
FOURTH RECENT ADVANCES IN QUANTITATIVE REMOTE SENSING

Auditori de Torrent, Spain
22 – 26 September 2014

Editor

José A. Sobrino
Global Change Unit
Universitat de València, Spain

FOURTH RECENT ADVANCES IN QUANTITATIVE REMOTE SENSING

Edited by

José A. Sobrino

Universitat de València, Spain

Publication coordinator: G. Sòria

Publication: J. C. Jiménez-Muñoz, Dražen Skoković and Y. Julien

Copyright © 2015 by the Authors

All rights reserved. This book or parts thereof may not be reproduced in any form or by any means, electronic or mechanical, including photocopying, recording or any information storage and retrieval system now known or to be invented, without written permission from the authors.

ISBN: 978-84-370-9808-1

Depósito legal: V-1854-2015

Printed in Spain by Guada Impresores

Preface

The Fourth International Symposium on Recent Advances in Quantitative Remote Sensing, was held in Torrent, Spain from 22 to 26 September, 2014. It was sponsored and organized by the Global Change Unit (GCU) from the Image Processing Laboratory (IPL), University of Valencia (UVEG), Spain. Other sponsors include:

- City Council of Torrent (Spain);
- L'Auditori Torrent (Spain);
- European Space Agency (ESA);
- Instituto Nacional de Técnica Aeroespacial (INTA), Ministerio de Defensa, Spain;
- Airbus Defence & Space;
- Elecnor Deimos Imaging;
- EOLAB;
- SM GEODIM

This Symposium addressed the scientific advances in quantitative remote sensing in connection with real applications. Its main goal was to assess the state of the art of both theory and applications in the analysis of remote sensing data, as well as to provide a forum for researcher in this subject area to exchange views and report their latest results. In this book 103 of the 237 contributions presented in both plenary and poster sessions are arranged according to the scientific topics selected. The papers are ranked in the same order as the final programme.

To conclude, I would particularly like to thank the participants who have contributed to constructive discussions and the members of the International Scientific Committee, who greatly contributed to select the papers presented at the Symposium providing an attractive scientific programme. The success is also due to the efforts made by the Organizing Committee. Many thanks to all of them.

José A. Sobrino
Symposium Chairperson
Global Change Unit,
Universitat de València

Valencia, 2015

International Scientific Committee:

Chairperson:

J. A. Sobrino University of Valencia, Spain

Members:

G. Asrar	PNNL, USA
F. Baret	INRA, Avignon, France
M. Berger	EC DG-RTD, Belgium
G. Chehbouni	IRD, France
Y. L. Desnos	ESA/ESRIN, Italy
J. Font	ICM-CSIC, Spain
A. Gillespie	University of Washington, USA
R. O. Green	NASA, JPL, Pasadena, USA
G. Gutman	NASA, Washington, D. C., USA
A. Huete	University of Technology, Sydney Australia
Y. Kerr	CESBIO, Toulouse, France
Z.-L. Li	University of Strasbourg, France
S. Liang	University of Maryland, USA
M. Menenti	Delft University of Technology, The Netherlands
J. Moreno	University of Valencia, Spain
F. Nerry	University of Strasbourg, France
A. Oliso	INRA, Avignon, France
F. Prata	NILU, Norway
J. Privette	NOAA, NCDC, USA
S. Quegan	University of Sheffield, UK
M. Rast	ESA/ESRIN, Italy
A. Royer	University of Sherbrooke, Canada
J. Shi	ICESS, UCSB, USA
Z. Su	University of Twente, The Netherlands
E. Vermote	NASA, GSFC, USA
Z. Wan	ICESS, UCSB, USA
J. P. Wigneron	INRA, Bordeaux, France
Y. Yu	NOAA, USA
P.J. Zarco-Tejada	IAS, CSIC, Spain

Organizing Committee:

Chairperson:

P. Gómez Symposium, Torrent, Spain

Members:

B. Franch	University of Maryland, USA
J. C. Jiménez-Muñoz	University of Valencia, Spain
Y. Julien	University of Valencia, Spain
R. Oltra-Carrió	ONERA, France
C. Mattar	University of Chile, Chile
G. Sòria	University of Valencia, Spain
D. Skoković	University of Valencia, Spain

CONTENTS

Preface

iii

Optical-thermal surface-atmosphere radiative transfer modelling with direct-diffuse atmospheric transfer functions and surface reflectance factors	1
W. Verhoef and C. van der Tol	
Prototyping of physically based methods to retrieve leaf area index and canopy water content from satellite data	7
M. Campos-Taberner, F.J. García-Haro, F. Camacho, G. Camps-Valls, M.A. Gilabert, B. Martínez, A. Moreno, S. Sánchez-Ruiz and J. Meliá	
Evaluation of LibRadtran Radiative Transfer Model for remote sensing applications	11
L. Carretero, E. de Miguel and M. Jiménez	
Land surface temperature retrieval from three thermal infrared data of MODIS for dust aerosol loading in the atmosphere	16
X. Fan, B.-H. Tang, H. Wu, G. Yan and Z.-L. Li	
Determining Optimal Conditions for Direct Detection of Sub-Pixel Archaeological Materials Using Airborne and Satellite Spectral Data	22
D.E. Sabol Jr and P. Buck	
Determination of the cloud radiative forcing and its relationship with the properties of clouds in the Iberian Peninsula	28
M.D. Freile-Aranda, J.L. Gómez-Amo, M.P. Utrillas and J.A. Martínez-Lozano	
Assessment of CALIOP level 2 daytime data during Saharan dust outbreaks in Southern Europe	32
C. Marcos, J.L. Gómez-Amo, R. Pedrós, M.P. Utrillas and J.A. Martínez-Lozano	
Atmospheric correction effect on land surface temperatures derived from Landsat-7 ETM+ data	37
M. Mira, A. Olioso, X. Pons, V. Rivalland, D. Courault, O. Marloie and P. Guillevic	
Generating land surface temperature products from MODIS data for agro-drought monitoring in China	42
Z. Qin, W. Li, C. Song, F. Wang, S. Zhao, B. Xu, J. Li and Y. Jin	
Estimating of air and deep temperature using thermal remotely sensed data	48
S.K. Alavipanah, A.A. Rezaei, M.E. Khusfi and M. Bakhtiari	
Future of Remote Sensing Applications: Thermal Remote Sensing of Human Emotions	54
S.K. Alavipanah and M.M. Rezvani	
Validation and analysis of land surface temperature from FengYun-2C (FY-2C) data	60
X. Song, Y. Wang, Z.-L. Li, B. Tang and P. Leng	
A split-window algorithm for estimating land surface temperature from Chinese FY-3 VIRR data	64
B.-H. Tang, Z.-L. Li, H. Wu, F. Nerry, K. Shao and G. Zhou	

Improvement on the universal triangle method to estimate soil moisture D. Zhang, Z.-L. Li, R. Tang, B.-H. Tang, H. Wu and K. Shao	69
A Comparison of Two LST Retrieval Methods with Simulated MODIS TIR and MIR Nighttime Data E.-Y. Zhao, C. Gao, Y. Qian, H. Huo, X. Jiang, Y. Zhang and Y. Du	75
Precipitable water vapor content derived from space-based passive radiometers over land surfaces F.-C. Zhou, X. Song, Z.-L. Li and R. Wang	80
INTA AHS and CASI hyperspectral images E. de Miguel, E. Prado, M. Jiménez, Ó. Gutiérrez de la Cámara, C. Linés and A. Fernández-Renau	86
Improvements on the estimation of land surface emissivity with NDVI thresholds method from MODIS data B.-H. Tang, Z.-L. Li, H. Wu and R. Tang	90
Impact of the frequency of conducting a white reference calibration on the accuracy of acquiring spectral reflectance coefficients using a spectroradiometer in laboratory conditions P. Kaminski, A. Orych and A. Jenerowicz	94
Remote sensing monitoring of grassland vegetation growth in China in 2012 H.L. Ma, B. Xu, X.C. Yang, Y.X. Jin, Z. Yang, S. Liu, J.Y. Li, T. Gao and H.D. Yu	98
Hyperspectral TIR sensor for building heat-loss detection L. Pipia, F. Pérez, A. Tardà, J. Corbera, M. Morera and A. Ruiz Casas	103
Landsat surface albedo product based on MODIS data B. Franch, E. F. Vermote and M. Claverie	108
Global Atmospheric Profiles from Reanalysis Information (GAPRI): a new dataset for forward simulations in the thermal infrared region C. Mattar, C. Durán-Alarcón, J.C. Jiménez-Muñoz and J.A. Sobrino	112
Functional attributes of the landscape surrounding the Temelin nuclear power plant (Czech Republic) P. Hesslerová and J. Pokorný	116
Bio-optical modelling to monitor submerged coastal vegetation N. Oppelt, K. Dörnhöfer and F. Uhl	121
Quantify the impact of cloud cover on radiation fluxes ground measurements from hemispherical images L. Roupioz, J. Colin, L. Jia, F. Nerry and M. Menenti	127
How atmospheric turbulence affects measurements of surface temperature from space? J.-P. Lagouarde, M. Irvine and S. Dupont	133
Data processing and temperature-emissivity separation for tower based imaging Fourier transform spectrometer data C. Borel, D. Rosario and J. Romano	139
Directional Hyperspectral Observations to Detect Plant Stress With The PRI and SIF in a Cornfield E. M. Middleton, Y.-B. Cheng, P. E. Campbell, K. F. Huemmrich, Q. Zhang, D. R. Landis, L. A. Corp , W. P. Kustas, C. S. T. Daughtry and A. L. Russ	144
30 years of land surface albedo from geostationary satellites: status of the scope-cm lags project A. Lattanzio, J. Matthews, M. Takahashi, K. Knapp, J. Schulz, R. Roebeling and R. Stöckli	150
Determining spectral reflectance coefficients of water in laboratory conditions P. Walczykowski	155
Determining methodology for acquiring spectral reflectance coefficients using a chosen monochromatic camera with interference filters P. Walczykowski, A. Orych and A. Jenerowicz	161

The use of optoelectronic filters for registering hyperspectral images in laboratory conditions	166
P. Walczykowski, M. Wilinska and D. Wierzbicki	
Comparison of Two Inversion Methods for Grassland Leaf Area Index Using Hyperspectral Remote Sensing	172
Q. Wu, Y.X. Jin, Y.H. Bao, Q.S. Hai, R.R. Yan, B.R. Chen, B.H. Zhang, H.B. Zhang, Z.W. Li, X.Y. Li and X.P. Xin	
Spectral-information-based atmospheric correction method for hyperspectral thermal infrared image	178
X. Zhong, H. Wu, B.-H. Tang, R. Tang and Z.-L. Li	
Index system and suitability evaluation of grassland vegetation growth for remote sensing monitoring in Xilingol grassland of Inner Mongolia, China	184
X. Yang, H. Yu, X. Zhu, Y. Jin, H. Ma, J. Li, F. Zhao, S. Chen and B. Xu	
Early water stress detection in desert Tamarugo trees based on leaf pulvinar movements	190
R. O. Chávez and J. G.P.W. Clevers	
A synoptic turbidity index for the Guadalquivir River with Landsat TM and ETM+ images: the turbiperiod	195
R. Díaz-Delgado, D. Aragonés, I. Afán and J. Bustamante	
Biomass and Soil Moisture Simulation and Assimilation over Hungary with the use of Surfex model	199
H. Tóth, B. Szintai and L. Kullmann	
Improved field method for determining land surface emissivity	203
F.-M. Götsche, F. S. Olesen and G. C. Hulley	
Surface temperature anomalies monitoring over the Amazon forests	209
J. C. Jiménez-Muñoz, J. A. Sobrino, C. Mattar and Y. Malhi	
Remote sensing on grassland growth monitoring and its correlativity with the meteorological factors in Xilingol's grassland of northern China	214
Y.X. Jin, B. Xu, J.J. Qiu, X.C. Yang, Z.H. Qin, Q. WU, H.L. Ma, J.Y. Li and F. Zhao	
Retrieving and broadcasting near-real time biophysical parameters from MODIS and SEVIRI receiving stations at the Global Change Unit of the University of Valencia	221
Y. Julien, J. A. Sobrino, G. Sòria, J.-C. Jimenez-Muñoz and D. Skoković	
Experimental study of angular effects on radiative surface temperature measurement	226
S. Peng, B.-H. Tang, H. Wu, R. Tang and Z.-L. Li	
Effects of Soil Moisture Content on Reflectance Anisotropy - Laboratory Measurements and RPV Model Inversions	230
P.P.J. Roosen, H.M. Bartholomeus and J.G.P.W. Clevers	
Estimate of daily surface albedo over highly heterogeneous area on the Tibetan Plateau using geostationary data	237
L. Roupioz, F. Nerry, L. Jia and M. Menenti	
Use of low-resolution satellites for permanent pasture yield estimation at regional scale	243
L. Seguini, R. Lopez-Lozano, S. Garcia Contado, G. Duveiller and B. Baruth	
Reconstruction of global NDVI time series dataset using a hybrid model – a prototype	249
J. Zhou, L. Jia and M. Menenti	
Rational design of sample location by Geostatistics for crop sown area estimation	255
D. Wang, Z. Chen, Q. Zhou and J. Liu	
Towards Buildings' Automatic Change Detection (Build-ACD) using VHSR Satellites Images: Application to Tetuan (Morocco)	262
O. Benarchid, N. Raissouni and J.A. Sobrino	

Application of the Mean-shift Segmentation Parameters Estimator (MSPE) to VHSR satellite images: Tetuan-Morocco	267
O. Benarchid and N. Raissouni	
Effect of Qinghai-Tibet Railroad on Vegetation Abundance	271
G. Wang, A. R. Gillespie, S. Liang, A. Mushkin and Q. Wu	
Effectiveness of MISR multiangular observations in the Earth Observation Land Data Assimilation System (EO-LDAS)	277
M. Chernetskiy, N. Gobron, J. Gomez-Dans, P. Lewis and C. Schmullius	
Crop cycle monitoring by combining medium and high resolution optical imagery	283
F.J. García-Haro, C. Gevaert and M. Campos-Taberner	
A first evaluation of an operational method (SSEBop) to estimate Actual Evapotranspiration by using MODIS data over the semi-arid region of Chile	288
L. E. Olivera-Guerra, C. Mattar, A. Santamaría-Artigas, C. Durán-Alarcón and R. Fuster	
Total and component evapotranspiration retrieval performances of a single-pixel energy balance model over agricultural crops.	292
G. Boulet, B. Mougenot, Z. Lili-Chabaane, P. Fanise, A. Olioso, M. Bahir, V. Rivalland, L. Jarlan, B. Coudert and J.-P. Lagouarde	
Remote Sensing of Water Resources in the semi-arid Mediterranean areas: The Joint International Laboratory TREMA	297
L. Jarlan, S. Khabba, M. Le Page, S. Er-Raki, L. Hanich, Y. Fakir, S. Mangiarotti, J. Ezzahar, M.H. Kharrou, B. Berjamy, O. Merlin, A. Saaïdi, S. Gascoin, A. Boudhar, M. Leblanc, G. Boulet, A. Benkaddour, J. Abaoui, A. Tavernier, V. Simonneaux, F. Driouech, S. Belaqqiz, G. Bigeard, F. Raïbi, J. Chirouze, B. Coudert, L. Drapeau, M. El Adnani, A. El Fazziki, O. Hagolle, N. Laftouhi, A. El Mandour, A. Marchane, A. Diarra, G. Aouade, J. Toumi, Y. Hajhouji, P. Fanise, H. Ibouh, N. Filali, B. Mougenot, H. Marah, A. Mokssit, Y. Kerr and G. Chehbouni	
Validation of evapotranspiration maps from 100-m to the 1-km scale over a semi-arid irrigated agricultural area	304
M. Bahir, G. Boulet, J. Chirouze, A. Olioso, V. Rivalland, B. Gallego-Elvira, M. Mira, O. Merlin, L. Jarlan and J.P. Lagouarde	
Use of remote sensing data fusion for daily evapotranspiration monitoring at watershed scale over a <i>dehesa</i> ecosystem	310
E. Carpintero, K. Semmens, M.C. Anderson, A. Andreu, F. Gao, W.P. Kustas and M.P. González-Dugo	
Improving Evapotranspiration Estimation Based on MOD16 Algorithm by Accounting for the Influence of Soil Moisture Variation	316
S. Di, R. Tang, H. Wu, B.-H. Tang, J. Lu and Z.-L. Li	
Daily evaporative fraction retrieval from MODIS data using two temporal information-based models	322
J. Lu, R. Tang, Z.-L. Li and Y. Bi	
Mapping daily gross primary production over Africa using SEVIRI/MSG satellite products	327
B. Martínez, A. Moreno, S. Sánchez, F.J. García-Haro, F. Camacho, J. Meliá, J. Ardö, W. Kutsch and M.A. Gilabert	
Spectroradiometer characterization for continuous operation in an Eddy Covariance flux tower	333
J. Pacheco-Labrador and M. P. Martín	
Impact of water stress on GPP estimation from remote sensing data in Mediterranean ecosystems	338
S. Sánchez-Ruiz, Á. Moreno, B. Martínez, M. Piles, F. Maselli, A. Carrara and M. A. Gilabert	
On the temporal upscaling of instantaneous evapotranspiration from the constant reference evaporative fraction method using public weather forecast information	344
R. Tang and Z.-L. Li	

The system for a quick estimate of agricultural crop quantity and surface for the purposes of a potential radioactive contamination using remote sensing data	349
J. Procházka, J. Brom and H. Vinciková	
Grassland sandy desertification in the Ongniud and Naiman Banners, China	355
J. Li, B. Xu, X. Yang, Y. Jin, F. Zhao, S. Chen, J. Guo, Z. Qin, H. Ma and L. Zhao	
Vegetation mapping with NASA's Terra/ASTER stereo images	361
A. Mushkin, A.R. Gillespie, V. Kane and J. Kane	
Cropland area mapping in Chad using MODIS time series	366
A. Pérez-Hoyos and F. Kayitakire	
Remote Sensing Monitoring and Analysis of Temporal and Spatial Change Characteristics of Grassland Desertification in Tibet	370
B. Xu, J.Y. Li, Y.X. Jin, Z.L. Wang, Z.H. Qin, M.Q. Wu, J. Zhang, H.L. Ma and X.C. Yang	
Recent land surface temperature trends over the Antarctic Peninsula	376
C. Durán-Alarcón, C. Mattar, J.C. Jiménez-Muñoz and J.A. Sobrino	
Monitoring pasture quality and production in extensive systems for an integrated management of oak savannas	380
P.J. Gómez-Giráldez, A. García-Moreno, P. Fernández-Rebollo, A.B. Caño, M.D. Carbonero and M.P. González-Dugo	
Quantitative Estimation of Sun-induced Fluorescence from the Apparent Reflectance	386
Z. Ni, Z. Liu, Z.-L. Li, F. Nerry, H. Huo and X. Li	
Adjacency effect correction of EO-1 ALI data using atmospheric point spread function	390
S.-B. Duan, Z.-L. Li, B.-H. Tang, H. Wu, R. Tang and Y. Bi	
Estimation of global soil moisture seasonal and inter-annual variability using SMOS satellite observations	396
M. Piles, E. Martínez, J. Ballabrera, M. Vall-llossera, E. Olmedo, J. Martínez and J. Font	
A new soil roughness parameter for the modelling of radar backscattering over bare soil	401
M. Zribi, A. Gorraeb and N. Baghdadi	
Cross-cutting validation of satellite products over France through their integration into a land surface model	406
J.-C. Calvet, A. Barbu, D. Carrer, D. Fairbairn, E. Gelati and C. Meurey,	
A Network of Sites for Ground Biophysical Measurements in support of Copernicus Global Land Product Validation	410
F. Camacho, R. Lacaze, C. Latorre, F. Baret, F. De la Cruz, V. Demarez, C. Di Bella, H. Fang, J. García-Haro, M. P. Gonzalez, N. Kussul, E. López-Baeza, C. Mattar, E. Nestola, E. Pattey, I. Piccard, C. Rudiger, I. Savin, A. Sanchez - Azofeifa, M. Boschetti, D. Bossio, M. Weiss, A. Castrignano and M. Zribi	
Landsat-8 TIRS Radiometric Performance	415
J. A. Barsi, M. Montanaro, B. L. Markham, S. J. Hook, J. R. Schott, N. G. Raqueno and A. Gerace	
Validation of an Experimental Cloud Infrastructure for Earth Observation Services	420
J. Becedas, R. Pérez, G. González, F. Pedrera, C. González and M. J. Latorre	
Continuous validation and algorithm improvement in LSA SAF FVC and LAI operational products over Africa	426
F.J. García-Haro, F. Camacho, B. Martínez, M. Campos-Taberner and J. Meliá	
Seasonal monitoring of FAPAR over the Barrax cropland site in Spain, in support of the validation of PROBA-V products at 333 m.	431
C. Latorre, F. Camacho, F. de la Cruz, R. Lacaze, M. Weiss and F. Baret	

Surface soil moisture retrieval over natural surfaces	436
P. Leng, X. Song, Z.-L. Li, Y. Wang and D. Wang	
Land Surface Temperature Product Validation by Using an Autonomous TIR Data Acquisition System Setup in Meteorological Stations	442
R. Niclòs, J. A. Valiente, M. J. Barberà, C. Coll, J. A. Benavent	
Calibration of Landsat-8 TIRS Bands with Ground-Truth Data over Different Land Covers at the Valencia Test Site	447
R. Niclòs, J. M. Sánchez, J. A. Valiente, M. J. Barberà, C. Coll, V. Caselles and D. Caselles	
Validation of a Forage Production Index derived from MODIS fCover time series - Methodology and main results	452
A. Roumigué, A. Jacquin, G. Sigel, H. Poilvé and O. Hagolle	
BEAM 5 and Sentinel Toolbox functions for image analysis and validation purposes	457
A. B. Ruescas, N. Fomferra and C. Brockmann	
Consistency assessment of PROBA-V and SPOT-VEGETATION GEOV1 LAI, FAPAR and FCover products for the continuity of the Copernicus Global Land Service.	461
J. Sánchez, F. Camacho, R. Lacaze and B. Smets	
GEOV2: Near real time estimation of LAI, FAPAR and cover fraction variables from VEGETATION data within Copernicus Global Land service	467
A. Verger, F. Baret, M. Weiss, B. Smets, F. Camacho and R. Lacaze	
Estimation of atmospheric water vertical content from MSG2-SEVIRI	472
X. Zhang , J. Pang and B. Wang	
Comparison of Split-Window and Single-Channel Methods for Land Surface Temperature Retrieval from Landsat-8	477
Y.-Z. Zhang, H. Wu, Z.-L. Li, X.-G. Jiang, Y.-Z. Du, E.-Y. Zhao	
Study on the methods of quantitative retrieval of farmland soil salinity based on remote sensing characteristic index—A Case Research in Xinjiang Shihezi Farming Area	482
S. Chen, C. Gao, B. Xu, Y. Jin, J. Li, H. Ma, F. Zhao, J. Guo, X. Yang	
Roughness parameterization for soil moisture optimum retrieval over the Valencia Anchor Station	488
R. Fernández-Morán, J.-P. Wigneron, E. Lopez-Baeza, P.M. Salgado-Hernanz, Y. Kerr, A. Mialon, M. Parrens, M. Miernecki, A. Coll-Pajaron, A. Alyaari, S. Wang and M. Schwank	
Potential of X-band SAR data from TerraSAR-X and COSMO-SkyMed sensors to retrieve physical soil properties	493
A. Gorrab, M. Zribi, N. Baghdadi, Z. Lili Chabaane and B. Mougenot	
Predictability of short-term quantitative precipitation nowcasting from radar scans using optical flow method	499
Y. Liu, D.-G. Xi and Z.-L. Li	
A statistical calibration for a combined Optical-Passive microwave method using remote sensing and reanalysis data	505
C. Mattar, A. Santamaría-Artigas, J.P. Wigneron and P. de Rosnay.	
LAB-net the First Chilean soil moisture network for Remote Sensing Applications	510
C. Mattar, A. Santamaría- Artigas, C. Durán-Alarcón, L. Olivera-Guerra and R. Fuster	
Synergistic usage of ERS, ASAR and PALSAR data for PSI based mining induced subsidence monitoring	513
N. Salepci, C. Thiel, A. Kuehl and C. Schmullius	
Performance comparison of downscaling methods on improving microwave soil moisture data spatial resolution with optical/infrared data	519
W. Zhao, A. Li, H. Jin, J. Bian, Z. Zhang and X. Nan	

Operational soil moisture mapping using multitemporal ASAR/Wide Swath ENVISAT data M. Zribi, F. Kotti, A. Gorrab, N. Baghdadi, Z. Lili Chabaane and R. Amri	524
Cloud screening and pixel characterization: moving to Sentinel requirements C. Brockmann, M. Paperin, A. Ruescas, O. Danne, G. Kirches and K. Stelzer	529
Integration of earth observation technologies in field-crop advisory services provided by sigAGROasesor platform. F.L.M. Padilla, M.P. González-Dugo, F. De la Cruz, A. Armesto, N. Abdat, J. Sillero, H. Lopez-Corcoles, A. Castilla, F. Perea, G. Besga, J. Serra, M. Jabargo, A. Mestre, M.R. Botey and A. Lafarga	533
Spatial analysis of the homogeneity of the Land Surface Temperature in three Spanish test sites D. Skoković, J. A. Sobrino, J. C. Jiménez-Muñoz, G. Soria and Y. Julien	538
 AUTHOR INDEX	 543
 FIGURES IN COLOUR	 553

Optical-thermal surface-atmosphere radiative transfer modelling with direct-diffuse atmospheric transfer functions and surface reflectance factors

Wouter Verhoef & Christiaan van der Tol

University of Twente, Faculty of Geo-Information Science and Earth Observation (ITC),
Water Resources Dept., Enschede, The Netherlands
w.verhoef@utwente.nl; c.vandertol@utwente.nl

ABSTRACT - Radiative transfer in the surface-atmosphere system can be described effectively with the so-called four-stream approach, which considers direct solar radiation, upward and downward diffuse fluxes, and the radiance in the observer's direction. Analyzing all possible radiative interactions between the Earth's surface and the atmosphere, for the surface we can identify four essential reflectance factors, two fluorescence terms, and in addition two thermal emissivities can be distinguished. For the atmosphere a total of 18 spectral transfer functions can be defined. These functions are uniformly applicable to the entire optical-thermal range, and they can be derived from four model runs with a radiative transfer code like MODTRAN. A Model Interrogation Technique (MIT) can be applied to extract the spectra of all 18 transfer functions from the outputs of the four model runs. The so-called T-18 system of atmospheric transfer functions can deal with problems related to the finite width of spectral bands, which leads to a violation of Beer's Law in strong atmospheric absorption bands. The system can be applied for the forward modelling of surface-atmosphere interactions involving surface BRDF effects, adjacency effects, directional fluorescence and directional thermal emissivity. It has been applied already for the generation of simulated Sentinel-3 satellite images. In addition, it can be used to study the impact of certain approximations often applied in the atmospheric correction of remotely sensed images, like the Lambertian assumption, and the assumption of a uniform Earth's surface. A particular application is illustrated with the generation of a database of simulated observations of vegetation reflectance and fluorescence by coupling the model SCOPE (Soil-Canopy-Observations, Photosynthesis and Energy balance) with MODTRAN5. For the calculation of the direct and diffuse incident radiation spectra at ground level, the propagation of emitted vegetation canopy fluorescence and for the calculation of top-of-atmosphere radiance spectra, use was made of the T-18 system of atmospheric transfer functions.

1 INTRODUCTION

Sensors on board remote sensing satellites operating in the solar reflective and thermal domains of the electromagnetic spectrum measure the top-of-atmosphere (TOA) radiance signals in a number of spectral bands. These radiance signals are influenced by the atmosphere and by the (bi-)directional properties of surface reflectance and emissivity. As the incident radiation on the surface is partly coming directly from the sun and partly consists of diffuse sky radiation caused by scattering in the atmosphere, it is beneficial to approximate the radiation field by dividing it in two major components, namely direct (collimated) radiation and isotropic diffuse radiation.

Reflected or emitted radiation from the earth's surface is mostly of a diffuse but anisotropic nature. However, most sensors measure only the radiance in a particular direction. In addition, hemispherical radiation from the surface is important for the radiation balance, so one can conclude that also for the upward radiation it is important to distinguish both the directional radiance and the diffuse flux. By considering direct solar flux, upward and downward

diffuse flux, as well as radiance in the direction of the observer we arrive at a so-called four-stream approach, which should not be confused with a four-stream implementation of the discrete ordinate method in radiative transfer modelling, where the four fluxes refer exclusively to discrete directions of radiation travel. The four-stream approach in the sense of the present paper has been applied for the first time by Gwynn H. Suits in his vegetation canopy reflectance model (Suits, 1972). This was an extension of earlier two and three-stream approaches applied by Kubelka & Munk (1931), Duntley (1942) and Allen, Gayle and Richardson (1970), which had not yet included a radiance in the observer's direction. All of these approaches were applied to describe radiative transfer inside a scattering and absorbing layer. In Verhoef (1985) it was shown that the system of four streams proposed by Suits (1972) could be applied to optically thick layers and to surfaces as well, and that multiple layers, or a layer and a surface, could be coupled by means of an adding algorithm (Van de Hulst, 1980). Examples are the coupling between a vegetation canopy layer with a background surface and the combination earth's surface – atmosphere. Although

the authors did not refer to the four-stream system as such, in Vermote et al. (1997) the 5S atmospheric model, and its interaction with the surface, were described in similar terms to explain atmospheric correction of remote sensing imagery. In Verhoef & Bach (2012) the four-stream approach was first applied for the simulation of satellite images from the Sentinel-3 mission, thereby including atmospheric transfer functions and thermal emission.

2 TERMINOLOGY

In this paper we first briefly describe the terminology of four-stream radiative transfer as first introduced in Verhoef (1985). In this terminology, reflectance factors get the symbol r if they originate from a “hard” opaque surface, and ρ if they originate from volume scattering in a layer. Transmittance factors always get the symbol τ . Two subscripts are used to indicate the type of incident and reflected or transmitted radiation, namely s for direct incident from the sun, d for diffuse upward or downward flux, and o for radiance in the observer’s direction. This radiance in the observer’s direction is represented by a term called flux-equivalent radiance, which is π times the radiance; i.e. it corresponds to the flux that would result if the radiance were isotropic. The reflectance of a non-Lambertian surface is now described with two linear equations, namely

$$\begin{aligned} E^+ &= r_{sd} E_s + r_{dd} E^- \\ E_o &= r_{so} E_s + r_{do} E^- \end{aligned} \quad (1)$$

where E_s is the direct solar flux, E_o the flux-equivalent radiance in the observer’s direction, and E^- and E^+ are the downward and upward diffuse fluxes.

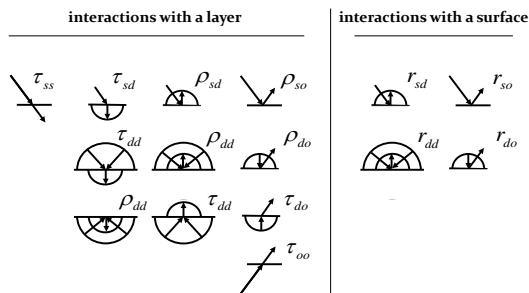


Fig. 1 RT interactions with a layer and a surface

The four reflectance factors used here are also known by the abbreviations DHRF, BHRF, BRF and HDRF, respectively (Nicodemus, 1970), which stand for directional-hemispherical, bi-hemispherical, bi-directional and hemispherical-directional reflectance factor. Fig. 1 illustrates not only the radiative transfer interactions with a surface, but also those for a scattering layer. Note that direct transmittances do not

involve scattering, so the direction and the type of the flux remain unchanged, and the subscripts therefore become ss for the direct transmittance of solar radiation and oo for the direct transmittance from the target to the observer.

3 SURFACE-ATMOSPHERE INTERACTIONS

Radiative transfer interactions between the earth’s surface and the atmosphere are illustrated conceptually in Fig. 2. The contributions to the radiance detected by a sensor on board a satellite above the atmosphere are identified as originating from (1) scattering of solar radiation with the atmosphere, (2) radiation reflected by the target and transmitted directly to the sensor, and (3) radiation reflected by the surroundings of the target and transmitted diffusely to the sensor. In both contributions (2) and (3) we can further distinguish between a contribution coming directly from the sun (a) and one that is coming from the sky (b) after scattering in the atmosphere.

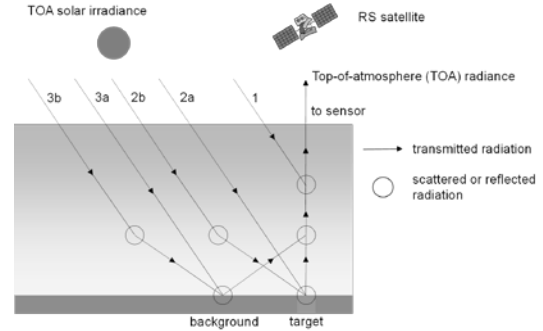


Fig. 2 Interactions with the atmosphere

The same interactions can be described more quantitatively with two systems of linear equations, one for the surface and one for the atmosphere. These are given by

$$\begin{aligned} E^+(b) &= \overline{r_{sd}} E_s(b) + \overline{r_{dd}} E^-(b) \\ E_o(b) &= r_{so} E_s(b) + r_{do} E^-(b) \end{aligned} \quad (2)$$

and

$$\begin{aligned} E_s(b) &= \tau_{ss} E_s(t) \\ E^-(b) &= \tau_{sd} E_s(t) + \rho_{dd} E^+(b) \\ E_o(t) &= \rho_{so} E_s(t) + \tau_{do} E^+(b) + \tau_{oo} E_o(b) \end{aligned} \quad (3)$$

where (b) stands for the bottom of the atmosphere and (t) for the top of the atmosphere. Eq. (2) differs from Eq. (1) in that the level (b) has been added and that for the hemispherical reflectance factors an over bar has been applied. This indicates that these reflectance factors refer to the surroundings of the target, obtained by a low-pass spatial filtering corresponding to the

point spread function related to the adjacency effect. The two systems of equations can be coupled by means of the first line in Eq. (2) and the second line in Eq. (3), from which the diffuse fluxes at the BOA level can be solved. These are next substituted in the second line of Eq. (2) and the third line of Eq. (3) to finally obtain the flux-equivalent radiance at TOA level. The result is given by the next equation, in which the 3 contributions of Fig. 2 are found in the terms in the square brackets in the same order.

$$E_o(t) = \left[\begin{aligned} &\rho_{so} + \left(\tau_{ss} r_{so} + \frac{\tau_{sd} + \tau_{ss} \overline{r_{sd} \rho_{dd}}}{1 - r_{dd} \rho_{dd}} r_{do} \right) \tau_{oo} \\ &+ \frac{\tau_{sd} r_{dd} + \tau_{ss} \overline{r_{sd}}}{1 - \rho_{dd} r_{dd}} \tau_{do} \end{aligned} \right] E_s(t)$$

Fig. 2 can also be replaced by a more quantitative alternative diagram, (Fig. 3) which includes all the quantities of Eqs. (2) and (3). This so-called flux interaction diagram describes all relevant upward and downward fluxes and these are connected by arrows which are accompanied by the associated reflectance or transmittance factor. Incident fluxes are placed in a box and reflected or transmitted fluxes in a circle. Since at the surface the transmitted fluxes coming from the atmosphere are at the same time incident to the surface, these are connected by solid bars to emphasize that these are identical.

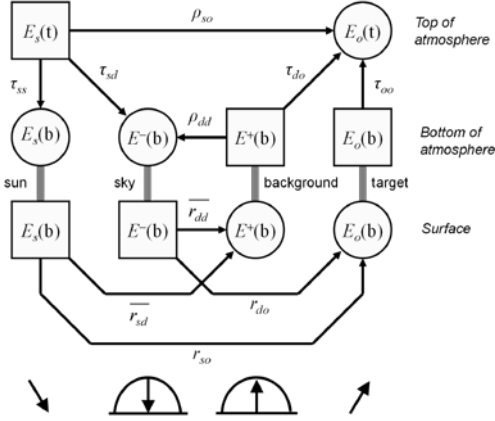


Fig. 3 Flux interaction diagram for the system surface – atmosphere.

4 INCLUDING THERMAL EMISSION AND FLUORESCENCE

In order to include the effects of emission from the surface and the atmosphere, Eqs. (2) and (3) must be extended with the following terms:

L_t = surface thermal blackbody radiance

L_a = atmospheric thermal radiance

F_s = target fluorescent radiance

F_d = fluorescent radiance of surroundings

Here L_a may refer to upward thermal path radiance at TOA as well as to downward sky radiance at BOA. The extended systems of equations are given by

$$E_o(b) = r_{so} E_s(b) + r_{do} E^-(b) + \pi(F_s + \varepsilon_o L_t) \quad (4)$$

$$E^+(b) = \overline{r_{sd}} E_s(b) + \overline{r_{dd}} E^-(b) + \pi(\overline{F_d} + \varepsilon_d L_t)$$

$$E_s(b) = \tau_{ss} E_s(t)$$

$$E^-(b) = \tau_{sd} E_s(t) + \rho_{dd} E^+(b) + \pi L_a(b) \quad (5)$$

$$E_o(t) = \rho_{so} E_s(t) + \tau_{do} E^+(b) + \tau_{oo} E_o(b) + \pi L_a(t)$$

Since the emission terms are assumed to be known, the extended equations are not more difficult to solve than Eqs. (2) and (3). The result is given by

$$L^{TOA} = E_s(t) \left[\begin{aligned} &\rho_{so} + \left(\tau_{ss} r_{so} + \frac{\tau_{sd} + \tau_{ss} \overline{r_{sd} \rho_{dd}}}{1 - r_{dd} \rho_{dd}} r_{do} \right) \tau_{oo} + \frac{\tau_{sd} \overline{r_{dd}} + \tau_{ss} \overline{r_{sd}}}{1 - \rho_{dd} r_{dd}} \tau_{do} \\ &+ L_a(t) + \left(\varepsilon_o L_t + \frac{L_a(b) + \varepsilon_d \overline{L_t} \rho_{dd}}{1 - r_{dd} \rho_{dd}} r_{do} \right) \tau_{oo} + \frac{L_a(b) \overline{r_{dd}} + \varepsilon_d \overline{L_t}}{1 - \rho_{dd} r_{dd}} \tau_{do} \\ &+ \left(F_s + \frac{\overline{F_d} \rho_{dd}}{1 - r_{dd} \rho_{dd}} r_{do} \right) \tau_{oo} + \frac{\overline{F_d}}{1 - \rho_{dd} r_{dd}} \tau_{do} \end{aligned} \right] \quad (6)$$

where the first line contains the optical part without fluorescence, the second line the thermal part, and the third line the part related to surface fluorescence. In Eq. (4) we observe that emission from the surface due to fluorescence in principle is indistinguishable from thermal emission by the surface. However, chlorophyll fluorescence by green leaves takes place in the wavelength region of 640 – 850 nm while thermal emission at temperatures around 300K mainly takes place at wavelengths greater than 2000 nm, so there will be no overlapping of both domains, unless the target is very hot, for instance due to a forest fire.

5 THE T-18 SYSTEM OF ATMOSPHERIC TRANSFER FUNCTIONS

Atmospheric transmittances (all τ), the spherical albedo ρ_{dd} , and the radiances L_a , are modulated by gaseous absorption lines. Over a finite spectral interval this introduces correlation between pairs of the above quantities. Due to this correlation, the spectral average of a product of two quantities will be larger than the product of their spectral averages, for instance:

$$\left(\frac{\langle \tau_{ss} \tau_{oo} \rangle}{\langle \tau_{ss} \rangle \langle \tau_{oo} \rangle} \right) > 1$$

or, in other words, the two-way transmittance from sun to target can be greater than the product of the one-way transmittances sun – target and target – sensor. Here, the angle brackets were used to indicate spectral averaging over a finite spectral interval, as well as to indicate “greater than”. Already a single absorption line can cause this effect, as the centre of the line might already be saturated while the wings are not, causing a violation of Beer’s Law, which is sometimes also called the “curve-of-growth” effect. In Eq. (6) we can observe many products of atmospheric

quantities, and these will all be subject to this effect. On the other hand, we may assume that surface spectra of reflectance, fluorescence and thermal emission are uncorrelated with atmospheric absorption bands, and the same holds for the spectral irradiance curve of the sun, which has Fraunhofer lines due to absorption by elements in the solar atmosphere, but these are mostly unrelated to gases in the terrestrial atmosphere. Therefore, both spectra of surface quantities and the solar irradiance curve are assumed to be uncorrelated with gaseous absorption lines in the atmosphere. In that case, one finds that a total of 18 atmospheric transfer functions are necessary to calculate radiance spectra both at TOA and BOA. These transfer functions are given in Table 1. The first 7 functions consist of T_1 , the solar radiance spectrum of a white reference panel placed parallel to the earth's surface at TOA, followed by the six primary optical atmospheric functions. The next seven are secondary optical functions, consisting of products of the primary ones, and the last four functions are thermal quantities, of which the last two are the thermal sky radiance multiplied by respectively the direct and the diffuse transmittance in the observer's direction. With the T-18 system one can model radiance spectra at BOA and TOA under the influence of BRDF and adjacency effects, thereby including observations of solar induced fluorescence and thermal emission effects. This system is universally applicable throughout the solar reflective and thermal spectral domains.

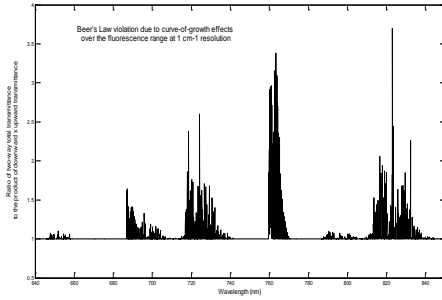


Fig. 4 Violation of Beer's Law in the fluorescence spectral region due to gaseous absorption lines (curve-of-growth effect) for the direct two-way transmittance

Table 1 Definition of the atmospheric transfer functions forming the T-18 system

Function	Name	Function	Name	Function	Name
$\langle E_s^+ \rangle \cos \theta_s / \pi$	T_1	$\langle \tau_{ss} \tau_{oo} \rangle$	T_8	$\langle L_{ss}(t) \rangle$	T_{15}
$\langle \rho_{ss} \rangle$	T_2	$\langle \tau_{ss} \tau_{oo} \rangle$	T_9	$\langle L_{ss}(b) \rangle$	T_{16}
$\langle \rho_{dd} \rangle$	T_3	$\langle \tau_{ss} \tau_{ds} \rangle$	T_{10}	$\langle L_{ss}(b) \tau_{oo} \rangle$	T_{17}
$\langle \tau_{ss} \rangle$	T_4	$\langle \tau_{ss} \tau_{ds} \rangle$	T_{11}	$\langle L_{ss}(b) \tau_{ds} \rangle$	T_{18}
$\langle \tau_{sd} \rangle$	T_5	$\langle \tau_{ss} \rho_{dd} \rangle$	T_{12}		
$\langle \tau_{oo} \rangle$	T_6	$\langle \rho_{dd} \tau_{oo} \rangle$	T_{13}		
$\langle \tau_{ds} \rangle$	T_7	$\langle \tau_{ss} \rho_{dd} \tau_{oo} \rangle$	T_{14}		

Although in general it is advisable to postpone the convolution with sensor spectral response functions until the last stage, the convolution with all functions of the T-18 functions is possible to obtain the corresponding functions for spectral bands of given sensors. For one standard case, the functions $T_1 - T_{18}$ are given in Figures 5 – 7. Figure 5 shows the function T_1 , the normalized solar spectral irradiance curve, for the spectral range 400 – 2500 nm, for a solar zenith angle of 45 degrees, and a sun-earth distance of 1 AU. Figure 6 shows the optical functions $T_2 - T_{14}$ for the spectral range 400 – 20000 nm (logarithmic scale) on a linear vertical scale. The thermal functions $T_{15} - T_{18}$ are shown in Figure 7 on double logarithmic scales to capture the large ranges in wavelength (1 – 50 microns) and radiance ($10^{-10} - 10^2 \text{ mW m}^{-2} \text{ sr}^{-1} \text{ nm}^{-1}$). The data shown in Figures 5 – 7 were obtained using the Model Interrogation Technique (MIT) applied to outputs from the radiative transfer code MODTRAN 5 version 2.1 (Berk et al., 2011). The MIT is briefly discussed in the next section.

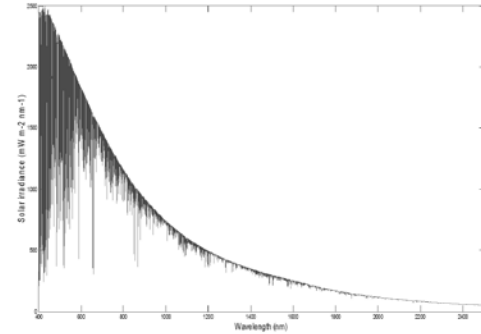


Fig. 5 Function T_1 , the solar spectral irradiance for the range 400 – 2500 nm

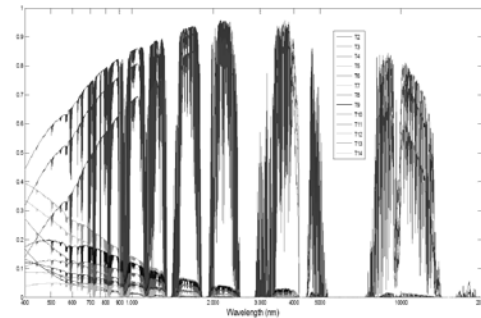


Fig. 6 Functions $T_2 - T_{14}$ for the range 400 – 20000 nm, on a logarithmic scale for the wavelength and a linear scale for transmittance or reflectance

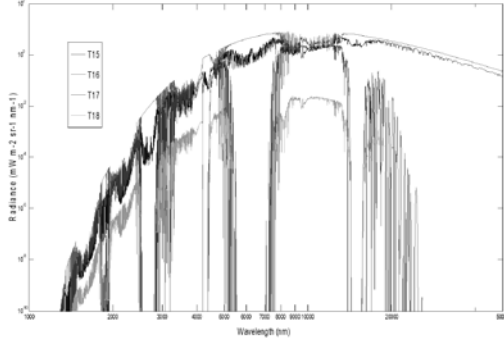


Fig. 7 Functions $T_{15} - T_{18}$ for the range 1 – 50 microns, on a logarithmic scale for wavelength and a logarithmic scale for spectral radiance

6 MODEL INTERROGATION TECHNIQUE (MIT)

The model interrogation technique can be applied to MODTRAN outputs or to those coming from other atmospheric transfer codes. In the MODTRAN .tp7 output file quite extensive information is provided about various spectral quantities, such as the target-sensor direct transmittance in column 2, and several contributions to the total sensed radiance, namely those related to path thermal radiance in column 3, surface emission in column 4, solar scattered radiance in column 5, ground-reflected radiance in column 7, direct solar reflected radiance in column 8, and finally the solar irradiance at TOA in column 14. If these contributions are calculated for two sensor altitudes (TOA and BOA) and two surface albedos for each altitude, one can derive all 18 transfer functions, although some assumptions must be made about the functions that contain products of primary transfer functions. In the current implementation of the MIT algorithm, at BOA the surface albedos used are 0.5 and 1.0, and at TOA 0.0 and 1.0 are used. With the T-18 system the radiances at BOA and TOA can be computed using the equations

$$L^{\text{BOA}} = T_1 \left[T_4 r_{so} + \frac{T_5 + T_{12} r_{sd}}{1 - r_{dd} T_3} r_{do} \right] + F_s + \varepsilon_o L_s + \left[\frac{T_{16} + [F_d + \varepsilon_d L_s] T_3}{1 - r_{dd} T_3} r_{do} \right] \quad (7)$$

$$L^{\text{TOA}} = T_1 \left[T_2 + T_8 r_{so} + \frac{T_9 + T_{14} r_{sd}}{1 - r_{dd} T_3} r_{do} + \frac{T_{10} r_{sd} + T_{11} r_{dd}}{1 - r_{dd} T_3} \right] + T_{15} + [F_s + \varepsilon_o L_s] T_6 + \left[\frac{T_{17} r_{do} + T_{18} r_{dd} + [F_d + \varepsilon_d L_s] (T_7 + T_{13} r_{do})}{1 - r_{dd} T_3} \right] \quad (8).$$

Note, that in this general case all of the 18 functions are employed if the radiances at BOA and TOA are both needed. However, huge simplifications are possible if one requires only the TOA radiance, and if one assumes a Lambertian surface reflection, no thermal emission, no fluorescence, and a uniform earth surface (no adjacency effects). In that case one can write

$$L^{\text{TOA}} = L_0 + \frac{gR}{1 - SR} \quad (9)$$

where

$L_0 = T_1 T_2$, which is the atmospheric path radiance (for a black surface);

$g = T_1 (T_8 + T_9 + T_{10} + T_{11})$, which is the total gain factor to convert reflectance differences into TOA radiance differences;

$S = T_3$, which is the spherical albedo at the bottom of the atmosphere.

Of course it would be helpful if atmospheric radiative transfer codes would provide these transfer functions directly as outputs, since in that case it would no longer be necessary to perform four runs, and the results would probably be more accurate.

7 APPLICATIONS

The T-18 system of atmospheric transfer function covers a very wide spectral range, and accommodates simulations of spectral radiance at BOA and TOA, thereby including BRDF and adjacency effects, as well as thermal emission and fluorescence. Therefore, this system is suitable for a wide range of applications, from image simulation and sensor design to its dedicated use in models such as SCOPE (Van der Tol et al, 2009).

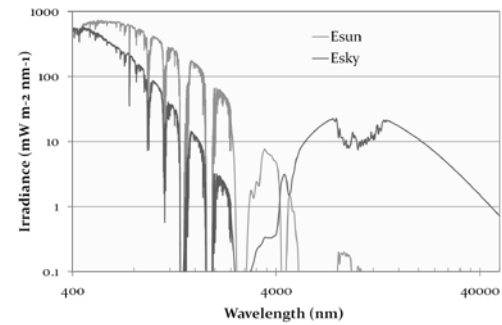


Fig. 8 Solar and sky irradiance from 400 nm until 50 μm as used in the SCOPE model on double logarithmic scales

Figure 8 illustrates this by showing the continuous spectra of the solar and sky irradiance used as input in SCOPE, which are needed to calculate the net radiation energy, amongst others. Other applications

are for instance the study of fluorescence retrieval from TOA radiance spectra, and the impact of BRDF and adjacency effects on atmospheric correction of satellite images.

REFERENCES

- Allen, W.A., Gayle, T.V., Richardson, A.J., 1970, Plant canopy irradiance specified by the Duntley equations, *J. Opt. Soc. Am.* 60(3): 372-376.
- Berk, A., Anderson, G.P., Acharya, P.K., Shettle, E.P., 2011, MODTRAN 5.2.1 User's Manual, Spectral Sciences Inc., Air Force Research Lab., USA.
- Duntley, S.Q., 1942, The optical properties of diffusing materials, *J. Opt. Soc. Am.* 32(2): 61-70.
- Kubelka, P., & Munk, F., 1931, Ein Beitrag zur Optik der Farbanstriche, *Ann. Techn. Phys.* 11: 593-610.
- Nicodemus, F.E., 1970, Reflectance nomenclature and directional reflectance and emissivity, *Appl. Optics* 9(6): 1474-1475.
- Suits, G.H., 1972, The calculation of the directional reflectance of a vegetative canopy, *Rem. Sens. Env.* 13: 133-129.
- Van de Hulst, H.C., 1980, Multiple light scattering, Academic, London.
- Van der Tol, C., Verhoef, W., Timmermans, J., Verhoef, A. and Su, Z., 2009, An integrated model of soil - canopy spectral radiances, photosynthesis, fluorescence, temperature and energy balance. *Biogeosciences* 6 (2009)12 pp. 3109-3129.
- Verhoef, W., 1985, Earth observation modeling based on layer scattering matrices, *Rem. Sens. Env.* 17: 165-178.
- Verhoef, W. and Bach, H., 2012, Simulation of Sentinel-3 images by four stream surface atmosphere radiative transfer modeling in the optical and thermal domains. *Rem. Sens. Env.* 120, pp. 197-207.
- Vermote, E. F., Tanré, D., Deuze, J. L., Herman, M. and Morcrette, J. J., 1997, Second Simulation of the Satellite Signal in the Solar Spectrum: an overview, *IEEE Transactions on Geoscience and Remote Sensing*, 35,3.

Prototyping of physically based methods to retrieve leaf area index and canopy water content from satellite data

M. Campos-Taberner¹, F.J. García-Haro¹, F. Camacho², G. Camps-Valls³, M.A. Gilabert¹, B. Martínez¹, A. Moreno¹, S. Sánchez-Ruiz¹, J. Meliá¹

¹*Facultat de Física, Universitat de València, Dr. Moliner, 50. 46100-Burjassot, Spain.*

²*EOLAB, Parc Científic Universitat de València. Catedrático José Beltrán, 2. 46980, Paterna, Spain.*

³*IPL, Parc Científic Universitat de València, Catedrático José Beltrán, 2. 46980 Paterna, Spain.*

Manuel.Campos@uv.es

ABSTRACT - Regional scale vegetation monitoring and yield forecasting require the estimation of biophysical parameters, such as Leaf Area Index (LAI), biomass and canopy water content (CWC). The CWC is also targeted for fire risk and drought monitoring. This work presents a methodology for jointly retrieval of Canopy Water Content (CWC) and Leaf Area Index (LAI) from coarse resolution satellite data. The method combines the use of databases generated by radiative transfer models (PROSAIL) and powerful nonlinear regression approaches. The advantage of physical models is that they can be coupled each other, thereby providing a physically-based linkage between optical data and biochemical or structural state variables. Suitable parameter combinations of leaf and optical properties were used as inputs into the model to avoid unrealistic simulated spectra.

1 INTRODUCTION

Leaf area index (LAI), defined as the one-side area of leaves per unit of ground area (m²/m²) (Jonckheere et al., 2004) and Canopy Water Content (CWC), defined as the total mass of the liquid water per unit ground area (kg/m²) (Cheng et al., 2008; Trombetti et al., 2008), are a key biophysical variables in agricultural and forestry applications.

Several studies have proved the relationship between canopy reflectance and biophysical parameters (Pasoli et al., 2010; Lázaro-Gredilla et al., 2014) such as LAI and CWC. In particular, the estimation of CWC from optical sensors is related to the water absorption features.

SEVIRI/MSG is a geostationary meteorological satellite system that provides much higher frequency of observation of the land surface than sun-synchronous systems. MSG SEVIRI bands are potentially suited to produce timely information on canopy water status and stress (Fensholt et al., 2010) due the potential of using water absorption band at 1640 nm for the retrieval of CWC.

We propose a retrieval method based on the inversion of a radiative transfer model PROSAIL (Jacquemoud et al., 2009), for the estimation of LAI and CWC maps from SEVIRI/MSG data.

2 METHODOLOGY AND DATA

2.1 Simulation

For the simulation of the SEVIRI spectra we considered a leaf optical properties model PROSPECT

(Jacquemoud and Baret, 1990) coupled with SAIL (Verhoef, 1984), a 1D turbid medium model for the canopy. This coupled modelling scheme called PROSAIL has been used in several remote sensing studies and has already been applied with success in a variety of crops (Duan et al., 2014).

The PROSPECT model simulates the leaf hemispherical transmittance and reflectance as a function of four structural and biochemical leaf parameters: leaf structure parameter N (unitless), equivalent water thickness C_w (g cm⁻²), dry matter content C_m (g cm⁻²) and leaf chlorophyll $a + b$ concentration C_{ab} (μg·cm⁻²). These leaf optical properties simulated by the PROSPECT model are the inputs of the SAIL model. The SAIL model simulates the top-of-the-canopy reflectances as a function of eight input parameters: LAI (m²/m²), average leaf angle ALA (°), fraction of diffuse incoming solar radiation $skyl$ (unitless), soil reflectance, hot-spot size parameter hot (m·m⁻¹), sun zenith angle t_s (°), sensor viewing angle t_o (°), and relative azimuth angle ϕ (°) between the sensor and sun.

The PROSAIL model was run in forward mode to simulate canopy reflectance on three SEVIRI spectral channels (0.6, 0.8 and 1.6 μm). 1000 parameter combinations were randomly generated with uniform distributions and were used to simulate the spectra. The specific ranges for the variables are shown in Table 1.

For leaf structure parameter N and average leaf angle ALA fixed values were chosen according to the values reported in the literature. ($N=1.5$, $ALA=45^\circ$)

2.2 Inversion

Many methods including neural networks have been used for reflectance model inversion (Baret *et al.*, 2007) and for estimation of CWC (Cernicharo *et al.*, 2013).

Table 1. Ranges of the input variables for the PROSAIL model.

Parameter	Min	Max
$C_w (\text{g} \cdot \text{cm}^{-2})$	0	0.08
$C_m (\text{relative})$	0.05	0.50
$C_{ab} (\mu\text{g} \cdot \text{cm}^{-2})$	20	30
$\text{LAI} (\text{m}^2/\text{m}^2)$	0	8
$hot (\text{m} \cdot \text{m}^{-1})$	0.001	1
$Soil$ (unitless)	0.7	2.3

Recently a new machine learning approach, based on the Gaussian Process (GP) theory, has been introduced in the literature (Rasmussen and Williams, 2006). According to this approach, the learning of a machine is formulated in terms of a Bayesian estimation problem, assuming that the parameters associated to the machine are a priori jointly drawn from a Gaussian distribution.

The inversion of the PROSAIL model was performed to estimate CWC and LAI. We proposed the use of Gaussian Process Regression (GPR) for canopy parameter retrieval. GPR is a nonparametric method that learns the relationship between the reflectance and canopy parameter by fitting a flexible nonlinear model directly from the data (Verrelst *et al.*, 2012). In general, GPR provides better estimation accuracies than other machine learning algorithms (Lázaro-Gredilla *et al.*, 2012) and may be of particular interest because they do not only provide pixel-wise predictions but also confidence intervals for the prediction.

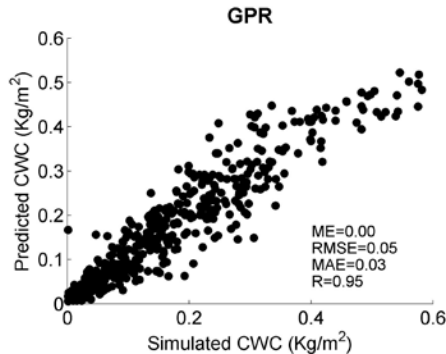


Figure 1. Simulated and predicted CWC

Figure 1 shows the scatterplot between the simulated data and predictions for the CWC. Model's performance was evaluated with the root-mean-squared error (RMSE), and Pearson's correlation coefficient (R) to account for the goodness-of-fit.

3 RESULTS

Extracting the relationship between the reflectance and canopy parameter, Gaussian Process Regression (GPR) provides an estimated map for LAI and CWC. Moreover it provides the variance associated to each pixel that can be interpreted as a confidence of the estimated parameter. Tree bands (0.6, 0.8 and 1.6 μm) of the SEVIRI/MSG reflectance given by the Ko BRDF parameter were used for the GPR.

The retrieved maps for LAI and CWC corresponding to 2013 June the 11th, are shown in the following figures.

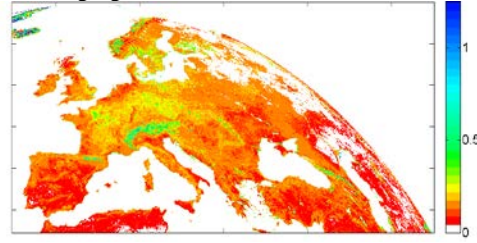


Figure 3. Canopy water content (Kg^2/m^2) estimated map retrieved with GPR (2013 June the 11th).

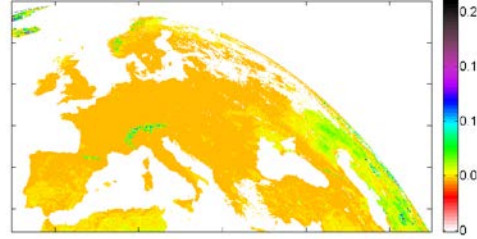


Figure 4. Confidence map (σ) retrieved with GPR for canopy water content (Kg^2/m^2) (2013 June the 11th).

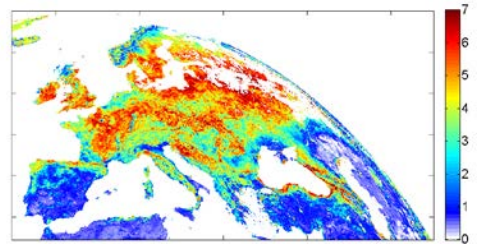


Figure 5. Leaf area index (m^2/m^2) estimated map retrieved with GPR (2013 June the 11th).

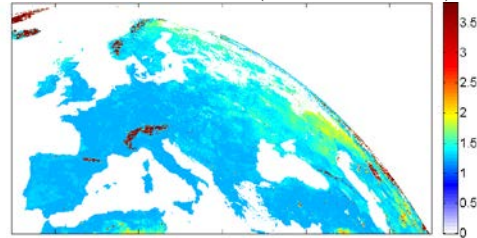


Figure 6. Confidence map (σ) retrieved with GPR for leaf area index (m^2/m^2) (2013 June the 11th).

4 QUALITY ASSESMENT

The retrieved LAI and CWC maps have been assessed through the comparison with ground measurements and operational products of biophysical parameters.

The SEN2Exp ground vegetation data set was used in order to perform a direct validation of the results obtained for CWC and LAI through the GPR. Indirect validation was performed comparing the estimations for LAI with Copernicus Global Land LAI GEOV1 product downloaded through the Copernicus Global Land Service. The LAI product is derived at 10-day temporal frequency. More details about the GEOV1 product are available on the following website (<http://land.copernicus.eu/global>)

4.1 Field campaign

As a part of SEN2Exp campaign supported by European Space Agency (ESA) for obtaining data to simulate the instruments on board Sentinel-2 satellite, a field campaign took place over Hart forest (France) between 11-12 of June, and 3-4 of September both conducted in 2013 (Sanchez et al. 2014).

In-situ vegetation characterization includes the sampling of the following variables: Leaf Area Index (LAI), Fraction of Absorbed Photosynthetically Active Radiation (FAPAR), Fraction of green Vegetation Cover (FCOVER), Fresh Weight (FW), Dry Weight (DW) and leaf area (A). LAI, FAPAR and FCOVER parameters have been obtained by using digital hemispheric photography (DHP), taking 12-15 pictures for Elementary sampling unit (ESU).

CWC was derived from the Leaf Area Index and the Leaf Water Content (LWC) as follows:

$$LWC = \frac{FW - DW}{A} \quad [Kg \cdot m^{-2}] \quad (1)$$

$$CWC = LAI \cdot LWC \quad [Kg \cdot m^{-2}] \quad (2)$$

Table 2. Comparison of LAI and CWC values with SEN2Exp and Copernicus product over Hart forest.

HARTH FOREST					
DATE	LAI (m ² /m ²)			CWC (kg/m ²)	
	GPR	GEOV1	SEN2Exp	GPR	SEN2Exp
06/11/2013	5.23	4.89	4.5	0.70	0.62
09/04/2013	2.55	2.79	3.8	0.41	0.55

To validate LAI estimates in a time series, we compared retrieved LAI values with Copernicus Global Land LAI GEOV1 product over 2013 (see Figure 7). Regarding CWC, there is no consistent product available to compare, nevertheless we can compare CWC estimates with ground measurements (see Figure 8). Note that error bars in Figure 7 and Figure 8 refer to RMSE of the Transfer Function used for the up-scaling process based on in situ measurements.

5 CONCLUSIONS

This study using MSG/SEVIRI data has explored the possible use of three of its spectral channels (0.6, 0.8 and 1.6 μm) for the estimation of CWC and LAI through the inversion of the PROSAIL radiative transfer model. Time series shows consistency of LAI GPR retrievals with Copernicus GEOV1 LAI product and the very limited ground measurements currently available. Results presented above indicate that the use of the MSG/SEVIRI data can be useful for the CWC and LAI retrieval. Producing CWC and LAI estimated maps using GPR provides also a confidence level for the predictions.

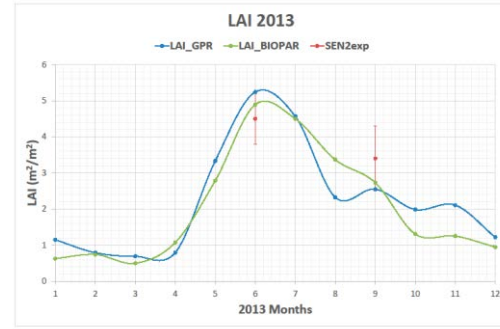


Figure 7. Comparison of the estimated LAI and Copernicus LAI GEOV1 over the 2013. Red points corresponding to ground measurements over Hart forest.

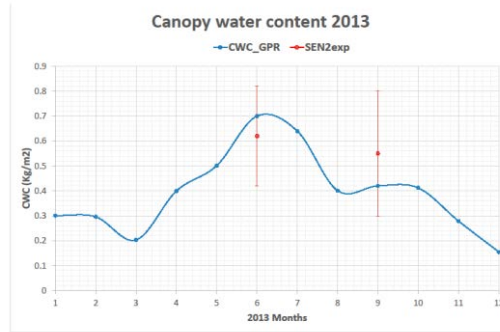


Figure 8. Comparison of the estimated CWC over the 2013 and SEN2Exp campaign. Red points corresponding to ground measurements over Hart forest.

Due to the high dependency of the parameter distribution used as input into PROSAIL, future work includes exploring various parameter distribution on RTM models for improving the database of simulated reflectance. Implementing a regression on multi-output parameter could be evaluated. Consider including other field campaigns will be useful to better validate the estimations.

ACKNOWLEDGMENT

Funding support of ERMES (EU FP7-Space-2013, Contract 606983), RESET CLIMATE (CGL2012–35831) and LSA SAF projects.

REFERENCES

- Baret, F., Hagolle, O., Geiger, B., Bicheron, P., Miras, B., Huc, M., et al., 2007, LAI, FAPAR and fCover CYCLOPES global products derived from VEGETATION. Part 1: Principles of the algorithm. *Remote Sensing of Environment*, **110**, 275–286.
- Cernicharo, J., Verger, A., Camacho, F., 2013, Empirical and Physical Estimation of Canopy Water Content from CHRIS/PROBA Data. *Remote Sensing*, **5**, 5265–5284.
- Cheng, Y. B., Ustin, S. L., Riaño, D., & Vanderbilt, V. C. 2008, Water content estimation from hyperspectral images and MODIS indexes in Southeastern Arizona. *Remote Sensing of Environment*, **112**, 363–374.
- Duan, S.-B., Li, Z.-L., Wu, H., Tang, B.-H., Ma, L., Zhao, E. et al., 2014, Inversion of the PROSAIL model to estimate leaf area index of maize, potato, and sunflower fields from unmanned aerial vehicle hyperspectral data, *International Journal of Applied Earth Observation and Geoinformation*, **26**, 12–20.
- Fensholt, R., Huber, S., Proud SR, Mbow, C., 2010, Detecting Canopy Water Status Using Shortwave Infrared Reflectance Data From Polar Orbiting and Geostationary Platforms. *Selected Topics in Applied Earth Observations and Remote Sensing*, *IEEE* (3), 3.
- Jacquemoud, S., Baret, F., 1990. PROSPECT: a model of leaf optical properties spectra. *Remote Sensing of Environment*, **34**, 75–91.
- Jacquemoud, S., Verhoef, W., Baret, F., Bacour, C., Zarco-Tejada, P.J., Asner, G.P., Francis, C., Ustin, S.L., 2009. PROSPECT + SAIL models: a review of use for vegetation characterization. *Remote Sensing of Environment*, **113**, S56–S66.
- Jonckheere, I., Fleck, S., Nackaerts, K., Muys, B., Coppin, P., Weiss, M. and Baret, F., 2004, Reviews of methods for in situ leaf area index determination. Part I. Theories, sensors, and hemispherical photography. *Agricultural and Forest Meteorology*, **121**, 19–35.
- Lázaro-Gredilla, M., Titsias, M.K., Verrelst, J., Camps-Valls, G., 2014, Retrieval of Biophysical Parameters With Heteroscedastic Gaussian Processes, *IEEE Geoscience Remote Sensing Letters*, **11**, 838–842.
- Pasoli, L., Melgani, F., Blanzieri, E., 2010, Gaussian Process Regression for Estimating Chlorophyll Concentration in Subsurface, *IEEE Geoscience Remote Sensing Letters*, **7**, 464–468.
- Rasmussen, C.E., and Williams, C.K.I., 2006, Gaussian Process for machine learning. Cambridge, Massachusetts: The MIT Press.
- Sánchez J., Sendra, V., Camacho, F., Baret, F., 2013, SEN2Exp: Analysis of ground level data & generating image products by up-scaling. CNN-VALSE2-TN-001-EOLAB. Issue 1.1, 29 pp
- Trombetti, M., Riaño, D., Rubio, M. A., Cheng, Y. B., & Ustin, S. L., 2008, Multi-temporal vegetation canopy water content retrieval and interpretation using artificial neural networks for the continental USA. *Remote Sensing of Environment*, **112**, 203–215.
- Verhoef, W., 1984. Light scattering by leaf layers with application to canopy reflectance modeling: the SAIL model. *Remote Sensing of Environment*, **16**, 125–141.
- Verrelst, J., Alonso, L., Camps-Valls, G., Delegido, J., Moreno, J., 2012, Retrieval of Vegetation Biophysical Parameters Using Gaussian Process Techniques, *IEEE T. Geoscience and Remote Sensing*, **5**, 1832–1843

Evaluation of LibRadtran Radiative Transfer Model for remote sensing applications

L. Carretero, E. de Miguel and M. Jiménez

Área de Teledetección, Instituto Nacional de Técnica Aeroespacial (INTA), Cta de Ajalvir, s/n, Torrejón de Ardoz, 28850, Madrid (Spain)
carreteroml@inta.es, demiguel@inta.es, jimenezmm@inta.es

ABSTRACT- *LibRadtran Radiative Transfer Model (RTM) is a free software package available from <http://www.libradtran.org>, commonly used so far in atmospheric applications. However, its flexibility in how and what input may be specified could make possible its implementation in remote sensing (RS) atmospheric correction and image simulations. In this study we present a comparison, focused in RS applications, between libRadtran and the MODerate resolution atmospheric TRANsmission code (MODTRAN), which is the standard RTM currently used in RS. For this purpose, we have compared at-surface VNIR (0.4 to 1.1 μm) and SWIR (2.0 to 2.2 μm) spectral direct irradiance and at-sensor VNIR-SWIR plus TIR (8 to 13 μm) spectral radiance obtained by the two RTMs, for several cases concerning different solar positions, observation geometries and atmospheric parameters, in order to notice their influence in the results. Finally, we have compared at-surface VNIR-SWIR (0.35 to 2.5 μm) spectral global irradiance measurements performed with the spectroradiometer ASD-FS3 and the simulations modelled with the two RTMs. Experimental data were obtained on 28 July 2014, during the collaboration of INTA RS group in the “Solar Irradiance Sensor Field Test 2014” (SISFT14) campaign, which took place in Merzouga (Morocco). LibRadtran calculations were generated using the line by line atmospheric transmittance and radiance model genln2 and the low-resolution (20 cm^{-1}) propagation band model LOWTRAN (Ricchiazzi et al., 1998) and MODTRAN calculations were performed employing different resolution band models (1 and 15 cm^{-1}).*

1 INTRODUCTION

The main objective of this study is to evaluate the use of libRadtran Radiative Transfer Model (RTM) in Remote Sensing (RS) applications as a complementary model to the MODerate resolution atmospheric TRANsmission code (MODTRAN), which is the most commonly RTM currently used in RS.

LibRadtran RTM is a software package freely available under the GNU General Public License, and developed by Bernhard Mayer, Claudia Emde, Josef Gasteiger, Robert Buras and Arve Kylling. It is a collection of C and FORTRAN functions and programs for the calculation of solar and thermal radiation in the Earth's atmosphere, which have been used so far in atmospheric applications (Mayer et al., 2005). MODTRAN is a commercial software that has been extensively validated and serves as a standard atmospheric band model for the RS community, developed by Spectral Sciences Inc. and the US Air Force Research Laboratory (Berk et al., 2008). To execute MODTRAN, the MODO front-end (ReSe, 2011) has been used.

In this study we present a comparison between libRadtran 1.7 and MODTRAN5, by evaluating the differences of the results obtained by the two models when calculating ground irradiances and at-sensor radiances for different cases.

Furthermore, we compare field measurements performed with the spectroradiometer ASD-FS3 on 28

July 2014, during the collaboration of INTA RS group in the “Solar Irradiance Sensor Field Test 2014” (SISFT14) campaign, with modelled data obtained by the two RTMs.

SISFT14 is a campaign included in ESA ExoMars project (exploration.esa.int/mars/48898-edm-science-payload/) that is aimed to test the Solar Irradiance Sensor (SIS). This sensor will become part of the meteorological station DREAMS (Dust characterisation, Risk assessment and Environment Analyser on the Martian Surface) that will be on-board the EDM 2016 (Entry and Descent Module) of the first ExoMars mission, to be launched on January 2016.

2 DATA AND METHODS

2.1 At-surface direct irradiance

For each case, two different spectral resolutions have been used, in order to assess the eventual differences when the spectral bandwidth is reduced.

The comparison of VNIR (0.4 to 1.1 μm) and SWIR (2.0 to 2.2 μm) direct ground irradiance has been performed for five scenarios (E1 to E5) concerning different solar positions, atmospheric parameters and ground altitude, as described in Table 1. The calculations have been performed using DISORT discrete ordinate algorithm (Stamnes et al., 1988) and the solar extraterrestrial irradiance from Kurucz (1992) for both libRadtran and MODTRAN.

	RTM	E1	E2	E3	E4	E5
Atmospheric profile	libRadtran	Afglus: US. Standard atmosphere, 1976				
	MODTRAN	1976 US. Standard				
Solar zenith (degrees)	libRadtran	30°				70°
	MODTRAN					
Atmospheric parameters	libRadtran	Rural aerosol model Visibility: 50 km wv: 1.5 cm		Rural aerosol Vis.: 20 km wv: 1.5 cm	Rural aerosol Vis.: 50 km wv: 2.8 cm	Rural aerosol Vis.: 50 km wv: 1.5 cm
	MODTRAN					
Ground altitude (km)	libRadtran	0 km	1 km	0 km		
	MODTRAN					
Slit function	libRadtran	Type: Gaussian; Resolution: 1 nm FWHM: VNIR (2 nm for low and high resolution) SWIR (2 nm for high resolution, 8 nm for low resolution)				
	MODTRAN					

Table1: Input parameters used by libRadtran and MODTRAN for the calculation of at-surface direct irradiance (sensor altitude=0 km) for day 150. Note: Each RTM may interpret these parameters in slightly different ways

2.2 At-sensor radiance

VNIR (0.4 to 1.1 μm) and SWIR (2.0 to 2.2 μm) at-sensor radiance has been computed for four cases (L1 to L4) concerning different solar positions and observation geometries, and TIR (8 to 13 μm) at-sensor thermal radiance for two scenarios (T1 and T2) with different sensor altitude (Table 2)

The calculations have been performed using DISORT discrete ordinate multiple scattering algorithm (Stamnes et al., 1988) and the solar extraterrestrial irradiance from Kurucz (1992), and a ground reflectivity of 0.2 for VNIR-SWIR and 0.02 for TIR has been considered for all wavelengths.

2.3 Solar Irradiance Sensor Field Test (SISFT14) campaign

At-surface VNIR-SWIR (0.35 to 2.5 μm) spectral global irradiance measurements were performed on 28 July 2014, during the collaboration of INTA RS group in SISFT14 campaign, which took place in Merzouga, Morocco (31° 12' 4" N, 4° 1' 37.9" W).

We have compared two datasets taken at 8:10 and 12:26 UTC, respectively, and the simulations modelled with the two RTMs, to evaluate the influence of the solar zenith angle in the results. Irradiance measurements were taken by the spectroradiometer ASD-FS3, and the atmospheric parameters (aerosol optical thickness at 1020 nm and water vapour column) by a Microtops sunphotometer. There was a great amount of dust in suspension during the measurements with an Aerosol Optical Depth (AOD) of 0.5 at 550 nm.

LibRadtran calculations were generated using the the low resolution (20 cm⁻¹) propagation band model LOWTRAN (Ricchiazzi et al., 1998), and MODTRAN calculations employing a 15 cm⁻¹ band model. Both RTMs simulations were performed using DISORT discrete ordinate algorithm (Stamnes et al., 1988) and the solar extraterrestrial irradiance from

Kurucz (1992), and a ground reflectivity of 0.3 has been considered for all wavelengths. Table 3 shows the parameters used by both RTMs.

3. RESULTS AND DISCUSSION

Results are represented as differences between libRadtran 1.7 and MODTRAN5 simulated radiances/irradiances, in order to show the discrepancies found. Figure 1 shows libRadtran – MODTRAN SWIR at-surface direct irradiances, Figure 2 VNIR at-sensor radiance differences and Figure 3 the same for TIR. In all the cases two different scenarios have been represented (E2 and E4 for SWIR irradiances, L2 and L4 for VNIR radiances and T1 and T2 for TIR radiances), as representative examples.

As we can see, differences between radiances/irradiances calculated by libRadtran and MODTRAN are larger in absorption zones than out of them (Figures 1, 2 and 3), even though the same water vapour content has been used in both RTMs. This fact could be explained assuming that both models use this input (water vapour content) differently, but we do not have any evidence of it yet, so we will do further investigations. The different behaviour found in and out absorption bands can be clearly seen in Figure 3, where there are great differences between cases T1 (sensor altitude= 100 km) and T2 (sensor altitude= 1 km) near the O3 absorption band. Comparing low resolution results (left of Figures 1, 2 and 3) with high resolution ones (right of the same figures) we can note that differences between radiances/irradiances obtained by both RTMs are larger when using high spectral resolution models than low spectral resolution ones. This could be due to the fact that the line by line atmospheric and transmittance model used with libRadtran has much more resolution than the 1 cm⁻¹ band model used by MODTRAN.

	RTM	L1	L2	L3	L4	T1	T2
Atmospheric profile	libRadtran	afglus: US. Standard atmosphere, 1976					
	MODTRAN	1976 US. Standard					
Solar angles (zenith/azimuth) (degrees)	libRadtran	(30°/0°)			(70°/0°)	—	
	MODTRAN						
Obs. angles (zenith/azimuth) (degrees)	libRadtran	(180°/180°)		(140°/180°)		(180°/180°)	
	MODTRAN						
Atmospheric parameters	libRadtran	Rural aerosol model Visibility: 50 km; wv: 1.5 cm					
	MODTRAN						
Sensor altitude (km)	libRadtran	100 km	1 km			100 km	1 km
	MODTRAN						
	RTM	L1	L2	L3	L4	T1	T2
Slit function	libRadtran	Type: Gaussian; Resolution: 1 nm FWHM: VNIR (2 nm for low and high resolution); SWIR: (2 nm for high resolution, 8 nm for low resolution)				Type: Gaussian Resolution: 1 nm FWHM: 10 nm for high res.; 260 nm for low res.)	
	MODTRAN						

Table 2: Input parameters used by both RTMs for the calculation of at-sensor radiance for day 180. Note: Each RTM may interpret these parameters in slightly different ways

	RTM	I1 (8:10 UTC)	I2 (12:26 UTC)
Atmospheric profile	libRadtran	Afglms: Midlatitude Summer	
	MODTRAN	Midlatitude Summer	
Solar zenith (degrees)	libRadtran	57.8°	12.3°
	MODTRAN		
Atmospheric parameters	libRadtran	Desert aerosol model (with wind speed of 30 m/s in MODTRAN) AOD (1020 nm): 0.465 wv: 0.84 cm	Desert aerosol model (with wind speed of 30 m/s in MODTRAN) AOD (1020 nm): 0.43 wv: 0.96 cm
	MODTRAN		
Ground altitude (km)	libRadtran	0.750 km	
	MODTRAN		
Slit function	libRadtran	Type: Gaussian; Resolution: 1 nm FWHM: 3 nm (350 to 1000 nm) 10 nm (1000 to 2500 nm)	
	MODTRAN		

Table 3: Input parameters used by both RTMs to model at-surface irradiance for SISFT14 campaign. Note: Each RTM may interpret these parameters in slightly different way

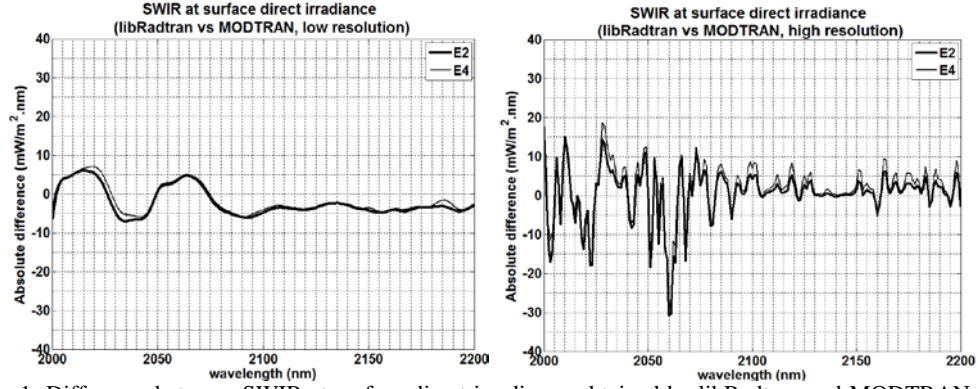


Figure 1: Difference between SWIR at-surface direct irradiance obtained by libRadtran and MODTRAN for cases E2 and E4. Band model results are represented on the left, and high resolution results on the right

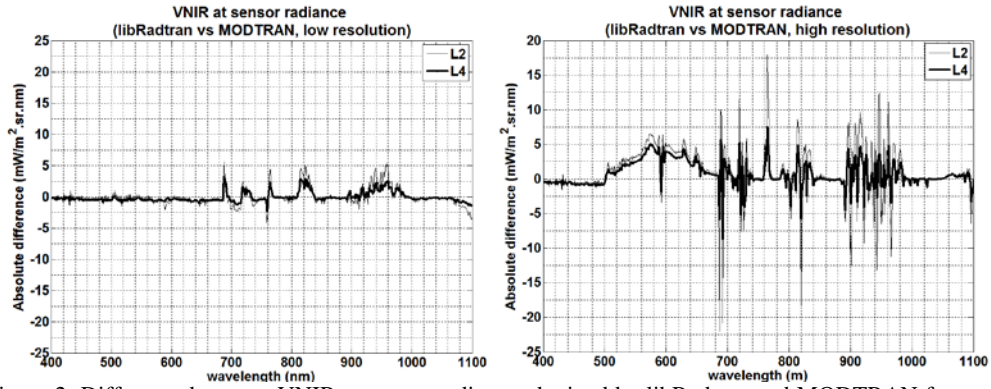


Figure 2: Difference between VNIR at-sensor radiance obtained by libRadtran and MODTRAN for cases L2 and L4. Band model results are represented on the left, and high resolution results on the right

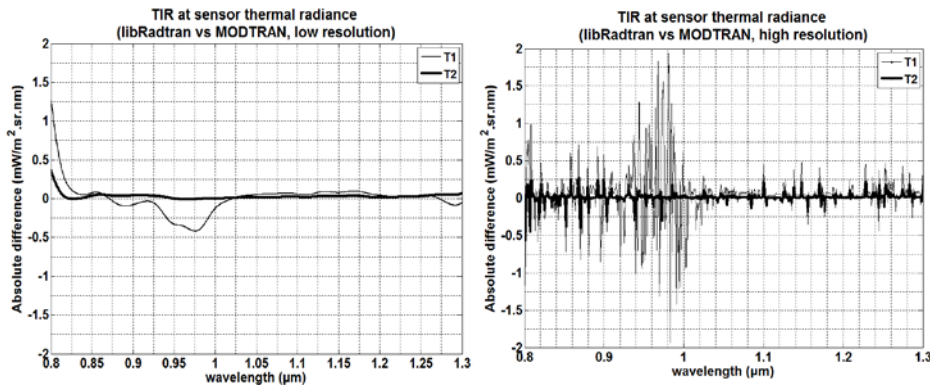


Figure 3: Difference between TIR at-sensor thermal radiance obtained by libRadtran and MODTRAN for cases T1 and T2. Band model results are represented on the left and high resolution results on the right

We will now compare ground irradiance modelled by libRadtran and MODTRAN with field measurements taken on 28 July 2014 in Merzouga (Morocco) with the spectroradiometer ASD-FS3 during SISFT14 campaign. Figure 4 shows ground irradiance differences between results obtained by both RTMs and the experimental data (RTM –

experimental data) for cases I1 (at 8:10 UTC, on the left) and I2 (at 12:26 UTC, on the right). The plots show that there are significant differences between expected and measured irradiance at short wavelengths. The differences must be linked to actual aerosol load and properties, which might be different to the models in MODTRAN and libRadtran.

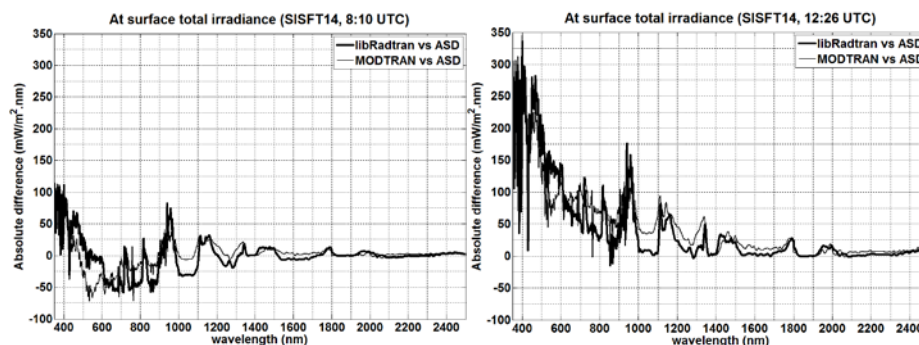


Figure 4: Difference between at-surface total irradiance obtained by each RTM and experimental data measured during the SISFT14 campaign. Left, comparison of experimental data with modelled results for 8:10 UTC. Right, the same comparison for 12:26 UTC.

4. CONCLUSIONS AND FUTURE WORK

In this study we have evaluated the use of libRadtran RTM in RS applications, as a complementary model to MODTRAN. For that purpose, we have compared irradiances/radiances modelled by both RTMs in order to visualize the differences between them.

Results obtained show that differences in radiances/irradiances calculated by libRadtran and MODTRAN are significant in absorption zones, reaching values of 20 mW/m².sr.nm and 30 mW/m².nm in worst cases, respectively. Outside absorption features both RTMs have similar results.

It can be noted as well a positive/negative alternance, which shows the problems in defining accurately the same spectral grid for both RTMs (Figures 1, 2 and 3).

As we can see, differences using high resolution results (right of Figures 1, 2 and 3) are larger than this magnitude for low resolution ones (left of the same figures), which may be associated to the fact that the line by line atmospheric and transmittance model genln2 used with libRadtran has much more resolution than the 1 cm⁻¹ band model used by MODTRAN. Differences between scenarios (E1 to E5, L1 to L4 and T1-T2) does not show any unexpected information; the main problems appear in all cases and increase when the atmospheric interference increases.

Comparing both RTMs with real data it can be noted that modelled results obtained by them differ significantly with the experimental data for desert conditions, mainly for wavelengths up to 1000 nm (Figure 4) what can be associated with the difficulty to model a severe case of aerosols just knowing AOD data at certain wavelength.

However, above 1000 nm the differences are negligibles. Apart from that, there could be instrument calibration errors and uncertainties in the atmospheric conditions, what would add more differences between modelled results and experimental data, especially in absorptions features. It is likely that the extrapolation of AOT from 1020 nm (as measured by Microtops) to

other wavelengths does not follow accurately the actual conditions.

The results obtained in this paper are a previous step for the use of libRadtran in RS applications at INTA, as an alternative to MODTRAN. The work performed shows the difficulties in configuring RTMs, not only for intercomparisons but also for RS applications.

REFERENCES

- Berk, A., Anderson, G.P., Acharya, P.K. and Shettle E.P., 2008, MODTRAN5.2.0.0 User's Manual. Spectral Sciences, Inc., Burlington, MA, Air Force Research Laboratory, Hanscom AFB, MA.
- ESA (2014) <http://exploration.esa.int/mars/48898-edm-science-payload/>
- Kurucz, R., 1992, Synthetic infrared spectra. In Proceedings of the 154th Symposium of the International Astronomical Union (IAU) (Tucson, Arizona, Kluwer, Acad., Norwell, MA).
- Mayer, B. and Kylling, A., 2005, Technical note: The libRadtran software package for radiative transfer calculations – description and examples of use. Atmos. Chem. Phys., 5, 1855–1877.
- Mayer, B., Kylling, A., Emde, C., Hamann, U. and Buras, R., 2012, LibRadtran User's Guide (<http://www.libradtran.org/doc/libRadtran.pdf>).
- ReSe, 2011, MODO: MODTRAN5 for Remote Sensing Applications, User Manual, Version 5 (http://www.rese.ch/pdf/MODO_Manual.pdf).
- Ricchiazzi, P., Yang, S., Gautier, C., and Sowle, D., 1998, SBDART: A research and Teaching software tool for plane-parallel radiative transfer in the Earth's atmosphere. Bulletin of the American Meteorological Society, 79, 2101–2114.
- Stamnes, K., Tsay, S.-C., Wiscombe, W., and Jayaweera, K., 1988, Numerically stable algorithm for discrete-ordinate-method radiative transfer in multiple scattering and emitting layered Media. Appl. Opt., 27, 2502–2509.

Land surface temperature retrieval from three thermal infrared data of MODIS for dust aerosol loading in the atmosphere

Xiwei Fan^{a,b,c}, Bo-Hui Tang^a, Hua Wu^a, Guangjian Yan^d, and Zhao-Liang Li^{a,c}

^a State Key Laboratory of Resources and Environment Information System, Institute of Geographic Sciences and Natural Resources Research, Chinese Academy of Sciences, Beijing 100101, China

^b University of Chinese Academy of Sciences, Beijing 100049, China

^c ICube, UdS, CNRS, 300 Bld Sebastien Brant, CS10413, 67412 Illkirch, France

^d State Key Laboratory of Remote Sensing Science, School of Geography, Beijing Key Laboratory for Remote Sensing of Environment and Digital Cities, Beijing Normal University, Beijing 100875, China

lizl@igsnr.ac.cn

ABSTRACT—Land surface temperature (LST) is a critical parameter for many applications. A default aerosol type and a fixed aerosol loading were commonly used in the development of LST retrieval algorithms. However, numerical simulations showed that a significant bias up to -3 K was found at nadir view if dust aerosol was not considered in the LST retrieval algorithm. To reduce the influence of dust aerosol on LST estimation, a three-channel algorithm was proposed with the measurements of MODIS channels 29, 31 and 32. The results showed that the LST could be estimated with a root mean square error (RMSE) of 1.1 K when viewing zenith angle (VZA) was 0° and aerosol optical depth (AOD) less than 1.0; the maximum RMSE was 1.6 K when VZA less than 60°. In case of clear-sky conditions, namely AOD=0, the RMSE was 1.1 K and 1.7 K when VZA=0° and 60°, respectively. It indicates that the proposed three-channel algorithm can be used to estimate LST not only for dust aerosol skies but also for clear-sky conditions. In addition, the sensitivity analysis in terms of the uncertainties of the input parameters and algorithm error itself showed that the total LST errors were less than 2.1 K.

1 INTRODUCTION

It is widely recognized that land surface temperature (LST) is a key parameter for many applications and the retrieval of LST from satellite infrared radiometers has proven to be useful. Note that a default aerosol type (rural aerosol) and a fixed aerosol loading (ground horizontal visibility equals to 23 km) were commonly used in the development of LST retrieval algorithms. However, numerical simulations showed that a significant bias up to -3 K was found at nadir view if dust aerosol was not considered in the LST retrieval algorithm (Fan *et al.*, 2014). Thus some LST and sea surface temperature (SST) correction methods were proposed to reduce the influence of dust aerosol on LST or SST retrieval based on dust aerosol optical depth (AOD) (Diazet *et al.*, 2001). Considering the difficulty to acquire reliable estimate of dust aerosol AOD in the nighttime, the objective of this study is to develop a nighttime LST retrieval algorithm for dust aerosol areas (frequently affected by dust aerosol). Because MODIS is widely used for the retrieval of LST, this study focuses on methodology development taking MODIS as an example.

2 DATA

The atmospheric radiative transfer model MODTRAN4 is used to simulate the MODIS data for

methodology development. Keeping in mind that a practical LST retrieval algorithm should accommodate atmospheric and land surface emissivity (LSE) variations wide enough to cover all possible real situations, the radiosonde observation databases Thermodynamic Initial Guess Retrieval (TIGR) database (Chedin *et al.*, 1985) and Advanced Spaceborne Thermal Emission Reflection Radiometer (ASTER) spectral library (Baldrige *et al.*, 2009) (<http://speclib.jpl.nasa.gov/>) are considered in our simulations. The TIGR atmospheric profiles constructed by the Laboratoire de Meteorologie Dynamique (LMD) contain 2311 atmospheric temperature, humidity and ozone mixing ratio profiles that show a total atmospheric water vapor content (WVC) ranging from 0.01 to 8.0 g/cm². Because the objective of this study focuses on LST retrieval in dust aerosol skies, only cloud-free atmospheric profiles are selected to exclude the influence from clouds. Thus the profiles with a relative humidity at any layer greater than 90% or at two consecutive layers greater than 85% are discarded (Wu *et al.*, 2013). Moreover, a subset of the remained profiles was further elaborately selected to insure that there was a nearly uniform probability distribution for WVC. At last, 60 atmospheric profiles with WVC ranging from 0.01 to 3.0 g/cm², nearly two atmospheric profiles for each 0.1

g/cm² interval, are extracted from the TIGR database. The ASTER spectral library is a compilation of more than 2300 spectra of materials, covering the wavelength range 0.4-15.4 μm . 54 land types, including soils (41), vegetation (4), and water/snow/ice (9), from the ASTER spectral library are used in the simulations.

3 METHODOLOGY

3.1 Radiative transfer in dust aerosol skies

To develop the new LST retrieval algorithm, the vertical atmospheric column profile is proposed to divide into two layers: the lower-layer (from ground to approximately 2 km height) affected by dust aerosol and the upper-layer (above 2 km height) without dust aerosol as Fig.1 shows. Thus the top of the atmosphere (TOA) radiance $B_i(T_i)$ in channel i can be expressed as:

$$B_i(T_i) = B_i(T_i^0)\tau_i + R_{i,atm-u}^{\uparrow} \quad (1)$$

where, $B_i(T_i^0)$ is the radiance in satellite direction at the interface of the two atmospheric layers, B_i is the Planck function in channel i ; $R_{i,atm-u}^{\uparrow}$ and τ_i are the upward radiance and transmittance of upper-layer atmosphere. McMillin (1975) used the mean value theorem to define the mean radiative temperature of the atmosphere in the upward direction, thus the upper-layer upward atmospheric radiance can be written as:

$$R_{i,atm-u}^{\uparrow} = B_i(T_{atm-u})(1 - \tau_i) \quad (2)$$

where T_{atm-u} is the equivalent temperature of the upper-layer atmosphere. Inserting Eq.(2) into Eq.(1), we can obtain:

$$B_i(T_i) = B_i(T_i^0)\tau_i + B_i(T_{atm-u})(1 - \tau_i) \quad (3)$$

To get an algorithm involving temperatures rather than radiances, the first-order Taylor series expansion is commonly used to approximate the Planck function, that is,

$$B_i(T) = B_i(T_i^0) + (T - T_i^0) \frac{\partial B_i(T_i^0)}{\partial T} \quad (T = T_i \text{ or } T_{atm-u}) \quad (4)$$

Sobrino *et al.* (1996) pointed out that in the 10.5-12.5 μm and for moderate temperature departures $|T - T_i^0| \leq 10-15$ K, Eq.(4) is accurate to better than 1 per cent. Thus approximating the Planck function in Eq.(3) using Eq.(4), we can obtain:

$$T_i = T_i^0\tau_i + T_{atm-u}(1 - \tau_i) \quad (5)$$

Eq.(5) means that the TOA brightness temperature T_i is the summation of T_i^0 and T_{atm-u} weighted by τ_i .

To retrieval LST in dust aerosol skies using TOA measured brightness temperatures T_i , the relationship between LST and T_i^0 need to be clarified. That is the radiation at the interface of the two atmospheric layers $B_i(T_i^0)$ is composed of five parts:

$$B_i(T_i^0) = B_i(T_s)\varepsilon_i(\tau_{di} + \tau_{si}) + R_{i,atm-l}^{\downarrow}(1 - \varepsilon_i)(\tau_{di} + \tau_{si}) + R_{i,atm-l}^{\uparrow} + R_{i,atm-u}^{\downarrow}(1 - \varepsilon_i)\gamma_i + R_{i,atm-u}^{\downarrow}\rho_i \quad (6)$$

where, the first part is the land surface radiation emitted by a temperature T_s with LSE equivalent to ε_i , τ_{di} and τ_{si} are the direct and scattering lower-layer atmospheric transmittances; the second and third parts are from the downward and upward radiations ($R_{i,atm-l}^{\downarrow}$ and $R_{i,atm-l}^{\uparrow}$) of lower-layer atmosphere; the fourth and fifth parts are the radiations from upper-layer atmosphere that reflected by the ground and dust aerosol; γ_i is the product of lower-layer atmospheric transmittances in downward and upward direction, and ρ_i is the spherical albedo reflectance of the lower-layer atmosphere that mainly caused by dust aerosol. Note that all the parameters in Eq.(1) to Eq.(6) are weighted by the channel spectral response function in channel i .

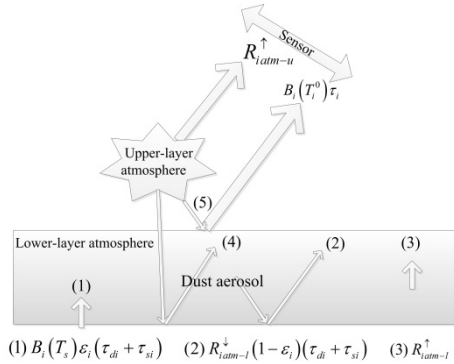


Fig.1. Illustration of radiative transfer equation in infrared regions with the presents of dust aerosol.

3.2 The three-channel LST retrieval algorithm

Assuming that the atmospheric profile is truncated at the top of the lower-layer atmosphere and no absorption is assumed in the upper-layer atmosphere, thus the radiation $B_i(T_i^0)$ measured at the interface of the two atmospheric layers is reduced to the sum of the first three parts in Eq.(6) and is labelled as $B_i(T_i')$ in this study. With the selected atmospheric profiles from TIGR, two groups of brightness temperatures T_i^0 and T_i' measured at the top of lower-layer atmosphere in MODIS channels 20, 22, 23, 29, 31 and 32 (centered at 3.8, 4.0, 4.1, 8.5, 11.0, and 12.0 μm) are produced respectively. T_i^0 and T_i' are the brightness temperatures without and with the truncation of the upper-layer atmosphere, respectively. It shows that the differences between T_i^0 and T_i' are less than 0.19 K, 0.37 K, 0.50 K, 0.19 K, 0.23 K and 0.22K for channels 20, 22, 23, 29 31 and 32 when AOD is equivalent to 1 and LSEs are 0.5, 0.5, 0.5, 0.8, 0.9, 0.9, respectively. It indicates that T_i^0 can be substitute with T_i' with a great accuracy.

In other words, the widely used two-channel or split-window algorithms can be used to estimate LST with the brightness temperatures measured at the height nearly 2-3 km above ground.

To get an accurate estimate of LST, many LST retrieval algorithms are proposed to reduce the influences from the second and third parts in Eq.(6). Sobrino and Raissouni (2000) proposed a two-channel algorithm with separate terms for the atmospheric and LSE corrections to retrieve LST from NOAA-AVHRR data. It can be written as:

$$T_s = T_i + a_1(T_i - T_j) + a_2(1 - \varepsilon_1) + a_3\Delta\varepsilon_1 + a_4W(1 - \varepsilon_1) + a_5W\Delta\varepsilon_1 + a_0 \quad (7)$$

where, T_s is the retrieved LST, T_i and T_j are the TOA brightness temperatures in channels i and j , ε_1 is the mean channel emissivity $\varepsilon_1 = (\varepsilon_i + \varepsilon_j)/2$, $\Delta\varepsilon_1$ is the emissivity difference $\Delta\varepsilon_1 = \varepsilon_i - \varepsilon_j$, W is the total atmospheric water vapor and a_i ($i=0-5$) is the numerical coefficient of the two-channel algorithm.

To study the possibility of the two-channel algorithm for the estimate of LST in dust aerosol skies with the data measured at the top of the lower-layer atmosphere. A simulated data (Dataset-1) is produced with the atmospheric profiles and LSEs selected from TIGR and ASTER discussed in section 2. To increase the representativeness of the simulations, the LSTs are varied from $T_0 - 5$ K to $T_0 + 5$ K in steps of 5 K according to the near surface atmospheric temperature (T_0) of the atmospheric profile. To simulate the influence of dust aerosol with different loadings, the AOD of dust aerosol is varied from 0.0 to 1.0 in steps of 0.1 using the optical properties of transported mineral aerosol type in Optical Properties of Aerosol and Cloud (OPAC) software package (Hess *et al.*, 1998). Thus the TOA brightness temperatures in channels 20, 22, 23, 29, 31 and 32, respectively, at vertical view condition are produced.

As the atmospheric WVC is relatively low when the presence of dust aerosol, the W in Eq.(7) is eliminated and the new Eq.(7) is expressed as:

$$T_s = T_i^0 + a_1(T_i^0 - T_j^0) + a_2(1 - \varepsilon_1) + a_3\Delta\varepsilon_1 + a_0 \quad (8)$$

where T_i^0 and T_j^0 are the brightness temperatures measured at the top of lower-layer atmosphere in channels i and j ; With the LSTs set in MODTRAN and the corresponding simulated brightness temperatures in Dataset-1, the coefficients in Eq.(8) are determined. Table 1 shows the RMSEs between the given LSTs and the estimated LSTs using Eq.(8) for different channel combinations.

Table 1 indicates that some of the channel combinations can be used to retrieval LST in dust aerosol skies with RMSEs less than 2 K. Considering the influence of the upper-layer atmosphere, the Eq.(5) in channel i and j are inserted in to Eq.(8):

$$T_s = \frac{T_i}{\tau_i} + a_1 \left(\frac{T_i}{\tau_i} - \frac{T_j}{\tau_j} \right) + T_{atm-u} \left[a_1 \frac{(1 - \tau_j)}{\tau_j} - a_1 \frac{(1 - \tau_i)}{\tau_i} - \frac{(1 - \tau_i)}{\tau_i} \right] + a_2(1 - \varepsilon_1) + a_3\Delta\varepsilon_1 + a_0 \quad (9)$$

To eliminate T_{atm-u} , another two-channel algorithms in channels i and k are selected:

$$T_s = \frac{T_i}{\tau_i} + b_1 \left(\frac{T_i}{\tau_i} - \frac{T_k}{\tau_k} \right) + T_{atm-u} \left[b_1 \frac{(1 - \tau_k)}{\tau_k} - b_1 \frac{(1 - \tau_i)}{\tau_i} - \frac{(1 - \tau_i)}{\tau_i} \right] + b_2(1 - \varepsilon_2) + b_3\Delta\varepsilon_2 + b_0 \quad (10)$$

Table 1. RMSEs of LST estimated using Eq.(8) for different channel combinations.

Channel combination	RMSE (K)	Channel combination	RMSE (K)
20,22	1.61	22,32	1.23
20,23	1.27	23,29	2.36
20,29	0.91	23,31	2.41
20,31	1.07	23,32	2.35
20,32	0.90	29,31	2.54
22,23	0.74	29,32	2.99
22,29	1.21	31,32	1.21
22,31	1.35		

Combining Eq.(9) and Eq.(10), the three channel LST retrieval algorithm is proposed as:

$$T_s = T_i + \frac{a_1 M_2}{\tau_j(M_2 - M_1)}(T_i - T_j) - \frac{b_1 M_1}{\tau_k(M_2 - M_1)}(T_i - T_k) + \frac{M_2}{M_2 - M_1} [a_2(1 - \varepsilon_1) + a_3\Delta\varepsilon_1] - \frac{M_1}{M_2 - M_1} [b_2(1 - \varepsilon_2) + b_3\Delta\varepsilon_2] + \frac{M_2 a_0 - M_1 b_0}{M_2 - M_1} \quad (11)$$

$$\text{with } M_1 = a_1 \frac{(1 - \tau_j)}{\tau_j} - a_1 \frac{(1 - \tau_i)}{\tau_i} - \frac{(1 - \tau_i)}{\tau_i}$$

$$\text{and } M_2 = b_1 \frac{(1 - \tau_k)}{\tau_k} - b_1 \frac{(1 - \tau_i)}{\tau_i} - \frac{(1 - \tau_i)}{\tau_i}$$

Considering the relatively low atmospheric WVC in the upper-layer atmosphere, the Eq.(11) is finally expressed as:

$$T_s = T_i + c_1(T_i - T_j) + c_2(T_i - T_k) + c_3\Delta\varepsilon_1 + c_4(1 - \varepsilon_1) + c_5\Delta\varepsilon_2 + c_0 \quad (12)$$

where T_i , T_j and T_k are the TOA brightness temperatures in channels i , j and k , respectively; ε_1 and $\Delta\varepsilon_1$ are the LSE mean and difference respectively in channels i and j ; $\Delta\varepsilon_2$ is the LSE difference in channels i and k ; c_i ($i=0-5$) is the numerical coefficient of the three-channel algorithm.

3.3 Results

To obtain the coefficients in Eq.(12), the simulated Dataset-2 is produced similarly as Dataset-1 but the brightness temperatures measured at the TOA. c_i ($i=0-5$) is determined from Dataset-2 by the statistical regression method. The RMSEs between actual LSTs (LSTs set in MODTRAN) and the LSTs estimated using Eq.(12) is given in Table 2.

Table 2. RMSEs of LST estimated using Eq.(12) for different channel combinations.

Channel combination	RMSE (K)	Channel combination	RMSE (K)
20,22,23	0.73	22,23,29	0.70
20,22,29	0.89	22,23,31	0.68
20,22,31	1.05	22,23,32	0.68
20,22,32	0.84	22,29,31	1.21
20,23,29	0.78	22,29,32	1.20
20,23,31	0.81	22,31,32	1.00
20,23,32	0.69	23,29,31	2.19
20,29,31	0.85	23,29,32	2.34
20,29,32	0.83	23,31,32	1.19
20,31,32	0.79	29,31,32	0.98

In Table 2, most of RMSEs are less than 1.2 K. The channel combinations (22, 23 and 31) and (22, 23 and 31) show the RMSEs less than other channels. Because of the scattering effect of dust aerosol, the radiations from the adjacent pixels around the target pixel can also be received by satellite. Thus compared with SST retrieval, the inhomogeneity of land surface is one of an important distinction for the retrieval of LST. The Dataset-2 with adjacent pixels' LST larger or less than 5 K of the target LST is added into Dataset-2. Thus the newly simulated dataset is two times larger than the original Dataset-2. After recalculate the coefficients of Eq.(12) using the new Dataset-2, the RMSEs of LST is given in Table 3. In addition, Fig 2 shows the extinction coefficient, single scattering albedo and asymmetry parameter of dust aerosol with extinction coefficient normalized to 1.0 at 0.55 μm . Besides that, the channel response functions of MODIS infrared window channels are also given in Fig 2.

Table 3 shows that the RMSE between actual LST and Eq.(12) estimated LST is 1.16 K when using MODIS channels 29, 31, and 32 ($i=31, j=29$ and $k=32$) and it is less than the RMSEs using other channel combinations. This is because the dust aerosol extinction coefficient and single scattering albedo of channels 29, 31, and 32 are less than the mid-infrared channels, as Fig.(2) shows.

Because the atmosphere WVC in Eq.(6) is eliminated in the reasoning process, to study the accuracy of the algorithm for different atmospheric WVC ranges, Fig. 3 shows the RMSEs of LST versus

AOD for WVC ranges of $[0, 1.0 \text{ g/cm}^2]$, $[1.0, 2.0 \text{ g/cm}^2]$, and $[2.0, 3.0 \text{ g/cm}^2]$ respectively in vertical view conditions.

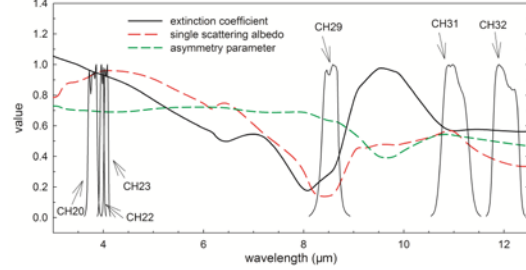


Fig.2. Variations of dust aerosol optical parameters (extinction coefficient, single scattering albedo and asymmetry parameter) with wavelength. The channel response functions of MODIS infrared window channels are also indicated. The extinction coefficients are normalized to 1.0 at 0.55 μm .

Table 3. RMSEs of LST estimated using Eq.(12) for different channels with considering the adjacency effect caused by the scattering of dust aerosol.

Channel combination	RMSE (K)	Channel combination	RMSE (K)
20,22,23	1.54	22,23,29	1.45
20,22,29	1.91	22,23,31	1.49
20,22,31	1.93	22,23,32	1.51
20,22,32	1.85	22,29,31	1.92
20,23,29	1.76	22,29,32	1.88
20,23,31	1.76	22,31,32	1.43
20,23,32	1.72	23,29,31	2.43
20,29,31	1.91	23,29,32	2.56
20,29,32	1.83	23,31,32	1.43
20,31,32	1.42	29,31,32	1.16

In Fig.3, there is no significant variations of the RMSEs of Eq.(12) retrieved LST among different AOD and atmospheric WVC ranges. When AOD less than 0.6 and atmospheric WVC less than 2 g/cm^2 , the RMSEs are less than 1.0 K; the RMSEs are larger than 1.0 K when AOD larger than 0.6 or atmospheric WVC larger than 2 g/cm^2 .

Considering different VZA conditions, the simulated data when $\text{VZA}=33^\circ, 44^\circ, 51^\circ, 56^\circ$, and 60° ($\text{Secant(VZA)}=1.2, 1.4, 1.6, 1.8$ and 2.0) are produced similar as Dataset-2 for channels 29, 31, and 32. Fig.4 is the RMSEs of LST retrieved employing channels 29, 31 and 32 versus AOD for six VZA conditions. It shows that the maximum RMSE is 2.1 K when $\text{VZA}=60^\circ$ and $\text{AOD}=1.0$, and larger VZA values produce a greater RMSE. In clear-sky conditions, namely AOD is equivalent to 0, the RMSE is 1.1 K and 1.7 K when $\text{VZA}=0^\circ$ and 60° , respectively. It indicates that the proposed three-channel algorithm can be used to estimate LST not only for dust aerosol skies but also for clear-sky conditions.

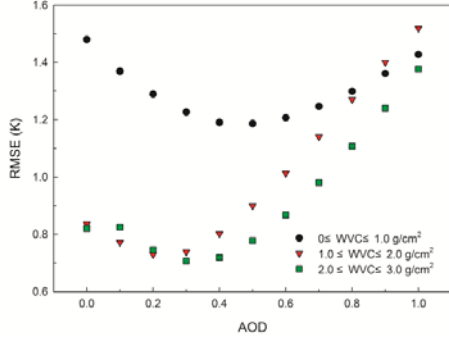


Fig.3. RMSEs of LST versus AOD for different atmospheric WVC ranges: [0, 1.0 g/cm²], [1.0, 2.0 g/cm²], and [2.0, 3.0 g/cm²] respectively in vertical view conditions.

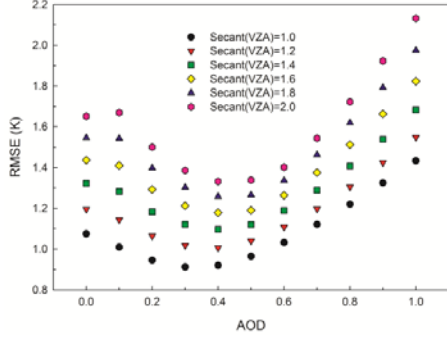


Fig.4. RMSEs between LST setting in MODTRAN and the LST estimated using Eq.(12) in six different VZAs.

4 SENSITIVITY ANALYSIS

To determine the influence of input variables' uncertainties on the performance of the proposed LST retrieval algorithm, a sensitivity analysis is performed. The LST errors of the proposed algorithm is primarily from the uncertainties of T_{29} , T_{31} , T_{32} , $\Delta\epsilon_1$, $\Delta\epsilon_2$, ϵ_1 and the algorithm accuracy itself, which can be expressed as:

$$\delta(LST_{total}) = \sqrt{\delta(T_{29})^2 + \delta(T_{31})^2 + \delta(T_{32})^2 + \delta(\Delta\epsilon_1)^2 + \delta(\Delta\epsilon_2)^2 + \delta(\epsilon_1)^2 + \delta(alg)^2} \quad (13)$$

with

$$\delta(T_{29}) = \left| \frac{\partial LST}{\partial T_{29}} \Delta T_{29} \right| \quad (14)$$

$$\delta(T_{31}) = \left| \frac{\partial LST}{\partial T_{31}} \Delta T_{31} \right| \quad (15)$$

$$\delta(T_{32}) = \left| \frac{\partial LST}{\partial T_{32}} \Delta T_{32} \right| \quad (16)$$

$$\delta(\Delta\epsilon_1) = \left| \frac{\partial LST}{\partial \Delta\epsilon_1} \Delta(\Delta\epsilon_1) \right| \quad (17)$$

$$\delta(\Delta\epsilon_2) = \left| \frac{\partial LST}{\partial \Delta\epsilon_2} \Delta(\Delta\epsilon_2) \right| \quad (18)$$

$$\delta(\epsilon_1) = \left| \frac{\partial LST}{\partial \epsilon_1} \Delta(\epsilon_1) \right| \quad (19)$$

where, ΔT_{29} , ΔT_{31} , ΔT_{32} , $\Delta(\Delta\epsilon_1)$, $\Delta(\Delta\epsilon_2)$ and $\Delta(\epsilon_1)$ are the uncertainties of the input variables T_{29} , T_{31} , T_{32} , $\Delta\epsilon_1$, $\Delta\epsilon_2$ and ϵ_1 , respectively, $\delta(T_{29})$, $\delta(T_{31})$, $\delta(T_{32})$, $\delta(\Delta\epsilon_1)$, $\delta(\Delta\epsilon_2)$ and $\delta(\epsilon_1)$ are the errors resulting from ΔT_{29} , ΔT_{31} , ΔT_{32} , $\Delta(\Delta\epsilon_1)$, $\Delta(\Delta\epsilon_2)$ and $\Delta(\epsilon_1)$, respectively, and $\delta(alg)$ represents the error from the algorithm itself.

Considering the noise equivalent temperature difference (NE ΔT) of MODIS channels 29, 31 and 32 with $\Delta T_{29} = \Delta T_{31} = \Delta T_{32} = 0.05$ K and assuming $\Delta(\Delta\epsilon_1) = \Delta(\Delta\epsilon_2) = \Delta(\epsilon_1) = 0.01$, the LST errors $\delta(T_{29})$, $\delta(T_{31})$, $\delta(T_{32})$, $\delta(\Delta\epsilon_1)$, $\delta(\Delta\epsilon_2)$ and $\delta(\epsilon_1)$ are shown in Fig. 5. The algorithm error $\delta(alg)$ and the total LST error $\delta(LST_{total})$ are also indicated in this figure.

Fig.5 shows that the LST errors caused by the uncertainties of T_{29} , T_{31} , T_{32} , $\Delta\epsilon_1$ and ϵ_1 are less than 0.5 K and the errors in the uncertainty of $\Delta\epsilon_2$ are approximately 1.2 K for all the VZA conditions. It indicates that to get an accurate LST using the proposed three-channel LST retrieval algorithm, the relatively high quality emissivity in channels 31 and 32 are necessary. Considering all the uncertainties of input parameters and model error itself, the total LST errors vary from 1.7 K to 2.1 K.

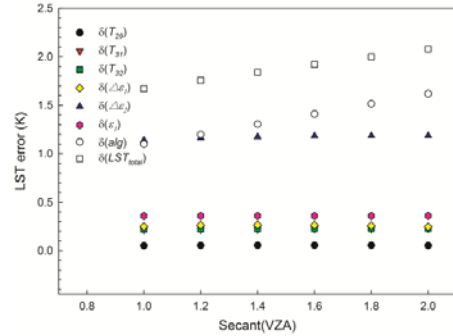


Fig.5. LST errors $\delta(T_{29})$, $\delta(T_{31})$, $\delta(T_{32})$, $\delta(\Delta\epsilon_1)$, $\delta(\Delta\epsilon_2)$, $\delta(\epsilon_1)$ and $\delta(alg)$ caused by the uncertainties of T_{29} , T_{31} , T_{32} , $\Delta\epsilon_1$, $\Delta\epsilon_2$, ϵ_1 and the algorithm error itself, and the total LST errors $\delta(LST_{total})$ versus Secant(VZA).

5 CONCLUSIONS

To acquire LST in dust aerosol skies, we have developed a three-channel LST retrieval algorithm based on a widely used two-channel algorithm for clear-sky conditions. Using MODIS channels 29, 31, and 32, the LST can be estimated with a root mean square error (RMSE) of 1.1 K when viewing zenith angle (VZA) is 0° and aerosol optical depth (AOD) less than 1.0; the maximum RMSE is 1.6 K when VZA is less than 60°. Note that the object of this study is to

develop a night-time LST retrieval algorithm in dust aerosol skies, but this algorithm can also be applied to daytime LST retrieval because we only use the MODIS thermal infrared channels (29, 31 and 32) that the influence from sun irradiance is ignorable. When AOD is equivalent to 0, namely clear-sky conditions, the RMSE is 1.1 K and 1.7 K when VZA=0° and 60°, respectively. It indicates that the proposed three-channel algorithm can be used to estimate LST not only for dust aerosol skies but also for clear-sky conditions, namely the areas frequently affected by dust aerosol. In addition, the sensitivity analysis in terms of the uncertainties of the input parameters and the algorithm error itself shows that the total LST errors are less than 2.1 K.

6 REFERENCES

- Baldrige, A. M., Hook, S. J., Grove, C. I., and Rivera, G., 2009, The ASTER spectral library version 2.0, *Remote Sensing of Environment*, 113, 711-715.
- Chedin, A., Scott, N. A., Wahiche, C., and Moulinier, P., 1985, The improved initialization inversion method: a high resolution physical method for temperature retrievals from satellites of the TIROS-N series, *Journal of climate and applied meteorology*, 24, 128-143.
- Diaz, J. P., Arbelo, M., Expósito, F. J., Podestá, G., Prospero, J. M., and Evans, R., 2001, Relationship between errors in AVHRR-derived sea surface temperature and the TOMS Aerosol Index, *Geophysical Research Letters*, 28, 1989-1992.
- Fan, X., Tang, B.-H., Wu, H., Yan, G., Li, Z.-L., Zhou, G., Shao, K., and Bi, Y., Extension of the generalized split-window algorithm for land surface temperature retrieval to atmospheres with heavy dust aerosol loading, *IEEE Journal of Selected Topics in Applied Earth Observations and Remote Sensing*, DOI: 10.1109/JSTARS.2014.2358584.
- Hess, M., Koepke, P., and Schult, I., 1998, Optical properties of aerosols and clouds: The software package OPAC, *Bulletin of the American Meteorological Society*, 79, 831-844.
- Sobrino, J. A. Li, Z.-L. Stoll, M. P., Becker, F., 1996, Multi-channel and multi-angle algorithms for estimating sea and land surface temperature with ATSR data, *International Journal of Remote Sensing*, 17, 2089-2114.
- Sobrino, J. A. and Raissouni, N., 2000, Toward remote sensing methods for land cover dynamic monitoring: Application to Morocco, *International Journal of Remote Sensing*, 21, 353-366.
- McMillin, L. M., 1975, Estimation of sea surface temperatures from two infrared window measurements with different absorption, *Journal of Geophysical Research*, 80, 5113-5117.
- Wu, H., Ni, L., Wang, N., Qian, Y., Tang, B.-H., and Li, Z.-L., 2013, Estimation of atmospheric profiles from hyperspectral infrared IASI sensor, *IEEE Journal of Selected Topics in Applied Earth Observations and Remote Sensing*, 6, 1485-1494.

Determining Optimal Conditions for Direct Detection of Sub-Pixel Archaeological Materials Using Airborne and Satellite Spectral Data

Sabol, Donald E. Jr., and Buck, Paul.

Division of Earth & Ecosystem Sciences, Desert Research Institute, Reno, Nevada, USA, 89512

Don.Sabol@dri.edu, Paul.Buck@dri.edu

ABSTRACT- *This project examines the detectability of sub-pixel artifacts (i.e. site midden, obsidian artifacts, and pottery sherds) using airborne and spaceborne image data. Our objectives are to: 1) use National Aeronautics and Space Administration (NASA-USA) image data in conjunction with actual field/laboratory measured spectra of archaeological materials to test the detection limits of the selected artifact classes at the sub-pixel scale by applying previously demonstrated theoretical detection limit modelling, 2) examine the influence that background, seasonal vegetation change and other on-site changes have for the detectability of these objects in image data, 3) establish the instrumentation, spatial scale, and spectral bands needed to improve the detectability of these objects, and 4) test predictions of new locations for artifacts at specific (spatial) densities in other image scenes and ground truth these predictions. Two field locations are examined: 1) Glass Mtn, California with variable concentrations of obsidian, and 2) the lower San Pedro River, Arizona with common concentrations of pottery and midden. Available image data include: NASA's MODIS/ASTER airborne simulator (MASTER) imaging system, the Airborne Visible/Infrared Imaging Spectrometer (AVIRIS), and the Advanced Spaceborne Thermal Emission and Reflection Radiometer (ASTER). Visible, SWIR, and TIR spectral characteristics of targets (archaeological material) and background (other non-archaeological materials) are measured in the field and laboratory. Detection thresholds (linking the spectra to the image data) are determined using Spectral Mixture Analysis (SMA). Subsequent success is evaluated by mapping predicted concentrations nearby and conducting ground truthing to determine accuracy.*

1 INTRODUCTION

Although many archaeological features such as the Egyptian pyramids and desert geoglyphs can be seen in aerial photographs and other remotely sensed images, most archaeological materials such as individual artifacts are usually considered too small to be readily detectable using remote sensing. However, direct detection of clusters of centimeter-sized artifacts may be possible combining high-spatial and spectral resolution image data with sub-pixel modelling.

The objectives of the proposed research are to:

- 1) use NASA aircraft and satellite data in conjunction with actual field/laboratory measured spectra of archaeological materials to determine the detection limits of selected artifact classes (obsidian, ceramics and midden) at the sub-pixel scale by applying previously demonstrated theoretical detection limit modelling (Sabol et al., 1992, Buck et al 2003).
- 2) examine the influence that background, seasonal vegetation change and other on-site changes have for the detectability of these objects in image data;
- 3) establish the instrumentation, spatial scale, and spectral bands needed to improve the detectability of these objects.

In particular we examine the detection threshold for obsidian artifacts, pottery sherds, and site midden at selected sites in southern Arizona and northern California. The final objective is to test predictions of new locations for these artifacts at specific (spatial) densities in other image scenes and ground truth these predictions.

2 BACKGROUND

Archaeological sites are typically discovered using traditional methods which include a well-designed random sample of geographic space in a region of interest, the results of predictive models based on quantitative relations between landscape features and site location tuned or "trained" on adjacent, well-studied areas, and on the archaeologist's field experience and intuition. A thorough archaeological evaluation of the landscape minimally requires locating artifact clusters and recording the density of artifacts within clusters (Dunnell and Dancey, 1983), as well as a quantification of the degree of error or bias inherent in the procedures used. However, these approaches are time- and labor-intensive, and it is not always possible to implement them fully if time and funding are limited. Innovative techniques that are quantitative and quick to apply over large areas may therefore be a welcome addition to the archaeologist's toolkit.

Exploration techniques based on remote sensing from aircraft or spacecraft have been developed over the past 20-30 years. Some of these techniques exploit differences in the reflectance (or emissive) spectra of different materials for identification and mapping and, in principle, these techniques can be adapted for use in archaeological surveys. They have the advantages of extending human perception, minimizing spatial bias in landscape analysis, and speed. Remote-sensing techniques are both quantitative and amenable to error analysis. Thus, remote sensing may be useful to the archaeologist for site discovery and analysis. However, it is important to recognize that the lessons learned with remote sensing in other fields such as geological prospecting and landscape analysis emphasize that remote sensing does not stand alone, but to be most effective must be used in conjunction with field inspection by scientists to verify, quantify, and evaluate findings made remotely.

Three advances in the past 20 years have made it feasible to pursue the remote-sensing approach in archaeological surveys. First, there is widespread recognition that a variety of materials, including some archaeological artifacts, may have unique spectral signatures distinguishable from the normal background materials against which they are viewed. This realization is relatively recent and not widely recognized in the archaeological literature. Second, the problem of subpixel detection (that is, how to determine compositional information at spatial resolutions below the spatial resolution of the scanner) has been successfully resolved. Third, laboratory and field instrumentation has advanced sufficiently to allow rapid and accurate characterization of spectra in dozens or hundreds of wavelengths with great precision, and at high spatial resolutions.

3 METHODS

We have shown previously (Buck et al., 2003, summarized above) that given the characteristics of available imaging systems and spectral properties of obsidian and ceramic artifacts on typical backgrounds, it should be possible to use aircraft and/or satellites to detect artifacts when above their theoretical detection thresholds on the ground surface. Previous research suggested that obsidian was detectable using selected wavelengths when it covered 4-25% of the ground with little obscuring vegetation, and that pottery could be detectable when it covered 12-48% of the ground surface again with little vegetation.

3.1 Field Locations

Two sites were selected for this study that have high densities of archaeological material including pottery shards, obsidian flakes, and midden material.

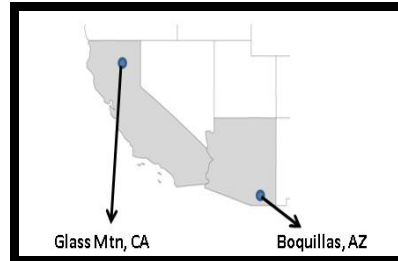


Figure 1: Location of the field sites.

3.1.1 Glass Mountain, northern California.

The Glass Mountain lava flow consists of about one cubic kilometer of lava from the Medicine Lake Highland Volcano (Eichelberger, 1981). This flow, comprising a variety of lithologies including dull stony porphyritic dacite charged with fine grained mafic xenoliths to shiny black phenolith free and xenolith free obsidian (Eichelberger, 1981). The obsidian was widely used for manufacture of chipped stone tools all over northern California because of its favorable flaking properties and sharp edges. Specific study sites were selected in an area northeast of the central Glass Mountain caldera because of the high density of obsidian scatters, indicating that it was clearly an important quarry area. Similar densities can be expected at habitation sites in this area of Medicine Lake Highlands.

3.1.2 Boquillas Ruin, San Pedro River Valley, Arizona.

The Boquillas Ruin is a large late prehistoric structural site on the east bank of the San Pedro River just north of the historic town site of Fairbank. Desert Archaeology, Inc. a private consulting firm has conducted surface survey and testing at this important site (Bill Doelle, personal communication 2011). The site has relatively high densities of pottery scatter as well as high spatial coverage of midden rich soils.

3.2 Field Methods

Field data collection consists of: 1) Spectral Data - collection of spectra of relevant target materials and backgrounds, and 2) Spatial Data - collection of data on the density or quantity of materials on the surface of the ground in each of the study areas.

3.2.1 Field Spectral Data

VIS-SWIR and TIR spectra are being collected on targets (artifacts) and background. Hand held devices at DRI are used to collect spectra in the field such as the ASD (Analytical Spectral Devices FieldSpec Pro) portable field spectrometer available for this purpose. TIR spectra of field samples are in the process of being measured using JPL's 520P Nicolet Fourier Transform Spectrometer with a Labsphere RSA-N1-

700D integrating sphere. The samples were either collected in the field (if permitted) or obtained from a curated collection. To date, only the VIS-SWIR spectra have been collected. TIR field data will be collected next year using three narrow-band thermal filters that we can use in conjunction with our thermal camera (FLIR SC640). Field images will be collected using three wavelengths at approximately 8 μ m, 9 μ m, and 10-11 μ m. These bands are primarily selected for silica (obsidian) detection and will allow us to construct color field TIR images at the sub-cm scale that we can correlate to the TIR airborne data as well as the laboratory spectra.

3.2.2 Field Spatial Data

The spatial surface distribution of pottery and midden (Boquillas) and obsidian (Glass Mountain) is measured for specific locations at each site. Specifically, estimates of the proportion of ground surface covered by these cultural materials, and also the background materials which include soil, rock, live vegetation, dead vegetation, and shade, must be determined to accurately assess whether the artifacts are spectrally detectable. Our analytical unit size as an 8 m x 8 m square (left). This unit size was chosen because it is approximately the same size as a “pixel” of the MASTER TIR data we have for the sites (~8.3 m). At each field area, 15-20 8X8 meter sites are selected. To estimate the portion of each 8m x 8m square covered by artifacts, we sampled the site surface using a 50 cm x 50 cm PVC pipe frame. Each of the 64 1 x 1 m squares of the larger unit were assigned a number from 1-64 then 20 randomly selected for counting. A photograph is made of each square, printed, and then examined in the field (on hands and knees) to identify all artifacts in the field of view.



Figure 2. Identifying artifacts in a field photo of sample sites. Artifacts in each photo of the 0.25 m² sample sites are identified. Later, in the laboratory, the photos are used to determine the percent surface coverage of the artifacts.

This is done in the field to preclude misidentification later in the laboratory. Later, back in the laboratory, the spatial coverage of each artifact type is determined for each photograph. These values will be used in conjunction with the MASTER data to: 1) determine artifact detectability, and 2) map areas of detectable artifacts in the image.

3.3 Image Spectral Analysis

MASTER image data (VIS-SWIR) is calibrated to reflectance using a combination of ACORN 6.0 (Atmospheric Correction Now) software and empirical line calibration using calibration sites in the field. The MASTER thermal bands will be corrected using an in-scene atmospheric correction (ISAC) routine. This will mitigate the impact of these atmospheric effects upon the radiance image data spectra (Johnson, 1998; Young, *et al.*, 2002). The ISAC algorithm relies upon the presence of a blackbody in the scene, the closest natural approximations to which are graybody objects such as water bodies or green vegetation stands in the scene. Although MASTER data is the primary data set being used in this study, other data such as ASTER (both sites) and AVIRIS (Boquillas) will also be analysed. ASTER data products already calibrated to reflectance and emissivity will be used in the analysis. These include: 1) VIS-SWIR cross-talk corrected data to reflectance (AST07XT) and 2) thermal data corrected to emissivity using the ASTER temperature-emissivity separation algorithm (AST05). Spectral data collected in the field (VIS-SWIR) and laboratory (TIR) are used as spectral “endmembers” in spectral mixture analysis (convolved to the appropriate imaging system bands) (Adams *et al.* 1993; Gillespie, 1992) to model the image data. This yields fractional spatial exposure of the major components in the scene. In cases where the fraction of the artifacts is very low, work in the next year will examine artifact detectability in the band residuals. Band residual analysis has been used on a high-resolution image data, such as AVIRIS (Gillespie, *et al.*, 1990) and lower resolution systems such as EOS/Aura for atmospheric studies (Krotkov, *et al.*, 2006).

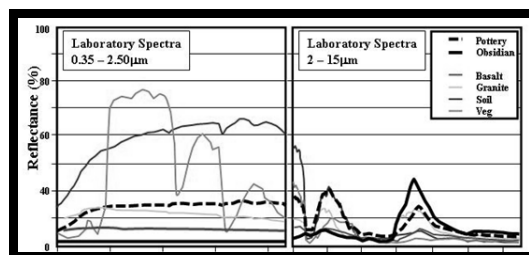


Figure 3. Typical VIS-SWIR and TIR spectra of background and artifacts.

The resultant fractions will be compared to our field measurements and fractional exposure determined from field photos to determine model accuracy.

3.4 Detection Threshold Model

Spectral detection analysis. The approach taken to determine target detectability is referred to as “spectral detection analysis” (Sabot et al., 1992). This method is designed to evaluate the spectral contrast between the target and background materials to determine detection thresholds using spectral mixture analysis. Endmember spectra from field and laboratory samples are incorporated into the analysis as well as system noise and endmember variability. The analysis yields an estimation of the minimum surficial coverage of target (artifact) within a pixel necessary to be detected in the image data.

3.5 Expansion as a Survey Tool in New Areas

Once the model has been evaluated in the study sites where artifact coverage has been determined, several new sites will be used as a test of the methodology. The purpose here is two-fold: 1) to find new areas that contain detectable artifacts, and 2) to use the theoretical detection model in conjunction with the fractions of major surface components to create a map that shows where (in image space) the background (composed of non-artifact components) is less likely to affect artifact detection. These are areas where artifact detection is most probable and can be used with ancillary data to use remote sensing for increased scrutiny for artifact detection (field checking, inclusion of a new spectral signature of artifact type or condition (i.e. different composition pottery than used in the initial phases of this study).

4. RESULTS TO DATE

The results shown here are preliminary and incomplete as this project is in the first of three planned years. So far, two field campaigns of each site have taken place; one during the growing season and one when plants are senescent (Table 1).

Table 1: Completed Fieldwork

Site	Wet Season	Dry Season
Glass Mountain, CA	4-6 June 2014	13-15 September 2014
Boquillas, AZ	27-30 July 2014	27-30 March 2014

4.1 Spectral Measurements

The spectral compositional complexity at Glass Mountain varies significantly by location. Sites located along the flow in sparsely wooded areas can be very complex. Here, components include green vegetation, dry vegetation (litter), vegetation, shade, soil, as well as the target (obsidian). However, there

are some sites at higher elevation that are simpler, composed only of white pumice and obsidian (Figure 4). The detection threshold for these different sites (in the VIS-SWIR) ranges from approximately 11% in the more complex sites to ~ 4% in the simpler sites.

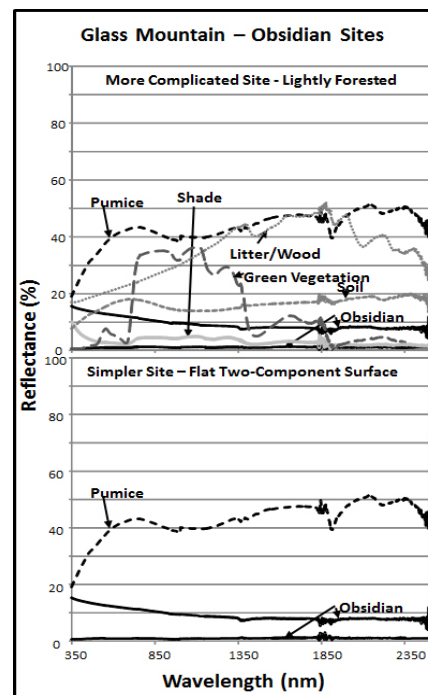


Figure 4. Spectra of target and background materials of Glass Mountain. As shown, some sites are spectrally more complicated than others.

The Glass Mountain study areas are dominated by coniferous vegetation and are, therefore, less affected by seasonal vegetation variability. This is not the case for the Boquillas site where the spectral contribution of the mesquite changes from being minor (<5% coverage from brown stems) to ~20% surface coverage from stems and refoliation during the late spring and summer. Figure 5 shows the difference in the seasonal background spectra measured at Boquillas. Although detection thresholds have yet to be determined for this site, the variation in backgrounds will likely affect artifact detectability.

Figure 6 shows the variability of the spectral signatures of the pottery sherds found at Boquillas as well as the spectra of the reddish soil that dominates the surface and midden soils that occur. Detection prediction scenarios are currently being developed for this site and will include the spectral variability of different types of pottery (slip painted, unpainted, corrugated utility ware).

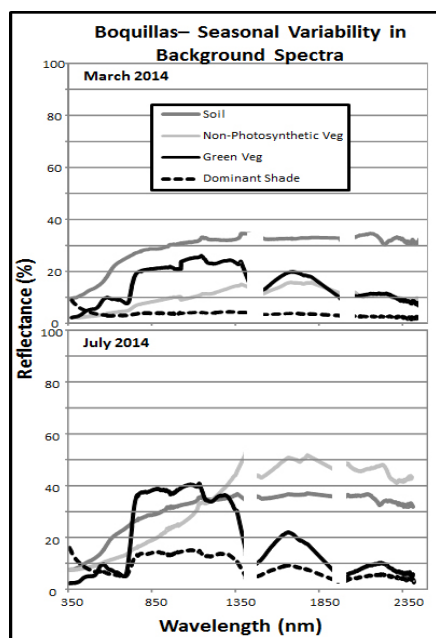


Figure 5. Spectra of the seasonal variability of background materials at Boquillas. March is a towards the end of the “dry” season and July is during the monsoon (wet) season.

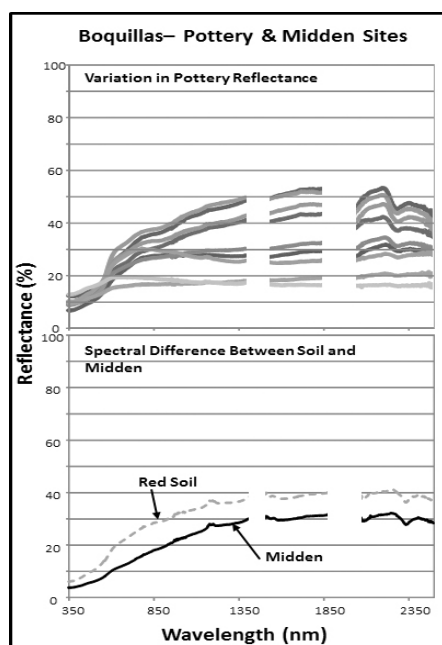


Figure 6. Spectra of the variability of pottery, soil, and midden of Boquillas. VIS-SWIR spectra of the pottery is highly variable. These pottery spectra include differently painted pot sherds as well as unpainted utility ware.

So far, 22 8m^2 sites have been located, gridded, with artifacts field verified in detailed photographs (Figure 7). Subsequent surficial exposed artifact counts have recently begun and counts made so far are summarized in Table 2.

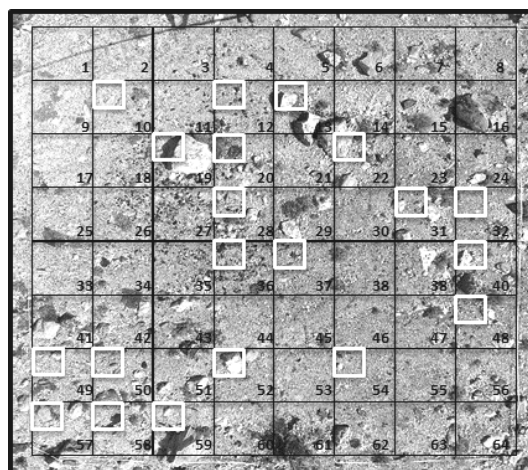


Figure 7. Example of the field sampling for detailed artifact counts in an 8X8 meter area. The white boxes are the 20 0.25m^2 areas measured in detail in the field and range from 0% obsidian to 28.2% obsidian.

Table 2. Summary of artifact counts to date.

Site	Glass Mtn, CA	Boquillas, AZ
# of 8m^2 Sites	14	8
# of 50cm^2 Sample Areas	280	160
# of Sample Areas Counted	20	20
% Coverage Range	0 – 55	0 – 18 (pottery) 0 – 34 (midden)

5. NEXT STEPS

This paper summarizes the first 10 months of work on this three year project. The first year has focused on initial field locations and site data collection. The next two years will include the following:

- 1) Continue field seasonal measurements at each site and complete determination of artifact coverage in each site using the field-verified photographs.
- 2) This next year, thermal measurements will begin with field samples measured in the laboratory using JPL's 520P Nicolet Fourier Transform Spectrometer with a Labsphere RSA-N1-700D integrating sphere.
- 3) Begin MASTER data calibration and georectification. Then, field (VIS-SWIR) and laboratory (TIR) spectra collected from field samples will be used to model the image data using spectral mixture analysis (Adams et al. 1993). This will give us the fractional spatial

exposure of the major components in the scene. In cases where the fraction of the artifacts is very low, the band residuals will be evaluated. The resultant fractions will be compared to our field measurements and fractional exposure determined from field photos to determine model accuracy.

- 4) Produce maps: a) detectable artifacts in MASTER scenes, and b) map areas in the MASTER scenes where different artifacts would be detectable given the background composition determined from the spectral mixture modeling.

6. ACKNOWLEDGMENTS

This study is funded by the NASA Space Archaeology program, NASA award #NNX12AP66G.

7. REFERENCES

- Adams, J.B., Smith, M.O., and Gillespie, A.R., 1993, A mixing-model strategy for analyzing and interpreting hyperspectral images. In C.M. Pieters and P.J. Englert, *eds.*, *Remote Geochemical Analysis: Elemental and Mineralogical Composition*, Cambridge University Press/Lunar and Planetary Institute, Cambridge.
- Buck, P.E., D.E. Sabol, and A.R. Gillespie (2003), Sub-pixel artifact detection using remote sensing. *Jour. Archaeological Science* 30 (2003) 973-989.
- Doelle, William (2011). Personal communication.
- Dunnell, R.C. and W.S. Dancey (1983), The siteless survey: a regional scale data collection strategy. In (M.B. Schiffer, ed.) *Advances in Archaeological Method and Theory* 6: 267-287. Academic Press: New York.
- Eichelberger, John C. (1981). Mechanism of magma Mixing at Glass Mountain, Medicine Lake Highland Volcano, California.
- Gillespie, A.R., Smith, M.O., Adams, J.B., Willis, S.C., Fischer, A.F. III, and Sabol, D.E., (1990). Interpretation of residual images: Spectral mixture analysis of AVIRIS images, Owens Valley, California, *Proc. Airborne Sci. Workshop: AVIRIS*, Jet Propulsion Laboratory, Pasadena, CA. 4-5 June, 243-270.
- Gillespie, A.R. (1992). Spectral mixture analysis of multispectral thermal infrared images. *Remote Sensing of the Environment* 42:137-145.
- Johnson, B.R. (1998) In-scene atmospheric compensation: application to the SEBASS data collected at the ARM site, Part I.
- Krotkov, N.A., Carn, S.A., Krueger, A.J., Bhartia, P.K., and Yang, K., (2006) Band residual difference algorithm for retrieval of SO₂ from the Aura Ozone Monitoring Instrument (OMI), *IEEE Trans Geosci. and Remote Sens.*, v.44, no.5.
- Sabol, D.E., J.B. Adams & M.O. Smith (1992). Quantitative sub pixel spectral detection of targets in multispectral images. *Journal of Geophysical Research* 97-E2: 2659-2672.
- Young, S. J., Johnson, B. R., Hackwell, J. A., (2002) An in-scene method for atmospheric compensation of thermal hyperspectral data. *Journal of Geophysical Research*, 107(D24), 4774.

Determination of the cloud radiative forcing and its relationship with the properties of clouds in the Iberian Peninsula

Freile-Aranda M.D.⁽¹⁾, Gómez-Amo J.L.⁽¹⁾⁽²⁾, Utrillas M.P.⁽¹⁾, Martínez-Lozano J.A.⁽¹⁾

(1) Departamento de Física de la Tierra y Termodinámica, Universidad de Valencia, Tel: 96 3543255, Fax: 96 3543385

(2) Laboratory for Earth Observations and Analyses, ENEA, Rome

M.Dolores.Freile@uv.es, Jose.L.Gomez-Amo@uv.es, Maria.P.Utrillas@uv.es, Jose.A.Martinez@uv.es

ABSTRACT- Clouds affect the propagation of the radiation in the atmosphere and, accordingly, they alter the Earth climate. They act scattering and absorbing solar and thermal radiation, making them play an important role in the Earth radiation budget. The magnitude used to quantify how much do clouds modify the radiation budget in the Earth-atmosphere system is the cloud radiative forcing (CRF), defined as the difference between the net flux in all sky and clear sky conditions. The aim of this work is to study the CRF at surface and at the top of the atmosphere (TOA), and its sensitivity to some of the properties of clouds, as cloud effective temperature or cloud visible optical depth, taking into account different cloud types. To avoid possible dependences on the solar zenith angle or the surface albedo, we will use the normalized cloud radiative forcing (NCRF), which is the CRF normalized to the net radiation flux on clear sky conditions. Shortwave and longwave spectral regions are considered. Daily products produced by CERES instrument, on board of Terra and Aqua satellites, has been used with a $1^\circ \times 1^\circ$ spatial resolution covering from March 2000 to December 2013. The selected region for this work is the Iberian Peninsula, which latitude goes from 44°N to 36°N and with a longitude between 10°W and 4°E . As expected, the effect of clouds on the radiation is not the same depending if we talk about the shortwave or longwave spectral region. Furthermore, the sensitivity of NCRF to the clouds properties will not be the same for surface and TOA. At surface, considering low clouds, the NCRF_{LW} changes by a 20% when the cloud effective temperature varies from 260K to 290K. In turn, changes in the liquid water path cause an increase of the NCRF_{SW} up to a 40%. These two effects are lower at the top of the atmosphere, as happens with high clouds too.

1 INTRODUCTION

Clouds have an important role on the Earth radiative energy balance. They modulate the solar radiative heating and the Earth thermal cooling, having an impact on weather and climate (Cheng et al., 2000). In addition, the cloud-radiation interaction depends on the cloud type and properties. Some studies show how the clouds effect on radiation changes with the cloud type considered (Cheng et al., 2000) or with cloud properties (Shupe et al, 2003).

Clouds act on the Earth radiative budget in two different ways. At shortwave they cool the system, while at longwave they heat it. The overall effect of clouds is of cooling. But when different cloud types are studied, this is not always accomplished, as it happens with cirrus (Cheng et al., 2000).

The cloud radiative impact is usually quantified by the cloud radiative forcing (CRF), defined as the difference between all-sky and clear-sky conditions. Another magnitude used is the normalized cloud radiative forcing (NCRF), obtained by normalizing the cloud radiative forcing to the net clear-sky flux.

Using satellite data produced by CERES, we derive the normalized cloud radiative forcing (NCRF) at surface and at the top of the atmosphere. Then, we

analyse the NCRF sensitivity according to different cloud properties at two different cloud types (low and high clouds). Longwave (5-100 μm) and shortwave (0.3-5 μm) spectral regions are studied separately.

As a preliminary study, we have work with the most important properties on each situation, although those are not the only ones that have influence on the NCRF. The Gaussian process regression (Lazaro-Gredilla et al., 2014; Verrelst et al., 2012) is used to know which of the cloud properties has to be studied.

2 DATA

Level 3 CERES daily product have been used, CERES_SYN1deg_Day Ed3A (Wielicki et al., 1996), from March of 2000 to December of 2012. Surface and TOA fluxes in longwave and shortwave spectral ranges and different cloud properties corresponding to different cloud types have been analysed in this study.

Table 1 – Definition of cloud types (1mb = 10^2Pa).

CLOUD LAYER	PRESSURE LEVEL (mb)	CLOUD HEIGHT (m)
HIGH	300 - 70	10000-13000
MID-HIGH	500 - 300	6000-10000
MID-LOW	700 - 500	3000-6000
LOW	Surface - 700	500-3000

The following cloud properties are chosen for the analysis: cloud effective temperature (CET), cloud visible optical depth (CVOD), liquid water path (LWP) and ice water path (IWP). Cloud area fraction (CAF) is also used.

The Level 3 CERES data are gridded with a $1^\circ \times 1^\circ$ (latitude \times longitude) spatial resolution covering the whole Iberian Peninsula between latitudes of 36°N to 44°N and longitudes from 10°W to 4°E (Fig. 9 and 10). Then a mask is used to avoid, when possible, ocean pixels.

3 METHODOLOGY

Cloud radiative forcing is obtained as the difference between the net radiation fluxes in all-sky and clear-sky conditions. At surface, the downward (F^\downarrow) and upward (F^\uparrow) fluxes are used. At TOA, only upward fluxes are considered. This way, to calculate the cloud radiative forcing, equation (1) is applied on each situation.

$$CRF = (F^\downarrow - F^\uparrow)^{all} - (F^\downarrow - F^\uparrow)^{clear} \quad (1)$$

Where the superscripts all and clear mean all-sky and clear-sky.

Sometimes, it is useful to normalize the cloud radiative forcing using the clear-sky net radiation. This procedure avoids possible dependences with the surface albedo or the solar zenith angle (Costa et al., 2000). To better compare the longwave and shortwave spectral regions, we use the absolute value of the normalized cloud radiative forcing.

$$NCRF = \frac{CRF}{(F^\downarrow - F^\uparrow)^{clear}} \quad (2)$$

We have to ensure that the normalized cloud radiative forcing belongs to the cloud type studied. To do this we have used the cloud area fraction. Pixels with a high cloud area fraction at the cloud type considered and with a low cloud area fraction at the other types have been selected.

We have used the Gaussian process regression (GPR), a non-linear regression model, to focus on the most relevant cloud properties on each case.

4 RESULTS

The GPR analysis reveals that the cloud effective temperature and the cloud optical depth are the most important cloud parameters that influence the longwave radiation. On the other hand, the liquid water path and the ice water path have affected mainly to the shortwave radiation.

In Figures 1 to 8 it is shown the NCRF in terms of the selected cloud properties. The average values and one standard deviation of NCRF are calculated at equal intervals of each evaluated property.

4.1 LOW CLOUDS (Fig. 1 to 4):

The cloud radiative forcing increases with the difference of temperature between the cloud and the surface. At surface, an increase of 30 K in the cloud effective temperature results in a decrease of $NCRF_{LW}$ from 55% to 35%. Therefore, the $NCRF_{LW}$ is lower when the cloud effective temperature gets closer to the surface temperature. The $NCRF_{LW}$ at the top of the atmosphere presents little dependency on cloud effective temperature and it is much lower than at surface (Fig.2). From the top of the atmosphere, the low clouds have similar temperature than the surface, resulting in a similar longwave fluxes in all-sky and clear-sky conditions. Consequently, the $NCRF_{LW}$ will be low.

In the shortwave, the cloud radiative forcing presents a notable sensitivity to the liquid water path. The impact that the liquid water path has on the $NCRF_{SW}$ is higher at surface than at the top of the atmosphere. In both situations, when the liquid water path reaches the 80 g/m^2 , the $NCRF_{SW}$ stabilizes and becomes less sensitive to this property.

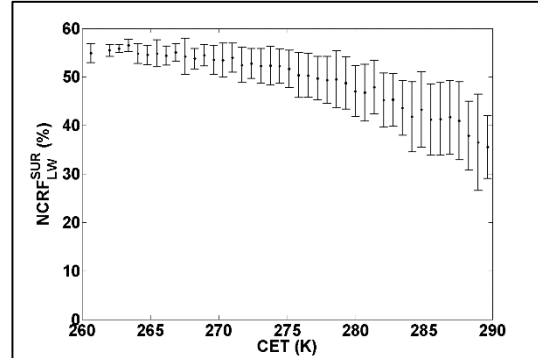


Figure 1: $NCRF_{LW}$ at surface as a function of the cloud effective temperature for low clouds.

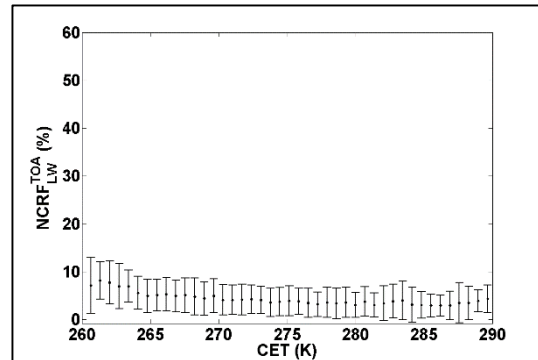


Figure 2: $NCRF_{LW}$ at TOA as a function of cloud effective temperature for low clouds.

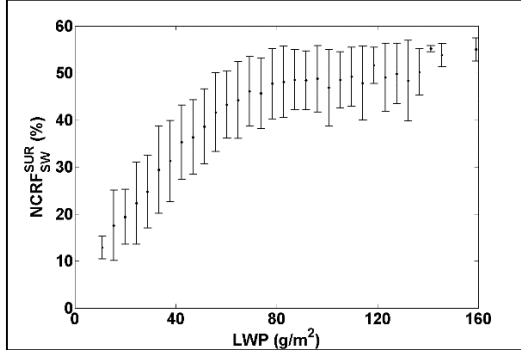


Figure 3: NCRFSW at surface as a function of liquid water path for low clouds.

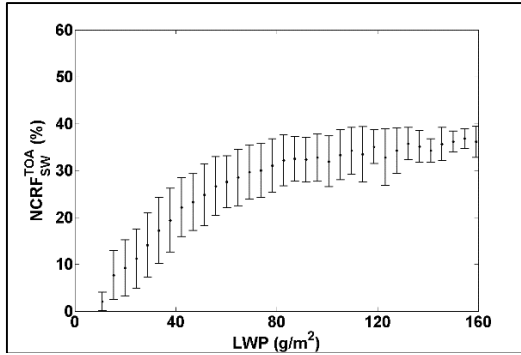


Figure 4: NCRFSW at TOA as a function of liquid water path for low clouds.

4.2 HIGH CLOUDS (Fig. 5 to 8):

Changes in the NCRFLW caused by the cloud optical depth at surface are more important than at the top of the atmosphere. As expected, thicker clouds (high COD) cause an increase in the NCRFLW values. When the cloud optical depth reaches 30 and 15, the NCRF stabilizes at a value of 45% and 38%, at surface and TOA, respectively.

The ice water path produces important variations in the NCRFSW at surface. The NCRFSW changes by a 40% for an ice water path variation between 15 g/m² and 215 g/m². For the same ice water path variation, the NCRFSW alters about a 20% at top of the atmosphere.

5 CONCLUSIONS

We have studied the variations that the cloud properties produce on the NCRF at surface and at the top of the atmosphere using CERES data collected during a 13-year period, between March of 2000 and December of 2012. From the Gaussian process regression, we have identified what cloud properties have a larger impact on NCRF at both, surface and TOA, taking into account the longwave and shortwave

spectral range. The results show that the parameters with more influence on the NCRFLW are the cloud effective temperature and the cloud optical depth, producing changes on the NCRFLW up to 20% and 30%, respectively. However, on the SW the most important parameters are the liquid water path and the ice water path, which increase the NCRFSW by a 40%.

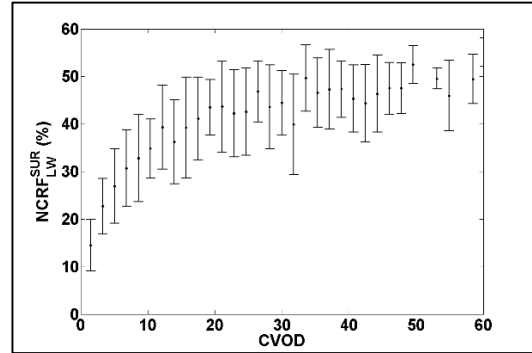


Figure 5: NCRFLW at surface as a function of cloud visible optical depth for high clouds.

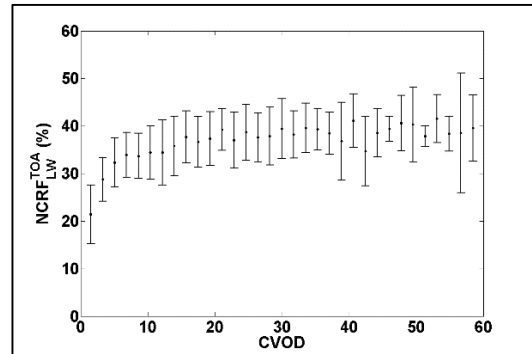


Figure 6: NCRFLW at TOA as a function of cloud visible optical depth for high clouds.

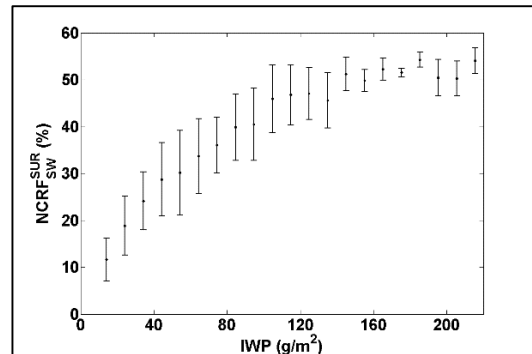


Figure 7: NCRFSW at surface as a function of ice water path for high clouds.

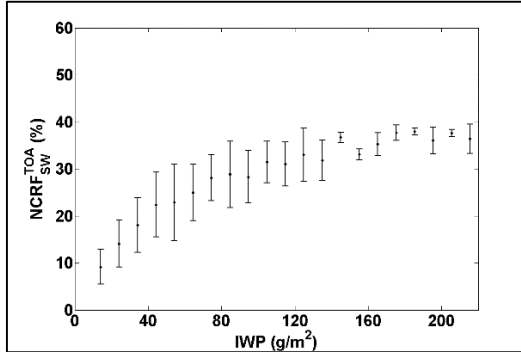


Figure 8: NCRF_{sw} at TOA as a function of ice water path for high clouds.

Thus, we can conclude that cloud properties have a large influence on the cloud radiative forcing. They may enhance or reduce the cooling or heating effects clouds have on surface or on the top of the atmosphere. Also, depending on the spectral regions we focus on, the property with more influence on cloud radiative forcing is different. As an extended and more thorough work, dependences between NCRF and the cloud properties not shown here can be also studied for a better understanding of clouds-radiation interaction.

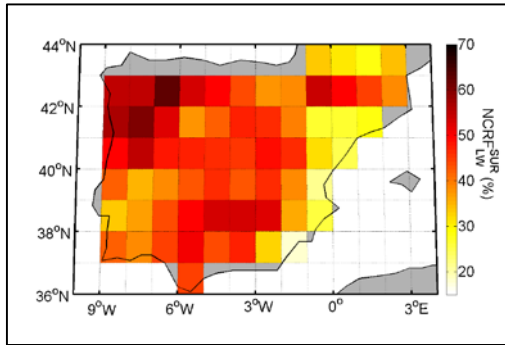


Figure 9: Daily mean of NCRF_{sw} at surface in the Iberian Peninsula (04/05/2012).

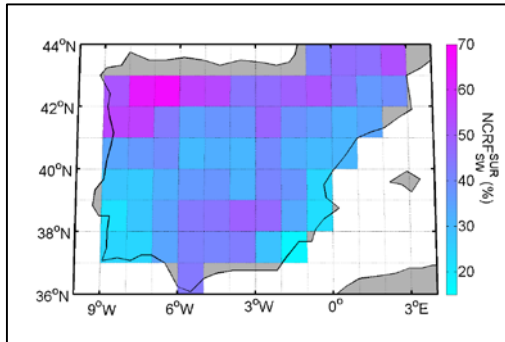


Figure 10: Daily mean of NCRF_{sw} at surface in the Iberian Peninsula (04/05/2012).

ACKNOWLEDGMENT

This work was financed jointly by the Spanish Ministry of Economy and Competitiveness and the European Regional Development Fund through projects CGL2011-24290 and CGL2012-33294, and by the Valencia Autonomous Government through projects PROMETEUII/2014/058 and ACOMP/2013/205. The CERES data were obtained from the Atmospheric Science Data Center at the NASA Langley Research Center.

REFERENCES

- Costa, M. J., Salgueiro, V., Santos, D., Bortoli, D., Silva, A. M. and Salgado, R. (2013). Surface cloud radiative forcing in the south of Portugal. *International Radiation Symposium: Radiation Processes in the Atmosphere and Ocean, IRS 2012*, Berlin, , 1531 684-687.
- Lazaro-Gredilla, M., Titsias, M. K., Verrelst, J. and Camps-Valls, G., 2014, Retrieval of biophysical parameters with heteroscedastic gaussian processes. *IEEE Geoscience and Remote Sensing Letters*, 11(4), 838-842.
- Shupe, M. D. and Intrieri, J. M., 2004, Cloud radiative forcing of the arctic surface: the influence of cloud properties, surface albedo, and solar zenith angle. *J. Climate*, 17, 616–628.
- Verrelst, J., Alonso, L., Camps-Valls, G., Delegido, J. and Moreno, J., 2012, Retrieval of vegetation biophysical parameters using gaussian process techniques. *IEEE Transactions on Geoscience and Remote Sensing*, 50(5), 1832-1843.
- Wielicki, B.A., Barkstrom, B.R., Harrison, E.F., Lee III, R.B., Smith, G.L. and Cooper, J.E., 1996, Clouds and the Earth's Radiant Energy System (CERES): An Earth Observing System Experiment, *Bull. Amer. Meteor. Soc.*, 77, 853-868.

Assessment of CALIOP level 2 daytime data during Saharan dust outbreaks in Southern Europe

Carlos Marcos (1), José L. Gómez-Amo (1,2), Roberto Pedrós (1), M^a Pilar Utrillas (1), J. Antonio Martínez-Lozano (1)

(1) Solar Radiation Group, Department of Earth Physics and Thermodynamics, University of Valencia, Spain

(2) Laboratory for Earth Observations and Analyses, ENEA, Italy

Email: Carlos.Marcos@uv.es

ABSTRACT- Saharan dust outbreaks are one of the major aerosol sources in Southern Europe, affecting the radiative balance and also being related to health problems. To improve our estimations on the effect of these events, information about the vertical distribution of dust in the atmosphere is needed. This kind of information is usually obtained through ground-based lidar measurements; however, these are only available at a limited number of locations. Because of this, spatially spread data provided by the satellite-based CALIOP lidar is especially valuable for the study of these events. In order to retrieve physical parameters such as aerosol extinction and backscattering coefficients, CALIOP level 1 data is processed by a series of algorithms which detect atmospheric features, separate them between clouds and aerosols, and classify these aerosols as one in six different subtypes, associated to a certain lidar ratio later used in the inversion of the data. The performance of these algorithms, however, can be limited by several factors, especially in the presence of background solar radiation. In this work we have analysed the retrievals of CALIOP algorithms during dust outbreaks over Southern Europe in a total of 23 cases, which have been selected using ground-based measurements and modelled air back-trajectory analysis. We observed that CALIOP level 2 aerosol optical depth is, on average, 50% lower than the aerosol optical depth measured by ground-based photometers. This discrepancy was found to be mainly caused by the misclassification of dust layers as clouds or clear sky by CALIOP algorithms.

1 INTRODUCTION

Southern Europe is frequently affected by dust outbreaks arriving from Northern Africa (e.g. Hamonou, 1999; Gobbi, 2004; Toledano, 2007; Papayannis, 2008; Gkikas, 2013). These events affect the earth-atmosphere radiative balance and are also associated to an increase in the concentration of particulate matter at ground level, which is linked to health issues (e.g. Rodríguez, 2001). In order to get a better understanding of the impact of these events, measurements of the vertical distribution of dust, like the ones performed by ground-based lidars (e.g. Papayannis, 2008), are needed. These measurements; however, are not available in most locations. Because of this, data from the satellite-based Cloud-Aerosol Lidar with Orthogonal Polarization (CALIOP) is especially valuable.

The CALIOP lidar, on board the Cloud-Aerosol Lidar and Infrared Pathfinder (CALPSO) platform, is a two-wavelength lidar elastic lidar operating at 532 and 1024nm, being the 532nm channel polarization sensitive (Winker, 2009). In order to retrieve physical parameters such as aerosol extinction and backscattering coefficients, CALIOP measurements are consecutively processed by a series of algorithms: first, the different features present in the atmosphere are detected at three different resolutions: 5, 20 and 80 km (Vaughan, 2009); second, these features are

separated between aerosols and clouds (Liu, 2009); and third, aerosol features are classified into 6 aerosol sub-types, corresponding to different values of lidar ratio, which are used for the inversion of the lidar signal (Omar, 2009; Young and Vaughan, 2009).

However, the performance of these algorithms can be affected by different factors when analysing dust aerosols. First, dense dust layers can be misclassified as clouds since they both can backscatter large amounts of signal in a similar spectral way (e.g. Liu, 2009; Naeger, 2013). Also, the lidar ratio associated to dust by CALIOP algorithms, 40sr, might be underestimated when dealing with Saharan dust (Schuster, 2012; Amaridis, 2013) and multiple-scattering effects (Wandinger, 2010). Finally, signal extinction caused by elevated dust layers reduces the signal-to-noise ratio in the lower altitudes, which might affect the detection of weaker lower layers. This limitation is even bigger during daytime cases, where the presence of solar background radiation already affects the aerosol detection ability of algorithms (Omar, 2013).

In this work we evaluate the performance of CALIOP algorithms during Saharan dust outbreaks happening over Southern Europe. First, we compare the aerosol optical depth values retrieved by CALIOP algorithms against ground-based measurements for 23 daytime cases distributed through Southern Europe.

Then, we relate the results of this comparison to the ability of CALIOP algorithms to correctly identify aerosols, with the help of aerosol extinction profiles obtained from the combination of CALIOP level 1 data and ground-based measurements.

2 DATA AND METHODS

In section 2.1, we describe the main datasets used in this work: CALIOP level 2 version 3 aerosol extinction coefficients, CALIOP level 1 version 3 total attenuated backscatter, and AERONET aerosol optical depth and Angstrom exponent. In section 2.2 we define the conditions for the selection of dust cases. In section 2.3, we describe the selection of CALIOP data for each case, and the cloud-screening process. Then, in section 2.4, the procedure for the combination of CALIOP level 1 and ground-based data is presented. Finally, in section 2.5 we show a summary of the available cases.

2.1 Experimental dataset

The aerosol extinction coefficient (σ) is offered in CALIOP level 2 data catalogue. It has a horizontal resolution of 5km, and a vertical resolution of 60m. Since this parameter cannot be directly compared to ground-based photometer measurements, σ is integrated for the whole profile to obtain the aerosol optical depth (AOD).

The total attenuated backscatter (β') is the main product in CALIOP level 1 catalogue (Hunt, 2009). For a certain altitude h , β' is defined as the backscattered signal by molecules, aerosols and clouds at that altitude, doubly attenuated by the atmospheric components between CALIOP and h . The horizontal resolution of β' is 333m, and its vertical resolution is 30m. In this work, we use this product as a reference for the selection of CALIOP level 2 data (see section 2.3). Also, β' is used in combination with ground-based measurements for the retrieval of aerosol extinction profiles, (see section 2.4).

Finally, we have also used ground-based measurements from photometers of the Aerosol Robotic Network (AERONET) to obtain three parameters: the aerosol optical depth at 532 nm (AOD_{532}), the aerosol optical depth at 870 nm (AOD_{870}) and the Angström exponent between 870 and 440nm (α). The AOD_{532} is used to evaluate CALIOP aerosol extinction retrievals, and also to obtain aerosol extinction profiles in combination with CALIOP level 1 data. Since most AERONET sites do not perform measurements at 532nm, the AOD at this wavelength is estimated as described by Eck et al. (1999). Finally, the last two parameters, AOD_{870} and α , are used to identify cases corresponding to dust outbreaks (see section 2.2).

2.2 Selection of dust cases

The selection of cases corresponding to desert dust outbreaks is based in 3 conditions:

- 1) The mean AOD_{870} and α averaged within 1 one hour centered on CALIOP overpass must be greater than 0.11 and lower than 0.8 respectively. These thresholds are based on the results obtained by Toledano et al. 2007; restricted by 30% to avoid false-positives.

- 2) CALIPSO overpass must be closer than 25km to an AERONET site to reduce the effect of aerosol spatial variability.

- 3) Air-masses arriving to a certain AERONET site must have travelled over Northern Africa anytime in the previous 6-day period to CALIPSO overpass. This condition is checked using the HYSPLIT model (Draxler and Hess, 1998).

2.3 Selection of CALIOP data and cloud-screening

For each case classified as dust outbreak, we select all CALIOP level 1 and level 2 profiles within a radius of 70km from its corresponding AERONET site. First, we use β' profiles, in combination with MODIS Aqua real-color images, to detect the presence of clouds, usually characterized by sharp changes in the backscattered signal. Then, the cloudy level 1 profiles, as well as their corresponding level 2 profiles, are discarded. Finally, once the cloudy profiles have been removed, the CALIOP level 2 AOD is calculated as the mean AOD of the remaining cloud-free profiles. By using this cloud-screening procedure, and not the level 2 Cloud-Aerosol discriminator product (Liu, 2009), we avoid potential misclassification of dust as clouds by CALIOP algorithms, which would result in the loss of valuable cases.

2.4 Combination of CALIOP and AERONET data

The combination of CALIOP level 1 β' profiles with ground-based values of AOD with the Fernald-Klett-Sasano method (Klett, 1981; Fernald, 1984; Sasano, 1985) allow us to obtain aerosol extinction profiles and mean lidar ratio values associated to them for each case. These lidar ratio values can be compared with those obtained from CALIOP level 2 data in order to evaluate to what extent this parameter is associated to biases in the retrieval of the AOD (see section 3.1). Also, the aerosol extinction profiles obtained with this method are an indicator of the presence of relevant aerosol layers, and can be used to evaluate and quantify the misclassification of aerosols as clouds or clear sky features (see section 3.2)

2.5 Available cases

A total of 23 cases were found to meet the conditions required in section 2.2 between July 2006 and January

2014. These cases were distributed mainly through the Iberian Peninsula, Southern France and Italy, with no available cases found for Eastern Mediterranean (Fig. 1). Most of these 23 cases were found in summer (18), a few in spring (4), and only one in winter.

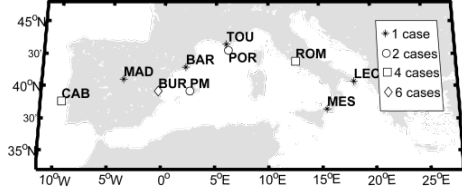


Fig. 1 Geographical distribution of the available cases, corresponding to the AERONET sites of Cabo da Roca (CAB), Madrid (MAD), Burjassot (BUR), Barcelona (BAR), Palma (PM), Toulon (TOU), Porquerolles (POR), Rome (ROM), Messina (MES) and Lecce (LEC).

3 RESULTS

In section 3.1 we present the evaluation of CALIOP level 2 AOD, in a comparison with ground-based measurements. Also, a brief analysis of the values of the lidar ratio is made. Then, in section 3.2 we quantify the effect that aerosol misclassification has on the retrieved AOD values.

3.1 Evaluation of level 2 AOD

We found that CALIOP level 2 AOD values are, on average, around 50% lower than the ones measured by ground-based photometers. While the mean AOD retrieved by CALIOP algorithms is 0.18, the mean value measured by ground-based photometers is 0.33. Moreover, we found little correlation ($R = 0.18$) between both datasets (Fig. 2).

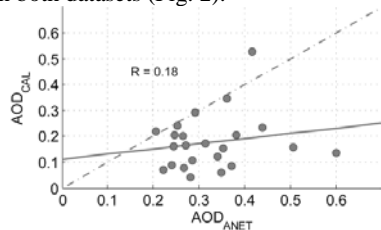


Fig. 2 CALIOP level 2 AOD (y axis) against AERONET AOD (x axis). The thicker line represents the linear fit ($y = 0.20x + 0.11$), while the thin dashed line is the 1:1 line, shown as reference.

An analysis of the CALIOP level 2 lidar ratio values reveals that all cases range between 39 and 51sr, with a mean value of 41sr. This mean lidar ratio value is a result of the aerosol classification made by CALIOP algorithms, which have identified the large majority of aerosols as dust, associated to a lidar ratio of 40sr. With regard to the results obtained from the

combination of CALIOP level 1 and AERONET data, we found a mean lidar ratio of 49, which is around 15% higher than the value given by CALIOP algorithms. Although the differences in the lidar ratio are noticeable, these are not big enough to explain the discrepancies found in the AOD.

3.2 Effect of aerosol misclassification

In order to quantify the effect of aerosol misclassification, we have calculated for each case the fraction of atmospheric features classified as aerosols by CALIOP algorithms, n_{aer} , as:

$$n_{aer} = \frac{\sum_{i=1}^{N_p} \sum_{j=1}^{N_h} [\delta(t_{i,h(j)}, aer) \cdot H(\sigma_{h(j)}^{L1+A} - 0.025 \text{ km}^{-1})]}{N_p N_h} \quad (1)$$

Where N_p is the number of cloud-free selected level 2 profiles; N_h is the number of bins per profile; $t_{i,h(j)}$ is the feature type (aerosol, cloud or clear sky) at profile i and altitude $h(j)$; and $\sigma_{h(j)}^{L1+A}$ is the aerosol extinction coefficient at an altitude $h(j)$ retrieved from the combination of CALIOP level 1 and AERONET data. The function δ is equal to 0, and becomes one when the feature $t_{i,j}$ has been classified as aerosol, while the function H is zero unless $\sigma_{h(j)}^{L1+A}$ is greater than 0.025 km^{-1} , when it becomes equal to one. This last condition is added since we only want to estimate the n_{aer} parameter in those zones above the CALIOP estimated detection threshold (Sheridan, 2012).

If we compare n_{aer} against the relative differences in the AOD obtained from CALIOP level 2 and AERONET data (ΔAOD), we find that these two parameters are strongly correlated, with $R = 0.85$ (Fig. 3). Nevertheless, there are two cases that show a different behaviour from the general trend, although a detailed analysis (not shown in this work) reveals that they are likely to be caused by inversion artefacts from CALIOP algorithms. These results indicate that, from the 21 available cases not affected by inversion artefacts, the main cause of discrepancy in the AOD is the misclassification of dust aerosols as clouds or clear sky features.

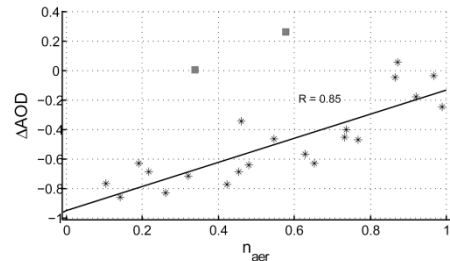


Fig. 3 Comparison between the n_{aer} parameter, defined in Eq. (1), and the relative difference in the AOD obtained from CALIOP level 2 and AERONET data (ΔAOD). Cases corresponding to inversion artefacts are shown with squares, and have not been taken into consideration for the linear fit.

CONCLUSIONS

In this work we have evaluated CALIOP level 2 aerosol optical depth (AOD) retrievals during dust outbreaks happening over Southern Europe. For a total of 23 daytime cases, we observed that CALIOP level 2 AOD was, on average, around 50% lower than the AOD measured by ground-based AERONET photometers (0.18 vs 0.33). With regard to the lidar ratio, the values obtained from CALIOP level 2 data were found to be, on average, lower than the ones obtained from the combination of CALIOP level 1 and AERONET data (41sr vs 49sr). However, these differences in the lidar ratio values, around 15%, were not large enough to explain the great differences found in the comparison of the AOD values.

With the help of aerosol extinction profiles obtained from the combination of CALIOP level 1 and AERONET data, we defined a parameter, n_{aer} , which accounted for the relative number of atmospheric features correctly classified as aerosols. We observed that the n_{aer} parameter and the relative differences in the AOD were strongly correlated. These results lead us to conclude that, for the studied events, aerosol misclassification by CALIOP algorithms is the major cause of error in the retrieval of AOD values.

ACKNOWLEDGEMENTS

The authors would like to acknowledge CALIPSO team for providing CALIOP data, which has been obtained from the NASA Langley Research Center Atmospheric Science Data Center. Also, we would like to thank the operators and investigators responsible for the AERONET sites of Barcelona, Burjassot, Cabo da Roca, Lecce, Madrid, Messina, Palma de Mallorca, Porquerolles, Rome and Toulon. This work was financed jointly by the Spanish Ministry of Economy and Competitiveness and the European Regional Development Fund through projects CGL2011-24290 and CGL2012-33294. The collaboration of J.L. Gómez-Amo was possible thanks to a postdoctoral fellowship of Spanish Ministry of Education (EX2010-1192). The collaboration of C. Marcos was possible thanks to the program: Ajudes per a la formació del personal investigador de caràcter predoctoral, en el marc del subprogram "Atracció del talent" de VLC-Campus.

REFERENCES

- Amiridis, V., Wandinger, U., Marinou, E., Giannakaki, E., Tsekeri, A., Basart, S., Kazadzis, S., Gkikas, A., Taylor, M., Baldasano, J., and Ansmann, A., 2013, Optimizing CALIPSO Saharan dust retrievals, *Atmos. Chem. Phys.*, 13, 12089-12106, doi:10.5194/acp-13-12089-2013.
- Draxler, R.R., and G.D. Hess, 1998: An overview of the HYSPLIT_4 modeling system of trajectories, dispersion, and deposition. *Aust. Meteor. Mag.*, 47, 295-308.
- Eck, T. F., B. N. Holben, J. S. Reid, O. Dubovik, A. Smirnov, N. T. O'Neill, I. Slutsker, and S. Kinne 1999, Wavelength dependence of the optical depth of biomass burning, urban, and desert dust aerosols, *J. Geophys. Res.*, 104(D24), 31333–31349, doi:10.1029/1999JD900923.
- Fernald, F., 1984: Analysis of atmospheric lidar observations: some comments, *Appl. Opt.* 23, 652-653
- Gkikas, A., Hatzianastassiou, N., Mihalopoulos, N., Katsoulis, V., Kazadzis, S., Pey, J., Querol, X., and Torres, O, 2013, The regime of intense desert dust episodes in the Mediterranean based on contemporary satellite observations and ground measurements, *Atmos. Chem. Phys.*, 13, 12135-12154, doi:10.5194/acp-13-12135-2013.
- Gobbi, G. P., Barnaba, F., and Ammannato, L., 2004, The vertical distribution of aerosols, Saharan dust and cirrus clouds in Rome (Italy) in the year 2001, *Atmos. Chem. Phys.*, 4, 351-359, doi:10.5194/acp-4-351-2004
- Hamonou, E., P. Chazette, D. Balis, F. Dulac, X. Schneider, E. Galani, G. Ancellet, and A. Papayannis, 1999, Characterization of the vertical structure of Saharan dust export to the Mediterranean basin, *J. Geophys. Res.*, 104(D18), 22257–22270, doi:10.1029/1999JD900257.
- Hunt, W. H., D. M. Winker, M. A. Vaughan, K. A. Powell, P. L. Luckey, and C. Weimer, 2009: CALIPSO Lidar Description and Performance Assessment. *J. Atmos. Oceanic Technol.*, 26, 1214–1228.
- Klett, J., 1981: Stable analytical inversion solution for processing lidar returns, *Appl. Opt.* 20, 211-220
- Liu, Z., M. Vaughan, D. Winker, C. Kittaka, B. Getzewich, R. Kuehn, A. Omar, K. Powell, C. Trepte, and C. Hostetler, 2009: The CALIPSO Lidar Cloud and Aerosol Discrimination: Version 2 Algorithm and Initial Assessment of Performance. *J. Atmos. Oceanic Technol.*, 26, 1198–1213. doi: http://dx.doi.org/10.1175/2009JTECHA1229.1
- Naeger, A.R.; Christopher, S.A.; Ferrare, R.; Zhaoyan Liu, "A New Technique Using Infrared Satellite Measurements to Improve the Accuracy of the CALIPSO Cloud-Aerosol Discrimination Method," *Geoscience and Remote Sensing, IEEE Transactions on*, vol.51, no.1, pp.642,653, Jan. 2013 doi: 10.1109/TGRS.2012.2201161

- Omar, A. H., D. M. Winker, M. A. Vaughan, Y. Hu, C. R. Trepte, R. A. Ferrare, K.-P. Lee, C. A. Hostetler, C. Kittaka, R. R. Rogers, R. E. Kuehn, and Z. Liu, 2009, The CALIPSO Automated Aerosol Classification and Lidar Ratio Selection Algorithm. *J. Atmos. Oceanic Technol.*, 26, 1994–2014. doi: <http://dx.doi.org/10.1175/2009JTECHA1231.1>
- Omar, A. H., D. M. Winker, J. L. Tackett, D. M. Giles, J. Kar, Z. Liu, M. A. Vaughan, K. A. Powell, and C. R. Trepte, 2013, CALIOP and AERONET aerosol optical depth comparisons: One size fits none, *J. Geophys. Res. Atmos.*, 118, 4748–4766, doi:10.1002/jgrd.50330.
- Papayannis, A., et al., 2008, Systematic lidar observations of Saharan dust over Europe in the frame of EARLINET (2000–2002), *J. Geophys. Res.*, 113, D10204, doi:10.1029/2007JD009028.
- Rodríguez, S., X. Querol, A. Alastuey, G. Kallos, O. Kakaliagou, 2001, Saharan dust contributions to PM10 and TSP levels in Southern and Eastern Spain, *Atmospheric Environment*, Volume 35, Issue 14, May 2001, Pages 2433–2447, ISSN 1352-2310, [http://dx.doi.org/10.1016/S1352-2310\(00\)00496-9](http://dx.doi.org/10.1016/S1352-2310(00)00496-9)
- Sasano, Y., Browell, E.V. e Ismail, S., 1985: Error caused by using a constant extinction/backscattering ratio in the lidar solution. *Appl. Opt.* 24, 3929–3932
- Schuster, G. L., Vaughan, M., MacDonnell, D., Su, W., Winker, D., Dubovik, O., Lapyonok, T., and Trepte, C., 2012, Comparison of CALIPSO aerosol optical depth retrievals to AERONET measurements, and a climatology for the lidar ratio of dust, *Atmos. Chem. Phys.*, 12, 7431–7452, doi:10.5194/acp-12-7431-2012
- Sheridan, P. J., Andrews, E., Ogren, J. A., Tackett, J. L., and Winker, D. M., 2012, Vertical profiles of aerosol optical properties over central Illinois and comparison with surface and satellite measurements, *Atmos. Chem. Phys.*, 12, 11695–11721, doi:10.5194/acp-12-11695-2012
- Toledano, C., V. E. Cachorro, A. M. de Frutos, M. Sorribas, N. Prats, and B. A. de la Morena, 2007, Inventory of African desert dust events over the southwestern Iberian Peninsula in 2000–2005 with an AERONET Cimel Sun photometer, *J. Geophys. Res.*, 112, D21201, doi:10.1029/2006JD008307.
- Vaughan, M. A., K. A. Powell, D. M. Winker, C. A. H., R. E. Kuehn, W. H. Hunt, B. J. Getzewich, S. A. Young, Z. Liu, and M. J. McGill, 2009: Fully Automated Detection of Cloud and Aerosol Layers in the CALIPSO Lidar Measurements. *J. Atmos. Oceanic Technol.*, 26, 2034–2050. doi: <http://dx.doi.org/10.1175/2009JTECHA1228.1>
- Wandinger, U., M. Tesche, P. Seifert, A. Ansmann, D. Müller, and D. Althausen, 2010, Size matters: Influence of multiple scattering on CALIPSO light-extinction profiling in desert dust, *Geophys. Res. Lett.*, 37, L10801, doi:10.1029/2010GL042815.
- Winker, D. M., M. A. Vaughan, A. Omar, Y. Hu, K. A. Powell, Z. Liu, W. H. Hunt, and S. A. Young, 2009: Overview of the CALIPSO Mission and CALIOP Data Processing Algorithms. *J. Atmos. Oceanic Technol.*, 26, 2310–2323. doi: <http://dx.doi.org/10.1175/2009JTECHA1281.1>
- Young, S. A., and M. A. Vaughan, 2009: The Retrieval of Profiles of Particulate Extinction from Cloud-Aerosol Lidar Infrared Pathfinder Satellite Observations (CALIPSO) Data: Algorithm Description. *J. Atmos. Oceanic Technol.*, 26, 1105–1119. <http://dx.doi.org/10.1175/2008JTECHA1221.1>

Atmospheric correction effect on land surface temperatures derived from Landsat-7 ETM+ data

Maria Mira (1,2,3), Albert Oliso (1,2), Xavier Pons (3), Vincent Rivalland (4), Dominique Courault (1,2), Olivier Marloie (5), Pierre Guillevic (6)

(1) INRA, EMMAH – UMR 1114, 84914 Avignon, France

(2) Université d'Avignon et des Pays de Vaucluse, EMMAH - UMR 1114, Avignon, France

(3) Universitat Autònoma de Barcelona, Department of Geography, 08193 Bellaterra, Spain

(4) CESBIO UMR 5126 UPS, CNRS, CNES, IRD, F-31401, Toulouse, France

(5) INRA, URFM – UR629, 84914 Avignon, France

(6) Jet Propulsion Laboratory, 4800 Oak Grove Drive, Pasadena, CA 91109

maria.mira@avignon.inra.fr, oliso@avignon.inra.fr, xavier.pons@uab.cat,

vincent.rivalland@cesbio.cnes.fr, dominique.courault@avignon.inra.fr,

olivier.marloie@avignon.inra.fr, Pierre.C.Guillevic@jpl.nasa.gov

ABSTRACT - The impact of using non-coincident radiosoundings to remove atmosphere effect from thermal radiances was analyzed here. We considered 27 Landsat-7 ETM+ images (thermal band 10.4-12.5 μm ; 60 m) acquired over a Mediterranean agricultural region, benefiting from nearby radiosoundings launched almost 2 hours later, and from the availability of a network of ground stations deployed over different types of ecosystems. We observed that, in the conditions of our images, surface temperature estimates slightly improved when considering one atmospheric profile interpolated to our particular time and location, in comparison with the use of non-coincident radiosoundings. However, it may imply an error up to 2.5 K for brightness temperatures (in particular for very high temperatures and during summer when the atmosphere was warmer and the vapor pressure was higher), leading to important errors in the derivation of surface energy fluxes. The characterization of the lowest atmosphere layer appeared to be essential to improve the estimates of brightness temperatures. The error on surface temperature estimates using Landsat-7 data ($\text{RMSE}_A=1.7$ K; $\text{Bias}=0.5$ K) was within the range of observed uncertainties due to atmospheric correction (from 0.6 to 2.5 K).

1 INTRODUCTION

Measurement of surface temperature using remote sensing techniques allows assessing surface energy balance at various spatial scales (i.e., from satellite and airplane platforms or from hand-held thermal infrared radiometers). However, surface temperature cannot be directly derived from thermal measurements. Measured radiation includes not only the radiation emitted by the surface but also the radiation emitted by the atmosphere. Further the signal from the surface is attenuated by the transfer through the atmosphere. Correction of these atmospheric effects requires knowing the atmospheric profile in temperature (T_a) and vapor pressure (e_a) along the atmospheric path of the thermal infrared measurement. The difficulty to obtain atmospheric profile at the same time and at the same position than thermal infrared measurement generates uncertainties in the derivation of surface temperature. The surface emissivity effect must also be accounted, since it directly affects the level of emitted radiation at a given temperature, inducing additional uncertainties. Poor knowledge in either surface emissivity or atmospheric and reflection effects results in uncertainty in the determination of

surface temperature from remote sensing measurement. These effects have been recognized for a long time (e.g. Idso and Jackson, 1968; Svendsen et al., 1990). An error of 0.01 on emissivity results in an error between 0.6 and 0.9 K on surface temperature (Oliso, 1995). This error increases if atmospheric radiation is not considered in the same spectral range as the sensor (Oliso et al., 2013), which measurement is particularly complex. Further, its determination is hindered by the fact that the lowest atmosphere layers are strongly affected by the underlying land surfaces (Jacob et al., 2003).

The work presented here complemented the analysis presented in Oliso et al. (2013), where we analyzed the impact of surface emissivity and atmospheric conditions on surface temperatures, while here we focused on the atmospheric correction effect. The objective of this study was to analyze the impact of using non-coincident radiosoundings to correct surface temperature retrievals from Landsat-7 ETM+ data for atmospheric effects. For that, we studied the sensitivity of the atmospheric parameters required to correct the temperatures measured at the top of the atmosphere, T_{TOA} (i.e., atmospheric transmission, τ and upwelling radiance, L^{\uparrow} , both band-averaged for the

10.4-12.5 μm spectral range) to errors in the estimation of the air temperature (T_a), pressure (P_a) and relative humidity (Rh) at surface level. After characterizing land surface emissivities (ϵ), land surface temperatures (T_s) derived from Landsat-7 were evaluated with their comparison with ground measurements.

2 MATERIALS

We considered 27 Landsat-7 images acquired at 10:15 UTC from 2007 to 2010 over the lower Rhône Valley in France (Avignon-Crau-Camargue area; 0 to 60 m above sea level). It was mainly a flat area presenting a wide variety of land uses (Mira et al., 2014).

Ground measurements were performed at six surface energy balance stations set on different ecosystems over the study area: dry grassland, irrigated meadow, salty marshes, wheat fields and rice. At the ground, surface temperatures were estimated from pyrgeometer measurements (Kipp & Zonen CNR1 sensors) applying the following Eq. (3) to the 5-50 μm spectral range.

3 METHODOLOGY

Top of atmosphere radiances measured by the instrument (L_{TOA}) were converted to top of canopy radiances (L_{TOC}), corrected for atmospheric effects but not for emissivity effects, by considering band-averaged magnitudes using [6]:

$$L_{TOC}(Tb) = \frac{L_{TOA} - L^\uparrow}{\tau} \quad (1)$$

where τ is the atmospheric transmission; L^\uparrow is the upwelling or atmospheric path radiance; and Tb is the surface brightness temperature (i.e., the temperature of a black body that would have the same radiance).

Radiance to temperature conversions were made using the inverted Planck function or the Landsat specific estimate of the Planck curve:

$$T = \frac{k_2}{\ln\left(\frac{k_1}{L(T)} + 1\right)} \quad (2)$$

where T is temperature in Kelvin; L is spectral radiance in $\text{W}/\text{m}^2 \cdot \text{sr} \cdot \mu\text{m}$; and k_1 and k_2 are calibration constants equal to $666.09 \text{ W}/\text{m}^2 \cdot \text{sr} \cdot \mu\text{m}$ and 1282.71 K , respectively, for the Landsat-7 ETM+ sensor (Chander et al., 2009).

Brightness to surface temperature (T_s) conversion was made using the approach proposed by Olioso (1995):

$$T_s - Tb \cong \frac{(1 - \epsilon)}{4\epsilon} Tb - \frac{(1 - \epsilon)}{4\epsilon f(Tb) \sigma Tb^3} Ra^\downarrow \quad (3)$$

where the spectral dependence of every parameter except T_s is obviated for simplicity. σ is the Stefan-Boltzmann constant. $f(T)$ is a factor corresponding to the fraction of energy emitted in this spectral band by a black body at temperature T relative to the emitted energy over the full spectrum, defined by Idso (1981) as:

$$f_{10.4-12.5}(T) = -0.2338 + 0.2288 \cdot 10^{-2}T - 0.3617 \cdot 10^{-5}T^2 \quad (4)$$

It varies between 0.12 and 0.13 for temperatures between -10°C and 45°C . Ra^\downarrow is the incoming atmospheric radiation in the spectral band, which can be expressed as a function of T_a and the atmospheric emissivity for the considered spectral band (ϵ_a) (Idso, 1981):

$$Ra^\downarrow = \epsilon_a \cdot f(T_a) \cdot \sigma \cdot T_a^4 \quad (5)$$

ϵ_a was estimated following the empirical equation proposed by Idso (1981), modified by the hypothesis considered by Rubio et al. (1997), as follows:

$$\epsilon_{a, 10.4-12.5 \mu\text{m}} = \gamma_{10.4-12.5 \mu\text{m}} \cdot 5.91 \cdot 10^{-6} \cdot e_a \cdot \exp(2450/T_a) \quad (6)$$

where $\gamma_{10.4-12.5 \mu\text{m}}$ is obtained according to García-Santos et al. (2012) as a function of W the atmospheric precipitable water:

$$\gamma_{10.4-12.5 \mu\text{m}} = 1.67 - 0.09 \cdot W \quad (7)$$

In our conditions, $\gamma_{10.4-12.5}$ ranged from 1.37 (for the wettest atmosphere) to 1.63 (for the driest atmosphere). For more details see Mira et al. (2014).

Surface emissivity (ϵ) is often estimated from NDVI using the relationship provided by Van de Griend and Owe (1993): see for example Bastiaanssen et al. (1998). In our study, a specific relationship was derived from the analysis of the shape of the NDVI – emissivity relationship performed by Wittich (1997) together with *in situ* measurements of soil and vegetation canopy emissivities performed in our study area (Coll et al., 2002) and laboratory measurements of soil spectra of samples collected in our study area (Lesaigroux et al., 2013). For more details see Mira et al. (2014).

Surface temperature (T_s) was calculated by considering brightness temperature derived from Eq. (1) and Eq. (2), and its conversion to surface temperature using Eq. (3). Atmospheric parameters τ and L^\uparrow from Eq. (1) were derived using:

- *Method 1*: The MODTRAN-4 radiative transfer code (Berk et al., 2003) and atmospheric information derived from nearby radiosoundings launched close to the Nîmes airport (20 to 40 km away; 60 m above sea level) 1 h and 45 minutes after satellite overpass, and

- *Method 2*: The operational atmospheric-correction tool available at <http://atmcorr.gsfc.nasa.gov>, developed for single-band thermal infrared Landsat sensors 5, 7 and 8,

which allows introducing the surface conditions (T_a , P_a and Rh) (Barsi et al., 2003). It uses atmospheric profiles from the National Centers for Environmental Prediction, interpolated to our particular date, time and location. To correct an entire image, we considered surface conditions acquired at the center of the scene at a certain time.

4 RESULTS

The spatial and temporal variability of T_a , P_a and Rh along the 27 considered dates was analyzed. The spatial variability could be assumed to be noise, while the temporal variability could be assumed to be a bias. The effect of the atmosphere spatial and temporal variability into atmospheric parameters τ and L^\uparrow were analyzed and results summarized in Table 1. These uncertainties may lead to errors up to 2.5 K and to a systematic underestimation up to 0.4 K for Tb (see Table 1), in particular in summer when the atmosphere was warmer and the vapor pressure was higher (values from a simulation study by considering TOA temperatures ranging from 0 to 40 °C, the usual range observed in our images, and the atmospheric conditions from the 27 considered days).

However, from the analysis of all pixels of our images, and particularly for completely clear sky days, there was a good correlation between Tb retrievals from *Method 1* and *Method 2* (absolute Root Mean Square Error, $RMSE_A$ and bias <1 K). The omission of surface atmospheric conditions (which characterize the lowest atmosphere layer) for the atmospheric correction following *Method 2* implied higher errors into Tb than considering those acquired at 12:00 UTC (the error in Tb was almost double, while the bias was smaller), confirming what Jacob et al. (2003) claimed.

As noted in Figure 1a, an underestimation of Tb implied an underestimation of Ts of about the same order or slightly higher, for any temperature, emissivity and atmospheric downwelling radiance (results from the analysis of Eq. (3)). However, an emissivity error of +0.01 implied an underestimation of Ts significantly increasing with temperature and the decrease of atmospheric downwelling radiance, and slightly decreasing with emissivity (Figure 1b). For an emissivity error of +0.02, the error in Ts was almost doubled (Figure 1b).

Table 1. Uncertainty in the atmospheric transmission (τ), the upwelling radiance (L^\uparrow), and the brightness temperature (Tb) in the 10.4–12.5 μm , the last for different temperatures top of atmosphere (T_{TOA}). It is calculated by considering retrievals from Method 1 and Method 2, the last considering surface conditions at satellite overpass. 22 days were analyzed, subject to the availability of data. $RMSE_A$ and $RMSE_R$ are absolute and relative Root Mean Square Error, respectively.

	$\delta\tau$	δL^\uparrow	δTb (K)					
$RMSE_A$	0.06	0.4	1.3	0.6	1.0	1.8	2.5	
$RMSE_R$	7%	31%	-	-	-	-	-	
Bias	0.012	-0.08	0.15	-0.009	-0.15	-0.3	-0.4	
			T_{TOA} (°C)					
			0	10	20	30	40	

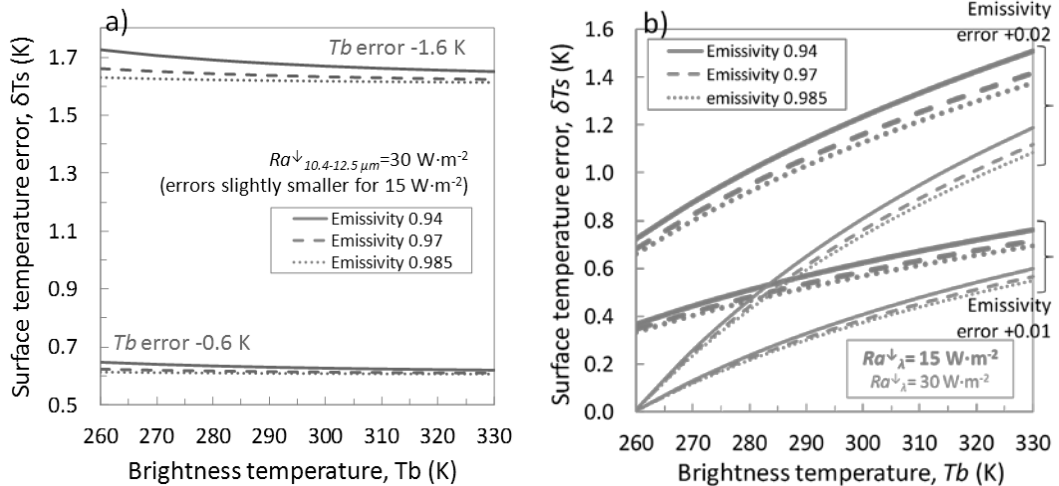


Figure 1. Error induced in the surface temperature estimation ($\delta Ts = Ts - Ts^*$) due to an error in the brightness temperature (δTb) estimates (a), or due to an emissivity error (b), for certain emissivity values, temperatures, and atmospheric conditions (atmospheric downwelling radiance in the 10.4–12.5 μm , $Ra_{10.4-12.5\mu m}^\downarrow$).

Consequently, the use of a temporal and spatial interpolated atmospheric profile together with surface conditions at satellite overpass (*Method 2*) for correcting for atmospheric effects, instead of using data from a nearby radiosounding launched almost 2 hours later (*Method 1*), just resulted in a decrease of 0.1 K for the $RMSE_A$ of T_s (and the bias remained the same). Figure 2 shows the comparison between

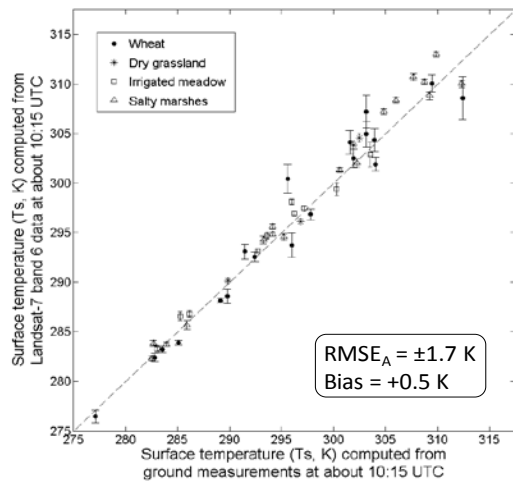


Figure 2. Comparison, over four measurement sites, between Landsat-7 retrievals from 22 days corrected for atmospheric effects using Method 2 and considering surface conditions at satellite overpass, and concurrent ground based measurements of surface temperature, T_s . Error bars show standard deviation of averaged data (i.e., 3×3 pixels 60-m resolution), only significant over the wheat field. $RMSE_A$: absolute Root Mean Square Error.

satellite estimates and ground measurements of T_s over each land use site. T_s were estimated with a bias of +0.3 K and an error of about 1.7 K, mostly due to larger scatter at high temperatures (probably caused by wrong characterization of emissivity over salty marshes) and the heterogeneity of the wheat field at Landsat scale. A deeper analysis is presented by Mira et al. (2014).

5 CONCLUSIONS

Our study showed that in the conditions of our images, the effect of the atmosphere was important for brightness temperatures top of canopy (T_b). This uncertainty was directly transmitted to surface temperature (T_s) which may have a significant impact on the derivation of surface energy fluxes (particularly the sensible heat flux, and exceptionally negligible for net radiation (Mira et al., 2014)). Uncertainties up to 2.5 K for T_b could be observed for high temperatures, with a warm atmosphere and high vapor pressure. We

demonstrated that the characterization of the lowest atmosphere layer is essential to improve T_b estimates. An improvement is expected with the retrieval of atmospheric parameters (L^1 and τ) for various points within the image. This process is being implemented in a processing chain by CESBIO. The error on surface temperature estimates using Landsat-7 data ($RMSE_A=1.7$ K; $Bias=0.5$ K) was within the range of observed errors due to atmospheric correction (from 0.6 to 2.5 K).

The procedure presented in this study is currently being implemented in a processing chain developed for mapping evapotranspiration (EVASPA tool, (Gallego-Elvira et al., 2013)). This work was performed through different projects funded by the CNES (TOSCA) and the European SIRRIMED FP7 project, and the CNES postdoctoral contract from M. Mira.

REFERENCES

- Barsi, J.A., Barker, J.L., and Schott, J.R., 2003, An atmospheric correction parameter calculator for a single thermal band earth-sensing instrument. In *IEEE International Geoscience and Remote Sensing Symposium*, Toulouse (France).
- Bastiaanssen, W.G.M., Menenti, M., Feddes, R.A., and Holtslag, A.A.M., 1998, A remote sensing surface energy balance algorithm for land (SEBAL) - 1. Formulation. *Journal of Hydrology*, **213**, 198-212.
- Berk, A., Anderson, G.P., Acharya, P.K., Hoke, M.L., Chetwynd, J.H., Bernstein, L.S., Shettle, E.P., Matthew, M.W., and Adler-Golden, S.M., 2003, MODTRAN4 Version 3 Revision 1 USERS MANUAL. *AFRL Technical Report*, Hanscom AFB, USA.
- Chander, G., Markham, B.L., and Helder, D.L., 2009, Summary of current radiometric calibration coefficients for Landsat MSS, TM, ETM+, and EO-1 ALI sensors. *Remote Sensing of Environment*, **113**, 893-903.
- Coll, C., Caselles, V., Rubio, E., Valor, E., Sospedra, F., Baret, F., Prévot, L., and Jacob, F., 2002, Temperature and emissivity extracted from airborne multi-channel data in the ReSeDA experiment. *Agronomie*, **22**, 567-573.
- Coll, C., Galve, J.M., Sánchez, J.M., and Caselles, V., 2010, Validation of Landsat-7/ETM+ thermal-band calibration and atmospheric correction with ground-based measurements. *IEEE Transactions on Geoscience and Remote Sensing*, **48**(1), 547-555.
- Gallego-Elvira, B., Oliso, A., Mira, M., Reyes-Castillo, S., Boulet, G., Marloie, O., Garrigues, S., Courault, C., Weiss, M., Chauvelon, P., and Boutron, O., 2013, EVASPA

- (Evapotranspiration Assessment from SPACE tool: An overview. *Procedia Environmental Sciences*, **19**, 303-310.
- García-Santos, V., Valor, E., Caselles, V., Mira, M., Galve, J.M., & Coll, C., 2012, Evaluation of different methods to retrieve the hemispherical downwelling irradiance in the thermal infrared region for field measurements. *IEEE Transactions on Geoscience and Remote Sensing*, **51**(4), 2155-2165.
- Jacob, F., Gu, X.F., Hanocq, J.F., Tallet, N., and Baret, F., 2003, Atmospheric corrections of single broadband channel and multidirectional airborne thermal infrared data: application to the ReSeDA experiment. *International Journal of Remote Sensing*, **24**, 3269-3290.
- Idso, S.B., and Jackson, R.D., 1968, Significance of fluctuation in sky radiant emittance for infrared thermometry. *Agronomy Journal*, **60**, 388-392.
- Idso, S.B., 1981, A set of equations for full spectrum and 8 to 14 μm and 10.4-12.5 μm thermal radiation from cloudless skies, *Water Resources Research*, **17**(2), 295-304.
- Lesaignoux, A., Fabre, S., and Briottet, X., 2013, Influence of soil moisture content on spectral reflectance of bare soils in the 0.4–14 μm domain. *International Journal of Remote Sensing*, **34**(7), 2268-2285.
- Mira, M., Olioso, A., Courault, D., Gallego-Elvira, B., Marloie, O., and Hagolle, O., Sensitivity of net radiation estimation from Landsat-7 ETM+ to errors in surface temperature and albedo. *Remote Sensing of Environment* (undergoing review).
- Olioso, A., 1995, Estimating the difference between brightness and surface temperatures for a vegetal canopy. *Agricultural and Forest Meteorology*, **72**, 237–242.
- Olioso, A., Mira, M., Courault, D., Marloie, O., and Guillevic, P., 2013, Impact of surface emissivity and atmospheric conditions on surface temperatures estimated from TOP of canopy brightness temperatures derived from Landsat-7 data. In *IEEE International Geoscience and Remote Sensing Symposium*, Melbourne (Australia), IEEE Catalog Number: CFP13IGA-USB.
- Rubio, E., Caselles, V., and Badenas, C., 1997, Emissivity measurements of several soils and vegetation types in the 8-14 μm wave band: Analysis of two field methods. *Remote Sensing of Environment*, **59**, 490-521.
- Svendsen H. Jensen H.E. Jensen S.E., Morgensen V.O., 1990, The effect of clear sky radiation on crop surface temperature determined by thermal thermometry. *Agricultural and Forest Meteorology*, **50**, 329-243.
- Van de Griend, A.A. and Owe, M., 1993, On the relationship between thermal radiation from a terrestrial surface. *Journal of Applied Meteorology*, **16**, 759-763.
- Wittich, K.P., 1997, Some simple relationships between land-surface emissivity, greenness and the plant cover fraction for use in satellite remote sensing. *International Journal of Biometeorology*, **41**, 58–64.

Generating land surface temperature products from MODIS data for agro-drought monitoring in China

Zhihao Qin¹, Wenjuan Li¹, Caiying Song², Fei Wang², Shuhe Zhao², Bin Xu¹, Jinya Li³, Yuanxiang Jin¹

1. *Institute of Agro-Resources and Regional Planning, Chinese Academy of Agricultural Sciences, Beijing 100081, China.*

2. *School of Geographic and Oceanographic Sciences, Nanjing University, Nanjing 210023, China.*

3. *Ecology Study Center, Chinese Academy of Sciences, Beijing, China*
qinzhihao@caas.cn, zhihaoqin@163.com

ABSTRACT - Water and heat are two important factors governing dynamic changes of soil moisture available for crop growing in farmland, hence become the basic indicators for agricultural drought monitoring. Due to its directly relating to soil moisture and heat flux characteristics, thermal remote sensing has been extensively applied to agricultural drought monitoring through soil water content estimation. In this paper, we present an applicable approach of split-window algorithm for quickly generating land surface temperature from MODIS thermal band data, which were extensively employed in agricultural drought monitoring in China. The characteristics of the algorithm were in its relatively high accuracy in LST retrieval while maintaining only the two essential parameters i.e. ground emissivity and atmospheric transmittance, for the LST retrieval. Focus was given to discussion of details about estimation of the algorithm's essential parameter, especially how to fastly estimate the ground emissivity and atmospheric transmittance from other bands of the same scene MODIS data. A complete procedure was present for quickly generating the LST product for agro-drought monitoring in China. Finally we conducted an experiment of applying the approach for agro-drought monitoring in February and March of 2009 in the winter wheat cropping region of China.. It had been observed that severe drought was happened in early spring in north China, the most important winter wheat cropping region. The results from the applications confirms the applicability of the proposed approach in quickly generating LST product from MODIS data required for agricultural drought monitoring in China.

1 INTRODUCTION

MODIS image data contains 8 thermal infrared (TIR) data (bands 29-36) with a spatial resolution of 1000m under nadir viewing to retrieving the distribution of surface heat, thereby establishing the model for hydrothermal arid farmland dynamic spatial and temporal estimates to determine the dynamic changes in agricultural drought and disaster. Land surface temperature (LST) is one basic parameter of agricultural drought monitoring model such as Vegetation Supply Water Index(VSWI), Thermal Inertia(TI) and Vegetation Temperature Condition Index(VTCI) (Kaufman & Gao, 1992; Goward & Czajkowski, 2002; Kogan, 1995). Due to its complicated process of LST, most drought monitoring models are directly using the brightness temperature transformed from the TIR data as input parameters. However, the measured LST is found to be about 5-10°C higher than the brightness temperature around the outlet of a nuclear power plant().

The objective of this paper is to develop an algorithm to quickly generating land surface temperature products from the thermal bands of

MODIS data for agricultural drought monitoring. In following sections we firstly present the derivation of the spit-window algorithm for the LST retrieval from the thermal bands of MODIS data. Then we establish the approaches to estimate the required parameters (i.e. atmospheric transmittance and ground emissivity) for the algorithm. Thirdly, we present a complete procedure for quickly generating the LST product for agro-drought monitoring in China. Finally we conduct an example of applying the algorithm for agro-drought monitoring in China.

2 SELECTION OF ALGORITHM FOR LST RETRIEVAL FROM MODIS DATA

Among the 8 thermal bands of MODIS data, bands 31 and 32 are the most comparable for land surface temperature retrieval required by agricultural drought monitoring. Qin et al. (2001) developed a split-window algorithm for LST retrieval from MODIS data, in which the characteristics of the algorithm were in its relatively high accuracy in LST retrieval while maintaining only the two essential parameters i.e. ground emissivity and atmospheric transmittance, for the LST retrieval. The split-window algorithm is calculated as follows:

$$T_s = A_0 + A_1 T_{31} - A_2 T_{32} \quad (1)$$

Where T_s is the LST in Kelvin degree; T_{31} and T_{32} are the brightness temperature of band 31 and band 32 for MODIS in Kelvin degree. The coefficients A_0 , A_1 and A_2 are defined as:

$$A_0 = E_1 a_{31} - E_2 a_{32} \quad (2)$$

$$A_1 = 1 + A + E_1 b_{31} \quad (3)$$

$$A_2 = A + E_2 b_{32} \quad (4)$$

Where a_{31} , b_{31} , a_{32} and b_{32} are the constants, giving as $a_{31} = -64.60363$, $b_{31} = 0.440817$, $a_{32} = -68.72575$, $b_{32} = 0.473453$ for LST range 0-50°C. The parameters A , E_1 , E_2 are computed as follows:

$$A = D_{31}/E_0 \quad (5)$$

$$E_1 = D_{32}(1 - C_{31} - D_{31})/E_0 \quad (6)$$

$$E_2 = D_{31}(1 - C_{32} - D_{32})/E_0 \quad (7)$$

$$E_0 = D_{32}C_{31} - D_{31}C_{32} \quad (8)$$

$$C_i = \varepsilon_i \tau_i(\theta) \quad (9)$$

$$D_i = [1 - \tau_i(\theta)][1 + (1 - \varepsilon_i)\tau_i(\theta)] \quad (10)$$

Where i represents MODIS thermal bands ($i=31$ and 32); τ_i is the atmospheric transmittance and ε_i is the ground emissivity of MODIS band i ($i=31$ and 32).

The algorithm requires brightness temperatures (T_{31} , T_{32}) calculated from MODIS thermal channels 31 and 32 and two essential parameters for LST retrieval: atmospheric transmittance (τ_i) and ground emissivity (ε_i). Details about accurate determination of the coefficients will be discussed in the following section.

3 COMPUTATION OF BRIGHTNESS TEMPERATURE

Since the observed thermal radiance for band i ($i=31, 32$) of MODIS TIR data is transformed into digital number (DN) for storage and transfer in a format of 16 digit, which give the range of 0-65535, we are able to compute the brightness temperature from MODIS TIR data through transformation of the DN value into thermal radiance and then conversion of the radiance into brightness temperature.

The DN value of MODIS TIR data can be converted into thermal spectral radiance through the radiance rescaling factors provided in the metadata file of MODIS data as follows:

$$I_i = RD_i (DN_i - RDOS_i) \quad (11)$$

Where I_i is the spectral radiance ($\text{W m}^{-2} \text{sr}^{-1} \mu\text{m}^{-1}$) of MODIS band i ($i=31, 32$); DN_i is the DN value ($DN=0-255$) for the quantized and calibrated standard product pixel of MODIS band i ($i=31, 32$); RD_i and $RDOS_i$ are the radiation constant of MODIS band i ($i=31, 32$) which can be obtained from the metadata file of MODIS image.

The thermal spectral radiance can be converted to brightness temperature through reversion of Planck

radiance function using the thermal constants provided in the metadata file:

$$T_i = K_{i2} / \ln(1 + K_{i1}/I_i) \quad (12)$$

Where T_i is brightness temperature (K) of MODIS band i ($i=31, 32$); K_{i1} and K_{i2} are the band-specific thermal conversion constants for MODIS band i ($i=31, 32$), with $K_{31,1} = 729.541636 \text{ W m}^{-2} \text{sr}^{-1} \mu\text{m}^{-1}$, $K_{31,2} = 1304.413871 \text{ K}$ for band 31 and $K_{32,1} = 474.684780 \text{ W m}^{-2} \text{sr}^{-1} \mu\text{m}^{-1}$, $K_{32,2} = 1196.978785 \text{ K}$ for band 32.

4 ESTIMATION OF ATMOSPHERIC TRANSMITTANCE

Atmospheric transmittance is a critical parameter affecting accuracy of LST retrieval using split-window algorithm, which strongly depends on the dynamics of water vapor content in the profile (Qin & Karnieli, 1999; Coll et al., 1994). Atmospheric water vapor content can be retrieved from MODIS data using the atmospheric water vapor algorithm with bands 2 and 19. The formula can be as follows (Gao & Goetz, 1992):

$$w = ((\alpha - \ln(\rho_{19}/\rho_2))/\beta)^2 \quad (13)$$

Where w is water vapor content in g cm^{-2} , α and β are constants with $\alpha=0.02$ and $\beta=0.651$; ρ_{19} and ρ_2 are reflectance of band 19 and 2 for MODIS respectively, which can be computed using the following formula:

$$\rho_i = RL_i (DN_i - RLOS_i) \quad (14)$$

in which DN_i is the digital number of MODIS band i ($i=19$ and 2), RL_i and $RLOS_i$ are the reflectance constants of MODIS band i ($i=19$ and 2), obtained from header file of MODIS image data.

In order to establish an approach to estimate atmospheric transmittance for MODIS TIR bands, we have to simulate the change of atmospheric transmittance with water vapor content under various atmospheric conditions. The relationship between transmittance and water vapor content in the atmosphere is shown in table 1. Therefore, if we know the content of water vapor in the atmosphere, we are able to use the equations in table 1 to estimate atmospheric transmittance for LST retrieval from MODIS data.

Table1. Relationship between transmittance and water vapor content in the atmosphere

Water vapor content (w) g cm^{-2}	Estimation equations	R^2
0.4-2.0	$\tau_{31}(10) = 0.99513 - 0.08082w$	0.9914
	$\tau_{32}(10) = 0.99377 - 0.11370w$	0.9932
2.0-4.0	$\tau_{31}(10) = 1.08692 - 0.12759w$	0.9992
	$\tau_{32}(10) = 1.07900 - 0.15925w$	0.9999
4.0-6.0	$\tau_{31}(10) = 1.07268 - 0.12571w$	0.9991
	$\tau_{32}(10) = 0.93821 - 0.12613w$	0.9955

Viewing angle on pixel scale and temperature in atmospheric profiles (Wan and Dozier 1996, Sobrino et al. 1991) are also two other factors of atmospheric transmittance. The transmittance gradually increases with increase of temperature in the atmosphere which gives the correction function of atmospheric temperature for atmospheric transmittance in Table 2.

The correction function of zenith viewing angle for atmospheric transmittance is calculated as follows:

$$\delta\tau_{31}(\theta) = -0.00247 + (2.3652 \times 10^{-5})\theta^2 \quad (15)$$

$$\delta\tau_{32}(\theta) = -0.00322 + (3.0967 \times 10^{-5})\theta^2 \quad (16)$$

in which θ is the zenith viewing angle of MODIS in degree which is computed as follows:

$$\theta = V_a * |D_0 - D_i| \quad (17)$$

Table2. The correction function of atmospheric temperature for atmospheric transmittance

band	correction function	Temperature range
band 31	$\delta\tau_{31}(T) = 0.08$	$T > 318K$
	$\delta\tau_{31}(T) = -0.05 + 0.003(T_{31} - 278)$	$278 < T < 318K$
	$\delta\tau_{31}(T) = -0.05$	$T < 278K$
band 32	$\delta\tau_{32}(T) = 0.095$	$T > 318K$
	$\delta\tau_{32}(T) = -0.065 + 0.004(T_{32} - 278)$	$278 < T < 318K$
	$\delta\tau_{32}(T) = -0.065$	$T < 278K$

Where θ is the zenith viewing angle of each pixel; D_0 is the ccolumn number of sub-satellite pixel; D_i is the ccolumn number of pixel i ; V_a is the viewing angle of sub-satellite pixel at a certain MODIS satellite height, giving as $V_a = 0.0812706^\circ$.

Therefore, atmospheric transmittance of MODIS band 31 and 32 for LST retrieval can be given as follows:

$$\tau_{31}(\theta) = \tau_{31}(10) + \delta\tau_{31}(T) - \delta\tau_{31}(\theta) \quad (18)$$

$$\tau_{32}(\theta) = \tau_{32}(10) + \delta\tau_{32}(T) - \delta\tau_{32}(\theta) \quad (19)$$

Where $\tau_{31}(\theta)$ and $\tau_{32}(\theta)$ are the atmospheric transmittance of MODIS band 31 and band 32; $\tau_{31}(10)$ and $\tau_{32}(10)$ are the sub-satellite atmospheric transmittance which can be estimated from the equation in table 1; $\delta\tau_{31}(T)$ and $\delta\tau_{31}(T)$ are the correction function of atmospheric temperature which can be estimated from the equation in table 2; $\delta\tau_{31}(\theta)$ and $\delta\tau_{32}(\theta)$ are the correction function of zenith viewing angle which can be estimated from the equation (15) and (16).

5 ESTIMATION OF GROUND EMISSIVITY

Ground emissivity is very important for LST retrieval from remote sensing data which is mainly depended on the structural composition of ground surface materials (Becker and Li 1995; Sobrino and Li,

2001; Humes et al., 1994). Therefore we can follow the approach developed in Qin et al. (2004b) to estimate the emissivity for the sub-pixels using the auxiliary VNIR band data.

$$\varepsilon_i = P_v R_v \varepsilon_{iv} + (1 - P_v) R_s \varepsilon_{is} + d\varepsilon \quad (20)$$

Where ε_i is the emissivity of the pixel for MODIS band i ($i=31, 32$); ε_{iv} and ε_{is} are the emissivity of vegetation and bare soil respectively for band i , with $\varepsilon_{31v}=0.98672$, $\varepsilon_{32v}=0.98990$, $\varepsilon_{31s}=0.96767$ and $\varepsilon_{32s}=0.97790$; P_v is the vegetation cover fraction in the pixel; $d\varepsilon$ is the term due to interaction of thermal emission between vegetation part and bare soil part; R_v and R_s are the radiance ratio of vegetation and bare soil respectively, which can be estimated with the fraction according to Qin et al. (2004) as follows:

$$R_v = 0.92762 + 0.07033P_v \quad (21)$$

$$R_s = 0.99782 + 0.08362P_v \quad (22)$$

The parameters P_v is computed as follows (Kerr et al. 1992):

$$P_v = (NDVI - NDVI_s) / (NDVI_v - NDVI_s) \quad (23)$$

Where P_v is the vegetation cover fraction of the pixel; $NDVI_s$ and $NDVI_v$ are the NDVI for a bare soil pixel and a fully vegetated one respectively, with $NDVI_v=0.9$, $NDVI_s=0.15$. If a pixel is with a NDVI value of greater than 0.9, it can be viewed as fully vegetated, or completely covered with vegetation, the fraction can be given as $P_v=1.0$. As a contrast, a pixel with $NDVI < 0.15$ can be termed as a bare surface without any vegetation cover, the fraction can be given as $P_v=0.0$. NDVI (normalized difference of vegetation index) can be calculated based on band 1st, 2nd for MODIS as follows:

$$NDVI = (B_2 - B_1) / (B_2 + B_1) \quad (24)$$

Where B_1 and B_2 are the reflection of band 1 (infrared band) and band 2 (red band) for MODIS data.

And we can follow the approach developed in Sobrino et al. (2004) to estimate the $d\varepsilon$, as follows:

$$d\varepsilon = \begin{cases} 0.0 & \text{for } P_v = 0.0 \text{ or } P_v = 1.0 \\ 0.003796P_v & \text{for } 0.0 < P_v < 0.5 \\ 0.003796(1 - P_v) & \text{for } 0.5 < P_v < 1.0 \\ 0.001898 & \text{for } P_v = 0.5 \end{cases} \quad (25)$$

in which P_v is the vegetation cover fraction of the pixel.

6 PROCEDURES OF MODIS LST PRODUCT

The procedures to conduct generation of land surface temperature products from MODIS data in China can be summarized as follows:

1. Estimating NDVI. This is done to the reflection of band 1 and band 2 from the auxiliary data with the digital number and the reflectance calibration.

Then the NDVI is used to the computation of vegetation cover fraction (P_v).

2. Classifying the auxiliary data. A classified image with 3 surface patterns for the pixels is generated: natural terrain, urban region, and water body from band 1 and band 2.

3. Estimating ground emissivity (ϵ_{31} and ϵ_{32}). This is done to the auxiliary data with assistance of classified images and the vegetation cover fraction (P_v).

4. Estimating water vapor content (w). This is done to the reflectance of band 2 and band 19. Then the water vapor content is used to the computation of sub-satellite atmospheric transmittance with $\tau_{31}(10)$ and $\tau_{32}(10)$.

5. Estimating the zenith viewing angle of each pixel (θ). Then the zenith viewing angle can be used to calculating the correction function of zenith viewing angle for atmospheric transmittance with $\delta\tau_{31}(\theta)$ and $\delta\tau_{32}(\theta)$.

6. Computing the brightness temperature (T_{31} and T_{32}). This is done to the reflectance of band 31 and band 32.

7. Estimating the correction function of atmospheric temperature for atmospheric transmittance with $\delta\tau_{31}(T)$ and $\delta\tau_{32}(T)$.

8. Estimating atmospheric transmittance of $\tau_{31}(\theta)$ and $\tau_{32}(\theta)$ with the equation (18) and (19).

9. Retrieving land surface temperature. This is done to the auxiliary data with assistance of essential parameters (ϵ_{31} , ϵ_{32} ; τ_{31} , τ_{32} ; T_{31} , T_{32}) and the equation (1).

9. Generating land surface temperature of the scene image. This is done with the Geometric Correction and Class Break Renderer.

10. Generating land surface temperature of different scene images in eastern, western and central China. This is done with the repeating steps from 1 to 10.

11. Generating land surface temperature product in China. This is done to overlay of administrative boundaries for each land surface temperature scene image.

The above procedures are illustrated in Figure 1 showing the technical process of the approach.

7 RESULT

According to the LST retrieval process of the split-window algorithm, the calculation process is divided into four modules, brightness temperature calculation module, atmospheric transmittance calculation module, surface emissivity calculation module and temperature derivation module. After validating detailed analysis of the results obtained in each step and its legitimacy, ultimately a complete

LST production generating process has been established. Experiments show that the program can quickly complete the calculation of China nationwide LST in 10 minutes under normal situation. We choose three images respectively located in the east, middle and west of China to analysis the LST spatial distribution as shown in figure 2.

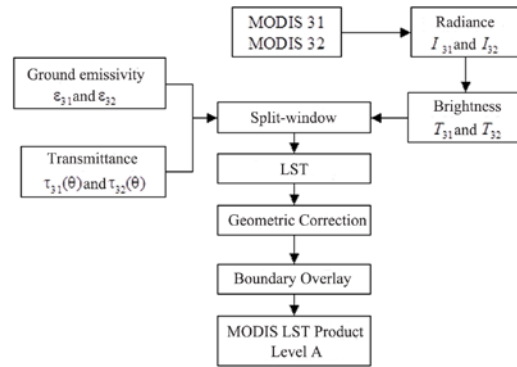


Figure 1 Process of generating LST products from MODIS data in China

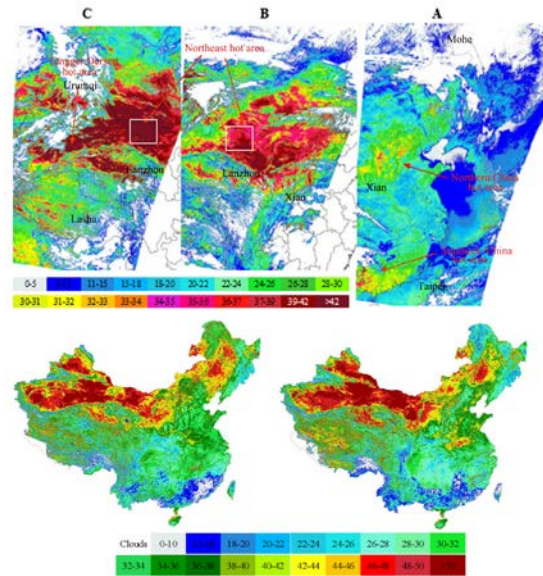


Figure 2 Spatial distribution of MODIS LST in China

Figure 2 is composed of three MODIS LST images. The acquired time when satellite passed at local time of images are respectively at April 4th, 2004 10:46 am of figure 2-A in the east of China, at April 17th, 2004 11:54 am of figure 2-B in the middle of China and at August 31st, 2004 12:42 pm of figure 2-C in the west of China. For the cloud cover area, we eliminate those data and fill them with white color. As figure 2-A shows, two relative high LST areas are

found in in the east of China. In the southeast of China, the summer is coming after April, so this area will performance as relative high LST area with the highest temperature achieved 35.49°C. And another high LST area emerges at the Loess Plate of China, because this area is at the period of spring drought with little rain. While in the same month, the Badan Jaran Desert and Tengger Desert in the northwest of China as shown in figure 5-B arise a huge hot area with the maximum LST achieved 45°C. The Taklamakan Desert will combine the Badan Jaran Desert and Tengger Desert as an extremely hot area in August as shown in figure 5-C. Compared this area in August with April, the average LST of the same area selected in the Badan Jaran Desert and Tengger Desert increase 11°C. The result of LST changes is caused by this region land-cover type (sand) and climate (less rain), which is consistent with the spatial distribution of land-cover type and the characteristics of climate in different areas.

8 CONCLUSION

Split-window algorithm is selected to quickly generating land surface temperature products from the thermal bands of MODIS data for agro-drought monitoring in China, which has relatively high accuracy in LST retrieval while maintaining only the two essential parameters i.e. ground emissivity and atmospheric transmittance, for the LST retrieval. Atmospheric transmittance strongly depends on the dynamics of water vapor content in the profile which could be retrieved by band 2 and band 19 for MODIS. The correction function of atmospheric temperature and zenith viewing angle for atmospheric transmittance are also considered in the calculation of atmospheric transmittance. Ground emissivity is estimated with assistance of classified images and the vegetation cover fraction.

Then we present a complete procedure for quickly generating the LST product for agro-drought monitoring in China with our algorithm, which is divided into four modules i. e. brightness temperature calculation module, atmospheric transmittance calculation module, surface emissivity calculation module and temperature derivation module.

The experiment of applying the approach for agro-drought monitoring in China shows severe drought happened in early spring in north China, the most important winter wheat cropping region in February and March of 2009 in the winter wheat cropping region of China. The results from the applications confirms the applicability of the proposed approach in quickly generating LST product from MODIS data required for agricultural drought monitoring in China.

REFERENCES

- Allen, R. G., Tasumi, M., & Trezza, R., 2007a. Satellite-based energy balance for mapping evapotranspiration with internalized calibration (METRIC)—Applications. *Journal of Irrigation and Drainage Engineering*, 133(4), 380-394.
- Allen, R. G., Tasumi, M., Morse, A., Trezza, R., Wright, J. L., Bastiaanssen, W., Kramber, W., Lorite, I., & Robison, C. W., 2007b. Satellite-based energy balance for mapping evapotranspiration with internalized calibration (METRIC)—Applications. *Journal of Irrigation and Drainage Engineering*, 133(4), 395-406.
- Anderson, M. C., Norman, J. M., Mecikalski, J. R., Otkin, J. A., & Kustas, W. P., 2007. A climatological study of evapotranspiration and moisture stress across the continental United States based on thermal remote sensing: 1. Model formulation. *Journal of Geophysical Research*, 112(D10117), doi: 10.1029/2006JD007506.
- Anderson, M., Kustas, W., 2008. Thermal remote sensing of drought and evapotranspiration. *Eos, Transactions American Geophysical Union*, 89(26), 233-234.
- Becker F., and Z. L. Li, 1995. Surface temperature and emissivity at various scales: definition, measurement and related problems. *Remote Sensing Review*, 12, 225-253.
- Coll, C., Caselles, V., Sobrino, J. A., & Valor, E., 1994. On the atmospheric dependence of the split-window equation for land surface temperature. *Remote Sensing*, 15(1), 105-122.
- Gao, B.C., and A. F. H. Goetz, 1992. Column atmospheric water vapor and vegetation liquid water retrieval from airborne imaging spectrometer data. *Journal of Geophysical Research*, 95(4), 3549-3564.
- Gao, M., Qin, Z., Zhang, H., Lu, L., Zhou, X., Yang, X., 2008. Remote sensing of agro-droughts in Guangdong Province of China using MODIS satellite data. *Sensors*, 8(8), 4687-4708.
- Goward, S. N., Xue, Y., & Czajkowski, K. P., 2002. Evaluating land surface moisture conditions from the remotely sensed temperature/vegetation index measurements: an exploration with the simplified simple biosphere model. *Remote sensing of environment*, 79(2), 225-242.
- Humes, K.S., W.P. Kustas, M. S. Moran, W. D. Nichols, and M.A. Weltz, 1994. Variability of emissivity and surface temperature over a sparsely vegetated surface. *Water Resource Research*, 30, 1299-1310.
- Kaufman, Y.J., and B.C. Gao, 1992. Remote sensing of water vapor in the near IR from EOS/MODIS. *IEEE Transactions on Geosciences and Remote Sensing*, 30(5), 871-884.

- Kerr, Y.H., J.P. Lagouarde, and J. Imbernon, 1992. Accurate land surface temperature retrieval from AVHRR data with use of an improved split window algorithm. *Remote Sensing of Environment*, 41, 197-209.
- Kogan, F. N., 1995. Application of vegetation index and brightness temperature for drought detection. *Advances in Space Research*, 15(11), 91-100.
- Qin, Z., and A. Karnieli, 1999. Progress in the remote sensing of land surface temperature and ground emissivity using NOAA-AVHRR data. 20: 2367-International Journal of Remote Sensing, 20: 2367-2393.
- Qin, Z., G. Dall' Olmo, A. Karnieli, and P. Berliner, 2001. Derivation of split window algorithm and its sensitivity analysis for retrieving land surface temperature from NOAA-AVHRR data. *Journal of Geophysical Research*, 106(D19): 22655-22670.
- Qin, Z., B. Xu, W. Zhang, W. Li, and H. Zhang, 2004a. Comparison of split window algorithms for land surface temperature retrieval from NOAA-AVHRR data. IEEE 2004 International Geosciences and Remote Sensing Symposium, VI: 3740-3743, September 20-24, 2004, Anchorage, Alaska, USA.
- Qin, Z., W.J. Li, B. Wu, Z.X. Chen, H.J. Tang, 2004b. Estimation of land surface emissivity for the
- Qin, Z., W.J. Li, B. Wu, Z.X. Chen, H.J. Tang, 2004. Estimation of land surface emissivity for the spectral range of Landsat TM6. *Remote Sensing for Land and Resources*, 3, 27-32.
- Sobrino, J. A., C. Coll, and V. Caselles, 1991. Atmospheric correction for land surface temperature using NOAA-11 AVHRR channels 4 and 5. *Remote Sensing of Environment*, 38, 19-34.
- Sobrino, J.A., N. Raissouni, and Z. L. Li, 2001. A comparative study of land surface emissivity retrieval from NOAA data. *Remote Sensing of Environment*, 75(2): 256-266.
- Sobrino, J. A., J. C. Jiménez-Muñoz, and L. Paolini, 2004. Land surface temperature retrieval from LANDSAT TM 5. *Remote Sensing of Environment*, 90, 434-440.
- Wan, Z., and J. Dozier, 1996. A generalized split-windows algorithm for retrieving land surface temperature from space. *IEEE Transactions on Geosciences and Remote Sensing*, 34, 892-905.
- Wan, Z., Wang, P., Li, X., 2004. Using MODIS land surface temperature and normalized difference vegetation index products for monitoring drought in the southern Great Plains, USA. *International Journal of Remote Sensing*, 25, 61-72.

Estimating of air and deep temperature using thermal remotely sensed data

Seyed Kazem Alavipanah¹, AbdolAli Rezaei², Mohsen Ebrahimi Khusfi², Mohsen Bakhtiari²

1. Professor at Remote sensing department, Faculty of Geography, University of Tehran, Iran. Tel: +982161113536, Email: Salavipa@ut.ac.ir

2. Ph.D students at Remote Sensing department, Faculty of Geography, University of Tehran, Iran (Mohsen_ebrahimi@ut.ac.ir, Rezai.al.65@gmail.com, M.bakhtiari_rs@ut.ac.ir)

ABSTRACT- *Temperature is an important factor in understanding some physico-chemical and biological properties. Computing surface, above surface temperature (AST) and subsurface temperature (SubST) are important issues that many sciences and Scientifics deal with them. There are a lot of ways to compute temperature; one of them that currently have been used extremely is thermal remote sensing. Many studies have been carried out, and different approaches have been proposed to derive land surface temperature (LST) from satellite TIR data. There have been earlier reviews on LST retrieval from space, the latest one is a review by Zhao-Liang et al. in 2013. These reviews focused on retrieving LST and there is a gap in reviewing algorithms in which we can estimate SubST and AST. There are some techniques to derive SubST and AST by using insitu data and empirical methods. Many of the parameterizations required in these complex heat flow models are not available at global scales. Remote sensing can provide such global data. A few studies have linked the TIR data and these methods to derive SubST and AST. The current study provides the theoretical basis for retrieving AST and SubST. Finally, directions for linking satellite-derived temperature and SubST-AST in future are then suggested. From the obtained results we generally concluded that different soil, plant, water and air related parameters are needed that must be taken into account for model validations and retrieval subsurface and air temperature.*

Key words: *Temperature, Surface, Subsurface, above surface, Thermal infrared remote sensing*

1 INTRODUCTION

Temperature that is an important factor in understanding some physico-chemical and biological properties and can be used for describing the state of materials and for studying environmental phenomenon can be estimated using both direct and indirect methodologies (Alavipanah, 2001). In direct ways we use a thermometer to retrieve the temperature in direct contact with the object. However, in large continuous areas using direct ways can't be useful and it's better to use indirect ways or remote sensing ways.

Temperature measurements are generally divided into three categories: Surface, Above and Sub surface. Computing each of them using satellite remote sensing has some limitations, advantages and conditions, but theoretical basis of all are the same.

Land surface temperature (LST) plays an important role in the study of land surface energy balance and as the direct driving force in the exchange of long-wave radiation and turbulent heat fluxes at the surface-atmosphere interface. It is one of the most important parameters in the physical processes of surface energy at local through global scales (Li et al., 2013). It combines the results of surface-atmosphere interactions and energy fluxes between the atmosphere

and the ground (Mannstein, 1987; Sellers et al., 1988). LST is of great interest to a variety of environmental studies including: Global warming, agriculture, urban affairs, climatology studies etc. LST is not only a good indicator of both the energy equilibrium of the Earth's surface and greenhouse effects, but also one of the key variables controlling fundamental biospheric and geospheric interactions between the Earth's surface and its atmosphere. Land surface temperature (LST) is an important factor controlling most physical, chemical and biological processes of the Earth. Knowledge of LST is necessary for many environmental studies and management activities of the Earth's resources (Li and Becker, 1993). In order to monitor macro-scale spatial changes of surface temperature, scanners designed for sensing in the thermal bands are placed onboard platforms for remote sensing of the Earth's resources from space (Sabins, 1986). Satellite-based thermal infrared (TIR) data is directly linked to the LST through the radiative transfer equation.

The air temperature is very vital for analyzing the human comfort, photosynthesis, and vegetation growth. Actually much of the discussion of global climate warming is given in terms of variations in

near-surface air temperature (Hansen et al., 1981). Air temperature near the surface of the earth is of interest because most terrestrial life occurs within this zone and air temperature regulates many land surface processes, such as photosynthesis, respiration, and evaporation. Thus, detailed measurements of spatiotemporal variations in air temperature across the earth's land areas are critical to the effective understanding of both the climate and the terrestrial life processes (Prihodko and Goward, 1997).

Near surface temperature is critical importance to the study of terrestrial hydrology (Dubayah et al. 2000), biospheric processes (Prince and Goward 1995) and other Earth System Science objectives (Ehrlich et al. 1994).

Prior to the advent of satellites, it was difficult to obtain temperature over extensive areas. Nowadays, thermal infrared observations of the earth's surface acquired from a satellite platform have long been recognized as a valuable key to evaluating the surface energy balance over large regions (Idso et al., 1975; Price, 1980). Over the past several decades, many studies have been carried out, and different approaches have been proposed to derive land surface temperature (LST) from satellite TIR data. The remotely sensed imagery provide an excellent cost-effective and time-saving path to analyses spatially and temporally distributed surface temperature, since the coverage of satellite imagery extends over a large area (Senanayake, 2013), this depends on spatial resolution of the images, while that is not case for meteorological data that have been measured at weather stations. Various methods have been presented for the retrieval of land surface temperature from satellite images. Liang Li et al (2013) reviewed the algorithms employed for obtaining LST from space-based TIR measurements. These algorithms can be roughly grouped into three categories: single-channel methods, multi-channel methods, and multi-angle methods (Li et al, 2013). Most of studies have been carried out focused on retrieving LST and there is a gap in reviewing algorithms in which we can estimate SubST and AST. However, Although most algorithms are related to LST retrieval (reviewed by Zhao-Liang et al. in 2013), but recent studies have showed that we also can estimate AST (Sahin, 2012; Benali et al., 2012) and SubST (Holmes et al., 2008) using some algorithms and models from satellite data. These algorithms and models have tried to calculate AST and SubST via establishing a relationship between LST to both of them. Therefore, it is important to review temperature retrieval algorithms and to direct future research into deriving AST and SubST.

The current study provides the theoretical basis for retrieving temperature and reviews methodologies, algorithms, techniques and procedures that have been

used for computing and validating AST and SubST. Section2 outlines the theoretical basis of SubST variations with depth and how sub surface temperature can be retrieved by using LST. Section 3 presents the theoretical basis of AST variations with height and its relation with LST. Section4 gives the conclusion and suggests future developments and provides perspectives on studying temperature from remotely sensed data.

2 SUB SURFACE TEMPERATURE

2.1 A SUMMARY HISTORY OF SUBST

Traditional exploration of geothermal reservoirs is done using subsurface imaging (using geophysical techniques) as input to reservoir modelling with limited use of field data besides the geochemical analysis of brines and hot springs. Earth observation, although this is a trivial remark addressing a remote sensing community, adds the geospatial component to the equation (earth surface information) as well as the time domain. Optical multi- and hyperspectral remote sensing can aid in better understanding surface geology and mineral alteration related to geothermal activity, thermal remote sensing allows to measure and map surface temperature distribution and heat flux, while with instruments like MODIS we gain insight into long-term thermal radiance variations (Van der Meer et al, 2014).

Thermal infrared (TIR) remote sensing provides data with synoptic coverage for investigating the surface and subsurface anomalies. TIR remote sensing data can be used to map and quantify temperature anomalies associated with surface geothermal features such as hot springs, geysers, fumaroles, and heated ground (Haselwimmer and Prakash, 2011). There are a number of papers demonstrating the use of thermal infrared data to map surface temperature and correlate that to geothermal heat. Much of the published research on the use of TIR remote sensing for mapping sub surface temperature anomalies has focused on the use of airborne thermal imagery acquired with broadband (Hodder, 1970; Lee, 1978; Haselwimmer and Prakash, 2011) or multispectral instruments (Mongillo, 1994; Seielstad and Queen, 2009). Although coarse spatial resolution satellite thermal sensors (60-90 m pixels), such as Landsat or ASTER, have limited potential for detailed mapping of discrete geothermal features a number of studies have exploited these datasets for broader scale detection of geothermal anomalies. These studies have commonly applied data processing techniques to enhance and detect what may be subtle surface temperature anomalies.

Table 1 shows some researches in which airborne and space borne thermal imagery has been used.

Table 1. Some researches in which thermal imagery has been used.

Application	Description	Reference
Detect geothermal anomalies by using airborne TIR	The thermal data provided an effective method for mapping of all the known and many previously unidentified geothermal features including hot springs, hot ground, and thermal seeps into lakes.	(Hodder, 1970; Lee, 1978; Mongillo, 1994; Seielstad and Queen 2009; Haselwimmer and Prakash 2011)
Detect subsurface archaeological remains by using airborne TIR	used airborne thermal infrared data to detect exposed and subsurface archaeological remains	(Ben-Dor et al., 2001; Rowlands et al., 2006; Eppelbaum, 2009)
Detect geothermal anomalies by using spaceborne TIR (Landsat, day/night pair of ASTER scenes, MODIS)	Mapping the locations of the known fumarole field, thermal springs, surface thermal anomalies, etc.	(Eneva et al., 2006; Coolbaugh et al., 2007; Kienholz et al., 2009; Vaughan et al., 2011)
investigating the potential of TIR remote sensing data to estimate the geothermal heat flux (GHF)	Radiant geothermal heat flux that allowed identifying background changes and seasonal effects to allow a better extraction of geothermal anomalies.	(Watson et al., 2008; Haselwimmer et al., 2013)

2.2 SUBST VARIATIONS WITH DEPTH

Soil temperature fluctuates annually and daily affected mainly by variations in air temperature and solar radiation. The annual variation of daily average soil temperature at different depths can be estimated using a sinusoidal function (Hillel, 1982; Wu and Nofziger, 1999). Soil temperature varies in response to changes in radiant, thermal and latent energy exchange processes that take place through the soil surface. The effects of these phenomena are propagated into the soil profile by a complex series of transport processes. There are three major heat transport processes in soils including: heat conduction, heat radiation.

2.3 SUBST RETRIEVAL ALGORITHM

The annual variation of daily average soil temperature at different depths is described with the following sinusoidal function (Hillel, 1982):

$$T(z, t) = T_a + A_0 e^{-z/d} \sin \left[\frac{2\pi(t-t_0)}{365} - \frac{z}{d} - \frac{\pi}{2} \right] \quad (1)$$

Where $T(z, t)$ is the soil temperature at time t (d) and depth z (m), T_a is the average soil temperature ($^{\circ}\text{C}$), A_0 is the annual amplitude of the surface soil -temperature ($^{\circ}\text{C}$), d is the damping depth (m) of annual fluctuation and t_0 is the time lag (days) from an arbitrary starting date (for example Julian day) to the occurrence of the minimum temperature in a year. The damping depth is given by d is a constant characterizing the decrease in amplitude with an increase in distance from the soil surface. It is defined as $d = (2Dh/\omega)^{0.5}$. Where ω is the frequency of a temperature fluctuation (For annual fluctuation $\omega = 2\pi/365 \text{ d}^{-1}$) and Dh is defined as thermal diffusivity is the change in temperature produced in a unit volume by the quantity of heat flowing through the volume in unit time under a unit temperature gradient. It can be

calculated from thermal conductivity and volumetric heat capacity.

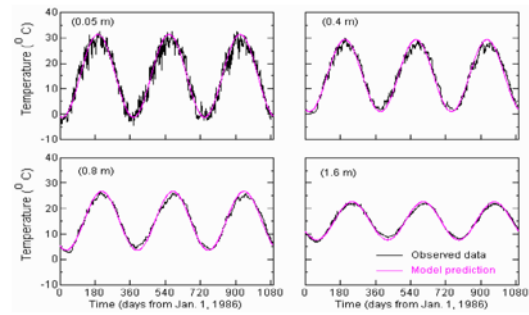


Figure 1. Measured mean and predicted soil temperatures at four depths based on measured soil surface temperatures (Wu and Nofziger, 1999)

3 ABOVE SURFACE TEMPERATURE

Different studies has dealt with and studied air temperature such as meteorology, climatology and etc. Air temperature is commonly measured at 2 m above the ground in weather stations, which are dependent on the regional infrastructure for weather data collection network. These data are collected as point samples whose distribution is rarely designed to capture the range of climate variability within a region. The spatial information available on air temperature is thus often limited, especially in sparsely populated and underdeveloped regions (Vancutsem et al., 2010). There are some limitations in air temperature measurements in the meteorology or climatology stations such as expensive measurements and samplings, low spatial resolution etc. Using complementary methods can be useful and make the measurements accurate and precise.

Benali et al. (2012) estimated T_{\max} , T_{\min} and T_{avg} for a 10 year period based on remote sensing LST product obtained from MODIS ,and auxiliary data using a

statistical approach. They developed the statistical models for their study and RMSE of T_{\max} and T_{\min} was 1.74 °C while RMSE of T_{avg} was 1.33 °C. Sahin et al (2012) introduce artificial neural networks for the estimation of land surface temperature using meteorological and geographical data in Turkey. The RMSE between the estimated and ground values was less than 1 k. Goward et al. (2002) estimated air temperature, from the thermal vegetation index procedure (TVX) in which a field of pixels is used to define the relationship between vegetation canopy cover, using a spectral vegetation index, and T_s from the split window technique. Prince et al (1998), assumes that the surface temperature of a closed canopy is equal to air temperature and so the air temperature can be obtained by interpolating the relationship to the spectral vegetation index and a closed canopy at which point surface temperature and the air temperature are the same.

Unlike surface temperature, few procedures exist for the estimation of surface air temperature from satellite observations. This is because the land surface energy balance is a complex phenomenon that depends on multiple variables (e.g., surface roughness, wind speed, soil moisture) whereas most sensors in orbit do not have the necessary spectral, spatial and temporal resolutions to constrain the problem adequately (Prince et al, 1998).

The derivation of near surface air temperature (T_a) from satellite information is far from straightforward. This includes two steps: (i) the derivation of skin surface temperature (T_s) from the thermal infrared (TIR) signal received by the sensor, and (ii) the estimation of T_a from T_s (Vancutsem et al., 2010).

To estimate T_a from T_s , two approaches may be distinguished according to the time of day. During the night, the retrieval of minimum T_a is simpler as the solar radiation does not affect the thermal infrared signal. During daytime, the difference between T_s and maximum T_a is mainly controlled by the surface energy balance, which is a complex system dependent on information not easily available (e.g. solar radiation, cloud-cover, wind speed, soil moisture and surface roughness) (Prince et al., 1998). Some studies have tried to derive maximum T_a from satellites through regression analysis. The most common one, known as the temperature-vegetation index method (TVX), is based on the assumption that the radiometric temperature of a fully vegetated canopy is in equilibrium with ambient air temperature, because of the similar heat capacity of dense vegetation and the surrounding air (Nemani& Running, 1989; Goward et al., 2002; Prince&Goward, 1995; Prihodko&Goward, 1997; Goetz, 1997; Goetz et al., 1995; Stisen et al., 2007).

The temperatures of the surfaces found in the surroundings influence decisively the temperature of the air parcel located at a given point (Unger et al, 2009).

Physically, surface temperature influences air temperature above the land surface because there is a heat transfer between atmosphere and surface. The equations used to estimate air temperature based on surface temperature is the same as equation for estimating sub surface temperature because the temperature above surface have relatively same pattern with it in the soil depth (Khomarudin et al, 2006). Khomarudin et al. (2006) in a study determined the best equation to calculate surface temperature from NOAA/AVHRR that it was Ulivieri et al.

Figure 2 compares the measured and predicted soil temperatures for the same site when model parameters are obtained from air temperatures instead of measured soil surface temperatures. The model consistently underestimates soil temperatures by about 2 degrees Celsius. These data and those of others suggest that good estimates of temperatures under bare soils can be obtained using by simply increasing the maximum and minimum air temperatures by 2 degrees when defining the model parameters. The correction for soils that are not bare will likely be less since those soil temperatures are somewhat less due to shading from the plants (Wu and Nofziger, 1999)

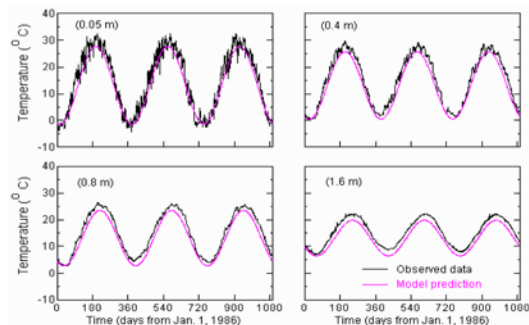


Figure 2. Comparison of measured and predicted soil temperatures at four depths based upon air temperatures at the site (Wu and Nofziger, 1999)

4 CONCLUSIONS, FUTURE DEVELOPMENT AND PERSPECTIVE

Remote sensing technology can be helpful to estimate temperature at surface, above surface and below surface. This research shows that thermal remote sensing is one of the most effective technologies for studies that deal with temperature. Using some techniques, algorithms and models, we can retrieve temperature from thermal remote sensing data.

As mentioned before, there is a gap in researches about the capability of thermal remote sensing in

retrieving AST and SubST based on LST which may provide valuable information for studying some phenomena and features. Thus, in this research, we investigated the relationship between LST to SubST and AST that can be used in many studies. We showed that LST can be a good indicator for estimating of SubST and AST. Therefore we generally conclude that when we have LST, estimating of SubST and AST is possible. However, there are some important limitation and restriction when we use LST to estimate AST and SubST that we should take in to account.

Even today, as a result of the resolution tradeoffs involved in using satellite data, it is difficult, and sometimes impossible, to acquire satellite temperature with high spatial and temporal resolutions.

From the obtained results we generally concluded that different soil, plant, water and air related parameters are needed that must be taken into account for model validations and retrieval subsurface and air temperature. Because of different natural of water and land, using LST for estimating SubST and AST can be affected by different parameters.

- Estimation of air temperature from the thermal signal is very complex due to atmospheric emission (Quattrochi and Luvall, 2004). Water and land based parameters must be taken in to account when dealing with retrieving AST from LST.
- Elevation and temperature inversions may affect surface temperature values and that these factors should ideally be taken into account when processing thermal images.
- Mixture of emitted radiance from various sources can be problematic to detect anomalies with confidence.
- Factors such as albedo, topographic slope/aspect, emissivity, and thermal inertia affect the temperature changes of Earth surfaces over the 24 hour temperature cycle.
- Shallow groundwater affects thermal properties of soil.
- Complexity of retrieval algorithms also is a subject that can be obstacle when using satellite data to estimate temperature.
- Some authors also pointed out that the effect of elevation should be treated with due care in the interpretation of temperature data to ensure false anomalies are filtered out (Eneva and Coolbaugh, 2009).

Beside all of these, Because of varying nature of various objects (such as vegetated surface) on the earth, understanding of LST is obscure. Another factor leading to the difficult understanding of LST is that the surface is not homogeneous at the spatial resolution (pixel scale) of remote sensing data (Qin and Karnieli, 1999). Usually, LST changes obviously in a small distance such as 1m (Ottle and Vidal Madjar

1992). However, the spatial resolution of most remote sensing data for LST is low compared with the difference of LST on the ground.

Future studies ought to focus on the following subjects to improve the methodologies of extracting AST and SubST from LST measurements:

- 1- Using hyperspectral TIR sensors with hundreds of channels are better able to extract land surface parameters than multispectral TIR sensors to enhance the accuracy of thermal data.
- 2- Taking into account other sciences such as geomorphology, soil, hydraulics, ground water, and etc. can improve the accuracy of TIR for detecting of AST and SubST.
- 3- Integration of remote sensing with other data sources, such as ground surveys data source can strongly improve our capacity to uncover unique and invaluable information.
- 4- InSAR data can add information on earth surface deformation, subsidence/uplift, which can be coupled to the development of the reservoir through reservoir modelling. However a number of steps need to be taken for a full uptake of remote sensing in geothermal exploration.

REFERENCES

- Alavipanah, SK., *Thermal Remote Sensing and its application in earth science. 2001: University of Tehran press Tehran.*
- Arya, S, P., (1998). Introduction to Meteorology. Academic Press, Inc. San Diego, California 92101.
- Benali, A., Carvalho, A. C., Nunes, J, P., Carvalhis, N., & Santos, A., (2012), Estimating air surface temperature in Portugal using MODIS LST data, *Remote Sensing of Environment*, 124, 108–121.
- Ben-Dor, E., M. Kochavi, L. Vinizki, M. Shionim & J. Portugal (2001) Detection of buried ancient walls using airborne thermal video radiometry. *International Journal of Remote Sensing*, 22, 3689-3702.
- Coolbaugh, M., C. Kratt, A. Fallacaro, W. Calvin & J. Taranik (2007) Detection of geothermal anomalies using advanced spaceborne thermal emission and reflection radiometer (ASTER) thermal infrared images at Bradys Hot Springs, Nevada, USA. *Remote Sensing of Environment*, 106, 350-359.
- Eneva, M., M. Coolbaugh & J. Combs (2006) Application of satellite thermal Infrared imagery to geothermal exploration in East Central California. *Geothermal Resources Council Transactions*, 30, 407-411.
- Eppelbaum, L. (2009) Near-surface temperature survey: An independent tool for delineation of buried archaeological targets. *Journal of Cultural Heritage*, 10, e93-e103.
- Flórides, G. and S. Kalogirou, *Ground heat exchangers—A review of systems, models and applications. Renewable Energy*, 2007. 32(15): p. 2461-2478.
- Goetz, S.J., 1997. Multi-sensor analysis of NDVI, surface temperature, and biophysical variables at a mixed grassland site, *International Journal of Remote Sensing*, 18 (1), 71–94.

- Goetz, S.J., Halthore, R., Hall, F.G., Markham, B.L., 1995. Surface temperature retrieval in a temperate grassland with multiresolution sensors, *Journal of Geophysical Research*, 100 (D12), 25397–25410.
- Goward, S. N., Xue, Y. K., & Czajkowski, K. P. (2002). Evaluating land surfacemoisture conditions
- Hansen, J., D. Johnson, A. Lacis, S. Lebedeff, P. Lee, D. Rind & G. Russell (1981) Climate impact of increasing atmospheric carbon dioxide. *Science*, 213, 957-966.
- Haselwimmer, C. & A. Prakash. 2011. Use of airborne thermal imaging to quantify heat flux and flow rate of surface geothermal fluids at Pilgrim Hot Springs, Alaska. In *AGU Fall Meeting*.
- Haselwimmer, C. & A. Prakash. 2013. Thermal Infrared Remote Sensing of Geothermal Systems. In *Thermal Infrared Remote Sensing*, 453-473. Springer.
- Hillel, D. 1982. *Introduction to soil physics*. Academic press New York.
- Hodder, D. (1970) Application of remote sensing to geothermal prospecting. *Geothermics*, 2, 368-380.
- Holmes, T., et al., *Estimating the soil temperature profile from a single depth observation: A simple empirical heatflow solution*. *Water Resources Research*, 2008. 44(2).
- Khomarudin, M. R., Bey, A & Khomarudin, I. (2006), Estimation of air temperature using remote sensing, based on thermal diffusivity approach, *Remote sensing and earth sciences*, 3, 24-30.
- Kienholz, C., A. Prakash & A. Kolker. 2009. Geothermal exploration in Akutan, Alaska, using multitemporal thermal infrared images. In *AGU Fall Meeting Abstracts*, 1009.
- Lee, K. (1978) Analysis of thermal infrared imagery of the Black Rock Desert geothermal area. *Q. Colo. Sch. Mines;(United States)*, 73.
- Li, Z.-L. & F. Becker (1993) Feasibility of land surface temperature and emissivity determination from AVHRR data. *Remote Sensing of Environment*, 43, 67-85.
- Li, Z.-L., et al., *Satellite-derived land surface temperature: Current status and perspectives*. *Remote Sensing of Environment*, 2013. **131**: p. 14-37.
- Mannstein, H., 1987, Surface energy budget, surface temperature and thermal inertia. In *Remote Sensing Applications in Meteorology and Climatology*, edited by R. A. Vaughan and D. Reidel (Dordrecht, Netherlands: A Reidel Publishing Co), NATO ASI Series C: Mathematical and Physical Sciences, 201, 391–410.
- Mongillo, M. (1994) Aerial thermal infrared mapping of the Waimangu-Waiotapu geothermal region, New Zealand. *Geothermics*, 23, 511-526.
- Montrith, J. L and Unsworth, M, H., (1989). *Principles of Environmental Physics* 2nd edn. Chapman and Hall, Inc. New York, NY.
- Nemani, R. R., Running, S. W., Pielke, R. A., & Chase, T. N. (1996). Global vegetation cover changes from coarse resolution satellite data. *Journal of Geophysical Research-Atmospheres*, 101(D3), 7157–7162.
- Prihodko, L., and Goward, S. N., (1997), Estimation of Air Temperature sensed surface observations from remotely sensed surface observations, *Remote Sensing of Environment*, 60, 335-346.
- Prihodko, L., & Goward, S. N. (1997). Estimation of air temperature from remotely sensed surface observations. *Remote Sensing of Environment*, 60(3), 335–346.
- Prince, S. D., & Goward, S. N. (1995). Global primary production: A remote sensing approach. *Journal of Biogeography*, 22(4–5), 815–835.
- Prince, S. D., Goetz, S. J., Dubayah, R. O., Czajkowski, K. P., & Thawley, M. (1998). Inference of surface and air temperature, atmospheric precipitable water and vapor pressure deficit using advanced very high-resolution radiometer satellite observations: Comparison with field observations. *Journal of Hydrology*, 213(1–4), 230–249.
- Qin, Z. and A. Karnieli, *Progress in the remote sensing of land surface temperature and ground emissivity using NOAA-AVHRR data*. *International Journal of Remote Sensing*, 1999. 20 (12): p. 2367-2393.
- Quattrochi, D.A. and J.C. Luvall, *Thermal Remote Sensing in Land Surface Processing*. 2004: CRC Press.
- Rowlands, A., A. Sarris & J. Bell (2006) Airborne multi sensor remote sensing of exposed and subsurface archaeological remains at Itanos and Roussolakkos, Crete. *BAR INTERNATIONAL SERIES*, 1568, 113.
- Şahin, M., et al., *Modelling and remote sensing of land surface temperature in Turkey*. *Journal of the Indian Society of Remote Sensing*, 2012. 40(3): p. 399-409.
- Seielstad, C. & L. Queen (2009) Thermal Remote Monitoring of the Norris Geyser Basin, Yellowstone National Park. *Final Report for the National Park Service Cooperative Ecosystem Studies Unit, Agreement*, 38.
- Sellers, P., F. Hall, G. Asrar, D. Strebel & R. Murphy (1988) The first ISLSCP field experiment (FIFE). *Bulletin of the American Meteorological Society*, 69, 22-27.
- Stisen, S., Sandholt, I., Norgaard, A., Fensholt, R., & Eklundh, L. (2007). Estimation of diurnal air temperature using MSG SEVIRI data in West Africa. *Remote Sensing of Environment*, 110(2), 262-274.
- Unger, J., Gal, T., Rakonczai, J., Mucsi, L., Szatmari, J., Tobak, Z., (2009), Air temperature versus surface temperature in urban environment, The seventh International Conference on Urban Climate, 29 June, 3 July 2009, Yokohama, Japan.
- Van der Meer, F., C. Hecker, F. van Ruitenbeek, H. van der Werff, C. de Wijkerslooth & C. Wechsler (2014) Geologic remote sensing for geothermal exploration: A review. *International Journal of Applied Earth Observation and Geoinformation*, 33, 255-269.
- Vancutsem, C., Ceccato, P., Dinku, T., & Connor, S. J. (2010). Evaluation of MODIS land surface temperature data to estimate air temperature in different ecosystems over Africa. *Remote Sensing of Environment*, 114, 449-465.
- Vaughan, R., L. Keszthelyi, J. Lowenstern, H. Heasler & C. Jaworowski. 2011. Measuring and monitoring heat flow and hydrothermal changes in the Yellowstone Geothermal System using ASTER and MODIS thermal infrared data. In *AGU Fall Meeting Abstracts*, 02.
- Watson, F.G.R., Lockwood, R.E., Newman, W.B., Anderson, T.N., Garrott, R.A., 2008. Development and comparison of Landsat radiometric and snowpack model inversion techniques for estimating geothermal heat flux. *Remote Sensing of Environment*. 112 (2), 471–481.
- Wu, J. & D. Nofziger (1999) Incorporating temperature effects on pesticide degradation into a management model. *Journal of environmental quality*, 28, 92-100.

Future of Remote Sensing Applications: Thermal Remote Sensing of Human Emotions

S.K.Alavipanah, M.M.Rezvani

Department of Cartography, Faculty of Geography, University of Tehran,

Salavipa@ut.ac.ir, Rezvani.m@ut.ac.ir

ABSTRACT - Today, with the increasing development of remote sensing science, saw a dramatic expansion of it in various scientific fields such as meteorology, geology, Global warming Risk assessment, Water resource etc, but place of this science in the field of humanities has always been empty. In this context, issues like global health and quality of human society life should be considered further. Therefore, some sciences such as medicine and psychology, new imaging systems have also remarkably grown in this field. Undoubtedly, All images were obtained in medicine obey the principles of remote sensing, but never have been studied from its perspective. Undoubtedly one of the key parameters that are studied in this field is heat and temperature of human body in different emotions. Meanwhile, in the approaches that are based on reflection of thermal electromagnetic waves, particularly in the area of thermal infrared range large gaps exist. To realizing this issue emotions must be defined and classified first, such as happiness, sadness, love, hate, fear, stress etc. then Proceeding to apply remote sensing capabilities within this range of waves and its techniques in diagnosis of these conditions. In this study, thermal properties of human body, short overview of the researches in the field of emotions and body temperature are offered, then human emotions are classified and the capabilities of remote sensing for better diagnostics are offered. Finally, in order to pave more the way suggestions will be raised.

1 INTRODUCTION

Emotions are psycho-physiological processes that play a key role in human life. They are an essential part of social interaction and can have strong regulatory influence on many important conscious and unconscious aspects of human behavior, While the human body temperature changes in different states of mind, is now well proven. Body temperature is stabilized and controlled by certain neurons in the hypothalamus that are sensitive to the surrounding blood temperature. The body can change its conductivity by expansion and contraction of the arteries that supply blood to the veins and capillaries of the outer skin layer below it. So therefore, the body shows its reaction with changes in skin surface temperature and thus the thermal long wave radiation, physically and psychologically. This does not concern only to the physical state but also correspond with many mental and psychological states. Today one of the new application of remote sensing is in medical science. Since the Medical images taken at very close intervals in some sources referred to as close range remote sensing. Most medical remote sensing is designed to "see into" the body without having to be invasive (cutting it open). While no one has ever Offered an appropriate investigation, which reflects the ability of remote sensing to detect and measure emotions.

Therefore, in this study in a comprehensive review, attempted to introduce some of the researches

which have been used Remote sensing capabilities in detection and measurement of emotions.

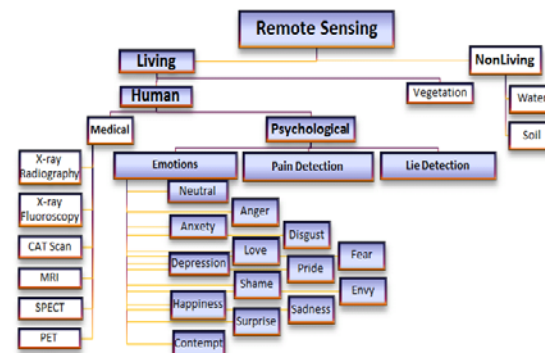


Fig. 1: Flowchart of remote sensing applications

2 REMOTE SENSING OF EMOTIONS

The first important point in the study of emotions is that emotional responses are the same for different people in the same situation, So the same definitions can be provided for different scenarios.

2.1 Which Parts of Body are Affected by Emotions

As mentioned above we can extract some rules for relation between body parts and emotions, in this regard, [2] With study on 701 volunteers Attempted to extract the common parts of the human body that affected by different emotional conditions.

Although no physical and imaging device were used in this study But 71% of volunteers had similar

response for same stimuli, which is the evidence for equal treatment of the human body in various emotional and sensory situations.

When a person experiences elevated feelings of alertness, anxiety, or fear increased levels of adrenaline regulate blood flow. Redistribution of blood flow in superficial blood vessels causes abrupt changes in local skin temperature. This is readily apparent in the human face where the layer of flesh is very thin. The human face and body emit both in the mid- (3-5 μm) and far infrared (8-12 μm) bands. Therefore, mid- and far infrared thermal cameras can sense temperature variations in the face at a distance, producing 2D images (thermograms). In this regard Many researchers and scientists have attempted to use thermal images to identify different states.

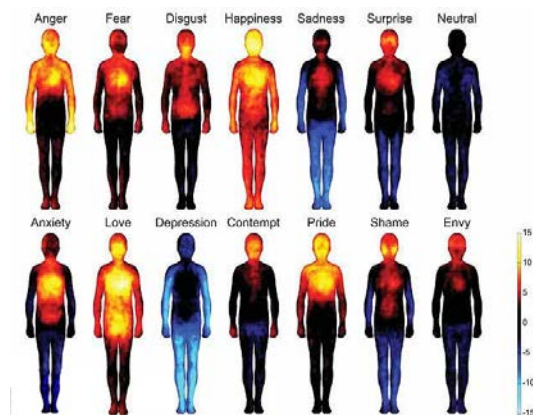


Fig. 2: result of study on 701 volunteers to extract affected regions of body by emotions stimuli with 71% similar volunteer response.

In a study [3] authors have attempted to analyze emotions on the Nasal Temperature Change Model. They suggested that human emotion is expressed as a vector in the plane with Pleasantness and Arousal axis. they analyzed basic psychology and the physiology change from the nasal thermal images. First, they focused to nasal thermal change depends on vasoconstriction as Pleasantness to Unpleasantness (P-U) estimation model. P-U estimation model was structured by biregressive; explanatory variables are nasal temperature changes. As results, they obtained good P-U estimates and the effectiveness was confirmed. Next, they focused to local fractal dimension of nasal thermal image depend on the complexity of nasal vasculosus plexus as Arousal to Sleepiness (A-S) estimation model. A-S estimation model was structured by biregressive; explanatory variables are local fractal degrees. As results, significant correlations with amplitude of α rhythm they reconfirmed. Finally, They attempted estimation

of emotions using thermal images in watching video programs using PU and A-S estimation models. AS results, emotional changes in time series re estimated. Moreover, estimates they redistributed corresponding to the video programs in the two-dimensional plane with P-U and A-S axis. The emotional strength and type was expressed as a vector from the origin.

Also in another similar study [4] by using thermal imagery detect the stress and fear .They propose a concept for detecting suspects engaged in illegal and potentially harmful activities in or around critical military or civilian installations. They investigate the use of thermal image analysis to detect at a distance facial patterns of anxiety, alertness, and/or fearfulness. This is a totally novel approach to the problem of biometric identification. Instead of focusing on the question .who are you. we focus instead on the question .what are you about to do?

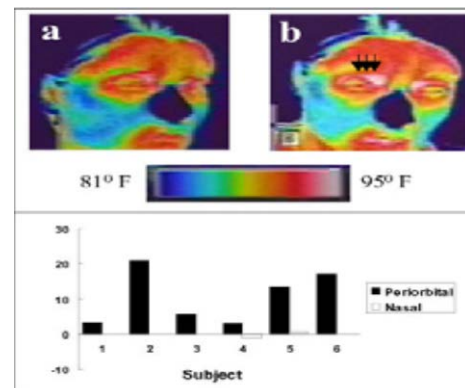


Fig. 3: Thermal images of the face for a subject (a) before and (b) 300 msec after an instantaneous startle.

Arrows indicate local warming in the periorbital area. The color bar depicts the false coloring scheme from the lowest (810 F) to the highest (950 F) temperature. (c) Changes of the average pixel value in the periorbital and nasal areas with auditory startle. The changes are depicted for each subject ($n=6$ subjects). Positive deviation represents local warming and negative deviation, cooling.

2.2 Emotions and its Thermal Signatures

When spectral and thermal signatures can be extracted for all kind of materials, why it could not for the emotions?

In some cases, researchers tried to apply different stimuli for extracting spectral signatures of different emotional states[5]. They considered three different conditions: stress induced by psychological pressure and other people judgement, pain and fear to feel pain, and sexual arousal and excitement.

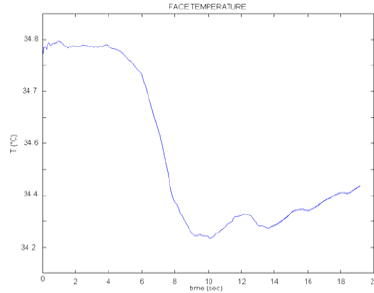


Fig. 4: Overall average Face Sympathetic Thermal Response to sub-painful stimuli.

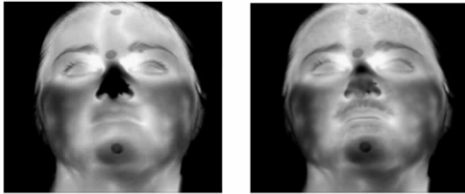


Fig.5: Facial Sudomotor Sympathetic Thermal Response. Left) Rest temperature distribution before receiving sub-painful stimulus; Right) Temperature decrease and onset of sudomotor sympathetic sweating especially appreciable on the perioral and forehead regions.

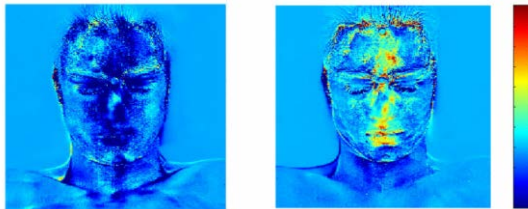


Fig. 6: Overall average of the cutaneous blood perfusion rate for one of the volunteers (in arbitrary units). On the left, the average distribution while watching sport movies; on the right, the average distribution while watching erotic content movies.

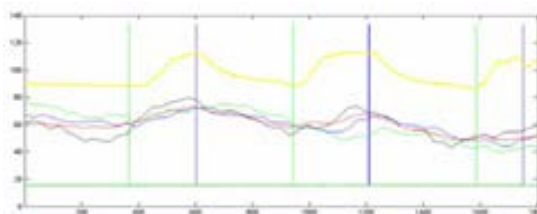


Fig. 7: Overall average time dynamics of the temperature of several facial regions and of the penis turgidity (yellow line). Temperature changes are phase locked to penis turgidity, then to sexual arousal.

2.3 Thermal Remote Sensing and Pain Regions Detection

Digital infrared thermal imaging is a noninvasive diagnostic technique that allows the examiner to visualize and quantify changes in skin surface temperature. In this regard [6] have been extracted pain area by using Thermal imagery. To evaluate the detection performance, they apply SOFES¹ algorithm to the well-known diseases which can be detected broadly to use the thermography. Figure 8 shows the detection results for a foot of the glycosuria, the degenerative

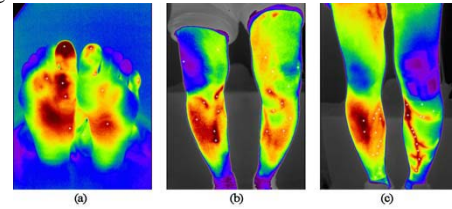


Fig. 8: Detection results of the suspicious pain regions. White asterisk marks represent those regions. (a) Foot of the glycosuria patient. (b) The degenerative arthritis. (c) The varicose vein.

2.4 HyperSpectral Imagery and Stress Detection

In some cases, Scientists have been used more specialized capabilities of remote sensing techniques in this context, for example, [6] by using hyper spectral imagery based on the principle that heat stress increases adrenaline detect the stress. Emotional or physical stresses induce a surge of adrenaline in the blood stream under the command of the sympathetic nerve system, which, cannot be suppressed by training. The onset of this alleviated level of adrenaline triggers a number of physiological chain reactions in the body, such as dilation of pupil and an increased feed of blood to muscles etc. This paper reports how Electro-Optics (EO) technologies such as hyper spectral and thermal imaging methods can be used for the detection of stress remotely.

This paper presents the hyperspectral characteristics of haemoglobin oxygenation for the representation of physiological responses to stress, and algorithms for characterizing haemoglobin saturated oxygenation have been established and subsequently validated using a set of test case data. Preliminary result has shown a positive identification of stress through an elevation of oxygenation saturation level in the facial region, and the effect due to physical stressors has been seen more prominently than the emotional one.

¹Survival Of the Fitness kind of the Evolution Strategy

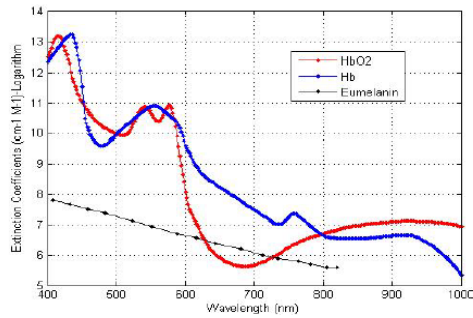


Fig. 9: shows the molar extinction coefficients (proportional to absorptivity) of deoxy-haemoglobin (Hb) and oxy-haemoglobin (HbO2) in the visible and near infra-red regions[9]. The HbO2 absorbs electromagnetic waves notably at wavelengths around 410, 545 and 578nm, while the absorptions of Hb are found predominately at around 415 & 555nm. It is found that the absorbance of the melanin varies linearly with the wavelength.

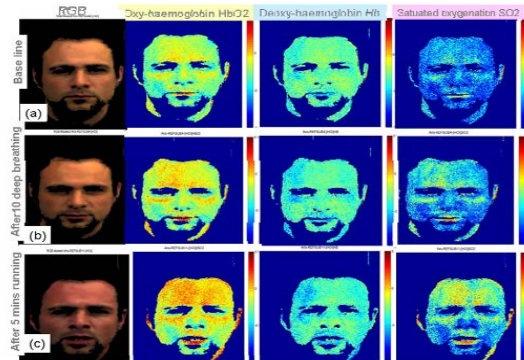


Fig. 10: shows the result for the detection of physical stress by sensing the increases of blood oxygenation using HSI technique. The experiment is arranged by requesting a subject to (a) sit on chair for rest as the base line condition, heart beat ~80BPM, (b) slow but deep breathing for 10 times while remain seated, heart beat increases to 90BPM, (c) after running for 5 minutes, heart beat increases to 140BPM. As in fig 4 all maps are presented in false colours with All maps are shown in false colours with hot (red) and cold (blue) colours representing high and low concentrations respectively.

2.5 Emotions Classification Using Thermal Imagery

As we know Emotions can be classified in this context [8] with interesting initiative study recognize and classify physical and emotional stress by using thermal images, They in a Comprehensive plan combine thermal imaging and hyper spectral methods for monitoring blood volume, and temperature of the

skin surface at the moment of stress. After reviewing and summarizing the physical changes in the body caused by stress, taking thermal images and compare them in different situation of stress and normal states.

Note that the thermal pattern in the prefrontal region (rectangular box) due to emotional stress is seen to be very distinct from that of the physical stressors .This paper reports the remote sensing of stress through one' sphysiological responses using EO imaging technique. Hyperspectral as well as thermal imaging have been employed for characterising physiological properties of physical as well as emotional stresses, they have found patches of alleviated temperature regions in the forehead forming patterns characteristic to the types of stressors, dependent on whether they are physical or emotional in origin. These stress induced thermal pattern shave been seen to be quite distinct to the one resulting from having high fever.

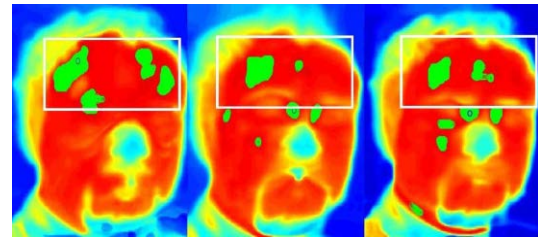


Fig. 11: shows the averaged thermal images of the subject after the emotional (left) and physical (middle and right) stressors are applied. All images are projected onto an arbitrary pose by using an image registration technique, and they are then averaged to give a more faithful representation of the thermal signatures due to various stressors.

In another interesting research [10] classified emotions by focusing on 8 different positions of forehead using near infrared spectroscopy (fNIRS) method on 8 volunteers. They composed a slideshow for audio-visual emotional induction containing stimuli from the International Affective Picture System (IAPS) [11] and International Affective Digital Sounds (IADS) [12]. Pictures and sounds with extreme ratings in valence and arousal according to the self assessment ratings in [13], [12] were selected and categorized into the following three emotion classes:

- VA - Maximum valence and maximum arousal: This class contained e.g. pictures of female erotica and exciting sports, rhythmic music and shouts of joy.
- Va - Maximum valence and minimum arousal: This class contained e.g. pictures of flowers and animals, calm classical music and environmental sounds.
- vA - Maximum arousal and minimum valence: This class contained e.g. pictures of mutilated persons and

threatening situations and sounds from air raid, and screaming persons.

The picture and sound items were selected to achieve a strong emotional stimulation and discriminability between the classes.

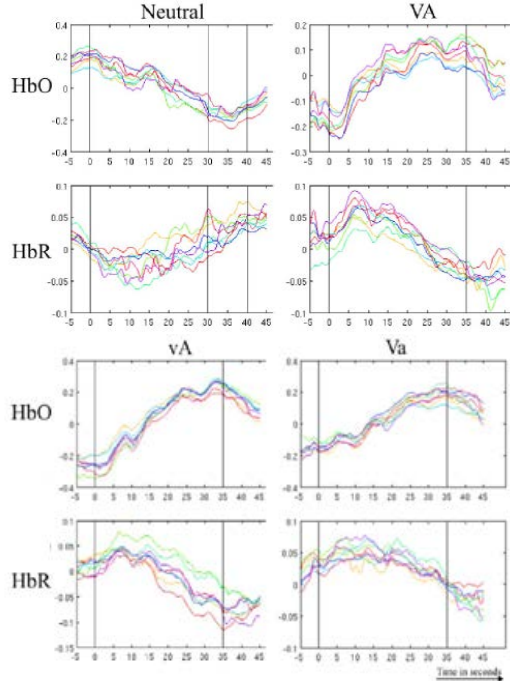


Fig. 12: Hemodynamic responses (grand averages) for the classes VA, vA, Va, and Neutral. The top row shows *HbO2* channels, the bottom row shows *HbR* channels. Signal epochs start 5 seconds before the beginning of an emotion induction or Neutral block and end 10 seconds after the end of the blocks. Vertical lines indicate begin and end of a block (as Neutral blocks have random length, the second and third vertical line in these plots indicate the time period where the blocks end). The x-axes show time in seconds, the y-axes concentration changes of *HbO2* and *HbR*.

Several different feature extraction methods have been used for fNIRS based BCIs, including simple statistical properties of the time-domain signals, such as mean, standard deviation, slope, kurtosis and skewness. These features intuitively express properties of the characteristic shape of hemodynamic responses, when applied to stimulus-locked fNIRS signals. However, in the case of continuous recognition, most of these features do not reflect easily interpretable signal properties. They decided to use only the mean value of short windows of the *HbO2* and *HbR* signals for the evaluations in this paper.

The columns correspond to the classes VA, vA, Va, and Neutral, respectively. Hemodynamic responses to the emotion induction are obviously present and show a typical shape at all channels and all classes. For the three emotion classes (VA, vA and Va), *HbO2* channels show an increase (hyper-oxygenation), while *HbR* show a decrease in concentration few seconds delayed after the beginning of each block. One can see that the hemodynamic responses remain stable.

In this paper, they presented a system for the continuous (i.e. asynchronous) recognition of affective states from fNIRS signals in response to different classes of audio-visual affective stimulation. In comparison to the results reported by previous studies, the performance of our system may appear inferior. However, continuous recognition is a much more challenging task than stimulus-locked evaluations. In this first study they chose a simple setup that allows an easy analysis and interpretation of all processing steps involved. Significant recognition results indicate that it is possible to discriminate Neutral signals from signals recorded during emotion induction. Discriminating different emotion classes against each other appeared to be more difficult. However, the results show that strongly different classes may also be discriminated using continuous recognition. The analysis of classification performance over time indicates that the continuous recognition of affective states of longer duration (such as mood) might be possible as recognition rates appear to remain stable for most of the evaluated binary classification tasks.

3 CONCLUSIONS

In this paper, we presented a totally novel approach of remote sensing. We attempted to review articles which recognizing emotions by using remote sensing tools and introduced another perspective of remote sensing called Emotional Remote sensing especially with the approach of heat and body temperature changes which has been less attentions paid.

First with the introduction of different psychological states, different body parts that affected by, and its response to changes in temperature are determined. Next we focused to apply different stimuli for extracting spectral signatures of different emotional states and then we reported the extraction of pain area by using Thermal imagery. Next we reported how Electro-Optics (EO) technologies such as hyper spectral and thermal imaging methods can be used for the detection of stress remotely then we recognize and classify physical and emotional stress by using thermal images. Finally, we reported classification of emotions by focusing on 8 different positions of forehead using near infrared spectroscopy.

Presented paper are just a few of many efforts which done by scientists in this context. with the purpose that temperature and its changes can be seen as an indicator for understanding human behavior and mental issues. in the other hand, it must be said that the feelings and reactions of the human body and the heat have conceivable relations.

This content is proof of truth and accuracy of the assumption that emotions can be also remotely sensed or even be able to extract the spectral signature of each human emotions. however, the complexity of this issue is too much, but its importance may be realized in near future years. but it is time to take more specialized and broader perspective on emotional remote sensing.

REFERENCES

- [1] Alavipanah, SK., *Thermal Remote Sensing and its application in earth science*,. 2001: University of Tehran press Tehran.
- [2] L.Nummenmaa., *Bodily maps of emotions*,PNAS,2014,v.11 no. 2, 646-651.
- [3] H.Tanaka,Y.Nagashuma,H.Ide., *An Attempt of Feeling Analysis by the Nasal Temperature ChangeModel*,.IEEE 2000, 0-7803-6583-6/00.
- [4] I.Pavlidis,J.Levine,P.Baukol.,*Thermal Imaging for Anxiety Detection*,.IEEE 2000, 0-7695-0640
- [5] A.Merla,L.Romani., *Thermal Signatures of Emotional Arousal: A Functional Infrared Imaging Study*,. IEEE EMBS 2007, 247-249.
- [6] J.Lee,S.Song., *Detection of Suspicious Pain Regions on a Digital Infrared Thermal Image using the Multimodal Function Optimization*,. IEEE EMBS 2008, 4055-4058.
- [7] P.Yuen,T.Chen., *Remote detection of stress using Hyperspectral imaging technique*,. Applied Remote Sensing 2009, 56-62.
- [8] P.Yuen,K.Hong., *Emotional & physical stress detection and classification using thermal imaging technique*,.2009, ESD09-SD10-16.
- [9] Prahl S, <http://omlc.ogi.edu/spectra/hemoglobin/>
- [10] D.Heger,R.Mutter,C.Herff., *Continuous Recognition of Affective States by Functional Near Infrared Spectroscopy Signals*,. IEEE 2013, 832-837.
- [11] P. J. Lang, M. M. Bradley, and B. N. Cuthbert.,*International affective picture system (iaps): Technical manual and affective ratings*,. 1999.
- [12] M. M. Bradley and P. J. Lang, *„The international affective digitized sounds (; iads-2): Affective ratings of sounds and instruction manual*,.University of Florida, Gainesville, FL, Tech. Rep. B-3, 2007.
- [13] P. Lang and M. M. Bradley.,*The international affective picture system (iaps) in the study of emotion and attention*,.Handbook of emotion elicitation and assessment, p. 29, 2007.

Validation and analysis of land surface temperature from FengYun-2C (FY-2C) data

Xiaoning Song^{1,*}, Yawei Wang¹, Zhao-Liang Li^{2,3}, Bohui Tang⁴, Pei Leng¹

1. College of Resources and Environment, University of Chinese Academy of Sciences, Beijing 100049, China;

2. ICube, UdS, CNRS, Boulevard Sebastien Brant, CS10413, Illkirch F-67412, France;

3. Key Laboratory of Agri-Informatics, Ministry of Agriculture/Institute of Agricultural Resources and Regional Planning, Chinese Academy of Agricultural Sciences, Beijing 100081, China

4. Key Laboratory of Water Cycle and Related Land Surface Processes, Institute of Geographical Sciences and Natural Resources Research, Chinese Academy of Sciences, Beijing, 100101, China

songxn@ucas.ac.cn

ABSTRACT—Land surface temperature (LST) is a key variable in the research of water cycle and energy budgets between the land and atmosphere interface, and also a vital parameter in the physics of land surface processes on regional and global scales. This study primarily addressed the theory of LST retrieval from the Chinese operational geostationary meteorological satellite FengYun-2C (FY-2C) data in two thermal infrared channels, using the Generalized Split-Window (GSW) algorithm. Accuracy of the FY-2C images derived LST was evaluated over the heterogeneous area of the Tibetan Plateau region using the Moderate-resolution Imaging Spectroradiometer (MODIS) LST product. The results revealed an overall significant correlation between the two datasets, the coefficient of correlation, R , varied from 0.72 to 0.95 and the root mean square error (RMSE) ranged from 0.44 to 3.87K during July and August in 2008. To analyze the possible sources of error that caused by the differences of emissivity, MOD11A1 was implemented to estimate emissivities of two thermal infrared channels of FY-2C images instead of MOD11A2 that originally used in the algorithm, the result showed that using MOD11A2 takes some uncertainties (the RMSE of two days in August 2008 were 0.75 K and 0.42K, respectively) to retrieve the hourly LST.

1 INTRODUCTION

Land surface temperature (LST) is an essential parameter in the research and applications in climate, hydrology and ecology, and it plays a significant role in the understanding of the water and energy balance of the Earth's surface. With the rapid development of the remote sensing technology, a number of methods and algorithms have been developed to retrieve LST using satellite data. In 1980s, Becker evaluated the effects of reflectance difference between the two thermal infrared channels of Advanced Very High Resolution Radiometer (AVHRR) data on the estimation of LST, and proved that using split-window algorithm for estimating of LST was practicable in theory (Becker 1987). Afterwards Vidal (1991) addressed that LST could be estimated from NOAA data with an error of 3K. In a later study, Qin and Karnieli (1999) estimated LST by split-window algorithm from AVHRR data which was based on assuming a fixed emissivity of 0.96. Compared with the polar-orbit satellites, geostationary satellites are capable of providing 48-96 images per day with a fixed observation angle for a given pixel, which is

most likely beneficial for the study of terrestrial water and energy budgets. In recent years, progressive attentions have been paid to the estimation of LST from geostationary meteorological satellite data. Trigo et al. (2008) produced LST product from the Meteosat Second Generation-Spinning Enhanced Visible and Infrared Imager (MSG-SEVIRI) data. For the first operational Chinese geostationary satellite, FengYun-2C (FY-2C), Tang et al. (2008) addressed the retrieval of LST using the generalized split-window algorithm proposed by Wan and Dozier (1996), results using the simulated data indicated that the split-window algorithm can be successfully applied to the LST retrievals from FY-2C data. However, persuasive validation is sorely lacking to further confirm the feasibility of using this method to obtain regional LST using FY-2C images. Followed by the FY-2C satellite, FY-2D was another operational geostationary satellite initiated by the China Meteorological Administration (CMA). In a recent study, Zhang et al. (2013) retrieved LST from FY-2D and validated it with MODIS data in a small scale; the coefficient of correlation (R) and the root mean square error (RMSE) were 0.5 and 4.4K, respectively. To date, the researches of heterogeneous

study areas are rarely seen probably due to the lacking in the validation and error analysis of the LST from FY data. The objective of this study is to address the LST retrieval from FY-2C observations and to evaluate the accuracy using Moderate-resolution Imaging Spectroradiometer (MODIS) data.

2 STUDY AREA AND DATA

2.1 Description of Study Area

The heterogeneous area of the Tibetan Plateau (26°00'12"-39°46'50"N, 73°18'52"-104°46'59"E) is chosen as the study area. With an average elevation over 4500 meters, the Tibetan Plateau is the world's highest and largest plateau, which has a great effect on climate the monsoon rains.

2.2 FY-2C Data

China announced FY-2 series project in 2001, which included three geostationary meteorological satellites, namely FY-2C, FY-2D and FY-2E. Located above the equator at longitude 105°E, FY-2C was launched on 19 October 2004 and becoming fully operational in 2006. The optical imaging radiometer onboard the FY-2C satellite is the Visible/Infrared Spin Scan-Radiometer (VISSR), which includes one visible channel and four infrared thermal channels with the characteristics of the instrument shown in Table 1. FY-2C can obtain one full disc image covering the earth surface from 60° N to 60° S in latitude and from 45° E to 165° E in longitude per hour and 30 minutes per acquisition for flood season. In this study, the FY-2C data are obtained from the National Satellite Meteorological Center (NSMC):

(<http://www.nsmc.cma.gov.cn/NSMC/Home/Index.html>)

Table 1. Main technical indicators of radiometer

Channel	Spectral range(μm)	Spatial resolution(km)
VIS	0.55-0.90	1.25
IR1	10.3-11.3	5
IR2	11.5-12.5	5
IR3	6.3-7.6	5
IR4	3.5-4	5

2.3 MODIS Data

MODIS is an instrument aboard the Terra (EOS AM) and Aqua (EOS PM) satellites. It covers the globe every 1-2 days, providing data in moderate spatial resolution (250 m at nadir) with large spectral range (36 channels). MOD11B1 (daily LST) at 6km spatial resolution, MOD11A1 (daily Land Surface Emissivity, LSE) at 1km spatial resolution and MOD11A2 (8-day composition LSE) at 1km spatial resolution are used in this study.

3 METHODOLOGY

The GSW algorithm proposed by Wan and Dozier (1996) was adopted to estimate LST from FY-2C satellite data. According to GSW algorithm, the LST can be expressed as

$$T_s = a_0 + (a_1 + a_2 \frac{1-\varepsilon}{\varepsilon} + a_3 \frac{\delta\varepsilon}{\varepsilon^2}) \frac{T_{IR1} + T_{IR2}}{2} + (a_4 + a_5 \frac{1-\varepsilon}{\varepsilon} + a_6 \frac{\delta\varepsilon}{\varepsilon^2}) \frac{T_{IR1} - T_{IR2}}{2} \quad (1)$$

Where T_{IR1} and T_{IR2} are the TOA brightness temperatures measured in channels IR1 and IR2. ε is the averaged emissivity of channels IR1 and IR2; $\delta\varepsilon$ is the emissivity difference between the two thermal infrared channels IR1 and IR2; a_0 - a_6 are unknown coefficients that can be derived from simulations by the moderate spectral resolution atmospheric transmittance algorithm and computer model (MODTRAN).

In the study proposed by Tang et al. (2008), relationships between LSE in MODIS channels 31 and 32 and thoes in S-VISSR channels IR1 and IR2 were developed by linear regressions as follows:

$$\varepsilon_{IR1} = -0.0611 + 1.0614\varepsilon_{31} \quad (2)$$

$$\varepsilon_{IR2} = -0.0210 + 1.0199\varepsilon_{32} \quad (3)$$

Figure 1 and Figure 2 shows the results of LSE calculated from the MOD11A2 products using Equations (2) and (3) on 5 August 2008.

RMSE	Percent (%)	Accumulation Percent (%)
0-1K	16.7	16.7
1-2K	39.6	56.3
2-4K	43.7	100

4 RESULTS AND ANALYSIS

To validate the result of LST retrieval, estimated LST from FY-2C data at 11:00 on 50 days during July and August 2008 in the Tibetan Plateau area is verified using the MOD11B1 data. Figure 3 depicts the coefficient of correlation for each of the selected day, and Table 2 details the distribution of RMSE. Clearly, the results reveal a significant correlation between the two dataset with R varying from 0.72 to 0.95 and RMSE ranging from 0.44 to 3.87K. Table 2 shows the RMSE which ranges from 0K to 1K is only 16.7%, and RMSE ranges between 2K to 4K is up to 43.7%, which indicates a certain error in the LST retrieval from FY-2C data.

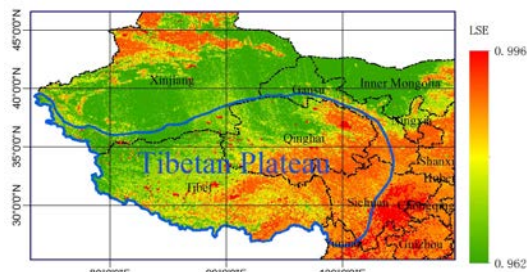


Figure 1. LSE in S-VISSR channel IR1 (10.3-11.3 μ m) on 5 August 2008

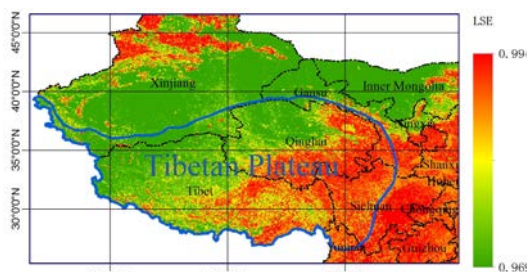


Figure 2. LSE in S-VISSR channel IR2 (11.5-12.5 μ m) on 5 August 2008

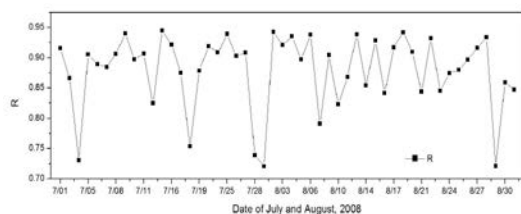
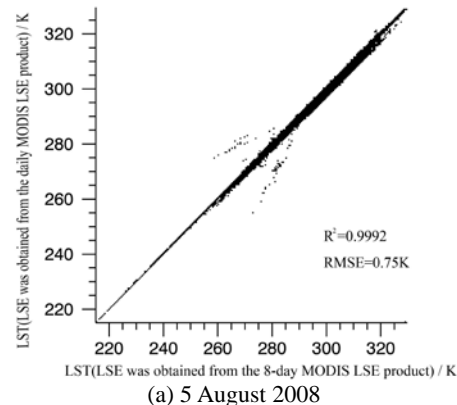
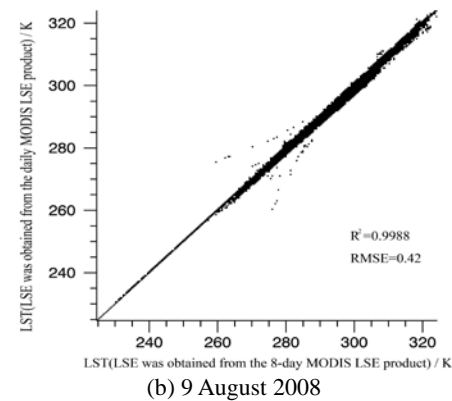


Figure 3. Correlation coefficient between FY-2C and MODIS-derived LST during July and August 2008
Table 2. Percent of the RMSE between FY-2C and MODIS-derived LST during July and August 2008

Because the 8-day composition LSE product (MOD11A2) was originally implemented by Tang et al (2008) to estimate LSE in their subsequent work, which probably led to a certain degree of uncertainty in the LST retrieval for a single day in the composition period. Namely, it is probably more reasonable to retrieve LST using the daily LSE product (MOD11A1) for a single day. Based on this, MOD11A1 were conducted to estimate LSE for the two thermal infrared channels of FY-2C, and further used for LST retrieval. Figure 4 reveals an $R^2=0.9992$ with $RMSE=0.75K$ on 5 August 2008, and an $R^2=0.9988$ with $RMSE=0.42K$ on 9 August 2008, which indicates that the 8-day LSE product is most likely to take some uncertainties in the retrieval of LST for a single day during the composing period.



(a) 5 August 2008



(b) 9 August 2008

Figure 4. Comparisons of the estimated LST with LSE obtained from the 8-day MODIS LSE product *versus* that from the daily LSE product. (a) 5 August 2008 (b) 9 August 2008.

In addition, there may be some other causes for the error. Firstly, the underlying heterogeneous surface has a great influence on the LST retrieval. Secondly, low Signal to Noise Ratio (SNR) of FY-2C data lead to a relatively low accuracy. Moreover, the different observation angle between FY-2C and MODIS is also a considerable error source. Last but not the least, the difference of observation time between FY-2C and MODIS is another error source.

5 SUMMARY AND CONCLUSIONS

This study primarily addresses the theory of LST retrieval using FY-2C data and validation using MODIS products over the study area. To analyze the influence of MODIS LSE product on the LST retrieval, MOD11A1 is implemented to estimate LSE instead of MOD11A2 that originally used.

The results indicate the following: (1) the generalized split window algorithms developed in this work are valid for LST retrieval from the FY-2C; (2) the validation with MOD11B1 reveals a significant correlation between the two dataset; and the

coefficient of correlation varies from 0.72 to 0.95 with RMSE ranges from 0.44 to 3.87K, and the average RMSE is 1.90K. (3) Using the MOD11A2 LSE product to retrieve LST for each of the composing day may be a considerable error source in the hourly LST estimation.

ACKNOWLEDGMENT

The work described in this article is supported in part by the National Nature Science Foundation of China [grant number 41271379]; partly supported by the Chinese Academy of Sciences (CAS) Key Research Program “Hydrological Impacts from Degrading Permafrost in the Sources Area of the Yellow River” [grant number KZZD-EW-13]. The authors greatly appreciate the LAADS for providing the MODIS data (<http://ladsweb.nascom.nasa.gov/data/search.html>) and NSMC for supplying FY data (<http://www.nsmc.cma.gov.cn/NSMC/Home/Index.htm>).

REFERENCES

- Becker, F., 1987, The impact of spectral emissivity on the measurement of land surface temperature from a satellite. *International Journal of Remote Sensing*, 8(10), 1509-1522.
- Qin, Z., and Karnieli A., 1999, Progress in the remote sensing of land surface temperature and ground emissivity using NOAA-AVHRR data. *International Journal of Remote Sensing*, 20, 2367-2393.
- Tang B. H., Bi Y., Li, Z.-L., and Xia, J., 2008, Generalized split-window algorithm for estimate of land surface temperature from Chinese geostationary FengYun meteorological satellite (FY-2C) data. *Sensors*, 8, 933-951.
- Trigo, I. F., Peres L. F., and DaCamara, C. C. , 2008, Thermal land surface emissivity retrieved from SEVIRI/Meteosat. *IEEE Transactions on Geoscience and Remote Sensing*, 46, 307-315.
- Vidal, A., 1991, Atmospheric and emissivity correction of land surface temperature measured from satellite using ground measurements of satellite data. *International Journal of Remote Sensing*, 12, 2449-2460.
- Wan, Z., and Dozier, J., 1996, A generalized split-window algorithm for retrieving land-surface temperature from space. *IEEE Transactions on Geoscience and Remote Sensing*, 34(4), 892-905.
- Zhang, X., Wang, J., 2013, Estimation of land surface temperature using geostationary meteorological satellite data. *Remote Sensing Technology and Application*, 28(1), 12-17.

A split-window algorithm for estimating land surface temperature from Chinese FY-3 VIRR data

Bo-Hui Tang^{1,3}, Zhao-Liang Li^{2,3,*}, Hua Wu¹, Françoise Nerry³, Kun Shao⁴, and Guoqing Zhou⁵

¹. State Key Lab of Resources and Environmental Information System, Institute of Geographic Sciences and Natural Resources Research, Chinese Academy of Sciences, Beijing, 100101, China.

². Key Laboratory of Agri-informatics, Ministry of Agriculture / Institute of Agricultural Resources and Regional Planning, Chinese Academy of Agricultural Sciences, Beijing, 100081, China.

³. ICube, UdS, CNRS, 300 Bld Sébastien Brant, CS10413, 67412 Illkirch, France.

⁴. HeFei University of Technology, Hefei, 230009, China.

⁵. Guangxi Key Laboratory of Spatial Information and Geomatics, Guilin University of Technology, Guangxi, 541004, China.

*. Corresponding to whom should be addressed: lizhaoliang@caas.cb

ABSTRACT: This work addressed the estimate of land surface temperature (LST) from the second generation of Chinese polar orbit FengYun-3 (FY-3) meteorological satellite data in two thermal infrared channels 4 (wavelength centered at 10.8 μm) and 5 (wavelength centered at 12.0 μm), using a split-window. The LST, mean emissivity, and atmospheric Water Vapor Content (WVC) were divided into several tractable sub-ranges with little overlaps to improve the fitting accuracy. The experimental results showed that the Root Mean Square Errors (RMSEs) are proportional to Viewing Zenith Angles (VZAs) and WVC, and they are less than 1.0 K for the sub-ranges with VZA less than 30° or for the sub-ranges with VZA less than 60° and the atmospheric WVC less than 3.5 g/cm², provided that the Land Surface Emissivity (LSE) are known. A preliminary validation showed that the split-window algorithm is capable of producing LST from FY-3 satellite data with RMSE less than 1.0 K.

Keywords: LST, FengYun-3 VIRR, split-window, LSE, WVC

1 INTRODUCTION

As one of the direct driving forces for the surface energy balance at the interface between the surface and the atmosphere, the land surface temperature (LST) is one of the key parameters in the physics of land surface processes at regional and global scales (Li et al., 2013). Many studies and applications including evapotranspiration, climate change, hydrological cycle, vegetation monitoring, urban climate and environmental require to know the knowledge of LST (Hansen et al., 2010). It is, consequently, crucial to have access to reliable estimates of LST over large spatial and temporal scales, such as the satellite observations in the Thermal Infra-Red (TIR) channels.

Up to now, many algorithms have been proposed for estimating the LST from polar-orbit satellite data (Wan and Dozier, 1996; Wan and Li, 1997; Gillespie et al., 1998) and geostationary satellite data (Tang et al., 2008; Jiang and Liu, 2014), respectively. Li et al. (2013) reviewed comprehensively the current different algorithms and pointed out that the major challenges for estimating LST from satellite data are the corrections of the effects caused by the atmosphere and the land surface emissivity (LSE). However, those

two issues are very difficult to address because the LST, the LSEs, and the downward atmospheric radiance are coupled together, and the great variability of the vertical profiles of atmospheric water vapor and temperature make the effects of atmospheric absorption, emission, and emission-reflection highly variable. Consequently, retrieval of the LST accurately from satellite measurements is a very difficult task.

FengYun-3 (FY-3), the second generation of Chinese polar orbit meteorological satellite, was launched into an 807-kilometer-high sun-synchronous orbit on 27 May 2008. It is an advanced earth observation satellite which carries ten payloads aboard of optical and microwave sensors to collect a range of remote sensing data, including temperature, humidity, air pressure, clouds, and radiation, through all-weather, multi-spectrum, three dimensional, and quantitative means. One of the major payloads onboard FY-3 is the Visible and InfraRed Radiometer (VIRR), which consists of seven visible and near infrared channels, and three infrared channels. Figure 1 shows the corresponding spectral response functions of FY-3 VIRR channels.

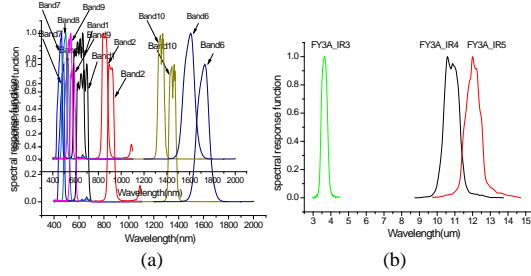


Figure1. Spectral response functions of FY-3 VIRR channels (a: visible and near-infrared channels; b: infrared channels)

The present work in this paper aims to estimate accurately the LST from FY-3 VIRR satellite data in two thermal infrared channels 4 (wavelength centered at 10.8 μm) and 5 (wavelength centered at 12.0 μm) by using a split-window technique. Section 2 describes the theory associated with the LST retrieval and presents the simulations made using atmospheric radiative transfer model MODTRAN 4. The results are explained in section 3 where the sensitivity and error analyses in terms of the uncertainty of Land Surface Emissivities (LSEs) and Water Vapor Content (WVC) in the atmosphere as well as the instrument noise are given. Section 4 gives an example of estimating the LST from actual FY-3 data for China region. The conclusions are drawn in section 5.

2 METHOD

2.1 Radiative transfer for split-window algorithm

On the basis of the radiative transfer theory, for a cloud-free atmosphere in thermodynamic equilibrium, the daytime channel radiance $B_i(T_i)$ measured at the Top Of the Atmosphere (TOA) in a Thermal Infra-Red (TIR) channel of the sensor onboard the satellite is given to a good approximation as (Li et al., 2000)

$$B_i(T_i) = \varepsilon_i B_i(T_s) \tau_i + R_{\text{atm}_i}^{\uparrow} + (1 - \varepsilon_i) R_{\text{atm}_i}^{\downarrow} \tau_i \quad (1)$$

Where T_i is the channel brightness temperature observed in channel i at the TOA, B_i is the Planck function, $B_i(T_i)$ is the radiance measured if the surface is a black body with surface temperature T_s , ε_i is the channel emissivity in channel i , τ_i is the total atmospheric transmittance along the target to sensor path in channel i , $R_{\text{atm}_i}^{\uparrow}$ is the thermal path atmospheric upwelling radiance in channel i , and $R_{\text{atm}_i}^{\downarrow}$ is the channel downwelling atmospheric radiance from the whole hemisphere in channel divided by π . It is possible to obtain an expression for LST determination if equation (1) is applied to two different channels. This two-channel technique is on the basis of the fact that the atmospheric attenuation

suffered by the radiation emitted by the surface is proportional to the difference between the at-sensor radiances measured simultaneously in two different infrared channels (McMillin, 1975).

2.2 Split-window algorithm development for FY-3 VIRR

The atmospheric radiative transfer model MODTRAN 4 was used to simulate at-sensor radiance with the latest version of the Thermodynamic Initial Guess Retrieval (TIGR) database TIGR2002, a variety of appropriate LSTs and LSEs change, as well as thermal infrared channel response function of the VIRR.

For different simulated values of the numerical experiments mentioned above, as done by Wan and Dozier (1996), the averaged emissivities are divided into two groups: one varies from 0.90 to 0.96 and the other ranges from 0.94 to 1.0. The atmospheric WVCs are divided into six sub-ranges with an overlap of 0.5 g/cm^2 : [0, 1.5], [1.0, 2.5], [2.0, 3.5], [3.0, 4.5], [4.0, 5.5], and [5.0, 6.5] g/cm^2 . The LSTs, T_s , are divided into five sub-ranges with an overlap of 5 K: $T_s \leq 280$ K, $275 \leq T_s \leq 295$ K, $290 \leq T_s \leq 310$ K, $305 \leq T_s \leq 325$ K, $T_s \geq 320$ K. We then propose to retrieve the LST according to the split-window algorithm developed by Sobrino et al. (1993) as

$$T_s = b_0 + b_1 * T_4 + b_2 * (T_4 - T_5) + b_3 * (T_4 - T_5)^2 + b_4 * (1 - \varepsilon) + b_5 * \Delta \varepsilon \quad (2)$$

where b_0 - b_5 are coefficients, obtained through statistical regressions method for each VZA and each sub-range. ε is the mean emissivity, and $\Delta \varepsilon$ is the emissivity difference between VIRR channels 4 and 5.

3 RESULTS AND ANALYSIS

3.1 Results

Figure 2 shows, the histogram of the difference between the actual T_s and the T_s estimated with the coefficients corresponding to the sub-range WVC $\in [1.0, 2.5]$, and $T_s \in [275\text{K}, 295\text{K}]$ for two different emissivity groups and VZA=0°, respectively.

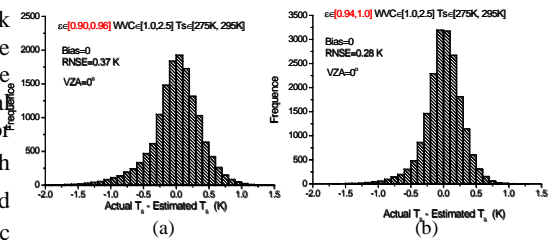


Figure 2. Histogram of the difference between the actual and estimated T_s for the sub-range with WVC ranging from 1.0 g/cm^2 to 2.5 g/cm^2 , and LST from 275 K to 295 K for VZA=0°. (a) for $\varepsilon \in [0.90, 0.96]$ and (b) for $\varepsilon \in [0.94, 1.0]$.

The Root Mean Square Errors (RMSEs) between the actual and estimated T_s is 0.37 K for the emissivity group $\varepsilon \in [0.94, 1.0]$, and 0.48 K for the other emissivity group $\varepsilon \in [0.90, 0.96]$. Similar results are obtained for the other VZAs.

3.2 Analysis

Wan and Dozier (1996) indicated that the errors of LST estimated by the split-window algorithm come mainly from the uncertainties of instrument noises, atmospheric properties and LSEs. In order to obtain the accuracy in LST retrieval, these three uncertainties of error were considered in this work.

3.2.1 Instrumental noises (NEAT) analysis

The noise equivalent temperature differences (NEAT) of FY-3 VIRR channels 4 and 5 are both 0.2 K. To see how significant the effect of the instrumental NEAT is on the retrieval of LST, a Gaussian random distribution error of 0.2 K is added to the simulated TOA brightness temperatures T_4 and T_5 in equation 2. We then estimate the LST using equation (2) with the noised TOA brightness temperatures and compare it to the actual LST. We find that, as one sub-range $\varepsilon \in [0.94, 1.0]$, $WVC \in [1.0, 2.5]$ and $T_s \in [275K, 295K]$ for an example, the effect of the instrumental NEAT on the retrieval of LST is small with RMSE 0.34 K. In contrast with the RMSE of 0.28 K for no-noise cases, the retrieval accuracy of LST is affected by 21% for NEAT=0.2 K.

3.2.2 Land surface emissivity

From equation (2), one can see that the accuracy of the retrieval LST related to the LSE is mainly dependent on the uncertainties of $(1-\varepsilon)$ and $\Delta\varepsilon$. The LST error σ_{LST} due to the uncertainty in $(1-\varepsilon)$ and $\Delta\varepsilon$ can be estimated by

$$\sigma_{LST} = \sqrt{b_4^2 \sigma(1-\varepsilon)^2 + b_5^2 \sigma(\Delta\varepsilon)^2} \quad (3)$$

where b_4 and b_5 are the regression coefficients obtained in section 2.2. Taking the sub-range $WVC \in [1.0, 2.5]$, $T_s \in [275K, 295K]$ for two emissivity groups for VZA=0 for an example, and assuming that the uncertainties of $(1-\varepsilon)$ and $\Delta\varepsilon$ are around 1%, we can obtain the LST error of 0.97 K for the high emissivity group $\varepsilon \in [0.94, 1.0]$, and of 1.1 K for the low emissivity group $\varepsilon \in [0.90, 0.96]$.

3.2.3 Atmospheric WVC

AS we know, the amount of the water vapor in the atmosphere is not easily determined from satellite data. Note that the WVC is divided into six sub-ranges with an overlap of 0.5 g/cm² in the present

split-window algorithm. The overlap WVC can be fallen into two adjacent sub-ranges. That is, it is included by two sub-ranges and corresponded to two pairs of coefficients b_0-b_5 . So the uncertainty of the WVC on the retrieval of LST is mainly due to the wrong sub-range selection of the WVC. In this work, we aim to analyze the effect of the overlap WVC on the retrieval of LST. As the overlap water vapour content $WVC \in [1.0, 1.5]$ in the high emissivity group $\varepsilon \in [0.94, 1.0]$ for an example, it can be fallen into two sub-ranges $WVC \in [0.0, 1.5]$ and $WVC \in [1.0, 2.5]$. We first estimate the LST with water vapor content $WVC \in [1.0, 2.5]$ using the coefficients corresponding to the sub-range $\varepsilon \in [0.94, 1.0]$, $WVC \in [0.0, 1.5]$, and $T_s \in [275K, 295K]$, the RMSE between the actual and the estimated is 0.21 K, while using the coefficients corresponding to the sub-range $\varepsilon \in [0.94, 1.0]$, $WVC \in [1.0, 2.5]$, and $T_s \in [275K, 295K]$, the RMSE is 0.26 K. This result shows that the uncertainty of the WVC can affect the accuracy of the retrieval LST by 24%.

3.2.4 Total error

The total maximum error is therefore calculated according to the expression given by

$$\sigma_{total}^2 = \sigma_{RMSE}^2 + \sigma_{noise}^2 + \sigma_{\varepsilon}^2 + \sigma_{WVC}^2 \quad (4)$$

Where σ_{total} is the total error associated with the present split-window algorithm, σ_{RMSE} is the error caused by the present algorithm itself, σ_{noise} is the error related to the instrumental noise, σ_{ε} is the error with respect to LSE, and σ_{WVC} is the error caused by the uncertainty of atmospheric WVC. As also the sub-range $\varepsilon \in [0.94, 1.0]$, $WVC \in [1.0, 2.5]$, and $T_s \in [275K, 295K]$ for an example, the retrieval accuracy of LST related to the algorithm itself is affected by 0.28 K. The errors caused by the instrumental noise, LSE, and the uncertainty of atmospheric WVC are 0.21, 0.97, and 0.24 K, respectively. Finally, the total error associated to the LST retrieval is about 1.1 K.

3.3 Preliminary test

To preliminary test the present algorithm, Some additional simulations are made using the same conditions as mentioned in section 2.2. The Viewing Zenith Angles (VZAs) and the six standard atmospheres of MODTRAN 4 are the main inputs for the simulations. The TOA brightness temperatures for VIRR channels 4 and 5 are obtained in combination with the MODTRAN outputs of atmospheric parameters (τ_i , $R_{atm_i}^{\uparrow}$, $R_{atm_i}^{\downarrow}$), and reasonable variations of LST (T_s) and LSEs (ε_i). We then

calculate the surface temperature by means of the proposed split-window algorithm. Figure 3 shows, for different types of land surfaces and atmospheric profiles, the comparison of the actual T_s and the T_s estimated using the proposed algorithm. The different RMSEs listed in this figure are due to estimating the LST at different VZAs. The results are quite well with the maximum RMSE less than 1 K. This result shows that the proposed split-window algorithm is feasible and reliable to retrieve the LST from FY-3 satellite data.

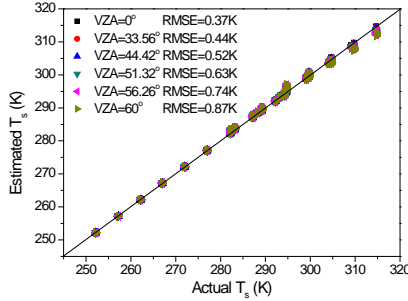


Figure 3. Comparison of the Actual LSTs and those estimated with the proposed split-window algorithm for different types of land surfaces and atmospheric profiles.

4 APPLICATION TO ACTUAL FY-3 DATA

4.1 Determination of LSEs

An NDVI-based threshold method is used to determine the LSEs for FY-3 VIRR channels 4 and 5. The spectral databases provided by the University of California Santa Barbara (UCSB) spectral database (<http://www.icess.ucsb.edu/modis/EMIS/html/em.html>) and the Johns Hopkins University (JHU) (<http://speclib.jpl.nasa.gov/>) spectral database are used to simulate the VIRR reflectances for visible and near-infrared channels and emissivities for infrared channels. The channels emissivities are determined by taking into account the characteristics of the soil present in each pixel and by identifying it as bare soil pixel, mixed pixel, and fully vegetated pixel, respectively.

4.2 Determination of WVC

Taking into account that the WVC is used to determine the optimal coefficients in the LST algorithm, accurate WVC is not required, provided that the estimated WVC is within the same sub-range as the actual WVC. The method proposed by Li et al. (2003) is used, which utilizes the transmittance ratio of two VIRR split-window channels 4 and 5 to derive the WVC.

$$WVC = d_1 + d_2 \times \frac{\tau_j}{\tau_i} \quad (5)$$

$$\text{With } \frac{\tau_j}{\tau_i} = \frac{\varepsilon_i}{\varepsilon_j} R_{ji}, \text{ and } R_{ji} = \frac{\sum_{k=1}^N (T_{i,k} - \bar{T}_i)(T_{j,k} - \bar{T}_j)}{\sum_{k=1}^N (T_{i,k} - \bar{T}_i)^2},$$

where d_1 and d_2 are unknown coefficients, τ_i and τ_j are the atmospheric transmittances in the split-window channels i and j , the subscript k denotes pixel k , and the \bar{T}_i and \bar{T}_j are the TOA mean (or the median) channel brightness temperatures of the N neighboring pixels considered for channels i and j , respectively. Based on the numerical simulated results obtained in Section 2.2, coefficients d_1 and d_2 can be respectively derived as functions of secant VZA as

$$d_1 = 25.156 - 13.572 / \cos(VZA) + 2.909 / \cos^2(VZA) \quad (6)$$

$$d_2 = -25.258 + 13.677 / \cos(VZA) - 2.931 / \cos^2(VZA) \quad (7)$$

The results of the comparison between the actual WVC and the ones estimated with equations (5), (6), and (7), show that the bias and RMSE are 0.08g/cm² and 0.16g/cm², respectively, which indicate that the estimated WVC can meet the need of the LST algorithm.

4.3 Estimation of LST

Figure 4 gives an example of the map of LST estimated from FY-3 VIRR satellite data on December 1, 2010 for China. The model inputs are the TOA brightness temperatures, VZA, LSEs, and WVC. All of these variables are extracted or derived directly from VIRR satellite data. From this figure one can see that the values of LST in the South and Easter China are higher, while those in the West and North China are relative lower.

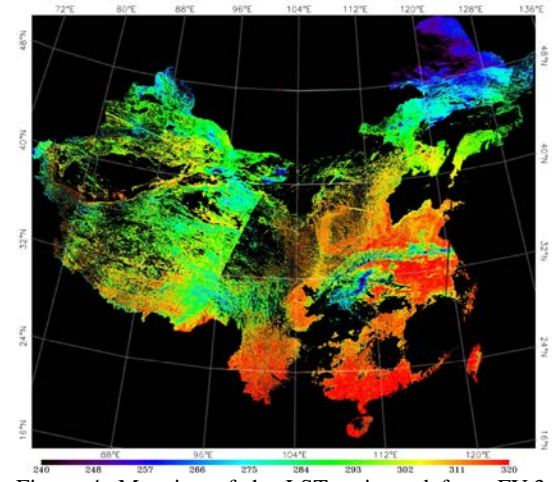


Figure 4. Mapping of the LST estimated from FY-3 VIRR data on December 1, 2010 for China.

5 CONCLUSIONS

In this paper, an operational split-window algorithm was developed to retrieve Land Surface Temperature (LST) from the second generation of Chinese polar orbit FengYun-3 (FY-3) meteorological satellite data in two thermal infrared channels 4.

Sensitivity and error analyses in term of the instrumental noise, the uncertainty of LSE and the atmospheric WVC showed that, given an instrumental noise $NE\Delta T=0.2$ K and the uncertainties of and around 1%, the total error associated to the LST retrieval is about 1.1 K.

In addition, a preliminary test has been done with a simulated database different from that used to obtain it. The testing error is less than 1 K which indicates that the split-window algorithm is capable of producing LST from FY-3 satellite data.

ACKNOWLEDGMENT

This work was jointly supported by the Excellent Young Talent Funds for Kezhen Distinguished Young Scholar in the Institute of Geographic Sciences and Natural Resources Research (IGSNRR), Chinese Academy of Sciences (CAS) under grant 2012RC101, the National Natural Science Foundation of China under grant 41171287, and the Hi-Tech Research and Development Program of China (863 Plan Program) under grant 2012AA12A302.

REFERENCES

- Gillespie, A.R., Rokugawa, S., Matsunaga, T., Cothren, J. S., Hook, S., & Kahle, A. B., 1998, A temperature and emissivity separation algorithm for Advanced Spaceborne Thermal Emission and Reflection Radiometer (ASTER) images. *IEEE Transactions on Geoscience and Remote Sensing*, 36, 1113-1126.
- Hansen, J., Ruedy, R., Sato, M., & Lo, K., 2010, Global surface temperature change. *Reviews of Geophysics*, vol. 48, pp. RG4004.
- Jiang, G.-M., & Liu, R., 2014, Retrieval of sea and land surface temperature from SVISSR/FY-2C/D/E measurements. *IEEE Transactions on Geoscience and Remote Sensing*, 52(10), 6132-6140.
- Li, Z. -L., Jia, L., Su, Z., Wan, Z., & Zhang, R., 2003, A new approach for retrieving precipitable water from ATSR2 split-window channel data over land area. *International Journal of Remote Sensing*, 24, 5095-5117.
- Li, Z. -L., Petitcolin, F., & Zhang, R. H., 2000, A physically based algorithm for land surface emissivity retrieval from combined mid-infrared and thermal infrared data. *Science in China Series E: Technological Sciences*, 43, 23-33.
- Li, Z.-L., Tang, B.-H., Wu, H., Ren, H. Z., Yan, G. J., Wan, Z., Trigo, I.F., & Sobrino, J.A., 2013, Satellite-derived land surface temperature: Current status and perspectives. *Remote Sensing of Environment*, 131, 14-37, doi: 10.1016/j.rse.2012.12.008.
- McMillin, L. M., 1975, Estimation of sea surface temperature from two infrared window measurements with different absorptions. *Journal of Geophysical Research*, 80, 5113-5117.
- Sobrino, J. A., Caselles, V., & Coll, C., 1993, Theoretical split-window algorithms for determining the actual surface temperature. *IL Nuovo Cimento C*, 16, 219-236.
- Tang, B.-H., Bi, Y., Li, Z.-L., & Xia, J., 2008, Generalized Split-Window algorithm for estimate of land surface temperature from Chinese geostationary FengYun meteorological satellite (FY-2C) data. *Sensors*, 8, 933-951.
- Wan, Z., & Dozier, J., 1996, A generalized split-window algorithm for retrieving land-surface temperature from space. *IEEE Transactions on Geoscience and Remote Sensing*, 34, 892-905.
- Wan, Z., & Li, Z.-L., 1997, A physics-based algorithm for retrieving land-surface emissivity and temperature from EOS/MODIS data. *IEEE Transactions on Geoscience and Remote Sensing*, 35, 980-996.

Improvement on the universal triangle method to estimate soil moisture

Dianjun Zhang^{a,b}, Zhao-Liang Li^{c,d,*}, Ronglin Tang^a, Bo-Hui Tang^a, HuaWu^a, Kun Shao^e,

^a State Key Laboratory of Resources and Environment Information System, Institute of Geographic Sciences and Natural Resources Research, Chinese Academy of Sciences, Beijing 100101, China

^b University of Chinese Academy of Sciences, Beijing 100049, China

^c ICube, UdS, CNRS, 300 Bld Sebastien Brant, CS10413, 67412 Illkirch, France

^d Key Laboratory of Agri-informatics, Ministry of Agriculture/Institute of Agricultural Resources and Regional Planning, Chinese Academy of Agricultural Sciences, Beijing 100081, China

^e HeFei University of Technology, Hefei, 230009, China;

* Authors to whom correspondence should be addressed: lizl@igsrr.ac.cn

ABSTRACT—Soil moisture is an important parameter that influences the exchange of water and energy fluxes between the land surface and atmosphere. Through the simulation by a SVAT model, Carlson proposed the universal triangle to determine soil moisture and stretched it to the remotely sensed data, which was insensitive to the initial atmospheric conditions. Due to the limitations of using observed limiting edges, this study developed a robust approach to determine the theoretical limiting edges with non-linear interpolation to estimate soil moisture from the universal triangular feature space. In order to simplify the soil moisture availability (Mo) equation but maintain the accuracy, this paper tried to use a quadratic polynomial model to regress the Mo, normalized land surface temperature (T^*) and fractional vegetation cover (FVC). This method was applied to retrieve soil moisture for the SEMACX campaign in the Walnut Creek watershed and the validation data were obtained on DOY 182 and 189 in 2002 that are coincident with the overpass of the Landsat satellite. When the estimations were verified by the in-situ measurement of soil water content at 6 cm depth, the RMSE was about $0.06 \text{ m}^3/\text{m}^3$ with a bias of $0.03 \text{ m}^3/\text{m}^3$ for Carlson's method while the developed method had a RMSE of $0.10 \text{ m}^3/\text{m}^3$ and a bias of about $0.05 \text{ m}^3/\text{m}^3$.

1 INTRODUCTION

Surface soil water content is a critical variable in environmental models and has been used in a wide range of applications, such as evapotranspiration, energy and water balance, global warming studies and agricultural management (Istanbulluoglu and Bras, 2006; Jackson, 1981; Li et al., 2009). Based on the previous studies, Carlson (2007) proposed the universal triangular feature space using normalized land surface temperature (T^*) and NDVI to determine the surface soil water content. In the study of Carlson, the limiting (dry and wet) points are determined from the remotely sensed scatter plots for bare soil and full vegetation cover. This determination is empirical and may be changeable for different areas of interest. A cubic polynomial model is used to interpolate soil moisture availability (Mo) in the feature space. Although the accuracy is high, the application is

relatively complex and requires more fitting coefficients. In view of the two above-mentioned limitations, this study aims to make improvements on the universal triangle feature space proposed by Carlson. First, the limiting edges are derived from the surface energy balance principle with a robust physical basis. The extreme warm and cold edges were determined with the constraints of the energy distribution. Second, a simplified quadratic polynomial interpolation function is proposed to obtain the Mo from the universal triangle. The number of the coefficients is reduced by a half compared to the Carlson's model.

2 METHODOLOGY

2.1 Carlson's method

The Carlson's approach (Carlson, 2007) is to use the model to create a matrix of T^* and Mo values for an entire range of input fraction of vegetation cover

(FVC). From this matrix, a set of polynomials are generated, which are then used to calculate Mo for all pixels (Carlson, 2007).

The relationship for Mo₁ is given by third order polynomial as:

$$Mo_1 = \sum_{i=0}^3 \sum_{j=0}^3 a_{ij} T^{*i} FVC^j \quad (1)$$

where the subscripts i and j pertain to the modeled T* and FVC; the coefficients for the two parameters are given in the study of Carlson (2007).

Carlson used a polynomial fit between the T* and FVC to obtain the warm edge as the upper boundary condition. On this edge, the Mo is equal to 0, the vegetation is restricted by the water stress and the evaporation is 0.

A reasonable equation for the warm edge is also given by a polynomial fit to the simulated model output:

$$T^*_{warm} = b + a_1 FVC + a_2 FVC^2 \quad (2)$$

where the coefficients for the polynomial are also given in Carlson's study (2007).

2.2 Our method

2.2.1 The limiting edge determination

In this study, the theoretical limiting edges were derived from radiation budget and energy balance equations (Long and Singh, 2012) (as shown in Fig.1); these extreme temperatures are associated with the longwave radiation component of the radiation budget equation and with the temperature gradient of the sensible heat flux component of the energy balance equation. Therefore, the derived limiting edges have a robust physical basis and are more accurate than the observed ones.

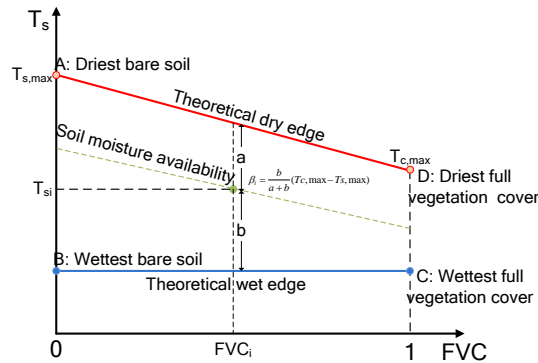


Fig.1. The trapezoidal space and the boundary conditions in the Mo estimation model establishment.

The land surface temperature at the dry point (T_{max}) can be obtained from the mathematical derivation of the energy balance equation:

$$T_{max} = \frac{R_{n,s0} - LE_s / (1 - c)}{\frac{\rho C_p}{r_{a,s}(1 - c)} + 4\sigma\epsilon_s T_a^3} + T_a \quad (3)$$

where R_{n,s0} is the net radiation for a bare soil surface. LE_s is the evaporation from a bare soil surface (W/m²). c is a calibrated scale coefficient (0.35). ρ is the air density, and C_p is the air heat capacity at constant pressure. T_a is the air temperature, and r_{a,s} is the aerodynamic resistance for bare soil. ε_s is the bare surface emissivity (e.g., 0.95). σ is the Stefan-Boltzmann constant. More details of the solution are given in the study of Long and Singh (2012).

2.2.2 The Normalization of LST and Soil Moisture

When the theoretical limiting edges are determined, the maximum and minimum LSTs can be fixed for a specific FVC. Then, the temperature can be normalized by the extreme temperatures using the following formula:

$$T^* = \frac{T_s - T_{min}}{T_{max} - T_{min}} \quad (4)$$

where T* is the normalized LST. T_{max} and T_{min} are the maximum and minimum LSTs (K) for bare soil and full vegetation cover, respectively. T_s is the LST for a specific FVC (K).

2.2.3 The Establishment of Mo Estimation Model

To simplify the Mo equation proposed by Carlson, a quadratic polynomial equation is used here to reveal the relationship among Mo, T* and FVC. Compared with the Carlson's model, the developed method has just 6 coefficients, i.e., the number is reduced by half. The equation is as follows:

$$Mo_2 = a_0 + a_1 FVC + a_2 T^* + a_3 T^{*2} + a_4 FVC^2 + a_5 T^* FVC \quad (5)$$

where a₀, a₁, a₂, a₃, a₄ and a₅ are the regression coefficients obtained with the following physical constraints.

For bare soil with the lowest temperature, the FVC and T* are both equal to 0 and the Mo is 1, which means a₀=1. Similarly, the FVC and Mo are equal to 0 and the T* is 1 for the bare soil with highest temperature, which means a₀+a₂+a₃=0. For full vegetation cover with adequate water content, both the FVC and Mo are equal to 1 and the T* is 0, which means a₀+a₁+a₄=1.

3 STUDY AREA AND DATA

3.1 Study area

The Soil Moisture-Atmosphere Coupling Experiment (SMACEX) campaign, conducted in central Iowa, located in latitude between 41.87°N and

42.05°N and in longitude between 93.83°W and 93.39°W (Fig.2), provides extensive measurements of soil, vegetation, and meteorological properties and states during the period from 15 June (DOY 166) through 8 July (DOY 189) in 2002 to give a greater understanding of mechanisms of water and heat exchanges with the atmosphere (Kustas et al., 2005; Long et al., 2012). The mean annual rainfall of this region is 835 mm, which is classified as a humid climate. The topography is characterized by low relief and poor surface drainage.

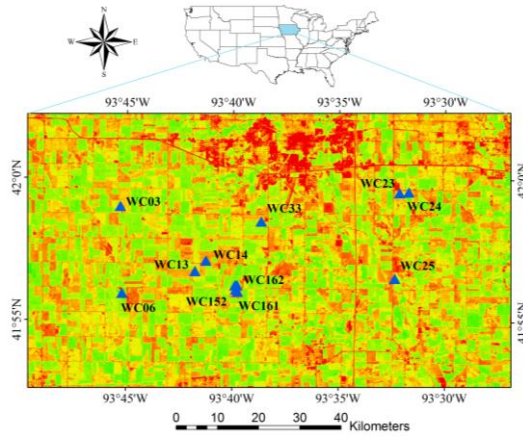


Fig.2. Location and fractional vegetation cover of Landsat TM imagery acquired on July 1 (DOY 182), 2002, of the SMACEX study site at Ames, central Iowa, U.S. (8 soil moisture monitoring site (WC) of the meteorological-flux network are selected in numbered triangles and the major crop types at each WC are soybean and corn).

3.2 Remotely sensed data

There were two cloud-free scenes of Landsat TM/ETM+ images acquired across the campaign period, i.e., the Landsat TM image acquired at 10:42 a.m. on DOY 182 with vegetated canopy cover from 75% to 90%, and the Landsat ETM+ image acquired at 10:45 a.m. on DOY 189 characterized from 85% to essentially full cover. Digital Elevation Models (DEMs) were obtained from the National Elevation Dataset produced and distributed by the U.S. Geological Survey (<http://seamless.usgs.gov/index.php>), with a spatial resolution of 1 arc sec (about 30 m). Terrain variables (e.g., elevation, slope, and aspect) were extracted directly from the DEMs.

3.3 Energy balance closure

The eddy covariance systems have been found to underestimate latent heat flux (LE) and sensible heat flux (H), i.e., $R_n - G > LE + H$, due to the mismatched source areas of LE and H with R_n and G; therefore the

measured LE and H need to be adjusted for energy balance closure (Twine et al., 2000). Fig.3 compares observed LE+H with $R_n - G$ at the Landsat overpass for two image acquisition dates, illustrating that in general the observed LE+H fluxes are less than $R_n - G$. The averaged closure ratio $[CR = (LE + H) / (R_n - G)]$ for all observations was found to be 0.85. The RMSE is approximately 39.2 W/m^2 and the BIAS is about 21.6 W/m^2 which is consistent with the findings of Long

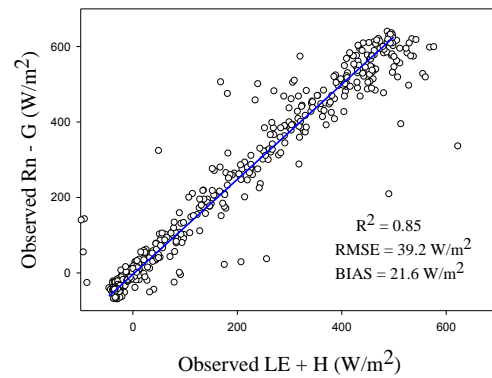


Fig.3. Comparison of observed available energy ($R_n - G$) and sum of observed sensible and latent heat fluxes (LE+H), showing the averaged closure ratio (CR) of 0.85.

3.4 In situ measurement data

The soil moisture probes measured the dielectric constant of the soil and the volumetric soil moisture was computed from previously determined relationships. Each probe was installed at a depth of 5 cm, which is appropriate for validating the retrieved surface soil moisture. Forty-two theta probe (TP) samples at 14 different locations and 4 gravimetric soil moisture (GSM) samples (coincident with 4 theta probe locations) were taken in every field. The gravimetric measurements of 0–6 cm were made with a coring tool, which also provided a reliable estimate of bulk density. The theta probe observations with a sampling depth of 0–6 cm were calibrated using the gravimetric observations taken in the field to estimate soil moisture. The average of the calibrated theta probe measurements were used as a field average.

Table 1. The soil moisture measurements on DOY 182 and 189 in 2002 in the Walnut Creek watershed. GSM is the Gravimetric Soil Moisture in grams/grams. VSM is the Volumetric Soil Moisture (VSM) in m^3/m^3 .

DOY	Site (WC)	Depth (cm)	GSM (g/g)	VSM (m^3/m^3)
182	03	0-6	0.166	0.186
	06	0-6	0.079	0.096

	13	0-6	0.048	0.053
	14	0-6	0.064	0.081
	23	0-6	0.078	0.110
	24	0-6	0.117	0.171
	25	0-6	0.134	0.128
	33	0-6	0.129	0.161
	03	0-6	0.259	0.286
	06	0-6	0.244	0.227
	13	0-6	0.157	0.218
	14	0-6	0.062	0.076
189	23	0-6	0.098	0.130
	24	0-6	0.186	0.250
	25	0-6	0.306	0.249
	33	0-6	0.272	0.306

4 Results and discussion

4.1 Noah simulation and Mo estimation model establishment

In this study, the Noah LSM version 3.2 is selected to simulate the soil moisture evolution under different FVCs and LSTs. The key input to the model includes land use (vegetation), soil texture, slope and secondary parameters that can be specified as a function of the three primary parameters. During the simulation, the land use is set to Cropland/ Woodland Mosaic, and the surface slope index is set to 1 (flat surface). Because the LST responds to the surface soil moisture content in the topsoil layers, the soil layer distribution is reformed and separated into seven layers with depths of 1, 2, 5, 10, 20, 50 and 150 cm. The average soil moisture in the top three layers represents the surface soil moisture to reduce the uncertainties.

The soil moisture is normalized by the wilting point ($0.05 \text{ m}^3/\text{m}^3$) and saturation water content ($0.45 \text{ m}^3/\text{m}^3$). The outputs contain various combinations of Mo, LST and FVC. The simulations are used to obtain the Mo estimation model.

The quadratic polynomial equation is:

$$Mo_2 = 1 - 0.08FVC - 1.57T^* + 0.58T^{*2} + 0.08FVC - 0.05T^* \cdot FVC \quad (6)$$

4.2 Comparison of the limiting edges with two methods

From Fig.4, it could be seen that the limiting edges derived using Carlson's method were different from these using our method. This difference was caused by the fact that Carlson used a cubic polynomial model while our method used a simple quadratic polynomial equation in fitting Mo to FVC

and T^* . Additionally, the use of the different SVAT models that were used for the simulations is another source of difference in the limiting edge determination.

The limiting edges from the two methods are fixed in the space of T^* -FVC. For low vegetation cover, the retrieved soil moisture between our method and Carlson's method has small differences because the limiting edges are close to each other. In contrast, the differences are large for the high vegetation cover area where the dry edges have the biggest differences but the wet edges are close.

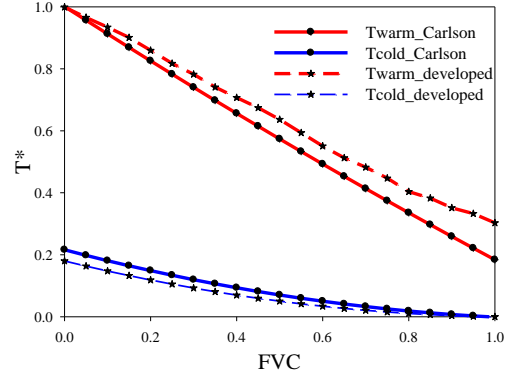


Fig.4. The comparison results of the derived limiting edges with two methods using the simulation outputs.

4.3 Comparison of the Mo with two methods using simulated data

To compare the estimation accuracy of the two methods, the simulation data on DOY 157 and 180 were selected to validate the estimated Mo (as shown in Fig.5). For DOY 157, the results obtained by Carlson showed a RMSE of 0.04 and a BIAS of 0.035. The developed method showed that the RMSE was 0.05 and the BIAS was 0.045. For DOY 180, the results obtained by Carlson showed a RMSE of 0.06 and a BIAS of 0.05. The developed method showed that the RMSE was 0.05 and the BIAS was 0.042. The comparison of the two methods shows similar performances in the surface soil moisture estimation.

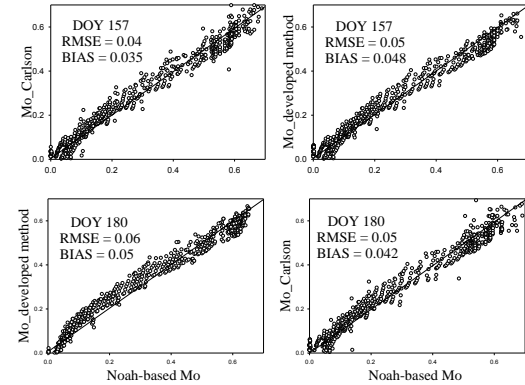


Fig.5. The results of the derived Mo for two days (DOY157 and 180); the abscissa is the simulated Mo by the Noah LSM, and the ordinate is the retrieved Mo by the developed and Carlson's model.

4.4 Validation of the soil moisture estimation based on the remotely sensed data

To further validate the estimation results, the in situ measurement of soil water content at 6 cm depth was used to compare with the remotely sensed surface soil moisture (as shown in Fig. 6). The wilting point and saturation water content at Walnut Creek watershed were applied to transform the available soil moisture to the surface soil water content.

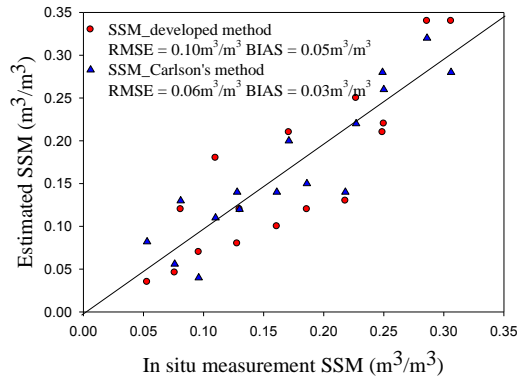


Fig.6. The validation results for two methods using the in situ measurement of soil moisture in Walnut Creek watershed.

The retrieved SSM by Carlson was a bit better than the developed method. This was attributed to the use of third order polynomial soil moisture availability equation. The RMSE was about $0.06 \text{ m}^3/\text{m}^3$ and the bias was approximately $0.03 \text{ m}^3/\text{m}^3$ for Carlson's method while the developed method had a RMSE of $0.10 \text{ m}^3/\text{m}^3$ and a bias of about $0.05 \text{ m}^3/\text{m}^3$. If the validation scale mismatch and uncertainties induced by the remotely sensed data were considered, the estimation accuracy was high and the two methods were almost equivalent in surface soil moisture estimation.

4.5 Discussion

Although the developed method can reach high soil moisture estimation accuracy, the following problems are still present:

- (1) Many uncertainties exist in the theoretical limiting edge determination. The use of the air temperature as the theoretical wet edge can overestimate the true wet edge, which makes the T^* larger for a fixed FVC in the normalization. The soil moisture availability will be overestimated by substituting the larger T^* into the soil moisture model.
- (2) Different land surface models provide different

simulation outputs because they have different physical mechanisms in soil moisture estimation. Additionally, using the remotely sensed data as inputs into the soil moisture model may induce some uncertainties. The mismatch of the scales when using the point-based data to validate the remotely sensed results would also induce many uncertainties.

5 CONCLUSIONS

Based on the universal triangular space, an improvement is conducted on the Carlson's method to estimate surface soil water content. First, the theoretical limiting edges are determined using the surface energy balance model that has a robust physical basis. The theoretical limiting edges are more accurate than the observed ones. Second, a simpler soil moisture availability estimation model is established using a quadratic equation to indicate the relationship among Mo, FVC and T^* . Finally, the simulation data and in situ measurements are used to validate the estimation results of the two methods. The results demonstrate that the accuracy of our method is rather equivalent with the Carlson's method. However, our developed model is easy and simple to operate in the practical application.

The simulation data on DOY 157 and 180 are used to validate the Mo of the two methods. The results obtained by Carlson show a RMSE of 0.04 and a BIAS of 0.035 on DOY157 and a RMSE of 0.06 and a BIAS of 0.05 on DOY 180. The developed method shows that the RMSE is 0.05 and the BIAS is 0.045 on DOY 157 and the RMSE is 0.05 and a BIAS of 0.042 on DOY 180. Additionally, using the in situ measurements as ground-truth data shows a RMSE of $0.06 \text{ m}^3/\text{m}^3$ and the bias is approximately $0.03 \text{ m}^3/\text{m}^3$ for Carlson's method and the developed method has a RMSE of $0.10 \text{ m}^3/\text{m}^3$ and a bias of about $0.05 \text{ m}^3/\text{m}^3$.

In this study, although the estimation accuracy is high, many problems still exist in surface soil moisture estimation. The theoretical limiting edges should be accurately determined for the universal triangular space construction. The differences among the land surface models should be considered for a robust soil moisture estimation model establishment. Moreover, the uncertainties of the remotely sensed data and the scale mismatch are still the conundrum in the soil moisture validation. These problems form the motivation for our future work.

ACKNOWLEDGEMENTS

This work was partly supported by the National Natural Science Foundation of China under Grant 41201366, the Institute of Geographic Sciences and Natural Resources Research funded outstanding young

talent project under Grant 2013RC201, the National High Technology Research and Development Program of China under Grant 2012AA121103, and the Exploratory Forefront Project for the Strategic Science Plan in IGSNRR, CAS under grant 2012QY006. We also wish to thank SMEX02 for providing in situ measurement of soil water content used in this work and greatly thank Di Long, who provided many constructive comments for improving this study.

REFERENCES

- Istanbulluoglu, E., and Bras, R. L., 2006, On the dynamics of soil moisture, vegetation and erosion: Implications of climate variability and change, *Water Resource Research*, 42, W06418, doi: 10.1029/2005WR004113.
- Jackson, R. D., Pinter, P. J., 1981, Detection of water stress in wheat by measurement of reflected solar and emitted thermal IR radiation, in *Spectral Signatures of Objects in Remote Sensing*, Institut National de la Recherche Agronomique, Versailles, France, pp. 399-406.
- Li, Z.-L., Tang, R. L., Wan, Z. M., Bi, Y. Y., Zhou, C. H., Tang, B. H., Yan, G. J. and Zhang, X. Y., 2009, A Review of Current Methodologies for Regional Evapotranspiration Estimation from Remotely Sensed Data, *Sensors*, 9, 3801-3853.
- Long, D. and Singh, V. P., 2012, A two-source trapezoid model for evapotranspiration (TTME) from satellite imagery, *Remote Sensing of Environment*, 121, 370-388.
- Carlson, T., 2007, An Overview of the Triangle Method for Estimating Surface Evapotranspiration and Soil Moisture from Satellite Imagery, *Sensors*, 7, 1612-1629.
- Kustas, W. P., Hatfield, J. L., and Prueger, J. H., 2005, The soil moisture - atmosphere coupling experiment (SMACEX) Background, hydrometeorological conditions, and preliminary findings. *Journal of Hydrometeorology*, 6, 791-804.
- Twine, T. E., Kustas, W. P., Norman, J. M., Cook, D. R., Houser, P. R., and Meyers, T. P., 2000, Correcting eddy-covariance flux underestimates over a grassland. *Agricultural and Forest Meteorology*, 103, 279-300.

A Comparison of Two LST Retrieval Methods with Simulated MODIS TIR and MIR Nighttime Data

En-Yu Zhao¹, Caixia Gao², Yonggang Qian², Hongyuan Huo¹, Xiaoguang Jiang^{1,3}, Yuze Zhang¹, Yuzhang Du¹,

¹University of Chinese Academy of Sciences, Beijing 100049, China;

²Key Laboratory of Quantitative Remote Sensing Information Technology, Academy of Opto-Electronics, Chinese Academy of Sciences, Beijing 100094, China;

³GuiLin University of Technology, GuiLin, 541004, China.

zhaoenyusdu@163.com

ABSTRACT - Land surface temperature (LST) is a good indicator of the energy equilibrium of the earth's surface. With the development of remote sensing, infrared sensors such as MODIS, AVHRR and SEVIRI, provide a valuable way for measuring LST over the entire globe, and various algorithms have been proposed from thermal infrared (TIR, 8~12μm) data. Moreover, due to the more transparent atmospheric window, less sensitive to land surface emissivity (LSE) and water vapor content (WVC) for LST retrieval, the mid-infrared (MIR, 3~5μm) data is also used to retrieve LST. Since the nighttime data in MIR spectral region is not affected by solar direct radiance, which is similar to the split-window method in TIR, LST also can be expressed as a linear combination of the brightness temperature measured in two adjacent MIR channels with coefficients depending on LSE, view zenith angle (VZA) and WVC. In this study, with the aid of simulated data under six VZAs (0°, 33.56°, 44.42°, 51.32°, 56.25° and 60°), various land surface and atmospheric conditions, a comparison is carried out between a LST retrieval method (denoted as Method1) using two MODIS TIR channels (channel 31: 10.78~11.28μm and channel 32: 11.77~12.27μm) and that (denoted as Method2) using two MODIS MIR channels (channel 22: 3.929~3.989μm and channel 23: 4.02~4.08μm) with the knowledge of LSE. The results show that the LST can be well estimated by the two methods with a root mean square error (RMSE) less than 1K at the VZA=0°. However, the RMSEs for Method1 increase significantly with the increase of WVCs, with a maximum of 1.6K, while the ones for Method2 is within 0.3K, and change little. Also, the sensitivity and error analyses for each method in terms of the uncertainty of the LSE, Noise Equivalent Temperature difference (NEAT) and WVC are also performed.

1 INTRODUCTION

Land surface temperature (LST) plays an important role in the physical processes of surface energy and water balance at local and global scales. Also, LST is the one of the most critical parameters in evapotranspiration, vegetation assessment, heat flux estimation, urban climate and environment studies (Li *et al.*, 2013). Therefore, it is essential to find a reliable way to acquire LST in regional and global scales. Whereas, the ground measured LST cannot practically provide values in large scale. With the development of remote sensing, infrared sensors provide a valuable way for measuring LST over the entire globe. Various algorithms have been proposed from thermal infrared (TIR, 8~12μm) data. Moreover, due to the more transparent atmospheric window, less sensitive to land surface emissivity (LSE) and water vapor content (WVC) for LST retrieval, the mid-infrared (MIR, 3~5μm) data is also used to retrieve LST (Zhao *et al.*, 2014).

In this paper, with the aid of simulated data under six VZAs (0°, 33.56°, 44.42°, 51.32°, 56.25° and 60°), various land surface and atmospheric conditions, a

comparison is carried out between a LST retrieval method (denoted as Method1) using two moderate resolution imaging spectroradiometer (MODIS) TIR channels (channel 31: 10.78~11.28μm and channel 32: 11.77~12.27μm) and that (denoted as Method2) using two MODIS MIR channels (channel 22: 3.929~3.989μm and channel 23: 4.02~4.08μm) with the knowledge of LSE. The sensitivity and error analyses for each method in terms of the uncertainty of the LSE, Noise Equivalent Temperature difference (NEAT) and WVC are also carried out.

2 METHODOLOGY AND DATA SIMULATION

2.1 Basic Theory

On the basis of the radiative transfer theory, under local thermodynamic equilibrium during a clear-sky day, the radiative transfer equation (RET) during night in the region (3~12μm) can be written as (Li *et al.*, 2013):

$$B_i(T_i) = \tau_i \left[\varepsilon_i B_i(T_s) + (1 - \varepsilon_i) R_{atm_i}^\downarrow \right] + R_{atm_i}^\uparrow \quad (1)$$

where B_i is the Planck function. $B_i(T_i)$ is the top of the atmosphere (TOA) radiance in channel i , and T_i is the

brightness temperature. ε_i and T_s are the surface emissivity and surface temperature, respectively. τ_i is the transmittance. $R_{atm,i}^{\uparrow}$ and $R_{atm,i}^{\downarrow}$ are the upward and downward atmospheric thermal radiances, respectively.

The split-window method applied to retrieve LST from TIR data is based on the differential absorption (especially for WVC) in two TIR channels by expressing LST as a linear function of the brightness temperatures T_i and T_j which are measured in the two adjacent TIR channels. The nighttime data in MIR spectral region is not affected by solar direct radiance, which is similar to the TIR region, therefore, LST also can be expressed as a linear combination of the brightness temperature measured in two adjacent MIR channels with coefficients depending on LSE, view zenith angle (VZA) and WVC. Therefore, the LST retrieval methods from TIR and MIR nighttime data can both be expressed as follows:

$$T_s = k_0 + (k_1 + k_2 \frac{1-\varepsilon}{\varepsilon} + k_3 \frac{\Delta\varepsilon}{\varepsilon^2}) \frac{T_i + T_j}{2} + (k_4 + k_5 \frac{1-\varepsilon}{\varepsilon} + k_6 \frac{\Delta\varepsilon}{\varepsilon^2}) \frac{T_i - T_j}{2} \quad (2)$$

where $\varepsilon = (\varepsilon_i + \varepsilon_j)/2$, $\Delta\varepsilon = \varepsilon_i - \varepsilon_j$, and $k_0, k_1, k_2, k_3, k_4, k_5$ and k_6 are unknown coefficients, which can be derived from simulated MODIS data. T_i and T_j are the TOA brightness temperatures in adjacent two channels. ε_i and ε_j are the LSEs in channel i and j , respectively. ε is the averaged emissivity, and $\Delta\varepsilon$ is the emissivity difference between the two channels.

2.2 Data

In this paper, the TOA radiances of the MODIS TIR channels (channel 31: 10.78~11.28 μ m and channel 32: 11.77~12.27 μ m) and MIR channels (channel 22: 3.929~3.989 μ m and channel 23: 4.02~4.08 μ m) are simulated by the moderate resolution atmospheric transmission (MODTRAN) 4.0. In total, 377 atmospheric profiles, which are used to gain the atmospheric parameters, are extracted from the TOVS Initial Guess Retrieval (TIGR) database, with the atmospheric bottom temperature (T_{air}) of 270~310K and the WVC of 0.06~5.39 g/cm² (Chedin *et al.*, 1985). Given the attenuation of the surface radiance, the uniformly mixed gases (CO₂, N₂O, CO and CH₄) and ozone, included in the standard atmospheres of the MODTRAN 4.0 code, are added to the water vapor taken from profiles in the TIGR radiosoundings (Sobrino *et al.*, 2004). To accomplish this, the surface temperatures are from $T_a - 15K$ to $T_a + 5K$ with a step of 5K. Furthermore, the VZAs are set to be 0°, 33.56°, 44.42°, 51.32°, 56.25° and 60° (corresponding values of $1/\cos(VZAs)$ are 1, 1.2, 1.4, 1.6, 1.8 and 2.0), respectively. Also, 70 different emissivities which are

obtained from the Johns Hopkins University (JHU) Spectral library (soils, vegetation and water, etc.) are considered. The TOA radiances could be determined according to Eq. (1) after the simulation. In total, for the TIGR database and the JHU Spectral library, 791700 different situations are simulated for retrieval.

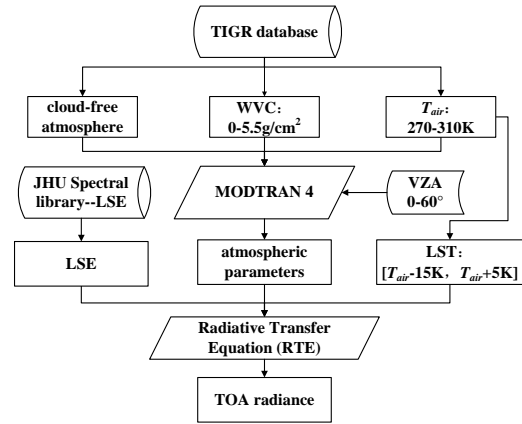


Figure 1. A flowchart of the simulation of TOA radiances

3 RESULTS AND ANALYSIS

3.1 Coefficients of LST Retrieval Method

In order to improve the accuracy of LST retrieval, WVCs and LSTs are divided into several sub-ranges. WVCs are divided into five sub-ranges: [0-1.5], [1-2.5], [2-3.5], [3-4.5] and [4-5.5] g/cm², and LSTs are divided into three sub-ranges: 255K<LST<285K, 280K<LST<300K and 295K<LST<315K. Then, the coefficients in Eq. (2) can be obtained through a statistical regression method for each sub-range under different VZAs. Figure 2 shows the coefficients of Method 1 and Method 2 as functions of the secant of VZAs at the sub-ranges of LST=295~315K, for the two WVC groups. The coefficients $k_0 \sim k_6$ for other VZAs can be linearly interpolated as function of the secant of VZA. Similar results are obtained for the other sub-ranges.

3.2 Results of LST Retrieval

It can be found from Figure 3 that the LST can be well estimated by the two methods with a root mean square error (RMSE) less than 1K at a VZA of 0°. However, the RMSEs for Method1 increase significantly with the increase of WVCs, with a maximum of 1.6K, while the ones for Method2 are within 0.3K, and change slightly. Generally, it can be found that the LST retrieval accuracy of Method2 is higher than that of Method1, which would be caused by more transparent atmospheric window and the less sensitivity to WVC in the MIR region.

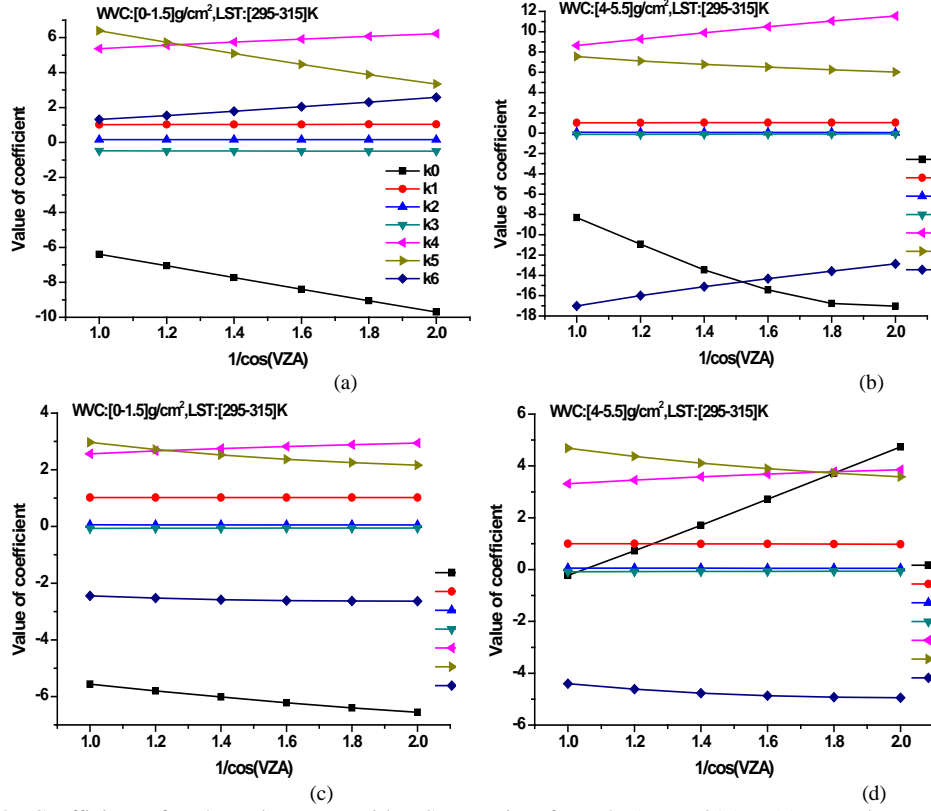


Figure 2: Coefficients for the sub-ranges with LST varying from 295K to 315K. (a) TIR dry atmosphere (WVC=0~1.5 g/cm²). (b) TIR humid atmosphere (WVC=4~5.5 g/cm²). (c) MIR dry atmosphere (WVC=0~1.5 g/cm²). (d) MIR humid atmosphere (WVC=4~5.5 g/cm²).

4 SENSITIVITY ANALYSIS

Sensitivity analysis is important to LST retrieval. In this study, the instrument noises (Noise Equivalent difference Temperature, NE Δ T), the uncertainties of LSEs and WVC are taken into account.

4.1 Sensitivity analysis to Instrumental Noises

To analyse the effect of NE Δ T on the LST retrieval using Eq. (2), a Gaussian random distribution error of 0.05K is added to T_i and T_j in channel 31 and channel 32 in Eq. (1), and an error of 0.07K is added to T_i and T_j in channel 22 and channel 23 (Zhao *et al.*, 2003). The errors for the sub-ranges of LST varying from 295K to 315K in the five WVC sub-ranges are shown in Figure 4. The results show that the LST errors caused by instrumental noises vary from 0.2K to 0.4K for Method1 and from 0.16K to 0.23K for Method2, respectively. It is noted that Method1 is more sensitive to NE Δ T than Method2.

4.2 Sensitivity analysis to LSEs

A Gaussian random distribution error of 0.01 is added to ε_i and ε_j in Eq. (1), and the LST retrieval errors for Method1 and Method2 are shown in Figure 5. It can be noted that, with the LSE uncertainty of 0.01, the LST retrieval errors vary from 0.4K to 2.2K for Method1 and the ones vary from 0.4K to 0.65K for Method2, respectively, at the condition of LST=295-315K. It is obvious that LST retrieval using TIR data is more sensitive to LSE than that using MIR data.

4.3 Sensitivity analysis to WVCs

The uncertainty of the WVC on the LST retrieval is investigated in this paper. A Gaussian random distribution error, where the mean of the distribution is 0 and the standard deviation is 20%, is added to WVC. Figure 6 (a) and (b) show the LST errors caused by a WVC uncertainty of 20% with the conditions of LST=295~315K. It can be seen from Figure 5 that RMSEs of Method1 vary from 0.2K to 1.7K and the ones of Method2 vary from 0.14K to 0.32K. Therefore, the uncertainty of WVC will make larger error in Method1 than Method2.

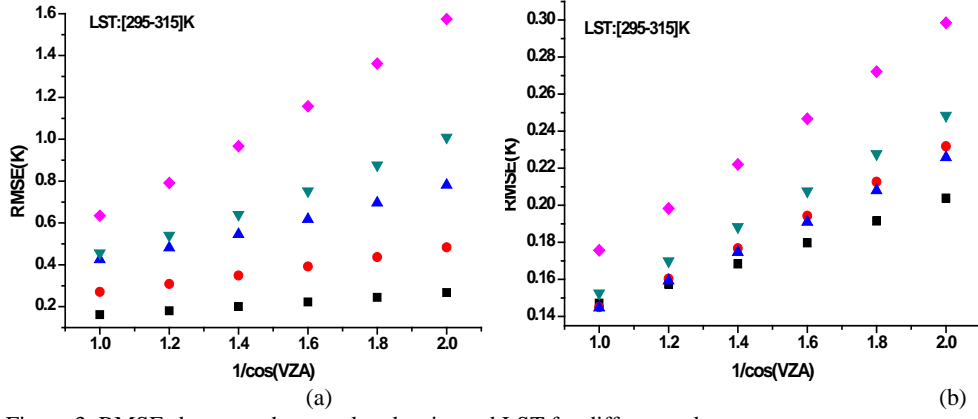


Figure 3. RMSEs between the actual and estimated LST for different sub-ranges.

(a) Method1. (b) Method2. WVC: ■0~1.5 ●1~2.5 ▲2~3.5 ▼3~4.5 ◆4~5.5 (g/cm²)

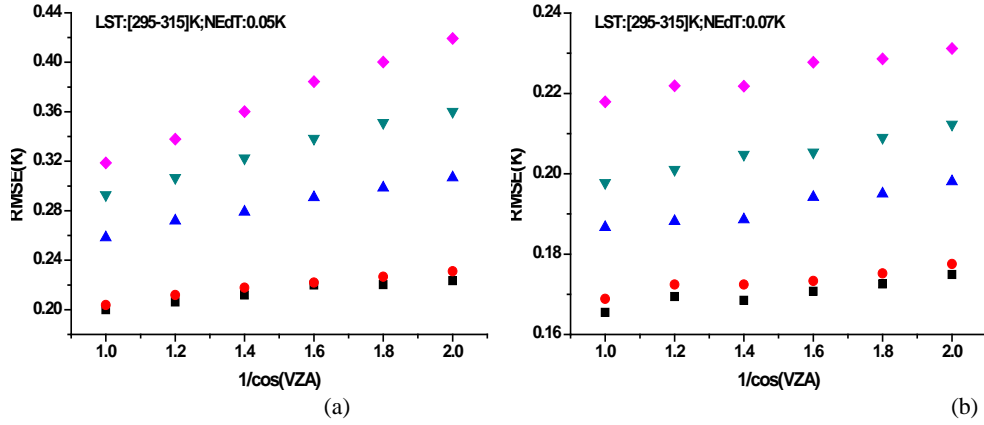


Figure 4. LST retrieval error caused by NEAT with LST=295-315K.

(a) Method 1. (b) Method 2. WVC: ■0~1.5 ●1~2.5 ▲2~3.5 ▼3~4.5 ◆4~5.5 (g/cm²)

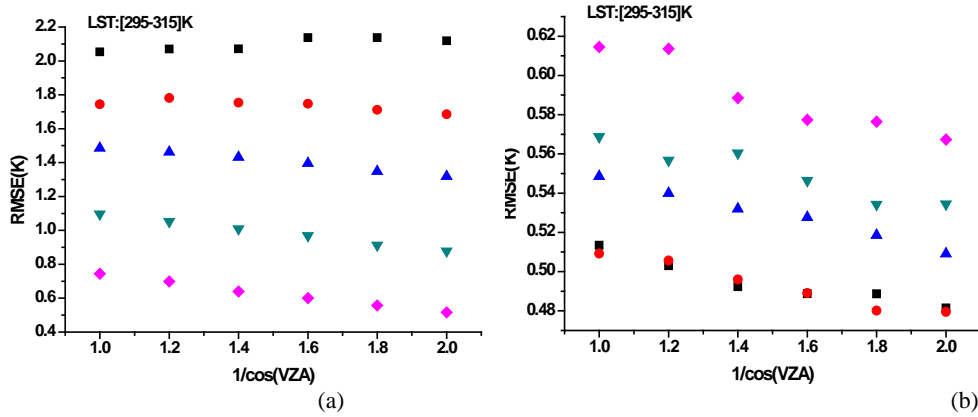


Figure 5. LST retrieval error caused by the emissivity uncertainty of 0.01.

(a) Method1. (b) Method2. WVC: ■0~1.5 ●1~2.5 ▲2~3.5 ▼3~4.5 ◆4~5.5 (g/cm²)

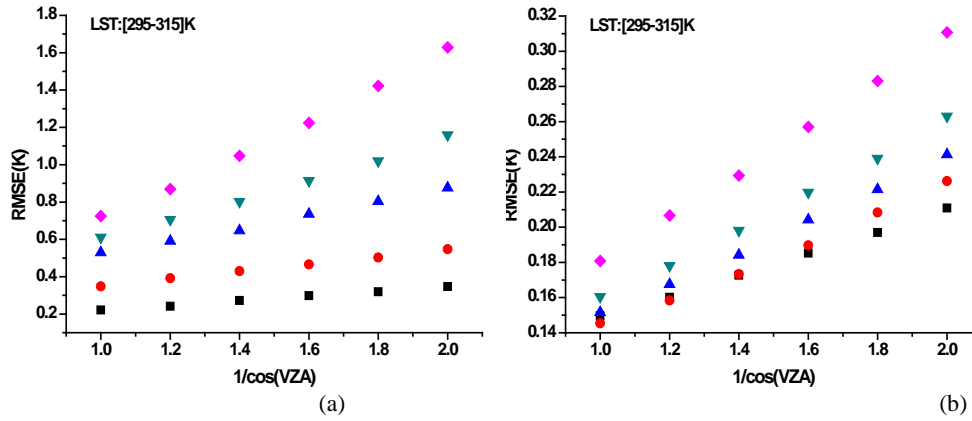


Figure 6. LST retrieval error caused by the WVC uncertainty of 20%.
(a) Method 1. (b) Method 2. WVC: ■ 0~1.5 ● 1~2.5 ▲ 2~3.5 ▼ 3~4.5 ◆ 4~5.5 (g/cm²)

5 CONCLUSION

The results show that at the conditions of VZA=0°, the LST can be estimated with the RMSEs less than 1K using the two methods. The sensitivity analyses show that the corresponding error is approximately 0.3K and 0.2K, respectively, with the NEΔT of MODIS (TIR: 0.05 K; MIR: 0.07K); the LST retrieval average errors are about 1.3K and 0.5K for Method1 and Method2, respectively, with a uncertainty of LSE of 0.01; the errors vary from 0.2K to 1.7K for Method1, and from 0.14K to 0.32K for Method2 when the uncertainty of WVC is 20%. It is noted that the same uncertainties of NEΔT, LSE and WVC cause more LST retrieval error for Method1 than that for Method2. Therefore, the LST retrieval from MIR nighttime data performs better than that from TIR data both in terms of retrieval accuracy and sensitivities to LSE, NEΔT and WVC using the MODIS simulated data with the help of LSE. However, in practice, due to the serious noise effect and high LSE uncertainty of nighttime data in MIR channels, the performance of the application of the two methods to satellite data need to be further studied in future.

6 REFERENCES

- Chedin, A., Scott, N., Wahiche, C., and Moulinier, P., 1985, The improved initialization inversion method: A high resolution physical method for temperature retrievals from satellites of the tiros-n series. *Journal of climate and applied meteorology*, **24**, 128-143.
- Li, Z. L., Wu, H., Wang, N., Qiu, S., Sobrino, J. A., Wan, Z., Tang, B., and Yan, G., 2013, Land surface emissivity retrieval from satellite data. *International Journal of Remote Sensing*, **34**(9-10), 3084-3127.
- Li, Z. L., Tang, B. H., Wu, H., Ren, H., Yan, G., Wan, Z., Trigo, I.F., and Sobrino, J. A., 2013, Satellite-derived land surface temperature: Current status and perspectives. *Remote Sensing of Environment*, **131**, 14-37.
- Sobrino, J. A., Jiménez-Muñoz, J. C., El-Kharraz, J., Gómez, M., Romaguera, M., and Soria, G., 2004, Single-channel and two-channel methods for land surface temperature retrieval from DAIS data and its application to the Barrax site. *International Journal of Remote Sensing*, **25**(1), 215-230.
- Zhao, E.Y., Qian, Y.G., Wang, N., Ma, L.L. and Tang, L.L., 2014, Retrieval of night-time land surface temperature from two mid-infrared channels data. *Infrared Millim.Waves*, **33**(3):303~310.
- Zhao, Y.S. *et al.*, 2003, Principles and Methods of Remote Sensing Application Analysis. In Chinese.

Precipitable water vapor content derived from space-based passive radiometers over land surfaces

Fang-Cheng Zhou^{a,b}, Xiaoning Song^{a,*}, Zhao-Liang Li^{b,c}, and Ruixin Wang^a

^a University of Chinese Academy of Sciences, Beijing 100049, China

^b State Key Laboratory of Resources and Environment Information System, Institute of Geographic Sciences and Natural Resources Research, Chinese Academy of Sciences, Beijing 100101, China

^c Key Laboratory of Agri-informatics, Ministry of Agriculture/Institute of Agricultural Resources and Regional Planning, Chinese Academy of Agricultural Sciences, Beijing 100081, China

*songxn@ucas.ac.cn

ABSTRACT—We have developed a physics-based algorithm for retrieving Precipitable Water Vapour (PWV) from passive microwave remote sensing data. The retrieval algorithm is developed from the radiative transfer analysis with the assumption that (1) the difference of brightness temperatures of adjacent channels is mainly influenced by PWV; (2) Land surface emissivities (LSE) of adjacent channels are identical. Brightness temperatures at horizontal polarization of 18.7 and 23.8 GHz are chosen as the best combination for retrieving PWV. Through some approximations made in the radiative transfer, a linear relationship between PWV and the difference of T_B at 18.7 and 23.8GHz has been established. The slope and intercept of the linear relationship are LSE-dependent. With LSE increase, the reliability of retrieval algorithm is getting worse, especially when the LSE is larger than 0.90 with determination coefficient (R^2) less than 0.60. This algorithm is validated with the measured data in Zhangye National Climate Observatory with the Root-Mean-Square Error (RMSE) of 3.94mm. The retrieval algorithm makes it possible to get daily PWV products from the daily brightness temperatures at horizontal polarization of 18.7 and 23.8 GHz.

1 INTRODUCTION

Precipitable Water Vapor (PWV) is the most variable component of the atmosphere in both space and time. It is very important for the meteorological applications, and the studies of climate change and global warming, since the water vapor is the most abundant greenhouse gas. Accurate, real-time knowledge of PWV presenting in the atmosphere is essential for the monitoring and forecasting tasks of many meteorological and hydrologic processes. In the field of remote sensing, knowledge of PWV can help improve the observation accuracy through the remote sensing atmospheric correction. Given the importance of PWV, it is necessary to monitor PWV accurately and timely.

Space-based passive microwave remote sensing have all-weather and all-times observed capabilities which can monitor the global distribution of PWV better than that of near-infrared remote sensing and ground-based instruments, while the algorithms for retrieving PWV suitable for passive microwave remote sensing data are few.

2 RADIATIVE TRANSFER ANALYSIS

The brightness temperature T_B measured from the space-based microwave radiometers consists of three radiative components: (1) upwelling radiation emitted

by the atmosphere T_a^\uparrow ; (2) surface-emitted radiation that attenuated by the atmosphere $\tau e T_s$; and (3) downwelling radiation from the atmosphere and cosmic background reflected by the surface and attenuated by the atmosphere $(1-e)\tau(T_a^\downarrow + T_{sky})$. With the assumption that the land surface is Lambertian and the upwelling and downwelling atmospheric radiances are identical, the radiative transfer equations for adjacent channels (i, j) can be written as

$$T_{Bi} = T_{ai} + \tau_i e_i T_s + (1 - e_i) \tau_i (T_{ai} + T_{sky}) \quad (1a)$$

$$T_{Bj} = T_{aj} + \tau_j e_j T_s + (1 - e_j) \tau_j (T_{aj} + T_{sky}) \quad (1b)$$

where T_{Bi} and T_{Bj} are the brightness temperatures of adjacent channels, respectively. τ_i and τ_j are the transmittances, T_{Bi} and T_{Bj} are the effective radiating temperatures of the atmosphere, e_i and e_j are the land surface emissivities (LSE) at the frequencies of i and j . T_s is the land surface temperature (LST), T_{sky} is the cosmic background radiation, about 2.75K. The dependence of the radiances on the sensor angle is implicit in these equations.

Here is the most important assumption in this study: LSE of the adjacent channels are identical. The equation of the split window temperature difference (ΔT_B) can be written as

$\Delta T_B = \Delta T_a + eT_s\Delta\tau + (1-e)(T_{ai}\tau_i - T_{aj}\tau_j + 2.75\tau_i - 2.75\tau_j)$ (2)
where

$$\Delta T_B = T_{Bi} - T_{Bj} \quad (3a)$$

$$\Delta T_a = T_{ai} - T_{aj} \quad (3b)$$

$$\Delta\tau = \tau_i - \tau_j \quad (3c)$$

e represent LSE of the adjacent channels. In the real application, once LST and LSE are known, ΔT_B is just a function of T_{ai} , T_{aj} , τ_i and τ_j , which are mainly influenced by the atmospheric conditions and the observed frequencies of microwave radiometers. When the adjacent observed frequencies are determined, ΔT_B will be only effected by the atmospheric conditions. PWV as an important parameter of atmosphere is chosen as the one which characterizes the atmospheric conditions. Westwater et al. (1990) found that there was an accurate and simple parameterization that relates τ to PWV, which was the linear relationship. Jia (2007) and Liu (2013) confirmed the linear relationship between τ and PWV with the simulation data calculated by the LIEBE93 model and Micro Wave radiative transfer MODEL (MWMOD), and further found that there was a positive relationship between T_a and PWV. Hence, ΔT_B can be considered as the function of PWV. This is the basis of the algorithm for retrieving PWV from passive microwave remote sensing data.

3 DATA AND METHODOLOGY

3.1 The Thermodynamic Initial Guess Retrieval (TIGR) dataset

TIGR was constructed by the Laboratoire de Meteorologie Dynamique (LMD) and has 2311 atmospheric profiles data from 80,000 radiosonde reports from all over the world. Each atmospheric profile has the values of the temperature, water vapour and ozone concentrations on a given pressure grid, from the surface to the top of the atmosphere. All these atmospheric profiles are grouped into five airmass types (Tropical, temperate -Midlat1-, cold temperate and summer polar -Midlat2-, Northern Hemisphere very cold polar -polar1-, winter Polar -Polar2-). TIGR dataset are downloaded from the Atmospheric Radiation Analysis (ARA) website (<http://ara.abct.lmd.polytechnique.fr/index.php?page=tigr>).

In this study, the original 2311 atmospheric profiles are selected by some rules to meet the needs of this study. Firstly, in order to eliminate the effect caused by the cloud liquid water (CLW) to ΔT_B , only the water vapour profiles whose relative humidity at any given pressure less than 80% are chosen, which represent the cloud-free days. Secondly, those located

on the oceans or lakes are filtered. Finally, 378 cloud-free and overland atmospheric profiles are left (Fig.1).

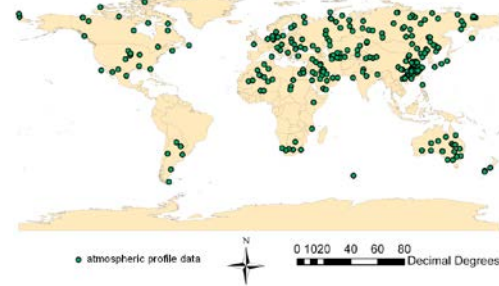


Fig.1. Locations of the 378 cloud-free and overland atmospheric profiles on the map of the world.

3.2 The Monochromatic Radiative Transfer Model (MonoRTM) overview

MonoRTM was constructed by Atmospheric and Environmental Research (AER) (http://rtweb.aer.com/monortm_frame.html) with the same physics as LBLRTM but is designed to process a limited number of monochromatic spectral output values. It is particularly useful in the microwave spectral region and can perform radiative transfer calculations for frequencies specified in the input stream. MonoRTM has a very high-precision with the application to the physical retrieval of PWV, which is expected to provide retrieval accuracies approaching 1% for PWV.

3.3 The best combination of frequencies and polarizations

3.3.1 The choice of the frequencies

The 22GHz is the most commonly used frequency to measure water vapor for atmospheric studies and weather prediction, often called as the water vapor line, so that a frequency located near 22GHz is necessary for estimating PWV. The choice of the other frequency should consist with the assumption in the previous section, which is the LSE of adjacent channels identical. Two frequencies near 20GHz are satisfactory, since the LSE of these two frequencies are proved very similar from the in situ measurements (Mätzler 1994). Referring to the frequency setting of the common space-based microwave radiometers and for the easy acquisition of the data, 18.7 and 23.8GHz are chosen which can be got from FengYun-3B.

3.3.2 The choice of the polarizations

Transform the Eq. (1), the physical algorithm for retrieving LSE can be written as

$$LSE = \frac{T_B - T_a - \tau(T_a + T_{sky})}{\tau T_s - \tau(T_a + T_{sky})} \quad (4)$$

where LSE and T_B are both influenced by the polarizations. To analysis the influence of the polarizations on the assumption, 12 radiosonde sounding observations in Zhangye National Climate Observatory from 1 May 2012 to 30 Sep. 2012 and daily MODIS LST products (MYD11A1) and FY-3B MicroWave Radiometer Imager (MWRI) L1 brightness temperature data at the corresponding time are got together to calculate LSE at horizontal and vertical polarizations according to Eq. (4), respectively. The ideal situation which consists with the assumption mostly is the polarization differences of LSE at adjacent channels closing to 0.

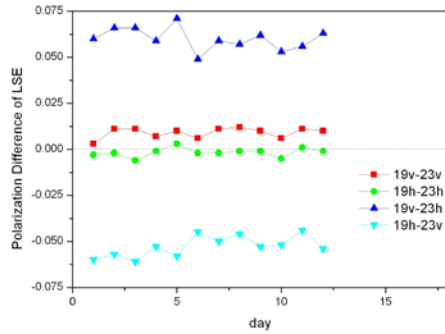


Fig.2. Four kinds of polarization differences of LSE, they are 18.7v-23.8v, 18.7h-23.8h, 18.7v-23.8h and 18.7h-23.8v (v and h represent vertical and horizontal polarizations, respectively).

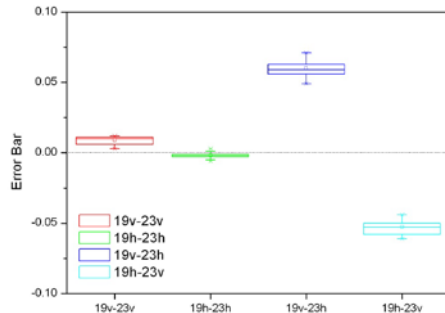


Fig.3. Error bars of four kinds of polarization differences of LSE, they are 18.7v-23.8v, 18.7h-23.8h, 18.7v-23.8h and 18.7h-23.8v (v and h represent vertical and horizontal polarizations, respectively).

From Fig.2, the line of (18.7h-23.8h) is closest to 0 line, and then the line of (18.7v-23.8v), the line of (18.7h-23.8v) and (18.7v-23.8h) are third and fourth, respectively. Fig.2 shows that the difference of the same polarization of LSE is less than that of different polarization, and difference at h polarization is less than that of v polarization. And this is further proved by Fig.3. So the best combination which most consist with our assumption is the brightness temperatures at horizontal polarization of 18.7 and 23.8 GHz.

3.4 Experimental design

To develop the relationship between ΔT_B and PWV, the databases of ΔT_B and PWV are needed. PWV database can be got through the simulation of MonoRTM with 378 atmospheric profiles. ΔT_B database can be got by the subtraction of simulated brightness temperatures of adjacent channels. For the simulation of brightness temperatures, according to Eq. (1), LST and LSE are needed except for T_a and τ (which can be calculated by MonoRTM). In this study, both LST and LSE are considered to vary in a wide range to consist with the real applications all over the world. For LST, it varies related to the surface air temperature of each atmospheric profile, which is expressed as T_0 . If $T_0 \geq 280$ K, LST varies from $T_0 - 5$ K to $T_0 + 20$ K in steps of 5 K. If $T_0 < 280$ K, LST varies from $T_0 - 10$ K to $T_0 + 15$ K in steps of 5 K. For LSE, it depends on several factors such as soil moisture content, vegetation cover, and also sensor parameters such as frequency, polarization, and incident angle. It is hard to assign LSE values just thinking of one or two factors. In this study, Advanced Integral Equation Model (AIEM) (Chen et al. 2003) is used to calculate LSE database for the following FY-3B sensor parameters: frequencies of 18.7 and 23.8 GHz, horizontal polarization, and 53° incidence angle. This database also covers a wide range of surface dielectric constants that are calculated from the corresponding volumetric soil moisture content (2%-44% in steps of 2%) by Dobson's dielectric mixing model, with a given soil texture property and surface roughness parameters (root-mean-square height from 0.25-3cm in steps of 0.25cm and the correlation length from 2.5-30cm in steps of 2.5cm).

4 RESULTS AND DISCUSSIONS

4.1 The relationship between ΔT_B and PWV

Fig.4 (a)-(f) show that there are linear relationships between ΔT_B and PWV. PWV increase with the increasing of ΔT_B . In fact, the change of PWV is the cause and the change of ΔT_B is the effect. The relationship between PWV and ΔT_B consists with the theoretic derivation of Eq. (2). The basis of Eq. (2) is the assumption that LSE of adjacent channels identical, so LSE are the main influence factor on this relationship. This is also proved by Fig.4 (a)-(f), for slopes and intercepts of the linear models varying with the change of LSE from 0.65 to 0.90 in steps of 0.05. With LSE increase, the slopes increase from 1.932 to 4.978, intercepts increase from -3.031 to 10.384, while the maximum brightness temperature difference decrease from 27.68K to 9.07K, and determination coefficient (R^2) decrease from 0.960 to 0.595 (see Table 1).

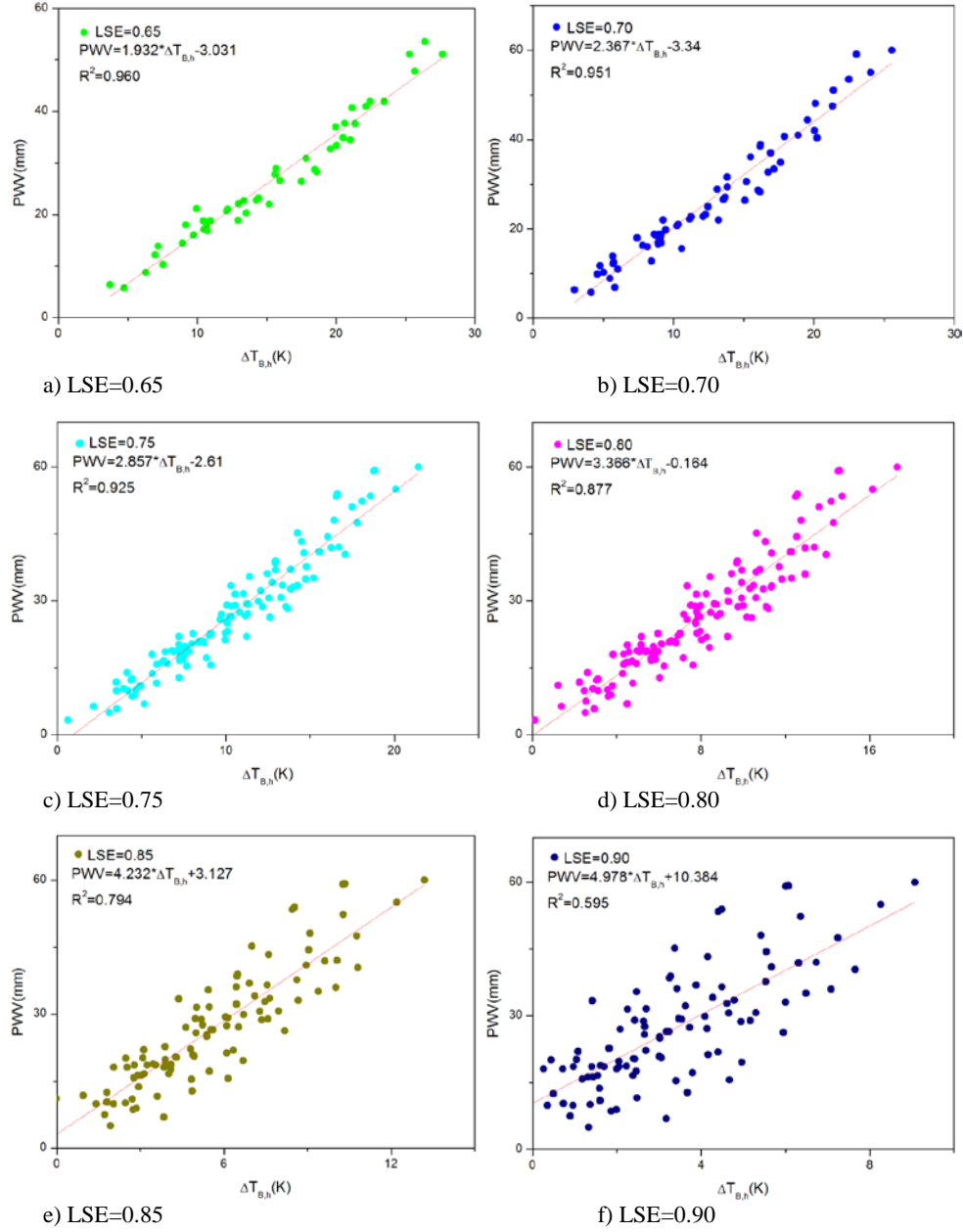


Fig.4. Linear relationships between PWV and ΔT_B with LSE=0.65, 0.70, 0.75, 0.80, 0.85, 0.90. These points are got by the following steps: firstly, the selected 378 atmospheric profiles data are entered in MonoRTM to calculate PWV; secondly, PWV with a wide range of LST and LSE, are all entered in Eq. (2) to calculate $\Delta T_{B,h}$ ($\Delta T_{B,h}$ represent the brightness temperature difference at horizontal polarization).

The change of maximum brightness temperature difference indicates that with the increasing of LSE, the change of ΔT_B caused by the change of PWV gradually decreases, and brightness temperatures of 18.7 and 23.8 GHz at h polarization become closer.

The decrease of R^2 indicates that the reliability of linear model is getting worse, especially when the LSE is larger than 0.90 with R^2 less than 0.60. In general, the value of LSE at horizontal polarization has an acceptable agreement with the land cover types. LSE

increases with the increasing of vegetation coverage (Norouzi et al. 2010). This means the linear model is more suitable for barren or sparsely vegetated zones than densely vegetated zones. This phenomenon may be caused by the Eq. (2), which ignores the influence of vegetation.

Table 1. Slopes and intercepts of linear models with LSE=0.65, 0.70, 0.75, 0.80, 0.85, 0.90.

Slope	Intercept	LSE
1.932	-3.031	0.65
2.367	-3.34	0.70
2.857	-2.61	0.75
3.366	-0.164	0.80
4.232	3.127	0.85
4.978	10.384	0.90

4.2 The relationships between slopes and LSE, intercepts and LSE

Be aware that the slopes and intercepts varying with the change of LSE, it is needed to develop the models between slopes and LSE, intercepts and LSE, respectively in order to calculate the slopes and intercepts when the LSE are known. Fig.5 shows that slopes have an exponential relationship with LSE with $R^2=0.998$; while the relationship between intercepts and LSE conforms to the dose-response function with $R^2=0.992$. Both slopes and intercepts increase with the increasing of LSE from 0.65 to 0.90.

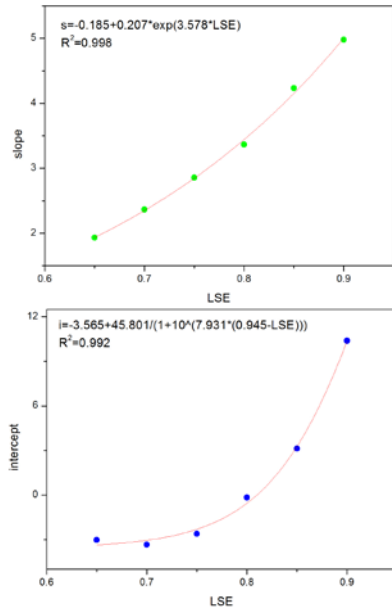


Fig.5. Relationships between slopes and LSE, intercepts and LSE, respectively. The range of LSE is from 0.65 to 0.90.

4.3 The algorithm for retrieving PWV from passive microwave remote sensing data

So far we can develop the algorithm for retrieving PWV from passive microwave remote sensing data, it can be written as

$$PWV = s \cdot \Delta T_{B,h} + i \quad (5)$$

where

$$s = -0.185 + 0.207 \cdot \exp(3.578 \cdot LSE) \quad (6a)$$

$$i = -3.565 + 45.801 / (1 + 10^{(7.931 \cdot (0.945 - LSE))}) \quad (6b)$$

where s stands for slopes, and i stands for intercepts. The retrieval model of PWV makes it possible to get PWV products from daily brightness temperatures at horizontal polarization of 18.7 and 23.8 GHz.

4.4 Sensitivity analysis

Except for the errors caused by the statistical regression method in the develop process of the retrieval model, the measuring errors of two parameters (LSE and ΔT_B) in the retrieval model also could cause errors to the retrieval PWV. In this study, LSE are assumed to be known. But in the real applications, LSE are generally got by some models, which usually have errors. According to the Fig.5, when the LSE are small, slopes and intercepts change slowly; while when the LSE are large, slopes and intercepts change sharply. That means when the LSE are larger, the errors of LSE will cause larger errors for slopes and intercepts and further cause larger errors for the retrieval PWV; while for the smaller LSE, the impact of LSE calculation errors for retrieval PWV is little. For the ΔT_B , errors mainly come from $NE\Delta T$ of the microwave radiometers. From the Eq.(5), the errors of retrieval PWV will be equal to $s \cdot NE\Delta T$ (s stands for slope, $NE\Delta T$ stands for the errors of ΔT_B). One of the ways to improve the precision of the retrieval model is to decrease the $NE\Delta T$.

4.5 Validation with measured data

To further assess the precision of the retrieval model of PWV, a preliminary validation is performed using the 12 radiosonde sounding observations from the Zhangye National Climate Observatory (39°5'15.68"N, 100°16'39.11"E), and the remotely sensed data at the corresponding time in this position, including MYD11A1 and FY-3B MWRI brightness temperature data. The reason of choosing this position as our validation site is this position has large areas of barren or sparsely vegetated zones, which conforms to the scope of application of our retrieval model. PWV are overestimated by the retrieval model with $R^2=0.524$, and the overestimation increase with the increasing of actual PWV. The reasons of R^2 a bit low are two: one is the calculated LSE may have some

errors, which can cause the errors of slopes and intercepts; the other may be the differences of the spatial resolutions and imaging time of the various input data. RMSE for the retrieval model is 3.94mm, which indicates good agreement.

5 CONCLUSIONS

We have developed a physics-based algorithm for retrieving PWV from passive microwave remote sensing data. The retrieval algorithm is developed from the radiative transfer analysis with the assumption that (1) the difference of brightness temperatures of adjacent channels is mainly influenced by PWV; (2) Land surface emissivities (LSE) of adjacent channels are identical. Brightness temperatures at horizontal polarization of 18.7 and 23.8 GHz are chosen as the best combination for the retrieval algorithm. Through some approximations made in the radiative transfer, a linear relationship between PWV and the difference of TB at 18.7 and 23.8GHz has been established. LSE determines the slopes and intercepts of the linear model. With the algorithm, PWV can be got just using the differences of brightness temperatures when LSE are known. The new PWV retrieval algorithm is validated with the measured data in Zhangye National Climate Observatory with the RMSE of 3.94mm, which indicates that the retrieval algorithm has a high precision. However, it has to be noted that the retrieval algorithm has poor R^2 when the LSE is large, which means the low precision when used in the densely vegetated zones.

6 REFERENCES

- Chen, K.S., Wu, T.-D., Tsang, L., Li, Q., Shi, J.C., and Fung, A.K., 2003, Emission of rough surfaces calculated by the integral equation method with comparison to three-dimensional moment method simulations. *Geoscience and Remote Sensing, IEEE Transactions on*, 41, 90-101.
- Jia, Y.-Y., 2007, Retrieval of land surface temperature using passive microwave remote sensing data. Doctor thesis. Institute of Geographical Sciences and Natural Resources Research, CAS, Beijing.
- Liu, Z.-L., 2013, Retrieval of land surface temperature from passive microwave remote-sensing data. Doctor thesis. Institute of Geographical Sciences and Natural Resources Research, CAS, Beijing.
- Mätzler, C., 1994, Passive microwave signatures of landscapes in winter. *Meteorology and Atmospheric Physics*, 54, 241-260.
- Norouzi, H., Temimi, M., and Khanbilvardi, R., 2010, Global microwave land surface emissivity retrieval at the AMSR-E microwave frequencies. In, *Microwave Radiometry and Remote Sensing of the Environment (MicroRad)*, 2010 11th Specialist Meeting on, pp. 90-95.
- Westwater, E.R., Snider, J.B., and Falls, M.J., 1990, Ground-based radiometric observations of atmospheric emission and attenuation at 20.6, 31.65, and 90.0 GHz: a comparison of measurements and theory. *Antennas and Propagation, IEEE Transactions on*, 38, 1569-1580.

INTA AHS and CASI hyperspectral images

Eduardo de Miguel, Elena Prado, Marcos Jiménez, Óscar Gutiérrez de la Cámara, Clara Linés and Alix Fernández-Renau

Área de Teledetección - Instituto Nacional de Técnica Aeroespacial (INTA).

Cta. de Ajalvir s/n Torrejón de Ardoz 28850, Spain

demiguel@inta.es, pradoe@inta.es, jimenezmm@inta.es, gutierrezcao@inta.es

ABSTRACT- *The INTA airborne hyperspectral system is based on the tandem use of the AHS and CASI-1500i hyperspectral sensors. This system is fully operational since 2009, having performed over 50 flight campaigns throughout Europe up to the present time. A specific processing chain is implemented within the INTA airborne data Processing and Archiving Facility. In this chain, raw data (level 0 product) are transformed to at-sensor radiance (level 1b) and geolocation information is attached (IGM and GMD files). Other processing levels, as atmospherically corrected reflectance/temperature/emissivity (L2b / L2c), can also be produced. The resulting image products are delivered to the users together with radiometric statistics, metadata and quality descriptors. In this paper, details about this processing chain are given. First, the overall processing approach is presented. Next, the specific procedures for radiometric calibration and image geolocation, which are critical for a quantitative use of the images, are discussed in detail. Then, the tools for retrieval of surface parameters are presented, including details on water vapour and aerosol optical thickness estimations for atmospheric correction. Some new features of the processing chain related to cloud and shadow masking and a tool to sample geolocated information from the original (not orthorectified) images are also presented. Finally, image metadata and quality descriptors are shown, discussing the difficulties in reporting in a simple and compact way the radiometric, spectral and spatial accuracy of the delivered products.*

1 INTRODUCTION

The INTA airborne hyperspectral system is based on the tandem use of the AHS and CASI-1500i hyperspectral sensors. This system is fully operational since 2009, having performed over 50 flight campaigns throughout Europe up to the present time.

A specific processing chain is implemented within the INTA airborne data Processing and Archiving Facility. In this chain, raw data (level 0 product) are transformed to at-sensor radiance (level 1b) and later to geolocated at-sensor radiance (level 1c). Other processing levels, as atmospherically corrected reflectance/temperature/emissivity (L2b / L2c), can also be produced. The resulting image products are delivered to the users together with radiometric statistics, metadata and quality descriptors.

Descriptions of this airborne remote sensing system have been recently published (de Miguel 2014a and 2014b). In this paper, we review its main characteristics and include some recent developments relevant for a quantitative use of the images.

Although some similar facilities exist through Europe which operate successfully complex airborne remote sensing systems, like the NERC ARSF (<http://arsf-dan.nerc.ac.uk/>), the APEX programme (<http://www.apex-esa.org/>) or the DLR OpAirs (Weide et al., 2010), the joint use of AHS and CASI makes the INTA system a unique tool for many airborne remote sensing applications.

2 THE ACQUISITION SYSTEM

2.1 The platform

The INTA platform for hyperspectral remote sensing is a C-212 aircraft, owned by INTA and operated by the Spanish Air Force. It is a high-wing twin-turboprop, modified for remote sensing surveys. Its main features are:

- Cruising speed: 140 Knots (72 ms⁻¹)
- Service ceiling: 25000 feet (7600 m)
- Maximum endurance: 6 hours
- Un-pressurized cabin, volume 22 m³
- Maximum pay-load: 2100 kg

This platform is part of EUFAR, the European Network of Aerial Facilities for Geo-Science Research (<http://www.eufar.net>).

2.2 The sensors

The CASI is a visible and near infrared (VNIR) pushbroom imager, manufactured by the Canadian company Itres (www.itres.com). It is based on a 1548 x 288 elements CCD, with a diffraction grating dispersing the output of a telescope on it. CASI has a 40° Field of View (FOV), and an instantaneous IFOV of 0.05 mrad. Spatial resolution ranges from 0.4 m to 1.5 m, depending on integration time and flight height. The maximum spectral resolution is 288 bands, corresponding to 2.4 nm inter-band distance; but spectral binning combined with the right integration

time allows for other spectral configurations, aimed to improve the signal to noise ratio.

The AHS is a linescanner, with a design similar to MODIS. It is based on a Cassegrain-type telescope, followed by a complex spectrometer based on gratings and dichroics. FOV is 90°, leading to some particular issues concerning atmospheric correction and pixel size, and IFOV is 2.5 mrad (so five times larger than in CASI). Accordingly, spatial resolution ranges from 2.5 m to 7 m. The sensor covers from VNIR to thermal infrared (TIR), including short wave infrared (SWIR, 2 to 2.5 microns) and 7 bands in the medium infrared (MIR, 3 to 5 microns). Total number of bands is 80, with medium/high spectral resolution. The telescope design enables perfect co-register between all bands.

2.3 Auxiliary elements

A number of elements are used to support the data acquired by the main sensors.

- Applanix POSAV 410 inertial navigation systems (one unit per sensor). They are used for retrieving accurate position and orientation information during image acquisition.
- Integrating spheres, used for absolute radiometric calibration, and spectral benches, including monochromators, for spectral calibration.
- Sunphotometers CIMEL 318 and Microtops II for retrieval of atmospheric parameters during flight campaigns.
- ASD FieldSpec 3 and TIR radiometer CIMEL 312 for ground radiometry, mainly used for calibration/validation activities.

3 THE PROCESSING CHAIN

3.1 Calibration and geolocation

Calibration and geolocation of each sample transforms the raw data into L1b products, which are the first step in the processing chain and its output for users who prefer to apply their own processing techniques (typically atmospheric correction).

Radiometric calibration is performed at the INTA facilities, using procedures defined by each sensor's vendor, but reviewed and adapted by INTA staff.

Spectral calibration is also performed at INTA. It is especially relevant for CASI, as its narrow bandwidth means that small shifts during system operation would represent a significant change in band position (this is not the case for the broader AHS bands). Therefore, a specific in-flight spectral shift detection has been implemented; it is based on matching the shape of the O2-a absorption feature at 762 nm to a theoretical curve. The estimated shift is computed per image column (therefore accounting for within FOV variations) and is used in a radiometric recalibration, in such a way that band positions delivered

to users remain constant, while the actual wavelength at each CCD row during the image acquisition might have been different to the nominal one.

The spectral characterization also includes the estimation of the actual FWHM. Laboratory tests give a typical value of 3.1 nm, with a small variation across the CCD; but the value in actual flight conditions might vary.

A further issue in the calibration process is spectral straylight, or out of band radiance. First, it disturbs the estimation of calibration coefficients; secondly, it is a source of noise in each pixel value. This out of band radiance might be significant when using quantitatively bands placed in absorption features. The CASI calibration process includes measuring the incoming light on a CCD column not illuminated by the optics slit, and subtracting the measured value from each pixel. However, this method does not consider the eventual variation of straylight across the CCD spatial dimension. Estimating such variation is possible using absorption features, but it is difficult because the coupled effect of straylight, small changes of actual FWHM across the CCD and the residual spectral shift after the recalibration procedure. Figure 1 illustrates this situation showing the depth of the O2-a absorption across the FOV for all pixels with a 25% reflectance in the [750,770] nm interval.

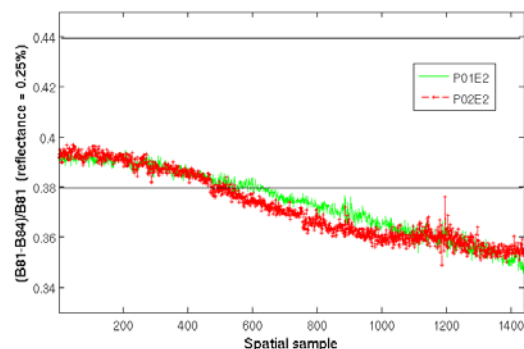


Figure 1. Relative depth of the O2-a absorption band as a function of across-track position for two CASI images acquired with spectral binning 2 (FWHM ~ 6 nm). The depth has been estimated for pixels with reflectance 25% in the [750,770] nm interval. The horizontal lines show the theoretical depth as computed with MODTRAN, considering i) the nominal band center and FWHM (depth 0.44), and ii) a shift of 0.5 nm blue-wards with FWHM 6.6 nm, which represents a worst case estimation (depth 0.38).

Geolocation of each pixel is performed from the exterior orientation information, a digital elevation model (DEM) and a detailed sensor model. For AHS the direct georeferencing code PARGE (Schläpfer, 2002) is used, while the Itres-provided *geocor* is used

in CASI. In both cases, the basic output of the process is an Input Geometry file (IGM) for each image. IGM image files denote the UTM Easting and Northing values derived by the geocoding process for each original image pixel. The IGM files have the same spatial size as the L1b imagery and contain the geolocation information for each original pixel.

3.2 Atmospheric correction and geometric resampling

Atmospheric correction is performed with ATCOR4 (Richter, 2002), where:

- water vapour is either estimated from external atmospheric data (ground measurements, MODIS...) or from CASI images using ATCOR4,
- aerosol optical thickness (or visibility) and aerosol type are estimated from external atmospheric data, like INTA CIMEL (see section 2.3), AERONET stations or others.

Resampling to a cartographic grid (usually based on UTM) is performed from the IGM described above by the use of a nearest neighbour algorithm. In the INTA PAF only a subset of spectral bands are systematically resampled, with the purpose of obtaining a kind of georectified quicklook for assessing the geolocation results and showing the result to the user. This quicklook is usually created with IDL GLT option. A specific problem here is the selection of the output pixel size during resampling, due to:

- the wide FOV in AHS, leading to large increase of GIFOV to the edges of the image,
- the selection of integration time in CASI might define an along-track pixel size which is significantly above the across-track pixel size defined by the instrument IFOV.

In such cases, resampling to a square grid must consider a compromise between redundancy (original samples that are used more than once when generating the resampled product) and data loss (raw original samples that are not mapped to the resampled product). The value used in the INTA PAF for the georeferenced quicklook is intended to optimize this compromise, and users are recommended to apply this value.

3.3 Metadata and quality descriptors

The ENVI header delivered with each product contains the basic image metadata; on the next level, quality information following the recommendations of EUFAR (Holzwarth et al., 2011) is delivered to users in a text file attached to each image product. Image statistics are also delivered per image, including parameters related to the radiometric quality, like an estimation of image noise and SNR.

A specific file is delivered with parameters reporting the geometrical features of each pixel. These

are the so-called geometric metadata (GMD), which are arranged as layers in an auxiliary file, with the same pixel-column dimensions as the radiometric data but with the following info as bands:

- View (scan) zenith angle
- View absolute azimuth
- Pixel distance (= view path length)
- Orthometric terrain height
- Actual GIFOV across-track
- Actual GIFOV along-track

These values are computed following rigorous models and using actual flight, sensor and terrain information.

Absolute radiometric, geometric and spatial accuracy of the image products is not systematically produced. These important quality parameters vary through each image and from image to image depending on many factors. For example, the CASI radiometric accuracy would depend (on top of any calibration errors) at least on the integration time selected, the spectral binning applied, time from the laboratory calibration (not in a linear way, but depending on the history of optics exposure to aerosols and humidity), CCD temperature, actual spectral shift in each pixel, detector linearity, and relative contribution of spatial and spectral straylight and of smearing effect to pixel value. As a second example, AHS TIR radiance is calibrated from two on-board black bodies (BBs), and therefore the uncertainty sources are mainly the accuracy of the BBs temperature monitoring, the actual emissivity of the BBs, which may differ from the specified value due to surface aging or contamination, the sensor head emission, which will contribute by reflection to the BBs radiance, the detector linearity and spectral straylight.

Considering, on top of this complex scenario, that there is usually no extensive and reliable reference or true value available for radiometric, geometric and spatial accuracy, the estimation of these quantities remains a challenge for AHS and CASI images.

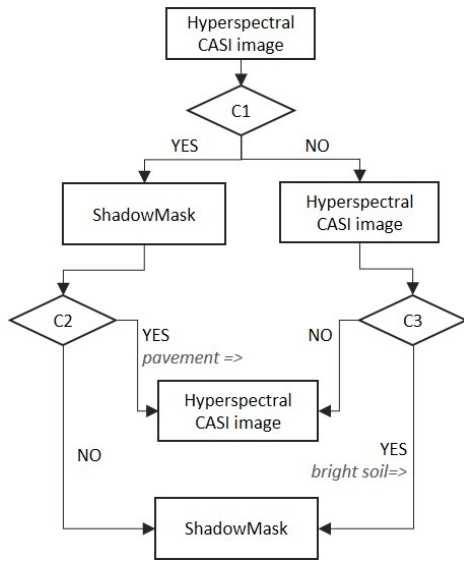
4 NEW FEATURES AND R+D ACTIVITIES

A recent addition to the processing chain is a tool to map a set of cartographic coordinates (for example from ground measurements) in the raw imagery, where row and column still corresponds to acquisition geometry. In this way, the user can skip the eventual problems linked to resampling. Working in raw geometry is also useful to avoid selecting a fixed pixel size. The tool is implemented in IDL, and is available to all users of INTA AHS / CASI images.

Cloud and shadow masks are currently not delivered systematically to users. INTA is working in implementing such masks, testing different algorithms based on the radiometric characteristics of clouds and shadows.

Although cloud detection could be performed with ATCOR4, specific algorithms tailored to AHS and CASI should improve the performance and, moreover, could be injected in the processing chain at the L1b level, where some users demand the images.

Shadow algorithms are problematic, unless a reliable digital surface model is available (which is not always the case), as the spectral signature of shaded surfaces may be quite similar to some pixels under sun light. Band ratios or absolute thresholds might be used: ratios usually show a lot of exceptions (mainly commission errors), but radiance thresholds must be computed for each image and are not free of commission errors. Empirical algorithms are being used at the INTA PAF while an automatic procedure is defined; to illustrate the problematic of accurate shadow detection, figure 2 displays the empirical algorithm used in the CASI Cazalegas 2012 campaign.



C1: $(1.005 * L_{558}) < L_{457} \ \& \ (1.005 * L_{543}) < L_{457} \ \& \ (1.4 * L_{413}) > L_{471}$ [Lx: image radiance at x (nm)]
 C2: $(1.05 * L_{687}) > L_{730} \ \& \ (L_{658} / L_{457}) > 0.8$
 C3: $(L_{558} / L_{615}) > 0.8 \ \& \ (L_{558} / L_{615}) < 1 \ \& \ (L_{457} / L_{615}) > 0.8$
 $\ \& \ (L_{413} / L_{457}) > 0.7 \ \& \ (L_{457} / L_{744}) > 0.8$

Figure 2. Empirical algorithm used for shadow detection in a CASI image acquired on October 10th, 2012 on a mixed urban-forest landscape.

5 CONCLUSIONS

The INTA hyperspectral airborne system is ready to be used by remote sensing scientists. In this system, the wide spatial and spectral coverage of AHS information is combined with the high spatial and VNIR spectral resolution of CASI, making it a unique tool for quantitative environmental research.

Although an operational processing chain is in place, specific (on request) processing algorithms can be used and improvements are always considered.

6 REFERENCES

- de Miguel, E., Fernández-Renau, A., Prado, E., Jiménez, M., Gutiérrez de la Cámara, O., Linés, C., Gómez, J.A., Martín, A.I., and Muñoz, F., 2014. A review of INTA AHS PAF. *EARSeL eProceedings*, 13(1): 20-29
- de Miguel, E., Fernández-Renau, A., Prado, E., Jiménez, M., Gutiérrez de la Cámara, O., Linés, C., Gómez, J.A., Martín, A.I., and Muñoz, F., 2014. The processing of CASI-1500i data at INTA PAF. *EARSeL eProceedings*, 13(1): 30-37
- Holzwarth, S., Bachmann, M., Freer, M., M Hofmann, 2011. Standards for airborne hyperspectral image data. In *Proceedings of the EARSeL 7th SIG-Imaging Spectroscopy workshop*.
- Richter, R. & Schläpfer, D. (2002): Geo-Atmospheric Processing of Airborne Imaging Spectrometry Data, Part 2: Atmospheric /Topographic Correction. *International Journal of Remote Sensing* 23(13), pp. 2631-2649.
- Schläpfer, D. & Richter, R. (2002): Geoatmospheric Processing of Airborne Imaging Spectrometry Data Part 1: Parametric Orthorectification. *International Journal of Remote Sensing*, 23(13), pp. 2609-2630.
- Weide, S., Bachmann, M., Gege, P., Schwarz, C., Holzwarth, S. and Müller, A. (2010) OpAiRS – Optical Airborne Remote Sensing and Calibration Facility. In: *Proceedings of Hyperspectral Workshop 2010*. ESA Communications (ESTEC, Noordwijk, The Netherlands).

Improvements on the estimation of land surface emissivity with NDVI thresholds method from MODIS data

Bo-Hui Tang^{1,3}, Zhao-Liang Li^{2,3,*}, Hua Wu¹, and Ronglin Tang¹

¹. State Key Lab of Resources and Environmental Information System, Institute of Geographic Sciences and Natural Resources Research, Chinese Academy of Sciences, Beijing, 100101, China.

². Key Laboratory of Agri-informatics, Ministry of Agriculture / Institute of Agricultural Resources and Regional Planning, Chinese Academy of Agricultural Sciences, Beijing, 100081, China.

³. ICube, UdS, CNRS, 300 Bld Sébastien Brant, CS10413, 67412 Illkirch, France.

lizhaoliang@caas.cb

ABSTRACT- This work proposed an improved NDVI thresholds method to estimate the land surface emissivities (LSEs) for bare soil and fully vegetation from MODIS data. The LSEs for MODIS channels 29 (8.4–8.7 μm), 31 (10.78–11.28 μm) and 32 (11.77–12.27 μm) are expressed respectively as functions of the atmospherically corrected reflectances of MODIS visible and near-infrared channels 1 to 7 with wavelength ranging from 0.4 μm to 2.2 μm for bare soil. To keep the angular information, the LSEs for vegetation are explicitly expressed in function of the NDVI. To validate the proposed method, the MODIS LST product MOD11_L2 with LSE derived using the classification-based method is used to compare with the resultant LSE. The results show that the statistics standard deviation of LSEs estimated with the improved method is significantly larger than that of the LSEs derived with the classification-based method for the same region for different land covers, which indicates that the proposed method is more feasible to depict the LSE variation of different land covers.

1 INTRODUCTION

Land Surface Emissivity (LSE), as a measure of the inherent efficiency of the surface in converting heat energy into radiant energy above the surface, is one of the key input parameters for the studies of surface energy budgets, climatic, hydrological, ecological, and biogeochemical models (Sobrino et al., 2001, 2005).

The estimation of land surface emissivity (LSE) has been ongoing for several decades and many methods up to now have been developed (Becker and Li, 1990; Li and Becker, 1993; Valor and Caselles, 1996; Wan and Li, 1997; Snyder et al., 1998; Sobrino and Raissouni, 2000; Li et al., 2000). Li et al. (2013) reviewed comprehensively the current different methods. Among them the Normalized Difference Vegetation Index (NDVI) thresholds method is an operative simplified method, which is based on a theoretical approach introducing surface effective parameters that model a given surface, considering it as constituted by a mixture of bare soil and vegetation. Note that the Thermal InfraRed (TIR) channel LSEs are usually derived as functions of the reflectance of red channel for bare soil and are often assigned as constants for fully vegetation (Sobrino and Raissouni, 2000; Sobrino et al., 2001, 2002).

However, it is well known that the LSE depends on the composition, roughness and moisture content of the surface and on the observation conditions (i.e., wavelength, pixel resolution and observation angle). It

is very difficult to accurately estimate the LSE with only one visible channel and may cause some significant errors for the types of soil when the relationship between the spectral emissivity and the reflectance of red channel is not good. In addition, it may introduce large errors for the estimation of Land Surface Temperature (LST) with fixed spectral emissivities for vegetation when the viewing zenith angle is larger than 50°.

The present work in this paper aims to propose an improved NDVI thresholds method to estimate the LSEs for bare soil and fully vegetation from the Moderate Resolution Imaging Spectroradiometer (MODIS) data. Section 2 describes the improvements of the NDVI thresholds method associated with the LSE retrieval from MODIS satellite data of channels 29, 31 and 32. The results and analysis are explained in section 3. Section 4 gives a preliminary validation of the present method. The conclusions are drawn in section 5.

2 IMPROVED NDVI THRESHOLD METHOD

On the basis of the theoretical model of deriving effective LSE for a row-distributed rough system (Valor and Caselles, 1996), Sobrino and Raissouni (2000) proposed a simple and operational NDVI-based threshold method to estimate the LSE from space data. This method assumes that: 1) the surface is only composed of soil and vegetation; 2) the emissivity of

the bare soil can be linearly represented by the surface reflectivity in the red channel; and 3) the LSE changes linearly with respect to the fraction of vegetation in a pixel. Therefore, the LSE of TIR channel i can be estimated using three linear functions corresponding to conditions in which a pixel is composed of full vegetation, of full soil, or of mixed soil/vegetation content, namely

$$\varepsilon_i = \begin{cases} a_i + b_i \rho_{red} & NDVI < NDVI_s \\ \varepsilon_{vi} P_v + \varepsilon_{si} (1 - P_v) + d\varepsilon_i & NDVI_s < NDVI < NDVI_v \\ \varepsilon_{vi} + d\varepsilon_i & NDVI > NDVI_v \end{cases} \quad (1)$$

where a_i and b_i are the channel-dependent regression coefficients, ρ_{red} is the reflectivity of the red channel and $NDVI_s$ is the NDVI corresponding to the bare soil. ε_{vi} and ε_{si} are the vegetation and soil emissivities in channel i , respectively.

It should be pointed out that the estimation of LSE in equation (1) for bare soil is only as a linear function of the reflectivity in the red channel, and is assigned as a constant for fully vegetation. However, for many bare soil types it is difficult to develop a good linear relationship between the spectral LSE and the reflectivity in red channel. In addition, a fixed spectral emissivity for full vegetation may cause some significant errors for the estimation of land surface temperature when the viewing zenith angle is larger than 50° . Consequently, we propose an improved NDVI threshold method to determine the LSE according to the characteristics of the soil present in one pixel, considering the magnitude of NDVI value for the pixel.

2.1 Determination of LSE for bare soil ($NDVI < 0.2$)

Values of NDVI lower than 0.2 are considered as bare soil. In this case, the typical soil spectra from the Johns Hopkins University (JHU) (<http://speclib.jpl.nasa.gov/>) spectral database are used to simulate the MODIS 1-7 visible/near-infrared channels reflectances and three thermal infrared emissivities (29, 31 and 32 channels), combining with the spectral response functions of those channels. Those soil types that do not comply with the majority of soil types are excluded in this investigation. Three statistical relationships have been obtained by correlating the emissivities 29, 31 and 32 respectively to the channel reflectances of the seven visible and near-infrared channels. The multiple linear regression relationships can be written as

$$\varepsilon_{si} = a_{i0} + \sum_{j=1}^7 a_{ij} \rho_j \quad (i = 29, 31, 32) \quad (2)$$

where ε_{si} represents the emissivity of bare soil, a_{i0} and a_{ij} are the regression coefficients, and ρ_j are the reflectances of MODIS visible/near-infrared channels.

2.2 Determination of LSE for dense vegetation ($NDVI > 0.5$)

For NDVI values larger than 0.5, the pixels are considered as fully vegetated ($P_v = 1$). The typical vegetation spectra provided by JHU are used to simulate the MODIS 1-2 channels reflectances and thermal infrared channel emissivities of 29, 31 and 32. Three statistical relationships are obtained by correlating the channel emissivities 29, 31 and 32 respectively to the NDVI, written by

$$\varepsilon_{vi} = b_{0i} + b_{1i} NDVI \quad (i = 29, 31, 32) \quad (3)$$

where ε_{vi} represents the emissivity of full vegetation, b_{0i} and b_{1i} are the regression coefficients.

2.3 Determination of LSE for soil/vegetation mixed area ($0.2 \leq NDVI \leq 0.5$)

When the NDVI value is between 0.2 and 0.5, the pixel is considered as being a mixture of bare soil and vegetation. In this case, the emissivity is calculated according to the mixed proportion of the bare soil and vegetation (Sobrino et al., 2001).

$$\varepsilon_i = \varepsilon_{vi} P_v + \varepsilon_{si} (1 - P_v) + C_i \quad (i = 29, 31, 32) \quad (4)$$

in which P_v is the vegetation proportion obtained by

$$P_v = \left[\frac{NDVI - NDVI_{min}}{NDVI_{max} - NDVI_{min}} \right]^2 \quad (5)$$

where $NDVI_{min} = 0.2$ and $NDVI_{max} = 0.5$. The term C in equation (4) includes the effect of the geometrical distribution of the natural surfaces and also the internal reflections (cavity effect) (i.e., for homogeneous and flat surfaces $C = 0$). A good approximation for this term can be given by

$$C_i = (1 - \varepsilon_{si})(1 - P_v) F \varepsilon_{vi} \quad (6)$$

where F is a shape factor whose value is ranged from 0 to 1. Since it cannot to evaluate this value from remotely sensed data, a mean value of 0.55 is usually used for different geometrical distributions. Figure 1 gives the flowchart of estimating LSEs for MODIS level-1B satellite data.

3 RESULTS AND DISCUSSION

To evaluate the present improved NDVI-based threshold method, Figure 2 shows the comparisons between the estimated LSEs and the actual ones obtained from ASTER spectral database for different bare soils for MODIS channels 29, 31 and 32, respectively. One can see that the fitting results are good with RMSE less than 0.01 for channels 31 and 32, and that of 0.02 for channel 29.

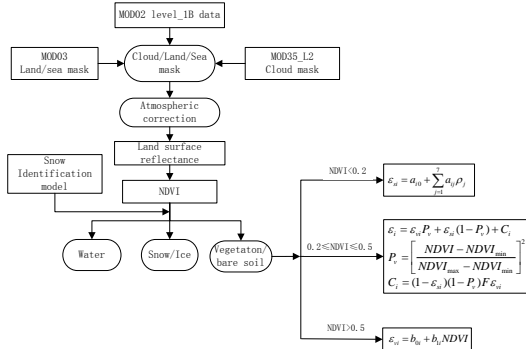


Figure1. Flowchart for estimating LSEs with improved NDVI thresholds method from MODIS data.

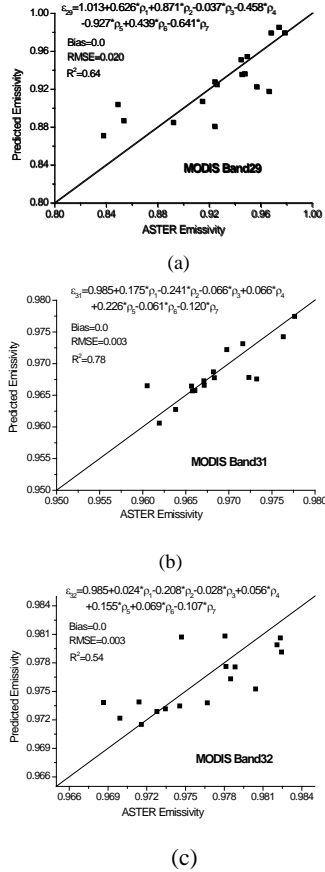


Figure 2. Comparisons between the estimated LSEs and the actual ones obtained from ASTER database for different bare soils ((a) for MODIS band 29; (b) for MODIS band 31; and (c) for MODIS band 32).

In addition, figure 3 gives the comparisons between the estimated LSEs and the actual ones from ASTER database for different vegetation for MODIS channels 29, 31 and 32, respectively. The fitting

results are well agreement with all of the RMSEs less than 0.01 for three channels.

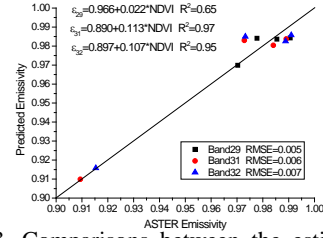


Figure 3. Comparisons between the estimated LSEs and the actual ones obtained from ASTER database for different vegetation for MODIS channels 29, 31, and 32, respectively.

4 PRELIMINARY VALIDATIONS

To validate the present method, the MODIS emissivity product MOD11_L2, derived with classification-based method, is used to validate the improved NDVI thresholds method. Figure 4 shows, as an example, the LSE map estimated with the proposed NDVI method and the classification-based method for MODIS channel 31 on December 1, 2010, respectively. The difference map between the two LSEs is also showed in this figure.

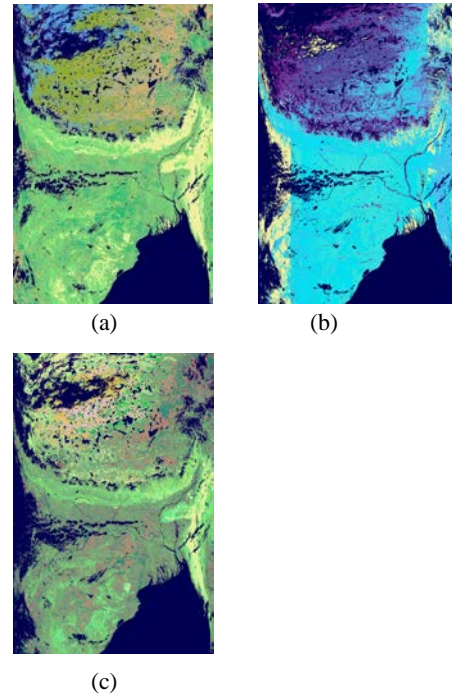


Figure 4. Mapping of LSEs obtained with different methods ((a) with NDVI method; (b) with classification-based method; and (c) the difference LSEs between (a) and (b)).

Table 1 also describes the statistics of the maximum, minimum, mean and standard deviation for the different LSE maps. One can see that the minimum, maximum, and the standard deviation of the LSEs estimated by the improved NDVI method are 0.826, 0.990 and 0.110, respectively, and those of the LSEs obtained from the classification-based method are 0.964, 0.992 and 0.006, respectively. These results indicate that the present improved NDVI threshold method can better depict the spectral variation for different land covers with standard deviation significantly larger than that of classification-based method.

Table 1. Statistics of the maximum, minimum, mean and standard deviation for the LSEs maps in figure 4.

	Minimum	Maximum	Mean	Standard deviation
Improved NDVI method (a)	0.826	0.990	0.976	0.110
Classification-based method(b)	0.964	0.992	0.979	0.006
Difference of two LSE maps	-0.163	0.018	-0.002	0.011

5 CONCLUSIONS

In this paper, an improved NDVI-based thresholds method was proposed to estimate the LSEs for MODIS channels 29, 31 and 32. To accurately depict the variation of the spectral emissivity for bare soil, the LSEs for MODIS channels 29 (8.4–8.7 μm), 31 (10.78–11.28 μm) and 32 (11.77–12.27 μm) are expressed respectively as functions of the atmospherically corrected reflectances of MODIS visible and near-infrared channels 1 to 7 with wavelength ranging from 0.4 μm to 2.2 μm . To keep the angular information, the LSEs for vegetation are explicitly expressed in function of the NDVI.

The results showed that the proposed improved NDVI-based threshold method can predict accurately the LSEs for bare soils with RMSE less than 0.01 for channels 31 and 32, and that of 0.02 for channel 29, and all of the RMSEs of the three channels are less than 0.01 for vegetation.

In addition, a preliminary validation has been done with one LSEs map, obtained from the MODIS emissivity product MOD11_L2 and derived with classification-based method. The results showed that the minimum, maximum, and the standard deviation of the LSEs estimated by the improved NDVI method are 0.826, 0.990 and 0.110, and those of the LSEs obtained from the classification-based method are 0.964, 0.992 and 0.006, respectively. It indicated that

the proposed method is more feasible than the classification-based method to depict the LSE variation of different land covers.

ACKNOWLEDGMENT

This work was jointly supported by the Excellent Young Talent Funds for Kezhen Distinguished Young Scholar in the Institute of Geographic Sciences and Natural Resources Research (IGSNRR), Chinese Academy of Sciences (CAS) under grant 2012RC101, the National Natural Science Foundation of China under grant 41171287, and the Hi-Tech Research and Development Program of China (863 Plan Program) under grant 2012AA12A302.

REFERENCES

- Becker, F., & Li, Z.-L., 1990, Temperature-independent spectral Indices in thermal Infrared bands. *Remote Sensing of Environment*, 32, 17-33.
- Li, Z.-L., & Becker, F., 1993, Feasibility of land surface-temperature and emissivity determination from AVHRR data. *Remote Sensing of Environment*, 43, 67-85.
- Li, Z.-L., Petitcolin, F., & Zhang, R. H., 2000, A physically based algorithm for land surface emissivity retrieval from combined mid-infrared and thermal infrared data. *Science in China Series E: Technological Sciences*, 43, 23-33.
- Li, Z.-L., Wu, H., Wang, N., Qiu, S., Sobrino, J. A., Wan, Z., Tang, B.-H., & Yan, G. (2013). Land surface emissivity retrieval from satellite data. *International Journal of Remote Sensing*, 34(9-10), 3084-3127.
- Snyder, W. C., Wan, Z., Zhang, Y., & Feng, Y. Z., 1998, Classification-based emissivity for land surface temperature measurement from space. *International Journal of Remote Sensing*, 19, 2753-2774.
- Sobrino, J. A., & Raissouni, N., 2000, Toward remote sensing methods for land cover dynamic monitoring: application to Morocco. *International Journal of Remote Sensing*, 21, 353-366.
- Sobrino, J. A., Raissouni, N., & Li, Z. -L., 2001, A comparative study of land surface emissivity retrieval from NOAA data. *Remote Sensing of Environment*, 75, 256-266.
- Sobrino, J. A., Jimenez-Munoz, J. C., Labed-Nachbrand, J., & Nerry, F., 2002, Surface emissivity retrieval from Digital Airborne Imaging Spectrometer data. *Journal of Geophysical Research-Atmospheres*, 107, 4729.
- Sobrino, J. A., Jimenez-Munoz, J. C., & Verhoef, W., 2005, Canopy directional emissivity: comparison between models. *Remote Sensing of Environment*, 99, 304-314.
- Valor, E., & Caselles, V., 1996, Mapping land surface emissivity from NDVI: application to European, African, and South American areas. *Remote Sensing of Environment*, 57, 167-184.
- Wan, Z., & Li, Z.-L., 1997, A physics-based algorithm for retrieving land-surface emissivity and temperature from EOS/MODIS data. *IEEE Transactions on Geoscience and Remote Sensing*, 35, 980-996.

Impact of the frequency of conducting a white reference calibration on the accuracy of acquiring spectral reflectance coefficients using a spectroradiometer in laboratory conditions

Paweł Kamiński, Agata Orych, Agnieszka Jenerowicz

Military University of Technology Department of Remote Sensing and Photogrammetry,
Institute of Geodesy, Faculty of Civil Engineering and Geodesy, 2 Kaliskiego st., Warsaw
00-908, Poland; tel. + 48 22 683 90 21

pkaminski@wat.edu.pl, aorych@wat.edu.pl, ajenerowicz@wat.edu.pl

ABSTRACT Determining spectral reflectance coefficients consists of measuring the intensity of the reflected electromagnetic radiation in specific wavelengths. These measurements are always calibrated using a white reference standard. Measurements of the reference standard should be carried out each time any geometrical parameters or lighting conditions change. Within the “IRAMSWater - Innovative remote sensing system for the monitoring of pollutants in rivers, offshore waters and flooded areas” (PBS1/B9/8/2012) research project financed by the Polish National Centre for Research and Development, the authors have built a laboratory measuring station, which will be used to acquire spectral reflectance coefficients. It consists of a spectroradiometer and a lighting system mounted on a specially constructed platform, which allows the user to conduct research using different geometrical parameters. This measuring station was used to conduct a cycle of measurements of the spectral reference standard. During these tests, the impact of the length of time allocated to warm up the measuring station on the accuracy and precision of the acquired data was researched. The next aspect, was testing the stability of the measurements on a fully warmed up (to an optimal temperature) measuring station. By conducting very long series of measurements, the authors had concluded how the accuracy of the determined spectral reflectance coefficients changes with time. This research was conducted in the 350-2500nm range. Based on these measurements and their analyses it was possible to determine the optimal frequency for calibrating the sensor using the white reference standard. This research was crucial in order to be able to determine the accuracy of the entire measuring station. They are the basis for correctly planning and conducting long measurement series of chosen water pollutants. These results will be the basis for developing a methodology for detecting these pollutants from multi- and hyperspectral imagery.

1 INTRODUCTION

A special measuring station located in the Department of Remote Sensing and Geodesy at the Military University of Technology consists of a spectroradiometer, a computer on which data is registered and a lighting system. Thanks to this measuring station we can conduct laboratory research in acquiring spectral reflectance coefficients of a variety of both liquid and solid state materials in the 350-2500nm range. There were conducted many accuracy assessments of different spectrometers (e.g. Chrien, et al., 1990; Green, et al., 1998), however they not included the influence of time on spectral measurements. In order to correctly perform measurements and later extract appropriate conclusions, it is essential to have thorough knowledge about the accuracy and precision which we can obtain from this measuring station in relation to the used white reference standard. Time regimes are also a very important aspect. These regimes concern both the amount of time needed for the instruments to warm-up and also concern the frequency with which it is necessary to calibrate (re-scale) the instrument using

a white reference panel (WR). This knowledge is essential for determining an optimal methodology for conducting measurements on this specific measuring station.

2 EXPERIMENTS

The authors' main task was to determine the precision and temporal stability of measurements of a white reference standard (Walczykowski, et al., 2013). This task was divided into two stages. The first stage consisted of measurements taken using a “cold set-up”. In practice this meant conducting experiments directly after switching on the instrument and lighting system. White reference calibration (WR) was performed directly after switching on the instrument and followed immediately with a series of measurements. An average value of the reflection coefficient was calculated from 25 subsequent measurements taken every 30seconds for each wavelength between 350-2500nm with 1nm increments.

The obtained results were all compared to the very first measurement. This was it was possible to observe how the spectral reflectance coefficients of the white

reference panel changes at different wavelengths with progression of time. That is to say, how the time that the instrument has to warm up affects the measurements.

After having conducted an over 2 hour measuring session with measurements recorded every 30seconds, the instrument was once again calibrated using the white reference panel (WR). After this a second measuring session was conducted on a “warmed-up set-up” which lasted 1,5 hours. These results were compared to the results obtained during the first measurement taken after the second calibration (WR). The purpose of this stage of the experiment was to examine the repeatability (precision) of results of the warmed-up instrument and to possibility determine the required frequency with which subsequent WR calibrations should be conducted. Calibrating may prove essential if the measuring station, whose measurement precision changes in time, exceeds certain criteria set by the intended end product of these measurements.

2.1 Cold instrument

The manufacturer of the spectroradiometer recommends warming-up the instrument before conducting measurements. According to the Analytical Spectral Devices, Inc. (ASD) Technical Guide this time should be at least 15 minutes (Hatchell , 1999; Mac Arthur, 2007).

The authors were expecting considerable fluctuations in the results as time progressed.

The authors have decided to investigate how the instruments parameters change as a function of time from the moment the instrument is switched on until it is fully warmed-up. Figure 1 shows the spectral reflectance coefficient in the studied spectral range taken directly after switching on the instrument compared to one measured after 2 hours from switching on the instrument, without recalibration. It is very visible, that there are differences between these two graphs (Figure 1).

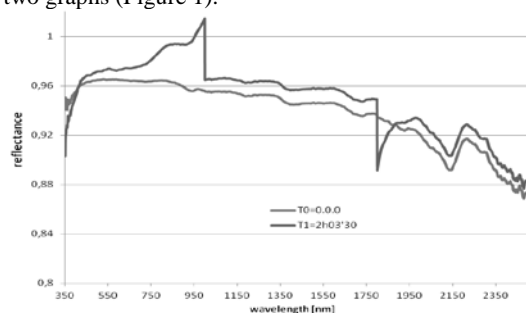


Figure 1 Spectral reflectance coefficient at different wavelengths (cold instrument)

In order to more fully show the scale of fluctuations introduced by the time the instrument needs to warm-up, the results have been presented as a proportion of the change with regards to the first measurement.

$$dp = \frac{D_1 - D_n}{D_1} \cdot 100\% \quad (1)$$

where:

dp - relative change with regards to the first measurement

D_1 – first measurement

D_n – subsequent measurements

Even though these fluctuations are both positive and negative in their sign, as can be seen in Figure 1, in the following graphs depicting the proportional changes, the authors have shown the absolute values (Figure 2).

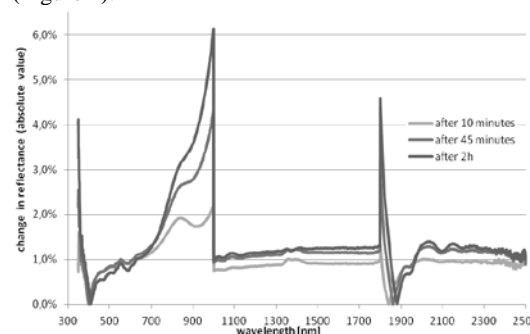


Figure 2 Relative change with regards to the first measurement (cold instrument)

On this graph it is visible that the relative change in increases with time. The greatest change, obtained after 2 hours from switching on the instrument, was over 6% compared to the first reading. However in most spectral ranges this change is no more than 1,5%. Figures 3 and 4 show in more detail these changes in the 400-700nm and 1100-1750nm ranges.

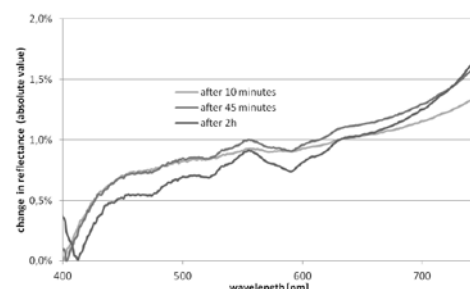


Figure 3 Relative change with regards to the first measurement in the 400-700nm range (cold instrument)

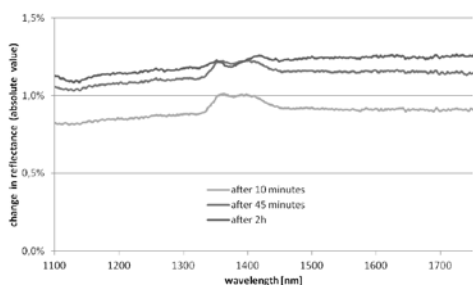


Figure 4 Relative change with regards to the first measurement in the 1100-1750nm range (cold instrument)

The existence of these changes proves that the measuring station's parameters change with time. The dynamics of these changes can be observed on specific examples of single wavelengths. Figure 5 shows the change dynamics of chosen vital measurement points – those wavelengths, at which the observed changes were greatest. Figure 6 shows the change dynamics of the spectral reflectance coefficient in the visible range – at 450nm and 600nm wavelengths.

Both of these plots show, that the greatest fluctuations occur in the first 20min from switching on the instrument. The change dynamics shown on Figure 5 visibly lessen at one point – the plot becomes saturated.

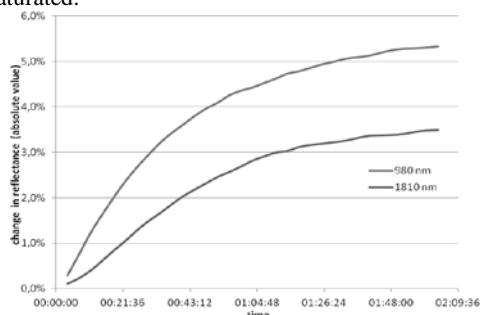


Figure 5 Change dynamics as a Function of time for 980nm and 1810 nm wavelengths.

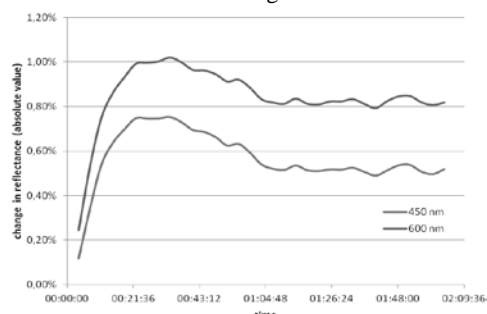


Figure 6 Change dynamics as a function of time for 450nm and 600nm wavelengths.

On figure 6, after an initial rapid increase in the relative change, it stabilizes after about 20minutes. After 35minutes these fluctuations start to lessen and then the value of relative change stabilizes at a specific level. Based on these results, it is most probably that 35 minutes will be the required time necessary for the instrument to warm up.

2.2 Warmed- up instrument

After 2 hours of operation, so after all elements of the measuring station has assumingly properly warmed-up, the instrument was recalibrated (WR).

The following figures show the results of measurements of reflection coefficients of the white reference panel obtained with a warmed-up instrument. The results – similarly to those obtained with a cold instrument, were taken every 30 seconds and are an average from 25 subsequent measurements.

Additionally measurements were averaged from 7 subsequent measuring time series. We therefore obtained average time series for each wavelength (every 1nm) from 350-2500nm with a 3,5minute time interval. This experiment lasted 1,5 hours from the moment the warmed-up instrument was recalibrated.

These results indicate, that despite the instrument being warm, its parameters still change in time. The relative change between the measurements taken directly after calibration and subsequent measurements is however much lower and oscillates around 0,1-0,15%, with a maximum observed value of 0,45% at the crucial wavelength 1000nm (wavelength at which there is a change between detectors within the instrument).

As shown in Figure 10, the changes in the registered reflectance coefficients are much smaller. For most wavelengths it does not exceed 0,15% in relation to the first measurement. Time does not have as big an impact on the results as it did in the case of using a cold instrument. The measuring station has a very high precision.

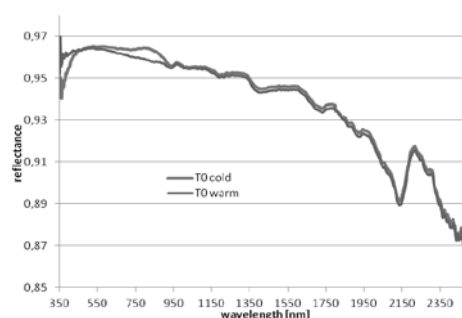


Figure 7 A comparison of spectral reflectance coefficients of the white reference panel obtained using a cold and warmed-up measuring station. Both measurements taken directly after WR calibration.

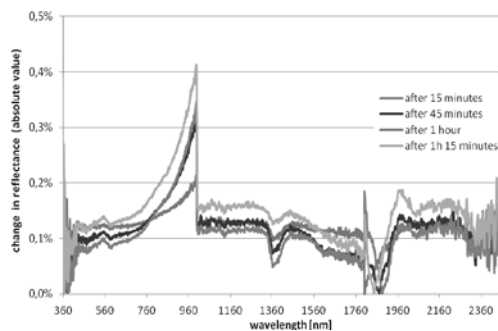


Figure 8 Relative change with regards to the first measurement (warmed-up instrument)

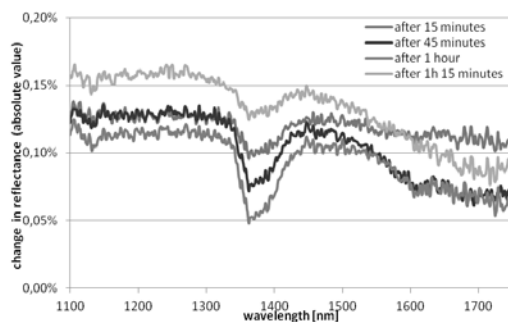


Figure 9 Relative change with regards to the first measurement in the 1100-1750nm range (warm instrument)

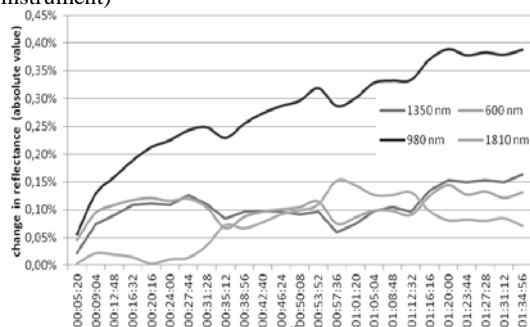


Figure 10 Change dynamics as a function of time for 600 nm, 980 nm, 1350 nm and 1810 nm wavelengths.

3 CONCLUSION

If the precision criteria set by the intended end product of these measurements is around 0,15%, then one can risk the assumption, that when working on a warm instrument set-up with unchanging lighting conditions, it is necessary to recalibrate the instrument every 1,5 hours.

Analyzing all of the experiments it is possible to conclude that before commencing laboratory measurements, the instrument must warm-up for at least 35 minutes. The instrument used in this study has two crucial wavelengths – 1000 and 1800 nm. At these two wavelengths we had observed the greatest fluctuations (lowest measurement precision) both in the cold and warm set-ups. Once the instrument is warmed-up sufficiently we had noticed a tenfold increase in the accuracy of measurements in the entire studies spectral range.

4 ACKNOWLEDGEMENTS

The presented article is part of research work carried out in the “Innovative remote sensing system for the monitoring of pollutants in rivers, offshore waters and flooded areas” project- PBS1/B9/8/2012 financed by the polish National Centre for Research and Development NCBiR.

5 REFERENCES

- Chrien, T. G., Green, R. O., Eastwood, M. L., 1990, Accuracy of the spatial and Radiometric Laboratory Calibration of the Airborne Visible/Infrared, Imaging spectroscopy of the terrestrial environment; Proceedings of the Meeting, Orlando, FL, Apr. 16, 17, 1990 (A91-36626 15-35). Bellingham, WA, Society of Photo-Optical Instrumentation Engineers, 1990, p. 37-49.
- Green, R. O., M. L. Eastwood, C. M. Sarture, T. G. Chrien, M. Aronsson, B. J. Chippendale, J. A. Faust, B. E. Pavri, C. J. Chovit, M. Solis, M. R., Olah, and O. Williams, 1998. Imaging spectroscopy and the Visible/Infrared Imaging Spectrometer (AVIRIS), Rem. Sens. Environ. 65, 227-248.
- Hatchell, D.C. (Managing Editor), 1999, Analytical Spectral Devices, Inc. (ASD) Technical Guide 4th Ed.
- Mac Arthur, A., 2007, Field Guide for ASD FieldSpec Pro- White Reference Mode Version 2, Field Spectroscopy Facility, Natural Environment Research Council, available at: http://fsf.nerc.ac.uk/resources/guides/pdf_guides/asd_guide_v2_wr.pdf
- Walczykowski, P., Orych, A., Dabrowski, R., Designing a modern Measuring Station for obtaining spectral response characteristics in laboratory conditions, in Proceedings in Research Conference In Technical Disciplines- RCITD 2013, 124-121.

Remote sensing monitoring of grassland vegetation growth in China in 2012

H.L. Ma^a, B. Xu^{a*}, X.C. Yang^a, Y.X. Jin^a, Z. Yang^b, S. Liu^b, J.Y. Li^a, T. Gao^a, H.D. Yu^a

^a Key Laboratory of Agri-informatics, Ministry of Agriculture / Institute of Agricultural Resources and Regional Planning, Chinese Academy of Agricultural Sciences, Beijing 100081, China;

^b Grassland Monitoring and Supervision Centre, Ministry of Agriculture, Beijing 100026, China;

mahailong@caas.cn, xubin@caas.cn

ABSTRACT- Grassland Vegetation Growth (GVG) refers to the overall growth status and trend of the grassland vegetation. The comparison between GVG at present and past is often used to illustrate the current growth status of GVG. The remote sensing monitoring of GVG is an approach to indirectly reflect GVG through processing of remote sensing data over different periods according to the characteristics of close correlation between ground remote sensing data and grassland vegetation status. This paper monitored and analyzed the GVG of China in 2012 using 3S technology and EOS/MODIS satellite remote sensing data. The result shows: (1) the GVG of China in 2012 is obviously better than the previous year., and the grassland area with better growth, poor growth and average growth accounts for 27.95%, 20.45% and 51.6% of China's total grassland respectively; (2) Compared with the same period in 2011, the areas with good GVG were mainly located in central and eastern and south-western Inner Mongolia, south-western Heilongjiang, western Jilin, southern Qinghai, eastern Gansu, most parts of Ningxia and eastern Xinjiang etc.; the areas with poor GVG were located in north-western Inner Mongolia, some parts of northern Xinjiang, western Tibet, southern Sichuan, and some parts of northern Yunnan etc.. The GVG in most provinces in South China was essentially flat with the previous year.

1 INTRODUCTION

Grassland Vegetation Growth (GVG) refers to the overall growth status and trend of the grassland vegetation. The comparison between GVG at present and past is often used to illustrate the current growth status of GVG. The remote sensing monitoring of GVG is an approach to indirectly reflect GVG through processing of remote sensing data over different periods according to the characteristics of close correlation between ground remote sensing data and grassland vegetation growth status (Xu et al. 2006, 2007, 2013). Normalized Difference Vegetation Index (NDVI) is one of the most relevant vegetation indices associated with herbaceous vegetation greenness values, which can better reflect the grassland vegetation coverage and yield information and has a significant correlation with grassland vegetation growth. Hence, it is currently widely used in grassland monitoring (Yu et al, 2012; Xing et al, 2005; Si et al, 2008). Natural grassland area accounts for about 41 percent of total land area in China. Conducting annual monitoring of grassland vegetation growth during the growing season from the beginning of turning green in May to the dry yellow period (Gao et al, 2006) in September has a very important role in understanding grassland vegetation growth conditions, providing valuable information for the protection and management of grassland ecosystems as well as

providing decision-making basis for grassland authorities and guidance for agricultural production and prevention of natural disasters.

2 MATERIALS AND METHODS

2.1 Study area

The remote sensing monitoring area includes all natural grasslands in China with an area of about 4×10⁸ hm². Grasslands in northern China are mainly concentrated contiguous natural grassland while grasslands in Southern China are more fragmented, mainly grassy hills and slopes. China is rich in grassland resources, with complex and diverse varieties, which mainly include 18 major categories such as alpine meadows, alpine steppes, temperate steppes, temperate deserts, lowland meadows, tropical shrub etc. The zonal distribution of grasslands in China is significant which is classified into three major regions by differences in heat and moisture, namely, Qinghai-Tibet Plateau alpine region, temperate grasslands and desert regions and Southern China and mountains in North China and coastal beach areas (Gao et al, 2012). Chinese grasslands have huge development potential with high utilization. However, due to serious overgrazing, grasslands are in varying degrees of degradation and desertification. As provinces with large area of grasslands, livestock accounts for a higher share of the local economy in

Inner Mongolia, Xinjiang, Tibet, Qinghai, Gansu and Sichuan (Ministry of Agriculture of the People's Republic of China, 2013; Gao et al, 2009).

2.2 Data and methods

The remote sensing data used in this study are derived from MODIS data of U.S EOS satellite. The data have a higher spatial resolution and good temporal resolution that can better reflect growth and spatial differences of various types of grassland over growing season and meet the requirements of remote sensing monitoring of grassland vegetation growth in the country (Yang et al, 2012; Xu et al, 2007, 2009, 2012; Jin et al, 2011, Wulantuya et al, 2009; Wang et al, 2009; Liu et al, 2007). The remote sensing data come from EOS-MODO2QKM 250M data on NASA LADSWEB website, downloaded daily data covering the whole territory of China over every May to September from 2011 till 2012. After the imageries are preprocessed, daily NDVI values are calculated. Then every ten-day period maximums are synthesized to get the maximum NDVI of every ten-day period over growing season during the two years. Then NDVI values of every ten-day period in 2012 and NDVI values of the same period in 2011 are used for computing by the established vegetation growth index formula and they are classified which are usually divided into five categories: better, good, balanced, poor and poorer to reflect the current status of GVG.

2.2.1 Vegetation Index NDVI calculation

Vegetation index refers to some values obtained through computation using near-infrared and red bands dominated multiple bands remote sensing data based on the spectral reflectance characteristics of green plants. These values reflect the status of plant growth and are a group of the most commonly used spectral variables. The normalized difference vegetation index (NDVI) is one of the indices that generally reflect the status of grassland vegetation growth with its range of values between -1 and 1. The range of green vegetation NDVI values is generally between 0.2 and 0.8. Generally, the higher are the NDVI values of the grassland, the higher is the grassland vegetation coverage and more exuberant of vegetation growth; conversely, the lower are the NDVI values, the lower is the vegetation coverage, namely, poor vegetation growth(Xing et al, 2005; Si et al 2008; liang, 2009; Pei, 2000). NDVI is expressed as:

$$NDVI = (NIR - RNIR) / (NIR + RNIR) \quad (1)$$

Where: RNIR is the reflectance of the red band of visible light; NIR is near-infrared reflectance.

Single-day NDVI values are seriously affected by sunshine. Synthesis of ten days NDVI maximum values can effectively eliminate the impact of the

cloud on the image, accurately reflecting large area of vegetation growth status. The formula is:

$$V(i) = \text{Max}[NDVI(d)] \quad (2)$$

Where, i represents ten-day data of different years; d=1, 2, 3...10, represents MODIS-NDVI daily data of every ten days.

Grassland vegetation growth is a relative concept, which through comparison between NDVI values of GVG of the year and NDVI values of the same period of the comparison year, indirectly reflects grassland vegetation growth status. The specific algorithm is as follows:

$$GI = [NDVI(m) - NDVI(n)] / [NDVI(m) + NDVI(n)] \quad (3)$$

Where, GI (Growth Index) is grassland vegetation growth index, NDVI(m) and NDVI(n) represent the NDVI values over the same period of different years, which in this article refer to the ten-day NDVI values of the same period in 2012 and 2011 (Xu et al, 2006, 2013).

2.2.2 Grassland vegetation growth classification

In order to make scientific evaluation of vegetation growth and objectively reflect the status of the grassland vegetation growth of the year, grassland vegetation growth classification is needed. Through extensive field surveys and experiments, the grassland growth index GI is identified. Based on grassland vegetation growth index difference value range, they are divided into five grades: good, relatively good, fair, relatively poor and poor. For some image elements which cannot be effectively monitored due to cloud cover and non-grassland type image elements, they are defined as non-monitoring area. By combining the NDVI vegetation growth chart, grassland distribution map and administrative map and classified computing, the spatial distribution of grassland vegetation growth is developed. Then ten-day period data statistics by provincial administrative unit is made for analysis of changes in grassland vegetation growth.

3 RESULTS AND ANALYSIS

3.1 The average condition of overall grassland vegetation growth over May-September 2012

The areas of grassland vegetation growth with good, relatively good, fair, relatively poor and poor over May-September 2012 accounted for 11.55%, 16.40%, 51.60%, 12.09% and 8.36% of the total monitoring area compared with the same period of 2011 respectively (Figure 1), of which the area with good and better growth accounted for 27.95%; the area with poor and poorer growth accounts for 20.45%. Overall, the national grassland vegetation growth in 2012 was slightly better than the previous year.

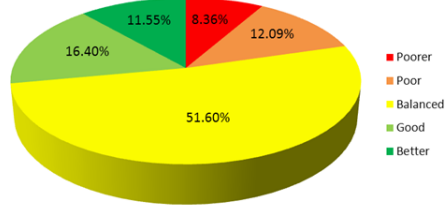


Figure 1. The production for Grassland vegetation growth of China in 2012

3.2 Sequential variation of grassland vegetation growth over May-September

The areas with good and better grassland vegetation growth over May-September 2012 were 25.45%, 31.40%, 30.37%, 25.56% and 26.51% , respectively, compared with the same period of the previous year; the areas with flat growth of grassland vegetation accounted for 57.78%, 49.10%, 46.92%, 51.91% and 52.63% respectively; and the areas with poor and poorer grassland vegetation growth accounted for 16.77%, 19.50%, 22.71%, 22.52% and 20.87% , respectively (Table 1, Table 2).

Table 1. Month dynamic change of grassland vegetation growth in China over May-September 2012 compared with the same period of 2011

Time period	Percentage of total grassland area (%)				
	Poorer	Poor	Balanced	Good	Better
May	6.83	9.94	57.78	16.64	6.83
June	8.30	11.20	49.10	17.46	8.30
July	9.95	12.76	46.92	17.35	9.95
August	8.98	13.54	51.91	13.36	8.98
September	7.40	13.47	52.63	17.60	7.40
Average	8.36	12.09	51.60	16.40	11.55

Table 2. Ten-day dynamic change of grassland vegetation growth in China over May-September 2012 compared with the same period of 2011

Time period	Percentage of total grassland area (%)				
	Poorer	Poor	Balanced	Good	Better
Early May	8.50	9.78	62.27	12.10	7.34
Mid-May	6.01	10.14	59.12	17.46	7.26
Late May	5.98	9.89	51.94	20.36	11.84
Early June	11.24	9.67	45.52	17.55	16.02
Mid-June	6.19	11.05	50.73	17.65	14.38
Late June	7.47	12.87	51.06	17.17	11.43
Early July	8.91	12.30	45.82	18.48	14.49
Mid-July	7.97	11.69	47.28	18.87	14.19
Late July	12.97	14.29	47.66	14.69	10.39
Early August	8.59	12.97	55.19	13.16	10.09
Mid-August	8.10	12.56	52.19	13.12	14.04
Late August	10.25	15.10	48.36	13.81	12.47
Early September	7.00	13.85	53.21	17.02	8.92
Mid-September	7.80	13.08	52.05	18.17	8.89
Average	8.36	12.09	51.60	16.40	11.55

To gain a more intuitive analysis of timing variation of grassland vegetation growth in the country, the growing vegetation index is merged into three grades - flat, good and better, poor and poorer for statistical analysis (Figure 2). From every ten-day period dynamic change of view, grassland vegetation growth for every ten-day period was mainly flat with the areas of flat vegetation growth within a narrow range between 45% -63%. The area of good and better vegetation growth over the period except late July was slightly more than the area with poor and poorer growth, of which there was a small difference in area between the two over early May and lately July to mid-September. Overall, the percentage of area with good/better, flat and poor/poorer grassland vegetation growth fluctuated around its mean value, respectively, without significant upward and downward trend and grassland vegetation growth was relatively stable throughout the year.

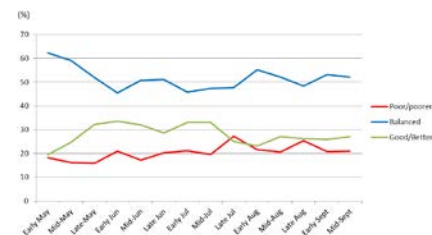


Figure 2. Ten-day dynamic change of grassland vegetation growth in China over May-September 2012 compared with the same period of 2011

3.3 Spatial pattern changes over time

The following are 14 ten-day period GVG figures during growing season in 2012 (Figure 3), which intuitively reflect the year-round growing season GVG changes, from which it can be seen that grassland vegetation growth has some regional differences in different periods. Of which grasslands with good and better growth in different periods were mainly located in Northern China while grassland vegetation growth in southwestern China showed flat and relatively good during the first half of growing season and flat and relatively poor in the latter half. Specifically, grassland vegetation growth in Gansu province in different periods of 2012 was better than that of the same periods of the previous year. Grassland vegetation growth in Inner Mongolia and Qinghai during most of the time except for a few periods was flat and relatively good. Grassland vegetation growth during most of the time in Xinjiang, Tibet and Sichuan was relatively poor than the same period of the previous year, especially during July and August, grassland vegetation with poor growth took a large percentage, of which the area with relatively poor grassland vegetation growth in late August in Tibet accounted for about half of the monitored area, the worst period of the annual grassland growth.

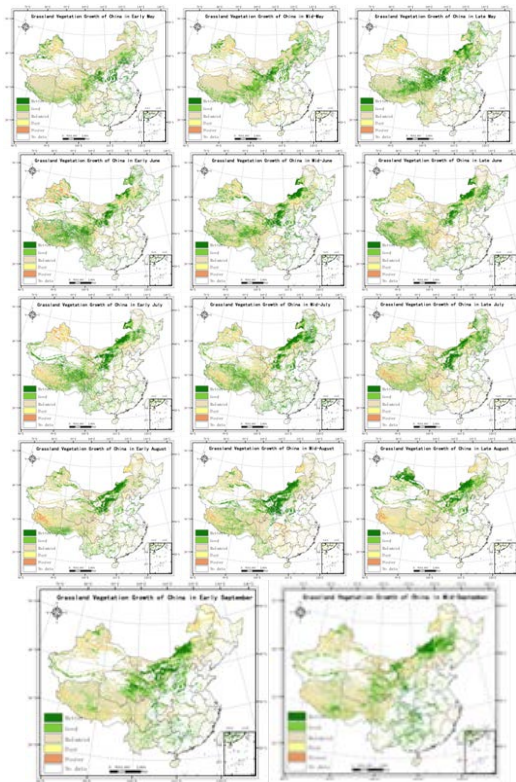


Figure 3. Spatial distribution map of vegetation growth during early May to mid-September 2012 compared with every ten-day period growth in 2011

3.4 Overall situation of grassland vegetation growth in China in 2012

Synthesis and mapping for the 2012 fourteen ten-day period NDVI data can be more intuitively reflect China's overall situation of grassland vegetation growth in 2012 (Figure 4). Due to impact such as uneven spatial precipitation, the regions with good and better growth were mainly located in central and eastern and southwestern Inner Mongolia, southwestern Heilongjiang, western Jilin, southern Qinghai, central and eastern Gansu, most parts of Ningxia and eastern Xinjiang etc.; the regions with poor and poorer growth were located in northwest of Inner Mongolia, some parts of northern Xinjiang, western Tibet, southern Sichuan, some parts of northern Yunnan etc. Grassland growth in most southern provinces was essentially flat with the previous year.

4 CONCLUSIONS AND OUTLOOKS

(1) MODIS-NDVI data have a good correlation with grassland vegetation growth which can reflect the status of grass growth and better serves for grassland monitoring, but there are some limitations. NDVI values between 0.1-0.7 can reflect vegetation growth,

but when NDVI values are less than 0.2, they will be largely interfered by other factors. Since grassland vegetation growth has complex process which is influenced by many factors such as precipitation, temperature, the earth's surface, etc., using the method by combining a variety of vegetation indices will improve the accuracy.

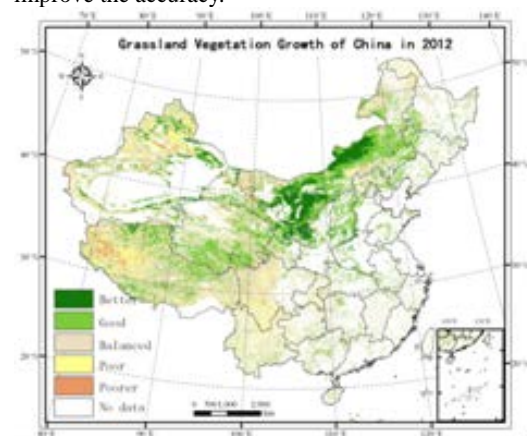


Figure 4 Spatial distribution map of grassland vegetation growth in 2012

(2) There is a greater impact on remote sensing of a large area by weather. Using ten-day period synthesized data in a state of continuous rainy weather may still be unable to eliminate the impact of the cloud on remote sensing data, which may affect the accuracy of the information extraction. How to improve the accuracy of remote sensing information extraction without extending the monitoring period is still an issue to be considered.

(3) Grasslands have the characteristics of a wide distribution area, homogeneous distribution and continuity. Using medium spatial resolution and high temporal resolution MODIS data can better meet the requirements of real-time dynamic monitoring of a large area, but for small area of grassland monitoring in terms of province or county, medium spatial resolution images cannot fully meet the requirements. As real-time and synchronization is important for dynamic monitoring of grasslands, using high spatial resolution and medium resolution of a variety of data sources combined can be considered to compensate for the lack of the temporal resolution on high spatial resolution images.

(4) Currently, growth indicators are established by empirical methods. Since grassland distribution types are diverse in China, using one method or one growth indicator to have a unified evaluation of the national grasslands has certain limitations. To evaluate grassland vegetation growth by region, method, index, respectively, can be considered to increase the accuracy of vegetation growth monitoring and is also the focus of our future work and research.

ACKNOWLEDGEMENTS

This work was supported by the National Natural Science Foundation of China (NSFC, 31372354), the International Science and Technology Cooperation Program of China under Grant 2013DFR30760, Grassland Monitoring and Supervision Center Ministry of Agriculture of China under Grant 425-1, and the Centre of Supervision Management of Grassland, Ministry of Agriculture

REFERENCE

- B.XU, W.G.Tao, X.C.Yang. MODIS-based remote sensing monitoring upon the vegetation growth of China's grassland. *Acta agrestia sinica*.2006,14 (3):242-247.
- B.XU, X.C.Yang. MODIS-based remote-sensing monitoring of the spatiotemporal patterns of China's grassland vegetation growth. *International Journal of Remote Sensing*, 2013.
- B.XU, X.C.Yang, X.Y.Hou. Advance of Technology of Remote Sensing Monitoring for Grassland Vegetation. *Science and technology review*, 2007,25(9):5-8.Dehaan, R. L., G R Taylor., 2002, Field-derived spectra of salinized soils and vegetation as indicators of irrigation-induced soil salinization. *Remote Sensing of Environment*, 80:406-417.
- H.D.YU, X.C.Yang, B.Xu. The Progress of Remote Sensing Monitoring for Grassland Vegetation Growth. *Progress in Geography*.2012,31(7):885-894.
- Q.Xing, A.J.Liu, Z.Y.Liu. Study on Change Rangeland Vegetation, Change Using MODIS-NDVI in Xilinguole Grassland. *Acta Agrestia Sinica*.2005,1
- Y.H.Si,W.Zhang. Monitoring Changes of Grassland Growth Based on Vegetation Index (NDVI) of MODIS——A Case Study of Xilin GolLeague. *Journal of Agricultural Science and Technology*, 2008,10(5):66-70.
- W.Gao,X.L.Qi,C.G.Li. Growth dynamic monitoring of natural grassland at returning green stage. *Journal of Resources and Ecology*. The proceedings on China grassland development forum.2006,9: 321-328
- H.B.Gao. *China Grassland*. China agriculture press. 2012,10.
- Ministry of Agriculture of the People's Republic of China. *Chinese grassland development report in 2011.. China agriculture press*.2013,7
- W.Gao , Q.Xing, D.F.Liu. Study on technical methods and index for monitoring the grassland degradation, desertization and salinization through remote sensing. *Grassland and turf*. 2007,123(4):40-44.
- Q Yang, Z.H.Qin, W.J.Li, B.Xu. Temporal and spatial variations of vegetation cover in hulunbeier grassland of Inner Mongolia, China, *Arid land research and management*,26,328-343,2012.
- B.Xu,X.C.Yang. Monitoring and evaluation of grassland livestock balance in pastoral and semi-pastoral counties of China, *geographical research*,2012,31(11),1998-2006.
- Y.X.Jin, B.Xu, X.C.Yang, et al. Remote sensing dynamic estimation of grass production in Xilinguole, Inner Mongolia. *SCIENTIA SINICA Vitae*, 2011, 41: 1185–1195
- B.Xu, X.C.Yang, et al. Calculation of grass production and balance of livestock carrying capacity in rangeland region of northeast China. *Geographical research*,2009,28(2): 402-408.
- Wulantuya, A.J.Liu, W.Gao. The dynamic remote sensing monitoring of Inner Mongolia natural grassland vegetation in 20 years. *Pratacultural Science* 2009,26(9):40-42.
- C.T.Wang, X.F.Li, Y.H.Ji. Remote sensing monitoring resolution upon the vegetation growth in Heilongjiang province. *Chinese journal of agro meteorology*. 2009,30(4):582-584.
- B.Xu, W.G.Tao,X.C.Yang, et al. Monitoring by remote sensing of vegetation growth in the project of grassland withdrawn from grazing in counties of china. *Acta Prataculturae Sinica*, 2007,16(5):13-21.
- A.J.Liu, J.G.Han. Remote sensing monitoring for the key phonological stages of rangeland a case study about Xilingol grassland. *Acta agrestia sinica*, 2007,15(3):201-205.
- A.J.Liu, J.G.Han. The study of method about monitoring grazing intensity in Xilingol rangeland using RS data. *Chinese journal of grassland*.2007,3:70-74.
- S.L.Liang. *Quantitative remote sensing*. Science Press. 2009,2.
- Z.Y.Pei, B.J.Yang. Analysis of multi-temporal and multi-spatial character of NDVI and crop condition models development. *Transactions of the Chinese society of agricultural engineering* , 2000, 16(5):20-22.

Hyperspectral TIR sensor for building heat-loss detection

Luca Pipia¹, Fernando Pérez¹, Anna Tardà¹, Jordi Corbera¹, Marta Morera² and Angel Ruiz Casas²

¹*Institut Cartogràfic i Geològic de Catalunya(ICGC)*

²*Ajuntament de Rubí*

luca.pipia@icgc.cat

ABSTRACT - *This work, carried out in the framework of Rubí-Brilla project, aims at detecting heat loss over industrial building covers in Rubí (Catalonia, Spain) using TASI-600 night acquisitions. The comparison of two hyperspectral TIR datasets acquired with a 6-hour time span led to the generation of a temperature gradient map and the detection of temperature change patterns related to heat-loss fluxes. A first study on the relationship between thermal behaviour and cover types was also carried out using the hyperspectral emissivity information. Different materials within the same roof were first discriminated by applying the Principal Component Analysis (PCA) technique to the emissivity profiles, and then characterized using the 32-band emissivity data.*

1 INTRODUCTION

Energy-efficiency is the first step toward achieving sustainability in buildings and infrastructures. Energy-efficiency helps control rising energy costs, reduce environmental footprints and increase the value and competitiveness. This issue, already important when dealing with private homes, becomes crucial for industrial facilities: a better management of the energy involved in the production activity leads to saving fixed production costs and, eventually, to a more competitive positioning in the market. Besides, buildings heat-loss and inefficient use of indoor heat cause a great waste of energy, with ultimate consequences on people's livelihood in terms of quality of the indoor thermal environment.

The Thermal Airborne Spectrographic Imager 600 (TASI-600) is a hyperspectral infrared sensor manufactured by the Canadian company ITRES®, which started being operated by the Institut Cartogràfic i Geològic de Catalunya (ICGC) at the end of 2009 [Pipia, 2010]. The system works in a

pushbroom configuration and provides the user with 32-band hyperspectral data in the 8-11.5µm spectral range. The nominal Field-Of-View (FOV) is approximately 40°, and it spreads over 600 spatial pixels. The TASI gives the opportunity to measure and retrieve information concerning skin-temperature and emissivity spectrum of the imaged scene. When flown over man-made areas, such as an industrial district, TASI-based absolute temperature becomes a reliable descriptor of heat leaks through roof covers, whereas patterns detected within hyperspectral emissivity images usually account for different properties of the cover material.

Following this approach, TASI data were acquired over an industrial area in Rubí, the second largest industrial district in Catalonia (Spain), in the framework of the project Rubí Brilla [Rubí,2013]. In this paper, the measurement campaign carried out by ICGC in the framework of the project Rubí Brilla is described. The temperature maps corresponding to each flight are compared in a pixel-by-pixel approach in order to detect changes in the temperature patterns, which



Figure 1 - TASI flight plan over Rubí

TASI field of view (FOV)	40°
Flight height	1600
# of Spectral Bands	32
# of Spatial Pixels	600
Along-track Pixel's size	2 m
Along-track Pixel's size	2 m
Swath	1100 m

Table 1 - Flight and sensor main parameters.

can be related to heat-loss fluxes. Similar thermal dynamics are looked for and compared to hyperspectral emissivity information. Finally, principal Component Analysis (PCA) is applied to stress the existence of possible relationships between thermal behaviours and cover materials.

2 TEST-SITE AND MEASURING CAMPAIGN

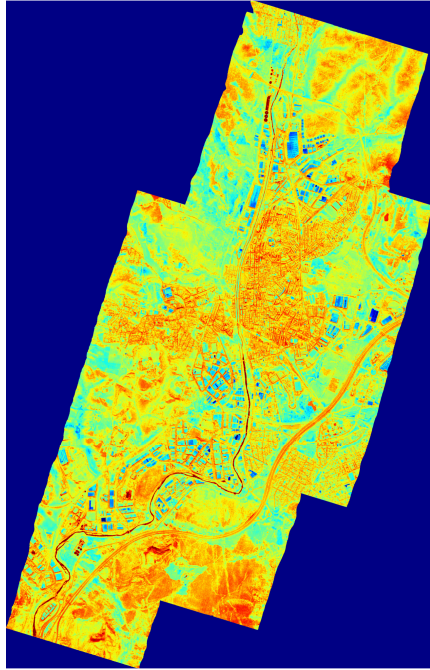
The municipality of Rubí, with a total area of about 35 km², is the second largest industrial district in Catalonia (Spain). In an attempt to generate an energy efficiency map of the industrial premises, the whole municipality was flown with the TASI sensor in the framework of a pioneering project called Rubí-Brilla. The project aims to make the town a reference, both at national and international scale, for energy efficiency and renewable energy use in industrial,

commercial and domestic scenarios. Among the specific strands of work planned by the project, there was the thermal characterization of a set of selected industrial premises using remote sensing. Accordingly, two TASI datasets were acquired over the whole municipality area on February 5th 2013. The two acquisition processes were carried out at 12am and 6am, which roughly correspond to the times when most of the product chains of the area are idle and resumed, respectively. A sketch of the flight plan defined to cover the whole municipality is shown in Fig. 1. The main flight and sensor parameters are summarized in Table 1.

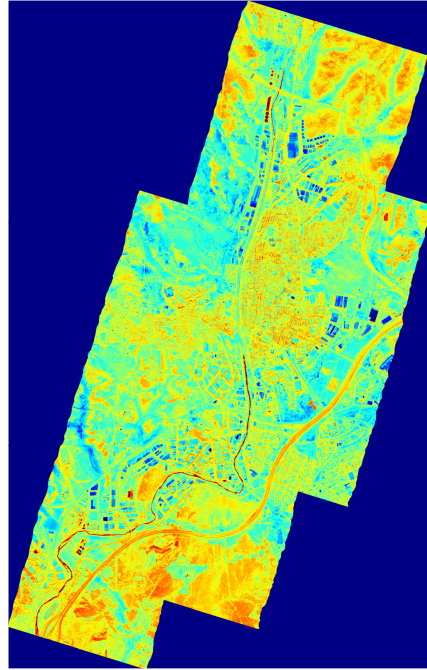
3 DATA ANALYSIS

A temperature geocoded image was retrieved from each flight track using the NCEP atmospheric profile [Barsi, 2003] tied to the ground information provided by the Cerdanyola del Vallès automatic weather station (5 km from Rubí downtown), and a version of the TES technique tailored to TASI spectral properties [Pipia, 2013]. Next, the five partially overlapped maps retrieved from each flight were mosaicked. The final temperature mosaics are shown in Figure 2a and 2b, respectively, whereas the temperature gradient map is shown in Figure 2c. Concerning the emissivity information, a noise-reduced hyperspectral map was calculated by invoking the time-stationarity of this parameter over man-made objects and averaging the two profiles available for each pixel of the imaged scene. An example of the result is provided with the image in Figure 2d, representing an RGB composition of the emissivity information at 9.6μm, 8.6μm and 8.2μm.

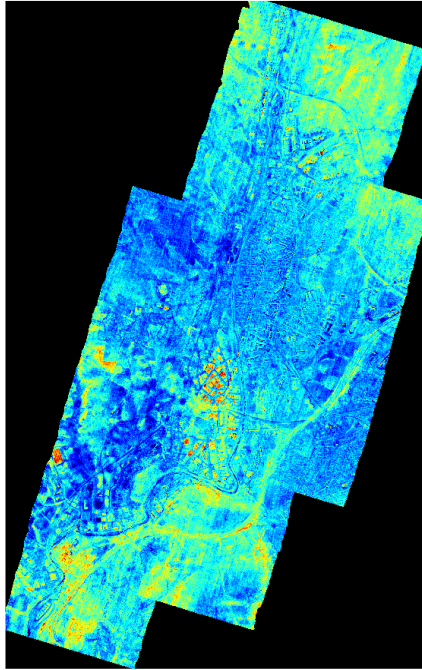
The thermal maps were compared on a pixel-by-pixel basis to detect changes in the roof temperature patterns that might be related to heat-loss fluxes. The study was applied to the 22 industrial facilities participating to Rubí-Brilla project. The temperature gradient ΔT was labelled as low, medium or high if $\Delta T < 1.5^\circ\text{C}$, $1.5^\circ\text{C} < \Delta T < 3^\circ\text{C}$ or $\Delta T > 3^\circ\text{C}$, respectively. Note that this segmentation was fixed after examining the overall thermal behaviour within the industrial district. The collection of images shown in Figure 3 provides an example of premises belonging to the



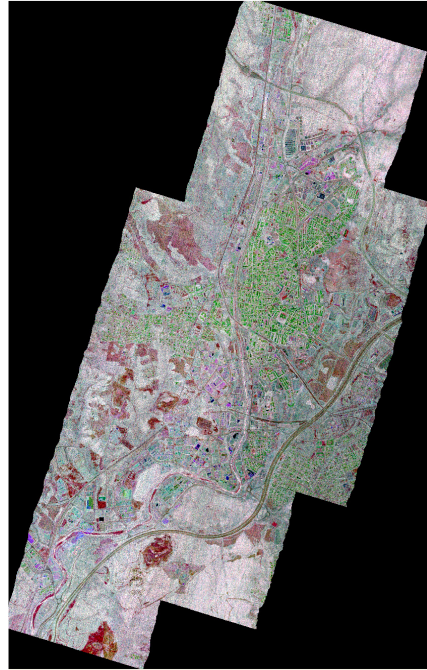
(a)Temperature mosaic -5/2/2013@12:00am



(b)Temperature mosaic - 5/2/2013@06:00



(c) ΔT mosaic: $T@6:00am - T@12:00am$



(d) $\langle \epsilon \rangle$ mosaic: $[\epsilon@6:00am + \epsilon@12:00am]/2$

Figure 2 – Mosaicks of temperature Mosaics in Rubí at 12am (a) and 6am (b), temperature gradient (c) and of emissivity at 9.6 μm (red), 8.6 μm (green) and 8.2 (blue) (d).

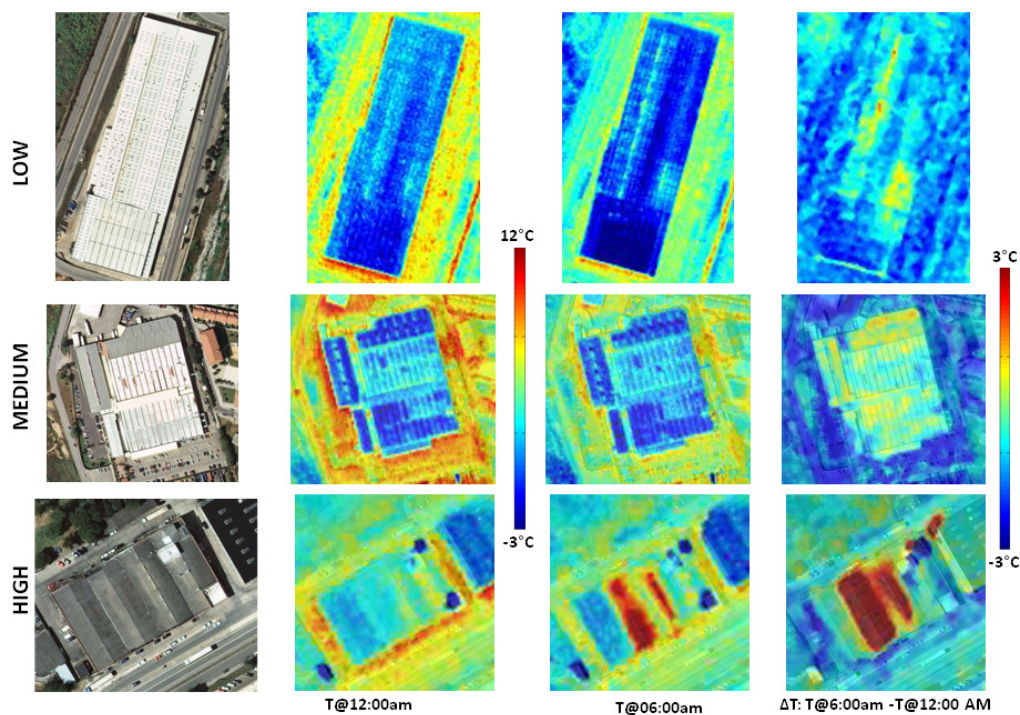


Figure 3 – Examples of industrial estates belonging to low (up), medium (centre), and high (bottom) temperature gradient classes.

three classes. Concerning the production activity carried out within each building, the low gradient case corresponds to the production of electric equipment, the medium gradient case to chemical products and the high gradient case to plastic part manufacturing.

In order to stress the existence of possible relationships between thermal behaviours and cover materials, the hyperspectral emissivity information was looked into. The areas within the same roof showing different emissivity features were detected using the Principal Component Analysis (PCA). Essentially, this technique makes it possible to reduce the hyperdata spectral dimension by transforming a set of observations of possible correlated variables (the spectral bands) into a set of values of linearly uncorrelated variables, through the maximization of the statistical variance. Accordingly, the RGB image obtained from the first three PCs was used to create a mask grouping all the pixels within the same cover

showing a homogeneous behaviour. The rationale is that each group should account for a specific cover material. Afterwards, a spatially averaged 32-band emissivity signature was calculated for each group of pixels detected within the same cover. An example of the study carried out for each of the 22 industrial facilities is shown in Figure 4.

PCA stressed the heterogeneity of materials that are often present within the same cover, independently of the indoor production activity. This result was confirmed by the survey carried out by ETSEIB of Universitat Politècnica de Catalunya (UPC) in the framework of Rubí-Brilla. Yet, covers labelled by the survey the same way, for example metal sheet, turned out to show different spectral signatures, bringing out the complexity of the material classification task to be carried out and the need of more exhaustive ground-truth information. Besides, additional information about building inside temperature becomes essential

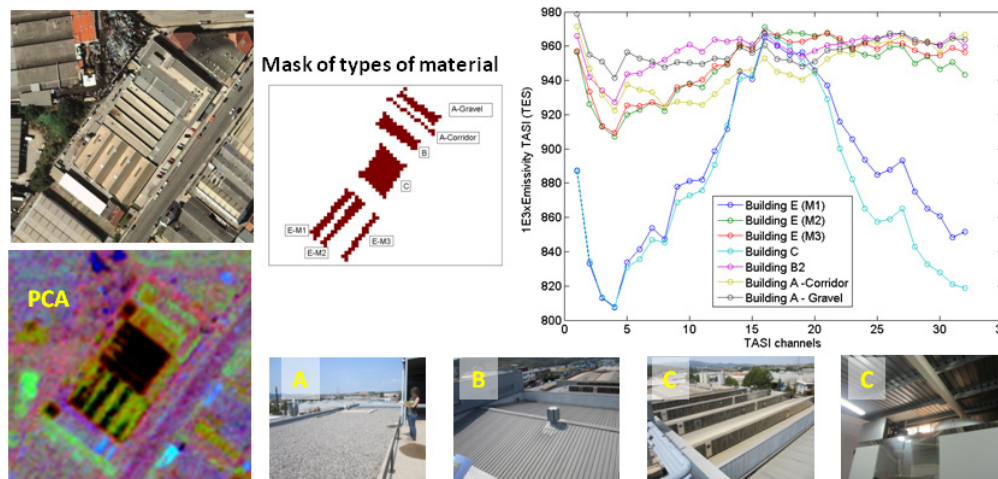


Figure 4 – Example of industrial facility cover in Rubí. RGB image from PCA is used to detect homogeneous areas and create a mask to estimate spatially-averaged 32-band emissivity profiles accounting for different materials.

to work out a quantitative descriptor of the energetic efficiency associable to each industrial building.

4 CONCLUSIONS

The two night TASI datasets acquired with a time-span of approximately 6 hours, made it possible to detect industrial building heat-loss through the estimation of the absolute temperature gradient, and discriminate cover materials using hyperspectral emissivity profiles. In-situ information concerning the material types is now required to create a hyperspectral TIR library for either supervised or non-supervised cover classifications. By cross-checking this information with building roof temperature gradient (TASI) and inside temperature gradient (related to specific production activities), it will be possible to quantitatively describe the cover thermal insulation, and provide valuable recommendations for saving production energy and, hopefully, achieving a more efficient management of the industrial buildings.

5 REFERENCES

L. Pipia, F. Pérez, A. Tardà, L. Martínez, V. Palà and R. Arbiol, "Thermal Airborne Spectrographic Imager for Temperature and Emissivity Retrieval," 3rd

International Symposium on Recent Advances in Quantitative Remote Sensing, 27 September - 1 October 2010, Torrent-Valencia (Spain), pp. 840-844.

Barsi, J.B., Barker J.L. and Schott J.R., "An Atmospheric Correction Parameter Calculator for a Single Thermal Band Earth-Sensing Instrument," *Geoscience and Remote Sensing Symposium* 2003, IGARSS'03 Proceedings, Vol. 5, pp. 3014-3016.

Rubí Brilla project :

http://www.rubi.cat/perfil/rubi/recursos/recursos/rubibrilla_project_short.pdf.

L. Pipia, F. Pérez, A. Tardà, L. Martínez and R. Arbiol, "Simultaneous usage of optic and thermal hyperspectral sensors for crop water stress characterization," *Geoscience and Remote Sensing Symposium* 2012, IGARSS'12 Proceedings, pp. 6661-6664.

Landsat surface albedo product based on MODIS data

B. Franch^{1,2}, E. F. Vermote^{2,1}, M. Claverie^{1,2}

¹ *Department of Geographical Sciences, University of Maryland, College Park MD 20742, United States*

² *NASA Goddard Space Flight Center, 8800 Greenbelt Road, Greenbelt, MD 20771, United States*

belen.franchgras@nasa.gov

ABSTRACT Surface albedo is an essential parameter not only for developing climate models, but also for most fluxes studies, which are mainly focused on agricultural applications and require a high spatial resolution. In this context Landsat is one of the most used remote sensing sensors. The albedo is estimated through the angular integration of the Bidirectional Reflectance Distribution Function (BRDF). Thus, it requires an appropriate angular sampling of the surface. However, Landsat sampling characteristics, with nearly constant illumination and observation geometry, prevent from deriving a surface albedo product. In this paper we present an algorithm to derive a Landsat surface albedo based on the BRDF parameters estimated from the MODerate Resolution Imaging Spectroradiometer (MODIS) Climate Modeling Grid (CMG) surface reflectance product (M{O,Y}D09). We base our method on Landsat unsupervised classification to disaggregate the BRDF parameters to the Landsat spatial resolution. We tested the proposed algorithm over five different sites of the Surface Radiation (SURFRAD) network. The results show that with this method we can derive the surface albedo with a Root Mean Square Error (RMSE) of 0.015.

1 INTRODUCTION

The increasing spatial resolution of modern climate models and the high spatial resolution required by most energy balance studies makes it necessary to examine spatial features of global surface albedo. There are several albedo products derived from different satellite sensors data, such as the MODerate Resolution Imaging Spectroradiometer (MODIS, Schaaf et al., 2002). However, in some cases the estimation of surface albedo from remotely sensed data is a challenging problem due to the low angular sampling of the sensor considered. This is the case of Landsat satellite series, which has the potential to provide medium resolution (30 m) images.

Shuai et al. (2011) presented a methodology to generate a Landsat surface albedo product based on the MODIS Bidirectional Reflectance Distribution Function (BRDF) MDC43 product at 500m (Schaaf et al., 2002). This method presents a Root Mean Square Error (RMSE) generally less than 0.03, but it is mostly determined by a negative bias (lower retrieved albedo than in situ data). The objective of this work is to present a method that improves upon the Shuai et al. (2011) albedo product. The algorithm presented, is based on the disaggregation of the BRDF parameters from MODIS to Landsat spatial resolution by matrix inversion and exploiting the information from all the pixels along the scene.

2 METHODOLOGY

In order to estimate the BRDF parameters from the MODIS surface reflectance images, we used the VJB method (Vermote et al., 2009). First, we start considering that the surface reflectance of a MODIS pixel can be written as a weighted sum of n Landsat classes:

$$K_0^{CMG} + K_1^{CMG} F_1(\theta_s, \theta_o, \phi) + K_2^{CMG} F_2(\theta_s, \theta_o, \phi) = A_s (K_0^C + K_1^C F_1(\theta_s, \theta_o, \phi) + K_2^C F_2(\theta_s, \theta_o, \phi)) + B_s (K_0^C + K_1^C F_1(\theta_s, \theta_o, \phi) + K_2^C F_2(\theta_s, \theta_o, \phi)) + \dots + N_s (K_0^C + K_1^C F_1(\theta_s, \theta_o, \phi) + K_2^C F_2(\theta_s, \theta_o, \phi))$$

this equation is valid for every F1 and F2. Thus, if we choose F1=F2=0:

$$K_0^{CMG} = A_s K_0^C + B_s K_0^C + \dots + N_s K_0^C \quad (1)$$

To solve this equation, where there are n unknowns (the same as classes), we will need a system of, at least, n equations that describe n MODIS pixels. One can therefore minimize the merit function, which leads to:

$$\begin{pmatrix} \sum_i A_i A_i & \sum_i A_i B_i & \dots & \sum_i A_i N_i \\ \sum_i A_i B_i & \sum_i B_i B_i & \dots & \sum_i B_i N_i \\ \vdots & \vdots & \ddots & \vdots \\ \sum_i A_i N_i & \sum_i B_i N_i & \dots & \sum_i N_i N_i \end{pmatrix} \begin{pmatrix} K_1^C \\ K_2^C \\ \vdots \\ K_n^C \end{pmatrix} = \begin{pmatrix} \sum_i K_1^{CMG} A_i \\ \sum_i K_1^{CMG} B_i \\ \vdots \\ \sum_i K_1^{CMG} N_i \end{pmatrix} \quad (2)$$

where the first element is a matrix that combines the proportion of classes within the CMG pixel.

Analogously, we get to the same solution for k1 and k2. Thus, with this method we can estimate the BRDF parameters at high resolution for each class considered

3 IMPLEMENTATION

First, we run an unsupervised classification over every Landsat image using the ENVI ISO data classification (ENVI reference). Next, we derive MODIS BRDF parameters using the VJB method. Next, we invert k_1^{Landsat} and k_2^{Landsat} for each class following the same structure as equation (12). In the inversion we consider every CMG pixel through the Landsat image that comprised at least 99% of land cloud/snow free Landsat pixels. Finally, we estimate the albedo (Strahler et al., 1999; Schaaf et al., 2002).

4. DATA

This study use the Landsat 30 m surface reflectance product generated by USGS using the Landsat Ecosystem Disturbance Adaptive Processing System (LEDAPS, Masek et al., 2006). We consider Landsat 5 Thematic Mapper (TM) images and Landsat 7 Enhanced Thematic Mapper Plus (ETM+). We worked over five different path/rows that included all the NOAA's Surface Radiation (SURFRAD) Measurement Network sites from 2003 to 2006.

We also processed MODIS CMG surface reflectance Collection 6 data (M{OY}DCMG) over the same areas and time period to derive the BRDF parameters.

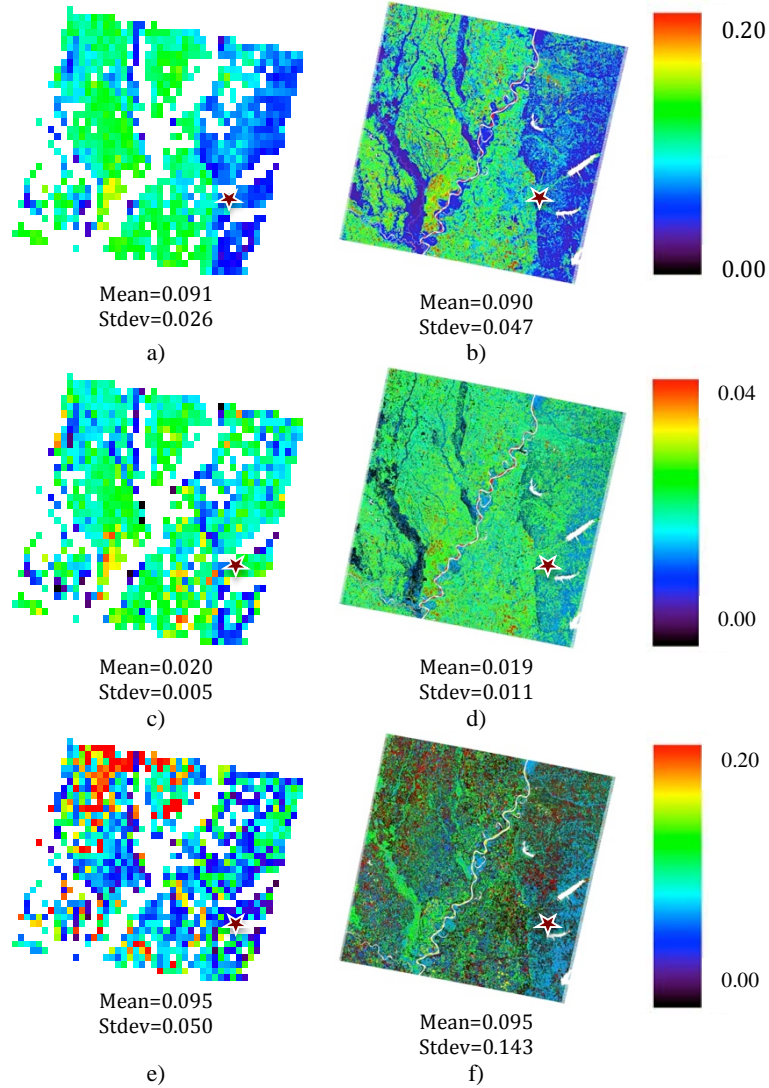


Figure 1. k_0 (a, b), k_1 (c, d) and k_2 (e, f) images in the red band in Goodwin Creek, MS.

5. RESULTS

Figure 1 shows the BRDF parameters k_0 , k_1 and k_2 for the red band in Goodwin Creek, MS, on September 30th of 2005.

The images on the left display MODIS CMG BRDF parameters derived with the VJB method while the images on the right correspond to Landsat resolution images resulting from the MODIS disaggregation after applying the methodology presented in this work. Both Landsat and MODIS images capture the heterogeneity of landscape through the scene. The left side of the image, composed mainly of forests, shows lower k_0 values in this band than the other areas. However, while both images at different spatial resolution show similar patterns with consistent variations through the scene, the higher resolution images show more variability along the scene than the coarser resolution. In fact, looking at the global statistics of each image, the high and low resolution scenes present the same mean with differences lower than 5%, while the high resolution ones have higher standard deviation than the lower resolution.

Figure 2 plots the validation of satellite-derived albedo with the in situ measurements. For validation purposes, we just consider the completely clear images over the tower site and with at least 30% of cloud free CMG pixels along the scene compared to the clearest (highest percentage of cloud free pixels) image of the same area. This filter is also applied to the original Landsat albedo results (Shuat et al., 2011), which are also represented in the plot, considering therefore the same amount of data.

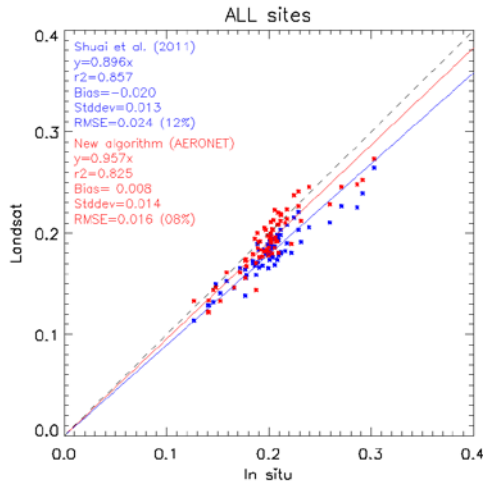


Figure 5. Validation of the proposed algorithm and Shuai et al. (2011) Landsat albedo products with in situ data retrieved from SURFRAD stations from 2003 to 2006.

The figure shows a good agreement of both Landsat products with field measurements with similar correlation coefficients. However, the Landsat albedo derived with the proposed algorithm lead to better statistics than the standard albedo with a decrease of the RMSE to 0.016 (on the order of 4%) and a slope nearer to one. The decrease in the RMSE is mainly caused by the correction of the bias, since both algorithms show similar standard deviation. Although the new method provides an improvement in the bias, we still observe a slight underestimation of Landsat albedo for albedos higher than 0.25.

Finally, following Roman et al. (2013) analysis about the possible sources of error in the Landsat product, we analyze the impact of the atmospheric correction on the albedo estimation. Taking advantage of the AERONET network in situ measurements we extract the particle size distribution of the aerosols (Vermote and Kotchenova, 2008) and the water vapor content. Then, we introduce this information in 6S (Vermote et al., 1997) and apply the atmospheric correction to Bondville and Table Mountain Landsat scenes (the only sites with AERONET data). Figure 3 shows the new validation of all the sites, where we replaced Bondville and Table Mountain original results with the albedo derived from the new atmospheric correction. Compared to Figure 2 statistics, the RMSE barely decreases from 0.016 to 0.015, improving the original Landsat albedo error around 5%, the correlation coefficient suffers a slight decrease (from 0.825 to 0.773) and, finally, we get a fitting slope nearer to one, with an improvement from 0.957 to 0.977 mainly caused by the improvement in the estimation of the high albedo values correcting the bias.

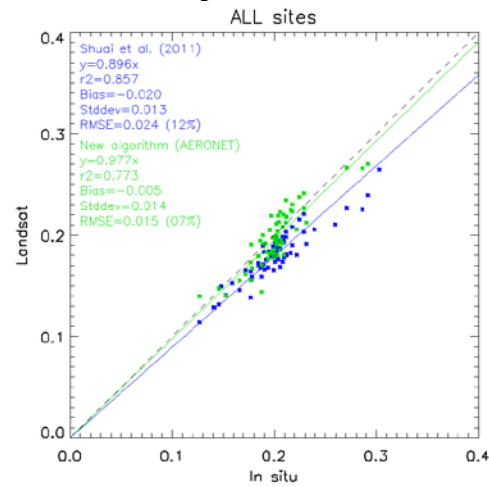


Figure 8. Validation of all the sites equivalent to Figure 5 but replacing Bondville and Table Mountain results with the albedo derived from the improved atmospheric correction.

6. CONCLUSIONS

This work presents a new method to estimate the Landsat albedo based on MODIS CMG BRDF data. This new method has three main differences with the method proposed by Shuai et al. (2011). First, we disaggregate the MODIS pixel into the Landsat spatial resolution including the information from all the cloud free pixels and working with the BRDF parameters. This supposes an advantage compared to the original Landsat albedo since we can provide BRDF maps at Landsat spatial resolution. Second, we work with the CMG product, instead of working at 500m spatial resolution. And, finally, we use a BRDF inversion method different to the heritage MCD43 product. However, this should not affect much to the surface albedo estimation since both models lead to equivalent results (Vermote et al., 2009; Breon & Vermote, 2012; Franch et al., 2014).

The validation for the five SURFRAD sites shows a better performance of the surface albedo product derived with the proposed method (RMSE of 0.016) when compared to the original Landsat albedo (RMSE of 0.024) caused by the partial correction of the bias. However, we still detect some bias for high albedo values. Among the possible errors that may cause this bias, we analyze the impact of the atmospheric correction. Thus, we applied a more accurate atmospheric correction by including AERONET in situ measurements of aerosol parameters (such as particle size distribution) and water vapor content. The results show the correction of such bias for high albedo values and similar results for the other albedo values. Therefore, this supports the good performance of the LEDAPS atmospheric correction for the broadband surface albedo estimation although it should be reviewed for high albedo values. Finally, after including the new results derived with the improved atmospheric correction, we get a RMSE of 0.015, which implies a decrease of 5% in the error compared to the original Landsat albedo (from 12% to 7%). We believe that the main improvement that causes the correction of the bias of Shuai et al. (2011) results is the proposed disaggregation method since the VJB provides equivalent albedo results than the MCD43 product and the atmospheric correction based on in situ atmospheric measurements just affect to the higher albedo values. With the proposed method we estimate that each image takes less than one hour to process with a standard processor server. The computation cost might be higher than Shuai et al. (2011) method but stay reasonable.

7. REFERENCES

- Bréon, F.M. & Vermote E.F. (2012). Correction of MODIS surface reflectance time series for BRDF effects. *Remote Sensing of Environment* 125, 1–9.
- Franch, B., Vermote, E.F., Sobrino, J.A. and Julien, Y. (2014). Retrieval of Surface Albedo on a Daily Basis: Application to MODIS Data. *IEEE Transactions on Geoscience and Remote Sensing*. Vol. 52, Issue 12, 7549-7558
- Masek, J.G., E.F. Vermote, N. Saleous, R. Wolfe, F.G. Hall, F. Huemmrich, F. Gao, J. Kutler & T.K. Lim. (2006). A Landsat surface reflectance data set for North America, 1990-2000, *Geoscience and Remote Sensing Letters*, 3, 68-72.
- Román, M.O., Gatebe, C.K., Shuai, Y., Wang, Z., Gao, F., Masek, J.G., He, T., Liang, S., & Schaaf, C.B. (2013). Use of In Situ and Airborne Multiangle Data to Assess MODIS- and Landsat-Based Estimates of Directional Reflectance and Albedo. *IEEE Transactions on geoscience and remote sensing*, Vol. 51, no. 3, pp. 1393-1404
- Schaaf, C. B., Gao, F., Strahler, A.H., Lucht, W., Li, X., Tsang, T., Strugnell, N.C., Zhang, X., Jin, Y., Muller, J.P., Lewis, P., Barnsley, M., et al., (2002). First operational BRDF, albedo nadir reflectance products from MODIS. *Remote Sens Environ*, 83(1-2), 135-148.
- Shuai, Y., Masek, J., Gao, F. & Schaaf, C. B. (2011). An algorithm for the retrieval of 30-m snow-free albedo from Landsat surface reflectance and MODIS BRDF. *Remote Sens. Environ.*, vol. 115, no. 9, pp. 2204–2216.
- Strahler A.H., Lucht W., Schaaf C.B., Tsang T., Gao F., Li X., Muller J.-P., Lewis P. & Barnsley M.J. (1999). MODIS BRDF Albedo Product: Algorithm Theoretical Basis Document. NASA EOS-MODIS Doc., V5.0.
- Vermote, E., Tanré, D., Deuzé, J.L., Herman, M. & Morcrette, J.J. (1997). Second simulation of the satellite signal in solar spectrum: An overview. *IEEE Trans. Geos. Rem. Sens.*, 35, 675 – 686
- Vermote, E. F. & S. Kotchenova, (2008). Atmospheric correction for the monitoring of land surfaces, *J. Geophys. Res.*, 113, D23S90, doi:10.1029/2007JD009662
- Vermote E.F., Justice C. & Bréon F.M. (2009). Towards a generalized approach for correction of the BRDF effect in MODIS directional reflectances. *IEEE Transactions in Geoscience and Remote Sensing*, 47 (3), pp. 898–908.

Global Atmospheric Profiles from Reanalysis Information (GAPRI): a new dataset for forward simulations in the thermal infrared region

C. Mattar¹, C. Durán-Alarcón¹, J.C. Jiménez-Muñoz² and J.A. Sobrino².

1. *Laboratory for Analysis of the Biosphere (LAB), University of Chile*

2. *Global Change Unit, Imaging Processing Laboratory, Parc-Cientific Universitat de Valencia.*

cmattar@uchile.cl

ABSTRACT - The new Global Atmospheric Profiles derived from Reanalysis Information (GAPRI) dataset is presented in this work. This data base can be used for forward simulations in the thermal infrared region. GAPRI is a comprehensive compilation of selected atmospheric vertical profiles at global scale which can be used for LST algorithms development. GAPRI includes information about geopotential height, atmospheric pressure, air temperature and relative humidity derived from ERA-Interim reanalysis data during year 2011. The vertical atmospheric profiles are structured for 29 vertical levels and extracted from a global spatial grid about $0.75^\circ \times 0.75^\circ$ latitude-longitude. The selection method was based to extract a clear sky profiles over different atmospheric weather conditions such as tropical, mid-latitude summer, sub-arctic and arctic considering sea and land areas and also daytime and nighttime conditions. Comparisons between GAPRI and other existing atmospheric profiles datasets shows the potential of this dataset for studies related to forward simulations. GAPRI dataset is available for users in MODTRAN format. The comparison was carried out for TERRA-MODIS and MSG-SEVIRI using the following data bases TIGR61, TIGR1761, TIGR2311 and STD66. The results obtained ranging between 0.1 and 0.3 K. GAPRI can also be modified for any specific user request such as vertical profile with low or high concentrations of precipitable water, day/night or masking the land or sea for every year between 1979 to the present.

1 INTRODUCTION

Atmospheric gases such as water vapour, carbon dioxide and ozone generate important energy absorption at wavelengths in the atmospheric window located in the thermal infrared (TIR) range (8 – 14 μm). This absorption reduces the land leaving radiance detected by Earth Observation (EO) sensors on board satellites, added to the atmospheric emission which is also detected by the sensor. Atmospheric absorption and emission must be removed from the at-sensor registered TIR radiance to retrieve surface parameters such as Land Surface Temperature (LST) and/or surface emissivity. This procedure is referred in the literature as to atmospheric correction or compensation, and it is a key factor for accurate retrieval of land products from remote sensing data. Although LST retrieval can be addressed from a direct inversion of the Radiative Transfer Equation (RTE), this procedure requires a detailed knowledge of the vertical structure of the atmosphere to account for the atmospheric transmissivity and radiances (both up- and down-welling) (e.g. Jiménez-Muñoz et al., 2010). Several methods have been developed to correct such atmospheric influences and retrieve LST from TIR data avoiding the detailed knowledge of the atmospheric profile, as reviewed in Li et al. (2013). In particular, the split-window algorithms have been traditionally used to retrieve LST from two TIR bands in the atmospheric window between 10 and 12 μm ,

which can be applied to a number of past and current EO sensors (Jiménez-Muñoz and Sobrino, 2008). Single-Channel algorithms have been also developed to retrieve LST from one single TIR bands, such as the Landsat series case (Jiménez-Muñoz et al., 2009).

In order to avoid the dependence on the atmospheric profile availability at the overpass time of the sensor, most of LST algorithms require the computation of certain algorithm coefficients obtained from simulation procedures using a number of atmospheric cases (and surface conditions). Once these coefficients are obtained, the LST algorithms can be applied in an operational way to generate LST products with minimum atmospheric input data (e.g. total atmospheric water vapour content). A few atmospheric profiles databases have been developed for simulation purposes, as for instance the Thermodynamic Initial Guess Retrieval (TIGR) data set (Aires et al., 2002), the Cloud-free latitude equally distributed SAFREE database (François et al., 2002), and the Cloudless Land Atmosphere Radiosounding (CLAR) database (Galve et al., 2008). However, these data bases did not present a wide density and range of atmospheric conditions. For instance, CLAR database does not include atmospheric profiles over sea, whereas the SAFREE database does not include atmospheric profiles over land. On the other hand, these databases do not include a clear night/day differentiation. The aim of this work is to present a

new Global Atmospheric Profiles derived from Reanalysis Information (GAPRI) dataset which includes more than 8,000 atmospheric profiles. Each individual profile is characterized by its geographical coordinate, and acquisition over land/sea or day/night is also differentiated. GAPRI dataset is supplied in MODTRAN code format (Berk et al., 1999) for forward simulations purposes.

2 DATA SET

ERA-Interim reanalysis products were used to generate the GAPRI dataset. ERA-Interim is generated by the European Centre of Medium-Range Weather Forecasts (ECMWF) continuing the ERA-40 reanalysis. The ERA-Interim improves the ERA-40 due to the use of a four-dimensional variational (4D) data assimilation bias correction for satellite radiance data (Dee, 2005; Dee and Uppala, 2009; Dee et al., 2011). ERA-Interim overlaps with ERA-40 from 1979 to 2001, and it is available from 1979 to present. In this work, the ERA-Interim air temperature, geopotential height and relative humidity data have been used at $0.75 \times 0.75^\circ$ spatial resolution at global scale during year 2011. These atmospheric variables were extracted at different mandatory pressure levels: 1000, 975, 950, 925, 900, 875, 850, 825, 800, 775, 750, 700, 650, 600, 550, 500, 450, 400, 350, 300, 250, 225, 200, 175, 150, 125, 100, 50 and 20 hPa.

3 METHOD

3.1. Profile Selection

Due to the large amount of ERA-interim data, different selection criteria were adopted in order to construct a robust database capable to be representative of global atmospheric conditions with a

moderate number of atmospheric profiles. The selection criteria refer to spatial conditions, precipitable water amount and temporal selection, although the criteria of clear sky conditions was always considered.

3.2. Global Spatial distribution

In order to extract atmospheric profiles at global scale over different locations, a normal random spatial sampling method was applied, selecting more than 8,000 pixels over the ERA-interim global grid. These pixels were divided into “sea” and “land” using a boolean mask (Figure 1). Once the pixels were selected, the atmospheric variables (geopotential height, air temperature, and relative humidity) were extracted and structured into 29 atmospheric mandatory levels. A cloud filter was applied to select only atmospheric profiles under clear sky conditions. The cloud filter is based on the maximum relative humidity for each level, so that “clear sky” profiles were selected when relative humidity values were lower than 80% at each level. A similar criterion was used in Wang et al. (2000) using radiosonde data. After application of the cloud filter, the total number of atmospheric profiles was reduced to 8,324, with 4,714 atmospheric profiles over land, and 3,610 atmospheric profiles over sea.

3.3. Precipitable water threshold

The integrated water vapour column (defined as precipitable water) is a key atmospheric parameter in the TIR region, since water vapour is the most important absorbing gas in this region. This parameter also appears explicitly in most of the LST algorithms.

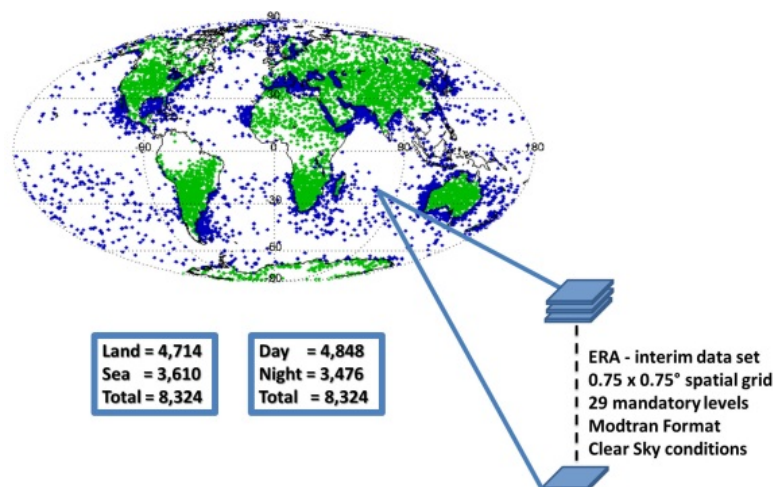


Fig1. Location of atmospheric profiles extracted from ERA-interim reanalysis to generate the GAPRI data base. Green and blue points indicate profiles extracted over “land” and “sea”.

Therefore, it is reasonable to classify the different atmospheric profiles according to well-distributed values of this parameter. In the GAPRI case, precipitable water (WP) was estimated from vertical integration of the specific humidity (q_v), which in turn was calculated from the saturation vapor pressure (e_s):

$$e_s = 611 * 10^{\left(\frac{17.27T}{237.3+T}\right)} \quad (1)$$

$$q_v = 0.622 \frac{e_s HR}{100p} \quad (2)$$

$$WP = 0.01 \int_{p_z}^{p_0} q_v dp \approx 0.01 \sum \bar{q}_v \Delta p \quad (3)$$

Where T is the air temperature ($^{\circ}\text{C}$), HR is the relative humidity (%), and p is the atmospheric pressure (hPa) at each atmospheric layer. GAPRI vertical profiles were classified into five intervals of WP: 0 – 10; 10 – 20; 20 – 30; 30 – 40; 40 – 60 cm.

3.4. Day/night classification

GAPRI atmospheric profiles were also classified into “day” and “night” acquisition. This time division was performed using the following expression:

$$lat_{light} = \frac{180 * \arctan(X)}{\pi \tan\left(\frac{\pi \varphi}{180}\right)} \quad (4)$$

$$X = \cos\left(\frac{\pi\left(\frac{\theta}{15} + UTC\right)}{12}\right) \quad (5)$$

Where θ is the geographical longitude ($^{\circ}$), φ is the sun declination ($^{\circ}$), UTC is the Universal Time Coordinated, and lat_{light} is the boundary between day and night. Based on this parameter, a given vertical profile is classified as “day” when $(lat_{light} - latitude(^{\circ})) > 0$ and $\varphi < 0$, or $(lat_{light} - latitude(^{\circ})) < 0$ and $\varphi > 0$, whereas it is classified as “night” when $(lat_{light} - latitude(^{\circ})) < 0$ and $\varphi < 0$, or $(lat_{light} - latitude(^{\circ})) > 0$ and $\varphi > 0$.

3.5. Conversion to MODTRAN format

MODTRAN radiative transfer code has been widely used for atmospheric correction of remotely sensed imagery. MODTRAN is an integrated 1 cm^{-1} spectral model based on LOWTRAN (20 cm^{-1}) with an accurate performance for brightness temperature simulations (less than 1 K) and radiance accuracy about 2%. Several versions have been released improving calculation methods and model discretization, among others details (Berk et al., 2006; Anderson et al., 2009).

MODTRAN allows the introduction of more than 30 vertical levels including meteorological parameters such as air temperature, relative humidity, dew point

temperature, mixing ratio, and geopotential height, among others. Moreover, it includes six standard atmospheric profiles representative of different climatic conditions (tropical, mid latitude summer, mid latitude winter, subarctic summer, subarctic winter, and US Standard Atmosphere). In this context, GAPRI profiles were converted to MODTRAN format ready for execution in thermal radiance mode with multiple scattering (16 streams) and surface emissivity equal to one. Geopotential height (km), air temperature (K), and relative humidity (%) for each layer was extracted from the ERA-Interim product, whereas the rest of atmospheric constituents were retrieved from default values included in the MODTRAN standard atmospheres depending on the location of the atmospheric profiles. Nevertheless, users can change the GAPRI format to adapt the input to other codes or other MODTRAN options.

4. RESULTS & DISCUSSION

Figures 2 and 3 show the histogram of the atmospheric profiles versus the WP content in terms of day/night and in terms of land/sea respectively. These results show also a robust distribution of the different atmospheric profiles included in the GAPRI database.

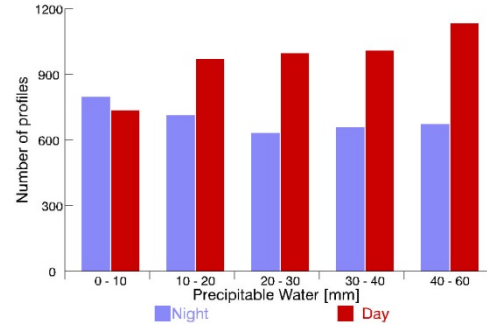


Fig2. Number of vertical profiles according to the precipitable water class and Day (red) and Night (blue) time.

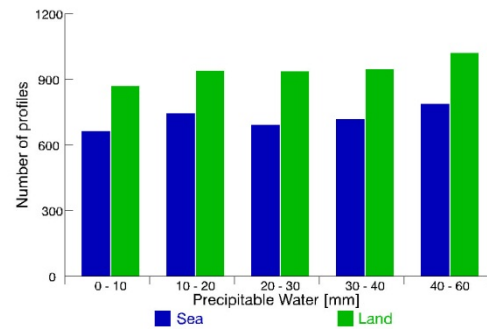


Fig3. Number of vertical profiles according to the precipitable water class Sea and Land distribution.

Table 1 shows the comparison between the GAPRI-derived Split-window algorithm and the other databases near to 0 K and standard deviations (1-sigma) typically below 0.7 K, which demonstrates the good performance of the GAPRI database, at least in comparison to other atmospheric profiles databases accepted by the scientific community.

Table 1. Comparison between the GAPRI-derived Split-window algorithm and AATSR, MODIS, AVHRR3, IMG and SEVIRI databases.

Satellite/Sensor	Database	N	bias \pm s
			(K)
ENVISAT-AATSR	TIGR61	6588	-0.1 \pm 0.5
	TIGR1761	190188	0.1 \pm 0.3
	TIGR2311	249588	0.2 \pm 0.6
	STD66	7128	0.0 \pm 0.3
TERRA-MODIS	TIGR61	6588	-0.1 \pm 0.4
	TIGR1761	190188	0.2 \pm 0.4
	TIGR2311	249588	0.2 \pm 0.6
	STD66	7128	-0.2 \pm 0.4
METOP-AVHRR3	TIGR61	6588	0.0 \pm 0.5
	TIGR1761	190188	0.2 \pm 0.3
	TIGR2311	249588	0.2 \pm 0.6
	STD66	7128	0.0 \pm 0.3
GOES13-IMG	TIGR61	6588	-0.3 \pm 1.1
	TIGR1761	190188	0.0 \pm 0.7
	TIGR2311	249588	0.0 \pm 1.2
	STD66	7128	-0.2 \pm 0.7
MSG2-SEVIRI	TIGR61	6588	-0.1 \pm 0.5
	TIGR1761	190188	0.2 \pm 0.3
	TIGR2311	249588	0.2 \pm 0.6
	STD66	7128	0.0 \pm 0.3

5 CONCLUSIONS

The main advantages of the GAPRI dataset is the complete description about location of the different atmospheric profiles, as well as the date and time when they were selected, covering both land and sea cases (which in turn allows the creation of a GAPRI-land or GAPRI-sea database). Moreover, the atmospheric profiles are converted to MODTRAN format to allow a direct execution of the database in this radiative transfer code. It is also important to note that GAPRI was constructed from an automatic selection implemented in an operational mode, which means that other configuration options can be chosen and adapted to the user requirements.

A web-based interface is foreseen in the future to freely download the GAPRI dataset. In the meanwhile, users interested on using the current GAPRI version (or other modifications on-demand) can contact directly to the authors.

6 ACKNOWLEDGMENTS

This Work is supported by Fondecyt-Initial 11130359 and U-Inicia VID 4/0612. The authors also acknowledge to ECMWF for the free distribution of ERA-interim data.

7 REFERENCES

- Aires, F., Chédin, A., Scott, N. A., and Rossow, W. B. 2002. A regularized neural net approach for retrieval of atmospheric and surface temperatures with the IASI instruments. *J. Appl. Meteorol.* 41(2), 144-159.
- Anderson, G.P., A. Berk, P.K. Acharya, L.S. Bernstein, S.M. Adler-Golden, J. Lee, and L. Muratov, "Reformulated Atmospheric Band Model Method for Modeling Atmospheric Propagation at Arbitrarily Fine Spectral Resolution and Expanded Capabilities," U.S. Patent #7593835, issued September 22, 2009.
- Berk, A. Anderson, G.P., Acharya, P.K., Chetwynd, J.H., Bernstein, L.S., Shettle, E.P., Matthew, M.W. and Adler-Golden, J.H. 1999. MODTRAN4 user's manual. Hanscom AFB, MA: Air Force Research Laboratory.
- Berk, A., G.P. Anderson, P.K. Acharya, L.S. Bernstein, L. Muratov, J. Lee, M. Fox, S.M. Adler-Golden, J.H. Chetwynd, M.L. Hoke, R.B. Lockwood, J.A. Gardner, T.W. Cooley, C.C. Borel, P.E. Lewis and E.P. Shettle, "MODTRAN5: 2006 Update," *Proc. SPIE*, Vol. 6233, 62331F, 2006.
- Dee, F., and Co-authors. 2011. The ERA-interim reanalysis: configuration and performance of the data assimilation system, *QJRM*, 137 (656), 553 – 597.
- François, C., Brisson, A., Le Borgne, L., and Marsouin, A. 2002. Definition of a radiosounding database for sea surface brightness temperature simulations. Application to sea surface temperature retrieval algorithm determination. *Remote Sensing of Environment*, 81, 309-326.
- Galve, J. A., Coll, C., Caselles, V., and Valor, E. 2008. An atmospheric radiosounding database for generating land surface temperature algorithms. *IEEE Transactions on Geoscience and Remote Sensing*, 36, 1113-1126.
- Jiménez-Muñoz, J. C., Cristóbal, J., Sobrino, J. A., Soria, G., Ninyerola, M., & Pons, X. 2009. Revision of the Single-Channel Algorithm for Land Surface Temperature Retrieval From Landsat Thermal-Infrared Data. *IEEE Transactions on Geoscience and Remote Sensing*, 47(1), 339-349.
- Jiménez-Muñoz, J.C. and Sobrino, J.A. 2008. Split-Window Coefficients for Land Surface Temperature Retrieval From Low-Resolution Thermal Infrared Sensors. *IEEE Geoscience and Remote Sensing Letters*, 5(4), pp. 806-809.
- Jiménez-Muñoz, J.C., Sobrino, J.A., Mattar, C. and Franch, B. 2010. Atmospheric correction of optical imagery from MODIS and Reanalysis atmospheric products. *Remote Sensing of Environment*, 144, 2195 – 2210.
- Li, Z.-L., Tang, B.-H., Wu, H., Ren, H., Yan, G., Wan, Z., Trigo, I. F., and Sobrino, J. A. (2013). Satellite-derived land surface temperature: Current status and perspectives. *Remote Sens. Environment*, 131, 14.

Functional attributes of the landscape surrounding the Temelin nuclear power plant (Czech Republic)

Petra Hesslerová, Jan Pokorný

ENKI, o.p.s. Dukelská 145, 379 01 Třeboň, Czech Republic

hesslerova@enki.cz; pokorny@enki.cz

ABSTRACT - The aim of this study is to demonstrate the importance of permanent vegetation in landscape. Indicators of key landscape functions (surface temperature, wetness and biomass content) were monitored from May to September in five catchments with different vegetation cover. The analysis of Landsat data illustrates that areas with a higher proportion of forest and wetlands provide a more balanced temperature-moisture regime throughout the growing season, reduce average and peak temperature, enhance humidity. In these areas, solar radiation is transformed into latent heat which leads to landscape cooling. This process indirectly leads to a reduction of soil erosion, loss of water, oxidation of organic matter and nutrient export. A landscape characterised by a balanced temperature-moisture regime also has a higher ability to bind and retain pollutants. Drainage and loss of natural wetlands are common across most of our agricultural landscape. Drained fields have a low capacity to retain water, nutrients and pollutants. Where crops dominate, the temperature - moisture regime evolves through different stages. With the exception of the early growth, maturity and senescence are characterised by high average and peak temperatures, high temperature variations and low humidity. As illustrated by the relationship existing between water electrical conductivity and cation concentration in relation to land cover, such landscapes have a lowered ability to retain chemical elements and pollutants. The sites that were object of our survey are situated within the emergency planning zone of the Temelín nuclear power plant, in order to demonstrate how our analytical approach may be applied to radiation risk management.

1 INTRODUCTION

Surface temperature is directly related to solar energy dissipation. Moderate surface temperatures and small temperature differences between adjacent sites within the landscape indicate an efficient solar energy distribution mediated by the water cycle. Temperature-balanced ecosystems possess the ability to retain water and nutrients; on the other hand, ecosystems characterised by high average temperatures with high spatial variation and seasonal or daily fluctuations, become easily desiccated and deprived of organic matter and mineral constituents including essential nutrients. In areas with high average temperatures (characterised by the absence of high moisture-dependant vegetation) solar energy is converted into sensible heat, causing the overheating of the soil surface with consequences such as soil drying, increased erosion, increased runoff, higher weathering rates and nutrient loss. Where average surface temperature is lower, this usually indicates the presence of vegetation well stocked with water. In such areas the solar energy is dissipated through water vaporisation. The transformation of solar energy into latent heat reduces the ambient temperature and cools down the landscape. These relations are well known and are supported by a number of field and experimental measurements (Monteith, 1981; Ryszkowski and Kedziora, 1987, 2007; Ripl, 2010; Hesslerová et al., 2013; Pokorný et al., 2010; M.

Eiseltová et al., 2012; Huryna and Pokorný, 2009; Brom et al., 2012).

This study evaluates the efficiency of energy dissipation processes in five different catchments comprised in the emergency planning zone of the Temelín nuclear power plant in southern Bohemia (Czech Republic). The studied catchments are characterised by significant differences in land cover. The evaluation of landscape functional processes is based on the intensive monitoring of surface temperature, humidity, green biomass, and proportion of land cover categories from May to September in different years. A key factor is represented by surface temperature, which is affected by land cover type and by water content. Temperature and humidity vary seasonally and the amplitude of their variation depends on the amount of green biomass. In areas with a heterogeneous landscape cover, with the presence of forest, and with a higher proportion of wet meadows and wetlands, we expect lower surface temperatures, higher humidity, and lower biomass fluctuations between seasons. The assessment is based on Landsat satellite data processing and interpretation.

Long term monitoring carried out in catchments of different land cover composition confirmed a direct effect of permanent vegetation and a balanced surface temperature regime on minimising nutrient and organic matter losses (Procházka et al., 2006, 2009; Ripl, 2003; Hesslerová et al., 2012). The issue concerning water and mineral element retention is highly relevant to sustainable landscape management

but also to radiation risk management and to strategies aimed at reducing population exposure (Fesenko et al., 2007). Our assessment indicates which type of land cover structure favours a balanced temperature and humidity regime which is then reflected in the ecosystem's capacity to retain water, nutrients and pollutants.

2 MODEL AREA, DATA, METHODS

The Temelín nuclear power plant (NPP) is located in the southern Bohemia (Czech Republic), approximately 65 kilometres from the Austrian border. The Emergency Planning Zone (EPZ) is defined by a 13 km diameter circle traced around the NPP. Our model area was selected as a 717 km² rectangle covering the whole EPZ and all five model catchments. Overall, arable land covers 45 %, forests nearly 35 %, pastures and areas which are only partly farmed 13 %, and water bodies not less than 3 % (CORINE Land Cover, 2006). A number of land cover categories were defined as follows:

- **Agriculture/water catchment** (32.17 km²) including 58 % of arable land, nearly 11 % of water bodies, 17% of pastures and heterogeneous agricultural areas; 6 % forest; and 3 % discontinuous urban areas.
- **Agriculture/drained** (6.14 km²) covers the area surrounding the nuclear power plant on south. Drained arable land predominates (58 %), with pastures and heterogeneous agricultural areas covering 33 %, forest 5 %, and water bodies 3 %.
- **Agriculture** (36.1 km²) has the highest proportion of arable land (60 %) and 15.5 % of pastures and heterogeneous agricultural areas; forest covers 21.5 %.
- **Heterogeneous** (18 km²) is characterised by 70 % of forest, completed by a mosaic of pastures and heterogeneous agricultural areas (23 %), transitional woodland-shrub (nearly 3 %) and water bodies 1.3 %; the arable land covers less than 3 %.
- **Forested** (4.5 km²) is covered by 81 % of forest, transitional woodland-shrub (nearly 5 %), arable land (9 %), while pastures and heterogeneous agriculture areas cover less than 5 %.

To characterise landscape functioning at the regional scale, the following spectral parameters were used:

- The relative amount of green biomass, determined on the basis of a spectral NDVI (Normalized Difference Vegetation Index) (Tucker, 1979).
- Relative humidity - evaluated using a NDWI (Normalized Difference Water Index) which is a good predictor of canopy water content and of water present in upper soil layers (Gao, 1996).
- Surface temperature - calculated from the thermal channel TM6 (Sobrino et al., 2005).

Due to the fact that data relative to single month were acquired in different years and under different imaging conditions (atmospheric, seasonality effects, etc.), values were standardized using a standard scores (z-scores) method to make them comparable. The method uses an approach introduced by (Brom et al., 2012). A formula (1) used for data standardization:

$$A_s = \frac{A_i - \bar{A}}{SD} \quad (1)$$

where A_s is a standardized value, A_i is the spectral parameter value (NDVI, NDWI, surface temperature) relative to pixel i , \bar{A} is the mean value of the parameter in the model area, SD is the standard deviation.

The land cover comparison between different catchments was performed as follows:

- The values of the spectral indices NDVI, NDWI and surface temperature were calculated in the model area
- A standardisation of all three parameters was performed. Individually standardized parameters relative to the model area were set equal to zero
- The values of the parameters assessed in individual catchments were retrieved by masking
- The interpretation of the differences between catchments within the model area was based upon time series and box plots representing seasonal changes in the assessment parameter

The spatially averaged standardized value of the parameters NDVI, NDWI and surface temperature was assessed from May to September in each one of the five catchments. The median value was retained as the basic statistical estimate for assessing differences between individual catchments within the model area. Spatial and seasonal variations of the parameters are shown by means of box plots (Fig. 1).

The model area standardized parameter values have by definition a mean equal to 0 and a standard deviation equal to 1. The data range is usually comprised in the range of -3 to 3.

In the assessment catchments, a standardized NDVI value > 0 indicates a higher amount of biomass than the model area mean (and vice versa). Similarly, a standardized NDWI value > 0 indicates less moisture than the model area mean (and vice versa). Finally, a standardized surface temperature index > 0 indicates a higher surface temperature than the model area mean (and vice versa).

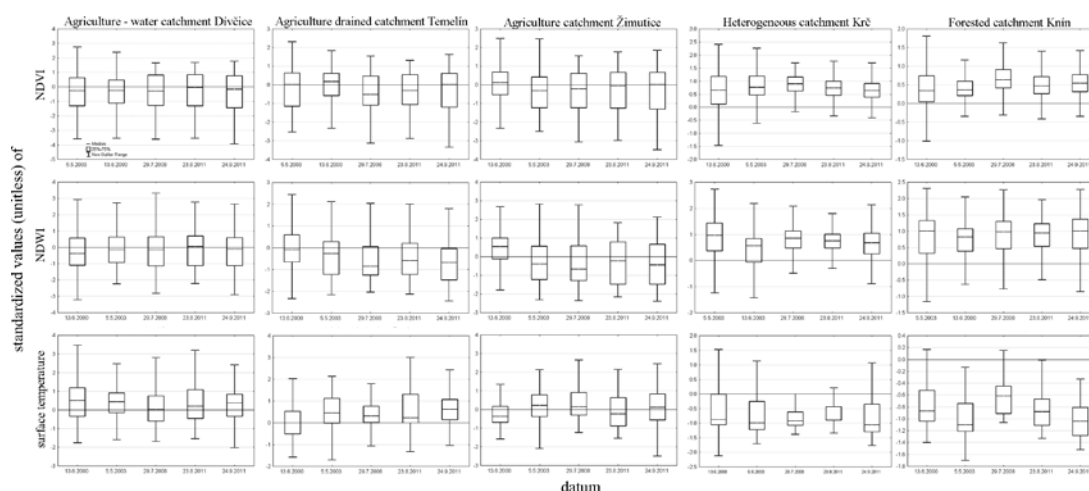


Fig. 1 Seasonal course of standardized values of indices NDVI (correlation with green biomass), NDWI (correlation with liquid water content in vegetation and soil) and surface temperature. The model area has a mean of standardized data equal to 0. Positive standardized values of: NDVI indicate higher amount of green biomass in the catchment than is the standard of model area; NDWI indicate higher moistness; Surface temperature indicate higher surface temperature in the cadastre than is the standard of model area. For negative values the interpretation is reversed.

3 RESULTS

The results are presented in Fig. 1. Three catchments, where arable land accounted for 58 - 60% (agriculture / water, agriculture, agriculture / drained), were characterized by lower than average values of vegetation and moisture indices reflected by higher surface temperature values.

Catchment areas covered by forest and by heterogeneous land cover typically had a large surface covered by permanent biomass well supplied with water throughout the whole season. The values of both spectral vegetation indices were higher than the model area average. This was positively reflected in temperature values which were significantly lower and relatively well seasonally balanced. This is evident especially in the case of heterogeneous catchment areas, where arable land covered < 3 %.

4 DISCUSSION AND CONCLUSIONS

Long term monitoring of three different catchments in the Šumava Mountains in southern Bohemia confirmed the influence of land cover on runoff and on the loss of organic matter and mineral elements (Procházka et al., 2008, 2009). Fifteen years of intensive hydrological and chemical monitoring demonstrated that forested catchments have a balanced outflow and low nutrients and matter losses (indicated by a moderate electrical conductivity of streamwater). Conversely, drained and intensively farmed catchments produced high export flows. The remote sensing of surface temperature using Landsat satellite data also confirmed the relationship between moderate

and balanced temperature with low nutrient and matter losses from forested areas as well as from areas rich in wetlands and in natural permanent vegetation (Hesslerová et al., 2012; Procházka et al., 2006; Bodlák et al., 2012).

Water samples were taken in order to analyze electrical conductivity and K^+ in relation to nutrient and matter losses, as well as to the ability of the territory eventually retain radionuclides (especially ^{137}Cs). As indicative values, samples were collected at 39 sites across the emergency planning zone.

Water conductivity measurements are related to the concentration of dissolved substances and provide an indication of nutrient and matter losses from catchments. The behaviour of radioactive ^{137}Cs is very similar to the behaviour of K^+ . Both cations may interact with the negative charges situated at the surface of soil particles, which determine cation exchange between particles and the solution. Alternatively they may become fixed between the layers of certain minerals - aluminosilicates. A higher fixation potential was observed for Cs^+ than K^+ , because it has a lower energy of hydration. The behaviour of Cs^+ in soils is usually controlled by clay particles. Organic matter contains primarily non-specific sites for the sorption of Cs^+ , which make it readily available to plants. Due to their similar properties and environmental fate, low concentrations of K^+ are also one of the factors that increase the effectiveness of Cs^+ uptake by plants from clay minerals.

It should be expected therefore, that in areas affected by an increased release of K^+ , in case of an accidental radionuclides release from a power plant, one may observe significant radionuclides leaching. This is unlikely to happen in areas where a balanced water cycle regulates matter and energy flows.

Despite irregular water sampling, water conductivity and dissolved cation concentrations indicated that the lowest values were reported from forested areas in southern, South-eastern and North-western parts of the territory surveyed consisting of areas characterized by heterogeneous land cover. Higher values were typical of the areas with a higher proportion of agricultural land, which includes all three model agricultural catchments.

This study shows the relevance of a holistic approach to landscape assessment encompassing energy flow indicators (remotely sensed surface temperature), as well as hydrological and elemental flow analysis indicating the ecosystem's capacity to retain water, nutrients and contaminants/radionuclides. The parallel analysis of surface temperature, humidity and biomass enables the mapping of the areas prone to higher water, matter and nutrient losses and thus to degradation or, on the other hand, areas that are capable to resist to accidental pollution because export flows are naturally buffered.

Where crops (for ex: cereals) predominate, the temperature - moisture regime varies considerably; i.e. it is characterised by high temperatures (both average and peak), high temperature variation amplitude and low humidity. This is true for most of the growing season but not at its beginning when temperature - moisture equilibria are more balanced. However, this period covers only 1-2 months within a year. During the rest of the growing season, at the stage of crops maturity, senescence, or after the harvest which leaves the soil surface barren, farmland is characterised by high surface temperature, similar to urban and industrialised built-up areas. On such surfaces where vegetation is absent and there is a frequent lack of water, solar radiation is converted primarily into sensible heat, which causes the overheating of the soil surface. The protection and the restoration of permanent vegetation and of small-scale water retention structures in the landscape are important tools for sustainable development and management. Conversely, the intensification of agriculture and urbanisation contribute significantly to the disruption of energy flows in the landscape. Drainage, the removal of permanent vegetation forest degradation as well as the decrease of sparse trees and shrubs, wetland drainage, wet meadows and floodplain degradation), the preference for thermophilous cereal crops lead to landscape overheating, its degradation and the decrease of its retention ability.

The study confirmed that a well structured land cover with a significant proportion of permanent

vegetation is an ideal tool for the mitigation of temperature and temperature differences within the landscape. A balanced flow of energy and matter mediated by the water cycle is essential to ensure good pollutant retention and therefore to lower the potential of exposing resident populations to harmful toxicants such as accidentally released radionuclides.

ACKNOWLEDGEMENTS

This paper was supported by The Ministry of Education, Youth and Sports of the Czech Republic through the programme: „The latest remote sensing technologies in the service of research, education and applications for regional development“ CZ.1.07/2.4.00/31.0213, and The Ministry of Interior of the Czech Republic with its programme: “Minimising the impact of landscape contamination by radiations in the emergency zone of nuclear power plant Temelín VG20122015100”.

REFERENCES

- Bodlák, L., Křováková, K., Nedbal, V. and Pechar, L., 2012, Assessment of Landscape Functionality Changes as One Aspect of Reclamation Quality – the Case of Velká Podkrušnohorská Dump, Czech Republic. *Ecological Engineering*, 43, 19–25.
- Brom, J., Nedbal, V., Procházka, J. and Pecharová, E., 2012, Changes in Vegetation Cover, Moisture Properties and Surface Temperature of a Brown Coal Dump from 1984 to 2009 Using Satellite Data Analysis. *Ecological Engineering*, 43, 45–52.
- Eiseltová, M., Pokorný, J., Hesslerová, P. and Ripl, W., 2012, Evapotranspiration – A Driving Force in Landscape Sustainability. In *Evapotranspiration - Remote Sensing and Modeling*, 305–28. InTech.
- Fesenko, S.V., Alexakhin, R.M., Balonov, M.I., Bogdevitch, I.M., Howard, B.J., Kashparov, V.A., Sanzharova, N.I., Panov, A.V., Voigt, G. and Zhuchenka, Y.M., 2007, An Extended Critical Review of Twenty Years of Countermeasures Used in Agriculture after the Chernobyl Accident. *Science of the Total Environment*, 383, 1–24.
- Gao, B., 1996, A Normalized Difference Water Index for Remote Sensing of Vegetation Liquid Water from Space. *Remote Sensing of Environment*, 58(3), 257–66.
- Hesslerová, P., Chmelová, I., Pokorný, J., Šulcová, J., Kröpfelová, L. and Pechar, L., 2012, Surface Temperature and Hydrochemistry as Indicators of Land Cover Functions. *Ecological Engineering*, 49, 146–52.
- Hesslerová, P., Pokorný, J., Brom, J. and Rejšková - Procházková, A., 2013, Daily Dynamics of Radiation Surface Temperature of Different Land Cover Types in a Temperate Cultural Landscape:

- Consequences for the Local Climate. *Ecological Engineering*, 54, 145–54.
- Huryna, H., and Pokorný, J., 2009, Comparison of Reflected Solar Radiation, Air Temperature and Relative Air Humidity in Different Ecosystems. In *Water and Nutrient Management in Natural and Constructed Wetlands*, edited by Jan Vymazal, 309–26. New York: Springer.
- Monteith, J.L., 1981, 'Evaporation and Surface Temperature'. *Quarterly Journal of the Royal Meteorological Society*, 107, 1–27.
- Pokorný, J., Brom, J., Čermák, J., Hesslerová, P., Huryna, H., Nadezhdina, N. and Rejšková, A., 2010, How Water and Vegetation Control Solar Energy Fluxes and Landscape Heat. *International Journal of Water*, 5(4), 311–36.
- Procházka, J., Brom, B. and Pechar, L., 2009, The Comparison of Water and Matter Flows in Three Small Catchments in the Šumava Mountains. *Soil and Water Research* 2, 4 (2), S75–82.
- Procházka, J., Brom, J., Pechar, L., Štíhová, J. and Pokorný, J., 2008, Changes in Concentrations of Dissolved Solids in Precipitation and Discharged Water from Drained Pasture, Natural Wetland and Spruce Forest During 1999–2006 in Šumava Mountains, Czech Republic. In *Wastewater Treatment, Plant Dynamics and Management in Constructed and Natural Wetlands*, edited by Jan Vymazal, 39–51. New York: Springer.
- Procházka, J., Včelák, V., Wotavová, K., Štíhová, J., and Pechar, L., 2006, Holistic Concept of Landscape Assessment: Case Study of Three Small Catchments in the Šumava Mountains. *Ekológia (Bratislava)*, 25(3), 5–17.
- Ripl, W., 2003, Water: The Bloodstream of the Biosphere. *Philosophical Transactions of the Royal Society B*, 358, 1921–34.
- Ripl, W., 2010, Loosing Fertile Matter to the Sea: How Landscape Entropy Affects Climate. *International Journal of Water*, 5(4), 353–64.
- Ryszkowski, L., and Kedziora, A., 1987, Impact of Agricultural Landscape Structure on Energy Flow and Water Cycling. *Landscape Ecology*, 1, 85–94.
- Ryszkowski, L., and Kedziora, A., 2007, Modification of Water Flows and Nitrogen Fluxes by Shelterbelts. *Ecological Engineering*, 29, 388–400.
- Sobrino, J.A., Jiménez-Muñoz, J.C. and Paolini, L., 2005, Land Surface Temperature Retrieval from LANDSAT TM 5. *Remote Sensing of Environment*, 90, 434–40.
- Tucker, C.J., 1979, Red and Photographic Infrared Linear Combinations for Monitoring Vegetation. *Remote Sensing of Environment*, 8, 127–50.

Bio-optical modelling to monitor submerged coastal vegetation

N. Oppelt, K. Dörnhöfer, F. Uhl

Kiel University, Dept. for Geography

oppelt@geographie.uni-kiel.de, doernhoefer@geographie.uni-kiel.de, uhl@geographie.uni-kiel.de

ABSTRACT - Hyperspectral sensors enable the detection of local absorption features of pigments and increased the number of possibilities to determine these features. This led to growing research interest to identify and monitor coastal vegetation using hyperspectral sensors. In this paper we discuss the performance of the bio-optical model WASI-2D to assess the distribution of sublittoral vegetation at the rocky shores of Helgoland (North Sea, Germany). In August 2010, an airborne flight campaign was conducted using the hyperspectral AISA_{eagle+} sensor. WASI originally was optimized for application in lakes; therefore we optimised its parameterisation for coastal waters. WASI-2D was able to derive plausible patterns of coverage fractions of vegetation and non-vegetated sediment. Problems occurred during quantitative accuracy assessment. The limited spatial accuracy of in situ kelp mappings (25 m) as well as its semi-quantitative performance prevented a successful quantitative accuracy assessment. Since sublittoral mapping is extremely difficult to obtain, a discussion about standards for accuracy assessment in the coastal zone is needed.

1 INTRODUCTION

In recent years, programmes such as the European Water Framework Directive or Marine Strategy Framework Directive have increasingly drawn public attention to coastal areas; they are important ecosystems offering wildlife habitat and tourist destinations, as well as functioning as important nutrient cycling capacity for maintaining water quality. According to the Marine Strategy Framework Directive, major threats to coastal ecosystems are climate change and entailing effects such as sea level rise as well as shifts and changes in flora and fauna. Information on the type and distribution of marine vegetation therefore is necessary for monitoring, management and understanding of coastal ecosystems.

While various attempts exist to monitor intertidal vegetation (e.g. Barillé et al., 2010, Godet et al., 2009, Oppelt et al., 2012, van der Waal et al., 2010), applications to quantitatively monitor the sublittoral vegetation are limited. To gather information about the bottom substrate in shallow waters bio-optical models can be applied. Applying these models, we gain insight into the habitat quality of shallow water bodies via assessing and monitoring bottom substrate. In the last decade bio-optical models such as WASI (Gege, 2004) or BOMBER (Giardino et al. 2012) became available. Just recently, a two-dimensional version of WASI has been published (Gege, 2014a). To analyse its potential for assessing sublittoral marine vegetation, we adapted WASI-2D to the coastal waters of Helgoland to assess the distribution of sublittoral vegetation.

2 STUDY AREA AND METHODOLOGY

2.1 Study area

The study was carried out in the sublittoral zone around the small archipelago Helgoland (North Sea; N 54°11', E 7°53', Figure 1). Semidiurnal tides with an approximate range of 2-3 m and turbid waters characterize the area around the rocky western main island and the "Düne" forming the archipelago. A small annual temperature range (annual mean = 9.8 °C) and evenly dispersed precipitation throughout the year (annual sum = 719 mm) characterise the maritime climate (German Weather Service). The mean water surface temperature is 10°C varying between 2 °C and 18 °C (Wiltshire and Manly, 2004). The study was carried out in water depths between 0.1 m and 5 m, the latter corresponding to Secchi depths measured during airborne data acquisition.

In this area sea floor is an eroded, rocky terrace, based on a tilted, red (Triassic) sandstone formation alternating with chalk and limestone resulting in a rugged terrain. Brown (e. g. *Fucus serratus*), red (e. g. *Mastocarpus stellatus*, *Chondrus crispus*) and green macroalgae (e. g. *Cladophora rupestris* and *Ulva* ssp.) dominate in the upper intertidal zone. Dense stands of large brown macroalgae, also known as kelp, predominate the subtidal waters: Mixed stands of *Fucus serratus*/*Laminaria digitata* grow around mean low water spring tide (MLWS). *Laminaria digitata* dominate between 0.7 m above and 0.9 m below (MLWS); *Laminaria hyperborea* form dense beds in the upper sublittoral below 1m, but can be found in water depths of up to 10 m (Pehlke and Bartsch, 2008). For this study we therefore focus on species of

the *Laminariales* order; they form dense stands covering the elevated ribs and rocky substrate, while avoiding the soft substrate at the north-eastern shore of the Düne and sediment which accumulates in the narrow channels.

2.2 AISA_{eagle+} data

An airborne hyperspectral AISA_{eagle+} sensor was used to acquire remote sensing data. AISA_{eagle+} is a CCD based imaging system consisting of a spectrograph, a global positioning system/inertia measurement unit (GPS/INS), a fibre optic downwelling irradiance system (FODIS), and a PC for data storage and display (SPECIM Images Ltd., 2011).

The system collected 122 spectral bands between 400 and 970 nm with an average spectral sampling rate of 4.6 nm. The aperture angle of the optical system was 0.7 mrad; the integration time was 74 ms and the swath width 512 pixels. The system was mounted on a Condor Stemme S10 motor glider flying at an altitude of 2000 m above sea level with a speed of 31 m/s. According to this setup, pixel spacing was 2.38 m along track and 2.89 m across track.

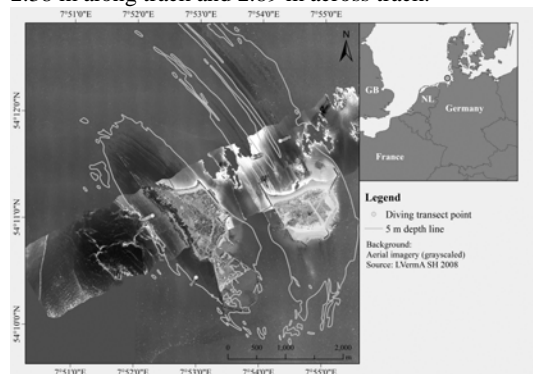


Figure 1. Test area Helgoland (upper right map) and location of AISA_{eagle} flight stripe and corresponding diving transects.

Pre-processing included radiometric calibration, atmospheric correction and masking, geometric correction, and cloud shadow masking. Radiometric calibration, using CaliGeoPro, included a correction of the sensor's dark current and homogeneity. Subsequent calibration to subsurface irradiance reflectance was conducted with the Modular Inversion Program MIP (Heege et al., 2004) and validated using tec5 HandySpec field spectra (spectral range: 350-900 nm, spectral sampling: 3 nm) collected simultaneously to the AISA overflight. Before atmospheric correction of the sublittoral waters, land surfaces including dried up intertidal pixels were masked. Cloud shadows were present over the shallow water regions and were masked as well applying the Cloud Shadow Detection Index (CSDI) method (Amin et al., 2013). Geometric

processing was conducted using CaliGeoPro involving the GPS/INS data acquired for each image line during data recording. Afterwards, we resampled image data to a pixel spacing of 2 x 2 m applying the nearest neighbour approach. For this study we use one flight stripe covering parts of the western and northern coastal waters of the main island, the northern sandy shores of the Düne (Figure 1).

2.3 Field survey

To provide validation data, divers conducted mappings covering the main growing areas around the islands. Data were collected along transects with a distance of 6 m between the measurement points. Measurements included the acquisition of percentage cover of brown algae and sediment using a semi-quantitative approach including six coverage classes, which afterwards are modified to 21 coverage classes as described by Pehlke and Bartsch (2008). At each measurement point bathymetry was measured using a digital depth gauge (Seemann Sub; precision: 40 cm). To locate measurement points a Magellan GPS 320 was installed on a buoy which also was attached to one of the divers. The resulting spatial accuracy of the mapping ranges about 25 m (Pehlke and Bartsch, 2008).

2.4 The bio-optical model WASI

Bio-optical models account for the attenuation of the water column, absorption and scattering by apparent and inherent optical properties, the reflectance of the bottom and influence of water depth. WASI-2D (Gege, 2014a) is a new module of the **water color simulator** (WASI; Gege, 2004) which enables processing of two-dimensional data. Therefore WASI-2D can be applied for analysing water bodies in remotely sensed imagery (e.g. remote sensing reflectance (R_{rs}), upwelling radiance). It includes several models to simulate the radiative transfer in the water body; in this study remote sensing reflectance R_{rs} is modelled following a method described by Albert and Mobley (2003). In shallow waters, bottom depth, bottom substrate, and the attenuation coefficients for downwelling and upwelling radiance in the water body are main coefficients to calculate R_{rs} as a function of the sun zenith angle, viewing direction and the concentrations of water constituents using equations derived by Albert (2004). In shallow waters inverting the model allows to generate maps of water constituents, bottom depth and up to six substrate classes.

WASI requires various input data including information on illumination and observation geometry, inherent and apparent optical properties of the water body and physical variables and constants; for an overview it is referred to Gege (2014b). Pre-defined parameterization of the water body, however, has been adapted to fresh water bodies, in particular to Lake

Constance. To optimize the model for our study site, we adapted some of the constant parameters; Table 1 lists constant parameters which were modified.

Table 1. Constant parameters modified to adapt WASI to coastal waters

Parameter	Unit	Value	Source
Backscattering coefficient b_{bw}	m^{-1} at 500 nm	0.00144	Morel (1974)
Chl-a	$\mu g l^{-1}$	2.000	<i>In situ</i>
SPM	$mg l^{-1}$	1.600	<i>In situ</i>
$Y_{(ay440nm)}$	m^{-1}	0.273	<i>In situ</i>
T_w	$^{\circ}C$	17.0	<i>In situ</i>
Diatoms	$\mu g l^{-1}$	0.30	<i>In situ</i>
Bottom reflectance	sr^{-1}	-	<i>In situ</i>

We changed the backscattering coefficient to a value corresponding to sea water (35 – 38 ‰ salinity; Morel, 1974). The hydro-chemical and biological components of the water body were defined according to *in situ* measurements during the AISA_{eagle+} overflight and data from the Helgoland Road, a time series of daily measurements of various water parameters including phytoplankton (Wiltshire 2012) and water temperature (T_w). According to Wiltshire (2011 and 2012) and Scharfe (2013) flagellates and, to a lesser degree, diatoms influence the microalgal community in the waters around Helgoland; therefore were implemented both as major phytoplankton types. Since the concentration of flagellates strongly varies in time (Wiltshire et al., 2010) and space (Scharfe, 2013), we selected the concentration of flagellates as a fit parameter, whereas concentration of diatoms was set as a constant value.

Table 2. Ranges and initialization of fit parameters

Parameter	Unit	Start	Min	Max
<i>Laminariales</i>	Coverage	0.694	0.0	1.0
Sediment	Coverage	0.188	0.0	1.0
BOB	M	1.100	0.1	5.0
Flagellates	$\mu g/l$	1.990	0.0	60

WASI provides a number of options for fine-tuning the inversion algorithm to known peculiarities of their dataset and to optimize processing for certain parameters of interest (Gege, 2014b), i.e. fit parameters are parameters which may vary within the scene. Due to the rugged terrain we therefore selected bathymetry as a second fit parameter (Table 2).

In WASI bottom reflectance is implemented for mixtures of different substrates each being characterized by a reflectance spectrum. In shallow waters, the influence of the bottom is modelled as a weighted sum of R_{rs} spectra representing the different

substrate types within a pixel. The weights are the products of the aerial fractions of the substrates and the fraction of radiation reflected in the direction of the sensor. WASI provides a database including spectra from German lakes (Gege, 2014a); to adapt WASI to the study area we therefore implemented reflectance spectra for *Laminariales* and sediment obtained in laboratory using an ASD field spectrometer (Analytical Spectral Devices, 2008).

WASI varies fit parameters within defined ranges (Table 2). For parameter fitting a downhill simplex algorithm is implemented; it converges towards a (local) minimum residuum which indicates the best match of all fit parameters. However, it may occur that no parameter set can be calculated which match the fit-parameters within a given maximum residuum R_{max} . To prevent the inversion algorithm from being trapped in an endless loop, a further parameter, i.e. the upper limit of iterations N_{max} is set to 1500. The simulation stops if N_{max} or R_{max} occur; in this study we selected the residual threshold between modelled and measured spectrum $R_{max} = 0.0001$. The spatial output includes maps of both fit parameters and fit criterions.

3 RESULTS AND DISCUSSION

Each pixel of the atmospherically corrected AISA image was inverted according to the methods described above. Figure 2 shows the numbers of iterations required and the resulting residuals. A high number of pixels with low residuals and a low amount of pixels with maximum number of iterations required indicate a good fit quality.

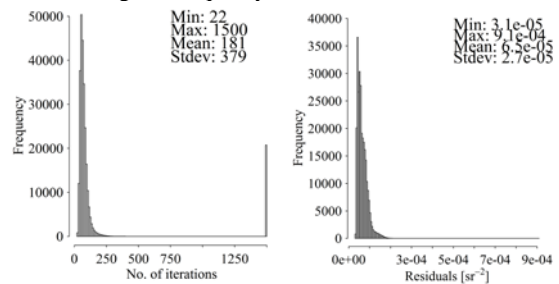


Figure 2. Numbers of iterations required (left) and residuals obtained for parameter fitting (right).

The concentration of flagellates varied within the pre-defined minimum and maximum values of 0 and 30 $\mu g/l$ with a mean value of 2.83 $\mu g/l$ and a standard deviation of 2.26 $\mu g/l$. Since the data from Helgoland Road have been used to define the boundary concentrations, using these values for validation of results should be avoided. In densely vegetated areas such as this study site, quantitative accuracy assessment using WASI bathymetry (Figure 3) is also unfeasible. WASI bathymetry mainly refers to the distance between the water surface and the main

scattering surface in the water column, which in our study site is the top of kelp canopy (Dörnhöfer and Oppelt, 2014); kelp thalli grow up to 5 m in length and form dense beds with a top of canopy between sea floor and water surface. Resulting absolute bathymetry values are reasonably lower than *in situ* measurements or official bathymetric maps. To avoid confusion we therefore refer to the modelled WASI bathymetry as bio-optical bathymetry.

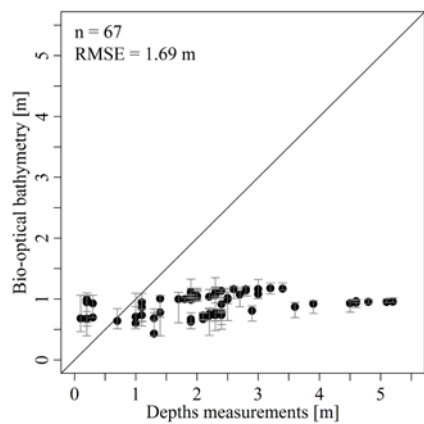


Figure 3. Scatterplot of mapped and modelled bathymetry; vertical bars indicate the range of modelled values within a 25 m area surrounding an *in situ* measurement point.

Taking into account the results of the diving mapping, analysis of fraction coverages of bottom substrates is practical for quantitative accuracy assessment. Figure 4 presents the spatial distribution of kelp and sediment as modelled with WASI-2D. The scatterplots of mapped and modelled bottom fractions

are given in Figure 5. Spatial patterns of kelp and sediment show plausible patterns with dense kelp beds in the western and northern rocky sublittoral of the main island; *Laminariales* also grow densely in the creeks of the tilted sandstone formation north of the Düne. The subtidal area North-East of the Düne is covered with sandy sediment and therefore kelp is missing. When looking at the scatterplots of mapped and calculated (modelled) coverage fractions (Figure 5), the results appear less promising.

In this context, however, the design of the *in situ* measurements may be more important than the WASI results. First, the diving mappings bear a high spatial inaccuracy (see also vertical bars in Figure 5). Second, the coarse coverage classes obtained from the diving mappings and their further modification into 21 final coverage classes appears to be a qualitative sampling which may be strongly affected by subjective. We therefore assume that also the diving data are insufficient to quantitatively validate the WASI results. These problems, in combination with WASI miscalculations, led to a low actual accuracy of the model represented by high root mean square errors (RMSE).

Diving mappings are time and cost intensive; moreover, they are extremely difficult to perform. To gain a higher usability of this kind of data we therefore need to discuss both performance of sublittoral *in situ* measurements and standards of current accuracy assessment procedures. An accuracy assessment optimised for coastal waters would be highly valuable. Nevertheless, low residuals indicate that WASI-2D fitted spectra with good quality underpinning its high potential even in the turbid waters in the German Bight.

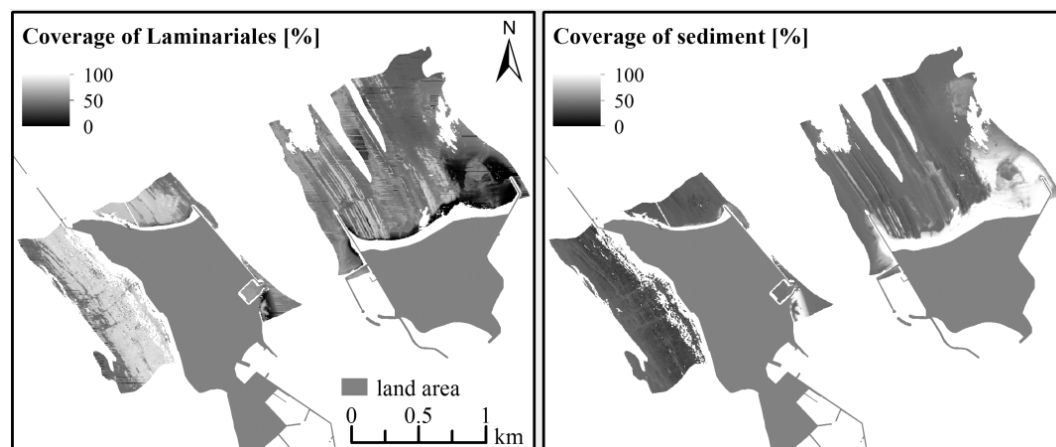


Figure 4. WASI results: coverage fractions of *Laminariales* (kelp) and sediment. Dried-up, intertidal areas and water depths > 5 m were masked.

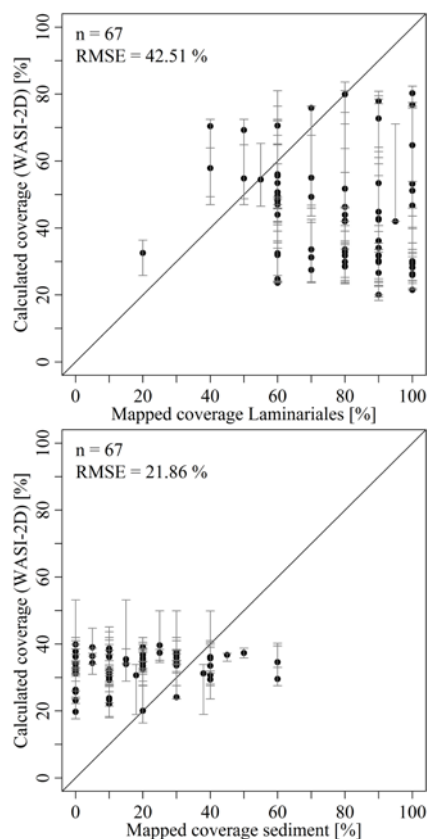


Figure 5. Scatterplots of mapped and modelled cover fractions of kelp (top) and sediment (bottom); vertical bars indicate the range of modelled coverage values within a 25 m buffer surrounding an *in situ* measurement point.

5 ACKNOWLEDGEMENTS

The authors would like to thank the German Federal Ministry for Technology and Economics for funding the project “Development of an EnMAP-based approach to assess sublittoral marine macroalgae (KelpMap)”. The airborne image acquisition and data processing was partly funded by the European Fond for Regional Development within the project “Flexihyp”. We gratefully acknowledge Franziska Nehring, Frederic Tardek (FIELAX GmbH) and EOMAP GmbH for processing the AISA data.

6 REFERENCES

- Albert, A., 2004, Inversion technique for optical remote sensing in shallow water. Ph.D. Dissertation, Universität Hamburg, Germany, 188 pp.
- Albert, A., and Mobley, C., 2003, An analytical model for subsurface irradiance and remote

- sensing reflectance in deep and shallow case-2 waters, *Optics Express*, **11**(22), 2873–2890.
- Analytical Spectral Devices Ltd., 2008, LabSpec User Manual, Boulder, Co, <http://support.asdi.com/Document/Viewer.aspx?id=41> (accessed 12.06.13).
- Barillé, L., Robin, M., Harin, N., Bargain, A., Launeau, P., 2010, Increase in seagrass distribution at Bourgneuf Bay (France) detected by spatial remote sensing, *Aquatic Botany*, **92**(3), 185–194.
- Amin, R., Gould, R., Hou, W., Arnone, R., and Zhongping, L., 2013, Optical Algorithm for Cloud Shadow Detection over Water, *IEEE Transactions on Geoscience and Remote Sensing*, **51**, 732–741.
- Dörnhöfer, K., Oppelt, N., 2014, Mapping benthic substrate coverage and bathymetry using bio-optical modelling – an EnMAP case study in the coastal waters of Helgoland, Proc. of the 6th Workshop on Hyperspectral Image and Signal processing (24–27 June, Lausanne (CH)), forthcoming.
- Godet, L., Fournier, J., Toupoint, N., Olivier, F., 2009, Mapping and monitoring intertidal benthic habitats: a review of techniques and a proposal for a new visual methodology for the European coasts. *Progress in Physical Geography* **33**(3), 378–402.
- Gege, P., 2004, The water color simulator WASI: an integrating software tool for analysis and simulation of optical in situ spectra, *Computers & Geosciences*, **30**(5), 523–532.
- Gege, P., 2014a, WASI-2D: A software tool for regionally optimized analysis of imaging spectrometer data from deep and shallow waters, *Computers & Geosciences*, **62**, 208–215.
- Gege, P., 2014b, The Water Colour Simulator WASI – User manual for version 4, DLR, 2014, Downloadable at the International Ocean Colour Consulting Group (IOCCG) web site <http://ioccg.or/data/software.html>.
- German Weather Service (DWD), “Langjährige Mittelwerte: 1961–1990 (in German)“.
- Giardino, C., Candiani, G., Bresciani, M., Lee, J., Gagliano, S., and Pepe, M., 2012, Bomber: A tool for estimating water quality and bottom properties from remote sensing images, *Computers & Geosciences*, **45**, 313–318.
- Heege, T., Häse, C., Bogner, A., and Pinnel, N., 2004, Physikalisch basierte Prozessierung multi-spektraler Fernerkundungsdaten von Binnengewässern. *Laufener Seminararbeit*, **2**, 67–71.
- Morel, A., 1974, Optical properties of pure water and pure sea water. In: Jerlov, N., Steeman Nielsen,

- E. (eds), *Optical Aspects of Oceanography*, Acad. Press London, 1-24.
- Oppelt, N., Schulze, F., Bartsch, I., Dörnhöfer, K. and Eisenhardt, I., 2012. Hyperspectral classification approaches for intertidal macroalgae habitat mapping: a case study in Helgoland, *Optical Engineering*, **51**(11), 111703.
- Pehlke, C., and Bartsch, I., 2008, Changes in depth distribution and biomass of sublittoral seaweeds at Helgoland (North Sea) between 1970 and 2005, *Climate Research*, **37**(2-3), 135–147.
- Scharfe, M., 2013, Analyse biologischer Langzeitveränderungen auf Basis hydroklimatischer Parameter in der südlichen Nordsee (Helgoland). PhD thesis, Hamburg University, Faculty for Geosciences, <http://ediss.sub.uni-hamburg.de/volltexte/2013/6250/pdf/Dissertation.pdf>, 105p.
- SPECIM Images Ltd., 2011, AISA Eagle hyperspectral sensor, http://www.specim.fi/files/pdf/aisa/datasheets/AisaEAGLE_datasheet_ver2-2012.pdf.
- Wiltshire, K.H., and Manly, B.F.J., 2004, The warming trend at Helgoland roads, North Sea: phytoplankton response, *Helgoland Marine Research*, **58**(4), 269–273.
- Wiltshire, K.H., Kraberg, A., Bartsch, I., Boersma, M., Franke, H.D., Freund, J., Gebühr, C., Gerdt, G., Stockmann, K., Wichels, A., 2010, Helgoland Roads, North Sea: 45 years of change. *Estuaries and Coasts*, **33**, 295-310.
- Wiltshire, K.H., 2011, Hydrochemistry at the time series station Helgoland Roads in 2010. *Alfred Wegener Institute for Polar and Marine Research*, Biological Institute Helgoland, doi:10.1594/PANGAEA.756613.
- Wiltshire, K.H., 2012, Total biovolume of phytoplankton at time series station Helgoland Roads in 2010. *Alfred Wegener Institute for Polar and Marine Research*, Biological Institute Helgoland, doi:10.1594/PANGAEA.783563.
- van der Wal, D., Wielemaker-van den Dool, A., Herman, P. J., 2010, Spatial Synchrony in Intertidal Benthic Algal Biomass in Temperate Coastal and Estuarine Ecosystems. *Ecosystems* **13**(2), 338-351.

Quantify the impact of cloud cover on radiation fluxes ground measurements from hemispherical images

L. Roupioz ^{a,b,c}, J. Colin ^a, L. Jia ^b, F. Nerry ^a, and M. Menenti ^c

^a ICube lab., UMR 7357 CNRS-U. Strasbourg, France

^b Alterra, Wageningen University and Research, Wageningen, The Netherlands

^c Faculty of Aerospace Engineering, TU Delft, Delft, The Netherlands

lroupioz@unistra.fr

ABSTRACT - Cloudy skies remain a challenge when quantifying solar radiation at the ground. From this observation, a fieldwork campaign has been set up in order to collect data about cloud cover conditions and daily evolution to directly analyse their impacts on solar radiation fluxes. To do so daytime hemispherical images have been collected at a very high frequency simultaneously to ground measurements of solar radiation fluxes in a scientific station close to the NamCo lake, China. After calibration, one of the main tasks was the classification of those hemispherical images and the extraction of meaningful indices to describe the cloud cover, such as cloud fraction or cloud cover distribution. The classification is based on automatic detection of threshold on the red band histogram. The results show that several cloud indices could be successfully derived from the hemispherical images even if very thin clouds can be difficult to detect. The indices are then correlated to the measured solar radiation values and the impact of cloud cover on surface radiation fluxes have been analysed. This analysis highlights that, more than the cloud fraction, the cloud distribution in the hemisphere was of importance when modelling radiation fluxes in the solar domain.

1 INTRODUCTION

Due to its location along with its geomorphological and physical characteristics, the Tibetan Plateau plays a major role in the hydrology and the climate scheme of the whole Asia. In the current context of climate change, estimations of surface radiation fluxes at fine spatial and temporal resolution are essential to understand and model convective exchanges in the troposphere and their evolution. The cloud coverage is a fundamental parameter influencing the radiation fluxes at the ground. Scattered cloud coverage can significantly impact the partitioning between direct and diffuse radiation, but also on the incoming infrared radiative forcing (Cess, 1995). Cloud cover is however poorly documented in operational weather stations. A common numerical representation of cloud cover is the octa, which is derived from visual observation from experimented operators. This index gives very little time granularity (usually one instantaneous observation, hourly), and no guarantee that such observations can be repeated from an operator or station to another (WWRP report, 2012). Dedicated commercial sensors have been designed in this scope, but remain expensive. This study is presenting an operational approach to capture short term variation of the cloud cover from a simple combination of hardware, and to record numerical information on cloud distribution. A result obtained from an experiment performed on the Tibetan Plateau illustrates the flexibility and reliability of the proposed setup and image processing approach for operational

or intensive observation. These observations are used to illustrate and analyse the impact of cloud cover on radiation fluxes measured at the ground.

First, the study area and the optical setup used for the data collection are presented. Then, the image classification and cloud indices extraction processes are developed followed by some results, conclusions and perspectives.

2 STUDY AREA AND DATA

2.1 Study area

The high temporal frequency hemispherical images have been collected during daytime, simultaneously to ground radiation fluxes measurements at the meteorological station of NamCo (30.46°N /90.57°E, 4730 m), located the South bank of the NamCo lake, 200 km North from Lhasa.

2.2 Data collection

The instrumental setup is composed of a standard reflex CCD camera, with two optical lenses: an 18 mm focal lens and a fisheye lens with a view angle of nearly 175°. A remote control is used to automate image acquisition at constant time step, a camera specific adapter ensures continuous power supply, and the whole system is conditioned in a weatherproof box with a glass hemisphere.

2.2 Data calibration

Prior to the processing of the images, a geometrical calibration of the whole system is performed to define

polar coordinates of each pixel. The methodology used here follows the one presented in the CAN-EYE user manual (2010). A polynomial fitting is then obtained to convert from pixel to polar coordinates. In the later text, azimuthal angles are expressed as such that 0° is north, and zenith angles are expressed as such that nadir is 0° , while elevation is expressed as 90 minus the zenith angle. It should be noted that geometrical and chromatic aberrations become significant for boundary pixels. Therefore, pixels corresponding to zenith angles larger than 75° are neglected in the later study. Other chromatic aberrations may also occur depending on the quality of the hemispheric glass protecting the lens, leading to small prism effects under direct solar radiation.

2.2 Ground measurements

Longwave and shortwave radiation fluxes are collected at the ground using a Kipp & Zonen CNR1 sensor combining two pyranometers and two pyrgeometers back to back, recording the four components of the radiative balance at a 10 min time step.

3 METHODOLOGY

The first step of the presented methodology is to classify the pixels of the hemispherical images as clear sky or clouds and then, integrating the calibration function, to extract the indices characterizing the cloud cover (Figure 1).

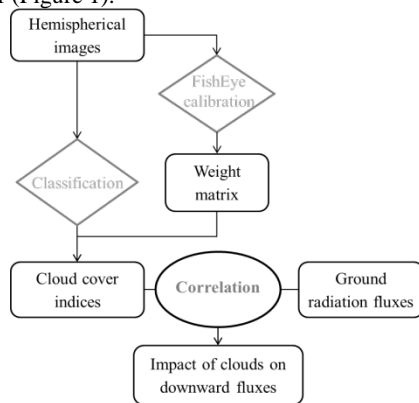


Figure 1: Hemispherical processing steps

3.1 Image classification

The processing sequence for the image classification phase is as follow:

1. Separation of the image pixels in two populations: within or outside of the sunspot;
2. Preprocessing of a band or combination of bands as an input for classification;
3. Classification of each population in either clear sky (0) or clouds (1);

Hiding the sunspot from the view of the camera using a belt or ball requires dedicated hardware and leads to lost pixels (Long, 2006). Here the sunspot is part of the image. Whether the sun is visible or not, the distribution of pixel values for a band or combination of band will strongly vary. Despite direct exposure to the sun, the CCD only saturates in the sunspot, and the overall image dynamic is preserved. However, as suggested by Calbò (2007), separating pixels in two populations according to the distance to sun centre improves classification results. Hence the exact sun location is computed from the location of the camera and the timestamp of a given image extracted from the EXIF meta-data. The diameter of the sunspot is fixed and slightly larger than the actual one to compensate for errors due to: 1. uncertainties in the horizontality and orientation of the instrument; 2. uncertainty in the timestamp provided by the camera clock, while limited when synchronized with a GPS clock. The pixels included in the sunspot are classified separately.

To find the most suitable approach for the cloud classification, several techniques found in the literature were tested. The most commonly used index to detect cloud is red over blue ratio (Shield, 2013). Some studies also suggest to use the red band (Ferreira, 2010), a normalized sky index (Yoshimura, 2013) or the red minus blue difference (Heinle, 2010). The conversion of the original image from the RGB to HSV colour space are also suggested by Martins et al. (2003) and Souza-Echer et al. (2006), since the saturation layer can help to discriminate between open sky and cloudy pixels. A preliminary analysis on a variety of cloud coverage situations shows that, with the CCD used for this study: 1. the red band usually provide most of the information as compared to red on blue indexes; 2. the saturation layer usually gives similar results as the red band, while requesting additional processing. In the later study, the red band is used after stretching the histogram and normalizing values. A gamma correction didn't prove to enhance the band contrast and is not used here.

The classification of images between clear sky and cloud pixels can be performed using either supervised or unsupervised classification approaches. An initial study with a large variety of images taken under different cloud cover and lighting conditions showed that: 1. a bi- or multi-modal distribution can usually be identified on a band or index; 2. a fixed threshold between open sky and cloud populations can give acceptable results for scattered sky conditions (its value is camera specific though); 3. a fix threshold doesn't give any good results for overcast sky or mixing of low and high clouds (e.g. cumulus and fuzzy cirrus). Moreover, a supervised approach can hardly be considered operational. Unsupervised classification approaches are used in some studies, i.e.

ANN (Cazorla, 2008). Considering our target acquisition frequency (one image every 10 to 30 seconds), the computation time has to be accounted for. Therefore, a simple histogram based classification is used. The detection of the modes in the distribution and identification of the local minimum between two modes is implemented, and combined with two validity ranges for the sunspot and the remaining sky.

The same classification method is applied to the pixels located within the sunspot but in that case the decision of the classification will classify all those pixels as clear or cloudy, providing information concerning the visibility of the sun.

3.2 Cloud cover indices

Once the hemispherical images are classified, it is possible to derive several indices in order to describe the cloud cover. Two types of indices can be derived: i. the indices that will be already usable products as such for other applications and ii. And indices that would be potentially useful to correlate with ground measurements to analyse the impact of cloud cover on radiation fluxes.

As output of the classification, two indices have been extracted:

- Cloud fraction
- Cloud distribution

In this study, several ways to calculate the cloud fraction have been experimented. The first one is the most used cloud fraction which corresponds to the total number of cloudy pixels divided by the total number of pixels, including the pixels within the sunspot (CF). The same total cloud fraction has been calculated but excluding the pixel within the sunspot (CF no sunspot). Another cloud fraction was calculated integrating a weight factor according to the distance of the clouds from the sunspot (CF Sun). In that case the closer the cloudy pixels are from the sunspot the higher weight value they have. A similar cloud fraction has been computed but weighted according to the distance to the nadir (CF Nadir). All those cloud fractions are accounting for the fisheye distortions

The indices to be correlated with the ground measurements have been selected on the basis of existing literature (Fu, 2013, Pfister, 2003) and according to their potential to relate the cloud cover characteristics to the variations in the radiation fluxes measured at the ground:

- Cloud fraction
- Sun visibility
- Cloud brokenness (ratio between total cloud edge length and total cloud area)
- Mean Red/Blue ratio over cloud or sunspot
- Number of saturated pixels and mean intensity level in sunspot

- Intensity mean and variance over the entire image and over cloudy pixels

4 RESULTS

4.1 Classification

A reference dataset is first generated from a set of 107 raw images chosen randomly. These images were classified and controlled manually, providing a validation dataset for a wide range of observed nebulousity. To perform this validation, the several cloud fractions described in the previous paragraphs have been computed from both the raw and reference images. Additionally, the visibility of the sunspot is checked both manually and with the automated approach. The validation has been performed for 4 solar zenith angle settings: 1. Images taken at all solar zenith angles, 2. for solar zenith angle lower than 75° , 3. for solar zenith angle lower than 70° and 4. for solar zenith angle lower than 65° . The results are summarized in Table 1, providing the root mean squared error (RMSE) between the cloud fractions derived from the images classified manually and the images classified automatically. From the validation, it appears clearly that the best results are obtained for hemispherical images collected when the solar zenith ranges from nadir up to 75° . Lowering the range from nadir to 70° or 65° does not significantly improve the results. This is directly related with the minimum illumination conditions required by the camera. Consequently, only images registered when the solar zenith angle is lower than 75° are considered for the rest of the study. The largest errors between the automatic and manual classifications are observed for the unweighted cloud fraction integrating the pixels within the sunspot. The best results are observed for the cloud fraction weighted according to the distance to the nadir. This can be explained by the fact that most of the classification errors are usually located on the edge of the hemisphere due to chromatic aberrations or more difficult classification conditions (Long, 2006). Generally, the weighted cloud fraction provides closer results than the unweighted ones. It is also important to mention that the measured differences are not only due to misclassification by the automatic method. Indeed, the cloud edges are sometimes very blurry and the boundary between clear sky and clouds can be very difficult to detect, even for human eyes. This is true in the vicinity of the sun as well. Then some errors can be done in the manually classified images concerning the exact limit of the clouds and also about what should be considered as thin clouds or not. In that regards, the automatic method is more consistent and objective and with a RMSE of maximum 8.3%, provided good results. However, the results concerning the classification of

the sunspot to determine the sun visibility is about 64% of correctly classified cases and will require further improvement.

When checking the results visually, the main problems observed with the automatic classification are mostly located over and around the sunspot, on the cloud edges, and for the detection of very thin or very dark clouds.

4.2 Cloud distribution

More than providing an accurate and consistent estimation of the cloud fraction, one of the main advantages of this method is to provide information about the spatial distribution of the clouds, as illustrated in Figure 2. Using the polar coordinates, the hemisphere is divided in segments, with zenith increment of 10° and azimuthal increment of 22.5° . Then a cloud fraction is computed for each segment.

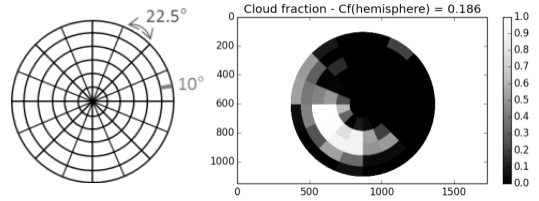


Figure 2: Segmentation grid (left) and example of cloud distribution maps (right)

4.3 Correlation to ground measurements

The different cloud fractions and the several indices extracted from the images have been correlated with the radiation fluxes measured at the ground. From this correlation analysis, it appears that only the cloud fractions provided interesting results. The Figure 3 illustrates the various cloud fractions (CF) used in the later analysis. A cloud fraction was also computed only in a buffer around the sunspot (CF close sun).

Concerning the downward longwave radiation, the correlation with the different cloud fractions is high except for the cloud fraction computed close to the sun. The correlation is mostly lower for the solar irradiance, for which the highest correlation is obtained with the cloud fraction computed close to the sun.

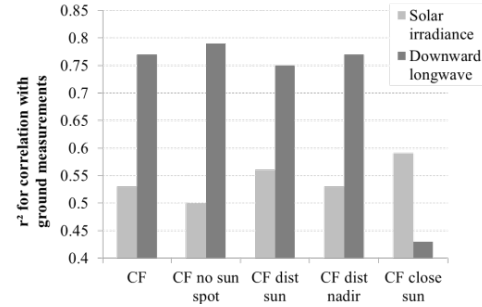


Figure 3: Correlation between downward ground fluxes measurement for shortwave (light grey) and longwave (dark grey) and the different cloud fractions

Figure 3 highlights the fact that regarding solar irradiance, more than the information about the amount of clouds, the localisation of those clouds in relation to the sun is of influence. This observation is confirmed by the results showed in Figure 4 where a time series of irradiance measured at the ground over 2 days is compared with the retrieved cloud fraction. An indication of the theoretical irradiance for completely clear sky is indicated by the dashed line. As expected, when the cloud cover is low, the measured irradiance is closed to the clear sky modelled irradiance, while when the cloud cover is higher the measured irradiance is lower than the modelled one. This is observed over the major part of the time series. However in two cases, highlighted in grey in Figure 4, there is a high cloud cover but almost no difference between the measured and the modelled irradiance. Those two cases were investigated and it comes out that even if the cloud fraction was correctly estimated from the hemispherical images, the sun was visible so direct sunlight was received at the ground, which explains the measured irradiance behaving as if it was clear sky. Those observations reinforce the results from Figure 3 about the necessity of cloud distribution information when working in the solar domain.

Table 1: RMSE between each cloud fractions retrieved from images classified automatically and the same cloud fractions retrieved from images classified manually

	All sun zenith angle	Sun zenith angle < 75°	Sun zenith angle < 70°	Sun zenith angle < 65°
Nb of images	107	93	89	84
RMSE CF	14.6%	8.3%	8.2%	8%
RMSE CF no sunspot	14.3%	7.8%	7.8%	7.7%
RMSE CF Sun	9.1%	5.7%	5.6%	5.5%
RMSE CF Nadir	9%	5.3%	5.3%	5.1%
% correct sunspot	63%	62%	63%	64%

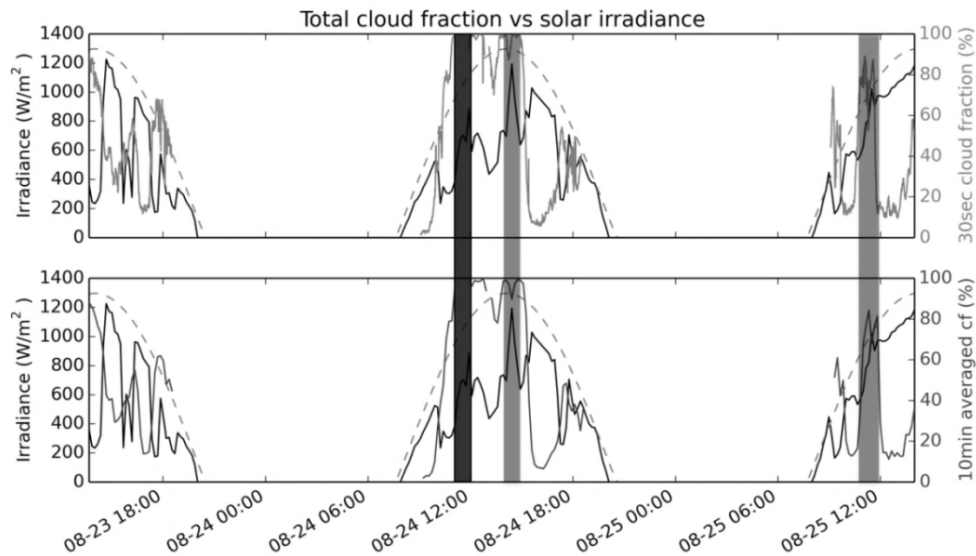


Figure 4: Time series of solar irradiance measured at the ground and cloud fraction estimates with missing data in dark grey and interesting phenomena in light grey. The measured irradiance is drawn in black, the cloud fraction in grey and the dashed line represents the clear sky modelled irradiance

5 CONCLUSION

This paper presented a methodology to accurately and consistently retrieve cloud fraction and cloud distribution from hemispherical images. The validation results showed very good results concerning the different cloud fractions estimates even if the thin clouds and the sunspot area are still difficult to classify. The main conclusion is that more than the cloud fraction, the cloud distribution is impacting the solar irradiance and this is the major asset of this method, to provide a distribution maps of the clouds over the hemisphere. As compared to existing system, this method is easy to set up and the retrieved information on cloud distribution could be very beneficial to several applications, for example the gap filling of time series of radiation fluxes and energy balance computed from VHR satellite data or also to account for the actual distribution of the radiative forcing in 3D radiative and energy balance models, especially for case studies where orientation effects may be strong (e.g. strong relief or urban areas).

Concerning the classification step, some work could be done to further improve the cloud detection and especially within and around sunspot. Some work could be done to extract further cloud information such as cloud thickness for example. A way to deepen the correlation analysis between ground solar irradiance and cloud cover would be to perform this analysis using higher frequency ground measurements. In this study, only one value every 10 min was available, even though the typical decorrelation time

of the sky is about 10 to 15 min (Long 2010). Furthermore, the ongoing experiment could also be completed by combining the presented system with additional sensors, such as a sun tracking system and an infrared camera, which would probably help for the validation of the sunspot and direct radiation detection.

6 REFERENCES

- Calbò, J., and Sabburg, J., 2008, Feature Extraction from Whole-Sky Ground-Based Images for Cloud-Type Recognition. *Journal of Atmospheric and Oceanic Technology*, 25(1), 3-14.
- Weiss M., and Baret, F., 2010, Can-Eye v6.1 User Manual, INRA.
- Cazorla, A., Olmo, F.J., and Alados-Arboledas, L., 2008, Development of a sky imager for cloud cover assessment. *Journal of the Optical Society of America A*, 25(1), 29-39
- Cess, R.D., Zhang, M.H., Minnis, P., et al., 1995, Absorption of Solar Radiation by Clouds: Observations versus Models. *Science*, 267(5197), 496-499.
- Ferreira, P.M., Martins, I.A.C., and Ruano, A. E., 2010, Cloud and clear sky pixel classification in ground-based all-sky hemispherical digital images. IFAC Conference on Control Methodologies and Technology for Energy Efficiency CMTEE'2010, Proceedings of the IFAC symposium held in Vilamoura, Portugal on 29-31 March 2010, pp.273-278

- Fu, C., and Cheng, H., 2013, Predicting solar irradiance with all-sky image features via regression. *Solar Energy*, 97, 537-550.
- Heinle, A., Macke, A., and Srivastav, A., 2010, Automatic cloud classification of whole sky images. *Atmospheric Measurement Techniques*, 3(3), 557-567.
- Long, C.N., Sabburg, J.M., Calbó, J., and Pagès, D., 2006, Retrieving Cloud Characteristics from Ground-Based Daytime Color All-Sky Images. *Journal of Atmospheric and Oceanic Technology*, 23(5), 633-652.
- Martins, F.R., Souza, M.P., and Pereira, E.B., 2003, Comparative study of satellite and ground techniques for cloud cover determination. *Advances in Space Research*, 32(11), 2275-2280.
- Pfister, G., McKenzie, R. L., Liley, J. B., et al., 2003, Cloud Coverage Based on All-Sky Imaging and Its Impact on Surface Solar Irradiance. *Journal of Applied Meteorology*, 42(10), 1421-1434.
- Shields, J.E., Karr, M.E., Johnson, R.W., and Burden, A.R., 2013, Day/night whole sky imagers for 24-h cloud and sky assessment: history and overview. *Applied Applied optics*, 52(8), 1605-1616.
- Silva, A.A., and de Souza Echer, M.P., 2013, Ground-based measurements of local cloud cover. *Meteorology and Atmospheric Physics*, 120(3-4), 201-212.
- Souza-Echer, M.P., Pereira, E.B., Bins, L.S., and Andrade, M.A.R., 2006, A Simple Method for the Assessment of the Cloud Cover State in High-Latitude Regions by a Ground-Based Digital Camera. *Journal of Atmospheric and Oceanic Technology*, 23(3), 437-447.
- WWRP (World Weather Research programme), 2012, Recommended Methods for Evaluating Cloud and Related Parameters. WMO, Switzerland.
- Yoshimura, M., and Yamashita, M., 2013, Contribution of Ground-Based Cloud Observation to Satellite-Based Cloud Discrimination. *Journal of Environmental Science and Engineering A* 2, 487-493.

How atmospheric turbulence affects measurements of surface temperature from space?

J.-P. Lagouarde, M. Irvine, S. Dupont
INRA, UMR 1391 ISPA, F-33140 Villenave d'Ornon, France
lagouarde@bordeaux.inra.fr

ABSTRACT- Atmospheric turbulence in both surface (SBL) and planetary (PBL) boundary-layers induce rapid temporal fluctuations of the surface temperature (T_s), with potentially important resulting errors on instantaneous satellite measurements in the thermal infrared (TIR). Several experimental studies have been performed over different surfaces (pine forest, maize, bare soil) using TIR cameras, either ground based or helicopter borne, designed to evaluate (i) how the spatial resolution operates a smoothing of the temporal fluctuations of the surface temperature measurements from space, and (ii) the resulting uncertainty on these measurements. Additionally, a simulation of instantaneous surface temperatures of a Maritime pine stand, performed using a Large Eddy Simulation (LES) airflow model coupled with a canopy model, is presented and a comparison between field measurements and numerical simulations is made using the classical assumption of frozen turbulence. The results confirm that the impact of the SBL turbulence rapidly vanishes with spatial resolution in the range of 50 to 100 m, and that T_s fluctuations are primarily governed by the low frequency PBL turbulence. For these resolutions, it is shown that the resulting uncertainty on T_s lies within a $\pm 1^\circ\text{C}$ interval. Recommendations are made for building the protocols of experiments devoted to the validation of TIR satellite data against ground measurements. The implications for designing the specifications of future high spatial resolution TIR missions, in particular NeDT and revisi, are also discussed.

1 INTRODUCTION

Surface temperature T_s displays temporal fluctuations due to micrometeorological field variability, wind speed in particular, whereas low orbit satellite flight speed typically being 7.5 km s^{-1} results in measurements of T_s from space representing a sampling of a randomly fluctuating signal. This may be an important source of uncertainty on satellite measurements. The high frequency turbulent structures within the surface boundary layer (SBL) correspond to typical times of a few seconds and scales of a few meters, and an illustration of their mechanical effect is given by the wind-induced wave-like structures ('honamis') observed on wheat fields. They induce similar spatial variability of T_s which is likely to be averaged by TIR sensors with resolutions of a few tens of meters (Lagouarde et al., 2013a). On the other hand, low frequency turbulent structures within the planetary boundary layer (PBL) correspond to large convective eddies -of a few hundreds of meters- which exceed the pixel size of TIR sensors at such a resolution; they induce significant T_s variations in amplitude which last several tens of seconds. A better assessment of T_s fluctuations is therefore necessary, especially as efforts are underway to propose innovative spatial missions with high spatial resolution (50 to 100m) in the TIR, such as HypsIRI (<http://hyspiri.jpl.nasa.gov/>), MISTIGRI (Lagouarde et

al., 2013b), or recently THIRSTY, a joint mission concept under study between the CNES and NASA (Crebassol et al., 2014). Moreover as most models deriving fluxes from surface temperature assume stationary conditions over time steps ranging from 15 to 30 minutes, the accuracy of fluxes retrieved from remotely sensed data closely depends on errors induced by the departure of the instantaneous measurements of T_s and their average value over the model time step. This paper addresses the problem of the uncertainty inherent in atmospheric turbulence on T_s measurements from space, and of its relation with the spatial resolution. The study is based on field and numerical experiments.

2 EXPERIMENTAL

Four experiments have been performed using TIR cameras placed on masts or towers. Three of them performed over a dry maize field, a bare soil, and a pine forest, are referred to as MAGR, BSGR, FOGR, the first two capital letters representing the surface type, the index GR for ground-based. A fourth experiment was conducted using a helicopter borne camera over a pine forest and is similarly referred to as FOHEL. A large eddy simulation (LES) experiment (referred to as FOLES) was also performed over a pine forest.

2.1 MA_{GR} and BS_{GR} experiments

2.1.1 Measurements

MA_{GR} and BS_{GR} experiments were performed on September 29, 2011 on two adjacent very large fields at the INRA test site of Bilos (44° 30' 03"N, 0° 57' 20"W) in SW France. The first one was covered with dry maize of about 2 m high. The second one was a bare soil field showing only shallow wheel tracks. Measurements were performed using an A40-M FLIR TIR 240x320 uncooled microbolometer camera. It has a 7.5 - 13 μm spectral response, with a 0.08 K thermal sensitivity (NeDT) at 30°C, and an accuracy of ±2%, i.e. ±0.6°C at this temperature. Emissivity was set to 1, so that brightness temperatures were only considered. As we are interested in fluctuations only, this has no impact here. The camera was installed at the top of a 5.40m mast. It was equipped with a 80° x 64.4° wide angle lens, which was inclined by about 60° (referred to nadir). The spatial resolution was therefore varying within the images and was calculated using simple geometric considerations. The zenith viewing angles also displayed a large range of variation within the images, and could differ from satellite ones, but we checked that this had no impact on the T_s fluctuations. A sequence of data 18 minutes long was acquired at 12.5 Hz over each surface in the beginning of a clear sky afternoon. This duration was chosen to statistically observe a few convective events of typically a few minutes time scale depending on PBL activity. Fluctuations of wind components and air temperature were simultaneously acquired at 10 Hz using a Young 81000V sonic anemometer.

2.1.2 Data processing

To remove possible systematic spatial variability and angular anisotropy effects, the average of all the images of the series were subtracted from each image of the series. Time series at different spatial resolutions (*r*) were produced for a specific location within the image. At any time *t*, the reconstruction of temperature T_s(*r*,*t*) at the resolution *r* is made by aggregating the *n* initial pixels of temperature T_{si}, contained within *r*, assuming a Stefan-Boltzmann TIR radiance conservation scheme, and weighing each initial pixel by its corresponding surface S_i at ground:

$$T_s(r, t) = [\sum_{i=1}^n S_i T_{si}(t)^4 / \sum_{i=1}^n S_i]^{1/4}, \quad (1)$$

with $r^2 = \sum_{i=1}^n S_i$.

2.2 FO_{GR} experiment

This experiment took place on September 10, 1999, over a 460 x 320 m maritime pine stand at Le Bray site (44° 43' 01.50"N, 0° 46' 09.0"W) in SW France. The mean tree height was 18.8 m, with rows oriented ENE-

WSW. Their width was 4 m, and the density of trees was 518 stems/ha. The crown cover was about 70%, leaving the understory vegetation partly visible. A micrometeorological tower on the site provided continuous wind speed and air temperature at a 40 m height using a Gill R3 sonic anemometer. A cooled MCT detector INFRAMETRICS M760 TIR camera was used here, working in a 8-12 μm spectral band with a ±1°C accuracy and a NeDT < 0.2°C. The camera placed on the tower was aiming at the forest with a 40° zenith angle. The lens had a 17 x 22° FOV, so that the trapezoidal area seen at the ground was about 19 m long, with 17 and 21 m bases, with corresponding dimensions of 12, 14 and 16 m at the top of canopy. Both crowns and soil were visible and contributed to the thermal signal. Two sequences of measurements of 30 minutes were performed under clear sky conditions, in two different directions. Two series of T_s images at 10 Hz were produced by averaging the temperatures over each 288 x 384 image according to a Stefan-Boltzmann aggregation scheme.

2.3 FO_{HEL} experiment

This experiment was performed on August 16th, 1995 on the same pine stand as for the FO_{GR} experiment. In 1995, the mean height of trees was 17.3 m, and the density was 615 stems/ha. A helicopter (Bell 206 'Jet Ranger') was used with the INFRAMETRICS M760 equipped with a 80 x 60° FOV wide angle lens aboard. The atmospheric flow measurements were performed with a Gill R2 anemometer located at 25 m. The helicopter was flown at a 700m height at the nadir of the stand. We checked that no contamination of the simulated time series by directional anisotropy effects occurred (Lagouarde et al., 2013a). Measurements were performed at 25 Hz during about 10 min.

The data processing includes (1) a correction for radiometric non-homogeneities within the FOV, and (2) a geometrical rectification to correct for the barrel-type distortions of the images leading to a final mean spatial resolution of 3.1 m, both made mandatory by the use of wide angle lenses. The correction of atmospheric effects is made using the LOWTRAN 7 model with radiosonde data from Merignac airport, 15 km North from le Bray site. Finally after applying an automatic process of geometric corrections described in Lagouarde et al. (2013a), a stack of coinciding images is produced. These are similarly gridded at a given spatial resolution (*r*). The temperature of each simulated pixel T_s(*r*,*t*) at time *t* is then estimated by aggregating the *n* pixels of temperature T_{si}(*t*) at 3.1 m initial resolution it contains, according to Eq.(1) with identical pixel size.

2.4 FO_{LES} experiment

The LES (large eddy simulation) ARPS model (Xue and al. 2001) extended so as to simulate turbulent flow within vegetation canopies (Dupont and Brunet 2008) is coupled with the SVAT model MuSICA (Ogé et al., 2003) to simulate the vegetation T_s , and its fluctuations in response to the turbulent structures present in the SBL and PBL. The coupled model is applied over a Maritime pine forest under convective conditions and clear sky typical of July in SW France. The forest is 22 m high, with a density of 410 trees/ha corresponding to a LAI~1.8. The computational domain extends over $3 \times 3 \times 2.5$ km, corresponding to $432 \times 432 \times 120$ grid points in the streamwise, spanwise and vertical directions respectively. The grid resolution is 7 m in the horizontal; in the vertical it is m below 23 m, and it is stretched above this level. The spatial fluctuations T_s are obtained at 13:00 UTC. Although the LES-simulated surface temperatures are thermodynamic and not brightness, they have been arbitrarily integrated as field experiments with Eq. (1).

3 RESULTS

Figures 1 and 2 present the temporal evolution of T_s , wind speed and air temperature for the MA_{GR}, and FO_{HEL} experiments aggregated at 50 and 60m respectively. The amplitude of the T_s variations reaches 3°C for maize, and 1.8°C for the pine forest of FO_{HEL}. The presence of higher frequency fluctuations for FO_{HEL} experiments compared to MA_{GR} ones are likely to be related to the fact we used for maize a camera based on a microbolometer technology which displays a slower response time than the MCT camera used over the forest stand for which the digitization of the data recorded on video tapes added noise. Nevertheless, the contribution of high frequency fluctuations in the surface temperature temporal signal remains low, which is consistent with the spatial integration effect of the high frequency fluctuations generated in the SBL (Lagouarde et al., 2013a). The low frequency PBL-induced turbulence therefore appears to be responsible for the most significant uncertainties in surface temperature. The effect of wind on surface temperature variations was confirmed by the analysis of the correlation between these two. Indeed the maximum correlation was found for lapse times exactly corresponding to the time necessary to cover the distance between the observed pixels and the instrumented mast for the measured wind speed. The simultaneity between the wind speed and surface temperature fluctuations observed confirms the prevailing effect of wind turbulence on the surface temperature variability. Conversely, no obvious correlation was found with the air temperature.

Similar results (not illustrated here) were found over the other surfaces: T_s varied within intervals of 1.8°C for bare soil at 50 resolution, and of 2.5 and 2.7°C for the two FO_{GR} sequences at 15-20 m resolution.

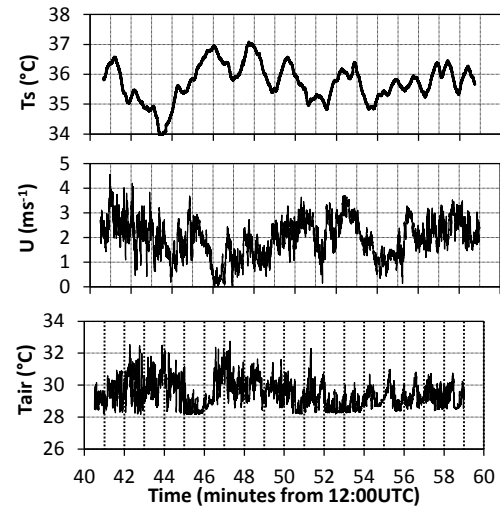


Figure 1. MA_{GR} T_s time-series at 50 m resolution, wind speed and air temperature over the maize field (Bilos, 2011/09/29, 12:41 - 12:59 UTC).

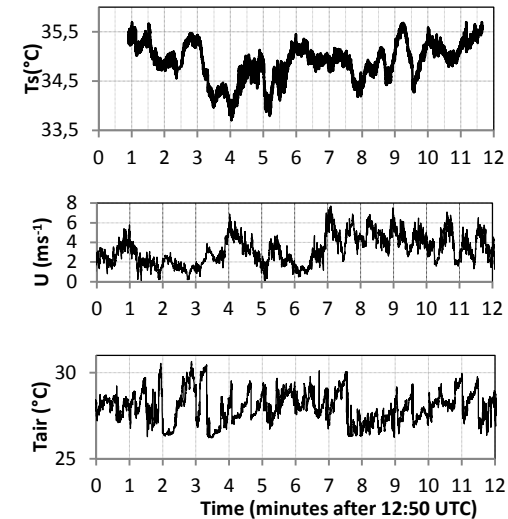


Figure 2. FO_{HEL} T_s time-series at 60 m resolution, wind speed and air temperature over Le Bray pine stand (1995/08/16, 12:51 - 13:02 UTC).

An instantaneous view of tree top surface temperature as simulated by ARPS-MuSICA shows surface temperature fluctuations of about 2-3°C in response to convective structures, an order of magnitude that is very consistent with previous field observations (Fig.

3a, see color plates, end of the proceedings book). The surface temperature field exhibits hexagonal patterns of a few hundred meters corresponding to the formation of convective plumes in the PBL. It is very consistent with the vertical velocity field (Fig 3b) and it confirms that the low frequency fluctuations of surface temperature observed from IRT camera can be explained by large-scale convective structures. Contrary to measurements in the solar domain for which reflectances are rather stable in time, measurements in the TIR are unavoidably affected by fluctuations related to atmospheric turbulence. We propose 2 indicators to quantify the inherent error induced by these fluctuations on TIR satellite data. First, a maximum error amplitude (MEA) can be defined for a specific spatial resolution as the difference between the extreme values of T_s during a time-series of duration T :

$$MEA = [\max(T_{si})] - [\min(T_{si})] \quad (2)$$

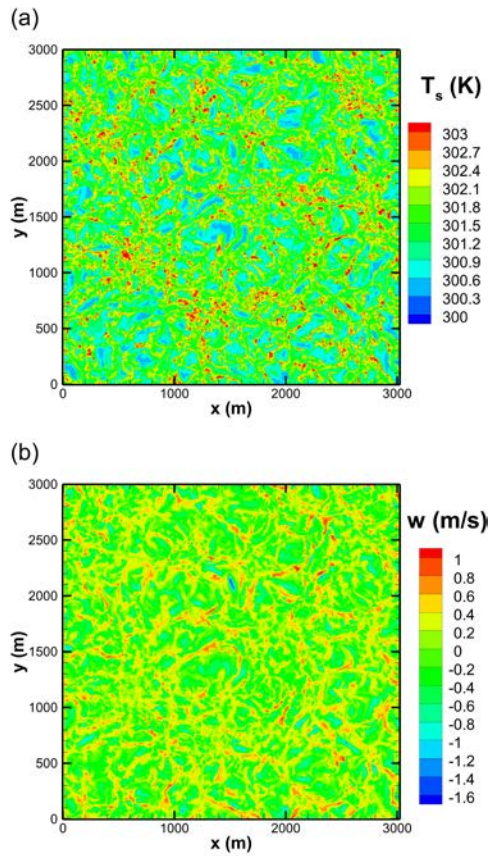


Figure 3. Snapshot of the tree top surface temperature T_s (a) and vertical wind velocity w at canopy top (b) as simulated by the LES model over a Maritime pine stand under convective condition.

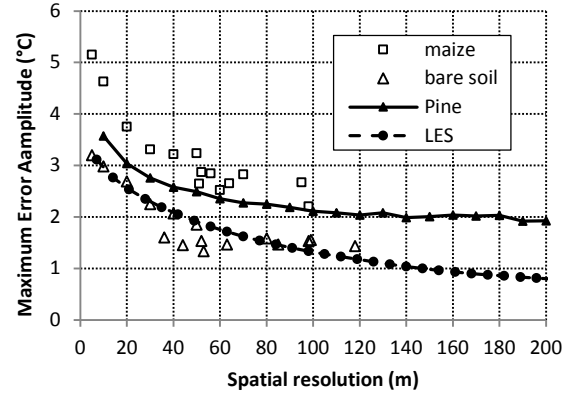


Figure 4. Relationship between MEA and spatial resolution for maize (MA_{GR}), bare soil (BS_{GR}), pine forest (helicopter measurements FO_{HEL}) and LES simulation.

If considering a time-series of images over a given surface, the MEA retrieved for each pixel can be averaged to provide a representative value smoothing possible spatial non-homogeneities. If considering a LES simulation, the assumption is made that the time period T and area L_s are long and large enough compared to the time and spatial scales of low frequency turbulent structures to give a representative value of the T_s fluctuation range. Fig. 4 presents MEA as a function of the spatial resolution for all experiments.

All curves reveal similar behaviour, with at first a rapid decrease with resolution, and a stabilization thereafter. The stabilization is reached at a 60-80 m resolution for bare soil and maize, whereas it occurs somewhat later for a forest, around 120 m for the Le Bray pine stand observed by helicopter, and 150-200 m for the LES simulation. The smoothing process of high frequency SBL-induced fluctuations operated by the integration over the pixel of turbulent structures of typically smaller size explains the decrease in the amplitude. After a given resolution limit, only low frequency turbulence remains; its typical kilometric scale - about the PBL height - makes that pixels up to a few hundreds meters are similarly affected, therefore explaining the plateau observed in Fig.4.

The second indicator to evaluate the uncertainty of satellite measurements is based on the statistics of the departure (in absolute value) of the surface temperature from its mean value over the sequences of measurements, and is referred to as DEP. The duration of the sequences is long enough to include several low frequency structures, which makes us confident in the estimation of the uncertainty for the cases studied. Fig. 5 shows the cumulated histogram of the DEP values obtained for MA_{GR}, BS_{GR} and FO_{GR}.

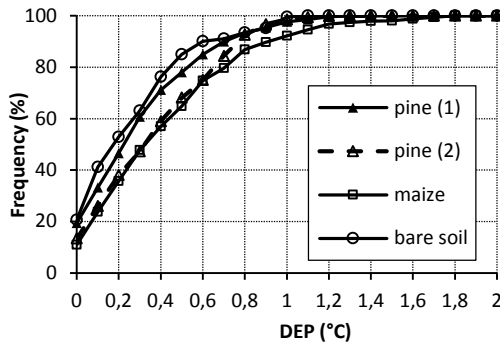


Figure 5. Probability of T_s uncertainty (DEP) for maize (MA_{GR}), bare soil (BS_{GR}) at 50m resolution and pine forest (FO_{GR}) ground experiments.

The error exceeds $\pm 0.5^\circ\text{C}$ for 35% to 15% of the cases depending on the surfaces, and $\pm 0.8^\circ\text{C}$ for about 10% of the instantaneous measurements. For maize, errors larger than $\pm 0.7^\circ\text{C}$ are made for 20% of the measurements. The fact that errors are smaller for bare soil, could possibly be attributed to lower roughness and therefore less interaction with the atmospheric layer above.

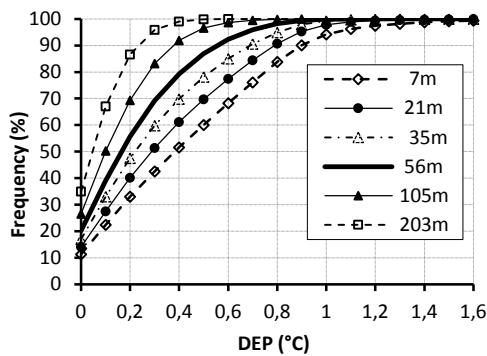


Figure 6. Idem Fig. 5 for pine forest (FO_{LES}) DEP derived from LES simulation at different spatial resolutions.

The DEP probability has also been derived from the LES simulation at different resolutions (Fig. 6). The results are consistent with those presented above and clearly confirm, as expected, the degradation of the accuracy of T_s measurements with the spatial resolution; for instance 40% of the data at 7m resolution are affected by an error larger than $\pm 0.5^\circ\text{C}$, and only 10% at 56m resolution, whereas the errors always remains lower than $\pm 0.5^\circ\text{C}$ at 200m resolution.

4 CONCLUSION

It has been shown that T_s displays important temporal fluctuations induced by atmospheric turbulence and the prevailing effect of wind has been demonstrated. T_s measurements from space are therefore prone to uncertainties. These depend on the spatial resolution and on the size of turbulent structures: because of an integration effect, large pixels are not impacted by high frequency structures which develop in the SBL and which have typical scales of a few meters only. On the opposite, measurements performed at high resolution may be dramatically affected by SBL turbulence. In the range 50-100m anticipated for future TIR missions, the measurements we performed and a simulation exercise based on a coupled LES-SVAT model (ARPS-MusiCA) both revealed that LST errors larger than $\pm 0.6\text{K}$ (resp $\pm 0.8\text{K}$) may be expected for about 25% (resp 15%) of the data. Nevertheless these results have to be generalized to more surface types and meteorological conditions. For remote sensing applications in the TIR, it results that several recommendations can be made:

- The uncertainty on satellite data must be taken into account when used in combination with SVAT models which generally have 30 mn to 1 hour time steps.
- Uncertainties both on satellite data and ground measurements must be taken into account in validation exercises.
- For continental biosphere studies, a 50 m resolution seems to be a reasonable trade off for observing the surface with enough details and an acceptable uncertainty.
- The possibility of relaxing the NeDT specification (would NeDT $<0.2-0.3\text{K}$ be enough?) is to be studied, at least for vegetation.
- Finally, a dense temporal sampling of LST allowing us to reduce the impact of turbulence induced uncertainty on LST, it emphasizes the need of high revisit for future TIR systems.

5 REFERENCES

- Crébasol P., Lagouarde J.-P., Hook S., Boissin B., Gamet P., Varinois A., Bret-Dibat T., Lum K., Foote M., Johnson W., Goullioud R. (2014). THIRSTY THERmal InfraRED SpaTial sYstem. International Geoscience and Remote Sensing Symposium (IGARSS), 13th-18th July, Québec City, Canada.
- Dupont S., and Brunet Y. (2008). Influence of foliar density profile on canopy flow: a large-eddy simulation study. *Agric. Forest Meteorol.* 148, 976–990.

- Lagouarde J.-P., Commandoire D., Irvine M., Garrigou D. (2013a). Atmospheric boundary-layer turbulence induced surface temperature fluctuations. Implications for TIR remote sensing measurements. *Remote Sens. Environ.* (138), 189-198.
- Lagouarde J.-P., Bach M., Sobrino J.A., Boulet G., Briottet X., Cherchali S., Coudert B., Dadou I., Dedieu G., Gamet P., Hagolle O., Jacob F., Nerry F., Oliso A., Ottlé C., Roujean J.L., & Fargant G. (2013b). The MISTIGRI Thermal Infrared project: scientific objectives and mission specifications. *Int. J. of Remote Sensing*. DOI:10.1080/01431161.2012.716921.
- Ogée J., Brunet Y., Loustau D., Berbigier P., Delzon S. (2003). MuSICA, a CO₂, water and energy multi-layer, multi-leaf pine forest model: evaluation from hourly to yearly time scales and sensitivity analysis. *Global Change Biology*, 9: 697-717.
- Xue M., Droegemeier K.K., Wong V., Shapiro A., Brewster K., Carr F., Weber D., Liu Y., Wang D. (2001). The advanced regional prediction system (arps) – a multiscale nonhydrostatic atmospheric simulation and prediction tool. Part II: model physics and applications. *Meteorol. Atmos. Phys.* 76 (3–4), 143–165.

ACKNOWLEDGEMENTS.

This work was supported by the Centre National d'Etudes Spatiales (CNES) through the TOSCA (Terre, Océan, Surfaces Continentales, Atmosphère) committee.

Data processing and temperature-emissivity separation for tower based imaging Fourier transform spectrometer data

Christoph Borel^a, Dalton Rosario^b, Joao Romano^c

^a*Department of Engineering Physics,*

Air Force Institute of Technology, WPAFB, OH 45433-7765, USA

^b*U.S. Army Research Laboratory, Adelphi, MD 20783-1197, USA*

^c*U.S. Army Armament RDEC, Picatinny Arsenal, NJ 07806, USA*

cborel@afit.edu; dalton.s.rosario.civ@mail.mil; joao.m.romano@us.army

ABSTRACT *In this paper we describe the end-to-end processing of image Fourier Transform spectrometry data taken at Picatinny Arsenal in New Jersey with the long-wave hyper-spectral camera from Telops. The first part of the paper discusses the processing from raw data to calibrated radiance and emissivity data. Data was taken during several months under different weather conditions every 6 minutes from a 213ft high tower of surrogate tank targets for a project sponsored by the Army Research Laboratory in Adelphi, MD. An automatic calibration and analysis program was developed which creates calibrated data files and HTML files. The first processing stage is a flat-fielding. During this step the mean base line is used to find dead pixels (baseline low or at the maximum). Noisy pixels are detected where the standard deviation over the part of the interferogram. A flat-fielded and bad pixel corrected calibration cube using the gain and offset determined by a single blackbody measurement is created. In the second stage each flat-fielded cube is Fourier transformed and a 2-point radiometric calibration is performed. For selected cubes a temperature-emissivity separation algorithm is applied. The second part discusses environmental effects such as diurnal and seasonal atmospheric and temperature changes and the effect of cloud cover on the data. To test the effect of environmental conditions the range-invariant anomaly detection approach is applied to calibrated radiance, brightness temperature and emissivity data.*

1 INTRODUCTION

The Spectral and Polarimetric Imagery Collection Experiment (SPICE) is a collaborative effort between the US Army Armament RDEC (ARDEC) and Army Research Laboratory (ARL) for the collection of mid-wave and long-wave infrared imagery using hyperspectral, polarimetric, and broadband sensors (Rosario, 2010). The data for this paper was taken from July 26-28 2011 from a 213ft high tower of surrogate tank targets with AFIT's HyperCam, a long-wave (LWIR) hyper-spectral camera from Telops. The project at AFIT was sponsored by the ARL in Adelphi, MD. Over a period of three days 200 GB of raw data were taken with varying instrument settings varying the nominal spectral resolution at 2, 4 and 8 cm⁻¹. Some of the cubes were averaged inside the instrument and some of them not. For each scene a pair blackbody measurements were taken at 25^o and 50^o C. The number of calibration cubes was limited to a maximum of 4 cubes to reduce the time the hot blackbody would shine into the instrument to prevent thermal drifts. Internal averaging was performed for 4, 8, 16 and 31 cubes to study the improvements in signal to noise. The integration time was fixed to 200 micro seconds for the low gain setting and to 80 when using high gain settings. When using the regular fore-optics, sub-windows were used to limit the size and time used

to acquire the data. On about one third of the data a telescope with a magnification of 3.5 was used to study the effects of spatial resolution and pointing jitter. The targets consisted of three surrogate tank targets with different orientation each at line-of-sight distances of 549 m (mid-range) and 1280 m (long-range) areas at Picatinny arsenal. The mid-range target area has a 2.4 by 2.4 m size aluminum sheet to reflect the down-welling radiance into the sensor. An automatic calibration and analysis program was developed which creates calibrated data files and HTML files. A special Quick Temperature-Emissivity Separation (QTES) algorithm was developed because the range to the target was relatively small making the retrieval of the atmospheric conditions, e.g. up/down-welling radiances and transmission difficult. QTES retrieves atmospheric parameters using the Amoeba algorithm (also known as Simplex, Nelder-Mead) (Press, 1988) by matching the MODTRAN5TM (Berk, 2006) outputs to the measured sky plate radiances. A special version of the Automatic Retrieval of Temperature-Emissivity using Spectral Smoothness (ARTEMISS) (Borel, 2008; Borel 2011) was developed. Rather than finding a temperature which creates a smooth emissivity over the entire bandwidth it uses a narrow spectral range to find the temperature which results in the emissivity with the smallest variance.

Assessment of the data calibration approach and temperature emissivity separation (TES) algorithm was performed via a robust anomaly detection method, which was specially designed to handling uncertainties in range and sensor-object viewing perspective. In this analysis, anomalies are defined as manmade objects or targets (e.g., equipments, military or commercial vehicles) in a natural background (trees, soil, grass). To assess the performance of the calibration approach and TES algorithm mentioned a simplified version of the Range-Invariant Anomaly Detector (RIAD) based on work in (Rosario, 2008) was developed.

2 LWIR HYPERCAM DATA PROCESSING

2.1 Flatfielding and radiometric calibration

The calibration was performed using an Interactive Data Language (IDL) program and processes data in several stages as described in (Borel, 2012) and shown in Figure 1. Intermediate results are stored so that the user can investigate the effects of various processing parameters and to minimize memory requirements. The first stage is a flat-fielding or non-uniformity correction operation. The gain or vignetting was estimated using the difference between the minimum and maximum extent of the interferogram. The offset is the mean value of the interferogram. Depending on the criterion the 320x256 pixel mercury cadmium telluride (MCT) detector used in the HyperCam has between 1 and 5 % bad pixels. To identify dead and stuck pixels the mean baseline is used. Dead pixels have a low baseline and stuck pixels have values near the maximum raw number range. Noisy pixels are found by computing the standard deviation of the interferogram away from the centerburst. The criterion for a pixel being classified as noisy is if its standard deviation is 5 times the standard deviation for good pixels. A bad pixel map for dead and noisy pixels is

created and for each scanline the bad pixel interferograms are replaced by their last “good” interferogram or by replacing them with the median interferogram. A median filter of size 5x5 pixels was used for our data. Then a flat-fielded and bad pixel corrected cube using the gain and offset determined by a single blackbody measurement is created. In the second stage each flat-fielded cube is Fourier transformed and a real-valued uncalibrated radiance cube is created for a predefined wavenumber range. Next the radiometric calibration is performed using a 2 point calibration computed from the two blackbody measurements and then applied to each data cube. The calibrated radiance, brightness temperature and emissivity cubes are then created in ENVI format. Finally a HTML file is created which contains quicklooks of spectra of selected pixels, the original and flat-fielded cubes as animated GIF images, and links to all the intermediate files that are created.

2.2 Quick temperature-emissivity separation

The scene observed by the HyperCam contains a unique feature in that a flat aluminium sheet of 2.4 by 2.4 m (sky plate) was mounted on a wooden structure to reflect down-welling light from the sky into the line of sight of the imager as shown in Figure 2. The distance to the targets was only 549 m, which makes it difficult to estimate the atmospheric parameters using the previously developed ARTEMIS method from high emissivity scene data. This is particularly true of the background pixels which consist mostly of vegetation which tends to have a similar temperature to the atmospheric temperature near the ground and a high emissivity. Thus, no useful atmospheric information, e.g. near horizontal atmospheric transmission between target and sensor which depends on water vapor, can be obtained.

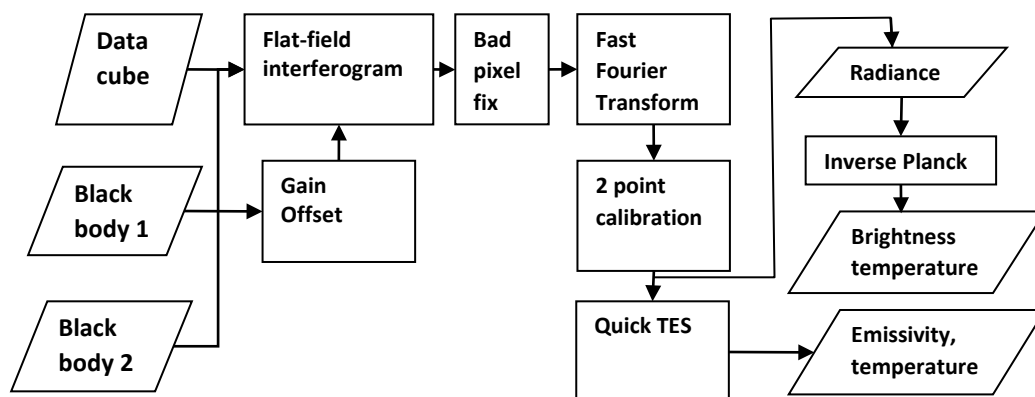


Figure 1 Data flow for the processing of raw interferogram data to calibrated radiances, brightness temperatures and emissivity cubes.

The only other possibility to obtain an estimate of the transmission is when the surrogate tank targets are much warmer than the air temperature which is the case on a sunny day. For that case, however, the emissivity of the paint of the surrogate targets is included in the transmission estimate and therefore cannot be easily separated. Hence the new temperature emissivity separation algorithm makes use of the low emissivity sky plate. For a pixel located on the sky plate the measured radiance L_c is given by:

$$L_c = \varepsilon_{plate} B(T_{plate}, \nu) + (1 - \varepsilon_{plate}) L_{\downarrow}(\nu) + L_{\uparrow}(\nu) \approx L_{\downarrow}(\nu) + L_{\uparrow}(\nu). \quad (1)$$

In most cases the emissivity of the sky plate will be close to 0 and thus the sky plate radiance is just the sum of down-welling L_{\downarrow} and up-welling L_{\uparrow} radiances. Thus the idea of QTES is to retrieve the atmospheric parameters by minimizing the difference between the measured sky plate radiance $L_c(\nu)$ and the sum of the MODTRAN5TM calculated up and down-welling radiances. Similar to the ARTEMIS (Borel, 2008) algorithm the temperature profile offset T_{offset} , the temperature scale height h_T , a scaling factor F_{RH} for the relative humidity, the relative humidity scale height h_{RH} and the columnar ozone amount O_3 are varied. To account for a possible small spectral shift the fractional wavelength offset is also varied. The amount of reflected sky radiance can be a complex mixture of clear sky radiance and radiance from clouds. Because of this a scaling factor a and offset b is introduced to better match the measured radiance L_c and the modeled down and up-welling radiances $L_{\downarrow} + L_{\uparrow}$. If the scaling factor a approaches 1 and the offset b is zero the sky is assumed to be clear. If a is less than one and b greater than zero then it is likely that partly cloudy conditions exist or a local minimum was found.

The Quick Temperature Emissivity Separation (QTES) algorithm consists of the following steps:

1. Find the coldest pixels L_c in the scene, which for this dataset are located on the sky plate.
2. Run the Amoeba algorithm (Borel, 2011) and change input parameters (T_{offset} , h_T , F_{RH} , h_{RH} , O_3 , ...) to MODTRAN5TM to minimize the difference $\sigma[L_c - a(L_{\downarrow} + L_{\uparrow}) - b]$, where a and b are scaling and offsets from 8-11.5 μm , and keep optimum L_{\downarrow} , L_{\uparrow} and τ . Note that multiple runs with different starting locations should be used to avoid local minima. To keep the notation in step 3 simple, a is set to 1 and b to 0.
3. For each pixel (i,j) do:
 - a. Estimate the surface brightness temperature $T_{BB} = BB^{-1}(L(i,j), \lambda_h)$ for a band λ_h with high transmission.

- b. For $T_k = \{T_{BB} - K/2dT + kdT\}$, $k=1,2,\dots,K$ compute the emissivity: $\varepsilon_k = (L_m - L_{\downarrow} - L_{\uparrow}) / (BB(T_k)\tau - L_{\downarrow})$.
- c. For narrow spectral range (9.5-10 μm) find T_{opt} which minimizes error: $\sigma(\varepsilon_k)$.

6. Save emissivity cube and temperature image T .

Fits achieved with this method are around $2 \mu W cm^{-2} sr^{-1} \mu m^{-1}$ (microFlicks) which is close to the noise performance achieved by the instrument as shown in Figure 3.



Figure 2 Surrogate tank targets and sky-plate (black).

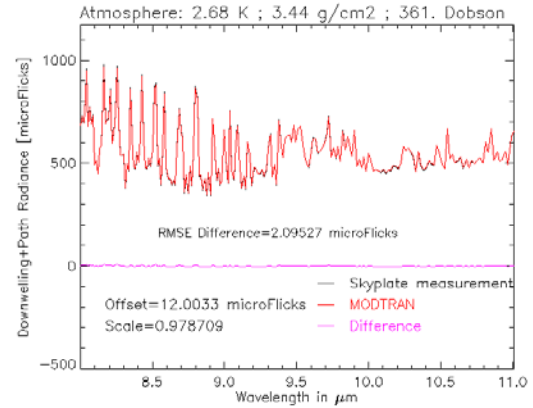


Figure 3 Measured and fitted spectrum of average over coldest pixels.

3 RANGE-INVARIANT ANOMALY DETECTION

Based on probability theory, the range-invariant anomaly detector method (Rosario, 2008) addresses range and background uncertainties by performing a repeated random sampling scheme, where N small blocks of data are randomly drawn from the input imagery in order to characterize the scene's clutter background on demand. The process is repeated M times with spatially independent samples to insure a statistically sound estimate of the background. The cumulative probability of spatially diverse samples can be modelled by the binomial distribution family. Using a repeated random sampling scheme jointly with an asymmetric metric constitutes the anomaly detection

method. In contrast to existing global methods, this method usually requires a small fraction of the hyperspectral imagery (less than 2%) to characterize the unknown clutter background and test the entire imagery for genuine scene anomalies.

Since a rather small number of pixels are used from the HyperCam data and the targets are quite large a simplified version was developed. The hyperspectral cube $d()$ with N_b bands and spatial dimension N_x by N_y pixels is treated as a random variable $x=d(ib,ix,iy)$, where $ib=1,...,N_b$, $ix=1,...,N_x$ and $iy=1,...,N_y$. Assuming that x has a finite range between $xmin=min(x)$ and $xmax=max(x)$ the distribution of $g1(x)$ can be calculated using a simple histogram operation over N_h bins. For a sub-block of N_b by N_t by N_t data points histograms $g0(x,i,j)$ are computed where $i=1,...,N_x/N_t$ and $j=1,...,N_y/N_t$. The range invariant anomaly detector uses the mean ratio R of the normalized histograms $R(i,j)=Mean[g0(x,i,j)/g1(x)]$. An anomaly is absent if the sub-block $g1(x,i,j)$ resembles $g0(x)$ causing the average ratio $R(i,j)$ to be close to unity. Otherwise an anomaly is present. By appropriate thresholding of $R(i,j)$, the anomalies are found for radiance, emissivity and brightness temperature data.

The simplified Range Invariant Anomaly Detector (RIAD) algorithm (Borel, 2012) has the following steps:

1. Compute the histogram $g0(x)$ in N_h bins ranging from $min(x)$ to $max(x)$.
2. Divide the cube into sub-cubes of size N_t by N_t by N_b bands and compute the histograms $g1(xk,i,j)$, where $i=1,...,N_x/N_t$, $j=1,...,N_y/N_t$ in $k=1,...,N_h$ bins ranging from $min(x)$ to $max(x)$.
3. Compute the mean ratio $R(i,j)=Mean[Rk(i,j)]$ where $Rk(i,j)=g1(xk,i,j)/g0(xk)$ for all non-zero elements of $g0(xk)$.

4. Decide that an anomaly is present when $R(i,j)>R_{thres}$, where R_{thres} is set to 2.

4 DETECTION RESULTS

To illustrate the RIAD a single dataset was selected from the over 200GB of data cubes. The image was taken at a nominal spectral resolution of 2 cm^{-1} from 0 to 1579.84 cm^{-1} . The two blackbodies were set at 25^0 and 50^0 C .

Figure 4 shows results of RIAD applied to radiance, emissivity and brightness temperature data cubes. The RIAD using radiance and brightness temperature finds all anomalies (surrogate tanks and sky plate) quite easily. When applying RIAD to the emissivity only the sky plate is found since its emissivity is low. The surrogate tanks were not found because their emissivity is similar to the background. Only pixels on horizontal surfaces of the surrogate tanks that reflect a significant amount of down-welling sky light where the retrieved emissivity is lower are flagged as anomalies. It is interesting to note that vertical surfaces on the surrogate tanks have a higher apparent emissivity than the background. This might be caused by multiple reflections between background (vegetation) and the surrogate tank surfaces which create a higher apparent emissivity similar to a black body cavity. Thus, the RIAD method seems not to work very well when applied to emissivity data. The same data was also analyzed using the global and local Reed-Xiaoli detector (RXD) (Lu, 1997) which yielded disappointing results (Figure 5). There was a large number of pixels misidentified as targets compared to the RIAD method. The skyplate was found in all results for the RXD. Parts of the tanks were somewhat visible in the global RXD. However the tanks were not visible in the local RXD using a window size of 5×5 pixels.

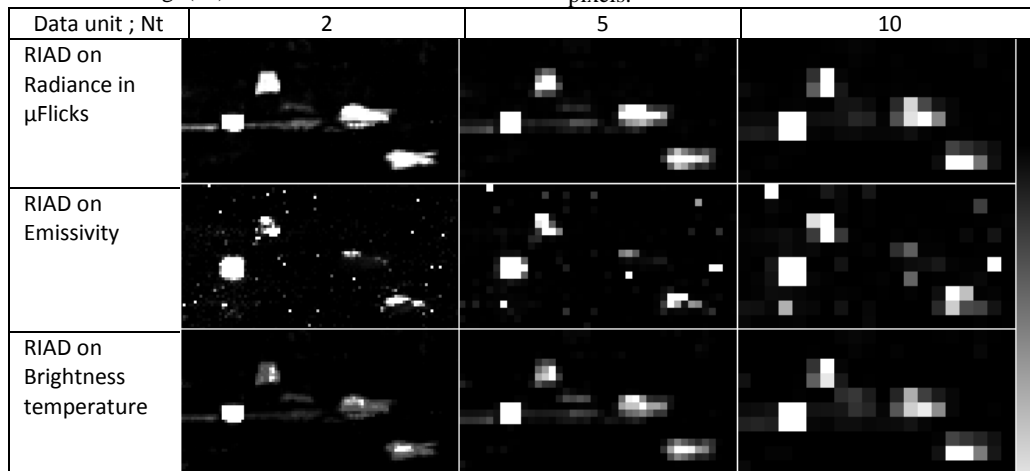


Figure 4 RIAD mean probability ratios using a 5% histogram stretched enhancement for the different units and block sizes N_t .

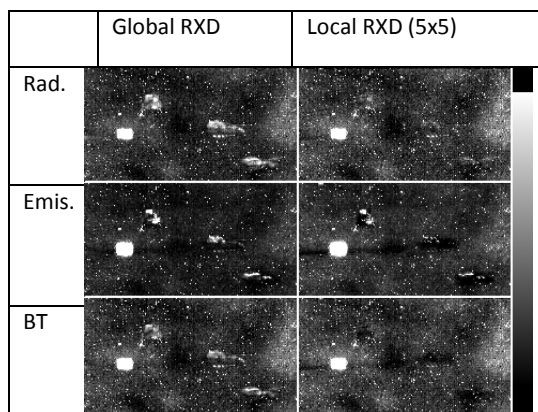


Figure 5 Results for radiance, emissivity and brightness temperature for global RXD and local RXD (5x5 window).

5 CONCLUSIONS AND FUTURE WORK

This paper shows how to process imaging Fourier transform data from raw to calibrated data. A sophisticated algorithm was able to match the measured radiances over a sky plate to MODTRAN⁵™ calculations to within a few microFlicks which then enabled us to compute an emissivity cube. More work is required in the future to compare these results with measured meteorological conditions at the site and retrieve emissivity under partly cloudy conditions. A simplified range-invariant anomaly detection (RIAD) was applied to simulated multi-spectral data and shown to find spectral anomalies. In the final application of RIAD to one set of measured long-wave hyperspectral data processed as radiance and brightness temperature, it appears that the best unit to use is brightness temperature, followed by radiance and then emissivity. The well established RXD did not find the surrogate tank targets with the sky plate present. More development and analysis of this set of algorithms is needed to find the optimum settings and test its robustness over a range of environmental conditions.

REFERENCES

- Berk, A., G.P. Anderson, P.K. Acharya, L.S. Bernstein, L. Muratov, J. Lee, M. Fox, S.M. Adler-Golden, J.H. Chetwynd, M.L. Hoke, R.B. Lockwood, J.A. Gardner, T.W. Cooley, C.C. Borel, P.E. Lewis and E.P. Shettle, 2006, MODTRAN5: 2006 Update, Proc. SPIE, Vol. 6233, 62331F.
- Borel, C.C., 2008, Error analysis for a temperature and emissivity retrieval algorithm for hyperspectral imaging data, International Journal of Remote Sensing, Volume 29, Numbers 17-18, pp. 5029-5045.
- Borel, C.C. and R.F. Tuttle, 2011, Recent advances in temperature-emissivity separation algorithms, 2011 IEEE Aerospace Conference, pp.1-14.
- Borel, C.C., D.S. Rosario, and J.M. Romano, Range-invariant anomaly detection applied to imaging Fourier Transform Spectrometry data, 2012, Optical Engineering+Applications SPIE Optics+Photonics, Conference: Imaging Spectrometry XVII (Shen/Lewis), Vol. 8515-85150J.
- Lu, X., L. E. Hoff, I. S. Reed, M. Chen, and L. B. Stotts, 1997, Automatic target detection and recognition in multiband imagery: A unified ML detection and estimation approach, IEEE Trans. Image Process., vol. 6, no. 1, pp. 143-156.
- Press, W. H., B. P. Flannery, S. A. Teukolsky, and W. T. Vetterling, 1988, Numerical Recipes in C: The Art of Scientific Computing, Cambridge University Press, Cambridge.
- Romano, J.M., D.S. Rosario, V. Farley and B. Sohr, 2010, Spectral imagery collection experiment, Proc. SPIE 7695, 76950K.
- Rosario, Dalton Souza, 2008, Algorithm development for hyperspectral anomaly detection, PhD thesis, University of Maryland, p.239.

Directional Hyperspectral Observations to Detect Plant Stress With The PRI and SIF in a Cornfield

E. M. Middleton^{*a}, Y.-B. Cheng^b, P. E. Campbell^c, K. F. Huemmrich^c, Q. Zhang^d, D. R. Landis^b, L. A. Corp^b, W. P. Kustas^e, C. S. T. Daughtry^e, and A. L. Russ^e

^aBiospheric Sciences Laboratory, NASA/Goddard Space Flight Center, Greenbelt, MD, USA

^bSigma Space, Inc. Inc., Lanham, MD 20706, USA

^cUniversity of Maryland at Baltimore County, Catonsville, MD, USA

^dUniversities Space Research Association, Columbia, MD, USA

^eUSDA-ARS Hydrology and Remote Sensing Laboratory, Beltsville Agricultural Research Center, Beltsville, MD

*Contact: Elizabeth.M.Middleton@nasa.gov;

ABSTRACT – We examined the impact of drought stress and temperature on plant hyperspectral, fluorescence, and photosynthetic responses during the 2012 growing season at an experimental USDA (United States Department of Agriculture) cornfield in Beltsville, MD USA. The manipulations included 4 nitrogen (N) application levels (0%N, 50%N, 100%N, and 200%N) and two water availabilities (W, drip irrigation; or NW, no irrigation) to produce 8 treatments. Hyperspectral observations were made in the solar principal plane at 7 view zenith angles: nadir (0°) ±30°, ±45°, and ±60° during morning and afternoon periods of 10 days throughout the season. Significant anisotropy was observed for the Photochemical Reflectance Index (PRI) and the far-red solar induced fluorescence (SIF₇₆₀), and diurnal and seasonal trends were obtained. We found that the nadir viewing configuration was optimal to discriminate among these 8 field treatments when environmental stresses were strongly expressed due to extreme drought and high temperatures. Nadir observations remained sufficient to describe responses even under more favorable conditions with lower environmental stresses, although values were similar among all treatments (and viewing configurations). The diurnal differences for each indicator, as well as the degree of anisotropy observed, can be largely attributed to drought induced changes in the canopy geometries of the treatment plots.

1 INTRODUCTION

Environmental conditions affect the physiological status of vegetation, inducing stress responses that influence growth and health. When environmental conditions are inadequate, the growth, accumulation of carbon as biomass, and soil-plant-atmosphere transport of water are reduced. An important objective of vegetation remote sensing for carbon uptake is to quantify plant stress levels that negatively impact photosynthetic function. Two physiological mechanisms have been identified that are associated with the light reactions component of photosynthesis, which can be measured using spectral information in the visible and near-infrared wavelengths (400-800 nm). Both mechanisms are related to the efficiency of utilization of absorbed photosynthetically active radiation (APAR). First is non-photosynthetic quenching (NPQ), the discarding of excess APAR as heat, primarily accomplished through the xanthophyll cycle and tracked by spectral changes at/near 531 nm [Gamon, 1990; Middleton, 2011]. Second is chlorophyll fluorescence (ChlF), the emission of excess APAR as photons across a broad wavelength range (~650-800 nm) [Middleton, 2011; Meroni, 2009]. The NPQ mechanism has been moni-

tored with the Photochemical Reflectance Index (PRI) which is the normalized difference ratio of reflectance from two green wavebands centered at the physiologically active wavelength (531 nm) and a reference wavelength (typically 570 nm) [Gamon, 1990]. PRI has been studied in many species and conditions, especially its relationship to photosynthetic light use efficiency (LUE) [Middleton, 2011 and references within]. The PRI is relatively easy to measure with field spectrometers having spectral resolutions <2-10 nm. Directional PRI observations have provided useful information under some circumstances, especially to discriminate between the light-stressed sunlit canopy sector vs. the less stressed shaded canopy sector [Cheng, 2009; Hilker, 2008; Middleton, 2009]. These sunlit and shaded canopy sectors occur at the hotspot and coldspot, respectively, at opposite positions along the instantaneous solar principal plane (SPP).

ChlF displays two distinctive peaks located in the red spectrum at 685 nm and in the far-red at 740 nm, associated with Photosystems II and I (PSII, PSI), respectively [Middleton, 2011; Meroni, 2009]. ChlF is an important physiological measurement because it serves as a probe for photosynthetic functionality, as has been established over decades of laboratory stud-

ies, most of which have been conducted with relatively low light intensities [Mohammed, 1995]. However, in the higher light levels of ambient natural settings this small ChlF emission signal is overwhelmed by reflected radiation except in specific wavelengths associated with narrow atmospheric absorption or transmission features where it can be retrieved as Solar-Induced chlorophyll Fluorescence (SIF). The easiest of these features to exploit is the oxygen A (O₂-A) band centered at 760 nm (SIF₇₆₀) which allows sampling of the broad second far-red ChlF peak produced by PSI emissions. The SIF emission signal of vegetation is typically assumed to be isotropic, or nearly so, so that the influence of canopy directional observations need not be considered. The FLuorescence EXplorer (FLEX) mission [Rascher, 2007] was selected in 2011 as one of the two European Space Agency (ESA) candidate satellite missions under the Earth Explorer 8 program, and is to be paired in tandem with ESA's forthcoming Sentinel-3 satellite. The FLEX mission would obtain approximately monthly observations to retrieve SIF in the red and far-red emission peaks as well as full-spectrum SIF (650-800 nm) and contemporary hyperspectral reflectance data in the VIS/NIR to retrieve the PRI and to enable vegetation classifications. These datasets would be collected in the morning (9-11am, depending on latitude) and provide monthly SIF and PRI observations at 300 m resolution over all land regions globally, thus providing critically important seasonal information about primary production and vegetation stress conditions at a spatial scale of value to ecosystem and agriculture studies. This study evaluates the role of both nadir and directional observations of PRI and SIF parameters (SIF₆₈₇, SIF₇₆₀). We examined canopies throughout a growing season in a USDA research cornfield with four nitrogen (N) application regimes coupled with water availability through a drip line (irrigated or non-irrigated) to produce 8 treatments. We found the nadir viewing configuration was optimal to discriminate among these field treatment plots when environmental stress was strongly expressed (drought, high temperatures) and nadir observations remained sufficient under low environmental stresses, when observations for all treatments and viewing configurations were similar.

2 METHODS

The research cornfield is located in Beltsville, MD, and managed by USDA-ARS (Agricultural Research Service). The field was planted with corn (*Zea mays* L.; variety, Pioneer 33A14) in late May 2012. For this study, we utilized the permanent N plots that were established over a decade ago: (i) the 100%N plot, the optimal fertilizer application treatment (140 Kg/ha); (ii) the 200%N over-fertilization plot (280 Kg/ha); (iii) the 50%N under-fertilization plot (70 Kg/ha); and (iv)

the 0%N plot (no additional N). In 2012, the USDA-ARS divided each N plot in half to create irrigated subplots, each ~15m x 15m in area. For this, an irrigation system consisting of parallel drip lines that were laid at 0.3m intervals throughout the half plots designated for water augmentation. Thus, 8 treatment plot types were established, with replicates, where each of the N plots (0%N, 50%N, 100%N and 200%N) had a rainfed-only half plot (no water, "nw") and a drip line water augmentation half plot (water, "w"). In addition to these experimental treatments, the study site experienced unseasonably high and sustained daytime temperatures (>32° C) with little precipitation (i.e., severe drought conditions) for the first half of the growing season. During this drought period, measureable precipitation was recorded on June 23, June 29, and July 9, and a significant rain event occurred on July 22 that ended the drought and lowered the daily maximum temperatures below 32° C. We examined these plots throughout the 2012 growing season as they progressed through different growth stages and a range in canopy leaf area indices (LAI 1-4) as measured with a LAI 2000 (Li-Cor, Lincoln, NE USA)). We made *in situ* leaf and canopy field measurements on 10 sunny days at various vegetative (V) growth stages (June 20, 28; July 5-6, 17) and reproductive (R) growth stages and senescence (July 25; Aug. 2, 16; Sept. 7, 11). On these 10 days (± 1 day), we collected *in situ* canopy and leaf fluorescence, *in situ* canopy hyperspectral reflectance, and canopy and leaf biophysical measurements (not discussed in this paper). The canopy spectra used for SIF retrievals were obtained with a high resolution spectrometer (Ocean Optics USB 4000, Dunedin, FL USA) using a pole-mounted fiber optic probe at late mornings (10-12 am) and early afternoons (1-3 pm). The canopy spectra used for PRI calculations were collected contemporaneously with an ASD FieldSpec spectroradiometer (Applied Spectral Devices, Boulder, CO USA). These canopy spectra were acquired at 7 view zenith angles (VZAs) along the SPP: nadir (0°), $\pm 30^\circ$, $\pm 45^\circ$, and $\pm 60^\circ$. Reference spectra were collected over a Spectralon panel (Labsphere, North Sutton, NH USA). These spectra were used for: (i) computing the PRI; and (ii) SIF₆₈₇ and SIF₇₆₀ retrievals, which were performed in the O₂-B, O₂-A atmospheric oxygen absorption bands centered at 687 and 760 nm, using the 3FLD retrieval approach [Meroni, 2009], and their ratio (SIF₆₈₇/SIF₇₆₀). We determined the corresponding quantities normalized to incoming Photosynthetically Active Radiation (PAR) as SIF yields (SIF/PAR). The bi-directional reflectance function (BRDF) responses in the SPP were determined for each sub-plot in mornings and afternoons for the PRI and SIF-related indices for each measurement day across the growing season. We determined the daily averages at the nadir

view angle (VZA=0°) for the PRI, NDVI (not shown), SIF₆₈₇ (not shown), SIF₇₆₀, and the SIF₆₈₇/SIF₇₆₀ ratio. Statistical analyses were performed using Systat 13 (Systat Software, San Jose, CA USA).

3 RESULTS

PRI values were always negative, indicative of stress, during the 2012 growing season, with the highest values close to zero (e.g., -0.005). The BRDFs for the PRI values in each of the 8 sub-plots during mornings and afternoons across the growing season were highly anisotropic in the SPP [Fig. 1]. In general, the BRDFs for plots before onset of senescence were bowl-shaped with the lowest PRI values associated with near-nadir VZAs (0°±30°). These BRDFs were more consistently bowl-shaped for the fully developed canopies (≥1m height, by June 28) during the first half of the season when drought was most severe and high temperatures prevailed (>32° C, mid-day). During this period, lower PRI values were observed for the sunlit canopy limbs as compared to the shaded limbs of the BRDF curves. A nested set of BRDFs were obtained for the 8 sub-plots in both mornings and afternoons,

especially between June 28 and July 17. These BRDFs naturally grouped into 4 higher curves associated with the well watered sub-plots (0%Nw; 50%Nw; 100%Nw; and 200%Nw) and 4 lower curves associated with the non-watered sub-plots (0%Nnw; 50%Nnw; 100%Nnw; and 200%Nnw). This gradient from highest to lowest BRDF is clearly evident for the stress conditions on the afternoon of June 28. A similar separation and ranking of the BRDFs according to nitrogen and water availability occurred on other days (e.g., afternoon of July 17) [Fig. 1]. During the drought period that accompanied the growth and maturation growth phases, the optimal treatment (100%Nw) always displayed the highest PRI values whereas the most deficient treatment (0%Nnw) always displayed the lowest PRI values, and this is most clear for the nadir or near-nadir (0°±30°) values [Fig. 1]. During this drought period, the forward scatter PRI values (VZAs: -30°, -45°, and -60°) were typically higher than those on the backscatter side (VZAs: +30°, +45°, and +60°), especially evident for the stressed *non-watered* subplots.

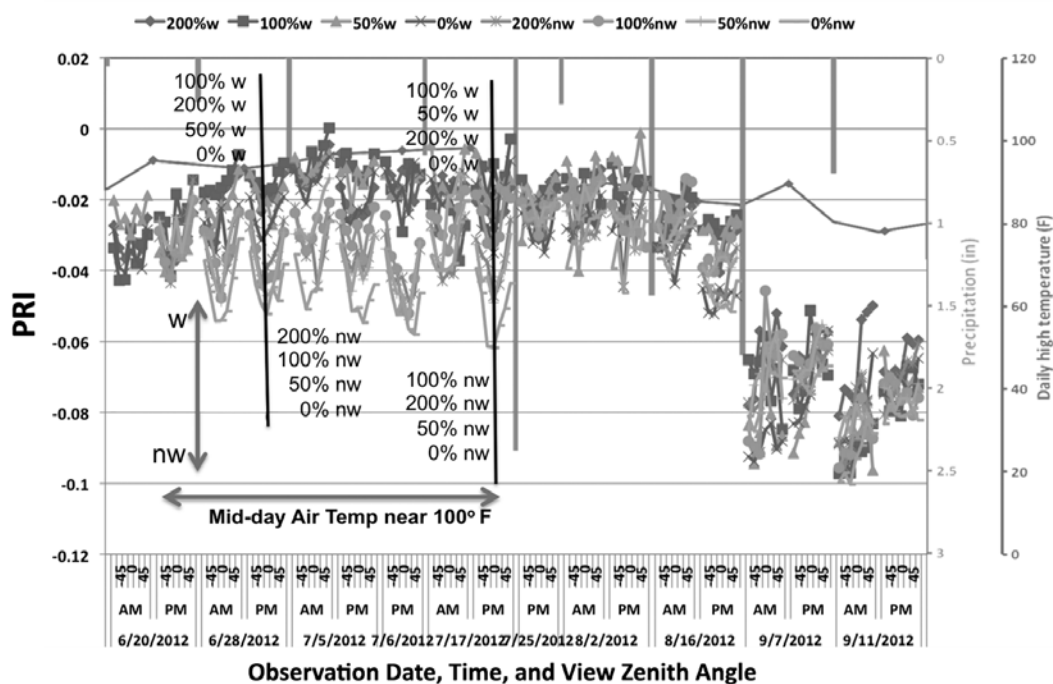
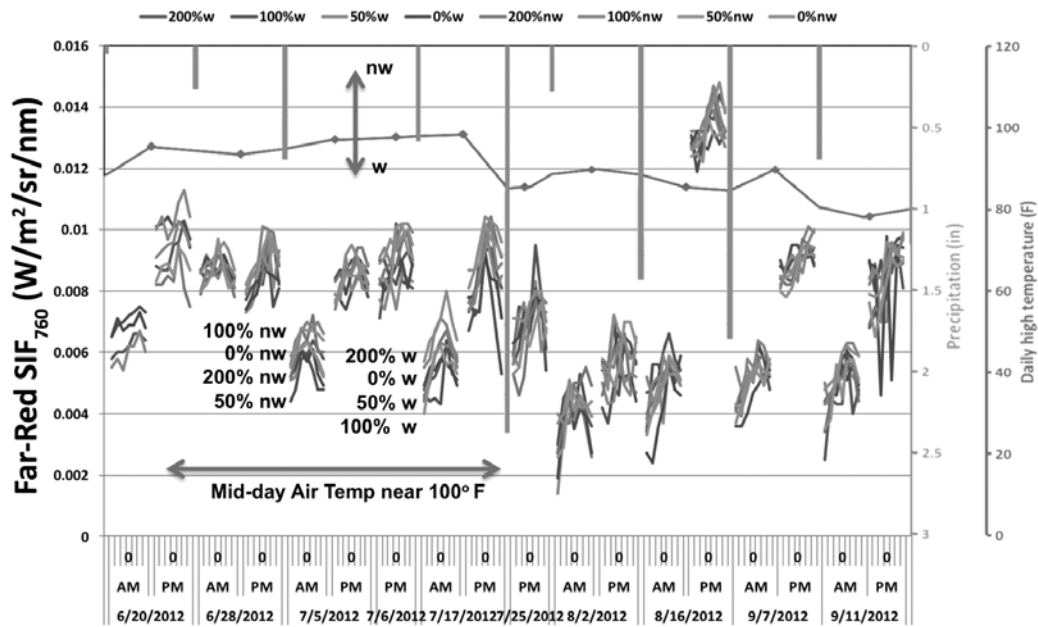


Figure 1. The seasonal change throughout the 2012 growing season for the 8 N/water treatment plots is documented with PRI responses for 10 observation days. For each observation date and time of day (AM or PM), the x-axis is the VZA in the SPP. Negative VZA represent forward-scattering directions and positive VZA represent backscatter directions. The lines show the PRI BRDF for the 8 different treatments. The bars extending from the top of the plot describe the timing and amount of rainfall, where the length of the bars indicates the amount of rain (in inches), and their position on the x-axis indicates the occurrence of rain between the observation days. The continuous line across the plot is the daily high temperature (in °F) on the observation days. The BRDFs capture the significant anisotropy of the stress responses.



Observation Date, Time, and View Zenith Angle

Figure 2. The bidirectional emission distribution functions for the far-red SIF retrieved for SIF₇₆₀ are shown for the data matching the PRI (Fig. 1). As with the PRI, significant anisotropy is apparent in the bidirectional emission for SIF₇₆₀. Note that the bidirectional emissions have inverted bowl shapes for almost all of the measurement sets, but that the highest SIF is emitted by the non-watered treatment groups whereas the least stressed groups had lower SIF. However, there was considerable overlap of the bidirectional emission and no consistent gradient from most to least SIF values. SIF₇₆₀ is lower in mornings than in afternoons, but afternoon SIF₇₆₀ is similar throughout the growing season.

However, this effect was variable for the watered sub-plots (e.g., afternoons, June 28, July 5). The discrimination among the sub-plots based on PRI BRDFs collapsed when the drought ended and the high daily ambient temperatures dropped, which occurred after the significant rain event of July 22. During the next month when field conditions were more favorable, the PRI values for all sub-plots remained relatively high (between -0.01 and -0.04) for all VZAs. However, with onset of senescence (Sept. 7, 11), the PRI values dropped to -0.06 or lower, and BRDF shapes were variable.

The corresponding bidirectional emission distribution functions for the SIF₇₆₀ also displayed significant anisotropy in the SPP (Fig. 2). Before onset of senescence, these SIF₇₆₀ curves were inverted bowl-shapes, an opposite trend to that exhibited by the PRI. The highest SIF₇₆₀ values were often produced by the 0%Nw, the most stressed subplot. Notably, the highest SIF₇₆₀ values (0.10-0.11 W m⁻² s⁻¹) were observed at near nadir VZAs in these sub-plots. This pattern was opposite to that observed for the PRI. The emission curves for the watered subplots tended to have lower SIF₇₆₀ values than the non-watered subplots, but there

was much overlap in the 8 curves (Fig. 2). For both SIF₇₆₀ and SIF₆₈₇, afternoon bidirectional emissions tended to be higher than in the morning throughout the season. After every rain event, the SIF values dropped, an effect especially apparent for the morning measurement sets. Anomalously high SIF values were observed for both the red and far-red SIF during the afternoon of Aug. 16, for which we have no explanation; however, their ratio fits within the seasonal pattern. Bidirectional SIF₆₈₇ emissions were much less anisotropic than either the SIF₇₆₀ or the PRI. However, when anisotropy was strongly expressed in mid-season the SIF₆₈₇ emission curves had inverted bowl-shapes (not shown). Typically, these overlapping SPP curves were flatter and/or more highly variable, so that a consistent gradient among the treatments was not apparent. However, the optimal 100%Nw treatment did consistently produce among the highest SIF₆₈₇ values. The SIF Ratio (SIF₆₈₇/SIF₇₆₀) was more stable across the growing season (Fig. 3) than either the SIF₆₈₇ or the SIF₇₆₀, except for perturbations caused by rain events. Much of the within-day and day-to-day variability was reduced with the SIF Ratio, for which the seasonal trend resembled that of the average PRI

values. This seasonal trend in daily nadir values per treatment for the PRI and the SIF Ratio is shown in Fig. 4, where both variables indicate higher responses for the optimal 100%Nw treatment across the season, maximum values in mid-season (early Aug.), and reductions during late season senescence. Consequent-

ly, these two variables are highly related ($r=0.96$, $n=63$). Higher values for both variables were associated with early season growth, whereas the lowest values were associated with the senescence period. Values were most variable during the reproductive growth phases.

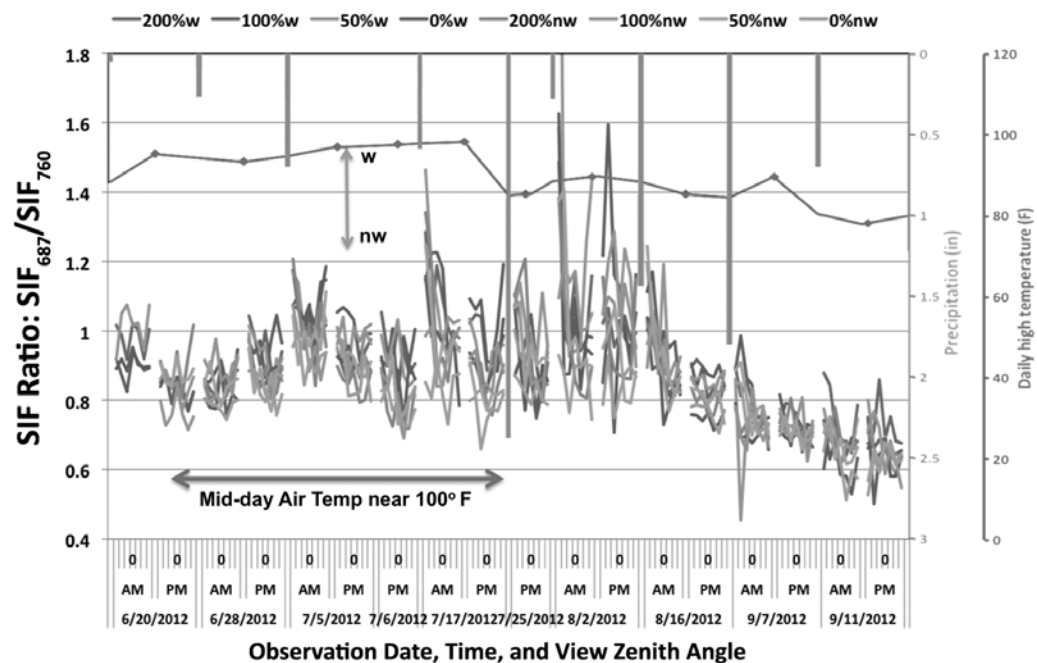


Figure 3. The bidirectional emission distribution functions for the Red/Far-Red SIF Ratio (SIF_{687}/SIF_{760}) are shown as in figs. 1 and 2. These curves exhibit overlapping and variable shapes across the SPP, so that the anisotropy is suppressed relative to that expressed by SIF_{760} . However, this ratio exhibits perturbations after rain events before stability is achieved. Within each measurement set, the highest values are typically associated with healthiest watered treatment groups. A general decline in the SIF_{687}/SIF_{760} ratio indicates a similar reduction in canopy photosynthetic efficiency.

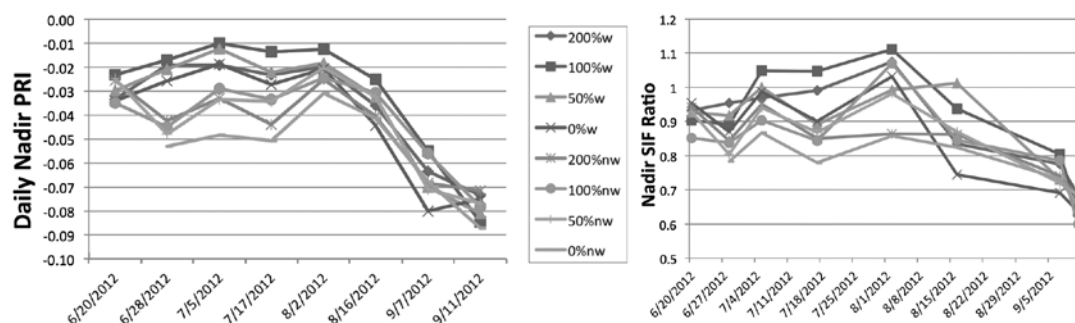


Figure 4. A) The average daily Nadir ($VZA = 0$) PRI observations and B) the average daily Nadir ($VZA = 0$) Red/Far-Red SIF Ratio (SIF_{687}/SIF_{760}) for the eight nitrogen/water treatments through the 2012 growing season in the USDA cornfield.

4. DISCUSSION

This study reveals that the BRDFs for several vegetation spectral stress indicators (PRI, SIF₇₆₀, SIF₆₈₇, SIF Ratio) acquired in the SPP in both mornings and afternoons throughout a corn crop's growing season exhibit: (i) differing expressions of surface anisotropy; (ii) differing values in morning vs. afternoons in pre-senescent period; and (iii) differing sensitivities to the nitrogen and water treatments applied to the experimental plots. It should be noted that the canopies of all treatments invoked various strategies to deal with the environmental conditions; the most obvious was generation of erectophile leaf angles and leaf roll, which placed the underside of leaves on the outside of the roll and oriented them approximately normal to the ground surface. This condition was observed by mid-morning in the non-watered treatments, and often by afternoon even in the well-watered treatments. The nadir PRI values were the most useful measures for discriminating among the various experimental treatments, and consistently identified the least stressed, well-watered plots separately from the stressed, no water plots. The optimal 100%Nw treatment produced the highest PRI values, whereas the 0%Nw treatment produced the lowest PRI values, especially during the severe drought period for fully developed mid-season canopies. PRI values were highest and similar for all treatments when the drought abated in mid-season. The PRI was the most anisotropic of these spectral indicators, exhibiting bowl-shaped BRDFs for which the lowest values occurred near nadir and the highest values occurred at the extreme VZAs ($\pm 60^\circ$). We could not corroborate published findings, primarily for forests from tower or satellite data, that the deltaPRI variable, the difference of the PRI values measured near the coldspot and the hotspot ($PRI_{\text{coldspot}} - PRI_{\text{hotspot}}$) [Hilker, 2008], was able to capture canopy stress. Instead, we found that the highest PRI values were as likely to be associated with the sunlit as with the shaded canopy sector. The two SIF variables also exhibited anisotropy, especially SIF₇₆₀, and both SIF indices showed higher emissions in afternoons as compared to mornings through the growing season until senescence. Both the PRI and the SIF Ratio showed similar seasonal trends, declining throughout the growing season.

These various observations can be explained by the observed canopy geometrical structure adjustments to stress. The canopy leaf distribution and energy management strategies (leaf roll, erectophile angles) that are typical of corn crops under stress put the underside of leaves as the interfacing plant tissue with the atmosphere, and the elements viewed by remote sensors. It is known from laboratory and field measurements that the leaf undersides have higher emis-

sions in the far-red spectrum, than in the red peak, and it has also been shown that the emission transmittance in the far-red through the leaf and viewed at the leaf underside amounts to ~40% of the emissions produced internally (Van Wittenberghe, 2014). A much smaller quantity is transmitted in the red region.

5. ACKNOWLEDGEMENTS

We would like to acknowledge NASA's Terrestrial Ecology program (TE) and Postdoctoral Program (NPP), and the Summer Student Internship programs at NASA/GSFC and UMBC/JCET, which provided funding and support for the research.

6. REFERENCES

- Cheng, Y.-B., et al., 2009, Dynamics of spectral bio-indicators and their correlations with light use efficiency using directional observations at a Douglas-fir forest, *Measurement Science and Technology*, 20 (9), 095107.
- Gamon, J.A., et al., 1990, Remote sensing of the xanthophyll cycle and chlorophyll fluorescence in sunflower leaves and canopies, *Oecologia*, 85 (1), 1-7.
- Hilker, T., et al., 2008, Separating physiologically and directionally induced changes in PRI using BRDF models, *Remote Sensing of Environment*, 112 (6), 2777-2788.
- Meroni, M., et al., 2009, Remote sensing of solar-induced chlorophyll fluorescence: Review of methods and applications, *Remote Sensing of Environment*, 113 (10), 2037-2051.
- Middleton, E.M., et al., 2009, Linking foliage spectral responses to canopy level ecosystem photosynthetic light use efficiency at a Douglas-fir forest in Canada, *Canadian Journal of Remote Sensing*, 35 (2), 166-188.
- Middleton, E.M., Huemmrich, K.F., Cheng, Y.-B., & Margolis, H.A. 2011, Spectral bio-indicators of photosynthetic efficiency and vegetation stress. In, *Hyperspectral Remote Sensing of Vegetation*, P.S. Thenkabail, J.G. Lyon, and A. Huete, (Eds.), Taylor & Francis, Cat. # K12019.
- Mohammed, G.H., Binder, W.D., & Gillies, S.L., 1995, Chlorophyll fluorescence: A review of its practical forestry applications and instrumentation, *Scandinavian Journal of Forest Research*, 10 (1), 383-410.
- Rascher, U., 2007, FLEX – Fluorescence Explorer: A remote sensing approach to quantify spatiotemporal variations of photosynthetic efficiency from space, *Photosynthesis Research*, 91, 293-294.
- Van Wittenberghe, et al., 2014, A field study on solar-induced fluorescence and pigment parameters along a vertical canopy gradient of four tree species in an urban environment, *Science of the Total Environment*, 466-467, 185-194.

30 Years Of Land Surface Albedo From Geostationary Satellites: Status Of The Scope-Cm Lags Project

Alessio Lattanzio^{1*}, Jessica Matthews², Masaya Takahashi³, Ken Knapp², Jörg Schulz¹, Rob Roebeling¹, Reto Stöckli⁴

¹EUMETSAT, Darmstadt, Germany;

²NOAA National Climate Data Center, Asheville, NC USA;

³JMA, Meteorological Satellite Center, Tokyo, Japan;

⁴Federal Office of Meteorology and Climatology MeteoSwiss, Zürich, Switzerland

alessio.lattanzio@eumetsat.int

ABSTRACT The Land surface Albedo from Geostationary Satellites (LAGS) project of the Sustained and Coordinated Processing of Environmental Satellite Data for Climate Monitoring (SCOPE-CM) activity is involving the operational meteorological satellite agencies in Europe (EUMETSAT), in Japan (JMA: Japan Meteorological Agency) and in the USA (NOAA: National Oceanic and Atmospheric Administration). The project started in January 2014 and aims at the generation of a Land Surface Albedo Climate Data Record enclosing almost 30 years starting in the early 1980s. The first issue addressed is the limitation in quality due to clouds not removed by the embedded cloud screening procedure. As also demonstrated in a study performed by independent researchers, the loss of quality in the retrieval is quite significant over dark dense vegetated areas. Two alternative strategies are followed to efficiently improve the cloud detection and removal. The first, in order to screen out outliers values, relies on a post processing analysis of the albedo seasonal variation together with the usage of a priori information contained in a background albedo map. The second is based on the application of a robust and reliable cloud mask from the Satellite Application Facility on Climate Monitoring (CM SAF) during the retrieval taking advantage of the information contained in the measurements of the infrared and visible channels. The second issue addressed in the project concerns the homogenization, for all exploited geostationary satellites, of the ancillary information needed for the atmospheric correction and of the input reflectance data. This paper discusses the activities performed and the results obtained.

1 INTRODUCTION

The Global Climate Observing System (GCOS) formulated scientific requirements for climate observations including a list of relevant parameters, the so-called Essential Climate Variables (ECVs), with associated observation requirements. One of the defined ECVs is the land surface albedo, a parameter defined as the ratio of the radiation flux reflected from the surface into the atmosphere to the incident radiation flux. It depends on both the anisotropy of the surface and the atmosphere. Land surface albedo is a key forcing parameter for the climate system controlling the radiative energy budget. Thus, its monitoring is of primary importance for an understanding of the climate system. Its value changes in space and time, depending on both natural processes (vegetation growth, rain and snowfall and snow melting, wildfires, etc.) and human activities (forestation and deforestation, harvesting crops, anthropogenic fires, etc.). Ground-based measurements of such a variable are of great importance for the assessment and evaluation of local and regional variability and change, while satellite remote sensing offers a unique opportunity for documenting and monitoring the spatial surface albedo

distribution, its variability and change at continental scales. Observations acquired by geostationary satellites have the advantages of offering both a long-term dataset and an angular sampling of the surface as well as providing diurnal sampling of key parameters influencing the retrieval such as cloud cover and aerosol load.

2 THE SCOPE-CM FRAMEWORK

The aim of the Sustained and Coordinated Processing of Environmental Satellite Data for Climate Monitoring (SCOPE-CM, <http://www.scope-cm.org/>) is the establishment of an international network of facilities for the continuous and sustained provision of high-quality products for climate monitoring. These satellite-based datasets, that have a goal to detect variability and trends of key climate variables, are referred to as Climate Data Records (CDR). They are defined as a “time series of measurements of sufficient length, consistency, and continuity to determine climate variability and change (NRC, 2004) and can be divided into two classes: (i) Fundamental Climate Data Records (FCDR), a homogenous long-term dataset of radiances or brightness temperatures encompassing different sensors and platforms with spatial and temporal overlap; and (ii) Thematic

Climate Data Record (TCDR), geophysical variables derived from the FCDRs, which can be understood as the satellite product associated with an Essential Climate Variable (ECV). The sustained and coordinated generation of FCDR and TCDR is the major objective of SCOPE-CM.

This initiative is one component of an end-to-end system with the final objective of climate monitoring having the satellite observations represented by the World Meteorological Organization (WMO) Integrated Global Observing System (WIGOS) at one end and the CDR user community at the other end (see Figure 1). Current participants of the network are the China Meteorological Administration (CMA), the European Organisation for the Exploitation of Meteorological Satellites (EUMETSAT), the Japan Meteorological Agency (JMA) and the National Oceanic and Atmospheric Administration (NOAA). The SCOPE-CM framework is currently running the phase-2 (SCOPE-CM, 2012), in which, 10 projects on CDR generation have been started. One of them is focusing on the retrieval of land surface albedo from geostationary satellites (Lattanzio et al., 2013). The three partners in the project are EUMETSAT, JMA and NOAA. The agencies share the same retrieval algorithm and each is processing its own satellite data.

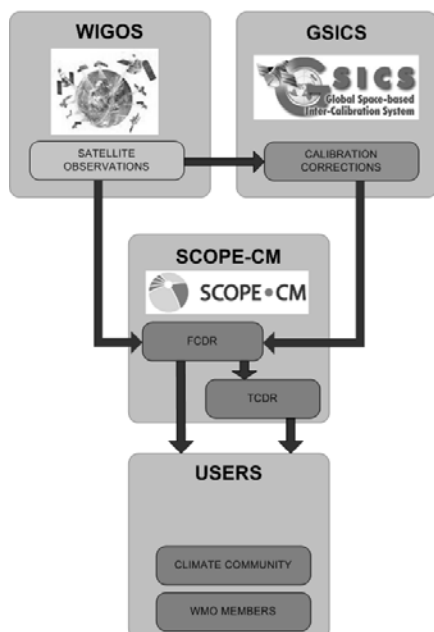


Figure 1: Conceptual view of the end-to-end system for the exploitation of satellite observations for climate monitoring.

3 RETRIEVAL OF SURFACE ALBEDO FROM GEOSTATIONARY SATELLITES

Geostationary satellites are very powerful devices for the measurement of surface albedo due to their ability to sense several times per day the same portion of the Earth's surface. On the other hand, the retrieval area is limited to a circle with a radius of ca. 65 degrees around the sub satellite point (SSP). The Geostationary Surface Albedo (GSA) algorithm performs the inversion of a fast Radiative Transfer Model (RTM) ingesting single visible band images and total column water vapour and total column ozone from reanalysis data. The GSA algorithm is based on a method proposed by Pinty et al. (2000). This method relies on daily accumulation of clear sky radiances acquired in a single visible band and on the applicability of the reciprocity principle (Lattanzio et al., 2006). According to this principle the Bidirectional Reflectance Distribution Function (BRDF) does not change when incident and reflected angles are reversed. The method applied in the GSA algorithm allows for a joint retrieval of aerosol load and surface albedo. An assessment of the measurement error and an estimation of the retrieval uncertainty are performed for each pixel (Govaerts and Lattanzio, 2007). The GSA algorithm however relies on run-time screening of cloudy pixels. This method does not recognize specific cloud patterns and the Directional Hemispherical Reflectance (DHR or black sky albedo) inversion is severely affected by cloud contamination. The surface albedo is retrieved as Bi-directional Hemispherical Reflectance isotropic (BHRiso or white sky albedo) and DHR. Those parameters can be used to estimate the real albedo (blue sky albedo) as explained in Pinty et al. (2005). The portion of the Earth land surface which can be sensed with instruments on board geostationary satellites is shown in Figure 2. The coverage in latitude is delimited within $\pm 65^\circ$ North and South.

4 VALIDATION

EUMETSAT coordinated a study for the validation of the surface albedo dataset. The study was performed by a group of independent researchers in Europe and the USA. A project report was delivered (Fell et al., 2012) and can be requested by interested users. The validation analysis focused on four main aspects: (1) uncertainty assessment, (2) temporal consistency, (3) validation against in-situ measurements and (4) comparison with other satellite estimates. NOAA and JMA started internal validation activities as well.

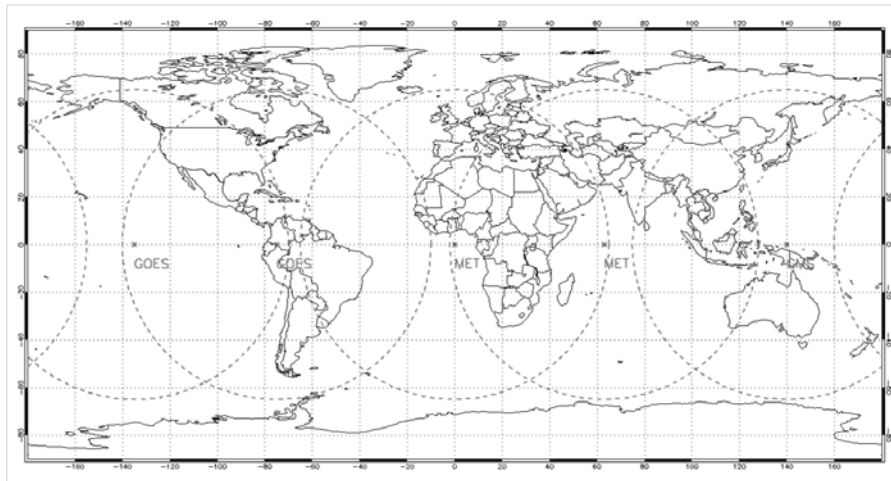


Figure 2: Portion of the Earth possible to sense with a ring of geostationary satellites. The temporal coverage is spanning from the beginning of the 1980s to the present with only one gap around 60°E where coverage only started late 1996 (see Figure 3).

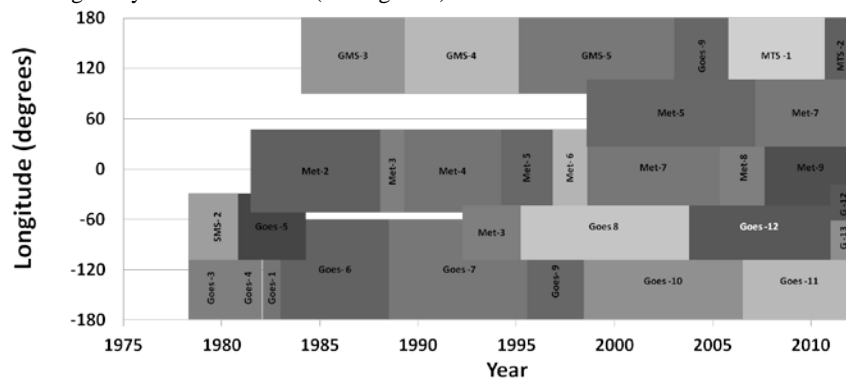


Figure 3: Temporal coverage possible to sense with a ring of geostationary satellites.

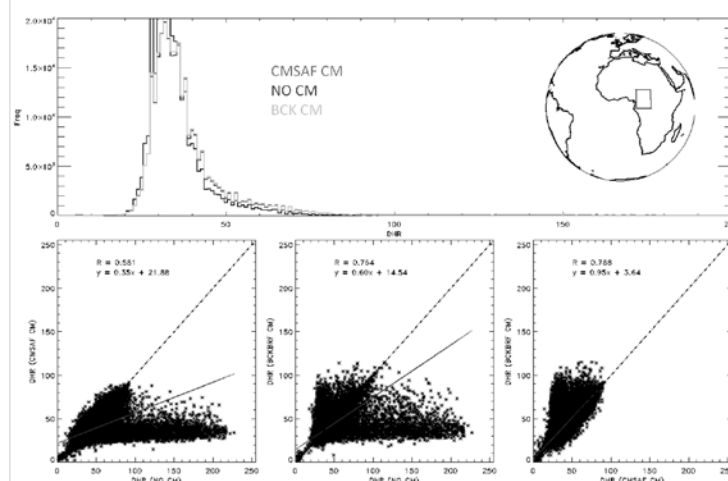


Figure 4: Region: tropical forest viewed under a small view zenith angle. Comparison of surface albedo retrieval with no cloud mask (NO CM), with a very simple one based on the VIS band only (BCK CM) and with a new cloud mask developed by CM SAF (CMSAF CM).

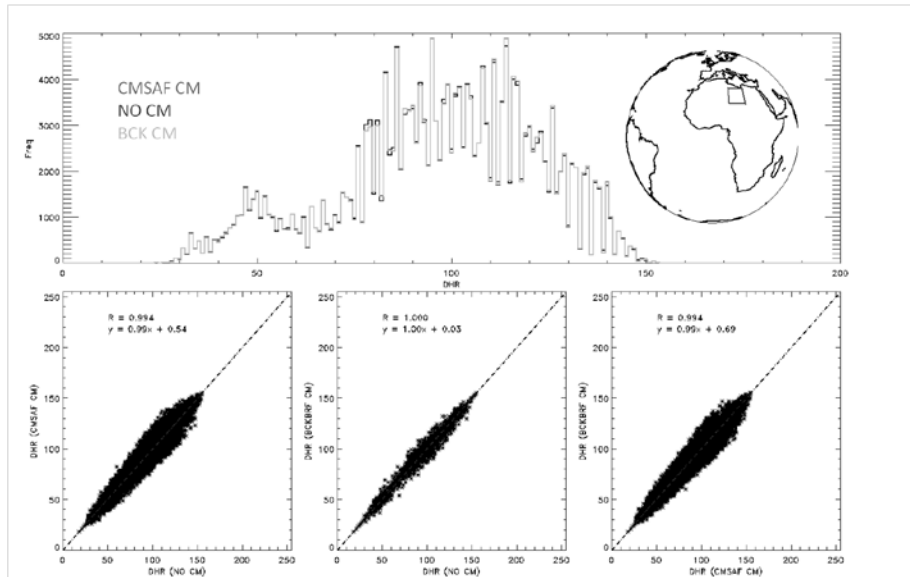


Figure 5: Same as Figure 4 but for a desert region.

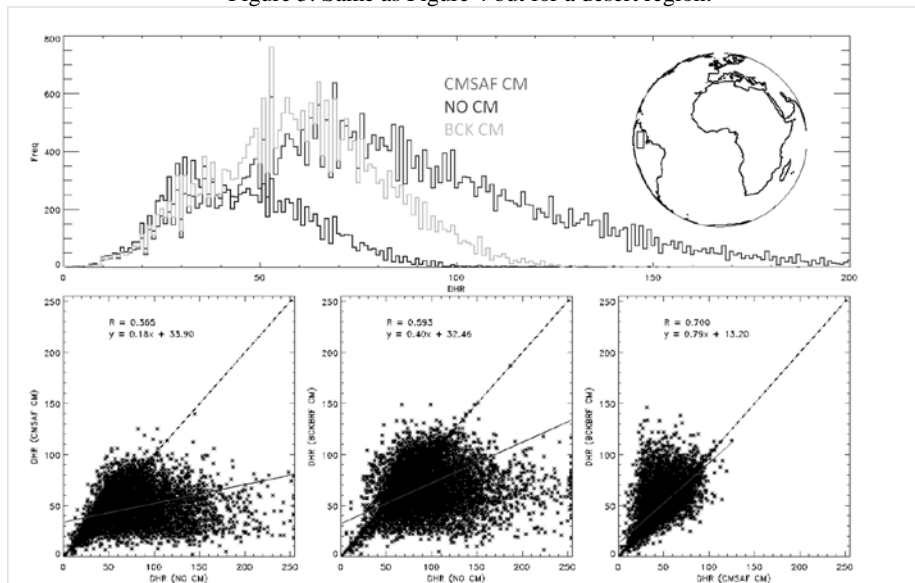


Figure 6: Same as Figure 4 but for a forest area viewed under a large view angle.

5 CURRENT ACTIVITIES

The project team is addressing some issues related with the current retrieval scheme: (1) development of a robust scheme for cloud screening (2) usage of common set of reanalysis data from ECMWF, and (3) cooperation with GSICS (Goldberg et al., 2011) and with the SCOPE-CM project focusing on inter-calibration among geostationary satellites (<http://www.scope-cm.org/projects/scm-06/>) for the exploitation of calibration coefficients derived with shared methods.

	Retrieved Pixels			Above Threshold ("0.45)		
	NO CM	CMSAF CM	BCK CM	NO CM	CMSAF CM	BCK CM
Forest (Africa)	90%	+92%	+91%	1%	0%	0.01%
Desert	100%	100%	100%	47.9%	47.7%	47.9%
Forest (SA)	51%	17%	36%	15%	0.03%	1.2%

Table 1: Impact of cloud masking on the number of retrieved pixels (total and higher than a threshold of 0.45).

A simple cloud mask based on the generation of a background reflectance map and a more sophisticated cloud mask currently developed by the Satellite

Application Facility on Climate Monitoring CM SAF (Stöckli, in prep.) have been used to study the impact on the pixel based albedo retrieval. Common to both methods is the fact that they can be applied to all past and current GEO satellites (MSG, GOES, GMS, MTSAT). They only depend on the availability of a visible (possibly broad band) and a thermal infrared (possibly at 10.8 micrometers) channel.

As exemplified for the tropical rain forest region (Figure 4) sensed under a small view zenith angle (VZA) the impact of using the CM SAF cloud mask over no cloud mask is to limit the DHR to values below 0.1 (left panel). The added value of the CM SAF cloud mask using both the visible and the infrared channels over the simple visible band only based cloud mask is to better constrain the DHR values on the range below 0.1 (right panel). As expected, cloud masking has almost no effect on DHR in a desert region (Figure 5). For a tropical rain forest region in South America sensed under large VZA the effect is two-fold (Figure 6). A cloud mask efficiently removes unrealistically high albedo values caused by cloud contamination. But secondly, as shown in Table 1, a more clear sky conservative cloud masking (CM SAF) also leads to a significant decrease of the number of retrieved DHR values. This result is not surprising as visible-only cloud masking at high VZA is likely to fail due to decreased contrast at higher atmospheric path lengths. The fewer but realistic and more reliable retained DHR observations will likely increase the overall quality of the DHR.

6 SUMMARY

SCOPE-CM is a framework established by the WMO for the sustained generation of CDRs. The main actors are satellite data providers. The second phase of the framework started middle 2014 with 10 projects. The SCOPE-CM project on land surface albedo retrieval from geostationary satellites has successfully implemented retrieval software at EUMETSAT, NOAA and JMA. A quality analysis and validation by independent scientists has shown that, among other problems, residual undetected clouds are an issue for product quality. The positive impact of a new cloud mask applicable to all historic and current geostationary satellites on the quality of the retrieval has been shown. Further work will focus on homogenisation of input data, in particular, inter-satellite calibrated reflectance, reanalysis data and the implementation of a reliable cloud mask.

7 REFERENCES

- Fell, F., et al. (2012): Evaluation of the Meteosat Surface Albedo Climate Data Record (ALBEDOVAL), Final Report, 119 pages.
- Goldberg M. et al. (2011): The Global Space-Based Inter-Calibration System. *Bull. Amer. Meteor. Soc.*, 92, 467–475.
- Govaerts, Y., and Lattanzio, A. (2007). Retrieval Error Estimation of Surface Albedo Derived from Geostationary Large Band Satellite Observations: Application to Meteosat-2 and -7 Data. *Journal of Geophysical Research* 112, doi:10.1029/2006JD007313
- Lattanzio, A. et al. (2006). Consistency of surface anisotropy characterization with Meteosat observations. *Advanced Space Research*, doi:10.1016/j.asr.2006.02.049
- Lattanzio A. et al. (2013). Land Surface Albedo from Geostationary Satellites: a multi-agency collaboration within SCOPE-CM. *Bulletin of the American Meteorological Society* - DOI:10.1175/BAMS-D-11-00230.1
- Loew, A. and Govaerts Y. (2010) Towards Multidecadal Consistent Meteosat Surface Albedo Time Series. *Remote Sens.*, 2(4), 957-967; doi:10.3390/rs2040957
- National Research Council (NRC), 2004: Climate data records from Environmental Satellites, National Academies Press, Washington DC, 150 pp.
- Pinty, B. et al. (2000) Surface albedo retrieval from Meteosat: Part 1: Theory, *Journal of Geophysical Research*, 105, 18099-18112.
- Pinty, B. et al. (2005). Coupling diffuse sky radiation and surface albedo. *J Atm Science* 62, 2580-2591
- SCOPE-CM, 2012: SCOPE-CM Phase 2 implementation plan. Version 1.0, pp. 28 (download from <http://www.scope-cm.org/history/>).
- Stöckli, R., et al. (in prep.) The Meteosat two channel CM-23011 Cloud Fractional Cover (CFC) dataset. Algorithm Theoretical Basis Document (ATBD) of the Satellite Application Facility on Climate Monitoring. XX pages

Determining spectral reflectance coefficients of water in laboratory conditions

Piotr Walczykowski

*Military University of Technology Department of Remote Sensing and Photogrammetry,
Institute of Geodesy, Faculty of Civil Engineering and Geodesy
2 Kaliskiego st., Warsaw 00-908, Poland; tel.+ 48 22 683 90 21
pwalczykowski@wat.edu.pl*

ABSTRACT *Water monitoring is one of the key areas of remote sensing applications. Water is a very important part of the environment. Remote, non-contact monitoring of pollutants can be performed based on the analysis of hyperspectral and multispectral imaging. In quantitative studies, particularly when detecting the percentage concentration of impurities in water, it is necessary to know the spectral reflectance coefficients of the water itself. It is very difficult to acquire these data with sufficient accuracy. For this purpose, the authors had constructed a specialized laboratory Measuring Station. It had been set up in a room isolated from any external factors. It consists of a ASD Field Spec 4 Spectroradiometer and a lighting system based on ASD Illuminator Reflectance Lamps. Both the spectroradiometer and lighting system are mounted on a specially constructed platform, which allows the user to conduct research using different geometrical parameters between the instrument, lighting system and the test sample. The test samples are placed in glass containers, which differ from one another in height and cubic volume. Due to the fact that water is characterized by a high translucency (transmission), the walls and the bottom of these tanks have to be covered with a suitable material impervious to radiation. This allowed for the elimination of external factors not related to the test samples. Two types of materials were used - one with high reflectance coefficients and the other with a low reflectance. The article presents a methodology for determining the spectral reflectance coefficients of water in the 350 – 2500nm range and the impact of various factors, such as the height and volume of the water, on the acquired values of spectral reflectance.*

1 INTRODUCTION

Remote, non-contact monitoring of water pollutants can be performed based on analyses of hyperspectral and multispectral imaging (Karafistan et al, 2003; Ritchie, et al., 2003). In quantitative studies, particularly when detecting the percentage concentration of impurities in water, inter alia, it is necessary to know the spectral reflectance coefficients of the water itself (Zibordi, 2012). It is possible to acquire spectral coefficients of natural reservoirs water with in situ measurements with spectroradiometers, from aerial and satellite images, both multispectral and hyperspectral, like it is presented in many research works that were conducted recently and in the past (e.g. Feng, et al., 2005; Froidefond, et al., 2002; Tomlinson, et al., 2004). However spectral reflectance coefficients acquired with multispectral and hyperspectral sensors can not be considered as reference for clear water due to many water contaminants (e.g., Kishino, et al., 2005; Matthews, et al., 2005). There are conducted some experiments in laboratory conditions, that could provide spectral reflectance coefficients of clear water, but still there it

is very difficult to acquire these data with sufficient accuracy (Han, 1997).

2 MEASURING STATION

A specialized measuring station had been constructed for the measurement of spectral coefficients of water in laboratory conditions. A separate room had been adapted for this purpose, which was specially modified for such experiments by covering the window openings and cover as well as lining the walls and ceiling of the room a special material that absorbs most of the radiation in the tested spectral range. The room had been fitted with special doors that, when closed, complete isolate the room from all external influences. The prepared room now houses our measuring station. It consists of a platform on which we had installed an ASD spectroradiometer Field Spec 4 and lighting system consisting of Illuminator Reflectance Lamps (Walczykowski, et al., 2013). The platform has been designed in such a way as to give the possibility of changing the geometry of the measuring station in terms of the angles between the spectroradiometers probe and the lighting system with respect to the studied sample.

When measuring the reflectance coefficients of water in laboratory conditions, the type of container used to store the water is a very big problem. The experiments described in this paper were all conducted using glass tanks. Due to the transparency of the glass, the containers' walls had been covered with a material impervious to radiation in the measured spectral range, while at the same time being characterized by a very high level of absorption (at 98%).

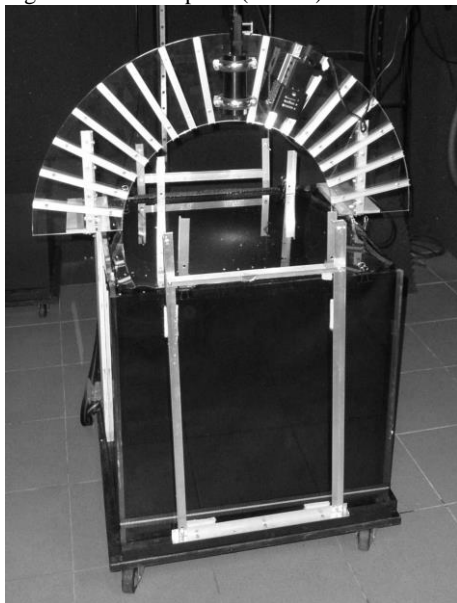


Figure 1. Measuring station

3 DETERMINING SPECTRAL REFLECTANCE COEFFICIENTS OF WATER

Determining spectral reflectance coefficients of water was done using a ASD Fieldspec4 spectroradiometer. The spectral reflectance coefficient was calculating using the following formula:

$$R = \frac{\text{Energy reflected from target}}{\text{Energy incident on target}} \quad (1)$$

Measurements of the amount of energy incident on a given sample had been done using a reference panel with a known spectral reflectance characteristic. Therefore, the methodology of determining these coefficients consists of measuring the radiance of the reference panel and then measuring the radiance of the tested sample, which in this case is water.

A reference panel (T1) with a known reflectance distribution was placed at the bottom of the tank. This acted as a background and additionally, going beyond the scope of laboratory experiments, could be used to

determine the impact of the type of material which makes up the riverbed or lakebed on obtained results. Thanks to a specially designed structure it was possible to locate the reference panel (T1) at different depths and therefore it was possible to conduct these experiments with different heights of the water column.

The next issue was the methodology of measuring spectral reflectance coefficients using the ASD FieldSpec 4 spectroradiometer (Hatchell, 1999). This instrument takes measurement in two phases – first a measurement of a reference panel (we used Zenith Lite SG3151 – T2) is taken and then a measurement of the studied sample. It is only possible to determine the spectral reflectance coefficients once we have both of these measurements. Such an approach determines the need to have a precisely stable geometry of the measurement station (Jung, et al., 2012). The distance between the spectroradiometer probe and the reference panel (T2) and the studied sample much be equal to each other. Even a small change causes large measurement errors. In order to collect accurate reflectance coefficient values it is necessary to provide stable illumination, an unchanging experiment set-up geometry (Jung, et al., 2012). To ensure a high accuracy of measurements, it was essential to place the reference panel (T2) on the waters surface. A specialized structure made this possible. After placing the reference panel (T2) on the waters surface and taking a measurement, the structure together with the reference panel was removed and the radiance measurement was the taken of the water together with a reference panel (T1) placed at the appropriate depth. The structure enabled the placing of the reference panel (T2) on the waters surface only when the water tank was at least 90% full. It was therefore impossible to conduct measurements with the tank filled to different levels. In order to study the affect of different heights of the water column, the position of the second reference panel (T1) submerged in the water was being changed.

The results of these measurements – the spectral reflectance coefficients of the water and reference panel (T1) submerged in the water at 15, 25, 35, 45 and 55 cm – have been shown in the figure below (Figure 2).

An interesting observation is the local maximum of the spectral reflectance coefficient curve visible at 1071nm, although this only occurs in the smallest water column. For a 15cm thick layer of water, the waters absorption was not total in this specific range, which lead to the reflectance being around 0,7%. For greater columns of water the reflectance value oscillates within the measuring errors of the spectroradiometer.

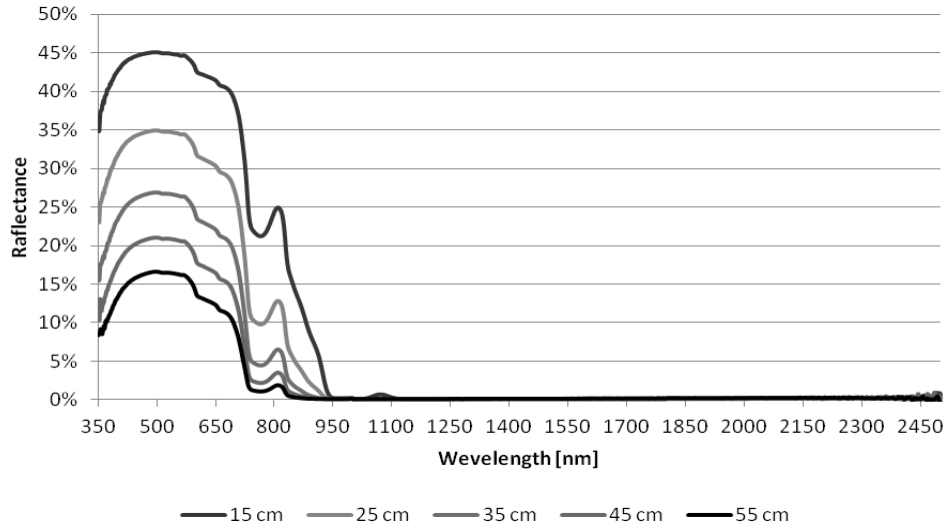


Figure 2. Spectral reflectance coefficients of the water and reference panel (T1)

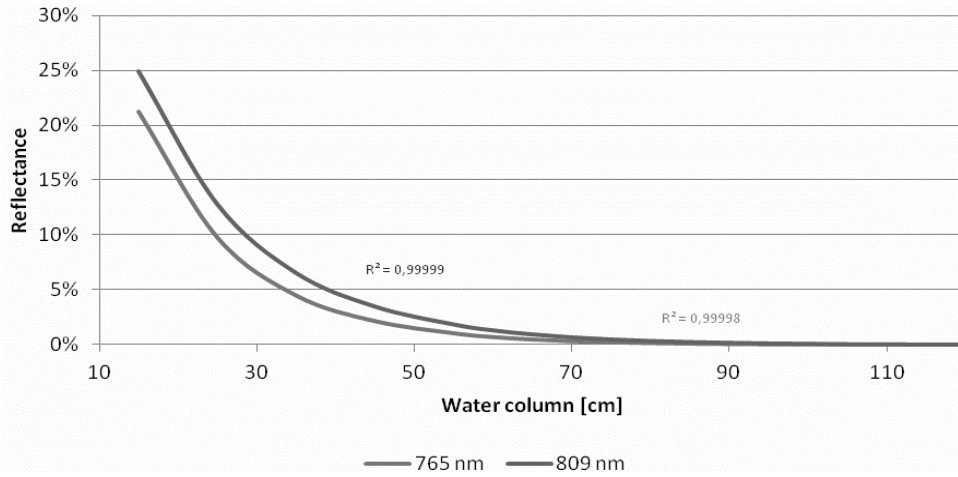


Figure 3. Approximation of the spectral reflectance coefficients at 765 and 809nm wavelengths with an exponential function.

When analyzing the spectral reflectance coefficients we had noticed two local extrema which occur in each of the studied water column Height – at $\lambda = 765$ and 809 nm.

The value of the spectral reflectance coefficients at these wavelengths in relation to the height of the water column can be described with an exponential function.

The mathematical formula, which enables the calculation of the spectral reflectance coefficient of the water depending on its depth for $\lambda = 765$ nm is as follows (2):

$$R_{765} = 0.64817e^{-0.06477h} \quad (2)$$

However for $\lambda = 809$ nm (3):

$$R_{765} = 0.64023e^{-0.07509h} \quad (3)$$

Assuming that the accuracy of measurements taken with the ASD FieldSpec 4 is equal to 0,02%, it is possible to precisely calculate the depth of clear water

up to 105cm using the 765nm wavelength and up to 125cm using the 809nm wavelength.

The height of the water column as a function of the spectral reflectance coefficient in the 765nm

wavelength is therefore described by the following formula and which had been illustrated in the Figure 4:

$$h = -13.31 \ln(R_{765}) - 5.92 \quad (4)$$

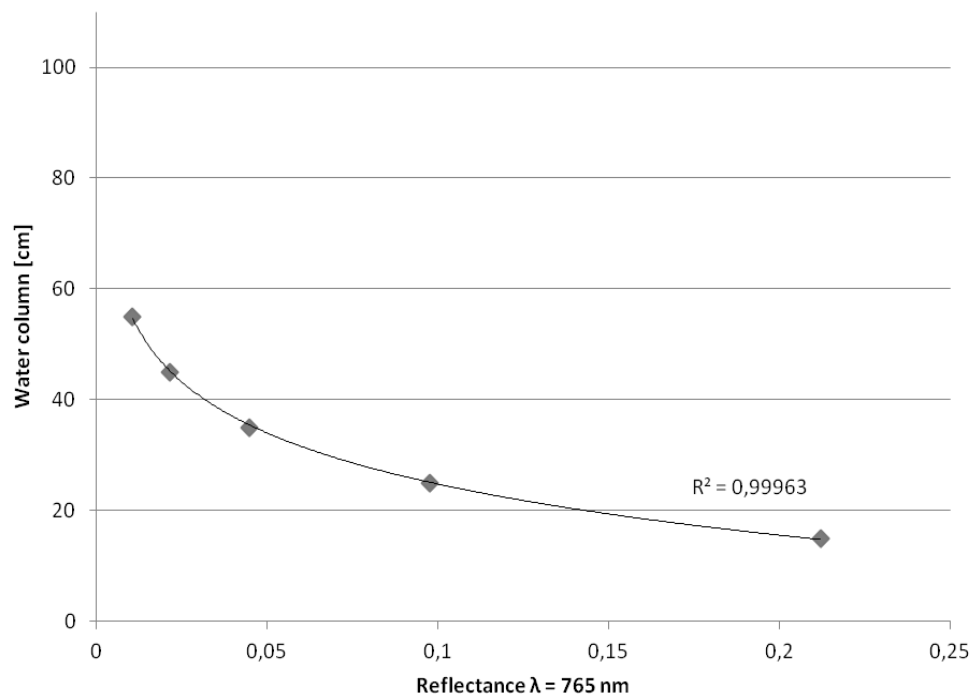


Figure 4. Logarithmic function for calculating the Height of the water column depending on the spectral reflectance coefficient at 765nm wavelength.

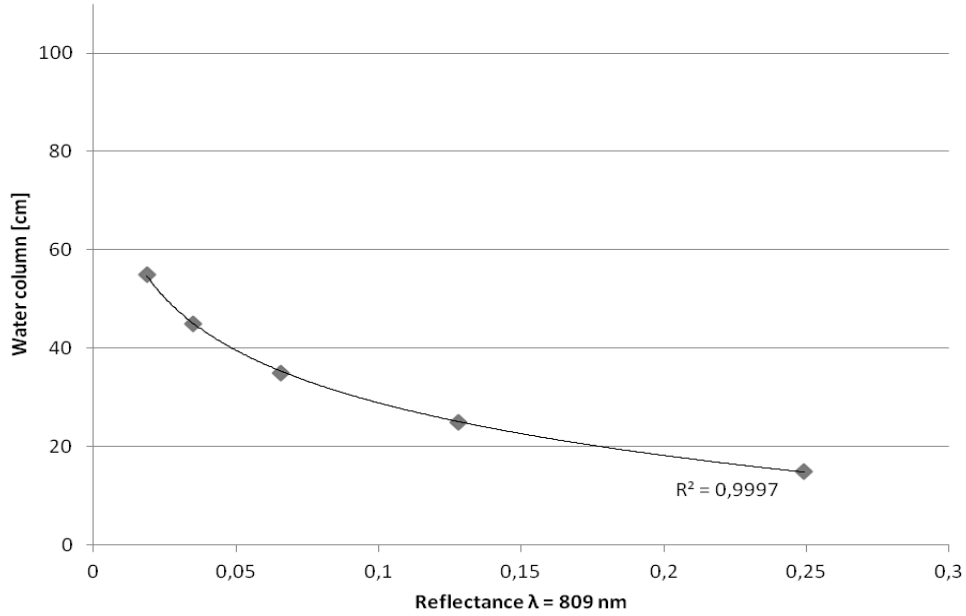


Figure 5. Logarithmic function for calculating the Height of the water column depending on the spectral reflectance coefficient at 809 nm wavelength.

The height of the water column as a function of the spectral reflectance coefficient in the 765nm wavelength is therefore described by the following formula and which had been illustrated in Figure 5:

$$h = -15.44 \ln(R_{809}) - 6.68 \quad (5)$$

The accuracy of calculating the height of the water column using the above mentioned methodology is very dependent on the accuracy of determining the spectral reflectance coefficients at 809 and 765nm wavelengths. This accuracy can be increased by using the coefficients measured in both of these wavelengths. Therefore we can propose the following formula:

$$h = \frac{\left(\frac{R_{809} - R_{765}}{R_{809} + R_{765}} \right) - 0.0233}{0.0046} \quad (6)$$

In his formula the accuracy of measuring the value of the spectral reflectance coefficient in the 765 and 809nm wavelengths has a much lesser affect on the accuracy of calculating the Height of the water column, in comparison to the methods described earlier.

4 SUMMARY

The conducted experiments have shown a visible relationship between spectral reflectance coefficients and the thickness of the water layer. They have resulted in mathematical formulas, which enable us to calculate the thickness of this water layer based on spectral reflectance coefficients in the 765 and/or 809nm wavelengths. This is possible with a reference panel submerged to a depth of up to 100cm.

The above research was carried out as part of the "IRAMSWater - Innovative remote sensing system for the monitoring of pollutants in rivers, offshore waters and flooded areas" (PBS1/B9/8/2012) project financed by the polish National Centre for Research and Development. The main aim of this research is to determine spectral reflectance coefficients of water. They will be the basis for later water pollutant detection methods. Using a reference panel (T1) submerged at different depths has a direct impact on the methods chosen for detecting water pollutants in field conditions and will also enable our results to be free of the affect of the type of material found on the bottom of the studied reservoirs.

5 ACKNOWLEDGEMENTS

The presented article is part of research work carried out in the “Innovative remote sensing system for the monitoring of pollutants in rivers, offshore waters and flooded areas” project- PBS1/B9/8/2012 financed by the polish National Centre for Research and Development NCBiR.

6 REFERENCES

- Feng, H., Campbell, J. W., Dowell, M. D., Moore, T. S., 2005, Modeling spectral reflectance of optically complex waters using bio-optical measurements from Tokyo Bay, *Remote Sensing of Environment* 99 (2005) 232 – 243.
- Froidefond, J., Gardel, L., Guiral, D., Parra, M., Ternon, J., 2002, Spectral remote sensing reflectance of coastal waters in French Guiana under the Amazon influence, *Remote Sensing of Environment* 80 (2002), 225- 232.
- Han, L., 1997, Spectral Reflectance With Varying Suspended Sediment Concentrations in Clear and Algae-laden Waters, *Photogrammetric Engineering & Remote Sensing*, 63, 701-705.
- Hatchell, D.C. (Managing Editor), 1999, *Analytical Spectral Devices, Inc. (ASD) Technical Guide* 4th Ed.
- Jung, A., Götze C., Glässer, C., Halle (Saale), 2012, Overview of Experimental Setups in Spectroscopic Laboratory Measurements – the SpecTour Project, PFG 2012 / 4, Stuttgart, August 2012.
- Karafisstan, A., Arik- Colakoglu, F., 2003, Physical, chemical and microbiological water quality of the Manyas lake, Turkey, *Mitigation and Adaptation Strategis for Global Change* (2005) 10, 127-143.
- Kishino, M., Tanaka, A., Ishizaka, J., 2005, Retrieval of Chlorophyll a, suspended solids, and colored dissolved organic matter in Tokyo Bay using ASTER data, *Remote Sensing of Environment* 99 (2005), 66 – 74.
- Matthews, M. W., Bernard, S., Winter, K., 2010, Remote sensing of cyanobacteria-dominant algal blooms and water quality parameters in Zeekoevlei, a small hypertrophic lake, using MERIS, *Remote Sensing of Environment* 114 (2010) 2070–2087.
- Ritchie, J.C., Zimba, P. V., Everitt, J. H., Remote sensing techniques to assess water quality, available at: http://www.asprs.org/a/publications/pers/2003journal/june/2003_jun_695-704.pdf.
- Tomlinson, M. C., Stumpf, R. P., Ransibrahmanakul, V., Truby, E. W., Kirkpatrick, G. J., Pederson, B. A., Vargo, G. A., Hei, C. A., 2004, Evaluation of the use of SeaWiFS imagery for detecting *Karenia brevis* harmful algal blooms in the eastern Gulf of Mexico, *Remote Sensing of Environment* 91 (2004), 293- 303.
- Walczykowski, P., Orych, A., Dabrowski, R., 2013, Designing a modern Measuring Station for obtaining spectral response characteristics in laboratory conditions, in *Proceedings in Research Conference In Technical Disciplines- RCITD* 2013, 124-121.
- Zibordi, G., Ruddick, K., Ansko, I., Moore. G., Kratzer, S., Icely, J., Reinart, A., 2012, In situ determination of the remote sensing reflectance: an inter-comparison, *Ocean Science*, 8, 2012, 567–586.

Determining methodology for acquiring spectral reflectance coefficients using a chosen monochromatic camera with interference filters

Piotr Walczykowski, Agata Orych, Agnieszka Jenerowicz
Military University of Technology Department of Remote Sensing and Photogrammetry,
Institute of Geodesy, Faculty of Civil Engineering and Geodesy
2 Kaliskiego st., Warsaw 00-908, Poland; tel. + 48 22 683 90 21
pwalczykowski@wat.edu.pl, aorych@wat.edu.pl, ajenerowicz@wat.edu.pl

ABSTRACT - Spectral reflectance coefficients are very useful in many different areas of interest, i.e. environmental and ecosystem studies, crop analysis, mineralogy and hydrology. They are usually acquired using discrete methods with spectrometers and spectroradiometers, which is very time consuming, therefore image-based methods are used more and more often. The research team from the Department of Remote Sensing and Photogrammetry from the Military University of Technology in Warsaw are proposing a method of extracting precise reflectance coefficients in quasi real time without the need for using a reference panel on the scene, that was obligatory in such measurements. This method is based only on the precisely determined exposure parameters of a chosen monochromatic camera together with interference filters. This research was conducted as part of the project entitled "IRAMSWater - Innovative remote sensing system for the monitoring of pollutants in rivers, offshore waters and flooded areas" (PBS1/B9/8/2012) financed by the polish National Centre for Research and Development. These analyses are conducted based on spectral characteristics of a wide selection of different pollutants.

1 INTRODUCTION

Spectral reflectance coefficients are one of the most widely used and most vital data of modern remote sensing. They are very useful in environmental and ecosystem studies, crop analysis, mineralogy and hydrology. They are usually acquired using discrete methods such as spectrometric measurements. These however can be very time consuming, therefore image-based methods are used more and more often. According to published studies, in order to acquire these spectral characteristics in a precise manner from hyperspectral data, it is necessary to have a reference panel visible on the photographed scene. This approach is based on acquisition the imagery first, ensuring that each scene contains at least one reference panel with a well know spectral characteristic, and then transforming the imagery and calculating the spectral response curves during post-processing.

1.1 Purpose of research

The research team from the Department of Remote Sensing and Photogrammetry from the Military University of Technology in Warsaw are proposing a method of extracting precise reflectance coefficients in quasi real time without the need for using a reference panel on the scene. This method is based only on the precisely determined exposure parameters of a chosen

monochromatic camera together with interference filters. This research was conducted as part of the project entitled "IRAMSWater - Innovative remote sensing system for the monitoring of pollutants in rivers, offshore waters and flooded areas" (PBS1/B9/8/2012) financed by the polish National Centre for Research and Development. Its main aim is the creation of a remote sensing system based on hyperspectral sensors which will enable the evaluation, detection and distribution of biological, physical and chemical pollutants in the examined waters in real time. These analyses are conducted based on spectral characteristics of a wide selection of pollutants. As most of these contaminants could only be measured in field conditions we needed to determine an optimal methodology for acquiring these data in an accurate and quick way.

2 ACQUIRING SPECTRAL REFLECTANCE COEFFICIENTS

Each object and substance due to different chemical and physical composition reflects a different amount of radiation and with a change in wavelength the value of this radiation varies. Spectral reflectance coefficients is represented by a function of wavelength, and its graphical representation is the dependence of the reflectance coefficients of an object's surface from the wavelength of the incident

radiation. These characteristics allow for the identification of the vast majority of objects (Von Kauzmann, 1957).

For direct measurements of spectral reflectance coefficients of different materials a spectrometers are used. This kind of instruments allows for discrete measurements. Spectral reflectance coefficients obtained with such devices are characterized by a high accuracy, but they can be obtained only from one point of the investigated object at any given time, which is extremely problematic when the structure of the investigated object is not homogenous or is changing in time (Kokaly, et al., 2001; Yen-Ben, et al., 2006). Methods based on spectrometric measurements can be very time consuming, therefore image-based methods are used more and more often.

The research team at the Military University of Technology has been working developing imaging methods for acquiring spectral reflectance coefficients. Over the decade we had proposed methods for processing data acquired from panchromatic, hyperspectral and multispectral sensors. In order to obtain spectral characteristics of an investigated object using a panchromatic imaging sensor, it is necessary to additionally use suitable filters – traditional inference filters or tuneable electro optical filters. Spectral reflectance coefficients are determined during post-processing on the basis of calculating the ratio between the digital number (DN) value of the investigated object in every band of the electromagnetic spectrum and the DN of a reference sample with a known reflectance value in each spectral band. This method therefore requires direct access to the objects of interest, in order to be able to place a reference panel in its vicinity (Debski et al., 2008; Guanter et al., 2005; Han, 2007). Therefore this approach is impossible to conduct in inaccessible areas. We had proposed a method for acquiring precise spectral information of objects using a panchromatic camera with a set of interference filters without the need to place a reference panel on the observed scene.

3 EXPERIMENT

The aim of this article is to describe methodology developed for determining the exposure parameters of two XEVA cameras with interference filters. In order to perform the task, an empirical approach was selected based on a series of measurements performed under laboratory and natural light conditions- outside the laboratory.

3.1 Monochromatic video sensors

For the study two different XENICS video cameras were used: XEVA 1.7- 320 and XS 1.7-320.

XEVA 1.7- 320 is a thermostabilized camera. It is a high quality digital video camera, with a thermo-

electrically cooled InGaAs detector head which registers spectral information in the 900-1700nm range. This camera has a wide range of possible applications, such as: image acquisition in the visible and infrared electromagnetic spectrum range, hyperspectral imaging, semiconductor inspection and high temperature thermography (300°C to 1200°C range or up to 2000°C).

The second camera is a compact XS-1.7-320. Like XEVA 1.7- 320 it allows to obtain images in visible and infrared electromagnetic spectrum range. The XS-1.7-320 unit has an InGaAs detector array which is sensitive up to 1.7 μm . Unlike XEVA, the XS camera does not have thermo-electrical cooling of the detector.

Both cameras have 16 mm lenses. Moreover both are small (XEVA 1.7- 320 : 90 x 110 x 110 mm; XS-1.7-320: 50 x 50 x 50 mm) and light (both up to 1 kg), what is a big advantage when using them in different conditions: both in laboratory and outdoors (Figure 1).



Figure 1. Cameras used for the experiment:
Xeva 1.7-320 and Xs 1.7-320

In order to determine spectral characteristics from images, the research team used a prepared set of interferometric filters (i.e. 900 nm, 950 nm, 1000 nm, 1050 nm, 1100 nm and 1150 nm).

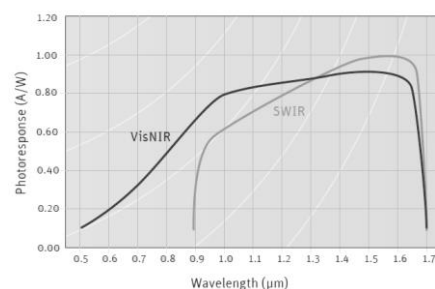


Figure 2. Sensitivity of cameras' detectors (SWIR)

3.2 Preliminary experiment set-up

To ensure the accuracy and repeatability of measurements, a number of assumptions about the measurement methods and measurement station were made, such as:

- Measurements were performed in a totally darkened lab, which provided full control over the light conditions in laboratory- with a constant and reliable light source- ASD Inc Pro Lamps. These lamps have a 70W power and give constant light in the 350-2500nm range. Three lamps were used to ensure the studied reference panel was evenly illuminated from all sides.
- Next measurements were conducted in natural light conditions.
- All calculations were done on DN values of exactly the same surface area of a white reference standard – the Zenith Lite SG3151- a reference panel which has a 95% lambertian reflectance in 250-2500nm range.
- Measurements of light intensity and light irradiance.
- In order to determine spectral characteristics from images, the research team used a prepared set of interferometric filters (i.e. 900 nm, 950 nm, 1000 nm, 1050 nm, 1100 nm and 1150 nm).
- High accuracy was provided by measuring the irradiance of the light radiation using a Spectroradiometer Field Spec4 instrument with the ASD Remote Cosine Receptor (RCR) placed near to the extension of the cameras optical probe, located directly behind the measured white reference panel. The RCR was set on a specially prepared tripod to ensure that all conducted measurements of irradiance were done always from the same place and in the same way.
- The experiment set-ups geometry had to be had to be controlled and stable. This was done by ensuring that the surface of the white reference panel was parallel to the surface of the sensors detector. Additionally it was made sure that the optical axis of the cameras always ran through the centre of the detector array, the centre of the screen opening, the centre of the white reference panel.

A experiment set-up's diagram is shown in Figure 3.

4 PRELIMINARY RESULTS

In theory of photography and optics, along with a double increase of the exposure time, the radiation that is reaching the detector also increases two-fold, so the pixel value should increase by the same factor until full saturation. The same relationship can be seen in the case of increasing light irradiance on the scene. In the case of the analog-to-digital converter used in the test cameras with interference filters to provide a greater dynamic range of the sensor, this relationship is expressed by a linear function, for each filter, with different transmission value. The aim was to determine this relationship by taking many measurements.

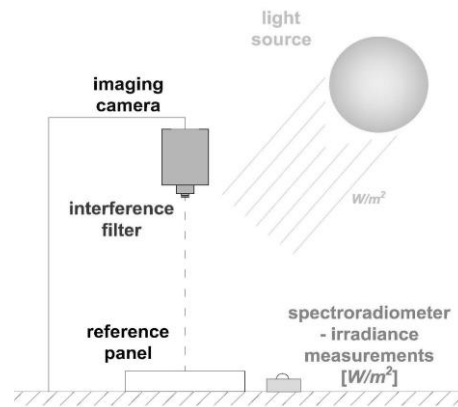
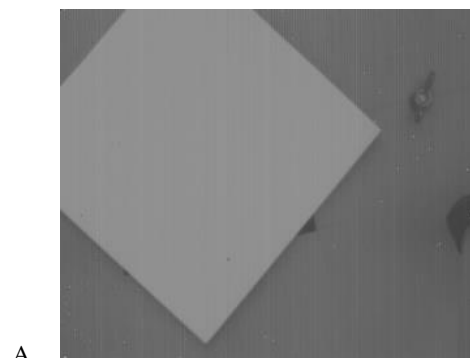


Figure 3. Measurement station

All experiments for both cameras were conducted in different lighting conditions (at different light irradiances) and with different exposure times (between 100 and 10000 μ s) with the prepared set of interference filters: 900 nm, 950 nm, 1000 nm, 1050 nm, 1100 nm and 1150 nm (Examples Figure 4).

Chosen preliminary results are show on the Figures 4 (A-C) and on the Figure 5.

The obtained results can not be as completely correct, when we reconsider are conditions, like exposure parameters, especially integration time and filter parameters, i.e. filter transmission, which is significantly different for all used filters, but according to obtained results it looks like they are equal. This is due to several conditions, that had influenced acquired images, in particular some scene parameters that could have been not fully controlled- its illumination in natural conditions, outside the laboratory. To fully control the state of light conditions it will be required a monitoring and continuous measurements of radiometric and photometric parameters of light. Moreover it will be necessary to fully and very precisely synchronize these measurements with data acquisition, especially in dynamically changeable weather conditions.



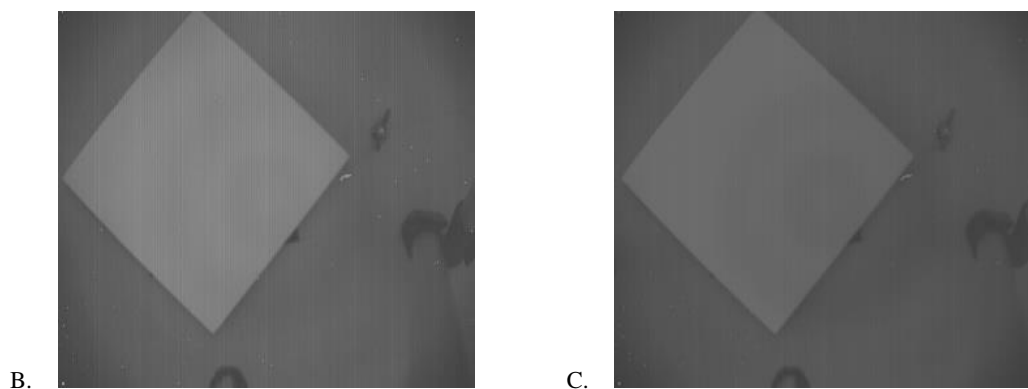


Figure 4. Examples of measurements for camera XS 1.7- 320, A- without filter, B- with filter 1050nm, C- with filter 1150 nm. Measurements taken in the same light conditions with the same integration time

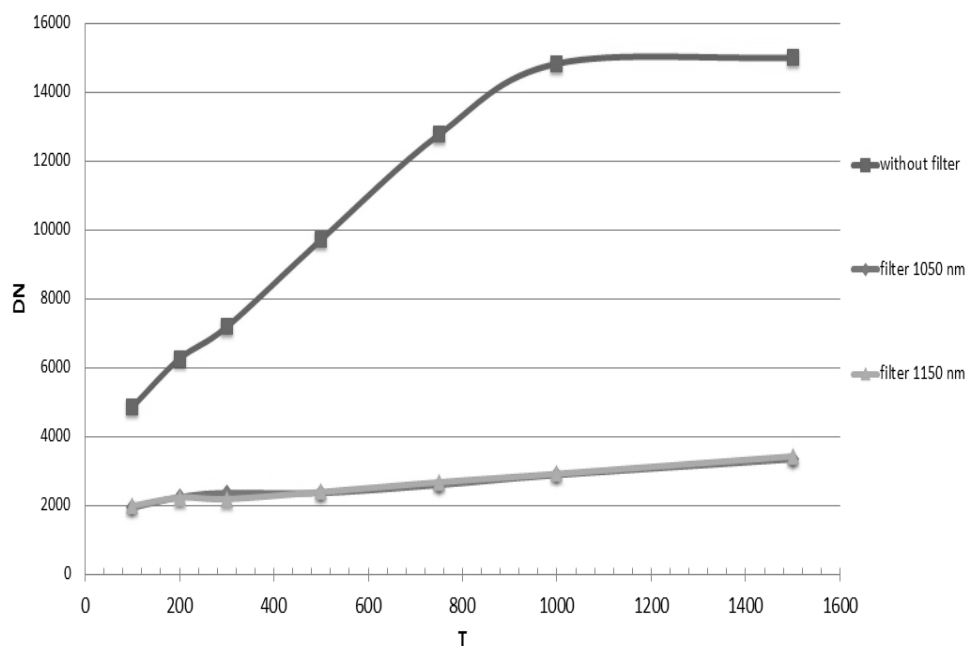


Figure 5. The relationship between pixel value (DN) and Integration Time for different filters (1050 nm and 1150 nm), example for XS-1.7-320

In addition to that it will be necessary to take into account sensor array sensitivity, both XEVA 1.7- 320 and XS 1.7 320, when preparing the set of interference filters. The appropriate selection of interference filters is highly recommended. For the purpose of preliminary experiment we purchased 6 filters: 900-1150, hoping images acquired using each filter will give us useable results. However due to the sensor low sensitivity in the 900- 950 nm range the images acquired with the 900 and 950 nm filters were practically unusable- exposure time were very long,

which is impractical for the final application of these sensors. Additionally this long time exposition resulted in very noisy images which in turn give very unreliable results.

Further experiments should be conducted using additional filters in the range 970- 1500 every 10- 20 nanometres.

5 CONCLUSION

It is possible to acquire spectral reflectance coefficients of different materials using Xenics sensors, both XEVA 1.7- 320 and XS 1.7- 320 with interference filters, without using white reference panels, only on the base of election proper exposure parameter. However there are many parameters which have negative influence on obtained images and therefore also on the resulting spectral information, i.e. camera sensor array sensitivity, filter transmission, influence of light conditions, etc. Therefore the research work on this topic should be continued to eliminate all parameters that affect negatively acquired images and to improve obtained results.

6 ACKNOWLEDGEMENTS

The presented article is part of research work carried out in the “Innovative remote sensing system for the monitoring of pollutants in rivers, offshore waters and flooded areas” project- PBS1/B9/8/2012 financed by the polish National Centre for Research and Development NCBiR.

7 REFERENCES

- Dębski, W., Walczykowski, P., 2008, Acquiring reflection coefficients using hyperspectral video imagery, XXIth ISPRS Congress, Beijing China, 353- 356.
- Guanter, L., Alonso, L., Moreno, J., 2005. First Results From the PROBA/CHRIS Hyperspectral/Multiangular Satellite System Over Land and Water Targets, IEEE GEOSCIENCE AND REMOTE SENSING LETTERS, vol. 2, no. 3, July 2005, 250- 254.
- Han, L., 1997. Spectral reflectance with varying suspended sediment concentration in clear and algae- laden waters, Photogrammetric Engineering & Remote Sensing, vol. 63, no 6, 701- 705.
- Von Kauzmann, W., 1957, Quantum Chemistry. An Introduction. Academic Press Inc., New York 1957., Chapter 15.
- Yen-Ben, Ch., Zarco-Tejada P.J., Riaño D., Rueda C. A., 2006. Estimating vegetation water content with hyperspectral data for different canopy scenarios: Relationships between AVIRIS and MODIS indexes, Remote Sensing of Environment Volume 105, Issue 4, 30.12.2006,354–366.
- Scientific brochure Xeva-1.7-320, http://www.xenics.com/documents/XB-003_04_Xeva-1.7-320_Scientific_LowRes.pdf (20 Sep. 2014)

Scientific brochure XS-1.7-320, http://www.xenics.com/documents/XB-001_03_XS-1.7-320_Scientific_LowRes.pdf (20 Sep. 2014)

The use of optoelectronic filters for registering hyperspectral images in laboratory conditions

Piotr Walczykowski, Michalina Wilinska, Damian Wierzbicki
Military University of Technology Department of Remote Sensing and Photogrammetry,
Institute of Geodesy, Faculty of Civil Engineering and Geodesy
2 Kaliskiego st., Warsaw 00-908, Poland; tel. + 48 22 683 90 21
pwalczykowski@wat.edu.pl, mwilinska@wat.edu.pl, dwierzbicki@wat.edu.pl

ABSTRACT In this article had been described a methodology of acquiring hyperspectral images using optoelectronic filters in laboratory conditions. It also presents the methodology for determining the transmission of two electronically tunable interference filters Varispec CRI-VIS and CRI-SNIR. The aim of the research was to determine the filter transmission values and to compare them with the results provided by the filter's producer. The tested interference filters are built with the intent of being integrated with panchromatic video cameras (400 - 1100 nm). The acquired data could then be used to determine spectral characteristics, and on that basis it will be possible i.e. detection of masked objects, examination of the vegetation and detection of water pollutants. The precise determination of the filters transmission values is necessary to establish the correct exposure parameters. Thanks to a correct methodology of data acquisition, the collected images could be used for qualitative and quantitative analyses. Within the framework of the presented research, laboratory measurements of the filter transmissions were carried out for the CRI-SNIR-10-20 filter (for the interval from 650 nm to 1100 nm) and the CRI-VIS-20-20 filter (for the interval from 400 nm to 720 nm). The main concept of the research was to calibrate a spectroradiometer using a reference panel and then to perform a series of measurements of the light transmitted through the filter which had been tuned to a specific wavelength. The measurements were conducted using Field Spec 3, Field Spec 4 Wide-Res spectroradiometers and a JASCO V670 spectrophotometer. Moreover there were carried out measurements with goniometer, that provided important data about the impact of the light angle on the filters transmission values. On the basis of the determined transmission filters' values, the methodology for obtaining hyperspectral images in laboratory conditions had been developed.

1 INTRODUCTION

For several years, we have been able to observe a growing interest in the search for innovative remote sensing methods for determining the various parameters of physical, biological and chemical properties of water (Álvarez-Romero JG, 2013). Usually we use multi- and hyperspectral data acquired from satellite imaging systems (Mannheim S., Segl K, 2004; Hu, C., Chen, Z, 2004) but the value of the ground sampling distance, which is often from ten to hundreds of meters, is primarily cause for restrictions. Therefore, it is possible to perform a rough estimate of the water quality only for large water basins. In addition, the most complicated process is often the search for relationships between the acquired satellite data and the values of water indicators measured directly in the field. Therefore, *in situ* measurements are a much more reliable research method (Graça, M. A, 2002). The paper presents a methodology for determining the transmission T of electronically tunable liquid crystal filters (Abdulhalim I, 2009; Hensley B, Wyble, 2012) D - LCTF CRI-VIS-20-20 and

CRI-SNIR-10-20. At the time of the research, the impact of the light incidence angle on the obtained values of the filters' transmissions was included. The developed methodology for determining the transmission of such filters, in the future will allow us to use them in *in situ* measurements for determining inland water depths, and thus to indirectly detect certain water quality indicators. These studies are extremely important from the point of view of future research in the "Innovative remote sensing system for the monitoring of pollutants in rivers, offshore waters and flooded areas" project.

2 EXPERIMENTS

Measurements of the LCTF transmission were conducted in a laboratory, although it is also possible to test and verify them outside of a laboratory. In the frame of research, the LCTF CRI-VIS-20-20 and CRI-SNIR-10-20 filters were studied, in a 400-720 nm and in 650 - 1100 nm ranges respectively. Knowledge of the filters transmission values is necessary to establish guidelines for future research concerning determining

spectral characteristics of the most common physical, biological and chemical water pollutants.

2.1 The spectrophotometric laboratory measurement set

The spectrophotometric laboratory measurement set consisted of a light source, white reflectance standard, a spectroradiometer and two interchangeably used LCTF filters (Figure 1). The white reference standard was positioned centrally relative to the pistol grip of the measuring device and was illuminated by a homogeneous non-polarized light, whose source was a halogen lamp.

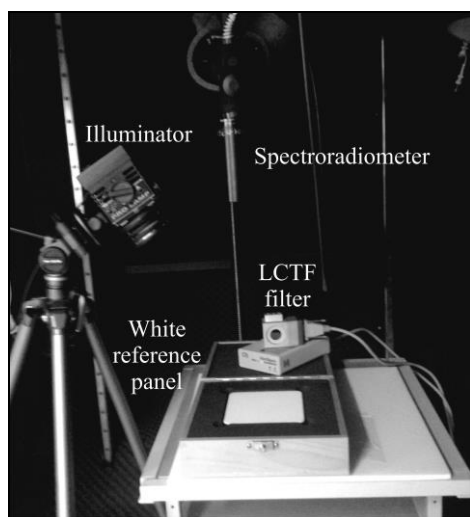


Figure 1 The spectrophotometric laboratory measurement set

Before starting the measurement, the spectroradiometer was calibrated using the reference standard. Then the tested filters were mounted directly to the pistol grip. To prevent the scattering of the radiation, the space between the end of the pistol grip and the surface of the filter was sealed with a light-impermeable material. During the measurements collected spectral data were generalized to intervals 10 nm, and for each spectrum 10 measuring series were performed. First, the filter was tuned electronically to a certain wavelength and next, after filter retuning, the received transmission was recorded using a portable computer. As a result of these measurements, the obtained data were used to plot graphs, which were in fact the tested filters transmission curves for a given wavelength.

2.2 ASD FieldSpec 3 spectroradiometer

The first set of the laboratory tests were carried out using the *ASD FieldSpec 3* spectroradiometer. As the result we obtained transmission values shown on Figure 2 and Figure 3. The results of transmission obtained for both filters differ significantly from the data presented by the manufacturer. We can conclude that, as expected, the transmission increases with increasing wavelength. The minimum value of the transmission was recorded at a wavelength of 400 nm and amounted to only 0.002%. The maximum transmission value was reached at a wavelength of 720 nm and amounted to 8.3%.

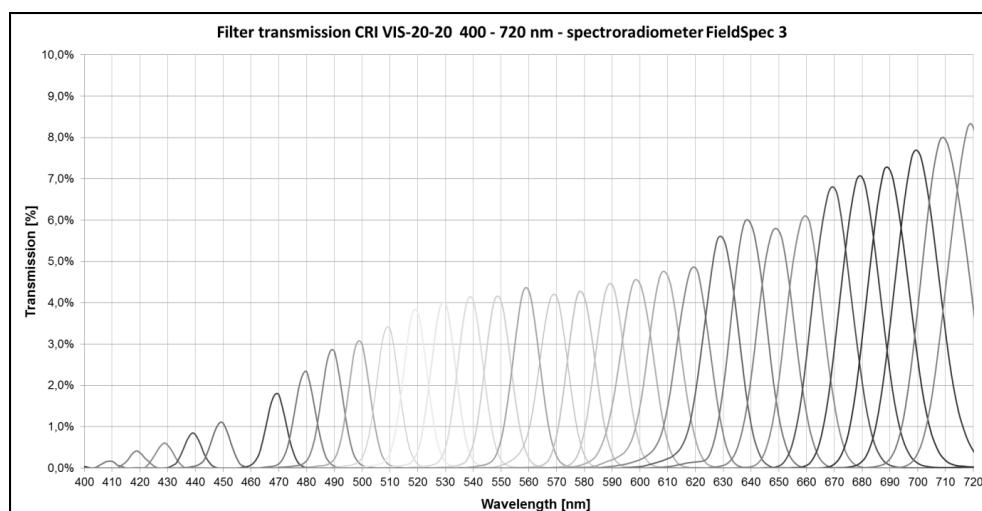


Figure 2 VariSpec CRI-VIS-20-20 transmission values measured with Field Spec 3 spectroradiometer

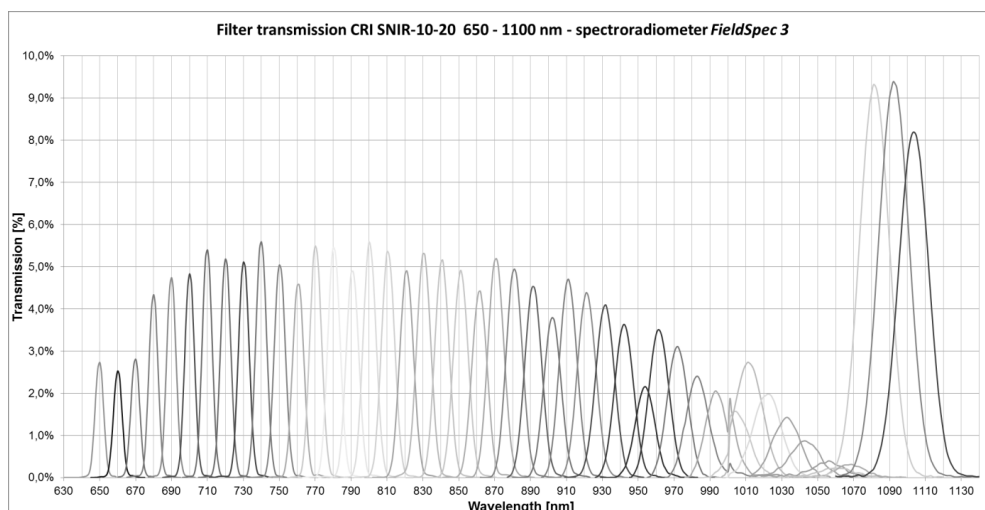


Figure 3 VariSpec CRI-SNIR-10-20 transmission values measured with Field Spec 3 spectroradiometer

As it can be seen on above figures, transmission values for wavelengths of 520 - 570 nm were at a similar level and its average value was 4.1%. For the transmission of the SNIR- CRI-10-20 filter, it can be concluded that for λ tuned every 10 nm in the range from 650 nm to 670 nm the transmission does not exceed the value 3.0%, and for the λ from 680 nm to 890 nm it reaches maximum values in the range from 4.3% to 5.6%. It then gradually decreases, to λ equal to 1050 nm, 1060 nm and 1070 nm achieving maximum transmission values below 0.4%. For λ

equal to 1080 nm, 1090 nm and 1100 nm the transmission increases rapidly and reaches a maximum equal to 9.3% , 9.4% and 8.2% respectively.

2.3 JASCO V670 spectrophotometer

As a control measurement we tested filters using a *JASCO V670* spectrophotometer (Figure 4 and Figure 5). The transmission values were found to be noticeably higher in relation to the results obtained in studies conducted *FieldSpec 3* spectroradiometer.

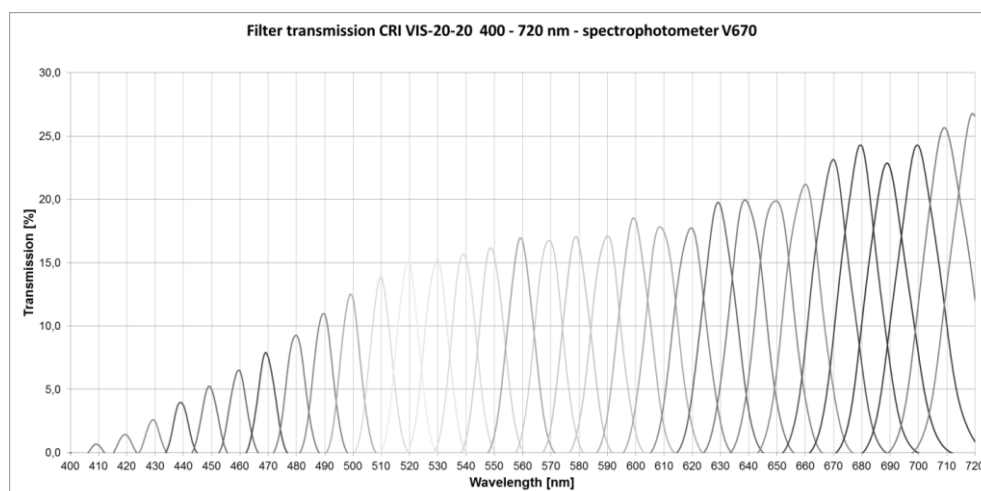


Figure 4 VariSpec CRI-VIS-20-20 transmission values measured with JASCO V670 spectrophotometer

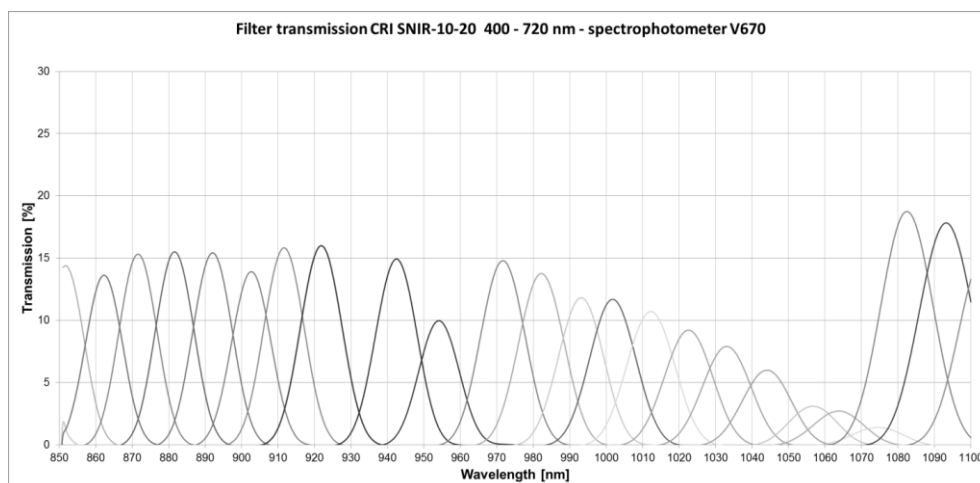


Figure 5 VariSpec CRI-SNIR-10-20 transmission values measured with JASCO V670 spectrophotometer

As it can be seen on Figure 4 and Figure 5, for the CRI-VIS-10-20 filter, the maximum recorded transmission value was achieved for $\lambda = 719$ nm, and it amounted to 26.8%. But for the CRI-SNIR-20-20 filter the transmission reaches its maximum for $\lambda = 1080$ nm, and it was equal to 18.7%. Although, values registered with a higher class equipment, such as the JASCO V670 spectrophotometer, were far greater than the values obtained with the *FieldSpec 3*, they are still several fold lower than those presented by the manufacturer.

2.4 Filters transmission values as a function of the illumination angle α

The purpose of this part of the research, was to assess the studied filters transmission variability as a function of illumination angle α . For this purpose authors designed a special goniometer (, so that it was possible to adjust the light incidence angle relative to the reflective pattern with an interval equal to 10° in the range from 10° to 80° . This time the *Field Spec4 Wide Res* spectroradiometer was used. The measurement results are shown in Figures 6 and 7.

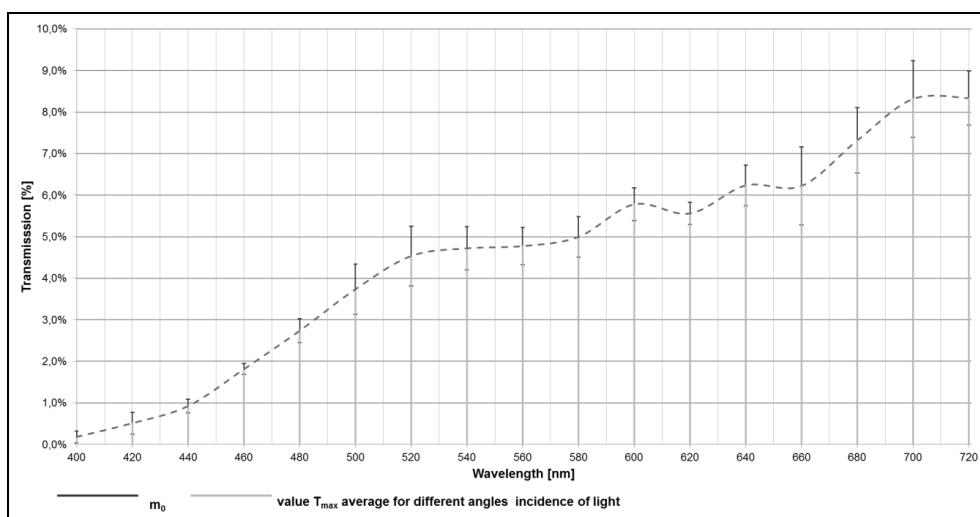


Figure 6 The maximum transmission values of the VIS LCTF VariSpec filter averaged for different light incidence angles with the distribution of the mean errors

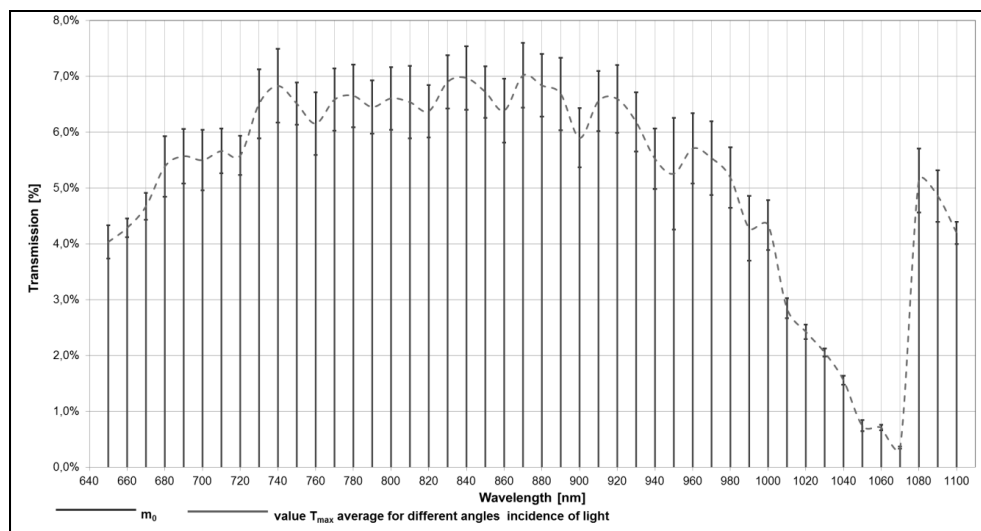


Figure 7 The maximum transmission values of the SNIR LCTF VariSpec filter averaged for different light incidence angles with the distribution of the mean errors

On the basis of Figures 5 and 6, it can be concluded, that the transmission values of the VariSpec filters vary depending on the lighting angle α . The standard deviation of the maximum of transmissions is on average 0.45% for CRI-SNIR-10-20 and 0.49% for CRI-VIS-20-20, which is within the measurement margin of error. Our research had confirmed that the obtained filter transmission values are dependent on the incidence angle of the light. However, the values by which the individual results differ, are of the order of the measurement error, and therefore they can be considered negligible.

3 CONCLUSION

Analyzing the results of transmission measurements obtained by three independent devices, we can conclude, that they are almost 10 times lower than the values given by the manufacturer and may not be possible to achieve in natural measurement conditions, especially in the case when it comes to the use of a filter-SNIR CRI-10-20 for recording the water surface and analyzing its contaminant. So for these filters it will be adequate to use a microscope etc., but when registering images of the Earth's surface, it is necessary to take into account the filter transmission determined using a spectroradiometer. Based on the study's results of the influence of illumination angle on the transmission values, it can be said, that it affects the transmission of VariSpec CRI-CRI-SNIR and VIS filters, but the differences are within the measurement error and can be considered as negligible.

In terms of the project IRAMS, designated tested filters transmission parameters will be particularly important in the image acquisition in laboratory

conditions, and therefore it was necessary to make a special test station, which is the subject of other research

4 ACKNOWLEDGEMENTS

The presented article is part of research work carried out in the "Innovative remote sensing system for the monitoring of pollutants in rivers, offshore waters and flooded areas" project- PBS1/B9/8/2012 financed by the polish National Centre for Research and Development NCBiR.

5 REFERENCES

- Abdulhalim I., 2009., Optimized guided mode resonant structure as thermooptic sensor and liquid crystal tunable filter, Chinese. Optics Letters. 7, 667–670 p
- Chrien, T. G., Green, R. O., Eastwood, M. L., 1990, Accuracy of the spatial and Radiometric Laboratory Calibration of the Airborne Visible/ Infrared, Imaging spectroscopy of the terrestrial environment; Proceedings of the Meeting, Orlando, FL, Apr. 16, 17, 1990 (A91-36626 15-35). Bellingham, WA, Society of Photo-Optical Instrumentation Engineers, 1990, p. 37-49.
- Álvarez-Romero JG, Devlin MJ, Teixeira da Silva E, Petus C, Ban N, Pressey RJ, Kool J, Roberts S, Cerdeira WA, Brodie J, 2013. A novel approach to model exposure of coastal-marine ecosystems to riverine flood plumes based on remote sensing techniques. J Environ Manage 119:194-207.

- Graça, M. A., Rodrigues-Capítulo, A., Ocón, C., & Gómez, N. 2002. In situ tests for water quality assessment: a case study in Pampean rivers. *Water research*, 36(16), 4033-4040.
- Hensley B, Wyble D. 2012. Spectral Imaging Using a Liquid Crystal Tunable Filter, [online] Available from Internet: <http://www.cis.rit.edu/DocumentLibrary/admin/uploads/CIS000196.pdf>.
- Hu, C., Chen, Z., Clayton, T. D., Swarzenski, P., Brock, J. C., & Muller-Karger, F. E. 2004. Assessment of estuarine water-quality indicators using MODIS medium-resolution bands: Initial results from Tampa Bay, FL. *Remote Sensing of Environment*, 93(3), 423-441.
- Mannheim S., Segl K., Heim B., Kaufmann H. 2004. Monitoring of lake water quality using hyperspectral CHRIS-PROBA data. *Proc. of the 2nd CHRIS/PROBA Workshop*, 28- 30 April 2004, ESA/ESRIN, Frascati, Italy (ESA SP-578, July 2004).

Comparison of Two Inversion Methods for Grassland Leaf Area Index Using Hyperspectral Remote Sensing

Q. Wu^{a,b,c}, Y.X. Jin^c, Y.H. Bao^b, Q.S. Hai^c, R.R. Yan^c, B.R. Chen^c, B.H. Zhang^c, H.B. Zhang^c, Z.W. Li^c, X.Y. Li^{a,b,c}, X.P. Xin^{c,*}

a. The Geographical Science College, Inner Mongolia Normal University, Hohhot 010022, China; b. Inner Mongolian Key Laboratory of Remote Sensing and Geographic Information System, Inner Mongolia Normal University, Hohhot 010022, China; c. National Hulunbuir Grassland Ecosystem Observation and Research Station / Institute of Agricultural Resources and Regional Planning, Chinese Academy of Agricultural Sciences, Beijing 100081, China

Email: wuqiong_0108@126.com; *xinxiaoping@caas.cn

ABSTRACT - The leaf area index (LAI) is one of the most important parameters for determining grassland canopy conditions. LAI controls numerous biological and physical processes in grassland ecosystems. Remote sensing techniques are effective for estimating the grassland LAI at a regional scale. Comparison of LAI inversion methods based on remote sensing is significant for accurately estimating the LAI in particular areas. In this study, we developed and compared two inversion models to estimate the LAI of a temperate meadow steppe in Hulunbuir, Inner Mongolia of China, based on hyperspectral images and field-measured LAI data. The BP neural network method was better than the statistical regression model for estimating the grassland LAI. The accuracy of the BP neural network method was 82.8%. We then explored the spatio-temporal distribution of the LAI for *Stipa Baicalensis* Roshev. in the meadow steppe of Hulunbuir including cut, grazed, and fenced sample plots. The LAI in the cut and grazed reflected the growth variations in *Stipa Baicalensis* Roshev.. However, because of the obvious litter layer, the LAI in the fenced was underestimated.

1 INTRODUCTION

The leaf area index (LAI) is defined as one half of the total green leaf area per unit horizontal ground surface area (Chen and Black, 1992) and is a key parameter for determining grassland vegetation growth conditions. LAI controls numerous biophysical processes of grassland ecosystems, and it is the most basic feature parameter in many models (Bonan, 1993; Fortin, et al., 2013), such as the grassland productivity model and the carbon cycle model (Darvishzadeh, et al., 2008). Monitoring grassland LAI is significant for assessing grassland growth, researching the carbon cycle and rationally utilizing grassland resources (Pu, et al., 2003). Remote sensing technology has the advantage of providing rapid and extensive dynamic observations, and it is an efficient approach for estimating the LAI at a local or regional scale (Chen and Cihlar, 1996; Haboudane, et al., 2004; Gray and Song, 2012).

LAI inversions based on remote sensing technology have mainly been applied to aspects of agricultural and forest ecosystems (Pu and Gong, 2004; Schlerf and Atzberger, 2006; Combal, et al., 2002; Bacour, et al., 2002; Vuolo, et al., 2008; Duan, et al., 2014). Few studies have been conducted on regional-

scale LAI inversions in grassland ecosystems, and those studies focused on LAI evaluations using a single inversion method (Fan, et al., 2008; Liu, et al., 2011; Darvishzadeh, et al., 2008; Vohland and Jarmer, 2008). Therefore, few studies have compared the different inversion methods. Applications and verifications of inversion methods during different vegetation growth seasons are lacking. Moreover, the verifications lack of mass ground data, which restrict the accuracy of LAI inversions.

In this study, we studied the meadow steppe of Hulunbuir *Stipa baicalensis* Roshev., Inner Mongolia, China. Based on HJ-1 remote sensing data and field measured data, we estimated the LAI in a meadow steppe of *Stipa Baicalensis* Roshev. using a statistical regression model and a BP neural network method. We then evaluated the accuracy of the two methods in different growth periods. The study is a reference for rapidly and extensively monitoring the grassland LAI and evaluating grassland growth.

2 MATERIALS AND METHODS

2.1 Study area

The data were obtained in the sample plots of the meadow steppe of Hulunbuir *Stipa Baicalensis* Roshev. around the Hulunbuir Grassland Ecosystem

Observation and Research Station, Chinese Academy of Agricultural Sciences (49° 19' N, 120° 03' E; altitude of 628 m) (Figure 1). This study area is a typical sample plot of Hulunbuir meadow steppe, where the annual average temperature is -3 to -1°C and the annual average precipitation is 350-400 mm. The precipitation is mainly concentrated in summer. The frost-free period is approximately 100-110 days. The major plant species include *Stipa Baicalensis* Roshev. and *Leymus Chinensis*. The soil types include chestnut soil and dark chestnut soil.

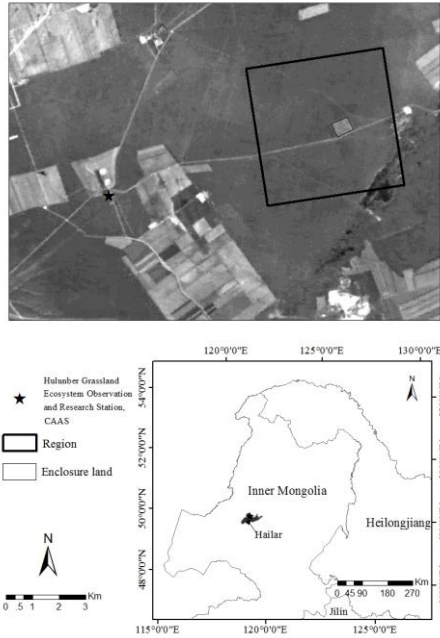


Figure 1 The location map of sample plots

2.2 LAI measurement

The LAI values were measured from early June to late August in 2013. Simultaneous ground observations and remote sensing measurements were conducted 8 times. Each measurement period was from 10:00 to 15:00(local time) in fine weather. The 3 km×3 km sample plot was designed to form 9 regular uniform grids, where we randomly chose four or five elementary sampling units (ESU) in each grid during each observation. The area of each ESU was 30 m×30 m and was equivalent to the resolution of the HJ satellite data. We selected three sample plots of approximately 1 square meter within each ESU to measure the LAI. Finally, we calculated the average measurement of the three sample plots as the LAI value in the ESU. Meanwhile, a GPS was used to record the geographical coordinates and altitude of each sample plot.

Because the sample data might influence the accuracy of the model evaluation, particularly abnormal data were eliminated from the sample plot data in accordance with the geographical information from the GPS. Finally, we obtained 326 sample data. The sample data were separated into two datasets (modeling data and validation data).

2.3 Remote Sensing Data Acquisition and Pre-processing

We selected 9 scenes from the HJ-1A/B-CCD image data that correspond to the simultaneous field sample data: HJ1B-CCD1 on June 4, 2013; HJ1B-CCD2 on June 11, 2013; HJ1B-CCD1 on June 23, 2013; HJ1B-CCD1 on June 29, 2013; HJ1B-CCD1 on July 6, 2013; HJ1B-CCD2 on July 13, 2013; HJ1B-CCD2 on July 21, 2013; HJ1B-CCD2 on August 11, 2013; and HJ1B-CCD2 on August 19, 2013. HJ-1A/B-CCD was downloaded from the website of the China Centre for Resources Satellite Data and Application (<http://www.cresda.com/n16/index.html>). Table 1 shows the major loading parameters of HJ-1-A and HJ-1-B.

The radiometric and system geometric corrections of the HJ data were processed, but a geometric precision correction was not conducted in this study. Thus, the nine scenes of the HJ images were preprocessed to obtain the actual ground surface reflectivity, which included radiation calibration, atmospheric correction and geometric correction.

2.4 Research Methods

2.4.1 Statistical Regression Model Method

HJ-CCD data has four bands after pre-processing, including blue band, green band, red band and near infrared band. Then we calculated the following three vegetation indices: NDVI, ARVI and MSAVI. The formulas are as follows:

$$NDVI = \frac{R_{NIR} - R_{Red}}{R_{NIR} + R_{Red}} \quad (1)$$

$$ARVI = \frac{R_{NIR} - R_{Red} + \theta(R_{Blue} - R_{Red})}{R_{NIR} + R_{Red} - \theta(R_{Blue} - R_{Red})} \quad (2)$$

$$MSAVI = \frac{2R_{NIR} + 1 - \sqrt{(2R_{NIR} + 1)^2 - 8(R_{NIR} - R_{Red})}}{2} \quad (3)$$

where R_{Blue} , R_{NIR} and R_{Red} are the blue band, near infrared band and red band, respectively, and θ is 1.

We extracted the reflectance value of the four bands and three vegetation indices of nine images in accordance with the simultaneous GPS ground coordinates. A regression analysis was conducted by assessing the relationships between the field-measured LAI and the four bands of the HJ data and the derived three vegetation indices. Based on our analysis of the

relationships between the LAI and the seven independent variables, we developed the following regression models: unary linear regression, logarithmic function, power function and exponential function. Following an F-test, the optimal model was selected according to the coefficient of determination (R^2).

2.4.2 BP Neural Network Method

The BP neural network consisted of three layers with multiple inputs and one output. We used 252 sample data to train the network and 74 sample data to verify the accuracy of the models. The optimal BP neural network model was obtained with the coefficient of determination (R^2).

2.4.3 Precision evaluation method

We calculated the root-mean-square error (RMSE) and mean relative error (MRE) to evaluate the precision of the two models based on the reserved 74-sample data. Finally, the optimal LAI inversion model was determined by the precision evaluation. The formulas for the RMSE and MRE are as follows:

$$RMSE = \sqrt{\frac{\sum (Y_i - Y_i')^2}{N}} \quad (4)$$

$$MRE = \sqrt{\frac{\sum [(Y_i - Y_i')/Y_i]^2}{N}} \quad (5)$$

where Y_i indicates the actual measured LAI value of sample points, Y_i' indicates the estimated LAI value of model and N indicates the number of sample points.

3 RESULTS

3.1 LAI inversion based on Statistical Regression Model

We conducted a Pearson correlation analysis of the LAI and reflectance of the four bands and three vegetation indices using SPSS software (Table 1). According to the correlation analysis, four variables, NDVI, ARVI, MSAVI and Band 3, were more highly correlated than the other variables. We then established the statistical models between the four variables and the LAI.

Table 1 Correlation between various parameters and LAI

LAI	NDVI	ARVI	MSAVI	Band 1	Band 2	Band 3	Band 4
Pearson correlation	0.714**	0.657**	0.715**	-0.276**	-0.217**	-0.564**	0.279**
Significance Two-tailed	0.000	0.000	0.000	0.000	0.000	0.000	0.000

** indicate significantly correlation at 0.01 level

Table 2 The statistical models between LAI ad vegetation indices

Vegetation Index	Model Formulation	R^2	F value	Sig.
NDVI	$LAI = 9.823NDVI - 4.783$	0.497	247.011	0.000
	$LAI = 6.762 \ln(NDVI) + 4.525$	0.495	244.963	0.000
	$LAI = 7.123NDVI^{3.597}$	0.536	288.530	0.000
	$LAI = 0.052e^{5.188NDVI}$	0.530	282.257	0.000
ARVI	$LAI = 6.759ARVI - 1.928$	0.419	179.928	0.000
	$LAI = 3.745 \ln(ARVI) + 4.065$	0.407	171.539	0.000
	$LAI = 5.636ARVI^{2.012}$	0.450	204.172	0.000
	$LAI = 0.229e^{3.604ARVI}$	0.455	208.843	0.000
MSAVI	$LAI = 13.933MSAVI - 9.366$	0.497	246.763	0.000
	$LAI = 11.310 \ln(MSAVI) + 4.316$	0.495	244.643	0.000
	$LAI = 6.399MSAVI^{6.039}$	0.539	292.732	0.000
	$LAI = 0.004e^{7.408MSAVI}$	0.537	290.109	0.000
Band3	$LAI = -0.004B3 + 4.190$	0.305	109.719	0.000
	$LAI = -1.950 \ln(B3) + 14.414$	0.301	107.882	0.000
	$LAI = 913.942B3^{-0.973}$	0.287	100.793	0.000
	$LAI = 5.670e^{-0.002B3}$	0.302	108.215	0.000

The results showed that the coefficients of determination were higher than 0.49 for the LAI-

NDVI and LAI-MSAVI models (Table 2). The models passed the significance test at the 0.01 level. The

coefficients of determination of the power and exponential function models were higher than those of the unary linear and logarithmic function models with three vegetation indices. The maximum coefficient of determination of the unary linear model with LAI-Band 3 was 0.305 and was significant at the 0.01 level. Therefore, the power function of LAI-MSAVI was ultimately obtained as the optimal statistical model after an integrated comparison of the R^2 and F values. The coefficient of determination (R^2) was 0.539, with an F value of 292.732.

3.2 LAI inversion based on BP neural network model

The design and optimization of the BP neural network included the design of the input, hidden and output layers. The input layer had seven nodes: blue, green, red, and near-infrared bands; and NDVI, ARVI and MSAVI. BP neural network model for the LAI inversion was obtained after continuous debugging of the neural network parameters and comparison of the coefficients of determination (R^2).

The BP neural network models were constructed with 252 sample data. When the hidden layer was 5, the transfer function in the 1st and 2nd layers of the network was "tansig", the transfer function in the output layer was "purelin" and the training function was "trainbr"; the maximum coefficient (R^2) was approximately 0.661 (Figure 2). Thus, the optimal model was the BP neural network model.

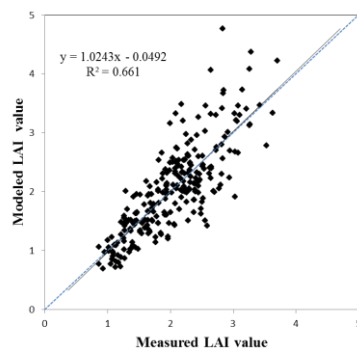


Figure 2 Relationship between the measured and estimated LAI based on BP neural network

3.3 Precision and comparison of two models

We used the remaining 74-sample data to verify the accuracy of the optimal power function between the LAI and MSAVI. The RMSE was 0.368, the MRE was 0.185 and the precision of the model was 81.5%. The optimal BP neural network model was verified by the same 74-sample data. The RMSE was 0.331, the MRE was 0.172 and the precision of the model was 82.8%. Compared with the two models, the precision of the BP neural network model was better than that of the statistical model (Figure 3).

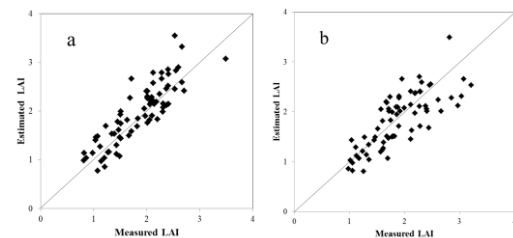


Figure 3 Measured LAI versus BP neural network and the regression-estimated LAI.

Note: a. Measured LAI versus BP neural network estimated LAI; b. Measured LAI versus the regression estimated LAI.

3.4 Spatial-temporal distribution of LAI

Considering the relative quality of the remote sensing data, we selected one image dataset of the ground surface reflectivity from the HJ satellite in June, July and August. We calculated the spatio-temporal distribution of the LAI with 30 m resolution using the optimal BP neural network model (Figure 4). In the beginning of June, a higher LAI value appeared in the grazed plot located in the southeastern region. The LAI value in the cut plot located in the northern and western regions was lower than that in the grazed area. The lowest LAI value appeared in the fenced plot located in the middle region. In the beginning of July, the LAI increased for different land uses (the grazed, cut and fenced plots). The LAI values from high to low were as follows: the cut, the fenced, the grazed plots. During the first ten-day period in August, the vegetation in the fenced and cut plots increased rapidly, and the LAI values were higher in the two regions. However, the LAI value in the grazed plot declined. Based on the time series, the LAI inversion results in the cut and grazed plots were consistent with the actual growth situations. It reflected the growth pattern of vegetation for the two land uses.

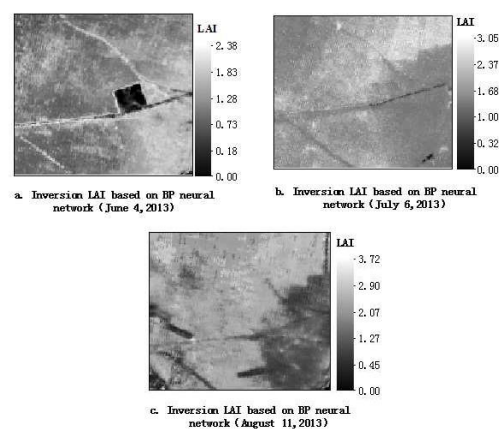


Figure 4 Distribution map of the LAI inversion of HJ-CCD images using BP neural network model

4 DISCUSSIONS

4.1 Relations between LAI and remote sensing data

We conducted a Pearson correlation analysis of the LAI and reflectance of the four bands and three vegetation indices (Table 2). Seven variables had significant correlations with LAI ($p < 0.01$). The blue, green and red bands in the visible wavelengths were negatively correlated with the grassland LAI, while the near-infrared band had a positive correlation with the LAI. Moreover, the correlations of the near-infrared and red bands with the LAI were better than those of the other two bands. The vegetation had strong reflection and absorption in the near-infrared and red bands; this finding could be related to the physiologic conditions of the vegetation. Three vegetation indices (NDVI, ARVI and MSAVI) were positively correlated with the LAI. The correlation coefficients between the VIs and LAI were better than those between the four bands and the LAI. Thus, establishing grassland LAI inversion models based on the vegetation index is feasible and suitable.

The coefficients of determination of the power and exponential function models based on the relationship between the LAI and three vegetation indices were higher than those of the unary linear and logarithmic function equations. The optimal inversion models established by the three vegetation indices were nonlinear. The LAI increased with the increase in the three vegetation indices. When the LAI was lower, the sensitivity was higher. When the LAI increased, the sensitivity declined. Because the three vegetation indices partly reflected the saturation, they were unable to reflect the actual changes in the LAI.

4.2 Compared between statistical regression model and BP neural network model

Compared between measured LAI and estimated LAI with two models (Figure 3), the sample points of LAI based on BP neural network model were closed to the 1:1 line. Moreover, *RMSE* and *MRE* of BP neural network model were less than those of statistical model. Because the BP neural network model had a strong nonlinear explanation, it could effectively avoid overestimating or underestimating the grassland LAI caused by the saturation of the vegetation indices. Furthermore, the BP neural network model was a feasible method for estimating the LAI at a regional level.

However, a specific and quantitative physical relationship was lacking in the neural network model for the LAI inversion, and many complex physical models were not placed on the inversion process because of deficient prior knowledge of the physiologic and biochemical parameters. The BP neural network model was the most accurate method for estimating the LAI for *Stipa Baicalensis* Roshev. in

the meadow steppe of Hulunbuir, Inner Mongolia, China; however, this may not be the case in other physiographical regions. In the future, the universality of LAI inversions using neural network models could be improved by confirming the mechanism's relationship between the LAI and input parameters.

4.3 Spatial-temporal distribution of LAI

Compared with the measured LAI (Figure 4), the result of the LAI inversion in the grazed and cut areas reflects the growth and changes of the LAI. In the fenced area, however, the vegetation exhibited withered leaves in the beginning of June. The withered leaves, which had accumulated from the previous year, influenced the reflectance of the near-infrared band. Because of the low reflectance of the near-infrared band in the HJ-CCD image, the model was unable to estimate the growth of the LAI, and the values were underestimated.

5 CONCLUSIONS

In this study, we developed a statistical regression model and a BP neural network model to estimate the LAI based on field-measured LAI and four bands (blue, green, red, and near-infrared) of the HJ satellite and derivative three vegetation indices. We further established an optimal model for exploring the spatio-temporal distribution of LAI in three land uses. The BP neural network model was better than the statistical regression model for estimating the grassland LAI. The precision of the BP neural network model was 82.8%. Based on the input of sensitive parameters, the grassland LAI inversion using a BP neural network could improve the accuracy of the LAI inversion. The LAI inversion in the grazed and cut plots detected the variation in the growth of the grassland LAI. Because of the obviously withered vegetation in the beginning of June in the fenced plot, the LAI inversion could not accurately detect the growth conditions in the LAI.

REFERENCES

- Bacour, C., Jacquemoud, S., Leroy, M., Hauteceur, O., Weiss, M., Prévot, L., Bruguier, N., Chauki, H., 2002, Reliability of the estimation of vegetation characteristics by inversion of three canopy reflectance models on airborne POLDER data. *Agronomie*, **22**, 555-565.
- Bonan, G. B., 1993, Importance of leaf area index and forest type when estimating photosynthesis in boreal forests. *Remote Sensing of Environment*, **43**, 303-314.
- Chen, J. M. and Black, T. A., 1992, Defining leaf area index for non-flat leaves. *Plant Cell Environment*, **15**, 421-429.
- Chen, J. M. and Cihlar, J., 1996, Retrieving leaf area index of boreal conifer forests using Landsat TM

- images. *Remote Sensing of Environment*, **55**, 153-162.
- Combal, B., Baret, F., Weiss, M., 2002. Improving canopy variables estimation from remote sensing data by exploiting ancillary information. *Case study on sugar beet canopies*, **22**, 205-215.
- Darvishzadeh, R., Skidmore, A., Schlerf, M., Atzberger, C., 2008. Inversion of a radiative transfer model for estimating vegetation LAI and chlorophyll in a heterogeneous grassland. *Remote Sensing of Environment*, **112**, 2592-2640.
- Duan, S. B., Zhao, L. L., Wu, H., Tang, B. H., Ma, L. L., Zhao, E. Y., Li, C. R., 2014. Inversion of the PROSAIL model to estimate leaf area index of maize, potato, and sunflower fields from unmanned aerial vehicle hyperspectral data. *International Journal of Applied Earth Observation and Geoinformation*, **26**, 12-20.
- Fan, L., Gao, Y., Brück, H., Bernhofer, C., 2009. Investigating the relationship between NDVI and LAI in semi-arid grassland in Inner Mongolia using in-situ measurements. *Theoretical and Applied Climatology*, **95**, 151-156.
- Fortin, J. G., Anctil, F., Parent, L. E., 2013. Comparison of physically based and empirical models to estimate corn (*Zea mays* L.) LAI from multispectral data in eastern Canada. *Canadian Journal of Remote Sensing*, **39**, 88-99.
- Gray, J. and Song, C., 2012. Mapping leaf area index using spatial, spectral, and temporal information from multiple sensors. *Remote Sensing of Environment*, **119**, 173-183.
- Haboudane, D., Miller, J. R., Pattey, E., Zarco-Tejada, P. J., and Strachan, I. B., 2004. Hyper-spectral vegetation indices and novel algorithms for predicting green LAI of crop canopies: Modeling and validation in the context of precision agriculture. *Remote Sensing of Environment*, **90**, 337-352.
- Liu, Y. B., Ju, W. M., Zhu, G. L., Chen, J. M., Xing, B. L., Zhu, Y. L., 2011. Retrieval of leaf area index for different grasslands in Inner Mongolia prairie using remote sensing data. *Acta Ecology Sinica*, **31**, 5159-5170.
- Pu, R., Gong, P., Biging, G. S., Larrieu, M. R., 2003. Extraction of red edge optical parameters from Hyperion data for estimation of forest leaf area index. *IEEE Transactions on Geoscience and Remote Sensing*, **41**, 916-921.
- Pu, R. and Gong, P., 2004. Wavelet transform applied to EO-1 hyperion data for forest LAI and crown closure mapping. *Remote Sensing of Environment*, **91**, 212-224.
- Schlerf, M. and Atzberger, C., 2006. Inversion of a forest reflectance model to estimate structural canopy variables from hyper-spectral remote sensing data. *Remote Sensing of Environment*, **100**, 281-294.
- Vohland, M. and Jarmer, T., 2008. Estimating structural and biochemical parameters for grassland from spectroradiometer data by radiative transfer modelling (PROSPECT+SAIL). *International Journal of Remote Sensing*, **29**, 191-209.
- Vuolo, F., Dini, L., D'Urso, G., 2008. Retrieval of leaf area index from CHRIS/PROBA data: an analysis of the directional and spectral information content. *International Journal of Remote Sensing*, **29**, 5063-5072.

Spectral-information-based atmospheric correction method for hyperspectral thermal infrared image

Xinke Zhong¹, Hua Wu², Bo-Hui Tang², Ronglin Tang² Zhao-Liang Li^{1,2}

1. ICube, UdS, CNRS, 300 Bld Sebastien Brant, CS10413, 67412, Illkirch, France

2. State Key Laboratory of Resources and Environmental information System, Institute of Geographic Sciences and Natural Resources Research, Chinese Academy of Sciences, Beijing, 100101, China

Email: lizl@igsrr.cn

ABSTRACT—Land surface temperature (LST) is an important parameter in climate system, and is widely used in numerical weather forecasting, drought monitoring, water resources management and global climate change studies. Atmospheric correction is one of key processes for the retrieval of LST from hyperspectral thermal infrared radiances measured at the top of the atmosphere (TOA). Nowadays, atmospheric correction methods for hyperspectral thermal infrared (HypTIR) images still require accurate atmospheric temperature and moisture profiles, but spatially and temporally collocated atmospheric profiles are usually not available. With an assumption of emissivity=1, LST can be directly expressed as a function of 13 brightness temperatures measured at TOA by a radiometer of spectral interval =800~1200cm⁻¹ and spectral resolution =0.25cm⁻¹. We have tested the accuracy of the proposed method and have analysed its sensitivity to spectral resolution and instrumental noise using simulation data. The results showed that LST can be retrieved by the proposed method with RMSE=0.16K if the instrumental noise (NEDT) is 0.1K. The results also indicated that the parameters in the developed function are dependent on the spectral resolution and LST can be retrieved accurately by the proposed method if appropriate values are used for each spectral resolution. Furthermore, the results demonstrated that the impact of instrumental noise on the accuracy of the LST retrieved by the proposed method is in the order of magnitude of the instrumental noise. This method is promising for retrieving LST from HypTIR image.

1 INTRODUCTION

Land surface temperature (LST) is a key parameter in climate system. LST retrieval is applied in thematic areas such as surface energy budget studies (Zhou et al, 2003), numerical weather/climate forecasting (Le Marshall et al., 2006), retrieving important climate variables (Vandenbussche et al., 2013) and soil moisture/evapotranspiration estimation (Rhee et al, 2010). Accuracy of the LST retrieval is strongly affected by atmospheric correction methods and LST and land surface emissivity (LSE) separation methods (Li et al., 2013).

Although several atmospheric correction methods for HypTIR image observed by airborne sensor have been developed (Gu et al., 2000; Young et al., 2002; Borel, 2008; Wang et al., 2009), there are few atmospheric correction methods for HypTIR data acquired by the space-borne sensor (Susskind et al., 2003; Pequignot et al., 2008; Paul et al., 2012). On the contrary, there is large HypTIR data observed by space-borne sensors. The first HyperTIR space-borne sensor, the Atmospheric InfraRed Sounder (AIRS), was observed in 2002, and have provided HypTIR data since then. Nowadays, there is HyperTIR data

observed by other space-borne sensors such as the Infrared Atmospheric Sounding Interferometer (IASI), the Cross-track Infrared Sounder (CrIS). In the future, the infrared sounder (IRS), another space-borne HypTIR sensor, will also provide this type of HypTIR data. There is a pressing need to develop atmospheric correction methods for HypTIR data measured by space-borne sensor. The objective of this paper is to develop a spectral-information-based atmospheric correction method for this type of HypTIR data. To be simple, we assume that LSE is equal to unity.

This paper is organized as follows: Section 2 presents the atmospheric correction method. The evaluation of the atmospheric correction method is given in Section 3. The sensitivity of the developed method to spectral resolution and instrumental noise is shown in Section 4, and the last section concludes.

2 METHODOLOGICAL DEVELOPMENT FOR ATMOSPHERIC CORRECTION

2.1 Physical base of the method

Assuming that land surface is Lambertian and LSE is unity, the radiance $L(\lambda_i)$ at TOA at a HypTIR channel can be written as

$$L(\lambda_i) = B(T_s, \lambda_i) \tau(\lambda_i) + L_p(\lambda_i) \quad (1)$$

where $B(T_s, \lambda_i)$ is the radiance of surface at a central wavelength λ_i of channel i with surface temperature of T_s , L_p is the upwelling radiance emitted by the atmosphere, τ is the transmittance.

If Equation (1) is linearized around average surface temperature and the wavelength λ_i in this equation is omitted, equation (1) can be rewritten as

$$Tb_i = \tau_i T_s + (1 - \tau_i) Ta_i, i = 1 \sim p \quad (2)$$

where Tb_i is the brightness temperature at TOA at channel i , Ta_i is the equivalent atmospheric temperature at channel i , τ_i is the transmittance at channel i , p is the number of channels selected for retrieving LST.

Inspired by the split-window method for LST retrieving, we propose a spectral-information-based atmospheric correction method for atmospheric correction. In this method, surface temperature can be written as

$$T_s = w_0 + \sum_{i=1:p} w_i Tb_i \quad (3)$$

where w_i are regression coefficients. The number of channels p , the center wavenumbers at channel i ($i=1 \sim p$) and coefficients w_i ($i=0 \sim p$) can be determined using stepwise regression with simulation data.

2.2 Determination of center wavenumbers at channel i ($i=1 \sim p$) and coefficients w_i ($i=0 \sim p$)

The scheme for determination of the channels and coefficients in Equation (3) is shown in Figure 1. Firstly, we fit a series of initial values of central wavenumbers at channel i ($i=1 \sim p$) and coefficients w_i using stepwise regression and Equation (3) with simulation data below for a series of number of channels in ascending order. For these numbers of channels, the root mean square error (RMSE) of the LST retrieved using Equation (3) and the corresponding initial values of central wavenumbers at channel i and coefficients w_i decreases with the increase of number of channels. Secondly, we find the number of channels with RMSE of the retrieved LST = 0.15K as the solution of the number of channels. The initial values of the central wavenumbers at channel i and the coefficients w_i corresponding to the solution of the number of channels are the solutions of the central wavenumbers and the coefficients. The threshold

RMSE for determination of the parameters are set according to Webster and Fieux's study (1984).

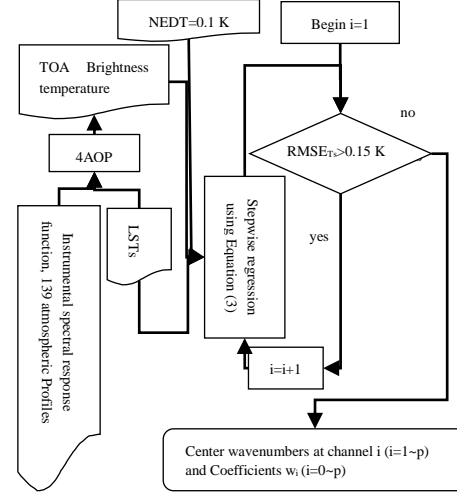


Figure 1. The scheme for determination of the central wavenumbers at channel i ($i=1 \sim p$) and the coefficients w_i ($i=0 \sim p$)

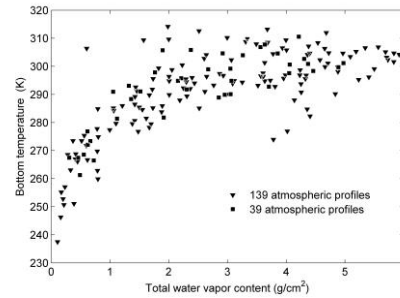


Figure 2. The variation of bottom temperature with the total water vapor content for the 139 atmospheric profiles and other 39 atmospheric profiles

The simulation data has been created using 4AOP to determine the center wavenumbers at channel i and the coefficients w_i in Equation (3). Spectral interval and spectral resolution for simulation were $800 \text{ cm}^{-1} \sim 1200 \text{ cm}^{-1}$ and 0.25 cm^{-1} respectively. Atmospheric profiles for simulation are 139 typical clear-sky profiles (Galve et al., 2008) from TIGR2000 database (Chedin et al., 1985) with total water vapor content ranging uniformly from 0 g/cm^2 to 6 g/cm^2 . The variation of bottom temperature with the total water vapor content for the 139 atmospheric profiles is presented in Figure 2. For each profile, six LSTs for simulation are the sums of the bottom temperature of atmosphere profile (Ta_0) and six differentiations dts. The dts are $[-15, -5, 0, 5, 10, 15]$ when $Ta_0 < 280\text{K}$, and are $[-10, -5, 0, 5, 10, 20]$ when $Ta_0 \geq 280\text{K}$ (Wang, 2011). The viewing angle for simulation is 90° . For each simulation case of HypTIR brightness temperature

data, the noise for simulation is a random noise of dimension = 1601 generated by a Matlab random number generator with NEDT of 0.1 K. The NEDT of noise is equal to that of the Infrared Atmospheric Sounding Interferometer (IASI) (Aires et al., 2002).

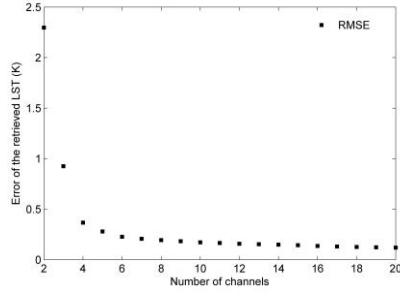


Figure 3. The variation of RMSE of the retrieved LST with number of channels in the process of center wavenumbers and coefficients determination

The variation of RMSE of the retrieved LST with the number of channels in the process of determination of the central wavenumbers at channel i and the coefficients w_i is shown in Figure 3. When the number of channels is larger than 13 the RMSE of the retrieved LST is less than 0.15K. The solution of the number of channels is 13.

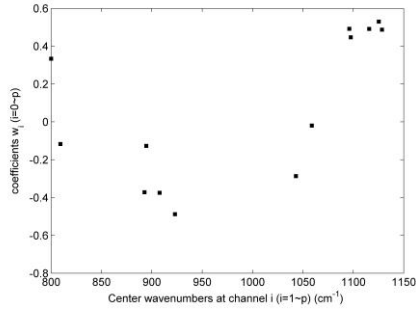


Figure 4. The determined center wavenumbers at channel i ($i=1\sim p$) and coefficients w_i ($i=0\sim p$). ($w_0=1.199$)

The solution of the center wavenumbers at channel i ($i=1\sim p$) and the coefficients w_i is shown in Figure 4. The center wavenumbers vary between 800cm^{-1} and 1128.5cm^{-1} . The coefficients are in the range of $-0.50\sim 0.53$.

3 EVALUATION OF THE METHOD

Firstly, we have evaluated the developed method by comparing the LST retrieved by the developed method with the true LST using simulation data in Section 2. The error of the retrieved LST is show in Figure 5. From this figure, we can see that the RMSE of the retrieved LST is about 0.15 K, and the error of LST ranges from -0.5 to 0.7K . Consequently, surface temperature can be accurately retrieved using Equation

(3) with the only 13 measurements in the spectral interval of $800\text{cm}^{-1}\sim 1200\text{cm}^{-1}$.

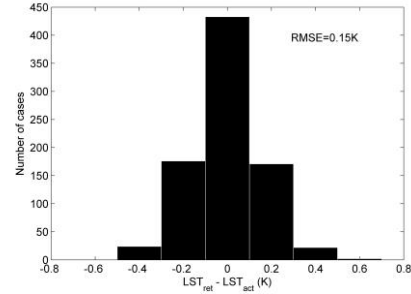


Figure 5. Error of the LST retrieved using our developed method (LST_{ret} =the retrieved LST, LST_{act} =the input LST)

We have also evaluated the developed method using the technique above with independent simulation data. The atmospheric profiles for this independent simulation are another 39 atmospheric profiles from TIGR database. The variation of bottom temperature with total water vapor content for the 39 atmospheric profiles is presented in Figure 2. Other parameters for independent simulation were the same as that in Section 2. The error of LST retrieved from this independent simulation data is shown in Figure 6. The RMSE of LST retrieved by Equation (3) from this independent simulation data is 0.16 K. Our developed method is very accurate and promising.

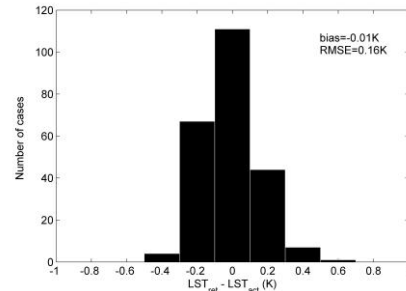


Figure 6. Error of the LST retrieved by Equation (3) from independent simulation data with the 39 atmospheric profiles

4 SENSITIVITY ANALYSIS OF THE METHOD

4.1 Sensitivity to spectral resolution

The developed method is affected by spectral resolution. We have retrieved LST using Equation (3) from five simulation database (spectral resolution = 0.25cm^{-1} , 0.5cm^{-1} , 1cm^{-1} , 2cm^{-1} , 5cm^{-1}) and have calculated error of the retrieved LST for each simulation database. The simulation data in these five simulation databases are a copy of the independent simulation data in Section 3 except for HypTIR brightness temperature dataset. The HypTIR brightness temperature dataset in each simulation

database contained 13 brightness temperatures which centered at the 13 wavenumbers described in Figure 4 and it is resampled from the independent simulation data in Section 3 using the different instrumental spectral response functions. The instrumental spectral response functions for the five simulation databases are rectangular impulse functions with spectral resolutions of the five values mentioned above and channel width of one spectral resolution. The errors of the LST retrieved from the five simulation databases using Equation (3) in function of spectral resolution are shown in Figure 7.

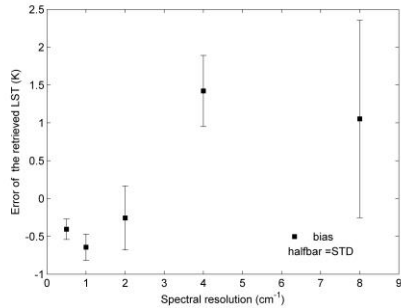


Figure 7. Sensitivity of our developed method to spectral resolution (STD = standard deviation)

The biases of the LST retrieved by Equation (3) from simulation databases for the five spectral resolutions are -0.41 K, -0.64 K, -0.26 K, 1.42 K, 1.05 K, and the corresponding standard errors of the retrieved LST are 0.14K, 0.17 K, 0.42 K, 0.47K, 1.30 K respectively. Therefore, we can conclude that coefficients in Equation (3) are dependent on spectral resolution. The coefficients in Equation (3) should be renewed for each spectral resolution.

4.2 Impact of spectral resolution on center wavenumbers at channel i ($i=1\sim p$)

Spectral resolution of HypTIR radiometer varies significantly between 0.25cm^{-1} and 10cm^{-1} . The coefficients w_i ($i=1\sim 13$) in our developed method are required to be refitted for each spectral resolution. Firstly, assuming that the center wavenumbers at channel i ($i=1\sim p$) are independent on spectral resolution, we have refitted coefficients w_i ($i=0\sim 13$) for each spectral resolution using linear regression with five simulation databases. The five simulation databases for refitting the coefficients w_i are resampled from simulation data described in Section 2 using technique and the five spectral resolutions mentioned in Section 4.1. After that, we have retrieved LST using Equation (3) and the refitted coefficients w_i from the five independent simulation databases mentioned in Section 4.1 and have calculated error of the retrieved LST for each independent simulation

database. The errors of the LST retrieved using Equation (3) and the refitted coefficients w_i from the independent simulation databases in function of spectral resolution are shown in Figure 8.

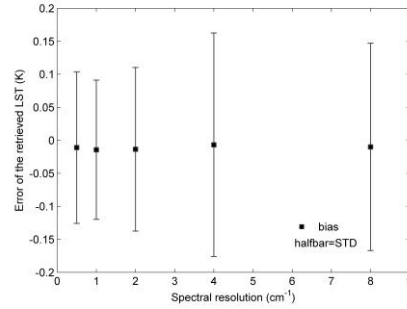


Figure 8. Errors of the LST retrieved using Equation (3) with refitted coefficients w_i ($i=1\sim 13$) from the five simulation databases in function of spectral resolution

For the five spectral resolutions, the biases of the LST retrieved by Equation (3) with refitted coefficients w_i from the five independent simulation databases are equal to -0.01 K, and the corresponding standard errors of the retrieved LST are 0.11K, 0.11 K, 0.12K, 0.17 K and 0.16 K respectively. The LST can be retrieved accurately using Equation (3) with the refitted coefficients w_i ($i=1\sim p$) for each spectral resolution.

4.3 Sensitivity to instrumental noise

The developed method is affected by instrumental noise. We have retrieved LSTs using Equation (3) from three simulation databases (NEDTs of noise = 0.1 K, 0.2 K, 0.3 K) and have calculated error of the retrieved LST for each simulation database. For each simulation database, simulation data is the same as that in Section 3 except for instrumental noise. To create independent instrumental noise, for each simulation case of HypTIR brightness temperature data, the random noises for simulation are 20 random noises of dimension =1601 generated by the Matlab random number generator. NEDTs of noise for the three simulation databases are the three values mentioned above. Errors of the LST retrieved using Equation (3) from the three simulation databases in function of instrumental noise are shown in Figure 9.

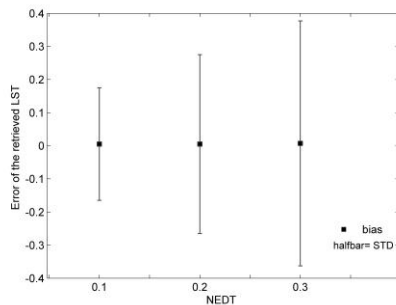


Figure 9. Sensitivity of our developed method to instrumental noise

With NEDT of instrumental noise growing from 0.1K to 0.3K, the RMSE of LST retrieved by Equation (3) for one level of instrumental noise goes up from 0.16 K to 0.37 K. Therefore, the impact of instrumental noise on the accuracy of the LST retrieved by Equation (3) is in the order of magnitude of the instrument noise.

5 CONCLUSIONS

With assumption of $LSE = 1$, we have developed an atmospheric correction method basing on 13 HypTIR measurements of a radiometer with spectral interval = $800\text{cm}^{-1} \sim 1200\text{cm}^{-1}$ and spectral resolution = 0.25 cm^{-1} and have evaluated the developed method using independent simulation data. Moreover, we have analyzed sensitivity of the developed method to spectral resolution and instrumental noise. From our work, we have drawn the following conclusions.

Firstly, land surface temperature can be retrieved by our developed method with RMSE of 0.16K. The developed method is very accurate and promising.

Secondly, the coefficients of the developed method are dependent on spectral resolution and LST can still be retrieved accurately by our developed method when the coefficients are refitted for each spectral resolution.

Furthermore, the impact of instrumental noise on the accuracy of the LST retrieved by the developed method is in the order of magnitude of the instrumental noise.

ACKNOWLEDGMENT

The authors would like to thank the LMD ARA for providing TIGR dataset and to thank LMD, NOVELTIS and CNES for providing the 4A/OP software. This work has been supported by the National High Technology Research and Development Program of China under Grant 2012AA121103 and by the National Natural Science Foundation of China under Grant 41231170.

REFERENCES

- Aires, F., Chedin, A., Scott, N. A., and Rossow, W. B., 2002, A regularized neural net approach for retrieval of atmospheric and surface temperatures with the IASI instrument. *Journal of Applied Meteorology*, 41, 144-159.
- Anderson, M. C., Hain, C., Wardlow, B., Pimstein, A., Mecikalski, J. R., and Kustas, W. P., 2011, Evaluation of drought indices based on thermal remote sensing of evapotranspiration over the continental United States. *Journal of Climate*, 24, 2025-2044.
- Borel, C., 2008, Error analysis for a temperature and emissivity retrieval algorithm for hyperspectral imaging data. *International Journal of Remote Sensing*, 29, 5029-5045.
- Chedin, A., Scott, N. A., Wahiche, C., and Moulinier, P., 1985, The improved initialization inversion method: A high resolution physical method for temperature retrievals from satellites of the TIROS-N series. *Journal of climate and applied meteorology*, 24, 128-143.
- Galve, J. M., Coll, C., Caselles, V., and Valor, E., 2008, An atmospheric radiosounding database for generating land surface temperature algorithms. *IEEE Transactions on Geoscience and Remote Sensing*, 46, 1547-1557.
- Gu, D., Gillespie, A. R., Kahle, A. B., and Palluconi, F. D., 2000, Autonomous atmospheric compensation (AAC) of high resolution hyperspectral thermal infrared remote-sensing imagery. *IEEE Transactions on Geoscience and Remote Sensing*, 38, 2557-2570.
- Le Marshall, J., Jung, J., Derber, J., Chahine, M., Treadon, R., Lord, S. J., ... and Tahara, Y., 2006, Improving global analysis and forecasting with AIRS. *Bulletin of the American Meteorological Society*, 87, 891-894.
- Li, Z.-L., Tang, B.-H., Wu, H., Ren, H., Yan, G., Wan, Z., Trigo, I.F., and Sobrino, J.A., 2013, Satellite-derived land surface temperature: Current status and perspectives. *Remote Sensing of Environment*, 131, 14-37.
- Masuda, K., Takashima, T., and Takayama, Y., 1988, EMISSIVITY OF PURE AND SEA WATERS FOR THE MODEL SEA-SURFACE IN THE INFRARED WINDOW REGIONS. *Remote Sensing of Environment*, 24, 313-329.
- Paul, M., Aires, F., Prigent, C., Trigo, I. F., & Bernardo, F., 2012, An innovative physical scheme to retrieve simultaneously surface temperature and emissivities using high spectral infrared observations from IASI. *Journal of Geophysical Research: Atmospheres* (1984–2012), 117(D11).

- Péquignot, E., Chédin, A., and Scott, N. A., 2008, Infrared continental surface emissivity spectra retrieved from AIRS hyperspectral sensor. *Journal of Applied Meteorology and Climatology*, 47, 1619-1633.
- Susskind, J., Barnett, C.D., and Blaisdell, J.M., 2003, Retrieval of atmospheric and surface parameters from AIRS/AMSU/HSB data in the presence of clouds. *IEEE Transactions on Geoscience and Remote Sensing*, 41, 390-409
- Vandenbussche, S., Kochenova, S., Vandaele, A. C., Kumps, N., and Mazière, M. D., 2013, Retrieval of desert dust aerosol vertical profiles from IASI measurements in the TIR atmospheric window. *Atmospheric Measurement Techniques Discussions*, 6, 4511-4550.
- Wang N., 2011, Simultaneous Retrieval of Land Surface Temperature, Emissivity and Atmospheric Profiles from Hyperspectral Thermal Infrared Data. PhD Thesis, Institute of Geographic Sciences and Natural Resources Research.
- Wang, X., OuYang, X., Li, Z. L., Jiang, X., and Ma, L., 2009, An atmospheric correction method for remotely sensed hyperspectral thermal infrared data. *IEEE International Geoscience and Remote Sensing Symposium*, 3, pp. 677-680.
- Webster, F., and Fieux, M., 1984, TOGA overview. In *Large-scale oceanographic experiments and satellites* (Springer Netherlands), pp. 17-24.
- Young, S. J., Johnson, B. R., and Hackwell, J. A., 2002, An in - scene method for atmospheric compensation of thermal hyperspectral data. *Journal of Geophysical Research: Atmospheres* (1984–2012), 107(D24).
- Zhou, L., Dickinson, R. E., Tian, Y., Jin, M., Ogawa, K., Yu, H., and Schmugge, T., 2003, A sensitivity study of climate and energy balance simulations with use of satellite - derived emissivity data over Northern Africa and the Arabian Peninsula. *Journal of Geophysical Research: Atmospheres* (1984–2012), 108(D24).
- Rhee, J., Im, J., and Carbone, G. J., 2010, Monitoring agricultural drought for arid and humid regions using multi-sensor remote sensing data. *Remote Sensing of Environment*, 114, 2875-2887.

Index system and suitability evaluation of grassland vegetation growth for remote sensing monitoring in Xilingol grassland of Inner Mongolia, China

Xiuchun Yang^{a,b}, Haida Yu^a, Xiaohua Zhu^c, Yunxiang Jin^a, Hailong Ma^a, Jinya Li^d, Fen Zhao^a, Shi Chen^a, Bin Xu^{a*}

^a Key Laboratory of Agri-informatics, Ministry of Agriculture / Institute of Agricultural Resources and Regional Planning, Chinese Academy of Agricultural Sciences, Beijing 100081, China; ^b College of Environment and Planning, Shangqiu Normal University, Henan 476000, China; ^c Institute of Geographic Sciences and Natural Resources Research, Chinese Academy of Sciences, Beijing 100101, China; ^d State Key Laboratory of Urban and Regional Ecology, Research Center for Eco-Environmental Sciences, Chinese Academy of Sciences, Beijing 100085, China
yangxiuchun@caas.cn; xubin@caas.cn

ABSTRACT—Grassland vegetation growth directly reflects the growth conditions of plants. In this study, the Xilingol Grassland in Inner Mongolia was used as the study area. Based on 16 days of Moderate-resolution Imaging Spectroradiometer (MODIS) data and ground sampling data, a monitoring indicator system for remote sensing of grassland vegetation growth was established. Ground data were used to assess the suitability of this indicator system. Using the year 2000 as the base year, with two vegetation indices, Normalized Difference Vegetation Index (NDVI) and Enhanced Vegetation Index (EVI), and the method of calculating difference as well as the method of calculating normalized difference, a monitoring indicator system for remote sensing of grassland vegetation, including Modified Growth Index (MGI)-NDVI, MGI-EVI, Growth Index (GI)-NDVI, and GI-EVI, was established. Then, determining the weights of vegetation coverage (c), height (h) and yield (y) in ground plots, a model for estimating the ground growth (g) was constructed: $g=0.2543c+0.1848h+0.5609y$. Also, on the basis of the partition, the ground growth value was calculated according to the ground growth model and that obtained from remote sensing indicators in the corresponding region were subjected to correlation analysis. It was found that the remote sensing growth indices suitable for the temperate steppe region, the meadow steppe region, and the desert steppe region were GI-EVI, MGI-NDVI, and GI-NDVI, respectively. Lastly, using the optimal remote sensing growth index for each region, the vegetation growth in the Xilingol Grassland was evaluated.

1 INTRODUCTION

China has about 400 million hm² of grassland, accounting for 41.7% of the total land area. In recent decades, grassland degradation and desertification have appeared on a large scale due to human over-exploitation and other factors. This is detrimental to the local production of livestock and results in the deterioration of the ecological environment. Monitoring of grassland vegetation growth can directly reflect changes in the status of grassland ecosystems as well as changes in vegetation caused by natural disasters, pests, and diseases, playing an important role in maintaining balanced and sustainable development of the grassland ecosystem. Meanwhile, grassland growth monitoring can also be used to monitor grassland vegetation biomass, making rational estimation of stock capacity easy and reducing

overgrazing, thus providing feedback for livestock management and production.

Monitoring of grassland vegetation growth can be divided into ground monitoring and remote sensing monitoring. Compared to ground monitoring, remote sensing monitoring has the advantages of monitoring over a large area, in real-time, and at a low cost and thus has become the main method of monitoring grassland growth. Existing remote sensing monitoring of grassland vegetation partially draws on methods of remote sensing crop growth monitoring. Current methods of remote sensing grassland growth monitoring include direct monitoring, vegetation growth process monitoring, and comparison over the same season (Wu et al., 2004; Meng et al., 2008; Svetlana et al., 2012; Xu et al., 2013).

Although currently there have been many studies on remote sensing monitoring of grassland vegetation

growth (Xu et al., 2007; John et al., 2013; Yu et al., 2013; Youngwook et al., 2014), there is a lack of studies on overall monitoring that targets different grassland types. Typically, the same indicator is used for all types of grassland which makes the results of the evaluation on grassland vegetation growth deviate from the actual situation, especially in areas with large spatial heterogeneity in grassland biomass. In addition, most existing remote sensing studies were not tested with ground data, and the accuracy of the monitoring results was not verified. In the present study, two vegetation indices, NDVI and EVI, and two growth calculation methods, the difference method and the normalized difference method, were used to construct a monitoring indicator system for remote sensing of grassland vegetation growth. The methods and vegetation indices suitable for remote sensing monitoring of different types of grasslands in Xilingol Grassland were analyzed. To quantitatively assess the suitability of different remote sensing monitoring indicators for the grassland growth in different types of grassland areas, ground grassland plots were used for verification. The conclusions obtained from this study will help to improve the accuracy of grassland growth monitoring via remote sensing.

2 MATERIALS AND METHODS

2.1 Study area

Xilingol League is located in the middle of the Inner Mongolia Autonomous Region of China at 115°13'-117°06'E, 43°02'-44°52'N. It is the grassland closest to the Beijing-Tianjin-Tangshan area. Xilingol League has a land area of 257,000 square kilometers, a population of one million, and 12 administrative counties. Xilingol Grassland has rich natural resources, and is one of the four most famous prairies in the world due to its characteristics such as a variety of grassland types, animal and plant species. It belongs to the Eurasian steppe zone, and has eight grassland types, some of which are temperate steppe, temperate desert steppe, and temperate steppe desert (Figure 1).

2.2 Data Sources

The remote sensing data used are the MOD13 product in MODIS data published by the United States National Aeronautics and Space Administration (NASA, <http://modis.gsfc.nasa.gov/>), belonging to level-2 land standard data products. The data contains rasterized vegetation indices, including synthetic NDVI, EVI, band reflectance, and other information over 16 days. The spatial resolution is 250 m. The downloaded vegetation indices were subjected to projection conversion, geometric correction, and other processing using the MODIS Reprojection Tool (MRT) to obtain the NDVI and EVI data during the 2000-2010 growing season (from May to September).

The ground data include plot data obtained from the Grassland Supervision Centre of the Ministry of Agriculture, as well as data from field research conducted by our research group in 2009 and 2010. There were a total of 175 ground grassland plots, and the time period involved was 2006-2010 (Figure 1).

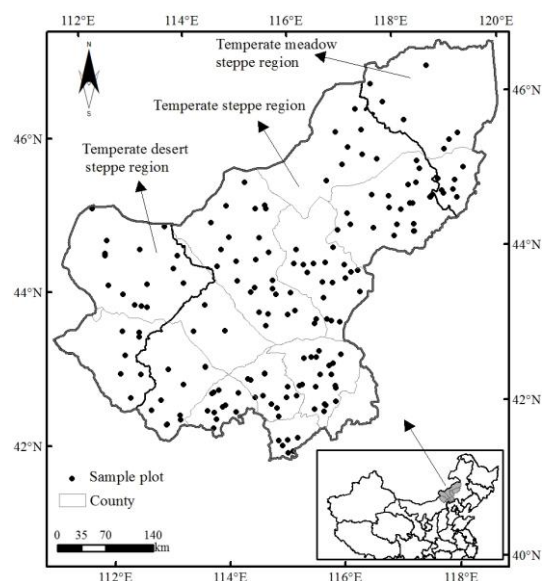


Figure 1. Grassland partitioning and distribution of ground plots

2.3 Methods

a) Grassland partitioning

Taking into consideration the spatial distribution of different grassland types in the Xilingol Grassland, hydrothermal and other natural conditions, the socio-economic conditions, and the animal husbandry layout, on the basis of maintaining the regional boundaries and the relatively completeness of county-level administrative units, following the principle of comprehensiveness combined with dominant type, as well as the principle of being practical, the Xilingol Grassland was divided into three regions, namely the temperate steppe region, the temperate meadow steppe region, and the temperate meadow steppe region, as shown in Figure 1.

b) The construction of the monitoring indicator system for remote sensing of grassland vegetation growth

NDVI and EVI each have their advantages in reflecting vegetation coverage. Hence, to compare the suitability of NDVI and EVI in different grassland types, four growth indices, namely GI-EVI, GI-NDVI, MGI-EVI, and MGI-NDVI, were used to construct the monitoring indicator system for remote sensing of

grassland vegetation growth. In other words, the indicator in the system was calculated based on either EVI or NDVI, using either the difference method or the normalized difference method.

Since 2000, China has started to implement the Beijing-Tianjin Sandstorm Source Control Project, the Grain for Green Project, and other key ecological construction projects. The study area in the present paper is located within the area of these ecological management projects. In order to objectively evaluate the continuous changes in the vegetation growth in the Xilingol Grassland, based on analysis of the Standardized Precipitation Index (SPI), the year 2000 was chosen as the base year.

GI is constructed using the difference method. The formula is:

$$GI = VI_m - VI_n \quad (1)$$

where VI_m is the vegetation index value in the year of monitoring, corresponding to $NDVI_m$ and EVI_m ; and VI_n is the vegetation index value in the base year (2000), corresponding to $NDVI_n$ and EVI_n .

The MGI is constructed using the normalized difference method. The formula is:

$$MGI = \frac{VI_m - VI_n}{VI_m + VI_n} \quad (2)$$

where VI_m is the vegetation index value in the year of monitoring, corresponding to $NDVI_m$ and EVI_m ; and VI_n is the vegetation index value in the base year (2000), corresponding to $NDVI_n$ and EVI_n .

The classification evaluation with the above two methods was mainly conducted based on the research results of Xu et al. (2013) and the verification test results using ground data. According to the magnitude of changes in the vegetation indices, the growth levels of different areas were divided into five scales: I: poor (negative growth), II: relatively poor (negative growth), III: unchanged, IV: relatively good (positive growth), and V: good (positive growth). Areas with questionable data or missing data were considered non-study areas.

c) The construction of grassland ground growth model

The height and coverage of grassland vegetation determine the condition of grassland vegetation growth, and yield can to a certain degree reflect grassland vegetation growth. First, the three indicators in three dimensions: height, coverage, and yield, were subjected to standardized dimensionless processing. Next, with growth assessment as the goal, height, cover, and yield as the participating factors, 30 experts in grassland science, ecology, and geography were invited to score the participating factors. Finally, the ground growth model was constructed using the AHP.

The questionnaire recovery rate of the present study was 100%, and the consistency index was 0.03, indicating rather a good consistency. The weights of all factors in the ground growth model were quantitatively determined: for height (h), 0.1848; coverage (c), 0.2543; and yield (y), 0.5609. The formula is:

$$g = 0.2543c + 0.1848h + 0.5609y \quad (3)$$

where g denotes the growth value; c denotes vegetation coverage; h denotes vegetation height; and y denotes vegetation yield.

3 RESULTS

3.1 Suitability evaluation of monitoring indicator in remote sensing

Data from 175 ground grassland plots were subjected to standardized dimensionless processing by calculating the proportions of the corresponding data. According to the magnitude of the correlation coefficients between the remote sensing growth value and the ground growth value in different grassland areas (Table 1), among the three areas, the remote sensing indicator best suitable for the temperate steppe region is GI-EVI, and that for the meadow steppe region is MGI-NDVI. In the desert steppe region, none of the correlation coefficients is high. Comparatively speaking, the remote sensing indicator best suitable for the desert steppe region is GI-NDVI.

Table 1. Correlation coefficients between remote sensing growth values and ground growth values

Regions	MGI-NDVI	MGI-EVI	GI-NDVI	GI-EVI
Temperate steppe region	0.310**	0.363**	0.386**	0.404**
Temperate meadow steppe region	0.521*	0.504*	0.407	0.446*
Temperate desert steppe region	-0.015	0.157	0.336*	0.203

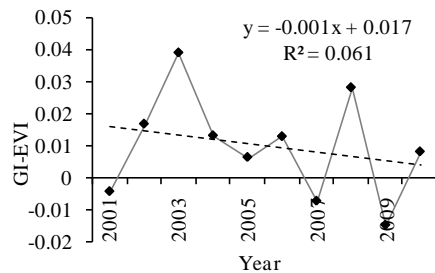
Notes: * $p < 0.05$; ** $p < 0.01$ (Pearson's correlation test).

3.2 The spatiotemporal analysis of grassland vegetation growth

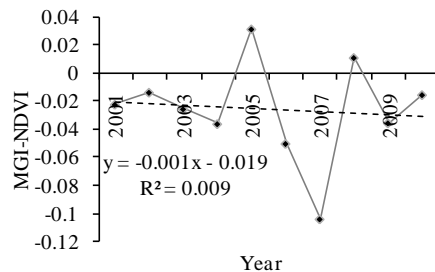
3.2.1 The spatiotemporal analysis of vegetation growth in the temperate steppe region

For the temperate steppe region, the coefficient of variation within the 10 years was 0.60, indicating relatively large changes. In Figure 2, the dotted line represents the linear curve fitting of annual vegetation growth in the temperate steppe region of the Xilingol League. Overall, the annual growth in the temperate steppe region showed a decreasing change. Among the 10 years, the growth values of 2001, 2007, and 2009 were smaller than that of 2000, whereas the growth

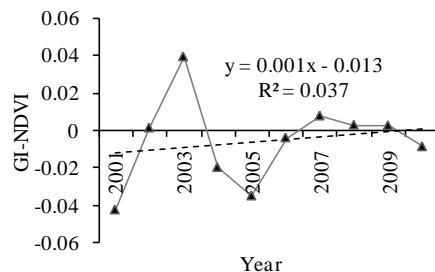
values of all other years were higher than that of 2000. The growth was the highest in 2003, followed by 2008.



a) Temperate steppe area



b) Temperate meadow steppe area



c) Temperate desert steppe area

Figure 2. Growth conditions in 2001-2010 in the temperate steppe region, meadow steppe region, desert steppe region

In the temperate steppe region, the proportion of areas with unchanged growth level in 2001-2010 was the largest, accounting for 60%-88% of the total area of the temperate grassland. In 2004, the area with unchanged growth level was the largest, reaching 116,982 km²; in 2008, it was minimal with only 8283 km².

For spatial variations in the study area, in general from 2001 to 2010, the growth of the Dong Ujimqin Banner and West Ujimqin Banner was relatively good, whereas that of Xianghuang Banner and Sonid Right Banner was relatively poor.

3.2.2 The spatiotemporal analysis of vegetation growth in the meadow steppe region

For the meadow steppe region, the coefficient of variation in 2001-2010 was 0.71. Overall the annual growth showed a decreasing trend (Figure 2), and the change was the largest among the three grassland

types. Using MGI-NDVI to represent the growth change in the meadow steppe region, it can be found that the growth was the best in 2005, followed by 2008. For the remaining eight years, the growth values were all negative (worse than 2000), and it was the lowest in 2007. Changes in 2001-2004 were relatively small.

The areas of regions in the meadow steppe region with different growth levels in each year are shown in Table 2. Within the 10 years studied, the area of regions with unchanged growth was 18%-62% that of the total area of the meadow grassland. This area with unchanged growth was the smallest in 2007, only 5388 km², and was the largest in 2008, reaching 18,056 km².

Table 2. The areas of meadow steppe regions with different growth levels (unit: km²)

Year	I	II	III	IV	V
2001	522	8153	17651	2730	179
2002	357	8281	16395	3630	573
2003	1006	10622	13456	3620	532
2004	593	12395	14536	1716	206
2005	107	2070	17340	8443	1275
2006	1730	13582	12162	1543	219
2007	7531	15816	5388	334	167
2008	181	4067	18056	6123	809
2009	1834	11729	11684	3171	816
2010	889	8886	14497	3963	1001

Spatially, the eastern part of the meadow steppe region showed relatively good growth in the years 2005, 2009, and 2010, and the remaining regions did not differ largely. Within the 10 years, the area of meadow grassland regions showing unchanged growth compared to 2000 was relatively large.

3.2.3 The spatiotemporal analysis of vegetation growth in the desert steppe region

For the desert steppe region, the coefficient of variation within 10 years was 0.23, and overall the annual growth showed an improving trend (Figure 2). Among the three grassland areas, the desert steppe region showed the smallest change in amplitude. It can be seen from changes in the growth as represented by GI-NDVI that the average vegetation growth of the desert steppe region in 2003 was substantially higher than 2000, whereas that in 2007-2009 was slightly better than 2000. In 2001 and 2005, the growth was worse than that in 2000.

The areas of region in the desert steppe region with different growth levels in each year are shown in Table 3. The desert grassland has a total area of 29,357.71 km², and is the smallest among the three grassland areas. Similar to the other two grassland types, the area of regions with unchanged growth in the desert steppe region was the largest, varying from 24,911-34,870 km². The area of grassland regions with

relatively good and good growth was the largest in 2003, accounting for 35.06% of the total area of the desert grassland and was the smallest in 2005, with a proportion of 0.13%.

The desert steppe region includes the majority of the Sonid Left Banner, a small part of the Sonid Right Banner, and Erenhot city of which the area is relatively small.

Table 3. The areas of desert steppe regions with different growth levels (unit: km²)

Year	I	II	III	IV	V
2001	1	13876	22909	64	1
2002	0	807	34646	1394	3
2003	0	21	23871	12881	77
2004	1	6779	29675	392	4
2005	3	11888	24912	44	3
2006	2	4648	29626	2566	8
2007	1	1460	31359	4020	11
2008	1	921	34814	1108	7
2009	2	1318	34036	1487	8
2010	2	4148	32068	627	6

3.2.4 The spatiotemporal analysis of vegetation growth in the entire study area

Within the entire study area, the area of regions showing unchanged growth was the largest. Except for the year 2008, in all the remaining years, the area of regions with unchanged growth was 60%-80% that of the total area; in 2008, it was the smallest, being only 61,151 km². The area of grassland regions showing relatively good and good growth accounted for 4.81%-33.47% of the total area, was the smallest in 2009 and largest in 2003. The area of grassland regions showing relatively poor and poor growth accounted for 5.40%-21.52% of the total grassland area, varying from 10,884 km²-12,309 km².

The spatial changes in grassland growth from 2001-2010 are as shown in Figure 3.

Figure 3. Spatial changes in grassland growth from 2001-2010

4 CONCLUSIONS AND DISCUSSION

4.1 Conclusions

In this study, based on years of field research data, remote sensing data, and weather information, a monitoring indicator system for remote sensing of grassland vegetation growth and a ground vegetation growth model were established. The latter was used to perform suitability evaluation on the monitoring indicatory system for remote sensing, and remote sensing monitoring indicators suitable for different grassland types were obtained. The main conclusions are as follows.

First, using two vegetation indices, NDVI and EVI, and two methods, the difference method and the normalized difference method, the grassland vegetation growth was calculated. Four monitoring indicators for remote sensing of growth were obtained: MGI-NDVI, MGI-EVI, GI-NDVI, and GI-EVI.

Second, using expert opinion scoring and AHP as methods, and grassland growth as the target goal, ground vegetation coverage (*c*), height (*h*), and yield (*y*) were selected to construct a model for estimating the ground growth (*g*): $g=0.2543c+0.1848h+0.5609y$. The obtained the ground growth values and the remote sensing growth values were subjected to correlation analysis, and it was found that the remote sensing growth indices suitable for temperate steppe regions, meadow steppe regions, and desert steppe regions were GI-EVI, MGI-NDVI, and GI-NDVI, respectively.

Third, using the optimal remote sensing growth index for each grassland type to monitor the vegetation growth over 10 years, it was found that the proportion of areas with growth improvement was the largest in the temperate steppe region, followed by the meadow steppe region. Vegetation growth improvement was not notable in the desert steppe region.

4.2 Discussion

The data sources used in the present study were remote sensing data and ground data. The nature of the remote sensing information determines that there is uncertainty in data acquisition, processing, and analysis. For ground data, such as vegetation coverage, there is relatively strong subjectivity in the measurement process, and different persons may obtain different values. Thus, there is also uncertainty in the ground data. Therefore, it is crucial to eliminate the data uncertainty as much as possible.

5. References

- John, A. G., K. F. Huemrich, S. S. Robert, E. T. Craig, 2013, Spatial and temporal variation in primary productivity (NDVI) of coastal Alaskan Tundra: Decreased Vegetation Growth Following Earlier Snowmelt. *Remote Sensing of Environment*, **129**: 144~153.
- Meng, J. H., B. F. Wu, 2008, Study on the Crop Condition Monitoring Methods with Remote Sensing. The International Archives of the Photogrammetry, *Remote Sensing and Spatial Information Sciences*, Beijing, XXXVII(B8): 940-950.
- Svetlana, M. K., T. A. Kazantsev, 2012, Derivative Vegetation Indices as a New Approach in Remote Sensing of Vegetation. *Frontiers of Earth Science*, **6**(2): 188-195.

- Wu, B. F., F. Zhang, C. L. Liu, L. Zhang, Z. M. Luo, 2004, An Integrated Method for Crop Condition Monitoring." [In Chinese with an English abstract.] *Journal of Remote Sensing*, **8(6)**: 498-514.
- Xu, B., W. G. Tao, X. C. Yang, Z. H. Qin, M. F. Gao, 2007, Monitoring by Remote Sensing of Vegetation Growth in the Project of Grassland Withdrawn from Grazing in Counties of China. [In Chinese with an English abstract.] *Acta Prataculturae Sinica*, **16(5)**: 13-21.
- Xu, B., X. C. Yang, W. G. Tao, J. M. Miao, Z. Yang, H. Q. Liu, Y. X. Jin, X. H. Zhu, Z. H. Qin, H. Y. Lv, J. Y. Li, 2013, MODIS-based Remote Sensing Monitoring of the Spatiotemporal Patterns of China's Grassland Vegetation Growth. *International Journal of Remote Sensing*, **34(11)**: 3867-3878.
- Youngwook, K., J.S. Kimball, K. Didan, G.M. Henebry, 2014, Response of Vegetation Growth and Productivity to Spring Climate Indicators in the Conterminous United States Derived from Satellite Remote Sensing Data Fusion. *Agricultural and Forest Meteorology*, **194**: 132-143.
- Yu, H. D., X. C. Yang, B. Xu, Y. X. Jin, T. Gao and J. Y. Li, 2013, Changes of Grassland Vegetation Growth in Xilin Gol League over 10 Years and Analysis on the Influence Factors. [In Chinese with an English abstract.] *Journal of geo-information science*, **15(2)**: 270-279.

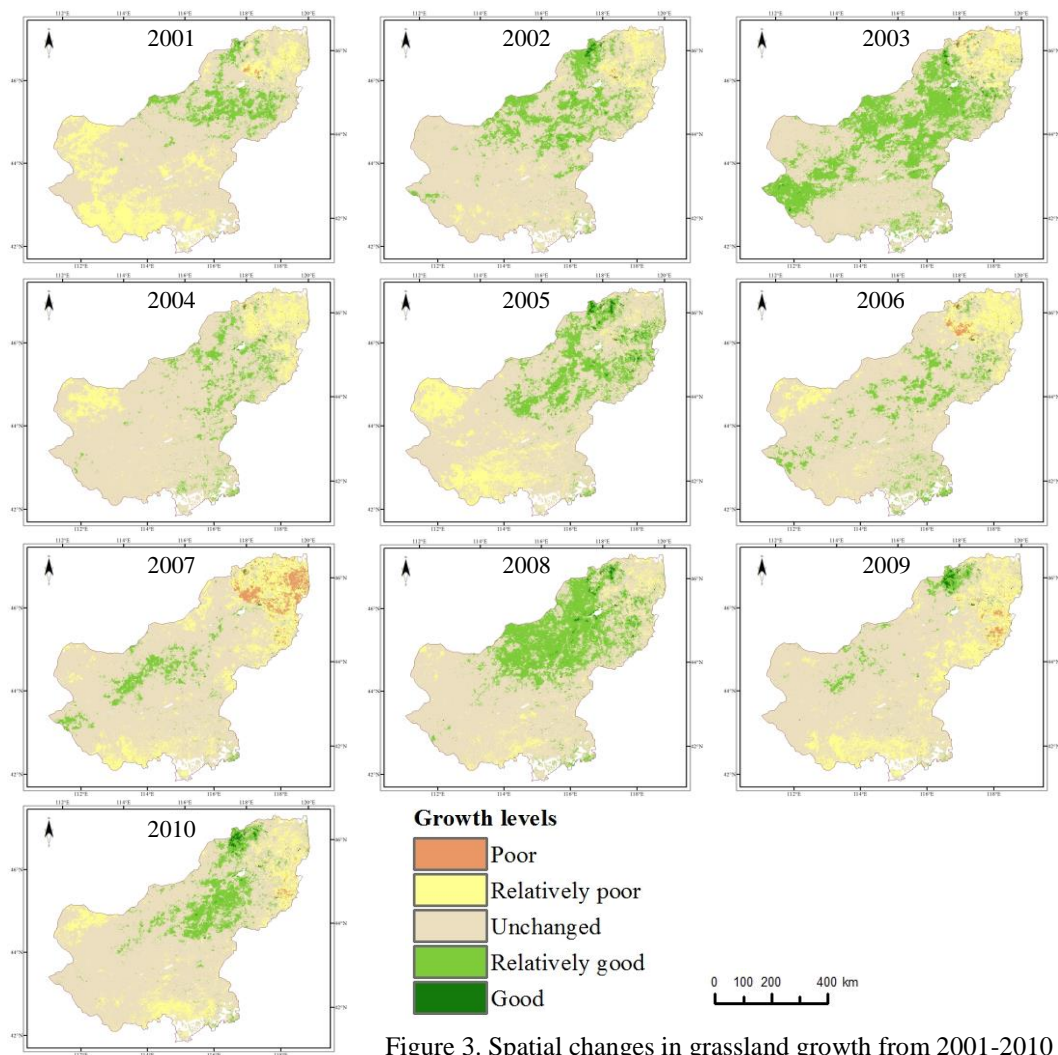


Figure 3. Spatial changes in grassland growth from 2001-2010

Early water stress detection in desert Tamarugo trees based on leaf pulvinar movements

Roberto O. Chávez, Jan G.P.W. Clevers,
Laboratory of Geo-Information Science and Remote Sensing, Wageningen University, P.O.
Box 47, 6700 AA Wageningen, The Netherlands
Roberto.Chavez@wur.nl, Jan.Clevers@wur.nl

ABSTRACT- A 25 years Landsat time series showed a strong seasonal variation in the normalized difference vegetation index (NDVI) for Tamarugo plantations with peak values in winter, which was negatively correlated to solar irradiation ($R^2 = 0.66$). This seasonal variation of the NDVI could be explained by movement of the leaves away from direct irradiation at high irradiation levels. This is caused by changes in turgor in pulvinus cells at the base of the leaves. Trees with water stress exhibited significantly less seasonal variation. In addition to the seasonal component, a decreasing trend in the Landsat NDVI series for the period 1996-2007 was observed, which was correlated to groundwater depletion. An analysis of 10 years MODIS data of the Tamarugo plantations showed a similar seasonal variation in NDVI as observed in the Landsat time series ($R^2 = 0.65$ with solar irradiation). In addition, a positive difference between the NDVI in the morning (Terra satellite) and the NDVI at midday (Aqua satellite) was observed, which again could be explained by the pulvinar movement. This difference was smaller for trees with water stress. This difference also became smaller in time because of an increasing ground water depletion, thus reducing the leaf pulvinar movement. This NDVI difference obtained from the MODIS Aqua and Terra satellites has potential to detect early symptoms of water stress for Tamarugo trees at the stand level.

1 INTRODUCTION

Heliotropic leaf movement or leaf “solar tracking” occurs in a wide variety of plants, including major crops like beans, as a response to changes in the position of the sun throughout the day (Ehleringer and Forseth, 1980). Contraction of the so-called pulvinus at the base of leaves and folioles is causing this movement. This may have an important effect on the canopy spectral reflectance measured from satellites. For this reason, monitoring systems based on remote sensing observations (e.g., using spectral vegetation indices like the normalised difference vegetation index, NDVI) should account for heliotropic movements in evaluating the actual condition of such species. Tamarugo (*Prosopis tamarugo* Phil.) is an endemic and endangered tree species adapted to the hyper-arid conditions of the Atacama Desert in Northern Chile. Diurnal leaf movements were observed in this Leguminosae tree species both in the laboratory (Chávez et al., 2012) and in the field (Chávez et al., 2013) and this had an important effect on canopy reflectance as measured with a radiometer. Tamarugo leaves moved towards an erectophile leaf angle distribution to decrease the direct solar irradiation on the leaves at the hottest time of the day (paraheliotropism) and this way minimize photoinhibition.

In this study, the hypothesis is that Tamarugo move their leaves away from direct irradiation under high irradiation conditions, causing a more erectophile leaf angle distribution within the canopy. As a result,

the NDVI will be lower under high irradiation conditions, in summer yielding a lower NDVI at midday than in the morning (Figure 1). Moreover, in summer the NDVI also will be lower than in winter when irradiation levels are lower (Figure 2).

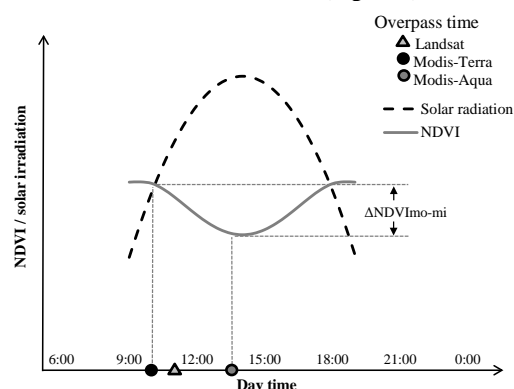


Figure 1: Conceptual diagram of the effect of leaf pulvinar movement on the NDVI difference between morning and midday ($\Delta\text{NDVI}_{\text{mo-mi}}$), occurring as solar irradiation changes during the day.

The Moderate Resolution Imaging Spectrometer (MODIS) seems suitable to detect the difference in NDVI between morning and midday, since the MODIS sensor on board of the Terra satellite acquires data at 10 a.m. for the test site, whereas the MODIS sensor on board of the Aqua satellite acquires data at 1.30 p.m. (local time). Both Terra and Aqua acquire

data on a daily basis. In addition to MODIS, the Landsat Thematic Mapper (TM) and Enhanced Thematic Mapper (ETM) seem to be suitable for detecting the difference in NDVI between summer and winter. Overall goal of this study is to find remote sensing based indicators for water stress of Tamarugo trees. Since pulvinar movement is triggered by cell water turgor and thus is limited for trees under water stress, expected changes in canopy spectral reflectance of Tamarugo plantations may be detected by remote sensing and used to assess water stress. Time series of MODIS and Landsat NDVI were used to study the effect of water stress on NDVI differences between winter and summer and between morning and midday.

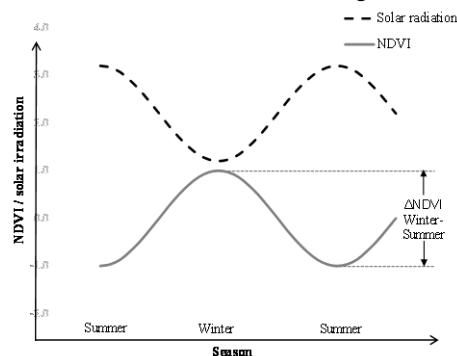


Figure 2: Conceptual diagram of the effect of leaf pulvinar movement on the NDVI difference between winter and summer ($\Delta\text{NDVI}_{\text{W-S}}$), occurring as solar irradiation varies between seasons.

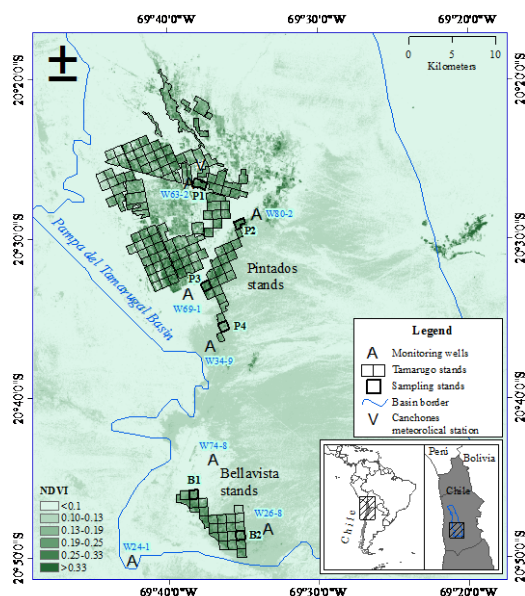


Figure 3: Landsat NDVI image (winter 2007) showing the location of the Tamarugo stands in the Pampa del Tamarugal basin in Chile.

2 MATERIAL AND METHODS

2.1 Test site

Tamarugo is an endemic tree of the hyper-arid Atacama Desert in Northern Chile (Figure 3). The Tamarugo forest, locally known as Pampa del Tamarugal, is important for its biodiversity (Espinoza and Galleguillo, 2008). Precipitation events are very rare and vegetation is fully dependent on ground water. However, competition for ground water is coming from mining industry and human consumption, leading to overexploitation of ground water. After being almost extinct in the 19th century, the Chilean government carried out an enormous reforestation effort by planting about 13,000 hectares of Tamarugo in the Pampa del Tamarugal basin (Zelada, 1986).

Tamarugo belongs to the Leguminosae family, Mimosaceae subfamily, and it can reach up to 25 meters height and 2 meters in stem diameter. The branches have twigs with composite leaves. The petioles have a distinctive structure called pulvinus, which is responsible for the ability to move the leaves (Figure 4). Changes in turgor of the pulvinus cells make the leaves to move.



Figure 4: Pulvinar structures of Tamarugo leaves. (a) Tamarugo trees, (b) leaf angle randomly distributed (morning), (c) leaf angle in erectophile position (at midday), (d) transversal section of a closed pulvinus (empty of water), (e) transversal section of an open pulvinus (filled with water), which allows leaves to reach an erectophile position, and (f) detail of the base of a Tamarugo pinna showing three levels of pulvinar structures.

2.2 Satellite data

For this study all available Landsat 5 TM and Landsat 7 ETM data as well as MODIS-Terra and MODIS-Aqua data of the study area covering the period 1989-2012 were used. This time frame was selected since this is the period of time with available ground water depth records for most of the monitoring wells located in the study area (Figure 3). For the Landsat NDVI time series cloud free images of 30 meters resolution and pre-processed using the Landsat Ecosystem Disturbance Adaptive Processing System (LEDAPS) were used to obtain surface reflectance values for all spectral bands (Masek et al., 2006). From this NDVI was calculated. For the MODIS-Terra and MODIS-Aqua NDVI time series the MODIS 16-day composites at 250 meters pixel resolution (MOD13Q1 and MYD13Q1 data products) were used. Both MODIS and Landsat data were downloaded from the USGS Earth Explorer website.

2.3 Ground water and irradiation data

Ground water records were obtained from the monitoring network (Figure 3) of the Dirección General de Aguas (DGA), the Chilean Water Service. Annual average values were calculated. This way representative ground water data for the period 1989-2012 were obtained. Solar irradiation records were obtained from the Canchones Experimental Station of the Universidad Arturo Prat (Chile), located in the northern part of the study area (Figure 3).

2.4 Data analysis

First, the natural dynamic of the NDVI time series was studied for the three satellite sensors. Using the annual records of ground water depletion for the monitoring wells (Figure 3), locations with low and high ground water depletion were compared. For this purpose a stand with almost no depletion was identified in the southern part of the study area (Figure 3, stand B1). The median NDVI value of the pixels inside the 1×1 km stand was used. In a similar way median values for a stand with severe ground water depletion (stand P2) were calculated.

After studying the dynamics of NDVI time series, the relationship between annual ground water depletion and relevant metrics derived from the NDVI signal was studied. The following metrics were studied:

- 1) The 16-day MODIS NDVI difference between morning (Terra) and midday (Aqua): $\Delta\text{NDVI}_{\text{mo-mi}}$;
- 2) The MODIS NDVI difference between winter and summer (using Terra): $\text{MODIS } \Delta\text{NDVI}_{\text{w-s}}$;
- 3) The Landsat NDVI difference between winter and summer: $\text{Landsat } \Delta\text{NDVI}_{\text{w-s}}$.

where the NDVI winter is calculated as the average of all scenes from the months May, June and July, whereas NDVI summer uses months November, December and January in a similar way.

3 RESULTS AND DISCUSSION

3.1 NDVI natural dynamic

In the situation with low ground water depletion, the NDVI signal of the Tamarugo stand presented a strong seasonal variation for the period 2005-2008, mainly explained by the seasonal variation of the monthly average solar irradiation (Figure 5). The MODIS-Terra and MODIS-Aqua showed the largest NDVI values in winter, when solar irradiation was lowest (Figure 6). The R^2 for the linear relationship between NDVI and solar irradiation was 0.65 for the MODIS-Terra NDVI, and 0.41 for the MODIS-Aqua NDVI. Moreover, NDVI values from MODIS-Terra in general were larger than those for MODIS-Aqua.

In a similar way the Landsat time series also showed largest NDVI values when solar irradiation was lowest (Figure 7). The R^2 for the linear relationship between NDVI and solar irradiation was 0.66 for the Landsat NDVI time series. Tamarugo seemed to react to the high solar irradiation in summer by having a predominantly erectophyle leaf angle distribution in order to minimize photoinhibition, similar to the diurnal mechanism reported by Chávez et al. (2013). As a result, the canopy spectral reflectance decreased causing the NDVI to drop in summer. Overall, the seasonal variation is the main feature of the annual NDVI signal, and therefore, the $\Delta\text{NDVI}_{\text{w-s}}$ may be used to detect the leaf pulvinar movement occurring in Tamarugo under natural conditions.

Figure 6 also shows that the difference in NDVI between Terra and Aqua ($\Delta\text{NDVI}_{\text{mo-mi}}$) was obvious in winter, but it was almost zero during summer. It is expected that Tamarugo start to move their leaves in winter towards midday, whereas in summer they will move there leaves already earlier in the morning when solar irradiation is already at high levels (yielding a smaller $\Delta\text{NDVI}_{\text{mo-mi}}$).

Notably the diurnal and seasonal variations in NDVI are not an effect of the bidirectional reflectance distribution function (BRDF). This would yield variations in reflectances and vegetation indices for a fixed canopy structure as a function of changing viewing and/or solar geometry. In the case of Tamarugo the tree canopy structure changes due to the movement of the leaves, which is different from a BRDF effect.

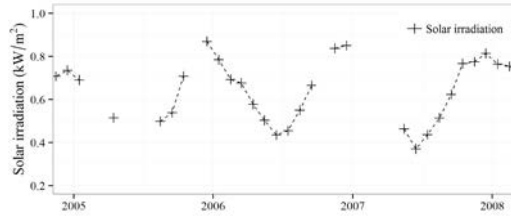


Figure 5: Solar irradiation records as measured at the meteorological station in the north of the study area.

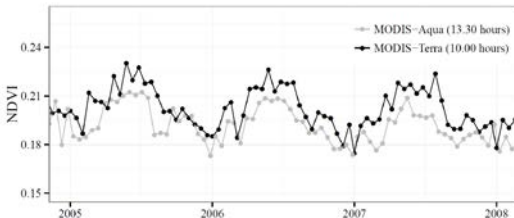


Figure 6: MODIS 16-days NDVI composite for a location with low ground water depletion (stand B1).

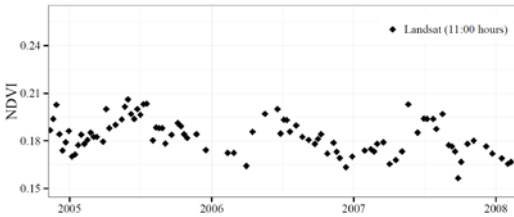


Figure 7: Landsat NDVI time series for a location with low ground water depletion (stand B1).

3.2 NDVI dynamic under high ground water depletion

In Figure 8 the MODIS-Terra and MODIS-Aqua NDVI time series are depicted for a stand with high depletion levels. The NDVI values are lower as compared to the stand without significant ground water depletion (Figure 6). Moreover, the difference between Terra and Aqua has decreased as compared to the time series of Figure 6. Severe ground water depletion is causing water stress, reducing turgor of cells (in particular in the pulvinus) and inhibiting the movement of leaves. Also for the Landsat NDVI time series lower values are observed (Figure 9) and the amplitude of the seasonal NDVI cycles has declined.

3.3 NDVI metrics

In Figure 10 an example is shown of a Tamarugo stand with severe ground water depletion. The annual time series of ground water depth, the Landsat NDVI in winter (NDVI_w) and the Landsat NDVI difference between winter and summer (Δ NDVI_{w-s}) is depicted. Both Landsat derived metrics showed a decreasing trend with increasing ground water depth.

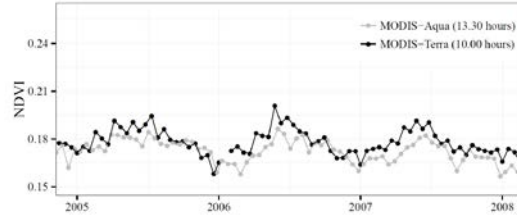


Figure 8: MODIS 16-days NDVI composite for a location with high ground water depletion (stand P2).



Figure 9: Landsat NDVI time series for a location with high ground water depletion (stand P2).

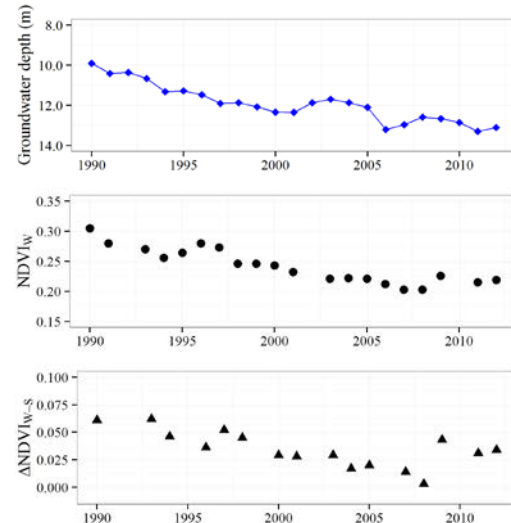


Figure 10: Example of annual ground water depletion and Landsat NDVI derived metrics NDVI_w and Δ NDVI_{w-s} (stand P2).

Figure 11 displays the NDVI values at pixel level of all Bellavista plantation stands (Figure 3) in the winter of 2007 (first row), the summer of 2006-2007 (second row), and the Δ NDVI_{w-s} of 2007 (third row) obtained from Landsat images (first column), MODIS-Terra images (second column), and MODIS-Aqua images (third column). The fourth column corresponds to the Δ NDVI_{mo-mi} in winter (first row) and summer (second row) based on Terra (morning) and Aqua (midday). This figure confirms that the Δ NDVI_{mo-mi} in winter and the Δ NDVI_{w-s} of 2007 was positive for the forested area.

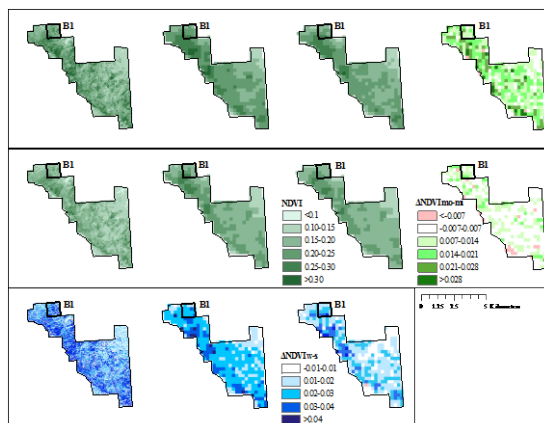


Figure 11: NDVI values at pixel level of all Bellavista plantation stands in the winter of 2007 (first row), the summer of 2006-2007 (second row), and the ΔNDVI_{w-s} of 2007 (third row) obtained from Landsat images (first column), MODIS-Terra images (second column), and MODIS-Aqua images (third column). The fourth column corresponds to the $\Delta\text{NDVI}_{mo-mi}$ in winter (first row) and summer (second row) based on Terra (morning) and Aqua (midday).

On the other hand, the $\Delta\text{NDVI}_{mo-mi}$ in summer was zero or close to zero. In a similar way the ΔNDVI_{w-s} was higher when using MODIS-Terra images than when using MODIS-Aqua images. Thus, the more promising indicators of pulvinar movement seemed to be the $\Delta\text{NDVI}_{mo-mi}$ in winter and the ΔNDVI_{w-s} in the morning (MODIS-Terra or Landsat). When using the NDVI as a potential indicator of the water status of Tamarugo trees, the signal in winter was stronger.

Previous papers (Chávez et al., 2013; Chávez et al., 2012) have shown that Tamarugo may show typical water stress symptoms, but additionally water stress may limit the normal functioning of the leaf pulvinar mechanism. These pulvinar movements are typical for heliotrophic species. Leaf pulvinar movement can be sensed by satellites using different NDVI metrics and these may be used for early water stress detection.

4 CONCLUSIONS

- Leaf pulvinar movements cause diurnal and seasonal variations in NDVI for Tamarugo stands;
- Negative correlation between NDVI and solar irradiation;
- NDVI difference between morning and midday can detect leaf pulvinar movement and this can be measured from Terra and Aqua satellites;
- NDVI difference between winter and summer can detect leaf pulvinar movement and this can be measured from Terra or Landsat time series;
- Leaf pulvinar movement can be limited by water stress;
- ΔNDVI_{w-s} and $\Delta\text{NDVI}_{mo-mi}$ have potential for early water stress detection.

5 REFERENCES

- Chávez, R.O., Clevers, J.G.P.W., Herold, M., Acevedo, E., & Ortiz, M. (2013). Assessing water stress of desert tamarugo trees using in situ data and very high spatial resolution remote sensing. *Remote Sensing*, **5**, 5064-5088
- Chávez, R.O., Clevers, J.G.P.W., Herold, M., Ortiz, M., & Acevedo, E. (2012). Modelling the spectral response of the desert tree *Prosopis tamarugo* to water stress. *International Journal of Applied Earth Observation and Geoinformation*, **21**, 53-65
- Ehleringer, J., & Forseth, I. (1980). Solar tracking by plants. *Science*, **210**, 1094-1098
- Espinoza, J., & Galleguillo, R. (2008). *Estrategia para la conservación de biodiversidad. Región de Tarapacá*: Comisión nacional del medio ambiente. Gobierno de Chile.
- Masek, J.G., Vermote, E.F., Saleous, N.E., Wolfe, R., Hall, F.G., Huemmrich, K.F., Gao, F., Kutler, J., & Lim, T.K. (2006). A landsat surface reflectance dataset for North America, 1990-2000. *IEEE Geoscience and Remote Sensing Letters*, **3**, 68-72
- Zelada, L. (1986). The influence of the productivity of *Prosopis tamarugo* on livestock production in the Pampa del Tamarugal - a review. *Forest Ecology and Management*, **16**, 15-31

A synoptic turbidity index for the Guadalquivir River with Landsat TM and ETM+ images: the turbiperiod

Ricardo Díaz-Delgado, David Aragonés, Isabel Afán and Javier Bustamante
Laboratorio de SIG y Teledetección (LAST). Estación Biológica de Doñana, CSIC. Avda. Américo Vespucio s/n. Sevilla. Spain.
rdiaz@ebd.csic.es

ABSTRACT *In late November 2007 there was an important increase in turbidity and salinity in the estuary of the Guadalquivir River (SW Spain). From that moment, high NTU values were periodically reached. The LAST-EBD participated in a large-scale watershed research project to reconstruct historical turbidity patterns by using Landsat TM and ETM+ time series of images. The aim of the work was to analyse historical trends and changes to infer the most relevant factors (tides, reservoir release, dredge...) determining such sudden turbid events and their frequency. Field work campaigns were carried out during two hydrological cycles coincident with 7 Landsat acquisitions. An empirical model was developed showing bands 2, 3 and 4 as significantly related to water turbidity of the River. Yearly composites were sought in order to extract historical patterns related to hydrological cycles. While average, summation and anomalies provided a rapid and synoptic picture of trend and peak years, the scarce occurrence of very turbid events was masked when they happened within an average year (low frequency turbid events). A new synoptic index, named turbiperiod was proposed to help identify such episodes. Index calculation considered the time span between images and assumed turbidity maintenance from one image to the next. This approach evidenced an increase in low frequency turbid events in the recent years, likely due to human activities in the Estuary.*

1 INTRODUCTION

In the past century, the Guadalquivir River was dramatically transformed for shipping, changing its ecological and hydrological functioning. The recent increase in frequency of high turbidity episodes at the Guadalquivir Estuary have caused serious problems for the historical water uses and services provided by the River (fishing, rice crops, aquaculture, tourism). Such disturbances come from the continuous demand of fresh water to retain tidal influence through regulatory dams and periodic labour to keep the canal depth for shipping. A new proposal for a deeper dredging plan of the navigation channel led to foster a large Scientific Consortium Project to extensively study the Guadalquivir Estuary. The Laboratory of Remote Sensing and GIS of Doñana Biological Station (LAST-EBD) participated in the project with the aim to reconstruct the historical river turbidity for the last 29 years using Landsat images (Díaz-Delgado et al., 2010).

Remote sensing has largely been used for quantifying water turbidity or Suspended Sediment Concentration (SSC) either in inland wetlands or coastal waters (Volpe et al., 2011; Matthews, 2011). Satellite mapping of turbidity is relevant both as an indicator of the optical environment for water quality monitoring purposes (Dogliotti et al. 2015). The spectral rationale relies on visible bands sensitivity to

SSC (Matthews, 2011). However, different factors contribute to final measurements in Nephelometric Turbidity Units (NTU) such as water depth, Chlorophyll Concentration (CC) and Dissolved Organic Matter (DOM) (Bustamante et al., 2009).

Several authors have addressed the issue of quantifying either water turbidity or SSC with Landsat TM and ETM+ images (REFs). Bustamante et al. (2009) developed an empirical model between Landsat bands reflectance and Doñana marshlands and River NTU values. This first model performed better for River than for marshland (78% vs. 40% of explained deviance). During the project different field campaigns increased ground-truth data and more Landsat scenes were available, what enabled to improve the model across a larger turbidity gradient (7-9000 NTU).

Although eventual River turbidity maps may help to reveal exceptional events, only historical analysis can contribute to determine the relevance of every factor (i.e. tidal influence, reservoir management, heavy rainfall, dredging, shipping intensity, etc.) on the observed dynamics. Time series analysis provided trends, averages and anomalies pointing out regular oscillations, trend shifts and dramatic cycles (Díaz-Delgado et al., 2010). The spatio-temporal reconstruction of river turbidity regime enabled to highlight local trends and the increase in the frequency of extreme turbid events. These events differed in magnitude and duration indicating the circumstances

and conditions at the origin (i.e. tidal influence, reservoir management, heavy rainfall, etc.). However, the scarce occurrence of very turbid events was masked when they happened within an average turbid year (low frequency turbid events). As the physical forcings keep contributing to current Estuary condition there is a strong need to use turbidity mapping as an essential indicator of the optical environment for water quality monitoring purposes (Dogliotti et al. 2015). The decision on increasing channel depth with new dredges may be enlightened by the understanding of historical turbidity regimes.

In this paper we present the results of applying an empirical model for River turbidity mapping to a long time series of Landsat TM and ETM+ images (1984-2013). We proposed a synoptic index able to represent the interannual variability due to differences in duration and magnitude of the turbid events. Such new annual index, named turbiperiod, provides similar information as the sum of annual turbidity, but distinguishing years with peak events from continuous high turbidity. Turbiperiod was calculated for the different hydrological years in the covered study period.

2 METHODS

2.1 Ground-truth

A network of probes and gauges were installed in 2008 by the scientific consortium along the Guadalquivir Estuary (Fig. 1) to systematically record river flow, temperature, salinity, and turbidity. In addition, the Andalusian Environment Agency carries out since 2006 periodical water sampling along the River measuring several physico-chemical parameters, including nephelometric water turbidity and Suspended Sediments Concentration (SSC). Since 2003 we measured periodically both *in situ* point turbidity and along transects aboard of a ship (the latter since 2008). This valuable and substantial ground-truth information was used to validate the turbidity model for every single scene coincident with sampling days.

2.3 Landsat Time Series

The image dataset used is a long time series (1984-2013) of more than 300 Landsat scenes (path 202, row 34) geometric and radiometrically corrected. Time series processing consists of metadata retrieval, automatic co-registration of every scene to a single geometrically corrected ETM+ panchromatic scene (independent RMS test value < 15m) and radiometric correction with the use of a Lambertian simple dark object model [Pons & Solé-Sugrañes 1994]. Finally, radiometric normalization is carried out in order to allow consistency of time series

analysis by using pseudo-invariant areas and cloud cover masking (Díaz-Delgado et al. 2010).

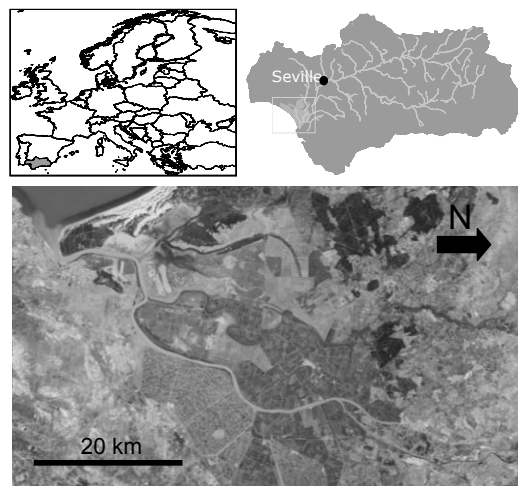


Figure 1. Location of Guadalquivir Estuary and watershed in the European context.

2.2 Empirical turbidity model

For water turbidity mapping we applied Generalized Additive Models (GAM) to extract the best predictor of measured Nephelometric Turbidity Units (NTU) and Suspended Sediments Concentration in mg/l (SSC). TM and ETM+ bands were entered as predictors for water turbidity. Ground-truth positions were crossed by buffering locations 50 m around.

The final (Eq. 1) model explained up to 78% of ground-truth NTU variability (both temporal and spatial). Reflectance (ρ) of bands 2 (0.52-0.60 μm), 3 (0.63-0.69 μm) and 4 (0.76-0.90 μm) from TM and ETM+ sensors are the most sensitive to water turbidity.

$$\log(NTU) = -4.3 + 85.22 * \rho TM_2 - 455.9 * (\rho TM_2)^2 + 594.58 * (\rho TM_2)^3 + 32.3 * \rho TM_3 - 15.36 * \rho TM_4 + 21 * (\rho TM_4)^2 \quad (1)$$

2.3 Model application

Although 60% of cloud-free scenes corresponded to summer acquisitions, there were still valid images from the rest of the year. A river and marshland water mask was used to discard model application on land. The model was systematically applied over every cloud-free scene and turbidity in $\ln(NTU)$ calculated for every single pixel. Scenes were grouped by hydrological cycle (Fig. 2) i.e. from September to August the following year.

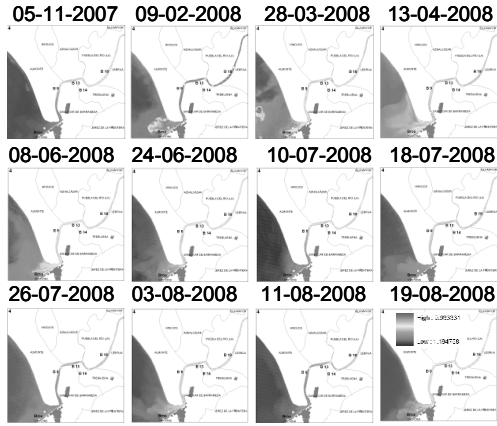


Figure 2. Turbidity maps for every cloud-free Landsat available scene during the 2007-2008 hidrological cycle in the Guadalquivir Estuary.

2.4 Looking for synopticity

It is widely known that tidal influence or freshwater release from upstream regulation reservoirs can determine NTU peaks in the Estuary (Allen et al. 1980; Díez-Minguito et al. 2014). This is clearly evidenced in single date mapping.

In order to assess progressive changes and shifts along the last 30 years, different synoptic metrics were calculated. Average NTU values per hydrological cycle should inform about systematic changes at every single pixel, both increase or decrease. On the other hand, summation of NTU values per hydrological cycle should depict the constancy of changes per year, making possible direct comparison between years. Finally, maxima NTU values per hydrological cycle would allow identifying turbidity peaks in the time series but not necessarily linked to above average or large summation values.

Concerning this limitation in conventional metrics, we propose a simple *turbiperiod* synoptic index accounting for the time lap between consecutive images and therefore for the duration of turbidity events within a hydrological cycle. The general calculation follows equation 2 where: T_1 -Today stands for the number of days between first available image at T_0 and the following at T_1 ; ΣNTU_{cycle} accounts for total summation of NTU values per pixel along the hydrological cycle; and NTU_{T_0} accounts for NTU pixel values at T_0 (first available image).

$$Turbiperiod = \frac{\Sigma NTU_{cycle}}{(T_1 - T_0 \text{ days} / NTU_{T_0}) + (T_2 - T_1 \text{ days} / NTU_{T_1}) + \dots} \quad (2)$$

Turbiperiod index is a ratio between total summation and total summation weighted by time

spans so that varies between 0 and 1. It is analogous to Gini coefficient of variable inequality (Díaz-Delgado et al, 2004), reaching high values for very unequal cycles along time in terms of NTU values.

3 RESULTS

3.1 Single date turbidity maps

Single date maps clearly matched the occurrence of dramatic events (Fig. 2), such as the ones observed during late November 2007 and early 2008 with maxima values of 3600 NTU. Figure 3 shows average single date NTU values for the last 30 years.

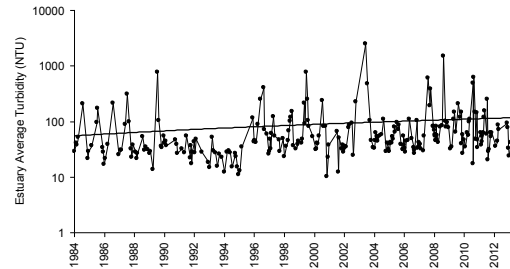


Figure 3. Average Estuary turbidity for every single available date for the last 90 km of the River. The non significant positive trend is also shown.

3.2 Trend analysis

While comparing average, maxima and summation NTU values per hydrological cycles, significant trends were found for everyone ($r^2=0.24$, $p<0.05$; $r^2=0.21$, $p<0.05$; $r^2=0.57$, $p<0.01$; Fig. 4).

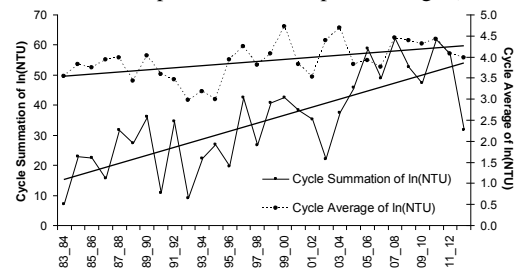


Figure 4. Average Estuary turbidity and total turbidity summation (in ln NTU) per hydrological cycle. Notice the low values during the drought period (1992-1995) and the important shift since 2004.

Both the average and summation clearly reveal an overall increase of turbid events and NTU values for the Estuary in the last 15 years. It is also evident the effect of the intense drought conditions from 1992 to 1995 in Southern Andalusia (Gonzalez-Hidalgo et al., 2010) when turbidity values and event frequency decreased due to dramatic River flow reduction.

3.3 The contribution of turbiperiod

While assessing about the duration and intensity of the turbidity events, the turbiperiod index was very useful to identify two extreme patterns: hydrological cycles with constant high turbidity *versus* hydrological cycles with high turbidity due to peak events (low frequency turbid events). Both cases show high summation NTU values. This is the case of cycles 1989-1990 and 2007-2008 (Figure 5).

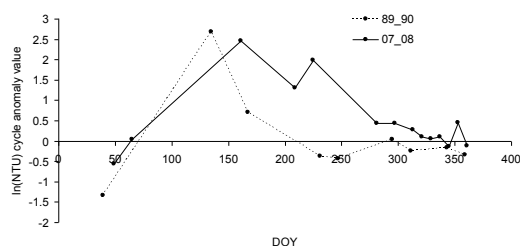


Figure 5. Anomalies of $\ln(\text{NTU})$ values for the Estuary per cycle showing a peak turbidity regime (1989-1990) and a constantly high turbidity regime (2007-2008).

Estuary turbiperiod values for every cycle also showed a strong significant trend (Table 1; $r^2=0.55$, $p<0.05$). Results show that although high turbidity values were reached at the beginning of the study period, most of them were due to peak events, while for the last decade the regime has become highly turbid during the longer time spans.

Table 1. Average value of turbiperiod index for the Estuary in the last 30 years. Certain cycles were excluded due to low number of scenes available.

Cycle	Turbiperiod	Cycle	Turbiperiod
84_85	0.27	00_01	0.48
85_86	0.46	01_02	0.57
86_87	0.21	02_03	0.49
87_88	0.37	03_04	0.71
88_89	0.28	04_05	0.56
89_90	0.40	05_06	0.66
91_92	0.36	06_07	0.63
93_94	0.25	07_08	0.85
94_95	0.25	08_09	0.65
95_96	0.21	09_10	0.71
96_97	0.55	10_11	0.75
97_98	0.33	11_12	0.67
98_99	0.49	12_13	0.38
99_00	0.56		

4 DISCUSSION

Many questions related to the Estuary functioning are tightly related to turbidity regime characterization. While data measurements from automatic probes and gauges have led to better understand current conditions, a mid-term historical perspective is needed to assess tendencies and time shifts on turbidity

regimes. Single date mapping allow to detect turbidity peaks but only synoptic metrics helped to identify trends and shifts like the observed in the Guadalquivir Estuary starting from 2006 up to 2012. The turbiperiod maps enabled to identify a consistent increase in the frequency of high turbid events in the last decade.

5 REFERENCES

- Allen, G. P., Salomon, J. C., Bassoullet, P., Du Penhoat, Y., and De Grandpre, C., 1980, Effects of tides on mixing and suspended sediment transport in macrotidal estuaries. *Sedimentary Geology*, 26(1), 69-90.
- Bustamante, J., Pacios, F., Díaz-Delgado R. and Aragonés, D., 2009, Predictive models of turbidity and water depth in the Doñana marshes using Landsat TM and ETM+ images, *Journal of Environmental Management*, 90, 2219-2225.
- Díaz-Delgado, R., Amezttoy, I., Cristobal, J. and Bustamante, J., 2010, Long time series of Landsat images to reconstruct river surface temperature and turbidity regimes of Guadalquivir Estuary. Proceedings of the 2010 IEEE International Geoscience & Remote Sensing Symposium (IGARSS2010) held in Honolulu, USA on 25th to 30th July 2010 (Honolulu: IEEE GRSS), pp. 233-236.
- Díaz-Delgado, R., Lloret, F. and Pons, X., 2004, Statistical analysis of fire frequency models for Catalonia (NE Spain, 1975-98) based on fire scar maps from Landsat MSS data. *International Journal of Wildland Fire*, 13, 89-99.
- Díez-Minguito, M., Baquerizo, A., de Swart, H. E., and Losada, M. A., 2014, Structure of the turbidity field in the Guadalquivir estuary: Analysis of observations and a box model approach. *Journal of Geophysical Research: Oceans*.
- Gonzalez-Hidalgo, J. C., Brunetti, M., and de Luis, M., 2010, Precipitation trends in Spanish hydrological divisions, 1946-2005. *Climate research*, 43(3), 215.
- Matthews, M. W., 2011, A current review of empirical procedures of remote sensing in inland and near-coastal transitional waters. *International Journal of Remote Sensing*, 32(21), 6855-6899.
- Volpe, V., Silvestri, S., & Marani, M. 2011. Remote sensing retrieval of suspended sediment concentration in shallow waters. *Remote Sensing of Environment*, 115(1), 44-54.

Biomass and Soil Moisture Simulation and Assimilation over Hungary with the use of Surfex model

Helga Tóth, Balázs Szintai and László Kullmann
Hungarian Meteorological Service, Hungary, Budapest
toth.h@met.hu; szintai.b@met.hu; kullmann.l@met.hu

ABSTRACT *In the framework of the ImagineS project a Land Data Assimilation System (LDAS) is applied at the Hungarian Meteorological Service (HMS - OMSZ) to monitor the above ground biomass, surface fluxes (carbon and water) and the associated root-zone soil moisture at the regional scale (spatial resolution of 8km x 8km) in quasi real time. In this system the SURFEX (SURFace EXternalisée) 7.3 model is used, which applies the ISBA-A-gs photosynthesis scheme to describe the evolution of vegetation. SURFEX is forced using the outputs of the ALADIN numerical weather prediction model run operationally at HMS. First, SURFEX was run in open-loop (i.e. no assimilation) mode. Secondly the Extend Kalman Filter (EKF) method was used to assimilate LAI Spot/Vegetation and SWI ASCAT/Metop satellite measurements. The EKF run was compared to the open-loop simulation and to observations (LAI and Soil Moisture satellite measurements) over the whole country and also to in-situ measurements of a selected site in West-Hungary (Hegyhátsál). A new diffusion soil scheme (ISBA-DIF) was tested and compared to the operational force-restore scheme.*

1 INTRODUCTION

One of the aim of ImagineS project (FP7 2012-2016) to develop and run the land data assimilation system (LDAS) which is capable of simulating the main processes above the ground biomass and to describe the carbon and water fluxes in the soil and on the surface. This LDAS is based on the SURFEX (SURFace EXternalisée) model which is a suitable tool to simulate these processes (Le Moigne, 2009). In our experiments the model was run on regular lat-lon grid with 8x8 km resolution over a domain covering Hungary. The model was running in cycling mode and the 24-hour forecast was produced with 6h outputs frequency. Evaluated model outputs are the LAI (Leaf Area Index), the WG2 (Volumetric soil moisture content), the GPP (Gross Primary Product) and the NEE (Net Ecosystem Exchange).

SURFEX was run in offline mode, this means that the surface fluxes have no influence on the atmospheric fields, but the model needs meteorological data (air temperature, humidity, wind speed, precipitation, long and short wave radiation). These information come from the ALADIN (Aire Limitée Adaptation dynamique Développement InterNational) numerical weather prediction model (Horányi et al., 2006) except for the radiation, which is derived from LandSAF (Land Surface Analysis Satellite Applications Facility) observation. The reason for this choice is that radiation influences to a great extent the photosynthesis and the NWP model's fields are not as accurate.

In this article the SURFEX model is presented with detailed description of the applied soil models and the

data assimilation system. In the second part of the report some results are showed, one- and two-dimensional evaluations of the model runs, which are compared to satellite and in-situ measurements.

2 MODELS AND METHODS

2.1 The SURFEX model

In SURFEX each surface grid point is separated into 4 different tiles: nature, sea, lake and town. The model handles each tile independently. In our work only the nature tile was treated. The nature tile is further divided into 12 patches according to the vegetation or surface types: bare soil, rock, permanent snow, deciduous tree, coniferous tree, broadleaf evergreen tree, C3 crops, C4 crops, irrigated crops, grassland, tropical grassland, parks and gardens. The model solves the prognostic equations and calculates the surface fluxes separately for the different patches.

The nature tile is simulated with the ISBA (Interaction between Soil, Biosphere and Atmosphere) scheme (Noilhan and Planton 1989), which contains a photosynthesis model, ISBA-A-gs (Calvet et al. 1998, Gibelin et al 2006). This model is suitable to describe the evolution of the vegetation. Biomass is a prognostic variable. Growing of biomass is due to photosynthesis (CO₂ assimilation) while the decline can be due to soil moisture stress or senescence. The model takes into account the soil moisture stress in the photosynthesis (Calvet, 2000). Plants can have two strategies to the stress: draught avoiding and draught tolerant strategy.

The GPP is calculated as the sum of net assimilation and the dark respiration of leaves. NEE is determined as a difference of Re (ecosystem respiration) and GPP. In ISBA-A-gs this is parametrized by a simple method depending on surface water content and the surface temperature.

2.2 ISBA-3L soil scheme

In ISBA a 3-layer soil scheme is used (surface 0-1 cm, root zone 0-2 m and deep soil 2-3 m). The soil prognostic variables (temperature, water content and intercepted water content) are calculated with force-restore method (Noilhan and Mahfouf 1996). The force terms for temperature are the radiation, latent and sensible heat-flux. The restore term relaxes the temperature to the mean soil temperature. The force terms for soil water content are the precipitation and evaporation. The restoring term describes how the system reaches the equilibrium.

2.3 ISBA-DIF (diffusion) soil scheme

ISBA-DIF is a new ISBA version including a soil multilayer diffusion scheme (Decharme et al., 2011, Parrens et al., 2014). With this technique the mass and heat-diffusive equations are solved explicitly. The total soil depth is discretized with several layers, and both moisture and temperature profiles can be explicitly computed according to soil texture properties. This multilayer diffusion scheme is theoretically superior to the simple force-restore scheme. It allows explicit representation of many processes those are more difficult to parameterize in bucket models: e.g. vertical distribution of root profile in the soil, surface capillarity exchanges, soil processes (heat exchange, infiltration, runoff). ISBA-DIF soil hydrology uses the mixed form of the Richard equation to describe the water mass transfer within the soil via Darcy's law.

2.4 Data Assimilation

To improve the accuracy of the initial fields Land Data Assimilation System (LDAS) is used. The analyzed variables are the Leaf Area Index (LAI) and the root-zone soil moisture (WG2). These variables have long memory (slow variability in time) and furthermore LAI and soil moisture influence to a high extent the evaluation of photosynthesis and through this the value of carbon fluxes. Observations for LAI are derived from SPOT-VGT satellite data. LAI values are produced by a statistical algorithm using two products: SPOT VGT CYCLOPES V3.1 and TERRA/AQUA MODIS collection 5 (Baret et al., 2013). The product is provided at a spatial resolution of 1 km and 10 days sampling time in regular latitude/longitude grid. To analyze the root-zone soil moisture, surface soil moisture (SSM) needs to be assimilated which is

derived from SWI (Soil Wetness Index) product. SWI is calculated from MetOp. ASCAT observations using a recursive exponential filter. SWI is provided at 10 km spatial resolution with daily sampling (Albergel et al., 2008). From SWI information to get SSM value we have to use the following relationship: $SSM = SWI \cdot (w_{max} - w_{min}) + w_{min}$, where w_{min} and w_{max} are the minimal and maximal SSM values that the model can take at a given grid point.

Extended Kalman Filter (EKF) assimilation method was performed to analyze LAI and SSM (Bouttier and Courtier 1999, Mahfouf 2010). To determine these values, observations and background (model forecast starting from a previous cycle) information need to be taken into account. The theory of Kalman Filter assumes that the analysis can be obtained by the following equation (1):

$$x_a = x_f + K(y_o - H(y_f)) \quad (1)$$

Where x is the model state vector (a means analysis, f means forecast), y is the observation vector, H is the non-linear observation operator, K is the Kalman gain.

The analysis equation is solved at each grid point independently, as we assume, there is no correlation between the neighbouring grid points

3 RESULTS

3.1 2-D Validation

Open-loop and Assimilation with using of ISBA-3L and Open-loop with using of ISBA-DIF scheme were performed and compared with satellite observations for year 2013. The observation error was set to 0.2 m²/m² for LAI and 0.04 m³/m³ for SSM. The model error was set to 0.2 m²/m² for LAI, 0.5 m³/m³ for SSM and 0.2 m³/m³ for WG2.

Fig. 1. shows the monthly averaged area-mean RMSE of LAI for the mentioned experiments. Patch averaged LAI values were taken into account in the calculations. From May-July the assimilated LAI fields were the closest to the observations but from the end of the summer all simulations produced similar and relatively good products. Similar results can be seen for SWI in Fig. 2. The assimilation is able to reduce the bias caused by the delay at the start of the growing season.

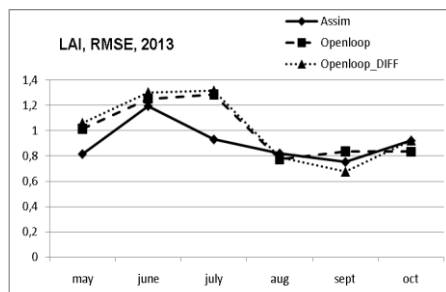


Fig 1. LAI area-mean RMSE for 2013. (solid: assimilation, dashed: openloop, dotted: openloop-diff)

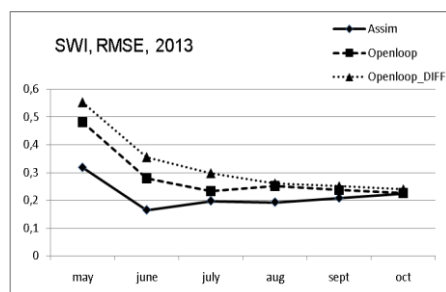


Fig 2. SWI area-mean RMSE for 2013. (solid: assimilation, dashed: openloop, dotted: openloop-diff)

3.2 1-D Validation

Experiment outputs were validated against in-situ measurements of Hegyhátsál (located in the Western part of Hungary lat.: 46° 57' 34", lon.: 16° 38' 30"). Data are available from two levels:

- 3 m height from a grassland area (valid for only the grassland patch):
 - LAI (weekly)
 - Soil Moisture (daily) (derived from 10-30 cm depth)
 - Carbon fluxes: GPP, Reco and NEE (daily)
 - Water flux: Latent Heat (LE) (daily)
- 82 m height (valid for the whole grid-point, consisting mainly of agricultural area):
 - Carbon fluxes: GPP and NEE (daily)
 - Water flux: LE (daily)

LAI is underestimated by the models (Fig. 3.). Unfortunately the assimilation of LAI and SWI could not improve the results. The carbon- and water flux forecasts were well represented by the open-loop simulations, but the assimilation run could not reproduce the events at is was in the reality (Fig.4. and Fig. 5.).

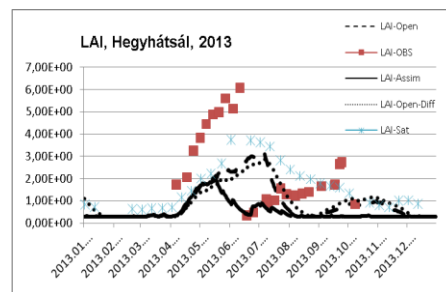


Fig. 3. LAI in Hegyhátsál over grassland area for 2013

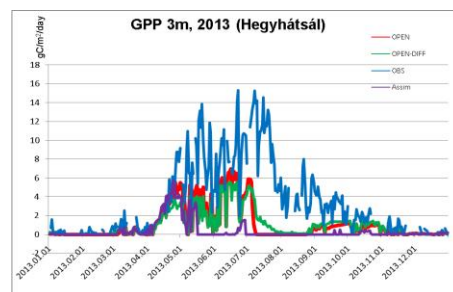


Fig.4. GPP in Hegyhátsál over grassland area for 2013

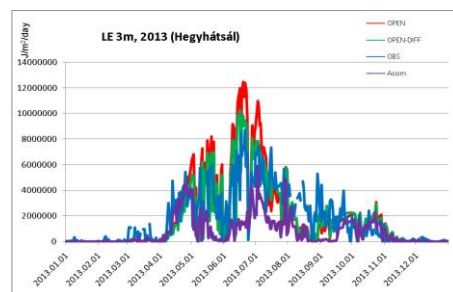


Fig. 5. LE in Hegyhátsál over grassland for 2013

4 CONCLUSIONS, PLANS

SURFEX model runs were performed for year 2013 over Hungarian domain. Three kind of experiments (open-loop and assimilation runs with using of ISBA-3L scheme and open-loop experiment with ISBA-DIF scheme) were done and evaluated against satellite and in-situ observations.

The models were able to simulate the annual cycle of the biomass and the arid period at the end of summer. But some deficiencies can be found in the carbon- and water flux analysis which requires further research.

In the near future we would like to focus on the correction of our LDAS, to eliminate the above mentioned deficiencies connected to carbon- and water flux analysis.

An other important challenge in the framework of ImagineS project to develop some drought indicators which are able to indicate the water shortage

periods. This kind of indicators can be very useful for farmers and agricultural experts as well.

5 REFERENCES

- Albergel, C., Rüdiger, C., Carrer, D., Calvet, J.-C., Fritz, N., Naeimi, V., Bartalis, Z., and Hasenauer, S., 2009: An evaluation of ASCAT surface soil moisture products with in-situ observations in South western France, *Hydrol. Earth Syst. Sci.*, **13**, pp. 115–124.
- Baret, F.; Weiss, M.; Lacaze, R.; Camacho, F.; Makhmara, H.; Pacholczyk, P.; Smets, B., 2013: GEOV1: LAI and FAPAR Essential Climate Variables and FCover global times series capitalizing over existing products. Part1: Principles of development and production. *Remote Sensing of Environment* **137**, pp. 299–309.
- Bouttier, F., and Courtier, P., 1999: Data assimilation concepts and methods. ECMWF, Meteorological Training Course Lecture Series
- Calvet, J.-C., Noilhan, J., Roujean, J.-L., Bessemoulin, P., Cabelguenne, M., Olioso, A., and Wigneron, J.-P., 1998: An interactive vegetation SVAT model tested against data from six contrasting sites, *Agric. For. Meteorol.*, **92**, pp. 73–95.
- Calvet, J.-C., 2000: Investigating soil and atmospheric plant water stress using physiological and micrometeorological data, *Agric. For. Meteorol.*, **103**, pp. 229–247.
- Decharme, B., Boone, A., Delire, C. and Noilhan, J., 2011: Local evaluation of the Interaction between Soil Biosphere Atmosphere soil multilayer diffusion scheme using four pedotransfer functions, *J. Geophys. Res.*, **116**
- Gibelin, A.-L., Calvet, J.-C., Roujean, J.-L., Jarlan, L., Los S. O., 2006: Ability of the land surface model ISBA-A-gs to simulate leaf area index at the global scale: comparison with satellites products. *J. Geophys. Res.*, **111**, D18102.
- Horányi A., Kertész S., Kullmann L. and Radnóti G., 2006: The ARPEGE/ALADIN mesoscale numerical modelling system and its application at the Hungarian Meteorological Service. *Időjárás*, **110**, pp. 203–227.
- Le Moigne, P., (2009), 'SURFEX scientific documentation'. *Note de Centre du Groupe de Météorologie a Moyenne Echelle*, No. **87**., CNRM, Météo-France: Toulouse, France.
- Mahfouf J.-F., 2010: Assimilation of satellite-derived soil moisture from ASCAT in a limited-area NWP model, *Q. J. R. Meteorol. Soc.*, **136**, pp. 784–798
- Noilhan, J. and Planton, S., 1989: A simple parameterization of land surface processes for meteorological models. *Mon. Weather Review*, **117**, pp. 536–549.
- Noilhan, J., and Mahfouf, J.-F., 1996: The ISBA land surface parameterization scheme. *Global Planetary Change*, **13**, pp. 145–159.
- Parrens, M., Mahfouf, J.-F. Barbu, A. L. and. Calvet, J.-C., 2014: Assimilation of surface soil moisture into a multilayer soil model: design and evaluation at local scale. *Hydrol. Earth Syst. Sci.*, **18**, pp. 673–689

Improved field method for determining land surface emissivity

Frank-M. Göttsche¹, Folke S. Olesen¹, Glynn C. Hulley²,

¹Karlsruhe Institute of Technology (KIT), Postfach 3640, 76021 Karlsruhe, Germany

²Jet Propulsion Laboratory, California Institute of Technology, Pasadena, USA

frank.goettsche@kit.edu, folke.olesen@kit.edu, glynn.hulley@jpl.nasa.gov

ABSTRACT Especially over arid regions the relatively high uncertainty in land surface emissivity (LSE) limits the accuracy with which land surface temperature (LST) can be retrieved from thermal infrared (TIR) radiance measurements. LSE uncertainty affects LST obtained from satellite measurements and in-situ radiance measurements alike and an accurate validation of LST products requires accurate knowledge of emissivity for the areas observed by the ground radiometers and the satellite sensor. Additionally, direct comparisons between satellite sensors and ground based sensors are complicated by spatial scale mismatch: ground radiometers usually observe some 10 m², whereas satellite sensors typically observe between 1 km² and 100 km². Therefore, LST validation sites have to be carefully selected and characterized on the scale of the ground radiometer as well as on the scale of the satellite pixel. Gobabeb (Namibia; hyper-arid desert climate) and Dahra (Senegal; hot-arid steppe-prairie climate) are two of KIT's four dedicated, permanent LST validation stations. At both stations in-situ emissivities of the dominant surface cover types were determined with an improved 'emissivity box method' and from emissivity spectra obtained for soil samples. The measurements performed with the box method were recorded at a sampling rate of 1 Hz, which significantly eases the identification of invalid data and allows the picking of undisturbed temperatures just before and after each change in box configuration. The results obtained with the box method are in good agreement with those from the emissivity spectra and give further confidence in the in-situ LST determined at KIT's validation sites.

1 INTRODUCTION

Accurate validation of LST satellite products, e.g. LST retrieved from MSG/SEVIRI by the Land Surface Analysis – Satellite Application Facility (LSA-SAF), requires knowledge of emissivity at the spatial scale of the in-situ measurements as well as at the – usually considerably larger – satellite spatial scale. At two of KIT's four dedicated LST validation stations, namely Gobabeb (Namibia; hyper-arid desert climate) and Dahra (Senegal; hot-arid steppe-prairie climate), LSE was determined from in-situ measurements performed with the so-called 'emissivity box method' (Combs et al., 1965)(Rubio et al., 1997). Outside their respective rainy seasons, KIT's validation sites Gobabeb and Dahra have relatively large fractions of bare ground. Therefore, the two sites are particularly prone to be misrepresented in satellite-retrieved LSEs (Göttsche and Hulley, 2012) (Jimenez-Munoz et al., 2014) and in-situ validation of LST strongly depends on accurate in-situ LSE.

The emissivity box method consists of a sequence of thermal infrared radiance measurements and employs a box with highly reflective inner walls (in the TIR) to control the radiation from the environment (Combs et al., 1965) (Rubio et al., 1997) (Rubio et al., 2003). In the field method employed by KIT all measured radiances are recorded at a sampling rate of one second, which allows the picking of undisturbed

temperatures directly before and after each change in box configuration (Göttsche and Hulley, 2012). The fast sampling also allows the later identification of erroneous measurements, e.g. caused by incorrect handling of the box during the experiment. Here, we describe the determination of in-situ LSEs with the one-lid emissivity box method and compare results obtained at Gobabeb and Dahra with emissivity spectra of soil and grass samples obtained in the laboratory using a Fourier Transform Infra-Red (FTIR) spectrometer.

2 ONE-LID EMISSIVITY BOX METHOD

(Rubio et al., 1997) studied the 'one-lid' and the 'two-lid emissivity box' methods in detail and derived correction terms for both. Gobabeb LST validation site has a very high frequency of clear sky conditions and the gravel plains form an open and unobstructed area. Furthermore, clear sky brightness temperature is regularly below -50°C while surface temperature can exceed 40°C: such high temperature differences improve the signal to noise ratio of the 'one-lid emissivity box' method considerably. KIT's emissivity box has inner walls of polished aluminium and the same dimensions as in (Rubio et al., 1997) (Rubio et al., 2003) and has been used to validate several satellite-retrieved emissivity products (Göttsche and Hulley, 2012) (Jimenez-Munoz et al., 2014).

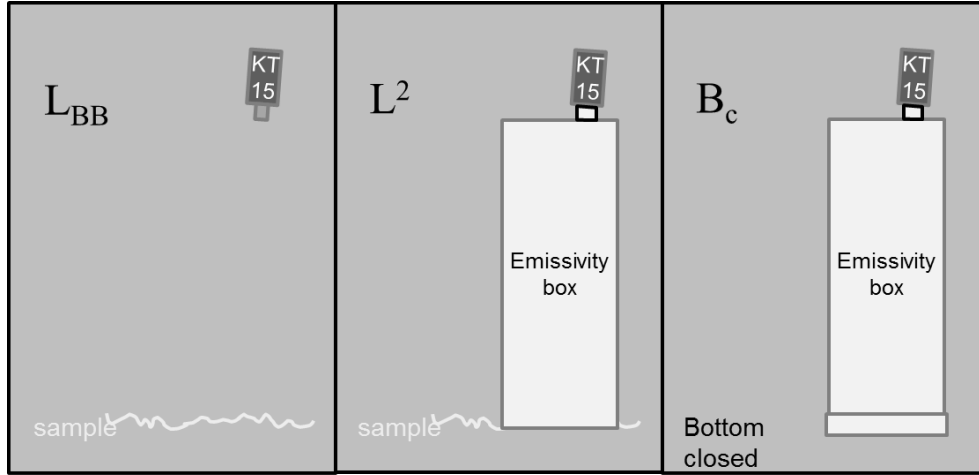


Figure 1 Radiometric measurements performed for the ‘one-lid emissivity box method’. Left: radiance emitted by the sample plus reflected down-welling radiance. Centre: radiance over the sample with box on top (temperature of the sample). Right: radiance inside the box when its bottom is also covered by highly reflective aluminium (temperature of inner box walls for correction).

Using the nomenclature of (Rubio et al., 2003), first the LSE uncorrected for the effect of the box is obtained from the measurements in Figure 1 and simultaneously measured down-welling sky-radiance L_a^\downarrow :

$$\varepsilon_0 = \frac{L_{BB} - L_a^\downarrow}{L^2 - L_a^\downarrow} \quad (1)$$

Where L_{BB} is the sample radiance measured under clear sky conditions (Figure 1, left) and L^2 is the radiance measured through the bottomless box when it is placed on the sample (Figure 1, centre). LSE corrected for the influence of the box given by

$$\varepsilon = \varepsilon_0 + \delta\varepsilon \quad (2)$$

with correction

$$\delta\varepsilon = (1 - \varepsilon_0) \left\{ 1 - \frac{L^2 - L_a^\downarrow}{L^2 - L_a^\downarrow - R(L^2 - B_c)} \right\} \quad (3)$$

$R = 0.265$ is a box-specific correction factor, which depends on box geometry and the spectral response of the inner walls (Rubio et al., 1997). The term B_c is the radiance measured through the box when its bottom is also covered by polished aluminium, i.e. the box is closed.

3 IMPROVEMENTS OF FIELD METHOD

Two improvements of the ‘one-lid box’ field technique were made: the first concerns the ‘Narcissus effect’ while the second improves the acquisition of the radiance measurements. Reliable data acquisition is especially important just before and after the

configuration of the emissivity box is changed, e.g. when it is put on or taken off the sample under investigation, since it is from these measurements that emissivity is obtained.

3.1 Avoiding the ‘Narcissus effect’

The Heitronics KT15.85 IIP radiometer used for the emissivity box measurements has an absolute accuracy of better than $\pm 0.3K$ (Theocharous et al., 2010) and a full field of view of 8.5° , which - together with a box height of 80 cm - results in an observed surface area of about 110 cm^2 . In order to avoid the ‘Narcissus effect’, i.e. the radiometer observing its own reflection on the sample or on the aluminium bottom, the opening for the radiometer in the top of the box is located 6 cm off-centre and the inserted radiometer is inclined by 5 degrees w.r.t. nadir. This ensures that the KT15.85 IIP is directed towards the centre of the sample but at the same time does not observe direct (specular) reflections of itself. Radiance emitted by the radiometer takes at least two reflections over the sample before being reflected back onto itself: over the spectral range of the KT15.85 IIP and over natural surfaces (Lambertian reflectors; reflectance $< 10\%$) the Narcissus effect can, therefore, be neglected.

3.2 Fast and continuous measurements

It is essential for the success of the emissivity box method that the sample temperature remains (at least approximately) constant between consecutive measurements (left & centre drawings of Figure 1): this requires experimenters to take fast readings while quickly (< 5 seconds) changing the box configuration.

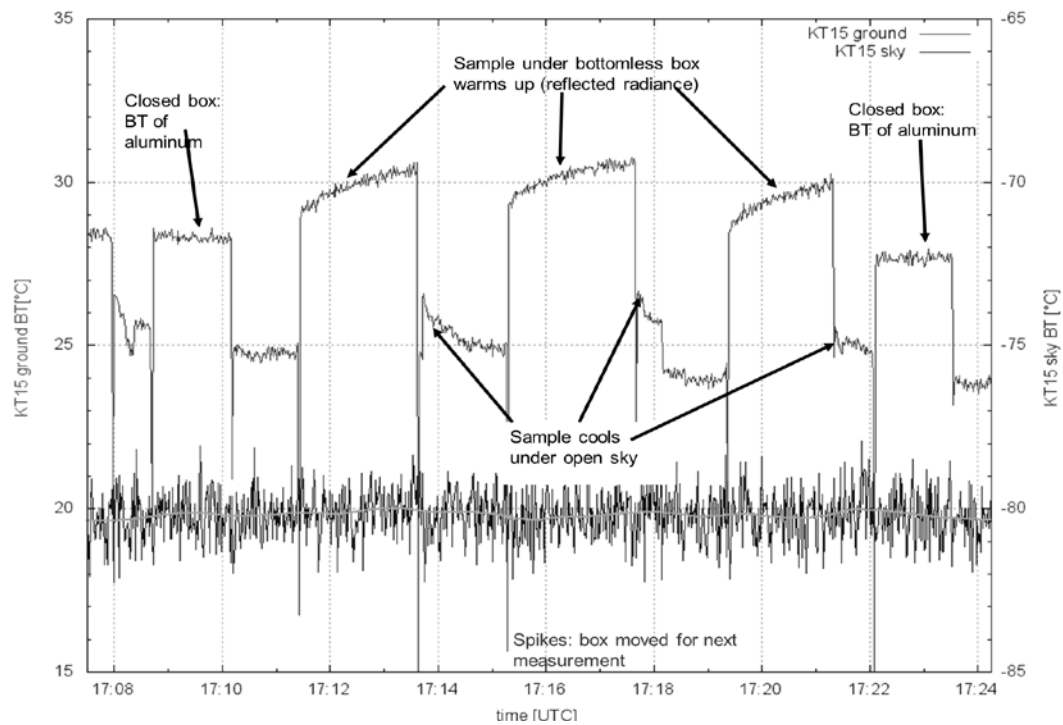


Figure 2 Brightness temperatures (BT) measured with the box method. Left axis: BT of sample and closed aluminium box. Right axis: measured ‘KT15 sky BT’ representative of the down-welling hemispherical radiance in the spectral range of the KT15.85 IIP radiometer (9.6–11.5 μm).

Here all brightness temperatures are continuously recorded once per second (Figure 2) and the optimum measurements for obtaining emissivity are selected later on ‘off-line’. Besides reducing errors, the fast sampling allows obtaining emissivity when the box is placed on the sample as well as when it is removed from the sample, i.e. it doubles the measurements that can be used to obtain emissivity. Furthermore, erroneous measurements, e.g. due to an incorrect position of the box on the sample, can be identified later on and excluded from the analysis.

Figure 2 shows examples of measurements performed with the different box configurations over sand dunes of the Namib Desert near Gobabeb. Emissivity is obtained from the BTs just before & after the box is put on the sample (at 17:11:25, 17:15:15, and 17:19:20 [hh:mm:ss]) as well as from the BT just before & after the box is taken off the sample (at 17:13:35, 17:17:40, and 17:21:25 [hh:mm:ss]). The key assumption of the box method is that the observed changes in BT are solely due to the different radiative environments, i.e. inside and outside the box, but do not reflect actual changes in thermodynamic temperature: this is the reason why the radiance measurements have to be performed quickly. The ‘BT of aluminium’ is used for

the correction term (eq. 2) and ‘KT15 sky BT’ is the measured zenith BT (right axis, here around $-80.3\text{ }^{\circ}\text{C}$) from which down-welling hemispherical radiance can be obtained (Rubio et al., 1997) (Rubio et al., 2003).

4 RESULTS

4.1 Gobabeb, Namibia

Gobabeb station is located on vast and flat gravel plains (several 100 km^2), which are mainly covered by coarse gravel, sand, and desiccated grass (Göttsche et al., 2013). The gravel plains are highly homogeneous in space and time, which makes them ideal for validating a broad range of satellite-derived products (Göttsche and Hulley, 2012) (Göttsche et al., 2013) (Jimenez-Munoz et al., 2014).

Some emissivities obtained over different surfaces with the one-lid box method (see section 3) are presented in Table 1. Due to the high level of uniformity and the small grain size of the investigated gravel and sand, their respective emissivities have small uncertainties. The ‘disturbed gravel’ (Table 1) was produced by briefly mixing the top layer of gravel with the sand directly underneath, which caused its LSE to become similar to that of the sand.

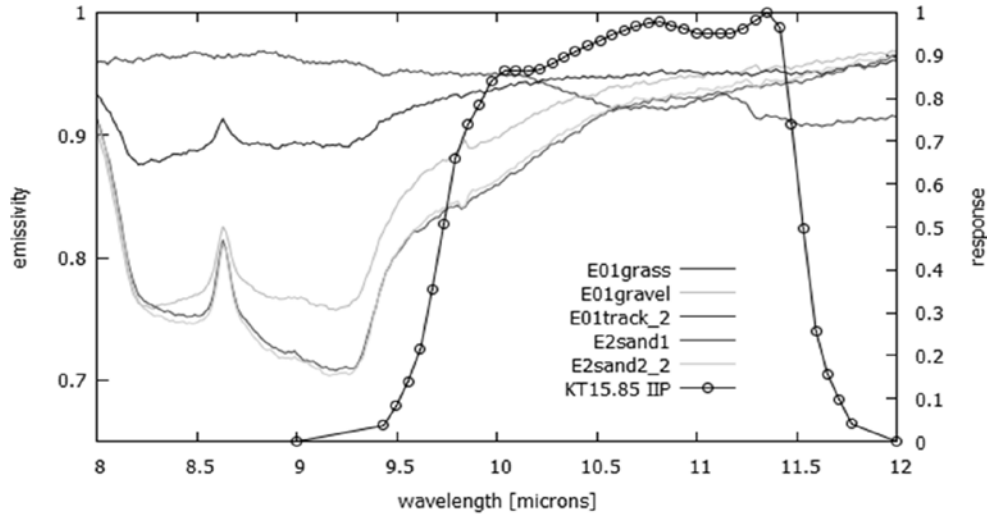


Figure 3 Emissivity spectra of some samples (Gobabeb) and KT15.85 IIP response function.

Furthermore, for meaningful comparisons between emissivities determined for different sensors, e.g. a KT15.85 IIP in-situ radiometer versus MSG/SEVIRI ch10.8, the different response functions of the two instruments have to be accounted for (Göttsche and Hulley, 2012). This is illustrated in Figure 3, which shows emissivity spectra obtained with a Nicolet 520 Fourier Transform Infra-red (FTIR) spectrometer for some samples from Gobabeb, Namibia.

Shown alongside with the emissivity spectra in Figure 3 is the KT15's response function (refers to right axis). The different response functions of the KT15.85 IIP (9.6-11.5 μm) and MSG/SEVIRI ch10.8 (9.8-11.8 μm ; see Figure 4) combined with the low emissivities of sand and gravel around the 'Reststrahlen bands' (8-9.5 μm ; SiO_2 -stretching) result in slightly different channel-effective emissivities for the two sensors; pronounced Reststrahlen bands are indicative of high quartz content.

Table 1 LSE and standard deviations determined with the one-lid box method at Gobabeb with the KT15.85 IIP radiometer. N gives number of measurements.

Surface type	$\varepsilon_0 \pm \text{stderr}$	$\varepsilon \pm \text{stderr}$	N
Gravel	0.919 ± 0.008	0.916 ± 0.007	10
Gravel (disturbed)	0.932 ± 0.003	0.931 ± 0.003	2
Grass (dry)	0.964 ± 0.012	0.962 ± 0.013	6
Sand (dunes)	0.930 ± 0.004	0.928 ± 0.004	16
Granite (inselberg)	0.914 ± 0.010	0.909 ± 0.011	5

For the mixture of 75% gravel and 25% dry grass determined for Gobabeb the emissivity for the KT15.85 IIP is slightly lower (0.940 ± 0.015) than the respective emissivity for SEVIRI ch10.8 (0.944 ± 0.015) (Göttsche and Hulley, 2012). Furthermore, Figure 3 shows that – in contrast to the sand and gravel – the emissivity of dry grass ('E01grass') decreases for wavelengths larger than about 9 μm .

4.2 Dahra, Senegal

Dahra station is located in so called 'tiger bush' and is covered by strongly seasonal grass (95%) and sparse, evergreen trees (dominantly acacia trees) with a background of reddish sand (Rasmussen et al., 2011). The strong seasonality is caused by a pronounced rainy season (about Jul/Aug to Sep/Oct), during which LST retrieval is highly challenging. Furthermore, the strong vegetation cycle, from nearly bare soil to full vegetation cover was shown to cause errors of up to 7% in some LSE products (Xu et al., 2014).

Using the emissivity box method as described in sections 2 and 3, on the 15th of January 2013 the following KT15.85 IIP emissivities were determined at Dahra: 0.960 ± 0.004 over a 'fire strip', i.e. an area cleared of remaining dry vegetation for fire protection, 0.953 ± 0.004 over areas of dry soil cleared just before the measurements, and 0.941 ± 0.005 for the unaltered validation site (mainly bare soil with some debris of desiccated vegetation lying on the surface). Additional measurements over dry grass yielded a KT15.85 IIP emissivity of 0.971 ± 0.011 . Since the vegetation at Dahra is highly seasonal, the value of 0.941 given above is only valid for the 15th of January 2013;

however, LSE is expected to be similar until the start of the next rainy season.

Figure 4 shows emissivity spectra of soil samples from Dahra and a dry grass spectrum from the ASTER spectral library (Baldrige et al., 2009). The spectrum labelled 'tree mast' is for a sample taken from the surface near the LST validation station, whereas the spectrum labelled '1m depth' is for a sample (mainly sand) from 1 m depth, which clearly contains a substantial amount of SiO₂.

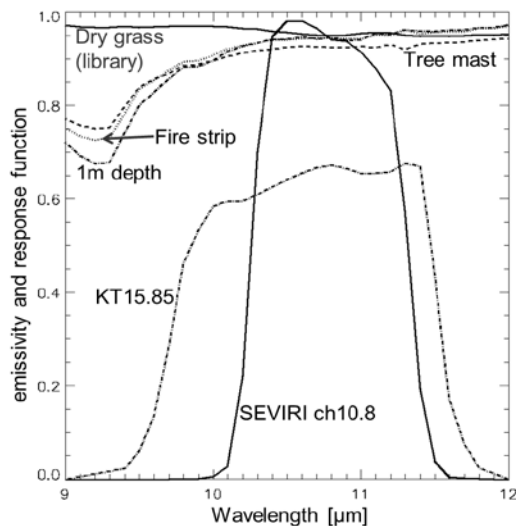


Figure 4 Emissivity spectra for samples from Dahra, a dry grass spectrum from the ASTER spectral library, and the KT15.85 IIP and SEVIRI ch10.8 response functions.

5 SUMMARY AND CONCLUSIONS

Gobabeb and Dahra (the latter during the dry season) both have generally favourable conditions for employing the one-lid emissivity box method:

- Frequently clear-sky with surface BT - sky BT > 80K give the radiance measurements a considerably higher SNR than usually achieved with the two-lid box method.
- The improved field technique gives accurate and stable results with fewer measurements and the fast sampling allows identifying and rejecting erroneous data.

Furthermore, in combination with the emissivity box the KT15.85 IIP has a sufficiently large field of view (12 cm diameter) to integrate over a larger number of small surface components, e.g. small pieces of gravel: for many surface types, gravel and grass, this yields more representative emissivities.

At Gobabeb, the determined in-situ LSE showed that several of the current LSE satellite products had errors of 3% or more (Göttsche and Hulley, 2012), whereas at Dahra the strong seasonal cycle (monsoon; from bare soil to full vegetation cover) caused errors of up to 7% in some LSE products. Therefore, the results presented here underline the importance of in-situ LSE for validating LST retrieval algorithms.

ACKNOWLEDGMENTS

The in-situ validation data for the Gobabeb and Dahra sites were obtained within the context of the Land Surface Analysis – Satellite Application Facility (LSA-SAF), a project funded by the European Organization for the Exploitation of Meteorological Satellites (EUMETSAT).

REFERENCES

- Baldrige, A., Hook, S., Grove, C., and Rivera, G., 2009. The ASTER spectral library version 2.0. *Remote Sensing of Environment*, 113(4), 711–715.
- Combs, A. C., Weickmann, H. K., Mader, C., and Tebo, A., 1965. Application of infrared radiometers to meteorology. *Journal of Applied Meteorology*, 4(2), 253–262.
- Göttsche, F.-M. and Hulley, G. C., 2012. Validation of six satellite-retrieved land surface emissivity products over two land cover types in a hyper-arid region. *Remote Sensing of Environment*, 124, 149–158.
- Göttsche, F.-M., Olesen, F.-S., and Bork-Unkelbach, A., 2013. Validation of land surface temperature derived from MSG/SEVIRI with in situ measurements at Gobabeb, Namibia. *International Journal of Remote Sensing*, 34(9–10), 3069–3083. Special Issue.
- Jimenez-Munoz, J. C., Sobrino, J. A., Mattar, C., Hulley, G., and Göttsche, F.-M., 2014. Temperature and emissivity separation from MSG/SEVIRI data. *IEEE Transactions on Geoscience and Remote Sensing*, 52(9), 5937–5951.
- Rasmussen, M. O., Göttsche, F.-M., Diop, D., Mbow, C., Olesen, F.-S., Fensholt, R., and Sandholt, I., 2011. Tree survey and allometric models for tiger bush in northern Senegal and comparison with tree parameters derived from high resolution satellite data. *International Journal of Applied Earth Observation and Geoinformation*, 13(4), 517–527.
- Rubio, E., Caselles, V., and Badenas, C., 1997. Emissivity measurements of several soils and vegetation types in the 8–14 μm wave band: analysis of two field methods. *Remote Sensing of Environment*, 59, 490–521.

- Rubio, E., Caselles, V., Coll, C., Valour, E., and Sospedra, F., 2003. Thermal-infrared emissivities of natural surfaces: Improvements on the experimental set-up and new measurements. *International Journal of Remote Sensing*, 24(24), 5379–5390.
- Theocharous, E., Usadi, E., and Fox, N. P., 2010. CEOS comparison of IR brightness temperature measurements in support of satellite validation. Part I: Laboratory and ocean surface temperature comparison of radiation thermometers. NPL REPORT OP3. Technical Report ISSN: 1754-2944, National Physical Laboratory, Teddington, UK.
- Xu, H., Yu, Y., Tarpley, D., Gottsche, F.-M., and Olesen, F.-S., 2014. Evaluation of GOES-R Land Surface Temperature Algorithm Using SEVIRI Satellite Retrievals With In Situ Measurements. *IEEE Transactions on Geoscience and Remote Sensing*, 52(7), 3812–3822.

Surface temperature anomalies monitoring over the Amazon forests

J. C. Jiménez-Muñoz¹, J. A. Sobrino¹, C. Mattar², Y. Malhi³

¹GCU/IPL, University of Valencia. SPAIN

²LAB, University of Chile. CHILE

³ECI, Oxford University. UK

jcjm@uv.es

ABSTRACT- *The occurrence of drought events is one major aspect of Amazonian climate change. In recent years several studies addressed the response of Amazonian forest to drought by analyzing anomalies in vegetation indices retrieved from satellite sensors. These studies were motivated by the occurrence of two major droughts in 2005 and 2010, which were considered amongst the most severe in a century. Variations in surface temperature are believed to be closely related to drought events, but very few studies have analyzed this variable over the Amazonian region. In this work we analyze the spatial and temporal patterns of Land Surface Temperature (LST) anomalies derived from Moderate Resolution Imaging Spectroradiometer (MODIS) in the last decade. Results show almost a sustained warming from year 2005 and a statistically significant ($p < 0.05$) warming trend in the last decade (2000 to present) when compared to previous decades (1989-2000) using climatic records. We also present a web-based tool (ipl.uv.es/thamazon) which allows the visualization of LST anomalies over the Amazon forests through a user-friendly interface.*

1 INTRODUCTION

The Amazon forests include more than 50% of the world's tropical forests and stores more than 100 billion tonnes of carbon (Malhi et al., 2006), so they are a key component of the global carbon cycle. In a global warming scenario, the monitoring of changes over the Amazon rainforest is critical to analyze the impact of these changes on the climate change. This analysis can be performed over a number of variables, but vegetation/air temperature is one of the key variables linked to the plant physiology. For example, some studies found a correlation between the decrease in tropical forest productivity and the increase in temperature, thus reducing the capability of carbon uptake and favoring the accumulation of atmospheric CO₂ (e.g. Clark et al., 2003).

Variations on temperature are also related to the occurrence of extreme events such as droughts. Precisely, the occurrence of drought events is one major aspect of Amazonian climate change (Malhi et al., 2008). Attention was paid to Amazonia because of two major droughts in 2005 (Marengo et al., 2008) and 2010 (Lewis et al., 2011), which were considered amongst the most severe in a century in such a short time of period. These drought events have been associated with increased tree mortality and losses of biomass, and also with temporary shutdown of the Amazon carbon sink (Phillips et al., 2009; Toomey et al., 2011; Gatti et al., 2014).

Analysis of Land Surface Temperature (LST) anomalies from remote sensing and climatic data

revealed a significant and sustained warming over this last decade, especially in 2005 and 2010 where the drought events took place (Jiménez-Muñoz et al., 2013). These thermal anomalies were related to Sea Surface Temperature (SST) anomalies over El Niño and Tropical North/South Atlantic regions, with a different location and extent of the thermal anomaly over the Amazon basin depending on the season and sea region.

On the other hand, the emergence of information technologies and the accessibility to internet connections has favored the design of web-based platforms to disseminate different products and/or results in a user-friendly manner instead of using the classical local machine-based platforms. This work shows the last results obtained from MODIS LST anomalies over the Amazon forests, and presents a new web-based visualization tool for monitoring thermal anomalies over the Amazon forests. It also provides information about a cal/val site in the Peruvian Amazon, where a thermal radiometer was recently installed.

2 DATA

Satellite imagery was acquired from the Moderate Resolution Imaging Spectroradiometer (MODIS) on board of NASA's Terra platform, whereas climatic data was extracted from the ERA-Interim reanalysis.

In the case of MODIS data, the monthly LST product MOD11C3 at 0.05° latitude/longitude Climate Modeling Grid (CMG) was used (Wan, 2007). This product is available from year 2000 to present, and it

includes both daytime and nighttime monthly averages of LST. A mean monthly LST was also obtained after averaging of daytime and nighttime LSTs. Due to failures of the MODIS Cloud Mask, some contaminated values could be included in the computation of the monthly values (Wan, 2008). Therefore, we also used the daily LST product MOD11C1 to reprocess the monthly LST by applying two filters: i) at least 50% of the daily values within a month are valid, and ii) LST values lower or higher than 3 standard deviations of the monthly mean were removed from the mean computation. This reprocessed product is denoted as MODrep.

Figure 1. General view of the Thermal Amazonia viewer (ipl.uv.es/thamazon).

The reanalysis data used included monthly means of skin temperature extracted from the ERA-Interim project developed by the European Centre for Medium-Range Weather Forecasts at $0.75^{\circ} \times 0.75^{\circ}$ latitude longitude global spatial resolution (Dee et al., 2011). It is available from 1979 to present, thus extending back the study period of the MODIS data.

3 THERMAL AMAZONIA VIEWER

The different products of thermal anomalies are available through the web-based platform “Thermal Amazonia Viewer”. This system is installed at the servers of the Image Processing Laboratory (IPL) of the University of Valencia (Spain), but it is highly portable and can be easily installed in any other server. The system is currently operational at the following link: <http://ipl.uv.es/thamazon>.

The development of the system is based in Open Source codes. All the algorithms for viewing and browsing the imagery included in the system were developed entirely in Javascript and Hyper Text Markup Language version 5 (HTML5). The viewer was tested on most modern browsers (eg., Safari, Google Chrome, Mozilla Firefox, and Internet Explorer 11).

Figure 1 shows a general view of the system. The left column is the “layers and views” menu, which includes the different products to be visualized. The current version of the system allows the visualization of thermal anomalies using MODIS and ERA-Interim products. Each main “standardized anomalies” layer includes different sub-layers to select the year and the month/season for which the thermal anomalies were calculated. It is also possible to visualize maps of LST anomalies trends, land cover, and graphs of time series of LST anomalies.

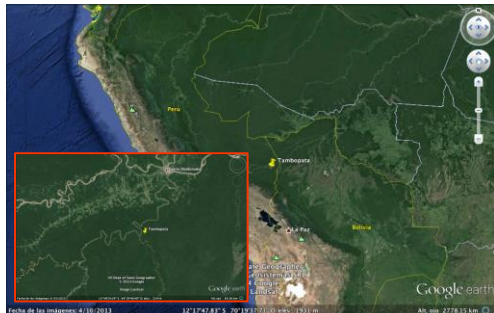


Figure 2. Location of the Tambopata cal/val site (extracted from Google Earth ®).



Figure 3. Pictures of the Tambopata's tower and the thermal radiometer.

5 RESULTS

Figure 4 shows LST standardized anomalies over the study area for the January-August-September (JAS) season from year 2005 to 2012 using the MOD11 product. In general, a warming pattern is observed over different regions, except for years 2006 and 2007, with no clear pattern or even a cooling pattern in some regions. A widespread warming is observed in 2010, when a severe drought occurred. Years 2009, 2011 and 2012 are also characterized by a widespread warming. However, the warming in 2005, when the first severe drought occurred, is only partly observed.

Because of the problems with the MODIS cloud mask, it is worth to compare the spatial patterns of the original MOD11C3 product with the spatial pattern of the ERA-Interim or MODrep products. Figure 5 shows the spatial pattern of LST anomalies obtained from the ERA-Interim reanalysis product. In despite of the different spatial resolution, we can observe that the spatial pattern for the widespread warming in 2010 is consistent with the pattern observed in the MOD11 product (Fig. 4). In the case of year 2005, some regions show also an agreement between MOD11 and ERA-Interim. However, significant differences are observed over other regions. In general, ERA-Interim enhances the warming in the drought of 2005. Figure 6 shows the comparison between the spatial pattern of LST anomalies using the MOD11 and the MODrep products. It is observed that the MODrep products provides a significant number of non-valid values because of the restriction of the cloud

filter. Most of the Northern Amazon is filtered in the MODrep product, whereas the spatial pattern for Southern Amazon is almost similar than the original MOD11 product. Figure 7 shows the map of the LST trends for the JAS season and the period 2000-2012 using MOD11 and ERA-Interim products. Both products show a significant ($p < 0.05$) warming over Southeastern Amazon, with a warming trend up to $1.5^{\circ}\text{C}/\text{decade}$. This sustained warming trend over SE Amazonia is also observed in the temporal series presented in Figure 8.

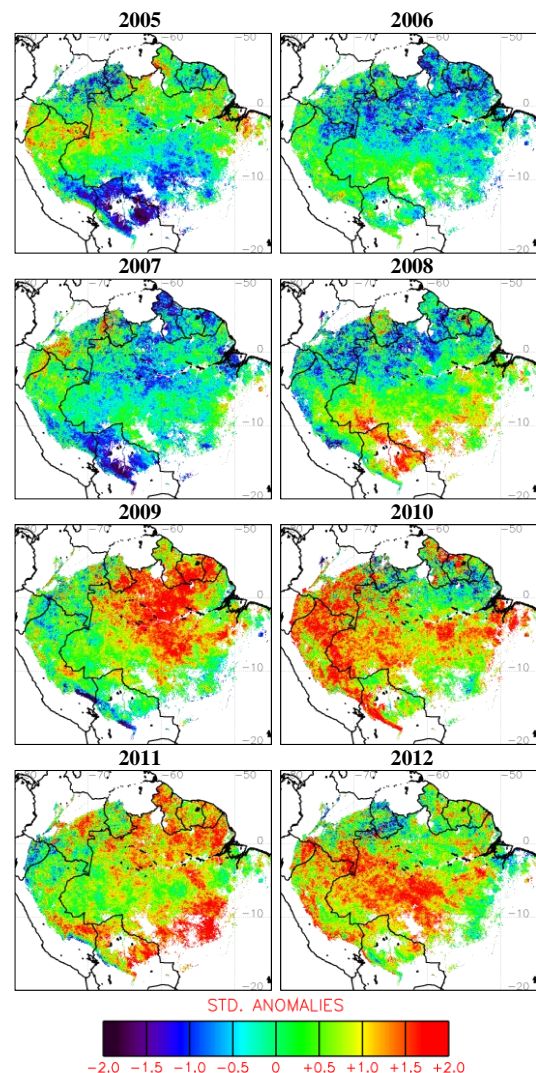


Figure 4. LST standardized anomalies for the JAS season using the MODIS product MOD11C3.

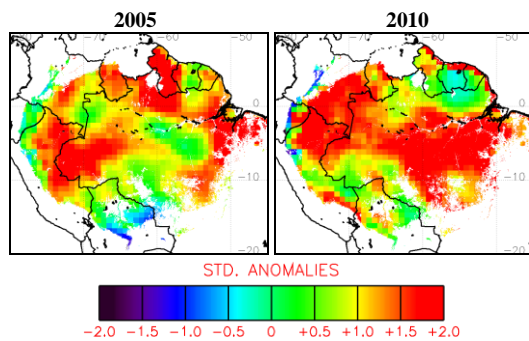


Figure 5. LST standardized anomalies for the JAS season using the ERA-Interim product.

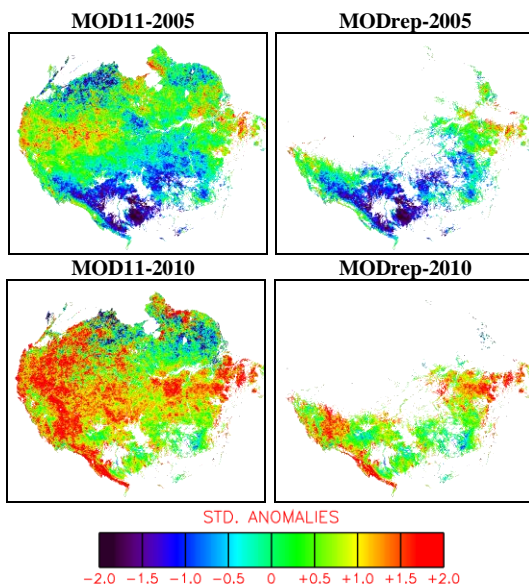


Figure 6. Comparison between LST standardized anomalies obtained from the MOD11C3 product (left column) and the MODrep product (right column) for years 2005 and 2010 and for the JAS season.

One aspect of the warming events over the Amazon forests is the link to the SST anomalies over different tropical sea regions, as discussed in Jiménez-Muñoz et al. (2013) and references therein. The visualization tool allows the simultaneous display of thermal anomalies over the Amazon forests and tropical Pacific, North Atlantic and South Atlantic sea regions around the Amazon basin. Figure 9 shows the land and sea surface thermal anomalies for two major El Niño events (1983 and 1998) for two different seasons (JFM and JAS). Since El Niño event is more related to the JFM season, most of the warming in the tropical Pacific and the Amazon basin is observed in this season. During the JAS season, the warming in the tropical Pacific is vanished, as is the warming over the

Amazon forests, although some warmed areas are still observed in this season. Note also that only warming over tropical Pacific is observed in 1983, whereas a widespread warming over tropical Pacific and North/South Atlantic is observed in the huge El Niño event in 1998. Figure 9 also shows the warming events occurred during the two major droughts of 2005 and 2010. It is clearly observed how these warming events are not related to El Niño events but to anomalous high temperatures over the tropical North Atlantic region, especially in 2010, where warming over the South Atlantic region is also evidenced.

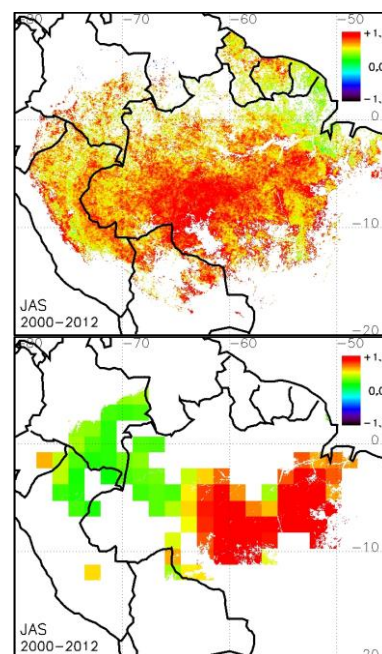


Figure 7. Trends ($^{\circ}\text{C}/\text{decade}$) in LST anomalies for the JAS season and the period 2000-2012 using MODIS product (top) and ERA-Interim reanalysis (bottom). Only pixels with $p < 0.05$ are displayed.

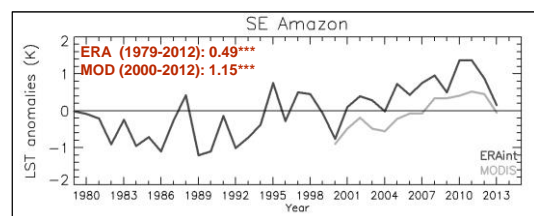


Figure 8. Time series of LST anomalies for the JAS season using MOD11 product (2000-2013) and ERA-Interim reanalysis (1979-2013) over SE Amazon. Warming rates ($^{\circ}\text{C}/\text{decade}$) are also provided (trend significance: *** $\rightarrow p < 0.01$).

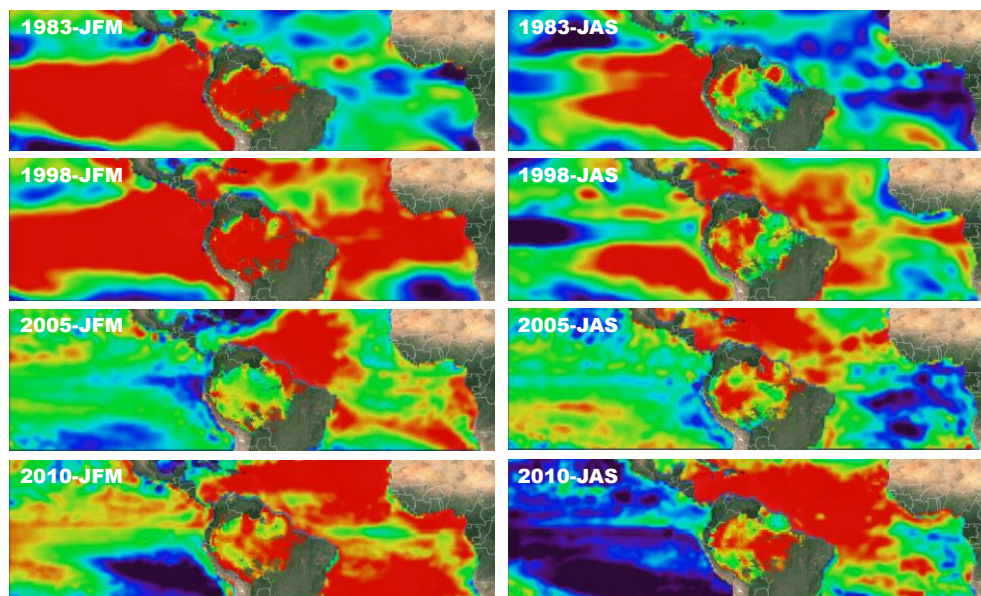


Figure 9. Sea and Land Surface Temperature anomalies for different seasons (JFM and JAS) and different years (1983, 1998: El Niño events; 2005,2010: severe droughts over Amazonia). Pictures extracted from *Thermal Amazonia Viewer*.

6 CONCLUSIONS

In this work we analysed temporal series of monthly/seasonal temperature anomalies over the Amazon forests using MODIS LST products and also ERA-Interim reanalysis data. A significant warming over Amazonia was evidenced in the last decade, especially over SE Amazon, with a mean warming rate higher than 1 °C/decade. Spatial patterns of LST trends obtained from MODIS and ERA-Interim over SE Amazon are consistent. However, significant discrepancies were found over other regions and years when seasonal anomalies were compared. It should be noted that some failures in the MODIS cloud mask lead to artefacts in the MODIS monthly LST product. We reprocessed MODIS daily values using a conservative cloud filter to avoid cloud contamination in the monthly values. As a result, values over most of Northern Amazon were not available. Over Southern Amazon, spatial patterns of thermal anomalies were similar than the MODIS original product.

In this work we also presented a web-based system, *Thermal Amazonia Viewer* (ipl.uv.es/thamazon), which allows the visualization of the thermal anomalies in a friendly interface. This system also includes a web site with different kind of information and also a ftp site for product download.

7 ACKNOWLEDGMENTS

We thank the Ministerio de Economía y Competitividad (CEOS-Spain, project AYA2011-29334-C02-01) and the Universitat de València (UV-INV-PRECOMP13-115366) for financial support. We also thank the MODIS and ERA-Interim projects for providing the data used in this work.

8 REFERENCES

- Clark, D. A., Piper, S. C., Keeling, C. D., and Clark, D. B. (2003). Tropical rain forest tree growth and atmospheric carbon dynamics linked to interannual temperature variation during 1984-2000. *Proc. Natl. Acad. Sci. U.S.A.*, 100(10), 5852-5857.
- Dee, D. P., S. M. Uppala, A. J. Simmons, P. Berrisford, P. Poli, S. Kobayashi, et al. (2011). The ERA interim reanalysis: configuration and performance of the data assimilation system, *Q. J. R. Meteorol. Soc.*, 137, 553-597.
- Gatti, L. V., Gloor, M., Miller, J. B., Doughty, C. E., Malhi, Y., Domingues, L. G., Basso, L. S., Martinewski, A., Correia, C. S. C., Borges, V. F., Freitas, S., Braz, R., Anderson, L. O., Rocha, H., Grace, J., Phillips, O. L., and Lloyd, J. (2014). Drought sensitivity of Amazonian carbon balance revealed by atmospheric measurements. *Nature*, 506, 76-80.

- Jiménez-Muñoz, J. C., Sobrino, J. A., Mattar, C., and Malhi, Y. (2013). Spatial and temporal patterns of the recent warming of the Amazon forest. *Journal of Geophysical Research*, 118, 5204-5215.
- Lewis, S. L., P. M. Brando, O. L. Phillips, G. M. F. van der Heijden, and D. Nepstad (2011), The 2010 Amazon drought, *Science*, 331, 554.
- Malhi, Y., Wood, D., Baker, T. R., Wright, J., Phillips, O. L., Cochrane, T., et al. (2006). The regional variation of aboveground live biomass in old-growth Amazonian forests. *Global Change Biology*, 12, 1107-1138.
- Malhi, Y., J. Timmons Roberts, R. A. Betts, T. J. Killeen, W. Li, and C. A. Nobre (2008), Climate Change, Deforestation, and the Fate of Amazon, *Science*, 319, 169-172.
- Marengo, J. A., C. A. Nobre, J. Tomasella, M. D. Oyama, G. S. de Oliveira, R. de Oliveira, H. Camargo, L. M. Alves, and I. Foster Brown (2008). The Drought of Amazonia in 2005, *J. Clim.*, 21(3), 495-516.
- Phillips, O. L., L. E. O. C. Aragao, S. L. Lewis, J. B. Fisher, J. Lloyd, G. López-González, et al. (2009), Drought sensitivity of the Amazon rainforest, *Science*, 323, 1344-1347.
- Strahler, A., Muchoney, D., Borak, J., Friedl, M., Gopal, S., Lambin, E., and Moody, A. (1999). MODIS Land Cover Product – Algorithm Theoretical Basis Document (ATBD) Version 5.0, Boston University.
- Toomey, M., D. A. Roberts, C. Still, M. L. Goulden, and J. P. McFadden (2011), Remotely sensed heat anomalies linked with Amazonian forest biomass declines, *Geophys. Res. Lett.*, 38, L19704, doi:10.1029/2011GL049041.
- Wan, Z. (2007), Collection-5 MODIS Land Surface Temperature Products Users' Guide, ICES, University of California, Santa Barbara.
- Wan, Z. (2008). New refinements and validation of the MODIS land-surface temperature/emissivity products. *Remote Sensing of Environment*, 112, 59-74.

Remote sensing on grassland growth monitoring and its correlativity with the meteorological factors in Xilingol's grassland of northern China

Y.X. Jin¹, B. Xu^{1,*}, J.J. Qiu¹, X.C. Yang¹, Z.H. Qin¹, Q. WU¹, H.L. Ma¹, J.Y. Li^{1,2}, F. Zhao¹
1. Key laboratory of Agri-informatics of the Ministry of Agriculture, Institute of Agricultural Resources and Regional Planning, Chinese Academy of Agricultural Sciences, Beijing 100081, China. 2. State Key Laboratory of Urban and Regional Ecology, Research Center for Eco-Environmental Sciences, Chinese Academy of Sciences, Beijing 100085, China.
Email: jinyunxiang@caas.cn; xubin@caas.cn

ABSTRACT - Vegetation growth is often used as an indicator of susceptibility to grassland degradation. Grassland vegetation growth monitoring using remotely sensed data, which is characterized by rapid and broad coverage, has the potential for wide application. Grassland ecosystems are an important component of the regional landscape. In this study, we developed an applicable method for monitoring grassland growth and analyzed its dynamic variation using the Moderate Resolution Imaging Spectroradiometer (MODIS) data. The normalized difference vegetation index (NDVI) was calculated from 2001 to 2010 during the grassland growth period. To evaluate the grassland growth, the growth index (GI) was proposed. According to the GI values, five grades were described: worse, slightly worse, balanced, slightly better and better. We explored the spatial-temporal variation of grassland growth and the relationship between grassland growth and meteorological factors. Our results indicated that, compared with the multi-year average, the spatial-temporal variation of grassland growth was significantly different between 2001 and 2010. The vegetation growth in 2009 compared with the multi-year average was worse than in other years. The vegetation growth in 2003 was the best of the years between 2001 and 2010. The GI during 2004 to 2008 exhibited significant fluctuation. Comparing the correlation coefficient between GI and precipitation or temperature, grassland vegetation growth had a positive correlation with precipitation and a negative correlation with temperature. This research provides an effective way to monitor grassland growth and a reference for the sustainable development of grassland ecosystems.

1 INTRODUCTION

Grasslands are important natural resources that cover 41% of the Earth's land surface (Moore, 1966). However, grasslands in arid and semi-arid regions are facing desertification or degradation caused by human activities and climate change. Xilingol's grassland is located at the center of Inner Mongolia, which consists of natural pastures that are among the highest in quality in northern China. The climate of Xilingol consists of long, cold winters with strong winds and warm summers with little rain (Huang et al., 2004; Chen et al., 2008).

Grassland vegetation growth relates to the overall growth state and conditions of the grassland vegetation. Grassland vegetation growth is a relative concept (Yang et al., 2014) and is calculated by comparing the present grassland state with a past state, including the overall or actual state during a certain period, i.e., year, season or month (Yang, 1999). Grassland vegetation growth monitoring includes ground monitoring and remote sensing monitoring. Grassland vegetation growth monitoring using remotely sensed data, which

are characterized by their rapid and broad coverage, has the potential for wide application (Jobbágy et al., 2002; Gao, 2006; Zhang and Guo, 2008; Yu et al., 2010; Xu et al., 2013). The remote sensing-based monitoring of grassland ecosystem processes at large spatial scales is an effective way to obtain knowledge regarding vegetation growth where the most important components of global change take place. Furthermore, the normalized difference vegetation index (NDVI) derived from MODIS is a key indicator for the monitoring of vegetation growth conditions and biomass (Tucker et al., 2001; Piao et al., 2006).

Meteorological factors have a major influence on vegetation growth. The relationships between vegetation and meteorological factors are important issues in ecology (Piao et al., 2011; Guo et al., 2012; Gao et al., 2013). Of numerous meteorological factors, precipitation and temperature are the key factors controlling vegetation spatial gradients and variability. In arid and semi-arid environments, precipitation exhibits a considerable positive correlation with vegetation growth and temperature displays a negative correlation with vegetation growth (Okin et al., 2001;

Fang et al., 2001; Weiss et al., 2004; Piao et al., 2007). Spatial interpolation methods are tools with which to study spatial metrological data. The thin-plate spline function method is considered as having high interpolation accuracy (Hutchinson, 2004; Liu et al., 2008.).

Monitoring vegetation growth dynamics is important for grassland management. The advances in the availability of remote sensing have proven very useful for observing vegetation activity at various scales. There are various applications and analyses of the relationships between grassland vegetation and meteorological factors. However, only a few studies have investigated the spatial-temporal variation between grassland vegetation growth and meteorological factors. In this paper, the vegetation growth index (GI) is presented. Based on GI, growth grade statistics and analyses were conducted to accomplish grassland vegetation growth monitoring. In addition, we explored trends of grassland growth and their correlation with meteorological factors.

2 MATERIALS AND METHODS

2.1 Study area

Xilingol League is located in the central part of Inner Mongolia, between 41°35' and 46°46'N and 111°09' and 119°58'E (Jin et al., 2014). Xilingol is dominated by natural grasslands, which cover 192,512 km², accounting for 95.03% of the total area of the region. This region has a typical temperate continental semi-arid climate. The mean annual temperature ranges from 1.3 to 4.8 °C, and the mean annual precipitation is approximately 150 - 400 mm. Precipitation distribution is mainly focused from June to August, though the inter-annual variation in precipitation can be larger. The Xilingol grassland is primarily dominated by temperate meadow steppe, temperate steppe and temperate desert steppe (Fig. 1).

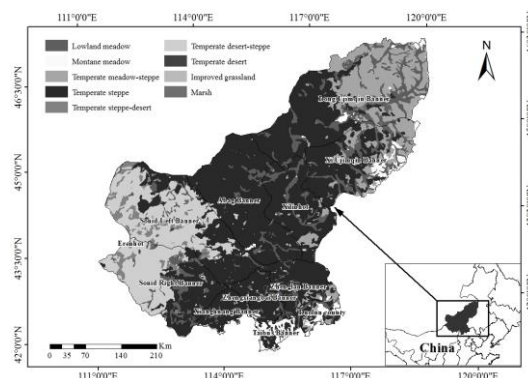


Fig. 1 The study region and spatial distribution of grassland types

2.2 Remote sensing data and climate data

MODIS data have spatial and temporal advantages for grassland growth research. NDVI data with a 250 m spatial resolution and 16 day composite were obtained from the MODIS land data set for August 2001 to 2010. The peak season included three periods from July 28 to September 14. The NDVI value was calculated by reprojection, format conversion and mosaic processes using MODIS Reprojection Tools (MRT) software. The NDVI data were developed using the maximum value composition (MVC), which can eliminate the interference caused by clouds, atmosphere aerosols and solar zenith angle (Holben, 1986). Then, the maximum NDVI values from 2001 to 2010 were averaged to obtain the multi-year average value.

Meteorological data included daily temperature and precipitation data from the National Meteorological Information Center (NMIC) for the years 2001 to 2010. The meteorological data were obtained from 36 climate stations distributed around the area. We calculated temperature and precipitation for the growing season (from May to September), the month of August and the period of July-August. To analyze the relationships between grassland growth and meteorological factors, the ANUSPLIN spatial interpolation method, which was developed in Australia by Hutchinson (Hutchinson, 2004), was used to generate a continuous spatial distribution of precipitation and temperature. Meteorological data were calculated by spline interpolation for the three time periods with longitude and latitude as independent variables and DEM as covariates. From these calculations, we obtained the spatial distribution of temperature and precipitation over the period 2001 to 2010. The mean relative error (MRE) was used to evaluate the interpolation accuracy. The MRE of the precipitation interpolation was 0.043, and the MRE of the temperature interpolation was 0.023.

2.3 Methods

Grassland vegetation growth accounts for the current vegetation growth compared with the status of previous growth, such as an average for multiple years. We used the vegetation GI to reflect the grassland growth condition. The GI was calculated between the NDVI of two periods using the following equation:

$$GI = \frac{(NDVI_m - NDVI_n)}{(NDVI_m + NDVI_n)} \quad (1)$$

where GI is the grassland growth index, $NDVI_m$ represents each NDVI from 2001 to 2010, and $NDVI_n$ represents the average NDVI value between 2001 and 2010.

Vegetation growth grades were established based on GI values. To enable a scientific and reasonable evaluation of vegetation growth, the GI was classified into five grades: better, slightly better, balanced, slightly worse and worse. The values of GI grades were confirmed by sampling data over several years (Xu et al., 2013). Values indicating the better classification are greater than 0.15, slightly better is between 0.05 and 0.15, balanced is between -0.05 and 0.05, slightly worse is between -0.15 and -0.05, and worse is lower than -0.15. The areas of non-grassland were considered to be non-monitored areas. Spatial statistics were conducted using ArcGIS software.

We selected Pearson's correlation method to analyze the correlations between GI and precipitation and temperature. Pearson's correlation coefficient measures the linear relationship between the interval scale variables when the two data sets are on the same line. The greater the absolute value of the correlation coefficient, the stronger the correlation; thus, the closer the correlation coefficient is to 1 or -1, the stronger the correlation, and the closer the correlation coefficient is to 0, the weaker the correlation.

$$r = \frac{N \sum x_i y_i - \sum x_i \sum y_i}{\sqrt{N \sum x_i^2 - (\sum x_i)^2} \cdot \sqrt{N \sum y_i^2 - (\sum y_i)^2}} \quad (2)$$

where x_i indicates one year of GI and y_i indicates one year of temperature or precipitation. $i = 2001, 2002, \dots, 2010$.

3 RESULTS

3.1 Grassland vegetation growth compared with the multi-year average

To compare the vegetation growth of the period from 2001 to 2010 with the multi-year average, GIs in different periods were obtained during the peak seasons (Table 1). The vegetation growth in 2001 compared with the multi-year average was on the worse side ('on the worse side' includes 'worse' and 'slightly worse'). The fractions of the area with GI grades of better, slightly better, balanced, slightly worse and worse accounted for 0.27%, 7.06%, 29.81%, 29.62% and 33.24%, respectively. The vegetation growth in 2002 compared with the multi-year average was principally in balance. The area with a GI of a balance grade accounted for 41.56% of the total. The vegetation growth in 2003 compared with the multi-year average was the best of all years between 2001 and 2010. The areas with GI grades of better, slightly better, balanced, slightly worse and worse accounted for 11.44%, 46.64%, 37.00%, 4.39% and 0.53%, respectively. The GI during 2004 to 2008 exhibited significant fluctuation. The vegetation growth in 2004, 2006 and 2008 was on the better side ('on the better side' includes 'better' and 'slightly better'). In particular, the GI in 2008 was similar to that in 2003. The areas with GI grades on the better side in 2008 accounted for 56.90%. However, the vegetation growth in 2009 and 2010 was worse. The area with GI grades on the worse side in 2009 and 2010 accounted for 66.73% and 54.14%, respectively.

Table 1 The comparative growth conditions of grassland vegetation growth between each year and the multi-year average

Period	Percentage of grassland area (%)				
	Worse	Slightly worse	Balanced	Slightly better	Better
2001	33.24	29.62	29.81	7.06	0.27
2002	5.51	17.22	41.56	30.51	5.2
2003	0.53	4.39	37.00	46.64	11.44
2004	4.66	14.41	41.25	37.17	2.51
2005	16.01	22.64	38.23	21.25	1.87
2006	3.03	9.97	37.66	39.32	10.02
2007	16.89	23.54	30.46	21.62	7.49
2008	0.52	5.16	37.42	46.73	10.17
2009	27.16	39.57	28.99	3.78	0.5
2010	14.86	39.28	36.84	8.59	0.43
Average	12.24	20.58	35.92	26.27	4.99

According to the grassland GI from 2001 to 2010, spatial distribution presented significant differences (Fig. 2). Grassland vegetation growth in 2001 was poor overall, with poor growth in the central and

western regions and better growth in part of the northeastern region. In 2002, grassland vegetation growth was poor in the central region and better in the north. Grassland vegetation growth in 2003 was

overall better, only showing poor growth in part of the central region. Grassland vegetation growth in 2004 was poor in the northwestern region and better in the southern and eastern regions. Grassland vegetation growth in 2005 was poor in the western region and better in the central region. Grassland vegetation growth in 2006 was better in the western region and poor in the northeastern region. In 2007, grassland vegetation growth in different regions was

significantly different, with poor growth in the northeastern region and better growth in the western region. In 2008, grassland vegetation growth was overall good and was better in the central region. Grassland vegetation growth in 2009 and 2010 was poor overall; it was relatively better in the central region in 2010, whereas vegetation growth for most of the other regions was poor.

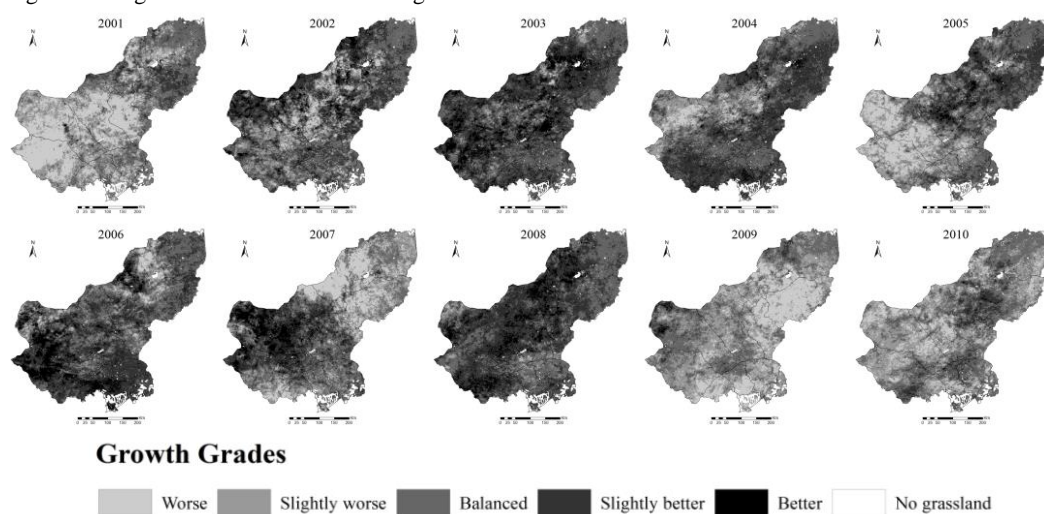


Fig. 2 Spatial distribution of Xilingol's grassland growth from 2001 to 2010 compared with the multi-year average

3.2 The relationship between grassland vegetation growth and precipitation

According to Pearson's correlation analysis (Fig. 3, Table 2), there was a positive correlation between vegetation growth and precipitation. Vegetation growth and growing season precipitation were significantly positively correlated, with the positive correlation area accounting for approximately 96.39%. There was a negative correlation in the central area, but the area accounted for only 3.37%. There was a significant positive correlation between vegetation growth and growing season precipitation in the eastern meadow grassland.

3.3 The relationship between grassland vegetation growth and temperature

According to Pearson's correlation analysis (Fig. 3, Table 2), there was mainly a negative correlation between vegetation growth and temperature. Vegetation growth and growing season temperature had some correlation. There was a negative correlation in the western region, whereas there was some positive correlation in the eastern region. The area with negative correlation accounted for 81.66%, whereas the area with positive correlation accounted for 17.96%.

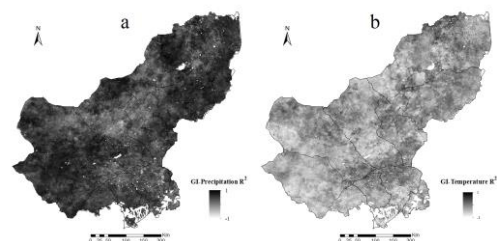


Fig. 3 The correlational relationships (R^2) between GI and precipitation (a) and temperature (b) from 2001 to 2010.

4 DISCUSSION

We monitored and analyzed grassland vegetation growth during the peak season between 2001 and 2010 in Xilingol's grassland. There were significant differences in annual vegetation growth. The grades of vegetation growth from 2002 to 2008 were principally balanced or better. The proportion of area with better grades in 2003 and 2008 reached more than 55%. Grassland vegetation growth in 2001, 2009 and 2010 was worse, with the proportion of area with worse grades reaching 66.73% in 2009. Many previous studies have indicated that grassland vegetation has a positive correlation with precipitation (Sala et al., 1988; Bai et al., 2000; Ni, 2004). Our study also showed that vegetation growth increased as

precipitation increased from 2001 to 2010. We also found that vegetation growth had a negative correlation with temperature. To further analyze the period during which meteorological factors had the greatest impact on vegetation growth, we selected the vegetation growing season to calculate Pearson's correlation. When the R^2 value was greater than 0.5, the area with a significant positive correlation between vegetation growth and growing season precipitation accounted for 52.47% of the total area. These results indicated that growing season precipitation had the greatest impact on the variation in vegetation growth. When the R^2 value was less than -0.5, the proportions of the area with a significant negative correlation between vegetation growth and growing season temperature were 18.69%. However, the precipitation factor plays a much more important role than temperature in vegetation growth.

5 CONCLUSIONS

The measurements from grassland vegetation growth monitoring provide an essential baseline for the long-term grassland management of a region. This study applied the grassland vegetation growth index (GI) to conduct remote sensing monitoring of grassland vegetation growth between 2001 and 2010. The following conclusions were derived from the results of the present study:

(1) On the whole, grassland growth was on the worse side in 2001, 2009 and 2010 compared with the multi-year average. The areas with a GI grade of worse during these years accounted for 33.24%, 27.16% and 14.86%, respectively, of the total area. The vegetation growth in 2003 compared with multi-year average was the best between 2001 and 2010. The area with a GI grade on the better side accounted for 58.08%. The GI from 2004 to 2008 exhibited significant fluctuations. The GI in 2008 was similar to that in 2003. In short, the spatial-temporal trends of grassland growth showed significant variation between 2001 and 2010.

(2) According to the correlation analysis of meteorological factors between 2001 and 2010, grassland growth had a positive correlation with precipitation and a negative correlation with temperature. Precipitation was one of the main factors in the arid and semi-arid region.

ACKNOWLEDGMENTS

We are grateful for support from the International Science & Technology Cooperation Program of China (2013DFR30760), the National Natural Science Foundation of China (NSFC, 31372354), and the Grassland Monitoring and Supervision Center Ministry of Agriculture, China (425-1). We thank the Grassland Monitoring and Supervision Center

Ministry of Agriculture, China, for providing the ground truth data.

REFERENCES

- Bai, Y.F., Li, L.H., Wang, Q.B., et al., 2000, Changes in plant species diversity and productivity along gradients of precipitation in the Xilin river basin, Inner Mongolia. *Acta Phytocologica Sinica*, **24**, 667-673.
- Chen, J., Hori, Y., Yamamura, Y., et al., 2008, Spatial heterogeneity and diversity analysis of macrovegetation in Xilingol region, Inner Mongolia, China, using beta distribution. *Journal of Arid Environments*, **72**, 1110-1119.
- Fang J. Y., Piao S. L., Tang Z. Y., et al., 2001, Interannual variability in net primary production and precipitation. *Science*, **293**, 479-480.
- Gao J., 2006, Quantification of grassland properties: how it can benefit from geoinformatic technologies. *International Journal of Remote Sensing*, **7**, 1351-1365.
- Gao T., Xu B., Yang X. C., et al., 2013, Using MODIS time series data to estimate aboveground biomass and its spatio-temporal variation in Inner Mongolia's grassland between 2001 and 2011. *International Journal of Remote Sensing*, **21**, 7796-7810.
- Guo Q., Hu Z., Li S., et al., 2012, Spatial variations in aboveground net primary productivity along a climate gradient in Eurasian temperate grassland: effects of mean annual precipitation and its seasonal distribution. *Global Change Biology*, **12**, 3624-3631.
- Holben, B. N., 1986, Characteristics of maximum-value composite images from temporal AVHRR data. *International Journal of Remote Sensing*, **11**, 1417-1434.
- Huang, D. M., Shiyomi, M., Chen, J., et al., 2004, Heterogeneity of vegetation in Inner Mongolia, China. *Grassland Science*, **50**, 319-328.
- Hutchinson, M. F., 2004, ANUSPLIN Version 4.3 User Guide. (Canberra, The Australia National University, Center for Resource and Environment Studies).
- Jin Y. X., Yang X. C., Qiu J. J., et al., 2014, Remote Sensing-Based Biomass Estimation and Its Spatio-Temporal Variations in Temperate Grassland, Northern China. *Remote Sensing*, **2**, 1496-1513.
- Jobbágy, E. G., Sala, O. E., Paruelo, J. M., 2002, Patterns and controls of primary production in the Patagonian steppe: a remote sensing approach. *Ecology*, **2**, 307-319.
- Liu, Z. H., Li, L. T., Tim, R. M., et al., 2008, Introduction of the professional interpolation software for meteorology data: ANUSPLIN. *Meteorological Monthly*, **2**, 92-100.

- Moore, C.W.E., 1966, Distribution of grasslands. In Grasses and Grasslands, edited by Barnard, C., (Macmillan, New York), pp. 182-205.
- Ni, J., 2004, Estimating net primary productivity of grasslands from field biomass measurements in temperate northern China. *Plant Ecology*, **174**, 217-234.
- Okin G. S., Murray B., Schlesinger W. H., 2001, Degradation of sandy arid shrubland environments: observations, process modeling, and management implications. *Journal of Arid Environments*, **47**, 123-144.
- Piao, S. L., Mohammat, A., Fang, J. Y., et al., 2006, NDVI-based increase in growth of temperate grasslands and its responses to climate changes in China. *Global Environmental Change*, **16**, 340-348.
- Piao, S. L., Friedlingstein, P., Ciais, P., et al., 2007, Growing season extension and its impact on terrestrial carbon cycle in the Northern Hemisphere over the past 2 decades. *Global Biogeochemical Cycles*, **21**, GB3018.
- Piao, S. L., Cui, M. D., Chen, A. P., et al., 2011, Altitude and temperature dependence of change in the spring vegetation green-up date from 1982 to 2006 in the Qinghai-Xizang Plateau. *Agricultural and Forest Meteorology*, **12**, 1599-1608.
- Sala, O. E., Parton, W. J., Joyce, L. A., et al., 1988, Primary production of the central grassland region of the United States. *Ecology*, **69**, 40-45.
- Tucker, C. J., Slayback, D. A., Pinzon, J. E., et al., 2001, Higher northern latitude normalized difference vegetation index and growing season trends from 1982 to 1999. *International Journal of Biometeorology*, **4**, 184-190.
- Weiss, J. L., Gutzler, D. S., Allred, C. J. E., et al., 2004, Seasonal and inter-annual relationships between vegetation and climate in central New Mexico, USA. *Journal of Arid Environments*, **4**, 507-534.
- Xu, B., Yang, X. C., Tao, W. G., et al., 2013, MODIS-based remote-sensing monitoring of the spatiotemporal patterns of China's grassland vegetation growth. *International Journal of Remote Sensing*, **11**, 3867-3878.
- Yang, B. J., Pei, Z. Y., 1999, Definition of Crop Condition and Crop Monitoring Using Remote Sensing. *Transactions of the Chinese Society of Agricultural Engineering*, **3**, 214-218.
- Yang, X. C., Xu, B., Jin, Y. X., et al., 2014, Remote sensing monitoring of grassland vegetation growth in the Beijing--Tianjin sandstorm source project area from 2000 to 2010. *Ecological Indicators*, DOI: 10.1016/j.ecolind.2014.04.044.
- Yu, H. Y., Eike, L. Xu, J. C., 2010, Winter and spring warming result in delayed spring phenology on the Tibetan Plateau. *Proceedings of the National Academy of Sciences of the United States of America*, **51**, 22151-22156.
- Zhang, C., Guo, X., 2008, Monitoring northern mixed prairie health using broadband satellite imagery. *International Journal of Remote Sensing*, **8**, 2257-2271.

Retrieving and broadcasting near-real time biophysical parameters from MODIS and SEVIRI receiving stations at the Global Change Unit of the University of Valencia

Y. Julien, J. A. Sobrino, G. Sòria, J.-C. Jimenez-Muñoz, D. Skoković
Global Change Unit, Image Processing Laboratory, Parque Científico, Universidad de Valencia, C/ Catedrático Jose Beltran n°2, 46980 Paterna, Spain.
yves.julien@uv.es

ABSTRACT - We present here the automatic processing chains implemented at the Global Change Unit of the University of Valencia. These allow for a near-real time retrieval of various biophysical parameters from sun-synchronous TERRA/AQUA MODIS (Moderate Resolution Imaging Spectroradiometer), and from geostationary MSG SEVIRI (Spinning Enhanced Visible and Infrared Imager) sensors. Retrieved parameters are similar for both sensors, and specific approaches have been developed and implemented for near-real time parameter retrievals: < 2 hours for MODIS, and < 5 minutes for MSG-SEVIRI. A BRDF (Bidirectional Reflectance Distribution Function) correction has still to be implemented in both processing chains, while more advanced parameters are already retrieved (hotspot detection, MSG-SEVIRI phenology), in good agreement with independent ground observations.

1 INTRODUCTION

With an ever increasing number of satellites orbiting our planet, the amount of data available for Earth Observation is rapidly growing. However, due to the amount of data processed, official repositories for remotely sensed biophysical products do not usually provide a near-real time access to the data. Moreover, proper analysis and validation of available data products over the Spanish territory have not been carried out.

Within the framework of the Spanish CEOS-SPAIN project, a processing and broadcasting scheme has been developed and implemented at the Global Change Unit of the University of Valencia, taking advantage of the received MODIS and MSG-SEVIRI data. The processing scheme has been designed with the goal of a near-real time processing of the data, estimating biophysical parameters as straightforwardly as possible. The selected parameters to estimate are the following: sea (SST) and land surface temperatures (LST), for which the total amount of water vapor (WV) and emissivities are needed, NDVI (Normalized Difference Vegetation Index), Vegetation Condition Index (VCI). However, different corrections are needed to retrieve accurately these parameters, such as an atmospheric correction and a BRDF (Bidirectional Reflectance Distribution Function) correction for visible bands.

This paper presents briefly the data received by the MODIS and MSG-SEVIRI stations located at the Global Change Unit, the processing chain for both streams of data, and a few applications of these data.

2 DATA

Two different streams of data are received at the Global Change Unit (see Figure 1): MSG-SEVIRI (top) and MODIS (bottom).

SEVIRI data are provided by the MSG geostationary platform, at 3 km resolution at nadir, with an image every 15 minutes, amounting to 21 GB/day before processing. MODIS data are sun-synchronous, at 250m to 1km spatial resolution depending on the spectral band, with around three overpasses during the day, and 3 during the night, amounting to 4GB/day before processing.



Figure 1. Antenna reception system at the Global Change Unit of the University of Valencia: MSG-SEVIRI reception system (top) and MODIS reception system (bottom).

MODIS data consist of the satellite overpasses within reach of the antenna located at the University of Valencia, overpasses which cover most of western Europe, while SEVIRI data consist of the whole hemisphere centred on the (0,0) latitude and longitude point. Figure 2 presents quicklooks for both MODIS and SEVIRI single acquisitions.

Each data stream is received respectively on a dedicated computer, and then processed by another dedicated computer, to be finally uploaded to a common server. A web of control routines between computers allow for the early detection of any reception, processing or archiving failures.

3 PROCESSING

Both MSG-SEVIRI and MODIS streams of data are processed linearly following a similar scheme (see Table 1). The selected algorithms have been chosen from a literature review, and are based on standard procedures (contextual fire detection – MOD14 – Giglio et al., 2003; MOD35 cloud screening – Ackerman et al., 2010; SMAC atmospheric correction – Rahman and Dedieu, 1994), completed with specific methods (threshold method for emissivities, band ratio for MODIS WV, SST, Split-window LST). For a complete description of these approaches, the reader is referred to the literature mentioned in Table 1. A specific algorithm (Julien et al., submitted) for instantaneous estimation of MSG-SEVIRI WV has been developed to allow for a near-real time processing of MSG-SEVIRI data stream. This algorithm makes use of the 6.2, 10.8 and 12 μm bands, and provides WV estimates with a worldwide accuracy

around 1 $\text{g}\cdot\text{cm}^2$, slightly below the accuracy of existing methods, although these latter do not allow for an instantaneous estimation of WV.

All products in bold characters in Table 1 are available for download from the CEOS-SPAIN online geo-portal (Figure 3), which allows for the selection of various MODIS and SEVIRI products: <http://ceosspain.lpi.uv.es>. The products can be downloaded over an area specified by the user and with a maximum amount of clouds over this area in the case of MODIS products, or for the whole disk in the case of SEVIRI products.

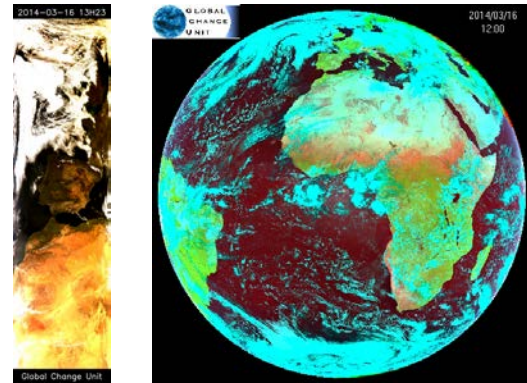


Figure 2. MODIS (left) and SEVIRI (right) quicklooks of received data at the Global Change unit of the University of Valencia.

Table 1. Description of the processing chain and retrieved products form both MODIS and MSG-SEVIRI data streams. Products in bold characters are available for download from CEOS-SPAIN online geo-portal: <http://ceosspain.lpi.uv.es>.

Processing steps	MODIS	MSG-SEVIRI
Data unpacking and calibrating	YES	YES
Geolocation	YES	NO
Hotspot Detection	MOD14 (Giglio et al. 2003)	Calle et al. (2006)
Cloud Detection	MOD35 (Ackerman et al., 2010)	NO
Water Vapor	Sobrino et al. (2003)	Julien et al. (submitted)
Atmospheric Correction	SMAC (Rahman and Dedieu, 1994)	SMAC (Rahman and Dedieu, 1994)
BRDF Correction	NOT YET	NOT YET
Sea Surface Temperature	El Kharraz (2004)	Romaguera et al. (2006)
NDVI	Tucker et al. (1979)	Tucker et al. (1979)
Vegetation Condition Index	Kogan (1995)	Kogan (1995)
Land Surface Emissivity	Sobrino et al. (2003)	Romaguera (2004)
Land Surface Temperature	Sobrino et al. (2003)	Atitar et al. (2008)
Quicklooks	YES	YES
Upload to webpage	YES	YES
Compression	YES	YES
Upload to server	YES	YES

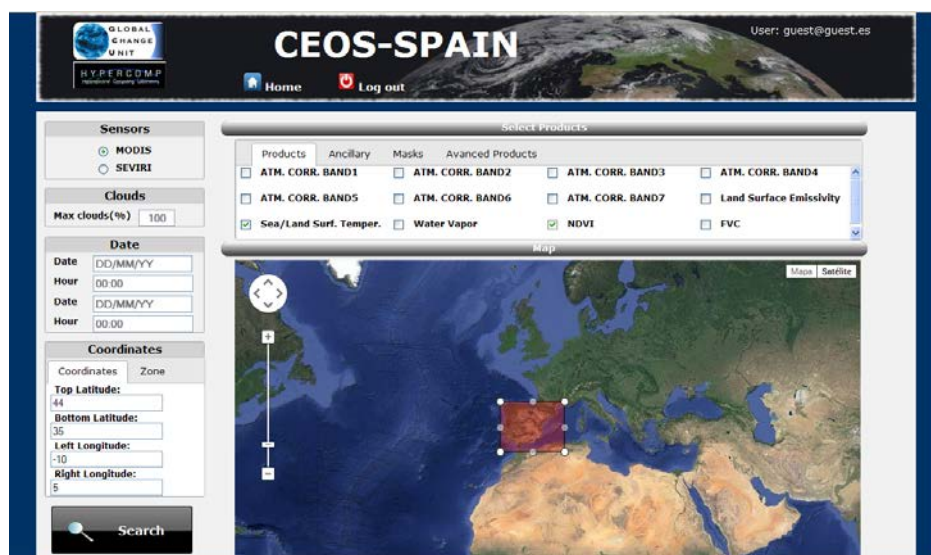


Figure 3. Overview of the geoportal from which all MODIS and SEVIRI products since 2007 can be downloaded: <http://ceosspain.lpi.uv.es>.

4 APPLICATIONS

With the availability of such a huge amount of data, countless applications can be carried out, from vegetation monitoring and forecasting to disaster early warning. Hereafter we present two among these applications, focused on one hand on hotspot detection, and on the other hand on phenology monitoring.

4.1 Hotspot detection

Forest fires are a considerable danger to human health, through corporal and property damage as well as air contamination, and play a key role in the carbon cycle through CO₂ emission, gas which has been evidenced as a major contributor to global warming. As regards spectral information, forest fires (and fires in general) present temperatures in the MIR (Mid-wave InfraRed) and TIR (Thermal InfraRed) higher than their surroundings, which allow for their detection from remote sensors such as MODIS (Giglio et al., 2003) and/or MSG-SEVIRI (Calle et al., 2006). In Table 2, we present a sample of 4 hotspots detected in Portugal from MSG-SEVIRI acquisition on the 2nd of September 2014 at 17:45 (UTC), along with the

estimated characteristics of the detected fire (Fire Radiative Power – FRP; fire temperature and burning area). The system is configured so that alert emails are sent to warn of forest fires in South-western Europe as soon as they are detected (within 5 minutes after the end of image reception).

4.2 Phenology estimation

Monitoring NDVI through a complete year allow for the estimation of phenological phases, such as the dates corresponding to the start and end of season (resp. SOS and EOS). This information is of utmost importance since they both play a role in water and carbon cycles, in direct relation with climate warming prediction, and are a known indicator of climate change through plant sensitivity to temperatures. In Figure 4 we present an example of EOS dates for year 2013 for the whole MSG-SEVIRI disk. To that end, instantaneous NDVI values at 12:00 UTC have been cloud corrected and gap-filled through a procedure similar to the one presented in Julien and Sobrino (2010) and then analyzed for yearly cycle characterization. Direct comparison with independent PEP725 ground station data show an error below 1 week for EOS in Europe (Sobrino et al. 2013).

Table 2. Coordinates and characteristics of the fire detected from MSG-SEVIRI acquisition on the 2nd of September 2014 at 17:45 (UTC).

Pixel	Latitude	Longitude	Fire Radiative Power (MW))	Temperature (°K)	Area (ha)
1	40.69	-6.89	19.7	1194	0.24
2	40.69	-6.85	28.5	932	0.87
3	40.25	-7.73	34.1	1495	0.22
4	40.25	-7.69	32.0	1857	0.12

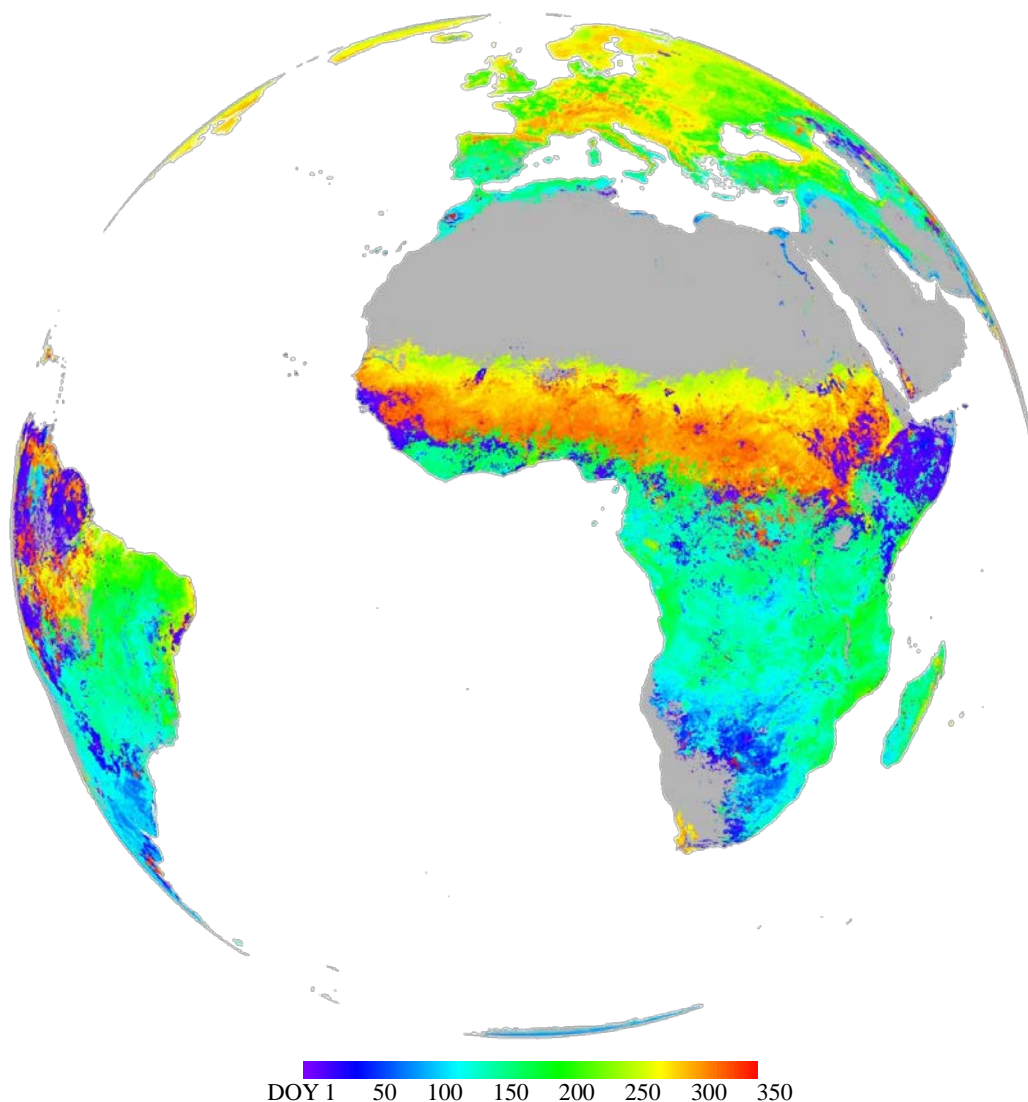


Figure 4. End Of Season (EOS) dates for year 2013 as retrieved from MSG-SEVIRI NDVI time series.

5 CONCLUSION

The MODIS and MSG-SEVIRI receiving stations at the Global Change Unit of the University of Valencia have been operational since mid-2007. All these data have been processed as described above, allowing for specific applications such as fire hotspot detection, phenology monitoring, or temperature spatial homogeneity studies (not described here). These data are available for download to the scientific community and the general public from the geo-portal located within the CEOS-SPAIN webpage: <http://ceosspain.lpi.uv.es>. Additional products (BRDF correction) will be added in a near future, and

presented products will be validated from multitemporal data recorded at various ground stations in Spain, representative of various land covers and land uses.

ACKNOWLEDGEMENT

The authors are grateful to all the members of the Global Change Unit of the University of Valencia for their dedication in keeping the MSG receiving station running over the years. This work was supported by the Spanish Ministerio de Ciencia y Tecnología (CEOS-SPAIN, project AYA2011-29334-C02-01).

REFERENCES

- Ackerman, Frey, Strabala, Liu, Gumley, Baum, & Menzel, 2010. *Discriminating Clear-Sky from Cloud with MODIS - Algorithm Theoretical Basis Document*. Products: MOD35. ATBD Reference Number: ATBD-MOD-06.
- Atitar, M., Sobrino, J.A., 2009. A Split-window Algorithm for Estimating LST From Meteosat 9 Data: Test and Comparison With In Situ Data and MODIS LSTs, *IEEE Geoscience And Remote Sensing Letters*, 6(1), 122-126.
- Calle, A, Casanova, JL, Romo, A (2006). Fire detection and monitoring using MSG spinning enhanced visible and infrared imager (SEVIRI) data, *Journal of Geophysical Research – Biogeosciences*, 111(G3), G04S06.
- El Kharraz, J., 2004. *Determinación de la temperatura de la superficie terrestre a partir de datos MODIS*, PhD Thesis, University of Valencia, Spain.
- Giglio, L., Descloitres, J., Justice, C.O., Kaufman, Y. 2003. An enhanced contextual fire detection algorithm for MODIS. *Remote Sensing of Environment*, 87:273-282.
- Julien, Y. & Sobrino, J. A. (2010). Comparison of cloud-reconstruction methods for time series of composite NDVI data, *Remote Sensing of Environment*, 114 (2010) 618–625.
- Julien, Y., Sobrino, J. A., Mattar, C. and Jiménez-Muñoz, J.-C. (submitted). Near Real-Time estimation of Water Vapor column from MSG SEVIRI thermal infrared bands: implications for Land Surface Temperature retrieval, *IEEE Transactions on Geoscience and Remote Sensing*, submitted.
- Kogan, F. N., 1995. Droughts of the late 1980s in the United States as derived from NOAA polar-orbiting satellite data, *Bulletin of the American Meteorological Society*, 76 (5) (1995), pp. 655–668.
- Rahman, H. & Dedieu, G., 1994. SMAC: a simplified method for the atmospheric correction of satellite measurements in the solar spectrum, *International Journal of Remote Sensing*, 1994, vol.15, No.1, 123-143.
- Romaguera, M., 2004. *Determinació de la temperatura de la superfície terrestre a partir de dades MSG1/SEVIRI*, DEA Research Report, University of Valencia, Spain.
- Romaguera, M., Sobrino, J. A. and Olesen, F.-S. 2006. Estimation of Sea Surface Temperature from SEVIRI Data: Algorithm Testing and Comparison with AVHRR Products, *International Journal of Remote Sensing*, 27: 5081–5086.
- Sobrino, J. A., El Kharraz, J. & Li, Z. L., 2003. Surface temperature and water vapour retrieval from MODIS data, *International Journal of Remote Sensing*, 24, 5161–5182.
- Sobrino, J. A., Julien, Y. & Sòria, G. (2013). Estimation of land surface phenology from Meteosat Second Generation SEVIRI data (2008–2011), *IEEE Journal of Selected Topics in Applied Earth Observations and Remote Sensing*, Vol. 6, No. 3, 1653-1659.
- Tucker, C. J., 1979. Red and Photographic Infrared Linear Combinations for Monitoring Vegetation, *Remote Sensing of Environment*, 8 (2), 127-150.

Experimental study of angular effects on radiative surface temperature measurement

Shuo Peng^{1,2}, Bo-Hui Tang^{1,*}, Hua Wu¹, Ronglin Tang¹ and Zhao-Liang Li^{3,4}

¹. State Key Laboratory of Resources and Environmental information System, Institute of Geographic Sciences and Natural Resources Research, CAS, Beijing, 100101, China.

². University of Chinese Academy of Sciences, Beijing, 100049, China.

³. Key Laboratory of Agri-informatics, Ministry of Agriculture / Institute of Agricultural Resources and Regional Planning, Chinese Academy of Agricultural Sciences, Beijing, 100081, China.

⁴. ICube, Uds, CNRS, 300 Bld Sebastien Brant, CS10413, 67412 Illkirch, France.

tangbh@igsrr.ac.cn

ABSTRACT –Land surface temperature (LST) is one of the key parameters in land surface processes. Notably the LST derived from satellite scale data is affected by the variation of viewing zenith angles, this paper briefly described the angular effect of the radiative surface temperature via field experimental study. The experiments were conducted over a homogenous and flat grassy lawn using two KT-15.99D infrared radiometers mounted on a multi-angle observation device. One radiometer measured the grass radiative surface temperature in different view angles through rotating the arm of the multi-angle observation device. The other radiometer measured the radiative surface temperature at nadir by a fixed arm. The results exhibited the radiative surface temperature increases with the increase of viewing zenith angle and it slightly depends on the variation of viewing azimuth angle. Comparing the off-nadir radiative temperatures to those obtained at nadir showed a maximum difference of 2.7 K when the viewing zenith angle is 75°, which indicates the angular effect of infrared radiation does exist and it must be taken into account in the application of satellite-derived LST with representing one fixed directional radiometer temperature.

1 INTRODUCTION

Land surface temperature is of great importance in many fields such as assessing the carbon, water, and energy fluxes at the surface-atmosphere interface (Li et al., 2013). Hemispherical radiative surface temperature is also an important input parameter for land surface models. However, satellite-derived LST is directional radiative temperature because the satellite observes the earth from one direction and the surface is heterogeneous. Replacing the hemispherical radiative surface temperature with the directional radiative surface temperature in land surface models will introduce an error of 1-2K (Harries et al., 2005). Therefore, it is necessary to develop methods to estimate the hemispherical radiative temperature from satellite-derived LST before inputting the hemispherical radiative temperature into the land surface models. Before that it requires a precise knowledge of the relation between the directional radiative temperature and the view angles. Several experimental studies over a wide range of surfaces have been reported to emphasize angular effect on the radiative temperature and several multi-angle radiative

temperature models have been developed (Chehbouni et al., 2001).

The directional brightness temperature is defined as the temperature of a black body that could have the same radiance as the radiance actually observed with the radiometer (Norman et al., 1995). Lacking of the knowledge of directional emissivity, it is difficult to infer the radiative temperature from the directional brightness temperature, so in this paper, we just carried out an experimental investigation of the angular variation of the brightness temperature and regard the brightness temperature as the radiative surface temperature over grassy lawn in China. The following sections provide a brief description of the experimental setup and the method of measurements, a discussion of the impact of changing view angles on the radiative surface temperature, a comparison between the measurements of this work and others' results, and a conclusion of the relationship between the view angles and the radiative surface temperature.

2 EXPERIMENT

The field measurements were carried out in China, near UCAS, where is semiarid climate. We selected grassy lawn for our initial measurements and analysis.

2.1 Experimental setup

An automatic multi-angle observation device used for multi-angle thermal infrared measurements consists of a goniometer and two KT-15.99D infrared radiometers.

The automatic multi-angle observation device (see figure1), which is mainly composed of a semicircular roadway of 1m radius, an elevator of 1m height to change the distance from the sensor level to the samples, a rotating arm and a fixed arm (Li et al., 2004). The two arms mounted on the elevator could move along the roadway simultaneously to change the view angle from 0° to 180° in the azimuth direction. Moreover, there is also something different between them. The rotating arm is used for changing the view angle from about -90° to 90° in the zenith direction and the fixed arm is used for letting the sensor on it measure the samples at nadir all the time.

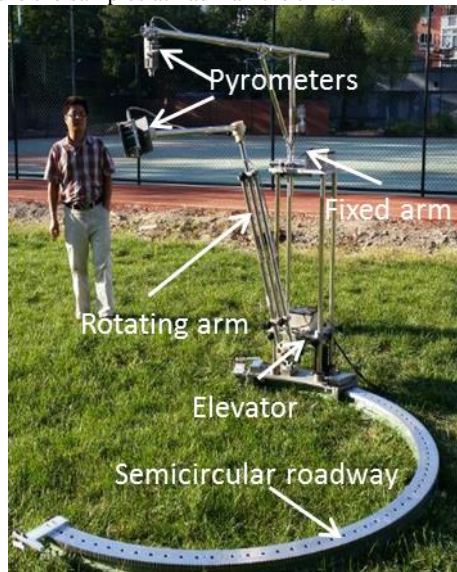


Figure1 Photo of the automatic multi-angle observation device setup for multi-angle thermal infrared measurements. It consists of a rotating arm and a fixed arm mounted on the elevator moving along the semicircular roadway.

The two arms are both equipped with KT-15.99D infrared radiometers operating at 10-13 μ m, with a temperature sensitivity of 0.2K and they have wide FOVs of 20°. The one on the rotating arm observes the samples from a 1.5m height at different view angles by rotating the arm to get the off-nadir radiative temperature and the other on the fixed arm is 0.1m higher than the former to obtain the radiative surface temperature at nadir.

2.2 Measuring procedures

A preliminary experimental investigation of the radiative surface temperature was made up over homogeneous surface (green grassy lawn) by the multi-angle observation device and sensors mentioned above.

Set up the multi-angle observation device and lay it opposite to the Sun (see figure2) to avoid the samples in the shadow of the system. Then we installed one radiometer on the rotating arm and the other on the fixed arm. Initially, we started measuring from -75° to 75° view angle in the zenith direction by pivoting the rotating arm at 0° viewing azimuth angle. Subsequently the arms moved an angle of 30 degrees to the 30° viewing azimuth angle along the roadway and then we started measuring at 75° and ended at -75° viewing zenith angle. As mentioned measuring method, it took 15 minutes to complete whole a hemispheric measurement if we made one measurement each 5° or 10° viewing zenith angle and each 30° viewing azimuth angle. However, measurements were actual operated by the steps of 5° from $\pm 75^\circ$ to $\pm 40^\circ$ view angle and 10° from $\pm 40^\circ$ to 0° view angle in the zenith direction. Simultaneously, the radiometer installed on the fixed arm always observed the surface at nadir. Meanwhile, nearby was a radiometer to measure the hemispherical incoming and outgoing long wave radiance over surface. In relation to the experimental weather condition, it was no wind and no cloud to ensure the thermal stabilization of the surface (Cuenca et al., 2004).

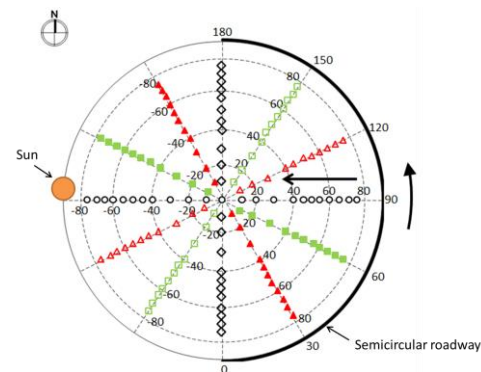


Figure2 Schematic representation of the hemispheric measurement in polar coordinate. Each point represents a measurement at the corresponding viewing zenith and azimuth angle.

3 RESULTS AND DISCUSSION

Now we represent the results obtained. To this end, we construct Figure3 and Figure4, which shows the case

of grass in terms of the zenith and azimuth angular dependence for the calculated relative-to-nadir radiative temperature. The relative-to-nadir radiative temperature ΔT is the difference between off-nadir observation of $T(\theta)$ and simultaneous observation of $T(0_i)$ at nadir.

ΔT is used because it minimizes the effect of temporal changes in temperature during an angular scan cycle. It should be mentioned that the two radiometers have been calibrated by comparing their readings to an absolute and differential temperature blackbody.

$$\Delta T = T(\theta) - T(0_i) \quad (1)$$

The X-axis of figure3 represents the viewing azimuth angle and the one of figure 4 represents the viewing zenith angle. The Y-axes of figure 3 and 4 represent the ΔT .

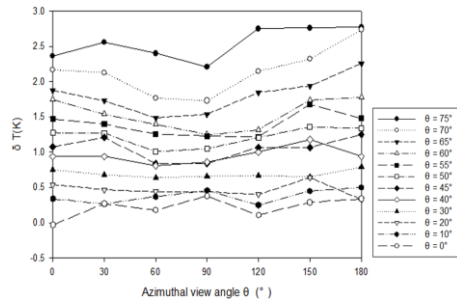


Figure3 ΔT of grassy lawn for different viewing azimuth angles.

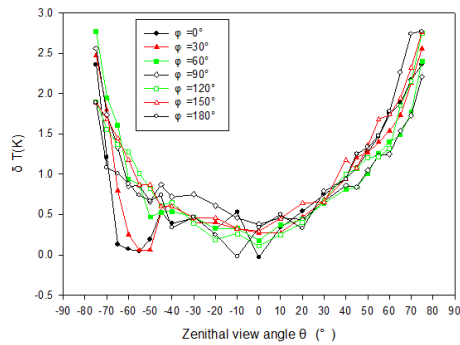


Figure4 ΔT of grassy lawn for different viewing zenith angles.

Figure3, which contains 12 curves of ΔT calculated at the 12 different viewing azimuth angles, shows that the ΔT is mainly influenced by the changes of viewing zenith angle and is slightly dependent on the viewing azimuth angle. And it is almost 2.7K of ΔT to the extent when the viewing zenith angle is 75° .

Figure 4, which consists of 7 curves, one for each azimuth angle, displays that the ΔT rises with increasing viewing zenith angle, with a symmetrical tendency, which is contrary to other results proposed by many papers. The other results reported that for most flat and homogeneous surfaces, brightness temperature decreases clearly with increasing viewing angle (Cuenca et al., 2005).

However, Lagouarde et al. (1995) proposed, for low solar elevations, ΔT is positive, that is to say, ΔT increases with increasing zenith angle. Actually, the time of our measurements is late afternoon, which means low solar elevation. The reason of the results can be explained by the vertical structure of the grass. At noon, the sun heats the grass and soil, but the soil is warmer than the grass. At nadir the mainly part of the sensor footprint is the warmer soil and at off-nadir is the cooler grass. Afternoon, the grass and soil are both cooling. Consequently, around the nadir, cool soil and shadow dominate the footprint of sensor, while for large viewing zenith angle the top of grass heated by the sun is domination.

With respect to the results, there are some regulations to the curves. To characterize the relationship between ΔT and the viewing zenith angle, we construct an empirical form

$$\Delta T = A\theta^2 + B\theta + C \quad (2)$$

where A is 0.0003, B is 0.0047 and C is 0.201, which R^2 is 0.8225.

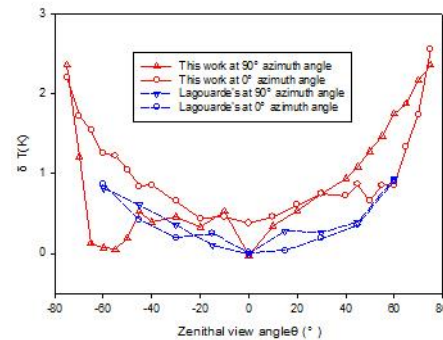


Figure5 Comparison between Lagouarde et al.'s results and ours.

Then we make a comparison between the relative-to-nadir radiative surface temperature measurements of this work and the results of the Lagouarde's (See figure 5). The solid lines show the results from this work and the dashed lines from Lagouarde's. The circle and triangle are used to represent the measurements at the 0° viewing azimuth angle and the 90° viewing azimuth angle. At the same viewing azimuth angle, the relative-to-nadir radiative temperature of the two results have the same

asymmetrical behaviour that effected by viewing zenith angle and they both reach about 1K at $\pm 60^\circ$.

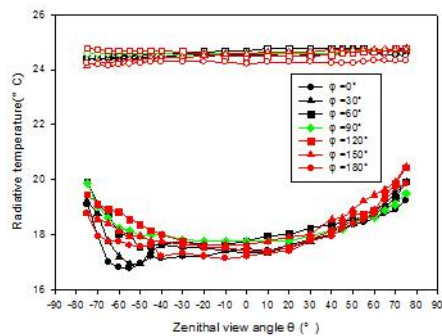


Figure6 Directional radiative temperature and hemispheric radiative temperature.

Figure6 shows the curves of directional radiative temperature and hemispheric radiative temperature. The solid curves are the directional radiative temperature and the hollow curves are the hemispheric radiative temperature at the corresponding azimuthal view angles. They show that the hemispheric radiative temperature is not dependent on view angles.

4 CONCLUSIONS

This paper studied the behaviour of angular effect on the radiative surface temperature through a multi-angle observation device and two infrared radiometers. The experimental study showed that the radiative surface temperature increases significantly with the increase of the viewing zenith angle and it slightly depends on the variation of viewing azimuth angle.

An empirical relationship was proposed to correlate the radiative temperature difference between the direction at nadir and off-nadir to the viewing zenith angle. More investigations will be conducted in the near future work.

5 ACKNOWLEDGMENT

This work was jointly supported by the Excellent Young Talent Funds for Kezhen Distinguished Young Scholar in IGSNRR under grant 2012RC101, and the National Natural Science Foundation of China under Grant 41231170.

6 REFERENCES

Chehbouni, A., Nouvellon, Y., Kerr, Y., Moran, M., Watts, C., Prevot, L., Goodrich, D. and Rambal, S., 2001, Directional effect on radiative surface temperature measurements over a semiarid grassland site. *Remote sensing of environment*, 76(3), 360-372.

Cuenca, J. and Sobrino, J. A., 2004, Experimental measurements for studying angular and spectral variation of thermal infrared emissivity. *Applied Optics*, 43(23), 4598-4602.

Cuenca, J., Sobrino, J. A. and Soria, G., 2005, An experimental study of angular variations of brightness surface temperature for some natural surfaces. MERIS (A) ATSR Workshop 2005.

Harries, J. E., Russell, J., Hanafin, J., Brindley, H., Futyran, J., Rufus, J., Kellock, S., Matthews, G., Wrigley, R. and Last, A., 2005, The geostationary earth radiation budget project. *Bulletin of the American Meteorological Society*, 86(7), 945-960.

Lagouarde, J., Kerr, Y. and Brunet, Y., 1995, An experimental study of angular effects on surface temperature for various plant canopies and bare soils. *Agricultural and Forest Meteorology*, 77(3), 167-190.

Li, Z.-L., Tang, B.-H., Wu, H., Ren, H., Yan, G., Wan, Z., Trigo, I. F. and Sobrino, J. A., 2013, Satellite-derived land surface temperature: Current status and perspectives. *Remote Sensing of Environment*, 131, 14-37.

Li, Z.-L., Zhang, R., Sun, X., Su, H., Tang, X., Zhu, Z. and Sobrino, J., 2004, Experimental system for the study of the directional thermal emission of natural surfaces. *International Journal of Remote Sensing*, 25(1), 195-204.

Norman, J. M. and Becker, F., 1995, Terminology in thermal infrared remote sensing of natural surfaces. *Agricultural and Forest Meteorology*, 77(3), 153-166.

Effects of Soil Moisture Content on Reflectance Anisotropy - Laboratory Measurements and RPV Model Inversions

P.P.J. Roosjen^a, H.M. Bartholomeus^a and J.G.P.W. Clevers^a

^aLaboratory of Geo-Information Science and Remote Sensing,
Wageningen University, P.O. Box 47, 6700 AA Wageningen, The Netherlands.
peter.roosjen@wur.nl, harm.bartholomeus@wur.nl, jan.clevers@wur.nl

ABSTRACT *The objective of this research was to study the effects of soil moisture content (SMC) on the anisotropic reflectance behaviour of soils. Biconical Reflectance Factors (BCRFs) of 5 different soil types were acquired at 24 positions in the principal plane in the 350 – 2500 nm range at different SMC levels using Wageningen University's laboratory goniometer facility. The Rahman-Pinty-Verstraete (RPV) model was inverted based on the best fit through the measured anisotropy curves at different SMC levels. The results show that the anisotropic reflectance behaviour of soils is strongly influenced by the SMC. Dry soils displayed strong backward scattering behaviour, with a maximum reflectance close to the hotspot position. An increase in SMC up to the saturation point caused the soils to scatter more in the forward direction and induced a weakening of the hotspot effect. At SMC levels past saturation point, the soils displayed a strong sun-glint like reflectance peak in the anti-solar direction. The RPV model was able to reproduce the measured anisotropy curves up to saturated SMC levels with $R^2 > 0.953$. It was not possible to fit the model through observations at SMC levels past saturation point. The asymmetry parameter (Θ) of the RPV model, which controls the proportion of forward and backward scattering, showed a strong linear correlation to SMC, also when all samples were considered together ($R^2 = 0.778$). The results of this study indicate that reflectance anisotropy contains information on SMC.*

1 INTRODUCTION

Soil moisture (SM) is an important parameter for environmental, ecological and agricultural processes. Knowledge about the distribution of soil moisture at high temporal and spatial scales is therefore interesting for many applications. Soil moisture is currently determined with methods such as gravimetry, neutron attenuation or time-domain reflectometry (TDR), but these methods are expensive, time consuming and in addition, they do not provide information on the spatial distribution. Remote sensing techniques can provide a cheap and quick alternative to provide information on SM. Although microwave remote sensing is an appropriate technique for estimating soil moisture (Kerr et al. 2001; Njoku et al. 2003), the greater temporal availability and generally higher spatial resolution of optical remote sensing data make optical remote sensing interesting for this purpose.

It is important to understand the relation between soil moisture content (SMC) and reflectance to extract information on soil moisture from optical data. One of the earliest studies on this relation was carried out by Ångström (1925), who investigated the fact that soils appear darker when they are wet. Ångström (1925) assigned this darkening of soils upon wetting to an increase of internal reflections within the water layer that covers the soil particles. Internal reflections within this layer increase the amount of

interactions between light and soil particles, which in turn increases the probability of light to be absorbed. Twomey et al. (1986) and Lekner and Dorf (1988) expanded on this theory by taking the different refractive indices (n) of air ($n \approx 1$), soil ($n \approx 1.5$) and water ($n \approx 1.33$) into account. The decrease of the relative refractive index when radiance transfers from air to soil, and from air to water when soils are wetted increases the probability of light to be scattered forward and thereby increases the probability of light to be absorbed by the soil particles. In addition to this, the absorption of light by water itself in the form of free water within the soil matrix or water bound to soil particles, plays an important role in changes in soil reflectance due to moisture (Bach and Mauser 1994).

Several experiments on the effects of SM on reflectance have been carried out. Lobell and Asner (2002) measured the reflectance of several soil samples in the 350-2500 nm range at different SMC levels under laboratory conditions and found an exponential decrease in reflectance when SMC is increased. Lobell and Asner (2002) also found that reflectance in the visible and near-infrared (VNIR) saturated at lower SMC levels compared to reflectance in the shortwave-infrared (SWIR). Weidong et al. (2002) performed a similar experiment and found that the decrease in reflectance is only valid up to a soil specific SMC level, which he referred to as the critical point. After the critical point, which has a good correlation with the point of near-saturation (-0.01

MPa water potential) of a soil, the soil reflectance increases with increasing soil moisture.

A lot of effort has been put in understanding, measuring (Lobell and Asner 2002; Weidong et al. 2002) and modelling (Bach and Mauser 1994; Lekner and Dorf 1988; Muller and Décamps 2001; Somers et al. 2010; Weidong et al. 2003) the effects of SMC on soil reflectance and predicting SMC based on reflectance data (Haubrock et al. 2008; Lesaignoux et al. 2012). Although there is a clear overview on the effects of SMC on spectral changes in reflectance, the effects of SMC on the anisotropic reflectance behaviour of soils did not receive much attention so far (Lobell and Asner 2002; Somers et al. 2010). Rosendahl et al. (2013) performed multi-angular laboratory measurements of glass and sand surfaces at different SMC levels with a Sony XCL-5005 imaging camera and found an increased proportion of forward scattering at higher SMC levels. Yang et al. (2011) performed multi-angular measurements with a FieldSpec FR2500 spectrometer under field conditions and found a similar behaviour at higher SMC levels. Besides that, Yang et al. (2011) also found a correlation between the equivalent water thickness parameter, obtained by inversion of the SWAP-Hapke model, and SMC measured with TDR. However, due to uncertainties in the multi-angular observations and TDR measurements, Yang et al. (2011) were not able to draw universal conclusions on their results.

The aim of this research is to explore the multi-angular reflective domain in relation to SMC (i) by measuring the effects of SMC on reflectance anisotropy and (ii) by modelling these effects with a simple Bidirectional Reflectance Distribution Function (BRDF) model, which is able to simulate the anisotropic reflectance behaviour of surfaces. Information on the anisotropic reflectance behaviour of soils at different SMC levels is important for the improvement and extension of existing remote sensing SMC models. Laboratory measurements obtained with a laboratory goniometer system and inversions of the Rahman-Pinty-Verstraete (RPV) model are presented in this paper to explain the effects of SMC on reflectance anisotropy.

2 METHODOLOGY

2.1 Soil samples

Five soil samples, collected at different locations in the Dutch provinces Friesland (53.1333° N, 5.8167° E) and Noord-Brabant (51.6667° N, 5.0000° E) in 2009 and 2010, respectively, were used in this experiment (table 1). For the experiments, the samples were placed in a mat-black coated cylindrical sample holder made of PVC, with a 20 cm diameter and a 0.1 cm depth. The sample holders were filled to the brim

with soil and flattened. Deionized water was added to the soil until a saturated state was reached. The samples were left to rest for 30 minutes so that the water could distribute uniformly along the sample. After distribution, any excess water after this point was drained from the surface.

Table 1. Properties of the soil samples used in this study.

Sample	Bulk density [gcm ⁻³]	Sand [%] [*]	Clay [%] [*]	Silt [%] [*]	OM [%] [*]
S09-131-34	1.26	-	+/-	+	-
S10-050-30	1.68	+	-	+/-	-
S10-081-12	1.14	+	-	-	+
S10-081-13	1.77	-	+	+	-
S10-081-17	1.29	-	+	+	-

^{*}Low = -, medium = +/-, high = +. Actual values will be displayed after laboratory results are back.

The volumetric soil moisture content (θ) of the samples was calculated based on the oven-dry (24h at 105°C) weight of the samples (m_0) and the weights of the sample collected during the drying process (m), using equation 1.

$$\theta = \frac{(m - m_0) / \rho_w}{m_0 / \rho_b} \quad (1)$$

Where ρ_w is the water density (0.998 gcm⁻³ at 23°C) and ρ_b is the bulk density of the soil sample.

2.2 Spectral measurements

The spectral measurements were taken with Wageningen University's laboratory goniometer facility (Roosjen et al. 2012). After preparation, the samples were placed on a data-logging balance with milligram accuracy, while they were illuminated by a 900 watt Quartz Tungsten Halogen (QTH) lamp, which was placed 70 cm from the sample at a 30° zenith angle. The reflectance of the samples was measured in the 350-2500 nm range during the drying process with an ASD FieldSpec 3 spectrometer (Analytical Spectral Devices, Boulder, CO). The spectrometer was equipped with a 1° fore optic and a diffuser. A white Spectralon panel (LabSphere Inc., North Sutton, NH) was used to calibrate the spectrometer. The robot arm that forms the core of the goniometer, was programmed to position the spectrometer around the sample at 24 different positions in the principal plane in step of 5° between a -65° and + 65° zenith angle, while maintaining a 40 cm distance between the sensor and the sample. A measurement cycle of the principal plane takes approximately 4 minutes, during which the SMC level

was assumed to be constant. There was a 15 minute break between each principal plane measurement cycle. The positions were repetitively measured until the soil reached a stable (air-dry) weight. The goniometer setup was built in a room that was covered with highly absorbent black materials to avoid unwanted scattering effects. During the measurements, the room was maintained at 23°C and at 50% humidity.

2.3 Rahman-Pinty-Verstraete model

The Rahman-Pinty-Verstraete (RPV) model (Rahman et al. 1993) was inverted based on a lookup table (LUT) approach. The RPV model was chosen since it is easily invertible and since it can simulate changes in intensity of forward and backward scattering intensity. The RPV model simulates the directional reflectance of a surface with varying viewing and illumination geometry using only 4 parameters. The model splits the reflectance into a scalar component ρ_0 and a directional component (equation 2).

$$\rho_s(\theta_1, \varphi_1; \theta_2, \varphi_2) = \rho_0 \frac{\cos^{k-1} \theta_1 \cos^{k-1} \theta_2}{(\cos \theta_1 + \cos \theta_2)^{1-k}} \cdot F(g)[1 + R(G)] \quad (2)$$

The Minnaert parameter (k) controls the bell-shape ($k > 1$) and bowl-shape ($k < 1$) of the anisotropy curve. The Henyey-Greenstein phase function $F(g)$ (Henyey 1941), is driven by the asymmetry parameter (Θ), which controls the amount forward ($0 \leq \Theta \leq 1$) and backward scattering ($-1 \leq \Theta \leq 0$), as given in equation 3.

$$F(g) = \frac{1 - \Theta^2}{[1 + \Theta^2 - 2\Theta \cos(\pi - g)]^{1.5}} \quad (3)$$

The hotspot function, driven by the hotspot parameter (ρ_c), is approximated by equation 4.

$$1 + R(G) = 1 + \frac{1 - \rho_c}{1 + G} \quad (4)$$

Where:

$$G = [\tan^2 \theta_1 + \tan^2 \theta_2 - 2 \tan \theta_1 \tan \theta_2 \cdot \cos(\varphi_1 - \varphi_2)]^{1/2} \quad (5)$$

Table 2 shows the minimum, maximum and the step size of the RPV parameter settings, as used for the inversion of the model.

All combinations of the parameters were tested to find the best fit between the measured and modelled reflectance values at each SMC level and each wavelength. The best fit was determined based on the lowest root mean squared error (RMSE) between the

measured and modelled reflectance at all positions in the principal plane (equation 6).

$$RMSE = \sqrt{\frac{\sum_{i=1}^n (\rho_{measured} - \rho_{modelled})^2}{n}} \quad (6)$$

Table 2. Range and the number of steps of the RPV parameters as used for the LUT model inversion.

Parameter	Min	Max	Steps
ρ_0 (VIS)	0.0	0.20	80
ρ_0 (NIR)	0.0	0.35	80
k	0.0	2.0	80
Θ	-1.0	1.0	80
ρ_c	0.0	2.0	20

3 RESULTS

3.1 Effects of SMC on reflectance

The effects of SMC on reflectance anisotropy that were measured with the goniometer under controlled laboratory conditions and simulated with the RPV-model will be presented in this section. Sample s09-131-34 is used as a representative for all investigated samples, because all samples showed similar responses to changes in SMC level.

Over the whole spectral domain, the spectrum of the air-dry measurement had the highest reflectance values, except for saturated SMC levels in the VNIR part (figure 1a).

The strongest spectral variations were found in the short wave infrared (SWIR) part of the spectrum, with emphasis on the water absorption bands centered at 1450 and 1900 nm, which resulted in a change of the shape of the spectral curve in this region. The shape of the curve hardly changed on wetting in the visible part of the spectrum, which is related to darkening of the soil without any change in the colour.

An increasing SMC level caused a non-linear and wavelength dependent decrease of the BCRFs (figure 1b). Wavelengths in the visible range were only sensitive to an increase of SMC level up to 25%. Longer wavelengths were sensitive to changes of SMC level within the whole range from air-dry to saturation point. The BCRFs decreased the strongest between an air-dry state and a SMC level of 25%. After this SMC level, the reflectance decreased slower with increasing SMC level. The BCRFs at 450, 574 and 986 nm increased again at SMC levels beyond the saturation point.

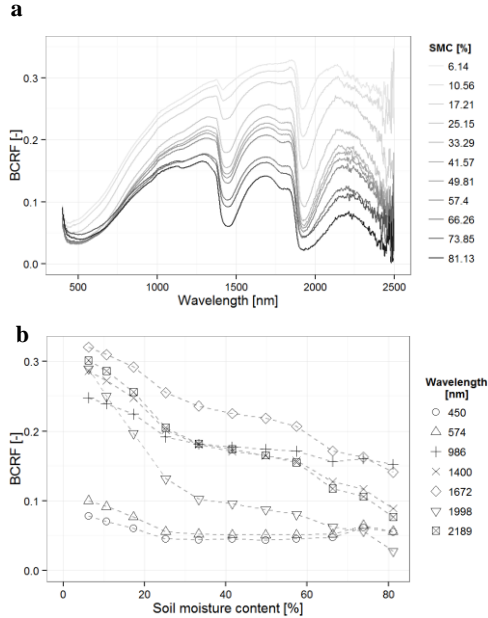


Figure 1. a) Spectra of sample s09-131-34, measured from nadir position at different SMC levels. b) BCRFs at several wavelengths as function of SMC.

3.2 Effects of SMC on reflectance anisotropy

Figure 2 shows the BCRFs and nadir normalized BCRFs, hereafter referred to as anisotropy factors (ANIFs), observed in the principal plane at air-dry, intermediate and saturated SMC levels. The BCRFs of the air-dry soil were higher compared to the intermediate and saturated levels at all positions in the principal plane. The highest BCRFs of the air-dry soil were measured in the backward scatter direction (negative view zenith angles), with a peak around the hotspot position (-30°). This so called hotspot effect was most pronounced for wavelengths in the visible range. The BCRFs measured in the forward scatter direction (positive view zenith angles) were lower than the BCRFs measured at nadir position. For all wavelengths a decrease in BCRF was observed when the SMC level increased. In addition, the hotspot effect and backward scattering intensity decreased, while the reflectance in the forward scatter direction increased. When the SMC level increased to a saturated level, the BCRFs drop even further and the reflectance in the backward scattering direction becomes approximately equal to, or lower than the BCRFs measured at nadir position. After the saturation point, a sun-glint like reflectance peak appeared at a 30° view zenith angle (VZA).

3.3 Modelling effects of SMC on reflectance anisotropy

The RPV model was inverted with a LUT that contained over 21 million different combinations of the ρ_c , Θ , k and ρ_0 parameters (table 2). Each model output was compared to the BCRF measurements. The combination of parameters that produced the lowest RMSE between measured and modelled reflectance factor in the principal plane between a VZA of -65° and 65° was considered the optimal parameter combination.

The RPV model was used to simulate the shape of the measured anisotropy curves with the parameters obtained from the model inversion (figure 3). The best fit of the model inversion resulted in a R^2 of 0.988 and 0.961 for the air-dry and saturated anisotropy curves, respectively (figure 3a-b). At all other intermediate SMC levels the RPV model was fit with a $R^2 > 0.953$. The model was not capable of reproducing the anisotropy curve after the saturation point where the sun-glint reflectance peak appeared (figure 3c).

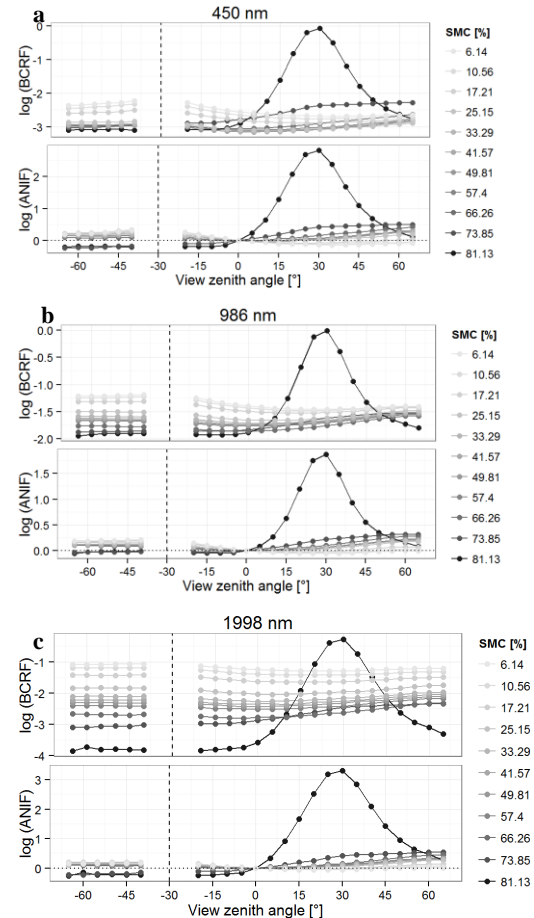


Figure 2. The effect of changes in SMC level on BCRFs and ANIFs in the principal plane. The y-axis is logarithmic to capture the specular lobe at a SMC level of 81.13%.

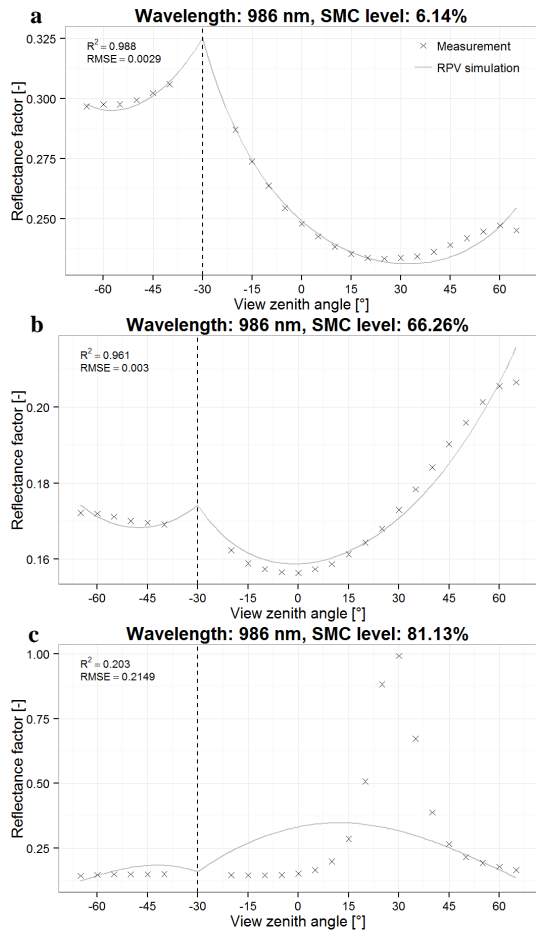


Figure 3. The fit of the RPV model inversion to the goniometer measurements at several SMC levels.

A linear regression analysis indicates that there is a strong correlation between the RPV parameters and the SMC level (figure 4a). When all samples are considered together there only seems to be a correlation between the Θ parameter and SMC (figure 4b). Figure 5 gives an overview of the correlation (R^2) between SMC and the RPV parameters.

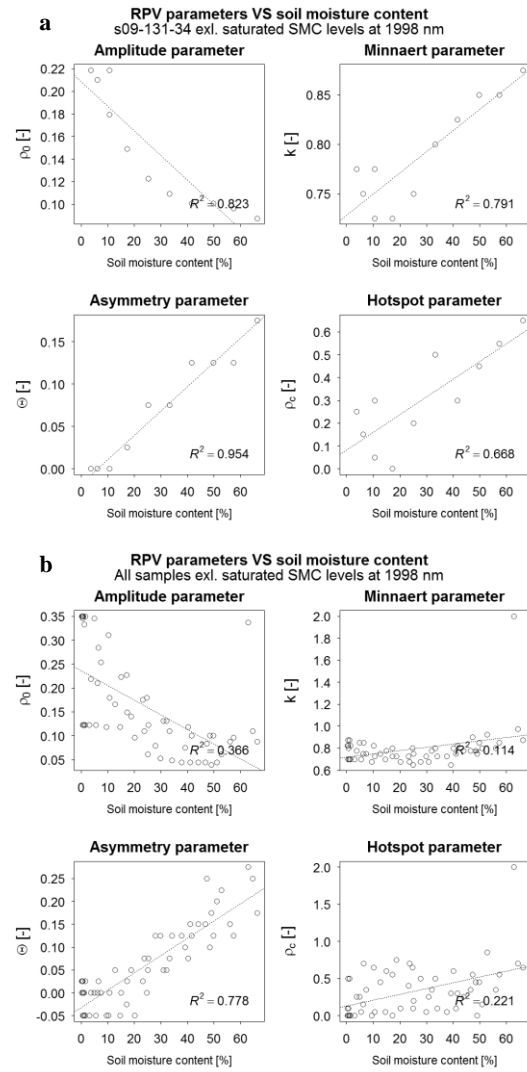
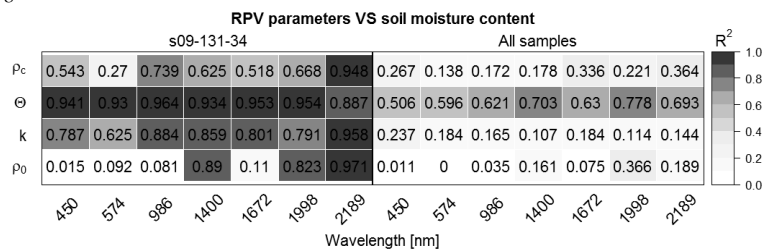


Figure 4. Correlation between the RPV parameters and SMC at 1998 nm. a) Sample s09-131-34; b) All samples considered together.

Figure 5. R^2 between the RPV parameters and SMC for Sample s09-131-34 (left) and all samples considered together (right) at several wavelengths.



4 DISCUSSION

In this research, the effects of SMC on reflectance anisotropy were studied based on laboratory goniometer measurements and RPV model inversions. The results of the measurements clearly indicate an effect of changes in SMC on the anisotropic reflectance behaviour of soils. An increased SMC level caused (i) an overall decrease in reflectance (ii) a decrease in backward scattering intensity and the hotspot effect and (iii) an increase in forward scattering intensity.

The decrease in reflectance upon wetting that we observed in this study is in line with observations of previous studies (Lobell and Asner 2002; Weidong et al. 2002). Like in these studies, we also observed that the reflectance at VNIR was sensitive only to lower SMC levels, while the reflectance in the SWIR was sensitive to the whole measured range of SMC levels (figure 1b). The parameters obtained by the inversion of the RPV-model are in good agreement with these observations. The amplitude parameter (ρ_0), which has no physical meaning but is related to the intensity of the reflectance (Rahman et al. 1993), had a poor correlation with SMC in the VNIR part of the spectrum, while stronger correlations were observed at wavelengths in the SWIR part (figure 5). This confirms the conclusion of Lobell and Asner (2002), who claimed that the SWIR region is better suitable for the measurement of changes in SMC, due to the response of reflectance up to high SMC levels in this region.

In the principal plane, we observed a decreased backward scattering intensity and hotspot effect, and an increased forward scattering intensity when the SMC level increased. These phenomena might be explained by the decrease in relative refraction index when radiance transfers from air to soil with the absence of water and from air to water for conditions where water is present in the soil. The forward scattering of radiance increases when the relative refraction index between two media decreases (Lekner and Dorf 1988; Twomey et al. 1986). This explains why we observed an increased intensity of forward scattering at higher SMC levels. As a result, this also induced a decreased backward scattering intensity and in addition, a decreased hotspot effect. The increased proportion of forward scattering is in good agreement with observations of Yang et al. (2011) and Rosendahl et al. (2013). The RPV model was capable of simulating the changes of the anisotropy curves in the principal plane for SMC levels ranging from air-dry to saturation point (figure 3). The asymmetry parameter of the RPV model (Θ), which controls the forward and backward scattering

intensity, showed strong correlations with SMC (figure 4 and 5). At very high SMC levels, we observed a sun-glint pattern, with a maximum reflectance around the angle of specular reflectance (figure 2). Although no visual water was present at the soil surface during the time of the measurements, it could be that all soil particles at the surface were surrounded by a water layer, which therefore made the soil act like a water surface. Rough water surfaces are known to display strong sun-glint patterns. The intensity and pattern of the sun-glint depends on the roughness of the surface, which is directly related to the surface slope distribution (Cox and Munk 1954). Therefore, it might be possible that the soil roughness of our samples is related to the sun-glint patterns that we observed in this study at high SMC levels. The RPV-model does not take sun-glint or specular reflectance into account and it was therefore not possible to fit the RPV-model through our observations (figure 3c).

The spectral measurements of this study were performed under controlled laboratory conditions with a constant illumination direction and at highly accurate observation positions. Different results might be obtained when repeating a similar experiment under field conditions due to the presence of diffuse illumination and the changing position of the sun over time. The natural presence of surface roughness and soil aggregates, which have a strong influence on reflectance anisotropy (Wang et al. 2012), were destroyed during the preparation of the samples. It might be possible that the anisotropic reflectance effects caused by soil surface structure and roughness overrule the effects caused by soil moisture. In addition, the presence of vegetation, rocks etcetera were not considered in this study. In combination with the acquisition time of the large number of observation positions that were used in this study, this limits the direct applicability for in situ measurements.

The results of this study indicate a strong influence of SMC on reflectance anisotropy. Therefore, it is recommended that reflectance anisotropy is taken into account when analysing data acquired under different viewing and illumination geometries. For future research we recommend to study the effects of moisture on the anisotropic reflectance behaviour of soils while taking the natural soil structure into account and, in addition, the effects of natural illumination conditions need to be studied.

5 CONCLUSIONS

The results of this study show that soil moisture has a strong influence on soil reflectance anisotropy. Increasing SMC levels caused a decrease of backward scattering intensity and hotspot effect, and an increase in forward scattering intensity. At SMC levels past

saturation point, a sun-glint reflectance pattern was observed. The RPV model was fitted through measurements that were performed in the principal plane and especially the asymmetry parameter (Θ), obtained by inversion of the RPV-model, showed a strong correlation to SMC. Although not directly applicable yet, the results of this study indicate that reflectance anisotropy contains information on SMC.

AKNOWLEDGEMENTS

This research was funded by a grant from the User Support Programme Space Research in The Netherlands.

6 REFERENCES

- Ångström, A. (1925). The Albedo of Various Surfaces of Ground. *Geografiska Annaler*, 7, 323-342
- Bach, H., & Mauser, W. (1994). Modelling and model verification of the spectral reflectance of soils under varying moisture conditions. In, *International Geoscience and Remote Sensing Symposium* (pp. 2354-2356)
- Cox, C., & Munk, W. (1954). Measurement of the Roughness of the Sea Surface from Photographs of the Sun's Glitter. *Journal of the Optical Society of America*, 44, 838-850
- Haubrock, S.N., Chabrillat, S., Lemmertz, C., & Kaufmann, H. (2008). Surface soil moisture quantification models from reflectance data under field conditions. *International Journal of Remote Sensing*, 29, 3-29
- Heney, L.G.G., J. L. (1941). Diffuse radiation in the galaxy. *Astrophysical Journal*, 93, 70-77
- Kerr, Y.H., Waldteufel, P., Wigneron, J.P., Martinuzzi, J.M., Font, J., & Berger, M. (2001). Soil moisture retrieval from space: The Soil Moisture and Ocean Salinity (SMOS) mission. *IEEE Transactions on Geoscience and Remote Sensing*, 39, 1729-1735
- Lekner, J., & Dorf, M.C. (1988). Why some things are darker when wet. *Applied Optics*, 27, 1278-1280
- Lesaignoux, A., Fabre, S., & Briottet, X. (2012). Influence of soil moisture content on spectral reflectance of bare soils in the 0.4–14 μm domain. *International Journal of Remote Sensing*, 34, 2268-2285
- Lobell, D.B., & Asner, G.P. (2002). Moisture effects on soil reflectance. *Soil Science Society of America Journal*, 66, 722-727
- Muller, E., & Décamps, H. (2001). Modeling soil moisture–reflectance. *Remote Sensing of Environment*, 76, 173-180
- Njoku, E.G., Jackson, T.J., Lakshmi, V., Chan, T.K., & Nghiem, S.V. (2003). Soil moisture retrieval from AMSR-E. *IEEE Transactions on Geoscience and Remote Sensing*, 41, 215-229
- Rahman, H., Pinty, B., & Verstraete, M.M. (1993). Coupled surface-atmosphere reflectance (CSAR) model 2. Semiempirical surface model usable with NOAA advanced very high resolution radiometer data. *Journal of Geophysical Research*, 98, 20791-20801
- Roosjen, P.P.J., Clevers, J.G.P.W., Bartholomeus, H.M., Schaepman, M.E., Schaepman-Strub, G., Jalink, H., van der Schoor, R., & de Jong, A. (2012). A laboratory goniometer system for measuring reflectance and emittance anisotropy. *Sensors*, 12, 17358-17371
- Rosendahl, S., Casselgren, J., & Sjö Dahl, M. (2013). Simplified model for light scattering from granular materials with varying moisture content. *Applied Optics*, 52, 4006-4012
- Somers, B., Gysels, V., Verstraeten, W.W., Delalieux, S., & Coppin, P. (2010). Modelling moisture-induced soil reflectance changes in cultivated sandy soils: A case study in citrus orchards. *European Journal of Soil Science*, 61, 1091-1105
- Twomey, S.A., Bohren, C.F., & Mergenthaler, J.L. (1986). Reflectance and albedo differences between wet and dry surfaces. *Applied Optics*, 25, 431-437
- Wang, Z., Coburn, C.A., Ren, X., & Teillet, P.M. (2012). Effect of soil surface roughness and scene components on soil surface bidirectional reflectance factor. *Source of the Document Canadian Journal of Soil Science*, 92, 297-313
- Weidong, L., Baret, F., Xingfa, G., Bing, Z., Qingxi, T., & Lanfen, Z. (2003). Evaluation of methods for soil surface moisture estimation from reflectance data. *International Journal of Remote Sensing*, 24, 2069-2083
- Weidong, L., Baret, F., Xingfa, G., Qingxi, T., Lanfen, Z., & Bing, Z. (2002). Relating soil surface moisture to reflectance. *Remote Sensing of Environment*, 81, 238-246
- Yang, G.J., Zhao, C.J., Huang, W.J., & Wang, J.H. (2011). Extension of the Hapke bidirectional reflectance model to retrieve soil water content. *Hydrology and Earth System Sciences*, 15, 2317-2326

Estimate of daily surface albedo over highly heterogeneous area on the Tibetan Plateau using geostationary data

L. Roupioz ^{a,b,c}, F. Nerry ^a, L. Jia ^b and M. Menenti ^c

^a ICube lab., UMR 7357 CNRS-U. Strasbourg, France

^b Alterra, Wageningen University and Research, Wageningen, The Netherlands

^c Faculty of Aerospace Engineering, TU Delft, Delft, The Netherlands

lroupioz@unistra.fr

ABSTRACT – In areas with very complex relief, such as the South part of the Tibet Plateau, the retrieval of albedo from satellite data remains difficult. To improve the surface reflectance retrieval and consequently the albedo estimation in such area, a method is developed to correct the satellite data for sub-pixel topographic effects. The analysis is performed using geostationary satellite FengYun-2E (FY-2E) data at kilometric level along with the high spatial resolution (30m) data of the Digital Elevation Model (DEM) from ASTER. The methodology accounts for the effects of sub-pixel topography on the estimation of the total irradiance received at the surface, allowing the computation of the topographically corrected surface reflectance. The corrected surface reflectance values obtained after this sub-pixel topographic correction are evaluated before being used for albedo retrieval. The results show significant improvement in surface reflectance retrieved from satellite data after sub-pixel topographic correction as compared to pixel level topographic correction. Furthermore, the albedo estimated using the corrected surface reflectance shows improvement when performed on synthetic data. Even if the results are less obvious with albedo retrieved from FY-2E data, the comparison with available ground data shows a gain in accuracy and leads to think that, in highly rugged terrain, the sub-pixel topography correction method provides more accurate results.

1 INTRODUCTION

Accurate estimates of net radiation at relatively high spatial resolution are essential to understand the energy and heat exchanges between the land and the atmosphere, as well as the impact of climate change on land surface processes. One of the essential parameters when modelling net radiation is the land surface albedo. There are several datasets providing albedo data at global level which have been proven reliable. However, in area with very complex relief, such as the South part of the Tibetan Plateau, the retrieval of albedo from satellite data is still difficult. One of the current method used to retrieve albedo from space, is to take advantage of the high temporal resolution and the variation in illumination angle of the geostationary satellite data to reconstruct the BRDF (Bidirectional Reflectance Distribution Function) and derive the surface albedo (Pinty, 2000, Govaerts, 2008). In the visible domain the geostationary satellite data can be available at the kilometric scale while current global DEM are available at a spatial resolution up to 30 m. Then, in order to improve the surface reflectance retrieval and consequently the albedo estimation, a method has been developed to correct the geostationary satellite data for sub-pixel topographic effects. The objective of this study is to account for the

effects of sub-pixel topography when retrieving land surface albedo from geostationary satellite FengYun-2E (FY-2E) data with kilometric spatial resolution using the high spatial resolution (30 m) data of the Digital Elevation Model (DEM) from ASTER. The methodology accounts for the effects of sub-pixel topography on the estimation of the total irradiance received at the surface, allowing the computation of the topographically corrected surface reflectance. The corrected surface reflectance values obtained after this sub-pixel topographic correction are evaluated before being used for albedo retrieval.

After presenting the study area and the data used in this analysis, the methodology applied to derive sub-pixel topographically corrected albedo is described. Then some results are provided, followed by some conclusions and recommendations.

2 STUDY AREA AND DATA

2.1 Study site

The Tibet Plateau is the largest and highest plateau area in the world spreading over 1.2 million km² and presenting an average elevation of over 5,000 meters. The South part of the plateau is characterised by a very rough relief affecting radiance measurements over space and time. For that reason, the study site has been

selected in that area, very suitable to work on the effects of topography. The study site presents a diversity of topography (Figure 1), from relatively flat to complex relief.

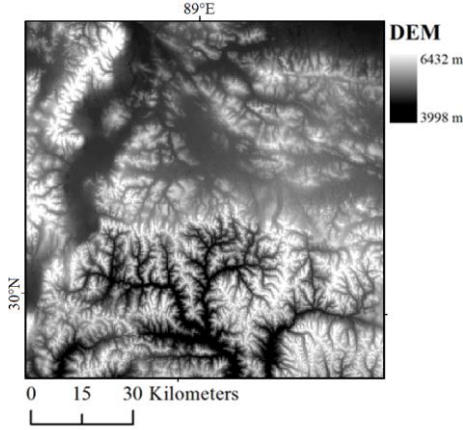


Figure 1: Study site digital elevation model

2.2 Satellite data

a) Landsat data

To validate the sub-pixel topographically corrected reflectance quantitatively, a cloud free Landsat-7 scene from the 27 October 2007 taken over the study site is used (Data available from the U.S. Geological Survey).

b) FY-2E data

To produce the land surface albedo, a time series of FY-2E data is used. FY-2E satellite belongs to the China's geostationary meteorological satellite program FY-2 managed by the Chinese Meteorological Administration (CMA). This dataset consists of a series of hourly daytime FY-2E full scene images for the whole year 2010. Only the visible band is used and the full scene is subset to the area described above (Figure 1). The visible band of FY-2E data spreads from 0.55 to 0.9 μ m and is available at 1.25 km resolution. For this study, the visible band of FY-2E is resampled to 1 km.

2.3 Topographic data

The characteristics of the topography are retrieved at 30 m resolution from the Global Digital Elevation Model (GDEM) version 2 provided by the Advanced Spaceborne Thermal Emission and Reflection Radiometer (ASTER) (ASTER GDEM is a product of METI and NASA). ASTER-GDEM2 is one of the most complete high-resolution digital topographic data sets in the world to date.

2.4 Ground data

In order to validate the estimated albedo from FY-2E, in situ measurements from two radiative balance stations located on the Tibetan Plateau are used: the NamCo station (30.46°N/90.57°E, 4730 m), located next to the NamCo lake over a relatively flat area and the Qomolangma station (28.36°N/86.95°E, 4293 m), located at the foot of the mount Everest, surrounded by steep slopes.

2.5 Actual albedo products

The produced albedo is also compared to existing albedo products: Globalbedo 8-days product (Data obtained from the ESA GlobAlbedo project downloaded from <http://www.GlobAlbedo.org>), MSA 10-days products (Meteosat Surface Albedo Product, EUMETSAT) and MODIS albedo 16-days product collection 5.1 (NASA Land Processes Distributed Active Archive Center (LP DAAC)).

3 TOPOGRAPHIC CORRECTION AT SUB-PIXEL LEVEL

To derive surface albedo from geostationary measured data, the radiance measured from the satellite needs to be converted in reflectance. Then, the reflectance values can be integrated over the considered spectra to obtain the corresponding albedo. The methodology proposed to improve the retrieval of land surface albedo in rugged area by integrating sub-pixel topography effect can be divided in three steps as shown in Figure 2:

- (1) Sub-pixel topographic correction: The method developed in this study is based on the topographic correction method presented in (Sandmeier, 1997) and applied in (Richter, 1998, Shepherd, 2003 and Wen, 2009) which estimates the corrected total solar irradiance as follow:

$$E = \Theta * E_d * \frac{\cos \theta_i}{\cos \theta_s} + E_f * \left[k * \frac{\cos \theta_i}{\cos \theta_s} + (1 - k) * V_d \right] + E_h * V_t * \rho_{adj} \quad (1)$$

In Equation 1, E represents the corrected irradiance, E_d and E_f the direct and diffuse irradiance, and E_h the total irradiance on a horizontal surface (W/m^2). Θ is the coefficient to control cast shadow, k is the anisotropy index, V_d and V_t are the sky-view and terrain-view factor, ρ_{adj} is the average reflectance of adjacent objects, θ_s and θ_i are the solar zenith angle and sun's incidence angle respectively.

Equation (1) is applied to each 30 m pixel of the DEM, considered as the sub-pixels of the geostationary satellite data. The resulting topographically corrected surface irradiance grid at 30 m can then be averaged into a sub-pixel topographically corrected irradiance grid at 1 km.

- (2) From radiance to reflectance: the sub-pixel topographically corrected irradiance at 1 km is used to convert satellite measured radiance to reflectance.
- (3) Albedo retrieval: The surface BRDF parameters are retrieved using the RPV model (Rahman, 1993). The inverted version of RPV requires a set of surface reflectance values measured at different view and illumination angles, along with some initial surface parameters values, to retrieve the real surface parameters values. The algorithm delivers the optimized set of RPV parameters characterizing the surface BRDF. The sub-pixel topographically corrected reflectance values obtained from the previous step are used to feed RPV. From the retrieved BRDF parameters the surface albedo is computed.

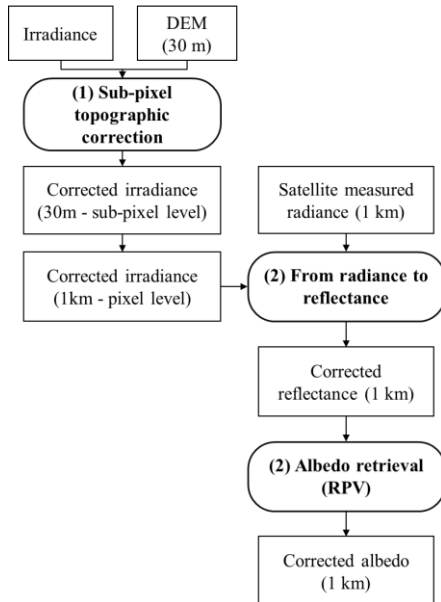


Figure 2: Sub-pixel topographically corrected albedo retrieval method

More details about the sub-pixel topographic correction can be found in (Roupioz, 2014a, Roupioz 2014b). Finally, the produced albedo is converted from narrowband to broadband albedo according to the method described in Loew (2010).

4 RESULTS

4.1 Surface reflectance

The Landsat-7 image is used to validate the sub-pixel topographically corrected surface reflectance. As the presented methodology is developed to retrieve albedo from geostationary data, only the panchromatic band (band 8) is used, being the closest to the visible band of FY-2E. The Landsat data, available at 30 m resolution, can be used as ground truth and the same Landsat data aggregated at 1 km resolution can be considered as radiance values measured by a geostationary satellite. Then, three datasets are produced and compared for the validation: (1) a Landsat data at 30 m corrected using the DEM at the same resolution, which is then aggregated at 1km. This dataset will be considered as the reference data; (2) a Landsat dataset upsampled at 1 km and corrected for topography at pixel level (DEM at 1 km); (3) a Landsat data upsampled at 1 km and corrected for topography at sub-pixel level (DEM at 30 m).

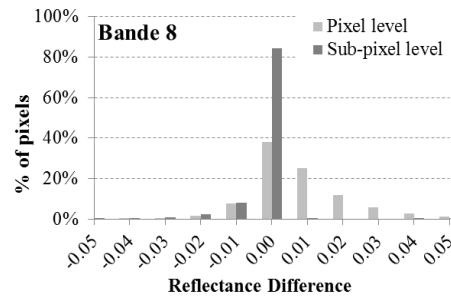


Figure 3: Difference between reference reflectance and pixel (light grey) or sub-pixel (dark grey) topographically corrected reflectance for the band 8 of Landsat-7

To highlight the improvement brought by integrating the sub-pixel topography effects in the reflectance retrieved at 1 km, the results of pixel level (2) and sub-pixel level (3) topographic correction are respectively compared to the reference map (1). The differences obtained are presented in Figure 3, which shows a larger dispersion of the values for the difference between the reference and the pixel level correction while the difference between the reference and the sub-pixel level is more compact and located around zero. Thus, the sub-pixel topographic correction method provides more accurate results than the pixel level correction method even if this method tends to slightly overestimate the retrieved reflectance. However this overestimation remains low and concerns less than 30% of the pixels and is mostly under 0.03. On the contrary, the pixel level correction

tends to overestimate the surface reflectance for more than 60% of the pixels and this error can reach 0.05. More detailed conclusion about the improvement of surface reflectance after sub-pixel topographic correction is presented in Roupioz et al. (2014b).

4.2 Albedo retrieval sensitivity

Prior to validate the albedo retrieved on real FY-2E data, an analysis has been performed to investigate the sensitivity of the method to sub-pixel topography but also to the sub-pixel land cover heterogeneity. To do so, 3 synthetic land cover maps with different degree of heterogeneity have been simulated: one with low (L), one with medium (M) and one with high (H) heterogeneity. For the relief, three topographic configurations have been selected from the DEM: one relatively flat (F), one hilly (M) and one rough area (S). In total, 9 land cover/topography combinations have been tested. The data being simulated, the actual albedo to be retrieved was known and could be used as reference. Then, four albedo computations have been run: (a) without integrating sub-pixel topography neither sub-pixel land cover heterogeneity, (b) integrating sub-pixel topography but neglecting sub-pixel land cover heterogeneity, (c) neglecting sub-pixel topography but integrating sub-pixel land cover heterogeneity and (d) integrating both sub-pixel topography and sub-pixel land cover heterogeneity.

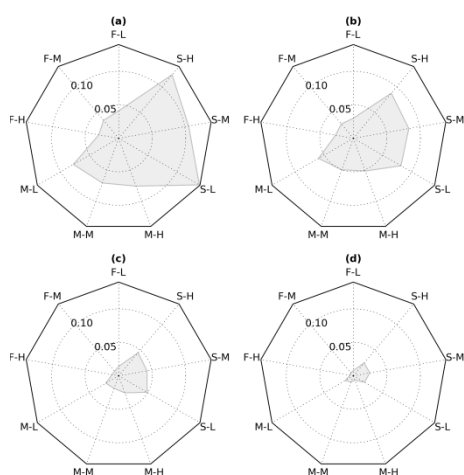


Figure 4: Comparison of RMSE obtained for the four different computations: (a) no correction, (b) only sub-pixel topography correction, (c) only sub-pixel land cover heterogeneity correction and (d) both corrections. Each spider diagrams shows the RMSE for each of the 9 topography-land cover combinations

Figure 4 shows in spider diagrams, the root mean squared error (RMSE) obtained for the 9 combinations for each of the computations. From this figure, it appears that the lowest RMSE is obtained when correcting for sub-pixel topography as well as for sub-pixel land cover heterogeneity and that the largest RMSE occurs when no correction at all is performed. Correcting for the sub-pixel topography can reduce the RMSE of up to 0.7 as compared to no correction at all, and accounting for sub-pixel land cover heterogeneity can reduce the RMSE of up to 1. The largest differences are observed when there is a strong relief and low land cover heterogeneity. Over a flat terrain the difference between the different computation methods are smaller.

4.3 FY-2E albedo

To accurately retrieve albedo from reflectance values measured at different illumination angles, RPV needs a minimum sample of measurements. When the set of measurements covers a good range of illumination angles, 6 valid observations can already be enough to retrieve satisfying surface BRDF characteristics (Govaerts, 2008). So, theoretically, as the FY-2E dataset used in this study contains hourly images, there should be enough data over a day to retrieve the land surface albedo. However, because of meteorological conditions and also because of the topography, the angular sampling of reflectance over a day is often not sufficient to accurately estimate the albedo. Then, in order to have accurate albedo estimates and to keep a good temporal resolution, a 3-days albedo time series was produced for the whole year 2010. Figure 5 highlights the sensitivity of the retrieved albedo to the angular sampling provided as input to RPV. In this figure, the mean illumination zenith angle of the reflectance measurements used is plotted against the difference between the retrieved albedo and the corresponding ground measurements. It shows that when measurements taken at large zenith angles only are available, the accuracy of the retrieved albedo as compared to the ground station is decreasing.

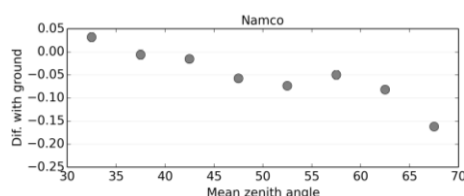


Figure 5: Relation between samples mean illumination zenith angle and accuracy of retrieved albedo

To validate the 3-days albedo time series produced from FY-2E data, the albedo values measured at the ground stations of NamCo and Qomolangma have been used as well as three well known global albedo products. The FY-2E albedo and the three albedo products are compared to their corresponding ground values. Concerning the FY-2E albedo, the sub-pixel topographically corrected (FY-2E) and uncorrected (FY-2E nc) albedo values have been used for the validation. Figure 6 shows the difference between ground measurement and the albedo retrieved from satellite data for each of the products. Looking at FY-2E and FY-2E nc, it appears that for NamCo, which is located in a relatively flat area, the mean difference between corrected and uncorrected albedo is not very different. Only the spread of the difference is lower for corrected data. Thus, the sub-pixel correction method does not introduce any bias in the albedo retrieval. For Qomolangma, there is a clear improvement of the corrected data as compared to the uncorrected ones.

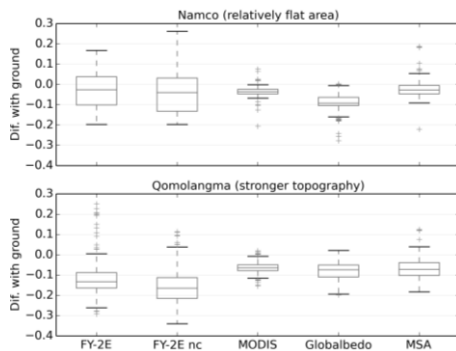


Figure 6: Comparison of the different albedo products with two ground stations data (FY-2E=sub-pixel topographically corrected albedo, FY-2E nc = uncorrected albedo)

As compared with the three other albedo products, the FY-2E corrected albedo seems to provides more accurate results over Namco but less accurate results over Qomolangma. In Namco the mean difference with ground data is lower MODIS and Globalbedo and similar to MSA. In Qomolangma the mean difference with ground data is higher than the three products. The differences observed for the FY-2E albedo are also more spread than for the other products. The main reason is that the other products come from operational algorithm including several filtering options, smoothing the extreme values that can be provided by mathematical algorithms. Furthermore, a simple cloud screening is used in this study, as compared to the more advanced ones applied

for the other products, leading to some of the largest differences observed.

The lower accuracy observed for the albedo retrieved over Qomolangma could be explained by two issues. First, the FY-2E data present some georeferencing inaccuracies up to 12km. Then, even if they have been corrected prior to be used in this study, some error can still remain and the fit between the DEM and the satellite data is maybe not perfect in that very heterogeneous area. The Namco area being more homogeneous, the impact is less important there. Second, it has been showed that the illumination angle sampling provided to RPV influences the accuracy of the retrieved albedo. The terrain being very rough around Qomolangma, the illumination angles corrected for the topography are larger than over a flat terrain, leading to an increase of the illumination zenith sample mean. The later could also explain some of the error in the retrieved FY-2E corrected albedo.

5 CONCLUSIONS

The presented methodology is made of three steps, the sub-pixel topographic correction of the irradiance, the estimation of the reflectance from satellite data using the corrected irradiance and the albedo retrieval from the corrected reflectance. Concerning the estimation of corrected reflectance, it appears clearly that the topographic correction at sub-pixel level leads to a significant improvement in surface reflectance retrieved from satellite data after sub-pixel topographic correction as compared to pixel level topographic correction. This is due to the integration in a more detailed way of the effects of the underlying topography. The main difference in estimating reflectance integrating a sub-pixel topographic correction comes from the use of more detailed irradiance estimates (Roupioz, 2014b). Regarding the albedo estimation, the sensitivity analysis performed using synthetic data highlighted the benefits of using sub-pixel level correction, especially in area presenting a strong relief. It also pointed out the necessity to consider the sub-pixel land cover heterogeneity as in Liu (2008). Even if the albedo values retrieved from FY-2E appears comparable or more accurate in average than other existing products over the Namco area, it did not perform very well over Qomolangma presenting there an underestimation as compared to the ground measurements. It is still interesting to notice that, in relatively flat area, the method does not bring any bias and in area with strong relief, the albedo retrieved after sub-pixel topographic correction provides better results. Because of the data georeferencing issue and the angle sensitivity of RPV, those results would need to be deepened in order to conclude more clearly about it. However those results are in line with the preliminary ones presented in

Roupioz (2014a). Thus, considering that an improvement was observed for the corrected reflectance values and using synthetic data, we can reasonably conclude that, in case of strong topography, the sub-pixel topography correction method gives the best results.

6 RECOMMENDATIONS

The sub-pixel topographic correction method has been proven to improve the retrieved reflectance and also the retrieved albedo when applied with synthetic data. To reinforce the conclusions concerning the albedo retrieved from the FY-2E, it would be very interesting to perform again this analysis but after georeferencing accurately the data or using other geostationary satellite data. Furthermore, the influence of the angles sampling provided to RPV should also be investigated more in details.

Despite the general improvement brought by the proposed methodology, the sensitivity analysis pointed out that, depending on its heterogeneity, the land cover also affects the albedo estimation. Thus, some work should be performed to integrate the sub-pixel land cover heterogeneity to further improve the proposed method. Another way to improve the method would be to work on the cloud screening step, in order to remove better the pixels contaminated by clouds.

ACKNOWLEDGMENTS

This work has been jointly supported by: the EU-FP7 project CEOP-AEGIS (Grant nr. 212921) (<http://ceop-aegis.org>) and the Dragon 3 young scientist grant from ESA.

REFERENCES

- Govaerts, Y.M., Lattanzio, A., Taberner, M., and Pinty, B., 2008, Generating global surface albedo products from multiple geostationary satellites. *Remote Sensing of Environment*, **112**(6), 2804-2816.
- Li, Y., Rong, Z.G., Zhang, L.J., Sun, L., and Xu, N., 2013, Multi-satellites normalization of the FengYun-2s visible detectors by the MVP method. 5th International Symposium on Photoelectronic Detection and Imaging, Proceeding of the ISPD1 2013, Symposium held in Beijing, China, on 25-27 June 2013, SPIE - The International Society for Optical Engineering, 8910.
- Liu, W., Hu, B., and Wang, S., 2008, Improving land surface pixel level albedo characterization using sub-pixel information retrieved from remote sensing. *Geoscience and Remote Sensing Symposium, Proceedings of the IGARSS 2008, Symposium held in Boston, USA, on 7-11 July 2008, IEEE International*, 2, pp.801-804.
- Loew, A., and Govearts, Y., 2010, Towards Multidecadal Consistent Meteosat Surface Albedo Time Series. *Remote Sensing*, **2**(4), 957-967.
- Pinty, B., Roveda, F., Verstraete, M.M., Gobron, N., Govearts, Y., Martonchik, J.V., Diner, D.J., and Kahn, A., 2000, Surface albedo retrieval from Meteosat 1. Theory. *Journal of Geophysical Research: Atmospheres*, **105**(D14), 18099-18112.
- Rahman, H., Verstraete, M.M., and Pinty, B., 1993, Coupled surface-atmosphere reflectance (CSAR) model 1. Model description and inversion on synthetic data. *Journal of Geophysical Research*, **98**(D11), 720-779.
- Richter, R., 1998, Correction of satellite imagery over mountainous terrain. *Applied optics*, **37**(18), 4004-4015.
- Roupioz, L., Jia, L., Nerry, F., and Menenti, M., 2014a, Correction of sub-pixel topographical effects on land surface albedo retrieved from geostationary satellite (FengYun-2D) observations. 35th International Symposium on Remote Sensing of Environment, Proceeding of the ISRSE 2013, Symposium held in Beijing, China, 22-26 April 2013, IOP Conference Series: Earth and Environmental Science, 17(1).
- Roupioz, L., Nerry, F., Jia, L., and Menenti, M., 2014b, Improved Surface Reflectance from Remote Sensing Data with Sub-Pixel Topographic Information. *Remote Sensing*, (In press).
- Sandmeier, S., and Itten, K.I., 1997, A physically-based model to correct atmospheric and illumination effects in optical satellite data of rugged terrain. *IEEE Transactions on Geoscience and Remote Sensing*, **35**(3), 708-717.
- Shepherd, J.D., and Dymond, J.R., 2003, Correcting satellite imagery for the variance of reflectance and illumination with topography. *International Journal of Remote Sensing*, **24**(17), 3503-3514.
- Wen, J., Liu, Q., Liu, Q., Xiao, Q., and Li, X., 2009, Parametrized BRDF for atmospheric and topographic correction and albedo estimation in Jiangxi rugged terrain, China. *International Journal of Remote Sensing*, **30**(11), 2875-2896.

Use of low-resolution satellites for permanent pasture yield estimation at regional scale

L. Seguini⁽¹⁾, R. Lopez-Lozano⁽¹⁾, S. Garcia Contado⁽¹⁾, G. Duveiller⁽²⁾, B. Baruth⁽¹⁾

⁽¹⁾ European Commission, Joint Research Centre (JRC), Institute for Environment and Sustainability (IES), MARS Unit, 21027 Ispra (VA), Italy.

⁽²⁾ European Commission, Joint Research Centre (JRC), Institute for Environment and Sustainability (IES), Climate Risk Management Unit, 21027 Ispra (VA), Italy

E-mail: Lorenzo.seguini@ext.jrc.ec.europa.eu

ABSTRACT *The main objective of this study is to evaluate the suitability of EO biophysical parameters to predict pasture yields, analysing their correlations between with the inter-annual variability of permanent pasture official yields statistics at regional scale. Within the EU, France was identified as a valid study case as consistent time series of pastures yield statistics are officially reported. Remote sensed data (JRC-fAPAR from SPOT VEGETATION) available in the MARS Crop Yield Forecasting System (MCYFS) were used to extract regional (NUTS3 scale) time-series over permanent pastures as defined by specific land cover maps. Cumulated fAPAR over specific time-windows were correlated to official regional yields. The results identified a marked regional distribution of the correlation between biophysical products time-series and official permanent pasture yields. Moreover, the variability of that correlation along the growing season was analysed to identifying the time window –region-specific– over which fAPAR becomes more reliable for yield forecasting.*

1. INTRODUCTION

The near real time monitoring of agricultural production, especially through the development of quantitative forecasting approaches, contributes to ensure a sustainable food supply. Pastures are an important agricultural land use in Europe representing about 13% of total EU land surface and constituting one of the main sources for livestock feed. An operational assessment of pastures productivity along the season is important in the management of agricultural markets: the share of livestock energy needs that are not satisfied by pastures creates a demand for other agricultural products, which may have a considerable impact on stocks and prices. In this context the JRC- MARS is developing in the recent time new tools focused in the monitoring of pasture productivity; in order to find stable and reliable methodologies to catch inter annual yields variability across the EU-28 regions.

Remote sensing at high observation frequency has proven to be a suitable monitoring tool thanks to the provision of coherent, in time and space, information of biophysical parameters like the fraction of absorbed photosynthetically active radiation (fAPAR). Previous studies have proven the existence of a strong relationship between remote sensed time series and

crop yield statistics (e.g. Rembold, 2013; Becker-Reshef, 2010, Duveiller, 2013).

This is an exploratory study to evaluate how reliable a system based on EO indicators could be to monitor and predict pastures productivity in Europe. A study case on France, based on the analysis of the correlation between yield statistics and fAPAR time-series from SPOT-VGT is presented here.

2. MATERIALS AND METHODS

2.1. Areas of study

We considered France as an optimal study site due to the following motivations: (1) France is one of the biggest crops and livestock producers and represents an important player in the European agricultural market; (2) the France Ministry of Agriculture makes available the most complete and large time series of statistics (area and yields) among the EU 28 states.

2.2. Pasture mask definition

The spatial pasture distribution was extracted following the CAPRI-DNDC-EUROPE framework (Leip, 2007). In that framework a spatialization model was used: it ingests as inputs different sources (regional statistics, Area Frame Survey and land cover

CORINE classes) and gives as outputs homogenous regions with the share of surface of a given land use/land cover. In this study the classes GRAE (Gras and Grazings production Activity Extensive) and GRAI (Gras and Grazings production Activity Intensive) were selected as pastures masks. The two classes resulted to have exactly the same distribution and thus we opted to use one single class that merged the two cited ones: the GRASS class. In *Figure 1* is displayed the GRASS class at 1km of pixel resolution - the same used by the CAPRI model.

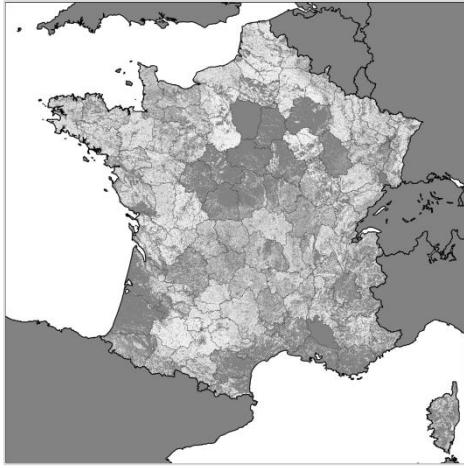


Figure 1: the distribution of pasture areas according to the CAPRI definitions of GRAE and GRAI.

2.3. Pasture statistics definitions and elaborations

Agreste is the official web data source of the France ministry of Agriculture. From the available Agreste databases we retrieved yields and area time series of different multiannual mowing pastures. Agreste defines two different time series 1989 – 2000 (TS1) and 2000 – 2012 (TS2). TS1 and TS2 identify five classes of pasture products that could have a relationship with the GRASS class as created from CAPRI model. In order a single homogeneous time-series we merged TS1 and TS2 assuming that no relevant difference occurred in the methodology of statistic data acquisition or computation. The new time series of yields and areas obtained (TS) are the ones we used as reference member.

1 - Prairies artificielles	Surfaces sowed with 80% of leguminous
2 - Prairies temporaires	Surfaces sowed with at least 20% of grasses
3 - Prairies naturelles ou semées depuis plus de 6 ans	Surfaces that for more than six years are covered with grasses, sowed or natural.
4 - STH peu productives (parcours, landes, alpages)	Like STH but with low production
5 - Surfaces toujours en herbe	Surfaces with perennial grasses used for pasture purposes.
6 - Prairies non permanentes et STH	Weighted average of classes 2 and 5

Table 1: description of the classes of pasture as defined by the French Ministry of Agriculture

Agreste statistics are provided at every administrative level, but we acquired only the smallest administrative level available: NUTS 3 (EUROSTAT - 2011)

We explored TS time series at country level and found a high co-linearity among the five classes main classes in both, yield and areas figures; we did not considered the last class in this part because is just derived from the others. We have found that, for yields statistics, the R^2 coefficient varies between 0.99 (*Prairies naturelles* VS *STH*) and 0.68 (*Prairies naturelles* VS *STH peu productives*). Regarding the areas the correlations are similar ranging from R^2 values of 0.99 (*Prairies naturelles* VS *STH*) to R^2 values of 0.74 (*Prairies naturelles* VS *STH peu productives*).

Given this analysis we have decided to use as statistical reference the sixth class that resume the classes of *STH* and *Prairies naturelles* through weighted means. Further in the document we refer to this class when we use the substantive of pasture, if not explicit defined otherwise.

2.4. Regional fAPAR time-series computation

The time series 1999 – 2013 of SPOT-VEGETATION daily top-of-atmosphere reflectance (TOA) images were acquired from CTIV (VEGETATION Image processing Centre run by VITO, Belgium). Cloud and snow pixels are masked, based on the methodology from Lissens et al. (2000). fAPAR is computed directly from TOA accordingly to Gobron et al. (2000) methodology. The algorithm computes fAPAR according to determined implementation for SPOT-VEGETATION is detailed in Gobron et al. (2002).

From the daily fAPAR images the processing chain applies a synthesis of a nominal temporal resolution of 10-days (*dekade*) using the maximum value composite

algorithm (Holben, 1986). The results are three images a month covering the period 1st – 10th, 11th – 20th, 21st – end of the month. In last step a smoothing algorithm is applied (Klisch, 2007).

The smoothed fAPAR values are thus aggregated at the same administrative level of the statistics: NUTS 3. The aggregation was done on the base of the class GRASS following the procedure of Genovese et al. (2001). The grid class could be seen as an area fraction image (AFI) containing in each pixel the share of surface covered by pasture and thus used as weight according to the following formula:

$$fAPAR_r = \frac{\sum_i^n (fAPAR_i * AFI_i)}{\sum_i^n (AFI_i)} \quad (1)$$

With fAPAR_r stands for the regional mean value at given date for the region *r*, fAPAR_i is the 10-day smoothed fAPAR value on pixel *i* at given date, AFI_i represents the area fraction value for the same pixel *i*, and *n* is the n-pixels over *n* total pixels included in the region *r*. With the given procedure pixels with higher GRASS density have more weight compared to the ones with low GRASS density in the overall regional mean.

To force the regional fAPAR means to be more representative of the pasture areas we decided to exclude the low-density pasture pixel. At the moment of the fAPAR_r computation we excluded all the pixels with GRASS density lower than 75%.

2.5. Regional fAPAR vs regional yields

A linear regression was used to evaluate the relationship between the time series of statistics yields and fAPAR.

Linear regression models were compute for each NUTS3 administrative unit between official statistics of the period 1998-2012 and a cumulated fAPAR over an optimal temporal window, defined by an initial dekad *i*, and a final dekad *i*+*x*, where *x* is the length, in dekads, of the window. The window length *x* ranges between 1 (a single dekad) up to 36 (a window including all the growing season). The purpose of cumulating fAPAR is having results only marginally influenced by to the quality of the composite (clouds, field of view, etc...) of the single dekads and that take into consideration the possible inter-annual shift of the phenological phases of the pasture development. For each NUTS 3, the correlation between fAPAR cumulated for all the possible temporal widows and yield statistics are explored, and mapped, as in the example of Figure 2> The possible windows are completely included in the growing season, starting on 1st October of year *y*-1 and finishing on 31st

September of year *y*. In our approached we have evaluate 666 regression models per region. Each regression model was based on time series from 1st October 1998 to 30th September 2012 divided into 14 agricultural seasons - the overlapping period between the available statistical yields time series and the available remote sensing time series.

Finally, the optimal window is selected as the one for which R² between cumulated fAPAR and observed yields is the highest (Figures 2 and 3). The methodology we applied considered all the first regions, in descended order, which covered the 90% of the total surface of the considered classes in at least one of the considered years.

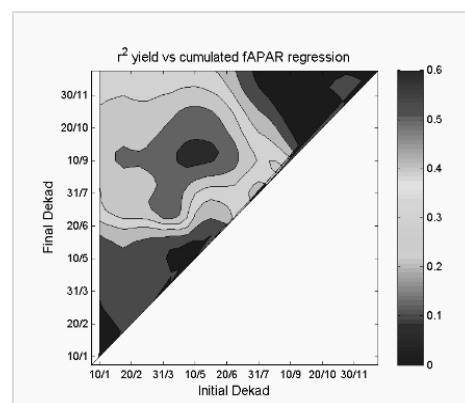


Figure 2: Nievre region. The distributions of the coefficients of determination values - R₂ - according to the possible combinations of the initial 10-Days period (Initial dekad - on the x axe) and final 10-days period (Final dekad - on the y axe). In red colours the combinations with the highest R² values.

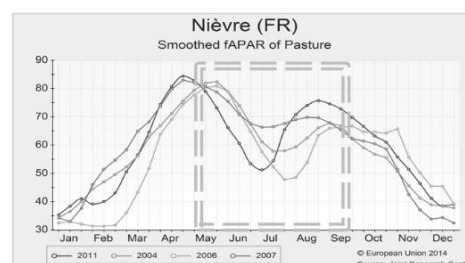


Figure 3: Nievre region. Example of optimal windows and its overlap to several time fAPAR seasons profiles. The window corresponds to the highest R² values as visible in Figure 2

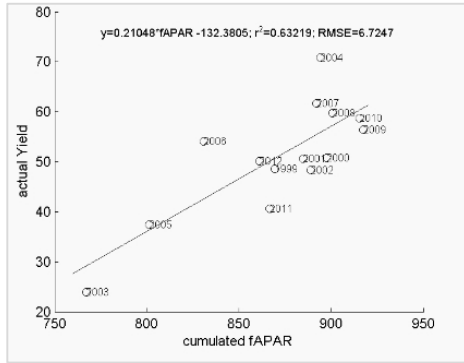


Figure 4: the scatterplot of the cumulated fAPAR computed inside the optimal window.

2.6. Reference values

We computed a set of reference values for each region with the following attributes: surface equal to the actual surface reported in the official statistics for 2012 and with yield equal to the average yield of the time series and normalized yield as obtained from Equation (2) – with x_n the normalized yield, x as the yield in the given region and MIN and MAX the minimum and maximum of the regional average yield) the model on the highest productive areas.

$$x_n = \frac{x - MIN}{MAX - MIN} \quad (2)$$

3. RESULTS

3.1. Correlation of cumulated fAPAR with yield statistics

From a visual analysis the highest R^2 ($R^2 > 0.5$) are distributed around the Massif Central (e.g. Auvergne, Limousine Rohn-alpes) and around the north-western provinces (Basse-Normandie, Pays de la Loire, Bretagne), see Figure 4.

In pure descriptive terms we had a group of 48 regions which correlation coefficient is more than 0.5 and in particular: 13% of the total France regions have a R^2 values above 0.75, and 20% of the total France regions have a R^2 between 0.6 and 0.75 and 23% of the regions between 0.5 and 0.6. The first two classes (33% of the total number of regions with R^2 above 0.6) count for the 40% of the whole statistical surface of the reference year.

3.2. Model performances associated to pastures density and average yields

We have searched for a relation between the regional model performances and the regional extension of a pasture area.

We have aggregated the results in four different classes of R^2 – ranges (Figure 5).

Computing the average regional P_d (pasture density, P_d is the share of pasture surface against the regional surface) in each of the ranges we observed that the model performs better if the regional P_d . For $R^2 > 0.75$ the average regional P_d is 30% of the total regional surface. This percentage decreases for lower R^2 values with percentages of 27%, 24% and 21% respectively for $0.6 < R^2 \leq 0.75$, $0.5 \leq R^2 \leq 0.6$ and $R^2 < 0.5$ ranges.

We have inspected the relation between the model performances and the average yield as computed in the reference year (§0). We observed that the distribution of medium-to-high normalized yield (normalized yield $\geq 50\%$) and medium-to-low normalized yields (normalized yield $\leq 50\%$) inside each R^2 ranges. The range with best regressions coefficients ($R^2 > 0.75$) has a relevant component (60%) of the medium-to-high normalized yields surface. In the others ranges where the medium-to-low yields areas are the main component in terms of surface. The medium-to-high component of $R^2 < 0.5$, $0.5 \leq R^2 \leq 0.6$ and $0.6 < R^2 \leq 0.75$ covers from 37%, 33% and 40% of the surface of each of their group, respectively.

As second step we have analysed the distribution of the medium-to-low and medium-to-high surfaces according to the model performances. We found that the share of the high-yields surfaces has no clear pattern among the four R^2 ranges: high shares in the $R^2 > 0.75$ and $R^2 < 0.5$ ranges (26% and 35%) and around 20% for the others two ranges. The low-yields surfaces tend to be more distribute in the ranges with low R^2 : 12% only in the $R^2 > 0.75$ range to 35% in the $R^2 < 0.5$. The results are summarized in Table 2.

R^2	% surface with normal yield >50 (*)	% surface with medium-to-low yield (**)	% surface with medium-to-high yield (**)
$R^2 > 0.75$	60,38	12,36	26,05
$0.6 \leq R^2 < 0.75$	37,65	23,45	19,59
$0.5 \leq R^2 < 0.6$	33,17	28,55	19,60
$R^2 < 0.5$	41,35	35,64	34,76

Table 2: (*) percentage of surface related to the whole R^2 range surface ;(**) percentage of R^2 surface related to the total yield range (medium-to-high or medium-to-low) surface.

3.3. Temporal windows

The model returns different *optimal integration windows* in terms of seasonal coverage and length of the windows. The disaggregation of both these variables over the four R^2 ranges gives no appreciable

results. The geographical distribution of the optimal integration windows was then studied, only for the regions that have $R^2 > 0.5$. We considered two areas: the north-western regions (Basse-Normandie, Pays de la Loire, and Bretagne) and some regions near to the Massif Central (Auvergne, Limousine and Rhône-Alpes) as samples (34 % of the total pasture class surface) of the main northern (17% of the total pasture class surface) and southern pasture regions (17% of the total pasture class surface). The two groups resulted quite different in terms of windows length. The northern regions have an average length of 19 dekades and a mode of 15 dekades while the southern ones an average length of seven and a mode of one. The seasonal distribution of the windows marks how the north-western regions windows start in winter (median in November, nominally during the dekade of 10-21 November) and end at the beginning of summer (median in June, nominally during the dekade of 11-20 June). The southern ones have different starting time (median in March, nominally during the dekade of 11-20 March) but the ending time is quite similar (median in May, nominally during the dekade of 21 – 31 May).

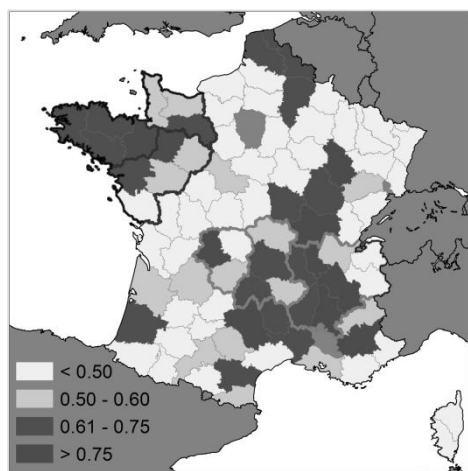


Figure 5: Geographical distribution of the R^2 across the France territory. The R^2 are divided into four ranges with decreasing values as displayed in the legend. In red and orange are marked the group of regions that were analyzed in §3.3.

4. DISCUSSION AND FURTHER DEVELOPMENTS

The model resulted to have better performances in regions with high density pasture, getting worst for low values of P_d . This could be due to the homogeneity in the surfaces observed from satellite:

the observations are more related to real pasture surface than to a mix of surfaces.

The analysis of the medium-to-low and medium-to-high normalized yields components highlights that the model performances get worst for medium-to-low yield regions. We have not yet analysed for this behaviour, we suppose that medium-to-low yields and low pasture density (P_d) could be highly correlated.

The study of the *optimal integration windows* suggests that the inter-annual variability in southern regions is explained by the $fAPAR_t$ due to the events that happen in the spring. In northern regions the events that determine the inter-annual variability happen in both the winter and spring months. In both of the cases the windows cover totally the spring period, when usually the most productive cuts happen. This suggests that the yield forecasting of the first cuts could be sufficient to explain the whole seasonal productivity.

These preliminary results are encouraging further analysis. In the further steps we will identify the outliers and will try to understand the causes of the model failure in those cases. The regression results will be further considered in their relation with the main climate variables to search about relationship between model performances and we will identify if climatic patterns.

REFERENCES

- Agreste, <http://agreste.agriculture.gouv.fr/page-d-accueil/article/donnees-en-ligne>.
- Becker-Reshef I., Vermote E., Lindeman M., Justice C., A generalized regression-based model for forecasting winter wheat yields in Kansas and Ukraine using MODIS data, *Remote Sensing of Environment*, 114 (6), 1312–1323, 2010
- Duveiller G., López-Lozano L. and Baruth B., Enhanced Processing of 1-km Spatial Resolution $fAPAR$ Time Series for Sugarcane Yield Forecasting and Monitoring, *Remote Sensing*, 5(3), 1091-1116; 2013.
- Eurostat, Regions in the European Union - Nomenclature of territorial units for statistics, *Publications Office of the European Union*, 2011.
- Genovese, G., Vignolles, C., Nègre, T., Passera, G., A methodology for a combined use of normalised difference vegetation index and CORINE land cover data for crop yield monitoring and forecasting. A case study on Spain. *Agronomie*, 21, 91-111, 2001

- Gobron N., Pinty B., Verstraete M. M. and Widlowski J.-L., Advanced Vegetation Indices Optimized for Up-Coming Sensors: Design, Performance and Applications, *IEEE Transactions on Geoscience and Remote Sensing*, 38(6): 2489-2505, 2000
- Leip, A., Marchi, G., Koeble, R., Kempen M., Britz W. and Li, C., Linking an economic model for European agriculture with a mechanistic model to estimate nitrogen losses from cropland soil in Europe *Biogeosciences Discussions* 4, 2215-2278, 2007.
- Lissens G., Kempeneers P., and Fierens F., Development of a cloud, snow and cloud shadow mask for VEGETATION imagery,” Proceedings of VEGETATION 2000 Symposium, pp. 3-6, 2000.
- Holben, H., Characteristics of maximum-value composite images from temporal AVHRR data, *International Journal of Remote Sensing* Vol. 7, pp 1417 – 1434, 1986.
- Rembold, F.; Atzberger, C.; Rojas, O.; Savin, I. Using low resolution satellite imagery for yield prediction and yield anomaly detection, *Remote Sensing*, 5(4), 1704-1733, 2013.

Reconstruction of global NDVI time series dataset using a hybrid model – a prototype

Jie ZHOU^{1,3,4}, Li JIA^{1,2}, Massimo Menenti³,

1 State Key Laboratory of Remote Sensing Science, Jointly sponsored by Institute of Remote Sensing and Digital Earth, Chinese Academy of Sciences and Beijing Normal University

2 Alterra, Wageningen University and Research Centre, Wageningen, The Netherlands

3 Technology University of Delft, Delft, The Netherlands

4 University of Chinese Academy of Sciences

Jiali@radi.ac.cn

ABSTRACT - *The Normalized Difference Vegetation Index (NDVI) time series observed by satellites, which reflects the evolution of terrestrial vegetation globally, is inevitably contaminated by clouds, aerosol, snow and ice cover. As such, both a negative bias and gaps often exist in the satellite based NDVI datasets. Intensive studies have been focused on developing methods to reconstruct time series and many of these methods have presented promising applications in some study areas. However, until now there is no consensus on which method outperforms other ones in all conditions. This study intends to develop a hybrid time series reconstruction model to reconstruct MODIS Climate Modelling Grid NDVI data over 13 years (2001-2013). This hybrid time series reconstruction model adaptively self-selects an optimal method among several alternative reconstruction methods with best performance for certain regions. The candidate methods include Harmonic Time Series Analysis (HANTS), Double logistic (DL), Asymmetric Gaussian (AG), Whittaker smoother (WS). The Preliminary result shows that the AG and DL methods outperform the WS and HA method in most regions between 30°N and 60°N as well as most of south Hemisphere, While WS gives best reconstruction performance in very high latitude region (higher than 60°N) as well as tropic forest region. The hybrid reconstruction model provides a framework for adaptive reconstruction model selection in different regions where annual curve of NDVI might have shown different number of gaps and position of gaps in the series. Other methods can be easily included in the hybrid model and the global selection result will benefit by using other NDVI dataset.*

1 INTRODUCTION

Long term archived medium resolution NDVI (Normalized Difference Vegetation Index) time series plays a critical role in climate and environment change related research topics like vegetation dynamics (Menenti et al., 1993; Jia et al., 2011; Andela et al., 2013), land cover or phenology variation (Zhu et al., 2012, Cong et al., 2013). However, as a measurement based on a ratio of satellite observed red band and infrared band reflectance, both of which are susceptible to some non-vegetation signal like atmosphere condition (cloud, ozone or aerosol) or snow cover, immediate NDVI products have less than ideal quality to capture the real vegetation condition (Holben, 1986). An array of methods has been developed to reconstruct contaminated NDVI time series and most of the methods work very well under specific conditions, although none of them can outperform all other methods under all conditions (Hird & Mcdermid, 2009; Musial et al., 2011).

This study developed a hybrid reconstruction model that pursues pixel wise optimal reconstruction

performance among several most popular purebred models. In particular, pixel wise reference series that roughly capture the vegetation seasonality and local noise conditions can be extracted from original NDVI time series and corresponding reliability information. Then the model with best reconstruction performance measured by the difference between reference series and simulated noisy series to which all candidate purebred models are applied will outperformed for a specific pixel.

2 Data & METHODOLOGIES

2.1 NDVI time series dataset and pre-processing

The 16 days 250 meters NDVI time series dataset derived from MODIS sensor i.e. MOD13Q1 from 2001 to 2013 are used in this study. For illustration, we only performed the hybrid model on 1221 globally distributed field sites (Fig.1) that released by Oak Ridge National Laboratory Distributed Active Center (ORNL DAAC). In addition, the pixel reliability layer of the NDVI dataset, which contains ranked values

describing overall quality, was also used to indicate different noise conditions (Roy et al, 2002).

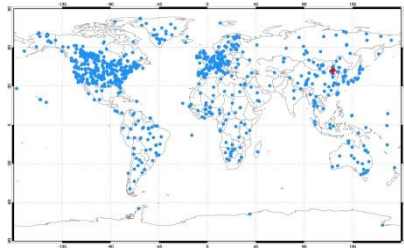


Fig.1 Distribution of MODIS subset field sites.(Provided by ORNL DAAC). The red star is the Duolun_cropland.

2.2 Four candidate remote sensing time series reconstruction methods

As the disturbances like cloud contamination or snow cover normally result in negative bias in NDVI time series, many reconstruction schemes tried to eliminate the bias effects by iterating to the upper envelop of curves (Verhoef, 1996; Jonsson & Eklundh, 2004). During each iteration, one smoothing method (either a curve fitting function or a series filter) is applied to time series where observations with large negative bias compared to previous iteration result are assigned reduced weight. Previous evaluation results indicated that the smoothing methods have large effects on reconstruction performance (Hird&Mcdermid, 2009; Musial et al., 2011). The hybrid model in this study intakes four most popular smoothing methods into the reconstruction framework under the same weight scheme.

2.2.1 Four candidate smoothing methods

Harmonic Analysis (HA) The vegetation growth cycle can be sketched rather well by several low frequency harmonic (or Fourier) components and the phase and amplitudes obtained from the harmonic decomposition are very relevant to the phenology of vegetation, which makes harmonic analysis technique is widely used in remote sensing time series processing and analysis (Menenti et al., 1993; Geerken et al., 2005; Menenti et al., 2010). Harmonic Analysis of NDVI Time Series (HANTS) (Verhoef, 1996) use selected low frequency harmonic components to fitting NDVI time series and remove outlier observation iteratively by assigning zero weight to largely negative biased observations. One of the most critical parameters of harmonic fitting is the number of harmonics to be used. For annual NDVI time series Verhoef (1996) used four harmonics during the fitting. To fit 13 years series, 13 harmonics with periods longer than one year

in addition to 3 harmonics with period shorter than one year has been applied in this study.

Whittaker Smoother (WS) Whittaker proposed the smoother minimizing a cost function that describes the balance between fidelity and roughness (Eilers, 2003). Generally, the quadratic difference between estimates and actual observations is used to measure fidelity while the roughness is expressed as the quadratic difference between successive estimates. This smoother has been successfully applied to processing various remote sensed time series (Atzberger & Eilers, 2011; Verhegghen et al., 2014), which reveals the effectiveness of this model in time series reconstruction.

Asymmetric Gaussian fitting (AG) Asymmetric Gaussian method that uses semilocal Gaussian function to fit asymmetric peaks in NDVI series has been implemented by Jonsson & Eklundh (2004) in TIMESAT program. Beck et al. (2006) found AG function can describe the vegetation dynamics very well. In addition, evaluation result reveals that the AG method outperform Fourier decomposition methods, i.e. HA method. One shortage of AG method is that the coarse seasonality of original series should be predetermined before fitting series to local Gaussian function. In TIMESAT program, a model function consisting three basic harmonic components with up to three order polynomial function is used to determine the number of season (Jonsson & Eklundh, 2004). However the WS smoother is selected to replace the original seasonality identification model in this study as the WS smoother is a flexible filter that doesn't need a priori assumption (Verhegghen et al., 2014).

Double Logistic fitting (DL) Similar to AG method, Double Logistic fitting (DL) has also been implemented in TIMESAT program to fit NDVI series using semi local function (Jonsson and Eklundh, 2004). The only difference is that the Gaussian function has been replaced by double logistic function (Beck et al., 2006).

2.2.2 Iteration to upper envelop

To find upper envelop a 13 years NDVI series, iteration fitting scheme is used in the model, during which each of above introduced smoothing methods are used to fitting NDVI series with predefined weights. Initial weights are set for each observation based on their reliability code. In practical, the weight of observations at reliability level of "Good", "Marginal", "Cloudy", "Snow", and "Filled" are set to 1, 0.5, 0, 0, and 0 respectively. For the k-th iteration, the weight is updated following equation after smoothing the series.

$$W_k = W_{k-1} + \frac{yr_{k-1} - yr_k}{(\max(yr_k) - \min(yr_k))} \quad (1)$$

Where W_k , yr_k are the weight vector and the smoothing result series in the k -th iteration. Under this weighting scheme, negative biased value compared to previous fitting will get decreased weight. To limit the range of the weight, all updated weights larger than 1.0 are set to 1.0. All weights less than 0.01 are set to 0.01 and corresponding observations are replaced by linear interpolation based on remaining observations with higher weights. The iterations will not terminated until either the difference between two successive iterations are very small or the number of iterations exceed 5.

2.3 The framework of the hybrid model

As shown in Fig.1, a 13 years reference series and noisy series are simulated based on the 13 years NDVI series and its reliability series for each pixel. Then both of the reference series and noisy series are reconstructed by all candidate reconstruction models. Finally, the difference between reconstructed reference series and reconstructed reference series in terms of Root Mean Squared Error (RMSE) is calculated for each reconstruction model. The model achieves the smallest RMSE is identified as the best reconstruction model for the pixel. In this context, the global distribution of pixel wise optimal reconstruction model can be expected after running above mentioned procedure over all vegetation covered pixel on earth. To synthesize a reference series for a pixel, the original 13 years NDVI series is reconstructed by WS model as WS model can give success reconstruction over most condition and capture basic vegetation cycles rather well. However, with a strong smooth effect, the WS cannot capture the vegetation variation around peak of NDVI time series, so the weighted residual between reconstruction result and original series are added to recover the peak feature of real vegetation variation.

The key point underlies the simulation of noisy NDVI series and reliability series is the contaminated observations of a pixel can be expected concentrated on similar season every year considering the main contamination source like cloud and snow always occur seasonally. In addition, the biased noise caused by cloud or snow cover in same season can also be considered to equivalent. By splitting all observation into five noise levels, i.e. “Good”, “Marginal”, “Cloudy”, “Snow”, and “filled” based on its reliability information, we assume the noise conditions on same day among different years follows multinomial distribution. The probability distribution for all noise level can be easily derived. Then 10 random reliability scenarios are simulated following the distribution for each pixel and each scenario corresponds to a simulated reliability series in Fig.2. The residual between reference series and original series are

rearranged based on simulated reliability scenarios and the result is added to reference series to construct noisy series. In practical, for a specific day of year, the noise added to reference observation labelled by simulated reliability information should be extracted from the residual in the same period among all years at the same reliability level.

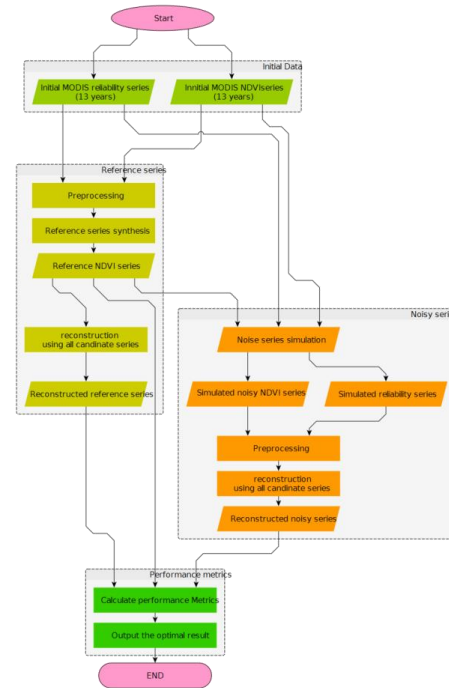


Fig.2 The flowchart of the hybrid model.

3 RESULTS

3.1 The validity of the hybrid model

The evaluation result for Duolun_cropland (42.05 N, 116.67E) is presented in Fig.3, where the reference series can capture the variation of original series very well and the simulated noisy series have the identical feature as the original NDVI series in terms of vegetation variation, biased noise level, and reliability labels based on visual checking. The reliability level maps, which are defined as the yearly superposition of a 13 years reliability label series of original NDVI series and simulated noisy NDVI series, are given in the left panel of Fig.3. The probability distribution map for the reliability level of duolun_cropland site for each composition day (Fig.4) shows clear seasonal variation of different reliability level of the site. In practical, the observations in winter can be contaminated by both snow and cloud with high

probability as very few observations have been labelled as “Good”. Also some problematic observations could be present in summer time because of marginal cloud cover. The observations during spring and autumn are most reliable. The three reliability level maps in Fig.3 for the simulated Scenarios that simulated based on the probability distribution in Fig. 4 are identical to the original reliability level map in terms of intra-annual variation (horizontal direction) but randomly distributed in terms of inter-annual variation (vertical direction). The different noisy scenarios do have different effects on the performance of different reconstruction models. For example, all models give rather good estimates in the winter of 2012 (the last valley of the series) in both scenario 1 and scenario 3. However, in the scenario 2, both HA and DL models give underestimations.

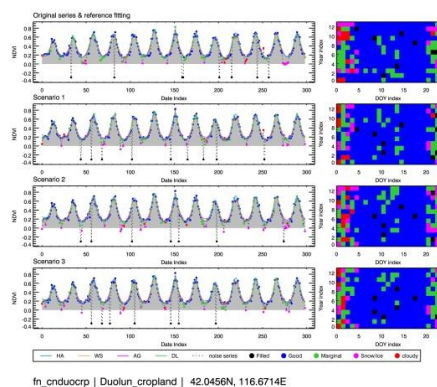


Fig. 3 The reference series and three scenarios for simulated noisy series and their reconstruction results by different candidate reconstruction methods. Left panel gives the yearly superposition of reliability information

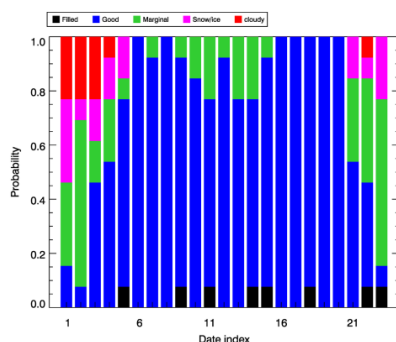


Fig.4. The probability distribution of the quality of NDVI observations from Duolun_cropland site. For each composition day, we assume the quality for different level follow multinomial distribution, with which random noisy series scenarios are simulated.

3.2 The primary reconstruction result of the Hybrid model

After running above mentioned hybrid model procedure over all MODIS subset sites in Fig.1, we get a global distribution of the pixel wise optimized reconstruction map as shown in Fig.5. The color of the filled circle in Fig.5 distinguishes the best reconstruction model while the size estimates the smallest reconstruction error can be expected from all candidate models for the pixel. The AG and DL methods outperform the WS and HA method in most regions between 30°N and 60°N as well as most of south Hemisphere. While WS gives best reconstruction performance in very high latitude region (higher than 60°N) as well as tropic forest region. Nevertheless, the superior performance of WS also can be found over other region over land occasionally. On the other hand, even using optimized reconstruction methods, the smallest reconstruction error on high latitude region and tropic forest region is apparently larger than other region, which can be attributed to heavy contamination from snow and cloud respectively.

4 DISCUSSIONS

As shown in Fig.5, the series of high latitude region between 30N and 60N, whose shape are mainly featured by strong seasonality and rapid green-up and senescence season, can achieve optimal reconstruction result by both asymmetric Gaussian and double logistic function based techniques, which is identical the conclusion of Hird & Mcdermid (2009). However, WS model seems a more stable model as the cases prevailed by WS can be found over global especially for very high latitude region and tropic forest region, which adds value to use WS method to construct a background for reference series globally in this study as well as in the study of Verhegghen et al. (2014). Over very few cases, HA model gets superior performance, which may be improved by selecting more appropriate harmonics for globally and multi – annual time series reconstruction.

In the most of previous work related to evaluate the performance of time series reconstruction models, it is normal to construct artificial noisy scenarios to test the stability of models by adding random uniformly distributed noise or gaps to reference data, during which the levels of noise or the percentage of gaps can be controlled (Hird & Mcdermid, 2009; Michishita et al., 2014). However, not only the levels but the distribution (position) of noise (or gaps) can influence the performance (Musial et al., 2011; Zhou et al., 2012). In this study, the simulation is performed on pixel wised gaps distribution and noise levels, which

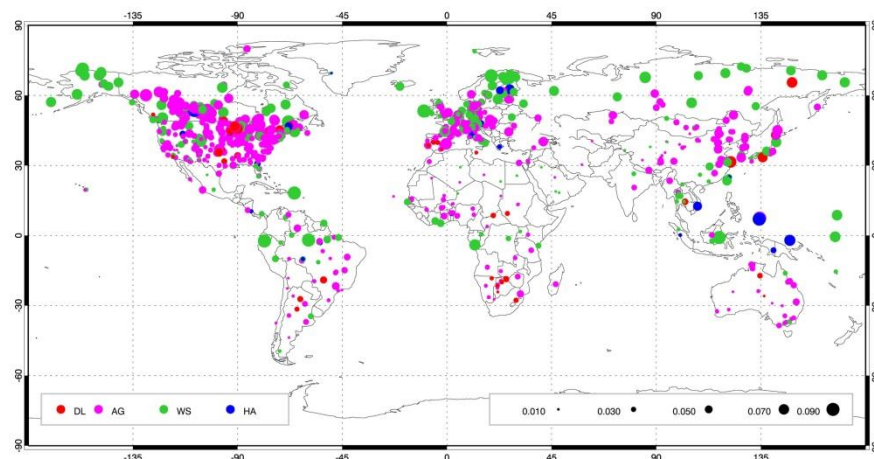


Fig.5. The Evaluation results for 1211 MODIS subset field sites. Coloured circles indicate the optimal reconstruction method for different sites. The smallest reconstruction error among all candidate methods is presented by different size of circles.

can be expected to give more reliable evaluation result.

5 CONCLUSIONS

The study prototyped a hybrid model for long term remote sensing time series reconstruction. The pixel wise optimal reconstruction model is promising to quantify the global distribution of expectable reconstruction error and stretch the distribution of regional optimal reconstruction method. Any new reconstruction models can be easily merged into the framework to evaluate their optimal application region and their ability to improve available models. More candidate reconstruction methods and more performance metrics should be added to the hybrid framework in the future work.

ACKNOWLEDGEMENT.

This study was jointly supported by the CAS/SAFEA International Partnership Program for Creative Research Teams (Grant nr. KZZD-EW-TZ-09) and the National Science Foundation of China projects (Grants nr. 41101331 and 9102500). The first author is financially supported for his PhD research by the China Scholarship Council with the project reference number of 201304910235.

REFERENCES

- Andela, N., Y. Y. Liu, A. I. J. M. van Dijk, R. A. M. de Jeu, and T. R. McVicar. 2013. "Global Changes in Dryland Vegetation Dynamics (1988–2008) Assessed by Satellite Remote Sensing: Comparing a New Passive Microwave Vegetation Density Record with Reflective Greenness Data." *Biogeosciences* 10 (10): 6657–76. doi:10.5194/bg-10-6657-2013.
- Atzberger, Clement, and Paul H. C. Eilers. 2011. "Evaluating the Effectiveness of Smoothing Algorithms in the Absence of Ground Reference Measurements." *International Journal of Remote Sensing* 32: 3689–3709. doi:10.1080/01431161003762405.
- Beck, Pieter S. A., Clement Atzberger, Kjell Arild Høgda, Bernt Johansen, and Andrew K. Skidmore. 2006. "Improved Monitoring of Vegetation Dynamics at Very High Latitudes: A New Method Using MODIS NDVI." *Remote Sensing of Environment* 100: 321–34. doi:10.1016/j.rse.2005.10.021.
- Cong, Nan, Tao Wang, Huijuan Nan, Yuecun Ma, Xuhui Wang, Ranga B. Myneni, and Shilong Piao. 2013. "Changes in Satellite-Derived Spring Vegetation Green-up Date and Its Linkage to Climate in China from 1982 to 2010: A Multimethod Analysis." *Global Change Biology* 19 (3): 881–91. doi:10.1111/gcb.12077.
- Geerken, R., B. Zaitchik, and J. P. Evans. 2005. "Classifying Rangeland Vegetation Type and Coverage from NDVI Time Series Using Fourier Filtered Cycle Similarity." *International Journal of Remote Sensing* 26 (24): 5535–54. doi:10.1080/01431160500300297.
- Hird, J. N., and G. J. McDermid. 2009. "Noise Reduction of NDVI Time Series: An Empirical

- Comparison of Selected Techniques.” *Remote Sensing of Environment* 113 (January): 248–58. doi:DOI 10.1016/j.rse.2008.09.003.
- Holben, B. N. 1986. “Characteristics of Maximum-Value Composite Images from Temporal Avhrr Data.” *International Journal of Remote Sensing* 7 (November): 1417–34.
- Jia, L., H. Shang, G. Hu, and M. Menenti. 2011. “Phenological Response of Vegetation to Upstream River Flow in the Heihe Rive Basin by Time Series Analysis of MODIS Data.” *Hydrology and Earth System Sciences* 15: 1047–64.
- Jonsson, P., and L. Eklundh. 2004. “TIMESAT - a Program for Analyzing Time-Series of Satellite Sensor Data.” *Computers & Geosciences* 30 (October): 833–45. doi:DOI 10.1016/j.cageo.2004.05.006.
- M. Menenti, L. Jia. 2010. “Analysis of Vegetation Response to Climate Variability Using Extended Time Series of Multispectral Satellite Images.” In *Remote Sensing Optical Observations of Vegetation Properties*, edited by F. Maselli, 131–63. Research Signpost.
- Menenti, M., S. Azzali, W. Verhoef, and R. van Swol. 1993. “Mapping Agroecological Zones and Time Lag in Vegetation Growth by Means of Fourier Analysis of Time Series of NDVI Images.” *Advances in Space Research* 13: 233–37. doi:10.1016/0273-1177(93)90550-u.
- Musial, J. P., M. M. Verstraete, and N. Gobron. 2011. “Technical Note: Comparing the Effectiveness of Recent Algorithms to Fill and Smooth Incomplete and Noisy Time Series.” *Atmos. Chem. Phys.* 11 (15): 7905–23. doi:10.5194/acp-11-7905-2011.
- Roy, D. P., J. S. Borak, S. Devadiga, R. E. Wolfe, M. Zheng, and J. Descloitres. 2002. “The MODIS Land Product Quality Assessment Approach.” *Remote Sensing of Environment* 83 (November): 62–76.
- Verhegghen, Astrid, Sophie Bontemps, and Pierre Defourny. 2014. “A Global NDVI and EVI Reference Data Set for Land-Surface Phenology Using 13 Years of Daily SPOT-VEGETATION Observations.” *International Journal of Remote Sensing* 35 (7): 2440–71. doi:10.1080/01431161.2014.883105.
- Verhoef, W. 1996. *Application of Harmonic Analysis of NDVI Time Series (HANTS)*. Fourier Analysis of Temporal NDVI in the Southern African and American Continents. DLO Winand Staring Centre, Wageningen, TheNetherlands.
- Zhou, Jie, Li Jia, Guangcheng Hu, and Massimo Menenti. 2012. “Evaluation of Harmonic Analysis of Time Series (HANTS): Impact of Gaps on Time Series Reconstruction.” In , 31–35. doi:10.1109/eorsa.2012.6261129.
- Zhu, Wenquan, Hanqin Tian, Xiaofeng Xu, Yaozhong Pan, Guangsheng Chen, and Wenpeng Lin. 2012. “Extension of the Growing Season due to Delayed Autumn over Mid and High Latitudes in North America during 1982–2006.” *Global Ecology and Biogeography* 21 (2): 260–71. doi:10.1111/j.1466-8238.2011.00675.x.

Rational design of sample location by Geostatistics for crop sown area estimation

Di Wang^{1,2}, Zhongxin Chen^{1,2*}, Qingbo Zhou^{1,2}, Jia Liu^{1,2}

1. Key Laboratory of Agri-informatics, Ministry of Agriculture, Beijing 100081, P.R.China

2. Institute of Agricultural Resources and Regional Planning, Chinese Academy of Agricultural Sciences, Beijing 100081, P.R.China

Email addresses: wangdicaas@126.com; *Corresponding author: chenzhongxin@caas.cn

ABSTRACT – Rational design of sample locations plays an important role for improving the accuracy of population extrapolation and decreasing the cost of survey sampling. Using remote sensing, Geographic Information Systems and traditional sampling methods combined with Geostatistics, this study's aims were to analyze the spatial correlation and variability of sampling units, quantitatively confirm the correlation threshold of sampling units, and sequentially optimize the samples layout. Mengcheng County in Anhui Province, China was chosen as the study area and winter wheat planting acreage as the study object in this paper. In order to evaluate the design effect of samples layout, simple random sampling method is selected as the control treatment. The experimental results demonstrate that, the variability of the proportion that winter wheat acreage accounts for that of one sampling unit (PWS) increases with sampling unit size increasing. Coefficient of variation (CV) of PWS varies from 32.75% to 43.46% at 8 sampling unit size levels; Spatial correlation thresholds of PWS increase with sampling unit size increasing; The relative error and CV of population extrapolation that samples layout is optimized are obviously less than those of simple random sampling method, when sampling unit size is small (500m×500m~2000m×2000m); Although the relative error and CV are not reduced after optimized design of sample locations, they occur an obvious decrease on sample size, when sampling unit size is larger (2500m×2500m~4000m×4000m). In this way, this research can provide a solution for improving the spatial sampling efficiency to estimate crop planting acreage.

1 INTRODUCTION

Sample location is a key factor for the formulation of spatial sampling scheme (Wanger 1995; Banjevic 2004; Nunes 2006). It has played a very important role that optimizing the samples layout for improving the representativeness of samples versus population and the accuracy of population extrapolation, and reducing the sampling cost (Warrick and Myers 1987; Van Groenigen 2000; Yan and Minsker 2006; Zimmerman 2006). In previous studies, simple random or systematic sampling is often used to formulate sample locations for estimating crop acreage at the large regional scale, e. g. simple random sampling is employed by National Agricultural Statistics Service (NASS), The United States (US) to make the layout formulation of samples units drawn at the second sampling stage, in order to monitor and estimate the main crop planting acreage on a national scale (Boryan et al 2011). Systematic sampling is served as sample locations of every sampling stage in Land Use/Cover Area Frame Statistical Survey (LUCAS) project, launched by European Union (EU), for estimating the main crop acreage in 15 member countries of EU (Delince 2001; Jacques and Gallego 2006; Gallego and Bamps 2008). In terms of the domestic studies on spatial sampling survey for crop area estimation, traditional sampling methods (e.g. stratified sampling,

systematic sampling and simple random sampling) are often combined with "3S" (RS, GIS and GPS) technology to formulate the spatial sampling scheme (Zhou 1996; Zhou et al 1998; Zhou, Yu and Zeng 1998; Chen et al 2000; Jiao and Yang 2002; Jiao, Yang and Pei 2002; Yang 2007; Wang, Zhou and Liu 2008; Zhang et al 2009; Wang et al 2012), however, simple random and systematic sampling are still used to design samples layout in these schemes. Although it has the advantages of simple and feasible that using simple random and systematic sampling to formulate samples layout, since the spatial correlation and variability of sampling units are not taken into account in two sample locations schemes, sequentially, the design reasonability using the two patterns is still poor and the accuracies of population inference are not high (Wang, Zhou and Liu 2012) (e. g. samples units are not all independent of each other, when simple random sampling method is used to design samples layout; sampling intervals are not reasonably defined, when systematic sampling method is used to allocate samples units in space).

Concerning these issue mentioned above, the objective of this paper is to present a method that uses remotely sensed data to estimate a semivariogram of the proportion that winter wheat acreage accounts for that of one sampling unit (PWS). The semivariogram is then employed to determine the spatial correlation

threshold of sampling units. Furthermore, the threshold is served as the sampling interval to optimize the sample location, following the rule that samples should be independent each other. In order to evaluate the results of optimization of sample location, simple random sampling is selected as the control treatment in this study.

2 MATERIALS AND METHODS

2.1 Technical route

The technical route consist of 5 steps: the first step is preparation of basic data used to formulate the spatial sampling scheme. The data include basic geographic information data, spatial distribution data of winter wheat of the study area; the second step is preliminary scheme of samples selection. The shape, size of sampling units and sampling method is formulated to evaluate the spatial correlation and variability of them in this step; the third step is calculation of spatial correlation threshold of sampling units. Variogram model is used to determinate the threshold (that is the range of variogram model), based on the sampled units drawn using simple random sampling method; the fourth step is optimization of samples layout. The sampled units are allocated in the systematic isometric pattern in space, and the correlation threshold is selected as the sampling interval; the last step is the evaluation of samples layout. The efficiency of population extrapolation is quantitatively evaluated after the samples layout is optimized, and simple random sampling is used as control treatment.

2.2 Study area

Mengcheng County is located in the northwest of Anhui Province, China (32°55'29" ~ 32°29'64" N latitude, 116°15'43" ~ 116°49'25" E longitude), with a total land area of 2091 km². It includes cultivated land area of 1.53×10⁵ hm² in the total land area. There is a sub-humid continental monsoon climate, and four seasons are distinct in Mengcheng County. The annual average temperature is 14.7°C, the average frost-free period is 216 days, the average annual precipitation is 872.4mm. Agricultural productivity is given priority with food crops, and cash crop is complementary. Food crops include wheat, maize, rice, soybean and cotton. Winter wheat is the most important food crop in Mengcheng County, and its planting acreage accounts for 70% of the total cultivated land of the study area.

2.3 Data

The experimental data consist of 2 parts: 1) Basic geographic information data. It refers to administrative boundary data of Mengcheng County (the scale is

1:250000, vector format); 2) The spatial distribution data of crop, it refers to spatial distribution data of winter wheat in 2009. It is derived from ALOS AVNIR-2 image (number: 162652930, date: 12-02-2009, spatial resolution: 10m) Fig 1 shows the spatial distribution of winter wheat of the study area in 2009.

2.4 Preliminary scheme of samples selection

Some samples units are needed to be drawn for calculating the variogram, because the spatial correlation and variability of sampling units can be evaluated by variogram model. Considering that simple random sampling method has the advantages of simple and feasible in the determination of sample size, sample selection and population inference, it is used to select the preliminary sample units for calculating the variogram. In addition, simple random sampling method is also selected as control treatment to evaluate the efficiencies of population extrapolation, based on the sampled units that the layout is optimized.

2.4.1 The design of sampling units

Square grid is selected as the shape of the sampling units to analyze the spatial correlation and variability of them. In addition, the sampling unit size is formulated into 8 levels to analyze the effect of the unit scale on spatial variability of them, and the interval of every level is 500m, 8 kinds of sampling unit size are 500m×500m, 1000m×1000m, 1500m×1500m, 2000m×2000m, 2500m×2500m, 3000 m×3000m, 3500m×3500m, 4000m×4000m, respectively. Then, the study area is divided by the formulated sampling unit size to construct the sampling frame. Furthermore, the winter wheat spatial distribution data are overlapped on the 8 sampling frame, and the winter wheat planting acreage proportion within the sampling units are calculated using GIS software as the population unit observation.

2.4.2 Preliminary selection of samples

(1) Sample size

Sample size is calculated according to Equations (1) - (4) (see Du [2005] and Li [2006]).

$$n_o = \left(\frac{t}{r}\right)^2 \frac{S^2}{Y^2} \quad (1)$$

$$n = \frac{n_o}{1 + \frac{n_o}{N}} \quad (2)$$

$$\bar{Y} = \frac{1}{N} \sum_{i=1}^N Y_i \quad (3)$$

$$S^2 = \frac{1}{N} \sum_{i=1}^N (Y_i - \bar{Y})^2 \quad (4)$$

Where n_0 is the initial sample size; t is the sampling probability degrees, when the confidence level is 95%, t is equal to 1.96; r is the relative error, 10% is used in the study; S^2 is the variance of all of population units; \bar{Y} is the population mean; n is modified sample size, when $n_0/N > 0.05$, n_0 is modified according to Equation (2); N is the population size; Y_i is winter wheat planting acreage proportion in the i -th population unit.

(2) Sample selection

The pseudo-random number method is used to draw the samples, after sample size is calculated according to the Equations (1)-(4). The process of sample selection is as follows: firstly, all population units are encoded in 1- N order using ArcGIS9.3 software; secondly, pseudo-random number with same amount as sample size are generated by SPSS software; Lastly, when the code of a population unit is same with the random number generated by SPSS, then the population unit is drawn as a sample.

(3) Sample observation

Samples observations are obtained with ArcGIS software calculating winter wheat sown area in the sampled units, when spatial distribution data of winter wheat sown area (retrieved by ALOS image) is overlapped with sampled units in the sampling frame.

(4) Population extrapolation and error estimation

Simple estimator is used to extrapolate population and estimate error, the equations used to estimate population values and sampling error can be found in (Du 2005) and (Li 2006). Relative error (r) and coefficient of variation (CV) are selected as index to quantitatively evaluate the efficiency of spatial sampling scheme for winter wheat planting acreage estimation.

2.5 Spatial correlation threshold of sampling units

The spatial correlation threshold is determined by analyzing the variability of sampling units using the variogram model. The procedures are as follows: firstly, the calculation of (x, y, z) coordinates of sampled units. (x, y) coordinates of sampled unit (that is the centre of the sampled unit) are calculated by GIS software, and the winter wheat planting acreage proportion within the sampled unit is selected as z coordinate; secondly, the (x, y, z) coordinates of sampled units are imported into GS+7.0 software, and then 4 kinds of variogram theoretical models (linear, spherical, exponential and Gaussian) are used to simulate the spatial correlation and variability of sampling units; finally, the optimal variogram model is constructed, based on the rule that the Residual Sum of

Squares (RSS) should be minimum. Consequently, the spatial correlation threshold can be determined using the optimal model.

2.6 Optimization method of samples layout

Considering the principle that sampling units should be independent each other in the tradition sampling theory, the layout of sampled units drawn by simple random sampling method is adjusted to meet the principle, and the spatial correlation threshold are selected as the sampling interval in space. The formulation process of samples layout is as follows: (1) One sampled unit is randomly drawn from the sampling frame, and the unit is served as a start point; (2) The rest of sampled units are drawn along the horizontal and vertical direction, and the spatial interval just is the threshold; (3) Simple random sampling is still used to extrapolate population and estimate errors, after the sample location is optimized.

3 RESULTS AND ANALYSIS

3.1 Descriptive statistical characteristics of PWS

Table 1 shows the characteristic of PWS at 8 sampling unit sizes. It is found that, although the change ranges of PWS are still large in 8 kinds of sampling frame, the CV varies from 33.38% to 43.46%, belongings to medium variation levels. Meanwhile, CV gradually increases with the sampling unit size increasing. It indicates that the variability of PWS increases with the sampling unit size increasing. In addition, it is also found that, although the sampling unit scales have a large change range, however, the changes of sample size are less than those of the sampling unit scale.

3.2 Normal distribution test

Normal distribution test is conducted to evaluate whether the data of PWS meet the second-order stationary hypothesis, consequently, the spatial correlation and variability of PWS can be analyzed by Geostatistics theory. Skewness and Kurtosis coefficient, that can be found Geostatistics module of GIS software, are used to test whether PWS meet the normal distribution at 8 sampling frames. Table 2 presents the results of normal distribution test of PWS without any conversion in 2009. It is found that PWS has a right skewed effect (skewness coefficient is less than 0) in 8 sampling frames, and most kurtosis coefficient of PWS are greater than those of normal distribution, therefore, the initial data of PWS need to make a conversion process to meet the normal distribution. Arcsine transformation method is used to process the initial data of PWS in this study. Table 2 shows the results of skewness and Kurtosis coefficient

of PWS that are processed by arcsine transformation method. It is found that, compared the initial data of PWS, the skewness and Kurtosis coefficient of PWS processed by arcsine transformation method nearly

meet normal distribution(skewness coefficient varies from -0.011to -0.084; and Kurtosis coefficient varies from 2.935 to 3.194).

Table 1. Statistical characteristics of PWS at 8 kinds of sampling unit sizes (based on the winter wheat spatial distribution data in the study area in 2009)

Sampling unit size (m×m)	Population size	Sample size	Minimum (%)	Maximum (%)	Mean (%)	Standard deviation (%)	Coefficient of variation (%)
500×500	8899	47	0.00	100.00	67.93	22.67	33.38
1000×1000	2292	41	0.00	99.65	65.54	22.70	34.63
1500×1500	1060	46	0.00	97.24	63.03	22.36	35.48
2000×2000	606	46	0.00	92.31	61.73	22.22	36.00
2500×2500	401	53	0.00	90.32	59.41	22.83	38.42
3000×3000	284	50	0.00	89.68	58.25	23.27	39.95
3500×3500	215	53	0.00	88.67	56.54	24.36	43.09
4000×4000	167	50	0.00	85.49	55.73	24.22	43.46

Table 2. Statistic distribution test of PWS at 8 kinds of sampling unit sizes (based on the winter wheat spatial distribution data in the study area in 2009)

Sampling unit (m×m)	Normal distribution test		Normal distribution test after a transformation of arcsine	
	Coefficient skewness	ofCoefficient of kurtosis	Coefficient skewness	ofCoefficient of kurtosis
500×500	-0.804	3.083	-0.011	2.985
1000×1000	-1.124	3.940	-0.052	3.164
1500×1500	-1.243	3.915	-0.084	3.194
2000×2000	-1.193	3.695	-0.081	3.057
2500×2500	-1.128	3.306	-0.074	2.935
3000×3000	-1.036	3.105	-0.076	2.989
3500×3500	-0.962	2.807	-0.072	2.957
4000×4000	-0.945	2.768	-0.073	2.942

3.3 Analysis of spatial variability of PWS

The variogram function is calculated and the scatter diagram of $\gamma(h) \sim h$ is displayed using the GS+7.0 software, based on the sampled units drawn by simple random sampling method in 8 kinds of sampling frames, the optimal variogram model and its parameters are found by comparing the RSS and R^2 of different models. The results of the optimal variogram model and corresponding parameters can be seen in Table 3. It is found that, the spatial variability of PWS can be simulated by Gaussian model very well at the different sampling unit size, except the size of 1000m×1000m and 2500 ×2500m. According to the results of RSS and R^2 (RSS varies from 0.0003 to 0.0023, R^2 varies from 0.759 to 0.943), it indicates that the variogram model can simulate the spatial variability characteristic of PWS. It is also found that there is a very strong spatial correlation among PWS at 8 kinds

sampling frames, due to the fact that the nugget coefficients vary from 0.13% to 9.17%, less than 25%. Furthermore, the spatial correlation of PWS is mainly dominated by structural factors (e. g. climate, topography, agrotype and so on), not are random factors (e. g. irrigation, tillage measures and soil improvement), in terms of the change of nugget coefficients. In addition, it can be also found that the range (A) gradually increases with sampling unit size increasing, which indicates that sampling unit scale has a certain effect on the spatial correlation scope of PWS.

3.4 Analysis on optimization results of sample location

The ultimate goal of optimizing the samples layout is to improve the accuracy of population extrapolation and reduce the sampling cost. In order to quantitatively evaluate the efficiency of spatial sampling survey that the samples layout has been

optimized, the simple random sampling method is selected as the control treatment, Table 4 shows the results of relative error, CV and sample size using spatial sampling scheme for winter wheat planting acreage estimation, after the samples layout is optimized. It is found that, the relative error and CV of population extrapolation that samples layout is optimized are obviously less than those of simple random sampling method at the same sample size, while sampling unit size is small (500m×500m~2000m×2000m); Compared those of simple random sampling method, although the relative error and CV are not decreased after optimized design

of sample location, there is an obvious decreasing on sample size, when sampling unit size is larger (2500m×2500m~4000m×4000m). Using the sampling unit size of 1000 m×1000 m and 2500 m×2500 m as an example, Fig 2 shows the initial and optimized samples layout of spatial sampling scheme for estimating winter wheat planting acreage of the study area in 2009. It can be found that the sampled units drawn by simple random sampling method often occur in a clustering pattern, consequently, the spatial correlation can be found among the sampled units, however, the problem cannot be found among the sampled units that the layout has been optimized.

Table 3. Semivariogram model of PWS and its corresponding parameters at 8 kinds of sampling unit sizes (based on the winter wheat spatial distribution data in the study area in 2009)

Sampling unit size (m×m)	Optimum model	Step length (m)	Nugget	Sill	Nugget coefficient (%)	Range (m)	RSS	R ²
500×500	Gaussian	500	0.0023	0.0433	5.31	6131	0.0018	0.762
1000×1000	Exponential	1000	0.0021	0.0542	3.87	6970	0.0023	0.759
1500×1500	Gaussian	1500	0.0011	0.0357	3.08	7156	0.0013	0.822
2000×2000	Gaussian	2000	0.0001	0.0475	0.21	5955	0.0012	0.826
2500×2500	Spherical	2500	0.0001	0.0464	0.22	7370	0.0015	0.776
3000×3000	Gaussian	3000	0.0001	0.0746	0.13	8175	0.0008	0.765
3500×3500	Gaussian	3500	0.0040	0.0436	9.17	11292	0.0006	0.907
4000×4000	Gaussian	4000	0.0001	0.0388	0.26	12470	0.0003	0.943

Table 4. Results of population extrapolation and error analysis of winter wheat planting acreage before and after reasonable formulation of samples layout in 2009

Sampling unit size (m×m)	Simple random sampling			Equi-spaced sample location		
	Sample size	Relative error (%)	CV (%)	Sample size	Relative error (%)	CV (%)
500×500	47	9.81	10.67	47	1.25	4.88
1000×1000	41	10.64	11.30	41	3.81	2.95
1500×1500	46	10.34	9.48	46	2.80	4.63
2000×2000	46	12.29	11.27	46	4.82	4.51
2500×2500	53	10.48	10.37	45	6.34	6.72
3000×3000	50	11.22	10.09	33	7.13	8.01
3500×3500	53	9.82	9.61	15	9.53	9.18
4000×4000	50	10.12	10.14	12	9.81	9.82

4 CONCLUSIONS

The experiments on optimization of spatial sampling layout are conducted to improve the efficiency of sampling survey for crop planting acreage estimation. Mengcheng County was selected as the study area and winter wheat planting acreage as the study object. Geostatistics, “3S” technology and traditional sampling method are used in this study. Simple random sampling method is selected as the control treatment, relative error, CV and sample size are used as the index to evaluate the efficiency of

spatial sampling scheme that the sample location has been optimized. The experimental results demonstrate as follows:

- (1) The variability of PWS increases with the sampling unit scale increasing, based on the descriptive statistical analysis. The CV of PWS varies from 33.38% to 43.46% at 8 kinds of sampling unit scales, belonging to the medium degree of variation.
- (2) There is a very strong spatial correlation among PWS of all sampling units in 8 kinds of sampling frames. The spatial correlation of PWS is mainly

- dominated by structural factors. Furthermore, the spatial correlation threshold gradually increases with the sampling unit scale increasing.
- (3) The relative error and CV of population extrapolation that samples layout is optimized are obviously less than those of simple random sampling method at the same sample size, while sampling unit size is small

(500m×500m~2000m×2000m); Compared those of simple random sampling method, although the relative error and CV are not decreased after optimized design of sample location, there is an obvious decreasing on sample size, when sampling unit size is larger (2500m×2500m~4000m×4000m).

Acknowledgements

This study was supported by National Nonprofit Institute Research Grant of CAAS (IARRP-2014-17); National Natural Science Foundation of China (41001247) and EU FP7 project (270351).

References

- Banjevic, M. 2004. Optimal network designs in spatial statistics. 114. California: Stanford University.
- Boryan, C., Z. W. Yang, R. Mueller, and M. Craig. 2011. Monitoring US agriculture: the US Department of Agriculture, National Agricultural Statistics Service, Cropland Data Layer Program. *Geocarto International* 26(5): 341-358.
- Chen, Z. X., H. Q. Liu, Q. B. Zhou, G. X. Yang, and J. Liu. 2000. Sampling and scaling scheme for monitoring the change of winter wheat acreage in China. *Transactions of the Chinese Society of Agricultural Engineering* 16(5): 126-129.
- Delince, J. A. 2001. European approach to area frame survey." Processing of the Conference on Agricultural and Environmental Statistical Applications, Rome, 1-10.
- Du, Z. F. 2005. *Sampling Techniques and Practices*. Beijing: Tsinghua University Press.
- Gallego, F. J., and C. Bamps. 2008. Using CORINE land cover and the point survey LUCAS for area estimation. *International Journal of Applied Earth Observation and Geoinformation* 10(4) : 467-475.
- Jacques, P., and J. Gallego. 2006. The LUCAS 2006 project-A new methodology. Joint Research Centre, European Commission. Available on-line: <http://mars.jrc.it/Bulletins-Publications/The-LUCAS-2006-project-A-new-methodology>.
- Jiao, X. F., and B. J. Yang. 2002. Design of sampling method for cotton area estimation using remote sensing at a national level. *Transactions of the Chinese Society of Agricultural Engineering* 18(4): 168-171.
- Jiao, X. F., B. J. Yang, and Z. Y. Pei. 2006. Paddy rice area estimation using a stratified sampling method with remote sensing in China. *Transactions of the Chinese Society of Agricultural Engineering* 22(5): 105-110.
- Li, J. C. 2006. *Application of Sampling Techniques*. Beijing: Science Press.
- Nunes, L. M. 2006. "Optimal estuarine sediment monitoring network design with simulated annealing." *Journal of Environmental Management* 78(3): 294-304.
- Van Groenigen, J. W. 2000. The influence of variogram parameters on optimal sampling schemes for mapping by kriging. *Geoderma* 97(3): 223-236.
- Wang, D., Q. B. Zhou, and J. Liu. 2008. Studies on experiment of optimizing of space sampling frame and sampling basic elements of crop areas. *Chinese Journal of Agricultural Resources and Regional Planning* 29(4): 9-15. (in Chinese)
- Wang, D., Q. B. Zhou, and J. Liu. 2012. A review on spatial sampling for crop area estimation. *Chinese Journal of Agricultural Resources and Regional Planning* 33(2): 9-14. (in Chinese)
- Wang, D., Q. B. Zhou, Z. X. Chen, J. Liu, and H. Deng. 2012. Spatial sampling method for estimating winter wheat sown area. *Transactions of the Chinese Society of Agricultural Engineering* 28(10): 177-184.
- Wanger, B. J. 1995. Sampling design methods for groundwater modeling under uncertainty. *Water Resources Research* 31(10): 2581-2591.
- Warrick, A. W., and D. E. Myers. 1987. Optimization of sampling locations for variogram calculations. *Water Resources Research* 23(3): 496-500.
- Yan, S. Q., and B. Minsker. 2006. Optimal groundwater remediation design using an Adaptive Neural Network Genetic Algorithm. *Water Resources Research* 42(5): 316-322.
- Yang, X. Q., W. Q. Zhu, Y. Z. Pan, and B. Jia. 2007. Spatial sampling design for crop acreage estimation. *Transactions of the Chinese Society of Agricultural Engineering* 23(12): 150-155.
- Zhang, J. S., Y. Z. Pan, T. G. Hu, L. Q. Chen, and Y. S. Dong. 2009. Analysis of influence factors about space sampling efficiency of winter wheat planting area. *Transactions of the Chinese Society of Agricultural Engineering* 25(8): 169-173.

- Zhou, H. M. 1996. A procedure of sampling investigation of paddy area. *Southwest China Journal of Agricultural Sciences* 7(3): 100-105. (in Chinese)
- Zhou, H. M., G. N. Yu, and L. X. Zeng. 1998. Application of sampling and stratified monitoring techniques in agricultural resources investigation using satellite remotely-sensed data. *Southwest China Journal of Agricultural Sciences* 11(3): 77-83. (in Chinese)
- Zhou, H. M., L. X. Zeng, G. N. Yu, and C. Zhang. 1998. A study on the technic methods of the macro-monitoring of the agricultural land resources in Sichuan Province by using satellite remote sensing. *Journal of Natural Resources* 3(1): 73-76. (in Chinese)
- Zimmerman, D. L. 2006. Optimal network design for spatial prediction, covariance parameter estimation, and empirical prediction. *Environmetrics* 17(6): 635-652.

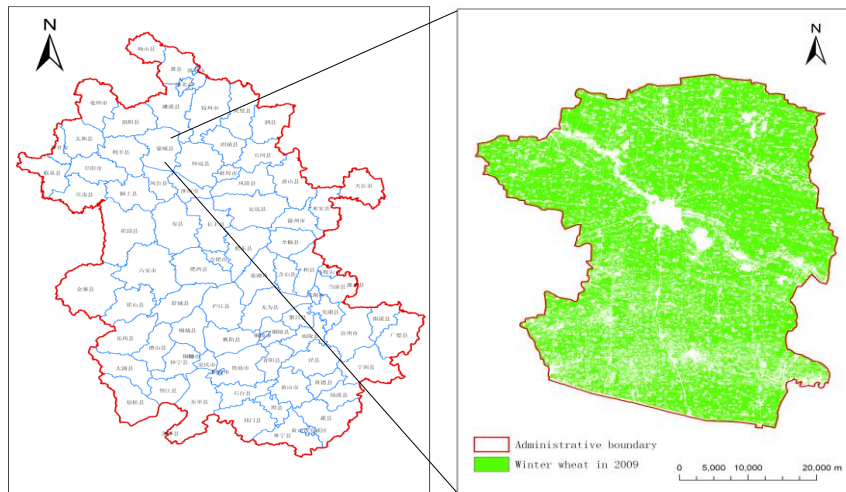


Fig 1. Spatial distribution of winter wheat in Mengcheng County in 2009

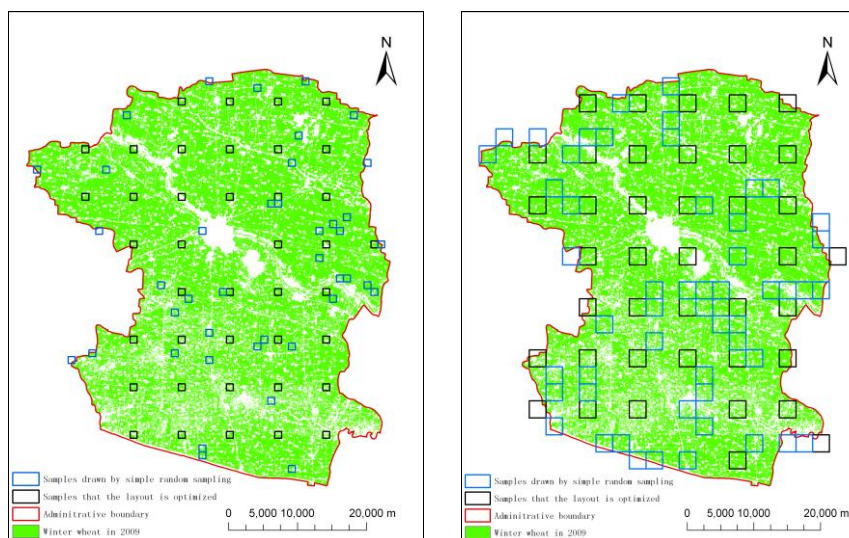


Fig 2. Samples layouts of winter wheat planting acreage before and after optimized formulation in the study area in 2009

Towards Buildings' Automatic Change Detection (Build-ACD) using VHSR Satellites Images: Application to Tetuan (Morocco)

O. Benarchid¹, N. Raissouni¹ and J.A. Sobrino²

¹ *RS&AID Laboratory, National School for Applied Sciences of Tetuan, University of Abdelmalek Essaadi, Mhaneech II. B.P. 2222, 93000 Tetuan, MOROCCO.*

² *GCU Unit, IPL Laboratory, Parque Científico, Universitat de València, C/ Catedrático José Beltran nº 2, 46980 Paterna (Valencia) SPAIN.*

obenarchid@remotesensing.ma; nraissouni@uae.ma; sobrino@uv.es

ABSTRACT- Nowadays, mapping agencies need to update their topographic and information systems databases in order to draw: i) urban planning (e.g., urban sprawl, road networks, etc.), and ii) environmental planning (e.g., ecological corridors, forest change, etc.). Until now, the update is achieved manually by using photogrammetric restitution and ground survey. This work is boring, time consuming, and does not satisfy the user's update frequency need. In this context, since 1999, Very High Spatial Resolution (VHSR) satellites images (e.g., IKONOS, QuickBird, GeoEye, and recently Pléiades) are interesting tools to satisfy the needs of both scientific community and decision makers in local authorities. Accordingly, the number of non-experts in using VHSR images is increasing, and the requirements of automated processing using less parameters is an expanding need. In the present research, we propose a method to automatically detect new buildings; we call Buildings' Automatic Change Detection (Build-ACD) which kernel is essentially and partially based on the Mean-shift Segmentation Parameters Estimator (MSPE) method for automatic selection of segmentation parameters. Build-ACD method has been applied and tested using GeoEye VHSR satellites images corresponding to Tetuan city (Northern Morocco).

1 INTRODUCTION

Nowadays, the availability of updated maps is essential for many applications. For example, having a frequent updating of urban planning is crucial to plan the sustainable development of a city. A recent representation of the road network allows solving the traffic jamming problems; knowing precisely the location of residential areas allows optimizing transport in underserved areas. Urban pollution can be better understood and controlled, thanks to an enhanced map of the altitude information of buildings.

In a very different context, that of natural disasters, the rapid production of maps of damage - in terms of infrastructure and destroyed buildings - is a key element in order to provide quick assistance to the people and allow effective rehabilitation.

For this, mapping agencies need to update their Vector Databases (VDB) in order to make decisions about: i) urban planning (e.g. urban sprawl, road networks, etc.), and ii) environmental planning (e.g. ecological corridors, forest change, etc.) (Hanson, Puissant, and Wolff, 2013).

Until now, the update is achieved manually by using photogrammetric restitution and ground survey. This work is boring, expensive, time consuming, and does not satisfy the user's update frequency need (Holland, Boyd, and Marshall, 2006; Hanson and

Wolff, 2010). Therefore, the requirements of semi-automatic/automatic updating process is an expanding need (Baltsavias, 2004).

Two principal objects of interest are identified by the data producers and the scientific community: roads and buildings which need the most frequent updates (Bouziani, Goïta, and He, 2010; Hanson and Wolff, 2010).

Despite all the solutions proposed, the automatic change detection remains an open matter of research (Baltsavias, 2004; Holland, Boyd, and Marshall, 2006; Bouziani, Goïta, and He, 2010).

The authors of (Knudsen and Olsen, 2003) propose a change detection method of buildings using scanned aerial photographs and VDB. First, they classified the scanned aerial images. Then, they overlaid the classification result with the VDB to detect the new buildings.

Holland, Boyd, and Marshall (2006) examine the potential of using VHSR satellite images (IKONOS and QuickBird) in the updating of VDB. The results have shown that VHSR images can play an important role in the update process.

In (Bouziani, Goïta, and He, 2010), the authors proposed a method for change detection of buildings using VHSR images and existing VDB. First, from the existing VDB, some change detection rules are defined. Then, the image is segmented. Thereafter, the

segmented image is analyzed in order to identify the change of buildings.

In (Cao, Liu, and Shang, 2014), an automatic change detection method based on level set evolution in remote sensing images is proposed. The problem is formulated as a segmentation issue to discriminate the changed class from the unchanged class in the difference images.

In the present research, we have proposed a method to automatically detect new buildings; we call Buildings' Automatic Change Detection (Build-ACD) which kernel is essentially and partially based on the Mean-shift Segmentation Parameters Estimator (MSPE) method for automatic selection of segmentation parameters.

2 STUDY AREA AND DATASET

This study is applied in the region of Tetuan city situated in northern Morocco (Figure 1).

However, two rural areas characterized by fields, hedges, and some isolated houses were extracted (Figure 3). The choice of this type is justified by the fact that the illegal construction work is done mainly in rural areas.

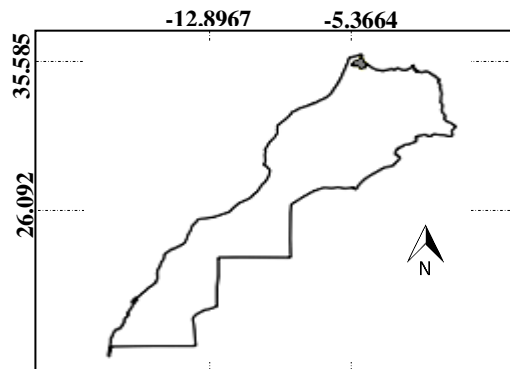


Figure 1 - Location of Tetuan (Morocco).

The test images are extracted from a GeoEye1 scene of 30 January 2013 (© DigitalGlobe Foundation) with an extent of 1 km by 1 km.

3 METHODOLOGY

The Build-ACD method is presented in Figure 2 and the principal steps are explained thereafter.

The image to database change detection method was chosen in this paper in order to: i) avoid radiometric correction between dates used in the image to image comparison, ii) avoid the matching between the old database's objects and the new ones detected by the image classification, and iii) use a priori knowledge from the VDB.

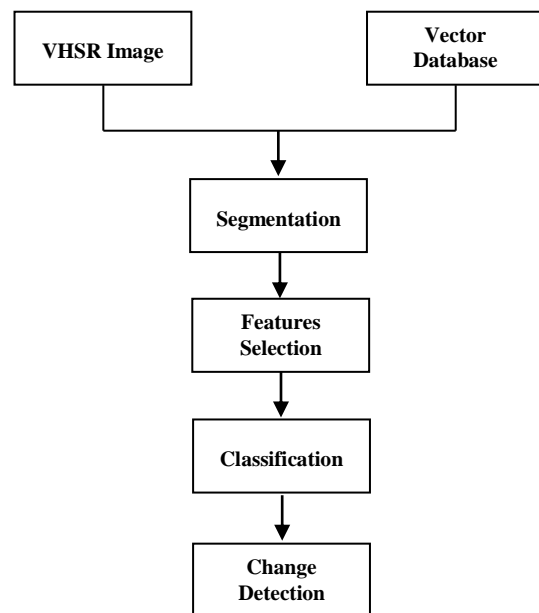


Figure 2 - Proposed methodology.

3.1 Segmentation

A new method, called Mean-shift Segmentation Parameters Estimator (MSPE), was proposed with the main objective of automating the selection of segmentation parameters values (Benarchid and Raissouni, 2014).

However, the outdated VDB can directly be used in the segmentation process. The authors of (Baillouel et al., 2003) show that the borders of database's objects are helpful to constrain the segmentation mainly in a difficult landscape where shadows cause problems in extraction.

3.2 Features Selection

After the segmentation process, the produced image segments will be used to calculate other information on top of spectral information (e.g., texture, morphology and context) which are essential in the VHSR images classification. However, these extra information are the features used in visual interpretation transposed to digital analysis. Usually, the visual interpretation keys are designed to interpret aerial photographs. Nevertheless, the sub-metric spatial resolution of VHSR satellite images has become a viable alternative and complementary to aerial photography, then the visual interpretation keys can also be used to interpret VHSR images (Carleer and Wolff, 2006).

After analyzing the landscape of the study area through the VDB and the VHSR images, four main object classes are defined: Vegetation, Soil, Roads, and

Buildings. Therefore, spectral and morphological features (e.g., size and shape) were used to classify these classes.

The spectral features consist on: i) NDVI (Normalized Difference Vegetation Index), ii) SBI (Soil Brightness Index), and iii) Shadow Index (SI). While, the morphological features include: i) Area, ii) Length/Width, and iii) Compactness.

Table 1 - Features used in the classification.

Indices	Formula
NDVI	$\frac{NIR - R}{NIR + R}$
SBI	$\sqrt{R^2 + NIR^2}$
SI	$\frac{R + G + B + NIR}{4}$
Area	$area(object)$
Length/Width	$\frac{length(object)}{width(object)}$
Compactness	$\frac{2\sqrt{\pi \cdot area(object)}}{perimeter(object)}$

3.3 Classification

The object's spectral features (NDVI, SBI, and SI) and the object's morphological features (Area, Length/Width, and Compactness) are compared with the thresholds of these features to assign an object to a given class. A function $m()$ is used to calculate the membership of an object to a given class. The chosen function uses the mean and the standard deviation of each feature for the building class. The membership function is given by:

$$\begin{cases} m(I_o) = 1 & \text{for } 0 \leq |I_o - m_{I_o}| \leq \sigma_{I_o} \\ m(I_o) = 0 & \text{for other } I_o \text{ values} \end{cases} \quad (1)$$

Where m_{I_o} and σ_{I_o} are respectively the mean and the standard deviation for any feature of for the building class; while I_o is the feature value for a given value.

3.4 Learning and Thresholds

Choosing a threshold for a feature is crucial to know if a condition is true or not. In several studies, the thresholds are chosen manually to achieve the best results. This is a trial-error approach and time consuming. For all the reasons above, a learning step is proposed to calculate the spectral properties and the geometric properties of buildings. Statistics on the features of buildings' segments are calculated using the existing VDB and the VHRS image (mean standard deviation, minimum value and maximum value). These values are used to calculate the

thresholds of the rules. Fuzzy logic was used in order to represent the distribution of the value of each feature. Thus, instead of having a rigid threshold value for a feature, it allows to introduce some fuzziness in the limitations.

3.5 Detection of New Buildings

The main objective is to detect the new buildings. First, the improbable areas are eliminated. Then, the segments belonging to the remaining areas are analyzed in details. Defining the probable zones of new buildings is based on the possible transition between the classes of the existing VDB.

The segments that could not be new buildings are: i) segments of the segmented image that correspond to the buildings on the existing VDB, and ii) segments of the segmented image that correspond to the roads on the existing VDB.

For the remaining segments, the rules used are the following: (R refers to "Rule"):

- **R1:** A segment with high NDVI cannot be a new building.
- **R2:** A segment with huge Area cannot be a new building.
- **R3:** If a segment has a Length/Width value close to 1, it probably is a new building.
- **R4:** A segment with high Compactness can be a new building
- **R5:** If the SBI index of a segment is high, it probably is bare soil.
- **R6:** If a segment has a low SI, it probably is shadow.

3.6 Quality Assessment

The evaluation of the described methodology for new buildings' detection was carried out on the area level. Reference new Buildings (*RB*) were manually delineated by direct photo-interpretation of the images.

The evaluation has been performed using a series of statistical parameters that have been repeatedly referred in the literature. *RB* and Detected new Buildings (*DB*) are spatially compared, and areas are categorized in three cases:

- i) True Positive (*TP*); number of buildings detected both manually and with the automatic approach.
- ii) False Positive (*FP*); number of buildings detected by the automatic approach but not manually.
- iii) True Negative (*TN*); number of buildings detected manually but not by the automatic approach.

The following area level quality metrics are defined using these cases:

- i) The Branching Factor (*BF*) (Equation 2) is a degree to which a system over-detects as buildings non-built areas.
- ii) The Detection Percentage (*DP*) (Equation 3) represents the percentage of reference built areas that is automatically detected.

$$BF = 100 \times \frac{FP}{TP + FP} \quad (2)$$

$$DP = 100 \times \frac{TP}{TP + TN} \quad (3)$$

4 RESULTS

The results of the statistical assessment of the Build-ACD for the two sites are shown in Table 2.

Table 2 - Statistical quality assessment of Build-ACD.

	Rural Site 1	Rural Site 2
Branching Factor (BF)%	18.75	12.50
Detection Percentage (DP) %	81.25	87.50

Build-ACD results obtained for rural site 1 show low value of *BF* (18.75%) meaning that few false alarms are detected. However, the *DP* value is 81.25% meaning that almost the totality of new buildings is detected. Figure 4 (a) shows an image detail illustrating the results for the rural site 1 of Tetuan.

Regarding the rural site 2, the *BF* value is lower than this obtained for the site 1. As a result the *DP* is 87.50%, meaning that the totality of new buildings is detected. Figure 4 (b) shows an image detail illustrating the results for the rural site 2 of Tetuan.

6 CONCLUSION

In this research, a method to automatically detect new buildings was proposed; we call Buildings' Automatic Change Detection (Build-ACD) which kernel is essentially and partially based on the Mean-shift Segmentation Parameters Estimator (MSPE) method for automatic selection of segmentation parameters.

The image to database change detection approach was chosen. The outdated VDB was used to constrain the segmentation and also in the classification process by using the database's objects as samples to define the thresholds for the spectral, textural, geometrical, and contextual features.

7 REFERENCES

- Bailloleul, T., J. Duan, V. Prinnet, and B. Serra. 2003. "Urban digital map updating from satellite high resolution images using GIS data as a priori knowledge." In The 2nd GRSS/ISPRS Joint workshop on Remote Sensing and Data Fusion over Urban Areas, Berlin, Germany, May 22-23.
- Baltsavias, E. P. 2004. "Object extraction and revision by image analysis using existing geodata and knowledge: Current status and steps towards operational systems." *ISPRS Journal of Photogrammetry and Remote Sensing* 58: 129-151.
- Benarchid, O. and N. Raissouni. 2014. "Mean-Shift Segmentation Parameters Estimator (MSPE): A new tool for very high spatial resolution satellite images." In International Conference on Multimedia Computing and Systems, Marrakech, Morocco, April 14-16.
- Bouziani, M., K. Goïta, and D. C. He. 2010. "Automatic change detection of buildings in urban environment from very high spatial resolution images using existing geodatabase and prior knowledge." *ISPRS Journal of Photogrammetry and Remote Sensing* 65: 143-153.
- Cao, G., Y. Liu, and Y. Shang. 2014. "Automatic change detection in remote sensing images using level set method with neighborhood constraints." *Journal of Applied Remote Sensing* 8.
- Carleer, A., and E. Wolff. 2006. "Urban land cover multi-level region-based classification of VHR data by selecting relevant features." *International Journal of Remote Sensing* 27: 1035-1051.
- Hanson, E., A. Puissant, and E. Wolff. 2013. "Local authorities' obligations about monitoring of urban and green areas and contribution of Very High Resolution images: examples in France and Belgium." In Joint Urban Remote Sensing Event, Sao Paulo, Brazil, April 21-23.
- Hanson, E. and E. Wolff. 2010. "Change detection for update of topographic databases through multi-level region-based classification of VHR optical and SAR data." In GEOBIA 2010: Geographic Object-Based Image Analysis, Ghent, Belgium, June 29-July 02.
- Holland, D. A., D. S. Boyd, and P. Marshall. 2006. "Updating topographic mapping in Great Britain using imagery from higher-resolution satellite sensors." *ISPRS Journal of Photogrammetry and Remote Sensing* 60: 212-223.

Knudsen, T., and B. Olsen. 2003. "Automated change detection for updates of digital map databases." *Photogrammetric Engineering and Remote Sensing* 69: 1289-1296..

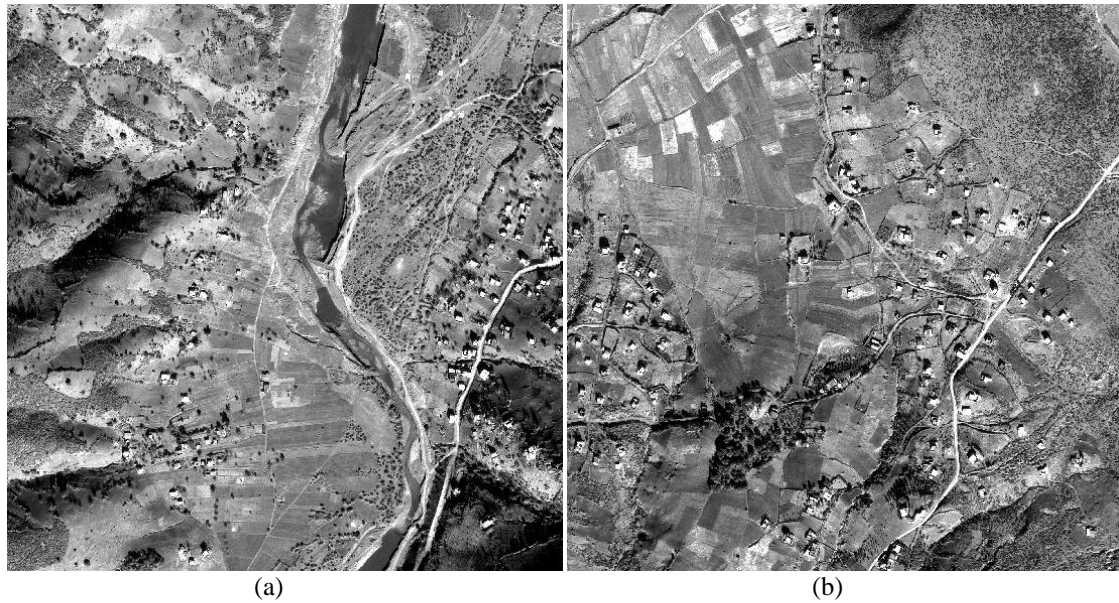


Figure 3 - Rural extracted areas: (a) site 1 and (b) site 2.

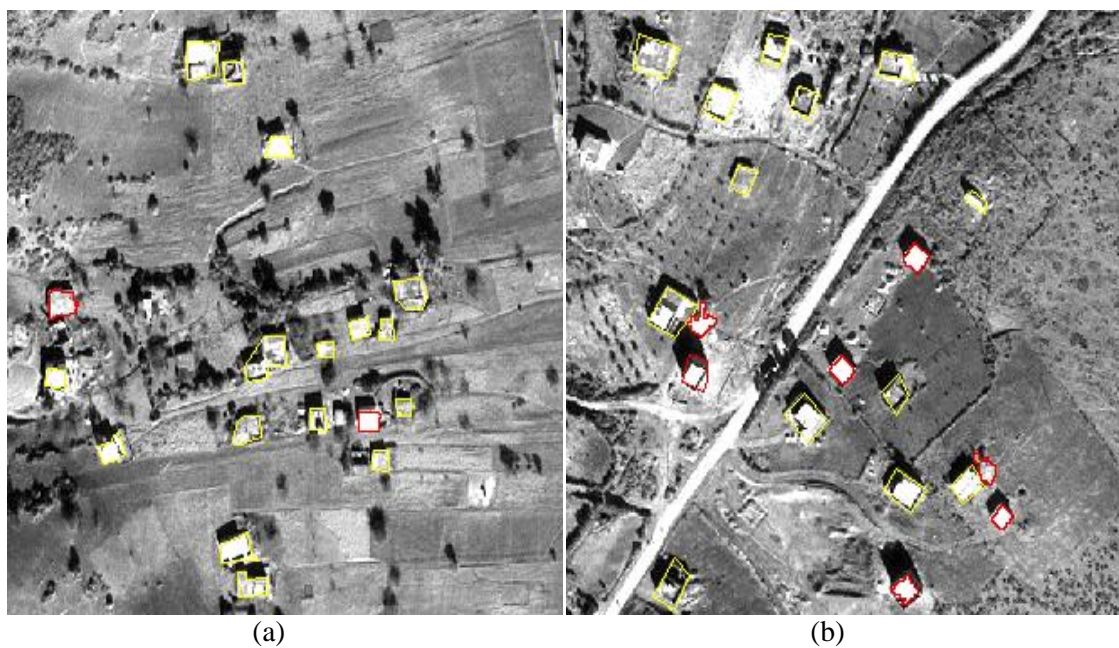


Figure 4 - Subsets of new buildings' detection: (a) rural site1 and (b) rural site 2. Old buildings are in yellow and new detected buildings are in red.

Application of the Mean-shift Segmentation Parameters Estimator (MSPE) to VHRS satellite images: Tetuan-Morocco

O. Benarchid and N. Raissouni

RS&AID Laboratory, National School for Applied Sciences of Tetuan, University of Abdelmalek Essaadi, Mhaneech II. B.P. 2222, 93000 TETUAN, Morocco
obenarchid@remotesensing.ma; nraissouni@uae.ma

ABSTRACT- Image segmentation is considered as crucial step dealing with Object-Based Image Analysis (OBIA) and different segmentation results could be achieved by combining possible parameters values. Optimal parameters selection is usually carried out on the basis of visual interpretation; therefore, defining optimal combinations is a challenging task. In the present research, Mean-shift Segmentation Parameters Estimator (MSPE) proposed tool is applied to automate the selection of segmentation parameters values to Very High Spatial Resolution (VHRS) satellite images in the region of Tetuan city (Northern Morocco). MSPE estimates the parameters values for the Mean-shift Segmentation (MS) algorithm. However, this algorithm needs as inputs: i) existing vector database and, ii) spectral data to define automatically the segmentation parameter values. Finally, application of the MSPE method on different landscape types show accurate results with Under Segmentation (US) values lower than 0.20.

1 INTRODUCTION

Image segmentation dates back to the 1970s. The first applications of segmentation methods are in the fields of industrial and medical image processing, and were not used widely in remote sensing in the 1980s and 1990s (Blaschke, 2010). Around the year 2000 and with the launch of Very High Spatial Resolution (VHRS) satellites, segmentation algorithms started to be used in remote sensing applications; because of segmentation is a fundamental step in Object-Based Image Analysis (OBIA) approach.

Nowadays, mapping agencies need to update their topographic and information systems databases in order to draw: i) urban planning (e.g. urban sprawl, road networks, etc.), and ii) environmental planning (e.g. ecological corridors, forest change, etc.). Until now, the update is achieved manually by using photogrammetric restitution and ground survey. This work is boring, time consuming, and does not satisfy the user's update frequency need (Hanson and Wolff, 2010). With the growth of non-experts in using VHRS remote sensing images, the requirements of semi-automated/automated processing using fewer parameters is an expanding need (Huth et al., 2012).

Two principal objects of interest are identified by the data producers: roads and buildings which need the most frequent update (Hanson and Wolff, 2010).

Moreover, Image segmentation is a crucial step in OBIA and different segmentation results can be achieved by combining the possible parameters values (spectral, and spatial) (Liu et al., 2012). The selection of optimal parameters is usually done by visual interpretation, that we called a trial-and-error way.

Therefore, defining the optimal combination of parameters values is a big challenge (Dragut, Tiede, and Levick, 2010).

Assessment of segmentation algorithms can be used to choose the optimal parameters. In general, there are two main methods: analytical methods and empirical methods. The analytical methods investigate and evaluate the segmentation algorithms themselves by analyzing their equations and required parameters.

In this paper, we have proposed a new Mean-shift Segmentation Parameters Estimator (MSPE) analytical method for automatic selection of segmentation parameters values using VHRS satellite images and Vector Database (VDB).

2 STUDY AREA AND DATASET

This study is applied in the region of Tetuan city situated in northern Morocco (Figure 1).

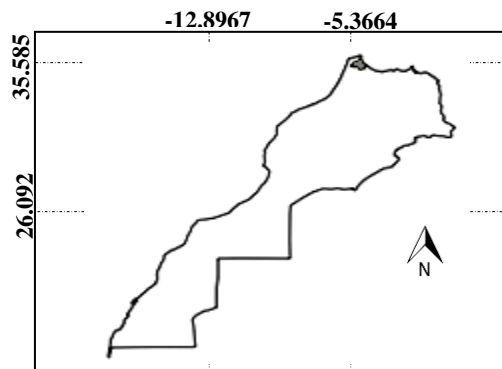


Figure 1 - Location of Tetuan (Morocco).

Various landscape types are extracted:

- Dense Residential (DW) zone: densely populated area, built in various material with few vegetation.
- Industrial zone: area with large constructions, few or no vegetation.
- Residential zone: residential area with isolated houses, large gardens, and some trees.
- Rural zone: rural area with fields, hedges and some isolated houses.

The test images are extracted from a GeoEye1 scene of 30 January 2013 (© DigitalGlobe Foundation).

3 MSPE TOOL

In this research, we propose a new tool, called Mean-shift Segmentation Parameters Estimator (MSPE), with the main objective of automating the selection of segmentation parameters values. MSPE estimates the parameters values for the Mean-shift Segmentation (MS) algorithm. Indeed, MSPE needs as inputs: i) existing VDB and ii) spectral data to define automatically the segmentation values.

The MS algorithm, generalized in (Fukunaga and Hostetler, 1975), is adapted to image analysis by Cheng (Cheng, 1995). This method is used in several image processing applications: smoothing, filtering, and segmentation (Comaniciu and Meer, 2002). MS is a simple iterative procedure that looks for a local mode within a set of data. It operates by taking the points in the feature space as empirical probability density function where dense regions (or clusters) correspond to local maxima or modes of the underlying distribution (Comaniciu and Meer, 2002).

First, the MS algorithm defines a window with a spatial radius h_r . Then, it groups together all the pixels within the defined window which are lower than the spectral threshold h_s , and calculates their mean.

Usually the Euclidean distance is the function used for measuring distances between pixels. Second, it shifts the center of the window to the mean and repeats the algorithm till it converges. Finally, it eliminates regions which are lower than the minimum region size M .

In order to calculate h_s , pixels that correspond to every reference polygon in the VDB are processed to calculate the Standard Deviation (SD) within 3×3 pixels filter, and the mean of the SD of reference polygons is h_s .

$$h_s = \frac{\sum_{i=1}^{N_{ref}} SD_i}{N_{ref}} \quad (1)$$

h_r is defined by calculating the radius R for each reference polygon in the VDB. Considering, the image

segments should overlap at least half area of the reference polygon.

$$h_r = \frac{\sum_{i=1}^{N_{ref}} R_i}{2 \times N_{ref}} \quad (2)$$

Finally, in order to calculate M , the area of each reference polygon in the VDB is calculated respecting corresponding-segment criteria.

Let $A = \{A_i: i = 1, 2, \dots, N_{ref}\}$ be the dataset of the reference polygons' area. Where $A_i = area(r_i)$; while $\mathcal{R} = \{r_i: i = 1, 2, \dots, N_{ref}\}$ is the dataset of reference polygons. The minimum region size M is given by:

$$M = \frac{\min(A)}{2} \quad (3)$$

4 ACCURACY ASSESSMENT

Segmentation results can be evaluated visually or quantitatively. Visual assessment is based on the expert knowledge. However, quantitative assessment compares the outputs to reference polygons using a set of metrics. For this study, we have chosen quantitative assessment evaluation method. High-quality image segmentation should result in a minimum of over segmentation and under-segmentation.

The first measure is Over-Segmentation (**OS**). It is the ratio between the total area of over-segments and the total area of reference polygons:

$$OS = \frac{\sum_{i=1}^{N_{ref}} area(r_i) - \sum_{i=1}^{N_{ref}} \sum_{j=1}^{N_{cor}} area(r_i \cap c_j)}{\sum_{i=1}^{N_{ref}} area(r_i)} \quad (4)$$

The second measure is Under-Segmentation (**US**) is the ratio between the total area of under-segments and the total area of corresponding segments:

$$US = \frac{\sum_{j=1}^{N_{cor}} area(c_j) - \sum_{i=1}^{N_{ref}} \sum_{j=1}^{N_{cor}} area(r_i \cap c_j)}{\sum_{j=1}^{N_{cor}} area(c_j)} \quad (5)$$

Where $C = \{c_j: j = 1, 2, \dots, N_{cor}\}$ is the dataset of corresponding segments, and $\mathcal{R} = \{r_i: i = 1, 2, \dots, N_{ref}\}$ is the dataset of reference polygons.

The values of these two indices are normalized, so the values range between zero and one. Zero values for US and OS indicate that there are no under-segments and no over-segments respectively.

These two parameters calculate only geometric discrepancies. Although, in an extreme case; a reference polygon can be overlapped by many small corresponding segments (pixels) with no over-segments or under-segments. This, geometrically desirable, does not give meaningful segments.

For this, we will use another metric that take in account also arithmetic relationship.

The third measure is a simple ratio between the number of corresponding segments and the number of reference polygons. This ratio is the Generalization (*Gen*), and is given by the following formula (Carleer, Deiber, and Wolff, 2005):

$$Gen = \frac{N_{cor}}{N_{ref}} \quad (6)$$

5 RESULTS

The parameters values of segmentation selected by using the MSPE method and their calculated accuracy metrics are shown in Table 1. However, the extracts of segmentation results are shown in Figure 2.

Table 1- MSPE results.

	DW	Industrial	Residential	Rural
h_s	64.80	19.15	40.52	30.50
h_r	14	17	10	5
M	536	1700	503	124
Gen	1.80	1.20	1.50	0.90
OS	0.64	0.19	0.10	0.09
US	0.35	0.20	0.16	0.10

The best accuracies were achieved for the Rural zone, the Industrial zone, and the Residential zone of Tetuan. As depicted by Table 1, all of the level-specific metrics were close to 0, even go nearly to the desirable combination of geometric and arithmetic match. Relatively, worse accuracies were obtained for DW zone Tetuan.

These results can be explained as the buildings of Rural zone, and the Residential zone of Tetuan are more spectrally homogenous within themselves than with nearby regions. Nevertheless, the worse accuracy of DW zone is due to: the buildings are much attached, the pixel values of roads and some buildings are similar, and the presence of shadow.

In conclusion, generally the MSPE tool gives better accuracies with more homogenous areas. By reason of: i) it is based on Mean-shift segmentation algorithm that focuses more on spectral feature, and ii) the use of spectral data to automatically determine the segmentation parameters.

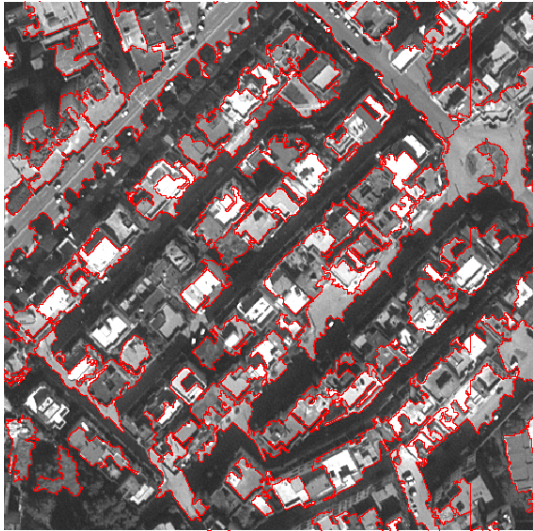
6 CONCLUSION

In this research, a proposition of a new Mean-shift Segmentation Parameters Estimator (MSPE) for automatic selection of segmentation parameters values using Very High Spatial Resolution (VHSR) satellite images and Vector Database (VDB) were carried out.

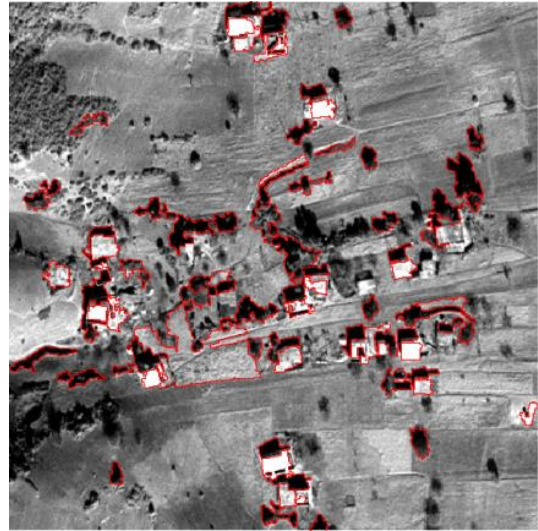
MSPE was applied to Tetuan city (Morocco) on different landscape' types and show accurate results with Under Segmentation (US) values lower than 0.20.

7 REFERENCES

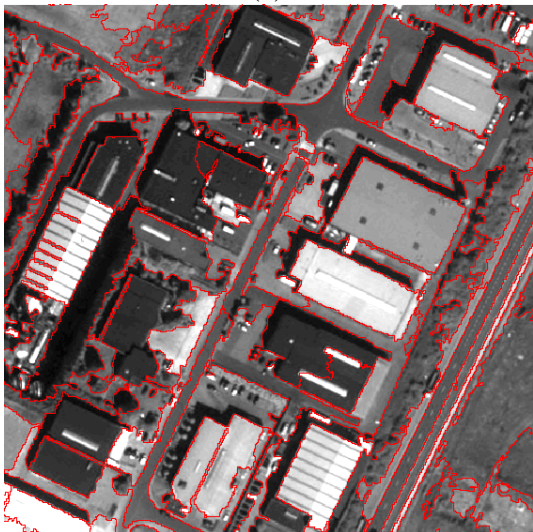
- Blaschke, T. 2010. "Object based image analysis for remote sensing." *ISPRS Journal of Photogrammetry and Remote Sensing* 65: 2-16.
- Carleer, A., O. Deiber, and E. Wolff. 2005. "Assessment of very high spatial resolution satellite image segmentations." *Photogrammetric Engineering and Remote Sensing* 71: 1285-1294.
- Cheng, Y. 1995. "Mean shift, mode seeking, and clustering." *IEEE Transactions on Pattern Analysis and Machine Intelligence* 17: 790-799.
- Comaniciu, D., and P. Meer. 2002. "Mean shift: A robust approach toward feature space analysis." *IEEE Transactions on Pattern Analysis and Machine Intelligence* 24: 603-619.
- Dragut, L., D. Tiede, and S. R. Levick. 2010. "ESP: a tool to estimate scale parameter for multiresolution image segmentation of remotely sensed data." *International Journal of Geographical Information Science* 24: 859-871.
- Fukunaga, K., and L. Hostetler. 1975. "The estimation of the gradient of a density function, with applications in pattern recognition." *IEEE Transactions on Information Theory* 21: 32-40.
- Hanson, E. and E. Wolff. 2010. "Change detection for update of topographic databases through multi-level region-based classification of VHR optical and SAR data." In *GEOBIA 2010: Geographic Object-Based Image Analysis*, Ghent, Belgium, June 29-July 02.
- Huth, J., C. Kuenzer, T. Wehrmann, S. Gebhardt, V. Q. Tuan, and S. Dech. 2012. "Land cover and land use classification with TWOPAC: towards automated processing for pixel- and object-based image classification." *Remote Sensing* 4: 2530-2553.
- Liu, Y., L. Bian, Y. Meng, H. Wang, S. Zhang, Y. Yang, X. Shao, and B. Wang. 2012. "Discrepancy measures for selecting optimal combination of parameter values in object-based image analysis." *ISPRS Journal of Photogrammetry & Remote Sensing* 68: 144-156.



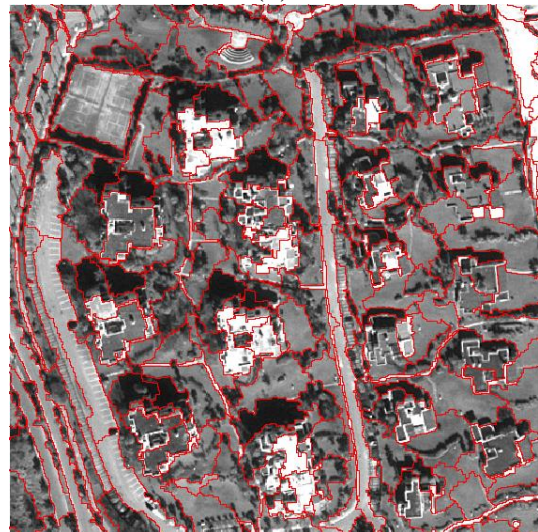
(a)



(b)



(c)



(d)

Figure 2 - Extracts of segmentation results using MSPE method of: Tetuan (Morocco): (a) DW, (b) Rural, (c) Industrial, and (d) Residential zones.

Effect of Qinghai-Tibet Railroad on Vegetation Abundance

Guangjun Wang^{1,2*}, Alan R. Gillespie², Shihai Liang³, Amit Mushkin², Qingbai Wu⁴

¹*School of Land Science and Technology, China University of Geosciences, Beijing 100083, China*

²*Department of Earth and Space Science, University of Washington, Seattle, WA 98105, United States*

³*School of Water Resources and Environment, China University of Geosciences, Beijing 100083, China*

⁴*State Key Laboratory of Frozen Soil Engineering, Cold and Arid Regions Environmental and Engineering Research Institute, Chinese Academy of Sciences, Lanzhou 730000, China*

Email: cugbwanggj@gmail.com; arg3@u.washington.edu; liangsh@cugb.edu.cn; qbwu@lzb.ac.cn

*Corresponding email address: cugbwanggj@gmail.com

ABSTRACT- Large-scale engineering projects such as mines and dams cause ecological damage that can persist after construction is complete. The Qinghai-Tibet Railroad (QTR) from Golmud to Lhasa was constructed entirely during the Landsat era and began operating in 2006. Therefore, it presents an opportunity for determining both the extent of ecological damage and the time required for some level of natural restoration after a major construction project. We have studied the effect of QTR construction on vegetation abundances measured using Multi-Endmember Spectral Mixture Analysis (MESMA) of a time series of Landsat TM/ETM+ images (2001, 2007, 2010) covering the 231 km stretch of the railroad from the south of Kaixinling Station to the north of Chumaerhe Station. It was found that the effect of QTR construction on vegetation abundances was limited to within 5.0 km of the tracks, and the largest decrease of vegetation abundances, 2.9%, occurred within 125 m of the tracks from 2001 to 2007. There was only 0.4% further decrease of vegetation abundances from 2007 to 2010. Moreover, the decrease of vegetation abundances within 125 m of the tracks occurred mainly west of the tracks, which we attributed to the prevailing west wind and measures adopted there to keep the sand from blowing across the railroad. It appears that in this sensitive cold desert, vegetation damage was limited to the period of the railroad construction.

1 INTRODUCTION

The Qinghai-Tibet Railroad (QTR), completed in October 2005 and in trial operation since July 1st 2006, is the world's highest-elevation railroad and the longest highland railroad. It is 1142 km from Golmud to Lhasa, the capital city of the Tibet Autonomous Region (Xizang) (Peng et al., 2007). Although railroad planners and builders did all they could do to minimize the negative impacts of the construction and try to make it an environment-friendly railroad, the potential long-term QTR environmental impacts should not be underestimated (Zhang et al., 2008; Peng et al., 2007). It is acknowledged that QTR construction had impacts on vegetation to some extent (Wang et al., 2005; Jin et al., 2008; Ding et al., 2006), but because of the complex variety of both man-induced and natural climatic changes along the railroad, there is no report available on the effect of vegetation abundances away from the tracks, especially the spatial and temporal patterns of vegetation abundances of the tracks. Yet we could gain insight into the vegetation degradation resulting from the QTR construction and rehabilitation from such an

analysis.

The objective of the present study is to estimate vegetation abundance in the vicinity of the QTR before, during and after railroad construction. The goal is to understand the temporary and lasting ecological changes accompanying construction projects in sensitive environments.

2 STUDY SITE AND MATERIALS

2.1 Study Site

One section of the QTR from south of Kaixinling Station to north of Chumaerhe Station is studied in this paper (Figure 1). The section is 231 km long and located in the Hoh Xil Nature Reserve, an unpopulated zone on the Qinghai - Tibetan Plateau. Because it has been only lightly used for human habitation and livestock grazing, the impact of construction is all the more evident. The elevation is from 4470 m asl to 5300 m asl, and the section experiences a continental climate with cold (to -30 °C) winters with blowing snow and warm (to +25 °C) summers, and widely variable annual precipitation of 50 to ~400 mm, thought to be mostly from the Southern Asian

monsoon during the May–August period (Jin et al., 2008). Strong winds ($> 17 \text{ m s}^{-1}$) are common in many sites along QTR and on average the number of strong

windy days at Tuotuohe and Wudaoliang stations is 168 and 136 yr^{-1} respectively (Zhang et al., 2010).

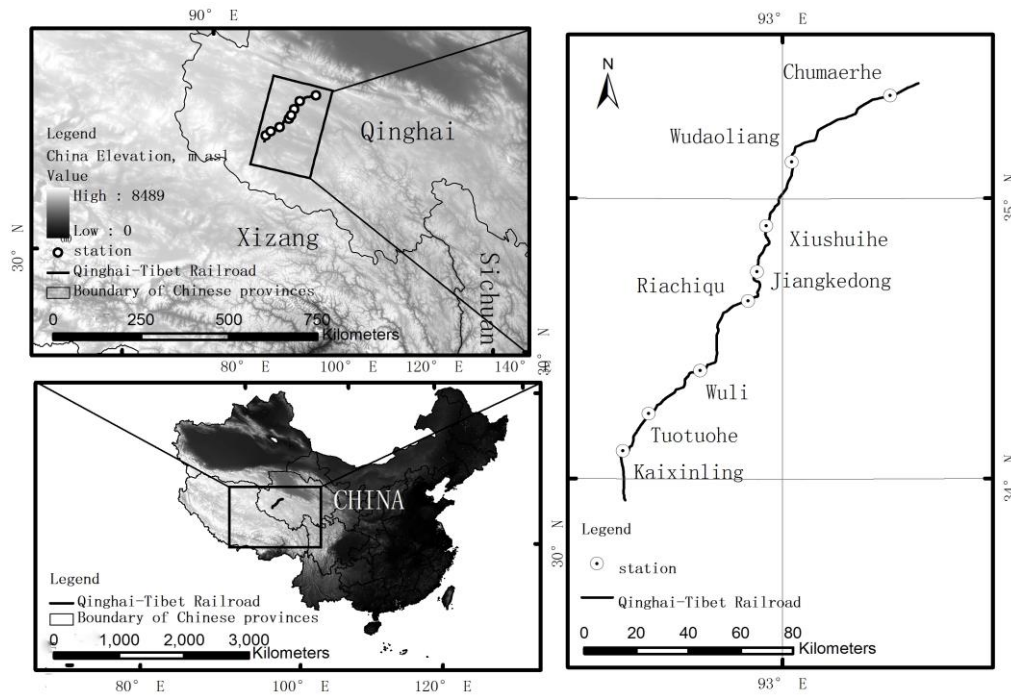


Figure 1. Location of the study area. Note: map boundary and locations approximate. Geographic features and the names do not imply any official endorsement or recognition.

Table 1 Vegetation communities along the QTR

Vegetation Community	Alpine meadow (Miehe et al., 2008)	Alpine steppe (Guo, 1993)	Alpine steppe (Guo, 1995)
Dominant species	<i>Kobresia pygmaea</i>	<i>Stipa purpurea</i>	<i>Littledalea racemosa</i>
Subordinate species	<i>Arenaria bryophylla</i> , <i>Arenaria kansuensis</i> , <i>Androsace tapeta</i> , <i>Leontopodium nanum</i> , lichens	<i>Carex moorcroftii</i> , <i>Oxytropis densa</i> , <i>Oxytropis falcate</i> , <i>Astragalus confertus</i> , <i>Pleurospermum hedinii</i>	<i>Carex moorcroftii</i> , <i>Lagotis brachystachya</i> , <i>Astragalus confertus</i>
Elevation range, m asl	4600–5400	4400–4700	4400–4700

Alpine meadow and alpine steppe are the two dominant vegetation communities across the study area, especially near the railroad (Xie and Qu, 2013), and each comprises specific vegetation species (Table 1). *Kobresia pygmaea* can occur in almost pure, completely closed stands and are often distributed in the pattern of polygonal cracks, which has been attributed to freeze-thaw cycles (Zhang, 1988). *Littledalea racemosa* is an endemic vegetation species and commonly located on scree slopes, rocky hillsides, gravelly ground and lake shores or in the valleys where there are abundant marly gravels or sandy soils

(Guo, 1995).

Frigid calcic soil classified as Cryepts and Cryids in the U.S. Soil Taxonomy (Soil Survey Staff, 2010) is the main soil type across the study area. There are two other main soils, frigid frozen soil (Cryorthents in U.S. Soil Taxonomy) and felty soil (Cryepts in U.S. Soil Taxonomy) distributed along the railroad. Moreover, there are sand and scree distributed near the rivers, around lakes or on rocky hillsides.

2.2 Materials

Three Landsat TM/ETM+ Level-1B products

measured on July 8 2001, August 2 2007, and July 25 2010 were used in this study. 2001 was before the railroad construction was started; 2010 was 5 yr after its completion; and 2007 was ~1 yr after its completion. No Landsat products after 2010 were used because of the Landsat 7 malfunction of the Scan Line Corrector (SLC), the retiring of Landsat 5, or excessive cloud cover. Data from the second version of the ASTER Global Digital Elevation Model (GDEM) and the vegetation and soil database digitalized and distributed by Chinese Qinghai-Tibet Plateau Data Center covering the study area were also used.

3 METHODS

3.1 Field Investigation and Image Pre-processing

Vegetation and soil types were confirmed in the field on July 15–25 2011. 31 ground-control points (GCPs) used for geometric correction were recorded by a GPS receiver with an accuracy of <1 m during the field investigation.

Geometric correction of the TM/ETM+ images was conducted using the selected GCPs. The correction using a second-order polynomial was accurate to <0.5 pixel Root Mean Squared Error (RMSE). Radiometric calibration and Fast Line-of-sight Atmospheric Analysis of Spectral Hypercubes (FLAASH) which incorporates the MODTRAN 4 radiation transfer model provided by ENVI software, were both applied to the images in order to compensate for atmospheric effects and to calibrate the encoded radiance measurements to reflectance. Finally, we implemented the “c-correction” (Teillet et al., 1982) using ASTER GDEM data to minimize the effect of topography in the TM /ETM+ images.

3.2 Spectral Mixture Analysis

3.2.1 SMA and MESMA

Spectral Mixture Analysis (SMA) assumes that different mixtures of a small number of surface materials or components in the scene are responsible for much of the spectral variation in remotely sensed images, and that these components with different spectra are called endmembers (Adams and Gillespie, 2006). The most commonly used approach in SMA modeling is Linear Spectral Mixture Analysis (LSMA) which minimizes the sum of band-wise errors of a least-squares model solution. In this approach, mixtures of specified spectral endmembers are taken to estimate the measured image spectra. LSMA has proven to be effective in vegetation abundance estimation.

Although LSMA is a useful technique, it accounts for materials not modeled by spectral endmembers or

their mixtures as residua, in some instances may lead to errors in mixing proportions (Adams and Gillespie, 2006). Because the number and identity of the endmembers are held fixed throughout an image or a sub-image area, violation of the above assumptions is a realistic possibility. In situations where the number and identity of endmembers within the field of the view is variable, MESMA may be helpful (Roberts et al., 1998). MESMA allows the types and number of endmembers to vary on a per pixel basis and has been widely tested on multi-spectral or hyper-spectral images.

3.2.2 Endmember selection

We extracted endmembers from the images themselves (“image endmembers”). The steps we used in selecting suitable endmembers and then in computing the endmember abundances or fractions were:

I. An area of 10 km × 10 km near the tracks and covering the main vegetation and soil types was selected for endmember spectra selection. The area centered around 34°05' N, 92°21' E;

II. We determined from the field inspection that only three endmembers appeared to be necessary in order to model the scene: vegetation, soil and “shade.” Three vegetation image endmembers (*Kobresia pygmaea*, *Stipa purpurea* and *Littledalea racemosa*) and five soil image endmembers (frigid calcic soil, frigid frozen soil, felty soil, sand and scree) plus an ideal shade endmember were selected to represent the range of possibilities within these three groups;

III. To reduce endmember variability, each candidate soil endmember was modeled by any other soil endmember mixed with shade. This was done to determine which soil endmembers composed a minimum endmember data set, and which were redundant. Only those soil endmembers that could not be modeled by any other soil endmember plus shade with all RMSE <0.004 (1 DN value) were selected as members of the minimum set. Similarly, a minimum set of vegetation endmembers was selected, consisting of only those endmembers that could not be modelled as mixtures of other vegetation and the selected soil endmembers.

IV. MESMA was applied to each pixel in the test area, comparing the fit of the different candidate endmember sets to the image reflectance. The model with the lowest RMSE was the one selected to model that pixel;

V. The abundance of shade (shadows and radiometric shading) generally increases with increasing vegetation abundance (Adams and Gillespie, 2006), and the fraction of sunlit soil should therefore decrease. Conversely, the fraction of shade should decrease with decreasing vegetation cover, whereas

the fraction of sunlit soil should increase. If the retrieved abundances conform to this observation in the test area, then the selected endmembers and retrieved abundances were confirmed and MESMA was applied to the whole image. If not, the endmember set was rejected and the next in order (Step III) was selected instead.

Twelve endmember spectra (three vegetation endmember spectra: *Kobresia pygmaea*, *Stipa purpurea* and *Littiedalea racemosa*, eight soil endmember spectra and one shade spectrum) were confirmed, and the vegetation abundances were computed.

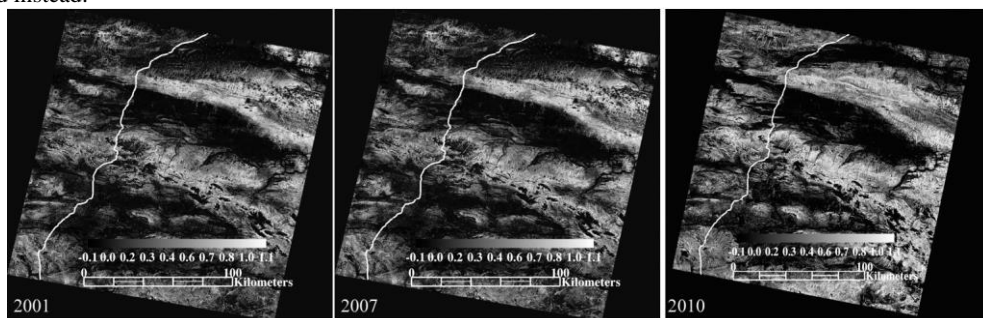


Figure 2. Vegetation fraction images. The white line shows the tracks of the QTR from the south of Kaixinling Station to the north of Chumaerhe Station.

4 RESULTS

4.1 Vegetation Abundance along the Railroad

The vegetation abundances across the study area are shown in Figure 2. The average vegetation abundance (AVA) was calculated for five buffer zones parallel to the QTR but different distances from it (on both sides of the tracks) (Figure 3). In 2001 the AVA decreased away from the tracks, whereas in 2007 and 2010 it increased within 5 km of the tracks, but decreased between 5 km and 10 km from the tracks.

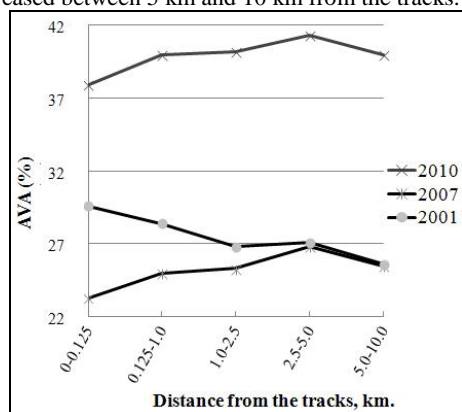


Figure 3. Average vegetation abundance (AVA) as a function of distance from the tracks. There are five buffer zones parallel to the QTR: 0–0.125 km, 0.125–1.0 km, 1.0–2.5 km, 2.5–5.0 km and 5.0–10.0 km.

4.2 Effect of QTR Construction on Vegetation Abundance

4.2.1 Assumptions

AVA images permit an intuitive snapshot view of spatial pattern of vegetation at one time. In order to estimate the effect of QTR construction on vegetation abundance quantitatively, we made the following two assumptions:

I. The vegetation communities in the nearby buffer zones are almost the same; the dominant species will vary little.

II. The vegetation communities in the nearby buffer zones are in the same growing environment and precipitation and temperature vary little.

Under the above two assumptions, the difference between nearby AVAs (“DAVA”) within each of the buffer zones can be calculated as

$$DAVA_i = AVA_{i+1} - AVA_i \quad (1)$$

where subscript i ranges from 0 to 4 indicating the buffer zone of 0–0.125 km, 0.125–1.0 km, 1.0–2.5 km, 2.5–5.0 km, and 5.0–10.0 km respectively. If the AVAs within the nearby buffer zones are the same, DAVA should be zero, signifying that QTR construction had no effect on the vegetation abundance. But if all the values of DAVA are greater than zero, it means that QTR construction reduced the vegetation abundance near the track.

In order to compare temporal changes in vegetation abundance, we introduced a third assumption to the analysis:

III The vegetation all has the same growth rate in the growing season.

With this assumption, the time difference of $DAVA$ ($DDAVA$) can be calculated to estimate the effect of railroad construction on the vegetation abundance from year to year. Thus,

$$DDAVA_i = DAVA_{ij} - DAVA_{ik} \quad (2)$$

where j and k are the year of the acquired remotely sensed images.

4.2.2 Spatial pattern of vegetation abundance

The $DAVA$ values showing the influence of QTR construction on vegetation abundance are shown in Figure 4. The same values for $DAVA_3$ in all three years mean that the impact of construction of QTR on vegetation abundance is limited to within 5.0 km from the tracks. However, the greatest value of $DAVA$ is $DAVA_0$ occurred in 2007 and 2010. This means that the greatest impact of QTR resulting in the decrease of vegetation abundance adjacent to the tracks occurred within 0.125 km of the tracks.

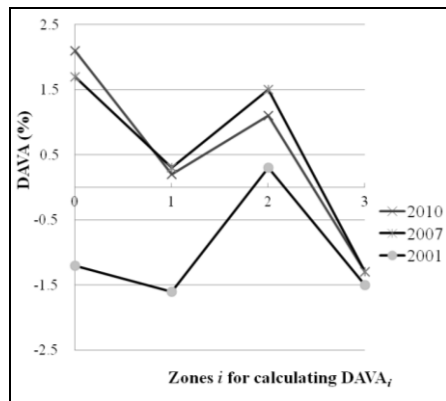


Figure 4. Differenced spatially averaged vegetation abundances ($DAVA$) in adjacent zones adjacent to the tracks (see Fig. 3). Zone i indicates that $DAVA$ for zones $i+1$ and i are differenced to create $DAVA_i$.

4.2.3 Temporal pattern of vegetation abundance

The temporal quantitative analysis of AVA within each buffer zone from year to year is summarized in Figure. 5. It is obvious that the value of $DDAVA$ is decreasing when the buffer zone is near the tracks between 2001 and 2007. The greatest decrease of 2.9% occurred for $DDAVA_0$, and the smallest decrease of 0.2% occurred for $DDAVA_3$. It means the greatest impact of QTR construction on AVA occurred within 125 m of the tracks between 2001 and 2007, when there was little effect >5 km from the tracks ($DDAVA_3$).

From 2007 to 2010, there was a further 0.4% decrease of vegetation abundance within 125 m of the tracks, and there is no change for $DDAVA_3$ with 0.0%

in the area beyond 5 km of the tracks. On the contrary, there was a slight restoration of vegetation at $DDAVA_1$ and $DDAVA_2$ with values of 0.1% and 0.4%, respectively.

5 Discussion: Causes of Vegetation Decrease Following QTR Construction

According to equation 1, values of $DAVA_0$ east of the tracks were 2.1%, 2.0% and 2.0% in 2001, 2007 and 2010, respectively. Thus there was little change east of the tracks, which means that QTR construction had little effect on vegetation abundance there. However, the pattern was asymmetric and values of $DAVA_0$ west of the tracks were -0.5%, 1.6% and 2.2% in 2001, 2007 and 2010, respectively. It was -0.5% on the west in 2001 before construction started, suggesting that there was then a slightly higher vegetation abundance within 125 m on the west relative to the zones farther away, but in 2007 after construction had been completed for ~1 yr, $DAVA_0$ had risen to 1.6%, implying that vegetation abundance within 125 m west of the tracks was decreasing. $DAVA_0$ was 2.2% in 2010, indicating a further vegetation decrease even after construction had been complete for >5 yr.

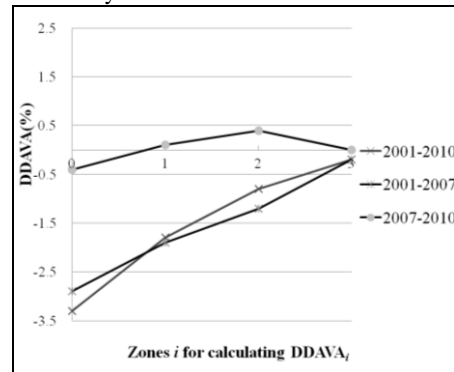


Figure 5. Time difference of $DAVA$ between 2001 and 2010, 2001 and 2007, 2007 and 2010 respectively.

The study area is located in a windy stretch of the Tibetan Plateau, and in one of the stretches of the railroad most strongly affected by blowing sand and sand accumulation. Zhang et al. (2010) found that QTR has suffered damage from blowing sand since 2006, when construction was completed, and the affected area is spreading. Although many measures have been adopted to keep the sand away from the railroad, the strong prevailing west winds still lead to sand accumulation of the tracks, especially west of the tracks. This can be seen if we compare the averaged sand abundance within the zones 125 m west and east of the tracks. The difference was -0.4% in 2001, rising to 3.1% in 2007, and then falling to 0.3% in 2010.

Thus our results suggest that this accumulation of drifting sand, and not direct effects of building the railroad, is what led to the observed greater decrease in vegetation abundance west of the railroad, and that the measures adopted to keep the sand away from the railroad have actually accelerated this decrease. Although this progress is too subtle to be perceived in the field, in our study it was measured by averaging the vegetation abundances calculated for a large number of pixels along the railroad.

6 SUMMARY AND CONCLUSIONS

The impact of the construction of QTR on vegetation abundance was limited to within 5.0 km of the tracks. The largest decrease of vegetation abundance (by 2.9%) occurred within 125 m of the tracks from 2001 when the railroad was not yet built, to 2007 when it had been completed for ~1 yr. There was a further 0.4% decrease of vegetation abundance in the next 5 yr.

We found that within 125 m of the tracks, the decrease of vegetation abundance occurred mainly west of the tracks, which we attributed to the prevailing strong west wind and measures adopted to keep blowing sand away from the railroad.

It appears that in this sensitive cold desert, vegetation damage was limited to the period of the railroad construction.

ACKNOWLEDGMENTS

We thank Batbaatar Jigjidsuren for his constructive comments that have greatly improved the quality of the paper. This work was in part supported by the National Natural Science Foundation (Grand No. 41330634; 41072191), China Geological Survey, China Scholarship Council and the Fundamental Research Funds for the Central Universities. Financial support does not constitute an endorsement of views expressed in this article.

REFERENCES

- Adams, John B, and Alan, R Gillespie, 2006, Remote sensing of landscapes with spectral images: A physical modeling approach (Cambridge, UK: Cambridge University Press).
- Ding, Mingjun, Zhang Yili, Shen Zhenxi, Liu Linshan, Zhang Wei, Wang Zhaofeng, Bai Wanqi, and Zheng Du, 2006, Land cover change along the Qinghai-Tibet Highway and Railway from 1981 to 2001. *Journal of Geographical Sciences*, 4, 387-395.
- Guo, Ke, 1993, Vegetation of Qinghai Hoh Xil region. *Acta Phytoecologica Sinica*, 2, 120-132. In chinese.
- Guo, Ke, 1995, Main characteristics of Littiedalea racemosa alpine steppe in Qinghai-Xizhang (Tibet) plateau. *Acta Phytoecologica Sinica*, 3, 248-254. In chinese.
- Jin, Huijun, Yu, Qihao, Wang, Shaoling, and Lü, Lanzhi, 2008, Changes in permafrost environments along the Qinghai-Tibet engineering corridor induced by anthropogenic activities and climate warming. *Cold Regions Science and Technology*, 3, 317-333.
- Miehe, Georg, Sabine, Miehe, Knut, Kaiser, Liu, Jianquan, and Zhao, Xinquan, 2008, Status and dynamics of the Kobresia pygmaea ecosystem on the Tibetan Plateau. *AMBIO: A Journal of the Human Environment*, 4, 272-279.
- Peng, Changhui, Hua, Ouyang, Gao, Qiong, Jiang, Yuan, Zhang, Feng, Li, Jun, and Yu, Qiang, 2007, Building a "Green" Railway in China. *Science*, 5824, 546-547.
- Roberts, Dar A, M Gardner, R Church, S Ustin, G Scheer, and RO Green, 1998, Mapping chaparral in the Santa Monica Mountains using multiple endmember spectral mixture models. *Remote sensing of environment*, 3, 267-279.
- Soil Survey Staff, 2010, Keys to Soil Taxonomy, Eleventh edition ed. (Washington DC: Government Printing Office).
- Teillet, PM, B Guindon, and DG Goodenough, 1982, On the slope-aspect correction of multispectral scanner data. *Canadian Journal of Remote Sensing*, 2, 84-106.
- Wang, Genxu, Wu, Qingbai, Wang, Yibo, and Guo, Zhenggang, 2005, The impacts of railroad engineering on the alpine grassland ecosystem in Qinghai-Tibet plateau. *Science & Technology Review*, 1, 8-13. In chinese.
- Xie, Shengbo, and Qu, Jianjun, 2013, Analyses on the types, distributions and characteristics of vegetation and soil along Qinghai-Tibet Railway. *Meteorological and Environmental Research*, 4, 15-18.
- Zhang, Jingwei, 1988, Vegetation of Xizang (Tibet) (Beijing, China: Science Press). In chinese.
- Zhang, Kecun, Qu Jianjun, Liao Kongtai, Niu Qinghe, and Han Qingjie, 2010, Damage by wind-blown sand and its control along Qinghai-Tibet Railway in China. *Aeolian Research*, 3, 143-146.
- Zhang, Tingjun, T Harry, W Baker, Cheng, GuoDong, and Wu, Qingbai, 2008, The Qinghai-Tibet Railroad: a milestone project and its environmental impact. *Cold Regions Science and Technology*, 3, 229-240.

Effectiveness of MISR multiangular observations in the Earth Observation Land Data Assimilation System (EO-LDAS)

M. Chernetskiy¹, N. Gobron², J. Gomez-Dans³, P. Lewis³, C. Schmullius¹.

¹ Friedrich Schiller University, Institute of Geography, Department for Earth Observation, Jena, Germany

² EC Joint Research Centre, Ispra (VA), Italy

³ University College London (UCL), United Kingdom

¹maxim.chernetskiy@uni-jena.de, ²nadine.gobron@jrc.ec.europa.eu, ³j.gomez-dans@ucl.ac.uk

ABSTRACT—The Earth Observation Land Data Assimilation System (EO-LDAS) is a system that allows interpreting spectral observations of the land surface to provide an optimal estimate of the Earth surface state. It allows a consistent combination of observations from different sensors despite the difference in spatial and spectral resolution and acquisition frequencies. The system is based on variational data assimilation (DA) scheme, and uses physically-based radiative transfer models (RTM) to map from state to observation. In addition the system takes into account observational uncertainty, prior information and a model of spatial/temporal evolution of the state. Such approach is very useful for the future satellite constellations as well as for reanalysis of historical data. In this study synergy of MISR and Landsat information in EO-LDAS was validated. Data of the ESA SPARC 2004 field campaign was used. The validation was made by reconstruction of CHRIS/PROBA spectral bands. In turn the reconstruction was made by combination of synthetic and real multiangular/multispectral data of MISR and Landsat ETM+. Synthetic data of ETM+ and MISR were generated by forward mode of the EO-LDAS observational operator. Then obtained reflectance bands were inverted with the different combinations of the sensors. First for ETM+ and MISR then for combinations of MISR-ETM+. Then obtained biophysical parameters were again used in a forward mode of the system to obtain hyperspectral information of CHRIS/PROBA. The same procedure was done for real data of ETM+ and MISR. In addition uncertainties of output spectra were considered.

1 INTRODUCTION

Earth Observation (EO) hyperspectral data provide detailed spectral information in the certain range of electromagnetic spectrum and it enables a significant improvement in comparison to the commonly used multispectral data in such areas as agriculture, forestry, soil and land management, etc. Currently only two hyperspectral sensors are orbiting the Earth - Hyperion on board of Earth Observing-1 satellite and Compact High Resolution Imaging Spectrometer (CHRIS) on board of Proba-1. However information of these sensors is not available on a global scale. At the same time nowadays there are a lot of multispectral instruments which provide wealth of information with different spectral ranges, spectral bandwidths, sun/view geometry, spatial resolutions and revisiting frequencies. Combination of these sensors through physically based models potentially can provide an estimation of a hyperspectral signal. One possible way to do it is the Earth Observation Land Data Assimilation System (EO-LDAS). It is a system which helps to interpret spectral observations over a land surface through providing an optimal estimate of state variables (Lewis et al. 2012). Several observations of different sensors can be used together

despite their differences in spatial and spectral resolution and acquisition frequencies. The principal is that the more accurate information is available the better results can be provided (Lewis et al. 2012; Knyazikhin et al. 1998). The EO-LDAS is based on variational Data Assimilation (DA) scheme together with a canopy radiative transfer model (RTM). The system takes into account observation uncertainties, prior information and a model of spatial/temporal evolution of land surface state.

The main purpose of EO-LDAS is the retrieval of biophysical land variables. However, once these state variables are retrieved from some observations, the system can be used in forward mode and predict observations of another sensor. For example it can be some observations of a hyperspectral sensor.

Despite of a set of constraints provided by EO-LDAS informational content of multispectral information still cannot be enough and some additional constraints are required. These additional constraints can be provided by multiangular information which are available globally and regularly by the Multiangle Imaging Spectroradiometer (MISR). It has nine view angles and spatial resolution from 275 m to 1.1 km (Diner et al. 1998). There are several studies which proofed what MISR multiangular

information can improve retrieval of some parameters such as Fraction of Absorbed Photosynthetically Active Radiation (FAPAR) or Leaf Area Index (LAI) (Knyazikhin et al. 1998; Gobron et al. 2000; Pinty et al. 2002; Widlowski et al. 2004; Laurent et al. 2011; Pisek et al. 2013).

This contribution is concentrated on validation of a combination of multiangular (MISR) and multispectral (ETM+) constraints in EO-LDAS for simulation of hyperspectral information at the Top of Canopy level (TOC).

2 STUDY SITE, DATA AND METHODS

The EO-LDAS is based on weak constrain data assimilation (DA), meaning that a model is not perfect and has a model error which regulated by so called regularization parameter (Zupanski 1997). The system implements mechanisms for constraining input remote sensing information in order to get an optimal estimate of vegetation parameters of land surface. In EO-LDAS, one can constraint the optimal solution by prior information, time or/and spatial regularization.

The main task of the system is the minimization of a cost function J_{post} which is the sum of three following terms:

$$J_{\text{post}} = J_{\text{prior}} + J_{\text{obs}} + J_{\text{model}} \quad (1)$$

where J_{prior} provides a priori knowledge of state variables, the second term J_{obs} corresponds to the observations cost function (the semidiscrete canopy radiative transfer model (Gobron et al. 1997)) and the J_{model} is a dynamic model cost function.

A test site for this study is an agriculture area near Barrax in Spain. It has availability of field measurements carried out by European Space Agency (ESA) - SPectraBArax Campaign (SPARC) campaign 2004 (Gandia et al. 2004).

A part of the SPARC campaign was acquisition by CHRIS/Proba which is an experimental space hyperspectral instrument. In the mode 1 it has 62 spectral bands from 411 to 997 nm; spatial resolution at nadir is 34m and 5 view zenith angles: $\pm 55^\circ$, $\pm 36^\circ$ and 0° (nominally).

A scene of CHRIS/Proba was acquired at the 16th July 2004. Geometrical properties of observations at the closest nadir PROBA camera are: 8.4° , 283.6° , 20.8° , 325.5° – view zenith angle (VZA), view azimuth angle (VAA), sun zenith angle (SZA) and sun azimuth angle (SAA) respectively.

The spectral data which were used for validation are taken from CHRIS/Proba image at the points of 18 SPARC field measurements. They represent different crop species and among measured parameters both LAI and chlorophyll a+b content.

The MISR is the operational multi-angular optical sensor which obtains information globally and simultaneously at nine view angles. We used the

MISR top of canopy reflectance at 275m spatial resolution produced by the sharpening method of (Verstraete et al. 2012) for 16 July 2004. The data were provided by Joint Research Centre (JRC) and contain: 4 spectral bands at 446, 558, 672 and 867 nm; 9 cameras at nadir, $\pm 26.1^\circ$, $\pm 45.6^\circ$, $\pm 60.0^\circ$, and $\pm 70.5^\circ$.

The Landsat ETM+ data were acquired at 18th July 2004 with 30m spatial resolution and 6 spectral bands. The atmospheric correction was performed by the Landsat Ecosystem Disturbance Adaptive Processing System (LEDAPS) software (Masek et al. 2012).

One important issue is to find an initial estimate of the state parameters because it determines starting values – first guess for an inversion process. First guess reduces chances to be trapped in a local minimum of parameter space and it makes the process faster. It was done by finding a minimum difference between an actual MISR measurement and a set of samples generated by the semidiscrete model. Sampling of 10 state parameters was done by the Latin Hypercube Sampling (LHS) from python library of the EO-LDAS new generation (Iman et al. 1980). The main advantage of LHS is that it is not required more samples for more dimensions.

In order to increase speed of computation uncertainties of forward modelling were estimated using Gaussian Process Emulator (Currin et al. 1991) which is implemented as a python library in the EO-LDAS new generation. It was used to increase speed of computation. The emulator establishes dependences between inputs (state parameters) and outputs (spectral bands) of the observational operator. Then it can be used for estimation of uncertainties (standard deviation) by forward run of a model. Nevertheless mean of the forward run was found by the EOLDAS observational operator without the emulator.

3 RESULTS

This section consists of the experiments which were carried out with synthetic and real data.

Synthetic MISR-like data were created for all 18 SPARC field measurements. The SPARC database (ESA 2004) was used to provide input information about LAI, chlorophyll a+b content, dry matter content and leaf water content. For each field we created nine measurements. Each measurement represents MISR-like one-pixel observation with several numbers of cameras. A number of cameras are increasing from nadir-only (An) to nine (Df-Da).

For each of nine measurements 10 state parameters were retrieved by inverse run of EO-LDAS. Then these parameters were used as an input in a forward run of EO-LDAS in order to obtain hyperspectral data.

Calculation of both mean the root-mean-square error (RMSE) and mean uncertainties for 18 field

measurements shows decrease of uncertainties for all considered measurements and doesn't show significant change in mean RMSE (Fig. 1). Especially significant decreasing of uncertainties (60%-80%) is appeared for the first 3-4 cameras. However as can be seen there is no meaningful change of RMSE with increasing a number of MISR cameras. In the case of synthetic data the advantage in combination of ETM+ and MISR

data in the terms of RMSE is about 10%. However for the real data there is a remarkable decrease (33%) of RMSE and also a decrease of variability of RMSE. If for MISR only decision it is 0.065 with $sd=0.055$ when in the case of joint decision it is 0.043 with $sd=0.018$. In addition second sensor always decrease uncertainty of the nadir only decision up to 30%-50%.

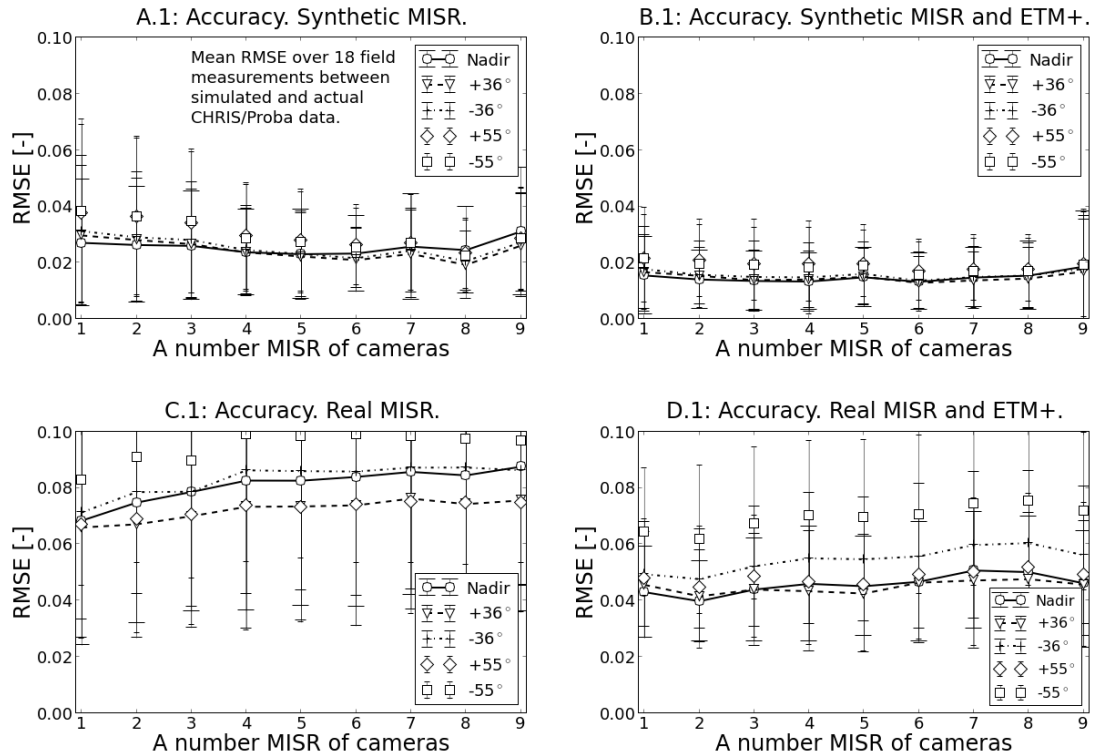


Figure 1. Mean RMSE between actual and simulated CHRIS/Proba spectra over 18 field measurements for 5 observational angles. Spectra were simulated by: A.1) synthetic MISR data; B.1) combination of synthetic MISR and ETM+ data; C.1) real MISR; D.1) real MISR and ETM+

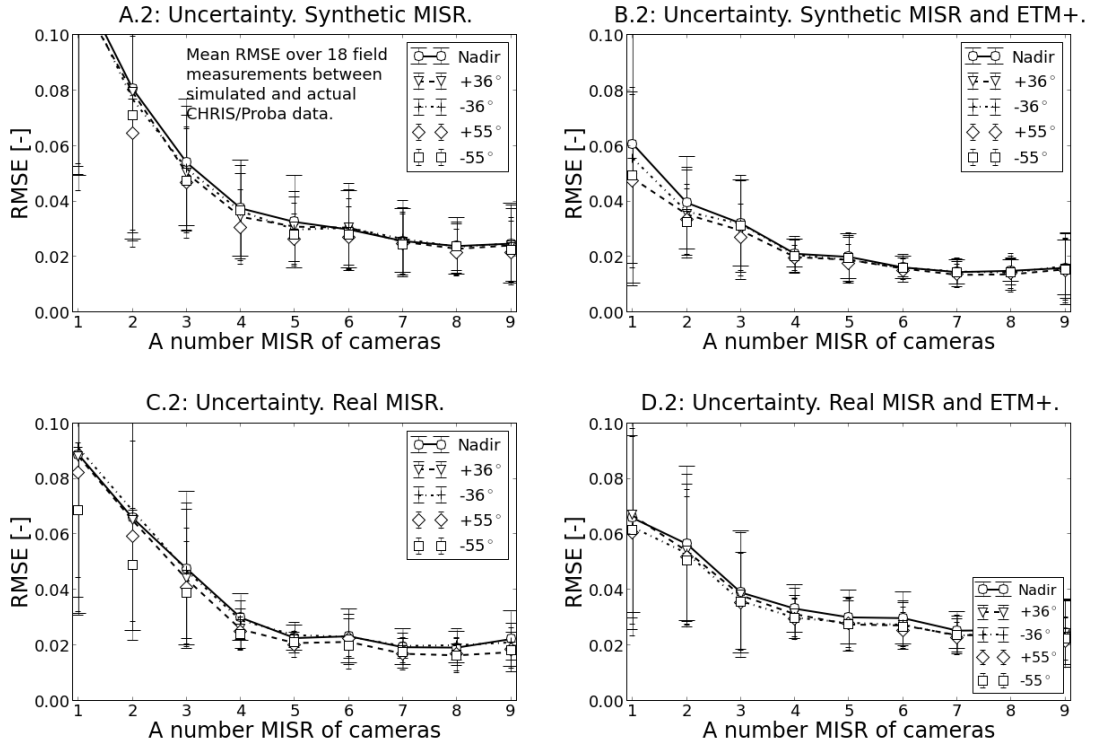


Figure 2. Mean posterior uncertainty (standard deviation) of simulated CHRIS/Proba spectra over 18 field measurements for 5 observational angles. Spectra were simulated by: A.2) synthetic MISR data; B.2) combination of synthetic MISR and ETM+ data; C.2) real MISR; D.2) real MISR and ETM+.

It is possible to explain decreasing of uncertainty by increasing a number of observations. However if to

generate synthetic MISR data with 9 identical nadir-only cameras uncertainties are not decreasing (Fig. 3).

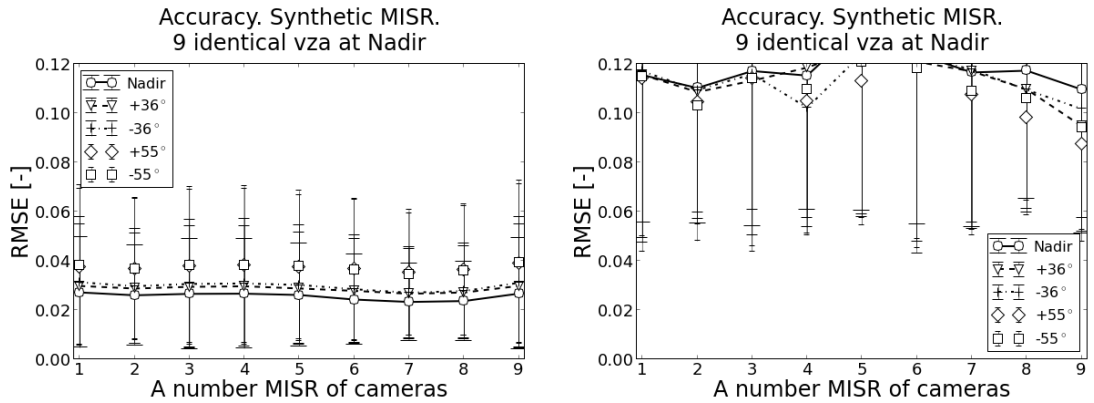


Figure 3. Mean posterior uncertainty (standard deviation) of simulated CHRIS/Proba spectra over 18 field measurements for 5 observational angles. All 9 cameras are identical to Nadir observation. Spectra were simulated by synthetic MISR data.

4 DISCUSSION AND CONCLUSIONS

This study presents a validation of multispectral and multiangular constraints of EOLDAS in a form of simulation of CHRIS/PROBA hyperspectral signal over the Barrax test site. The process of validation can be summarized in the three parts: making a first guess; retrieval of the state parameters by EOLDAS; obtaining simulated spectral profiles by running the semidiscrete model in forward mode and calculation of uncertainties by Gaussian Process Emulators (GP).

The simulation has been conducted for four data sets with 18 measurements in each: synthetic MISR, synthetic MISR and ETM+, real MISR, real MISR and ETM+. In all cases number of MISR cameras were increased one by one from nadir camera (An) to cameras up to 70 deg. (i.e. Df and Da). It was found that in all considering cases posterior uncertainties are decreasing with increasing of MISR cameras. I.e. the problem becomes more constrained with increasing amount of multiangular information. The results based on the real MISR data have highest values of RMSE because due to low spatial resolution its signal is mixed and it has high discrepancy with CHRIS/PROBA. However adding spectral information of ETM+ always increase accuracy and decrease uncertainties relative to both ETM+-only and MISR-only results, for synthetic as well as for real datasets.

Presented results demonstrate that EO-LDAS can be used for simulation of hyperspectral data when hyperspectral information is not available. In addition it can be used for validation of biophysical parameters retrieval if hyperspectral information is available but field measurements are not available. In addition was shown a way of combination of mixed coarse spatial resolution data and high resolution data (only in spectral domain).

The quite important issue which was not considered here is how to propagate a priori uncertainties through the pre-processing chain: i.e. calibration, georeferencing, atmospheric correction, dependency on spatial resolution, etc. So further efforts are required because this can provide a proper balance between the cost function terms: models, radiometric information and prior information and can significantly improve results.

ACKNOWLEDGEMENTS

We gratefully acknowledge financial support of this project through GIONET, funded by the European Commission, Marie Curie Programme Initial Training Network, Grant Agreement number PITN-GA-2010-264509. We also acknowledge European Space Agency for providing data access by the "EO-Support" system (projects ID 13803 and 13931) and Olivier Morgan (JRC) for his technical support.

REFERENCES

- Curran, C., Mitchell, T., Morris, M. and Ylvisaker, D., 1991. Bayesian Prediction of Deterministic Functions, with Applications to the Design and Analysis of Computer Experiments. *Journal of the American Statistical Association*, 86, 953–963.
- Diner, D.J., Beckert, J.C., Reilly, T.H., Bruegge, C.J., Conel, J.E., Kahn, R.A., Martonchik, J. V., Ackerman, T.P., Davies, R., Gerstl, S.A.W., Gordon, H.R., Muller, J.-P., Myneni, R.B., Sellers, P.J., Pinty, B. and Verstraete, M.M., 1998. Multi-angle Imaging SpectroRadiometer (MISR) instrument description and experiment overview. *Geoscience and Remote Sensing, IEEE Transactions on*, 36(4), 1072–1087.
- ESA, 2004. SPARC Data Acquisition Report., Contract no: 18307/04/NL/FF, University of Valencia [Online]. Available: <http://earth.esa.int/campaigns/>.
- Gandia, S., Fernández, G., García, J.C. and Moreno, J., 2004. Retrieval of vegetation biophysical variables from CHRIS/PROBA data in the SPARC campaign. In *Proc. 2nd CHIRS/Proba Workshop*, ESA/ESRIN, Frascati, Italy.
- Gobron, N., Pinty, B., Verstraete, M.M. and Govaerts, Y., 1997. A semidiscrete model for the scattering of light by vegetation. *Journal of Geophysical Research*, 102, 9431–9446.
- Gobron, N., Pinty, B., Verstraete, M.M., Martonchik, J. V., Knyazikhin, Y. and Diner, D.J., 2000. Potential of multiangular spectral measurements to characterize land surfaces: Conceptual approach and exploratory application. *Journal of Geophysical Research*, 105(D13), 17539.
- Iman, R.L., Davenport, J.M. and Zeigler, D.K., 1980. Latin hypercube sampling (program user's guide),
- Knyazikhin, Y., Martonchik, J. V., Myneni, R.B., Diner, D.J. and Running, S.W., 1998. Synergistic algorithm for estimating vegetation canopy leaf area index and fraction of absorbed photosynthetically active radiation from MODIS and MISR data. *Journal of Geophysical Research*, 103(D24), 32257.

- Laurent, V.C.E., Verhoef, W., Clevers, J.G.P.W. and Schaepman, M.E., 2011. Inversion of a coupled canopy–atmosphere model using multi-angular top-of-atmosphere radiance data: A forest case study. *Remote Sensing of Environment*, 115(10), 2603–2612.
- Lewis, P., Gómez-Dans, J., Kaminski, T., Settle, J., Quaife, T., Gobron, N., Styles, J. and Berger, M., 2012. An Earth Observation Land Data Assimilation System (EO-LDAS). *Remote Sensing of Environment*, 120, 219–235.
- Masek, J.G., Vermote, E.F., Saleous, N., Wolfe, R., Hall, F.G., Huemmrich, F., Gao, F., Kutler, J. and Lim, T.K., 2012. LEDAPS Landsat Calibration, Reflectance, Atmospheric Correction Preprocessing Code. Model product. Available on-line [<http://daac.ornl.gov>] from Oak Ridge National Laboratory Distributed Active Archive Center, Oak Ridge, Tennessee, U.S.A. <http://dx.doi.or>.
- Pinty, B., Widlowski, J., Gobron, N., Verstraete, M.M., Diner, D.J. and Member, A., 2002. Uniqueness of Multiangular Measurements — Part I: An Indicator of Subpixel Surface Heterogeneity From MISR. , 40(7), 1560–1573.
- Pisek, J., Ryu, Y., Sprintsin, M., He, L., Oliphant, A.J., Korhonen, L., Kuusk, J., Kuusk, A., Bergstrom, R., Verrelst, J. and Alikas, K., 2013. Retrieving vegetation clumping index from Multi-angle Imaging SpectroRadiometer (MISR) data at 275m resolution. *Remote Sensing of Environment*, 138, 126–133.
- Verstraete, M.M., Member, S., Hunt, L.A., Scholes, R.J., Clerici, M., Pinty, B. and Nelson, D.L., 2012. Generating 275-m Resolution Land Surface Products From the Multi-Angle Imaging SpectroRadiometer Data. *IEEE Transactions on Geoscience and Remote Sensing*, 50(10), 3980–3990.
- Widlowski, J.-L., Pinty, B., Gobron, N., Verstraete, M.M., Diner, D.J. and Davis, A.B., 2004. Canopy structure parameters derived from multi-angular remote sensing data for terrestrial carbon studies. *Climatic Change*, 67, 403–415.
- Zupanski, D., 1997. A general weak constraint applicable to operational 4DVAR data assimilation systems. *Monthly Weather Review*, 125, 2274–2292.

Crop cycle monitoring by combining medium and high resolution optical imagery

F.J. García-Haro¹, C. Gevaert², M. Campos-Taberner¹

¹*Facultat de Física, Universitat de València, Dr. Moliner, 50. 46100-Burjassot, Spain.*

²*Department of Earth Observation Science, Faculty ITC, University of Twente, P.O. Box 6, Enschede 7500AA, Enschede, The Netherlands.*

j.garcia.haro@uv.es

ABSTRACT-This work is focussed on evaluating data fusion methods between medium-resolution imagery such as MODIS and high-resolution datasets such as Landsat. A recently developed method, namely Spatial and Temporal Reflectance Unmixing Model (STRUM) is evaluated. The study area is the rice district in Valencia (Spain) and the overall objective consists in obtaining time series of Landsat-like reflectance imagery using MODIS time series and a limited number of Landsat 8 imagery. The results are suitable to monitor an agronomic season with enhanced spatial resolution within the context of ERMES (EU FP7). This will contribute to produce timely information to force model simulation to the conditions observed by satellite monitoring at a local scale.

1 INTRODUCTION

Information of the phenological development is a fundamental element in crop monitoring because it describes the actual state of the cultivated species/varieties and their relation with the pedo-climatic conditions. Multitemporal satellite imagery may provide occurrence estimation of the phenological stages in a spatially distributed model. However, factors such as inadequate spatial or temporal resolution and cloud cover have limited the effectiveness of utilizing satellite imagery.

Landsat mission provides one of the most extensively used high-resolution data sets. Landsat TM, ETM+ and OLI sensors have a spatial resolution of 30 m for the multispectral bands, which is adequate for many environmental applications. However, Landsat satellites have a revisit time of 16 days, and an average of 35% of the images are plagued by cloud cover (Roy et al., 2008). On the other hand, medium-resolution MODIS TERRA imagery have a daily revisit period, but a lower spatial resolution which limits its effectiveness for fine-scale environmental applications.

In order to overcome this problem we focussed on evaluating data fusion methods between MODIS and Landsat. Two prevalent data fusion methods are the Spatial and Temporal Adaptive Reflectance Fusion Model (STARFM) (Gao et al. 2006) and unmixing-based data fusion (Zurita-Milla, 2009, 2011; Amorós-López, 2013). In this study we apply a recently developed algorithm, namely the Spatial and Temporal Reflectance Unmixing Model (STRUM), which combines the strengths of both algorithms (Gevaert

and García, 2015). The potential of this method is demonstrated using Landsat and MODIS imagery.

The ability of fused images to capture phenological variations is also assessed using temporal NDVI profiles. The study area is the rice district in Valencia (Spain) and the overall objective consists in obtaining time series of reflectance imagery during an agronomic season with enhanced spatial resolution. Improvement is achieved by downscaling time series of MODIS products to disaggregate the product medium resolution using the information about their pixel composition provided by high resolution data.

2 METHODOLOGY

STRUM is an unmixing based method inspired by STARFM principles, i.e. assuming that MODIS and Landsat surface reflectance are radiometrically and temporally comparable. Similar to the STARFM, this method requires three input images: a Landsat and MODIS image on the same base date (t_0), and a MODIS image on the prediction date (t_k). A residual image is defined as the difference between the two MODIS images, i.e.

$$residual = M(t_k) - M(t_0) \quad (1)$$

The definition of this residual implies that STRUM requires corresponding spectral bands between the high- and medium-resolution data, as opposed to the unmixing method which can be applied to all the spectral bands of the medium-resolution data.

Unmixing-based image fusion applies four steps to solve the linear mixing model (see figure 1):

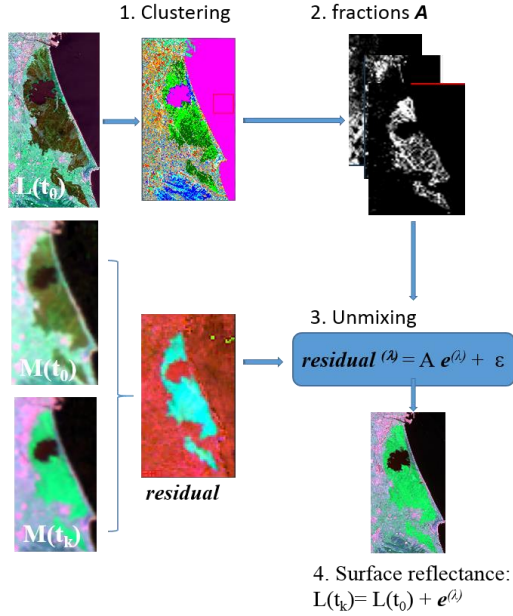


Figure 1. Flow chart of the algorithm for FVC determination

(1) Cluster the high-resolution dataset to define the endmembers. The present study applies the k-means algorithm to identify k spectral clusters.

(2) Apply a sliding window of $[n \times n]$ MODIS pixels to the clustered image to record the endmember fractions **A**, a $[n^2 \times k]$ matrix with the abundances of each endmember within each medium-resolution pixel. The use of a sliding window allows for spectral differences between pixels of the same cluster in different locations.

(3) Unmix the medium-resolution residual. The aim is to solve for $e^{(\lambda)}$ a $[k \times I]$ column vector that contains temporal changes of each endmember spectra in MODIS band (λ). $residual^{(\lambda)}$ is a $[n^2 \times I]$ column vector residual values (Ec. 1) of each MODIS pixel in the $n \times n$ moving window for the MODIS band λ which is currently being unmixed. This is achieved by minimizing the residuals (ϵ) of the linear model (Eq. 2).

$$residual^{(\lambda)} = A e^{(\lambda)} + \epsilon \quad (2)$$

We propose a Bayesian approach, which allows specifying the variances σ_0^2 and σ_r^2 assigned to the prior of $e^{(\lambda)}$ and the noisy reflectance data $r^{(\lambda)}$, respectively. For a detailed description, we refer to Murphy (2012). If the precision assigned to the prior is strong relative to the data strength (σ_0 is large relative to σ_r), more emphasis is put on the prior and

vice versa. The relative importance of the prior is controlled in this study by optimizing the ratio $\sigma_{ratio} = \sigma_r / \sigma_0$.

(4) Create the fused image. The temporal change of the relevant endmember is assigned to each Landsat pixel in the window to its class label, and added to the input Landsat image on the base date:

$$L(t_k) = L(t_0) + e^{(\lambda)} \quad (3)$$

The fused results therefore provide Landsat-like reflectances containing information regarding temporal variation in surface reflectances obtained from the input MODIS imagery.

3. RESULTS

3.1 Study area

The study area is in the Albufera National park region near Valencia, Spain (39.33°N, 0.36°W). It is a rectangular area of 1008 km², which corresponds to 808×1399 Landsat pixels. The lands occupied by the cultivation of rice amounts to 16,000 ha, which is the area that has remained stable in recent years. The area has a typical Mediterranean climate, mild, with an average annual humidity of 65%. The average annual temperature is 17° C. Their mean values ranging from 11° C in January and 27° C in August. The mean annual precipitation is approximately 430 mm. Precipitation tends to be intense and concentrated in autumn.

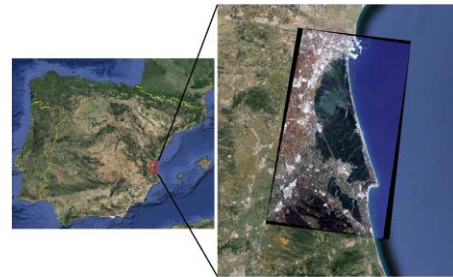


Figure 2. Location of the study area

3.2 Satellite image preprocessing

The current study uses Landsat 8/OLI imagery for the high-resolution input data. The Landsat 8 images were downloaded as a Level 1T product and corrected to TOA reflectance using the parameters provided in the metadata file. The images were atmospherically

corrected using the Dark Object Subtraction (DOS) method (Chavez, 1988). As the study area lies in two Landsat paths, images are available every 8 days rather than the usual interval of 16. However, only six corresponding cloud-free Landsat 8/OLI images were available within the time frame: May 3, May 19, June 4, June 20, July 15, July 31 and September, 1, 2014.

The Moderate Resolution Imaging Spectroradiometer (MODIS) sensor, on board satellites Terra and Aqua, is used for medium-resolution imagery. The MODIS MCD43A4 Nadir BRDF-Adjusted Reflectance product with a 463 m resolution was utilized, as previous studies have indicated that MODIS BRDF products provide more accurate data fusion results than daily MODIS surface reflectances (Roy et al., 2008; Walker et al., 2012). This product is a 16-day composite of both Aqua and Terra satellites, produced every 8 days. MCD43A4 images corresponding to the same periods were used.

All images were subsetting to the study area, low-quality pixels identified by the quality flag information were removed, and the images were reprojected to UTM coordinates. Furthermore, the geometric co-registration of each Landsat-MODIS image pair was optimized. This was done by determining the optimal offset which maximized the Pearson's correlation coefficient between all spectral bands of the MODIS image and resampled Landsat image.

Inspection of the data revealed significant differences between the Landsat and MODIS reflectance data sets, caused by differences in image processing chains and spectral band difference effects (Teillet et al. 2007). In order to reduce this bias, a radiometric normalization method was applied, which assumes a linear relationship between the reflectance of both images. The critical aspect is the determination of suitable invariant pixels (at MODIS scale) upon which to base the normalization. We applied Iteratively Reweighted Multivariate Alteration Detection (IRMAD) transformation (Nielsen, 2007) to select pixels with a high no-change probability (i.e., >0.95). The method is completely automatic and compares favorably with normalization using hand-selected invariant features (Canty & Nielsen, 2008). We regressed the (resampled) Landsat images onto the corresponding MODIS images at no-change locations (see Figure 3). For each band, slope and intercept parameters were obtained using orthogonal linear regression, since it outperformed the ordinary least squares regression.

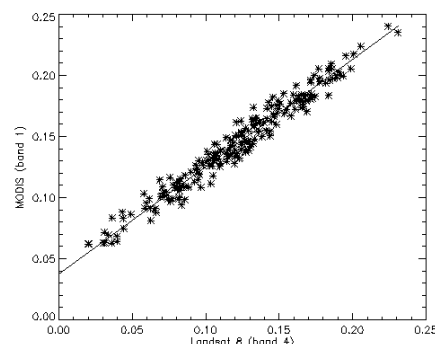


Figure 3. Example of radiometric normalization in red waveband, corresponding to Landsat8/OLI June 4 (target) vs. MCD43 May, 25 – June, 10 (reference). Solid line: orthogonal regression.

3.3 Data fusion optimization

Optimal input parameters were identified using the Landsat 8/OLI image on June 4, 2014 and the MODIS composite from May 25-June 10th as base images, and the MODIS composite from July 12-28th to represent the prediction date (see Figure 4). The number of clusters was varied using the values $k=10, 20, 40$, and 80 . The window size was also varied from $w=5$ to 41 MODIS pixels in steps of 4 . The weight of the *a priori* endmember information was varied, using the values $\sigma_{ratio}=0.01, 1, 2$, and 5 .

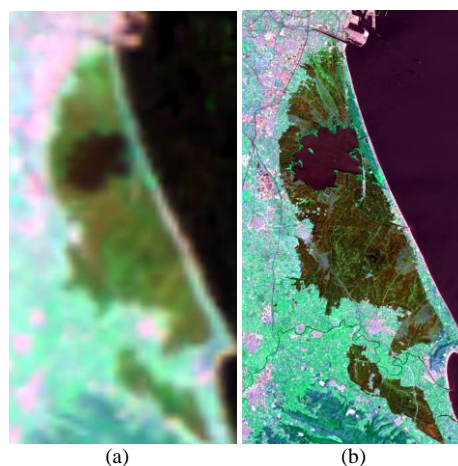


Figure 4. The base pair ($M(t_0), L(t_0)$) used to predict surface reflectance for each $M(t_k)$. (a) MODIS composite from May, 25 – June, 10th; (b) Landsat 8/OLI image on June 4.

The accuracy was evaluated taking into account the *Erreur Relative Globale Adimensionnelle de Synthèse* (ERGAS) (Wald, 2002) and the correlation coefficient as a quality indicators. ERGAS was higher for smaller numbers of clusters (lower ERGAS and higher correlation coefficient). Few clusters (i.e. $k=10$ or 20)

produced better indicator values, and reduced the sensitivity to variations in moving-window size. In order to preserve the spectral variability while maintaining fusion quality, a small value of neighborhood size (i.e. less than 20) was preferred. Furthermore, it was observed that the inclusion of *a priori* spectral information allows to significantly improve the results. The optimal parameters in the current study were defined as $w=9$, $k=20$ and $\sigma_{ratio}=1.0$, although other combinations are also possible.

3.4 Creation of fused Landsat 8/OLI Reflectance

The application of these optimal parameters produced surface reflectances very similar to Landsat imagery, as indicated in Figure 5. These results correspond to a case with significant temporal change and suggest that a significant time between the base image date and prediction date did not significantly affect the ability to correctly predict Landsat-8 reflectance. Even better results were found in cases with little temporal change.

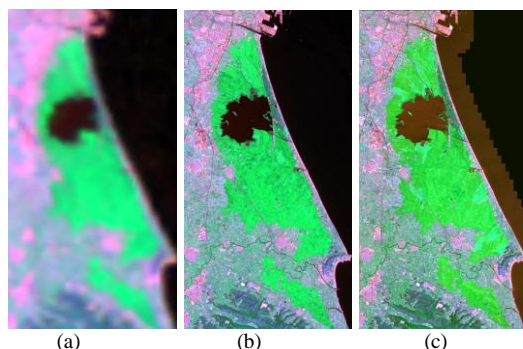


Figure 5. Results of data fusion in a case with significant temporal change: using June 3th as a base date to predict reflectance on September 1st. (a) The MODIS composite of August 21-September 6, 2014; (b) the predictions using STRUM. (c) a reference (unused) Landsat image on September 1st. All images are displayed with the band combination R:Red, G:NIR, B: SWIR.

3.5 Derivation of temporal profiles

In order to assess whether the fused images are suitable for studying vegetation dynamics, the final experiment consisted of applying the STRUM algorithm to create NDVI temporal profiles of 8 fused images. The NDVI time series were assessed by examining seasonal variations over representative agricultural fields. The aim of the experiment was to fill gaps in the Landsat 8 temporal profiles by using only one Landsat 8 image to create the time series and 8 MODIS data. This simulates realistic situations in

which few high-resolution images are available. Furthermore, it allows unused Landsat images to act as a testing dataset to analyze the quality of the fused NDVI predictions.

The reconstruction of the Landsat-like rice cycle (May-September 2014) is illustrated in Figure 1. The Landsat image on June 4 and the MODIS composite from May 25-June 10th were used as base images.

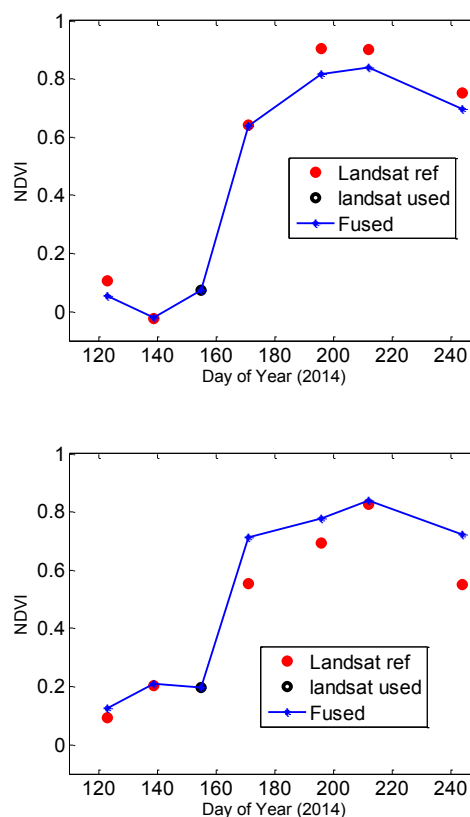


Figure 6. Temporal profiles of the STRUM NDVI predictions for a scenario using a single Landsat image to create the temporal profiles. Results correspond to two representative agricultural fields.

Results confirm that STRUM has the potential to transfer temporal information from MODIS to Landsat in order to capture phenological variations. The method clearly outperforms existing literature methods at observing temporal dynamics in situations where limited high-resolution images are available. For example, Gevaert and García-Haro (2015) found that STARFM fails to capture phenological variations when having only 1 or 2 input Landsat 8 images and predictions are highly dependent on the number input images.

3 CONCLUSIONS

Multi-sensor data fusion provides an opportunity to obtain imagery products which transcend physical sensor limitations. The STRUM algorithm has been recently proposed to produce Landsat-like reflectances while preserving the spatial patterns found in Landsat images. This paper explores the potential of this method to monitor an agronomic season of rice fields with enhanced spatial resolution, while incorporating information regarding temporal variation in reflectances obtained from the input MODIS imagery.

The STRUM produced surface reflectances very similar to Landsat imagery, even in challenging scenarios with a significant time between the base image date and prediction date. The ability of fused images to capture phenological variations has been also demonstrated. Temporal profiles of STRUM NDVI closely resembled Landsat NDVI profiles in experiments simulating situations where few input high-resolution images are available.

The results of this study confirm previous findings that STRUM is well suited for data fusion applications requiring Landsat-like surface reflectances, such as gap-filling and cloud replacement. The method has potential to generate high resolution imagery to monitor the rice agronomic season and provide timely information to force model simulation to the conditions observed by satellite monitoring at a local scale.

4 ACKNOWLEDGMENTS

Funding support of ERMES (EU FP7-Space-2013, Contract 606983), RESET CLIMATE (CGL2012-35831) and LSA SAF (EUMETSAT) projects is acknowledged.

5 REFERENCES

- Amorós-López, J., Gómez-Chova, L., Alonso, L., Guanter, L., Zurita-Milla, R., Moreno, J., & Camps-Valls, G., 2013, Multitemporal fusion of Landsat/TM and ENVISAT/MERIS for crop monitoring. *International Journal of Applied Earth Observation and Geoinformation*, **23**, 132–141.
- Canty, M. J., & Nielsen, A. A., 2008, Automatic radiometric normalization of multitemporal satellite imagery with the iteratively re-weighted MAD transformation. *Remote Sensing of Environment*, **112**, 1025–1036.
- Chavez, P. S. J., 1988, An improved dark-object subtraction technique for atmospheric scattering correction of multispectral data. *Remote Sensing of Environment*, **24**, 459–479.
- Gao, F., Masek, J., Schwaller, M., & Hall, F., 2006, On the blending of the Landsat and MODIS surface reflectance: predicting daily Landsat surface reflectance. *IEEE Transactions on Geoscience and Remote Sensing*, **44**, 2207–2218.
- Gevaert, C.M. and F.J. García-Haro, 2015, A Comparison of STARFM and an Unmixing-based Algorithm for Landsat and MODIS Data Fusion, *Remote sensing of Environment*, **156**, 34–44.
- Murphy, K., 2012, *Machine learning: a probabilistic perspective* (p. 1098). Cambridge, Massachusetts, USA: MIT Press.
- Nielsen, A. A., 2007, The regularized iteratively reweighted MAD method for change detection in multi- and hyperspectral data. *IEEE Transactions on Image Processing*, **16**, 463–78.
- Roy, D. P., Ju, J., Lewis, P., Schaaf, C., Gao, F., Hansen, M., & Lindquist, E., 2008, Multi-temporal MODIS–Landsat data fusion for relative radiometric normalization, gap filling, and prediction of Landsat data. *Remote Sensing of Environment*, **112**, 3112–3130.
- Teillet, P. M., Fedosejevs, G., Thome, K. ., & Barker, J. L., 2007, Impacts of spectral band difference effects on radiometric cross-calibration between satellite sensors in the solar-reflective spectral domain. *Remote Sensing of Environment*, **110**, 393–409.
- Zurita-Milla, R., Kaiser, G., Clevers, J. G. P. W., Schneider, W., & Schaepman, M. E., 2009, Downscaling time series of MERIS full resolution data to monitor vegetation seasonal dynamics. *Remote Sensing of Environment*, **113**, 1874–1885.
- Zurita-Milla, R., Gómez-Chova, L., Guanter, L., Clevers, J. G. P. W., & Camps-Valls, G., 2011, Multitemporal Unmixing of Medium-Spatial-Resolution Satellite Images : A Case Study Using MERIS Images for Land-Cover Mapping. *IEEE Transactions on Geoscience and Remote Sensing*, **49**, 4308–4317.
- Wald, L., 2002, *Data Fusion: Definitions and Architectures: Fusion of Images of Different Spatial Resolutions* (p. 198). Paris, France: Presses des MINES.

A first evaluation of an operational method (SSEBop) to estimate Actual Evapotranspiration by using MODIS data over the semi-arid region of Chile

Luis E. Olivera-Guerra¹, Cristian Mattar¹, Andrés Santamaría-Artigas¹, Claudio Durán-Alarcón¹, Rodrigo Fuster²

1. Laboratory for Analysis of the Biosphere (LAB), University of Chile

luis.enrique.olivera@gmail.com

2. Laboratory for Territorial Analysis (LAT), University of Chile.

ABSTRACT - Evaluation of evapotranspiration (ET) estimations over large areas is necessary before they can be used. This work presents the preliminary results of the “Hydric demand model for improving basin water management” project carried out in the Copiapó Basin, Chile. This basin is located in the southern boundary of the Atacama Desert over a semi-arid climate and high influences of the desert. As a first approach to evaluate an operational ET estimation model, the 8-day MODIS 1 km ET products (MOD16) and the Operational Simplified Surface Energy Balance (SSEBop) were compared over a basin with Vineyards and Olive Orchards that is currently under water supply problems. For this, the daily MODIS 1 km MOD11 land surface temperature (LST) product and meteorological data for the whole year 2013 were used to estimate the evaporative fraction of 8-day time periods as an input for the SSEBop model in order to obtain ET images of the study area aggregated over 8 days. Similar ET values were obtained in the comparison between model-estimated ETr and the ETr provided by the MOD16 product, achieving a R² for olives of 0.622 and a RMSE of 3.79 mm/8day, for vineyards the R² was 0.634 and the RMSE obtained was 3.62 mm/8day. This approach shows that the SSEBop model is able to estimate the spatial and temporal variability of ET at basin scale throughout the year, which could allow having an operational approach to monitor the water consumption of crops.

1 INTRODUCTION

Evapotranspiration (ET) has been recognized as the most important parameter in the energy and water exchange processes between land's surface and the atmosphere. In semi-arid environments, knowledge of daily ET values becomes more significant since it represents a large proportion of the water budget, estimated at more than 70% of incoming precipitation (Moussa et al., 2007). In addition, water resources have become scarcer in relation to demand, thus any attempt to improve water use efficiency must be based on reliable estimates of ET.

In Chile, agricultural activities generate one of the most important economic incomes. A significant portion of these activities are located in semi-arid conditions, where the productivity depends upon root zone moisture and irrigation. Thus, agricultural water consumption need to be efficient and estimated in order to maximize the crop productivity.

The agricultural activities in the semi-arid region of Chile, in addition to being one of the main water demanding activities, present a particular framework in respect to the water users. These activities are always developed under water use conflicts because other commercial activities such as mining and industrial uses. Thereby, water is a key strategic

resource in the development of all sectors of the economy.

In this context, an estimate of the actual water demand in the Copiapó Basin is a useful tool for farmers and decision makers. Thus, the aim of this work focuses on the first evaluation of an operational and dynamic model to estimate the water demand at regional scale using remote sensing data over the Copiapó Basin.

2 STUDY AREA

2.1 Study Area

The study area is located in the southern boundary of the Atacama Desert, Chile. The area of analysis corresponds to two sub-basins of the Copiapó Basin: Río Copiapó Bajo and Río Copiapó Medio (called *Copiapó Basin* in this work), in which agricultural crops are grown. This 4600 km² area, extends from sea level in the west to 4150 masl in the mountainous areas in the east. The basin is dominated by sandy soil of the Atacama Desert and crops are grown in a narrow valley along the basin. Agriculture is mainly dominated by vineyards and olive orchards under drip irrigation.

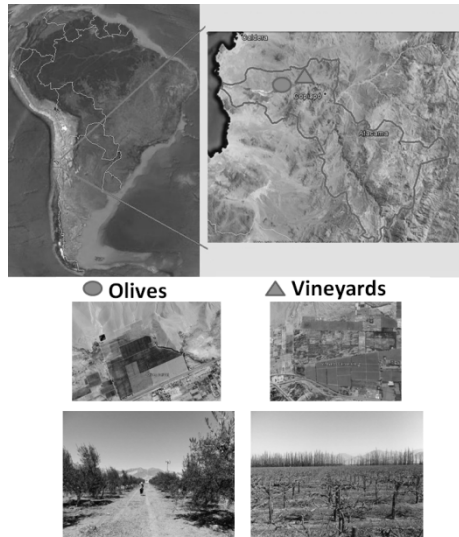


Figure 1. Study area.

3 DATA AND METHODOLOGY

3.1 Data

Land surface temperature derived from the Moderate Resolution Imaging Spectroradiometer (MODIS) 8-day average at 1km spatial resolution MOD11A2 product was used to estimate the SSEBop-based dataset for the whole year 2013. This dataset was generated using the algorithm Operational Simplified Surface Energy Balance (SSEBop; Senay et al., 2013). To evaluate the dataset generated with SSEBop we used the global MODIS ET datasets aggregated over 8 days at 1km spatial resolution (MOD16A1) for the year 2013 obtained from the University of Montana's Numerical Terra dynamic Simulation Group website (<ftp.nts.umt.edu/pub/MODIS/Mirror/MOD16/>) which are produced using an improved remote sensing ET algorithm proposed by Mu et al. (2011).

Daily minimum and maximum air temperature data for 2013 was obtained from a meteorological station located in the Copiapó Basin (27°57'35"S., 70°0'3"W.). The daily reference ET (ET₀) was obtained from this station using the standardized Penman-Monteith equation (Allen et al., 1998).

3.2 Methodology

The SSEBop algorithm was used to estimate the ET throughout the year 2013. This method use a predefined temperature difference (dT) between the "hot/dry" and "cold/wet" reference points that are seasonally dynamic and boundary conditions that are unique for each pixel, unlike the original SSEB formulation or similar models based in the surface energy balance (e.g., METRIC, SEBAL, S-SEBI) that use a set of reference hot and cold pixel pairs

applicable for a limited, uniform hydro-climatic region. The difference between the hot and cold values is assumed nearly constant for a given location and period (day or eight day) under clear-sky conditions. The cold boundary condition is obtained as a fraction of the air temperature T_a.

This simplification allows to estimate ET (ET_r) as a fraction of the ET₀ as:

$$ET_r = ET_f \times k \times ET_0 \quad (1)$$

Where k is a coefficient that scales the grass reference ET into the level of a maximum ET experienced by an aerodynamically rougher crop. The magnitude of k was determined accordingly to k_c coefficients of the dominating crops in the basin (vineyards and olives) and the fraction of the cover of vegetation. The k coefficient was established as 0.65. The ET_f is the ET fraction calculated as follow:

$$ET_f = \frac{T_{hot} - LST}{T_{hot} - T_{cold}} \quad (2)$$

Where LST is remotely sensed land surface temperature from MOD11A2 filtered from clouds or other processing failures using quality control (QC) values. T_{hot} is the reference "hot" condition of each pixel estimated as LST at the idealized reference "hot" condition; T_{cold} is the cold reference value as LST at the idealized reference "cold" condition. Temperatures LST, T_{hot} and T_{cold} are estimated over a given time period for each pixel, thus allowing to calculate ET_f of each pixel on the given time period, either daily (with a product such as MODIS MOD11A1) or as an eight day average (MOD11A2). The difference between T_{hot} and T_{cold} is simply the dT.

Assuming that there was a clear sky over the eight day period, ET rate will be equal to the potential rate (well-watered vegetation or well-watered bare soil), LST is close to the near-surface air temperature (i.e., little or no sensible heat flux). Thus T_{cold} is approximated to the corresponding T_a with a correction factor. The value of this correction factor "c" was determined in Senay et al. (2013) as a single spatially and temporally averaged factor for a diversity of environments, so the same coefficient equal to 0.993 was used in this work since it is steady in space and time.

T_{hot} was determined by a constant difference (dT) added to the T_{cold} of each pixel on the given time period. The difference dT is estimated from energy balance based on the assumption of a clear-sky condition. The dT is solved from the net radiation equation for a bare, dry soil where ET is assumed to be 0 and sensible heat is assumed to be maximum (Bastiaanssen et al., 1998; Roerink et al., 2000; Allen et al., 2007) in the radiation balance:

$$R_n = LE + H + G \quad (3)$$

where LE is the latent heat flux (W/m²), H is the sensible heat flux (W/m²) and G is the ground heat flux (W/m²). Since for a bare and dry soil LE and G are considered 0, the magnitude of the R_n can be equated with the sensible heat equation as:

$$R_n = H = \frac{\rho_a * C_p * dT}{r_{ah}} \quad (4)$$

where ρ_a is air density (kg/m³), C_p is specific heat of air at constant pressure (~1.013 kJ/kg/K), and r_{ah} is the aerodynamic resistance of heat (s/m). From the Equation (4) dT can be solved by rearranging in function of R_n, C_p , ρ_a , and r_{ah} . Net radiation is estimated using the series of equations of FAO-56 (Allen et al., 1998) in function of daily minimum and maximum air temperature data and the day of year. Air density can be solved as a function of the mean daily air temperature and atmospheric pressure according to elevation from the digital elevation model (DEM) ASTER GDEM resampled to 1km.

Aerodynamic resistance for heat on dry soil was fixed at 110 s/m according to Calder (1977) and Qiu et al. (1998) that determined that r_{ah} for this boundary conditions of dry soil is spatially uniform and has not significant variation with wind speed.

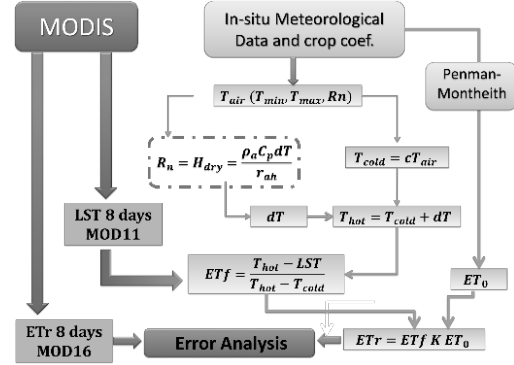


Figure 2. Flowchart of the scheme to estimate ETr.

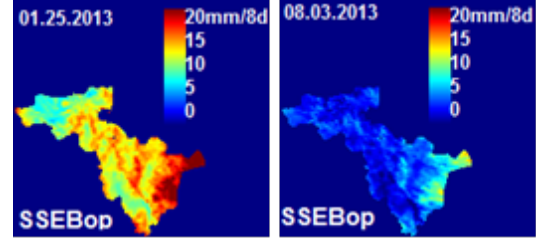


Figure 3. Evapotranspiration at dry (25-Jan-2013) and wet (03-Aug-2013) edges over the study area.

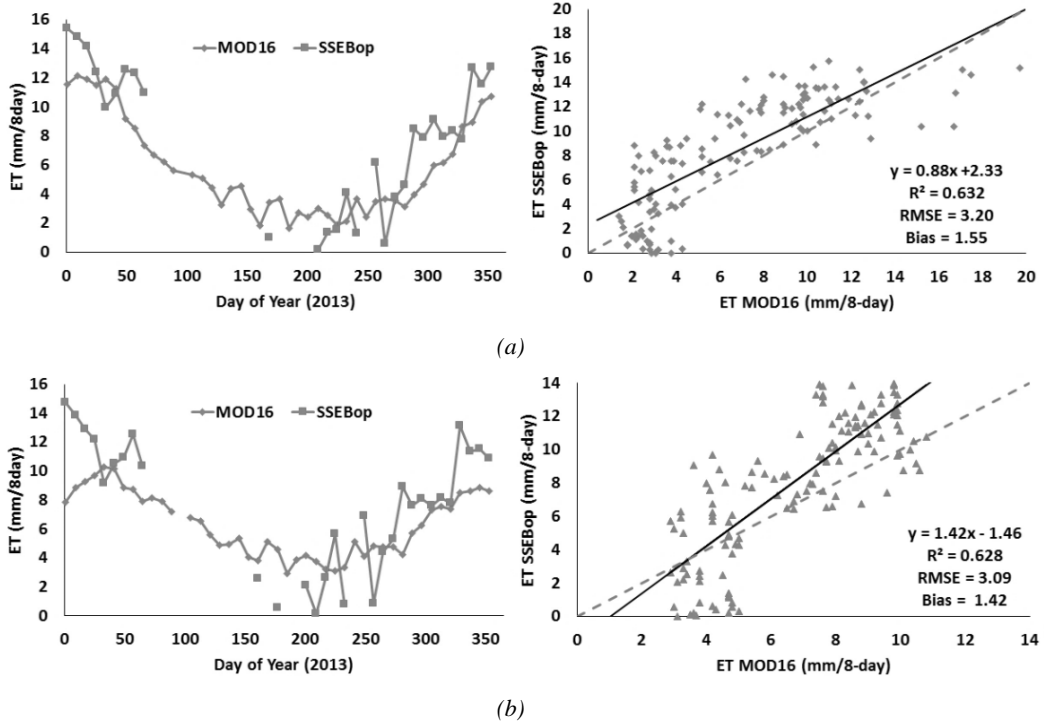


Figure 4. Time series of ETr(SSEBop) and ETr(MOD16) every 8 days and the statistical relationship for vineyards (a) and olives (b).

4 RESULTS AND DISCUSSION

The ETr estimates obtained from SSEBop model were compared with the ETr from the MOD16 dataset. Figure 3 shows the estimation of ETr at dry and wet edge over the study area. It is clear that in January the ETr is higher than the values of August. There are also high differences over the irrigated areas in about 10 mm/8days. It seems that the highest values of ETr could be related to low values of LST (influences of DEM) in the east (right) of the basin.

Figure 4 shows the time series and linear relationship between ETr from MOD16 and ETr every 8 days retrieved from the operational model (SSEBop). The gap in the time series is due to lack of data from the meteorological station and/or from clouds in the LST values from MODIS images.

The minimum ETr occurs in the months of winter (July-August) showed by both MOD16 values and SSEBop estimates. In the ETr time series its showed that the maximum value from MOD16 occurs between days 33 and 40 of the year for both crops, while SSEBop shows a relative minimum in this date. This relative minimum is due to variations of ET0 that ETr using SSEBop follow the same variations of ET0. The RMSE is close to 3 mm/8days for both olive and vineyard crops; R2 is greater than 0.6 for both crops, and bias is close to 1.5 mm/8days. Values close to zero could be attributed to cases when *Thot* is close to *LST*.

5 CONCLUSIONS

The SSEBop model is able to estimate the spatial and temporal variability of ET at basin scale throughout the year, which allow to count with an operational approach for the monitoring the water consumption of crops.

Further improvements will consider the use of structural vegetation parameters (i.e. LAI) and gap function of olive orchards (Connor et al., 2009).

6 ACKNOWLEDGMENTS

This Work is partially supported by Fondecyt-Initial 11130359 and the project FONDEF-IDeA CA13I10102. The authors also acknowledge to ECMWF for the free distribution of ERA-interim data and NASA for the free distribution of MODIS products.

7 REFERENCES

- Allen R., Pereira L., Raes D., Smith M., 1998, Crop evapotranspiration: guidelines for computing crop water requirements. *FAO Irrigation and Drainage Paper No. 56*. FAO, Rome.
- Allen, R.G., M. Tasumi, and R. Trezza, 2007, Satellite-Based Energy Balance for Mapping Evapotranspiration with Internalized Calibration (METRIC) – Model. *ASCE Journal of Irrigation and Drainage Engineering*, **133**, 380-394.
- Bastiaanssen, W.G.M., M. Menenti, R.A. Feddes, and A.A.M. Holtslag, 1998, The Surface Energy Balance Algorithm for Land (SEBAL): Part 1 Formulation. *Journal of Hydrology*, **212-213**, 198-212.
- Calder, I.R., 1977, A Model of Transpiration and Interception Loss From a Spruce Forest in Plynlimon, Central Wales. *Journal of Hydrology*, **33**, 247-265.
- Connor, D.J., Centeno, A. and Gómez-del-Campo, M. 2009. Yield determination in olive hedgerow orchards. II. Analysis of radiation and fruiting profiles. *Crop & Pasture Science*, **60**, 1-10.
- Moussa, R., Chahinian, N., Bocquillon, C., 2007. Distributed hydrological modelling of a Mediterranean mountainous catchment – model construction and multi-site validation. *Journal of Hydrology*, **337**, 35–51.
- Mu, Q., Zhao, M., & Running, S. W., 2011, Improvements to a MODIS global terrestrial evapotranspiration algorithm. *Remote Sensing of Environment*, **115**, 1781–1800
- Qiu, G.Y., Yanob, T., and Momiic, K. 1998, An Improved Methodology to Measure Evaporation from Bare Soil Based on Comparison of Surface Temperature with a Dry Soil Surface. *Journal of Hydrology*, **210**, 93-105.
- Roerink, G.J., Su, Z., and Menenti, M., 2000, S-SEBI: A Simple Remote Sensing Algorithm to Estimate the Surface Energy Balance. *Physics and Chemistry of the Earth*, **25**, 147-157.
- Senay, G. B., Bohms, S., Singh, R. K., Gowda, P. H., Velpuri, N.M., Alemu, H., et al. (2013). Operational evapotranspiration mapping using remote sensing and weather datasets: A new parameterization for the SSEB approach. *Journal of the American Water Resources Association*, **49**, 577-591.

Total and component evapotranspiration retrieval performances of a single-pixel energy balance model over agricultural crops.

G. Boulet^{*1,2}, B. Mougenot^{1,2}, Z. Lili-Chabaane², P. Fanise¹, A. Olioso^{3,4}, M. Bahir¹, V. Rivalland¹, L. Jarlan¹, B. Coudert¹ and J.-P. Lagouarde⁵

¹ CESBIO - UMR 5126 UPS, CNRS, CNES, IRD, Toulouse, France

² Institut National Agronomique de Tunisie, Tunis, Tunisie

³ INRA, EMMAH – UMR1114, 84914 Avignon, France

⁴ UAPV, EMMAH – UMR1114, 84000 Avignon, France

⁵ INRA, UMR 1391 ISPA, 33140 Villenave d'Ornon, France

* Gilles.Boulet@ird.fr

ABSTRACT - Evaporation is an important component of the water cycle, especially in semi-arid lands. Its quantification is crucial for a sustainable management of scarce water resources. A way to quantify evapotranspiration is to exploit the available surface temperature data from remote sensing as a signature of the surface energy balance, including the latent heat flux. Remotely sensed energy balance models enable to estimate stress levels and, in turn, the water status of continental surfaces. Two source models, such as TSEB (Norman et al., 1995) allow deriving a rough estimate of the water stress of the vegetation instead of that of a soil-vegetation composite. For the latter, a realistic underlying assumption enables to invert two unknowns (evaporation and transpiration) from a single piece of information. This assumption states that, in most cases, vegetation is unstressed, and that if vegetation is stressed, evaporation is negligible. In the latter case, if vegetation stress is not properly accounted for, the resulting evaporation will decrease to unrealistic levels (negative fluxes) in order to maintain the same total surface temperature. This work challenges the limits of such hypothesis by 1- studying evaporation and transpiration retrievals using two versions (parallel and series resistance networks) of a two source energy balance model similar to TSEB, and 2- testing the water stress retrievals (vegetation water stress and moisture-limited soil evaporation) over contrasted test sites (irrigated wheat, rainfed wheat). Bounding relationships and temporal consistency tests are proposed to ensure that convergence is reached at all times to provide robust estimates of evaporation and transpiration.

1 INTRODUCTION

Two source energy balance models allow us to derive a rough estimate of the water stress of the vegetation instead of that of a soil-vegetation composite. Such frameworks can be used with either component surface temperatures (e.g. soil and vegetation components retrieved from directional surface temperature data) or a single soil-vegetation composite surface skin temperature as input data. For the latter, the TSEB model proposes a realistic underlying assumption to downsize the number of unknowns from two (evaporation E and transpiration T) to one (E or T , Norman et al., 1995).

The TSEB model assumes that in most cases vegetation has access to enough water in the root zone to transpire at a potential rate. This assumption implies that, if vegetation stress is not properly taken into account, the resulting evaporation will decrease to unrealistic levels (negative fluxes) in order to maintain the same total surface temperature.

The model used here is a generalization of the TSEB model using a linearization of the full set of energy

budget equations and the Shuttleworth and Wallace (1985) expressions of the aerodynamic resistances.

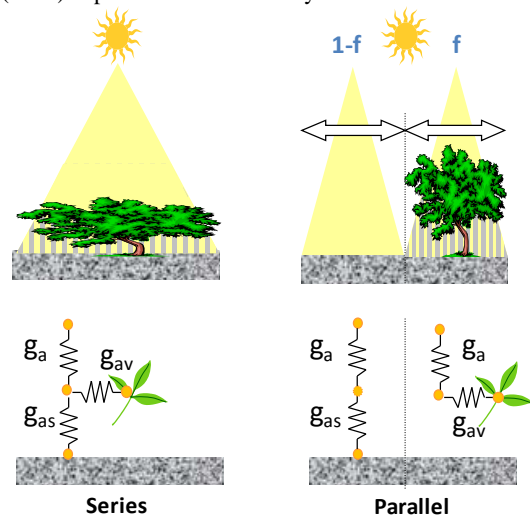


Figure 1: Schematic showing the series and parallel approaches

2 SERIES AND PARALLEL VERSIONS OF THE TSEB_SW MODEL

5 main equations are used to solve the energy budget of the soil and the vegetation, the continuity of the latent and sensible heat fluxes and the link between the radiative surface temperature and its components (soil and vegetation):

$$\begin{cases} Rn_s = LE_s + H_s + G \\ Rn_v = LE_v + H_v \\ H = H_s + H_v \\ LE = LE_s + LE_v \\ T_{rad}^4 = f_c T_v^4 + (1 - f_c) T_s^4 \end{cases} \quad (1)$$

(Rn_s and Rn_v : soil and vegetation net radiation components (resp.); LE_s and LE_v : corresponding latent heat flux components; H_s and H_v : corresponding sensible heat flux components; G : soil heat flux; T_{rad} , T_s and T_v : broadband radiative, soil and vegetation surface temperatures, respectively)

Two versions are derived, which can be regarded as fully coupled (Series) and fully uncoupled (Parallel) soil – vegetation - air exchanges (Figure 1 and Lhomme et al., 2012). The various aerodynamic resistances are computed according to Shuttleworth and Wallace (1985) while the stomatal resistance is modelled according to Braud et al. (1995) for all environmental

control factors except water stress (which is replaced by a transpiration efficiency β_v). TSEB_SW Series and Parallel versions are described in Annex.

3 SYNTHETIC RETRIEVAL TEST

In order to assess the limits of the main TSEB underlying assumption regarding vegetation stress, we built a synthetic simulation experiment. The target is the capacity to retrieve accurate evaporation efficiencies (ratio between actual and potential latent heat fluxes) with the TSEB_SW model from synthetic surface temperature generated from prescribed combinations of soil evaporation and transpiration efficiency values.

It consists in computing a radiative mixed surface temperature (T_{rad}), soil evaporation (LE_s), transpiration (LE_v) and evapotranspiration (LE) for each combination of soil evaporation ($\beta_s \in [0,1]$) and transpiration ($\beta_v \in [0,1]$) efficiencies using the direct mode (prescribed mode of Annex), then using it as an input to the TSEB_SW model to retrieve LE_s , LE_v , LE as well as the corresponding efficiencies (β_s , β_v and β for the total) and compare the retrieved β_s , β_v and β to the prescribed ones.

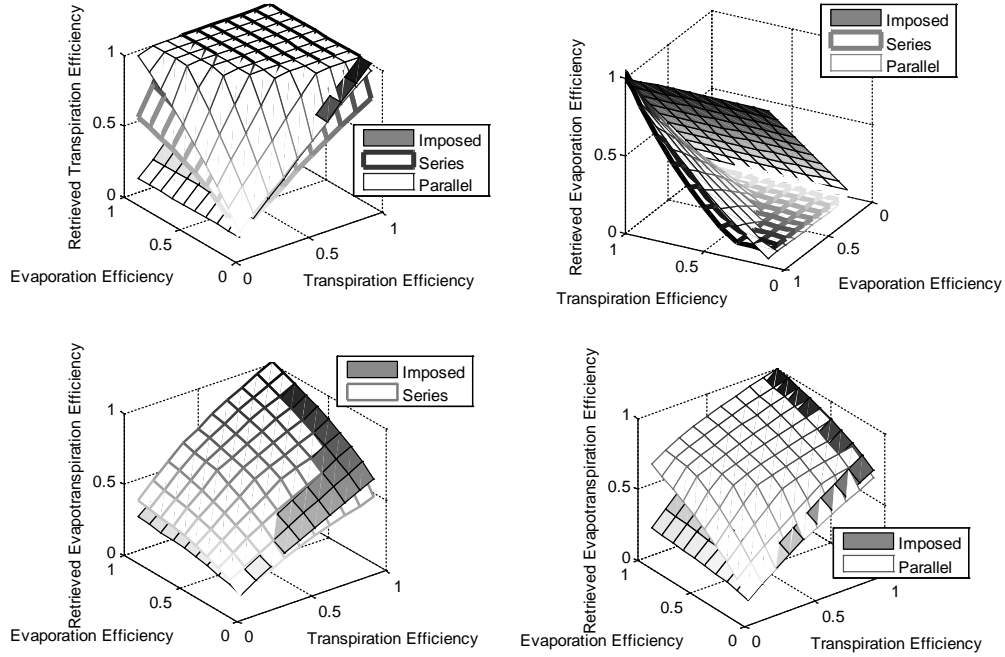


Figure 2: Retrieval test for total (top) and component (bottom) evapotranspiration: retrieved total (β) and component (β_s , β_v) efficiencies when using T_{rad} values as input to TSEB for given combinations of prescribed or imposed β_s and β_v values.

One expects rather good retrieval performances close to the initial TSEB assumptions (transpiration close to potential conditions, i.e. $\beta_v \cong 1$ and low soil evaporation i.e. $\beta_s \cong 0$) with a degradation when soil evaporation is high and transpiration is low. This is illustrated in Figure 2 for typical dry climate conditions and a Leaf Area Index characteristic of maximum development conditions of a cereal cover (LAI=3). The most interesting information from this test is that the Series model is much more efficient to retrieve total heat flux, and that evaporation and transpiration retrieval efficiencies decrease rapidly when β_v is lower than 0.8 and β_s is above 0.2.

4 APPLICATION

4.1 Dataset

Two datasets were used to assess the performance of the Series and Parallel versions of the TSEB_SW model over an entire growing season. The first is a rainfed wheat with Leaf Area Index values up to 2 and the second is an irrigated wheat with LAI up to 4. Both have been grown in a semi-arid climate (central Tunisia and Morocco). Surface temperature data was acquired with an Apogee thermoradiometer, while energy fluxes were measured according to classical FLUXNET recommendations (Baldocchi et al., 2001) with CSAT sonic anemometers and Krypton fast response hygrometers. Observed and simulated latent heat flux values (half hourly averages in W/m²) are compared at midday in all sky conditions.

Bounding	Rainfed Wheat		Irrigated Wheat	
	No	Yes	No	Yes
Series	75	65	58	56
Parallel	80	73	77	68
Kustas et al.	99	74	83	67

Table 1: performances of instantaneous latent heat flux retrieval at midday (Root Mean Square Error in W/m²);

Two sets of simulations are derived for each model version (Series and Parallel): in the set close to the original TSEB, outputs are not compared to potential heat fluxes; in the second, outputs are, like in SEBS, bounded by the potential flux rates considered at absolute maximum reachable values. This is legitimate for the Parallel version, but for the Series version one must inquire if oasis effects do not enhance latent heat flux values over the total potential value of a uniformly wet surface. No calibration is performed, the minimum stomatal resistance value is set to 100 s/m and the G/Rn_s ratio ξ to 40%.

4.2 Evapotranspiration and water stress

Low RMSE values do not warranty that total water stress (or total efficiency) is correctly simulated. Retrieved and observed efficiencies are shown in Figure 5 and 6. Surface stress is much higher (lower efficiency values) for the rainfed than the irrigated wheat field. The scatter is quite large, therefore showing the natural limit of stress retrieval from naturally noisy TIR data. However, broad tendencies are well reproduced, which is encouraging.

4.3 Soil evaporation

In order to assess the performance not only of the, total flux or total stress retrieval, we decided to compare the retrieved soil evaporation to an independent evaluation based on a soil efficiency β_s derived from the observed time series of soil moisture in the top 5 cm, according to:

$$\beta_{s,e}(\theta_{0-5cm}) = \left[0.5 - 0.5 \cos\left(\pi \frac{\theta_{0-5cm}}{\theta_{sat}}\right) \right]^p \quad (2)$$

With p fixed to 1 for the loamy site (rainfed wheat) and 0.5 for the clay site (irrigated wheat). $\beta_{s,e}$ is multiplied by the simulated soil potential evaporation rate (see Annex). Results are shown on Figure 7 (rainfed wheat) and 8 (irrigated wheat). For the rainfed site, tendencies are consistent but many outliers (inconsistent retrievals at some points) remain, while for the irrigated site the Series model provides estimates very close to those obtained from the surface soil moisture, while the parallel models underestimate consistently the soil evaporation with $\beta_s=0$ during senescence while some wetting events are present.

5 CONCLUSION

Theoretical limitations of the evapotranspiration components (E and T) retrieval from a single radiative surface temperature have been inferred. For low vegetation transpiration efficiencies it is almost impossible to retrieve a non-zero soil evaporation efficiency. Within these limits, the new TSEB_SW series model shows good retrieval performances of ET as well as E and T components compared to the original TSEB.

Total flux values are shown in Figures 3 and 4 for the bounded sets and RMSE values for both bounded and unbounded sets in Table 1. In both cases (Series and Parallel versions) the RMSE values are similar and consistent with values found in the literature (cf. Li et al., 2006). The bounded Series outputs display the best performances. RMSE values for the parallel TSEB version of Kustas et al. (1999) are very close to that of the TSEB_SW parallel version.

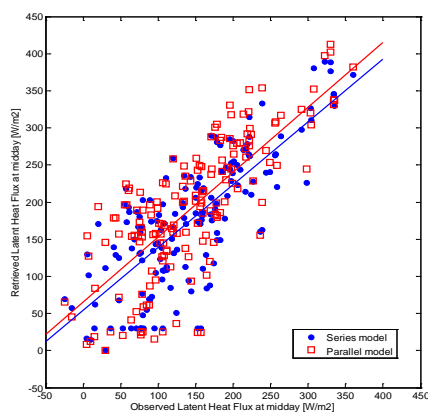


Figure 3 : scatterplot of retrieved vs observed latent heat flux at midday at the rainfed wheat site

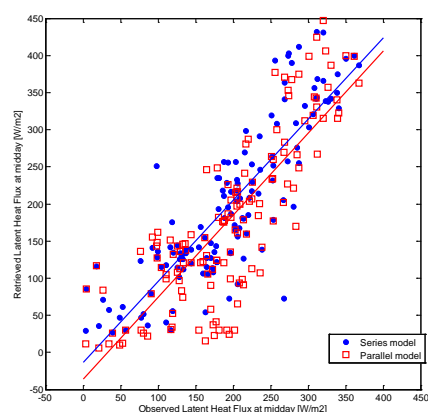


Figure 4 : same as Figure 3 for the irrigated wheat site

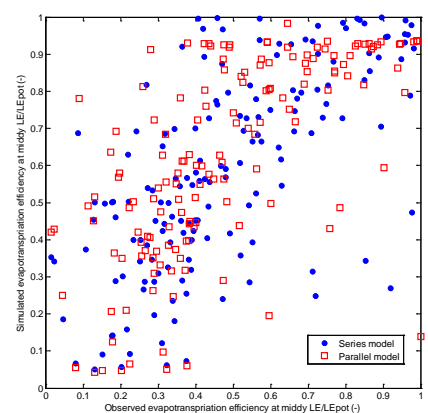


Figure 5: scatterplot of retrieved vs observed evapotranspiration efficiency at midday at the rainfed wheat site

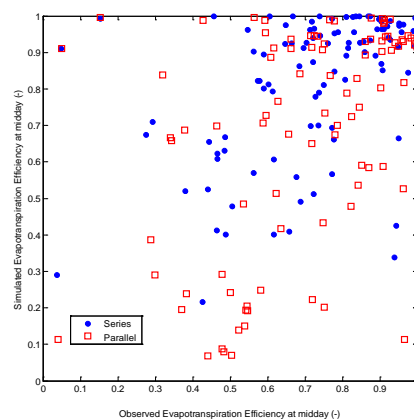


Figure 6: same as Figure 5 the irrigated wheat site

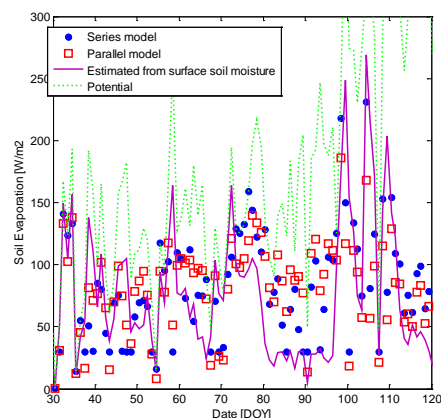


Figure 7: Evolution of the retrieved evaporation fluxes compared to the potential evaporation and the simulated evaporation using observed surface soil moisture time series for the rainfed wheat site

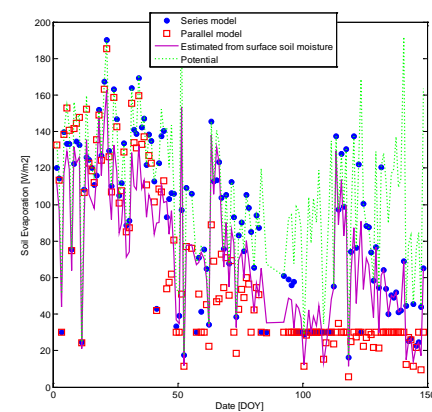


Figure 8: same as Figure 7 for the irrigated wheat site

6 REFERENCES

- Baldocchi, D., et al., 2001, FLUXNET: A New Tool to Study the Temporal and Spatial Variability of Ecosystem-Scale Carbon Dioxide, Water Vapor, and Energy Flux Densities, *Bulletin of the American Meteorological Society*, **82**(11): 2415-2434.
- Braud, I., Dantas-Antonino, A. C., Vauclin, M., Thony, J. L. and Ruelle, P., 1995, A Simple Soil-Plant-Atmosphere Transfer model (SiSPAT), development and field verification, *Journal of Hydrology*, **166**: 231-260.
- Kustas, W.P., Norman, J.M., 1999, Evaluation of soil and vegetation heat flux predictions using a simple two-source model with radiometric temperatures for partial canopy cover, *Agricultural and Forest Meteorology*, **94**(1): 13-29.
- Li, F.Q., Kustas, W.P., Prueger, J.H., Neale, C.M.U., Jackson, T.J., 2005, Utility of remote sensing-based two-source energy balance model under low- and high-vegetation cover conditions, *Journal of Hydrometeorology*, **6**(6): 878-891.
- Lhomme, J.P., Montes, C., Jacob, F., Prevot, L., 2012, Evaporation from Heterogeneous and Sparse Canopies: On the Formulations Related to Multi-Source Representations. *Boundary Layer Meteorology*, **144**(2): 243-262.
- Norman, J.M., Kustas, W.P., Humes, K.S., 1995, Source approach for estimating soil and vegetation energy fluxes in observations of directional radiometric surface temperature, *Agricultural and Forest Meteorology*, **77**(3-4): 263-293.
- Shuttleworth, W.J., and Wallace, J.S., 1985, Evaporation from sparse crops - an energy combination theory, *Quarterly Journal of the Royal Meteorological Society*, **111**: 839-855.

ANNEX: TSEB_SW model

The **series** model of the energy balance system (1) translates into:

$$\left[\begin{array}{l} (1 - f_c)(1 - \xi)A = (1 - f_c)g_{rad}(T_s - T_a) + \rho c_p g_{as}(T_s - T_0) + \beta_s(\rho c_p / \gamma)g_{as}[D_0 + \Delta(T_s - T_a)] \\ f_c A = f_c g_{rad}(T_v - T_a) + \rho c_p g_{av}(T_v - T_0) + \beta_v(\rho c_p / \gamma)g_{av}[D_0 + \Delta(T_v - T_a)] \\ g_a(T_0 - T_a) = g_{as}(T_s - T_0) + g_{av}(T_v - T_0) \\ g_{as}[D_0 + \Delta(T_v - T_a)] = \beta_s g_{as}[D_0 + \Delta(T_s - T_a)] + \beta_v g_{av}[D_0 + \Delta(T_v - T_a)] \\ T_{rad}^4 = f_c T_v^4 + (1 - f_c)T_s^4 \end{array} \right]$$

Where $A = (1 - \alpha)R_g + \varepsilon_s \sigma (\varepsilon_a T_a^4 - 1)$ and $g_{rad} = 4\varepsilon_s \sigma T_a^3$ (α albedo, R_g global incoming radiation, σ Stefan-Boltzman constant, ε_s and ε_a surface and air emissivities; f_c : fraction cover function of Leaf Area Index; ξ : ratio between G and R_n ; T_s , T_v , T_a , T_0 , T_{rad} : soil, vegetation, air, aerodynamic and radiative temperatures (resp.); β_s and β_v : imposed or retrieved soil evaporation and transpiration efficiencies (resp.); the vapour pressure deficit at the aerodynamic level is $D_0 = e_{sat}(T_a) - e_0$ where e_0 is the partial pressure of vapour at the aerodynamic level and $e_{sat}(T_a)$ is the saturated vapour pressure at air temperature; Δ is the slope of the saturation vapour curve at air temperature; ρc_p is the product of air density and specific heat; g_{as} , g_{av} , g_a : soil to aerodynamic level, vegetation to aerodynamic level and aerodynamic level to air aerodynamic conductances).

While the **parallel** model corresponds to:

$$\left[\begin{array}{l} (1 - \xi)A = g_{rad}(T_s - T_a) + \rho c_p (g_a + g_{as})(T_s - T_a) + \beta_s(\rho c_p / \gamma)(g_a + g_{as})[D_a + \Delta(T_s - T_a)] \\ A = g_{rad}(T_v - T_a) + \rho c_p (g_a + g_{av})(T_v - T_a) + \beta_v(\rho c_p / \gamma)(g_a + g_{av})[D_a + \Delta(T_v - T_a)] \\ H = \rho c_p g_a(T_0 - T_a) = (1 - f_c)\rho c_p (g_a + g_{as})(T_s - T_a) + f_c \rho c_p (g_a + g_{av})(T_v - T_a) \\ LE = (1 - f_c)\beta_s(\rho c_p / \gamma)(g_a + g_{as})[D_a + \Delta(T_s - T_a)] + f_c \beta_v(\rho c_p / \gamma)(g_a + g_{av})[D_a + \Delta(T_v - T_a)] \\ T_{rad}^4 = f_c T_v^4 + (1 - f_c)T_s^4 \end{array} \right]$$

In **prescribed** (potential or fully stressed) conditions, the system is solved in a direct mode for the following unknowns: T_s , T_v , D_0 and T_0 ; in potential conditions, $\beta_s = \beta_v = 1$ while in fully stressed conditions $\beta_s = \beta_v = 0$; T_{rad} in this direct mode is then an output of the system, while for heat fluxes retrieval (inverse mode) it is an input.

In **retrieval** conditions (inverse mode), unknowns are β_s or β_v , T_s , T_v , D_0 and T_0 . At first, β_v is set to 1, if a negative β_s is obtained, $\beta_s = 0$ and β_v is retrieved, if β_v is negative, fully stressed conditions are imposed. In inverse or retrieval mode, the fifth equation is linearized: $T_{rad} = f_c T_v + (1 - f_c)T_s$.

Remote Sensing of Water Resources in the semi-arid Mediterranean areas: The Joint International Laboratory TREMA

L. Jarlan^{1*}, S. Khabba^{2*}, M. Le Page¹, S. Er-Raki³, L. Hanich³, Y. Fakir², S. Mangiarotti¹, J. Ezzahar⁴, M.H. Kharrou⁵, B. Berjamy⁶, O. Merlin¹, A. Saaïdi⁷, S. Gascoin¹, A. Boudhar⁸, M. Leblanc⁹, G. Boulet¹, A. Benkaddour³, J. Abaoui⁷, A. Tavernier¹, V. Simonneaux¹, F. Driouech⁷, S. Belaiz², G. Bigeard¹, F. Raïbi⁷, J. Chirouze¹, B. Coudert¹, L. Drapeau¹, M. El Adnani², A. El Fazziki², O. Hagolle¹, N. Laftouhi², A. El Mandour², A. Marchane³, A. Diarra², G. Aouade³, J. Toumi², Y. Hajhouji², P. Fanise¹, H. Ibouh³, N. Filali⁷, B. Mougenot¹, H. Marah⁴, A. Mokssit⁷, Y. Kerr¹, G. Chehbouni¹

¹Centre d'Etudes Spatiales de la Biosphère, Toulouse, France. e-mail: lionel.jarlan@cesbio.cnes.fr

²Faculté des Sciences Semalia (FSS), Université Cadi Ayyad (UCAM), Marrakech, Maroc. e-mail: khabba@uca.ac.ma

³Faculté des Sciences et Techniques (FST), Université Cadi Ayyad, Marrakech, Maroc. e-mail: hanich@fstg-marrakech.ac.ma

⁴Centre National d'Etudes sur les Sciences, les Techniques et l'Energie Nucléaire (CNESTEN), Rabat, Maroc. Unité Eau et Climat. e-mail: marah@cnesten.org.ma

⁵Office Régional de Mise en Valeur de l'Eau Agricole du Tensift Haouz (ORMVAH), Marrakech, Maroc. e-mail: hakimkharroul@yahoo.fr

⁶Agence de Bassin Hydraulique du Tensift (ABHT), Marrakech, Maroc. e-mail: berjamy@eau-tensift.net

⁷Direction de la Météorologie Nationale (DMN), Casablanca, Maroc. e-mail: mokssit.abdalah@yahoo.fr

⁸Université Sultan Moulay Slimane, Beni Mellal, Maroc. e-mail: abdelghani99@gmail.com

⁹UMR G-EAU, Montpellier, France

*Corresponding authors : lionel.jarlan@ird.fr and khabba@uca.ma

ABSTRACT - Anticipate and develop measures to adapt to climate and water use are based on the monitoring of water resources and a better understanding of the eco-hydrological processes governing their dynamics. This paper presents some lessons learned within the frame of a bilateral project on how remote sensing can help better monitoring of and predicting water resources in the semi-arid mediterranea. The study region is the Tensift catchment located near Marrakech (Morocco); a typical watershed of the Southern Mediterranean with a water production area in the mountain and a downstream consumption mainly by agriculture. After a description of the institutional context and of the experimental network, this paper presents some recent research results including: (1) methodological development for the retrieval of key component of the water cycle (disaggregated soil moisture from SMOS at the kilometric scale, snow covered area based on MODIS products); (2) the use of remote sensing products together with surface modeling for the monitoring of evapotranspiration; (3) phenomenological modeling based on the sole time series of various remote sensing data sets with application to cereal yields prediction. Finally, the issue of transfer of research results to water resource managers is also addressed through two remote sensing based tools developed together with our management partners.

1 INTRODUCTION

Water shortage in semi-arid region associated is likely to become a crucial issue of the 21th century. Semi-arid Mediterranean regions are characterized by a strong spatio-temporal variability of precipitation associated to a marked seasonality of evaporative demand, resulting in a period of high water deficit in summer. Flows are thus intermittent and river beds are

dry during a large part of the year. For many watersheds in the Mediterranean semi-arid zone, water production is located in the mountains with numerous irrigated areas located downstream and the presence of snow acts as a flow buffer with high run-off shifted during spring snow melting. In addition, Driouech *et al.* (2010) have highlighted a possible drop of up to 15% in winter precipitation, with an increase in dry periods by 2050 over Morocco that could impact

drastically the water cycle of the semi-arid catchments. There is thus an imperious need for a better understanding of the main processes governing the water redistribution at the catchment scale in order to develop likely scenario of water evolution under both climate and water use change.

A common feature of South Mediterranean semi-arid regions is the scarcity of the *in situ* meteorological network, in particular in the mountains for obvious access reasons, while these areas show high climate variability. Remote sensing, by taking advantage of contrasting spectral signature of land surface is an interesting alternative for extracting surface information such land use, vegetation characteristics, snow cover and, in combination with surface modelling, higher level products such as evapotranspiration For instance, in the visible and infrared domain, spectral properties of snow are well-known, with high reflectance in the visible part of the electromagnetic spectrum and, by contrast, low reflectance in the medium infrared. This contrasted spectral behavior was exploited to build the Normalized Difference Snow Index (NDSI). For crop monitoring, optical satellite data were also intensively used to provide regular observations of several key biophysical variables of plants derived from the Normalized Difference Vegetation Index (NDVI). Time series of remote sensing observations exist since the beginning of the 80's. Those time series are good proxies of land surface evolution under climatic and anthropic constraints.

After a brief description of the institutional context and the experimental network implemented on the Tensift catchment, this paper will present an overview of recent research results obtained within the frame of the Joint International Laboratory TREMA (<http://trema.ucam.ac.ma>) dealing with (1) methodological development for the retrieval of key component of the water cycle at the catchment scale (kilometric soil moisture based on the disaggregation of SMOS data, snow covered area based on daily MODIS data); (2) the use of remote sensing products together with surface modeling through data assimilation techniques; (3) phenomenological modeling based on the sole time series of various remote sensing data sets with application to evapotranspiration and cereal yields prediction. Finally, the issue of transfer of research results to water resource managers is also addressed through two remote sensing based tools developed together with our management partners: (1) the Satellite Monitoring of Irrigation (SAMIR) for irrigation scheduling and (2) a decision support system for the surface and ground water management at the scale of the Tensift catchment.

2 Context and study region

2.1 The Joint International Laboratory TREMA

The laboratory, based at the Cadi Ayyad University, involves a multidisciplinary team of researchers and professors from several research institutions in Morocco and in France. It has been created in 2011 based on a long lasting collaboration between CESBIO and actors of the Marrakech region within the frame of the SUDMED program (Chehbouni et al., 2008). The scientific objective of the LMI articulates around the sustainable management of the water resources for catchments typical of the South of the Mediterranean area. It is twofold : (1) to improve our understanding of the main processes of the water redistribution at the catchment scale through the development of a numerical platform of modelling and observation in order to establish evolution scenarios of the water resources in a changing climate context and (2) to get a better understanding of the terrestrial water cycle at the continental scale and in particular, the linkages between the continental water cycle and the large scale climate pseudo-oscillations.

Our second goal is to help bring together researchers and managers whose objectives and vocabulary often appear divergent because of differing vocabulary, working time scales, tools ... To this objective, the two main institutions in charge of the water management of the Tensift catchment have been involved since the beginning of the project and contributed to define the main scientific and development questions underlying the creation of the Laboratory.

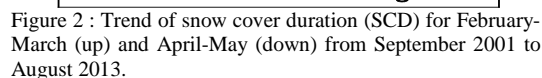
2.2 The Tensift Catchment

In the Tensift catchment, precipitation are mostly concentrated on the High Atlas mountain and fall in a significant proportion in the form of snow stored in winter which contribute to the streamflow in summer. This water is mainly used for irrigation in the Haouz plain. The plain is crossed from South to North by several *wadis* which are the tributaries of two large collectors, the Tensift and Oum er Rbia, which gave their name to their respective watershed. The plain climate is semi-arid, with average annual rainfall of 250 mm concentrated between November and April, whilst evaporative demand according to the reference evapotranspiration (ET_0) is about 1600mm per year. The agricultural sector is managed by the *Office Régional de Mise en valeur Agricole du Haouz*, or ORMVAH. About two thirds of the 473,000 hectares of croplands are irrigated, and half of them (144,600 ha) are irrigated from dams.

The research activities rely on an experimental network of *in situ* and satellite observations. This data base is used to feed, validate and calibrate the remote sensing retrievals and the hydro-ecologic models. The "Tensift" observatory is interested in the documentation of the main processes of water redistribution and use of the water at the soil-vegetation-atmosphere interface and between the surface and the aquifer at the scale of the whole catchment. The "TENSIFT" observatory samples three interconnected processes (1) the hydrologic functioning of the irrigated crops in plain with a sampling of the main cultures of the region which will be updated according to the "Plan Vert" for Moroccan agriculture; (2) the mountain hydrology by focusing on the dynamics of the snow-covered area; (3) the dynamic of streamflow and water table.

3 RESULTS

Snow cover is a concern for many studies of climate change impact highlighting a possible change in seasonal pattern, including a shift of the snowy season towards earlier ablation. Within the South Mediterranean region, an earlier melting could penalize water availability in the summer. Remote sensing has been used to monitor Snow Covered Areas (Boudhar et al., 2010). The study presented here used the daily MODIS product of Fractional Snow Cover (MOD10A1). These products have been (1) validated against in situ automatic snow depth measurements acquired by 5 stations installed within the frame of the IMPETUS and SUDMED programs and (2) used to characterize spatio-temporal trend (Man-Kendall test) of snow cover areas at the scale of all Moroccan catchments with a snow-rain functioning (Marchane et al., 2014, RSE in revision).



299

test. Most of this observed decrease has been detected below 2,500 masl, with 76.1% of the pixels located below this elevation showing a decreasing trend (15.1% significant).

It is interesting to also highlight that most of the observed patterns are in line with some previous studies. Bormann *et al.* (2012), in particular, demonstrated in South-East Australia a close behavior with a decreasing trend of snow cover duration mainly attributed to an earlier melt in spring. The snowpack in this region is subject, similarly to the Atlas region, to frequent melt-refreeze cycles because the diurnal course of temperature passes through the freezing point. By contrast, the significant increase of snow duration on the higher elevation areas during the core of the winter was attributed by these authors to more intense accumulation. Some work also studied the processes governing the snow melt in those semi-arid mountains (Boudhar *et al.*, 2014).

3.2 Hydric functioning of irrigated crops

Focus has been put on the evaluation of the water demand of the irrigated crops, the partition of water between soil evaporation, plant transpiration and deep infiltration through modeling and experimentation for the main crops of the region (Er-Raki *et al.*, 2012; Khabba *et al.*, 2013). From experimental data analysis, it is shown that 28% of water inputs are lost by evaporation for the flooding irrigation site. These quantities of water losses were confirmed by the stable isotopic method (Keeling plot approach) over olive, orange and winter wheat crops (Amenzou *et al.*, 2013). Concerning the losses of water by infiltration, results are surprising as the inadequate use of the drip technique, whose use is encouraged within the Green plan for Moroccan agriculture, can lead to substantial infiltration losses with values in the range of 29-41 %.

Concerning the modeling component, several models ranging from the most simple (FAO-56; Allen *et al.*, 1998) to the most complex (i.e. SVAT: Soil Vegetation Atmosphere Transfer) were implemented to estimate the spatio-temporal variability of ET. The results showed that the physically based SVATs such as ISBA (Tavernier *et al.*, not yet published) provide good estimates of surface fluxes (RMSE of about 40 W/m²) over all sites once a proper calibration is carried out, but they required several input parameters that are not routinely available at the appropriate spatial scale. For operational purposes, simpler approaches such as the FAO-56 and the TSEB models showed a good estimate of ET at field scale : Kharrou *et al.*, 2011 and Diarra *et al.*, 2013, Chirouze *et al.*, 2014, respectively.

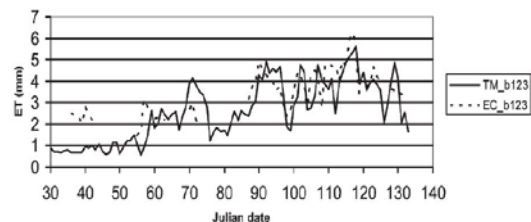


Figure 3 : Comparison of actual ET estimated using SAMIR, based on Landsat TM data (TM), and ground measurements achieved by Eddy Correlation systems (EC) for one wheat plots in 2003.

Also, the FAO-56 approach was adapted to use a satellite-based vegetation index (Simonneaux *et al.*, 2008; Er-Raki *et al.*, 2010) and calibrated and validated on the Haouz plain, for the main crops (wheat, olive and citrus). Its implementation was validated using a Landsat TM image time series (Simonneaux *et al.*, 2008), and also using low resolution images (Benhadj *et al.*, 2012). The results showed that despite the simplicity of the model and some theoretical limitations of its parameterizations for the soil water balance, plain scale estimates of ET were reasonable (Figure 3). This model was converted in a software for Satellite Monitoring of Irrigation (see section 3.4). However, the FAO-56 method combined with solar remote sensing data alone was not sufficient to accurately estimate water consumption, especially when soil evaporation and stress under full vegetation cover conditions occurred (Er-Raki *et al.*, 2007).

In this regard, Er-Raki *et al.*, 2008 directly assimilated snapshot evaporation data that could be obtained through the resolution of a simple energy budget forced by TIR observations. These preliminary results showed a clear improvement of the seasonal ET estimates. Improvements in ET estimates were also obtained when a dual source SVAT model in conjunction with TIR measurements (Ezzahar *et al.*, 2012), even for a heterogeneous surface of Agdal olive trees.

3.3 Disaggregation of remote sensing products

Data disaggregation (or downscaling) is becoming a recognized modeling framework to improve the spatial resolution of available remote sensing products. Disaggregation has been applied to medium resolution optical data by Benhadj *et al.* (2012) to evaluate land use of mixed pixel. The downscaled data set presented here (Figure 4) is obtained from the disaggregation of 40 km resolution SMOS soil moisture at 1 km resolution using MODIS data and DISPATCH (DISaggregation based on Physical And Theoretical scale Change ; Merlin *et al.*, 2012) methodology.

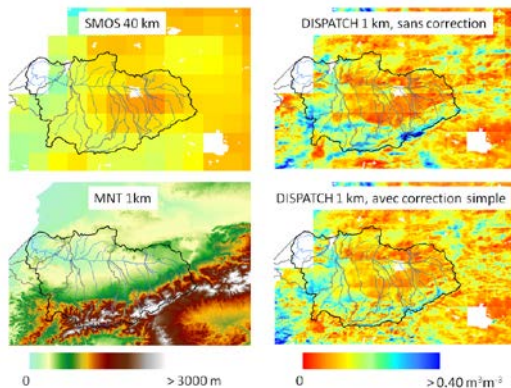


Figure 4 : disaggregated soil moisture : SMOS at full resolution, disaggregated product at 1 kms with and without temperature correction, MNT.

The on-going validation of the DISPATCH at 1 km resolution in the Tensift catchment is especially challenging due to i) potentially strong topographic effects on MODIS temperature and ii) the presence of crop irrigation at a scale (typically 3-4 ha) much smaller than the target downscaling resolution. These conditions are however particularly suitable for our analysis since DISPATCH is expected to cover a large range of performance with possible significant biases in the output data relative to in situ measurements. In order to evaluate soil moisture disaggregation, Merlin et al. (2014, RS, submitted) also define a new metric.

3.4 Decision support for water management

Satellite Monitoring of Irrigation (SAMIR) is a software for the spatialization of ET and water balance of irrigated crops on large areas, based on the use of satellite images. The water demand of the crops is calculated using the FAO method, well suited to computation on large areas where the available information on soil and crops is limited.

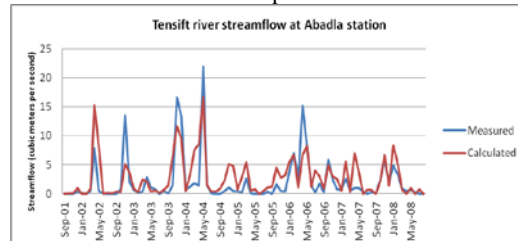


Figure 5 : Measured and predicted streamflow of the SAMIR-WEAP-MODFLOW tool at the plain outlet (Abadla station) without calibration.

As an irrigation manager, the Regional Office of Agricultural Development of the Haouz plain (ORMVAH) is interested in short term management of the irrigation sectors. Le Page et al. (2014) described a life size experiment aiming to evaluate the potential

water saving that could be expected by using the FAO-56 to schedule irrigation. Belaiz et al. (2013) introduced successfully, in SAMIR software, a new irrigation priority index (IPI) based on remote sensing data for assessing the networks irrigation scheduling. Also, Belaiz et al. (2014) have succeeded to optimize the spatiotemporal distribution of water irrigation, by minimizing the IPI with a multi-criterion approach taking into account most of the constraints in the existing system of concrete channels. By taking into account an information on the plant water demand for irrigation scheduling, the theoretical results obtained within an irrigated perimeter showed a potential water saving of up to 25%. Kharrou et al. (2013) evaluated the potentiality of the SAMIR tool to quantify the adequacy of the actual water distribution with regards to the plant water demand and the equity between farmers.

As a planning agency, the Hydraulic Basin Agency (ABHT) is interested in longest term information regarding water consumption including irrigated agriculture. SAMIR was used to derive monthly ET estimates of irrigated sectors in the Haouz plain and incorporated in the decision support system for water management developed in collaboration with GiZ. This tool, named SAMIR-WEAP-MODFLOW is a numerical platform feeded with remote sensing data reproducing the integrated functioning of the Haouz plain including surface and groundwater (Le Page et al., 2012). Figure 5 shows the predicted streamflow at the watershed outlet without calibration.

3.5 Seasonal prediction of cereal grain yield

Over the South Mediterranean countries, no studies exploited the predictive capacity of large scale climate for the prediction of wheat yields. We analyzed the relationships between NDVI and wheat yields at the agricultural province scale in Morocco and large-scale climate variables and indices: NAO, Sea Surface Temperature (SST), 500 hpa geopotentials (Jarlan et al., 2013, 2014).

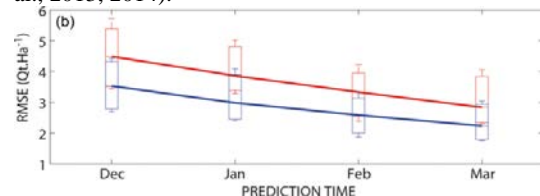


Figure 6: Evolution of rmse between predicted cereal grain yields and province statistics for the 11 most productive province in Morocco as a function of prediction time from December to March (about 2 months before harvest) ; (red) Multi-linear regression ; (blue) Support Vector Machine

This kind of lagged correlation can then be used to build statistical models for the early prediction of grain yields. Figure 6 displays the results of a non-linear

regression model based on support vector machine that allows forecasting yields province with a good accuracy from February, meaning 3 to 4 months before harvest. It takes into account information on the tropical Atlantic SST in October, 500 hpa geopotentials in November, NAO in December, February rainfall amount and March NDVI.

4 DISCUSSION AND CONCLUSION

The scientific activities of the Joint International Laboratory LMI-TREMA are supported by an experimental design of in situ and satellite data sets structured as an observatory of the Water Resources of the Haouz catchment. The study of the Soil-Plant-Atmosphere process and the integrated hydrological functioning of the catchment are the main objectives of these two scientific programs. The irrigated crops, that use 85% of plain water, are particularly studied to quantify water exchanges by ET and deep drainage. Also, various models of different complexity levels based on in-situ data or/and feeded by remote sensing data were used/developed to estimate heat and water fluxes in soil-plant-atmosphere system. At larger scale, long term monitoring of snow cover or grain yield based on remote sensing offers the opportunity to evaluate observed change and feed modelling tools to develop likely scenario of water evolution. To this objective, our current work deals with the implementation of a mechanistic approach based on the hydrometeorological chain SIM (Habets et al., 2008) to evaluate not only integrated variable such as streamflow but also intermediate processes and assess the impact of climate change through disaggregated scenario forcing. As a logical perspectives of these results, the use of the multi-spectral satellite data (optical, thermal-infrared and radar remote sensing) in conjunction with a disaggregation scheme and data assimilation to control the water balance in the FAO-56 and other SVAT models.

Beside these research activities, the project has reached the level of maturity to propose decision support tools to major institutions in charge of the water management of the catchment as evidenced by the two recent achievements SAMIR and SAMIR-WEAP-MODFLOW.

REFERENCES

- Amenzou, N., Marah, H., Raïbi, F., Ezzahar, J., Khabba, S., Jarlan L., Ismaili, M.; Estimation of soil evaporation and infiltration losses using stables isotopes, Fluxmeter and Eddy-Covariance system for citrus orchards in a semi-arid region (Morocco); *Academia Journal of Environmental Sciences*, 1 (1): 001-008 (2013).
- Belaqziz, S., Khabba, S., Er-Raki, S., Jarlan, L., Le Page, M., Kharrou, M.H., Adnani, M.E., Chehbouni, A., 2013, A new irrigation priority index based on remote sensing data for assessing the networks irrigation scheduling, *Agricultural Water Management*, 119, pp. 19.
- Belaqziz S., Mangiarotti S., Le Page, M., Khabba S., Er-Raki S., Agouti T., Drapeau L., Kharrou M.H., El Adnani M., Jarlan L., 2014, Irrigation scheduling of a classical gravity network based on the Covariance Matrix Adaptation – Evolutionary Strategy algorithm, *Computers and Electronics in Agriculture*, 102, 64-72.
- Benhadj I., Duchemin B., Simonneaux V., Maisongrande P., Khabba S., Chehbouni A.G., 2012, Automatic unmixing of MODIS multi-temporal data for inter-annual monitoring of land use at regional scale (Tensift, Morocco). *International Journal of Remote Sensing*, 33(5):1325-1348.
- Boudhar, A.; Duchemin, B.; Hanich, L.; Jarlan, L.; Chaponniere, A.; Maisongrande, P.; Boulet, G.; Chehbouni, A. (2010). Long-term analysis of snow-covered area in the Moroccan High-Atlas through remote sensing. *INTERNATIONAL JOURNAL OF APPLIED EARTH OBSERVATION AND GEOINFORMATION*, 10.1016/j.jag.2009.09.008, WOS:000275612600018.
- Boudhar A., Boulet G., Hanich L., Sicar J.E., Chehbouni G., 2014, Energy fluxes and melt rate of a seasonal snow cover in the Moroccan High Atlas, *Hydrological Sciences Journal*, in press.
- Chebouni, a., Escadafal, R., Duchemin, B., Boulet, G., Simonneaux, V., Dedieu, G., ... Sobrino, J. a. (2008). An integrated modelling and remote sensing approach for hydrological study in arid and semi-arid regions: the SUDMED Programme. *International Journal of Remote Sensing*, 29(17-18), 5161–5181. doi:10.1080/01431160802036417
- Chirouze, J., Boulet, G., Jarlan, L., Fieuzal, R., Rodriguez, J. C., Ezzahar, J., Er-Raki, S., Bigeard, G., Merlin, O., Garatuza-Payan, J., Watts, C., and Chehbouni, G.: Intercomparison of four remote-sensing-based energy balance methods to retrieve surface evapotranspiration and water stress of irrigated fields in semi-arid climate, *Hydrol. Earth Syst. Sci.*, 18, 1165-1188, 10.5194/hess-18-1165-2014, 2014.
- Erraki S., Chehbouni A., Khabba S., Simonneaux V., Jarlan L., Ouldbba A., Rodriguez J., Allen R., 2010. Assessment of reference evapotranspiration methods in semi-arid regions: Can weather forecast data be used as alternate of ground meteorological parameters? *Journal of Arid Environments*, 74(12):1587-1596.

- Er-Raki S., Chehbouni A., Boulet G., Williams D. G., 2010. Using the dual approach of FAO-56 for partitioning ET into soil and plant components for olive orchards in a semi-arid region. *Agricultural Water Management*, 97(11):1769-1778.
- Er-Raki S., Chehbouni A., Duchemin B. (2010). Combining satellite remote sensing data with the FAO-56 dual approach for water use mapping in irrigated wheat fields of a semi-arid region. *REMOTE SENSING*, 10.3390/rs2010375.
- Ezzahar, J., Er-Raki, S., Marah, H., Khabba, S., Amenou, N. Chehbouni, G., 2012. Coupling Soil-Vegetation-Atmosphere-Transfer model with Energy Balance model for estimating energy and water vapor fluxes over an olive orchard in semi-arid region. *Global Changes*, 1 (e1): 1-8.
- Ezzahar J. , Er-Raki, S., Bouarifi W., Jarlan L., Marah H., Khabba S., Ed Dabdoub M., Chehbouni G., 2012. Estimation of the evapotranspiration over sparse and tall vegetation using the Large Aperture Scintillometer. In: *Evapotranspiration: Processes, Sources and Environmental Implications*. Nova Science Publishers, Inc., 167-181. ISBN: 978-1-62417-138-3.1
- Diarra, A., Jarlan, L., Er-Raki, S., Le Page, M., Khabba, S., Bigeard G., Tavernier, A., Chirouze, J., Fanise, P., Moutammani, A., Ezzahar, J., Kharrou, M.H., Chehbouni, G. 2013. Characterization of evapotranspiration over irrigated crops in a semi-arid area (Marrakech, Morocco) using an energy budget model. *Procedia Environmental Sciences*, 19, 504-513
- Driouech, F., Déqué, M., & Sánchez-Gómez, E. (2010). Weather regimes—Moroccan precipitation link in a regional climate change simulation. *Global and Planetary Change*, 72(1-2), 1–10. doi:10.1016/j.gloplacha.2010.03.004
- Habets F., A. Boone, J.L. Champeaux, P. Etchevers, L. Franchisteguy, E. Leblois, E. Ledoux, P. Le Moigne, E. Martin, S. Morel, J. Noilhan, P. Quintana-Segui, F. Rousset-Regimbeau, P. Vienne, 2008 : The SIM hydrometeorological model over France, *J. Geophys. Res.*, 113
- Hadria R., B. Duchemin, L. Jarlan, G. Dedieu, F. Baup, S. Khabba, A. Olioso, T. Le Toan, 2010, Potentiality of optical and radar satellite data at high spatio-temporal resolutions for the monitoring of irrigated wheat crops in Morocco, *International Journal of Applied Earth Observation and Geoinformation*, 12S, S32-S37, doi:10.1016/j.jag.2009.09.003.
- Jarlan L., Abaoui J., Duchemin B., Ouldbba A., Tourre Y., Khabba S., Balaghi R., Mokssit A., Chehbouni G., 2013, Linkages between Wheat Yields and Climate (1982-2008), *International Journal of Biometeorology*, 10.1007/s00484-013-0753-9.
- Jarlan L., Driouech F., Duchemin B., Tourre Y., Abaoui J., Bouysse M., Ouldbba A., Mokssit A. and Chehbouni G, 2014, Vegetation dynamics over Morocco (1982 – 2008): Linkages with climate signals and seasonal prediction, *International Journal of Climatology*, 34:4, pp. 1245-1261, DOI: 10.1002/joc.3762.
- Khabba, S., Jarlan, L., Er-Raki, S., Le Page, M., Ezzahar, J., Boulet, G., Simonneaux, V., Kharrou, M.H., Hanich, L., Chehbouni, G. 2013. The SudMed program and the Joint International Laboratory TREMA: A decade of water transfer study in the Soil-Plant-Atmosphere system over irrigated crops in semi-arid area. *Procedia Environmental Sciences*, 19, 524-533.
- Kharrou M.H., M. Le Page, A. Chehbouni, V. Simonneaux, S. Er-Raki, L. Jarlan, L. Ouzine, S. Khabba, G. Chehbouni, 2013. "Assessment of equity and adequacy of water delivery in irrigation systems using remote sensing-based indicators in semi-arid region, Morocco", *Water Resources Management*, DOI: 10.1007/s11269-013-0438-5.
- Le Page M., Berjamy B., Fakir Y., Bourgin F., Jarlan L., Abourida A., Benrhanem M., Jacob G., Huber M., Sghrer, F., Simonneaux V., Chehbouni G., 2012, An integrated DSS for groundwater management based on Remote Sensing. The case of a semi-arid aquifer in Morocco, *Water Resources Management*, 26(11) : 3209-3230.
- Le Page M., Toumi J., Khabba S., Tavernier A., Kharrou H., Er-Raki S., Huc M., Kasbani M., El outamanni A., Yousfi M., Jarlan L., 2014, A life-size and near real time Test of Irrigation scheduling with a sentinel-2 like time series (SPOT4-Take5) in Morocco, *Rem. Sens*, 6(11), 11182-11203.
- Merlin, O.; Rüdiger, C.; Al Bitar, A.; Richaume, P.; Walker, J.; Kerr, Y. 2012, Disaggregation of SMOS soil moisture in southeastern Australia. *IEEE Trans. Geosci. Remote Sens.* 2012, 50, 1556–1571.
- Merlin, O., Chirouze, J., Olioso, A., Jarlan, L., Chehbouni, G., and Boulet, G., 2014, An image-based four-source surface energy balance model to estimate crop evapotranspiration from solar reflectance/thermal emission data (SEB-4S), *Agricultural and Forest Meteorology*, 184, 188-203.

Validation of evapotranspiration maps from 100-m to the 1-km scale over a semi-arid irrigated agricultural area

Bahir, M.*¹, Boulet, G.^{1,2}, Chirouze, J.¹, Oliso, A.³, Rivalland, V.¹, Gallego-Elvira, B.⁴, Mira, M.^{3,5}, Merlin, O.¹, Jarlan, L.¹, Lagouarde, J.P.⁶

¹ CESBIO-UMR 5126, Toulouse, France ² Institut National Agronomique de Tunisie, Tunis, Tunisie ³ INRA, EMMAH /UAPV– UMR1114, Avignon, France ⁴ NERC, Oxfordshire, United Kingdom ⁵ Autonomous University of Barcelona, Spain ⁶ INRA, ISPA - UMR1391, Villenave d'Ornon, France

*Malik.Bahir@cesbio.cnes.fr

ABSTRACT-Evapotranspiration (ET) estimates are particularly needed for monitoring the available water of arid lands. Remote sensing data offer the ideal spatial and temporal coverage needed by irrigation water management institutions to deal with non sustainable groundwater uptakes. Validation of ET products remains a difficult task. The objective of this study is to evaluate ET instantaneous fluxes obtained using two Energy Balance models (SEBS, Su, 2002; TSEB, Norman et al., 1995) forced by local meteorological observations and remote sensing data (in VIS, NIR and TIR domains) from ASTER and MODIS. The study zone is a 4 by 4 km² semi-arid irrigated agricultural area located in the north west of Mexico. Land surface products for both sensors are resampled at 100 and 1km resolutions. ET retrievals from ASTER have been first validated using eddy covariance data at 7 locations sampling the area main crps. Those high resolution ET estimates provide reference ET maps at low resolution once linearly aggregated at the km scale. We first compared fluxes obtained by running SEBS and TSEB using ASTER reflectances and radiances aggregated at the km scale (aggregated inputs) to the latter reference maps to investigate the impact of input aggregation. Then, we compared ET maps obtained with SEBS and TSEB from MODIS data to this reference dataset. The first results show that MODIS ET estimates compare well with the reference simulation (relative bias is about 6% for SEBS and 8% for TSEB). Discrepancies are mainly related to fraction cover mapping for TSEB and vegetation height mapping for SEBS.

1 INTRODUCTION

In semi-arid areas, more than 80% of the annual available water is used by irrigated agriculture. ET estimate quantifying the actual water use by the plant is thus of crucial importance for such water managers as agricultural office. Remote sensing products offer important opportunities to monitor ET at large spatial scales.

We aim here at evaluating ET Remote Sensing (RS) estimates by two Energy Budget (EB) models, SEBS and TSEB at high (ASTER, 100 m) and low (MODIS, 1000 m) spatial resolutions. First, high resolution (HR) estimates are validated with EC data. Second, averaging of HR estimates to the km scale provides a reference to evaluate estimates from low resolution (LR) RS data. (Fig. 1).

2 MATERIAL AND METHODS

2.1 Study Area

The study area (see Fig. 2) is located in the Yaqui valley (27.4° N, 19.9° W), Sonora, in the North-West Mexico. The dominant crop is winter wheat and the climate is considered as semi-arid. Irrigation water represents 90% of the water uses.

2.1 In Situ Dataset

The meteorological dataset is acquired at a height of 10-m from an automatic weather station located at the center of the 4x4 -km² square. The solar and atmospheric incoming radiation, the air temperature, the relative humidity and the wind speed are measured.

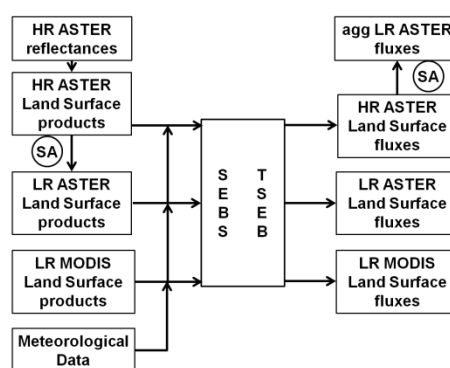


Figure 1. Methodology scheme. SA symbolizes a linear Simple Aggregation.

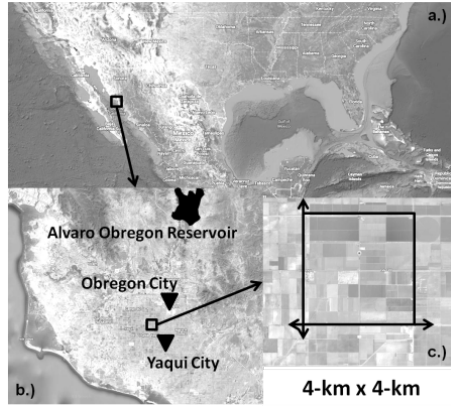


Figure 2. Study zone location in .a.)North america. b.) the Sonora state. c.) local fetch.

Fluxnet type EC towers are installed at seven sites located on different crops (Fig.2). They measure net radiation, soil heat, latent and sensible heat fluxes as well as surface temperature and soil moisture (Chirouze et al, 2013). Crop heights were measured manually almost every two weeks at each plot and then linearly interpolated and spatialized for the 7 ASTER overpasses dates. In this remote sensing based approach the use of spatialized ground measured crop heights is discussable but it's important to compare the accuracy of ET estimates at high spatial resolution, obtained with models forced by in situ crop height measurements and by Remote sensing products derived crop heights, when compared to EC measurements.

2.2 ASTER Dataset

The ASTER dataset is built from 4 products and 7 dates between the 30th December of 2007 and the 13th May of 2008 (surface reflectance in several bands and surface temperature). For each date, the overpass local time is between 10:30 AM and 11:00AM.

Albedo is computed as in Liang et al. (2000):

$$\alpha^{ASTER} = 0.484 \times \text{Band1} + 0.335 \times \text{Band2} - 0.324 \times \text{Band5} + 0.551 \times \text{Band6} + 0.305 \times \text{Band8} - 0.367 \times \text{Band9} - 0.0015 \quad (1)$$

Emissivity is computed as in Ogawa et al. (2004):

$$\epsilon^{ASTER} = 0.121 \times \text{Band11} + 0.194 \times \text{Band12} + 0.323 \times \text{Band14} + 0.242 \quad (2)$$

Leaf Area Index LAI and Fraction Cover FC are derived according to Fieuzal et al.(2011):

$$\text{LAI}^{ASTER} = -\frac{1}{1.14} \times \ln \frac{\text{NDVI}_{\max} - \text{NDVI}}{\text{NDVI}_{\max} - \text{NDVI}_{\min}} \quad (3)$$

$$\text{FC}^{ASTER} = \frac{\text{NDVI}_{\max} - \text{NDVI}}{\text{NDVI}_{\max} - \text{NDVI}_{\min}} \quad (4)$$

with $\text{NDVI}_{\max} = 0.94$ and $\text{NDVI}_{\min} = 0.14$.

This produces the High Resolution (HR) ASTER inputs dataset (~100-m resolution). Its aggregation of reflectances and radiances to a ~1000m resolution provides the LR ASTER inputs (Fig.3).

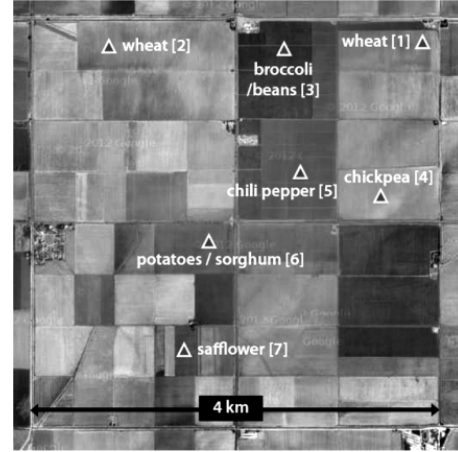


Figure.3. Satellite view of the studied zone with respective positions of the EC stations (Imagerie© 2012 Cnes/Spot Image).

2.3 MODIS Dataset

The MODIS dataset is also a blend of four products. MODIS NDVI and Surface Temperature are compared to the LR ASTER inputs dataset to identify any spatial shift between both sensors using a maximum of correlation method. LAI and Fc are estimated from the MODIS NDVI products with the same relations used for the HR ASTER inputs dataset. Albedo is estimated with the Lewis & Barnsley (1994). relation:

$$\alpha^{MODIS} = 0.85 \times \alpha_{\text{Black Sky}} + 0.15 \times \alpha_{\text{White Sky}} \quad (5)$$

Emissivity is computed with the relation detailed in Liang et al (2006):

$$\epsilon^{MODIS} = 0.4587 \times \epsilon_{b31} + 0.5414 \times \epsilon_{b32} \quad (6)$$

Finally, the MODIS land surface properties fits the LR ASTER inputs grid and constitute the MODIS inputs dataset (Fig. 3).

2.4 Models

In this study two Energy Balance (EB) models are used to compute the instantaneous fluxes a single source model, SEBS and a double source model, TSEB. SEBS (Su et al. 2000) computes the latent heat flux as the residual term of the energy balance equation, $R_n - G = H + LE$. The originality lies in the equation that relates the roughness length for heat transfer to the roughness length for momentum transfer. TSEB (Norman et al, 1995) solves the soil and vegetation energy budgets individually.

3 HR FLUXES VALIDATION

We first evaluate the latent heat LE fluxes, obtained with SEBS and TSEB models when forced by the HR ASTER inputs dataset, the meteorological dataset and the in situ crop height measurements, comparing them to EC measurements at the satellite overpass time.

3.1 In Situ measured Crop Heights

Both models are able to provide a good estimate (Chirouze et al., 2013) of the instantaneous ET fluxes at the satellite overpass time with an advantage for SEBS on TSEB (Table1). To evaluate the accuracy of ET maps obtained through energy balance models forced only by remote sensing products and easily available meteorological data, the crop height will be estimated from other remote sensing products.

3.2 NDVI derived Crop heights

The crop height will be, for each pixel, estimated as a linear regression between the maximum and minimum NDVI and a theoretical maximum and minimum cereal crop height (1.3m and 0.05m). This crop height data set is called "hc RS". The use of hc RS do not have a major impact on the retrieval performance (Table 1). This, validates the simple approach to derive crop heights from NDVI products.

To evaluate the use of LR RS products to force the two models at low resolution for estimating ET fluxes these last ASTER outputs will be aggregated to a 1000-m scale to approach the original MODIS resolution and considered as a reference dataset named AST agg (aggregated).

	SEBS		TSEB	
	in situ hc	RS hc	in situ hc	RS hc
RMSE [W/m^2]	109,8	109,1	111,25	112
mbias [W/m^2]	6,65	2,24	66,7	62
rel bias [%]	2	1	20	18
Nash [-]	0,39	0,4	0,35	0,55

Table 1. Statistics between EC measurements and SEBS and TSEB LE fluxes obtained with the HR ASTER inputs dataset.

4 INPUTS AGGREGATION PROPERTIES

To estimate the accuracy of using LR RS products as inputs for EB models to compute large ET maps, the LR ASTER inputs are used to force the models. The output fluxes, constituting the LR ASTER dataset, are compared to the reference fluxes agg ASTER dataset.

4.1 SEBS

The averaged results show good performances (relative bias=5%, Nash= 0.61) of SEBS to estimate instantaneous latent heat fluxes with LR inputs. Fig. 4 presents an underestimation of the ASTER LR LE fluxes, when the NDVI starts to decrease and an overestimation when the vegetation is dry. Those errors compensate each other for the whole data set which explains the good average performance. However, the relative biases can reach values higher than 19% due to the method used to derive crop heights from NDVI products. It provides higher LR ASTER crop heights than HR ASTER, inducing roughness lengths differences and explaining the LE fluxes biases.

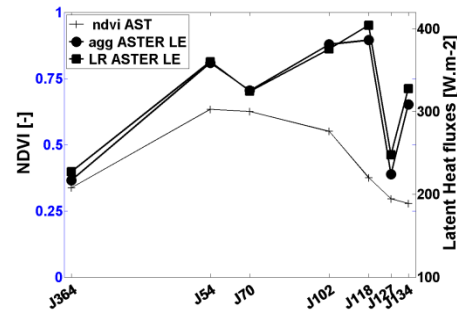


Figure 4. Time series - agg ASTER LE, LR ASTER SEBS LE fluxes and ASTER NDVI.

4.2 TSEB

The averaged results (relative bias =0.9% Nash =0.96) show very good performances (Fig.5) of TSEB to estimate instantaneous latent heat fluxes with LR inputs. The results show a better accuracy of TSEB compared to SEBS and illustrate the TSEB robustness to crop height variations in latent heat fluxes estimation.

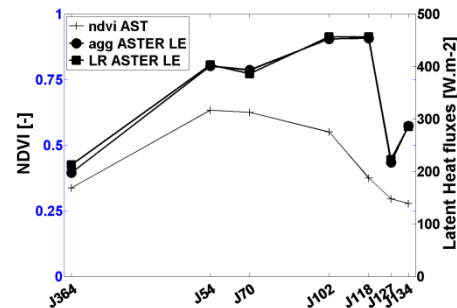


Figure 5. Time series - agg ASTER LE, LR ASTER TSEB LE fluxes and ASTER NDVI.

These good results are due to a good balance between the soil and vegetation components of the total latent heat flux (Fig.6). In this agricultural irrigated area, the

LR inputs tend to overestimate the vegetation cover inducing higher crop (relative bias =6% Nash =0.97) and lower soil (relative bias =-6.5% Nash =0.96) latent heat fluxes. This illustrates the sensibility of TSEB to the partition of the available energy between the two sources composing the surface through the Fc parameter.

5 MODIS INPUTS USE VALIDATION

To evaluate the use of a common LR sensor to provide energy balance models inputs for estimating LE fluxes, MODIS and agg ASTER outputs are compared.

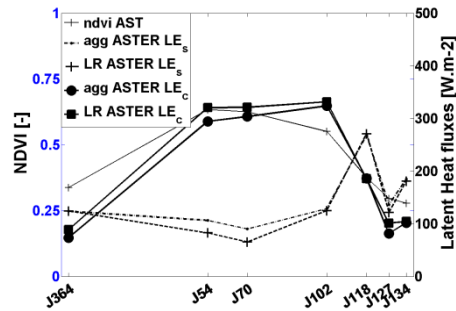


Figure 6. Time series agg ASTER LE_s /LE_c, LR ASTER TSEB LE_s /LE_c fluxes and ASTER NDVI.

5.1 SEBS

The averaged results show good performances (relative bias=5%, Nash= 0.65) of SEBS to estimate instantaneous latent heat fluxes with MODIS LR inputs.

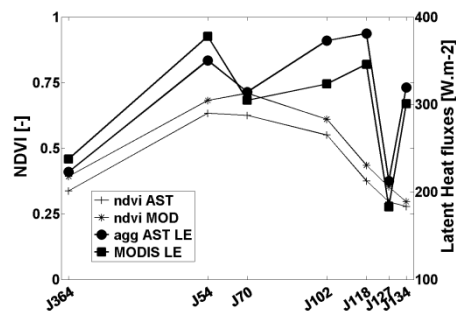


Figure 7. Time series - agg ASTER LE, MODIS SEBS LE fluxes and both sensors NDVI.

The good seasonal results are not representative of the model's response to the different sensor forcing datasets at the different vegetation stages (Fig.6). In fact, the relative bias can reach -24% the 10th of March, -19% the 11th of April and 18% the 6th of May. As explained in 3.1, the model sensitivity to the NDVI derived crop height parameter induces the LE fluxes discrepancies.

5.2 TSEB

The averaged results (relative bias =6.2% Nash =0.87) show very good performances of TSEB to estimate instantaneous latent heat fluxes with MODIS LR inputs (Fig. 8). The results show a better accuracy of TSEB compared to SEBS and illustrate again the TSEB robustness to crop height variations in latent heat fluxes estimation.

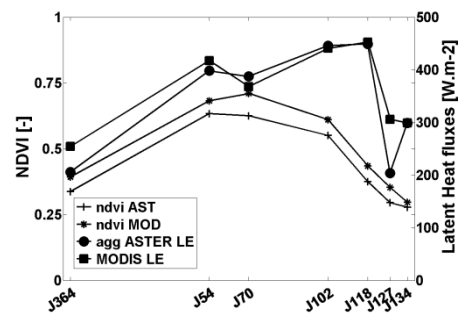


Figure 8. Time series - agg ASTER LE, MODIS TSEB LE fluxes and both sensors NDVI.

The model performances regarding soil and crop LE fluxes separately are also good (relative bias = -18% and 25%; Nash = 0.75 and 0.92, respectively for LE_s and LE_c) and induce a good balance between the two LE fluxes terms (Fig.9).

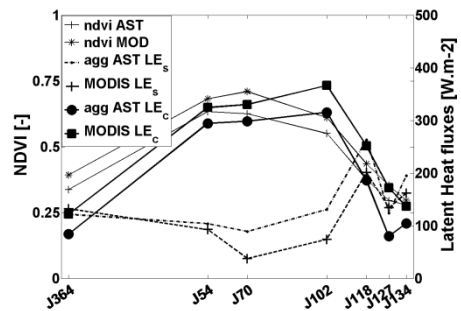


Figure 9. Time series agg ASTER LE_s /LE_c, MODIS TSEB LE_s /LE_c fluxes and both sensors NDVI.

Relative biases are well balanced between soil and crop parts considering the whole season giving a low seasonal relative bias for LE fluxes (6.2%). As explained in Section 3.2, the model sensitivity to the NDVI derived vegetation Fc parameter induces different available energy partitions and explains the LE fluxes discrepancies.

6 CROOP HEIGHT AGGREGATION ISSUE

To reduce biases for the LE fluxes using SEBS model with LR inputs, different ways to determine an effective crop height parameter at LR (Boulet et al., 1999) were tested and used as part of the LR ASTER and MODIS input datasets to force the model.

	Relative bias [%]											
	ref		RS		HR agg lin		HR agg geo		HR agg harmo		grad min	
	LR AST	MO D	LR AST	MO D	LR AST	MO D	LR AST	MO D	LR AST	MO D	LR AST	MO D
J370	0,2	-0,8	-9,8	-2,5	-9,7	6,6	-6,2	12,6	4,7	12,6	-14,1	2,1
J54	-0,4	-1,3	-11,5	-3,3	-8,7	7,9	-5,2	11	0,4	3,8	-7,5	1,4
J70	-1	-0,3	-20,4	-24,3	-14,9	-3	-8,9	1,2	-0,3	-7,2	-12,5	-10,4
J102	-0,7	-1,6	-11,4	-19,4	-9,1	-13,3	-7	-10	-1,5	-6,4	-8,4	-8,8
J118	0	0,5	2,1	-3,2	0	-9,3	0,5	-7	4,6	3,2	0,3	1,2
J127	-0,4	11,5	13	19	-10,1	-14,1	-7,7	1,4	10,4	25,4	-0,9	23,3
J134	-0,6	-6,2	6,7	8,7	-6,8	-5,8	-5,5	-0,3	6,2	0,8	-8,8	-5
Average	-0,4	-0,3	-5,2	-5,1	-8,1	-4,6	-5,5	0,4	3	2,9	-7,2	-0,8

Table 2. Relative biases between the agg AST LE fluxes and the LR ASTER /MODIS LE fluxes, forced with the different LR crop height parameters.

6.1 Reference crop height

First a low resolution reference crop height was inversed considering the minimum difference between the aggregated sensible heat flux from high resolution flux values and the one computed at low resolution.

6.2 Aggregation Methods

The HR ASTER inputs dataset crop heights were aggregated to the LR ASTER inputs dataset resolution (~1000-m) using different averaging methods as the linear, the geometric and the harmonic ones.

6.3 Neutral Atmospheric Conditions Aerodynamic Conductance Inversion

Another way to compute a LR crop height dataset with HR VIS/NIR data is to find values reducing as much as possible the difference between the HR and LR conductances, g_a in neutral conditions. In fact, in these conditions the sensible heat flux expression is reduced to:

$$\begin{aligned}
 H &= \frac{\rho \times C_p \times k \times u_* \times (\theta_0 - \theta_a)}{\ln\left(\frac{z-d_0}{z_{0h}}\right)} \\
 &= \frac{\rho \times C_p \times k^2 \times u \times \ln\left(\frac{z-d_0}{z_{0m}}\right) \times (\theta_0 - \theta_a)}{\ln\left(\frac{z-d_0}{z_{0h}}\right)} \quad (7) \\
 &= \frac{\rho \times C_p \times (\theta_0 - \theta_a)}{r_a} \\
 g_a &= 1/r_a = (A + kB^{-1}) \times A \text{ with } A = \ln\left(\frac{z-d_0}{z_{0m}}\right)
 \end{aligned}$$

7 RESULTS

The reference crop height gives good performances (average relative bias =0.4% and biases never exceeds 1%) showing that a good estimation of the crop height at low resolution reduce considerably the biases on the LE fluxes and proves again the sensibility of the SEBS model to this input. The results show a good reduction of relative biases on the LE fluxes. The harmonic aggregation shows the best performances using LR ASTER inputs and the geometrical aggregation using MODIS inputs (Table .2).

The aerodynamic conductance inversion is not efficient because the hypothesis of a neutral atmosphere is not consistent.

8 CONCLUSIONS

Both models are accurate enough for estimating instantaneous LE fluxes using RS data at different scales. TSEB gives excellent results using LR inputs. Its two sources balance very well the different perceptions of the soil/vegetation flux partition at different scales. SEBS shows good performances but some limits with LR inputs due to its sensibility to the crop height derived roughness length parameter were identified. Methods to derive LR crop heights using VIS/NIR HR data offer good options to reduce the error made using LR inputs with SEBS model.

9 REFERENCES

Boulet et al, 1999. An assessment of effective land surface parameterisation in regional-scale water balance studies. *Journal of Hydrology*, 217(3–4): 225-238.

- J. Chirouze et al, 2013, Inter-comparison of four remote sensing based surface energy balance methods to retrieve surface evapotranspiration and water stress of irrigated fields in semi-arid climate. *Hydrology and Earth Sciences Discussions*, **10**, 895-963
- R. Fieuzal et al, 2011. Combined use of optical and radar satellite data for the monitoring of irrigation and soil moisture of wheat crops. *Hydrology and Earth System Sciences*, 15(4): 1117-1129).
- Lewis, P., & Barnsley, M.J, (1994). Influence of the sky radiance distribution on various formulations of the earth surface albedo. In, *Proceedings on the 6th International Symposium on Physical Measurements and Signatures in Remote Sensing* (pp. 707-715).
- S.Liang, 2000, Narrowband to broadband conversions of land surface albedo I Algorithms, *Remote Sensing of Environment*, 76, 213-238.
- S.Liang et al, 2002, Narrowband to broadband conversions of land surface albedo II Validation, *Remote Sensing of Environment*, 84, 25-41.
- J.M.Norman et al, 1995, Source approach for estimating soil and vegetation energy fluxes in observations of directional radiometric surface temperature, *Agricultural And Forest Meteorology*, 77, 263-293.
- K. Ogawa et al, 2004, Mapping Surface Broadband Emissivity of the Sahara Desert Using ASTER and MODIS Data, *Earth Interactions*, V8, 7, p.1.
- Z.Su, 2002, The Surface Energy Balance System (SEBS) for estimation of turbulent fluxes, *Hydrology & Earth System Sciences*, 6, 85-89.

Use of remote sensing data fusion for daily evapotranspiration monitoring at watershed scale over a *dehesa* ecosystem

E. Carpintero⁽¹⁾, K. Semmens⁽²⁾, M.C. Anderson⁽²⁾, A. Andreu⁽¹⁾, F. Gao⁽²⁾, W.P. Kustas⁽²⁾, M.P. González-Dugo⁽¹⁾

(1) IFAPA Centro Alameda del Obispo, 14080 Córdoba, Spain. Ph: +34671532700, Fax: +34957016043.

(2) Hydrology and Remote Sensing Laboratory, USDA ARS, Bldg. 007. BARC West Beltsville, MD 20750. United States.

E-mail: elisabet.carpintero@juntadeandalucia.es

ABSTRACT- Thermal-based energy balance models use radiometric temperature for estimating evapotranspiration (ET). With the adequate spatial and temporal resolution, ET fluxes may be used to improve the modelling of hydrological processes occurring in an area. In this work, the Atmosphere-Land Exchange Inverse (ALEXI) energy balance model (Anderson et al., 1997) has been applied to obtain daily continental-scale ET estimations at coarse resolution. These fluxes constrained higher resolution ET retrievals from both MODIS and Landsat images using an associated flux disaggregation scheme (DisALEXI). Finally, a model data fusion, STARFM (Gao et al. 2006), was used to fuse MODIS and Landsat ET maps in order to obtain both fine spatial and temporal resolution. The results suggest the utility of the ALEXI/DisALEXI scheme to accurately estimate turbulent and radiative fluxes at 1 Km spatial resolution over the complex canopy structure of *dehesa* ecosystem, with a MAD value for convective fluxes of 59 Wm⁻² for H and 31 Wm⁻² for ET and an average value for radiative fluxes of 27 Wm⁻². The application of STARFM over this ecosystem has proved a significant improvement in the heterogeneity assessment of ET values, with a slight quantitative improvement of fused images (5 %) when compared with flux measurements.

1 INTRODUCTION

The *dehesa* is the largest agroforest ecosystem in Europe, covering about 3 million hectares between the Iberian Peninsula and Greece (Papanastasis et al., 2004). In spite of being an example of sustainable use of resources, it is currently exposed to multiple threats from socio-economic changes and intensive agricultural use and livestock, which have led to changes in hydrological processes and soil properties (Coelho et al., 2004). A better understanding of hydrological processes at watershed scale and the role of vegetation in them can help to improve their management and contribute to its preservation.

In this sense, evapotranspiration (ET) is a useful indicator of plant ecosystem health (Moran et al., 2004), especially in complex water-controlled ecosystems of semiarid regions, such as the *dehesa* ecosystem. Its regularly estimation may improve our tools for hydrological planning, watershed management and drought impact evaluation.

Thermal-based energy balance models use the radiometric temperature registered by the sensor as the primary boundary condition for estimating surface energy fluxes, and therefore in the estimation of ET. Between them, the Two Source Energy Balance model (TSEB) distinguishes between soil and vegetation

contribution to the temperature measured by the sensor and to the exchange of superficial energy fluxes, in order to obtain a physical representation of evaporation process (Norman et al, 1995; Kustas et al., 1999).

Anderson et al. (1997) suggested an improvement of the two-source diagram by means of the incorporation of a simple description of the global contour layer dynamic. The result was the energy balance model Atmosphere-Land Exchange Inverse (ALEXI) and an associated flux disaggregation scheme (DisALEXI) (Norman et al., 2003). For the estimation, it uses thermal data from multiple sensors without the need of local observations, e.g. meteorological information. It can also minimize the deviation effect in the estimation of temperature registered by the sensor because it works at differential mode using information obtained twice a day.

However, current sources of satellite thermal data are limited in having both high spatial and temporal resolutions, useful for daily ET monitoring purposes. For example, 16-day revisit cycle of Landsat, together the cloud cover, reduce the actual temporal frequency. On the other hand, moderate resolution sensors present difficulties for capturing the ET variability in heterogeneous and complex areas.

Therefore, the use of remote sensing data fusion from multiple sensors is an alternative for improving the spatial-temporal resolution and combines the best characteristics of each data source. In this sense, the Spatial and Temporal Adaptive Reflectance Fusion Model (STARFM) by Gao et al. (2006), allows the integration of the inputs or energy fluxes maps resulting of the models application.

The objective of this work is to address a continuous evapotranspiration monitoring at watershed scale over the complex *dehesa* ecosystem. The ability of the remote sensing data fusion STARFM will be assessed, which combines ET maps provided by the Landsat and MODIS sensors and previously generated using the ALEXI/DisALEXI models. The advantages and limitations of this modelling system will be analyzed, discussing, the refinements required to reliably monitor ET over this complex landscape.

2 METHODOLOGY

2.1 Study area description and ground measurements

The study area is the Martín Gonzalo watershed, located in Southern Spain (Fig. 1). The homogeneous landscape of *dehesa* ecosystem is the predominant use, characterized by widely-spaced oak trees (mostly *Quercus Ilex* L.) combined with crops, pasture and shrubs in the sub-canopy layer, with some conifer forest and olives groves. The climate is characterized by an average rainfall of 720 mm per year, with cold winters, long dry summers and severe periodic droughts.

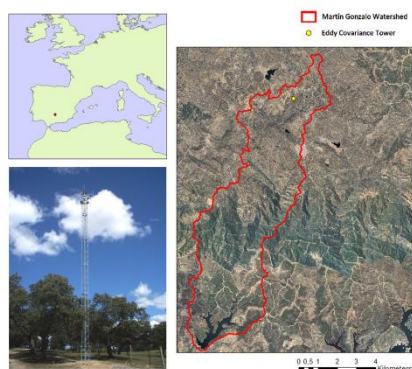


Figure 1. Location of the study area and eddy covariance tower (ECT).

In this watershed is currently installed an eddy covariance tower (ECT) system (Fig. 1) and all instrumentation needed for measuring the energy balance components (Santa Clotilde, 38°12' N; 4°17' W, 736 m a.s.l). The equipment was installed on a 18

m tower in order to minimize roughness sub-layer effects caused by tree height, open canopy structure and terrain on the turbulence measurements. The data have been post-processed in order to remove anomalies and make corrections (Andreu et al., 2013).

In this work, the force of the balance closure for calculating LE values was performed with the residual method. Daily fluxes were obtained by averaging half-hourly values over 24 h, with overnight fluxes equal to 0.

2.2 Modelling framework description

The Atmosphere-Land Exchange Inverse (ALEXI) energy balance model (Anderson et al., 1997) has been applied to obtain daily continental-scale ET estimations at coarse resolution (3 Km), using hourly thermal data from the geostationary MSG satellite.

These fluxes constrained higher resolution ET retrievals from both MODIS (1 Km, daily) and Landsat (100 m, 16 days) images over the study area for the year 2013 using the associated flux disaggregation scheme (DisALEXI). For its application, a set of meteorological inputs, biophysical parameters, regional data and information from MODIS and Landsat sensors has been required.

Finally, the data fusion technique STARFM was applied on MODIS and Landsat ET maps to provide data with both fine spatial and temporal resolution. This ET data fusion methodology was successful tested by Cammalleri et al. (2013, 2014) over rain-fed and irrigated agricultural areas in the Midwest US and over irrigated crops in Texas.

The ALEXI/DisALEXI/STARFM system is described further below.

2.2.1 The ALEXI/DisALEXI model

The two-source energy balance (TSEB) model considers the surface radiometric temperature to be a combination of both soil/substrate (T_s) and vegetated canopy (T_c) temperatures, weighted by the local vegetation cover fraction at the sensor view angle, $f(\theta)$:

$$T_{RAD}(\theta) \approx (f(\theta)T_c^4 + [1 - f(\theta)]T_s^4)^{1/4} \quad (1)$$

The equations to estimate surface energy-balance fluxes can be formulated for the whole system soil-canopy-atmosphere, or for each individual component as:

$$Rn_s = H_s + LE_s + G \quad (2)$$

$$Rn_c = H_c + LE_c \quad (3)$$

Where the subscripts “s” and “c” refer to soil and canopy, respectively. R_n identifies the net radiation, G the soil heat, and H and LE are the turbulent fluxes, sensible and latent heat, respectively. The complete model and equations formulation can be found in Norman et al. (1995) with modifications in Kustas and Norman (1999).

The ALEXI model and the associated flux disaggregation scheme, DisALEXI, are built upon the two source energy balance (TSEB) model. ALEXI was specifically designed to accommodate errors due to the inconsistency between radiometric and air temperature inputs by applying the TSEB in a time-differencing mode to thermal observations collected by geostationary satellites, over the morning hours (Anderson et al, 1997). TSEB is coupled with an atmospheric boundary layer model to internally simulate the effect of land-atmosphere feedback on near-surface air temperature (Anderson et al., 2012a). As a result, ALEXI provides an assessment of surface energy fluxes at continental scale, but at coarse spatial resolution.

For higher spatial resolutions of ET estimations, Norman et al. (2003) developed an associated flux disaggregation scheme (DisALEXI). It uses the air temperature diagnosed by ALEXI at the second time as the upper boundary condition for the implementation of the TSEB in DisALEXI, and therefore to disaggregate the ALEXI fluxes, by using higher resolution data from polar systems, as MODIS or Landsat (Anderson et al., 2012a).

2.2.1 ET maps fusion approach

The stage before applying fusion techniques consists on filling gaps in time series of MODIS ET due to cloud cover, in order to obtain a set of continuous daily data at 1 km resolution. This procedure was based on the preservation of the ratio between actual ET and reference ET (ET_0) as described by Anderson et al. (2012a).

The temporally sparse ET maps of Landsat at 30 m resolution and daily ET maps at MODIS-scale have been combined using the STARFM model (Gao et al., 2006). STARFM compares one or more pairs of observed Landsat/MODIS maps, collected on the same day to predict maps at Landsat spatial scale on other MODIS observations date, obtaining daily Landsat-like images.

Estimations of ET for a generic day (t_0), between Landsat overpasses, is based on a weighing function (W), which considers spatial differences between the Landsat (L) and MODIS (M) images on the acquisition date t_k and temporal difference between MODIS images from observed and predicted dates, t_k and t_0 respectively. The model computes the predicted

ET at 30 m for the central pixel of a selected moving window, with the following expression (eq. 4):

$$L(x_w/2, y_w/2, t_0) = \sum_{i=1}^w \sum_{j=1}^w \sum_{k=1}^n W_{ijk} [M(x_i, y_j, t_0) + L(x_i, y_j, t_k) - M(x_i, y_i, t_k)] \quad (4)$$

where w is the searching window size; $(x_w/2, y_w/2)$ is the central pixel of this moving window; n is the number of Landsat and MODIS pairs used (in this case only one pair) and W is the weighting factor. The complete model was described by Gao et al. (2006).

2.3 Remote sensing data processing

The daily ET maps at 3 km spatial resolution used for DisALEXI application have been obtained from routine estimates provided by the ALEXI model on the CONUS grid (Anderson et al., 2007). The remote sensing data from polar sensors required some preprocessing.

2.3.1 MODIS data processing

Remote sensing inputs for DisALEXI/MODIS application included products at 1 Km each 8-16 days of LAI (MDC15A3), NDVI (MOD13A2) and albedo (MDC43B3), which have been bilinearly interpolated in time to provide daily data. The instantaneous swath LST product (MOD11_L2) was used to derive radiometric temperature on daily basis as input of DisALEXI/MODIS. The TsHARP sharpening procedure (Kustas et al, 2003) was applied to reduce effects of off-nadir pixel smearing.

2.3.2 Landsat data processing

Scenes from Landsat 8 during the period April-December 2013 (DOY 102, 134, 150, 166, 198, 246, 262, 278, 294, 310 and 342) have been used. Bad pixels and clouds have been masked out. The optical bands were calibrated and atmospherically corrected using the Landsat Ecosystem Disturbance Adaptive Processing System (LEDAPS) (Masek et al., 2006). To obtain LAI data at 30 m resolution, a regression tree approach was applied, correlating Landsat reflectances with the MODIS LAI product (Gao et al., 2012).

For the atmospheric correction of thermal band the MODTRAN model (Berk et al., 1989) was used. Afterwards, LST maps were sharpened to 30 m resolution (typical of optical bands) using the TsHARP sharpening procedure (Kustas et al., 2003),

based on the conservation of the relation NDVI-TRAD at multiple spatial resolutions.

2.4 Meteorological, biophysical and regional data

Meteorological data were obtained from the Fifth-Generation Pennsylvania State University/National Center for Atmospheric Research Mesoscale Model (MM5) at a spatial resolution of 36 Km, while insolation data were obtained from a MSG product at 20 Km resolution.

Biophysical data such as fractional vegetation cover, canopy height, clumping factor, etc. in the area have been described by Andreu et al. (2013).

The Andalusian land cover map 2007 and Elevation Digital Model from Andalusian Government 2009-2010 at 10 m spatial resolution were used in this application.

3 RESULTS

3.1 Analysis of surface energy fluxes using MODIS images

Figure 2 shows the relationship between observed and modeled energy fluxes using DisALEXI application for MODIS images. In the figure 2(a), the fluxes were obtained at overpass time for 66 measurements and figure 2(b) shows the daytime-integrated fluxes of 49 days. It can be seen an acceptable correspondence between ECT observations and modeled outputs for all fluxes and over a wide range of variability in fluxes, although it is shown that there are a slight underestimation of sensible heat (H) and overestimation of latent heat (LE). The possible reasons may be limitations of the Priestley-Taylor coefficient or due to the daytime upscaling procedure.

These results are further corroborated by statistical metrics: mean absolute difference (MAD), root mean square difference (RMSD) and relative error (RE, ratio between MAD and observed average flux).

For the instantaneous turbulent fluxes, the MAD was 31 Wm^{-2} for LE and 59 Wm^{-2} for H, with RMSD of 41 and 69 Wm^{-2} , respectively. The RE in LE was 23.7% and 20.6% for H. The indices for radiative fluxes were around 27 % for MAD and 32% for RMSD.

The RMSD of LE is slightly higher than the values found by other authors (30 Wm^{-2}) over agricultural areas (González-Dugo et al., 2009), but it is similar to the results under irrigated conditions, semiarid regions and other studies over dehesa ecosystem, ranging between 45 and 55 Wm^{-2} (Cammalleri et al, 2010; Andreu et al., 2013).

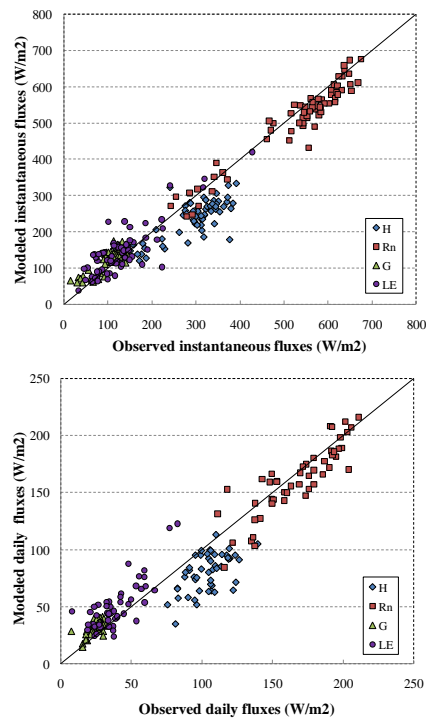


Figure 2. Comparison between observed and modeled energy fluxes by DisALEXI application using MODIS images: (a) instantaneous fluxes at overpass time and (b) daytime-integrated fluxes.

On the other hand, the statistical metrics for daily fluxes are slightly higher, with MAD for turbulent fluxes around $14\text{--}24 \text{ Wm}^{-2}$, and RE of 35 % for LE and 23% for H.

3.2 Analysis of surface energy fluxes using Landsat images

In figure 3, the comparison between observed and modelled daytime-integrated fluxes by DisALEXI application on Landsat dates is shown.

The plot was sampled on five cloudless Landsat images, in the tower area in which there were ECT observations (DOY 150, 198, 246, 262 and 342). For the comparison, the average fluxes of 3×3 Landsat pixels were estimated.

Figure 3 demonstrates a general agreement between pairs of fluxes. The values of MAD between observed and modeled ones were 17 Wm^{-2} for H and 9 Wm^{-2} for LE, with RMSD of 21 and 12 Wm^{-2} respectively. The RE was 19 and 20 % for LE and H, and around 11% for radiative fluxes (Rn and G). These results show a value of RE for LE higher than the value found by

Cammalleri et al. (2013), around 8%, but lower RE in other fluxes as H, with value around 55%.

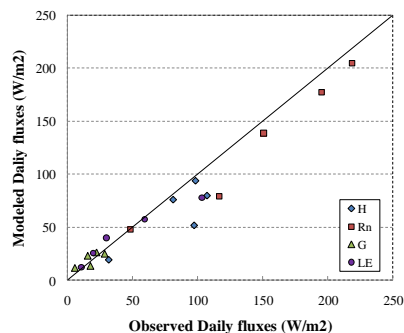


Figure 3. Comparison between observed and modeled daytime-integrated fluxes by DisALEXI application on Landsat dates.

3. 3 Evaluation of STARFM fusion method

A series of daily ET maps at 30 m resolution has been generated by STARFM model, for the period April-December 2013. The figure 4 shows the evolution of spatially distributed ET (mm) in the area on different days between DOY 141-240.

The comparison between daily ET from STARFM and ECT for 76 days between the period DOY 145-262 obtained a value of MAD of 0.36 mm with RE of 24 %. Besides, the application of remote sensing data fusion has supposed a slight improvement, in quantitative terms, in daily estimation of ET, around 5 % compared with gapfilled ET from application DisALEXI/MODIS, and using information measured by the ECT.

In spite of that, it is observed that the STARFM model better reflects the heterogeneity of the ET at watershed scale, reproducing the ET spatial variability, which supposes a noticeable improvement for interpreting the results and planning applications.

4 CONCLUSIONS

These results suggest the utility of the ALEXI/DisALEXI model to accurately estimate turbulent and radiative fluxes at 1 Km spatial resolution over the complex canopy structure of *dehesa* ecosystem, with a MAD value for convective fluxes of 59 Wm^{-2} for H and 31 Wm^{-2} for ET, and an average value for radiative fluxes of 27 Wm^{-2} , with RMSD of 69 and 41 Wm^{-2} for H and ET, and average value of 32 Wm^{-2} for Rn and G. These values are in the range of previous application of this model to other natural landscapes.

The application of remote sensing data fusion, STARFM, over this ecosystem has proved a significant improvement in heterogeneity assessment of ET values. The spatial resolution of the resultant dataset allows for further applications on vegetation and hydrological processes monitoring at watershed scale.

When compared with flux measurements, a slight quantitative improvement of fused images is observed (5 %).

This preliminary results highlights the need for further development and integration of cloud mask and gap filling procedures on Landsat images. Both correction would help to increase the number of available images, resulting in a significant gain in the fusion process.

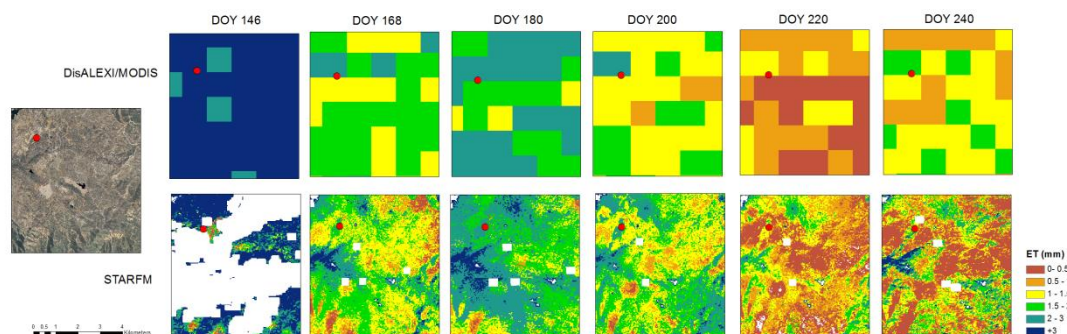


Figure 4. Maps of spatial distribution of daytime-integrated ET (mm) on different days between DOY 141-240

5 REFERENCES

- Anderson, M.C., Kustas, W.P., Alfieri, J.G., Hain, C.R., Prueger, J.H., Evett, S.R., Colaizzi, P.D., Howell, T.A. and Chávez, J.L., 2012a, Mapping daily evapotranspiration at Land-sat spatial scales during the BEAREX'08 field campaign. *Adv. Water Resour.* 50, pp. 162–177.
- Anderson, M.C., Norman, J.M., Diak, G.R., Kustas, W.P. and Mecikalski, J.R., 1997, A two-source time-integrated model for estimating surface fluxes using thermal infrared remote sensing. *Remote Sensing Environment* 60, pp.195-216.
- Andreu, A., González-Dugo, M.P., Kustas, W.P., Polo, M.J. and Anderson, M.C., 2013, Modelling surface energy fluxes over a dehesa ecosystem using a two-source energy balance model and medium resolution satellite data. *Remote Sensing for Agriculture, Ecosystems, and Hydrology XV*, (eds.) CMU Neale, A Maltese. Proc. SPIE, 888717. doi:10.1117/12.2029235.
- Berk, A., Bernstein, L.S. and Robertson, D.C., 1989, MODTRAN: A Moderate Resolution Model for LOWTRAN 7. GL-TR-89-0122. Air Force Geophysics Lab, Bedford, MA, pp. 38.
- Cammalleri, C., Agnese, C., Ciraolo, G., Minacapilli, M., Provenzano, G. and Rallo, G., 2010, Actual Evapotranspiration Assessment by Means of a Coupled Energy/Hydrologic Balance Model: Validation over an Olive Grove by Means of Scintillometry and Measurements of Soil Water Contents. *Journal of Hydrology*, 392, pp.70-82.
- Cammalleri, C., Anderson, M.C., Gao, F., Hain, C.R. and Kustas, W.P., 2013, A data fusion approach for mapping daily evapotranspiration at field scale. *Water Resour. Res.*, 49, pp. 4672-4686.
- Cammalleri, C., Anderson, M.C., Gao, F., Hain, C.R. and Kustas, W.P., 2014, Mapping daily evapotranspiration at field scales over rainfed and irrigated agricultural areas using remote sensing data fusion. *Agricultural Forest Meteorology* 186, pp. 1-11.
- Coelho, C. O. A., Ferreira, A. J. D., Laouina, A., Hamza, A., Chaker, M. et al., 2004, Changes in land use and land management practices affecting land degradation within forest and grazing ecosystems in the Western Mediterranean. *Adv. GeoEcology*, 37, pp. 137-154.
- Gao, F., Masek, J., Schwaller, M. and Hall, F., 2006, On the blending of the Landsat and MODIS surface reflectance: Predicting daily Landsat surface reflectance. *IEEE Transactions Geosci. Remote Sensing*. 44(8), pp. 2207-2218.
- Gao, F. et al., 2012, Simple method for retrieving leaf area index from Landsat using MODIS leaf area index products as reference. *Journal of Applied Remote Sensing*. 6(1), pp. 1-15.
- González-Dugo, M. P., Neale, C. M. U., Mateos, L., Kustas, W. P., Prueger, J. H., Anderson, M. C. and Li, F., 2009, A comparison of operational remote sensing-based models for estimating crop evapotranspiration. *Agricultural and Forest Meteorology*, 149 (11), pp.1843-1853.
- Kustas, W. P. and Norman, J. M., 1999, Evaluation of soil and vegetation heat flux predictions using a simple two source model with radiometric temperatures for partial canopy cover. *Agricultural Forest Meteorology*, 94 (1), pp. 13-29.
- Kustas, W.P., Norman, J.M., Anderson, M.C. and French, A.N., 2003, Estimating subpixel surface temperatures and energy fluxes from the vegetation index–radiometric temperature relationship. *Remote Sens. Environ.* 85, pp. 429–440.
- Masek, J.G., Vermote, E.F., Saleous, N.E., Wolfe, R.E., Hall, F.G., Huemmrich, K.F., Gao, F., Kutler, J. and Lim, T.-K., 2006, A Landsat surface reflectance dataset for North America, 1990–2000. *IEEE Geosci. Remote Sens. Lett.* 3 (1), pp. 68–72.
- Moran, M.S., Peters-Lidard, C.D., Watts, J.M., McElroy, S.A., 2004, Estimating soil moisture at the watershed scale with satellite-based radar and land surface models. *Canadian J. Rem. Sens.*, 30, pp. 805-826.
- Norman, J. M., Kustas, W. P. and Humes, K. S., 1995, Source approach for estimating soil and vegetation energy fluxes in observations directional radiometric surface temperature. *Agricultural Forest Meteorology*. 77, pp. 263–293.
- Norman, J.M., Anderson, M.C., Kustas, W.P., French, A.N., Mecikalski, J., Torn, R., Diak, G.R., Schmugge, T.J. and Tanner, B.C.W., 2003, Remote sensing of surface energy fluxes at 101-m pixel resolution. *Water Resour. Res.* 39, pp. 1221–1237.
- Papanastasis, V.P., 2004, Vegetation degradation and land use changes in agrosilvopastoral systems. In: Schnabel S, Ferreira A eds. Sustainability of agrosilvopastoral systems. *Advances in GeoEcology*, 37, pp. 2–12.

Improving Evapotranspiration Estimation Based on MOD16 Algorithm by Accounting for the Influence of Soil Moisture Variation

Su-chuang Di ^{1,2,3}, Ronglin Tang ¹, Hua Wu ¹, Bo-Hui Tang ¹, Jing Lu ⁴, Zhao-liang Li ^{1, 5, *}

1. Institute of Geographic Sciences and Natural Resources Research, China;

2. University of Chinese Academy of Sciences, China;

3. Beijing Water Science and Technology Institute, China;

4. Institute of Remote Sensing and Digital Earth Chinese Academy of Sciences, China;

5. ICube, UdS, CNRS, France;

* Email : lizl@unistra.fr

ABSTRACT - To integrate the influence of soil moisture into MOD16 Evapotranspiration (ET) algorithm, two improvements were made by combining the two layers of relative soil moisture parameters with the surface resistance model and by substituting the Penman-Monteith (P-M) method for the complementary relationship to estimate the dry soil surface evaporation. In the vegetation surface resistance model, a multiplier R_{sm1} was added and the influence of relative soil moisture in root zone was accounted for. In the soil surface model, an empirical exponent relationship was used. Both the MOD16 method and the improved method were validated at nine flux tower sites from 2000 to 2009. In the arid region, the improved method performed better than the MOD16 method. The mean absolute BIAS value was reduced from 0.37 mm/d to 0.14 mm/d and the mean Root Mean Square Error (RMSE) value was reduced from 0.99 mm/d to 0.74 mm/d. However, in the humid region, the improved method performed worse than the MOD16 method. The mean absolute BIAS value was increased from 0.26 mm/d to 0.58 mm/d and the mean RMSE value was increased from 1.02 mm/d to 1.57 mm/d. Furthermore, the uncertainties associated with the improvement method in the MODIS Leaf Area Index products, flux tower measurements, soil texture, soil moisture and model parameter were analyzed and the outlook of future modifications was also provided.

1 INTRODUCTION

Evapotranspiration (ET) is an important component both in surface energy balance and in hydrology cycle. Many kinds of ET estimation models were developed to estimate regional ET based on remote sensing products. These models could produce good estimation results on sunny days and on regional scales. However, when they are applied on the global spatial scale or to estimate continuous regional ET on daily or weekly temporal scale, the disadvantages emerge and mainly include: (1) there are no surface temperature parameters from thermal infrared remote sensing data under cloudy conditions. (2) The advection energy which is an important driving factor for ET in heterogeneous underlying regions is not accounted for. (3) ET results from remote sensing based models are instantaneous and the errors are generated when the instantaneous ET values are transformed into daily or weekly ET values, especially under cloudy conditions (Li et al., 2009).

To deal with these problems, the Penman-Monteith (P-M) approach based the MOD16 model was developed and improved (Cleugh et al., 2007; Mu et al., 2007; Mu et al., 2011). Although this model has been proved to estimate with certain success the global

ET, the inaccuracies were found between the flux tower measured ET and the MOD16 ET products for different cases (Kim et al., 2012; Jia et al., 2012; Ramoelo et al., 2014).

Vegetation surface resistance is expressed as a function of stomata conductance, cuticular conductance, boundary-layer resistance, leaf area index (LAI), vapour pressure deficit (VPD), temperature and other parameters in the MOD16 method. Soil moisture is the water source of ET and it plays an important role in controlling the canopy resistance and soil surface resistance. Some researchers found that after incorporating the surface soil moisture into the ET estimation model, results were improved (Gokmen et al., 2012; Sun et al., 2013). However, in the MOD16 algorithm the influence of soil moisture on ET was not accounted for directly.

The objective of this paper is to improve the daily ET estimation by integrating the influence of soil moisture into the MOD16 method. First, two layers of relative soil moisture in soil surface zone and root zone are integrated into the surface resistance sub-model and the relative soil moisture are inferred from the volumetric water content and soil hydraulic parameters. Second, the dry soil surface evaporation is estimated with the P-M method instead of the integration of the complementary relationship and the

Potential Evapotranspiration (ETP). The MOD16 method and the improved method are tested at 9 flux tower sites with crops or grass vegetation types in different climates in Contiguous United States. The uncertainties associated with the improved method are analyzed.

2. METHODOLOGY

2.1 MOD16 Algorithm

The MOD16 ET calculation algorithm is based on the P-M equation. On the temporal scale, the daily ET is divided into daytime ET and nighttime ET. On the spatial scale, the ET surface is divided into 4 parts: the wet canopy surface, the dry canopy surface, the wet soil surface and the dry soil surface. The details on the MOD16 method are found in Mu et al. (2011).

2.2 Improving canopy surface resistance

$$R_{sm1} = \begin{cases} 1 & SM_1 > Fc \\ \frac{SM_1 - Wp}{Fc - Wp} & Wp \leq SM_1 \leq Fc \\ 0 & SM_1 < Wp \end{cases} \quad (1)$$

$$G_{s-day} = C_L \times m(T_{min}) \times m(VPD) \times R_{sm1} \times r_{corr} \quad (2)$$

$$C_{C-day} = \frac{Gs2 \times (G_{s-day} + G_{CU})}{Gs2 + G_{s-day} + G_{CU}} \times LAI \times (1 - Fwet) \quad (3)$$

$$r_{cs-day} = 1 / C_{c-day} \quad (4)$$

where R_{sm1} is the root zone relative soil moisture; SM_1 is the volumetric water content in root zone; C_{C-day} is the daytime canopy conductance; $Gs2$ is the leaf boundary-layer conductance; G_{s-day} is the daytime stoma conductance; $G_{s-day,org}$ is the daytime stoma conductance calculated from the original MOD16 method; G_{CU} is the cuticular conductance; C_L is the potential stoma conductance; r_{cs-day} is the canopy daytime resistance. $Fwet$ is wet surface area ratio. Fc and Wp are the field capacity and wilting point, respectively. See Section 2.4 for their computations.

2.3 Improving dry soil surface evaporation

$$R_{sm2} = SM_2 / Sp \quad (4)$$

$$r_{ss} = \exp(a - b \times R_{sm2}) \quad (5)$$

$$\lambda E_S = \frac{\Delta(R_{ns} - G_s) + \rho Cp(1 - Fc) \times VPD / r_{as}}{\Delta + \gamma(1 + r_{ss} / r_{as})} \times (1 - Fwet) \quad (6)$$

where R_{sm2} is the soil surface relative soil moisture and the maximum value is set 1; SM_2 is the volumetric water content on soil surface; r_{ss} is the soil surface resistance; R_{ns} is the soil surface net radiation; G_s is the soil heat flux; a , b are the constants. r_{as} is the aerodynamic resistance on soil surface resistance. Sp is the saturation point. See Section 2.4 for its computation.

2.4 Soil hydraulic parameters estimation

In the improved method, the three soil hydraulic parameters (Fc , Wp and Sp) were estimated from the soil texture information according to Saxton et al. (1986).

$$\psi = A \times \theta^B \quad (7)$$

$$A = \exp(-4.396 - 0.0715(\% \text{ clay}) - 4.88 \times 10^{-4}(\% \text{ sand})^2 - 4.285 \times 10^{-5}(\% \text{ sand})^2(\% \text{ clay}))100 \quad (8)$$

$$B = -3.14 - 2.22 \times 10^{-3}(\% \text{ clay})^2 - 3.484 \times 10^{-5}(\% \text{ sand})^2(\% \text{ clay}) \quad (9)$$

$$Sp = 0.332 - 7.251 \times 10^{-4}(\% \text{ sand}) + 0.1276 \log_{10}(\% \text{ clay}) \quad (10)$$

where ψ is the soil water potential; θ is the soil water volumetric content; A , B are the parameters determined from the soil texture. If $\psi = 30$ KPa, $\theta = Fc$, field capacity; If $\psi = 1500$ KPa, $\theta = Wp$, wilting point.

3. STUDY SITES AND DATA

3.1 Study Sites

The original MOD16 method and the improved method are tested at 9 AmeriFlux tower sites in Contiguous USA. The latitudes range from 31.73° N to 44.35° N and the longitudes from 88.29° W to 120.95° W. The vegetation types around these sites are grass and crops. The climate types include: (1) Mid latitude Desert Climate; (2) Semiarid Steppe Climate; (3) Mediterranean Climate; (4) Humid continental Climate(cool summer); (5) Humid continental Climate(warm summer); (6) Humid Subtropical Climate. The mean annual precipitation ranges from

281 mm to 1142 mm and the mean annual temperature ranges from 6.27 °C to 17.30 °C.

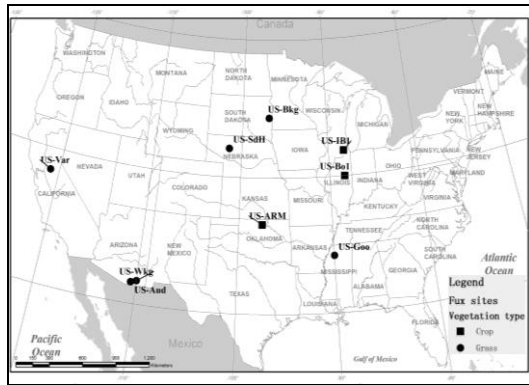


Fig.1 Test Flux sites distribution and vegetation types

3.2 Input datasets

The aggregated daily meteorological datasets from the half-hour measurements are used in this study. The Level 2 measured meteorological data, soil moisture data, and surface flux data at 9 tower site are obtained.

The LAI and vegetation coverage fraction (FC) datasets are from the 1-km² MODIS collection FPAR/LAI (MOD15A2).

3.3 Pre-processing datasets

For valid days, the daily, daytime and nighttime averaged values of meteorological data, surface flux data and soil moisture data are estimated based on the 30-min time series.

The 8-day MODIS LAI and FC products are interpolated to obtain the daily values under the assumption that there is no obvious change in the vegetation within the 8 days.

According to Saxton et al. (1986), the Fc, Wp and Sp are calculated. The results show that the Fc ranges from 0.20 to 0.48, the Wp ranges from 0.09 to 0.26, and the Sp ranges from 0.39 to 0.49. Generally, the silty clay soil is characterized by high hydraulic parametric values while the sandy loam soil is characterized by small hydraulic parameters.

4. RESULTS AND DISCUSSION

4.1 Daily ET comparison from two methods

Both the results of MOD16 method and improved method were compared with the measured daily ET and the 3 indicators of BIAS, root mean square error (RMSE) and correlation coefficient (R) were selected to evaluate the performances of the two methods. After improving the parameterization of original MOD16 method, R values were increased at 8 sites, absolute BIAS values reduced at 3 sites and RSME values reduced at 4 sites.

For 4 sites in the arid region, the averaged absolute BIAS and RMSE were decreased from 0.37 mm/d to 0.14 mm/d and from 0.99 mm/d to 0.74 mm/d, respectively, after integrating soil moisture parameters. For 5 sites in the humid region, the averaged absolute BIAS and RMSE were increased from 0.22 mm/d to 0.58 mm/d and from 1.02 mm/d to 1.37 mm/d, respectively.

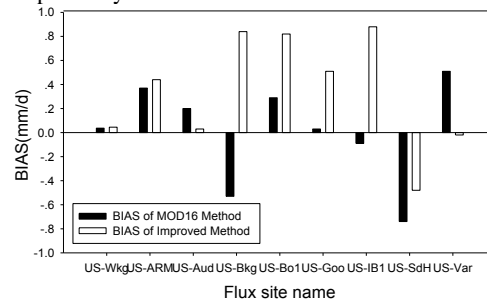


Fig.2 BIAS in the validation of the MOD16 and improved methods at 9 test Flux sites

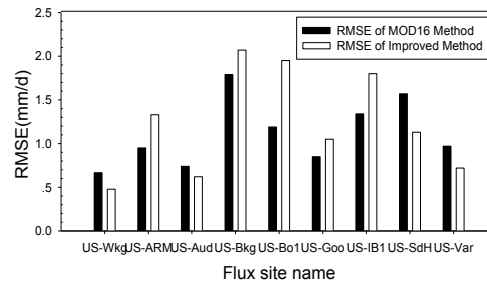


Fig.3 RMSE in the validation of the MOD16 and improved method at 9 test Flux sites

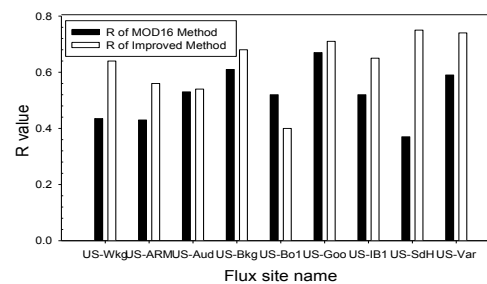


Fig.4 R value in the validation of the MOD16 and improved method at 9 test Flux sites

4.2 Daily ET comparison at arid site - US-Wkg

To compare the ET time series from the MOD16 and the improved method in arid region, the measured flux data at the US-Wkg site from 1st January, 2005 to 31st December, 2009 was used. Compared with the MOD16 method, the improved method produced similar BIAS, smaller RSME and larger R values at this site. For the MOD16 method, the BIAS, RSME and R were 0.04 mm/d, 0.67 mm/d and 0.44 respectively. For the improved method, they were 0.05

mm/d, 0.48 mm/d and 0.64, respectively.

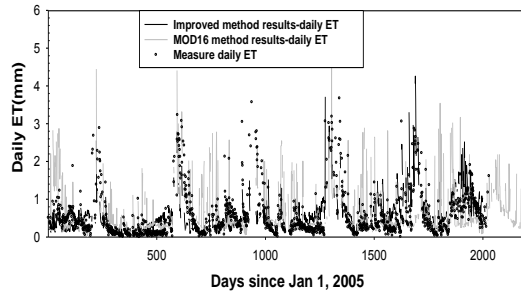


Fig.5 Comparisons of estimated daily ET time series from MOD16 and Improved method with measured data at US-Wkg

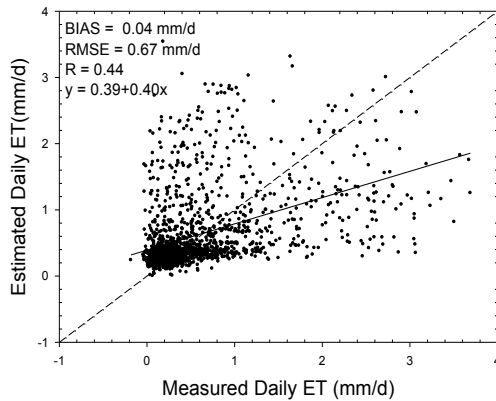


Fig.6 Comparisons of MOD16 daily ET with measured values at US-Wkg

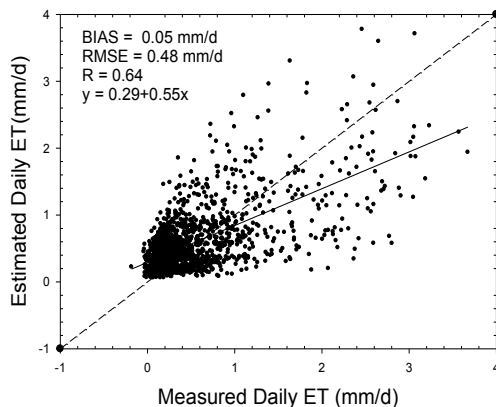


Fig.7 Comparisons of improved daily ET with measured values at US-Wkg

4.3 Daily ET comparison at humid site - US-IB1

To compare the ET time series from the MOD16 and the improved method in the humid region, the US-IB1 site was selected. The calculation period was from Mar.29, 2005 to Oct.31, 2009.

Compared with the MOD16 method, the improved method produced larger BIAS, larger RSME and higher R values at this site. For the MOD16 method, the BIAS, RSME and R were -0.09 mm/d, 1.34 mm/d and 0.52, respectively. For the improved method, they were 0.88 mm/d, 1.80 mm/d and 0.65, respectively.

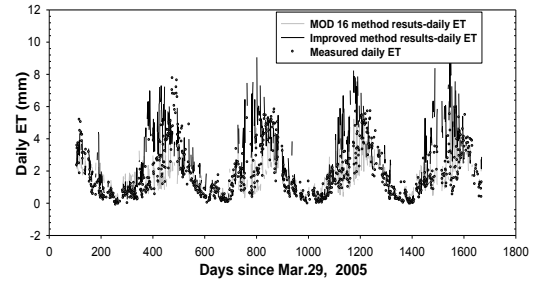


Fig.8 Comparisons of estimated daily ET time series from MOD16 and improved method with measured data at US-IB1

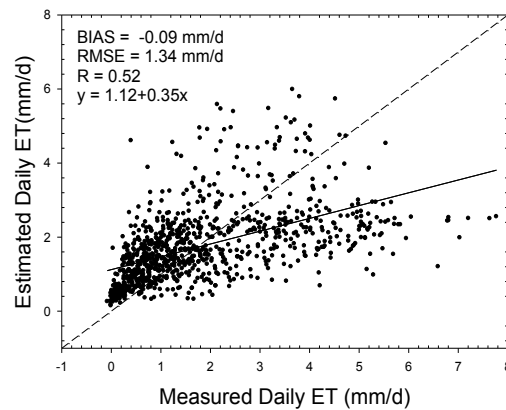


Fig.9 Comparisons of MOD16 daily ET with measured values at US-IB1

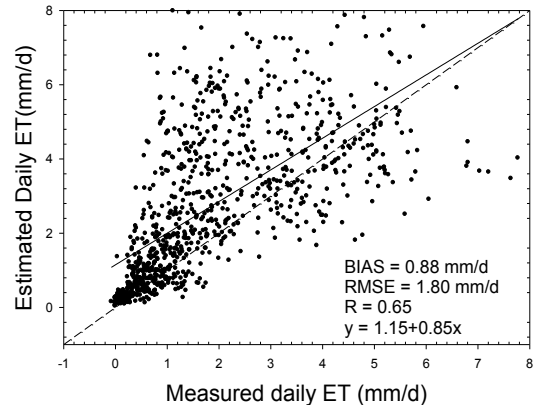


Fig.10 Comparisons of improved daily ET with measured values at US-IB1

4.4 Discussion

The mean R value of 9 sites was 0.52 for the original method and 0.63 for the improved method. The phenomenon that 8 out of total 9 sites were with higher R values for the improved method than for the MOD16 method indicated that daily ET produced by the improved method was more correlated with the observed values than the Mod16 method. The soil moisture is the water source of ET and it is highly related to the observed daily ET. Therefore, the R values from the improved method were higher than

from the MOD16 method.

For 4 sites in the arid region, the mean absolute BIAS and RMSE were decreased after integrating the soil moisture parameters, because water was the major limiting factor for ET in arid region. Soil moisture in root zone was usually near wilting point and R_{sml} value was very small in arid region. Therefore, the surface resistance for transpiration was very high and the vegetation transpiration was reduced in the improved method. The ET components from the other 3 surfaces were very small in arid region. The MOD16 ET in arid region was found larger than the ET values estimated from water balance model (Xue et al. 2012). The deviation was reduced in the new method, so the new method produced more accurate daily ET than the MOD16 method in arid region.

For 5 sites in the humid region, the mean absolute BIAS and RMSE were increased after integrating soil moisture parameters, primarily because in humid region the ET limiting factor was usually the available energy. The root zone soil moisture was usually near filed capacity and R_{sml} was near 1, so the vegetation transpiration results were similar between the MOD16 method and our improved method. In humid region the surface soil moisture was also usually very high and the soil surface resistance was smaller. In the improved method, the P-M method was used to estimate the ET at the dry soil surface. Sun et al. (2010) found that the ET from the P-M method had an tendency to be overestimated in humid region, so the improved method produced higher ET than the MOD16 method. The deviation between the measured and estimated ETs was larger for the improved method.

Discrepancies between the calculated ET from the improved method and the measurement might originate from such factors as MODIS products accuracies, flux tower measurement errors, soil texture uncertainties, soil moisture uncertainties and other model parameter accuracies.

5. SUMMERY AND CONCLUSION

In this study, the MOD16 algorithm was improved by integrating two layers of soil moisture into the surface resistance sub-model and substituting the complementary relationship by the P-M method to estimate the evaporation at the dry soil surface. The ET components from the dry canopy surface and dry soil surface were estimated based on the P-M model. The other two ET components from wet canopy surface and wet soil surface were estimated in the same way as the original MOD16 method because the influence of soil moisture had little effect on these two ET components. By summing the ET results from the 4 ET components, the total daily ET could be estimated in the improved method.

The performances of the original MOD16 method and the improved method were evaluated based on the observed daily ET at 9 flux sites in Contiguous United States. Generally, the improved method performed better at arid sites than at humid sites. For 4 sites in arid region, the averaged absolute BIAS and RMSE were decreased from 0.37 mm/d to 0.14 mm/d and from 0.99 mm/d to 0.74 mm/d, respectively, after integrating soil moisture parameters. For 5 sites in humid region, the averaged absolute BIAS and RMSE were increased from 0.22 mm/d to 0.58 mm/d and from 1.02 mm/d to 1.37 mm/d, respectively, after integrating soil moisture. There was a tendency of underestimation of transpiration and total ET in arid region compared with the MOD16 method. However, there was a tendency of overestimation of soil surface evaporation and total ET in humid region.

The results of the improved method were influenced by such factors as MODIS LAI and FC products accuracies, flux tower measurement errors, soil texture uncertainties, soil moisture uncertainties and other model parameter accuracies.

Future work will be conducted to combine the improved model with the soil moisture information derived from remote sensing data or land surface models so that the improved model could be applied at regional scale.

6. ACKNOWLEDGMENT

The measurements at the 9 flux tower sites were downloaded from the AmeriFlux FTP servers. We gratefully thank the researchers at these sites for their efforts on making these data available. Information on LAI and FC was downloaded from the MODIS collections. This work was partly supported by the National Natural Science Foundation of China under Grant 41201366, the Institute of Geographic Sciences and Natural Resources Research funded outstanding young talent project under Grant 2013RC201, and the National Natural Science Foundation of China under Grant 41101332.

7. REFERENCES

- Cleugh H, R. Leuning, Q. Mu and S. W. Running. 2007. "Regional Evaporation Estimates from Flux Tower and MODIS Satellite Data." *Remote Sensing of Environment* 106(3): 285-304.
- Jia, Z., S. Liu, Z. Xu, Y. Chen and M. Zhu. 2012. "Validation of Remotely Sensed Evapotranspiration over the Hai River Basin, China." *Journal of Geophysical Research* 117: 2156-2202.
- Kim, H. W., K. Hwang, Q. Mu, S. O. Lee, and M.

- Choi. 2012. "Validation of MODIS 16 Global Terrestrial Evapotranspiration Products in Various Climates and Land Cover Types in Asia." *KSCE Journal of Civil Engineering* 16(2): 229-238.
- Li, Z.-L., R. L. Tang, Z. Wan, Y. Bi, C. Zhou, B. Tang, G. Yan, and X. Zhang. 2009. "A Review of Current Methodologies for Regional Evapotranspiration Estimation from Remotely Sensed Data." *Sensors* 9: 3801-3853.
- Mu, Q., F. A. Heinsch, M. Zhao and S. W. Running. 2007. "Development of a Global Evapotranspiration Algorithm Based on MODIS and Global Meteorology Data." *Remote Sensing of Environment* 111(4): 519-536.
- Mu, Q., M. Zhao and S. W. Running. 2009. "Improvements to a MODIS Global Terrestrial Evapotranspiration Algorithm." *Remote Sensing of Environment* 115(8): 1781-1800.
- Ramoelo, A., N. Majozi, R. Mathieu, N. Jovanovic, A. Nickless and S. Dzikiti. 2014. "Validation of Global Evapotranspiration Product (MOD16) using Flux Tower Data in the African Savanna, South Africa." *Remote Sensing* 6(8): 7406-7423.
- Saxton, K. E., W.J. Rawls, J.S. Romberger and R. I. Papendick. 1986. "Estimating Generalized Soil-water Characteristics from Texture." *Soil Science Society of America Journal* 50(4): 1031-1036.
- Sun, L., S. Liang, W. Yuan and Z. Chen. 2013. "Improving a Penman-Monteith Evapotranspiration Model by Incorporating Soil Moisture Control on Soil Evaporation in Semi-arid Area." *International Journal of Digital Earth* 10: 134-156.
- Xue, B.-L., L.Wang, X. Li, K. Yang, D. Chen and L. Sun. 2013. "Evaluation of Evapotranspiration Estimates for Two River Basins on the Tibetan Plateau by a Water Balance Method." *Journal of Hydrology* 492: 290-297.

Daily evaporative fraction retrieval from MODIS data using two temporal information-based models

Jing Lu^{a,b}, Ronglin Tang^b, Zhao-Liang Li^{c,d,*}, Yuyun Bi^c

a. State Key Laboratory of Remote Sensing Science, Institute of Remote Sensing and Digital Earth, Chinese Academy of Sciences, Beijing 100101, China

b. State Key Laboratory of Resources and Environmental Information System, Institute of Geographic Sciences and Natural Resources Research, Chinese Academy of Sciences, Beijing, 100101, China

c. Key Laboratory of Agri-informatics, Ministry of Agriculture/Institute of Agricultural Resources and Regional Planning, Chinese Academy of Agricultural Sciences, Beijing 100081, China

d. ICube, UdS, CNRS, Bld Sebastien Brant, CS10413, 67400, Illkirch, France

* Authors to whom correspondence should be addressed: lizl@unistra.fr

ABSTRACT—This study compared two evaporative fraction (EF) methods using the day-night difference of land surface temperature (LST) over the Southern Great Plains. One is a new developed method for estimating daily EF by a semi-empirical parameterization based on the day-night differences of LST, air temperature, and incoming solar radiation, and the fractional vegetation cover, the other is the triangular feature space method constructed by the day-night difference of LST and fractional vegetation cover. The results showed that the two methods can reasonably estimate EF in spatial distribution. The coefficient of determination in the EF comparison between these two methods is 0.824. Compared with the in-situ measurements from Energy Balance Bowen Ratio system, the EF from the new developed parameterization is closer to the measured values with a bias of -0.011, whereas the triangular feature method slightly underestimates EF.

1 INTRODUCTION

Remote sensing (RS) is an economically viable approach of obtaining evapotranspiration (ET) at the regional scale. A large number of RS-based ET methods from the simple empirical formulas to the sophisticated land surface models have been proposed, such as the triangle feature method, the surface energy balance system (SEBS), the surface energy balance algorithm for land (SEBAL), the Penman-Monteith (PM) equation, the assimilation method, and so on (Li et al. 2009). However, the retrieval errors and uncertainties of remotely sensed data make the accurate ET estimation at the regional and global scales become a challenge. Multi-times observations from remote sensing sensors can help to solve this problem. On the basis of the two-source model proposed by Norman et al. (1995), and coupling with a simplified conservation equation describing the growth of a convective boundary layer, Anderson et al. (1997) developed a two-source time-integrated model for estimating surface fluxes, which is not sensitive to the retrieval error of land surface temperature (LST). Wang et al. (2006) and Stisen et al. (2008) used the day-night difference of LST from MODIS products

and the change rate of LST during the morning from the meteorological satellites to construct LST-vegetation index feature space for improving the EF estimates, respectively. Assimilating multi-times observations of the remotely sensed data from satellites into the land surface process models is also an approach to reduce the uncertainties of remote sensing data. Recently, Lu et al. (2013, 2014) provided a new EF parameterization based on temporal variations of surface temperature, air temperature, and net radiation, and it was further improved by using incoming solar radiation. To further clarify the performance of this method for EF estimates at the regional scale, the study will compare this new method with the triangular feature space method improved by Wang et al. (2006). The reasons for choosing the improved triangular method as the reference model are that: (1) both methods can directly determine EF without calculating various surface resistances, and (2) they are all dependent on the day-night difference of LST and the fractional vegetation cover. Lu's method and Wang's method are denoted as EF_L method and EF_T method for short hereinafter, respectively.

2 METHODS

2.1 EF_L method

On the basis of the surface energy balance equation and with the assumption of relatively invariant EF during the daytime and low evaporation at night, Lu et al. (2013, 2014) derived a new parameterization scheme of directly estimating daily EF. Daily EF is parameterized as a function of day-night differences in surface temperature, air temperature (T_a), and incoming solar radiation (R_g), i.e.,

$$EF_L = 1 - (-13.52 \times f_c^2 + 41.81 \times f_c + 24.26) \frac{\Delta T_s - \Delta T_a}{\Delta R_g} \quad (1)$$

where ΔT_s , ΔT_a , and ΔR_g are day-night differences of T_s , T_a , and R_g , respectively, i.e., the differences between 1:30 P.M. and 1:30 A.M., corresponding to MODIS/Aqua day and night overpass times. f_c is the fractional vegetation cover. Those coefficients in equation (1) were obtained using the simulated data with different surface and atmospheric characteristics. Details are found in the paper of Lu et al. (2013, 2014). Although the formula is semi-empirical, those coefficients don't strongly rely on the surface and atmospheric characteristics, and has been assessed at the Yucheng station in North China and at some America flux sites with different vegetation types.

2.2 EF_T method

Wang et al. (2006) constructed the feature space by using ΔT_s and the normalized difference vegetation index (NDVI). The ϕ value in the Priestley-Taylor equation is then obtained by a two-step linear interpolation according to ΔT_s and NDVI over the study region. EF is finally calculated by multiplying $\Delta/(\Delta+\gamma)$ which is an air temperature factor. In this study, there are two aspects different from the original Wang et al. (2006)'s method. One is to use f_c instead of NDVI to construct the triangle feature space with the consideration that f_c is more representative of the relative proportionality between soil and vegetation within a pixel (Tang et al., 2010). The other is to directly interpolate EF rather than ϕ value in the Priestley-Taylor equation with the assumption that ET or EF is minimum on dry edge and reaches the maximum on wet edge (Jiang and Islam, 2003). In this study, the dry edge is formed by fitting f_c interval and their corresponding maximum ΔT_s , whereas the wet edge is determined by averaging the minimum ΔT_s for all f_c intervals (de Tomás et al., 2014). EF on dry edge is linearly proportional to f_c , and EF on wet edge is equal to 1. After determining the dry and wet edges, EF for each pixel in the feature space is linearly interpolated between the maximum and minimum of ΔT_s corresponding to each f_c . As a result, EF is calculated by the following equation.

$$EF_T = \frac{(1 - EF_{dry})(\Delta T_{s,i,dry} - \Delta T_{s,i})}{(\Delta T_{s,i,dry} - \Delta T_{s,wet})} + EF_{dry} \quad (2)$$

with $EF_{dry} = 1 - (f_{c,max} - f_{c,i})/f_{c,max}$.

where $f_{c,max}$ corresponds to the abscissa of the intersection of dry and wet edges, which is not always equal to 1. The subscripts of 'dry' and 'wet' denote the values on the dry and wet edges, respectively. i represents a given value in the feature space.

3 STUDY AREA AND DATA

The Southern Great Plains (SGP) region is an ideal area for performing the comparison of temporal information-based models because of a large number of intensive observations over the region. The SGP region is located in the south of the United States of America, from 95.5°W to 99.5°W in longitude and from 34.5°N to 38.5°N in latitude. This region is mainly covered by grasslands, croplands, and savanna sparsely vegetation (see Fig. 1).

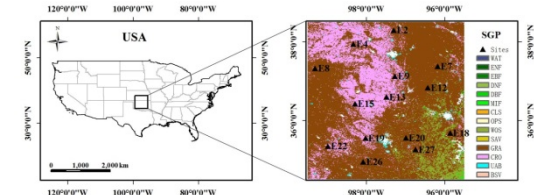


Fig. 1. The location of the Southern Great Plains and the distribution of Energy Balance Bowen Ratio sites

Annual precipitation is about 500 mm (Wan et al., 2004). Water supplied as irrigation in the region amounts to billions of cubic meters annually and is governed by the determination of ET in the region (Batra et al., 2006). Surface fluxes from 14 Energy Balance Bowen Ratio (EBBR) sites, which are almost uniformly distributed over the SGP region, are collected to evaluate the EF estimates using remotely sensed data (see Fig. 1). Basic information about those sites is list in Table 1. MYD11A1 and MYD13A2 products on 8 September (DOY 252) in 2004 are used in this study because of the minimum cloud cover on the day. The f_c required by the two methods is calculated by a nonlinear model proposed by Carlson and Ripley (1997), i.e.,

$$f_c = \left(\frac{NDVI - NDVI_{min}}{NDVI_{max} - NDVI_{min}} \right)^2 \quad (3)$$

where $NDVI_{min}$ and $NDVI_{max}$ are the NDVI for bare soil and dense vegetation at full coverage, and are assigned to be 0.2 and 0.86, respectively.

In addition, T_a and R_g are also required by the EF_L method, which are from NLDAS-2 forcing dataset with a spatial resolution of 0.125° and a temporal resolution of an hour.

Table 1. The basic information of sites

Sites ID	Site name	Location	Latitude	Longitude	Elevation(m)	Land cover
EF2	Hillsboro	Kansas	38.305 N	97.301 W	447	Grass
EF4	Plevna	Kansas	37.953 N	98.329 W	513	Rangeland (ungrazed)
EF7	Elk Falls	Kansas	37.383 N	96.180 W	283	Pasture
EF8	Coldwater	Kansas	37.333 N	99.309 W	664	Rangeland (grazed)
EF9	Ashton	Kansas	37.133 N	97.266 W	386	Pasture
EF12	Pawhuska	Oklahoma	36.841 N	96.427 W	331	Native prairie
EF13	Lamont	Oklahoma	36.605 N	97.485 W	318	Pasture and wheat
EF15	Ringwood	Oklahoma	36.431 N	98.284 W	418	Pasture
EF18	Morris	Oklahoma	35.688 N	95.856 W	217	Grass
EF19	El Reno	Oklahoma	35.557 N	98.017 W	421	Pasture (ungrazed)
EF20	Meeker	Oklahoma	35.564 N	96.988 W	309	Pasture
EF22	Cordell	Oklahoma	35.354 N	98.977 W	465	Rangeland (grazed)
EF26	Cement	Oklahoma	34.957 N	98.076 W	400	Pasture
EF27	Earlsboro	Oklahoma	35.269 N	96.740 W	300	Pasture

4 RESULTS AND DISCUSSION

4.1 Spatial distribution of EF estimates over the SGP region

The EF over the SGP region estimated by the EF_L method and the EF_T method are shown in Fig.2a-b. It is obvious that EF in the east of the SGP region is larger than that in the west. This trend is also consistent with the output of NLDAS-2 (Fig. 2c). The mean EF over the SGP region from EF_L method is 0.59 with a standard deviation of 0.16, and the mean EF from the EF_T method is 0.47 with a standard deviation of 0.15. The result estimated by EF_L method is closer to the EF from NLDAS_2 with the mean value of 0.61 and the standard deviation of 0.1.

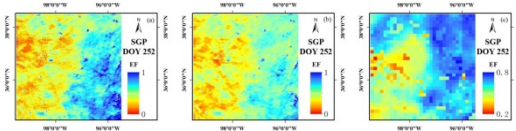


Fig. 2. The EF distribution over the Southern Great Plains from (a) the EF_L method, (b) the EF_T method, and (c) NLDAS-2.

The spatial distribution of EF mainly depends on T_s and f_c . From Fig.3, it can be observed that T_s in the east is lower than that in the west, which may be caused by the cooling of high ET. High ET may be also from more vegetation in the east. The spatial variation of T_s on DOY 252 is independent of R_g . From Fig.3a, it can be observed that R_g over the SGP region almost varies along latitudinal trend, decreasing from the north to the south according to the altitude of sun, about 40 W/m² difference over the region. Therefore, T_s is the result of joint action of radiation

and surface characteristics. As a result, the spatial distribution of T_a is similar to T_s , gradually decreasing from the west to the east. The maximum difference of T_a over the SGP region is not more than 5 K, that is, the atmospheric condition over the SGP region doesn't change dramatically. Relatively homogeneous atmospheric condition and flat terrain can meet the precondition of the EF_T method. This is also the reason that the EF estimate from the EF_L method is not strongly related to R_g and T_a .

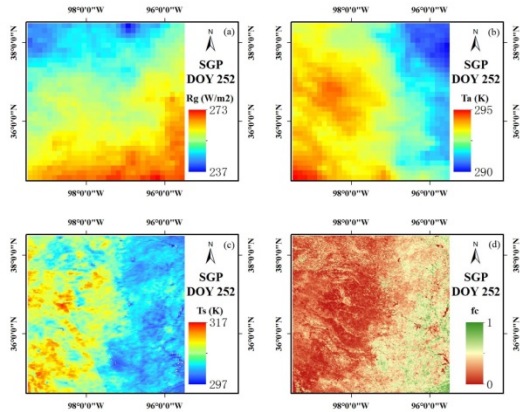


Fig. 3. Spatial distribution of (a) R_g , (b) T_a , (c) T_s , and (d) f_c over the SGP region

4.2 Comparison of two temporal information-based methods for estimating EF

The EF from the EF_L method is strongly related to that from the EF_T method with the coefficient of determination of 0.824. The values from the EF_L method are generally overestimated compared with the EF_T method with a bias of 0.126 (see Fig. 4a). The

large relative biases between the estimated EF from the two methods occur in the west with low ET (see Fig. 4b). This is consistent with the previous study, which concluded that larger uncertainties often happen on the surface with low ET and low f_c . The calculation of f_c driven by the NDVI also caused the error of EF estimates. 0.2 variations in f_c can lead to about 0.1 variations in EF. Besides the error of input variables from remotely sensed data, the determination of coefficients in the EF_L method may be also an error source. The coefficients in equation (1) were determined using simulated data by a SVAT model for variable atmospheric conditions at four stations with different vegetation cover and soil moisture conditions. The simulated data may be limited and cannot represent all surface and atmospheric conditions. This will lead to the uncertainties for EF estimates by equation (1). For the EF_T method, the errors in EF estimates are mainly from the uncertainties in determining the dry and wet boundaries (Long et al., 2012). The dry and wet edges from the linear regression may not be the true theoretical boundaries. The assumptions of EF on the dry edge linearly proportional to f_c and linearly interpolating EF between the minimum and maximum of T_s for each f_c also lead to errors in estimating EF. Particularly for the pixels close to the dry and wet edges, larger errors are produced.

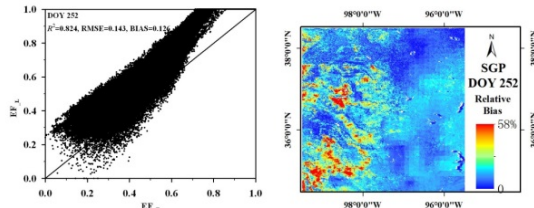


Fig. 4 (a) Comparisons of EF estimates between the EF_L and EF_T methods and (b) the spatial distribution of their absolute relative bias

4.3 Evaluation of EF estimates with in situ measurements

When the estimated EF from the two temporal information-based methods are compared with the measured values from EBBR system, EF estimates from the EF_L method are closer to the in-situ measurements with the root mean square error of 0.170 and a bias of -0.011. The mean measured EF at 14 EBBR stations on DOY 252 is 0.57. This value can represent the EF over the SGP region because the EBBR stations are uniformly distributed in the region. Therefore, the EF estimates from the EF_L method are more reasonable over the SGP region. Additionally, the inconsistency between the estimated and measured EF is also from the measurement error and the

different observation scales between the MODIS pixel and EBBR system. The spatial resolution of 1 km is generally larger than the source area of EBBR system. How to accurately validate the estimated ET from the remotely sensed data using in situ measurements is still a challenge.

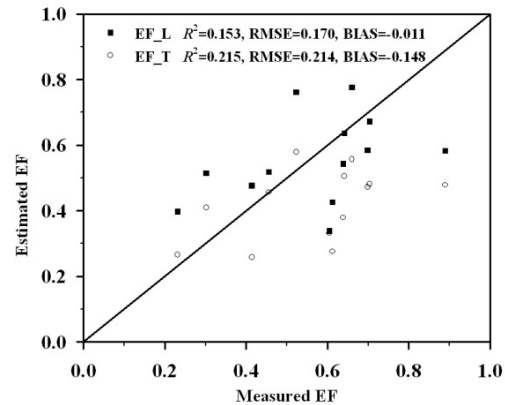


Fig. 5 Comparisons of EF estimates from two methods with the in-situ measurements

5 CONCLUSIONS

This study compared two EF methods driven by the day-night difference of surface temperature over the SGP region. The results showed that the two methods can reasonably estimate daily EF in spatial distribution. The spatial distribution of EF over the SGP region is dependent of the surface temperature and vegetation cover rather than atmospheric condition. Low surface temperature corresponds to low EF because of the cooling of ET, whereas high vegetation cover leads to high EF. Although there are a lot of uncertainties for remotely sensed input variables and the parameterizations of EF, the EF from the new developed method is strongly related to that from the improved triangular method with the coefficient of determination of 0.824. Compared with the EF from feature space method, the EF from the new developed EF method is closer to the in-situ measurements. The independence on the domain size and the spatial resolution of remotely sensed image make the new developed method superior to the feature space method. The biggest disadvantage for the LST-based ET method is that LST from the thermal infrared remote sensing is easily contaminated by the cloud. However, the LST is still the direct variable reflecting surface thermal states, which has the maximum potential to estimate surface ET.

6 REFERENCES

- Anderson, M. C., Norman, J. M., Diak, G. R., Kustas, W. P., and Mecikalski, J. R., 1997, A Two-Source Time-Integrated Model for Estimating Surface Fluxes Using Thermal Infrared Remote Sensing. *Remote Sensing of Environment*. **60** (2),195-216.
- Batra, N., Islam, S., Venturini, V., Bisht, G., and Jiang, L., 2006, Estimation and comparison of evapotranspiration from MODIS and AVHRR sensors for clear sky days over the Southern Great Plains. *Remote Sensing of Environment*. **103** (1),1-15.
- Carlson, T. N., and Ripley, D. A., 1997, On the relation between NDVI, fractional vegetation cover, and leaf area index. *Remote Sensing of Environment*. **62** (3),241-52.
- de Tomás, A., Nieto, H., Guzinski, R., Salas, J., Sandholt, I., and Berliner, P., 2014, Validation and scale dependencies of the triangle method for the evaporative fraction estimation over heterogeneous areas. *Remote Sensing of Environment*. **152** (0),493-511.
- Jiang, L., and Islam, S., 2003, An intercomparison of regional latent heat flux estimation using remote sensing data. *International Journal of Remote Sensing*. **24** (11),2221-36.
- Li, Z.-L., Tang, R., Wan, Z., Bi, Y., Zhou, C., Tang, B., Yan, G., and Zhang, X., 2009, A review of current methodologies for regional evapotranspiration estimation from remotely sensed data. *Sensors*. **9** (5),3801-53.
- Long, D., Singh, V. P., and Scanlon, B. R., 2012, Deriving theoretical boundaries to address scale dependencies of triangle models for evapotranspiration estimation. *Journal of Geophysical Research*. **117** (D5),D05113.
- Lu, J., Tang, R., Tang, H., and Li, Z.-L., 2013, Derivation of Daily Evaporative Fraction Based on Temporal Variations in Surface Temperature, Air Temperature, and Net Radiation. *Remote Sensing*. **5** (10),5369-96.
- Lu, J., Tang, R., Tang, H., Li, Z.-L., Zhou, G., Shao, K., Bi, Y., and Labed, J., 2014, Daily Evaporative Fraction Parameterization Scheme Driven by Day–Night Differences in Surface Parameters: Improvement and Validation. *Remote Sensing*. **6** (5),4369-90.
- Norman, J. M., Kustas, W. P., and Humes, K. S., 1995, Source Approach for Estimating Soil and Vegetation Energy Fluxes in Observations of Directional Radiometric Surface-Temperature. *Agricultural and Forest Meteorology*. **77** (3-4),263-93.
- Stisen, S., Sandholt, I., Norgaard, A., Fensholt, R., and Jensen, K. H., 2008, Combining the triangle method with thermal inertia to estimate regional evapotranspiration - Applied to MSG-SEVIRI data in the Senegal River basin. *Remote Sensing of Environment*. **112** (3),1242-55.
- Tang, R., Li, Z.-L., and Tang, B., 2010, An application of the Ts–VI triangle method with enhanced edges determination for evapotranspiration estimation from MODIS data in arid and semi-arid regions: Implementation and validation. *Remote Sensing of Environment*. **114** (3),540-51.
- Wan, Z., Wang, P., and Li, X., 2004, Using MODIS land surface temperature and normalized difference vegetation index products for monitoring drought in the southern Great Plains, USA. *International Journal of Remote Sensing*. **25** (1),61-72.
- Wang, K. C., Li, Z. Q., and Cribb, M., 2006, Estimation of evaporative fraction from a combination of day and night land surface temperatures and NDVI: A new method to determine the Priestley-Taylor parameter. *Remote Sensing of Environment*. **102** (3-4),293-305.

Mapping daily gross primary production over Africa using SEVIRI/MSG satellite products

B. Martínez¹, A. Moreno¹, S. Sánchez¹, F.J. García-Haro¹, F. Camacho², J. Meliá¹, J. Ardö³, W. Kutsch⁴, M.A. Gilabert¹

¹ *Facultat de Física, Universitat de València, Dr. Moliner, 50. 46100-Burjassot, Spain*

² *EOLAB SPAIN, Pol. La Coma s/n, 46980 Paterna, Spain*

³ *Physical Geography and Ecosystem Science, Lund University, Sölvegatan 12, SE-223 62 Lund, Sweden*

⁴ *Johann Heinrich von Thünen Institute, Institute for Agricultural Climate Research, Bundesallee 50, 38116 Braunschweig, Germany*

Beatriz.martinez@uv.es

ABSTRACT - This work aims at providing gross primary production (GPP) estimates over Africa for 2008 using SEVIRI/MSG satellite products delivered in LSA SAF system. The GPP estimates rely on the use of the Monteith's simple approach, which considers GPP as proportional to the flux density of photosynthetically active radiation (PAR), the fractional absorption of that flux (f_{APAR}) and the light-use efficiency (ϵ), by means of the general relation $GPP = \epsilon f_{APAR} PAR$. In this work the PAR relies on the daily MSG down-welling surface shortwave radiation flux (DIDSSF) product. The PAR is considered as the 46% of the DIDSSF, which is produced from the daily integration of the down-welling surface shortwave radiation flux (DSSF) product acquired every 30 minutes. For the f_{APAR} input, the daily MSG f_{APAR} (MDFAPAR) product has been used. Lastly, a constant ϵ was used since it has been demonstrated that the most significant inputs in the Monteith's model are PAR and f_{APAR} . The feasibility of the proposed GPP product is demonstrated by means of a comparison with in situ GPP estimates from eddy covariance (EC) data (local assessment) and an inter-comparison with MODIS GPP product (regional assessment). The intra-annual variability of the two EC fluxes towers has been well reproduced by the daily MSG GPP although larger GPP values have been obtained on the dry season. The comparison at regional scale has indicated large discrepancies between MSG and MODIS GPP, particularly over broadleaved forest and dry savanna ecosystems in the Sahel.

1 INTRODUCTION

Africa's role in the global carbon cycle has been increasingly recognized. According to Williams et al. (2007), the African continent contributes as much as one-fifth of the net primary production and a half of the interannual variability of the carbon balance at the global scale. However, estimates are highly uncertain and there is a need to better understand the temporal and spatial dynamics of ecosystem productivity across the continent. Thus, a procedure mostly independent of ground measurements and driven by remote sensing data would be extremely useful to yield frequent spatial estimates of gross primary production (GPP) (Running et al., 1999).

In this paper, daily GPP estimates over Africa for 2008 using SEVIRI/MSG satellite products delivered from the LSA SAF system (<http://landsaf.ipma.pt>) are

computed. The geostationary-orbiting MSG satellite offers a good alternative to characterize this continent due to its 30-minutes temporal resolution and its nominal 3.1 km spatial resolution.

GPP is estimated using Monteith's light use efficiency (LUE) concept. This concept provides the theoretical basis for most models of gross primary production based on optical remote sensing and considers GPP ($\text{g C m}^{-2} \text{ day}^{-1}$) as proportional to the incoming photosynthetically active radiation (PAR) ($\text{MJ m}^{-2} \text{ day}^{-1}$), the fractional absorption of that flux (f_{APAR}) (dimensionless) and the light-use efficiency (ϵ) (g C MJ^{-1}), by means of the general relation:

$$GPP = \epsilon f_{APAR} PAR \quad (1)$$

2 DATA AND METHODS

2.1 PAR

In this work the PAR is considered to be 46% (Iqbal, 1983) of the daily MSG down-welling surface shortwave radiation flux (DIDSSF). The DIDSSF for 2008 has been produced from the daily integration of the down-welling surface shortwave radiation flux (DSSF) product acquired every 30 minutes (Moreno et al., 2013).

Figure 1 shows incoming PAR for four dates over Africa. Higher values are observed in the more temperate areas (southern and northern Africa) whereas intermediate values are found in equatorial and tropical areas. Noteworthy, the effect of the clouds, which leads to a diminution of the irradiation (blue patches) and consequently non-uniform spatial irradiation gradient as it would be expected.

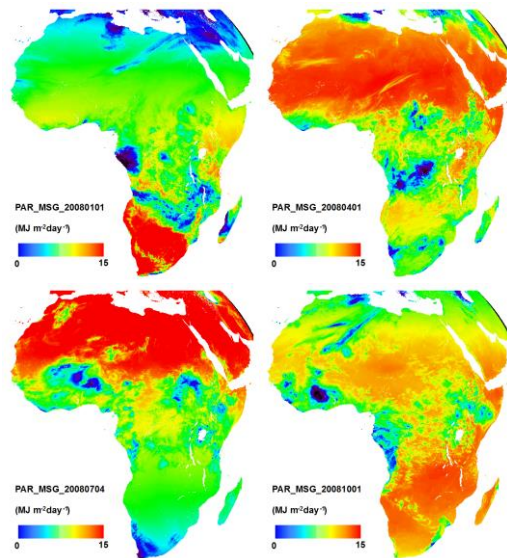


Figure 1. PAR derived from the daily down-welling surface shortwave radiation flux (DIDSSF) product for four dates.

2.2 f_{APAR}

The MSG f_{APAR} product (MDFAPAR) has been used. It is delivered by the LSA SAF network at 3.1 km spatial resolution (sub-satellite point) and daily frequency over the geostationary MSG grid (García-Haro et al., 2008).

The MSG FAPAR product is based on a linear relationship between the Renormalized Difference Vegetation Index (RDVI), computed from the reflectance in the visible (R_R) and near infrared (R_{NIR}) bands for an optimal angular geometry in the solar principal plane and daily-integrated f_{APAR} (Roujean et al., 1995). The R_R and R_{NIR} have been obtained using the BRDF parameters (k_0 , k_1 and k_2) from the clear-sky top of the canopy reflectances observations along the

day (each 15 minutes) and the method proposed by Roujean et al. (1992).

Subsequently, the f_{APAR} time series has been filtered using an adapted local regression filter LOESS (locally weighted scatterplot smoothing) in order to remove undesirable day-to-day variability (noise) resulting from cloud, ozone, dust, and other aerosols that generally lead to spurious drops in the data (Moreno et al., 2014). Figure 2 shows an example for two sites in Africa (see Table 1) where smoother f_{APAR} profiles are generated capturing the upper envelope and removing unrealistic high frequency noise. Figure 3 shows the f_{APAR} filtered and its error for all Africa.

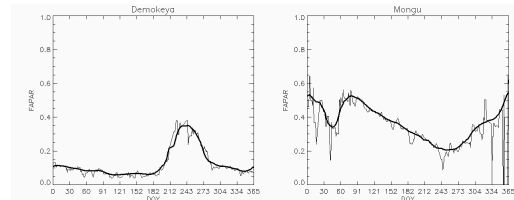


Figure 2. Original and filtered f_{APAR} product for two sites in Africa, Demokeya (13.28°N, 30.47°E) and Mongu (-15.43°N, 23.25°E).

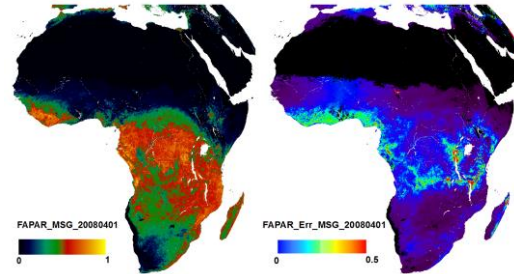


Figure 3. f_{APAR} filtered (left) product with its error (right) for April 1st, 2008.

2.3 ε (Light-Use Efficiency)

The ε can be operationally parameterized as a function of a maximum value (ε_{max}) which is downregulated by different estimators related with types of stress that affect the functionality of the plant, such as water and thermal stress. The ε_{max} can be set as invariant across sites and biomes (Myneni et al., 1995) or be derived from biome-dependent values (Garbulsky et al., 2010).

A constant ε for the entire year and for all vegetation types is used for simplicity. An intermediate value of 1.2 is used according to Garbulsky et al. (2010). In a first approximation, the main concern is to analyse the influence of PAR and f_{APAR} inputs in GPP estimates since it has been demonstrated that they explained about the 60% of the GPP variance in the Monteith's model (Moreno, 2014).

This indicates that the GPP results from MSG are suggestive of potential rather than actual carbon assimilation estimates, since the influence of different types of stress, such as water and thermal stress, are not accounted for.

2.4 Quality assessment

The resulting daily MSG GPP images have been assessed by means of a comparison with *in situ* GPP estimates from the EC data (local assessment) and an inter-comparison with MODIS product at a regional scale (local and regional assessment). The MODIS GPP product is also included in the local study in order to explore the MSG GPP capabilities in comparison with an operational product. A statistical analysis is performed for MSG GPP and MODIS GPP as compared to EC GPP.

The *in situ* GPP data are derived from two EC (Table 1): a grassland site located in the semi-arid Sahel area (Demokeya) and a deciduous broadleaved forest site located in the sub-humid region of southern Africa (Mongu). GPP data were obtained via the flux-partitioning model by Reichstein et al. (2005) approach. Figure 4 shows the positions of both EC flux towers over a land cover derived from the 23-class Global Land Cover 2000 (GLC2000) (Mayaux, et al., 2004). A generalized classification has been used by aggregating several similar land cover classes from the GLC2000. The study area is described through a generalized thematic legend of 6 major biomes: broadleaf evergreen forest (7.6%), broadleaf deciduous forest (13.9%), mosaic of cropland, tree cover and grassland (4.6%), shrubland (12.1%), grassland (16.9%), cultivated areas and mosaic (11.5%), and bare Soil (33.2%). This generalization reduces the number of classes while preserving the essence of the geographical patterns of the study area.

The 8-day MODIS GPP product (MOD17A2 version-55) at 1 km is considered. The version-55 is a post-processed MODIS GPP version-5 dataset where the contaminated MODIS FPAR/LAI inputs to the MOD15 algorithm have been cleaned (Zhao and Running, 2010). The MOD15A2 version-55 is validated to Stage-3 which means that its accuracy was assessed and uncertainties were well-established via independent measurements representing global conditions. The MODIS products were geo-located to a standard SEVIRI grid in order to reproduce the characteristics of the MSG product. The reprojection step is calculated by averaging all fine resolution pixel values of the MODIS product that overlap with a given SEVIRI pixel. Those pixels identified as water, snow or unreliably calculated, were excluded during the averaging process (García-Haro et al., 2008).

Table 1. Coordinates, ecosystem type and mean annual precipitation (MAP) for the two EC flux towers considered in the quality assessment of the MSG GPP.

Site	Lat (°)	Lon (°)	Ecosystem	MAP (mm)
Demokeya (SD-DEM)	13.28E	30.48E	Grassland/Savanna	320
Mongu (ZM-MON)	15.44S	23.25N	Deciduous Broadleaved forest	945

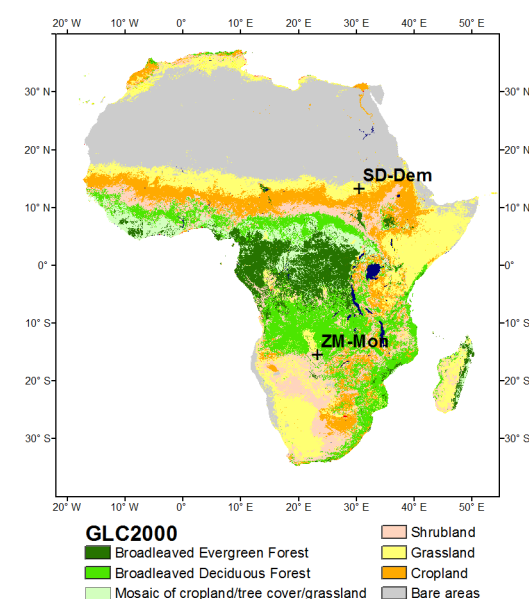


Figure 4. Distribution of 6 major biomes in Africa derived from the 23-class Global land cover 2000 (GLC2000). Locations of the two EC flux towers considered.

3 RESULTS

Figure 5 shows the GPP derived from MSG data over Africa for four dates. As expected, higher GPP are observed on forest areas (central part of Africa) as compared to the lower GPP observed on grasslands and shrublands (southern Africa and Sahel area). The great influence of the PAR in GPP is stressed. Higher GPP values are observed on central and southern Africa near the southern hemispheric summer (Figure 5a) with suddenly diminution of GPP estimates due to the presence of clouds (small patches in blue in Figure 1). An increase in productivity is observed on the Sahel zone (8°-18°N, 17°W-20°E) from January to October, partly explained by the rainy season which takes place during the June-October period. Precipitation varies widely throughout this zone, with the northern regions typically recording 100-300 mm

during the season and the southern areas receiving well in excess of 500 mm.

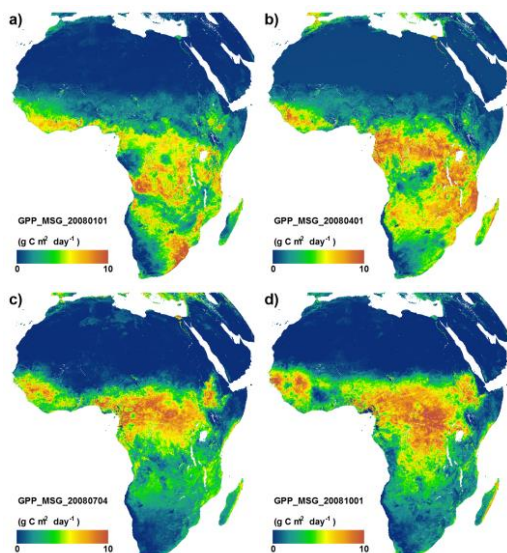


Figure 5. Daily GPP derived from MSG data for four dates along the 2008.

3.1 Quality assessment

3.1.1 Local assessment

Figure 6 shows the f_{APAR} and DIDSSF products used in the MSG GPP calculation for the Demokeya (top) and Mongu (bottom) sites along with the f_{APAR} error bars (grey). Figure 7 shows the temporal profiles of the MSG GPP along with the MODIS GPP and the GPP EC data.

According to the EC GPP data, the MSG GPP captures the seasonal variation well. However, MSG GPP seems to overestimate the GPP over the dry season (GPP up to $4 \text{ g C m}^{-2} \text{ day}^{-1}$) as compared to the MODIS GPP and EC data.

The mean bias error (MBE), mean absolute error (MAE), root mean square error (RMSE) and correlation coefficient (R) are computed (Table 2). The results show a better agreement between MSG GPP and EC GPP (MBE=0.03; RMSE=0.90) for the Demokeya site as compared to the MODIS product. The MODIS GPP product shows major deviations during the growing season (MBE= -0.71; RMSE=1.7). However, a worst agreement is observed for the MSG GPP product at the Mongu site, mainly due to its inability to characterize lower values.

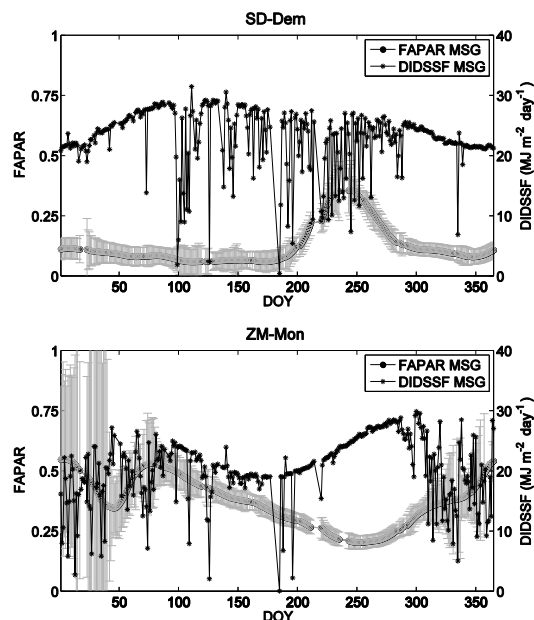


Figure 6. f_{APAR} and DIDSSF products use in the MSG GPP calculation for the Demokeya (top) and Mongu (bottom) sites along with the f_{APAR} error bars (grey).

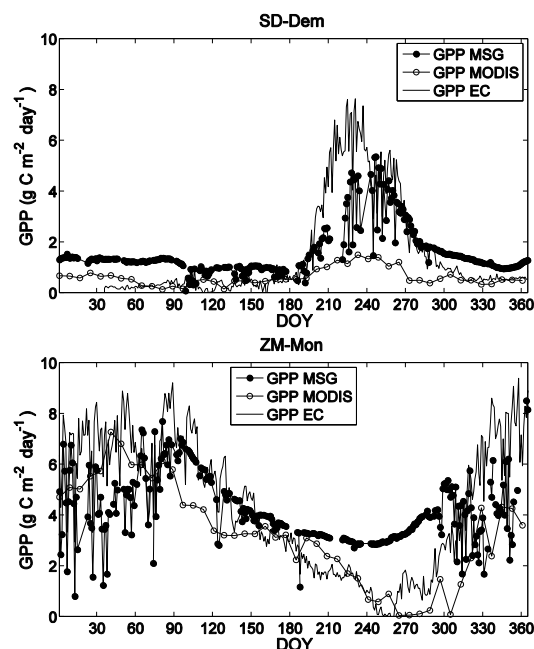


Figure 7. MSG GPP along with the MODIS GPP and the GPP derived from the EC tower for the Demokeya (top) and Mongu (bottom) sites.

Table 2. MBE, MAE, RMSE and R for MSG and MODIS GPP as compared to EC data for the two sites considered. The analyses is done using the GPP units ($\text{g C m}^{-2} \text{ day}^{-1}$).

Site	MBE	MAE	RMSE	R
GPP MSG-GPP EC				
Demokeya (SD-DEM)	0.03	0.50	0.90	0.90
Mongu (ZM-MON)	-0.02	1.2	1.8	0.59
GPP MODIS-GPP EC				
Demokeya (SD-DEM)	-0.71	0.73	1.7	0.90
Mongu (ZM-MON)	-0.91	1.1	1.7	0.81

3.1.2 Regional assessment

This analysis has been performed by means of the intercomparison of the annual GPP derived from MSG and MODIS for 2008. Figure 8 (top) shows as the highest GPP values ($> 2.5 \text{ kg C m}^{-2} \text{ year}^{-1}$) are located in forest areas: broadleaved evergreen forests (see Figure 4) and mixed forest, whereas the lowest values mainly correspond to grasslands and shrubs covers (around $0.5 \text{ kg C m}^{-2} \text{ year}^{-1}$).

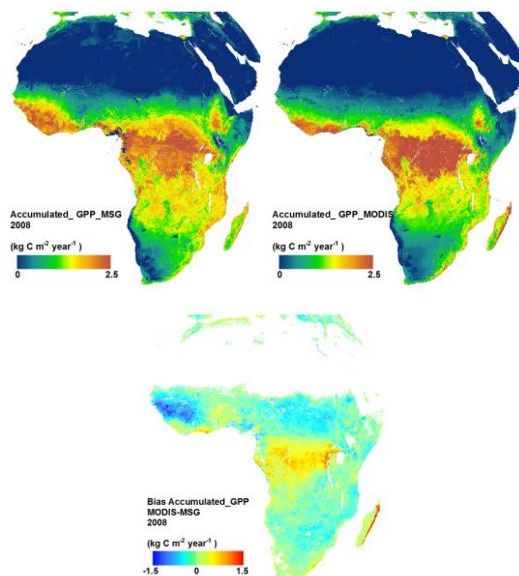


Figure 8. Annual MSG and MODIS GPP for 2008 (top) and bias between accumulated MODIS and MSG (bottom).

The difference between the annual MSG and MODIS GPP (Figure 8-bottom) shows as the largest discrepancies occurred over forests with higher values given by the annual MODIS GPP ($\text{MBE}=0.32 \text{ kg C m}^{-2} \text{ year}^{-1}$ and $\text{RMSE}=0.51 \text{ kg C m}^{-2} \text{ year}^{-1}$) (see table 3). For the rest of the land cover classes, the annual MSG GPP provides us higher values than the MODIS GPP.

The highest negative bias is observed for the dry savanna ecosystems in the Sahel (blue dark patches corresponding mainly to the mixed of cropland/tree cover/ grassland and shrubland land covers) as was reported by Sjöström et al., 2011. The best agreement is found over grassland ($\text{MBE}=-0.13 \text{ kg C m}^{-2} \text{ year}^{-1}$; $\text{RMSE}=0.21 \text{ kg C m}^{-2} \text{ year}^{-1}$).

Table 3. MBE between MSG and MODIS GPP according to land cover types. The analysis is done using the GPP units ($\text{kg C m}^{-2} \text{ year}^{-1}$).

Land Cover	MBE	MAE	RMSE
Broadleaved evergreen forest	0.32	0.43	0.51
Broadleaved deciduous forest	-0.19	0.29	0.37
Mixed of mosaic cropland/tree cover/grassland	-0.07	0.39	0.48
Shrubland	-0.23	0.30	0.37
Grassland	-0.13	0.19	0.21
Cultivated/Mosaic	-0.27	0.31	0.36

4 DISCUSSION

The feasibility of the daily MSG GPP over Africa combines results of EC measurements along with MODIS GPP product over different ecosystems. From the local assessment, the f_{APAR} product is thought to be a key source of the GPP seasonal variation as it was reported in Moreno (2014) (see Figure 6). The overestimation of MSG GPP as compared to the MODIS GPP and EC data can be also attributed to the f_{APAR} input which values do not reach to zero in any case and a parameterization of ε including controlled water stress factors are not accounted for.

The major deviations of the MODIS GPP product during the growing season were also reported by Sjöström et al. (2013) who associated the problem to the f_{APAR} linear fitting of the MODIS GPP algorithm that failed to reproduce the green up observed in the field f_{APAR} data.

The positive offset observed between the annual MSG and MODIS GPP (Figure 8-bottom) over forest can be partly explained by the f_{APAR} . As it was stated in Martínez et al. (2013), the lack of representation of clumping in the MSG f_{APAR} product and different MODIS algorithm assumptions on canopy architecture specific per biome class (i.e. leaf angle distribution and optical properties of leaf, wood, litter and soil) were the main explanations.

5 CONCLUSIONS

The daily GPP MSG product over Africa for 2008 has indicated reliable estimates at spatial and temporal domains. The comparison with EC data has revealed that seasonality has been captured well but GPP was overestimated specifically on the dry season when lower values are expected. A better agreement was

found at the grassland site (Demokeya) as compared to MODIS GPP. The comparison at regional scale has indicated large discrepancies between GPP MSG and GPP MODIS over broadleaved forest and dry savanna ecosystems in the Sahel.

Moreover, a better quality assessment will be needed over a wider range of biomes using EC tower data to analyse the uncertainties and potential of the MSG GPP estimates. Further improvements on the MSG GPP by the parameterization of the maximum light use efficiency by biomes and the analysis of the MSG f_{APAR} product are expected.

6 ACKNOWLEDGMENTS

This research has been supported by the projects: LSA SAF (EUMETSAT), RESET CLIMATE (Spanish Ministry of Economy and Competitiveness, CGL2012-35831) and ERMES (EU FP7-Space-2013, Contract 606983). Special thanks are also given to the CARBOAFRICA network for providing us the EC towers data and Alirio Arboleda (RMI) for facilitating archived LSA SAF data.

7 REFERENCES

- Garbulsky, M. F., Peñuelas, J., Papale, D., Ardö, J., Goulden, M. L., Kiely, G., et al., 2010, Patterns and controls of the variability of radiation use efficiency and primary productivity across terrestrial ecosystems. *Global Ecology and Biogeography*, **19**, 253–267.
- García-Haro, F.J., Camacho, F., Meliá, J., 2008. *Vegetation Parameters Validation Report (VEGA VR)*, SAF/LAND/UV/VR VEGA/2.1, January 2008, 91 pp. Available on-line at <<http://landsaf.meteo.pt>>.
- Iqbal, M., 1983, An introduction to solar radiation, Academic Press, Orlando, FL.
- Martínez, B., Camacho, F., Verger, A., García-Haro, F.J., Gilabert, M.A., 2013, Intercomparison and quality assessment of MERIS, MODIS and SEVIRI FAPAR products over the Iberian Peninsula. *International Journal of Applied Earth Observation and Geoinformation*, **21**, 463–476.
- Mayaux, P., Bartholomé, E., Fritz, S., Belward, A., 2004, A new land cover map of Africa for the year 2000. *Journal of Biogeography*, **31**, 861–877.
- Moreno, A., Gilabert, M.A., Camacho, F., Martínez, B., 2013, Validation of daily global solar irradiation images from MSG over Spain. *Renewable Energy*, **60**, 332–342.
- Moreno, A., García-Haro, F.J., Martínez, B., Gilabert, M.A., 2014, Noise Reduction and Gap Filling of fAPAR Time Series Using an Adapted Local Regression Filter. *Remote Sensing*, **6**, 8238–8260; doi:10.3390/rs6098238.
- Moreno, A. 2014. Retrieval and assessment of CO₂ uptake by mediterranean ecosystems using remote sensing and meteorological data. Doctoral Dissertation. Universitat de València. 172 pp.
- Myneni, R.B., Los, S.O., Asrar, G., 1995. Potential gross primary productivity of terrestrial vegetation from 1982–1990. *Geophysical Research Letters*, **22**, 2617–2620.
- Reichstein, M., Falge, E., Baldocchi, D.D., + 28 authors., 2005, On the separation of net ecosystem exchange into assimilation and ecosystem respiration: review and improved algorithm. *Global Change Biology*, **11**, 1–16.
- Roujean, J.L., Leroy, M., Dechamps, P.Y., 1992, A bidirectional reflectance model of the earth's surface for the correction of remote sensing data. *Journal of Geophysical Research*, **97** (D18), 20455–20468.
- Roujean, J.L., Bréon, F.M., 1995, Estimating PAR absorbed by vegetation from bidirectional reflectance measurements. *Remote Sensing of Environment*, **51**, 373–384.
- Running, S.W., Baldocchi, D. D., Bakwin, P. S., Hibbard, K.A., 1999. A global terrestrial monitoring network integrating tower fluxes, flask sampling, ecosystem modeling and EOS satellite data. *Remote Sensing of Environment*, **70**, 108–127.
- Sjöström, S.D., Ardö, J., Arneth, A., Boulain, N., Cappelaere, B., Eklundh, L., et al., 2011, Exploring the potential of MODIS EVI for modelling gross primary production across Africa ecosystems. *Remote Sensing of Environment*, **115**, 1081–1089.
- Sjöström, S.D., Zhao, M., Archibald, S., et al., 2013, Evaluation of MODIS gross primary productivity for Africa using eddy covariance data. *Remote Sensing of Environment*, **131**, 275–286.
- Zhao, M., Running, S. W., 2010, Drought-induced reduction in global terrestrial net primary production from 2000 through 2009. *Science*, **329**, 940–943.
- Williams, C. A., Hanan, N. P., Neff, J. C., Scholes, R. J., Berry, J. A., Denning, A. S., et al., 2007. Africa and the global carbon cycle. *Carbon Balance and Management*, **2**, 3, doi:10.1186/1750-0680-2-3.

Spectroradiometer characterization for continuous operation in an Eddy Covariance flux tower

Javier Pacheco-Labrador, M. Pilar Martín

Environmental Remote Sensing and Spectroscopy Laboratory (SpecLab), Instituto de Economía, Geografía y Demografía (IEGD), Consejo Superior de Investigaciones Científicas (CSIC), Albasanz 26-28, 28037, Madrid, Spain
javier.pacheco@cchs.csic.es; mpilar.martin@cchs.csic.es

ABSTRACT – *In this paper we describe the characterization of a field spectroradiometer dedicated to the study of vegetation status. The instrument is installed in a continuous automated system outdoors, facing a wide range of environmental conditions. Dark current, non-linearity, thermal dependence, spectral calibration and the directional response of the cosine head are characterized. Laboratory experiments are used to produce the models needed for the correction of the spectral measurements. Moreover, a spectral diffuse-to-direct radiation ratio model is generated by means of simulation in order to retrieve this variable from a broadband pyranometer data installed in the field site. Correction models will allow to remove instrumental artifacts from the spectral variables and the analysis of the impact of each of these artifacts on the measurements.*

1 INTRODUCTION

Eddy covariance sites allow the estimation of the biospheric fluxes in the different ecosystems of the Earth (Baldocchi et al. 2001). Optical sensors have been installed in these sites to provide information that can be related with these fluxes and used to upscale the information provided from remote platforms (Gamon et al. 2006a, Gamon et al. 2010). Though single channel and multi-channel sensors have been mainly used; there is an increasing interest on the installation of hyperspectral sensors (Balzarolo et al. 2011). These provide spectrally detailed information about the ecosystem observed, but are also subject of large levels of uncertainty (Milton et al. 2009). Therefore, an adequate control and characterization of these instruments is needed to ensure the quality of the measurements. These uncertainties can become more acute in the case of spectroradiometers installed in automated continuous systems that operate outdoors. Since, these would face a wide range of environmental conditions and acquisition settings, environmental and instrumental artifacts must be separated from the vegetation signals.

Dark current, non-linearity, thermal dependence, spectral calibration and the directional response of the cosine head are among the factors that need to be carefully characterized in order to be able to identify potential uncertainties in the spectral measurements related to instrument performance.

Sensor temperature (T) is largely related with the dark current (Kusk, 2011) and the sensitivity to radiation of the pixels (Saber et al., 2011). In field

spectroradiometers, the integration time (t_{int}) is adjusted according to the signal received, however, the dark current (Kusk, 2011) depend also on this parameter. Some instruments combine different sensors to measure the different components of the reflectance factors, in these dual-channel spectroradiometer, the spectral calibration of each sensor is key, especially in the regions close to the absorption features of the atmosphere or of the targets measured (Bachman et al. 2012). Cosine diffusers allow in these systems measure incoming irradiance in a continuous basis. However, the directional response of these devices is usually different to the one expected, which is the cosine of the illumination angle. Therefore, this response must be characterized, and the diffuse and direct fractions of the incoming radiations considered (Meywerk et al., 1999).

We describe here the characterization of a dual channel field spectroradiometer installed in an outdoors automated system (AMSPEC-MED) that allows correcting the abovementioned instrumental artifacts.

2 INSTRUMENTATION AND METHODS

2.1 Instrumentation

We characterized a Unispec-DC spectroradiometer (PP Systems, Amesbury, USA). It is a double-channel instrument equipped with two twin spectrometer modules (module-1 and module-2) MMS-1 (Carl Zeiss, Inc., Thornwood, NY, USA). The first channel samples incoming irradiance through a cosine diffuser and the second the reflected radiance through an optical fibre; both measurements are integrated to

measure the Hemispherical-Conical Reflectance Factor (HCRF) (Nicodemus et al., 1977).

For the characterization different light sources were used: an 10 W tungsten bulb into an ASD RTS-3ZC integrating sphere (Analytical Instrumental Analytical Spectral Devices Inc., Boulder, Colorado); a mercury-argon calibration source (Ocean Optics, Dunedin, FL, USA); and a 250 W tungsten lamp (OSRAM GmbH, Munich, Germany). An ASD FR3 spectroradiometer (Analytical Instrumental Analytical Spectral Devices Inc., Boulder, Colorado) was used to characterize the atmospheric diffuse-to-global radiation ratio (DGr). The temperature of the instrument was modified using a CTP 31213 fridge (Lieberh, Ochsenhausen, Germany) and a Raypa DOD-90 oven (R. Espinar, Terrasa, Spain).

2.2 Methodology

Table 1 summarizes the configuration of the different characterization experiments. Dark current and temperature dependence were calibrated modifying the instrument temperature while measurements were taken. Dark signal (Equation 1) was characterized also as a function of the integration time separating the electronic bias (N_{bias}) from the thermal-current or dark current (N_0). For each pixel a set of 5 coefficients was fit by means of Least Squares (LS).

$$N_{dark} = N_{bias} + N_0 = (a_0 + a_1 T) + t_{int} (a_2 + a_3 T + a_4 T^2) \quad (1)$$

Experiment	t_{int} (ms)	T (°C)	Samples
Dark signal	4 - 1000	9.5-45.4	3840
Non-linearity	4 - 741	22.7-23.9	419
Temperature dependence	190 - 469	13.9-46.1	1102
Wavelength calibration	7	15.6-48.3	430
Cosine directional response	400	26.4-29.3	200

Table 1. Experiments configuration

The signal measured corresponding to the photocurrent (N_{phot}) plus N_0 , notated as N_{meas} was always first calculated removing N_{bias} from the raw spectra. Non-linearity was then characterized using the method described in Pacheco-Labrador et al. (in press), which separates the non-linearity related with the gray level measured (\Re_{GL}) from the related with

the integration time (\Re_{IT}). The correction, that includes the removal of the dark current, was then performed as follows (Equation 2):

$$N_{NL} = \frac{N_{meas}}{\Re_{GL}(N_{meas}) \Re_{IT}(t_{int}, N_{meas})} - N_0 \quad (2)$$

Temperature dependence (TD) was measured sampling radiance through an open port of the integrating sphere while the temperature of the sensor was modified. The corrected signals N_{NL} measured at an arbitrary temperature of 30 °C were used to normalize the measurements. For each pixel, the deviation from ratio one was characterized adjusting a 5th degree polynomial by LS. The correction was later applied as in Equation 3:

$$N_{TD} = \frac{N_{NL}}{TD(T)} \quad (3)$$

Spectral calibration of each module was done by fitting a normal distribution to up to 9 emission lines of the mercury-argon lamp. Then a 2nd degree polynomial was adjusted to predict the central wavelength of each pixel. The experiment was carried out at different temperatures, but the significance of its impact on spectral calibration was eventually discarded. For the computation of HCRF, the spectra measured in module-2 would be linearly interpolated to the centre bands of module-1 (N_{SC}).

The directional response of the cosine diffuser was measured rotating the diffuser against an irradiance source between 0 ° and 90 ° in a dark room. Diffuse radiation was also measured and removed, in order to characterize the response exclusively to direct radiation. The measurement at nadir was used to normalize the measurements at different angles, and the difference with the cosine of the illumination angle was calculated (β). Eventually, irradiance spectra measured in module-1 are corrected (N_{CR}) using the method described in Maywerk et al. (1999), summarized in Equation 4:

$$N_{CR} = N_{TD} \left[\frac{1 - DGr \cdot \int_0^1 \beta(\theta_s) \theta_s d\theta_s - (1 - DGr \beta(\theta_s))}{1 - DGr \cdot \int_0^1 \beta(\theta_s) \theta_s d\theta_s} \right] \quad (4)$$

where DGr is the diffuse-to-global radiation. DGr can be measured in the field from a broadband pyranometer; but for the correction, DGr is needed at

each wavelength of the sensor. For that, a model to estimate spectral DGr from broadband measurements was developed. Diffuse and global irradiance measurements from an ASD FR3 spectroradiometer and the pyranometer spectral response function were used to simulate the pyranometer's DGr and this related to DGr in each pixel in module-1 by means of a linear model. Eventually, HCRF was then calculated as in Equation 5 (Gamon et al, 2006b):

$$\rho_{HCRF} = \frac{(N_{WC,Mod-2})_{tar} (N_{CR,Mod-1})_{ref}}{(N_{CR,Mod-1})_{tar} (N_{WC,Mod-2})_{ref}} \rho_{ref} \quad (5)$$

3 RESULTS

Figure 1 shows the estimated N_0 and N_{bias} vs T at different integration times, for a single pixel in module-1. The electronic bias detected was inversely related with T , whereas dark current increased quadratically with this variable, and linearly with the integration time. Root Mean Squared Errors (RMSE) were 6.2 DN and 5.5 DN in module-1 and module-2 respectively.

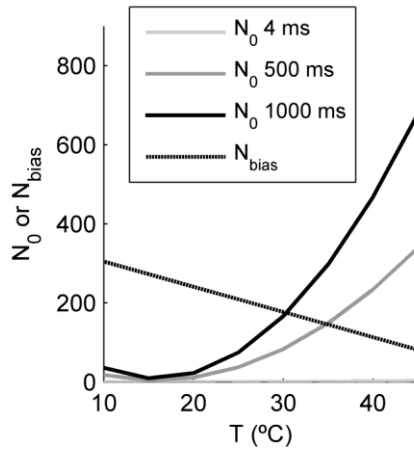


Figure 1. Modelled N_0 and N_{bias} .

Non-linearity models corrected for the effects related to the gray level measured and the integration time set in the instrument, though this second effect also depends on the irradiance impinging each pixel. \mathcal{R}_{GL} values slowly decreased with the gray level but abruptly dropped above the 50000 DN. \mathcal{R}_{IT} hyperbolically decreased with the integration time, whereas it increased with the pixel irradiance until a saturation level. These functions were fit with a RMSE of 0.003 and 0.004 in \mathcal{R}_{GL} and 0.17 DN/ms and 0.20 DN/ms in \mathcal{R}_{IT} for module-1 and module-2 respectively.

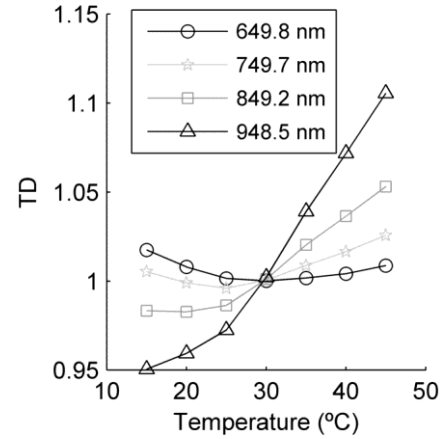


Figure 2. Modelled TD at different wavelengths

Temperature dependence models found large noise in the pixel located in the extremes of the sensor, where the signal-to-noise (SNR) is low. Figure 2 shows the modelled TD for different pixels of the module-1. As can be seen, the temperature dependence effect is low in the Visible region (400 nm -700 nm), decreasing smoothly around 30 °C. However, in the Near Infrared (NIR) values increased from below 1, up to close 1.2 in pixels above 1000 nm.

The spectral calibration of each spectrometer was accomplished with a RMSE of 0.9 nm in module -1 and 0.7 nm in module-2. The effects of temperature were also analysed, but the differences produced were lower than the precision of the fit and, therefore, excluded from the models.

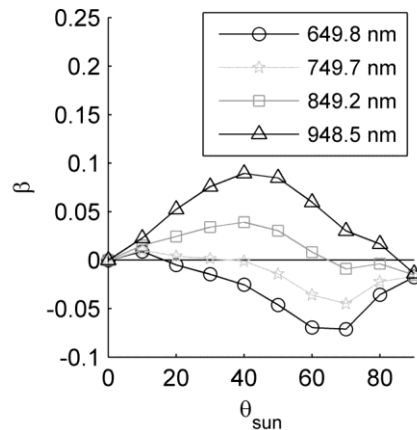


Figure 3. Directional response bias of the cosine head at different wavelengths.

The cosine head showed a directional response that differed from the cosine of the angle of illumination in a different way for each spectral region. Figure 3 shows the value of the correction factor for different wavelengths. As can be seen, at the Visible wavelengths, the factor β goes below 0, which means that the irradiance is overestimated, this effect is maximum around 40°. However, as the wavelength increases irradiance is underestimated, especially around 60°.

Coefficients of a linear model were fit to estimate diffuse-to-global radiation in each pixel of module-1 from the broadband *DGr* provided by the field pyranometer. The RMSE obtained was 0.21.

4 DISCUSSION

Laboratory experiments have been used to characterize and calibrate correction models for a field spectroradiometer to be deployed in the field as the core of an automated system to monitor vegetation covers. Models allow the correction of the digital signal (in DN) of each sensor module, later used to compute the HCRF. Dark current has been modelled as a function of IT and temperature, but an electronic bias was prior separated. As shown, at low temperatures and integration times, this bias is significantly larger than the signal related to the dark current. The final impact of this factor on the HCRF should be low, since eventually it has to be removed as well as the thermally generated current, but for this, non-linearity correction related with the gray level has to be applied. Two sources of non-linearity have been characterized which allowed a correction that, in the range of situations that the instrument would have to face, performs better than other methods usually applied (Pacheco-Labrador, in press). This can be relevant in the study of variables which are related with the quantity of radiance measured, such as the Bi-Directional Reflectance Factor or with the irradiance levels, such as vegetation stress (Pacheco-Labrador et al. 2014).

Thermal dependence of the sensor has shown to be more acute in the NIR wavebands which can be explained by the presence of a silicon band gap, sensible to temperature. Thermal stabilization or thermal dependence characterization would be, therefore, important in the study of vegetation. NIR radiation is usually related with vegetation structure, leaf area index and other biophysical variables of interest, whose estimation could be affected by this effect.

The spectral calibration was performed using several emission lines. The impact of temperature was analysed, but given the spectral resolution -10 nm- and

the uncertainties in the calibration models, the shifts produced by temperature were considered negligible. However, this effect might be significant in sensors with high spectral resolution, as those used in the estimation of vegetation fluorescence. The cosine head showed a directional response biased from the cosine of the illumination angle. This bias depended on this angle and also on the wavelength; therefore, biases introduced would affect the calculation of HCRF in different ways. Visible reflectance would be overestimated whereas an overestimation would occur in the NIR. The impact would also depend on the diffuse and the direct fractions of the irradiance reaching the device. Since *DGr* changes across the spectrum, we have modelled the *DGr* of each band of the module-1 using the simulated broadband value of a pyranometer that operates in the site where the spectrometer is installed. Accurate estimation of spectral *DGr* could be of interest for different applications. In this case, a direct measurement was not possible, and a simple model was developed. The method is empirical, and assumes that diffuse radiation is heterotrophic, therefore, uncertainties related with these estimates could be large; though at least provide a closer approach that direct use of the pyranometer ratios.

A field measurements dataset large enough would give an estimation of the impact of each correction under different situations. Part of the effects here analysed could partially cancel out during the calculation of HCRF, though would remain for the quantification of radiance or irradiance. The corrections applied are expected to improve the inter-comparability of the data acquired by this instrument and separate instrumental artifacts from others related with the properties of the surfaces measured.

5 CONCLUSIONS

We have characterized five instrumental sources of uncertainty in a field spectroradiometer installed in an outdoors continuous automated system (AMSPEC-MED). The objective of this characterization was to generate the models needed for the correction of the measurements acquired with this system. This way, the spectral variables generated are expected to be related with the chemical and physical properties of the vegetation studied, and not with the instrument performance. Further effort is needed to quantify the impact of each artifacts characterized under real operation conditions; identifying environmental and instrumental variables of most relevance in these automated systems.

REFERENCES

- Bachmann, C.M., Montes, M.J., Parrish, C.E., Fusina, R.A., Nichols, C.R., Li, R.-R., Hallenborg, E., Jones, C.A., Lee, K., Sellars, J., White, S.A., & Fry, J.C. (2012). A dual-spectrometer approach to reflectance measurements under sub-optimal sky conditions. *Optics Express*, 20, 8959-8973
- Baldocchi, D.D. (2003). Assessing the eddy covariance technique for evaluating carbon dioxide exchange rates of ecosystems: past, present and future. *Global Change Biology*, 9, 479-492
- Balzarolo, M., Anderson, K., Nichol, C., Rossini, M., Vescovo, L., Arriga, N., Wohlfahrt, G., Calvet, J.-C., Carrara, A., Cerasoli, S., Cogliati, S., Daumard, F., Eklundh, L., Elbers, J.A., Evrendilek, F., Handcock, R.N., Kaduk, J., Klumpp, K., Longdoz, B., Matteucci, G., Meroni, M., Montagnani, L., Ourcival, J.-M., Sánchez-Cañete, E.P., Pontailier, J.-Y., Juszczak, R., Scholes, B., & Martín, M.P. (2011). Ground-Based Optical Measurements at European Flux Sites: A Review of Methods, Instruments and Current Controversies. *Sensors*, 11, 7954-7981
- Gamon, J.A., Coburn, C., Flanagan, L.B., Huemmrich, K.F., Kiddle, C., Sanchez-Azofeifa, G.A., Thayer, D.R., Vescovo, L., Gianelle, D., Sims, D.A., Rahman, A.F., & Pastorello, G.Z. (2010). SpecNet revisited: bridging flux and remote sensing communities. *Canadian Journal of Remote Sensing*, 36, S376-S390
- Gamon, J.A., Cheng, Y., Claudio, H., MacKinney, L., & Sims, D.A. (2006a). A mobile tram system for systematic sampling of ecosystem optical properties. *Remote Sensing of Environment*, 103, 246-254
- Gamon, J.A., Rahman, A.F., Dungan, J.L., Schildhauer, M., & Huemmrich, K.F. (2006b). Spectral Network (SpecNet)—What is it and why do we need it? *Remote Sensing of Environment*, 103, 227-235
- Kuusk, J. (2011). Dark Signal Temperature Dependence Correction Method for Miniature Spectrometer Modules. *Journal of Sensors*, 2011
- Meywerk, J., & Ramanathan, V. (1999). Observations of the spectral clear-sky aerosol forcing over the tropical Indian Ocean. *Journal of Geophysical Research: Atmospheres*, 104, 24359-24370
- Milton, E.J., Schaepman, M.E., Anderson, K., Kneubühler, M., & Fox, N. (2009). Progress in field spectroscopy. *Remote Sensing of Environment*, 113, Supplement 1, S92-S109.
- Pacheco-Labrador, J., & Martin, M.P. (2014). Nonlinear Response in a Field Portable Spectroradiometer: Characterization and Effects on Output Reflectance. *Geoscience and Remote Sensing, IEEE Transactions on*, 52, 920-928
- Pacheco-Labrador, J.; Martín, M.P., Characterizing integration time and gray level related nonlinearities in a NMOS sensor. *Applied Optics*, in press.
- Saber, G.R.S., Fox, N.P., Theocharous, E., Sun, T., & Grattan, K.T.V. (2011). Temperature and nonlinearity corrections for a photodiode array spectrometer used in the field. *Applied Optics*, 50, 866-875.

Impact of water stress on GPP estimation from remote sensing data in Mediterranean ecosystems

S. Sánchez-Ruiz¹, Á. Moreno¹, B. Martínez¹, M. Piles², F. Maselli³, A. Carrara⁴, M. A. Gilabert¹

¹ *Departament de Física de la Terra i Termodinàmica, Facultat de Física, Universitat de València, Dr. Moliner, 50. 46100-Burjassot, Spain*

² *Remote Sensing Laboratory/IEEC, Universitat Politècnica de Catalunya and SMOS Barcelona Expert Center, Jordi Girona, 1-3. 08034-Barcelona, Spain*

³ *IBIMET-CNR, Via Madonna del Piano, 10. 50019-Sesto Fiorentino, Italy*

⁴ *Fundación CEAM, Charles Robert Darwin, 14, Parc Tecnològic. 46980-Paterna, Spain*
sergio.sanchez@uv.es +34 963 543 113

ABSTRACT- Terrestrial carbon fixation is usually estimated by production efficiency models (PEMs) following the Monteith's approach. This study aims to characterize and quantify, by means of remote sensing data, the impact of water stress in the gross primary production (GPP) of vegetation in the Spanish Iberian Peninsula. Three different water stress factors were calculated: C_{ws}^1 using only meteorological data, C_{ws}^2 combining meteorological data and MSG/SEVIRI imagery, and C_{ws}^3 using only SMOS-derived imagery. They were included in the PEM as light use efficiency down-regulating factors. The calculated GPP series were then compared to GPP estimated from eddy covariance (EC) data retrieved in two sites: a meadow in Las Majadas del Tiétar (LMa) and a shrubland in Cortes de Pallás (CPa). The inclusion of a water stress factor in the PEM improved the GPP estimates both in terms of explained variance and accuracy. C_{ws}^3 option showed very promising results obtaining the highest explained variance ($R^2 = 0.89$ in LMa and $R^2 = 0.81$ in CPa). However, it needs to be optimized to avoid its high bias ($1.8 \text{ g m}^{-2} \text{ day}^{-1}$ in LMa and $1.2 \text{ g m}^{-2} \text{ day}^{-1}$ in CPa). C_{ws}^1 option obtained the best accuracy ($RMSE = 1.0 \text{ g m}^{-2} \text{ day}^{-1}$ in LMa and $RMSE = 0.9 \text{ g m}^{-2} \text{ day}^{-1}$ in CPa) and a high explained variance ($R^2 = 0.86$ in LMa and $R^2 = 0.75$ in CPa), but it was calculated using only meteorological data.

1 INTRODUCTION

The monitoring of CO₂ emission and fixation fluxes between the atmosphere and the land surface is a key factor in climate change studies (IPCC, 2007). Only remote sensing offers suitable spatial coverage and revisiting frequency to monitor CO₂ fluxes at regional and global scales.

Carbon fixation by terrestrial vegetation, which is a significant sink, is usually estimated by Production Efficiency Models (PEMs) in terms of carbon mass converted to biomass through photosynthesis. According to the Monteith's approach (Monteith, 1972), the Gross Primary Production (GPP) is proportional to the Absorbed Photosynthetically Active Radiation (APAR), which is calculated as the product of f_{APAR} (Fraction of APAR) and PAR (Photosynthetically Active Radiation). The proportionality constant is the light use efficiency ε , which accounts both for the conversion from radiation units to carbon mass units and for the efficiency in this transformation. ε is in turn modeled as the product of ε_{max} , the maximum ε corresponding to an optimal ecosystem functioning, and other factors generally

ranging from 0 to 1 which down-regulate the former due to different environmental stresses. In Mediterranean ecosystems, ε is mainly affected by the water stress typical of summer time.

The aim of the present work is to characterize and quantify, by means of remote sensing data, a down-regulating factor which accounts for short-term vegetation water stress in the Spanish Iberian Peninsula and to evaluate its impact on GPP. In order to do this, time series of the needed variables for the year 2011 were utilized.

2 DATA SET

2.1 Sites description

Two sites in Spain with different vegetation type were selected. Las Majadas del Tiétar (LMa) (39° 56' 29'' N, 5° 46' 2'' W) is a meadow at 258 m of altitude with a mean annual precipitation of 572 mm and a mean annual air temperature of 18.5 °C. Cortes de Pallás (CPa) (39° 13' 26'' N, 0° 56' 11'' W) is a shrubland at 810 m of altitude with a mean annual precipitation of 600 mm and a mean annual air temperature of 14.1 °C.

2.2 Flux data

Daily Net Ecosystem Exchange collected from the two Eddy Covariance (EC) towers located in the two study sites were partitioned to estimate GPP according to Reichstein *et al.* (2005) methodology. The EC towers belong to the European Fluxes Database Cluster (<http://www.europe-fluxdata.eu>).

2.3 Meteorological data

The following daily meteorological measurements were provided by AEMet from 400 stations distributed around the Spanish Iberian Peninsula: accumulated precipitation, maximum temperature and minimum temperature. These data were spatially interpolated by ordinary kriging to build images of 1 km spatial resolution.

2.4 Satellite data

MSG/SEVIRI products DIDSSF (daily downward surface shortwave flux) and DMET (daily evapotranspiration) were downloaded from the LSA SAF Server (<http://landsaf.meteo.pt>). These images were reprojected to a 1 km spatial resolution latitude/longitude projection regular grid. MODIS products MCD43A1 and MCD43A2 were downloaded from the Warehouse Inventory Search Tool (<http://wist.echo.nasa.gov>). SMOS-derived L4 High resolution Delayed (HDE) soil moisture time series were supplied by the SMOS Barcelona Expert Center (<http://cp34-bec.cmima.csic.es>).

3 METHODOLOGY

3.1 Gross Primary Production

The following Monteith-like equation was used to calculate daily GPP in $\text{g m}^{-2} \text{day}^{-1}$:

$$\text{GPP} = \text{PAR } f_{\text{APAR}} \varepsilon_{\text{max}} \varepsilon(W) \quad (1)$$

where $\varepsilon(W)$ is the down-regulating factor accounting for the water stress of vegetation. The different inputs were derived as follows.

3.1.1 Photosynthetically Active Radiation

PAR was computed in $\text{MJ m}^{-2} \text{day}^{-1}$ as the 46 % of the daily global solar radiation (Iqbal, 1983). DIDSSF from MSG/SEVIRI were used as global solar radiation estimations.

3.1.2 Fraction of Absorbed Photosynthetically Active Radiation

f_{APAR} was computed according to the methodology set out by Roujean & Breon (1995) using MODIS products MCD43A1 and MCD43A2: first near infrared and red reflectances were obtained from

bidirectional reflectance distribution function for an optimal geometry in order to reduce the influence of external factors, then RDVI was calculated using these two reflectances, and finally f_{APAR} was calculated as a linear function of RDVI. In addition, the f_{APAR} series were filtered and gap-filled as explained in Moreno *et al.* (2014) so that sudden drops and missing data due to the presence of clouds or poor atmospheric correction were avoided.

3.1.3 Maximum light use efficiency

ε_{max} values depend on vegetation type and were extracted from literature: 1.6 g MJ^{-1} for Las Majadas del Tiétar and 1.1 g MJ^{-1} for Cortes de Pallás (Garbulsky *et al.*, 2010).

3.1.4 Water stress factor

$\varepsilon(W)$ was characterized by means of the water stress coefficient (Maselli *et al.*, 2009) C_{ws} :

$$C_{\text{ws}} = (1 + \text{AET}/\text{PET})/2 \quad (2)$$

where AET and PET are the actual and potential evapotranspiration in mm day^{-1} , respectively. This factor ranges from 0.5 (when short-term water stress reduces photosynthesis to half of its potential value) to 1 (when vegetation does not suffer water stress). MSG/SEVIRI product DMET was used as actual evapotranspiration. If actual evapotranspiration is not available, precipitation (P) can be used instead only if it does not exceed the potential evapotranspiration. If precipitation exceeds potential evapotranspiration, C_{ws} is set to 1. Potential evapotranspiration in mm day^{-1} is calculated by means of the Jensen-Haise equation (Jensen & Haise, 1965):

$$\text{PET} = R_g(0.025 T_a + 0.08)/2450 \quad (3)$$

where R_g is the global solar radiation in $\text{kJ m}^{-2} \text{day}^{-1}$ and T_a is the averaged air temperature in $^{\circ}\text{C}$. MSG/SEVIRI DIDSSF product was used as global solar radiation. Maximum and minimum daily temperatures images were used to compute the mean daily temperatures.

The linear relationship between evapotranspiration ratio AET/PET and soil moisture (Kirkham, 2005) was also considered. Therefore, three different water stress factors were calculated as follows:

$$C_{\text{ws}}^1 = (1 + P/\text{PET})/2 \quad (4)$$

$$C_{\text{ws}}^2 = (1 + \text{AET}/\text{PET})/2 \quad (5)$$

$$C_{\text{ws}}^3 = (1 + \text{SM})/2 \quad (6)$$

where SM refers to soil moisture in the first 5 cm of depth in $\text{m}^3 \text{m}^{-3}$. SM was estimated by means of an algorithm that combines SMOS brightness temperatures and MODIS LST and NDVI into 1 km soil moisture estimates (Piles *et al.*, 2014). Since SMOS provides two images per day (morning and afternoon orbits) and the downscaling algorithm uses MODIS data from TERRA or AQUA platforms day passes, up to four HDE daily soil moisture images can be obtained. In this work, 1 km SMOS-derived soil moisture series using both TERRA and AQUA data were used to minimize the number of gaps due to clouds masking MODIS measurements.

Numerator and denominator in equations (4) and (5) were accumulated with the values from the n^{th} previous days until the day of the C_{ws} calculation, with $n = 0, 1, 2 \dots 89$. Therefore 90 values of each C_{ws} were obtained for each day. In the case of equation (6), this accumulation was accounted in the calculation of SM mean.

By maximizing the explained variance (R^2) of the estimated GPP, an optimal accumulation period (ranging from 0 to 89 days) was found for each of the three C_{ws} and each of the two study zones. The followed criterion is explained at the beginning of section 4.

3.2 Statistical analysis

Four series of daily GPP were obtained by means of the PEM model (equation (1)) using the three C_{ws} mentioned above and $C_{ws} = 1$, i. e., assuming no water stress. Explained variance (R^2), mean biased error (MBE), mean absolute error (MAE) and root mean squared error (RMSE) were calculated between each of the four daily GPP series and the one estimated from EC data. Then a separated study using the same statistics but considering only the period of the year when vegetation is affected by water stress was also carried out. This period was extracted from Figure 1, where both the profiles of the estimated and the calculated GPP by the model without C_{ws} for both EC towers sites (LMa and CPa) are shown. It can be appreciated how the two curves decouple around DoY = 150 and DoY = 180, and couple back around DoY = 300 and DoY = 320 approximately in LMa and CPa, respectively.

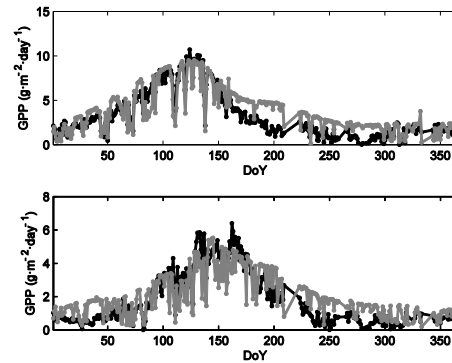


Figure 1. GPP temporal variation for the year 2011. Top: Las Majadas del Tiétar. Bottom: Cortes de Pallás. Black: estimated GPP from EC data. Gray: calculated GPP by the model without C_{ws} .

4 RESULTS AND DISCUSSION

The variance of estimated GPP explained by the calculated GPP through eq. (1) as a function of the accumulation period of C_{ws} in LMa is shown in Figure 2. Since some of the curves present an intense variation along the first days of accumulation and then they tend to reduce its variation considerably, a criterion to choose the optimal period of accumulation was established. First the accumulation period with the highest R^2 is found, then a threshold is set in this R^2 minus its 2 %, and finally the first accumulation period whose R^2 overcomes the threshold is taken. C_{ws}^1 (Fig. 2 top) needs an accumulation period to raise a high correlation. Its R^2 curve presents an absolute minimum before ten days of accumulation and then it grows rapidly until it stabilizes and almost saturates after around 40 days of accumulation (60 for CPa, not shown). The chosen accumulation periods were 38 and 52 days for LMa and CPa respectively. On the other hand, R^2 curves of C_{ws}^2 (Fig. 2 center) are rather flat and almost all their values are above the threshold, including the no accumulation case. This fact supports the following idea: since carbon dioxide enters the plant through the same way that water vapor exits from it, the evapotranspiration ratio accounts for the short-term response of vegetation to water stress almost immediately. If they are not well watered, plants close their stomata in order to maintain its water inside them and carbon dioxide cannot enter so easily. Finally, in the case of C_{ws}^3 (only morning orbits are shown) only the no accumulation case is over the threshold (Fig. 2 bottom). The behavior of the explained variance in function of the C_{ws} accumulation period in CPa is very similar to the one exposed in Figure 2, but it presents lower values.

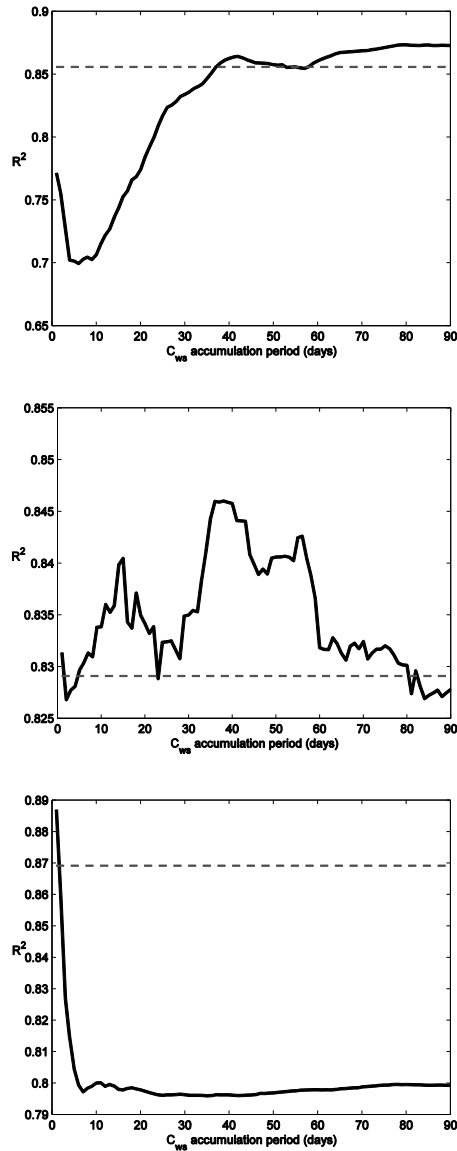


Figure 2. Variance of estimated GPP explained by the calculated GPP through equation (1) model as a function of C_{ws} accumulation period in Las Majadas del Tiétar. From top to bottom: $\varepsilon(W) = C_{ws}^1$, C_{ws}^2 , C_{ws}^3 morning orbits. Black solid line: R^2 . Gray dashed line: threshold.

The statistics resulting from the comparison between the calculated and the estimated GPP for the whole year 2011 are presented in Table 1. In LMa the C_{ws}^1 option achieves a considerably improvement regarding to the model without water stress: it explains a 9 % more of the temporal variance of GPP and it reduces the differences between the estimated values with lower errors and a small negative bias in comparison with the initial large positive bias. The C_{ws}^2 option exhibits a similar behavior, but its improvement

respect to the initial model is less notable, especially in terms of the accuracy. C_{ws}^3 option achieves the highest coefficient of determination. However it also presents the highest errors, probably due to the low values of SM, which result in low values of C_{ws}^3 . This issue needs to be optimized. R^2 is higher for morning orbits and errors are lower for afternoon orbits, where SM values are higher. Similar results are obtained for CPa. It presents a similar accuracy, but a lower correlation. It may be due to the lower vegetation fraction cover in CPa in comparison to LMa. In general, when the model includes a water stress factor, it is able to better track the temporal variability of the GPP explaining a considerably amount of its variance (especially when C_{ws}^3 is used) and it presents a rather good agreement with the estimated GPP. The change in the sign of the bias when C_{ws}^1 and C_{ws}^2 are used is probably caused by the tendency to overestimate measured PET of the Jensen-Haise equation (eq. (3)) (Jensen & Haise, 1965; Vörösmarty *et al.*, 1998).

Table 1. R^2 , MBE, MAE and RMSE presented by the different options of equation (1) model in Las Majadas del Tiétar and Cortes de Pallás for the whole year 2011. The super index *m* and *a* indicate morning and afternoon orbits respectively. Errors are expressed in $g\ m^{-2}\ day^{-1}$.

Las Majadas del Tiétar

	R^2	MBE	MAE	RMSE
$\varepsilon(W) = 1$	0.77	0.6	1.1	1.4
$\varepsilon(W) = C_{ws}^1$	0.86	-0.09	0.8	1.0
$\varepsilon(W) = C_{ws}^2$	0.83	-0.4	1.0	1.3
$\varepsilon(W) = C_{ws}^{3m}$	0.89	-0.8	1.2	1.8
$\varepsilon(W) = C_{ws}^{3a}$	0.86	-0.8	1.2	1.7

Cortes de Pallás

	R^2	MBE	MAE	RMSE
$\varepsilon(W) = 1$	0.67	0.2	0.8	1.0
$\varepsilon(W) = C_{ws}^1$	0.75	-0.2	0.6	0.9
$\varepsilon(W) = C_{ws}^2$	0.69	-0.5	0.8	1.2
$\varepsilon(W) = C_{ws}^{3m}$	0.81	-0.6	0.8	1.2
$\varepsilon(W) = C_{ws}^{3a}$	0.79	-0.5	0.8	1.2

Figure 3 shows the temporal variation of the GPP calculated by the three alternatives of the model together with the estimated GPP from EC data. It can be seen how the model has improved its performance during the water stress period in comparison with Figure 1. However, now the model underestimates GPP in the maximum production period and it keeps slightly overestimating it at the beginning of the year.

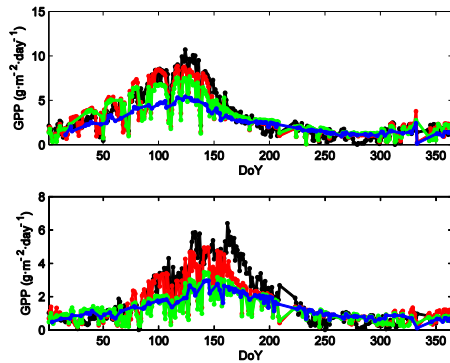


Figure 3. Temporal variation for the year 2011 of GPP estimated EC data (black), and calculated by equation (1) with $\varepsilon(W) = C_{ws}^1$ (red), $\varepsilon(W) = C_{ws}^2$ (green), and $\varepsilon(W) = C_{ws}^3$ (blue). Top: Las Majadas del Tiétar. Bottom: Cortes de Pallás.

The statistics shown in Table 2 are calculated only for late spring/summer (DoY = 150-300 and DoY = 180-320 for LMa and CPa, respectively) when water stress affects the study areas. It must be noticed the strong improvement of the model with the water stress factor in terms of accuracy, although it is probably caused by the lower GPP values during this period. Comparing to Table 1, it can be appreciated that the coefficient of determination is lower during the water stress period, i.e. the model cannot track the estimated GPP as good as the rest of the year, but its improvement regarding the alternative without C_{ws} is generally greater. The diminution of R^2 during the water stress period is related with the more complex temporal evolution of GPP associated with the effects of water stress in photosynthesis.

5 CONCLUSIONS

In this study, three different factors which account for short-term water stress vegetation were tested in a PEM for two EC tower sites in Spain. The three demonstrated a significant improvement in the model estimates in terms of gross primary production. The inclusion of the water stress factor helps the model tracking GPP temporal variability and reduces the differences with the estimated values, especially during the water shortage period typical of Mediterranean ecosystems. Although the C_{ws}^1 option performs rather well, the C_{ws}^2 one could be a better option since it reduces the use of meteorological data to only one variable (air temperature), which could be estimated from remotely sensed land surface temperature. C_{ws}^3 seems to be a very promising option since it does not need meteorological data and it presents the highest coefficients of determination. However, its temporal series present several gaps and a revision is needed to account for the high bias.

Table 2. R^2 , MBE, MAE and RMSE presented by the different options of equation (1) model in Las Majadas del Tiétar and Cortes de Pallás for water stress period of the year 2011. The super index m and a indicate morning and afternoon orbits respectively. Errors are expressed in $g\ m^{-2}\ day^{-1}$.

Las Majadas del Tiétar

	R^2	MBE	MAE	RMSE
$\varepsilon(W) = 1$	0.64	1.6	1.7	1.9
$\varepsilon(W) = C_{ws}^1$	0.76	0.07	0.6	0.7
$\varepsilon(W) = C_{ws}^2$	0.71	0.2	0.7	0.8
$\varepsilon(W) = C_{ws}^{3m}$	0.78	0.10	0.7	0.8
$\varepsilon(W) = C_{ws}^{3a}$	0.76	0.014	0.6	0.8

Cortes de Pallás

	R^2	MBE	MAE	RMSE
$\varepsilon(W) = 1$	0.48	0.8	0.9	1.1
$\varepsilon(W) = C_{ws}^1$	0.51	-0.04	0.5	0.6
$\varepsilon(W) = C_{ws}^2$	0.51	-0.08	0.5	0.7
$\varepsilon(W) = C_{ws}^{3m}$	0.69	0.007	0.5	0.6
$\varepsilon(W) = C_{ws}^{3a}$	0.65	0.08	0.4	0.5

6 ACKNOWLEDGEMENTS

This work was partially funded by the RESET CLIMATE Project from the Spanish Ministry of Economy and Competitiveness (Project CGL2012-35831) and LSA SAF (EUMETSAT). Part of the data was kindly provided by the SMOS Barcelona Expert Center (under the project MIDAS 7: AYA2012-39356) and by AEMet.

7 REFERENCES

- Garbulsky, M. F., Peñuelas, J., Papale, D., Ardö, J., Goulden, M. L., Kiely, G., Richardson, A. D., Rotenberg, E., Veendaal, E. M., and Filella, I., 2010, Patterns and controls of the variability of radiation use efficiency and primary productivity across terrestrial ecosystems. *Global Ecology and Biogeography*, **19** (2), 253–267. doi:10.1111/j.1466-8238.2009.00504.x
- IPCC., 2007, Climate Change 2007: The physical science basis. (Solomon, S., Qin, D., Marquis, M., Averyt, K., B., and Tignor, M., Eds.).
- Iqbal, M., 1983, An Introduction to Solar Radiation. (Academic Press, Canada).

- Jensen, M. E., and Haise, H. R., 1965, Estimating evapotranspiration from solar radiation. *Journal of Irrigation and Drainage Division*, **89**, 15–41.
- Kirkham, M. B., 2005, Potential Evapotranspiration. In *Principles of Soil and Plant Water Relations*. (Elsevier Academic Press, Ed.), pp. 455–468.
- Maselli, F., Papale, D., Puletti, N., Chirici, G., and Corona, P., 2009, Combining remote sensing and ancillary data to monitor the gross productivity of water-limited forest ecosystems. *Remote Sensing of Environment*, **113** (3), 657–667. doi:10.1016/j.rse.2008.11.008
- Monteith, J. L., 1972, Solar Radiation and Productivity in Tropical Ecosystems. *Journal of Applied Ecology*, **9**, 747–766.
- Moreno, A., García-Haro, F., Martínez, B., and Gilabert, M. A., 2014, Noise Reduction and Gap Filling of fAPAR Time Series Using an Adapted Local Regression Filter. *Remote Sensing*, **6** (9), 8238–8260. doi:10.3390/rs6098238
- Piles, M., Sánchez, N., Vall-llossera, M., Camps, A., Martínez-Fernández, J., Martínez, J., and González-Gambau, V., 2014, A Downscaling Approach for SMOS Land Observations: Evaluation of High-Resolution Soil Moisture Maps Over the Iberian Peninsula. *IEEE Journal of Selected Topics in Applied Earth Observations and Remote Sensing*, **7** (9). doi:10.1109/JSTARS.2014.2325398
- Reichstein, M., Falge, E., Baldocchi, D., Papale, D., Aubinet, M., Berbigier, P., Bernhofer, C., Buchmann, N., Gilmanov, T., Granier, A., Grunwald, T., Havrankova, K., Ilvesniemi, H., Janous, D., Knohl, A., Laurila, T., Lohila, A., Loustau, D., Matteucci, G., Meyers, T., Miglietta, F., Ourcival J. M., Pumpanen, J., Rambal, S., Rotenberg, E., Sanz, M., Tenhunen, J., Seufert, G., Vaccari, F., Vesala, T., Yakir, D., and Valentini, R., 2005, On the separation of net ecosystem exchange into assimilation and ecosystem respiration: review and improved algorithm. *Global Change Biology*, **11** (9), 1424–1439. doi:10.1111/j.1365-2486.2005.001002.x
- Roujean, J., and Breon, F., 1995, Estimating PAR Absorbed by Vegetation from Bidirectional Reflectance Measurements. *Remote Sensing of Environment*, **51**, 375–384.
- Vörösmarty, C. J., Federer, C. A., and Schloss, A. L., 1998, Potential evaporation functions compared on US watersheds: Possible implications for global-scale water balance and terrestrial ecosystem modeling. *Journal of Hydrology*, **207**, 147–169.

On the temporal upscaling of instantaneous evapotranspiration from the constant reference evaporative fraction method using public weather forecast information

Ronglin Tang¹, Zhao-Liang Li^{2, 1, *}

¹ State Key Laboratory of Resources and Environment Information System, Institute of Geographic Sciences and Natural Resources Research, Beijing 100101, China

² Key Laboratory of Agri-informatics, Ministry of Agriculture/Institute of Agricultural Resources and Regional Planning, Chinese Academy of Agricultural Sciences, Beijing 100081, China

* Author to whom correspondence should be addressed: lizhaoliang@caas.cn

ABSTRACT- Quantification of land surface evapotranspiration (ET) is of great significance in water resources management, climate change study, and numerical weather prediction. The constant reference evaporative fraction (the ratio of actual to reference ET) method, which assumes the equality of the daily reference evaporative fraction (EF_r) to that at the satellite overpass time, is one of the representative schemes that have been widely applied for the remote sensing instantaneous ET upscaling. To overcome the difficulties encountered in the acquisition of the tower-based meteorological variables, this paper investigates the feasibility of using publicly available weather forecast information to estimate the daily reference ET in the constant reference evaporative fraction method. Results show that using the meteorological variables converted from the daily weather forecast information produced a small bias of 0.1 mm/d and a RMSE of 0.6 mm/d when the estimated daily reference ET was compared with that derived using completely the ground-based meteorological measurements. When the remote sensing instantaneous ET and half-hourly reference ET are estimated with accuracies that are of similar magnitude to those of the ground-based measurements, the upscaling method can produce daily ET using the meteorological variables converted from the weather forecast information, with the bias of 0.1 mm/d and the RMSE of 0.7 mm/d.

1 INTRODUCTION

Quantification of land surface evapotranspiration (ET) is of great significance in water resources management, climate change study, and numerical weather prediction. A number of methods, primarily based on surface energy budget theory, have been developed using thermal infrared data over the past decades to estimate regional and continental ET (see the reviews by Li et al. (2009)). However, these one- and two-source energy balance models in most cases only provide the ET estimates at an instantaneous time scale.

The constant reference evaporative fraction (the ratio of actual to reference ET) method, which assumes the equality of the daily reference evaporative fraction (EF_r) to that at the satellite overpass time, is one of the representative upscaling methods that have been widely applied (Colaizzi et al., 2006; Chávez et al., 2008; Tang et al., 2013a). The key in the application of the constant EF_r method is to properly estimate the instantaneous and daily reference ET (ET_r), which generally requires as inputs the meteorological variables of global solar radiation, air temperature, vapor pressure deficit (relative humidity),

wind speed. For the daily ET_r estimations using the FAO Penman-Monteith (PM) equation, meteorological data on daily global solar radiation, maximum and minimum air temperature, relative humidity, and wind speed are required. However, due to the limited number of observation sites and the high cost of the equipped instruments, such daily data may not be easily accessed, especially for developing countries.

This paper aims to investigate the feasibility of using publicly available weather forecast information to estimate the daily ET_r when the constant reference evaporative fraction method is applied to upscale the remote sensing model-derived instantaneous ET.

2 METHODOLOGY

2.1 Constant reference evaporative fraction upscaling method

The constant reference evaporative fraction upscaling method was first proposed by Trezza (2002) to convert instantaneous remote sensing ET to daily values. It assumes that the ratio of actual instantaneous ET to daily ET values is equivalent to the ratio of the corresponding reference instantaneous ET to reference daily ET values, namely,

$$\frac{ET_{a,i}}{ET_{a,d}} = \frac{ET_{r,i}}{ET_{r,d}} \quad (1)$$

where ET_a is the remote sensing model-derived ET; ET_r is the reference ET estimated from the FAO-PM equation; and subscripts i and d are indicative of the values at the instantaneous and daily time scales, respectively.

Assuming that a hypothetical grass with an height of 0.12 m has an albedo of 0.23 and a fixed surface resistance of 70 s/m or variables resistances of 50 s/m and 200 s/m during daytime and nighttime, respectively, daily and half-hourly reference ETs can be estimated from the Penman-Monteith equation as suggested by Allen et al. (1998) and ASCE-EWRI (2005).

2.2 Two-source energy balance model

The two-source energy balance (N95) model developed by Norman et al. (1995) was used in this study for the remote sensing instantaneous ET estimation. The remarkable superiority of the N95 model towards the conventional one-source energy balance models is that the satellite view geometry is incorporated and the empirical correction of the excess resistance can be avoided. Moreover, the energy fluxes and surface temperature are partitioned into soil and vegetation components and the sensitivity of the model to the atmospheric and vegetation inputs is not so high compared with the commonly used one-source bulk transfer models. The N95 model has been demonstrated to be robust under a wide range of landscape and hydrometeorological conditions for the soil and canopy ET estimation (Kustas & Norman, 1997; Tang et al., 2011).

2.3 Weather forecast information translation

Publicly available forecast information for short, medium, and long-term time scales includes the daily maximum and minimum air temperature, the cloudiness condition, and the wind scale and direction. With the increase of cloud, the forecasted cloudiness condition is classified into five categories—clear sky, clear to cloudy, cloudy, overcast sky, and rainy (Cai et al., 2007). Assuming an equal increment between 0 and N under the five cloudiness conditions, the ratio of actual and maximum sunshine durations is supposed to be averagely 0.9, 0.7, 0.5, 0.3, and 0.1 for the clear sky, the clear to cloudy sky, the cloudy sky, the overcast sky, and the rainy sky, respectively. Daily global solar radiation can be estimated using the empirical equation following the work of Allen et al. (1998) provided that the ratio of actual and maximum sunshine durations is known. The forecasted wind scale is classified into 13 categories (from 0 to 12) and

each category represents a certain range of wind speed at 10 m height according to the standards of meteorological observation. The wind speed at 10 m height needs to be further converted to that at 2 m height using the equation following the work of Allen et al. (1998).

3 MATERIALS AND DATA

3.1 Yucheng station

Ground-based data measurements that are collected for the inputs of ET retrieval model and the validation of ET upscaling method in this study are conducted between January 2011 and October 2012 at the Yucheng Comprehensive Experimental Station (hereafter referred to as Yucheng station), which is located in the North China Plain with a latitude of 36.8291° N and a longitude of 116.5703° E.

A suite of standard sensors are equipped at the Yucheng station to measure meteorological variables (e.g., air temperature, air pressure, actual vapor pressure, and wind speed/direction) and profiles of soil water and temperature. Moreover, a CNR-1 device and a HFP-01 soil heat flux plate buried at a depth of 2 cm are also setup to measure the downward and upward shortwave and longwave radiations and the soil heat flux. The Yucheng station was also equipped with an eddy covariance (EC) system that consists of an open-path CO₂/H₂O gas analyzer (model LI-7500, Licor Inc., Lincoln, Nebraska) and a 3-D sonic anemometer/thermometer (model CSAT3, Campbell Scientific Inc., Logan, Utah). This EC system measures regularly the sensible heat flux (H) and latent heat flux (LE). All mentioned measurements above are stored as a 30-min averaged value.

Our previous study showed that the residual energy (RE) correction method produces the best agreement between remote sensing instantaneous ET and ground-based EC measurements at the Yucheng station (Tang et al., 2013b). We therefore applied the RE correction method to correct the 30-min averaged daytime EC measurement to close the energy imbalance of the EC measurements in this study.

3.2 MODIS data

Remote sensing data used to drive the two-source ET model are acquired from the MODIS/Terra and MODIS/Aqua satellite platforms. The MODIS data involved in this study consist of the Land Surface Temperature and Emissivity 5-min L2 Swath 1 km data set product (MOD11_L2 for the Terra satellite and MYD11_L2 for the Aqua satellite) produced using the generalized split-window LST algorithm (Wan & Dozier, 1996), the geolocation dataset product (MOD03 and MYD03) at 1 km spatial resolution, and

the MODIS Atmospheric Profiles product (MOD07 and MYD07) at 5 km spatial resolution. Totally, Sixty-five MODIS overpass times (35 MODIS/Terra + 30 MODIS/Aqua) over 58 calendar days from January 2011 to October 2012 were selected for the remote sensing instantaneous ET estimation and the daily ET upscaling.

MODIS temperature is corrected using the simultaneous ground-based longwave radiation measurement to provide the most accurate inputs for driving the N95 model, as presented in Tang et al. (2011).

3.3 Weather forecast information

China Meteorological Administration issues the weather forecast three times (8:00 AM, 11:00 AM, 18:00 PM Beijing time) a day. The weather forecast information at the Yucheng County issued at 8:00 AM was collected from January 2011 to October 2012 in this study for the daily reference ET estimation. This forecast information includes the cloudiness condition, daily maximum and minimum air temperature, and wind scale and direction over the next 24 hours (8:00 AM today ~ 8:00 AM next day).

4 RESULTS AND DISCUSSION

4.1 Comparison of daily reference ET

For the purpose of investigating the feasibility of using publicly available weather forecast information to estimate the daily reference ET when the constant reference evaporative fraction method is applied to upscale remote sensing instantaneous ET, it is necessary to test how well the daily reference ET can be estimated from the converted meteorological variables.

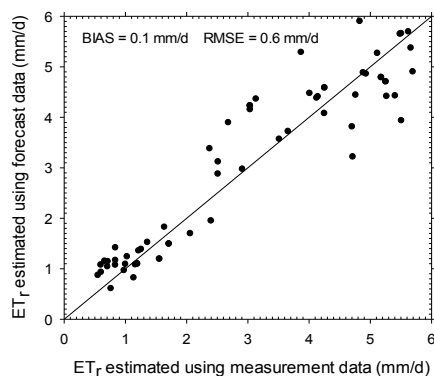


Figure 1 Comparison of daily reference ET using forecast meteorological information with that computed using ground-based measurements.

Figure 1 compares the daily reference ET estimated using the meteorological variables converted from weather forecast information with that derived completely using ground-based meteorological measurements at the Yucheng station over the selected 58 MODIS overpass days from January 2011 to October 2012. A small bias of 0.1 mm/d and an RMSE of 0.6 mm/d were observed. It can also be seen that when the daily reference was below 2.5 mm/d, a good agreement can be observed between the daily reference ET estimated from weather forecast information and that using ground-based measurements. However, when the daily reference was above 2.5 mm/d, a relatively large scatter was found.

4.2 Comparison of the remote sensing-based instantaneous LE and half-hourly reference ET using MOD07 air and dew-point temperatures

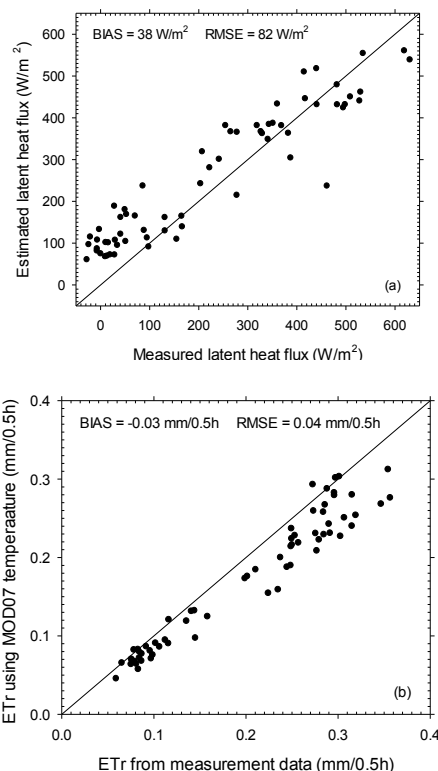


Figure 2 (a) Comparison of remote sensing-based N95-derived instantaneous latent heat flux with the ground-based EC measurements. (b) Comparison of half-hourly reference ET estimated using MOD07 air and dew-point temperatures with that using ground-based meteorological variables.

Figure 2a compares the remote sensing instantaneous LE from the two-source N95 model with EC measurements corrected by the RE correction method at the 65 MODIS/Terra and MODIS/Aqua overpass times over the 58 selected days. The instantaneous LE was overestimated by 38 W/m^2 and a large scatter was observed with a RMSE of 82 W/m^2 . The overestimation tended to become more serious when the LE is in a small magnitude. The N95 model did not produce instantaneous LE estimates as expected from the previous studies, which would inevitably affect the daily ET upscaled from the constant evaporative fraction method. Figure 2b compares the half-hourly reference ET estimated using MOD07 air and dew-point temperatures with that derived completely using ground-based meteorological measurements at the MODIS overpass times. Using MOD07 air and dew-point temperatures in most cases produced lower reference ET than using ground-based air temperature and humidity measurements, with a bias of -0.03 mm/0.5h and a RMSE of 0.04 mm/0.05h . The underestimation was found to be more serious when the half-hourly reference ET is in a large magnitude.

4.3 Validation of the upscaled daily ET

Figure 3 compares the upscaled daily ET (using the daily reference ET estimated from forecast meteorological information) with the corresponding RE method-corrected EC measurements of daily ET over the selected 58 MODIS overpass days. One can see from this figure that the bias and scatter in the remote sensing instantaneous ET estimation have significantly impacted the upscaled daily ET. The tendency to overestimate the upscaled daily ET, which results from the overall overestimation in the remote sensing instantaneous ET, has been further enhanced by the underestimation in the half-hourly reference ET using MOD07 air and dew-point temperatures. The constant reference evaporative fraction upscaling method under this condition was shown to in most cases overestimate the daily ET with a bias of 1.0 mm/d and a RMSE of 1.6 mm/d . When the N95 model-estimated ET was changed to the EC-measured half-hourly LE corrected by the RE method (with the half-hourly reference ET and daily reference ET unchanged), the bias and RMSE were significantly reduced to 0.5 mm/d and 1.0 mm/d , respectively, which demonstrated the significance of the accurate estimation of remote sensing instantaneous ET in the constant reference evaporative fraction upscaling method. When the N95 model-estimated instantaneous ET and the half-hourly reference ET using MOD07 air and dew-point temperatures were changed to the ground-based EC-measured ET and the half-hourly reference ET using ground-based meteorological

variables (implicitly assuming that the instantaneous ET and the half-hourly reference ET were accurately estimated with similar accuracies to the ground-based measurements), respectively, both the bias and the RMSE were further decreased to 0.1 mm/d and 0.7 mm/d .

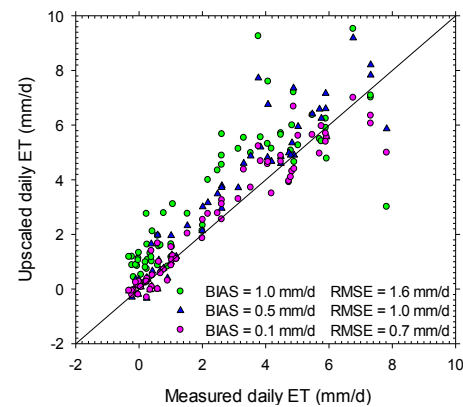


Figure 3 Comparison of upscaled daily ET with the corresponding ground-based ET measurements or reference ET computed using ground-based measurements. Filled green circle represents the daily ET upscaled using N95-estimated instantaneous ET, half-hourly reference ET estimated using MOD07 air and dew-point temperatures, and daily reference ET estimated using forecast meteorological information. Filled blue triangle represents the daily ET upscaled using EC-measured half-hourly LE corrected by the RE method, half-hourly reference ET estimated using MOD07 air and dew-point temperatures, and daily reference ET estimated using forecast meteorological information. Filled purple circle represents the daily ET upscaled using EC-measured half-hourly LE corrected by the RE method, half-hourly reference ET estimated using ground-based meteorological variables, and daily reference ET estimated using ground-based meteorological variables.

5 SUMMARY AND CONCLUSION

Using the constant reference evaporative fraction upscaling method in most cases overestimated the daily ET with a bias of 1.0 mm/d and a RMSE of 1.6 mm/d when we made use of the N95 model-derived instantaneous ET, the half-hourly reference ET estimated using MOD07-based air and dew-point temperatures, and the daily reference ET estimated from the meteorological variables converted from the weather forecast information. When the N95 model-estimated ET was changed to the EC-measured half-hourly LE corrected by the RE method (with the half-hourly reference ET and daily reference ET unchanged), the

bias and RMSE were significantly reduced to 0.5 mm/d and 1.0 mm/d, respectively. When the N95 model-estimated instantaneous ET and the half-hourly reference ET using MOD07 air and dew-point temperatures were changed to the ground-based EC-measured ET and the half-hourly reference ET estimated using ground-based meteorological variables, respectively, both the bias and the RMSE were further decreased to 0.1 mm/d and 0.7 mm/d. These results demonstrated the significance of the accurate estimation of remote sensing instantaneous ET and half-hourly reference ET in the constant reference evaporative fraction upscaling method. When these two factors are estimated with accuracies that are of similar magnitude to those of the ground-based measurements, the upscaling method can produce reasonable daily ET using the meteorological variables converted from the weather forecast information.

6 ACKNOWLEDGMENTS

The staff members at the Yucheng site are acknowledged for their hard-work on the setup and maintenance of the ground-based instruments and data collection. Associate Professor Yuanyuan Jia and Professor Chuanrong Li in the Academy of Opto-Electronics, Chinese Academy of Sciences, are thanked for their cooperation in providing the surface measurements. This work was supported by the National Natural Science Foundation of China under Grant 41201366 and 41101332, the Institute of Geographic Sciences and Natural Resources Research funded outstanding young talent project under Grant 2013RC201, and the National High Technology Research and Development Program of China under Grant 2012AA121103.

7 REFERENCES

- Allen, R. G., Pereira, L. S., Raes, D., and Smith, M., 1998, Crop evapotranspiration—Guidelines for computing crop water requirements. FAO Technical Paper 56, Food and Agricultural Organization of the United Nations, Rome.
- ASCE-EWRI., 2005, The ASCE Standardized Reference Evapotranspiration Equation. Technical Committee report to the Environmental and Water Resources Institute of the American Society of Civil Engineers from the Task Committee on Standardization of Reference Evapotranspiration. ASCE-EWRI, 1801 Alexander Bell Drive, Reston, VA 20191-4400, 173 pp.
- Cai, J., Liu, Y., Lei, T., and Pereira, L. S., 2007, Estimating reference evapotranspiration with the FAO Penman–Monteith equation using daily weather forecast messages. *Agricultural and Forest Meteorology*, **145**(1), 22–35.
- Chávez, J. L., Neale, C. M., Prueger, J. H., and Kustas, W. P. (2008). Daily evapotranspiration estimates from extrapolating instantaneous airborne remote sensing ET values. *Irrigation Science*, **27**, 67–81.
- Colaizzi, P. D., Evett, S. R., Howell, T. A., and Tolck, J. A., 2006, Comparison of five models to scale daily evapotranspiration from one-time-of-day measurements. *Transactions of the ASAE*, **49**, 1409–1417.
- Kustas, W. P., and Norman, J. M., 1997, A two-source approach for estimating turbulent fluxes using multiple angle thermal infrared observations. *Water Resources Research*, **33**, 1495–1508.
- Li, Z. -L., Tang, R. L., Wan, Z., Bi, Y., Zhou, C., Tang, B., Yan, G., and Zhang, X., 2009, A Review of current methodologies for regional evapotranspiration estimation from remotely sensed data. *Sensors*, **9**, 3801–3853.
- Norman, J. M., Kustas, W. P., and Humes, K. S., 1995, A two-source approach for estimating soil and vegetation energy fluxes from observations of directional radiometric surface temperature. *Agricultural and Forest Meteorology*, **77**, 263–293.
- Tang, R. L., Li, Z. -L., and Sun, X., 2013a, Temporal upscaling of instantaneous evapotranspiration: An intercomparison of four methods using eddy covariance measurements and MODIS data. *Remote Sensing of Environment*, **138**, 102–118.
- Tang, R. L., Li, Z. -L., Jia, Y., Li, C., Chen, K. S., Sun, X., and Lou, J., 2013b, Evaluating one-and two-source energy balance models in estimating surface evapotranspiration from Landsat-derived surface temperature and field measurements. *International Journal of Remote Sensing*, **34**(9–10), 3299–3313.
- Tang, R. L., Li, Z. -L., Jia, Y., Li, C., Sun, X., Kustas, W. P., and Anderson, M. C., 2011, An intercomparison of three remote sensing-based energy balance models using Large Aperture Scintillometer measurements over a wheat–corn production region. *Remote Sensing of Environment*, **115**, 3187–3202.
- Trezza, R., 2002, Evapotranspiration using a satellite-based surface energy balance with standardized ground control. Ph.D. dissertation, USU, Logan, UT, 339 pp.

The system for a quick estimate of agricultural crop quantity and surface for the purposes of a potential radioactive contamination using remote sensing data

Jan Procházka, Jakub Brom, Hana Vinciková

University of South Bohemia in České Budějovice, Faculty of Agriculture, Department of Landscape Management, Laboratory of Applied Ecology, Studentská 13, České Budějovice, CZ 37005, Czech Republic

prochaz@zf.jcu.cz; jbrom@zf.jcu.cz; hanavincikova@seznam.cz

ABSTRACT - The experience of the Chernobyl or Fukushima NPP accidents has shown the agricultural landscape contamination poses an environmental as well as economic and cultural issue in the long term. In order to mitigate the consequences of an accident and subsequent action, it is important to quickly estimate the quantity and distribution of the vegetation (crops) aboveground biomass in farmed land and also the distribution of radioactive material deposition between the vegetation cover and soil surface. The evaluation system involves: the analysis of the radiation situation (total deposition) in the area of interest; the analysis of crop spatial distribution in the area of interest; the estimate of crop biomass quantity and the distribution of radionuclide on the vegetation cover surface and ground; the evaluation of situation and subsequent action. For the purposes of the crop spatial distribution analysis, a supervised classification of remote sensing data can be used with the possibility to immediately create a landscape cover map for relatively large areas. The classification of crop distribution output enters the system of cover production indicator and crop and soil contamination estimate for the area of interest. The SARCA (Spatial Assessment of Radioactive Contamination of Agricultural Crops) programme was developed for these purposes, enabling us to estimate the average specific activity of radionuclide deposition on the vegetation cover and soil surface for individual agricultural areas ($Bq \cdot m^{-2}$), after entering the layer of the specific deposited activity of the given radionuclide in the given area and the crop spatial distribution layer.

1 INTRODUCTION

As a precaution against a possible emergency associated with radioactive material release into the environment, it is important to have access to timely information on agricultural crop situation and distribution in the wider surroundings of nuclear power plants, among other things. The issues of agricultural production and landscape protection against radioactive material contamination and steps to be taken in the event of a radiation accident affecting agricultural activities and the environment have been subject of ongoing discussions (cf. e.g. the EURANOS documents, <http://www.euranos.fzk.de/>). Such information is necessary for the logistics of action to be taken in view of a potential disposal of the agricultural produce in order to reduce the radioactive contamination of the landscape as well as the risk of food chain contamination. In order to mitigate the consequences of an accident and take subsequent action, it is important to quickly estimate the quantity and distribution of the vegetation biomass to be found above the ground (crops) in farmland and also the distribution of radioactive material deposition between the vegetation cover and soil surface.

The spatial distribution of crops can be assessed using the geographic information system (GIS) tools (see e.g. Priya and Shibasaki, 2001) and also remote sensing (RS) methods (see Oetter et al., 2000; Pinter et al., 2003; Fumin et al., 2010). Direct field measurement, RS or mathematic models (summarized by Ahamed et al., 2011; Květ et al., 1971; Paine et al., 2012) can be used to evaluate quantitative production characteristics. Current complex systems used in order to estimate agricultural production provide reliable results with sufficient estimate accuracy of monitored quantities; however, their use for the purposes of agricultural crop radiation protection seems rather complicated due to the large amount of input data required. Given the fact the data acquisition and processing is very demanding in terms of time, staff and financial resources in view of the area considered for the event of a potential radiation accident and prompt action to be taken, it is necessary to adopt a more straightforward approach, drawing on a smaller amount of input data, even though it involves a less accurate estimate. This was the reason why we used a simple mathematic model, able to quickly estimate crop production characteristics in the specified time and crop and soil surface radioactive contamination in

the affected area upon entering the layer of the specific deposited activity of the given radionuclide in space (e.g. prediction model output data, aerial or field measurement).

The aim of this paper is to present a study covering a quick estimate of the quantity and distribution of the aboveground vegetation biomass (crops) to be found in farmland using RS data in order to determine potential deposition of radioactive material in vegetation (crops) or soil surface.

2 METHODS

The purpose of the assessment of the area of interest in terms of currently grown crops is to determine the distribution of the individual crop types and their production properties and characteristic in time. As the current crop distribution in the area of interest is not registered in any central database, it is necessary to search for alternative sources of information. In case of a crop contamination and subsequent steps to be taken the need for the acquisition of relevant information is a question of a few days. It is therefore possible to only use a limited number of the various methods available. The selected methods have both advantages and disadvantages for our purpose (Tab. 1).

The assessment involves also the information on current or long-term climatic characteristics. This is associated with a general knowledge of growing conditions of the individual crops.

The following approaches can be adopted in order to assess the amount of biomass and its development during the growing season:

- Remote Sensing (estimates based on spectral indices)
- Measurement *per se*
- Use of mathematic models

Remote sensing (RS) distance data enable landscape cover classification for large areas. Crop species composition and spatial distribution in the area of interest can be determined and their surface representation can be calculated based on the classification of satellite images. Quantitative indices, such as the amount of biomass, can be estimated based on the distance data using spectral (vegetation) indices. The most frequent vegetation index is the NDVI (Tucker, 1979), which can be used for a number of applications.

The advantage of measurement *per se* lies in the acquisition of real and relatively accurate data for individual crops which can subsequently be used for the whole of the area assessed with similar conditions. The disadvantage, on the other hand, is that the method is time-consuming and material intensive, and also the impact of different seasonal conditions (weather, agrotechnology).

From the currently available methods, the use of information on crop spatial distribution provided by farms emerged as the most suitable evaluation approach for the area of interest, and such information is further used in order to calculate the amount of the aboveground biomass based on a mathematic model, RS data and methods.

Apart from the identification by field research or satellite data analysis, crop production characteristics can be determined and analyzed using mathematic models covering plant growth analysis. The advantage of the use of growth analysis models is that studied characteristics can be estimated throughout the considered period, and in particular time actually, and that the models can be combined with other inputs such as the information on cover radioactive contamination, for example. The disadvantage, on the other hand, lies in a certain simplification, given by the mathematic method as well as the quality and availability of the data used.

Table 1- Methods used to assess crop distribution – advantages (+) and disadvantages (-)

Method	+	-
Field investigation	Accurate (depending on the mapping method!)	Labour intensive, time-consuming
Information from farms + GIS processing	Time-consuming data collection	Accuracy depends on the reliability of provided information
Monitoring of landscape cover changes using RS data	Good quality, both optical and geometric (data with high spatial resolution) Acquired in the wide part of the spectrum Usability given by the resolution and wavelength range of scanned reflected radiation Low price per data area unit	Software and technology intensive Interpretation errors Depends on weather conditions in thermal and optical RS

Fig. 1 - SARCA programme input form (in Czech, English version will be available soon)

3 MODEL STUDY

The radioactive contamination modelling system draws on a simple approach involving the estimation of crop aboveground biomass based on a growth model parametrized for the individual monitored crops. The system also takes into account the distribution of radioactive contaminant deposition between agricultural crop surface and soil surface through the calculation of the interception factor according to Müller and Pröhl (1993). For the purposes of calculation the primary data on an accident and subsequent spread of radioactive contamination can be the outputs from dispersion forecast models covering the radioactive contamination spread, and aerial or field measurements. The actual calculation of all the parameters in the spatial scale is carried out using the SARCA (Spatial Assessment of Radioactive Contamination of Agricultural Crops) software (for more details see Brom et al., 2013, 2014) (Fig.1).

The input data for the purposes of this case study included the digital layer of crop spatial distribution in the area of interest, crop attributes for the calculation of crop biomass (Fig. 3A) and other characteristics using a growth model and a model data file of radioactive contaminant deposition from the HARP RP forecast model (Institute of Information Theory and Automation, ASCR; <https://dss.utia.cas.cz/>) (Pecha, Hofman, 2007). Radioactivity reference levels for plant material and soil handling are determined according to the OIL (IAEA, 1997).

The calculation involves the aspect of precipitation, an important factor in the distribution of a contaminant between the cover surface and soil surface. The value of aggregate rainfall was set to zero

for the whole area of interest given the fact there was no rainfall in the considered period.

The Temelín Nuclear Power Plant (Temelín NPP) Emergency Planning Zone (Fig. 2A) – covering an area of 13km in diameter with the centre corresponding to the location of the containment building of the first production block – was primarily chosen as the model test area for the estimate of agricultural crop and soil contamination using the SARCA programme.

The analysis was carried out for July 2013, i.e. just before the harvest of most of the agricultural crops. Based on the supervised classification of a Landsat 8 satellite image (27.07.2013) the whole of the Temelín NPP territory was classified in terms of crop distribution (Fig. 2B) using the source data on grown crops acquired during the field investigation.

The outcome of the calculation is a digital vector layer in the shp format, spatially corresponding to the specification of the input digital layer capturing the crop spatial distribution. The information contained in the following columns is important when it comes to the decision-making process on the activities to be carried out in the area of interest:

- “RU”: Reference Level (Fig.3B) . Values 0, 1 and 2 describe the level of the total radionuclide deposition in the given part, providing a rough outline of potential interventions for the individual parts.
- “B_HA” and “B_POL”: the amount of biomass in t.ha⁻¹ and t per land (field), providing an overview of the amount of aboveground biomass in the individual lands located in the monitored area.
- “DEP_POR” and “DEP_PUD”: radioactive material deposition on the cover and soil surface. These columns provide information on the degree

of cover and soil contamination (Bq.m^{-2}) and can therefore give a guideline to decide on the removal of the aboveground biomass growing in the monitored area in order to protect the soil.

- “HYG_LIM” and “KONT_POR”: level of the sanitary limit category (0 and 1) and the degree of weight contamination of the crop aboveground biomass. These values indicate if the given sanitary limit was reached/exceeded or not and the degree of the aboveground biomass contamination in Bq.kg^{-1} and give us the guideline to decide how the crop aboveground biomass is to be used.
- “NAKLADY”: Costs of the aboveground biomass removal. This column contains rough information on the financial costs of biomass removal from the individual lands. The removal costs are calculated for all parts of the area of interest covered by biomass.
- “ODSTR”: Recommendation of biomass removal in view of a potential reduction of the arable land. Biomass removal is recommended considering the total contamination of the particular land and the amount of biomass to be found in the area.

In accordance with the evaluation of the SARCA programme output, almost 70% (13,000 hectares) of the monitored area of farmland in the area of interest could be classified in the reference level category no. 0, 18% in category no. 1, and 12.2% (2,267 ha) in reference level no. 2 based on the model radiation situation from July 2013. The total crop aboveground biomass in these categories is 166,000 t in the 0 “RU”, 43,000 t in the 1 “RU” and 27,000 t in the 2 “RU”. If biomass removal in the “RU” no. 1 category was considered (not necessary for “RU” no. 0, not possible for “RU” no. 2), the biomass removal costs for the particular area would amount to more than 6 million CZK (approx. €215,000).

In the model example 36% of radioactive deposition was captured on the vegetation surface, which clearly demonstrates the importance of vegetation cover for the protection of soil against radioactive contamination. Vegetation cover removal can therefore become an important step for a potential reduction of the radioactive contamination of the landscape.

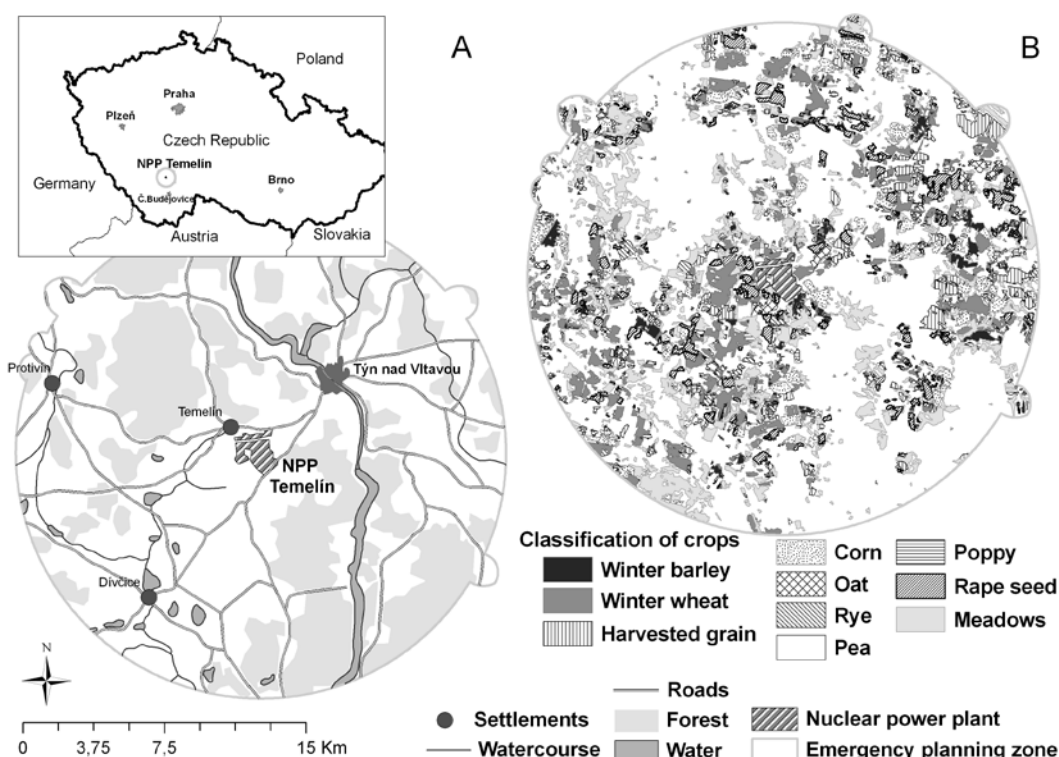


Fig. 2 - A) Study area of emergency planning zone of NPP Temelin located in South Bohemia, Czech Republic B) Classification of agricultural crops in the vicinity of NPP Temelin in 2013 from Landsat 8 (data available from the U.S. Geological Survey), using data from the field monitoring

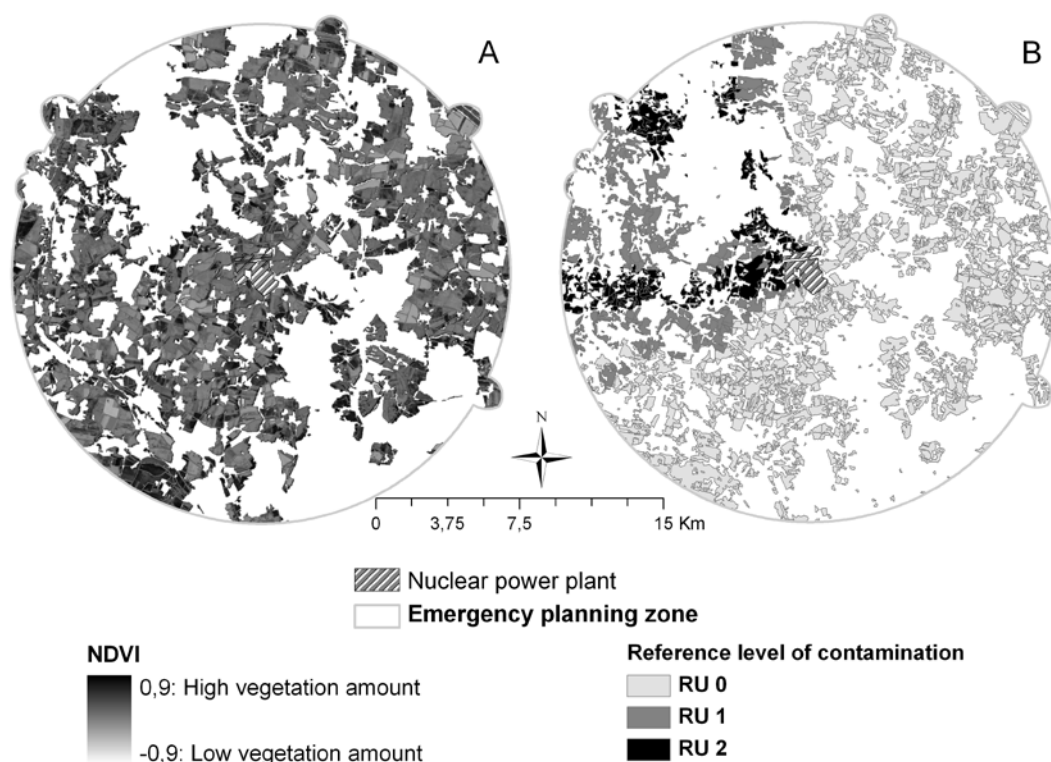


Fig. 3 - A) Amount of biomass expressed by NDVI index (only on agricultural land); B) Level of contamination: RU 0 = areas with no necessary action ($0-5\text{ kBq.m}^{-2}$), RU 1 = areas with limited action ($5\text{ kBq.m}^{-2}-3\text{ MBq.m}^{-2}$) and RU 2 = areas displaying radiation specific activity posing a Great to human health ($>3\text{ MBq.m}^{-2}$)

4 CONCLUSIONS

The presented evaluation system provides a solution to quickly estimate the quantity and distribution of the aboveground vegetation biomass (crops) in farmland and also the distribution of radioactive material deposition between the vegetation cover and soil surface in the event of radioactive contamination. The system is based on 1) the analysis of crop (vegetation cover) spatial distribution; 2) the calculation of crop production characteristics; and 3) the analysis of cover and soil surface contamination using the SARCA software under the conditions of both wet and dry deposition of radioactive material. In view of the OIL reference levels (IAEA, 1997), the lands are divided into three classes based on the level of contamination: areas with no action required, limited action, and areas displaying radiation specific activity posing a threat to human health. Functions, solution steps and examples of output were applied on the example of a simulated accident and radiation release potentially taking place in the Temelín power plant for the area of the Emergency Planning Zone. Based on the outputs obtained using the proposed methodology, it will be

possible to estimate the risks and propose action to be taken to reduce the contamination of farmland. The issue of a flexible reduction of farmland contamination is important in terms of the possible use of farmland from both the current and long-term perspective.

5 ACKNOWLEDGEMENTS

The Study was supported by projects of The Ministry of the Interior of the Czech Republic number VF20102015014 (Research on advanced methods for detection, assessment and subsequent managing of radioactive contamination) and VG20122015100 (The minimizing impact of radiological contamination on the landscape in an emergency zone of the NPP Temelín)

6 REFERENCES

- Ahamed, T., Tian, L., Zhang, Y., Ting, K. C., 2011, A review of remote sensing methods for biomass feedstock production. *Biomass and Bioenergy*, 35, 2455-2469.

- Brom, J., Procházka, J., Nedbal, V., Vinciková, H., 2013, The GIS tool used for timely spatial evaluation of radioactive contamination of agricultural soil and crops. *Bepečnost jaderné energie*, 21(59)(1/2), 48–52(in Czech).
- Brom, J., Procházka, J., Vinciková, H., Nedbal, V., 2014, SARCA, Software for Spatial Assessment of Radioactive Contamination of Agricultural Crops. University of South Bohemia, Faculty of Agriculture, České Budějovice (in Czech).
- Fumin, Z., Zaichun, Z., Yaozhong, P., Tangao, H., Jinshui Z., 2010, Application of remote sensing technology in crop acreage and yield statistical survey in China. Meeting on the Management of Statistical Information Systems (MSIS 2010), Daejeon, Republic of Korea, pp.26-29.
- IAEA (1997): Generic Assessment Procedures for Determining Protective Actions During a Reactor Accident. IAEA-TECDOC-955, IAEA, Vienna.
- Květ, J., Ondok, J.,P., Nečas, J., et Jarvis, P.,G., 1971, Methods of growth analysis. In Plant Photosynthetic Production. Manual of Methods, edited by Z., Šesták, J., Čatský, and P.,G., Jarvis (Dr. W. Junk, Publ., The Hague), pp. 343-391.
- Oetter, R., Cohen, W.B., Berterretche, M., Maiersperger, T.K., Kennedy, R.E., 2000, Land cover mapping in an agricultural setting using multiseasonal Thematic Mapper data. *Remote Sensing of Environment*, 76, 139-155.
- Paine, C.E.T., Marthews, T.R., Vogt, D.R., Purves, D., Rees, M., Hector, A., Turnbull, L.A., 2012. How to fit nonlinear plant growth models and calculate growth rates: an update for ecologists: Nonlinear plant growth models. *Methods in Ecology and Evolution*, 3, 245–256.
- Pecha, P., Hofman, R., 2007, Integration of data assimilation subsystem into environmental model of harmful substances propagation. Proceedings of International Conference on Harmonisation within Atmospheric Dispersion Modelling held in Cambridge, (Cambridge Environment Research Institut), pp.111-115.
- Pinter, P.J., Hatfield, J.L., Schepers, J.S., Barnes, E.M., Moran, M.S., Daughtry, C.S.T. and Upchurch, D.R., 2003, Remote Sensing for Crop Managament. *Photogrammetric Engineering & Remote Sensing*, Vol. 69. No. 6, 647-664.
- Priya, S., Shibasaki, R., 2001, National spatial crop yield simulation using GIS-based crop production model. *Ecological Modelling*, 135, 113–129.
- Tucker, C.J., 1979, Red and photographic infrared linear combinations for monitoring vegetation. *Remote Sens. Environ*, 8, 127-150.

Grassland sandy desertification in the Ongniud and Naiman Banners, China

Jinya Li^{a,b}, Bin Xu^{b,*}, Xiuchun Yang^b, Yunxiang Jin^b, Fen Zhao^b, Shi Chen^b, Jian Guo^b, Zhihao Qin^b, Hailong Ma^b, Lina Zhao^c

^aState Key Laboratory of Urban and Regional Ecology, Research Center for Eco-Environmental Sciences, Chinese Academy of Sciences, Beijing 100085, P.R. China;

^bKey Laboratory of Agri-informatics of the Ministry of Agriculture, Institute of Agricultural Resources and Regional Planning, Chinese Academy of Agricultural Sciences, Beijing 100081, P.R. China;

^cInstitute of Botany, Chinese Academy of Sciences, Beijing 100093, P.R. China

Jinya Li(jiyli@rcees.ac.cn); Bin Xu(xubin@caas.cn);

Xiuchun Yang(yangxiuchun@caas.cn); Yunxiang Jin(jinyunxiang83@163.com);

Fen Zhao(zhaofen198931@163.com); Shi Chen(shic11@126.com);

Jian Guo(guojianxiaobai@163.com); Zhihao Qin(qinzhihao@caas.cn);

Hailong Ma(mahailong@caas.cn); Lina Zhao(zhaoln@ibcas.ac.cn)

ABSTRACT- In the face of increasingly serious grassland sandy desertification, China has made great efforts to combat desertification, and a series of key national ecological projects have been launched. In this paper, the Naiman and Ongniud Banners were studied because they cover the main desertified grassland in Horqin. Next, a desertification classification and grading system was designed for Horqin sandy land after conducting fieldwork. Based on the Spectral Mixture Analysis (SMA) and decision-tree methods, we interpreted Landsat TM/ETM+/OLI images of the study area from four years, 1985, 1992, 2001 and 2013. Overall, the following results were obtained. The total area of desertified grassland in Naiman and Ongniud Banner increased from 5979 km² in 1985 to 9195 km² in 1992 (an increase of 53.79%) and then decreased to 7828 km² in 2001 and 6023 km² in 2013. The areas of desertified grassland with different degrees of desertification followed the same changing trends as the total desertified grassland area. The annual rates of desertified grassland growth during the three periods (1985–1992, 1992–2001 and 2001–2013) were 7.68, -1.65 and -1.92%, while the areas of severely desertified grassland were 14.12, -3.48 and -1.19%. During the study period, the coupling relationship between wind and precipitation did not benefit the reversion of grassland sandy desertification. Furthermore, the growing population, livestock and farmland area inhibited the reversion trend of grassland sandy desertification. These results show that ecological engineering measures have helped reverse desertification and have promoted the restoration of grassland vegetation.

1 INTRODUCTION

Desertification, land degradation in arid, semi-arid and part of sub-humid regions due to natural and/or anthropogenic factors, is a serious global socio-economic and environmental problem (Collado et al. 2002; Reynolds et al. 2007; Zucca et al. 2012). With a population of over 1.3 billion and limited farmland area, the efficient and sustainable management of grasslands is a survival issue in China, which has the second-largest grassland area in the world (Li et al. 2013; The Department of Animal Husbandry and Veterinary of the Ministry of Agriculture and the National Animal Husbandry and Veterinary Station 1996). In the face of increasing grassland degradation, state and local governments in China have implemented a series of grassland protection and recovery projects. Monitoring and accurate assessments of the status of and trends in grassland desertification are important for

understanding grassland desertification processes and for developing efficient environmental management strategies (Reynolds et al. 2007; Rubio and Bochet 1998).

Grassland desertification research has mainly relied on field surveys, which are expensive, labor-intensive and often limited in spatio-temporal scale (Li et al. 2013). Many methods derived from remote sensing have been used to monitor and assess grassland desertification. These methods incorporate visual interpretation methods, the vegetation index, and computer-assisted digital processing methods that are highly subjective with low efficiency (Zhang et al. 2014). Spectral mixture analysis (SMA) has been promoted as an efficient sub-pixel classification for deriving coverage information from multispectral and hyperspectral images in arid and semi-arid areas (Elmore et al. 2000; García Haro et al. 2005; Okin 2007; Somers and Asner 2014). In addition, SMA is used to

transform radiation or reflectance data into a few dominant end member fractions, and the derivation of vegetation coverage and bare-sand ratios is a prerequisite for the quantitative evaluation of grassland desertification.

The objectives of this paper are 1) to design a grassland desertification and grading system that conforms to the situation occurring on Horqin sandy land after conducting seminars and demonstration projects for experts and field survey and 2) to monitor and analyze the dynamics of grassland desertification in representative counties containing Horqin sandy land in the last 30 years.

2 MATERIALS AND METHODS

2.1 Study site

The study area is located in Naiman and Ongniud Banners, covering a total area of 20,058 km² from a longitude of 117°49'E to 121°35'E and a latitude of 42°15'N to 38°10'N. This area is located in the southwestern portion of the Horqin sandy land in Inner Mongolia, northern China.

This site is typical of an agro-pastoral transition zone in a temperate continental semiarid monsoonal climate with an annual mean precipitation of 368 mm and an annual mean potential evaporation of 1935 to 2197 mm. The annual mean temperature is 6–6.5°C.

2.2 Data acquisition and pre-processing

The successful launch of Landsat8 further extended the 40-year Landsat record by at least 5 years. This extension is very important for global change research (Roy et al. 2014). Based on the data quality, precipitation and our goal of analyzing the influences of implementing a series of ecological protection and recovery policies for grassland desertification before and after 2000, we selected the Landsat Thematic Mapper (TM5) scenes that were acquired in 1985, 1992 and part of 2001, a portion of the Landsat Enhanced Thematic Mapper plus (ETM+7) scenes that were

acquired in 2001 and the Landsat Operational Land Imager (OLI) scenes that were acquired in 2013. With a resolution of 30 m, the time series Landsat images were acquired during the region's typical growing season (during July and early September) and were downloaded from the United States Geological Survey (USGS) web site (<http://glovis.usgs.gov>) at no cost. Geometric correction, atmospheric correction and other image processing operations were performed by using ENVI 5.1 (ITT Exelis Visual Information Solutions Inc.).

Other study area data, including annual land-use maps, meteorological data (rainfall, temperature, etc.), socioeconomic data (population, cattle stocks, etc.), grassland type and soil type, were collected and collated.

2.3 Grading system for Horqin sandy desertification

Dispersed, patchy vegetation cover and sand sheets are the main landscape characteristics of areas undergoing grassland desertification and serve as good visual indicators of environmental changes and the severity of desertification (Diouf and Lambin 2001; Wang et al. 2012). Based on relevant classification criteria, studies on grassland desertification and China's national standard "parameters for degradation, sandification and salification of rangelands" (GB19377-2003), we used vegetation coverage and the bare-sand ratio as the main criteria for deriving the desertification status. Next, we combined field inspection and verification data with expert opinions to determine the appropriate gradation system for using remote sensing to determine grassland desertification in Horqin (Table 1). In addition, we classified the land cover of the study area into the ten following categories (shrubland was treated as grassland): farmland, forest, human settlements, salinization land, water, nondesertified grassland (non-DG), slightly desertified grassland (SIDG), moderately desertified grassland (MDG), severely desertified grassland (SeDG) and others.

Table 1. Remote sensing grading system of grassland desertification in Horqin.

Grassland desertification intensity classification	Vegetation community characteristics		Bare-sand ratio (%)	Geomorphologic features
	Vegetation composition	Vegetation coverage(%)		
SIDG	Psammophytes become the main accompanying species.	45–60	15–30	Relatively moderate sand, fixed sand dunes.
MDG	Psammophytes become the dominant species.	25–45	30–50	Moderate sand, small blowout pits or semi-fixed sand dunes.
SeDG	Vegetation is very sparse, only a few psammophytes remaining.	<25	>50	Medium and large sand dunes, large blowout pits, semi-mobile or mobile sand dunes.

2.4 Grassland desertification extraction method

In remote sensing images of arid and semiarid environments, especially in areas undergoing desertification, the pixel usually contains several objects (Dawelbait and Morari 2012). We selected the Linear Spectral Mixture Model (LSMM), an SMA that is widely used due to its simplicity, reasonable level of effectiveness and interpretability (Bioucas-Dias et al. 2012; Collado et al. 2002; Elmore et al. 2000; Yang et al. 2012), to calculate the proportion of each target surface feature within a pixel. In an LSMM, the reflectance of each pixel at each spectral band is considered to be a linear combination of the reflectance of each end-member and its relative abundance, which is described as follows (Eq. 1):

$$\rho(\lambda_i) = \sum_{j=1}^m F_j \rho_j(\lambda_i) + \varepsilon(\lambda_i) \quad (1)$$

here $j=1, 2, \dots, m$ is the pixel component (end-member); $i=1, 2, \dots, n$ is the spectral band; $m \leq n+1$; $\rho(\lambda_i)$ is the reflectance of the mixed pixels for each band i ; $\rho_j(\lambda_i)$ is the reflectance of the end-member j at band i ; F_j refers to the abundance of end-member j in the pixel (a parameter to be estimated); and $\varepsilon(\lambda_i)$ is the difference between the actual and modeled reflectance. In addition, F_j represents the best-fit coefficient that minimizes the root-mean-squared (RMS) error (Eq. 2).

$$RMS = \sqrt{(\sum_{i=1}^n \varepsilon^2(\lambda_i))/n} \quad (2)$$

where n is the number of bands and $\varepsilon(\lambda_i)$ is the residual term at band i .

The derived fractions of end-members are often subject to the unity constraint, which is derived as follows (Eq. 3):

$$\sum_{j=1}^m F_j = 1 \quad (3)$$

The key to successful LSMM is the appropriate selection of the end-members that are chosen to represent surface components (Tompkins et al. 1997). In this study, we conducted a comprehensive field investigation to identify the optimal/most representative surface types and to find preferable locations for the development of a spectral library from the Landsat images. Based on the field investigation, the “pure” spectral end-members of vegetation, bare sand and bare soil were extracted using the PPI (Pixel Pure Index), which is a common approach for end-member selection that is available through ENVI (Jiapaer et al. 2011; Pan and Li 2013). Next, these end-members were input into a LSMM algorithm.

The number of the end-members was constrained by the dimensionality of the satellite images (Theseira et al. 2002). To focus on the desertification-dominated information and to simplify the analysis process of the

LSMM, the Normalized Difference Infrared Index (NDII) was used to mask the farmland, while the Tasseled Cap (TC), band5 and NDVI were used to mask the forest, the Modified Normalized Differential Water Index was used to mask the water area, and the TC1 (the first band of TC) and MNDWI were used to mask the salinization land. Next, the masked image was placed in the LSMM algorithm, and a grading desertification map was produced from the bare sand fraction map by using the decision-tree method according to the grading system (Table 1).

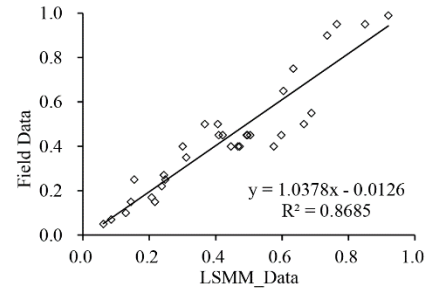


Figure 1. The linear regression relationship between the field-measured and LSMM-estimated vegetation fraction in 2013.

2.5 Field survey

To establish interpretation symbols and a grading system that would be more consistent with the actual conditions of the Horqin sandy land, a field survey was conducted between August 5 and August 20, 2013. In this study, 66 plots (size 1×1 m for herbs or stunted brushwood plots, and 10×10 m for shrub plots) were selected. After excluding the plots (plots with bare sand information) used for end-member selection and without bare sand information or a vegetation fraction (those used to establish interpretation symbols), 32 plots remained for validation. The accuracy was estimated by using a linear regression between the field vegetation cover in each plot and the pixel values from the vegetation fraction image. The regression result (presented in Figure 1) showed that the correlation was significant, which indicated satisfactory accuracy.

3 RESULTS

3.1 Status of grassland sandy desertification during four periods

The desertified grassland was mainly distributed northeast of Ongniud and northwest of Naiman, which is the main grassland desertification area in the Horqin sandy land. The statistical results in Table 2 show that the Total DG covered approximately 35% of the study area, increasing from 5979 km² in 1985 to 9195 km² in 1992 (an increase of 53.79%) before gradually decreasing to 6023 km² in 2013. The area of SeDG and MDG peaked in 1992, exhibiting the same trend as the total DG. In contrast, the SiDG peaked in 2001. Among

other categories, the area of farmland increased steadily from 2574 km² in 1985 to 5807 km² in 2013 (an increase of 125.60%), while the area of human settlement increased from 43 km² in 1985 to 332 km² in 2013 (an increase of 677.78%).

3.2 Annual rate

The annual change rate was calculated and is presented in Table 3. The annual rates of MDG, SeDG and Total DG growth between 1985 and 1992 were all positive. These values became negative during the other two periods, which suggested an overall grassland desertification development trend between 1985 and 1992 and reversion trends between 1992 and 2001 and between 2001-2013. The annual rate of reduction in the MDG area was 0.94% between 1992 and 2001, with a higher reduction rate occurring during the subsequent period with a rate of 4.07%. The SeDG area significantly increased between 1985 and 1992 and decreased during the two subsequent periods, with reduction rates of 3.48% and 1.19%. Farmland and Human settlement rapidly increased in the area during the three periods, which suggested that the pressure on land resources by humans increased.

4 DISCUSSION

Grassland desertification is a typical form of degradation that is induced by climate change and anthropogenic factors and could be influenced at the

regional landscape level (Dawelbait and Morari 2012; Seifan 2009; Xue et al. 2013). Horqin sandy land is located in the east section of the interlaced agro-pastoral zone of northern China at the edge of the monsoon climate zone. Thus, this area displays environmental sensitivity and ecological fragility that are typical of this region (Zhao et al. 2014).

Temperature and precipitation are two important climate factors that affect grasslands in the study area (Wang et al. 2012; Zhao 2003). During the study period, the annual mean temperature raised with fluctuations between 1985 and 2002, then decreased between 2002 and 2012. In addition, the annual precipitation decreased between 1985 and 2006 and increased between 2006 and 2012. The upward trend in annual temperature and the downward trend in annual precipitation created a warm and dry climate for the period of 1985-2006 (Figure 2), which likely affected the growth of vegetation. These effects are especially strong in the MDG and SeDG areas with poor water-holding capacities and low soil nutrient contents, which exacerbated grassland desertification processes. When the annual precipitation increased and the annual temperature decreased between 2006 and 2012, the soil was likely more stable and more difficult to erode because as the soil was less exposed. Under these conditions, soil moisture, biomass and biodiversity would increase, which would result in more vegetation (Ge et al. 2013).

Table 2. Changes in the areas of each major category from 1985 to 2013 in Ongniud Naiman Banners (area: km²; proportion: %).

Land types	1985		1992		2001		2013	
	Area	Proportion	Area	Proportion	Area	Proportion	Area	Proportion
SIDG	2255	11.24	2883	14.37	2902	14.47	2619	13.06
MDG	1852	9.23	2590	12.91	2371	11.82	1214	6.05
SeDG	1872	9.33	3723	18.56	2555	12.74	2189	10.91
Total DG	5979	29.81	9195	45.84	7828	39.03	6023	30.03
Non-DG	10226	50.98	6830	34.05	6757	33.69	7569	37.74
Farmland	2574	12.83	3284	16.37	4795	23.91	5807	28.95
Forest	113	0.56	67	0.33	68	0.34	147	0.74
Water	305	1.52	292	1.46	145	0.72	60	0.30
Salinization land	621	3.10	187	0.93	222	1.11	48	0.24
Human settlement	43	0.21	57	0.29	124	0.62	332	1.66
Others	198	0.99	146	0.73	117	0.58	74	0.37

Table 3. Annual change rates for each major category in the Ongniud and Naiman Banners during different periods. Positive values represent an increase and negative values represent a decrease. Unit: %.

	SIDG	MDG	SeDG	Total DG	Non -DG	Farmland	Forest	Water	Salinization Land	Human settlement
1985-1992	3.98	5.69	14.12	7.68	-4.74	3.94	-5.84	-0.59	-9.99	4.93
1992-2001	0.07	-0.94	-3.48	-1.65	-0.12	5.11	0.21	-5.59	2.12	12.83
2001-2013	-0.81	-4.07	-1.19	-1.92	1.00	1.76	9.76	-4.87	-6.54	14.02

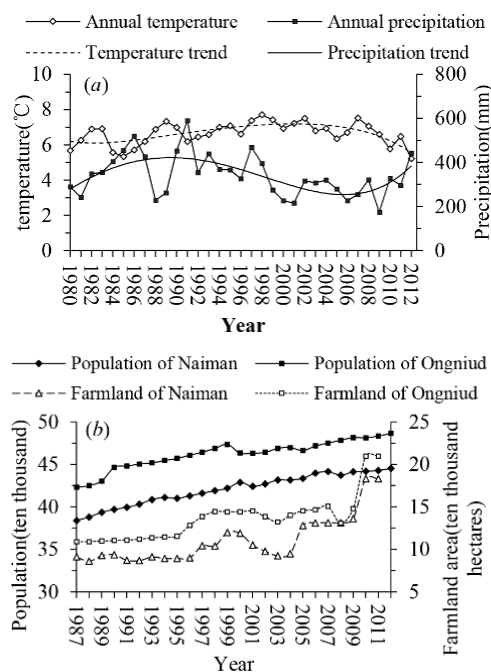


Figure 2. The changes in the main climate and humanity factors in the study area. In Figure (A), only the Ongniud data were used.

The vulnerability of grasslands to desertification was a function of both anthropogenic pressures and climate change. Between 1985 and 1992, grassland desertification was exacerbated by excessive land use activities and warm and dry conditions. After this period, the state and local governments in this region considered grassland desertification control and ecological restoration as highly important. Projects were implemented that adjusted the land use structure, including Grain for Green Projects, the Beijing and Tianjin Sandstorm Source Treatment Project, the Three-North Shelterbelt Project, the financial subsidies for grassland protection, and many other policies and measures to address grassland degradation. Thereafter, despite the overall trends in the climate conditions that were not conducive to reversing desertification and the great pressure from the increasing population and economic development, desertification was reversed between 1992 and 2001. This reverse was maintained as the warm and dry conditions became less severe and increased input from governments occurred between 2001 and 2013.

5 CONCLUSIONS

Monitoring and assessing grassland desertification is helpful and valuable for developing efficient environmental management strategies (Li et al. 2013). In this paper, satellite data were shown to be useful for long-term grassland desertification monitoring.

However, it is difficult to precisely monitor grassland desertification because remote sensing images only offer a snapshot of the conditions. In addition, vegetation growth varies according to climate conditions and other factors. Thus, the information extraction method and the assessment indicators must be further perfected.

6 ACKNOWLEDGEMENTS

This work was jointly supported by the National Natural Science Foundation of China (NSFC, 31372354), the International Science and Technology Cooperation Program of China under Grant 2013DFR30760, Grassland Monitoring and Supervision Center Ministry of Agriculture of China under Grant 425-1, and the Centre of Supervision Management of Grassland, Ministry of Agriculture, China.

7 REFERENCES

- Bioucas-Dias, J.E.M., Plaza, A., Dobigeon, N., Parente, M., Du, Q., Gader, P., and Chanussot, J. 2012. Hyperspectral unmixing overview: Geometrical, statistical, and sparse regression-based approaches. *Selected Topics in Applied Earth Observations and Remote Sensing, IEEE Journal of*, **5**, 354-379
- Collado, A.D., Chuvieco, E., and Camarasa, A. 2002. Satellite remote sensing analysis to monitor desertification processes in the crop-rangeland boundary of Argentina. *Journal of Arid Environments*, **52**, 121-133
- Dawelbait, M., and Morari, F. 2012. Monitoring desertification in a Savannah region in Sudan using Landsat images and spectral mixture analysis. *Journal of Arid Environments*, **80**, 45-55
- Diouf, A., and Lambin, E.F. 2001. Monitoring land-cover changes in semi-arid regions: remote sensing data and field observations in the Ferlo, Senegal. *Journal of Arid Environments*, **48**, 129-148
- Elmore, A.J., Mustard, J.F., Manning, S.J., and Lobell, D.B. 2000. Quantifying Vegetation Change in Semiarid Environments: Precision and Accuracy of Spectral Mixture Analysis and the Normalized Difference Vegetation Index. *Remote Sensing of Environment*, **73**, 87-102
- García Haro, F.J., Sommer, S., and Kemper, T. 2005. A new tool for variable multiple endmember spectral mixture analysis (VMESMA). *International Journal of Remote Sensing*, **26**, 2135-2162
- Ge, X., Ni, J., Li, Z., Hu, R., Ming, X., and Ye, Q. 2013. Quantifying the synergistic effect of the precipitation and land use on sandy desertification at county level: A case study in Naiman Banner, northern China. *Journal of Environmental Management*, **123**, 34-41

- Jiapaer, G., Chen, X., and Bao, A. 2011. A comparison of methods for estimating fractional vegetation cover in arid regions. *Agricultural And Forest Meteorology*, **151**, 1698-1710
- Li, J.Y., Yang, X.C., Jin, Y.X., Yang, Z., Huang, W.G., Zhao, L.N., Gao, T., Yu, H.D., Ma, H.L., Qin, Z.H., and Xu, B. 2013. Monitoring and analysis of grassland desertification dynamics using Landsat images in Ningxia, China. *Remote Sensing of Environment*, **138**, 19-26
- Pan, J., and Li, T. 2013. Extracting desertification from Landsat TM imagery based on spectral mixture analysis and Albedo-Vegetation feature space. *Natural Hazards*, 1-13
- Reynolds, J.F., Smith, D.M.S., Lambin, E.F., Turner II, B.L., Mortimore, M., Batterbury, S.P.J., Downing, T.E., Dowlatabadi, H., Fern A Ndez, R.J., Herrick, J.E., and Others 2007. Global desertification: building a science for dryland development. *Science*, **316**, 847-851
- Roy, D.P., Wulder, M.A., Loveland, T.R., Allen, R.G., Anderson, M.C., Helder, D., Irons, J.R., Johnson, D.M., Kennedy, R., Scambos, T.A., and Others 2014. Landsat-8: Science and product vision for terrestrial global change research. *Remote Sensing of Environment*, **145**, 154-172
- Rubio, J.L., and Bochet, E. 1998. Desertification indicators as diagnosis criteria for desertification risk assessment in Europe. *Journal of Arid Environments*, **39**, 113-120
- Seifan, M. 2009. Long-term effects of anthropogenic activities on semi-arid sand dunes. *Journal of Arid Environments*, **73**, 332-337
- Somers, B., and Asner, G.P. 2014. Tree species mapping in tropical forests using multi-temporal imaging spectroscopy: Wavelength adaptive spectral mixture analysis. *International Journal of Applied Earth Observation and Geoinformation*, **31**, 57-66
- The Department of Animal Husbandry and Veterinary of the Ministry of Agriculture and the National Animal Husbandry and Veterinary Station. 1996. Chinese grassland resources. Beijing: China Science and Technology Press
- Theseira, M.A., Thomas, G., and Sannier, C.A.D. 2002. An evaluation of spectral mixture modelling applied to a semi-arid environment. *International Journal of Remote Sensing*, **23**, 687-700
- Tompkins, S., Mustard, J.F., Pieters, C.M., and Forsyth, D.W. 1997. Optimization of endmembers for spectral mixture analysis. *Remote Sensing of Environment*, **59**, 472-489
- Wang, T., Yan, C.Z., Song, X., and Xie, J.L. 2012. Monitoring recent trends in the area of aeolian desertified land using Landsat images in China's Xinjiang region. *Isprs Journal of Photogrammetry And Remote Sensing*, **68**, 184-190
- Xue, Z., Qin, Z., Li, H., Ding, G., and Meng, X. 2013. Evaluation of aeolian desertification from 1975 to 2010 and its causes in northwest Shanxi Province, China. *Global And Planetary Change*, **107**, 102-108
- Yang, J., Weisberg, P.J., and Bristow, N.A. 2012. Landsat remote sensing approaches for monitoring long-term tree cover dynamics in semi-arid woodlands: Comparison of vegetation indices and spectral mixture analysis. *Remote Sensing of Environment*, **119**, 62-71
- Zhang, X., Shang, K., Cen, Y., Shuai, T., and Sun, Y.L. 2014. Estimating ecological indicators of karst rocky desertification by linear spectral unmixing method. *International Journal of Applied Earth Observation and Geoinformation*, **31**, 86-94
- Zhao, H.L. 2003. Desertification processes and its restoration mechanisms in the Horqin sand land. Beijing: Ocean Press
- Zhao, H.L., Li, J., Liu, R.T., Zhou, R.L., Qu, H., and Pan, C.C. 2014. Effects of desertification on temporal and spatial distribution of soil macroarthropods in Horqin sandy grassland, Inner Mongolia. *Geoderma*, **223**, 62-67
- Zucca, C., Peruta, R.D., Salvia, R., Sommer, S., and Cherlet, M. 2012. Towards a World Desertification Atlas. Relating and selecting indicators and data sets to represent complex issues. *Ecological Indicators*, **15**, 157-170

Vegetation mapping with NASA's Terra/ASTER stereo images

Amit Mushkin^{1,2}, Alan R. Gillespie², Van Kane³, Jonathan Kane³

1. Geological Survey of Israel, Jerusalem, Israel

2. Department of Earth and Space Sciences, Univ. of Washington, Seattle WA, USA

3. School of Environmental and Forest Sciences, Univ. of Washington, Seattle WA, USA

mushkin@uw.edu, arg3@uw.edu, vkane@uw.edu, jontkane@uw.edu

ABSTRACT - Multispectral images acquired by Terra's sensors are a resource for mapping Earth's surface properties for scientific investigations and environmental monitoring. Terra products now include a seamless global DEM produced from ASTER's 15 m/pixel stereo images, which have been routinely acquired since March 2000. ASTER's stereo images can also be used for mapping <m-scale surface roughness, a fundamental but typically unresolved property of Earth's land surfaces that is significant for a wide range of surface-process studies as well as for remote-sensing applications. Ratio images between ASTER's stereo channels provide a robust measure of the deviation from Lambertian surface reflection caused by unresolved shadows cast by sub-pixel roughness elements. Here, we examine the utility of ASTER stereo ratio images (3B/3N) as a quantitative proxy for estimating forest canopy structure. We focus on a xeric forest in northwestern USA and demonstrate that ASTER 3B/3N values effectively capture the variability in forest tree heights (0-40 m) as measured with ~8 pulse/m² airborne LiDAR data for open- and closed-canopy tree stands. ASTER 3B/3N images provide a new tool for addressing common ambiguities in 'conventional' spectrally based (e.g., NDVI) mapping of forests from space.

1 INTRODUCTION

Measuring vegetation state and quantifying its change in response to climatic changes and mankind's activities (e.g., Froking et al., 2009; Bergen et al., 2009) provide prime motivators for quantitative remote-sensing studies of Earth's surface. In this context, data from spaceborne sensors continue to be a pivotal resource (NRC, 2007) because of their unique spatial perspective, relatively frequent sampling intervals and readily accessible historic coverage spanning the past few decades.

The standard approaches currently utilized for measuring vegetation state from space are largely based on spectral recognition of chlorophyll absorption, or its absence, in green leaves. Vegetation indices such as NDVI (Tucker, 1979) and/or the Tasseled Cap Transformation (TCT: Kauth and Thomas, 1976) can provide effective measures for vegetation state. Yet, quantitative interpretation of the spatial variability and/or change over time of these indices may become ambiguous due to factors such as atmospheric effects, soil background, chlorophyll saturation, and low or non-photosynthetic vegetation (NPV). For example, robust characterization of mature through old-growth forests from space remains an often challenging task because these forest stages are differentiated primarily by roughness variability within their canopies (Cohen and Spies, 1992) rather than by predictable variations in their spectral properties at the typical pixel-scale of spaceborne imagers.

Spectral mixture analysis (SMA) provides a widely applicable approach for reducing ambiguities in spectrally derived vegetation indices (Adams and Gillespie, 2006) and for obtaining complementary information about canopy structure (Gillespie et al., 2006). However, SMA is also sensitive to atmospheric effects and non-unique spectral properties of common sub-pixel scene elements. Radar-based spaceborne measures of vegetation cover (e.g., Evans and Smith, 1991; Lardeaux et al., 2008), height and biomass (e.g., Simard et al., 2007) also offer a promising tool for reducing ambiguities in spectral-based vegetation indices. However, saturation problems in closed-canopy forests (Saatchi et al., 2007) and additional complications such as soil moisture effects appear to impede broad and standard application of such radar techniques.

High-resolution airborne LiDAR has been established as an effective approach for measuring canopy roughness as well as vegetation height and structure (e.g., Lefsky et al., 2002; Hudak et al., 2009; Kane et al. 2010, 2011) and likely offers the most direct approach for remotely measuring such vegetation parameters. And yet, limited spatial coverage, infrequent sampling intervals and the high costs associated with acquiring airborne LiDAR data currently limit its utilization for large, systematic global-scale studies.

Here, we test the utility of a simple and robust space-based measure of unresolved shadows (Fig. 1) (Mushkin and Gillespie, 2005; 2006; 2010) as a new mapping approach for canopy roughness and tree

heights in open- and closed-canopy forest stands. We focus on a 16 km² subset of the Deschutes National forest in Oregon USA (Fig. 2) where LiDAR data were used to measure canopy coverage and structure ‘directly’ (Figs. 3-5), and ratio images between Terra/ASTER’s 15 m/pixel stereo channels were used to map sub-pixel shadow variations (integrated over all sub-pixel scales) (Fig. 6). We use the LiDAR data as ‘ground truth’ and evaluate the correlation between sub-pixel shadowing as measured with stereo images from space and canopy structure (Fig. 7).

2 METHODOLOGY

2.1 ASTER Stereo Ratio images

ASTER is a multispectral sensor (Yamaguchi et al., 1998) on board the Terra satellite, continuously acquiring ‘on-demand’ data since early 2000. ASTER images are ~60 × 60 km and consist of 14 spectral channels between 0.56 and 11.5 μm. ASTER’s stereoscopic imaging capability is facilitated by a backwards-pointing channel (3B) of 15-m data acquired at the same wavelengths and resolution as the nadir channel (3N) at ~0.81 μm, but ~55 seconds later resulting in a 27.6° stereo angle aligned with Terra’s NNE-SSW track (Fig. 1). 3B data were primarily designed for independent generation of ~30-m DEM’s now available as a validated standard ASTER product (<http://asterweb.jpl.nasa.gov/gdem.asp>), and are included with nearly all ASTER level-1B data sets.

Variations in the ratio between surface-reflected solar radiance measured from two view angles at nearly the same time is primarily a function the difference between the amount of sub-pixel shadows that are ‘visible’ from the two view angles (Fig. 1). Because ASTER’s 3B and 3N channels are acquired at the same wavelength and through ~the same atmosphere their ratio is largely independent of surface composition and atmospheric effects (Mushkin and Gillespie, 2010). Accordingly, the ratio between ASTER’s stereo channels can be used as a proxy for the roughness of bare surfaces with the implied assumption that roughness and shadowing on the surface are correlated (Mushkin and Gillespie, 2005; 2010). ASTER’s 3B/3N ratio can also provide a calibrated proxy for vegetation cover in semi-arid plains (Mushkin et al., 2009).

2.2 LiDAR Data and Processing

LiDAR data were acquired by Watershed Sciences, Inc. (now Quantum Spatial, Inc.) in July and August 2010 using Leica ALS50 Phase II and ALS60 sensors with an average pulse density of 8.6 pulses m⁻². We used the USDA Forest Service Fusion v3.42 software (<http://forsys.cfr.washington.edu/fusion.html>) to generate a 1 m² canopy-surface model, which

assigned each grid cell the value of the highest LiDAR return elevation within a given grid cell.

2.3 Study Site

The study site is located within the Deschutes National Forest in western Oregon, USA, ~2 km east of the intersection of HWY 97 and HWY 58 (Fig. 2). Ponderosa pine (*Pinus ponderosa*) and Lodgepole pine (*Pinus contorta*) are common within this region. Most of this xeric forest has been harvested in the past and current stands were generally planted and thinned to different densities. Based on tree heights, a variety of stand ages are present in the 16 km² area we examined, in which terrain slopes are <3° so that topographic shading has a minimal effect on canopy self-shadowing.

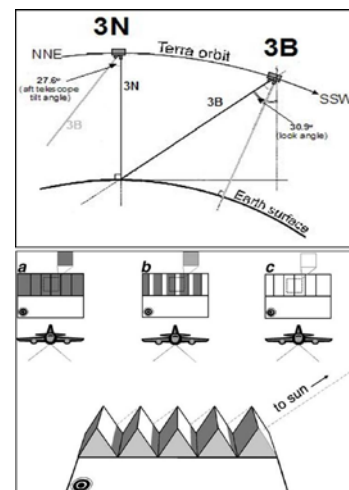


Figure 1. Illustration of the ASTER 3B/3N stereo viewing geometry (top) and the effects of viewing geometry on DN values (bottom). The nadir view (b) will have a lower DN value than the same surface viewed down-sun (c) because shadows become hidden behind sunlit surface elements. The same surface in an up-sun view (a) will appear darker because sunlit elements become hidden from the sensor. DN values for the smooth surface in the foreground (no shadows) do not change with view angle (i.e., Lambertian reflection). The sun in all cases is in the same location to the right.



Figure 2. Study site in the central Oregon, USA.

3 RESULTS

3.1 LiDAR-based Forest Classification

Four main classes of forest stands occur in the study area: ‘clear cut’ (A), ‘replanted sparse’ (B), ‘replanted dense’ (C) and ‘legacy’ (D) (Figs 3,4). Using a 1 m/pixel canopy surface model derived from the LiDAR data (Fig. 3) we characterized the variability in % canopy coverage and the size-frequency distribution of trees within 3-4 plots belonging to classes B, C and D (Fig. 5).

‘Clear cuts’ exhibit low canopy cover (<10%) and few, well-spaced legacy trees with a height mode of ~27 m. For ‘replanted sparse’, canopy cover increases from <20 to ~40% as tree-height mode increases from ~3 to 5 m. For ‘replanted dense’, tree-height mode increases from ~3 to 14 m while canopy cover remains ~constant at 70-80%. For ‘legacy’ plots, canopy cover increases from 45 to 70 % as tree-height mode decreases from ~28 to 20 m (Fig. 5). This complex co-variance of % canopy cover and canopy structure suggests that independent measures of both attributes may be required to capture the variability amongst the examined forest stands using satellite data.

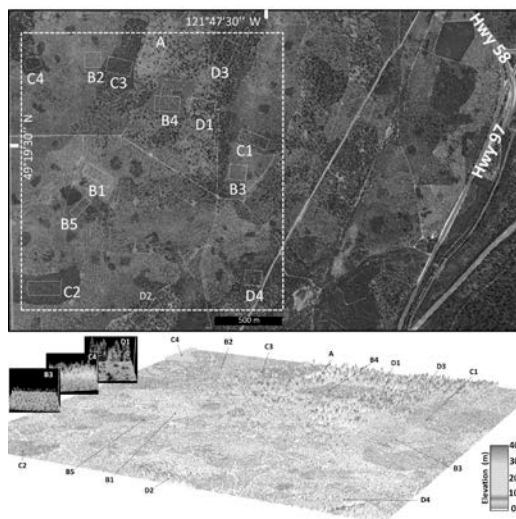


Figure 3. Google Earth image of the study site (top) and a 1 m/pixel canopy surface model (bottom) for the 4 × 4 km area boxed in white (See Fig. S1 for color version). Insets are point-cloud rendering of the LiDAR data used for the surface model. The different classes of forest stands are marked in both images.

3.2 ASTER-based NDVI and Sub-pixel Shadow images

ASTER data acquired Sep. 26 2011 were used to produce 15 m/pixel NDVI and 3B/3N ratio images for the study site (Fig. 6). Whereas NDVI responds primarily to chlorophyll abundance on the surface

3B/3N ratios respond primarily to sub-pixel shadowing (Fig. 1), which in forested terrains is expected to vary as a function of canopy roughness/structure (Gillespie et al., 2006). Below, we compare between ASTER-derived NDVI and 3B/3N values and the canopy-surface characteristics of the different forest stands as measured with LiDAR data.

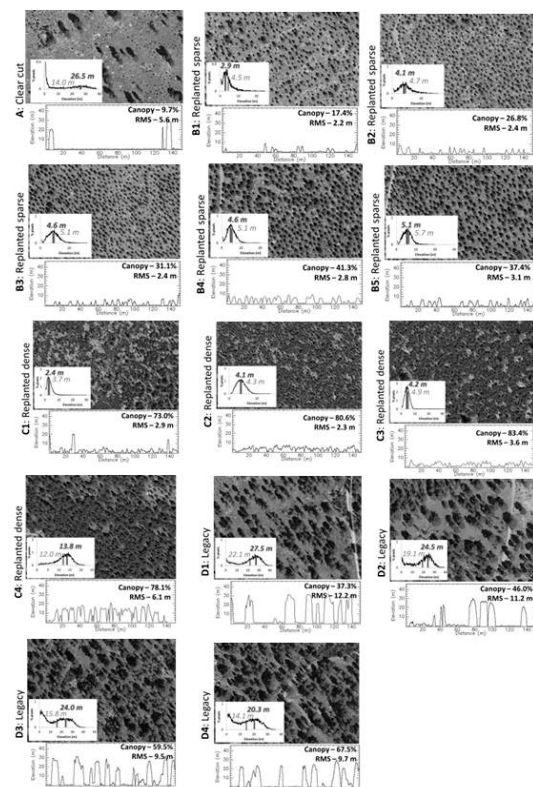


Figure 4. Google Earth images and elevation profiles extracted from the canopy surface model. Insets are histograms for non-ground (i.e. elevation ≥ 0.5 m) LiDAR pixels with tree-height mean (grey) and mode (black). ‘Replanted sparse’ and ‘replanted dense’ display uni-modal tree-height distributions and ‘legacy’ and ‘clear cut’ display bi-modal distributions.

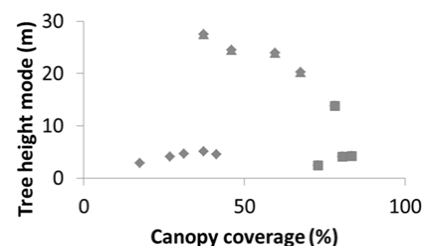


Figure 5. Complex co-variance between tree heights and canopy coverage for ‘replanted sparse’ (diamonds), ‘replanted dense’ (squares) and ‘legacy’ stands (stars)

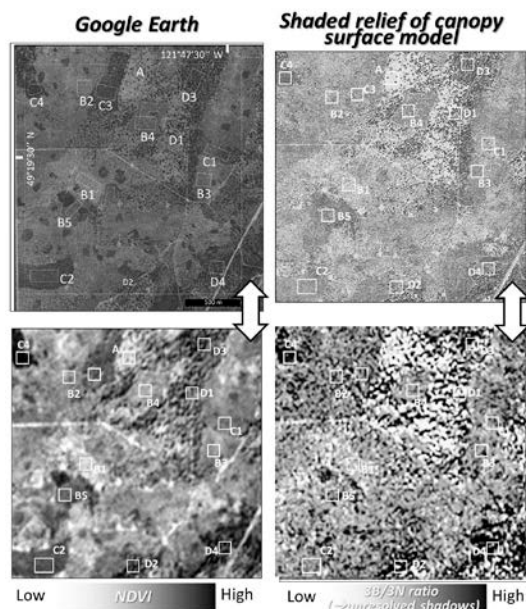


Figure 6. ASTER-derived 15 m/pixel NDVI displays a 1st-order resemblance to a high-resolution panchromatic aerial photo (Google Earth) of the study site. The ASTER 3B/3N 15 m/pixel ratio image, which corresponds to variation in the amount of unresolved shadows in each pixel, displays a 1st-order resemblance to a 1 m/pixel shaded relief image of the canopy-surface model. Solar illumination for the shaded relief image was set to resemble the sun's position at the time of the ASTER data acquisition.

4 DISCUSSION

Spatial variability of grey levels in the ASTER-derived NDVI image of the study area exhibits a 1st order resemblance to the high-resolution Google Earth (GE) image (Fig. 6). For example, the dark plots C2, C3 and D3 in GE correspond to high NDVI values and the light toned 'clear cut' plot (A) along the northern limit of the study area as well as the bare roads crossing the study area display low NDVI values. This 1st order correspondence between the NDVI and GE images likely reflects their dependency on chlorophyll abundance. NDVI values are also well-correlated with % canopy cover in the different plots examined (Fig. 7) and it thus appears that NDVI in such settings can provide a fairly robust estimate for % canopy cover.

However, as indicated by the LiDAR data (Fig. 5) we find that % canopy cover is a poor predictor for tree-height variability (Fig. 7). For example, 'replanted sparse' plots, which have trees of similar heights, display distinct NDVI values and 'replanted dense', which have significantly different tree heights, display similar NDVI values (Fig. 7).

This ambiguity in inference of canopy structure from the GE and/or the NDVI images is also apparent in the 1 m/pixel canopy surface shaded relief image in figure 7. For example, B2 and C3, which ~similar tree-height modes of 2.3 and 3.6 m, respectively, display distinct GE and/or NDVI grey-levels whereas their shading in the shaded relief image of the canopy surface model is similar.

Spatial variability of grey levels across the ASTER 3B/3N image and the canopy-surface (LiDAR) shaded relief image display a 1st order resemblance (Fig. 6). This similarity between 15 m/pixel 3B/3N ratios and the 1 m/pixel shading of the canopy structure suggests that the former are largely dependent on unresolved shadows at 1-15 m scales. We also find that ASTER's 3B/3N ratios are positively correlated with tree height modes for 'replanted sparse' and 'replanted dense' forest stands (Fig. 7). For 'legacy' stands we find that 3B/3N ratios are inversely correlated to tree height mode.

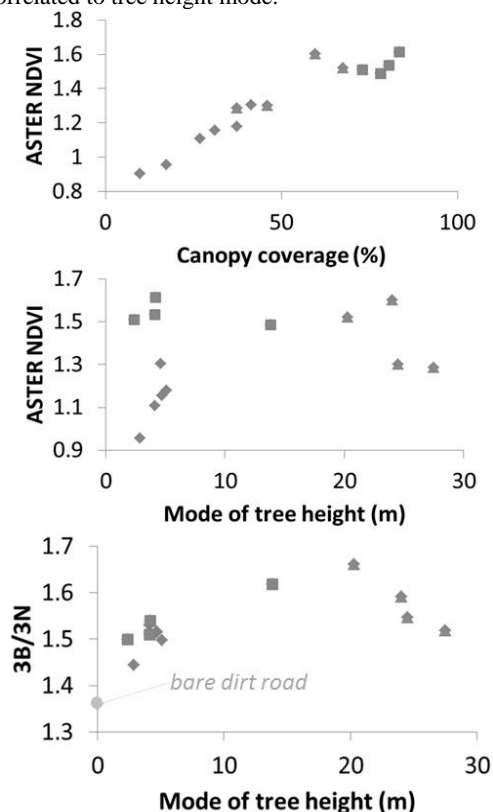


Figure 7. NDVI is a robust predictor for canopy cover (top) but a poor predictor for tree heights (center). ASTER 3B/3N ratios offer a robust predictor for tree height (bottom) provided that 'replanted sparse' (diamonds) and 'replanted dense' (squares) stands can be independently distinguished from 'legacy' stands (stars).

The positive correlation between 3B/3N ratios and tree heights for 'replanted sparse' and 'replanted dense' stands implies that the amounts of unresolved shadows at the ASTER 15 m/pixel scale increase as these stands mature and trees become higher. Unresolved shadowing likely increases in these stands because more height variability (i.e., roughness) is introduced by the differential growth of individual trees in the stand. The inverse correlation between tree height and unresolved shadows for 'legacy' stands may be associated in part with an upper limit in the heights that trees can attain in this forest (~25-30 m). As more trees reach this maximum height canopy roughness and 3B/3N ratios would be expected to decrease.

Our results indicate that 3B/3N ratio values can be used to resolve ambiguities in tree-height inference from NDVI (Fig. 7). We therefore propose that ASTER-derived 3B/3N ratios and tree-height estimates derived from them can be used as a simple and widely applicable new approach for quantitatively evaluating biomass and relative age variability amongst forest stands from space.

5 REFERENCES

- Adams, J. B., and Gillespie, A. R., 2006. Remote Sensing of Landscapes with Spectral Images. Cambridge University Press, Cambridge UK.
- Bergen, K. M., Goetz, S. J., Dubayah, R. O., Henebry, G. M., Hunsaker, C. T., Imhoff, M. L., Nelson, R. F., Parker, G. G., and Radeloff, V. C., 2009. Remote sensing of vegetation 3-D structure for biodiversity and habitat: Review and implications for lidar and radar spaceborne missions. *Journal of Geophysical Research-Biogeosciences* 114, G00E06, doi:10.1029/2008JG000883.
- Cohen, W.B., and Spies, T.A., 1992. Estimating structural attributes of Douglas-fir western hemlock forest stands from Landsat and SPOT imagery. *Remote Sensing of Environment* 41, 1-17.
- Evans, D. L., and Smith, M. O., 1991. Separation of vegetation and rock signatures in thematic mapper and polarimetric SAR images. *Remote Sensing of Environment* 37(1), 63-75.
- Frolking, S., Palace, M. W., Clark, D. B., Chambers, J. Q., Shugart, H. H., and Hurtt, G. C., 2009. Forest disturbance and recovery: A general review in the context of spaceborne remote sensing of impacts on aboveground biomass and canopy structure. *Journal of Geophysical Research - Biogeosciences* 114, G00E02, doi:10.1029/2008JG000911.
- Gillespie, A. R., Gilson, L., O'Neal, M. A., and Kane, V. R., 2006. A framework for estimating unresolved spectral shade. In J. A. Sobrino, ed., *Second Recent Advances in Quantitative Remote Sensing*, Publicacions de la Universitat de València, Spain, ISBN: 84-370-6533-X; 978-84-370-6533-5, 385-390.
- Hudak, A. T., Evans, J. S., and Smith, S., and Matthews, A., 2009. LiDAR utility for natural resource managers. *Remote Sensing* 1, 934-951.
- Kane, V.R., Bakker, J.D., McGaughey, R.J., Lutz, J.A., Gersonde, R.F., Franklin, J.F., 2010. Comparisons between field- and LiDAR-based measures of stand structural complexity. *Canadian Journal of Forest Research* 40, 761-773. doi:doi:10.1139/x10-024
- Kane, V.R., Gersonde, R.F., Lutz, J.A., McGaughey, R.J., Bakker, J.D., & Franklin, J.F. (2011). Patch dynamics and the development of structural and spatial heterogeneity in Pacific Northwest forests. *Canadian Journal of Forest Research* 41, 2276-2291
- Kauth, R. J., and Thomas, G. S., 1976. The tasseled Cap -- A Graphic Description of the Spectral-Temporal Development of Agricultural Crops as Seen by LANDSAT. *Proceedings of the Symposium on Machine Processing of Remotely Sensed Data*, Purdue University of West Lafayette, Indiana, 1976, pp. 4B-41 to 4B-51.
- Lardeux, C., Frison, P.-L., Souyris, J.-C., Tison, C., Stoll, B., Rudant, J.-P., 2008. Contribution of radar polarimetric data for the cartography in tropical environment. *Proceedings of SPIE, the International Society for Optical Engineering* 7154.
- Lefsky, M. A., Cohen, W. B., Parker, G. G., and Harding, D. J., 2002. Lidar remote sensing for ecosystem studies. *Bioscience* 52, 19-30.
- Mushkin, A., and Gillespie, A. R., 2005. Estimating sub-pixel surface roughness using remotely sensed stereoscopic data. *Remote Sensing of Environment* 99 75-83.
- Mushkin, A., and Gillespie, A. R., 2006. Mapping sub-pixel surface roughness on Mars using high-resolution satellite image data. *Geophysical Research Letters* 33(18), L18204 (6 pp), doi: 10.1029/2006GL027095.
- Mushkin, A., Gillespie, A. R., Abbott, E. A., Smith, M., Avalia, J., Brudsky, E., (2009). Vegetation effects on sub-pixel roughness measurements from NASA's Terra/ASTER stereo images. *Eos Transactions, American Geophysical Union*, 90(52), Fall Meeting Supplement, Abstract U33B-0071.
- Mushkin, A., and Gillespie, A., 2010. Using ASTER stereo images to quantify surface roughness. In Ramachandran, B., Justice, C., Abrams, M., eds., *Land Remote Sensing and Global Environmental Change: NASA's Earth Observing System and the Science of ASTER and MODIS*, Springer-Verlag.
- National Research Council (NRC), 2007. *Earth Science and Applications From Space: National Imperatives for the Next Decade and Beyond*, Committee on Earth Science and Applications From Space: A Community Assessment and Strategy for the Future, 456 pp., National Academies Press Washington, D. C.
- Saatchi, S. S., R. A. Houghton, R. C. Dos Santos Alvala, J. V. Soares, and Y. Yu (2007), Distribution of aboveground live biomass in the Amazon basin. *Global Change Biology* 13, 816-837.
- Simard, M., Rivera-Monroy, V.H., José Ernesto Mancera-Pineda, Castaneda-Moya, E. Twilley, R., 2007. A Systematic Method for 3D Mapping of Mangrove Forests Based on Shuttle Radar Topography Mission Elevation Data, ICESat/GLAS Waveforms and Field Data: Application to Ciénaga Grande de Santa Marta, Colombia. *Remote Sensing of Environment* 112(5), 2131-2144, doi:10.1016/j.rse.2007.10.012
- Tucker, C. J. (1979) Red and photographic infrared linear combinations for monitoring vegetation. *Remote Sensing of Environment* 8, 127-150.

Cropland area mapping in Chad using MODIS time series

A. Pérez-Hoyos, F. Kayitakire

European Commission Joint Research Centre, Via Enrico Fermi, 2749, I-21027 Ispra (VA), Italy

Ana.Perez-Hoyos@jrc.ec.europa.eu

ABSTRACT - Mapping cropland is a very important issue in areas such as sub-Saharan Africa, where the availability of accurate cropland information is needed for food security assessment. In this sense, Remote sensing data from satellite-based data has been proven useful for land cover characterization. This study aims to evaluate the performance of Moderate Resolution Imaging Spectroradiometer MOD13Q1 (16-day composite of normalized difference vegetation index at 250 m resolution) to classify cropland areas in Chad. The proposed methodology involves masking the non-vegetative areas (e.g. water bodies), stratifying the area into characteristic regions based on the spatio-temporal analysis of the vegetation indices and perform an unsupervised classification for each stratum and class identification with the legend (cropland/non-cropland) to each cluster. Finally, the resulted map was compared with existing coarse-resolution global land cover datasets (MODIS, GLC2000, GlobCover and JRC Crop Mask).

1. INTRODUCTION

Accurate and reliable spatial information on cropland is essential for a wide range of applications, e.g. analyse agricultural spatio-temporal dynamics and its environmental impacts.

Cropland monitoring is the main scope of a large number of operational initiatives at the international, regional and national scale. The primary international monitoring systems include the USAID Famine Early Warning System (FEWS-NET), the UN Food and Agriculture Organization (FAO) Global Information and Early Warning System (GIEWS), and the Group on Earth Observations Global Agricultural Monitoring (GEOGLAM)(Becker-Reshef *et al.*, 2010). Monitoring croplands is also a core aim for the Monitoring Agriculture by Remote Sensing (MARS) Project of the European Commission, at the Joint Research Center (JRC), with particular emphasis on food security assessments in food insecure countries (Atzberger, 2013).

Global cropland extent can be obtained from global land cover products such as the GLC-2000 (Mayaux *et al.*, 2004), the MODIS land cover product (Friedl *et al.*, 2010) and the GlobCover maps (Bontemps *et al.*, 2011). The problem with these products is that they are more focused on land cover classification and are not accurate enough to provide a reliable estimate of croplands (See *et al.*, 2014). Furthermore, the comparative analysis of these land cover products revealed large inconsistencies among them in Africa (Kaptué-Tchuente *et al.*, 2011). In particular, discrepancies regarding the extent of the cultivated area and its spatial distribution have already been documented (Fritz *et al.*, 2010). Actually, these global products are not expected to be suitable or reliable for the analysis of fragmented and heterogeneous African

rural landscapes, because of sub-pixel heterogeneity (Lobell and Asner, 2004). Cropland monitoring in the Sahel belt presents a number of particular challenges, such as the high variability in terms of agricultural system and crop calendar due to its own localization in a transition zone from the Sahara Desert to the more humid savannas and woodlands in the south (Vintrou *et al.*, 2012). Moreover, seasonal activity of vegetation varies according to the period, the number and duration of rainfall events (Mayaux *et al.*, 2004).

The mapping of crops using remote sensing data has shown good potential for characterizing the extent, distribution and condition of croplands (Lunetta *et al.*, 2010). In this sense, the MODerate resolution Imaging Spectroradiometer (MODIS) offers a high potential for cropland monitoring at regional scales due to its high spatial and temporal resolution.

The objective of this study was: 1) to examine the explanatory power of multi-temporal MODIS NDVI data for regional-scale crop mapping in sub-Saharan Africa and 2) develop a repeatable method for monitoring croplands in a consistent way. To this end, Chad was selected as a representative country. The need of more accurate information on cropland has been recently highlighted in Chad due to its high vulnerability from a food security perspective and because it is the country where the highest uncertainties in cropland classification lies (See *et al.*, 2014).

2. DATA

2.1 Time series MODIS NDVI data

MOD13Q1 products (16-Day L3 Global 250 m version 5) spanning from February 2000 to December 2013 were acquired from the NASA Earth Observation System Data Getaway. MOD13Q1 products were

provided every 16 days at a spatial resolution of 250 m in the sinusoidal projection. For each date, the tiles covering Chad were mosaicked and re-projected from their native Sinusoidal projection to the World Geodetic System (WGS-84). The layers of interest for our study were the Normalized Difference Vegetation Index (NDVI) and the pixel-reliability layer that refers to the reliability of the spectral measures on the pixel-level.

2.2 Google Earth reference data collection

Reference data was obtained from the human interpretation of high-resolution imagery in Google Earth (GE, <http://www.earth.google.com>). The high-resolution Google Earth images were selected especially because of free accessibility of these images. In Chad, most of the imagery is from Landsat ETM+ and SPOT imagery.

2.3 Global land cover datasets

Among the global land cover products, the following three products have been used: GLC2000 (Mayaux *et al.*, 2004), GlobCover 2009 (Bontemps *et al.*, 2011) and MODIS Land Cover (MOD12Q1) for the year 2009 (Friedl *et al.*, 2000). These products are the most widely used datasets for a variety of applications, including environmental studies, agriculture, forestry and landscape management and planning.

3. METHODOLOGY

The workflow included six major steps, as follows: (1) a smoothing algorithm to remove bad values in time-series NDVI was applied, (2) no vegetation areas were masked, (3) a stratification of Chad based on metrics derived from the annual NDVI curve was performed, (4) the classification by region of the smoothed time-series NDVI was implemented by ISODATA algorithm, (5) results of ISODATA were labelled and (6) the final result was compared with global land cover datasets.

3.1 Pre-processing of the time series

The method of noise reduction (Chen *et al.*, 2004) was used to smooth out noise in the time series MODIS NDVI data, specifically that caused primarily by cloud contamination and atmospheric variability (Chen *et al.*, 2004). This method is based on the Savitzky-Golay filter based on local least-squares polynomial approximation, in an iterative manner and preserving the upper NDVI envelope. Figure 1 shows an original NDVI profile and the filtered NDVI profile at a randomly agricultural selected pixel. It shows that the filter effectively eliminates data noise and improves the quality of the data.

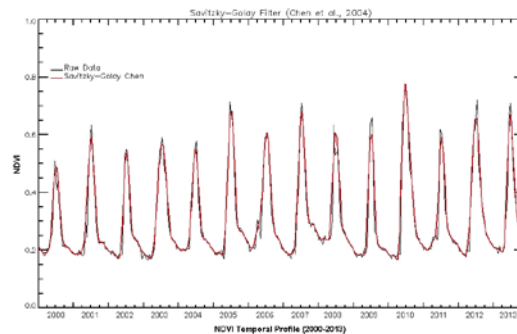


Figure 1. Time series MODIS NDVI profile before and after filtering.

3.2 Mask no vegetation

To minimize the error during the classification, the non-vegetative zones were masked. In this study, three land cover types were considered as non-vegetative classes: artificial, water and bare areas. The mask process followed two phases: 1) a combination of the main global land cover products (GLC2000, MODIS and GlobCover) were used to identify the non-vegetative classes and 2) the temporal profiles of the agreed non-vegetative zones were analysed over the period 2000-2013 to determine an optimum threshold of 0.16 that mask these areas properly.

3.3. Stratification

A stratification of the study region was performed before classifying the cropland/non-cropland areas. Stratification reduces the variability in data that can result in a more accurate classification with improved spatial patterns. Stratifying landscape into sub-regions of similar biophysical and spectral characteristics is a common method of isolating spectral gradients.

In this work, the stratification was based on a set of five metrics that describe the patterns of the radiation by vegetation that have previously been demonstrated to be adequate for this purpose (Pettorelli *et al.*, 2012). These metrics derived from the NDVI average year (2000-2013) included: (1) NDVI mean that can be used to estimate fAPAR and thus net primary production, (2) the relative range of NDVI as the annual amplitude normalized by the NDVI annual mean that provides an indicator of the seasonality of the photosynthetic activity, (3) the date of maximum that provides additional description of vegetation phenology, (4) the date of minimum that provides information of presence/absence of vegetation during the dry season and (5) the date where the maximum is reached that allows to discriminate natural cycles from crop cycles.

3.4 Classification

The classification of cropland and non-cropland cover was conducted for annual MODIS-NDVI dataset corresponding to year 2010. This year was an above-normal agricultural year according the CILSS (*Comité permanent Inter-États de Lutte contre la Sécheresse dans le Sahel*) that justifies its selection as a reference year to assess the method.

For each strata, an Iterative Self-Organizing Data Analysis Technique (ISODATA) (Ball and Hall, 1965) was applied to the 23-date NDVI time series. This is a type of unsupervised classification based on the natural grouping of pixels. The main parameters used in the ISODATA method were a number of classes varying from 40 to 100 classes, with a maximum number of 100 iterations and a convergence threshold of 0.95.

3.5 Labelling

The clusters were recoded and labelled into two classes (cropland/no-cropland) according to two criteria. First, the cluster's mean multi-temporal NDVI signature was evaluated for class determination. Second, the cluster was evaluated by visual interpretation of high-resolution imagery from Google Earth to confirm the presence or absence of cropland.

3.6 Global land cover comparison

The accuracy of the cropland mask was assessed by visual comparison with the three global land cover products.

4. RESULTS

Preliminary results of the cropland classification are presented in this section. Figure 2 shows the mask of non-vegetative areas.

The stratification obtained with the MODIS time series resulted into 22 strata. The number of strata was further grouped into four strata based on a dendrogram of a hierarchical cluster analysis. The resulted stratification (Figure 3) followed the north-south bioclimatic gradient.

The resulted cropland classification is shown in Figure 4. The ISODATA clustering evidence the great variability within class spectral heterogeneity in the croplands of Chad. The number of clusters varies from 47, for strata 4, to 73 for strata 3. Strata 1 and 3 have both 50. Visual analysis of the crop mask showed that compared with previous land cover datasets (Figure 4), the cropland mask adequately delineates the main cropland areas of Chad. Moreover, compared to GLC2000, the crop mask avoids overestimation of croplands, and properly detects the cropland areas of the south of Chad that are not mapped in GLC2000, MODIS and GlobCover.

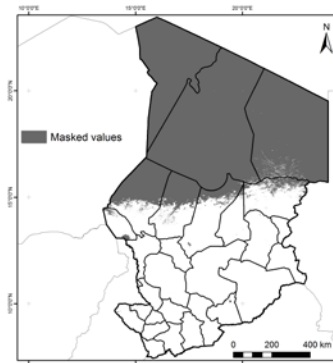


Figure 2. Mask of artificial surfaces, bare soils and water bodies (in grey).

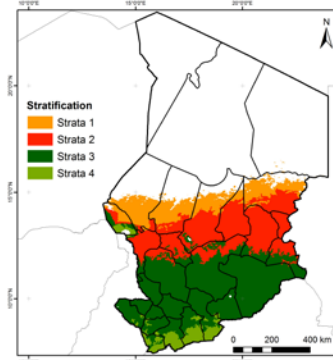


Figure 3. Stratification of Chad based on MODIS dataset.

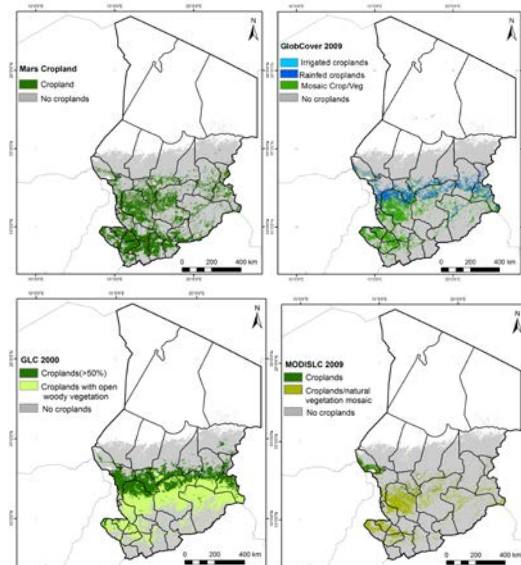


Figure 4. Top-left) Crop mask compared to top-right) GlobCover, bottom-left) GLC2000 and bottom-right) MODIS Land Cover.

5. CONCLUSIONS

MODIS Normalized Vegetation Index (NDVI) have been used to map crops in sub-Saharan Africa through unsupervised classification. Results demonstrated the potential utility of MOD13Q1 for identifying and mapping croplands in Chad. The preliminary results are quite promising to encourage the authors to further in-depth research in cropland classification in Chad. Further work could also consider including other variables (e.g. red spectral band) in order to better characterise the croplands in this region.

6. REFERENCES

- Atzberger, C., 2013. Advances in Remote Sensing of Agriculture: Context Description, Existing Operational Monitoring Systems and Major Information Needs. *Remote Sensing*, **5**, 949-981.
- Ball, G.H., and Hall, D.J., 1965. Isodata: a Method of Data Analysis and Pattern Classification. Stanford Research Institute, Menlo Park, California, United States.
- Becker-Reshef, I., Justice, C.O., Sullivan, M., Vermote, E.F., Tucker, C., Anyamba, A., Small, J., Pak, E., Masuoka, E., Schmaltz, J. et al. 2010. Monitoring global croplands with coarse resolution Earth observation: The Global Agriculture Monitoring (GLAM) project. *Remote Sensing*, **2**, 1589-1609.
- Bontemps, S., Defourny, P., van Bogaert, E., Arino, O., Kalagrou, V., Pérez, J.R. 2011. GLOBCOVER 2009: Products description and validation report.
- Chen, J., Jonsson, P., Tamura, M., Gu, Z.H., Matsushita, B., and Eklundh, B. 2004. A simple method for reconstructing a high-quality NDVI-time series data set based on the Savitzky-Golay filter. *Remote Sensing Environment*, **91**, 332-344.
- Friedl, M.A., Sulla-menahse, B., Tan, A., Schneider, N., Ramankutty, A., Sibley, A., and Huang, X. 2010. MODIS Collection 5 global land cover: algorithm refinements and characterization of new datasets. *Remote Sensing of Environment*, **114**, 168-182.
- Fritz, S., See, L., and Rembold, F. 2010. Comparison of global and regional land cover maps with statistical information for the agricultural domain in Africa. *International Journal of Remote Sensing*, **31**, 2237-2256.
- Kaptué-Tchuenté, A.T., Roujean, J.L., and Daroux, J.L. 2011. Comparison and relative quality assessment of the GLC2000, GLOBCOVER, MODIS and Ecoclimap land cover data sets at the African continental scale. *International Journal of Applied Earth Observation and Geoinformation*, **13**, 207-219.
- Lobell, D.B., and Asner, G.P., 2004. Cropland distributions from temporal unmixing of MODIS data. *Remote Sensing of Environment*, **93**, 412-422.
- Lunetta, R.S., Shao, Y., Ediriwickrema, J., Lyon, J.G. 2010. Monitoring agricultural cropping patterns across the Laurentian Great Lakes Basin using MODIS-NDVI data. *International Journal of Applied Earth Observation and Geoinformation*, **12**, 81-88.
- Mayaux, P., Bartholomé, E., Fritz, S., and Belward, A. 2004. A new land cover map of Africa for the year 2000. *Journal of Biogeography*, **31**, 861-877.
- Pettorelli, N., Chauvenet, A.L.M., Duffy, J.P., Cornforth, W.A., Meillere, A., and Baillie, J.E.M. 2012. Tracking the effect of climate change on ecosystem functioning using protected areas: Africa as a case study. *Ecological Indicators*, **20**, 269-276.
- See, L., Fritz, S., You, L., Ramankutty, N., Herrero, M., Justice, C., Becker-Reshef, I., Thrnton, P., Erb, K., Gong, P., Tang, H., van der Velde, M., Ericksen, P., McCallum, I., Kraxner, F., Obersteiner, M. 2014. Improved global cropland data as an essential ingredient for food security. *Global Food Security*, In Press.
- Vintrau, E., Desbrosse, A., Bégué, A., Traoré, S., Baron, C., and Lo Seen, D., 2012. Crop area mapping in West Africa using landscape stratification of MODIS time series and comparison with existing global land products. *International Journal of Applied Earth Observation and Geoinformation*, **14**, 83-93.

Remote Sensing Monitoring and Analysis of Temporal and Spatial Change Characteristics of Grassland Desertification in Tibet

B. Xu^{a,*}, J.Y. Li^{a,c}, Y.X. Jin^a, Z.L. Wang^b, Z.H. Qin^a, M.Q. Wu^b, J. Zhang^d, H.L. Ma^a, X.C. Yang^{a,*}

a Key Laboratory of Agri-informatics of the Ministry of Agriculture, Institute of Agricultural Resources and Regional Planning, Chinese Academy of Agricultural Sciences, Beijing 100081, China; b College of Geography and Planning, Ludong University, Yantai 264025, China; c State Key Laboratory of Urban and Regional Ecology, Research Center for Eco-Environmental Sciences, Chinese Academy of Sciences, Beijing 100085, China; d Planning and Design Institute of Forest Products Industry, State Forestry Administration, Beijing 100714, China

Email: xubin@caas.cn; yangxiuchun@caas.cn

ABSTRACT - This thesis takes Amdo, Baingoin, Coqên and Zhongba Counties in Tibet as the study areas; employs remote sensing data, including Landsat TM/ETM+ and SPOT; and builds Tibetan grassland desertification classification indexes on the basis of field surveys. Moreover, this study uses spectral mixture analysis (SMA) methods to interpret the remote sensing image data of study areas during three periods, namely 1990, 2000 and 2009, and takes the bare sand area proportion and vegetation coverage degree as the main bases for the grassland desertification evaluation. The study results show that the slightly, moderately and severely desertified grasslands of the monitoring zone covered a total area of 114,113.16 km² in 1990, accounting for 82.12% of the study area. The area exhibited no change in 2000 and declined by 4,472.31 km² in 2009. The area of non-desertified grassland markedly increased from 1990 to 2009. The area of slightly desertified grassland also markedly increased from 1990 to 2000 but rose gradually from 2000 to 2009. The area of moderately desertified grassland increased gradually from 1990 to 2000 and decreased significantly from 2000 to 2009. The severely desertified grassland declined from 1990 to 2009. The grassland desertification degree of the four Tibetan counties was alleviated from 1990 to 2009, and the grassland desertification area exhibited a gradual reduction during the same period. With regard to other soil coverage types, the ice and snow area markedly changed and declined to approximately one-third of the original ice and snow area during the 20 years, and most of the ice and snow was changed into bare sand and different types of desertified grasslands.

1 INTRODUCTION

The Qinghai-Tibet Plateau is the highest plateau in the world, covering an area of approximately 2,400,000 km², including all areas in Tibet and Qinghai and portions of Sichuan, Xinjiang, Gansu and Yunnan. As the largest region of the Qinghai-Tibet Plateau, Tibet covers a total area of 1202.2 thousand km², accounting for approximately half of the Qinghai-Tibet Plateau. Natural grasslands cover an area of 810.7 thousand km², accounting for approximately 67.43% of the total area of Tibet. Cropland and garden plots account for approximately 0.3% of the total area of Tibet, and woodlands accounts for approximately 10.55%. Grasslands are the largest ecosystem in Tibet, and Tibet boasts the largest grassland area in China. Tibetan grasslands include high-cold meadows, high-cold steppes and high-cold desert steppes. Their common characteristics are low temperature, severe environment, and

difficulties in spontaneous recovery after grassland deterioration or desertification (The Bureau of land management of Tibet Autonomous Region, 1994). It is difficult to conduct traditional ground monitoring of grassland desertification because Tibet grasslands have a severe environment and belong to a no-man zone. Thus, it is timesaving, labor saving and feasible to use remote sensing technology to monitor grassland desertification. Moreover, the remote sensing technology used to monitor the spatial-temporal change dynamics of grassland desertification plays an important role in adopting measures, controlling grassland desertification, and protecting and managing Tibetan grasslands.

Four counties in the Tibet Autonomous Region are considered as the study areas in this thesis. The thesis, based on Landsat TM/ETM+ remote sensing image and field inspection and investigation, and after the expert's demonstration, builds a Tibetan grassland desertification classification and staging hierarchy and

sets up remote sensing interpretation symbols for different grassland desertification ranking types. Moreover, this thesis adopts methods such as spectral mixture analysis (SMA) to interpret the remote sensing images covering the study areas in 1990, 2000 and 2009. The thesis takes the bare sand area percentage and vegetation coverage for the assessment basis of grassland desertification types to monitor and analyze the spatial-temporal dynamic change characteristics of Tibetan grassland desertification, providing a basis for sand prevention and control in Tibetan grasslands.

2 STUDY AREA

The study area mainly consists of Amdo County, Baingoin County, Coqên County and Zhongba County, covering an area of 13,896 km². The four counties have suffered severe grassland desertification, which is typical in Tibet. Amdo County and Baingoin County belong to Nagqu Prefecture, Coqên County belongs to Ngari Prefecture, and Zhongba County belongs to Xigatse Prefecture. The main grassland types include high-cold meadow, high-cold meadow steppe, high-cold steppe and high-cold desert steppe. See Fig. 1 for the location of the study area, which is situated in the northern and south-central regions of Tibet. The mean altitude is 4000-5000 m, the annual precipitation is 200-400 mm, the annual mean temperature is -0.9-3.3°C, the frost-free period only lasts several days to dozens of days, and the high-altitude zones experience no absolute frost-free periods. The severe natural conditions lead to low, short, rare and simply composed grass communities, together with cushion plants, and the set up group of species are mainly local endemic species.

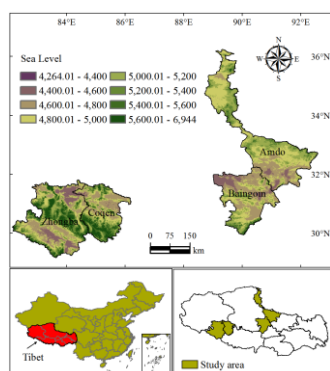


Fig.1 Location of Study Area

3 DATA AND METHODS

3.1 Study Data and Pre-treatment

TM/ETM+ images of the study area in 1990, 2000 and 2009 were used as the main data sources, covering four counties in the Tibet Autonomous Region,

including Amdo, Baingoin, Zhongba and Coqên. The four counties include major grassland types in Tibet and have many typical grassland desertification types. The spatial resolution of remote sensing data is 30 m, and complete coverage of the four counties requires 18 scenes every period, totaling 54 scenes for three periods of time. The data imaging period is mainly in summer (from July to August), when the vegetation conditions are favorable. Some data were downloaded from the United States Geological Survey (USGS) website (<http://glovis.usgs.gov>), and other data were purchased from The Center for Earth Observation and Digital Earth, Chinese Academy of Sciences. Moreover, the SPOT data for the study area in 2009 were purchased for the accuracy test. The radiation calibration, atmospheric correction and precise geometric correction (the error is less than 1 pixel) were conducted for each scene data.

This thesis collects and refines the meteorological data of the study area, including the precipitation and temperature, grassland resource type diagram (vector), DEM landform data, and soil type distribution diagram. This study involved a field inspection of the study area from July 25 to August 10 in 2010 and obtained multiple ground grassland desertification data, which mainly included the grassland desertification type, spatial position information on the interpretation symbol, ground sample plot and sample plot data, and pasturing and desertification situations in the neighborhood of the sample plots to set up a grassland desertification classification index system suitable for the study area.

3.2 Grassland Desertification Evaluation System and Index

This thesis divides the land cover types of the study area into 9 categories, including river, lake, ice and snow, bare sand, salinization land, non-desertified grassland (DG), slightly DG, moderately DG, and severely DG, in accordance with the study results of China's relevant desertification classification indexes (Li, J. Y., et al, 2013; Li, J. Y., et al, 2011; Ding, G.D., et al, 2004) and national standards of *Classification Indexes of Degradation, Desertification and Salinization of Natural Grasslands* (GB19377-2003). This classification is based on the field inspection in combination with basic desertification features and grassland types of the study area as well as the scientific soundness, operability and interpretation of remote sensing images. This study includes an integrated survey and measurement of typical grassland desertification types, establishes a parallel relationship with the remote sensing data, and develops the grassland desertification remote sensing interpretation index system to divide the DG into 3 categories, including slightly DG, moderately DG and severely DG

3.3 Methods of Grassland Desertification Information Extraction

The thesis uses the bare sand area percentage and vegetation coverage as the main assessment bases of grassland desertification and uses SMA as the major method for abstracting the bare sand area percentage and vegetation coverage. The linear spectral mixture model (LSMM), a type of SMA, is extensively used due to define physical meanings and ensure high scientific soundness and simple modeling (Dawelbait, M. and Morari, F., 2012; Yang, J., et al, 2012; Dawelbait, M. and Morari, F., 2012). In LSMM, the pixel reflectivity (brightness value) in a certain spectral band is a linear combination that takes the area proportion of the reflectivity of endmember components forming the pixel to the pixel (abundance) as the weight coefficient (Li, J. Y., et al, 2013; Li, J. Y., et al, 2011). The model is expressed as follows:

$$\rho(\lambda_i) = \sum_{j=1}^m F_j \rho_j(\lambda_i) + \varepsilon(\lambda_i) \quad (1)$$

In this formula, $j=1,2,\dots, m$ is the pixel component; $i=1,2,\dots, n$ is the spectral channel; and $m \leq n+1$. $\rho(\lambda_i)$ is the gray-scale value of the pixel in the i wave band; $\rho_j(\lambda_i)$ is the spectral reflectance value of land type in the i wave band; $\varepsilon(\lambda_i)$ is the error term of the its spectral channel; F_j is the non-evaluated parameter that satisfies the area proportion of pixel components to the pixel when the RMSE is minimal in the following formula. RMSE refers to the root-mean-square error in the solution process.

$$RMSE = \sqrt{\left(\sum_{i=1}^n \varepsilon^2(\lambda_i) \right) / n} \quad (2)$$

The proper and precise endmember is crucial for

the LSMM. The selection of ground objects as endmembers, quantity of endmembers and confirmation of characteristic spectrum are the keys to determining the pixel decomposition of the LSMM (Li, J. Y., et al, 2013; Elmore, A.J., et al, 2000). The following standards are usually adopted to evaluate the endmember selection: (1) the root-mean-square error should be small as possible; (2) $0 \leq F \leq 1$; (3) the endmember should be a representative and valid component of most pixels in the image. The thesis conducts a complete field survey of the study area, masters the land coverage characteristics and environmental background, and integrates the results of the minimum noise fraction (MNF) in the construction of a two-dimensional scatter diagram, ultimately selecting grassland, bare sands (gravel) and bare sand (gravel) as the terminal endmembers of selected models after many tests.

3.4 Classification Precision Verification

The ground verification points and high-resolution SPOT images are used to appraise the precision of the grassland desertification and land coverage classification results, respectively. There are 55 actual measurement points on the ground. The actual measurement verification on the ground is 86.67%, indicating a high classification precision. The high-resolution SPOT images are used in the precision verification. The classification precision of the two remote sensing data sets is 82%.

4 RESULTS AND ANALYSIS

The monitoring results principally include the time and spatial changes in grassland desertification in four Tibetan counties.

Table 1 Grassland Desertification Status of Study Areas of Four Tibetan counties in Three Periods of Time (Area: km²; Scale: %)

Land Types	1990		2000		2009	
	Area	Scale	Area	Scale	Area	Scale
Slightly DG	17,612.68	12.7	19,714.08	14.2	20,701.38	14.9
Moderately DG	53,577.11	38.6	54,583.54	39.3	49,907.91	35.9
Severely DG	42,923.37	30.9	39,906.43	28.7	39,031.56	28.1
Subtotal of DG	114,113.16	82.12	114,204.05	82.19	109,640.85	78.90
Non-DG	6898.49	4.96	10,612.21	7.64	14,976.47	10.80
Subtotal of Different Grasslands	121,585.70	87.50	125,335.34	90.20	125,445.09	90.27
River	782.61	0.56	810.01	0.58	735.92	0.53
Lake	7348.42	5.29	7647.46	5.50	8482.92	6.10
Ice and Snow	8516.61	6.13	4471.58	3.22	2821.60	2.03
Bare Sand	728.17	0.52	683.36	0.49	1481.34	1.07
Salinization Soil	574.05	0.41	519.08	0.37	827.77	0.60
Subtotal of Land Types	138961.5	100	138947.8	100	138966.9	100

Note: DG stands for desertified grassland.

4.1 Time Change Characteristics of Grassland Desertification

The period 1990 to 2009 is divided into two periods (1990-2000 and 2000-2009), for the change analyses.

4.1.1 Grassland Desertification Change Characteristics

See Fig. 2 for the monitoring results of Tibetan grassland desertification during 3 periods. Statistical calculations of the results in the figure are presented in Table 2.

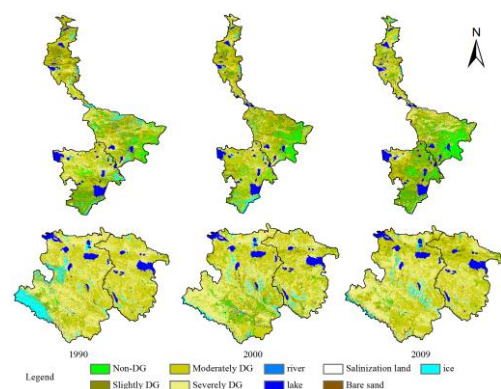


Fig. 2 Chart of Soil Coverage Type Change, such as Tibetan Grassland Desertification

Note: Because the study area is divided into two location zones, Amdo and Baingoin are connected, Zhongba and Coqên are connected, and the two location zones are far from each other, the spatial positions and dimension scales of different counties are changed and removed for convenience; DG stands for desertified grassland.

According to the classification figure and statistical results for the three time periods, the DG areas of three ranks totaled 114,113.16 km² in 1990, accounting for 82.12% of the total study area. This area was similar to that in 2000. The DG areas accounted for 78.90% of the total study area in 2009, a reduction of 4,472.31 km². The non-DG areas increased from 6898.49 km² in 1990 to 10,612.21 km² in 2000 and 14,976.47 km² in 2009. The slightly DG areas markedly increased from 17,612.68 km² to 19,714.08 km² during the periods of 1990 and 2000,

Table 2 Change Velocity of Different Grassland Desertification and Land Types (%)

Period	Slightl y DG	Moderat ely DG	Severe ly DG	Total of DG	Non- DG	River	Lake	Ice and Snow	Bare Sand	Salinizati on Soil
1990-2000	11.93	1.88	-7.03	0.07	53.83	3.50	4.07	-47.50	-6.15	-9.57
2000-2009	5.01	-8.57	-2.19	-4.00	41.12	-9.15	10.92	-36.90	116.77	59.47
1990-2009	17.54	-6.85	-9.07	-3.92	117.10	-5.97	15.44	-66.87	103.43	44.20

Note: The change velocity (%) = (Ni-Ni-1)/ Ni-1 *100. In the formula, Ni is the quantity of a certain land type in a certain time, whereas Ni-1 is the quantity of the related land types in the preceding time, and DG stands for desertified grassland.

in Different Time Periods

According to the land coverage characteristics in Tibet, slightly DG, moderately DG, severely DG, salinized grassland, non-DG, river surface, lake surface, ice and snow, and bare sand are selected as the land coverage types.

an increase of 2,101.4 km². However, the slightly DG areas increased gradually from 2000 to 2009. The moderately DG areas increased slowly from 1990 to 2000 and markedly decreased from 2000 to 2009, down 4,675.63 km². The severely DG areas decreased gradually during the two periods. Overall, the grassland desertification degree and areas of four Tibetan counties were alleviated during the nearly 20 years from 1990 to 2009.

The coverage area of ice and snow exhibited a significant reduction during this period, from 8,516.61 km² in 1990 to 4,471.58 km² in 2000 and to 2,821.60 km² in 2009. The areas declined 3-fold during the 20 years. The area of bare sand increased by 100% during the same period, and the lake area exhibited a sharp increase. The area change is most likely attributed to the rising temperature of the Qinghai-Tibet Plateau and to global climate change.

4.1.2 Change Velocity of Different Grassland Desertification and Land Coverage Types

The slightly DG area increased by 11.93% and 5.01%, respectively, during the two periods from 1990 to 2000 and from 2000 to 2009. The moderately DG area increased by 1.88% from 1990 to 2000 and declined by 8.57% from 2000 to 2009. The severely DG area decreased gradually, down 7.03% from 1990 to 2000 and 2.19% from 2000 to 2009.

The river area increased from 1990 to 2000 and decreased from 2000 to 2009. The lake area rose gradually after 1990, up 4.07% from 1990 to 2000 and 10.92% from 2000 to 2009; the ice and snow area decreased significantly, down 47.50% from 1990 to 2000 and 36.90% from 2000 to 2009. The areas of bare sand and salinized soil were relatively small; the areas decreased from 1990 to 2000 while increasing sharply from 2000 to 2009.

4.2 Spatial Change Characteristics among Land Coverage Types, Particularly Grassland Desertification

Because the study area is divided into two location zones, Amdo and Baingoin are connected, Zhongba and Coqên are connected, and the two location zones are far from each other, the spatial pieces and dimension scales of different counties are changed and removed for convenience (Fig. 3).

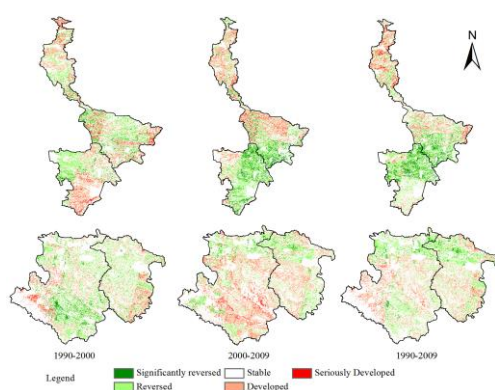


Fig. 3 Dynamic Change Chart of the Grassland

4.2.1 Spatial Change of Grassland Desertification

The grid computing is conducted via ArcGIS to obtain the Spatial Dynamic Change Chart of Grassland Desertification (Fig. 3) from 1990 to 2000, from 2000 to 2009 and from 1990 to 2009. The figure stipulates that “developed” means an increase in desertification degree (for instance, non-DG are changed into slightly DG); “seriously developed” means a sharp increase in desertification degree (for instance, slightly DG are changed into severely DG). In contrast, “reversed” means a decline in desertification degree, “significantly reversed” means a sharp decline, and “stable” means the desertification degree is the same for the two periods.

The function of spatial change detection statistics in the ENVI software is used to obtain the transfer matrixes of the study area for different periods.

Fig. 3 indicates that from 1990 to 2000, grassland desertification occurred north and partially east of Amdo and south of Baingoin, reversed grassland desertification formed in central Amdo and northwest of Baingoin, and reversed grassland desertification also formed in Coqên and most of Zhongba. From 2000 to 2009, the grassland desertification formed in mid-northern Amdo, mid-southern Zhongba and west of Coqên; south of Amdo and most of Baingoin exhibited reversed grassland desertification. From

1990 to 2009, grassland desertification occurred in northern and the southeast corner of Amdo, reversed grassland desertification occurred across most of Baingoin and southern Amdo, and desertification and reversed desertification both occurred in Zhongba and Coqên.

4.2.2 Analysis of Temporal and Spatial Change Characteristics of Grassland Desertification and Land Coverage Types

To gain a better understanding of the grassland change conditions in different periods, the analysis is conducted for the classification results of the study area for the two periods.

The areas of slightly DG that changed into moderately and severely DG and non-DG were 7,250.70 km², 1,583.50 km² and 3,000.68 km², respectively, from 1990 to 2000. The areas of moderately DG that changed into slightly DG were 9,307.9 km²; and the areas of moderate DG that changed into severely DG and non-DG were, respectively, 11,926.50 km² and 2,579.49 km². The areas of severely DG that changed into slight and moderately DG were 3,118.46 km² and 15,297.06 km², respectively, and few areas were changed into non-DG. In addition, the areas of ice and snow that changed into slightly, moderately and severely DG and other land types were 556.4 km², 1,410 km² and 3,185.5 km², respectively.

The areas of slightly DG that changed into moderately and severely DG and non-DG were 8,385.59 km², 2,275.57 km² and 33,220.54 km², respectively, from 2000 to 2009; the areas of moderately DG that changed into slightly DG were 10,525.09 km², and the areas of moderately DG that changed into severely DG and non-DG were 13,374.17 km² and 3,741.43 km², respectively. The areas of severely DG that changed into slightly and moderately DG were 2,718.73 km² and 13,537.03 km², respectively, whereas few areas were changed into non-DG. In addition, the areas of ice and snow changed into slightly, moderately and severely DG were 463.17 km², 456.06 km² and 1,127.49 km², respectively.

5 CONCLUSION AND DISCUSSION

Tibet covers half of the total area of the Qinghai-Tibet Plateau, and thus forms the main part of the Qinghai-Tibet Plateau. Although natural grasslands account for 67.43% of the total area of Tibet, Tibet has suffered severe grassland deterioration and desertification due to human factors, including overgrazing, and natural factors, including rising temperatures. Moreover, the Tibetan high-cold meadow and steppe are difficult to restore after such

degradation. To effectively address the problem of heavy grazing, the government of the Tibet Autonomous Region determined in 2009 to establish a grassland ecology protection and encouragement mechanism in which the livestock carrying capacity is determined in accordance with the grass, the core wood substitutes other sweep energy for the subsidy, and a livestock electronic identification system and grassland ecology monitoring system was built. The mechanism covers the four counties in which remote sensing of grassland desertification was conducted in this study. Adopting the remote sensing technology for monitoring and mastering the Tibetan grassland desertification conditions is critical for protecting and managing grasslands. We conducted remote sensing monitoring of grassland desertification in four Tibetan counties using field and indoor evaluations in 2010. Landsat TM/ETM+ remote sensing data were primarily used because these data have a long time sequence and provide optimum data for monitoring grassland desertification changes over many years. Precipitation has a substantial impact on grassland vegetation. The remote sensing data were selected for three periods to approximate the average for several years of precipitation and ultimately decrease misjudgments of the grassland desertification classification level due to the effect of precipitation on vegetation. We adopted the SMA method to analyze grassland desertification during two periods spanning approximately 20 years to reveal the temporal and spatial change characteristics of Tibetan grasslands.

ACKNOWLEDGMENTS

This thesis project is financed by the National Natural Science Foundation of China (Serial Number: 31372354) and the agricultural and rural resource monitoring statistics (grassland monitoring) project. We received extensive support and guidance from leaders of The Center of Supervision Management of Grassland, Ministry of Agriculture during the study period. Moreover, we acknowledge units such as the grassland management stations in Tibet Autonomous Region and Nagqu, which provided us with great support and assistance during the field survey.

REFERENCES

- Dawelbait, M. and Morari, F., 2010, Limits and potentialities of studying dryland vegetation using the optical remote sensing. *Italian Journal of Agronomy*, **3**, 97-106.
- Dawelbait, M. and Morari, F., 2012, Monitoring desertification in a Savannah region in Sudan using Landsat images and spectral mixture analysis. *Journal of Arid Environments*, **80**, 45-55.

- Ding, G.D., Zhao, Y.N., Fan, J.Y. and Du, H., 2004, Analysis on development of desertification assessment indicator system. *Journal of Beijing Forestry University*, **01**, 92-96.
- Elmore, A.J., Mustard, J.F., Manning, S.J., and Lobell, D.B. 2000. Quantifying Vegetation Change in Semiarid Environments: Precision and Accuracy of Spectral Mixture Analysis and the Normalized Difference Vegetation Index. *Remote Sensing of Environment*, **73**, 87-102
- Li, J.Y., Xu, B., Yang, X.C., Jin, Y.X., Li, Y.Y., Zhang, J., Zhao, L.N. and Li, R.L., 2011, Dynamic changes and driving force of grassland sandy desertification in Xilin Gol. A case study of Zhenglan Banner. *Geographical Research*, **9**, 1669-1682.
- Li, J.Y., Yang, X.C., Jin, Y.X., Yang, Z., Huang, W.G., Zhao, L.N., Gao, T., Yu, H.D., Ma, H.L., Qin, Z.H., and Xu, B. 2013, Monitoring and analysis of grassland desertification dynamics using Landsat images in Ningxia, China. *Remote Sensing of Environment*, **138**, 19-26
- The Bureau of land management of Tibet Autonomous Region, 1994, The Bureau of animal husbandry of Tibet Autonomous Region. Grassland resources of Tibet Autonomous Region. (Beijing, Beijing: Science Press).
- Yang, J., Weisberg, P. J., Bristow, N. A., 2012, Landsat remote sensing approaches for monitoring long-term tree cover dynamics in semi-arid woodlands: Comparison of vegetation indices and spectral mixture analysis. *Remote Sensing of Environment*, **119**, 62-71.

Recent land surface temperature trends over the Antarctic Peninsula

C. Durán-Alarcón¹, C. Mattar¹, J.C. Jiménez-Muñoz², J.A. Sobrino².

1. Laboratory for Analysis of the Biosphere, University of Chile, Chile

claudioduran@ug.uchile.cl, cmattar@uchile.cl

2. Global Change Unit, Image Processing Laboratory, University of Valencia, Spain

jcjm@uv.es, sobrino@uv.es

ABSTRACT- *The Antarctic Peninsula has experienced a significant warming rate during the middle of last century, which has been the subject of important efforts in research, since not yet the role of these changes is understood in the global climate system. For instance, the consequences of ice-mass loss on the global sea level rise. Thus, to assess the spatial and temporal changes over the Antarctic Peninsula, satellite-derived and reanalysis temperature data can provide an alternative to examine the climate variations of the Antarctica in areas which are not represented by stations. Several studies have made assessments of the quality of satellite derived and reanalysis products in the Antarctic region. In this work we analysed the spatio-temporal trend of the Land Surface Temperature over the Antarctic Peninsula the last decade (2001-2013). To perform this analysis, satellite data derived from the Moderate Resolution Imaging Spectroradiometer (MODIS) land products MOD11C3 (LST) and reanalysis data Skin Temperature (Tskin) extracted from ERA-Interim were used. Additionally, Tskin extracted from ERA-Interim reanalysis data in the period 1979 – 2013 were also processed in this work. Seasonal Anomalies for each variable were analysed at monthly level, and the magnitude and statistical significance of the trends were computed using the non-parametric tests of Sen's Slope and Mann-Kendall respectively. Results obtained from MODIS LST data showed a not significant decrease (p -value < 0.05) on surface temperature over the Antarctic Peninsula in the last decade except summer (DJF), that showing a non-significant trend of increasing temperature (+0.6°C per decade). Different results were obtained when using ERA-Interim reanalysis data in same time period, because only winter (June July August) reveals a significant rate of increase in temperature (+1.7°C per decade). These differences could be explained due to the infrared temperature satellite-derived might be affected by cloud cover. Finally, in the last three decade, the results obtained from reanalysis data achieved similar sign of trends that the last decade, although lower magnitude trends and not statistically significance during the last 30 years.*

1 INTRODUCTION

Antarctica is one of the most important ice surfaces in the World. It is sensitive to global warming and therefore global change. LST (Land Surface Temperature) over Antarctic region has been rising during the last decades. Therefore, a sustained warming over Antarctica has the potential to affect the global climate system. In Polar zones, LST also affects the growth and decay of sea ice, the salinity and heat fluxes between the sea ice and the atmosphere, and the ice extent. Moreover, it affects the area coverage of continental surface melt, evaporation and sublimation, accumulation rate, the stability of the ice sheet, and the variation in the circulation patterns in the atmosphere and the boundary layer (Comiso, 2000).

The spatial and temporal patterns of the trends have been addressed using different data sets (i.e. in-situ data, models and remote sensing information). Researches have shown significant changes in the surface temperature of the Antarctica (Turner et al. 2002, Turner et al., 2006). In-situ data have shown that Antarctic Peninsula has experienced significant

warming in the last decades (Vaughan et al, 2003; Jacka et al, 2004), while there has been a cooling of the interior of the Antarctic region with a highly seasonally dependent (Doran et al. 2002; Thompson and Solomon, 2002). Moreover, the trends in Land Surface Temperature over the Antarctic Peninsula using remote sensing and reanalysis data have also shown widespread and non-uniform changes of the Antarctic surface temperatures in the last decades, with warming over Antarctic Peninsula (Comiso, 2000, Simmonds et al. 2004; Johanson et al. 2007; Steig et al., 2009).

To assess the LST trends over Antarctic Peninsula in the last decade, Monthly LST-MODIS data and skin temperature generated by ERA-interim reanalysis data were used. The reanalysis data set also retrieves temperatures for a longer period of time, 1980-2013, which is necessary for demonstrating decadal changes. This manuscript includes the following sections: description of study area and data used in this work; presentation of method used to estimate surface trends and its statistical significance; the results and the discussion and finally conclusions are presented.

2 MATERIALS AND METHODS

2.1 Data and study area

In this work, land surface temperature trend was assessed over the Antarctic Peninsula, located in West Antarctic (see figure 1). Previous researches have shown that this area has experienced a rapid warming, which could impact on the global climate. (Comiso, 2000, Vaughan, et al., 2003, Steig et al, 2009). Therefore it is very important to maintain a continuous monitoring of temperature changes in this region.

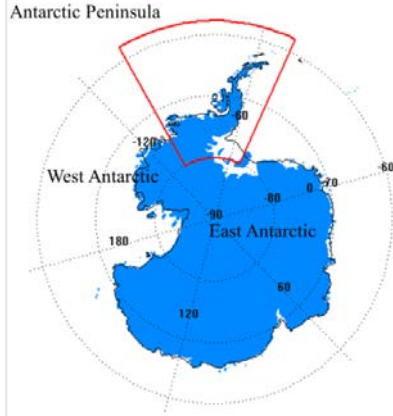


Figure 1. Antarctic Peninsula, study area in red region.

We used the MODIS products at 0.05° latitude/longitude Climate Modelling Grid (CMG) from 2001 to 2013. Daytime and nighttime LST imagery was extracted from Terra monthly Land Surface Temperature product (MOD11C3), and these were averaged to obtain a mean monthly temperature for each time. The Version 5.0 MODIS land surface temperature products have been used in this work. These products were obtained by TERRA satellite and the products provided radiometrically corrected surface temperature measurements using the generalized split window approach (Wan and Dozier, 1996; Wan, 2008).

On the other hand, reanalysis data including monthly means of skin temperature were processed from the ERA-Interim dataset from 1979 to 2013. This data was developed by the European Centre for Medium-Range Weather Forecasts (ECMWF) at 0.75° × 0.75° latitude-longitude global spatial resolutions. It has several features, such as four – dimensional variational data assimilation and variational bias correction of satellite radiance data (Dee et al., 2011).

2.2 Non-parametric trend analysis

In order to analyse the LST time series, the temperature anomaly from remote sensing data (land surface temperature) and reanalysis data (skin temperature) was carried out.

Once the anomaly for each data set was estimated, a trend analysis was applied considering its significance and slope magnitude. To this end, Mann-Kendall's analysis (Kendall, 1975) was used to identify the sign (eq. 1) and level of significance (eq. 2 and 3) in decadal trend.

$$t = \sum_{i=1}^{n-1} \sum_{j=i+1}^n \text{sign}(x_j - x_i) \quad (1)$$

Where t corresponds to sign of trend, x_i and x_j are anomalies of temperature time series.

$$\text{var}(t) = \frac{1}{18} \left(n(n-1)(2n+5) - \sum_{q=1}^g t_q(t_q - q)(2t_q + 5) \right) \quad (2)$$

$$Z = \begin{cases} \frac{t-1}{\sqrt{\text{var}(t)}} & \text{if } t < 0 \\ 0 & \text{if } t = 0 \\ \frac{t+1}{\sqrt{\text{var}(t)}} & \text{if } t > 0 \end{cases} \quad (3)$$

From t and t variance of, the parameter of the normal distribution is estimated. Therefore it is possible to submit to a test of hypothesis. Then, the Sen's method (Sen, 1968) was used to estimate the slope (warming/cooling rates) through the calculation of the median obtained by the equation (4).

$$m_q = \frac{y_j - y_i}{x_j - x_i} \quad \forall \quad i < j \quad (4)$$

Where corresponds to a slope time series combination. Both, Mann-Kendall and Sen-Slope method are non-parametric test and make no assumptions on distribution of data trends were computed on a pixel-by-pixel basis for each data set trends were calculated when at least 70% of the data included in the temporal series will be a valid data. To establish different statistical confidential levels, three different levels of significance will be considered for the trends: 0.1, 0.05 and 0.01 p-levels, with confidence levels of 90%, 95% and 99%, respectively.

The trends were characterized by temporal resolution such as monthly mean, seasonal and yearly. The results were associated with previous results widely documented in literature.

3 RESULTS AND DISCUSSION

3.1 Monthly trends MODIS-ERA

The results of monthly trends of LST on the Antarctic Peninsula are presented. Figure 2 shows the monthly mean slopes for ERA and MODIS data. The results show significant differences between the trends obtained from MODIS-LST and TSKIN-ERA. This difference is pronounced in the extreme of the Antarctic Peninsula where the trends is +0.7°C/decade for ERA and -1.1°C/decade for MODIS.

The differences between the results obtained from both sources of data may be associated to different spatial resolution between MODIS products and ERA.

The Antarctic Peninsula shows the highest variation in the trend and where a largest pixel is influenced by the effects of sea.

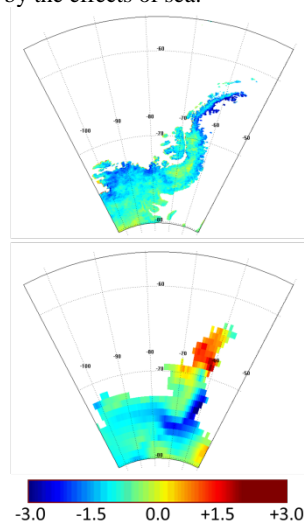


Figure 2. (a) Monthly LST-MODIS trend between 2001 – 2013 and (b) Monthly TSKIN-ERA in same period, in $^{\circ}\text{C}/\text{decade}$.

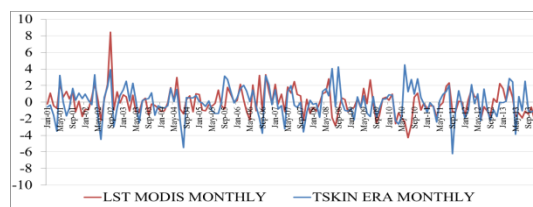


Figure 3. Monthly anomalies ($^{\circ}\text{C}$) of LST-MODIS (red line) and TSKIN-ERA anomalies (blue line) between 2001 and 2013.

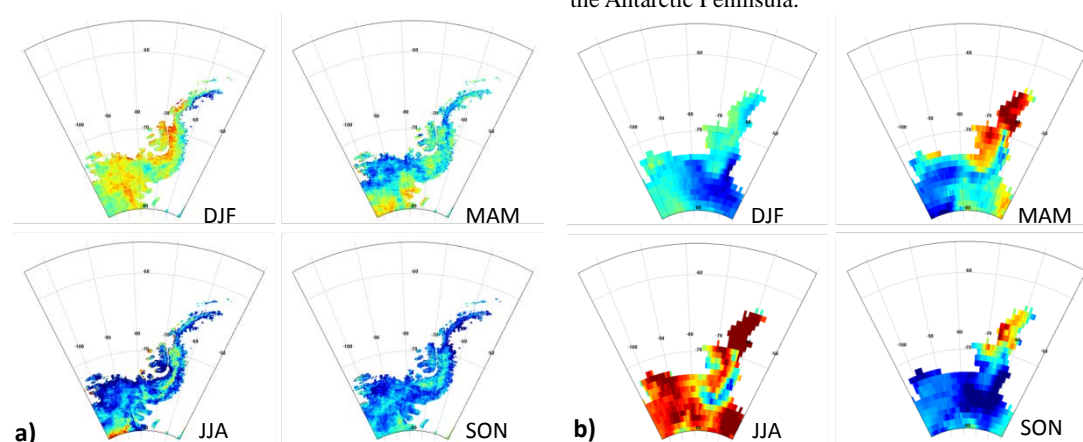


Figure 4. Seasonal LST-MODIS trend (in a) and Seasonal TSKIN-ERA (in b) between 2001 – 2013.

The monthly mean anomalies of remote sensing data and reanalysis shown certain differences over the period 2001-2013, pronounced in the winter months. In Figure 3 the anomalies over the whole Antarctic Peninsula are displayed and it can be clearly seen that in the winter months when the higher bias between MODIS and ERA occurs, just as likely to find the cloud cover is higher in the year.

Another important cause that explains the differences obtained between LST MODIS and skin temperature ERA-Interim trends is the influence of cloudiness that strongly affects the acquisition of remote sensing data in the thermal region, creating a gap between the results generated from different data set. These cloud effects cannot be influenced by ERA-interim reanalysis since these products were generated in a global assimilation model without thermal remote sensing data.

3.2 Seasonal trends MODIS-ERA

In this section the main results of the seasonal trends shown of LST on the Antarctic Peninsula are presented. It seems that for MODIS seasonal anomalies, non-significant warming was retrieved, probably to clouds effect. In contrast, the JJA season reveals a strong warming by using ERA skin temperature. In average the trend is about to $+1.7^{\circ}\text{C}/\text{decade}$.

It seems that for MODIS seasonal anomalies, non-significant warming/cooling is retrieved, probably due to clouds effects and quality assessment of MODIS products. In contrast, the JJA season reveals a strong warming by using ERA skin temperature. In average the trend is about to $-1.7^{\circ}\text{C}/\text{decade}$ for SON, a cooling trend is observed but non-statistically significant. Figure 4 shows the differences in trends of ERA Interim and MODIS anomalies spatially distributed in the Antarctic Peninsula.

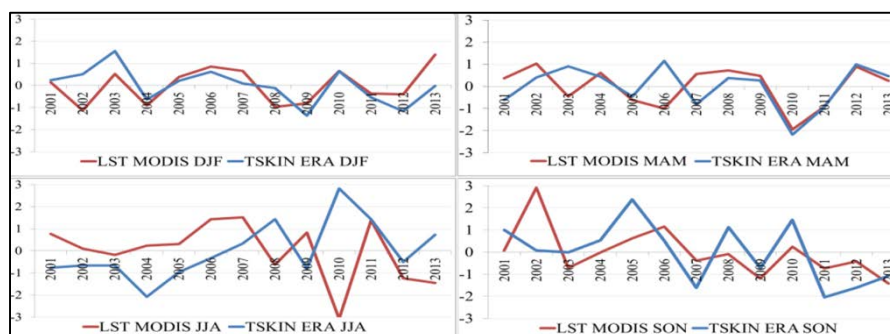


Figure 5. Seasonal anomalies (°C) of LST-MODIS and TSKIN-ERA between 2001–2013 for DJF, MAM, JJA and SON.

Previous results reported in the literature are consistent with results obtained from ERA-Interim which describe a strong seasonality trends in surface temperature and a significant winter warming on the Antarctic Peninsula (Vaughan et al, 2003; Jacka et al, 2004).

Figure 5 shows the seasonal anomalies of MODIS LST and ERA-Interim skin temperature in the period 2001–2013 for the whole area of the Antarctic Peninsula. In both data sets similar behaviors are observed over the time, except for the winter season, where MODIS trends and ERA show different sign and magnitude.

4 CONCLUSIONS

Land surface temperature trends over the Antarctic Peninsula present different patterns at comparing MODIS and ERA-Interim data. Seasonal warming was revealed during JJA by using ERA-Interim. The rest of seasons have not evidence statistically significant changes.

5 ACKNOWLEDGMENTS

This Work is supported by Fondecyt-Initial 11130359 and U-Inicia VID 4/0612. The authors also acknowledge to ECMWF for the free distribution of ERA-interim data and NASA for the free distribution of LST-MODIS products.

6 REFERENCES

Comiso, J. C. 2000. Variability and trends in Antarctic surface temperatures from in situ and satellite infrared measurements. *Journal of Climate*, 13, 1674–1696.

Dee, D. P. & Coauthors. 2011. The ERA - Interim Reanalysis: configuration and performance of the data assimilation system. *Quarterly Journal of the Royal Meteorological Society*, 137, 553–597.

Doran, P. T., & Coauthors. 2002. Antarctic climate cooling and terrestrial ecosystem response. *Nature*, 415, 517–520.

Holmes, T. R. H., R. A.M. De Jeu, & A. j. Dolman. 2009. Land surface temperature from Ka band (37 GHz) passive microwave observations. *Journal of Geophysical Research*, 114(D4), p.D04113.

Jacka, T. H., W. F. Budd, & A. Holder. 2004. A further assessment of surface temperature changes at stations in the Antarctic and Southern Ocean, 1949–2002. *Annals of Glaciology*, 39, 331–338.

Johanson, C. M., & Q. Fu. 2007. Antarctic atmospheric temperature trend patterns from satellite observations. *Geophysical Research Letter*, 34, L12703.

Kendall, M. G. 1975. *Rank Correlation Methods*. Charles Griffin: London.

Monaghan, A. J., D. H. Bromwich, W. Chapman, and J. C. Comiso, “Recent variability and trends of Antarctic near-surface temperature,” *J. Geophys. Res.*, vol. 113, no. D4, p. D04105, Feb. 2008.

Sen, P. K. 1968. Estimates of the regression coefficient based on Kendall’s tau. *Journal of the American Statistical Association*. 63, 1379–1389.

Simmons A. J., P. D. Jones, V. da Costa Bechtold, A. C. M. Beljaars, P. W. Kallberg, S. Saarinen, S. M. Uppala, P. Viterbo, and N. Wedi. 2004. Comparison of trends and low-frequency variability in CRU,ERA-40, and NCEP/NCAR analyses of surface air temperature. *Journal Of Geophysical Research*, Vol. 109, D24115.

Steig, E. J., D. P. Schneider, S. D. Rutherford, M. E. Mann, J. C. Comiso & D. T. Shindell. 2009. Warming of the Antarctic ice-sheet surface since the 1957 International Geophysical Year. *Nature*, 457, 459–462.

Thompson, D. W. J. & S. Solomon. 2002. Interpretation of recent Southern Hemisphere climate change. *Science*, 296, 895–899.

Turner, J., J. C. King, T. A. Lachlan-Cope & P. D. Jones. 2002. Climate change Recent temperature trends in the Antarctic. *Nature*, 418, 291–292.

Turner, J., T. A. Lachlan-Cope, S. Colwell, G. J. Marshall, & W. M. Connolley. 2006. Significant warming of the Antarctic winter troposphere. *Science*, 311, 1914–1917.

Vaughan, D.G., Marshall, G.J., Connelley, W., Parkinson, C., Mulvaney, R., Hodgson, D. A., Turner, J. (2003). Recent Rapid Regional Climate warming On The Antarctic Peninsula. *Climatic Change*, 60, 243–274.

Wan, Z., & Dozier, J. 1996. A generalized split-window algorithm for retrieving land surface temperature from space. *IEEE transactions on geoscience and remote sensing*, 34(4), 892–905.

Wan, Z. 2008. New refinements and validation of the MODIS land-surface temperature/emissivity products. *Remote Sensing of Environment*, 112(1), 59–74.

Monitoring pasture quality and production in extensive systems for an integrated management of oak savannas

P.J. Gómez-Giráldez^{a1}, A. García-Moreno^{a2}, P. Fernández-Rebollo^{b3}, A.B. Caño^{a4}, M.D. Carbonero^{a5}, M.P. González-Dugo^{a6}

^a IFAPA. Consejería de Agricultura, Pesca y Desarrollo Rural. Apdo. 3092 Córdoba, Spain

^b Departamento de Ingeniería Forestal. ETSIAM. Universidad de Córdoba. Campus de Rabanales 14071 Córdoba, Spain

¹pjesus.gomez@juntadeandalucia.es, ²alma.garcia@juntadeandalucia.es, ³ir1ferep@uco.es,

⁴antoniab.cano@juntadeandalucia.es, ⁵mariad.carbonero@juntadeandalucia.es,

⁶mariap.gonzalez.d@juntadeandalucia.es

ABSTRACT- This work explores the monitoring of grassland production and quality in extensive systems using remotely sensed data with different spatial and temporal scales. Pastures net primary production was estimated using an adaptation of Monteith model. A regional approach for dehesa (oak savannah) area in the north of Cordoba (Spain) has been developed combining MODIS products at 250 m of spatial resolution with spatially interpolated meteorological data. When compared with field measurement, grassland production estimations presented an overestimation at the beginning of the growing season, with a mean absolute error (MAE) equal to 118 kg/ha that decreases to 61 kg/ha at the end of the season. In order to estimate pasture quality, canopy hyperspectral reflectance was measured in the 350-2500 nm wavelength range over natural pastures and Nitrogen concentration of the ground samples was determined using an automated combustion instrument. The equation calculated by PLS regression allowed for a good prediction N concentration (calibration $r^2=0.76$ and validation $r^2=0.86$). The relationship obtained between Canopy chlorophyll concentration index (CCCI) and N concentration was poor ($r^2=0.16$), slightly improved when N values were lower than 2.0 ($r^2=0.47$). When the total data set was analyzed by farms the improvement of relationship accuracy was different between them ($r^2=0.22$, 0.41 and 0.42 respectively).

1 INTRODUCTION

Extensive livestock is the main economic activity supporting Mediterranean pastures. These areas provide important ecosystem services as the prevention of forest fires, the protection of soils or the conservation of key habitats for biodiversity, and they possess significant cultural and historical values. Oak savannas, known as *dehesas* in Spain and *montados* in Portugal, cover about 3 million hectares in the Iberian Peninsula and Greece. The monitoring of these large areas requires effective tools that provide timely and accurate data to assist management and decision-making at different levels. This work focuses in the estimation of pasture production and quality using remotely sensed data at different scales.

Regarding pasture production, biomass estimation models integrating remote sensors are often used in agriculture to provide input data for crop models that predict or estimate crop yield. Empirical models are easy to apply but difficult to extrapolate, the approaches with a more physical basis, such as biomass estimate model of Monteith (1977), allow to incorporate remote data, as satellite derived fraction of PAR radiation absorbed by the plant, and combine it with meteorological information to provide accurate biomass estimation (Padilla et al., 2012). For pasture

production there are several empirical models like Hobbs (1995). In forestry, there are many studies of biomass production for homogeneous forest or forest plantations mixed with different techniques, such mechanistic models with eddy covariance systems, or forest inventories (Van Tuyl et al., 2005). Some studies (Sjöström et al., 2008; Ma et al., 2014) focus in savannah. However, the particular structure of dehesa system presents some difficulties for this type of studies, previous experiences are rare, focusing on general grass production models without remote sensors (e.g. Haydock and Shaw, 1975).

On the other hand, the pasture quality is important for pasture management and livestock since it determine the production response per unit of pasture consumed by the animals. Traditional laboratory analyses of grass nutritive value are time-consuming and costly. Some studies (Pullanagari et al., 2012; Starks et al., 2008) suggested that functional relations may be obtained between vegetation reflectance provided by remote sensing and biochemical variables, successfully predicting quality. Changes in variables, such as nitrogen concentration (N) and in-vitro dry matter digestibility (IVDMD), therefore, should affect properties of canopy reflectance in a wide range of spectra from 400 to 1695 nm (Starks et al., 2008).

Previous studies have found high correlations (>0.95) between crude protein (CP), acid detergent fibre (ADF), neutral detergent fibre (NDF) and organic matter digestibility (OMD) and spectral information comes from dry and ground pasture samples, offering a rapid and inexpensive approach to assess these properties.

The final purpose of this work is to test the ability of remote sensing to support the development of an advisory service in the framework of LIFE bioDEHESA project, which may help farmers to make appropriate decisions and minimize feed costs of animals in extensive grazing systems, preventing overexploitation, and seeking to ensure the conservation of the system but guaranteeing profitability. To do this, a first approach has been developed in a dehesa region located in the North of Cordoba (Spain, Fig. 1).

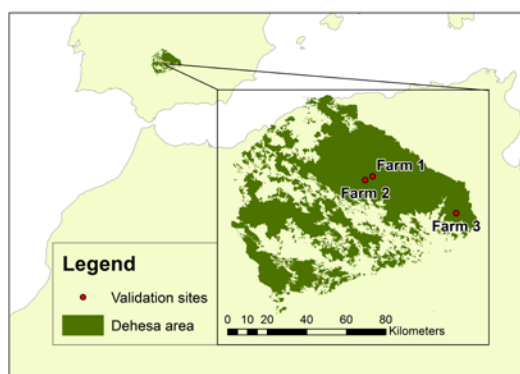


Figure 1. Study area and validation farms.

2 METHODOLOGY

2.1 Pasture production

Daily values of meteorological variables such as solar radiation (R_d), minimum air temperature (T_{min}) and vapour pressure deficit (VPD) were obtained for the study period (pasture growing season 2013-2014) by 18 meteorological stations, part of the Andalusian Agroclimatic Network stations (RIA), distributed along the region. These variables were spatially interpolated. For these interpolations the IDW (Inverse Distance Weight) was applied directly for DPV. T_{min} used IDW corrected through DEM using a gradient of -0.6°C each 100 meters of height. In the case of R_d , the effect of clouds and atmosphere was included by means of a clarity index (Herrero et al. 2011).

The estimation of pasture net primary production has been obtained using an adaptation of Monteith model (1977):

$$NPP = \int fAPAR \cdot PAR \cdot \epsilon \cdot dt \quad (1)$$

where:

NPP (g/ha): Net primary production

fAPAR (dimensionless): Fraction of photosynthetically active radiation absorbed by the vegetation. It is estimated from daily NDVI series, based on MODIS reflectance products (MOD09Q1). This estimation used an experimental expression obtained for wheat by Padilla et al. 2012:

$$fAPAR = 1.16 \cdot NDVI - 0.19 \quad (2)$$

Previously, an annual average value of NDVI corresponding to sparse oak trees canopies is subtracted from daily data for each pixel. This value is taken from values obtained during the dry season, when annual pasture is dry and the only photosynthetic activity canopy corresponded to oak trees. The stability of this value during the year was verified with field measurements with an ASD FieldSpec FR spectroradiometer during the 2013/2014 growing season.

PAR (MJ): Photosynthetically active radiation. It is derived from total solar radiation data, provided by weather stations, using a reduction factor of 0.48 for PAR as average.

ϵ (g/MJ): Light use efficiency. A maximum value of 0.768 gC/MJ have been used. This constant value is modified according to climatic variables that reduce plant efficiency, as the daily minimum temperature and humidity. Thresholds values for both variables (-8 and 11.39°C for T_{min} ; 0.65 and 3.1 kPa for VPD) were taken from previous studies in wooded grassland (Running et al. 2000).

This model was applied from February to June of 2014. This period was chosen according to the first rainfall event that is supposed to trigger the beginning of pasture growth.

Three pilot farms were chosen in the study area (Fig. 1) as validation sites. Farms 1 and 2 had presence of livestock during the study period.

Pastures biomass samples were taken at plot level to serve as validation dataset. These biomass samples were collected during the growing season (March to June 2014) in the three farms. The production was calculated using the Comparative Yield Method (Haydock and Shaw, 1975).

2.2 Pasture quality

Ground surface reflectance was measured in the 350-2500 nm wavelength range over natural pasture in three dehesa farms from early January to late June 2013 using a portable ASD FieldSpec FR spectroradiometer (Analytical Spectral Devices Inc., Boulder, CO, USA). A total set of 93 samples of canopy reflectance was measured at each sampling site with and without presence of livestock. Thereafter, all above-ground vegetation in plots of 0.16 m^2 area were immediately clipped to a height of about 1 cm above the soil surface. The herbage samples were dried at 65°C for 48 h in a forced-air oven and ground through a 2-mm screen in a laboratory mill. Nitrogen

concentration of ground samples was determined in the laboratory using an automated combustion instrument (LECO, St Joseph, MI, USA).

The estimation of nitrogen content using the spectral data was carried out by two different methods:

i) Partial least-squares regression (PLSR). This method reduces high dimensional data into a limited number of uncorrelated components based on the covariance between the predictors and response variables. Reflectance values in two ranges (i.e. 1830-1940 nm and 2400-2500 nm) were first omitted from the reflectance data sets because of instrument noise, giving a total of 2290 wavebands. The model was calculated with 71 samples and was subsequently evaluated by external validation set of 22 samples, which were selected randomly from the total set.

The predictive ability of the model was evaluated by coefficient of determination (r^2) and the root mean square error (RMSE).

ii) The canopy chlorophyll concentration index (CCCI) (Barnes et al., 2000). It is a two dimensional index, utilizing NDVI as an estimate of percent cover, and the normalized difference far red index (NDFR), which is sensitive to plant chlorophyll content or nitrogen status.

$CCCI = \frac{NDFR - NDFR_{MIN}}{NDFR_{MAX} - NDFR_{MIN}}$
where upper (MAX) and lower (MIN) bounds for NDFR are determined as a function of NDVI.

3 RESULTS

3.1 Net Primary Production

Figure 2 shows an example of the daily spatial interpolation for meteorological variables (Rd, Tmin and VPD).

Daily Tmin and VPD maps were used to reduce the light-use maximum efficiency and Rd maps were applied to estimate, along with fAPAR images, the available energy to produce biomass. Regional estimations of net primary production were produced at daily scale using the modified Monteith approach. Daily net production was aggregated at seasonal level for the grasslands growing season (February to June).

In Figure 3 it can be seen the final net primary production (accumulated from February to June).

The validation of biomass estimated values was performed comparing the available observations over the field sites and the seasonal estimations. The results are shown in Figure 4, the estimations presented a mean absolute error (MAE) at the beginning of the season of 118 kg/ha, that represents the 43% of error, while at the end of the growing season the model deviation was reduced to a MAE equal to 61 kg/ha equivalent to the 9.3% of measured average production of grasslands, with a global error for the whole season of 28.4%.

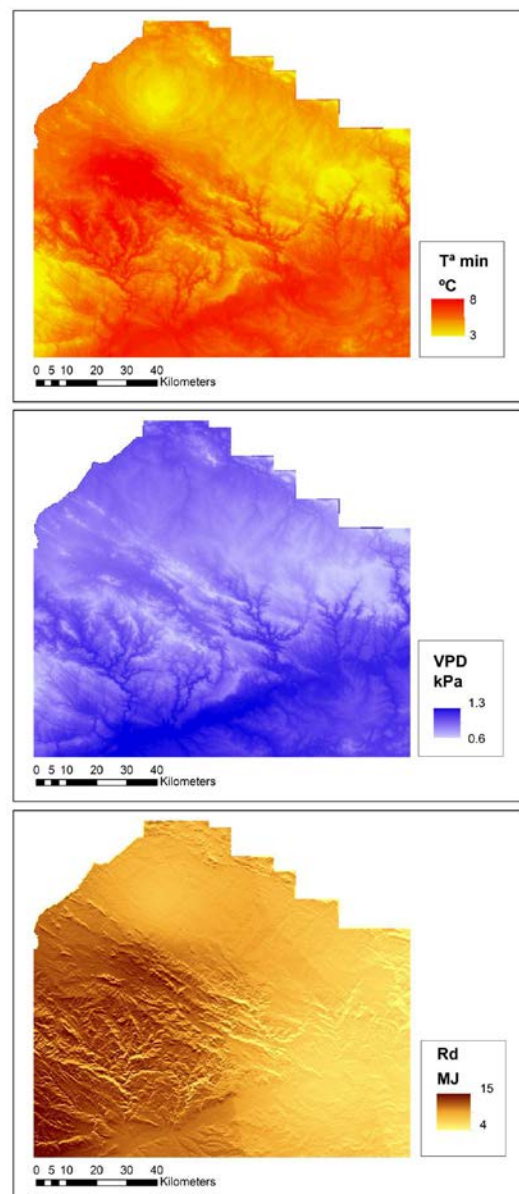


Figure 2. Spatial interpolation of Rd, Tmin and VPD for the 28th of February, 2014.

The error at the end of growing season (<10%) can be considered as excellent for authors like Jamieson et al. (1991), Bannayan and Hoogenboom (2009) and Dettori et al. (2011) in their classification for crops, while the strong error at the beginning corresponded with the presence of livestock in Farms 1 and 2 during that period (February to March). This effect can be observed in Figure 5, where the three farms are represented at temporal scale. The global one is acceptable (between 20 and 30%).

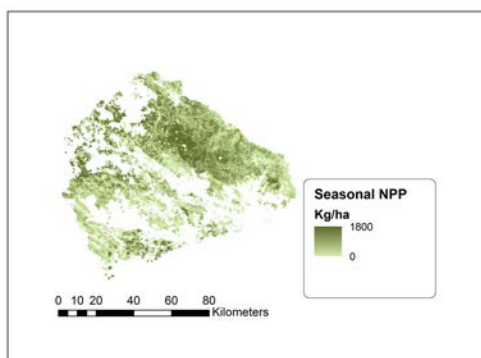


Figure 3. Seasonal Net Primary Production (February to June of 2014) over the study area

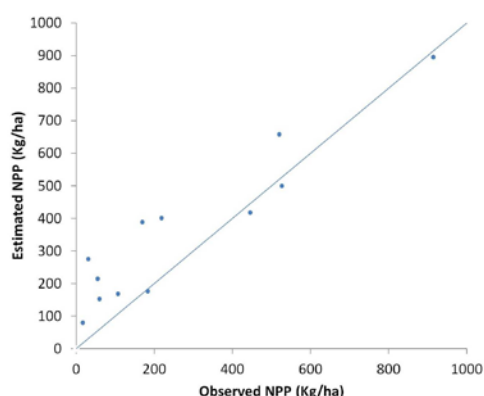


Figure 4. Comparison of estimated and measured grassland production at plot level.

3.2 Pasture quality

The calibration model calculated by PLS regression method provided a good prediction of N concentration, pointing out the value of this method for extracting important information from multiple wavelengths. The estimated values were well correlated with the measured ones (calibration $r^2=0.76$; RMSE=0.41 and validation $r^2=0.84$; RMSE=0.35) (Fig.6).

Relationship between CCCI and N concentration considering all data sets was poor ($r^2=0.16$) (Fig. 7). For N values lower than 2.0, which were obtained from May to June, the relationship accuracy was improved ($r^2=0.468$). When the total analytical data set was divided into individual farms, the relationship accuracy was also improved. However, this improvement was variable by farm, and required further research.

4 CONCLUSIONS

The results of pasture production showed an overestimation at the beginning of the growing season, which might be due to the grazing management of the study plots. Farm 1 was the most grazed, in opposite to Farm 3 that was not grazed during the measurement

period. The mean absolute error (MAE) at the beginning of the season, when farms 1 and 2 were grazed, was 118 kg/ha, while at the end of the growing season the model deviation was reduced to a MAE equal to 61 kg/ha. This estimation is considered appropriate to the scale and objectives of potential applications in pasture management and the initial error will require further data and analysis to account for overestimation.

Regarding the pasture quality assessment, the equation calculated by PLS-regression allowed for a good prediction of N concentration, demonstrating the potential of using canopy hyperspectral reflectance to estimate N concentration of grasses through PLS regression, which uses all wavebands. However, the CCCI showed little sensitivity to nitrogen concentration, presenting a poor relationship ($r^2=0.16$) when all data were considered. When the total analytical dataset was divided into individual farms or were considered N values lower than 2.0, the accuracy of the estimations was improved, suggesting an influence of external factors not considered in this analysis.

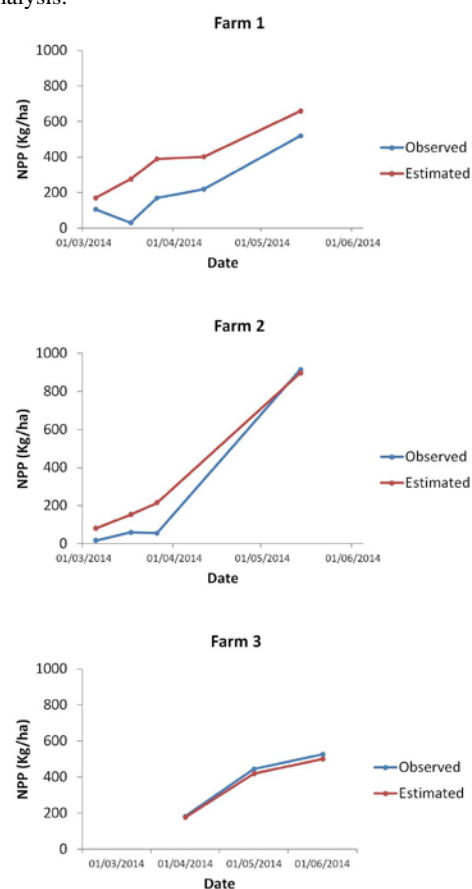


Figure 5. Temporal evolution of observed and estimated NPP in the three validation farms.

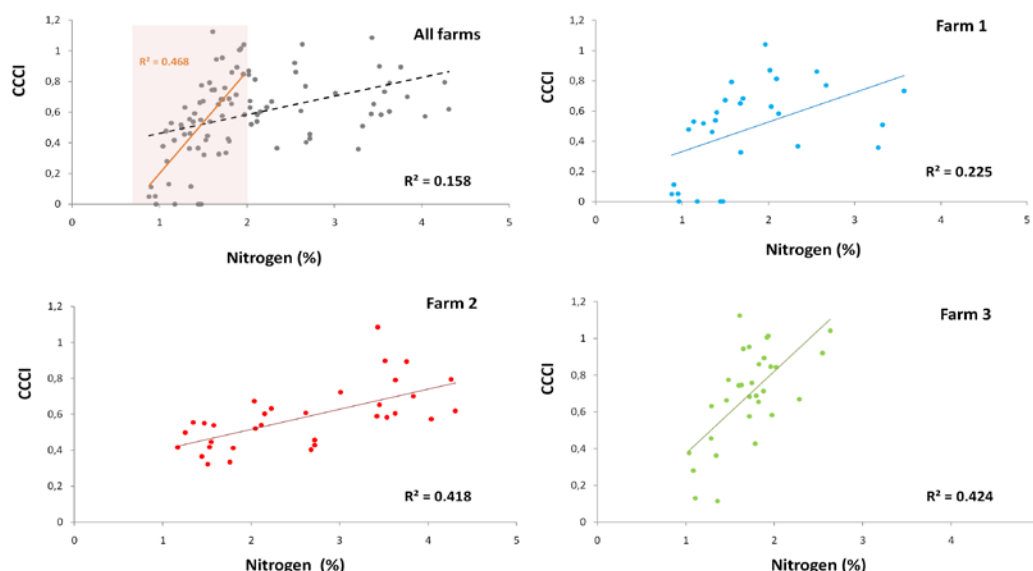


Figure 6. Relation between CCCI and nitrogen concentration (%), in all farms together and each farm separately

4 CONCLUSIONS

The results of pasture production showed an overestimation at the beginning of the growing season, which might be due to the grazing management of the study plots. Farm 1 was the most grazed, in opposite to Farm 3 that was not grazed during the measurement period. The mean absolute error (MAE) at the beginning of the season, when farms 1 and 2 were grazed, was 118 kg/ha, while at the end of the growing season the model deviation was reduced to a MAE equal to 61 kg/ha. This estimation is considered appropriate to the scale and objectives of potential applications in pasture management and the initial error will require further data and analysis to account for overestimation.

Regarding the pasture quality assessment, the equation calculated by PLS-regression allowed for a good prediction of N concentration, demonstrating the potential of using canopy hyperspectral reflectance to estimate N concentration of grasses through PLS regression, which uses all wavebands. However, the CCCI showed little sensitivity to nitrogen concentration, presenting a poor relationship ($r^2=0.16$) when all data were considered. When the total analytical dataset was divided into individual farms or were considered N values lower than 2.0, the accuracy of the estimations was improved, suggesting an influence of external factors not considered in this analysis.

Ground-based remote sensors offer an alternative for estimating natural pasture N concentrations, however their utility seems limited when only few bands are used.

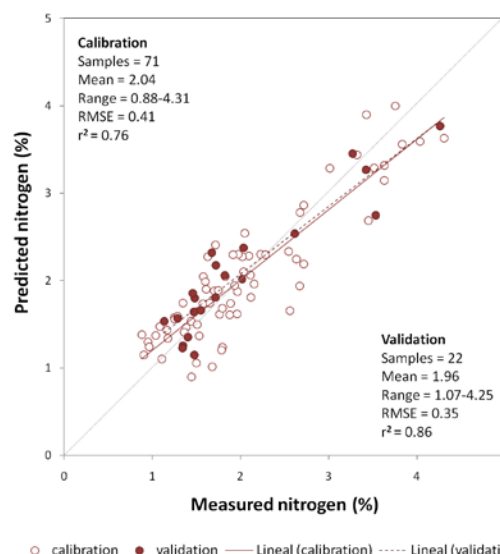


Figure 7. Relationship between laboratory measured nitrogen and predicted nitrogen using the calibration and validation sets.

5 ACKNOWLEDGMENTS

This work has been partially funded by LIFE+bioDehesa project (LIFE11/BIO/ES/000726).

6 REFERENCES

- Barnes, E.M., Clarke, T.R., Colaizzi, P., Haberland, J., Kostrzewski, M., Riley, E., Moran, S., Waller, P., Choi, C., Thompson, T., Richards, S., Lascano, R., Li, H., 2000, Coincident detection of crop water stress, nitrogen status, and canopy density

- using ground-based multispectral data. In: Proceedings of the Fifth International Conference on Precision Agriculture, 16–19 July, at Bloomington, MN, USA.
- Bannayan, M., Hoogenboom, G., 2009, Using pattern recognition for estimating cultivar coefficients of a crop simulation model. *Field Crops Research*. 111, 290-302.
- Dettoni, M., Cesaraccio, C. Motroni, A., Spano, D., Duce, P., 2011, Using CERES-Wheat to simulate durum wheat production and phenology in Southern Sardinia, Italy. *Field Crops Research*. 120, 179-188.
- El-Shikha, D.M., Waller, P., Hunsaker, D., Clarke T., Barnes E., 2007. Ground-based remote sensing for assessing water and nitrogen status of broccoli. *Agricultural water management*, 92, 183-193.
- Haydock, K.P., Shaw, N.H., 1975, The comparative yield method for estimating the dry matter yield of pasture. *Australian Journal of Experimental Agriculture and Animal Husbandry*. 15: 663-670.
- Herrero, J., Millares, A., Aguilar, C., Díaz, A., Polo, M. J., Losada, M. A., 2011. WiMMed. Base teórica. (WiM-Med. Theoretical basis). Grupo de Dinámica de Flujos Ambientales, (University of Granada) and Grupo de Dinámica Fluvial e Hidrología, (University of Córdoba), Granada, available at: http://www.uco.es/dfh/images/stories/20110614%20wimmed_teoria1.pdf
- Hobbs, T.J., 1995, The use of NOAA-AVHRR NDVI data to assess herbage production in the arid rangelands of Central Australia. *International Journal of Remote Sensing*. 7(16), 1289-1302.
- Jamieson, P.H., Porter, J.R., Wilson, D.R., 1991, A test of the computer simulation model ARCWheat on wheat crops grown in New Zealand. *Field Crops Research*. 27, 337-350.
- Ma, X., Huete, A., Yu, Q., Restrepo-Coupe, N., Beringer, J., Hutley, L.B., Kanniah, K.D., Cleverly, J., Eamus, D., 2014, Parameterization of an ecosystem light-use-efficiency model for predicting savanna GPP using MODIS EVI. *Remote Sensing of Environment*. 154, 253-271.
- Monteith, J., 1977, Climate and efficiency of crop production in Britain. *Philosophical Transactions of the Royal Society of London, Ser. B*: 277-294.
- Padilla, F.L.M., Maas, S.J., González-Dugo, M.P., Mansilla, F., Rajan, N., Gavilán P. and Domínguez, J., 2012, Monitoring regional wheat yield in Southern Spain using the GRAMI Model and satellite imagery. *Field Crops Research*. 130, 145-154.
- Pullanagari, R.R., Yule, I.J., Tuohy, M.P., Hedley, M.J., Dynes, R.A. and King, W.M., 2012, Proximal sensing of the seasonal variability of pasture nutritive value using multispectral radiometry. *Grass Forage Science Journal*. 68, 110–119.
- Running, S.W., Thornton, P.E. Nemani, R. Glassy, J.M., 2000, Global terrestrial gross and net primary productivity from the Earth Observing System. *Methods in Ecosystem Science*. O. Sala, R. Jackson and H. Mooney. New York, Springer Verlag: 44-57.
- Sjöström, M., Ardö, J., Eklundh, L., El-Tahir, B.A., El-Khidir, H.A.M., Hellström, M., Pilesjö, P. and Seaquist, J., 2009, Evaluation of satellite based indices for gross primary production estimates in a sparse savanna in the Sudan. *Biogeosciences*. 6, 129–138.
- Starks, P.J; Zhao, D. and Brown, M.A., 2008, Estimation of nitrogen concentration and in vitro dry matter digestibility of herbage of warm-season grass pastures from canopy hyperspectral reflectance measurements. *Grass Forage Science Journal*. 63, 168–178.
- Van Tuyl, S., Law, B.E., Turner, D.P. and Gitelman, A.I., 2005, Variability in net primary production and carbon storage in biomass across Oregon forests—an assessment integrating data from forest inventories, intensive sites, and remote sensing. *Forest Ecology and Management*. 209, 273-291.

Quantitative Estimation of Sun-induced Fluorescence from the Apparent Reflectance

Zhuoya NI^{1,2}, Zhigang LIU^{1,*}, Zhao-Liang LI^{2,3}, Françoise NERRY², Hongyuan HUO⁴ and Xiaowen LI¹

¹State Key Laboratory of Remote Sensing Science, School of Geography, Beijing Key Laboratory of Environmental Remote Sensing and Digital City, Beijing Normal University, Beijing, 100875, China; E-Mails: nizhuoya@gmail.com; lix@bnu.edu.cn

²ICube, CNRS, Université de Strasbourg, 300 Boulevard Sébastien Brant, CS10413, Illkirch 67412, France; E-Mails: lizl@unistra.fr; f.nerry@unistra.fr

³Key Laboratory of Agri-informatics, Ministry of Agriculture/Institute of Agricultural Resources and Regional Planning, Chinese Academy of Agricultural Sciences, Beijing 100081, China

⁴Tianjin Normal University, Tianjin 300387, China; E-Mail: huohongyuan2008@163.com

*E-Mail: zhigangliu@bnu.edu.cn; Tel.: +86-010-5880-7698; Fax: +86-010-5880-5274.

ABSTRACT - In this paper, we developed a new method based on reflectance index to quantitatively extract the sun-induced fluorescence. The sensitivity analysis was conducted with the FluorMOD model to define which parameters affected mostly the $L(F)761$ (fluorescence radiance at the wavelength 761nm simulated by FluorMOD). From the results of sensitivity analysis, we considered that sun zenith angle (θ), fluorescence quantum efficiency (F_i), leaf inclination distribution function (LIDF), leaf temperature (T), leaf area index (LAI) and leaf chlorophyll $a+b$ content (Cab) accounted for most of the $L(F)761$ variations. Sensitivity analysis paved the way to generate the simulated data including the reflectance spectrum and fluorescence radiation. Based on the simulated data, the quantitative relationship analysis were done between the existing reflectance indices and $L(F)761$, and $R740/R630$, $R685/R850$ and $R750/R710$ which could be proved to be best candidates to extract the fluorescence radiation. The result showed that this method could be used to retrieve the fluorescence and provide a new way to estimate the fluorescence quantitatively. It demonstrated that it was feasible to use the hyperspectral remote sensing and thermal infrared remote sensing to retrieve the fluorescence radiation.

1 INTRODUCTION

Remote sensing is a reliable and operational way to relate remote sensing measurement to the biochemical at earth surfaces in. It is feasible to extract Sun-induced Fluorescence (SIF) from hyperspectral image. SIF is considered to be an ideal, fast, non-invasive and sensitive probe to detect the physiological state of the vegetation and provides a new way for global vegetation monitoring and global biomass estimating (Genty, Briantais et al. 1989).

Quantify detecting SIF was first reported in vegetation canopies in 1980 by McFarlane et al., who use the Ha Fraunhofer line at 656nm to measure SIF (McFarlane, Watson et al. 1980). According to previous literatures, the methods of detecting fluorescence have radiance-based methods and reflectance-based methods (Meroni, Rossini et al. 2009). The first methods are FLDs. Fraunhofer Line Depth (FLD) principle which was proposed by Plascyk (Plascyk 1975) and Plascyk and Gabriel (Plascyk and Gabriel 1975). FLD used downward solar irradiance and the upward canopy radiance inside the Fraunhofer line and the other measurement outside. The weakness

of FLD was that the reflectance and fluorescence of inside bands were assumed to be the same that of outside bands. As to the weakness of FLD, a series of methods were proposed by modify this restriction, which include 3FLD (3 Fraunhofer Line Depth) (Maier, Günther et al. 2003), cFLD (corrected Fraunhofer Line Depth) (Maier, Günther et al. 2003; Moya, Daumard et al. 2006), iFLD (improved Fraunhofer Line Depth) (Alonso, Gomez-Chova et al. 2008), eFLD (extended Fraunhofer Line Depth) (Mazzoni 2007) and SFM (Spectral Fitting Methods) (Meroni, Busetto et al. 2010). FLD methods were radiance-based methods which calculated SIF in physic units (radiance unit). The second category was reflectance-based approaches. These methods utilized some optical indices to enhance fluorescence, including reflectance ratios (Zarco-Tejada, Miller et al. 2000; Zarco-Tejada, Pushnik et al. 2003; Dobrowski, Pushnik et al. 2005), derivatives ratios (Zarco-Tejada, Miller et al. 2000; Zarco-Tejada, Pushnik et al. 2003) and in-filling method (Pérez-Priego, Zarco-Tejada et al. 2005). It exploited two or three wavelengths to create the indices related to the fluorescence, including at least one wavelength affected by the fluorescence (closer to

the peaks of the fluorescence spectrum) and one wavelength less or not affected. Although these methods only computed the F_s qualitatively, they were only the methods under some conditions, such as using the artificial light or the radiance-based methods failing (Meroni, Rossini et al. 2009).

Within these two methods, the reflectance-based approaches had paid little attention because these methods qualitatively analyzed the F_s using only two or three bands to build different indices related to F_s and compute the F_s without real physical meaning. However, these methods were the ways to obtain F_s quickly and easily. In this paper, the quantitative relationship between the reflectance index and $L(F)761$ was built. The results showed that some other parameters, such as θ , F_i and T , were needed in the process of using the reflectance index to quantitatively extract SIF.

2 FLUORMOD MODEL AND SENSITIVITY ANALYSIS

2.1 FluorMOD

The FluorMOD project was developed by European Space Agency (ESA) to advance the science of vegetation fluorescence simulation through the development and integration of leaf and canopy fluorescence model based on physical methods (Zarco-Tejada, Miller et al. 2004; Zarco-Tejada 2005).

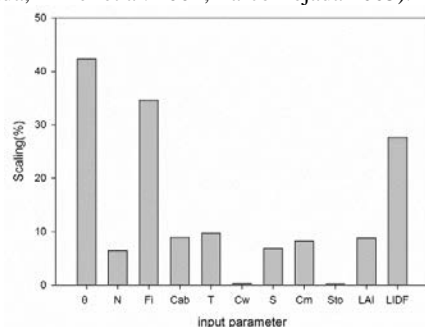


Figure 1. Result of sensitivity analysis for FluorMOD as a function of input parameter.

2.2 Sensitivity analysis

Sensitivity analysis was used to determine what effect each individual input, or pair of inputs, has on the output. The software GEM-SA (Gaussian Emulation Machine for Sensitivity Analysis) was used to perform the sensitivity analysis work. The GEM-SA used a Gaussian process prior probability distribution to describe beliefs about an unknown code output, as a function of the code inputs. Total effects could be generated within GEM-SA and it represented the sum of all main interactions and higher order terms in which a parameter was involved.

Among the parameters whose total effect exceeded 10%, θ whose total effect accounted for 42.32% was the most important. Sun zenith angle is an important parameter because it affects the total intensity of the incoming sunlight. F_i whose total effect accounted for 34.62% was the second important parameter. F_i showed the ability of emitting the fluorescence signal by the leaf, and related with the light absorbed and plant physiological status. The third important parameters were canopy structure parameters including the LAI and LIDF, which directly affected the light intensity accepted by the canopy. Other parameter whose total effects were close to 10%, such as the leaf temperature T and leaf chlorophyll a+b content (Cab), should be considered. The most of energy absorbed by leaf is used to photosynthesis, while the extra energy dissipates in the form of heat dissipation and fluorescence emission. The leaf chlorophyll content is related to the fluorescence yield and heat dissipation has a very close relationship with photosynthesis and fluorescence. Therefore, the variations of these two parameters were also considered in the generation of simulated data.

3 BUILD QUANTITATIVE RELATIONSHIP BETWEEN THE REFLECTANCE INDEX AND $L(F)761$

In this method, LIDF was assumed to spherical distribution, and the FluorMOD model was used to generate the simulated data using the fixed step input parameters F_i (0.01-0.1), T (5-25°C), LAI (0.1-8), Cab (10-90 $\mu\text{g}/\text{cm}^2$) and 13 kinds of atmosphere files (different sun zenith angle θ). The simulated data including the apparent reflectance spectra and fluorescence radiance were used to generate a database which was composed of input parameters (θ , F_i , T , LAI and Cab), the reflectance indices and $L(F)761$.

Based on the simulated data, the optimal reflectance indices were selected. The results showed $R685/R850$, $R740/R630$, $R750/R710$ could be used to retrieve the fluorescence. $R740/R630$ was taken as an example. In the first, the relationship between $R740/R630$ and $L(F)761$ which corresponded to input parameters θ (30), F_i (0.04), T (20°C), LAI (4) and Cab (10-90 $\mu\text{g}/\text{cm}^2$) was analyzed. It showed that this index and $L(F)761$ had same performances along with the increase of chlorophyll content: $R740/R630$ and $L(F)761$ gradually increased with Cab rising (see Figure2a). Under the condition of θ (30), F_i (0.04), T (20°C), LAI(0.1-8) and Cab (10-90 $\mu\text{g}/\text{cm}^2$), $R740/R630$ and $L(F)761$ increased along with rising of LAI (seeing Figure2b), and relationship between $R740/R630$ and $L(F)761$ was insensitive to the variation of LAI and Cab . $L(F)761$ could be expressed as the no-linear function of $R740/R630$: $y=a(1-e^{-bx})+c$, y represented $L(F)761$, and x represented $R740/R630$.

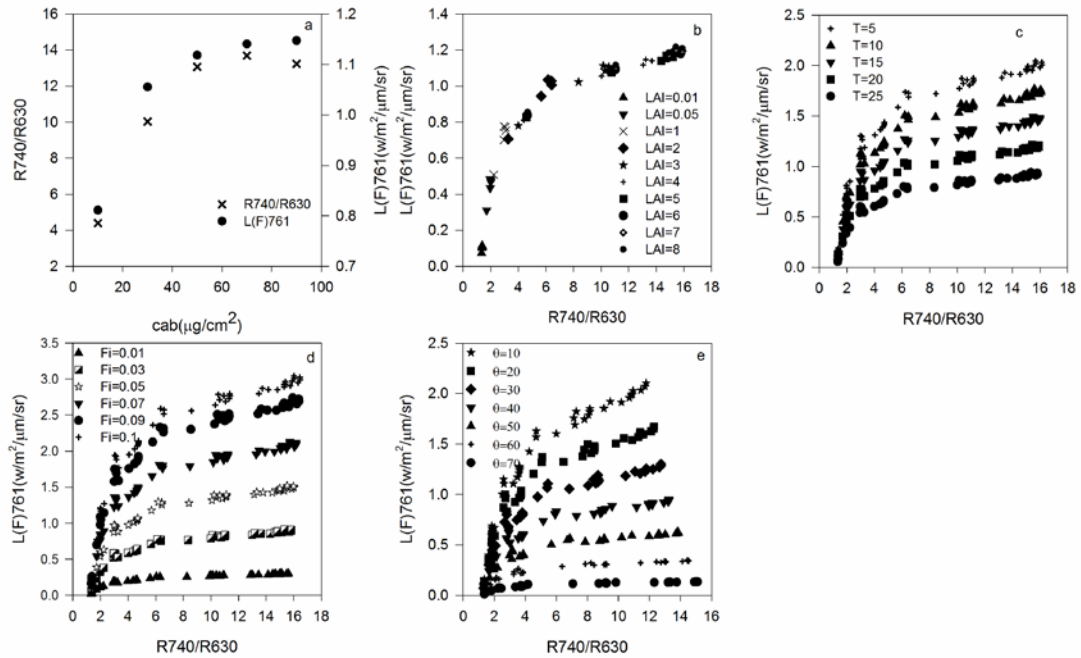


Figure 2. Relationship between L(F)761 and R740/R630. a. $\theta=30^\circ$, $Fi=0.04$, $T=20^\circ\text{C}$, $LAI=4$ and $Cab=10\text{--}90\mu\text{g}/\text{cm}^2$; b. $\theta=30^\circ$, $Fi=0.04$, $T=20^\circ\text{C}$, $LAI=0.1\text{--}8$ and $Cab=10\text{--}90\mu\text{g}/\text{cm}^2$; c. $\theta=30^\circ$, $Fi=0.04$, $T=5\text{--}25^\circ\text{C}$, $LAI=0.1\text{--}8$ and $Cab=10\text{--}90\mu\text{g}/\text{cm}^2$; d. $\theta=30^\circ$, $Fi=0.01\text{--}0.1$, $T=20^\circ\text{C}$, $LAI=0.1\text{--}8$ and $Cab=10\text{--}90\mu\text{g}/\text{cm}^2$; e. $\theta=10\text{--}70^\circ$, $Fi=0.04$, $T=20^\circ\text{C}$, $LAI=0.1\text{--}8$ and $Cab=10\text{--}90\mu\text{g}/\text{cm}^2$.

In the third condition, Fi was set to constant value 0.04, T varied from 5°C to 25°C , LAI changed from 0.1 to 8, and cab was from 10 to $90\mu\text{g}/\text{cm}^2$, $R740/R630$ was compared with $L(F)761$. From the result (seeing Figure 2c), $L(F)761$ decreased with temperature T rising, and the relationship between $R740/R630$ and $L(F)761$ varied regularly. It also revealed that the variation of T was opposed to the variation of fluorescence radiance. In the Figure 2d, the preconditions were Fi varied from 0.01 to 0.1, T was set to 20°C , LAI varied from 0.1 to 8 and cab varied from 10 to $90\mu\text{g}/\text{cm}^2$, the variation of $L(F)761$ proportionated to the variation of Fi . In the Figure 2e, with the increasing of sun zenith angle, the $L(F)761$ decreased, and the function between the $L(F)761$ and $R740/R630$ also changed regularly. According to the above analysis, $L(F)761$ was expressed as the non-linear function of $R740/R630$, θ , Fi and T , such as $y=a*f(b*x)+c$, a , b and c were the function of θ , Fi and T , the variations of θ .

The 26000 simulated data generated by FluorMOD, including sun zenith angle θ , Fi , T , $R685/R850$, $R740/R630$, $R750/R710$ and $L(F)761$, was used to be built a database. By data fitting, the coefficients of formula were obtained. The quantitative model about the reflectance index and $L(F)761$ were obtained. The fluorescence extracted using the quantitative model

was compared with $L(F)761$. By the comparison, it was possible to use this method to retrieve the fluorescence.

4 DISCUSSIONS

Reflectance indices, such as $R740/R630$, which had one wavelength or two wavelengths located between 740nm and 850nm, are less affected by LAI and Cab . It was obvious that a good linear or non-linear relationship existed between $L(F)761$ and some reflectance indices computed from the simulated data. Therefore, these reflectance indices are the best candidates for retrieving the fluorescence quantitatively.

According to the research goal, the reflectance indices which were insensitive to LAI and cab gained more attention. By the analysis, $R740/R630$, $R685/R850$ and $R750/R710$ were selected and the quantitative model in which fluorescence on the canopy was the function of the reflectance index, Fi , T and θ was built. The fluorescence estimated from the quantitative model yielded the best results ($R^2=0.94$, $RMSE=0.32\text{w}/\text{m}^2/\mu\text{m}/\text{sr}$ for $R685/R850$ vs. $L(F)761$; $R^2=0.95$, $RMSE=0.30\text{w}/\text{m}^2/\mu\text{m}/\text{sr}$ for $R750/R710$ vs. $L(F)761$; $R^2=0.95$, $RMSE=0.29\text{w}/\text{m}^2/\mu\text{m}/\text{sr}$ for $R740/R630$ vs. $L(F)761$).

Based on the FluorMOD model, we used the reflectance index, fluorescence quantum efficiency, temperature and sun zenith angle to build the quantitative model to estimate fluorescence radiation. This method gave us new insight to retrieve the fluorescence from the reflectance spectrum and enabled us to retrieve fluorescence quantitatively without determining reference irradiation or sun irradiation.

5 REFERENCES

- Alonso, L., L. Gomez-Chova, et al., 2008. Improved Fraunhofer Line Discrimination method for vegetation fluorescence quantification, *Geoscience and Remote Sensing Letters, IEEE* 5(4), 620-624.
- Dobrowski, S., and J. Pushnik, et al., 2005, Simple reflectance indices track heat and water stress-induced changes in steady-state chlorophyll fluorescence at the canopy scale, *Remote Sensing of Environment*, 97(3), 403-414.
- Genty, B., and J.-M. Briantais, et al., 1989, The relationship between the quantum yield of photosynthetic electron transport and quenching of chlorophyll fluorescence, *Biochimica et Biophysica Acta (BBA) - General Subjects*, 990(1), 87-92.
- Krause, G. H., and E. Weis, 1984, Chlorophyll fluorescence as a tool in plant physiology, *Photosynthesis Research*, 5(2), 139-157.
- Larcher, W., 1994, Photosynthesis as a tool for indicating temperature stress events, *Ecophysiology of photosynthesis*, Springer: 261-277.
- Maier, S. W., and K. P. Günther, et al., 2003, Sun-induced fluorescence: A new tool for precision farming., *Digital imaging and spectral techniques: Applications to precision agriculture and crop physiology* (digitalimaginga), 209-222.
- Mazzoni, M., Agati, G., Del Bianco, S., and Cecchi, G., & Mazzinghi, P., 2007, High resolution measurements of solar induced chlorophyll fluorescence in the Fraunhofer Ha and in the atmospheric oxygen lines. Proceedings of the 3rd International Workshop on Remote Sensing of Vegetation Fluorescences. Florence, Italy.
- McFarlane, J., and R. Watson, et al., 1980, Plant stress detection by remote measurement of fluorescence, *Applied Optics*, 19(19), 3287-3289.
- Meroni, M., and L. Busetto, et al., 2010, Performance of spectral fitting methods for vegetation fluorescence quantification, *Remote Sensing of Environment*, 114(2), 363-374.
- Meroni, M., and M. Rossini, et al., 2009, Remote sensing of solar-induced chlorophyll fluorescence: Review of methods and applications, *Remote Sensing of Environment* 113(10), 2037-2051.
- Moya, I., and F. Daumard, et al., 2006, First airborne multiwavelength passive chlorophyll fluorescence measurements over La Mancha (Spain) fields., Second recent advances in quantitative remote sensing, pp 820-825.
- Pérez-Priego, O., and P. J. Zarco-Tejada, et al., 2005, Detection of water stress in orchard trees with a high-resolution spectrometer through chlorophyll fluorescence *in-filling* of the O₂-A band, *Geoscience and Remote Sensing, IEEE Transactions*, 43(12), 2860-2869.
- Plascyk, J. A., 1975, The MK II Fraunhofer line discriminator (FLD-II) for airborne and orbital remote sensing of solar-stimulated luminescence, *Optical Engineering*, 14(4), 339-0.
- Plascyk, J. A. and F. C. Gabriel, 1975, The Fraunhofer line discriminator MKII-an airborne instrument for precise and standardized ecological luminescence measurement, *Instrumentation and Measurement, IEEE Transactions*, 24(4), 306-313.
- Zarco-Tejada, P., 2005, Development of a Vegetation Fluorescence Canopy Model, Paris, ESA Scientific and Technical Publications Branch, ESTEC.
- Zarco-Tejada, P. J., and J. Miller, et al., 2004, FluorMODgui: a graphic user interface for the spectral simulation of leaf and canopy fluorescence effects.
- Zarco-Tejada, P. J., and J. R. Miller, et al., 2000, Chlorophyll fluorescence effects on vegetation apparent reflectance: I. Leaf-level measurements and model simulation, *Remote Sensing of Environment*, 74(3), 582-595.
- Zarco-Tejada, P. J., and J. R. Miller, et al., 2000, Chlorophyll fluorescence effects on vegetation apparent reflectance: II. Laboratory and airborne canopy-level measurements with hyperspectral data, *Remote Sensing of Environment*, 74(3), 596-608.
- Zarco-Tejada, P. J., and J. Pushnik, et al., 2003, Steady-state chlorophyll *a* fluorescence detection from canopy derivative reflectance and double-peak red-edge effects, *Remote Sensing of Environment*, 84(2), 283-294.

Adjacency effect correction of EO-1 ALI data using atmospheric point spread function

Si-Bo Duan^{1,2,3}, Zhao-Liang Li^{3,4,*}, Bo-Hui Tang¹, Hua Wu¹, Ronglin Tang¹, and Yuyun Bi³

1. State Key Laboratory of Resources and Environment Information System, Institute of Geographic Sciences and Natural Resources Research, Chinese Academy of Sciences, Beijing 100101, China

2. University of Chinese Academy of Sciences, Beijing 100049, China

3. Key Laboratory of Agri-informatics, Ministry of Agriculture/Institute of Agricultural Resources and Regional Planning, Chinese Academy of Agricultural Sciences, Beijing 100081, China

4. ICube, UdS, CNRS, 300 Bld Sebastien Brant, CS10413, Illkirch 67412, France

* Author to whom correspondence should be addressed: lizhaoliang@caas.cn

ABSTRACT - We aim to propose an atmospheric correction method with adjacency effect correction to derive surface reflectance from EO-1 ALI data. Adjacency effects are corrected using an atmospheric point spread function. An analytical expression of the atmospheric point spread function is presented based on a single scattering approximation. This method was applied to ALI imagery acquired through WATER (Watershed Airborne Telemetry Experimental Research) on 20 May 2008. Compared with the surface reflectance before the adjacency effects were corrected, after the adjacency effects were corrected, the surface reflectance exhibited increased between-pixel contrast.

1 INTRODUCTION

Adjacency effects are caused by radiation reflected from the observed target environment and scattered into a sensor's instantaneous field of view (IFOV) (Burazerovic et al. 2013; Richter et al. 2006). This effect includes four radiation components. Radiation component 1 is the radiation scattered by the atmosphere before detection by the sensor (i.e., the atmospheric path radiance). Radiation component 2 is the radiation reflected by the target and transmitted to the sensor. Radiation component 3 is the radiation reflected by the background and scattered before detection by the sensor. Radiation component 4 is multiple scattering between the atmosphere and surface. The latter two radiation components compose adjacency effects. Adjacency effects reduce between-pixel contrast (i.e., dark pixels appear brighter, but bright pixels appear darker). This effect is one of the most intricate problems that must be solved during surface reflectance retrieval from remotely sensed data at a high spatial resolution.

Previous studies associated with adjacency effect correction can be summarized into two categories: 1) empirical methods (Ouaidrari and Vermote 1999; Richter 1998; Tanré et al. 1987) and 2) atmospheric point spread function (PSF)-based methods (Sanders et al. 2001; Semenov et al. 2011).

Although certain theoretical modeling and simulations experiments have been performed (Minomura, Kuze, and Takeuchi 2001; Sei 2007; Yang et al. 2009), few examples of applied adjacency effect corrections for satellite or airborne data have been published (Liang et al. 2001; Sterckx, Knaeps, and Ruddick 2011). Therefore, the adjacency effect deserves further investigation due to increasingly high spatial resolution satellite sensors. The objective of this study is to develop a method for correcting adjacency effects using an atmospheric PSF. The atmospheric PSF is derived based on a single scattering approximation. This paper is organized as follows: Section 2 introduces the method for atmospheric and adjacency effect corrections. The study area and data used in this study are described in Section 3. Section 4 presents the results and discussion, and the last section concludes.

2 METHODOLOGY

2.1 Radiative transfer equation

For a non-homogeneous Lambertian surface, the surface reflectance can be expressed as follows:

$$\rho_{NHL} = \frac{1 - \langle \rho \rangle S}{1 - \rho_{HL} S} \left(1 + \frac{t_d(\mu_v)}{e^{-\tau/\mu_v}} \right) \rho_{HL} - \frac{t_d(\mu_v)}{e^{-\tau/\mu_v}} \langle \rho \rangle \quad (1)$$

where ρ_{NHL} is the non-homogeneous Lambertian surface reflectance; ρ_{HL} is the homogeneous Lambertian surface reflectance; F_d is the total solar flux at the ground; μ_v are the cosine values of the viewing zenith angles; τ is the atmospheric optical depth; $e^{-\tau/\mu_v}$ and $t_d(\mu_v)$ are the direct and diffuse transmittances from the ground to the sensor; S is the spherical albedo of the atmosphere; $\langle \rho \rangle$ is the average reflectance of the environment, which is the spatial average of each pixel reflectance over the whole surface.

The spatial average must be weighted by an atmospheric PSF, which considers the contribution of each adjacency pixel based on the distance from the target (Vermote et al. 1997).

$$\langle \rho \rangle = \int_{-\infty}^{+\infty} \int_{-\infty}^{+\infty} PSF(x, y) \rho(x, y) dx dy \quad (2)$$

2.2 Atmospheric point spread function

As mentioned previously, the radiation components 3 and 4 are associated with adjacency effects. Nevertheless, the contribution of radiation component 4 is significantly smaller than radiation component 3 due to multiple scattering between the atmosphere and surface. Therefore, we only analyze the adjacency radiance that corresponds to radiant component 3. Assuming that, after reflection by an adjacent pixel, a photon is only scattered once by the atmosphere before detection by the sensor IFOV. The geometry for computing the atmospheric PSF based on the single scattering approximation is shown in Figure 1. The single scattering approximation is reasonable when the atmospheric optical depth is much less than unity (Minomura, Kuze, and Takeuchi 2001). Based on the single scattering approximation, the adjacency radiance L_{adj} can be written as follows (Sanders et al. 2001):

$$L_{\text{adj}} = \frac{\omega}{4\pi} \int_0^{\tau_{\text{TOA}}} \int_{-\infty}^{+\infty} \int_{-\infty}^{+\infty} \frac{E_g(x, y)}{\pi} \rho(x, y) P(\Theta) e^{-\tau_a/\mu_r} e^{-\tau_b/\mu_v} \frac{\mu_r}{r^2} dx dy d\tau \quad (3)$$

where ω is the single scattering albedo, τ_{TOA} is the atmospheric optical depth from the ground to the top of the atmosphere (TOA), $E_g(x, y)$ is the solar irradiance at the ground, $\rho(x, y)$ is the surface reflectance, $P(\Theta)$ is the scattering phase function, Θ is the scattering angle, $e^{-\tau_a/\mu_r}$ is the atmospheric transmittance from the ground to the scattering point, τ_a is the atmospheric optical depth from the ground to the scattering point, μ_r is the cosine value of the reflection angle θ_r , $e^{-\tau_b/\mu_v}$ is the atmospheric transmittance from the scattering point to the sensor, τ_b is the atmospheric optical depth from the scattering point to the sensor, and r is the distance from the ground to the scattering point.

We assume that the solar irradiance at the ground is constant in a given spatial range (i.e., $E_g(x, y) = E_g$ in Equation (3)), and $\langle \rho \rangle$ can be expressed as follows.

$$\langle \rho \rangle = \frac{\omega}{4\pi} \int_0^{\tau_{\text{TOA}}} \int_{-\infty}^{+\infty} \int_{-\infty}^{+\infty} \rho(x, y) P(\Theta) e^{-\tau_a/\mu_r} e^{-\tau_b/\mu_v} \frac{\mu_r}{\pi r^2} dx dy d\tau \quad (4)$$

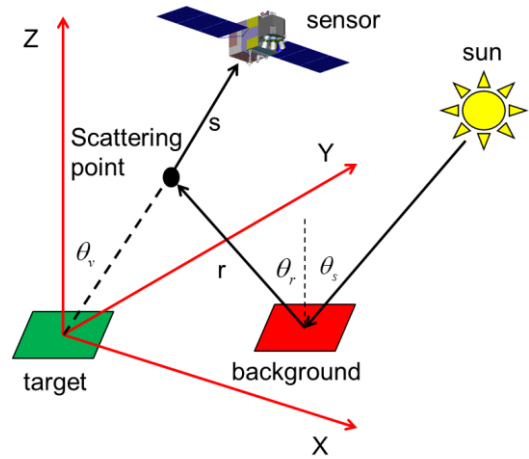


Figure 1. Geometry for computing the atmospheric point spread function based on the single scattering approximation.

We assume that the atmosphere is horizontally layered with a uniform optical parameter in each layer; the atmospheric PSF is derived by comparing Equation (4) with Equation (2) (Borel and Gerstl 1992):

$$PSF(x, y) = \frac{\omega}{4\pi} \sum_{l=1}^N P(\Theta) e^{-\tau_a/\mu_r} e^{-\tau_b/\mu_v} \frac{\mu_r}{\pi r^2} \Delta \tau \quad (5)$$

where l denotes the l th-layer atmosphere, and N is the number of atmospheric layers.

To calculate the relative weight of each adjacent pixel, it is necessary to normalize the atmospheric PSF (i.e., the atmospheric PSF must integrate to unity) (Sanders et al. 2001). The normalized atmospheric PSF can be expressed as follows:

$$PSF(x, y) = \frac{\sum_{l=1}^N P(\Theta) e^{-\tau_a/\mu_r} e^{-\tau_b/\mu_v} \frac{\mu_r}{r^2}}{\sum_{i=-n}^n \sum_{j=-n}^n \sum_{l=1}^N P(\Theta) e^{-\tau_a/\mu_r} e^{-\tau_b/\mu_v} \frac{\mu_r}{r^2}} \quad (6)$$

where n corresponds to the number of pixels for the effective range of the adjacency effects.

$\langle \rho \rangle$ can then be calculated using the discrete form of Equation (2), as follows.

$$\langle \rho \rangle = \sum_{i=-n}^n \sum_{j=-n}^n PSF(i, j) \rho(i, j) \quad (7)$$

In theory, on the right-hand side of Equation (7), ρ should be the actual reflectance; however, the actual reflectance is not available at this stage. Therefore, an iterative procedure is used to reduce the error introduced by replacing the actual reflectance with ρ_{HL} or ρ_{NHL} (Putsay 1992).

3 STUDY AREA AND DATA

3.1 Study area

The study area is located in the southern portion of the Zhangye oasis (Gansu, China: 38.77° N, 100.32° E). A false-color subset image from the ALI data is shown in Figure 2. This area belongs to the arid region hydrology experimental area of the Watershed Allied Telemetry Experimental Research (WATER). WATER simultaneously collects satellite, airborne, and ground-based remote sensing data in the Heihe River Basin (Li et al. 2009). The study area ground elevation ranges from approximately 1500 to 2000 m. The annual precipitation is less than 200 mm. This area is mainly characterized by artificial oases, desert, the Gobi, and transitional zones between oases and desert.

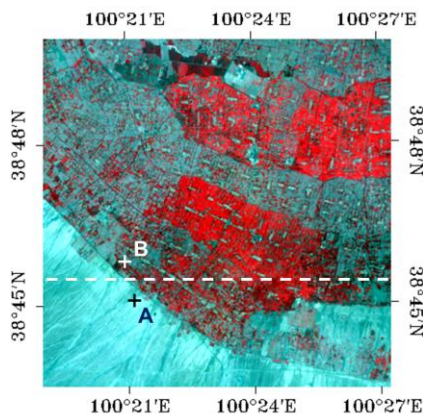


Figure 2. A false-color subset image from ALI data collected in the study area. (R: band 4, G: band 3, B: band 2)

3.2 ALI data

ALI data acquired over the study area on 20 May 2008 were downloaded from the U.S. Geological Survey (USGS) Earth Resources Observation and Science (EROS) Center website (<http://glovis.usgs.gov/>). The radiometric calibration coefficients shown in Table 1 were used to convert the data from a calibrated digital number (Q_{cal}) to at-sensor spectral radiance (Chander et al. 2009):

$$L_{\lambda} = \left(\frac{LMAX_{\lambda} - LMIN_{\lambda}}{Q_{\text{cal max}} - Q_{\text{cal min}}} \right) (Q_{\text{cal}} - Q_{\text{cal min}}) + LMIN_{\lambda} \quad (8)$$

where L_{λ} is the spectral radiance at the sensor's aperture, Q_{cal} is the quantized calibrated pixel value, $Q_{\text{cal min}}$ is the minimum quantized calibrated pixel value that corresponds to $LMIN_{\lambda}$ ($Q_{\text{cal min}}=1$), $Q_{\text{cal max}}$ is the maximum quantized calibrated pixel value that corresponds to $LMAX_{\lambda}$ ($Q_{\text{cal max}}=32767$), $LMIN_{\lambda}$ is the spectral at-sensor radiance that is scaled to $Q_{\text{cal min}}$, and $LMAX_{\lambda}$ is the spectral at-sensor radiance that is scaled to $Q_{\text{cal max}}$.

Table 1. ALI spectral range, center wavelength, and radiometric calibration coefficients.

No.	Spectral range (μm)	Center wavelength (μm)	$LMIN_{\lambda}$ ($\text{W m}^{-2} \text{sr}^{-1} \mu\text{m}^{-1}$)	$LMAX_{\lambda}$ ($\text{W m}^{-2} \text{sr}^{-1} \mu\text{m}^{-1}$)
1p	0.43-0.45	0.443	-3.36	1471
1	0.45-0.51	0.483	-4.36	1405
2	0.52-0.60	0.565	-1.87	915.5
3	0.63-0.69	0.662	-1.28	588.5
4	0.77-0.80	0.790	-0.84	359.6
4p	0.84-0.89	0.868	-0.64	297.5
5p	1.20-1.30	1.250	-1.29	270.7
5	1.55-1.75	1.650	-0.59	91.14
7	2.08-2.35	2.215	-0.20	29.61

3.3 In situ measurements

The in situ spectral reflectance and atmospheric parameters were measured when the ALI data were acquired on 20 May 2008. The spectral reflectance was collected with wavelengths from 350 to 2500 nm using an Analytical Spectral Devices (ASD) spectrometer. Only the reflectance spectra in the wavelength range 350-950 nm were used in this study because the sensitivity of the ASD spectrometer silicon detector is reduced at approximately 1000 nm. The measurement procedure consisted of pointing from a nadir perspective while walking across the target. Five measurements for each target were averaged to yield a representative reflectance spectrum. The spectral reflectance was measured over one vegetated and one bare soil site. The representative reflectance spectrum was convolved with the ALI spectral response function to derive the ALI bands' in situ surface reflectance. The in situ surface reflectance was used to validate the surface reflectance before and after the adjacency effects were corrected.

The aerosol optical depth (AOD) and columnar water vapor (CWV) were measured using an automatic CIMEL CE318 sunphotometer. The

sunphotometer has nine channels at the nominal wavelengths 340, 380, 440, 500, 670, 870, 936, 1020, and 1640 nm. The CWV was derived from the 936 nm channel measurements using an algorithm developed by Bruegge et al. (1992) with the coefficients from Halthore et al. (1997). The Ångström law was used to derive the AOD at 550 nm from measurements using the other channels (Estellés et al. 2006). The AOD values measured at 550 nm and the CWV values measured when the ALI data were acquired are 0.5 and 1.9 g cm⁻², respectively. The AOD and CWV values were input into MODTRAN to derive the atmospheric parameters and PSF.

4 RESULTS AND DISCUSSION

Previous studies show that the effective range for adjacency effects is approximately 1 km for satellite imagery (Kaufmann 1984). The appropriate filter window size ($m=2n+1$) in Equation (6) is the pixel equivalent of approximately 1 km. Because adjacency effects are a second order effect, the precise filter window size does not critically influence the final reflectance values. In this study, the constant filter window size 33×33 pixels was used for all ALI bands with a 30 m spatial resolution. Figure 3 shows the atmospheric PSF with a 33×33 pixel filter window size in ALI band 1p. As expected, the atmospheric PSF peak value was in the target pixel because the aerosol scattering phase function strongly peaks in the forward direction, and the near-target pixel influence is substantially greater.

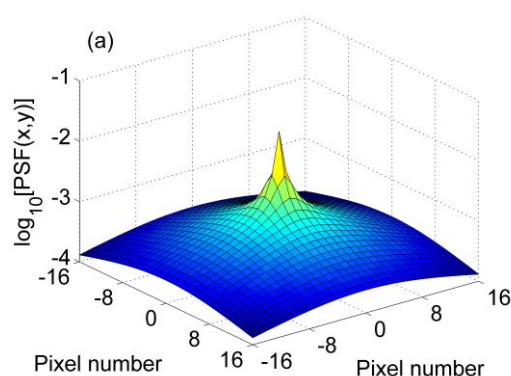


Figure 3. Atmospheric point spread functions in the ALI band 1p (443 nm).

The surface reflectance before the adjacency effects were corrected (i.e., ρ_{HL}) was derived from the ALI data at-sensor radiance L_{sensor} by inverting Equation (1). The surface reflectance after the adjacency effects were corrected (i.e., ρ_{NHL}) was derived by combining ρ_{HL} with $\langle \rho \rangle$. Figure 4 shows the surface reflectance before and after the adjacency

effects were corrected in the ALI band 1p. Compared with the surface reflectance after the adjacency effects were corrected, the surface reflectance before the adjacency effects were corrected lacks contrast (i.e., the dark pixels appear brighter, and the bright pixels appear darker). Nevertheless, the surface reflectance after the adjacency effects were corrected clearly exhibits enhanced between-pixel contrast.

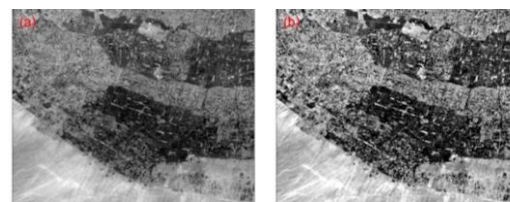


Figure 4. Comparison of the surface reflectance (a) before and (b) after the adjacency effects were corrected in the ALI band 1p (443 nm).

To compare the surface reflectance before and after the adjacency effects were corrected, one surface reflectance profile was randomly selected and is shown in Figure 2. Figure 5 shows the surface reflectance profiles before and after the adjacency effects were corrected in ALI band 1p. Shown in Figure 5, after the adjacency effects were corrected, the peak reflectance is greater, and the valley reflectance is lower. In other words, correcting the adjacency effects enhances the between-pixel contrast and ALI imagery details.

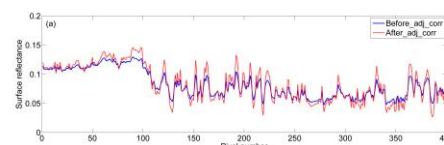


Figure 5. Surface reflectance profiles before and after the adjacency effects were corrected for ALI band 1p (443 nm).

To further analyze the discrepancies between the surface reflectance before and after the adjacency effects were corrected, we selected a vegetated pixel (pixel A) and a bare soil pixel (pixel B) shown in Figure 2 along the transitional zones between the oasis and desert. Figure 6 shows a comparison of the surface reflectance before and after the adjacency effects were corrected over the vegetated and bare soil pixels. The surface reflectance before the adjacency effects were corrected is higher than after the adjacency effects were corrected for the vegetated pixel with relatively low surface reflectance. These results are due to the greater number of photons present from adjacency effects on pixels than the number of photons that escape from the sensor IFOV (i.e., the dark pixels appear brighter). In contrast, the surface reflectance

before the adjacency effects were corrected is lower than that after the adjacency effects were corrected for the bare soil pixel with a relatively high surface reflectance. These results are due to photons that escape from the sensor IFOV and are not counterbalanced by photons from adjacent pixels (i.e., bright pixels appear darker). Furthermore, the discrepancies between the surface reflectance before and after the adjacency effects were corrected decrease as a function of the wavelength for both the vegetated and bare soil pixels.

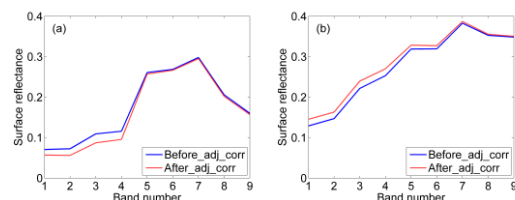


Figure 6. A comparison of the surface reflectance before and after the adjacency effects were corrected over (a) vegetated and (b) bare soil pixels.

5 CONCLUSIONS

We propose a method to correct the ALI data atmospheric and adjacency effects. The atmospheric correction was performed using the atmospheric radiative transfer code MODTRAN and ground-based atmospheric parameter measurements. The adjacency effects were corrected using the atmospheric PSF. The atmospheric PSF was derived based on a single scattering approximation.

A comparison of the surface reflectance before and after the adjacency effects were corrected indicates that the surface reflectance before the adjacency effects were corrected reduced the contrast, but the surface reflectance after the adjacency effects were corrected clearly enhanced the between-pixel contrast.

ACKNOWLEDGMENT

This work was supported by the Chinese 973 Program under Grant 2013CB733402, by the Excellent Young Talent Funds for Kezhen Distinguished Young Scholar in IGSNRR, CAS under grant 2012RC101, and the Hi-Tech Research and Development Program of China (863 Plan Program) under Grant 2012AA12A302.

REFERENCES

Borel, C. C., and Gerstl, S. A. W., 1992, Adjacency-Blurring-Effect of Scenes Modeled by the Radiosity Method. *Proceedings SPIE*, 1688, 620-624.

Bruegge, C. J., Conel, J. E., Green, R. O., Margolis, J. S., Holm, R. G., and Toon, G., 1992, Water Vapor Column Abundance Retrievals during FIFE. *Journal of Geophysical Research*, 97, 18759-18768.

Burazerovic, D., Heylen, R., Geens, B., Sterckx, S., and Scheunders, P., 2013, Detecting the Adjacency Effect in Hyperspectral Imagery with Spectral Unmixing Techniques. *IEEE Journal of Selected Topics in Applied Earth Observations and Remote Sensing*, 6, 1070-1078.

Chander, G., Markham, B. L., and Helder, D. L., 2009, Summary of Current Radiometric Calibration Coefficients for Landsat MSS, TM, ETM+, and EO-1 ALI Sensors. *Remote Sensing of Environment*, 113, 893-903.

Duan, S.-B., Li, Z.-L., Tang, B.-H., Wu, H., Ma, L., Zhao, E., and Li, C., 2013, Land Surface Reflectance Retrieval from Hyperspectral Data Collected by An Unmanned Aerial Vehicle over the Baotou Test Site. *PLoS ONE*, 8, e66972.

Duan, S.-B., Li, Z.-L., Tang, B.-H., Wu, H., Ma, L., Zhao, E., and Li, C., 2014, Inversion of the PROSAIL model to estimate leaf area index of maize, potato, and sunflower fields from unmanned aerial vehicle hyperspectral data. *International Journal of Applied Earth Observation and Geoinformation*, 26, 12-20.

Estellés, V., Utrillas, M. P., Martínez-Lozano, J. A., Alcántara, A., Alados-Arboledas, L., Olmo, F. J., Lorente, J., de Cabo, X., Cachorro, V., Horvath, H., Labajo, A., Sorribas, M., Díaz, J. P., Díaz, A. M., Silva, A. M., Elías, T., Pujadas, M., Rodrigues, J. A., Cañada, J., and García, Y., 2006, Intercomparison of Spectroradiometers and Sun Photometers for the Determination of the Aerosol Optical Depth during the VELETA-2002 Field Campaign. *Journal of Geophysical Research*, 111, D17207.

Halothore, R. N., Eck, T. F., Holben, B. N., and Markham, B. L., 1997, Sun Photometric Measurements of Atmospheric Water Vapor Column Abundance in the 940-nm Band. *Journal of Geophysical Research*, 102, 4343-4352.

Kaufman, Y. J., 1984, Atmospheric Effect on Spatial Resolution of Surface Imagery: Errata. *Applied Optics*, 23, 4164-4172.

Li, X., Li, X., Li, Z., Ma, M., Wang, J., Xiao, Q., Liu, Q., Che, T., Chen, E., Yan, G., Hu, Z., Zhang, L., Chu, R., Su, P., Liu, Q., Liu, S., Wang, J., Niu, Z., Chen, Y., Jin, R., Wang, W., Ran, Y., Xin, X., and Ren, H., 2009, Watershed Allied Telemetry

- Experimental Research. *Journal of Geophysical Research*, 114, D22103.
- Liang, S., Fang, H., and Chen, M., 2001, Atmospheric Correction of Landsat ETM+ Land Surface Imagery. I. Methods. *IEEE Transactions on Geoscience and Remote Sensing*, 39, 2490-2498.
- Minomura, M., Kuze, H., and Takeuchi, N., 2001, Adjacency Effect in the Atmospheric Correction of Satellite Remote Sensing Data: Evaluation of the Influence of Aerosol Extinction Profiles. *Optical Review*, 8, 133-141.
- Ouaidrari, H., and Vermote, E. F., 1999. Operational Atmospheric Correction of Landsat TM Data. *Remote Sensing of Environment*, 70, 4-15.
- Putsay, M., 1992, A Simple Atmospheric Correction Method for the Short Wave Satellite Images. *International Journal of Remote Sensing*, 13, 1549-1558.
- Richter, R., 1998, Correction of Satellite Imagery over Mountainous Terrain. *Applied Optics*, 37, 4004-4015.
- Richter, R., Bachmann, M., Dorigo, W., and Mueller, A., 2006, Influence of the Adjacency Effect on Ground Reflectance Measurements. *IEEE Geoscience Remote Sensing Letters*, 3, 565-569.
- Sanders, L. C., Schott, J. R., and Raqueño, R., 2001, A VNIR/SWIR Atmospheric Correction Algorithm for Hyperspectral Imagery with Adjacency Effect. *Remote Sensing of Environment*, 78, 252-263.
- Sei, A., 2007, Analysis of Adjacency Effects for Two Lambertian Half-Spaces. *International Journal of Remote Sensing*, 28, 1873-1890.
- Semenov, A. A., Moshkov, A. V., Pozhidayev, V. N., Barducci, A., Marcoionni, P., and Pippi, I., 2011, Estimation of Normalized Atmospheric Point Spread Function and Restoration of Remotely Sensed Images. *IEEE Transactions on Geoscience and Remote Sensing*, 49, 2623-2634.
- Sterckx, S., Knaeps, E., and Ruddick, K., 2011, Detection and Correction of Adjacency Effects in Hyperspectral Airborne Data of Coastal and Inland Waters: the Use of the Near Infrared Similarity Spectrum. *International Journal of Remote Sensing*, 32, 6479-6505.
- Tanré, D., Deschamps, P. Y., Duhaut, P., and Herman, M., 1987, Adjacency Effect Produced by the Atmospheric Scattering in Thematic Mapper Data. *Journal of Geophysical Research*, 92, 12000-12006.
- Vermote, E. F., Tanre, D., Deuze, J. L., Herman, M., and Morcette, J. J., 1997, Second Simulation of the Satellite Signal in the Solar Spectrum, 6S: An Overview. *IEEE Transactions on Geoscience and Remote Sensing*, 35, 675-686.
- Yang, G., Liu, Q., Liu, Q., Huang, W., and Wang, J., 2009, Simulation of High Resolution Mid-Infrared (3-5 μm) Images Using An Atmosphere Radiative Transfer Analytic Model. *International Journal of Remote Sensing*, 30, 6003-6022.

Estimation of global soil moisture seasonal and inter-annual variability using SMOS satellite observations

M. Piles^{1,3}, E. Martínez³, J. Ballabrera^{2,3}, M. Vall-llossera^{1,3}, E. Olmedo^{2,3}, J. Martínez^{2,3} and J. Font^{2,3}

¹Remote Sensing Laboratory/IEEC, Universitat Politècnica de Catalunya, Jordi Girona 1-3, E-08034 Barcelona, Spain

²Departament d'oceanografia física i Tecnològica, Institut de Ciències del Mar/CSIC, Pg. Marítim de la Barceloneta 37-49, E-08003 Barcelona, Spain

³SMOS Barcelona Expert Centre, Pg. Marítim de la Barceloneta 37-49, E-08003 Barcelona, Spain

maria.piles@tsc.upc.edu

ABSTRACT - The SMOS mission is providing the first ever global observations of soil moisture over land and surface salinity over the oceans. With almost five years of mapping these two variables, it is now possible to start analysing their spatial variability at seasonal and inter-annual scales. A preliminary analysis has been performed to determine trends and anomalies in SMOS soil moisture time series, analyse their spatial coherence, and study their relationships through precipitation. By relating temporal series of soil moisture anomalies to North Atlantic Oscillation climate index, we show that SMOS information can be used to monitor major global patterns of weather alterations over land (e.g. areas affected by drought/heavy rain).

1 INTRODUCTION

Knowledge of global soil moisture dynamics is expected to play an important role in monitoring climate trends. However, measuring soil moisture is challenging because of its high variability. As point-scale in situ measurements are still scarce, remote sensing is the only practical means to obtain regional- and global-scale soil moisture estimates. The ESA's Soil Moisture and Ocean Salinity (SMOS) is the first satellite mission ever designed to measuring the Earth's surface soil moisture at daily time scales with an unprecedented level of accuracy (Kerr, 2010). Since its launch in November 2009, significant efforts have been dedicated to validate, and fine-tune, the retrieval algorithms so that SMOS-derived soil moisture estimates meet the standards required for climate research applications.

The SMOS Barcelona Expert Centre (BEC) is the Spanish ground segment for the SMOS data, and distributes global soil moisture (SM) and ocean salinity maps in near real time. The SM data are available since SMOS launch until present, and global SM information (with a spatial and temporal resolution of 25 km and three days respectively) has proved to be useful for different applications, such as assessing drought conditions and monitoring water stress (Scaini, 2014). Also, fine scale (< 1 km spatial resolution) soil moisture estimates have been obtained by merging SMOS and NASA's Moderate Resolution Imaging Spectroradiometer (MODIS) data, extending the applicability of the data to regional and local studies (Piles, 2013; Piles, 2014).

Today, with more than four years of SMOS data, it is now possible to provide new insight into temporal changes in soil moisture, and their links with the Earth's water cycle and climate system. This work is a first step in this direction. A preliminary analysis has been performed to determine trends and anomalies in SMOS SM time series, analyse their spatial coherence, and study their relationships through precipitation. The analysis includes determination of variability at seasonal and inter-annual scales, focusing on four target regions representative of arid, semi-arid, sub-humid and humid areas across global land biomes. In addition, the relationship between temporal series of SM anomalies and the North Atlantic Oscillation (NAO) climate index has been explored.

2 DATA

2.1 SMOS soil moisture

Four years of SMOS-BEC L3 binned soil moisture (9-day composite, generated every 3 days), are used in the present study, starting on January 1, 2010. Data are projected on a 25-km EASE grid and can be accessed online through the SMOS-BEC web service (<http://cp34-bec.cmima.csic.es/>).

2.2 MERRA precipitation

Global daily precipitation for the study period is obtained from the Modern Era Retrospective Analysis (MERRA) 300 reanalysis products (Rienecker, 2011). Data are 1/2 x 2/3 degrees resolution and can be obtained online through the NASA Goddard Earth

Sciences Data and Information Services Center (disc.sci.gsfc.nasa.gov/mdisc).

2.3 NAO index

The NAO is traditionally defined as the normalized pressure difference between a station on the Azores and one on Iceland. An extended version of the index has been derived for the winter half of the year by using a station from Gibraltar (Jones et al., 1997). The daily NAO index is obtained from the KNMI Climate Explorer (<http://climexp.knmi.nl>). It is calculated from stations in south west Iceland (Reykjavik), Gibraltar and Ponta Delgada (Azores).

3. ANALYSIS OF GLOBAL VARIABILITY

To enable spatial and temporal consistency, all data sets used in this work have been resampled to the SMOS-BEC L3 product grid sampling: that is, 9-day average generated every 3 days on a 25km EASE grid. The dry/normal/humid ranges of SMOS soil moisture are estimated in a monthly basis and an annual cycle is created to provide maps of their spatial and seasonal distribution. This soil moisture climatology is used to calculate the SM anomalies during the four years of SMOS in orbit.

4. RESULTS

4.1 Soil moisture variability at target areas

A suite of target regions across global land biomes was designated to cover as large a variety of geographic regions, land cover types, and climates as possible (Martínez, 2014). Four of them have been selected as representative for this work (Fig. 1). Time series of precipitation and SMOS-derived soil moisture over the four focus regions are shown in Fig. 2. It can be seen that soil moisture estimates follow the precipitation dynamics over the Iberian Peninsula, Sahel and Gibson desert. On the contrary, the US Midwest region has a totally distinctive behaviour, with soil moisture reaching maximums during periods of low precipitation and vice-versa. This can be explained by the fact that this area is dominated by irrigated fields, and receives water from the Mississippi River. This is a clear example of an area where soil moisture is not driven by natural phenomena, so SMOS is able to provide valuable, independent information for land surface-atmospheric models and agricultural applications, among others.

Soil moisture temporal series over Sahel and Gibson desert in Fig. 2 reflect their dry and wet seasons occur in opposite times of the year, with maximum precipitation occurring in July for Sahel (northern hemisphere) and January for Gibson desert (southern hemisphere). In these areas the soil moisture seasonal variability is dominated by the Inter Tropical

Convergence Zone (ITCZ). The ITCZ is a band of low pressure that encircles the globe near the equator where the trade winds of the Northern and Southern Hemispheres converge. The area is characterized by convective thunderstorm activity. The meridional position of the ITCZ varies seasonally following the sun: it moves north in the northern summer and south in the northern winter (Oliver, 2006). Figure 3 shows the map of global correlation between the temporal evolution of soil moisture of a given pixel in Sahel (black triangle), and the temporal evolution of precipitation at every pixel. It can be seen that soil moisture estimates at Sahel are highly correlated with precipitation near the equator in latitudes from 0 to 20° ($R > 0.7$), and highly anti-correlated with precipitation in latitudes from 0 to -20° ($R < -0.7$). The correlation pattern closely matches the position of the ITCZ, which is responsible for progression of the wet and dry seasons in the tropics.

4.2 Soil moisture relationship with the NAO

The NAO time series manifests the north-south dipole of sea level pressure anomalies in the North Atlantic Ocean, with one center located over Greenland and the other center of opposite sign spanning the central latitudes of the North Atlantic between 35°N and 40°N. The positive phase of the NAO reflects below-normal heights and pressure across the high latitudes of the North Atlantic and above-normal heights and pressure over the central North Atlantic, the eastern United States and Western Europe. The negative phase reflects an opposite pattern of height and pressure anomalies over these regions (Oliver, 2006). Figure 4 shows the map of global correlation between the temporal evolution of the NAO index and the soil moisture anomalies during the study period. The lack of data in the Labrador Peninsula and Northern Europe is due to the presence of ice, which prevents retrieving soil moisture. Although correlation values are generally low, a clear correlation/anti-correlation pattern is observed, consistent with the positive and negative modes of dominant winter climate variability in the North Atlantic region (i.e. the North Atlantic Oscillation).

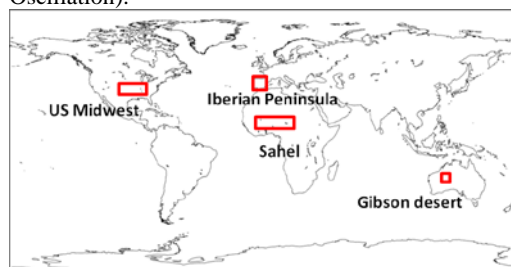


Fig 1. Four target regions selected across global land biomes

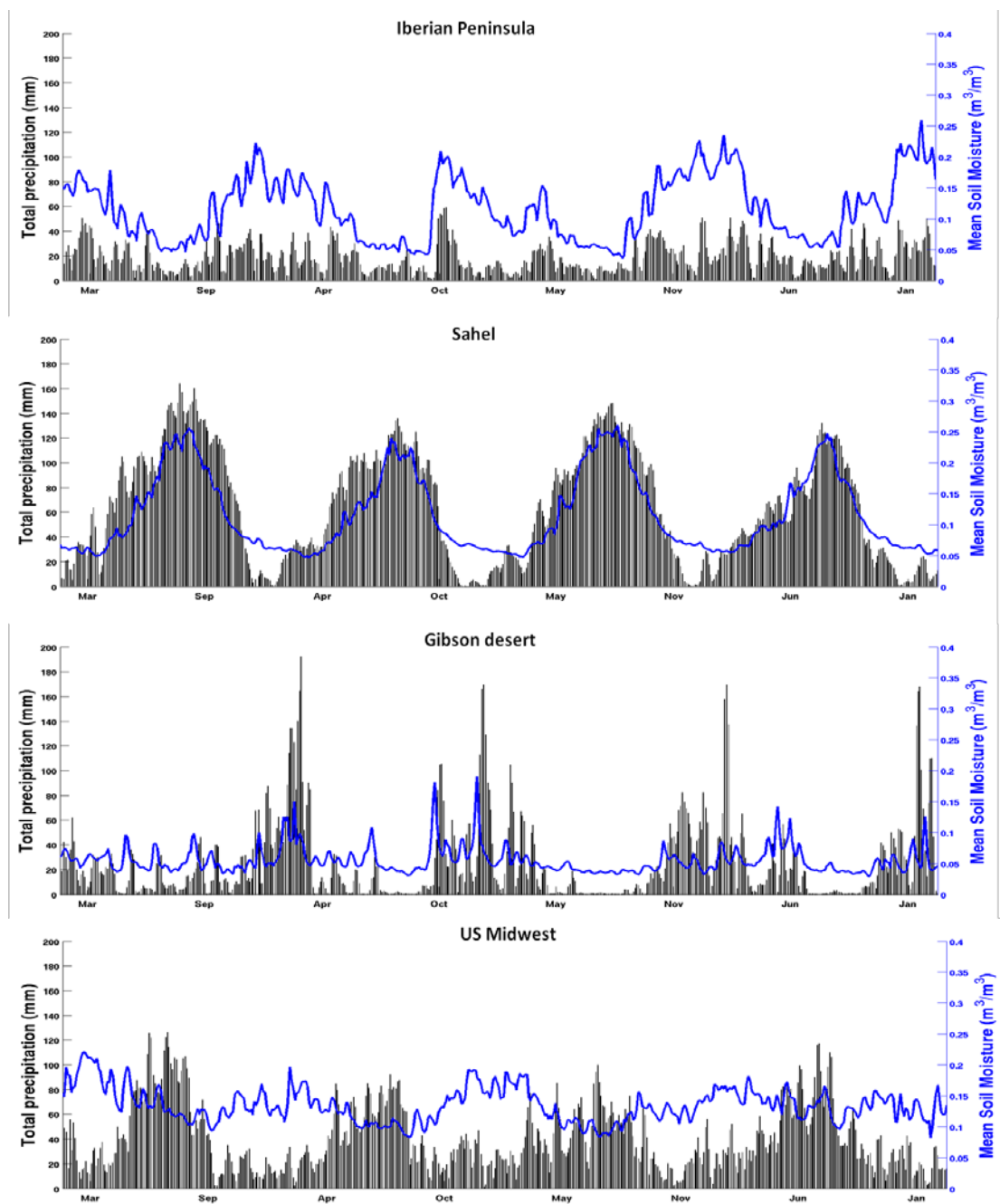


Figure 2. Time series of SMOS soil moisture and MERRA precipitation over the four target areas: US Midwest (32° to 39° N; 85° to 105° W), Iberian Peninsula (36° to 44° N; 10° W to 4° E), Sahel (8° to 14° N; 0° to 23° E), and Gibson desert (22.5°-27° S; 122° to 128.5° E).

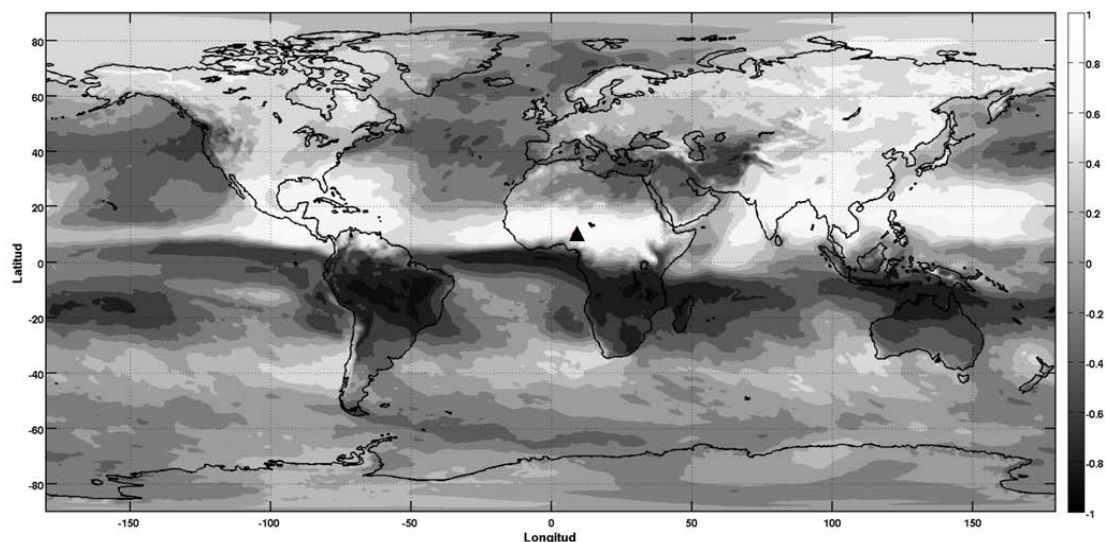


Figure 3. Correlation of the soil moisture temporal evolution of a given location in Sahel (black triangle) with the temporal evolution of global precipitation.

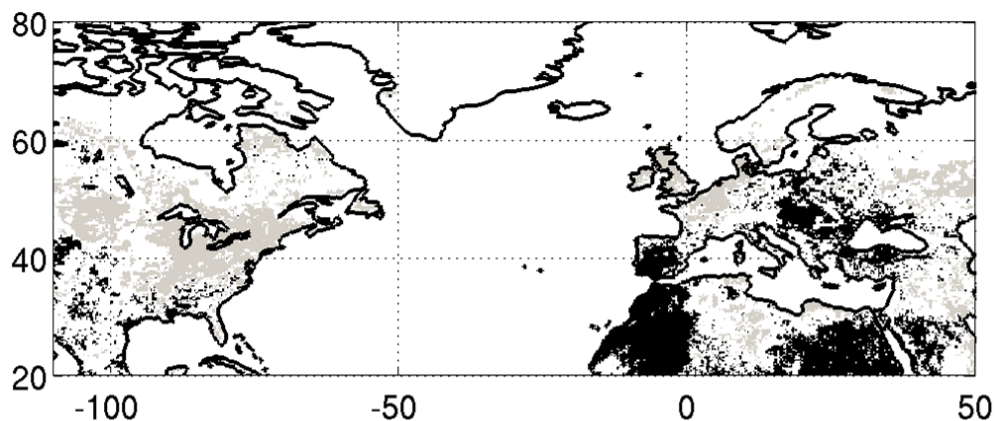


Figure 4. Correlation map of the NAO index and the soil moisture evolution during the 4-year study period. Grey and black colours indicate positive and negative values, respectively.

5 CONCLUSION

Results shown in this work provide new insight into changes in a key variable of the water cycle: soil moisture. SMOS-derived SM presents coherent spatial and temporal distribution at seasonal and inter-annual scales. SM estimates reproduce precipitation wet-up and dry-down events, but is also able to identify phenomena not directly related to precipitation, such as irrigation. By relating temporal series of SM anomalies to the NAO climate index, we have shown that SMOS data are able to monitor global patterns of weather alterations over Western Europe and western United States (areas affected by drought/heavy rain). It is anticipated that the uncertainty of SM representation in climate models could be reduced by using satellite

information such as the one provided by SMOS and the upcoming SMAP mission, which will help improving future climate projections.

6 ACKNOWLEDGEMENTS

This work was supported by the Spanish Ministry of Science and Innovations through the project AYA2012-39356-C05.

7 REFERENCES

- Jones, P.D., Jónsson, T. and Wheeler, D., (1997) Extension to the North Atlantic Oscillation using early instrumental pressure observations from Gibraltar and South-West Iceland. *Int. J. Climatol.* 17, 1433-1450.

- Kerr, Y; P. Waldteufel, J.-P. Wigneron, S. Delwart, F. Cabot, J. Boutin, M.-J. Escorihuela, J. Font, N. Reul, C. Gruhier, S. Juglea, M. R. Drinkwater, A. Hahne, M. Martin-Neira, and S. Mecklenburg, (2010) The SMOS mission: New Tool for Monitoring Key Elements of the Global Water Cycle, *Proc. IEEE*, vol. 98, pp. 666–687
- Martínez, E (2014) Soil moisture and ocean teleconnexion, *Master de oceanografia i gestió del medi marí, Universitat de Barcelona*.
- Oliver, J.E. (2006) Encyclopedia of World Climatology. Second Edition. Edited by J.E. Oliver. Springer, ISBN:978-1402048708, pp. 854.
- Piles, M; M. Vall-llossera; A. Camps; N. Sánchez; J. Martínez-Fernández; J. Martínez; V. González-Gambau. (2013), On the synergy of SMOS and Terra/Aqua MODIS: high resolution soil moisture maps in near real-time, *Proc. IEEE International Geoscience and Remote Sensing Symposium*, pp. 3423 - 3426. 2013.
- Piles, M; N. Sánchez; M. Vall-llossera; A. Camps; J. Martínez-Fernández; J. Martínez; V. González-Gambau (2014). A downscaling approach for SMOS land observations: two year evaluation of high resolution soil moisture maps over the Iberian Peninsula. *IEEE Journal of Selected Topics on Applied Earth Observations and Remote Sensing*, in press.
- Rienecker, M, M. Suarez, R. Gelaro, R. Todling, J. acmeister, E. Liu, M.G.Bosilovich, S. Schubert, L. Takacs, G.-K. Kim, S. Bloom, J. Chen, D. Collins, A. Conaty, A. da Silva, W. Gu, J. Joiner, R. D. Koster, R. Lucchesi, A. Molod, T. Owens, S. Pawson, P. Pegion, C. R. Redder, R. Reichle, F. R. Robertson, A. G. Ruddick, M. Sienkiewicz, and J. Woollen, (2011) MERRA: NASA's Modern-Era Retrospective Analysis for Research and Applications, *Journal of Climate*, vol. 24, pp. 3624–3648.
- Scaini, A.; N. Sánchez, S.M. Vicente-Serrano, J. Martínez-Fernández (2014). SMOS-derived soil moisture anomalies and drought indices: a comparative analysis using in situ measurements. *Hydrological processes*, in press.

A new soil roughness parameter for the modelling of radar backscattering over bare soil

M. Zribi^a, A. Gorraab^{a-b} and N. Baghdadi^c

a-CESBIO (CNRS/UPS/IRD/CNES), 18 av. Edouard Belin, bpi 2801, 31401 Toulouse cedex9, France

b-INAT/LRSTE (Université de Carthage), 43 av. Charles Nicolle 1082, Tunis, Mahrajène Tunisie

c-IRSTEA, UMR TETIS, 500 rue François Breton, 34093 Montpellier cedex 5, France

Emails: zribim@cesbio.cnes.fr; azzagorrah@gmail.com; nicolas.baghdadi@teledetection.fr;

ABSTRACT- The characterisation of soil surface roughness is a key requirement for the correct analysis of radar backscattering behaviour. It is noteworthy that an increase in the number of surface roughness parameters in a model also increases the difficulty with which data can be inverted for the purposes of estimating soil parameters. In this paper, a new description of soil surface roughness is proposed for microwave applications. This is based on an original roughness parameter, Z_g , which combines the three most commonly used soil parameters: root mean surface height, correlation length, and correlation function shape, into just one parameter. Numerical modelling, based on the moment method and integral equations, is used to evaluate the relevance of this approach. It is applied over a broad dataset of numerically generated surfaces characterised by a large range of surface roughness parameters. A strong correlation is observed between this new parameter and the radar backscattering simulations, for the HH and VV polarizations in the C and X bands. It is proposed to validate this approach using data acquired in the C and X bands, at several agricultural sites in France. It was found that the parameter Z_g has a high potential for the analysis of surface roughness using radar measurements. An empirical model is proposed for the simulation of backscattered radar signals over bare soil.

1 INTRODUCTION

Soil moisture and roughness parameters play a key role in hydrological and climate studies. In recent years, various efforts have been devoted to the analysis of the backscattering characteristics of bare soils. In this context, Zribi and Dechambre (2003) introduced a description based on the parameter $Z_s = s^2/l$, where s is the rms surface height and l is the correlation length. Baghdadi et al. (2006, 2011) proposed an empirical correlation length, computed as a function of the rms height, radar frequency, incidence angle and polarization, in order to obtain a better fit between Integral Equation Model (Fung et al., 1992, Fung, 1994) simulations and radar observations. Lievens et al. (2011) show that roughness parameters differ between SAR acquisitions, as they are related to the observed backscatter coefficients and variations in local incidence angle. A statistical model was thus developed, to allow the effective roughness parameters to be estimated from microwave backscattering observations. Despite these contributions, the influence of roughness is still poorly modelled in currently known inversion techniques.

In the present study, a new surface description is proposed, in which the analysis uses the moment method to numerically simulate the backscattering integral equations. Our paper is organised into five

sections, of which Section 2 presents the principles of the numerical backscattering simulations. It discusses the influence of roughness on the backscattering simulations and introduces the new roughness parameter, Z_g . Section 4 describes the potential of this parameter, through the use of experimental analyses based on different types of ground and radar measurements. Finally, our conclusions are presented in Section 5.

2 ANALYSIS OF SIMULATED RADAR BACKSCATTERING AS A FUNCTION OF ROUGHNESS

2.1 Backscattering modelling

A numerical backscattering model based on the moment method is used to simulate radar signals over bare soils (Harrington, 1968). With this approach, the computations are made using simulated surfaces, with various roughness and soil moisture characteristics. The first step in this process thus involves the generation of soil roughness profiles.

In this section, it is proposed to generate soil surfaces with different correlation functions $\rho(x) = \exp\left(-\left(\frac{x}{l}\right)^\alpha\right)$,

in which the parameter α can range between 1 and 2, with these extremes corresponding to exponential and Gaussian functions, respectively (Fung et al., 1985).

2.2 Influence of roughness on the backscattering simulations

In order to study the influence of the soil roughness parameters on radar signal backscattering, Moment Method (MM) simulations were run in the *HH* and *VV* polarizations, at 20 and 40° incidence angles, and at three different values of soil moisture: 10%, 20% and 30%. The results shown in Figs. 1 and 2 were computed at a 40° incidence angle, since the radar signals are known to be more sensitive to roughness at higher incidence angles (Fung, 1994). Various surface parameters were used: rms heights $s=0.4$ cm, $s=0.6$ cm, $s=0.8$ cm, $s=1$ cm, $s=1.2$ cm, $s=1.4$ cm, $s=1.6$ cm; correlation lengths $l=4$ cm, $l=6$ cm, $l=8$ cm and $l=10$ cm; α parameter $\alpha=1$, $\alpha=1.25$, $\alpha=1.5$ and $\alpha=1.75$. The latter range (for the parameter α) was based on the values retrieved during various experimental campaigns.

Fig. 1-a shows the simulated backscattered signal, for the *HH* polarization, assuming volumetric moisture condition of 10% in the C band at 40° incidence, for all of the above roughness configurations, plotted as a function of the rms surface height. Simulations show that the backscattered signal is moderately well correlated with the rms surface height (in the C band, R^2 is equal to 0.65 and 0.66, and in the X band it is equal to 0.58 and 0.51, for volumetric moistures of 10% and 30%, respectively). This outcome is influenced, in particular, by the correlation length, which is not taken into account in the above relationships. Fig. 1-b plots the simulated backscattered radar signals for the *HH* polarization, for volumetric moisture of 10%, in the C at 40° incidence, for all of the above roughness configurations, plotted as a function of the parameter Z_s . Since the latter parameter is defined as $Z_s = s^2/l$ (Zribi and Dechambre, 2003), it combines the influence of both the soil's rms height and its correlation length: it is in effect given by the product of the rms height s , which is related to the power of the surface height variations, and the ratio s/l , which represents the local slope of the soil. The underlying motivation for the introduction of Z_s was to introduce the influence of *slope*, which is an important soil feature in the estimation of σ° . It can clearly be seen that the simulated backscattering is more strongly correlated with Z_s ($R^2 = 0.82$, 0.81 in the C band, and $R^2 = 0.71$, 0.62 in the X band, for volumetric moistures of 10% and 30%, respectively), than with the rms height. When the exponential correlation function is considered alone, the correlation between Z_s and the simulated backscattered signal is very high ($R^2 > 0.9$). When different function shapes are considered, corresponding to different values of α (1, 1.25, 1.5 and 1.75), the correlation coefficient decreases, as shown

in Fig.1-b. This outcome could be explained by the influence of the slope component (s/l) on backscattering, which depends on the shape of the correlation function.

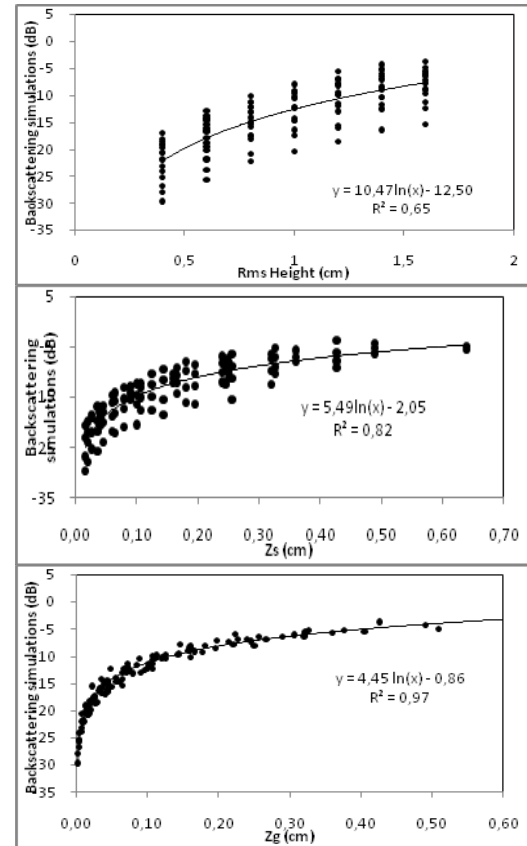


Fig. 1: Backscattering simulations in the *HH* polarisation at 40° incidence, as a function of the rms height, Z_s and Z_g parameters

2.3 Generating the Z_g parameter

The parameter Z_s was initially proposed for use with an exponential correlation (Zribi and Dechambre, 2003), and weaker correlations are observed between Z_s and the simulated backscattering when other correlation function shapes are considered. However, with agricultural and natural soils, differing correlation function shapes are retrieved during the same period. In practice, new tillage is often associated with an exponential function, whereas rain-eroded and ploughed soils are often found to have correlation functions with a shape lying between that of an exponential and a Gaussian function. For these reasons, the use of a single roughness parameter, with an rms height, correlation length and correlation function shape, could be very useful for inversion

studies based on the analysis of radar measurements, which generally make use of a small number of radar configurations.

Since the contribution of the ratio s/l must be different from one correlation shape to another, as a result of differences in the high frequency spectrum of the soil profile, we propose to introduce a new parameter, which is a global representation of the Z_g parameter, written as:

$$Z_g = s \left(\frac{s}{l} \right)^\alpha \quad (1)$$

For a fixed value of α , small values of Z_g correspond to small values of s and/or large values of l , whereas large values of Z_g correspond to large values of s or small values of l . In the case of a fixed correlation length, small values of Z_g correspond to small values of s and/or large values of α , whereas large values of Z_g correspond to large values of s or small values of α . A smooth soil surface (without clods) is generally characterised by a small value of s and a medium to large value of l , thus to a small value of Z_g . Ploughed soil, corresponding to new tillage, is generally associated with a large value of s , a medium to large value of l , and a value of α close to 1, and thus to a large value of Z_g .

Fig. 1-c shows a plot of simulated backscattered signals as a function of Z_g , for various ranges of roughness and four correlation function shapes ($\alpha=1$, $\alpha=1.25$, $\alpha=1.5$, $\alpha=1.75$), in the C band and for the HH polarization, with volumetric moisture value of 10%. Firstly, it can be seen that the simulated backscattering increases with Z_g , and that there is a strong correlation between the backscattering and Z_g , equal to 0.97 and 0.97 for 10% and 30% volumetric moistures in the C-band and equal to 0.97 and 0.93 for 10% and 30% volumetric moistures in the X-band.

A high dynamic range can be observed at small values of Z_g , and near saturation can be seen when Z_g reaches approximately 0.3-0.35. The highest values of α produce the weakest backscattering. From this initial result, Z_g appears to be a useful parameter for the characterization of surface roughness, in the case of a given (fixed) radar configuration. This result can be explained by the fact that Z_g takes the influence on radar backscattering behaviour of s , l and the correlation function shape into account.

To simplify the combination of backscattering simulations made at different radar frequencies, the former were considered as a function of electromagnetic roughness, written in the form: $k \cdot Z_g$ (k : radar wave number). Fig. 2 plots the simulated backscattered signals as a function of $k \cdot Z_g$, in the HH , at a 40° incidence angle, and with the volumetric moisture equal to 10%, thus allowing all roughness conditions and C- and X-band simulations to be combined.

A least squares approach was then used to establish an empirical relationship between $k \cdot Z_g$ and the backscattered signals, taking the form:

$$\sigma^0 = \alpha + \beta \left(1 - e^{-\mu k Z_g} \right) \quad (2)$$

where σ^0 is expressed in dB, k in cm^{-1} , and Z_g in cm. The backscattered signals can be seen to be strongly correlated with $k \cdot Z_g$. All of studied configurations are characterised by a strong correlation between $k \cdot Z_g$ and the radar simulations (greater than 0.77).

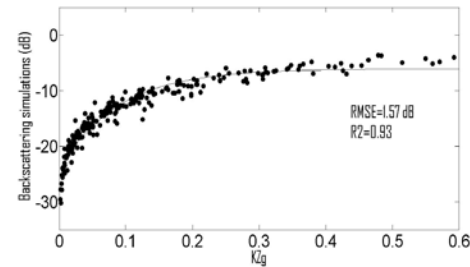


Fig. 2: Backscattering simulations as a function of the parameter kZ_g .

3 EXPERIMENTAL ANALYSIS

In this study, we use data acquired over agricultural watersheds, during the course of three experimental campaigns (Orgeval'94, Pays de Caux'94, Villamblain'2003). For each of these campaigns, radar data (SIRC, ERASME, ASAR/ENVISAT) was acquired with different configurations (Table 1).

Campaign	Sensor	date	Configuration
Orgeval'94	SIRC	12/04/94 - 18/04/94	C band, HH, 44°
Pays de Caux'94	ERASME	February 1994	C and X bands, HH, VV, 20°, 25°, 30°, 35°
Villamblain'03	ASAR/ENVISAT	October 2003	C band, HH, ~43°

Table 1: Radar satellite configurations corresponding to the radar data acquisitions, for the three studied sites.

Simultaneously to the radar acquisitions, ground measurements were carried out in a large number of test fields: the soil moisture was measured within the top 5 cm soil using a gravimetric method and/or a TDR probe, and roughness measurements were made using a pin-profiler (total length equal to 2 m, resolution equal to 10 mm).

3.1 Comparing backscattering simulations with radar signal data

In Figs. 3-a and 3-b, the results derived from the moment method simulations made in two dimensions

are compared with real radar data, for the *HH* and *VV* polarizations, respectively. Two-dimensional (rather than three-dimensional) simulations were used, since the analysed experimental fields had very little directional structure. For each individual test field, ground measurements (*rms* height, correlation length, α parameter, soil moisture) were used as input for the radar backscattering simulations. Fig. 3-a shows the *HH* polarization data obtained from several different configurations: C and X bands, and five different incidence angles: 20°, 25°, 30°, 35° and 44°, whereas Fig. 3-b shows *VV* polarization results for the same set of configurations. In the *HH* polarization, the simulations can be seen to deviate from the radar measurements, with an RMSE equal to 3.34 dB. In the *VV* polarization, a good agreement can be observed, with an RMSE equal to 1.62 dB. These results illustrate some of the limitations encountered, particularly in the *HH* polarization, when the MM model is used to simulate all surface conditions. This is probably due to the greater sensitivity of *HH* polarization to soil roughness (Fung, 1994). In the following section, it is proposed to use empirical relationships to express the backscattered radar signals as a function of the surface parameters.

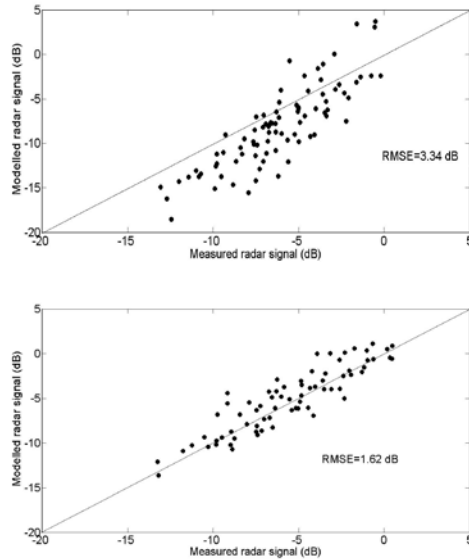


Fig. 3: Numerically simulated radar signals as a function of measured radar signals, a) *HH* pol (C and X bands, at five incidence angles: 20°, 25°, 30°, 35° and 44°), b) *VV* pol (C and X bands, at four incidence angles: 20°, 25°, 30° and 35°).

3.2 Analysis of the relationship between roughness and radar data

All of the ground data analysed in the present study was acquired under very similar soil moisture

conditions (close to 30%). Fig. 4 shows the radar signals measured over the test fields, as a function of kZg , for various configurations (both polarizations and several incidence angles). As in the case of the simulations described in last section, the radar signals are characterized by a high dynamic range at small values of kZg , and near saturation can be observed when kZg reaches approximately 0.3-0.35.

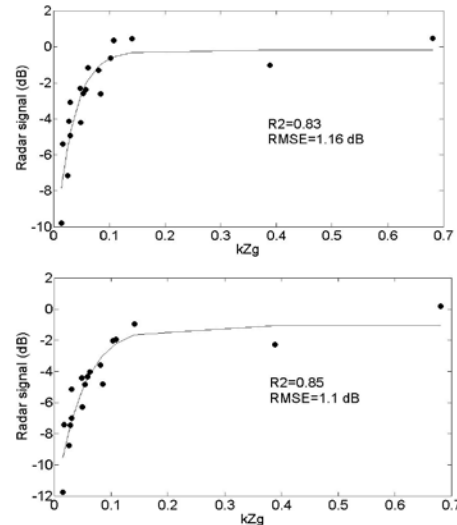


Fig. 4: Relationship between kZg and measured radar signals, for: a) *HH* polarization at 20° incidence, b) *VV* polarization at 20° incidence.

Figs.4-a, 4-b, correspond to observations made at the Pays de Caux site, using the ERASME airborne FM-CW scatterometer. This data was acquired in the *HH* and *VV* polarizations, in the C-and X-bands at 20°, incidence. In both polarizations, the roughness parameter kZg and the radar measurements are strongly correlated. Empirical relationships can be used to express the backscattered radar signals as a function of kZg , for various multi-incidence and polarization configurations. These are written:

$$\sigma_{p\theta}^0 = \alpha_{p\theta} + \beta_{p\theta} \left(1 - e^{-\mu_{p\theta} k Zg} \right) \quad (3)$$

where the coefficients $\alpha_{p\theta}$, $\beta_{p\theta}$ and $\mu_{p\theta}$ are adjusted using a least squares optimisation, p is the polarization and θ is the incidence angle.

4 CONCLUSION

It is very difficult to separately estimate the influences of *rms* height (*s*), correlation length (*l*) and correlation function shape, on the backscattering behaviour of a rough soil surface. In practice, the availability of only a limited number of radar configurations can make it impossible to retrieve all of these parameters with soil moisture.

In the present study, a new approach is proposed for the description of surface roughness and its influence on the backscattering behaviour of radar signals. The resulting expressions make use of a numerical backscattering algorithm based on the moment method, applied to synthetically generated surfaces and assuming a correlation function described

by $\rho(x) = \exp\left(-\left(\frac{x}{1}\right)^\alpha\right)$. The correlation between the

simulated and measured rms soil heights is weak, as a consequence of influences related to the correlation length of the surface roughness and the shape of the correlation function. These influences must be accounted for, in order to retrieve accurate surface roughness or moisture estimations. The parameter Z_s , which allows the influence of soil surface height and slope to be taken into account, can be used to improve the correlation strength. Nevertheless, the simulated radar signals are still affected by strong fluctuations, resulting from variations in the shape of the correlation function. By introducing a new roughness parameter (Z_g), written in the form $Z_g = s\left(\frac{s}{1}\right)^\alpha$, the influence of the rms surface height, the slope of the soil surface, and a third parameter α related to the shape of the correlation function, can be taken into account. A very good correlation is then observed between kZ_g and the simulated radar signals in the C and X bands, with R^2 equal to 0.93 and 0.9 at 40° incidence for the HH and VV polarizations, respectively. Empirical functions are proposed to describe these relationships. The usefulness of this new parameter is demonstrated through the analysis of radar signal data acquired at three experimental sites in France (Orgeval, Pays de Caux and Villamblain).

5 ACKNOWLEDGEMENTS

This study was funded by: ASCAS (TOSCA/CNES) and AMETHYST (ANR-12-TMED-0006-01) projects.

6 REFERENCES

- Baghdadi, N., Holah, N., and Zribi, M., 2006. Calibration of the Integral Equation Model for SAR data in C-band and HH and VV polarizations. *International Journal of Remote Sensing*, 27 (4), 805-816.
- Baghdadi, N., Abou Chaaya, J., and Zribi, M., 2011. Semi-empirical calibration of the Integral equation Model for SAR data in C-band and cross polarization using radar images and field measurements. *IEEE Geoscience and Remote Sensing Letters*, 8 (1), 14-18.
- Fung, A., and Chen, M. F., 1985. Numerical Simulation of Scattering from Simple and Composite Random Surfaces, *J. Opt. Am. A*, 2 (12).
- Fung, A. K., 1994. *Microwave Scattering and Emission Models and their Applications*, Norwood: Artech House.
- Fung, A. K., Li, Z., and Chen, K. S., 1992. Backscattering from a randomly rough dielectric surface. *IEEE Transaction on Geoscience and Remote Sensing*, 30, 356-369.
- Harrington, R. F., 1968. *Field Computation by Moment Method*. IEEE PRESS, Series on Electromagnetic Waves.
- Lievens H., Verhoest N.E.C., De Keyser E., Vernieuwe H., Matgen P., Álvarez-Mozos J., De Baets B. (2011). Effective roughness modelling as a tool for soil moisture retrieval from C- and L-band SAR. *Hydrology and Earth System Sciences*, 15(1), 151-162.
- Zribi, M. and Dechambre, M. 2003. A new empirical model to retrieve soil moisture and roughness from Radar Data. *Remote Sensing of Environment*, 84 (1), 42-52.

Cross-cutting validation of satellite products over France through their integration into a land surface model

Jean-Christophe Calvet, Alina Barbu, Dominique Carrer, David Fairbairn, Emiliano Gelati, and Catherine Meurey,
CNRM-GAME, Météo-France, CNRS, UMR3589, Toulouse, France
jean-christophe.calvet@meteo.fr

ABSTRACT - Météo-France develops the ISBA-A-gs generic land surface model (LSM) able to represent the diurnal cycle of the surface fluxes together with the seasonal, interannual and decadal variability of the vegetation biomass. The LSM is embedded in the SURFEX modeling platform together with a simplified extended Kalman filter. These tools form a Land Data Assimilation System (LDAS). The current version of the LDAS assimilates SPOT-VGT LAI and ASCAT surface soil moisture (SSM) products over France (8km x 8km), and a passive monitoring of surface albedo (SA), FAPAR and Land Surface temperature (LST) is performed (i.e., the simulated values are compared with the satellite products). The LDAS-France system is developed in the framework of the FP7 IMAGINES project and is used in the European Copernicus Global Land Service (<http://land.copernicus.eu/global/>) to monitor the quality of upstream products. The LDAS generates statistics whose trends can be analyzed in order to detect possible drifts in the quality of the products: (1) for LAI and SSM, metrics derived from the active monitoring (i.e. assimilation) such as innovations (observations vs. model forecast), residuals (observations vs. analysis), and increments (analysis vs. model forecast); (2) for SA, LST, and FAPAR, metrics derived from the passive monitoring such as the Pearson correlation coefficient, z-score, RMSD, SDD, mean bias. The results obtained over the 2007-2014 period are presented.

1 INTRODUCTION

Long (more than 30 years) time series of satellite-derived products over land are now available. They concern Essential Climate Variables (ECV) such as LAI, FAPAR, surface albedo, and soil moisture. The direct validation of such Climate Data Records (CDR) is not easy, as in situ observations are limited in space and time. Therefore, indirect validation has a key role to play. It consists in comparing the products with similar pre-existing products derived from satellite observations or from land surface model (LSM) simulations. The most advanced indirect validation technique consists in integrating the products into a LSM using a data assimilation scheme. The obtained reanalysis accounts for the synergies of the various upstream products and provides statistics which can be used to monitor the quality of the assimilated observations.

2 TOOLS

2.1 SURFEX

The SURFEX modelling platform of Météo-France (Masson et al. 2013) is used to represent the ocean, urban, lakes, and soil/vegetation processes in research and operational applications. It is interoperable with

real-time applications in numerical weather forecast, hydrology, and atmospheric chemistry. It is used in the CNRM-ARPEGE IPCC climate simulations. SURFEX is shared by many national meteorological services in Europe and North Africa and the newly released Version 8 is open-source.

2.2 ISBA-A-gs

The ISBA-A-gs model (Calvet et al. 1998, Gibelin et al. 2006) is a version of the ISBA land surface model in SURFEX able to simulate photosynthesis and plant growth. It was designed to simulate biophysical variables observable from space such as LAI, FAPAR, SA, LST, and SSM. In ISBA-A-gs, LAI is flexible and can be analyzed at a given time. LAI is completely driven by photosynthesis and no growing degree-day phenology model is used. All the atmospheric variables impact LAI and the annual maximum LAI is modelled. Moreover, the impact of long-term changes in the atmospheric CO₂ concentration can be simulated.

Szczypta et al. (2014) have evaluated the ISBA-A-gs over the Euro-Mediterranean area using LAI and SSM data records produced by the geoland2 and by the ESA-CCI Soil Moisture projects, respectively.

2.3 LDAS-France

Barbu et al. (2014) have implemented a LDAS chain over France (LDAS-France). The system is able to jointly assimilate LAI and SSM in ISBA-A-gs at a spatial resolution of 8km x 8km. It simulates other variables such as FAPAR, SA and LST. A demonstration of the capabilities of LDAS-France is made using the Copernicus Global Land SPOT-VGT-derived LAI and the ASCAT-derived SSM.

3 ASSIMILATION OF VEGETATION PRODUCTS

Since ISBA-A-gs is able to simulate LAI and FAPAR, both quantities can be assimilated. Assimilating LAI is more easy than assimilating FAPAR for several reasons:

- FAPAR has very little sensitivity to LAI changes for high LAI values (typically for $\text{LAI} > 2 \text{ m}^2\text{m}^{-2}$);
- FAPAR is a radiative product and has a diurnal cycle; it depends on atmospheric variables and the satellite-derived FAPAR corresponds to cloudless conditions by definition, while the atmospheric conditions imposed to the model may be different;
- New LAI products are designed to limit the saturation effect (e.g. GEOV1, Baret et al. 2013).

However, FAPAR is highly informative at wintertime at mid-latitudes, especially for grasslands as shown by Fig. 1.

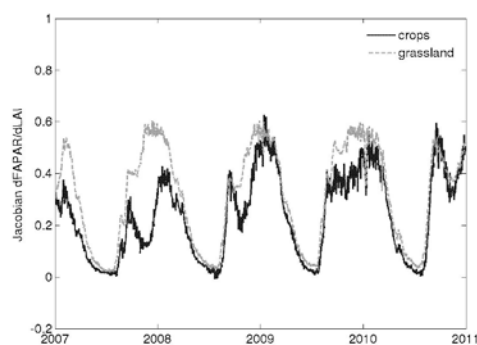


Figure 1 - $\Delta\text{FAPAR}/\Delta\text{LAI}$ Jacobians simulated by the ISBA-A-gs model from 2007 to 2010 for a model grid-cell near Toulouse in France for (grey dashed line) grasslands and (dark solid line) straw crops.

4 ASSIMILATION OF SSM

One has to face a number of difficulties when implementing the assimilation of ASCAT-derived SSM observations:

- Soil moisture is model-dependent and the SSM observations have to be rescaled to be consistent with the range of modelled soil moisture values;
- The ASCAT product has seasonal and interannual issues related to the empirical correction of the vegetation effects, based on fixed parameters ignoring the interannual variability of the vegetation biomass.

A way to cope with these problems is to implement a seasonal-based CDF (Cumulative Distribution Function) matching technique using a three-month moving window (Barbu et al., 2014).

Another issue is the decoupling of the soil moisture content between surface and deep soil layers that may occur in dry conditions. This is illustrated by the SSM Jacobians shown in Fig. 9 of Parrens et al. (2014): using a detailed multilayer soil model, they show that in dry conditions at summertime, the sensitivity of SSM to small perturbations of the soil moisture of a deep soil layer is very low for soil layer below 0.15 m. This means that soil moisture cannot be correctly analyzed by a multi-layer model below this depth. This problem is less acute using a bulk root-zone soil hydrology model such as in the current version of LDAS-France.

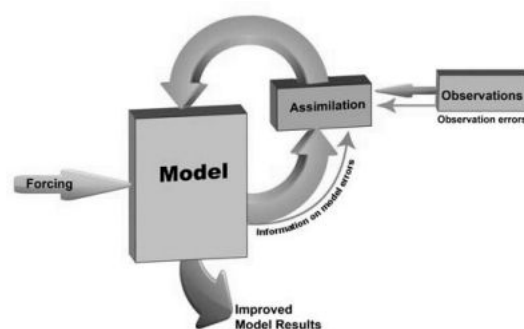


Figure 2 - General principles of the sequential data assimilation of observations into a model (reproduced from <http://www.coastlab.org/reanalyse.htm>).

5 APPLICATIONS

Integrating observations into a land surface model is a way to improve the model results (Fig. 2). It is also a way to assess and monitor the observation errors through time. In the context of this work, the added value of data assimilation is shown for drought monitoring (Sect. 5.1) and examples of satellite product quality monitoring results are shown in Sect. 5.2.

5.1 Drought monitoring

During the spring of 2011, France was affected by an extreme drought event, never seen in 50 years of meteorological records. Figure 3 shows that the assimilation of LAI and SSM tends to enhance the drought impact on root-zone soil moisture in western France.

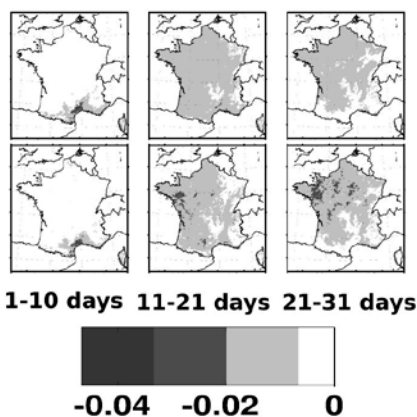


Figure 3 - Negative changes in the root-zone soil moisture during the three ten-daily periods of April 2011, from one period to another, in $\text{m}^3\text{m}^{-3} / 10\text{-d}$ as produced by (top) open-loop simulations and (bottom) LDAS-France.

5.2 Cross-cutting validation of satellite products

LDAS-France is used operationally since 1 January 2013 to produce metrics permitting the quality monitoring of LAI, FAPAR, SSM, SA, and LST. Figures 4-6 present monthly standard deviation of differences (SDD) scores of the observations vs. (1) the open-loop simulations and (2) the analysis. The analysis is an optimal, best estimation of the

considered variable as it combines the information brought by the model (and indirectly the atmospheric observations such as the in situ precipitation observations) and the assimilated LAI and SSM satellite products.

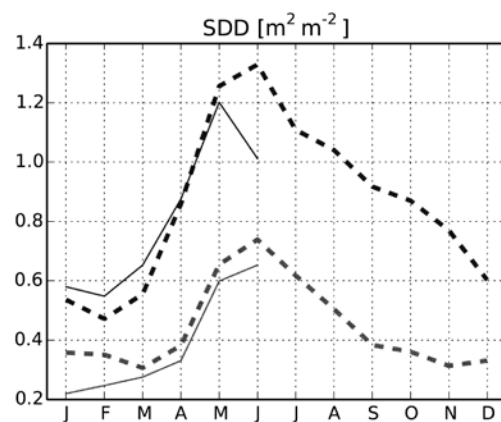


Figure 4 - Monthly LAI scores of the observations vs. (dark lines) model open-loop simulations, (grey lines) analysis, over France at $8\text{ km} \times 8\text{ km}$ spatial resolution: for (thick dashed lines) all data pairs from 2007 to 2013, and for (fine solid lines) data pairs in 2014, from January to June. Model-analysis differences show the impact of assimilating LAI and SSM on the simulated LAI.

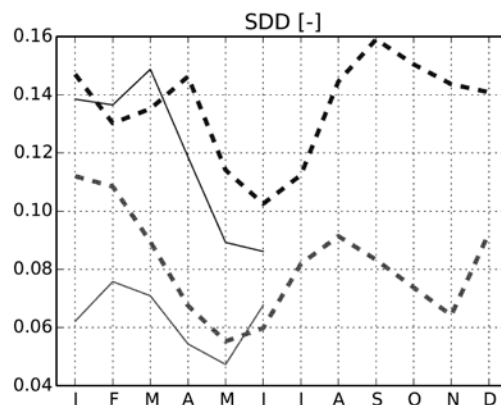


Figure 5 - As in Fig. 4, except for FAPAR.

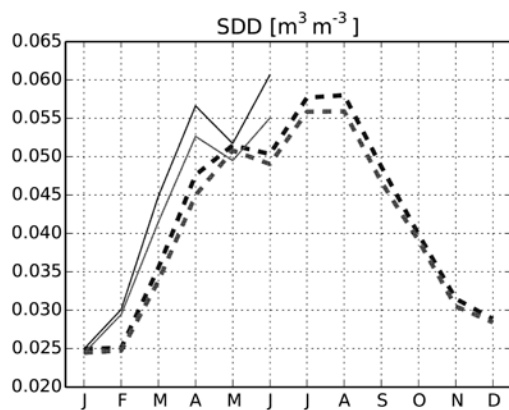


Figure 6 - As in Fig. 4, except for SSM.

6 CONCLUSIONS

For the first time, an operational LDAS able to sequentially assimilate LAI together with SSM is used at a country scale over France. The LDAS-France is used to perform a cross-cutting validation of key biophysical variables produced by the Copernicus Global Land service.

The feasibility of extending the LDAS at a global scale ("LDAS-Monde") is being tested. Note that over France, thousands of in situ raingages are used as input to LDAS-France in near-real-time. Today, this is not possible outside France. The LDAS-Monde chain will first be tested over the Euro-Mediterranean area. Eventually, a multi-decadal global land reanalysis integrating the existing vegetation and soil moisture satellite-derived products will be built and compared with other land reanalyses.

7 REFERENCES

Barbu, A.L., J.-C. Calvet, J.-F. Mahfouf, and S. Lafont: Integrating ASCAT surface soil moisture and GEOV1 leaf area index into the SURFEX modelling platform: a land data assimilation application over France, *Hydrol. Earth Syst.*, 18, 173–192, doi:10.5194/hess-18-173-2014, 2014.

Baret, F., Weiss, M., Lacaze, R., Camacho, F., Makhmara, H., Pacholczyk, P., and Smets, B.: GEOV1: LAI and FAPAR essential climate variables and FCOVER global time series capitalizing over existing products. Part1: Principles of development and production, *Remote Sens. Environ.*, 137, 299–309, 2013.

Calvet, J.-C., Noilhan, J., Roujean, J.-L., Bessemoulin, P., Cabelguenne, M., Olioso, A., and Wigneron, J.-P.: An interactive vegetation SVAT model tested against data from six contrasting sites, *Agr. Forest Meteorol.*, 92, 73–95, 1998.

Gibelin, A.-L., Calvet, J.-C., Roujean, J.-L., Jarlan, L., and Los, S. O.: Ability of the land surface model ISBA-A-gs to simulate leaf area index at the global scale: Comparison with satellites products, *J. Geophys. Res.*, 111, D18102, doi:10.1029/2005JD006691, 2006.

Masson, V., Le Moigne, P., Martin, E., Faroux, S., Alias, A., Alkama, R., Belamari, S., Barbu, A., Boone, A., Bouyssel, F., Brousseau, P., Brun, E., Calvet, J.-C., Carrer, D., Decharme, B., Delire, C., Donier, S., Essaouini, K., Gibelin, A.-L., Giordani, H., Habets, F., Jidane, M., Kerdraon, G., Kourzeneva, E., Lafaysse, M., Lafont, S., Lebeaupin Brossier, C., Lemonsu, A., Mahfouf, J.-F., Marguinaud, P., Mokhtari, M., Morin, S., Pigeon, G., Salgado, R., Seity, Y., Taillefer, F., Tanguy, G., Tulet, P., Vincendon, B., Vionnet, V., and Voldoire, A.: The SURFEXv7.2 land and ocean surface platform for coupled or offline simulation of Earth surface variables and fluxes, *Geosci. Model Dev.*, 6, 929–960, doi:10.5194/gmd-6-929-2013, 2013.

Parrens, M., Mahfouf, J.-F., Barbu, A., and Calvet, J.-C.: Assimilation of surface soil moisture into a multilayer soil model: design and evaluation at local scale, *Hydrol. Earth Syst. Sci.*, 18, 673–689, doi:10.5194/hess-18-673-2014, 2014.

Szczypta, C., Calvet, J.-C., Maignan, F., Dorigo, W., Baret, F., and Ciais, P.: Suitability of modelled and remotely sensed essential climate variables for monitoring Euro-Mediterranean droughts, *Geosci. Model Dev.*, 7, 931–946, doi:10.5194/gmd-7-931-2014, 2014.

A Network of Sites for Ground Biophysical Measurements in support of Copernicus Global Land Product Validation

F. Camacho⁽¹⁾, R. Lacaze⁽²⁾, C. Latorre⁽¹⁾, F. Baret⁽³⁾, F. De la Cruz⁽⁴⁾, V. Demarez⁽⁵⁾, C. Di Bella⁽⁶⁾, H. Fang⁽⁷⁾, J. García-Haro⁽⁸⁾, M. P. Gonzalez⁽⁹⁾, N. Kussul⁽¹⁰⁾, E. López-Baeza⁽⁸⁾, C. Mattar⁽¹¹⁾, E. Nestola⁽¹²⁾, E. Pattey⁽¹³⁾, I. Piccard⁽¹⁴⁾, C. Rudiger⁽¹⁵⁾, I. Savin⁽¹⁶⁾, A. Sanchez - Azofeifa⁽¹⁷⁾, M. Boschetti⁽¹⁸⁾, D. Bossio⁽¹⁹⁾, M. Weiss⁽³⁾, A. Castrignano⁽²⁰⁾, M. Zribi⁽⁵⁾

⁽¹⁾ EOLAB, Valencia, Spain, ⁽²⁾ HYGEOS, Toulouse, France, ⁽³⁾ INRA, Avignon, France, ⁽⁴⁾ ITAP, Albacete, Spain, ⁽⁵⁾ CESBIO, Toulouse, France, ⁽⁶⁾ INTA, Buenos Aires, Argentina, ⁽⁷⁾ LREIS, Beijing, China, ⁽⁸⁾ UVEG, Valencia, Spain, ⁽⁹⁾ IFAPA, Córdoba, Spain, ⁽¹⁰⁾ NAS, Kiev, Ukraine, ⁽¹¹⁾ U. Chile. Santiago de Chile, Chile, ⁽¹²⁾ IBAF-CNR, Porano, Italy, ⁽¹³⁾ Agri-Food, Ottawa, Canada, ⁽¹⁴⁾ VITO, Mol, Belgium, ⁽¹⁵⁾ U. Monash, Melbourne, Australia, ⁽¹⁶⁾ DSSI, Moscow, Russia, ⁽¹⁷⁾ U. Alberta, Edmonton, Canada, ⁽¹⁸⁾ IREA-CNR, Milano, Italy, ⁽¹⁹⁾ CIAT, Nairobi, Kenya, ⁽²⁰⁾ CRA-SCA, Bari, Italy
fernando.camacho@eolab.es

ABSTRACT – Provision of reliable ground reference datasets is mandatory for the validation of satellite products. The ground data should be collected considering the spatial variability of the sites in agreement with recommendations of the CEOS WGCV Land Product Validation sub-group for validation of moderate resolution satellite products. This paper describes a network of sites established in support of the validation of Copernicus Global Land biophysical products (LAI, FAPAR and FCover) where ground measurements are collected. Protocols for field data collection based on optical instruments and reporting, as well as for up-scaling of local ground data to the site extent are also detailed. Currently, 10 different sites have been sampled in 45 field campaigns; reaching the number of one-thousand Elementary Sampling Units (ESU) sampled with digital hemispherical photograph (DHP), LAI-2200 or AccuPAR devices in two years (2013 and 2014). Moreover, autonomous PAR systems (PASTIS) have been installed over a few sites for the continuous monitoring of FAPAR and PAI. A number of additional sites (mostly from the JECAM network) where ground activities are being conducted are also considered to provide a comprehensive database for the validation of Copernicus Global Land products. This database will be shared through the FP7 ImagineS web site and CEOS On-Line Validation Experiment (OLIVE) tool for the validation of medium resolution satellite biophysical products.

1 INTRODUCTION

The Copernicus program is the EU response to the increasing demand for reliable environmental data. The Copernicus Global Land Service (<http://land.copernicus.eu/global/>) aims to continuously monitor the status of land territories and provide a series of bio-geophysical products (e.g. Albedo, LAI, FAPAR, Burnt Areas, Land Surface Temperature...) on the status and evolution of continental ecosystems at global scale.

Provision of consistent ground biophysical variables (i.e., LAI, FAPAR, FCover) is essential for the validation of biophysical satellite products. The biophysical variables should be collected and processed according to the CEOS WGCV Land Product Validation (LPV) guidelines to be directly comparable with the medium resolution satellite product. Up to know, the largest compilation of ground

reference data processed according to CEOS LPV guidelines was mainly achieved from a range of initiatives (VALERI, NASA, CCRS, ESA...), but none of them are currently providing updated biophysical ground reference values. Existing networks are not fully dedicated to the validation of LAI/FAPAR satellite products and the sites, methodologies or measured variables do not always match properly the validation requirements for global biophysical satellite products.

Consequently, building a network of sites for the provision of regular and consistent ground biophysical datasets is necessary for the validation of Copernicus Global Land products whose quality needs to be verified regularly. In the context of the FP7 ImagineS (2012-2016) project (<http://fp7-imagines.eu/>), in support of the evolution of the Global Land Service, a network of demonstration sites for the validation of Copernicus Global Land products has been established over cropland/grassland areas. The initial network has

been expanded with additional sites where ground data are being collected thanks to the collaboration with other research teams involved in JECAM (www.jecam.org/), FLUXNET (fluxnet.ornl.gov/) or Environet (www.envir-net.org/) networks.

This paper describes the status of the current activities, including established protocols, the network of sites, the achieved field campaigns and the perspectives.

2 DEFINITIONS AND METHODS

2.1 Leaf Area Index (LAI)

Leaf area index (LAI) corresponds to one half the total green leaf area per unit horizontal ground surface area. However, if no distinction between leaves and other plants elements is made the correct term is Plant Area Index (PAI), which is the variable estimated from indirect methods. If we refer only to green elements, the correct term is GLAI (Green Leaf Area Index) or GAI (Green Area Index) if no distinction is made between leaves and other plant elements. GAI may be also estimated from indirect methods based on downward looking measurements of the green fraction with hemispherical cameras. GAI is probably the most pertinent definition to be used for remote sensing observations (Baret and Fernandes, 2012). Note that the community uses commonly the term LAI in place of GLAI.

Indirect methods are commonly used for measuring PAI (GAI) from gap (green) fraction (Weiss et al., 2004). As we are interested in GLAI estimates, we should avoid to measure when the yellow-to-total leaf area ratio is large (i.e., during the senescent periods). Digital Hemispherical Photos (DHP) have the advantage to discriminate green from non-green elements during the processing of the digital photos, and thus is easily related to GAI. Moreover, most of the indirect methods estimate an 'effective' PAI (GAI) value, assuming random distribution of the elements within the canopy volume (i.e., no clumping). The clumping should be also measured to obtain the actual value. We refer here as "LAI" and "LAI_e", the actual and effective GLAI based on indirect methods.

The devices most often used in our sites are DHP and LAI-2000 or LAI-2200 (LI-COR Inc. Lincoln, Nebraska).

2.2 Fraction of Absorbed PAR (FAPAR)

FAPAR refers to the fraction of PAR (0.4-0.7 μm) that is absorbed by a vegetation canopy. Since FAPAR is mainly used as a descriptor of photosynthesis and evapotranspiration processes, only the green photosynthetic elements (leaves, needles, or other green elements) should be accounted for. FAPAR

depends also on the illumination conditions, i.e. the angular position of the sun and the relative contributions of the direct and diffuse illumination. Both black-sky (assuming only direct radiation) and white sky (assuming that all the incoming radiation is in the form of isotropic diffuse radiation) FAPAR values may be considered. Satellite FAPAR products are currently mainly defined as the black-sky FAPAR value for the same sun position as that observed at the satellite overpass. Black-sky FAPAR computed at 10:00 local solar time is a good approximation of the daily integrated black-sky FAPAR. The fraction of intercepted radiation, FIPAR (although it is not restricted to the PAR domain) is a very close approximation of FAPAR.

The PAR absorbed by canopies may be either measured directly by PAR sensors (PAR balance) or estimated using ceptometers dedicated to measure PAR transmitted at the bottom of the canopy or estimated using the gap fraction, i.e. light transmission assuming that leaves are perfect black absorbers (i.e., FIPAR) (Baret and Fernandes, 2012).

In our sites most of the FAPAR measurements are based on FIPAR using DHP or PAR transmitted using ceptometers such as AccuPAR (Decagon, USA). Moreover, INRA has developed the PAI autonomous system from transmittance sensors in the PAR domain (PASTIS) that allows continuous monitoring of FAPAR and PAI (see Weiss et al., 2014) that have been installed in several sites as detailed hereafter.

2.3 Fraction of Vegetation cover (FCover)

It corresponds to the green fraction as seen from the nadir direction. FCOVER is mainly assessed using digital photography. Note that the field of view of the camera should be restricted as much as possible to better match the vertical direction assumed in the FCOVER definition. A $\pm 10^\circ$ field of view is admitted as a proxy for the vertical direction. DHP is the main device used for FCOVER estimates in our database.

3 PROTOCOLS FOR FIELD DATA AND UP-SCALING

Based on the previous achievements mainly during the VALERI project (<http://w3.avignon.inra.fr/valeri/>), guidelines for running a field campaign, and reporting the data has been established (Baret and Fernandes, 2012), as well as for the up-scaling of the ground data according to the CEOS LPV recommendations (Fernandes et al., 2014). These protocols have been provided to the teams operating on the ImagineS sites for consistent ground data acquisitions.

3.1 Field Measurements

a) Site selection

A validation site should be selected according to several criteria.

- The site should be relatively flat to simplify the interpretation.
- The extent should be around few km² ($\approx 3 \times 3$ km²) so that ground sampling would be relatively easy.
- It should present a significant range of vegetation types and development stages. Note that ImagineS is focused on agriculture indicators. The sites are thus located over agricultural areas.
- The site should be composed of patches of vegetation large enough to minimize border effects.

b) Sampling the site

A single pixel constitutes the Elementary Sampling Unit (ESU) that should be associated with the ground measurements representative of the corresponding area. To sampling the site the following rules are proposed:

- Considering the site heterogeneity a minimum of around 30 ESUs should be sampled over the study site. Note that additional control points over bare areas should be considered.
- The ESUs should be around 20 m in agreement with the pixel size of high resolution products for up-scaling.
- The ESUs should sample the variability observed over the site, both in terms of landcover and conditions. A stratified sampling based on the prior knowledge of the landcover is optimal. Adjacency effects should be minimized. ESUs should therefore be located at a reasonable distance (i.e. 50 m) from borders and surrounded by pixels with approximately the same type of vegetation as that of the considered ESU. Note that each ESU should be geo-referenced.

c) Sampling a ESU

Over each ESU, a sampling scheme is proposed for the measurement of the several biophysical variables.

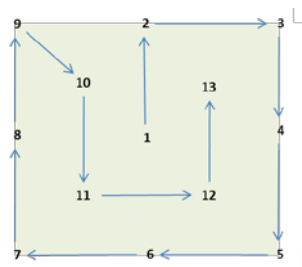


Figure 1. Typical sampling scheme proposed for an ESU.

The GPS coordinates of the centre of the ESU (point 1) are measured within few metres accuracy. The sampling thus includes 13 individual measurements.

It is proposed to use digital hemispherical photography to estimate LAI, FAPAR and FCover simultaneously. This technique has been proven very efficient. However, great care should be taken to:

- Illumination conditions: better use diffuse conditions to avoid problems with shadows.
- Use color cameras with high resolution (minimum 10 Mega pixels).
- Sample both overstory (looking upward) and understory (looking downward) when needed.
- It is very important to minimize problems related to the presence of non-green vegetation elements avoiding up-ward looking photos when dry elements are presents.

The processing could be conveniently achieved using the CAN-EYE software (<http://www6.paca.inra.fr/can-eye/>) that provides estimates of effective and actual LAI, FAPAR (actually FIPAR) for a range of sun positions and FCover.

d) Reporting

Finally, guidelines for reporting a ground campaign in a consistent way have been proposed, including description of the site and sampled vegetation, description of protocols and ancillary information. A format for providing the ground measurements with header information is used.

3.2 Up-scaling ground measurements

The local measurements acquired over a sample of ESUs should be extended to the whole site (i.e. up-scaling). Guidelines for up-scaling of ground measurements using high spatial resolution imagery are also well established (Fernandes et al., 2014).

The up-scaling of ground data is carried out by EOLAB. A multiple robust regression method between ESUs reflectance and the ground biophysical variable is applied (Martínez et al., 2009). The 'robustfit' function from the Matlab statistics toolbox is used. It uses an iteratively re-weighted least squares algorithm, with the weights at each iteration computed by applying the bi-square function to the residuals from the previous iteration. This algorithm provides lower weight to ESUs that do not fit well. The results are less sensitive to outliers in the data as compared with ordinary least squares regression. At the end of the processing, two errors are computed: weighted RMSE (using the weights attributed to each ESU) and cross-validation RMSE (leave-one-out method).

The multiple robust regression method is applied to the different band combinations of the high resolution satellite imagery. The final band combination for the

transfer function is selected based on a good compromise between the low cross-validation RMSE, the weighted RMSE (lowest value) and the number of rejected points. As the method has limited extrapolation capacities, a quality flag image based on the convex hull technique is included in the final ground based map in order to inform the users on the reliability of the estimates. The convex hull test allows evaluating also the suitability of the spatial sampling. An example of this procedure can be found in this issue (Camacho et al., 2014).

4 THE NETWORK OF SITES

A network of 17 demonstration sites over cropland areas has been established in ImagineS where research teams are able to collect ground data and/or to evaluate the satellite products. LAI/FAPAR is measured in 13 ImagineS sites (see Table 1).

Site Name	Country	Lat.	Long.	Biome
SouthWest(*)	France	43.48	1.27	Cropland
Barrax	Spain	39.03	-2.07	Cropland
Tula (*)	Russia	53.08	37.23	Cropland
Upper Tana Basin	Kenia	-0.55	36.48	Cropland
Merguellil (*)	Tunisia	35.75	10.08	Cropland
Ottawa	Canada	45.30	-75.50	Cropland
San ernando	Chile	-34.70	-70.96	Cropland
25 Mayo	Argentina	-37.90	-67.73	Crops/Shrubs
Yanco	Australia	-34.75	146.07	Grassland
Córdoba	Spain	37.78	-4.73	Cropland
La Albufera	Spain	39.27	-0.316	Rice
Rosasco	Italy	45.25	8.562	Rice
Pshenichne(*)	Ukraine	50.07	30.11	Cropland

Table 1. List of ImagineS demonstration sites where ground LAI/FAPAR measurements are acquired. Asterisks indicates sites of the JECAM network.

Site Name	Country	Lat.	Lon.	Biome
Guangdong	China	20,87	110,08	Rice
Belgium-France	Belgium	50,65	5,00	Cropland
Collelongo	Italy	41,85	13,59	Deciduous Broadleaf Forest
SantaRosa	CostaRica	10,84	-85,62	Tropical Forest.
Heilongjiang Farm-Heilongjiang	China	47,65	133,52	Rice
Utiel	Spain	39,58	-1,26	Vineyard
Capitanata	Italy	41,53	15,63	Cropland

Table 2. Additional sites where ground LAI/FAPAR measurements are acquired and shared with ImagineS.

Moreover, seven additional sites where ground data is being collected shared the measurements for the validation of Copernicus Global Land products (Table 2). Note that the protocols for ground data collection over these few sites coming from JECAM such as Guangdong, Belgium-France, Heilongjiang (Fang et al., 2014) or Capitanata, FLUXNET (i.e., Collelongo) or ESA SMOS/Sentinel-3 (i.e., Utiel) validation sites could be slightly different than those described above followed in ImagineS

5 DATA COLLECTED

A large dataset of more than 1000 ESUs has been already collected on the ImagineS sites during 2013 and 2014 (Table 3).

SITE	# CAMPAIGNS	DATES (2013)	# ESUS
SW France	5	19-26 June	113
		09-11 July	
		24-29 July	
		16-20 August	
		2-6 Septem.	
Merguellil	9	31 January	91
		20 February	
		8 March	
		26 March	
		11 April	
		17 April	
		3 May	
		15 May	
Ottawa	4	19 December	34
		10-26 June	
		3-31 July	
		15,26 August	
Pshenichne	3	10,18 Septem.	102
		14-17 May	
		12-15 June	
		14-17 July	
SITE	# CAMPAIGNS	DATES (2014)	# ESUS
Barrax	1	29-30 May	30
Tula	5	9 April	155
		23 May	
		26 June	
		25 July	
		3 September	
Merguellil	6	21 January	77
		14 February	
		21 March	
		15 April	
		8 May	
		28 May	
25 de Mayo	1	7-9th February	44
Cordoba	1	19-20 May	55
Albufera	9	17 June	257
		24-25 June	
		29 June	
		6 July	
		15 July	
		22 July	
		31 July	
		7 August	
		22 August	
Rosasco	1	3-4 July	43

Table 3. Number of field campaigns, dates in 2013 and 2014 and total number of ESUs collected up to now in the ImagineS sites.

Note that for most of the sites multi-temporal campaigns have been performed in order to characterize the crop cycle. In addition, PASTIS-PAR data has been collected during 2014 in Barrax (Latorre et al., 2014), Ottawa and Yanco sites, and will be installed in Pshenichne and Collelongo in 2015.

6 CONCLUSIONS AND PERSPECTIVES

Reliable ground dataset of biophysical variables are essential for the accuracy assessment of satellite biophysical products. In the context of the FP7 ImagineS project a network of cropland sites has been established in support of the validation of Copernicus Global Land products. Protocols for field acquisitions and up-scaling of ground data using high resolution imagery in agreement with the CEOS LPV recommendations have been promoted among the different sites. Protocols were previously established during the VALERI initiative.

Up to now, 45 field campaigns have been conducted in 10 different cropland sites; biophysical (LAI_{eff}, LAI, FAPAR, FCOVER) variables were characterised in more than 1000 ESU over croplands using indirect methods. In several sites, multi-temporal acquisitions have been conducted allowing the proper characterization of the vegetation cycle. Moreover, autonomous systems (PASTIS-PAR) for continuous monitoring of PAI and FAPAR have been installed over three sites. This dataset is complemented with several additional sites where ground data is collected from other initiatives (e.g. JECAM, Environet). Ground data are up-scaled when a cloud-free high-resolution image is available. Uncertainties of ground estimates under different vegetation conditions should be better accounted for with destructive measurements as in Fang et al., (2014).

This ground database as well as the ground-based high resolution maps constitutes an important contribution for the validation of the medium resolution products. This dataset will be shared to the scientific validation community through the ImagineS web page and the mean values of the 3x3 km² site through the CEOS OLIVE tool (<http://calvalportal.ceos.org/web/olive/>). This network based on collaborative research with different institutions should be extended in the near future with the inclusion of new sites targeting different biomes. The ImagineS achievements should be a first step towards the establishment of a network of sites supporting the continuous validation of satellite biophysical products.

7 REFERENCES

- Baret, F. and R. Fernandes, 2012. Validation Concept. ESA Report. VALSE2-PR-014-INRA.39 pp.
- Camacho, F., C. Latorre et al., (2014). Characterization of vegetation parameters over the Río Colorado basin in La Pampa (Argentina) with ground data and multi-scale satellite imagery. This issue.
- Fang, H., W. Li, S. Wei, C. Jiang (2014). Seasonal variation of leaf area index (LAI) over paddy rice fields in NE China: Intercomparison of destructive sampling, LAI-2200, digital hemispherical photography (DHP), and AccuPAR methods. *Agricultural and Forest Meteorology*, 198–199: 126–141.
- Fernandes, R., Plummer, S., Nightingale, J., et al. (2014). Global Leaf Area Index Product Validation Good Practices. CEOS Working Group on Calibration and Validation - Land Product Validation Sub-Group. Version 2.0: Public version available on LPV website.
- Latorre, C., F. Camacho, et al. (2014). Seasonal monitoring of FAPAR over the Barrax cropland site in Spain, in support of the validation of PROBA-V products at 333m. This issue.
- B. Martínez, F. Camacho, A. Verger, F.J. García-Haro, M.A. Gilabert (2013). Intercomparison and quality assessment of MERIS, MODIS and SEVIRI FAPAR products over the Iberian Peninsula. *International Journal of Applied Earth Observation and Geoinformation* 21 : 463–476
- Weiss, M., F. Baret, B. de Solan, M. Hemmerlé (2014). Monitoring Plant Area Index at ground level: PAI autonomous system from transmittance sensors (PASTIS). This issue.
- Weiss, M., Baret, F., Smith, G.J., Jonckheere, I. and Coppin, P., 2004. Review of methods for in situ leaf area index (LAI) determination Part II: Estimation of LAI, errors and sampling. *Agricultural and Forest Meteorology*, 121(1-2): 37-53.

8 ACKNOWLEDGEMENTS

Special thanks are given to all researchers and institutions involved in the acquisition of field data. This research is supported by the FP7-SPACE-2012-1 ImagineS project.

Landsat-8 TIRS Radiometric Performance

Julia A. Barsi, Matthew Montanaro, Brian L. Markham, Simon J. Hook, John R. Schott, Nina G. Raqueno, Aaron Gerace
Science Systems and Applications, Inc.; Sigma Space Corp.; NASA/Goddard Space Flight Center; NASA/Jet Propulsion Laboratory; Rochester Institute of Technology; Rochester Institute of Technology
julia.barsi@nasa.gov; matthew.montanaro@nasa.gov; brian.l.markham@nasa.gov; simon.j.hook@nasa.gov; schott@cis.rit.edu; nina@cis.rit.edu; adgpci@cis.rit.edu

ABSTRACT – *Landsat-8 was launched on February 11, 2013 and continues the long record of earth imaging by Landsat sensors. The Thermal Infrared Sensor (TIRS) is the satellite's thermal band imager. The TIRS instrument is a significant departure from the previous Landsat thermal imagers; it is a pushbroom design, rather than a whiskbroom. TIRS acquires data in two spectral channels covering 10.60-11.19 μm (Band 10) and 11.50-12.51 μm (Band 11) rather than a single wide spectral bandpass channel. The spatial resolution is 100 m as opposed to 60 m on Landsat-7 and 120 m on Landsat-5.*

TIRS was well characterized and calibrated on the ground prior to launch. Monitoring of the calibration continues on-orbit using the on-board variable temperature blackbody and a view to deep space. The on-board calibration is validated by in situ measurements of large water bodies. Periodic views of the moon have been used to diagnose and characterize stray light.

While the TIRS instrument has been stable to 0.2% per year and the noise is about a factor of four better than ETM+ based on on-board assessments, a stray light issue has affected the absolute calibration. In-situ validation revealed an average calibration error of 0.29 $\text{W/m}^2 \text{ sr } \mu\text{m}$ in Band 10 and 0.51 $\text{W/m}^2 \text{ sr } \mu\text{m}$ in Band 11. This calibration error varies with the temperature of the surroundings and has been demonstrated to be due to stray light far out-of-field. A bias correction was made in February 2014 to account for the average additional radiance reaching the focal plane and studies are on going to determine the best way to correct for the stray light.

1 INTRODUCTION

The Thermal Infrared Sensor (TIRS) continues the 30 year legacy of imaging in the long-wave infrared for the Landsat program. Landsat-8 is a departure from the previous Landsat instruments in a number of ways: 1) there are two instruments on-board, TIRS for the thermal measurements and the Operational Land Imager (OLI) for the reflective band measurements, 2) the instruments are both pushbroom designs meaning they have long linear arrays of detectors that push across the Earth to image rather than having a mirror sweep across the Earth with a limited number of detectors, 3) the images are acquired in 12-bit radiometric resolution. Though the instruments are different, Landsat-8 maintains the swath width, scene framing, radiometric and geometric accuracy and precision, and general spectral bandwidths of the prior Landsat missions.

This paper will cover the basic characteristics and early calibration results of TIRS. Where applicable, results will be compared to the previous instruments, Landsat-5 Thematic Mapper (TM) and Landsat-7 Enhanced Thematic Mapper+ (ETM+). More details about OLI can be found in Knight, 2014 and Markham, 2014.

2 THE TIRS INSTRUMENT

2.1 Instrument Design

The TIRS instrument is a four optical element refracting telescope with focal plane array consisting of three distinct sensor chip assemblies (SCAs). The Scene Select Mechanism (SSM), a flat folding mirror located in front of the telescope, allows the instrument view to switch between the nadir view port, the deep space port, and the on-board blackbody. The deep space and blackbody views are used for on-board calibration and characterization, typically twice an orbit. The spatial resolution of the TIRS is 100 m and it has a 185 km ground swath.

Unlike prior Landsat instruments, TIRS has two spectral bands. The two TIRS bands split the ETM+ bandpass roughly in half. Band 10 is 10.60-11.19 μm and Band 11 is 11.50-12.51 μm . Figure 1 shows the band-average relative spectral responses (RSRs) of the TIRS and ETM+ bands. The TIRS RSRs can be found at <http://landsat.gsfc.nasa.gov/?p=5698>.

The three SCAs are staggered on the focal plane, such that two SCAs are slightly forward-looking and one is slightly rearward looking. The chips are each 520x640 but the spectral filters only cover about 30 rows of the arrays per band and only two rows per

band are transmitted to the ground. In ground processing the majority of data are taken from one of the rows to form the final image product, though poorly performing detectors in the primary row are substituted with detectors from the second row. The SCAs overlap each other by about 28 detectors, which provides a narrow swath of ground that is imaged by two SCAs. This provides some measure of how well the SCAs can be normalized to each other.

More details on the TIRS instrument design can be found in Reuter, 2014.

2.2 On-Orbit Performance

There are many metrics that are used to quantify TIRS performance. Here, we will only focus on noise and stability, as they are essential to a functioning calibration process. Additional metrics can be found in Montanaro, 2014a.

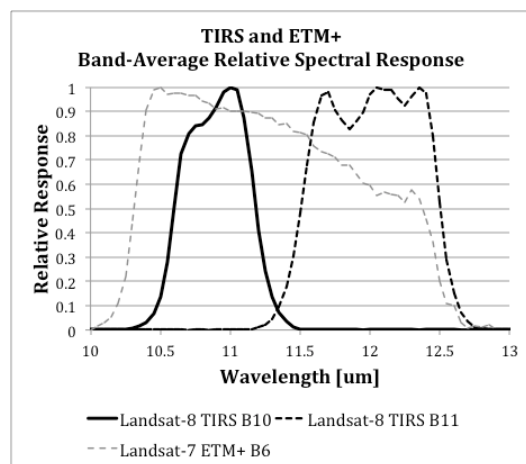


Figure 1. The relative spectral responses of the two Landsat-8 TIRS bands and the Landsat-7 ETM+ thermal band.

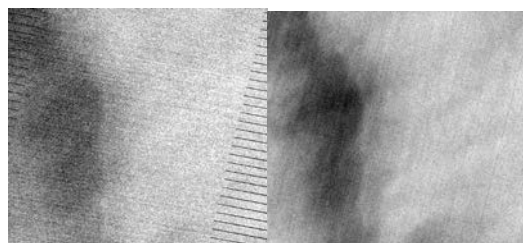


Figure 2. Landsat-7 ETM+ Band 6 (left) and Landsat-8 TIRS Band 10 (right) image subset of the same region of the Atlantic Ocean, acquired within 10 minutes of each other when the two satellites were in nearly the same orbit (March 2013). The noise is clearly visible in the ETM+ image while the TIRS image is much smoother (though per-detector striping is visible).

2.2.1 Noise

The noise in the TIRS instrument is at a level that is not readily visible in the imagery (Figure 2). There is no detectable coherent noise. The overall noise in TIRS is expressed as Noise Equivalent Delta Temperature (NEAT). TIRS acquires images of its blackbody at multiple temperatures at monthly intervals and thus an NEAT can be calculated at many temperature levels. At the standard performance level of 300 K, the NEAT is less than 0.06 K for every detector in both bands.

The Landsat-5 TM and Landsat-7 ETM+ NEAT were calculated based on the calibration shutter, which was ~280 K (Schott, 2012). Table 1 compares the NEAT at 280 K for the three instruments. The pushbroom design of the TIRS instrument allows for considerably longer dwell time such that the noise characteristics are about a factor of four better than the TMs.

Table 1. NEAT at 280 K for the Landsat thermal bands. The Landsat-7 NEAT is provided for the High gain setting. Landsat-5 NEAT is provided as a range due to the effect of the build up of ice on the Dewar window and its periodic removal.

Instrument	Band	Band-Average NEAT at 280 K [K]
Landsat-8 TIRS	10	0.05
Landsat-8 TIRS	11	0.06
Landsat-7 ETM+	6 (H)	0.21
Landsat-5 TM	6	0.17-0.30

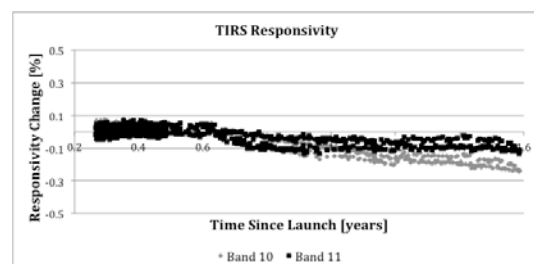


Figure 3. Responsivity of the TIRS bands as a function of change over time. This shows that the instrument is internally stable to better than 0.2% per year over the lifetime.

2.2.2 Stability

The stability of TIRS is monitored on many time-scales using the blackbody and deep space images. Here, we present the lifetime stability using a responsivity metric, g ,

$$g = (Q_{BB} - Q_0) / (L_{BB} - L_{space}) \quad (1)$$

Where: Q_{BB} is the bias-subtracted, linearized digital counts extracted from the blackbody image, Q_0 is the instrument offset which incorporates the instrument

and electronic biases, L_{BB} is the spectral radiance of the blackbody as converted from the monitor thermistor and L_{space} is the spectral radiance of deep space, assuming a 4 K background.

The band-average responsivity is calculated for all cases when the blackbody is set at 295 K. The responsivity has decreased by 0.2% per year in Band 10 and by 0.1% per year in Band 11 (Figure 3). This shows that the instrument is internally stable to better than 0.2% per year over the lifetime. This degradation is being tracked and can be accounted for in the calibration process when the change is determined to be significant.

3 VICARIOUS CALIBRATION

3.1 Methodology

The vicarious calibration of the TIRS bands is performed by two groups out of the NASA/Jet Propulsion Laboratory (JPL) and the Rochester Institute of Technology (RIT) on large water bodies in and around the continental United States. Water is a good thermal calibration target because it is homogeneous, spectrally uniform, and has a known and stable emissivity. Large water bodies, like large lakes and oceans, change temperature slowly, making the measurement less time sensitive, and the water is always mixing, so the skin temperature is generally close to the bulk (near-surface) temperature.

JPL operates four instrumented buoys on Lake Tahoe on the California/Nevada boarder and an instrumented permanent platform on the Salton Sea in southern California. RIT makes use of the NOAA buoy network; instrumented buoys are distributed around the coastal United States (Great Lakes, Atlantic Ocean, Pacific Ocean and Gulf of Mexico).

The teams use a combination of surface and subsurface measurements of the temperature and radiance to estimate surface-leaving radiance in the TIRS bands. They propagate the surface-leaving radiance to the spacecraft using MODTRAN, a radiance propagation tool, and an atmosphere derived from reanalysis data. This estimate of the top-of-atmosphere (TOA) radiance is compared to the radiance measured by TIRS (Hook, 2007 and Schott, 2012).

A robust calibration is built up over time, as the water bodies change temperature with location as well as throughout the seasons.

3.2 Results

The data were collected at every opportunity once TIRS was on orbit and by September 2013, just seven months after launch, it was clear that there was a calibration error in both bands. There did not appear to be an error in the gain of the instrument, but the

biases seemed to be off by a significant amount. The TIRS image radiances were hotter than the vicarious radiances, by $0.29 \text{ W/m}^2 \text{ sr } \mu\text{m}$ in Band 10 and $0.51 \text{ W/m}^2 \text{ sr } \mu\text{m}$ in Band 11, or about 2.1 K and 4.4 K at 300 K respectively.

New calibration coefficients were calculated and on Feb. 3, 2014, were implemented in the processing system at USGS. The existing data in the USGS archive was purged, so that all data available from USGS after Feb. 3, 2014 included the correction for the bias error (USGS, 2014).

The image data were reprocessed and the dataset continued to grow. After reanalysis, the reprocessed data have no statistically significant error (Figure 4, Table 2). However, the variability in the results was still larger than expected and desired.

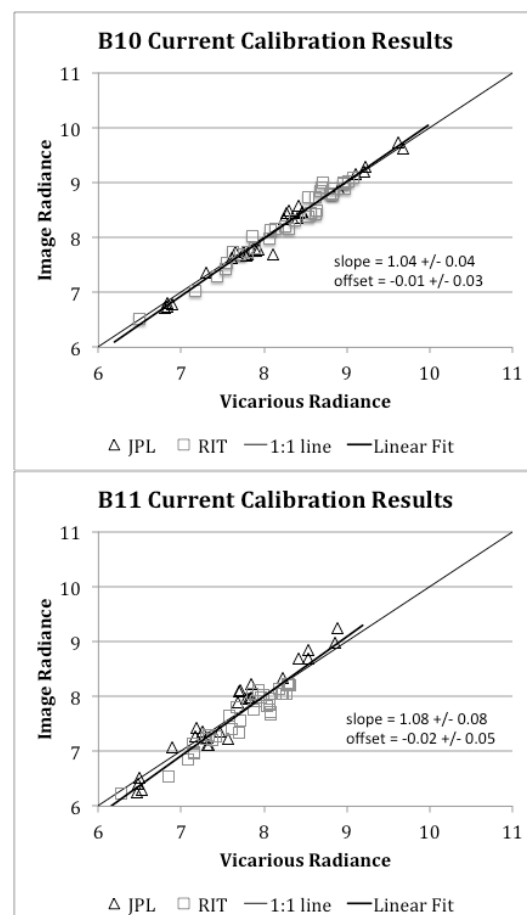


Figure 4. The current vicarious calibration results for TIRS Band 10 (top) and TIRS Band 11 (bottom). There is no statistically significant residual error in gain or offset in these data. Radiances are in units of $[\text{W/m}^2 \text{ sr } \mu\text{m}]$.

Figure 5 shows the calibration error plotted as a function of day of year. The seasonal trend apparent in these results could indicate a gain error, regardless of the statistics indicating that there was no significant error in slope. However, other evidence was building that there was stray light present in the images.

More details on the vicarious calibration results can be found in (Barsi, 2014).

4 STRAY LIGHT

While the vicarious calibration effort was ongoing, odd non-uniform structure was being seen in the image data. It did not appear consistently in images but when it was visible, it seemed to change within an image. This is not behaviour indicative of a stable instrument, but all the on-board evidence indicated the TIRS instrument was stable.

Figure 6 shows a TIRS Band 11 image of the Red Sea, stretched to illustrate the non-uniform behaviour. There are distinct edges, at the boundaries of the SCAs, and the contrast between the two edges is not constant as the spacecraft travels south.

This, along with the evidence of the seasonal trend in the JPL Band 11 data, is an indication of stray light getting in the TIRS telescope.

Table 2. Residual calibration error for the vicarious calibration data after the February 2014 reprocessing. The error calculation assumes that all the error is in the bias. The variability in the results is provided for all Landsat thermal bands for comparison. While there is no residual calibration error, the variability in the TIRS data is much larger than ETM+ and TM.

Instrument	Band	Calibration Error \pm 95% confidence interval [W/m ² sr μ m]	RMS Variability [K at 300K]
Landsat-8 TIRS	10	-0.01 \pm 0.03	0.87
Landsat-8 TIRS	11	-0.02 \pm 0.05	1.67
Landsat-7 ETM+	6		0.48
Landsat-5 TM	6		0.53

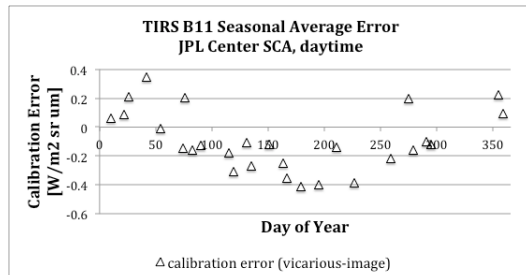


Figure 5. Seasonal trend in the JPL Band 11 vicarious calibration results.

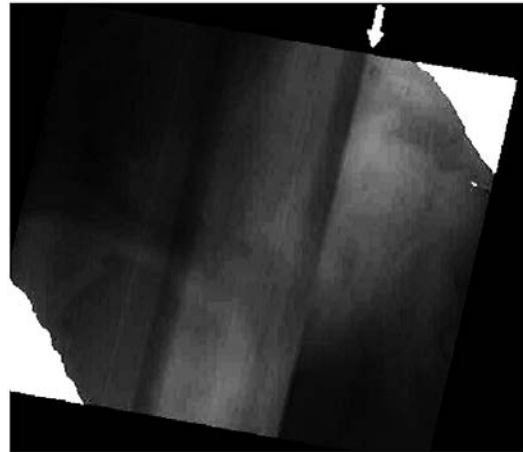


Figure 6. TIRS Band 11 image of the Red Sea, contrast stretched to make the non-uniformities visible. If the instrument were stable, the contrast between the SCA edges should not change as the spacecraft travelled south.

To detect stray light on-orbit, Landsat-8 performed a maneuver to image deep space while the moon was between $\pm 15^\circ$ outside of the field of view. The satellite slewed across space and images were acquired as the moon moved in and out of the field-of-view. The results showed that the focal plane would light up when the moon was in an arc about 15° off-axis. Several scans were made to build up a map of the out-of-field locations from where stray light would originate.

This effort produced a sparse map of the origin of the stray light. The data was provided to the optics group at NASA/GSFC to see if they could detect the origin of stray light in the telescope.

The optics group quickly determined that the reflection was coming off one of the rings that holds the third lens of the telescope in place. The reflection was not detected during pre-launch testing because of deficiencies in the test setup.

The optics model allowed for a full mapping of the locations of the source of the stray light for each detector on the focal plane. Figure 7 shows the locations in the out-of-field from where the stray light originates for two detectors, one in the center of the focal plane and the other on the edge of the focal plane. The stray light contribution is significantly different for the two detectors.

The per-detector optics model map can be used in an algorithm to correct for stray light. However, to correct for the out-of-field radiance, one needs to know the out-of-field radiance or be able to approximate it.

Several methods of stray light correction are being considered for implementation in the USGS processing system: (1) using coincident external data that have a wider field-of-view which would provide actual information about the out-of-field radiance; (2) using only the TIRS interval to approximate the out-of-field contributions; or (3) using historical or database data as a guide to what the out-of-field radiance might be. Each of the methods has advantages and disadvantages and will be thoroughly tested and validated before a correction will be implemented in the processing system.

More details about the stray light investigation are available in (Montanaro, 2014b).

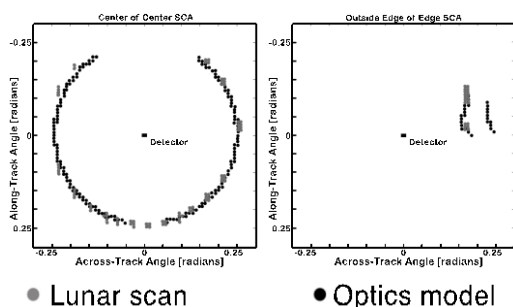


Figure 7. The map of the origin of the stray light for two detectors, one in the center of the focal plane (left), the other on the edge of the focal plane (right). The stray light is mapped from each detector's optical axis, not the optical axis of the center of the focal plane. The optics model filled in the relatively sparse map generated by the lunar scans.

5 SUMMARY AND RECOMMENDATIONS FOR USERS

TIRS is extremely stable radiometrically on orbit. The NEAT is about 0.05 K for all detectors and there is no discernable coherent noise. Long-term trending indicates that the responsivity may be decreasing, 0.2% per year in the worst case (Band 10) over the lifetime, though this degradation can be accounted for in the processing system when it is deemed to be significant.

The vicarious calibration effort determined there was a calibration error just seven months after launch. TIRS was estimating radiances that were too hot by 0.29 and 0.51 W/m² sr μm in Band 10 and 11 respectively. The error was corrected in the processing system on Feb. 3, 2014 though it was later determined that the bias error was due to stray light, not strictly a calibration error.

The stray light is adding a varying signal to the focal plane. Using lunar scans and the optics model,

maps of the out-of-field stray light contribution were made for every detector. Several stray light correction methods are being tested presently.

We believe that Band 10 is usable for most applications as its variability (0.87 K) is much lower than Band 11 (1.87 K). Users should avoid using Band 11 until a stray light correction can be implemented. Split-window atmospheric correction techniques should be avoided as they depend on a stable relationship between the two bands. The stray light has a much larger effect in Band 11 than Band 10, so the difference between the two bands will vary with the out-of-field radiance contribution.

If users are using Band 10 data and are acquiring data from the USGS, they should verify they are using data processed after Feb. 3, 2014 by checking the FILE_DATE field in the metadata file.

6 REFERENCES

- Barsi, J.A., Schott, J.R., Hook, S.J., Raqueno, N.G., Markham, B.L., 2014, TIRS Vicarious Radiometric Calibration. *Remote Sensing*, **6**, in press.
- Hook, S. J., Vaughan, R. G., Tonooka, H., Schladow, S. G., 2007, Absolute radiometric in-flight validation of mid infrared and thermal infrared data from ASTER and MODIS on the terra spacecraft using the Lake Tahoe, CA/NV, USA, automated validation site. *IEEE Transactions on Geoscience and Remote Sensing*, **45**(6), 1798–1807.
- Knight, E.J. and Kvaran, G., 2014, Landsat-8 Operational Land Imager Design, Characterization, and Performance. *Remote Sensing*, **6**(11), 10286–10305.
- Markham, B.L., Barsi, J.A., Kvaran, G., Ong, L., Kaita, E., Biggar, S., Czaplá-Myers, J., Mishra, N., Helder, D.L., 2014, Landsat-8 Operational Land Imager Radiometric Calibration and Stability. *Remote Sensing*, **6**, in press.
- Montanaro, M., Levy, R., Markham, B.L., 2014a, On-Orbit Radiometric Performance of the Landsat 8 Thermal Infrared Sensor. *Remote Sensing*, **6**, in press.
- Montanaro, M., Gerace, A., Lunsford, A., Reuter, D., 2014b, Stray Light Artifacts in Imagery from the Landsat 8 Thermal Infrared Sensor. *Remote Sensing*, **6**(11), 10435–10456; doi:10.3390/rs61110435.
- Reuter, D.C., Richardson, C., Pellerano, F., Irons, J.R., Allen, R., Anderson, M., Jhabvala, M., Lunsford, A., Montanaro, M., Smith, R., Tesfaye, Z., Thome, K., 2014, The Thermal Infrared Sensor (TIRS) on Landsat 8: Design Overview and Pre-Launch Characterization. *Remote Sensing*, **6**, in press.
- Schott, J.R., Hook, S.J., Barsi, J.A., Markham, B.L., Miller, J., Padula, F.P., Raqueno, N.G., 2012, Thermal infrared radiometric calibration of the entire Landsat 4, 5, and 7 archive (1982–2010). *Remote Sensing of Environment*, **122**, 41–49.
- USGS. January 29, 2014 notice. https://landsat.usgs.gov/calibration_notices.php. Accessed October 24, 2014.

Validation of an Experimental Cloud Infrastructure for Earth Observation Services

J. Becedas*, R. Pérez, G. González, F. Pedrera, C. González, M. J. Latorre
Elecnor Deimos

Francia 9, Pol. Industrial La Nava, 13500 Puertollano, Ciudad Real.

**Corresponding author e-mail: jonathan.becedas@elecnor-deimos.es*

ABSTRACT

Earth Observation (EO) accumulates spatial and temporal records of the world. It is applied in diverse sectors such as monitoring of the environment, natural disasters, emergencies and civil security among others. However, Earth Observation still presents critical challenges to cover the current demand of services that require the processing, storage and distribution of massive amounts of data. EO industries implement on-site conventional infrastructures with limited scalability and flexibility capabilities. In addition, the information provided by traditional EO systems is expensive because the technology used, such as optical satellites, is costly, and the infrastructure required to process and store the data has very high prices that have to be recovered.

In this work we made use of the Future Internet technologies to create a cloud-based system to process, store and distribute data acquired from Earth Observation satellites. We validated the system by implementing a virtual model of a constellation of 17 satellites and a network of 12 ground stations that imaged the surface of the Earth in a daily basis. Those images were processed and stored in cloud to provide advanced services through the Internet. We enhanced and exploited the current geospatial stack and infrastructures to provide demand-driven EO services. In order to test the cloud based system, a scenario emulating a realistic situation was used to offer the service: the earthquake that occurred in the Spanish city of Lorca in 2011.

Keywords: *Earth Observation, Remote Sensing, Distributed Systems, Cloud Computing, Future Internet.*

1 INTRODUCTION

The Earth Observation space market segment was mainly focused in space developments and military programmes; however during the last years this trend has changed. In the year 2000, \$200 million were reached in commercial data sales. Ten years later, at the end of 2009, the sales reached \$1.1 billion, and the forecast for 2019 is of \$4 billion (Keith, 2011), (Euroconsult, 2010). Regarding the Earth Observation satellites market, almost a double number of satellites are planned to be launched in the second decade of this century compared to the first (353 versus 149) (Euroconsult, 2014). Growth is experimented at each level of the value chain: manufacturing, launch, data and services; Earth Observation becoming a field of new business opportunities and work.

The enhancement of in orbit Earth Observation satellites recording images of the world's surface increases the amount of generated data to be managed by existing infrastructures. The process of recording data from Earth observations from an increasing number of satellites generates massive amounts of

spatiotemporal geospatial information that has to be intensively processed. This is a major challenge (Yang, et al., 2011) and a complex problem because the data recorded increases over time.

On-site traditional infrastructures or data centres are not designed to manage variable and increasing amounts of Earth Observation data, because they were sized to operate a defined number of satellites. They are then really limited in flexibility and scalability. Two main drawbacks are extracted: i) traditional infrastructures are not flexible to operate an increasing number of satellites and ii) they have the risk of over/under sizing the infrastructure to offer services to highly variable demands such as crisis management, natural disasters monitoring and civil security among others (Deren, 2007). The services requested by these users have to be more flexible with instantaneous and easy web access.

In this work we make use of Future Internet technologies provided by the Fed4FIRE infrastructure to experiment a cloud-based system capable of covering the demand of highly variable Earth Observation services through the GEO-Cloud

experiment (Becedas, 2014). The system is constituted of i) a Space System Simulator implemented in Virtual Wall (Kavoussanakis, et al., 2013) reproducing the behaviour of a constellation of 17 satellites and 12 ground stations and generating the images that are ingested in the cloud, and ii) a data centre implemented in the BonFIRE multi-cloud system (Kavoussanakis, et al., 2013), which ingests, processes, archives, catalogues and on demand distribute the images to the end users (Pérez, et al., 2014).

The system was tested in a realistic scenario of natural disaster monitoring and management; specifically, the Lorca's Earthquake in Spain, which occurred in 2011. The constellation of satellites captured images of the region of Murcia for their processing and distribution through a web service. The whole process was carried out automatically.

The main results of the system performing under the conditions of the previous scenario are here analysed. They include the processing times of the processors, time from acquisition to delivery to the end user, real-time scalability of the cloud system and the availability of the delivery layer among others.

The paper is structured into five sections: Section 2 describes the scenario in which the system is tested; Section 3 is devoted to explain the architecture of the system; Section 4 shows the main results of the experiment, Section 5 summarizes the main conclusions of the work.

2 SCENARIO DESCRIPTION

In May 11th of 2011, an earthquake took place in Lorca, in the Region of Murcia (Spain) at 18:47 local time. It had a moderate magnitude 5.1 in moment magnitude scale (M) and was preceded by a 4.5M foreshock at 17:05 local time. The seismic affected to other Spanish regions: Almería, Albacete, Granada, Jaén, Málaga, Alicante, Ciudad Real and Madrid.

In this type of natural disasters, emergency units and humanitarian organizations demand accurate imagery of the affected area after the disaster occurred. They are used to do a preliminary damage assessment and have situational awareness to identify possible focus areas in which victims can be concentrated, and to analyse accesses and evacuation routes.

The hypothesis is the following: after the earthquake occurred there was a demand to record the region of Murcia in Spain. The area to record was 11311 km².

The first satellite that passed over the area of interest was the GEO-Cloud_011. The characteristics of the satellite are the following: resolution 6.7 m, swath 160 km, 5 bands (4 Multispectral [RGB and NIR] and 1 Panchromatic). Due to the wide swath of the satellite, the area of interest was acquired in a single pass of the satellite. Because the satellite was inside the visibility area of Puertollano ground station (GS_Puertollano), the GEO-Cloud_011 downloaded the recorded data there at a transfer rate of 160 Mbps. Figure 1 shows an image of the scenario. Notice that at the same time, the rest of satellites were working in parallel acquiring images of other areas and downloading them in other ground stations of the network.

3 SYSTEM ARCHITECTURE

The entire system was composed by the following parts: i) The Space System Simulator, which reproduced a constellation of 17 satellites imaging the Earth's surface and a network of 12 ground stations in which the satellites downloaded the acquisitions; ii) The Geo-images Management System on cloud which was also divided into two layers: a) Layer 1 ingested, processed and catalogued the acquired images from satellites and b) Layer 2 which used the catalogued images to provide a web service to distribute and visualize the images (see Figure 2). The instance types used in BonFIRE to carry out the experiment are described in Table 1.

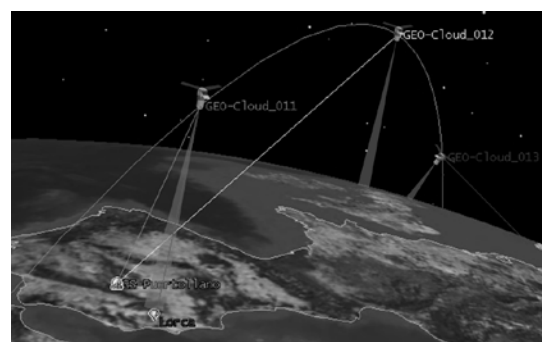


Figure 1 Image of the Lorca's earthquake scenario.

Table 1 Instances used in BonFIRE

Instance Type	Virtual CPU	RAM
xlarge	4	8 GB
Medium	2	2 GB

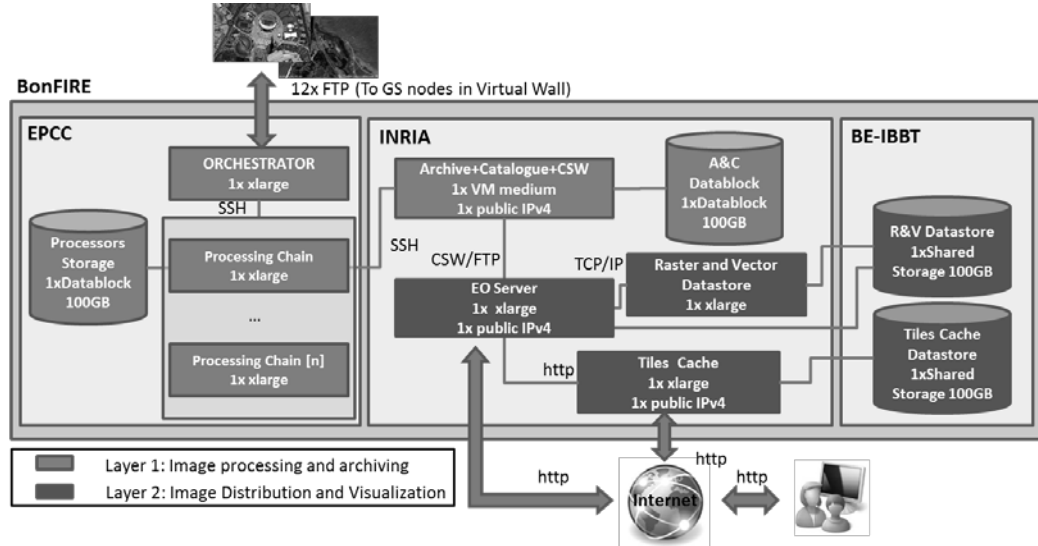


Figure 2 GEO-images Management Architecture

3.1. Space System Simulator

The Space System Simulator was implemented in Virtual Wall. This system simulated a constellation of 17 satellites acquiring images of the Earth's surface which were downloaded to a network of 12 ground stations. The Satellite System Simulator executed 17 Satellite Simulators, each one reproducing the individual behaviour of a specific satellite. The Ground Station System Simulator aggregated 12 Ground Station Simulators, each one reproducing the individual behaviour of a ground station (for more information on the Space System Simulator see (Pérez, et al., 2014)). The network links between each ground station implemented in Virtual Wall and BonFIRE were customized by manually configuring the bandwidth, loss-rate and delay impairments of the network. They were previously measured in an emulated network implemented in PlanetLab (see (González, et al., 2014) for more information). These values are summarized in Table 2.

3.2. Cloud: Layer 1 – Image processing and archiving

The architecture of this layer was constituted of the Orchestrator, the Processing chains and the Archive and Catalogue.

The Orchestrator performed over BonFIRE and controlled all the interactions between all the components implemented there (see Figure 3). It had the following functions: i) To identify the outputs to be generated by the processors.

Table 2 Table of network impairments

Ground Station	Average Bandwidth (Mbps)	Average Latency (ms)	Loss-rate (%)
GS_Irkutsk	2.21	242.29	0.024
GS_Puertollano	15.59	27.19	0.005
GS_Svalbard	7.32	59.23	0.006
GS_Troll	1.42	340.9	0.204
GS_Chetumal	3.36	154.20	0.010
GS_Córdoba	0.20	302.68	0.240
GS_Dubai	2.29	70.08	0.001
GS_Kourou	1.56	317.20	0.076
GS_Krugerdsorp	2.29	207.36	0.010
GS_Malaysia	2.23	201.51	0.063
GS_Prince_Albert	3.39	166.63	0.008
GS_Sidney	1.33	375.31	0.004

ii) To generate the Job Orders, which contained all the information needed to make the product processors perform correctly. iii) To manage the ingestion of raw data from the satellite constellation. When a ground station simulator created a new raw data file, the Orchestrator downloaded it through an FTP connection. If there were several raw data pending of download, a thread for downloading the data was created. iv) To control the Processing chains by managing the product processors. v) To manage the Archive and Catalogue.

The Orchestrator was implemented in an xlarge instance in BonFIRE. It had FTP interfaces with the ground stations and SSH interfaces with the Processing Chains and with the Archive and Catalogue.

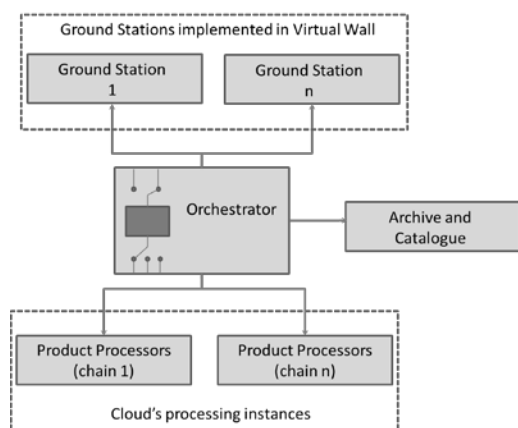


Figure 3 Orchestrator interactions

Each Processing chain was in charge of processing the raw data from the satellites to provide image products. The most important operations that they performed were the following: i) decoding of the data and packaging into square scenes (L0 and L0R); ii) a calibration, to convert the pixel elements from instrument digital count into radiance units (L1A); iii) geometric corrections, to eliminate distortions due to misalignments of the sensors in the focal plane geometry and a geolocation, to compute the geodetic coordinates of the input pixels (L1B); and iv) an ortho-rectification, to produce ortho-photos with vertical projection, free of distortions (L1C).

For this first implementation, seven Processing chains were requested and instantiated. When there was new incoming raw data, the Orchestrator selected one of the Processing chains by using a simple load balancing algorithm which started processing the data. Thus, the processing was dynamically done and queues were avoided.

In the Archive and Catalogue the processed images were stored and catalogued with the following features: i) the Catalogue stored an inventory database with the metadata of archive files; and ii) provided a CSW standard interface to provide web service.

Regarding the storage, two implementations were done. First by using datablocks (the local storage of the Processing Chain instances), as shown in Figure 2. Second by using a shared storage provided by the BE-IBBT testbed in BonFIRE (see Figure 4). This storage was implemented by using a Network File System (NFS) protocol.

3.3. Cloud: Layer 2 – Image Distribution and Visualization

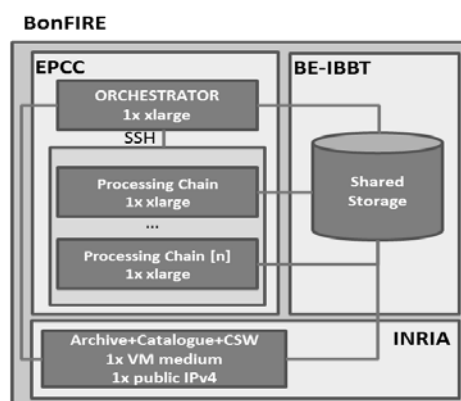


Figure 4 Architecture of Layer 1 with NFS

To distribute the images to the end users, a scalable Image Distribution and Visualization infrastructure (IDV) was designed and implemented. It offered direct access and visualization of the satellite imagery and high added value services mainly through standard (OGC) web services. It was connected to Layer 1 through the CSW interface provided by the Archive and Catalogue (see Figure 2).

The logical components of the IDV were the following: i) A Datastore module whose function was to store processed and optimize images taken from the Layer 1. It managed both raster in a shared file system and vector data in a PostGIS database (metadata, value added products). ii) An EO server implemented with GeoServer, which implemented OGC web services (WMS, WFS, WCS, etc.), and designed to horizontally scale and optimize EO images delivery. iii) A Tiles cache implemented with GeoWebCache stack, which cached map tiles coming from the EO server to optimize the visualization of the products. It was designed to horizontally scale in the Cloud infrastructure when needed.

4 RESULTS

The results obtained in the experimentation are separately presented for each of the two layers to facilitate understanding.

4.1. Layer 1 results

The experiment started with a petition of recording one image of the city of Lorca. The first satellite passing over the city was the GEO-Cloud_011. It entered into the area of interest and started the image

recording and the simultaneous download into the GS_Puertollano ground station. 23.4 s later, the GEO-Cloud_011 finished downloading the image into the ground station. During that time the satellites GEO-Cloud_005, GEO-Cloud_006, GEO-Cloud_008, GEO-Cloud_013 downloaded 4 images recorded out of the area of interest, GEO-Cloud_005 and GEO-Cloud_006 in the simulated GS_Troll ground station, GEO-Cloud_8 in GS_Krugersdorp and GEO-Cloud_013 in GS_Svalbard.

In the very instant a ground station had new available data; the Orchestrator ingested it into the BonFIRE cloud. In this scenario, at time 23.4 s from the start of the acquisition, the 302 MB of raw data was ingested from the GS_Puertollano ground station at a transfer rate of 15.59 Mbps (see Table 2). 25 s later, the image was in the cloud and the Orchestrator launched a new processing chain to process the raw data. The raw data was transferred to the processing chain. Once the Processing chain was activated, it processed the raw data to produce L0, L0R, L1A, L1B, L1BR and L1C products. After processing, the resultant image was archived and catalogued. The time for archiving was 36 s since the image was sent from the Processing chain to the Archive and Catalogue module. Cataloguing was instantaneously done without delay.

The scenario was tested in the architecture with local storage (datablocks), shown in Figure 2, and in the architecture with shared storage, shown in Figure 4.

The results of the Processing chain working in the two architectures are shown in Figure 5. There was a high difference in the processing time when using the architecture with datablocks and with shared storage. This can be noticed in the accumulated diagram. The processing time of the whole chain when using shared storage was almost 16.93 hours (16 hours, 55 minutes), while with datablocks was 2.35 hours (2 hours, 21 minutes). That difference was produced because the processing chain was continuously consulting the stored images to compare pixels and metadata. Since the shared storage, implemented in an NFS, was located in the BE-IBBT testbed (Ghent, Belgium), and the processing chain in the EPCC testbed (Edinburgh, UK), the processing time incremented. Note that all the I/O operations such as reads and writes were performed by using the Internet network. The delays on the communications, the congestion of the network and the packets distribution algorithms of the network provoked more delays than when using datablocks located in the EPCC nodes, where the transfer time between the memory and the processors was highly reduced.

To corroborate that hypothesis, performance tests were done in the shared and in the datablocks local storages. These tests consisted of executing the *dd* software copying information in both storage configurations. With the shared storage 2.7 GB of information were copied in 1174.6 s (at 2.3 MB/s) and in the local storage (datablock) 2.7 GB were copied in 50.97 s (52.7 MB/s). Thus it can be concluded that the implementation of the architecture with shared storage produced a bottleneck in the system performance.

Regarding the time from the acquisition until the products were available in the catalogue, it depended on the product. The L1A, which was a georeferenced image with radiometric correction, was available 5 minutes and 10 seconds from acquisition. While a radiometric corrected, georeferenced and orthorectified image (L1C) was available at time 2 hours and 25 minutes from acquisition.

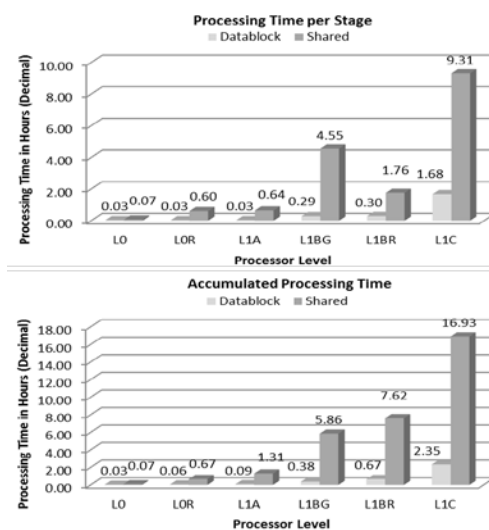


Figure 5 Products processing time. Top: per stage. Bottom: accumulated.

4.2. Layer 2 results

The Layer 2 was integrated with Layer 1 by using the CSW interface. The scenario was then executed. Because the requirements of this scenario for Layer 2 are not highly demanding, load tests were carried out to measure the availability of the offered WMS service. WMS requests were simulated for selected locations (BBOX) and a fixed resolution (WIDTH and HEIGHT) of 950×1000 pixels in its original reference system (SRS) EPSG:23030.

A static configuration was used at this stage to test the capabilities of the IDV to deliver imagery to the end

users for this scenario in the simplest configuration without auto-scaling. The load testing was implemented using an Open Source Framework named Locust, which enabled load testing requests from distributed nodes in a virtual network. Sampling was done by using a variable number of users requesting images from 1 master and 3 slave nodes. The following metrics were measured for each node: number of requests, number of fails, median response time, average response time, minimum and maximum request time, content size and requests per second.

Additionally, the load testing managed the HTTP response codes to measure successful average response times that provided the main metric for the performance of the IDV. In Table 3 this metric is shown with the average successful response times for the 4 nodes. The system has a stable performance up to 80 concurrent users, with response times below 1 s for up to 30 concurrent users. From 80 concurrent users, the system degrades mainly due to CPU overload. As a result, if more than 80 users access the web service autoscaling would be required.

Table 3 Successful WMS requests response time

Users	1	10	30	60	80	100
Average Response Time (ms)	694	762	796	1035	1481	53307

5 CONCLUSIONS

The architecture implemented in the BonFIRE multi-cloud system, and described in this paper is able of on demand processing and distributing satellite imagery. It was demonstrated that using local storage for image processing was faster than using the NFS shared storage and that the architecture proposed is capable of covering the demand of simultaneous users, being the autoscaling feature of cloud computing a feasible solution when the number of simultaneous users is higher than 80 when using xlarge type instances.

It worths to mention that the automation of the whole process from acquisition until having the images in the catalogue highly reduces the delivery times: L1A products are available after 5 minutes from acquisition, and L1C after 2 hours and 25 minutes, in the scenario studied with the hypothesis considered.

6. ACKNOWLEDGMENT

This work was carried out with the support of the FP7 Fed4FIRE-project ("Federation for FIRE"), an Integrated project funded by the European Union's Seventh Programme for research, technological development and demonstration under grant

agreement No [318389]. It does not necessarily reflect the views of the European Commission. The European Commission is not liable for any use that may be made of the information contained herein.

7 REFERENCES

- Ambrust, M., 2010. A view of cloud computing. *Communications of the ACM*, 53(4), pp. 50-58.
- Becedas, J., 2014. The GEO-Cloud Experiment: Global Earth Observation System Computed in Cloud. *The 8th Int. Conference on Innovative Mobile and Internet Services in Ubiquitous Computing*, July 2-4, Birmingham, UK.
- Deren, L., 2007. Remote Sensing Can Help Monitoring and Predication Natural Disasters. *Science & Technology Review*, 25(6), p. 3.
- Euroconsult, 2010. Satellite-based Earth Observation: Market Prospects to 2019, Euroconsult.
- Euroconsult, 2014. Satellite-Based Earth Observation: Market Prospects to 2023, Euroconsult.
- Farres, J., 2012. Cloud computing and content delivery network use within Earth Observation Ground Segments: experiences and lessons learnt. *ESA*.
- Ge, X. and Wang, H., 2009. Cloud-Based Service for Big Spatial Data Technology in Emergency Management, *Proceedings of the ISPRS 2009*, pp. 126-129.
- González, G. et al., 2014. Measurement and modelling of PlanetLab network impairments for Fed4FIRE's geo-cloud experiment. *26th IEEE International Teletraffic Congress*, pp. 1-4.
- Hume, A.C. et al., 2012. BonFIRE: A Multi-cloud Test Facility for Internet of Services Experimentation in Testbeds and Research Infrastructure. *Development of Networks and Communities, Springer Berlin Heidelberg*, pp. 81-96.
- Instituto Geográfico Nacional et al., 2011. Informe del seismo de Lorca del 11 de mayo de 2011.
- Kavoussanakis, K. et al., 2013. BonFIRE: the Clouds and Services Testbed. *5th IEEE Int. Conference on Cloud Computing Technology and Science*.
- Keith, A., 2011. Emerging markets, partnerships set to fuel global growth. *Earthwide Communications LLC*, pp. 1-3.
- Pérez, R. et al., 2014. Test Cloud Computing for Massive Space Data Processing, Storage and Distribution with Open-Source Geo-Software. *FOSS4G-E2014, OSGeo's European Conference on Free and Open Source Software for Geospatial Bremen, Germany*.
- Yang, C. et al., 2011. Spatial cloud computing: how can the geospatial sciences use and help shape cloud computing?. *International Journal of Digital Earth*, 4(7), pp. 305-329.

Continuous validation and algorithm improvement in LSA SAF FVC and LAI operational products over Africa

F.J. García-Haro¹, F. Camacho², B. Martínez¹, M. Campos-Taberner¹, J. Meliá¹

¹Facultat de Física, Universitat de València, Dr. Moliner, 50. 46100-Burjassot, Spain.

²EOLAB, Parc Científic Universitat de València. Catedrático José Beltrán, 2. 46980 Paterna, Spain.
j.garcia.haro@uv.es

ABSTRACT -

The EUMETSAT Satellite Application Facility on Land Surface Analysis (LSA SAF) generates, on an operational basis, daily and 10-day vegetation parameters from the SEVIRI/MSG satellites. They include the Fractional Vegetation Cover (FVC) and Leaf Area Index (LAI), which are important structural properties of land surface areas occupied by plant canopies.

This study presents updated validation results, which are mandatory to ensure the quality of the products. Despite the overall consistency with Copernicus Global Land and MODIS products, a positive bias of MSG FVC and LAI is observed in the southern Africa region, particularly over savannas and sparsely vegetated areas. A modified version of the algorithm is also proposed to minimize this possible bias by improving the characterization of different soil types in the Bayesian model.

1 INTRODUCTION

The main purpose of the LSA SAF is to take full advantage of remotely sensed data, particularly those available from EUMETSAT sensors, to generate, on an operational basis, land surface variables. The LSA SAF system is fully centralized at Portuguese Institute for the Ocean and Atmosphere (IPMA), which generates and disseminates the operational products by EUMTETCast and off-line from LSA SAF website (<http://landsaf.ipma.pt>) that contains products as well as updated information.

Current LSA SAF vegetation products are the Fractional Vegetation Cover (FVC), the Leaf Area Index (LAI) and the Fraction of Absorbed Photosynthetically Active Radiation (FAPAR). These products are produced in near real time from the MSG/SEVIRI observations at a spatial resolution of 3 km at equator (~5 km over central Europe) on a daily and 10-day basis, in the geostationary grid. The high rate of acquisition provided by the SEVIRI instrument guarantees the availability of spatially consistent cloud-free data for adequately monitoring both the seasonality of vegetation and the long-term trends in the state of vegetation.

The coverage of the products is the MSG disk. The technical properties of final products of FVC, LAI and FAPAR (spatial and temporal resolution, thematic

accuracy, etc.) depend on the input data, and the retrieval algorithms. According to LSA SAF requirements (Trigo et al., 2011) target accuracy should be better than 15% for FVC and FAPAR (i.e. about 0.08 in absolute terms for a FVC/FAPAR value of 0.5), and better than 1 in absolute terms for LAI. The characteristics of SEVIRI based VEGA products provided by the LSA SAF are summarized in Table 1 (for a detailed description we refer to García-Haro et al., 2014a).

Table 1. Product Requirements for MSG vegetation products, in terms of temporal resolution and accuracy. MD stands for MSG Daily, and MT for MSG Ten-days.

Product	Identifier	Temporal resolution	Target accuracy
MDFVC	LSA-401	1-day	15%
MTFVC	LSA-402	10-days	15%
MDLAI	LSA-404	1-day	1
MTLAI	LSA-405	10-days	1
MDFAPAR	LSA-407	1-day	15%
MTFAPAR	LSA-408	10-days	15%

The aim of this work is two-fold. Firstly, it presents updated validation results as well as evaluation of their temporal and spatial consistency. It includes inter-

comparison with equivalent satellite products, in particular, SPOT/VGT Global Land Copernicus products and MODIS/TERRA. Secondly, the bias has been minimized by improving the characterization of different soil types in the Bayesian model and the use of temporal information.

2 METHODOLOGY AND RESULTS

2.1 FVC and LAI algorithms

The algorithms of the SEVIRI/MSG vegetation products use as input BRDF parameters (Roujean and Lacaze, 2002). This minimizes surface anisotropy effects, which constitute one of the main drawbacks of using geostationary satellites for vegetation monitoring. The characteristics of SEVIRI based VEGA products provided by the LSA SAF are summarized in Table 1. A detailed description is provided in García-Haro et al. (2014a).

The algorithm for retrieving FVC and LAI from SEVIRI/MSG in LSA SAF relies on optimised Spectral Mixture Analysis (SMA) methods in which endmember signatures are no longer treated as constants, but they are represented by multi-modal probability density functions (García-Haro et al., 2005). The use of standardized SMA improves understanding of the impact of endmember variability on the derivation of subpixel vegetation fractions at a global scale. The LAI is estimated from a FVC following the methodology developed by Roujean and Lacaze (2002), which proved to be more effective than traditional techniques based on spectral vegetation indices. This method relies on a tractable physical model for interception of solar irradiance by vegetative canopies.

The LSA SAF methodology (see figure 1) has been applied to different remotely sensed data, including SPOT/VEGETATION, MODIS and Sentinel-2 like data, showing good performances (García-Haro et al. 2005b, Verger et al. 2009a, b, Camacho et al. 2013).

2.2 Validation of the LSA SAF products

The SEVIRI/MSG products are continuously validated using a limited number of ground measurements available from international initiatives such as VALERI, BigFoot, NASA SAFARI-2000, CEOS/OLIVE, IMAGINES FP7 and ESA validation campaigns. Indirect validation includes inter-comparison with equivalent satellite products from different sensors (MERIS, VGT, MODIS), as well as evaluation of their temporal and spatial consistency. The fraction of valid pixels (i.e. processed with reliability) for LSA SAF FVC and LAI products over

Africa zones is nearly 100% through the whole year which is clearly one of the main advantages of using MSG data, instead of polar-orbiting satellite products thanks to the high-frequency of observations that allows getting a much higher number of cloud-free observations.

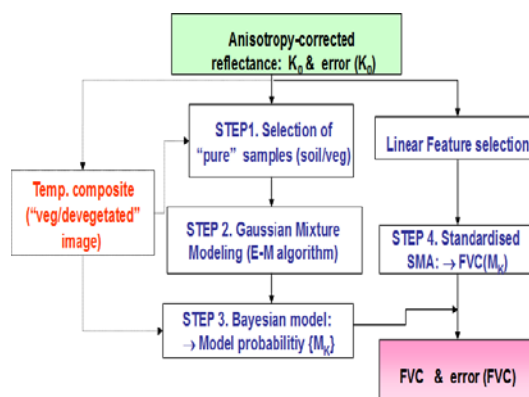


Figure 1. Flow chart of the algorithm for FVC determination

The above exercises have shown the consistency of spatial and temporal FVC, LAI and FAPAR distributions per main biomes, with values within the baseline of equivalent reference products. The validation results are highly significant and allow concluding that SEVIRI/MSG vegetation products have reached a validation stage level 2 according to CEOS LPV criteria (e.g., Camacho et al., 2010; Martínez et al., 2013; García-Haro et al., 2014b).

In the present study, the SEVIRI/MSG products are further evaluated against two prominent satellite products:

- (i) The first version of global biophysical products (i.e., LAI and FCOVER), namely GEOV1, developed in the framework of Copernicus Global Land Service from SPOT/VGT data at 1 km spatial resolution and 10-days temporal frequency (using a temporal window of 30 days). GEOV1 products have reached a validation stage level of 2 according to CEOS LPV criteria. Full validation results can be found in Camacho et al. (2013, 2014).
- (ii) Terra MODIS LAI/FAPAR (MOD15A2) is produced at 1 km spatial resolution and 8 days step over a sinusoidal grid. The MODIS LAI products have been extensively validated (Yang et al., 2006; Garrigues et al., 2008). The main drawbacks of MODIS LAI/FAPAR c5 products are its unrealistically strong temporal variability (Kobayashi et al., 2010).

The intercomparison with Global Land Copernicus (FVC, LAI, FAPAR) & MODIS (LAI, FAPAR) products reveals a high consistency between products. Results confirm that the LSA SAF vegetation products have a good quality: a spatial distribution realistic over the SEVIRI disk, temporal profiles shows realistic variations, smoothness and consistency from year to year (see further details in Camacho and Sánchez (2014)). However, a systematic overestimation of SEVIRI/MSG FVC and LAI regarding equivalent products is observed for low values in the southern Africa region (open savannas, sparsely vegetated and semidesertic areas), as illustrated in Figure 2.

The evaluation of the actual differences among product is inconclusive since there is a very reduced number of sites and periods in which ground data is available in South Africa region, and available data correspond to the 2000-2003 period. The spatial and temporal variation of the LSA SAF LAI and FVC vegetation products in southern Africa was validated using data collected by Privette et al. (2002) and Huemmrich et al. (2005) along the International Geosphere Biosphere Programme (IGBP) Kalahari Transect. Both FVC and LAI MSG products showed a good correspondence with ground estimates from Kalahari transect SAFARI 2000 initiative (Trigo et al., 2011, García-Haro et al., 2014b).

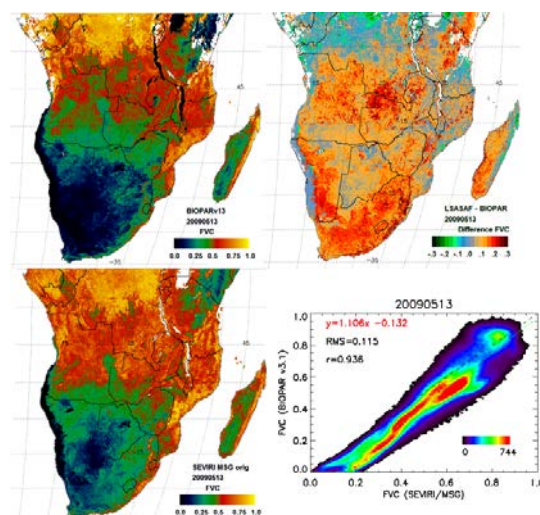


Figure 2. Comparison (image maps, difference and scatterplot) between SEVIRI FVC (currently available in LSA SAF) and Copernicus Global Land (VGT, GEOV1), products on mid May, 2013.

2.3 Algorithm improvement

In order to reduce possible biases in sparsely vegetated areas, a refinement of the current algorithm is proposed here, by taking into account three main features:

- (i) A more detailed characterization of different soil types using finer resolution data such as Google Earth and ancillary information.
- (ii) Use of temporal information to improve the purity of the training database, by generating a composited reflectance corresponding to the period which presents the maximum (or minimum) amount of vegetation.
- (iii) Improve the identification of the vegetation/soil components on a per pixel basis using multiple reflectance observations over a seasonal period (temporal trajectory).

2.4 Results of the new algorithm

To evaluate the performance of the new version of the algorithm, FVC and LAI were retrieved from SEVIRI/MSG over South Africa region during the 2006-2014 period. MSG maps were compared with very limited ground truth available and with equivalent satellite products from Copernicus Global Land (VGT, GEOV1) and MODIS c5. For this reason, all validation datasets were geo-located to a standard SEVIRI grid. The reprojection step was calculated by averaging all pixel values of the reference product that overlap with a given SEVIRI pixel. Those pixels identified as water, snow or unreliably calculated, were excluded. This intercomparison is thus limited by geolocation uncertainties, the sensor point spread functions (PSF) and differences in temporal compositing, which differs from one product to another.

The FVC and LAI values derived from the new algorithm clearly increase the consistency with Copernicus Global Land and MODIS products (see examples in Figures 3 and 4). This improved consistency could be regarded as an improvement to be incorporated in the future LSA SAF processing chain for the reprocessing of SEVIRI FVC and LAI products.

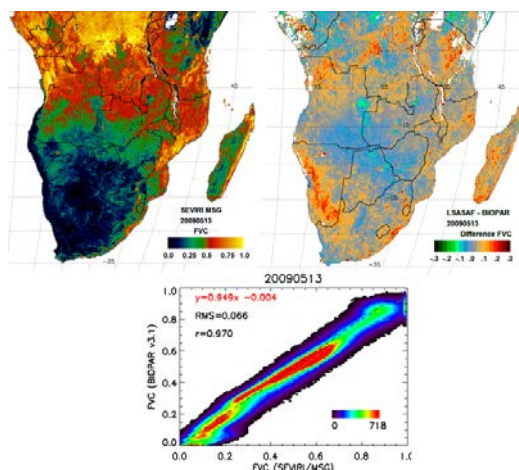


Figure 3. Comparison (image maps, difference and scatterplot) between SEVIRI F FVC (resulted from the new LSA SAF algorithm) and Copernicus Global Land (VGT, GEOV1), products on mid May, 2013.

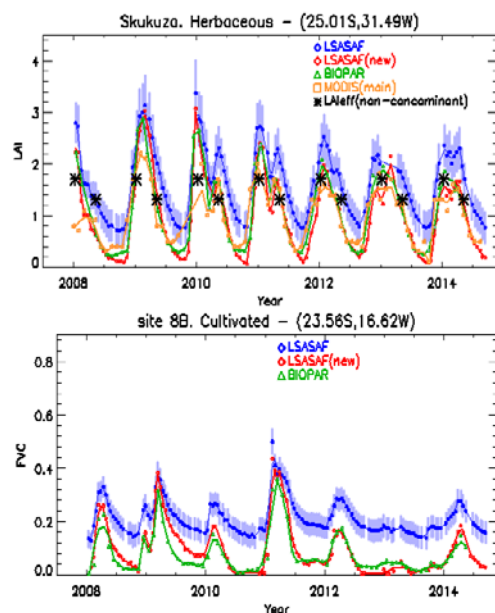


Figure 4. Temporal profiles of LSA SAF (current and new), Copernicus GEOV1 and NASA MODISC5 LAI (top) and FVC (bottom) products over two sites in Southern Africa. Black symbols refer to (non concomitant) in situ measurements acquired in the SAFARI 2000 initiative (2000-2003).

3 CONCLUSIONS

The LSA SAF vegetation products offer important improvements on the spatial coverage and temporal continuity. The products are spatially and temporally consistent with equivalent satellite products. However, the intercomparison with Copernicus Global Land and

MODIS products reveals a possible positive bias of FVC and LAI in the southern Africa region (particularly over savannas and sparsely vegetated areas). This evaluation is inconclusive and further validation activities are required to collect ground truth over sparse vegetation areas in Southern Africa.

In order to reduce this possible bias, a new version of the LSA SAF algorithm is here developed, which improves the characterization of different soil types in the Bayesian model. The training process makes use of the very detailed information coming from land cover classifications, finer resolution data such as Google Earth and ancillary information. This new version of the algorithms may enhance the quality of the current LSA SAF products. This improvement, along with changes made to algorithm inputs and version, justifies the reprocessing of SEVIRI-based vegetation products, now foreseen for the current LSA SAF CDOP-2 phase.

4 ACKNOWLEDGMENTS

Funding support of LSA SAF (EUMETSAT), ERMES (EU FP7-Space-2013, Contract 606983), RESET CLIMATE (CGL2012-35831) projects is acknowledged.

5 REFERENCES

- Camacho, F., Cernicharo, J., García Haro, F.J., Verger, A., Meliá, J., 2010, Consistency assessment of FVC and LAI operational products over Africa. Proceedings of the RAQRS'III 3rd International Symposium on Recent Advances in Remote Sensing, 27 September-1 October 2010 (Publ. Univ. Valencia: Valencia), Ed. J. Sobrino, ISBN: 978-84-370-7952-3 pp: 694-699.
- Camacho, F., Cernicharo, J., Lacaze, R., Baret, F., Weiss, M., 2013, GEOV1: LAI, FAPAR essential climate variables and FCOVER global time series capitalizing over existing products. Part 2: Validation and intercomparison with reference products. *Remote Sensing of Environment*, **137**, 310-329.
- Camacho, F., Lacaze, R., Baret, F., Latorre, C., De la Cruz, F., Demarez, V., Di Bella, C., Fang, H., García-Haro, J., Pat Gonzalez, M., Kussul, N., López-Baeza, E., Mattar, C., Nestola, E., Pattey, E., Piccard, I., Rudiger, C., Savin, I., Sanchez-Azofeifa, A., Zribi, M., 2014, A Network of Sites for Ground Biophysical Measurements in support of Copernicus Global Land Product Validation, this issue.

- Camacho, F., Baret, F., Weiss, M., Fernandes, R., Berthelot, B., Sánchez, J., Latorre, C., García-Haro, J., Duca, R., 2013, Validación de algoritmos para la obtención de variables biofísicas con datos Sentinel2 en la ESA: proyecto VALSE-2, XV Congreso de la Asociación Española de Teledetección (AET), Teledetección. Sistemas Operacionales de Observación de la Tierra. (Eds. A. Fernández-Renau González-Anleo & E. de Miguel Llanes), INTA, Torrejón de Ardoz (Madrid), 22-24 de Octubre 2013 pp. 144-147.
- Camacho, F., Sánchez, J., 2014, GIOGL1 Quality Monitoring Report January – June 2014. LAI-FAPAR-FCOVER GEOV1, GEOV0. GIO-GL Lot 1, GMES Initial Operations, 77 pp.
- García-Haro, F.J., Sommer, S., Kemper, T., 2005a, Variable multiple endmember spectral mixture analysis (VMESMA). *International Journal of Remote Sensing*, **26**, 2135-2162.
- García-Haro, F.J., Camacho-de Coca, F., Meliá, J., Martínez, B., 2005b, Operational derivation of vegetation products in the framework of the LSA SAF project. Proceedings of 2005 EUMETSAT Meteorological Satellite Conference. Dubrovnik (Croatia). 19-23 September, (Eumetsat Publ.: Darmstad), ISBN 92-9110-073-0, ISSN 1011-3932, pp 247-254
- García-Haro, F.J., Camacho, F., Meliá, J., 2014, The EUMETSAT Satellite Application Facility on Land Surface Analysis: Vegetation Parameters Product User Manual, reference number SAF/LAND/UV/PUM_VEGA/2.1-4, issue 2.1-4, 11 December 2013, 46 pp.
- García-Haro, F.J., Camacho, F., Martínez, B., Meliá, J., 2014, The EUMETSAT Satellite Application Facility on Land Surface Analysis: Vegetation Parameters Validation Report, reference number SAF/LAND/UV/VEGA_VR/2.1-4, issue 2.1-4, 11 December 2013, 111 pp.
- Garrigues, S., Lacaze, R., Baret, F., Morissette, J. T., Weiss, M., Nickeson, J. E., et al., 2008, Validation and Intercomparison of Global Leaf Area Index Products Derived From Remote Sensing Data. *Journal of Geophysical Research*, **113**, G02028, doi: 10.1029/2007JG000635.
- Huemmmrich, K.F., Privette, J. L., Mukelabai, M., Myneni, R. B., Knyazikhin, Y., 2005, Time-series validation of MODIS land biophysical products in a Kalahari Woodland, Africa. *International Journal of Remote Sensing*, **26**, 4381–4398.
- Martínez, B., Camacho, F., Verger, A., García-Haro, F.J., Gilabert, M.A., 2013, Intercomparison and quality assessment of MERIS, MODIS and SEVIRI FAPAR products over the Iberian Peninsula. *International Journal of Applied Earth Observation and Geoinformation*, **21**, 463-476.
- Privette, J.L., Myneni, R.B., Knyazikhin, Y., Mukelabai, M., Roberts, G., Tian, Y., Wang, Y., Leblanc, S.G., 2002, Early spatial and temporal validation of MODIS LAI product in the Southern Africa Kalahari. *Remote Sensing of Environment*, **83**, 232–243.
- Roujean, J.L., Lacaze, R., 2002, Global mapping of vegetation parameters from POLDER multiangular measurements for studies of surface-atmosphere interactions: A pragmatic method and its validation. *Journal of Geophysical Research*, **107D**, 10129-10145.
- Verger, A., Camacho, F., García-Haro, F.J., Meliá, J., 2009a, Prototyping of Land-SAF leaf area index algorithm with VEGETATION and MODIS data over Europe. *Remote Sensing of Environment*, **113**, 2285–2297.
- Verger, A., Martínez, B., Camacho, F., García-Haro, F.J., 2009b, Accuracy assessment of fraction of vegetation cover and leaf area index estimates from pragmatic methods in a cropland area. *International Journal of Remote Sensing*, **30**, 2685–2704.
- Trigo, I. F., DaCamara, C., Viterbo, P., Roujean, J.L., Olesen, F., Barroso, C., Camacho-de Coca, F., Carrer, D., Freitas, S.C., García-Haro, F.J., Geiger, B., Gellens-Meulenberghs, F., Ghilain, N., Meliá, J., Pessanha, L., Siljamo, N., Arboleda, A., 2011, The Satellite Application Facility on Land Surface Analysis, *International Journal of Remote Sensing*, **32**, 2725-2744.
- Weiss, M., Baret, F., Block, T., Koetz, B., Burini, A., Scholze, B., Lecharpentier, P., Brockmann, C., Fernandes, R., Plummer, S., Myneni, R., Gobron, N., Nightingale, J., Schaepman-Strub, G., Camacho, F., Sanchez-Azofeifa, A., 2014, On Line Validation Exercise (OLIVE): A Web Based Service for the Validation of Medium Resolution Land Products. Application to FAPAR Products. *Remote Sensing*, **6**, 4190-4216.
- Yang, W., Tang, B., Huang, D., Rautiainen, M., Shabanov, N.V, Wang, Y., et al., 2006, MODIS Leaf Area Index products: from validation to algorithm improvements. *IEEE Transactions on Geoscience and Remote Sensing*, **44**, 1829-1842.

Seasonal monitoring of FAPAR over the Barrax cropland site in Spain, in support of the validation of PROBA-V products at 333 m.

C. Latorre⁽¹⁾, F. Camacho⁽¹⁾, F. de la Cruz⁽²⁾, R. Lacaze⁽³⁾, M. Weiss⁽⁴⁾, F. Baret⁽⁴⁾

⁽¹⁾ EOLAB, Parc Científic Universitat de València. Catedrático José Beltrán, 2. 46980 Paterna (Valencia), SPAIN, ⁽²⁾ ITAP, Albacete, SPAIN, ⁽³⁾ HYGEOS, Toulouse, FRANCE, ⁽⁴⁾ INRA, Avignon, FRANCE
consuelo.latorre@eolab.es

ABSTRACT

This paper describes the ground activities to capture the seasonality of FAPAR during the growing season (spring-summer 2014) in Las Tiesas experimental farm located in Barrax (Albacete), one of the demonstration and validation site of the FP7 ImagineS project. The continuous monitoring of FAPAR (and PAI) was achieved using the PASTIS-PAR sensors developed at INRA-Avignon. 20 PASTIS-PAR systems, each with 6 PAR sensors, were installed in the largest fields of up to 1 km diameter (wheat, sunflower, barley, legumes, pappaver somniferum). Moreover, an intensive field campaign was performed with Digital Hemispherical Photographs (DHP) in the middle of the period (29th – 30th May) to characterize biophysical variables (LAI, FAPAR, FCover) over the main crop types. The ground DHP estimates were up-scaled using Landsat-8 imagery and empirical transfer function. The processing of the ground data set shows the ability of the PASTIS-PAR system to capture the seasonality of the FAPAR for several crops, whereas DHP data was used as complementary information to generate an empirical high resolution map for a particular date. These dataset constitutes an useful information for the validation of Copernicus Global Land products based on PROBA-V at 1 km and 333m.

1. INTRODUCTION

The Copernicus Global Land service provides Essential Climate Variables such as the Leaf Area Index (LAI), the Fraction of PAR absorbed by the vegetation (FAPAR) or the surface albedo. Most of them are currently derived from SPOT/VGT observations at 1km spatial resolution.

For the service continuity, research and development are performed within the FP7/ImagineS (Implementing Multi-scale Agricultural Indicators Exploiting Sentinels) project, which is focused on the retrieval of LAI, FAPAR, vegetation cover fraction and surface albedo from PROBA-V sensor data with an improved spatial resolution of 333 m. Therefore, validation activities are mandatory to evaluate the uncertainty attached to these new products.

The objective of this paper was two-fold: (1) to produce ground biophysical variable maps for product validation. This was achieved by an intensive field campaign in May in Las Tiesas – Barrax (Albacete, SPAIN), on 29th - 30th May, 2014 with Digital Hemispherical Photos (DHP) (2) to characterize the FAPAR and LAI temporal evolution during spring and summer time, by setting up the recent PASTIS-PAR (PAI Autonomous System from Transmittance Sensors) systems in specific locations. Continuous measurements were collected during 2014 inter-annual

campaign to capture the seasonality of FAPAR during the growing season (Latorre et al., 2014).

2. METHODOLOGY

2.1 STUDY AREA

The study area was located in “Las Tiesas” farm (39.074 N, 2.104 W) in Barrax (Albacete, Spain). The area is characterized by a flat morphology and large, uniform land-use units. The test site of Barrax has been used for agricultural research and ESA validation activities for many years.

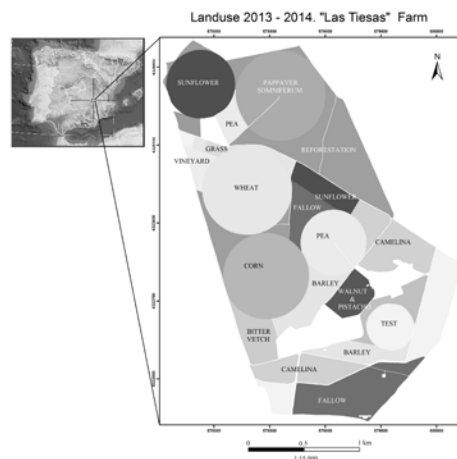


Fig. 1 Location and Land Use map.

Figure 1 shows the land use map during the field campaign. Among the irrigated fields we found Corn (C) crops at different stage of development, Onion (O), Garlic (G), Potato (P), Wheat (W) and Sunflower (S) among other crop types in minor proportion (e.g., vineyard, fruit trees, papaver). Note that Camelina (Ca), and Barley (B) fields were senescent at the time of the field campaign, and many fields were harvested.

2.2 INSTRUMENTATION

Two main devices were used for measuring biophysical variables in the study area: (1) digital hemispherical photography (DHP), (2) PASTIS-PAR systems.

2.2.1 Digital Hemispherical Photographs.

The system for DHP measures is composed by a professional camera and a fisheye lens: CANON EOS 6D and a SIGMA 8mm F3.5 – EX DG. Hemispherical photos allow the calculation of LAI, FAPAR and FCOVER measuring gap fraction through an extreme wide-angle camera lens (i.e. 180°) (Weiss et al., 2004). It produces circular images that record the size, shape, and location of gaps. These hemispherical photos acquired during the field campaign were processed with the CAN-EYE software (www6.paca.inra.fr/can-eye) to derive PAI, FAPAR and FCOVER. It is based on a supervised RGB color classification of the image to discriminate vegetation elements from background (i.e., gaps). This approach allows exploiting downward-looking photographs for short canopies (background = soil) as well as upward-looking photographs for tall canopies (background = sky). CAN-EYE software processes simultaneously up to of 25 images acquired over the same ESU (Elementary Sampling Unit).

Figure 2 shows several examples of DHPs acquisitions over different crops and photographs of ESUs where PASTIS-PAR systems were installed.

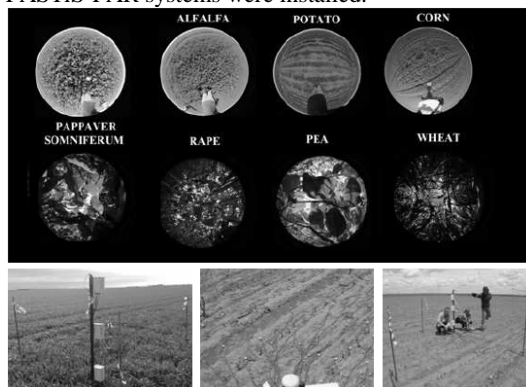


Fig.2 Top: DHPs of several ESUs. Bottom: PASTIS PAR systems.

2.2.2 PASTIS - PAR description

The PASTIS systems allow monitoring continuously the crop phenology. The device includes a data logger associated to 6 wired hemispherical quantum sensors measuring instantaneous PAR signal. The PASTIS systems require to be first calibrated against an absolute reference. During the field campaign, some sensors are installed looking upward at the top of the canopy or in an open area close to the canopy to measure the incident PAR, while others are positioned at the ground level to measure the transmitted flux and thus compute canopy PAR transmittance. The data visualization, filtering and processing for both calibration and field campaigns are performed with the PASTIS Analyzer software. The derivation of the PAI is achieved using a look-up-table based on Poisson model simulations. The direct and diffuse components of the PAR signal are taken into account in the computation.

2.3 GROUND SAMPLING STRATEGY

The DHP spatial sampling scheme was predefined to cover the existing variability over the study area (see Figure 3). Moreover, a visual inspection was conducted to identify bare areas and senescent crops (i.e., non photosynthetic vegetation) such as Camelina and Barley. A pseudo-regular sampling scheme was used within each ESU of approximately 20x20 m². The centre of the ESU was geo-located by GPS. The number of hemispherical photos per ESU ranges between 12 and 15 (see protocol in Camacho et al., 2014).

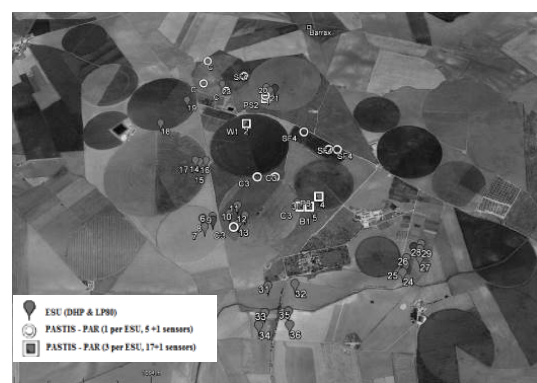


Fig. 3 Sampling of ESUS over the Barrax site

A total of 36 ESUs of 11 different land cover types were characterized during the intensive field campaign (Figure 4). The percentage of distribution of the vegetation types sampled during the intensive campaign was 22% of corn fields in early stage of growing and 17% of sampling was wheat fields. The

other more representative ESUS were: Pappaver, Onion and Alfalfa crops.

On the other hand, four ESUs (Barley, Wheat, Pea and Papaver) were characterised during spring and three ESUs (Corn and Sunflower) in summer. Each ESU was equipped using one PASTIS-PAR system (6 individual sensors). On few ESUs two additional systems (i.e. a total of 18 sensors) were installed in order to better evaluate the influence of the number of sensors in the measurement.

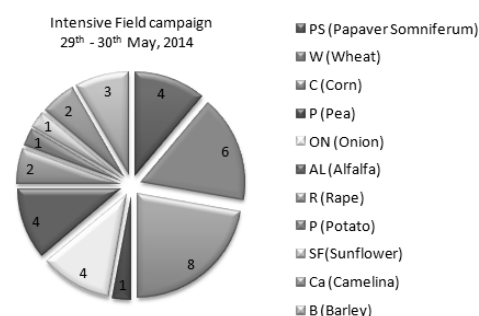


Fig. 4 Vegetation types sampled in the intensive field campaign.

3. RESULTS

3.1 GROUND DATA – INTENSIVE FIELD CAMPAIGN

The FAPAR (instantaneous at 10 a.m.) values cover approximately the full dynamic range, with minimum values for corn (0.01 - 0.22) and medium absorption values, around 0.5, for potato. The highest absorption was for Pappaver and Alfalfa field (see Figure 5).

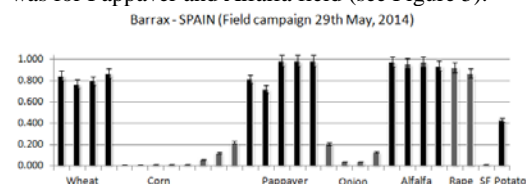


Fig. 5 FAPAR measurements acquired during the intensive field campaign.

3.2 UP-SCALING GROUND DATA – INTENSIVE FIELD CAMPAIGN

The standard procedure to produce validation maps follows the best practices of CEOS/LPV (Committee on Earth Observation Satellites) group (Morissette et al., 2006, Fernandes et al. 2014). Protocols are also described in Camacho et al. 2014. The up-scaling of field measurements is performed using a Landsat-8 decametric resolution image, provided by the GloVis - USGS Global Visualization service (https://lpdaac.usgs.gov/data_access/glovis). The

Landsat-8 image was acquired the 26th May 2014. Four spectral bands (Green - band 3 (0.53-0.59 μm), Red - band 4 (0.64-0.67 μm), NIR - band 5 (0.85-0.88 μm) and SWIR1 - band 6 (1.58-1.65 μm)) of Top of Atmosphere reflectance with a nadir ground sampling distance of 30 m, were selected for the transfer function analysis, in UTM 30 North projection and Datum WGS-84.

A transfer function between the ground measurements and the corresponding pixel reflectance values is first calibrated, and then applied to the whole decametric image (an area of 10x10 km^2 was selected).

3.2.1 Evaluating the spatial sampling

The ESUs were preferentially located in the most representative crops. The evaluation of the sampling strategy was performed by comparing the distribution of the NDVI values over the ESUs with that obtained over the whole area using the decametric resolution image. Associated to the biophysical variable map, a quality flag is generated to indicate if the pixel is within, close to, or outside the Convex Hull defined by the ESU pixel reflectance (see Figure 6).

Results show that the sampling achieved represents well the whole site since the NDVI distribution of the ESUs is comprised between the lowest and highest cumulative frequencies (Figure 6, Left). The Quality Flag (Figure 6, Right) also indicates that 77% of the pixels are within the Convex Hull or close to its borders.

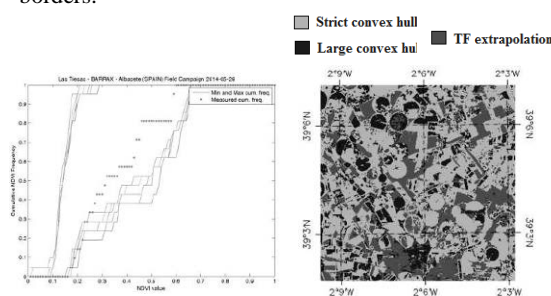


Fig.6 Left: Comparison of NDVI (TOA) distribution between ESUs (green dots) and over the whole image. Right: Convex-Hull quality flag over the 10x10 km^2 area centered at the test site.

3.2.2 Production of ground-based maps.

3.2.2.1 The Transfer Function

The estimation of the transfer function between TOA reflectances and biophysical variable is based on an iteratively re-weighted least squares algorithm. The weights are computed at each iteration by applying the bi-square function to the residuals from the previous iteration (Martínez et al., 2009). At the end of the processing, two errors were computed: weighted RMSE (RW) using the weights attributed to each ESU

and cross-validation RMSE (RC) or leave-one-out method. Among all the possible band combinations, the best performances were obtained when using the Landsat-8 visible (green, red), near infrared and shortwave infrared bands, with a RW of 0.19 and RC of 0.28 for FAPAR. The resulting scatterplot shows a good correlation: the points are distributed along the 1:1 line with no bias. Some scattering is however observed mainly for the lowest values (growing sunflower crops) where the TF overestimates the ground values (see Figure 7).

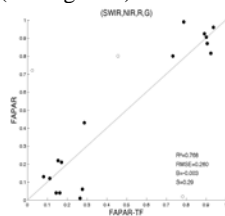


Fig.7 Right: Scatter plot between ground data and transfer function estimates.

3.2.2.1 The High Resolution Ground Based Maps

The high resolution maps are obtained by applying the selected transfer function to the Landsat-8 TOA reflectances. Figure 8 presents the FAPAR TF biophysical variable over the 10x10 km² area.

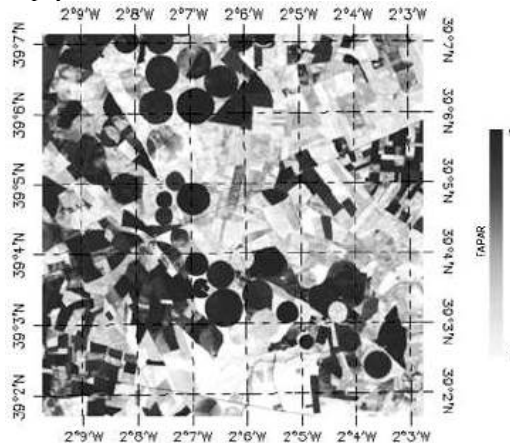


Fig.8 Map for FAPAR (black-sky 10 am) results for regression on reflectance using 4 bands combination (over Landsat 8 -TOA image).

A validation area of 3x3 km² was considered around the central coordinates where mean values were derived for validation of 1 km satellite products.

3.3 Continuous Monitoring with PASTiS systems

This section shows the first results of the analysis and filtering of the PASTIS-PAR data recorded over Sunflower and Corn (other plots are currently under analysis).

3.3.1 Sensor calibration

The calibration experiment took place in January 2014 in Avignon, France. The PASTiS systems were all synchronized and aligned on a bench during 15 days along with a PAR reference Kipp&Zonen sensor. Data were acquired every minute and we selected only the clear days. Then, the calibration coefficients between the reference and PASTiS sensors are obtained by applying a robust regression technique (see Figure 9).

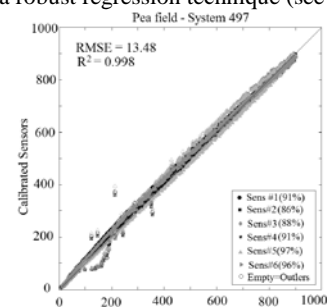


Fig.9 Example of a calibration result for a given PASTiS system. Empty symbols correspond to outliers identified by the robust regression technique.

3.3.2 Transmittance computation

In agreement with the cosine response limitation of the quantum sensors, the data are first filtered to eliminate data acquired at solar zenith angles higher than 80°. Then, the data can be visualized and manually eliminated in case of a wrong behavior of the sensor (eg. dis-functioning such as battery loss or wire eating by rabbits).

The incident PAR is then computed every 5 minute by averaging all the measurements acquired in the incident mode. For each system, the transmittance is then computed as the ratio between the average signal of the sensors over one day installed in “transmitted mode” and the incident PAR (Figure 10).

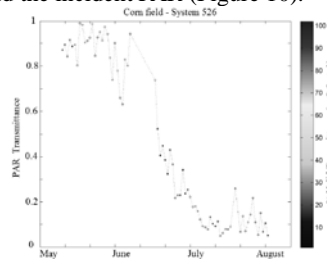


Fig.10 Example of PASTiS PAR transmittance in a corn field. The color of each point is proportional to the number of valid data acquired at the corresponding date.

3.3.3 FAPAR and PAI computation

3.3.3.1 FAPAR

The daily FAPAR is computed as:

$$FAPAR(d) = \frac{\sum_d (PAR_i(\theta_S) - PAR_t(\theta_S))}{\sum_d PAR_i(\theta_S)} = 1 - \frac{\sum_d PAR_t(\theta_S)}{\sum_d PAR_i(\theta_S)} \quad (1)$$

where PAR_i and PAR_t are respectively the incoming and transmitted PAR measurement for each acquisition time throughout day. An example of the FAPAR temporal profile is provided in Figure 11.

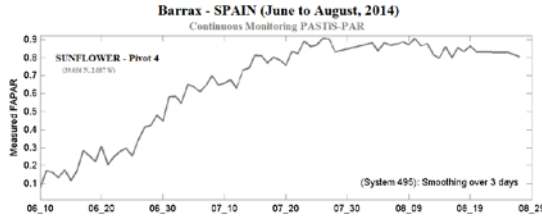


Fig.11 Example of PASTIS-PAR FAPAR in a Sunflower field.

3.2.2.2 Estimation of the diffuse fraction

The diffuse fraction of the incoming PAR is required to estimate the black sky, white sky and PAI variables. The diffuse fraction is estimated with a neural network (NNET) calibrated on experimental data acquired with a BF2 PAR sensor during the 2001-2014 period. We used 85% of the data to calibrate the neural network and 15% for the validation (total number 47666). Inputs are the optical path, the Earth-Sun distance correction factor and the incident PAR. Results show that the diffuse fraction is well estimated, with a R^2 of 0.89, and a RMSE of 0.091 computed over the validation data set.

3.2.2.3 PAI computation

To compute PAI, Look-Up-Tables (LUT) of 5000 cases were built based on the Poisson model (Weiss et al, 2004) assuming turbid medium and an ellipsoidal distribution of leaf inclination. The input of the LUT is the instantaneous black sky and white sky FAPAR, and the outputs are the corresponding PAI and Average Leaf Angle (ALA). All the data collected over a 3 days moving window are used to estimate PAI and ALA. The required diffuse fraction corresponding to each instantaneous observation is derived from the estimate based on the incident PAR value (see previous section). The 30 LUT cases providing the lowest RMSE between the PASTIS measured FAPAR and the LUT simulations were selected. Results show a consistent and rather smooth evolution of the PAI as expected (see Figure 12).

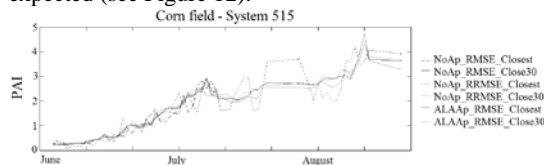


Fig. 12 Example of PASTIS PAR PAI in a corn field.

4. CONCLUSION

The FP7 ImagineS project continues the innovation and development activities to support the operations of the Copernicus Global Land service. The field activities support the validation of Copernicus Global Land LAI/FAPAR products based on PROBA-V observations.

DHP estimates were used for producing empirical transfer function maps of the study area. We also have demonstrated that the PASTIS-PAR systems are able to capture the seasonal variation of FAPAR (over the limited ESUs already processed). PASTIS-PAR FAPAR and PAI data will contribute to the validation of PROBA-V products at 333 m.

5. ACKNOWLEDGEMENTS

We wish to thank the ITAP (*Instituto Técnico Agronómico Provincial de Albacete*) for the support and the organization of the Field Campaign, and the facilities which allow us to characterize the site. PASTIS-PAR devices installed in las Tiesas are distributed by INRA and HIPHEN (www.hiphen-plant.com).

This research is supported by the FP7-SPACE-2012-1 ImagineS project, under Grant Agreement N°311766.

6. REFERENCES

- Baret, F and Fernandes, R. (2012). Validation Concept. ESA Report. VALSE2-PR-014-INRA, 42 pp.
- Camacho, F., Lacaze, R., Latorre, C., Baret, et al. (2014). A network of Sites for Ground Biophysical Measurements in support of Copernicus Global Land Product Validation. This issue.
- Fernandes, R., Plummer, S., Nightingale, J., et al. (2014). Global Leaf Area Index Product Validation Good Practices. CEOS Working Group on Calibration and Validation - Land Product Validation Sub-Group. Version 2.0: Public version made available on LPV website.
- Martínez, B., García-Haro, F. J., and Camacho, F. (2009). Derivation of high-resolution leaf area index maps in support of validation activities: Application to the cropland Barrax site. *Agricultural and Forest Meteorology*, 149, 130–145.
- Morissette, J. T., Baret, F., Privette, J. L., Myneni, R. B., et al. (2006). Validation of global moderate-resolution LAI products: A framework proposed within the CEOS land product validation subgroup. *IEEE Transactions on Geoscience and Remote Sensing*, 44, 1804–1817.
- Latorre, C., Camacho, F., de la Cruz, F., Atienzar, F. C. (2014). Vegetation Field Data and Production of Ground-Based Maps “Las Tiesas – BARRAX site, Albacete, Spain. 29th-30th May, 2014” report. FP7 ImagineS project (available at website).
- Weiss, M., Baret, F., Smith, G.J., Jonckheere, I. and Coppin, P., (2004). Review of methods for in situ leaf area index (LAI) determination. Part II. Estimation of LAI, errors and sampling. *Agricultural and Forest Meteorology*. 121, 37–53.
- Weiss, M, Baret, F., et al. (2014). Monitoring Plant Area Index at ground level: PAI autonomous system from transmittance sensors (PASTIS). This issue.

Surface soil moisture retrieval over natural surfaces

Pei Leng^{1,2}, Xiaoning Song^{1,*}, Zhao-Liang Li^{3,2}, Yawei Wang¹, Di Wang³

1. College of Resources and Environment, University of Chinese Academy of Sciences, Beijing 100049, China

2. ICube, UdS, CNRS, Bld Sebastien Brant, CS10413, Illkirch F-67412, France

3. Key Laboratory of Agro-informatics, Ministry of Agricultural/Institute of Agricultural Resources and Regional Planning, Chinese Academy of Agricultural Sciences, Beijing 100081, China

Email: songxn@ucas.ac.cn

ABSTRACT - Surface soil moisture (SSM) is a fundamental variable for understanding hydrology cycle, earth's energy budget and climate change. To achieve the quantitative SSM content retrieval over natural surfaces, effects of fractional vegetation cover (FVC) and soil texture on a previously developed SSM retrieval model are primarily evaluated using simulated data from the Common Land Model (CoLM). The results indicate that (1) both the accuracy and the five model parameters of the previous SSM retrieval model show relatively consistent variations when the fractional vegetation cover (FVC) varies from 0 to 0.7 and (2) the SSM exhibits a generally significant and exponential relationship with the rotation angle when the clay content is lower than 30%, with the FVC ranging from 0 to 0.7. These findings make it possible to estimate SSM directly under the conditions that the underlying surface is in the presence of spatially variable FVC and soil texture. On this basis, we further confirm the feasibility of using the previous bare SSM retrieval model to estimate SSM for FVC varying from 0 to 0.7 with a clay content lower than 30%. For the simulated data on eight cloud-free days, the total root mean square error (RMSE) of the retrieved SSM and the coefficient of determination (R^2) are $0.033 \text{ m}^3\text{m}^{-3}$ and 0.758, respectively. Ultimately, a preliminary validation is conducted using the ground measurements in Bondville; an $R^2=0.328$ and a $\text{RMSE}=0.058 \text{ m}^3\text{m}^{-3}$ are obtained for 14 cloud-free days.

1 INTRODUCTION

As a source of water for evapotranspiration over continents, surface soil moisture (SSM) is profoundly involved in both the water and energy cycles at the land/atmosphere interface. SSM is also a critical factor in the environment and climate system, as well as in various applications, such as drought monitoring (Mozny et al. 2012; Anderson et al. 2012), runoff generation (Meyles et al. 2003; Penna et al. 2011), irrigation scheduling (Bailey and Spackman 1996; Intrigliolo and Castel 2004), weather forecasting (Huang et al. 1996; Scipal et al. 2008) and carbon/nitrogen cycling (Porporato et al. 2003; Yurova and Lankreijer 2007).

Because remote sensing instruments can observe the atmosphere and Earth's surface over a large area within a short time, remote sensing is becoming the preferred method for obtaining SSM information at the regional scale, and a number of methods have been developed to estimate SSM or remotely sensed proxies of soil moisture in recent decades (Price 1980; Sandholt, Rasmussen, and Andersen 2002; Li et al. 2009; Li, Tang et al. 2013; Song et al. 2013; Li, Wu et al. 2013; Zhao and Li 2013; Zhao et al. 2013). However, several challenges make obtaining direct

and accurate quantitative SSM values (the actual volumetric water content or gravimetric water content rather than soil moisture proxies) over natural surfaces difficult. In particular, vegetation cover has a significant effect on the ability of passive microwave radiometers to detect changes in near-surface soil moisture (Jackson et al. 1982). Hence, intensive validations of passive-microwave-derived soil moisture products are only conducted in sparsely to moderately vegetated regions, according to previous studies. Nevertheless, passive-microwave-derived soil moisture products exhibit only a low to moderate accuracy compared with ground measurements, simulations and remotely sensed soil moisture (Wanders et al. 2012; Su et al. 2013). Moreover, because soil moisture exhibits completely different transfer characteristics in bare soils and vegetated conditions, it is also regarded as a critical factor that greatly determines the physical basis and method for estimating SSM using optical and thermal infrared observations. For example, consider the commonly used thermal inertia (TI) or apparent thermal inertia (ATI). Although TI and ATI are widely recognized as feasible proxies of soil moisture, they are only appropriate for bare soils and sparse vegetation. Likewise, the empirical relationships that convert the

evaporative fraction (EF) derived from optical and thermal infrared data to soil moisture values generally work better for bare soils and shallowly-rooted plant cover (Davies and Allen 1973). In addition to vegetation, soil texture also greatly affects the direct observation of quantitative SSM values when using remotely sensed images. In particular, the empirical relationships that link the ATI (or TI) and soil moisture content are not unique and are variable with the soil texture characteristics. Moreover, the “universal triangle” method and the following indices developed on the basis of this triangle principle that have been commonly used to infer soil moisture conditions and evapotranspiration do not provide quantitative volumetric soil moisture values. Specifically, the concept of soil surface moisture availability (M_0), which is defined as the soil water content compared with the field capacity, was originally used in the triangle methods (Carlson et al. 2007). Hence, these indices couple soil moisture and soil texture similarly to proxies, rather than provide the actual volumetric water content or gravimetric water content that are usually expected.

Considering natural surfaces, the underlying surface is most likely associated with spatially variable vegetation coverage and soil texture. In that case, both vegetation and soil texture affect soil moisture transfer and land surface parameters that are used in the methods or algorithms for SSM estimations; therefore, the quantitative soil moisture content is likely difficult to obtain directly using an inversion model with the same physical basis and model expression. Nevertheless, because optical and thermal infrared remote sensing of soil moisture has a fine spatial resolution that better satisfies the requirements of various applications, quantitative SSM content values directly obtained over natural surfaces, where vegetation cover and soil texture are spatially variable, are important. In a previous study, Leng et al. (2014) developed a bare SSM retrieval model from the synergistic use of land surface temperature (LST) and net surface shortwave radiation (NSSR). The SSM retrieval model was proved to be independent of soil texture, and it has the ability to estimate quantitative volumetric soil water content directly without establishing an empirical relationship between ground SSM measurements and satellite-derived proxies of SSM. These advantages indicate a potential possibility to estimate SSM quantitatively and directly for natural surfaces in intended developments. Following the previous work, this study aims to analyze the effects of fractional vegetation cover (FVC) and soil texture on the previous SSM retrieval model and to achieve the quantitative SSM retrieval using a uniform expression with the underlying surface in the presence of spatially variable vegetation cover and soil textures.

2 MATERIALS AND METHODS

2.1 Bare SSM Retrieval Model

Based on the derivation of the elliptical relationship between the daytime LST and NSSR, as well as the simulated data from the Common Land Model (CoLM), a novel SSM retrieval model was developed and proven to be feasible in bare soils with both simulated data and field measurements (Leng et al. 2014). The model is expressed as:

$$SSM = n_1 \times x_0 + n_2 \times y_0 + n_3 \times a + n_4 \times \theta + n_0 \quad (1)$$

where SSM is the daily average SSM (m^3m^{-3}); x_0 , y_0 , a and θ are the ellipse parameters derived from the elliptical relationship between the diurnal LST and NSSR cycles, i.e., the ellipse center horizontal coordinate, ellipse center vertical coordinate, semi-major axis and rotation angle, respectively; and n_i ($i = 0, 1, 2, 3, 4$) are the model parameters (m^3m^{-3}). The SSM retrieval model is independent of the soil texture, and the five model parameters n_i ($i = 0, 1, 2, 3, 4$) depend only on the atmospheric conditions of each cloud-free day.

2.2 CoLM Simulation

To achieve the SSM retrieval over a nature surface where FVC and soil texture are spatially variable, it is quite necessary to investigate the effects of FVC and soil texture on the bare SSM retrieval model. Analogously to previous study (Leng et al. 2014), meteorological variables, including downward solar radiation, downward longwave radiation, precipitation, air temperature, wind speed, wind direction, atmospheric pressure at the surface and specific humidity that collected at the Bondville site (40.0062°N, 88.2904°W) on eight cloud-free days in 2001, are selected to drive the CoLM to produce simulated data. In general, the initializations of soil properties and soil moisture can be also referred to Leng et al. (2013). Figure 1 depicts the scheme of the simulation in detail.

3 RESULTS AND ANALYSIS

3.1 EFFECTS OF VEGETATION

Effects of vegetation on the previously developed bare SSM retrieval model are primarily investigated using the dataset from Simulation 1. Similarly to the previous study, the simulated dataset on DOY 274 in 2001 is obtained to assess the effects of FVC on the SSM retrieval model, as described in Equation (1). Figure 2 shows the results of the model parameters versus FVC using the simulated data on DOY 274. Clearly, the five model parameters n_i ($i = 0, 1, 2, 3, 4$) generally maintain a relatively gradual variation when the FVC varies from 0 to 0.7. However, when the FVC

exceeds 0.7, the model parameters are most likely experience anomalous variations as the FVC increases.

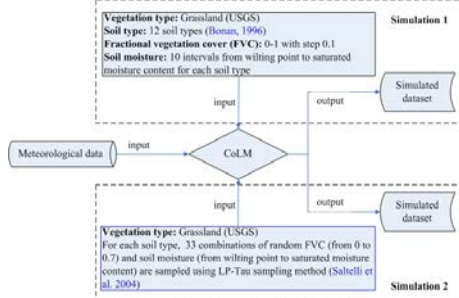


Figure 1. Scheme for Common Land Model (CoLM) simulation.

In addition to the variations in the model parameters with different FVCs, the coefficient of determination (R^2) and root mean square error (RMSE) also exhibit completely different variations, depending on whether the FVC is equal to 0.7. As depicted in Figure 3, the accuracy generally shows a consistent decrease as the FVC increases within the range from 0 to 0.7. In particular, both R^2 and RMSE exhibit quite anomalous variations when the FVC is higher than 0.7, which is quite similar to that of the irregular variations in the five model parameters.

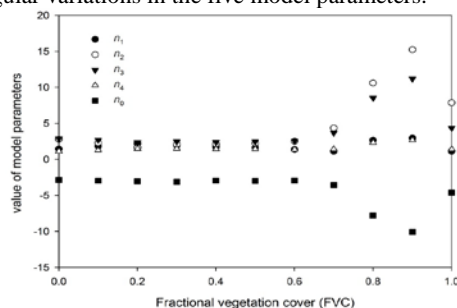


Figure 2. Variations of model parameters *versus* fractional vegetation cover (FVC) with simulated data on DOY 274 in 2001 at Bondville site.

Under dense vegetation coverage ($FVC > 0.7$), satellite-derived LST and NSSR contain weak information on the soil surface. In that case, estimating SSM using such weak information from the optical and thermal measurements most likely generates various uncertainties. Nevertheless, because both the model parameters and accuracy exhibit consistent variations when the FVC varies from 0 to 0.7, the SSM can potentially be estimated using an identical expression in such conditions. Moreover, this FVC range well represents the natural surfaces that generally cover the vegetation conditions from bare soils to moderate and high coverage. Based on these results, we define a FVC range (from 0 to 0.7) to discuss SSM retrievals.

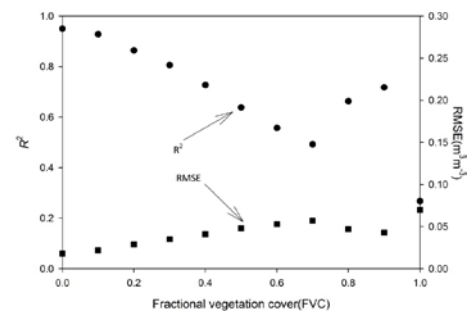


Figure 3. Variations of the accuracy of SSM retrieval *versus* fractional vegetation cover (FVC) with simulated data on DOY 274 in 2001 at Bondville site.

3.2 EFFECTS OF SOIL TEXTURE

To achieve the SSM retrieval over natural surfaces in which the FVC and soil texture are spatially variable, the effects of soil texture on the SSM retrieval in partial vegetation coverage, with the FVC ranging from 0 to 0.7, are discussed in the following section. Hereafter, the dataset from Simulation 2 is utilized to evaluate the effects of soil texture on the SSM retrieval in various vegetation coverage conditions within this FVC range.

Because the rotation angle is the ellipse parameter most sensitive to the SSM, the behavior of SSM response to the rotation angle for different soil textures with the simulated data on DOY 274 is investigated. When the clay content is lower than 30%, the SSM generally exhibits a significant exponential relationship with the rotation angle; while clay content exceeds 30%, the SSM approximately follows a linear relationship with the rotation angle, as depicted in Figure 4. In particular, only several typical soil textures are presented in the Figure and the other soil textures generally follows the similar variations for each group depending on whether the clay content is over 30%. Note that for each soil texture, because the initial settings of the simulated data contain different random combinations of soil moisture (from the wilting point to the saturated moisture content) and FVC (from 0 to 0.7), the exponential or linear relationship between the SSMs and rotation angles for each soil texture is independent of the FVC. Moreover, the coefficients of determination of the linear relationship are generally not as significant as those of the exponential relationship.

Based on these results, we divide all the soil textures into two groups: clay content lower than 30% and clay content higher than 30%. Coincidentally, except for the tropical rain forest areas and forest ecosystems, most of the continent has no more than 30% clay content, according to the present global soil datasets (Wei et al. 2014). Subsequently, we evaluate the previous bare SSM retrieval model using three

cases: case I represents all 12 soil textures, and case II and case III denote the soils with clay contents lower than 30% and higher than 30%, respectively. Note that all the three cases assume fractional vegetation in the presence of spatially variable FVC ranging from 0 to 0.7.

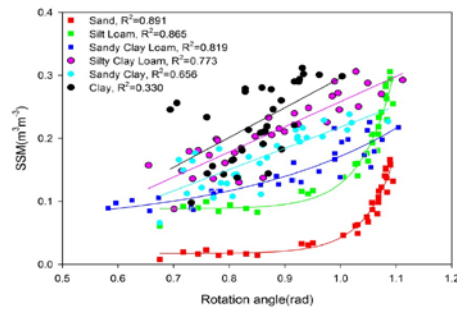


Figure 4. Relationships between SSMs and rotation angles for different soil textures.

Because the previous bare SSM retrieval model is capable of estimating SSM directly without the knowledge of soil texture, to achieve the direct estimation of SSM quantitatively using an uniform model expression shown in Equation (1) under the conditions that the underlying surface is in the presence of spatially variable FVC and soil texture, it is quite necessary to further assess the feasibility of using the five model parameters n_i ($i = 0, 1, 2, 3, 4$) obtained for bare soils to retrieve SSM in spatially variable FVC and soil texture conditions. Figure 5 shows the accuracy of the SSM retrieval using Equation (1) on this purpose. In this Figure, the five model parameters n_i ($i = 0, 1, 2, 3, 4$) for each of the eight cloud-free days are obtained from the simulated data for bare soils. Clearly, case II generally exhibits higher accuracy than the other two cases. In case II, the estimated SSM conforms well to the simulated values, with R^2 approximately 0.80 throughout the eight cloud-free days. For the other two cases, accuracy does not maintain a relatively stable value. In particular, case III shows the overall lowest accuracy regarding both R^2 and RMSE, which indicates that the previous bare SSM retrieval model is unsuited to the conditions that the underlying surface is with clay content high than 30% and FVC ranging from 0 to 0.7. Furthermore, although case I reveals an overall moderate accuracy between case II and case III, R^2 varies unsteadily according to the eight cloud-free day.

In summary, although the previous SSM retrieval model is independent of soil texture in bare soils, the model is most likely not independent of all the soil textures with moderate to high vegetation coverage. Specifically, the effects of combined vegetation and soil texture for a natural surface make it difficult to

estimate SSM using the previous model. However, the significant exponential relationship between SSM and the rotation angle presents the possibility of retrieving SSM using ellipse parameters with a uniform expression shown in Equation (1) when the FVC ranges from 0 to 0.7 and when the clay content is lower than 30%.

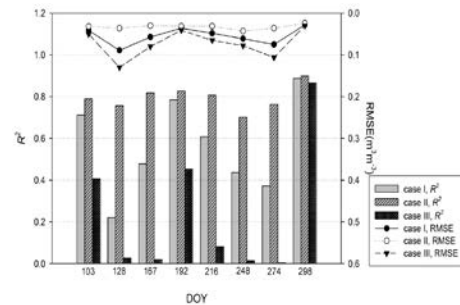


Figure 5. Accuracy of SSM retrieval with the three cases under vegetation condition (FVC ranging from 0 to 0.7) with simulated data on the eight cloud-free days in 2001 at Bondville site. Case I represents all the 12 soil textures, while case II and case III denote the soils with clay content lower than 30% and higher than 30%, respectively.

3.3 SSM Retrieval

The previous sections define the vegetation and soil texture conditions with respect to the SSM retrieval using the previous developed bare SSM retrieval model described in Equation (1). The model assumes the underlying surface is associated with spatially variable vegetation and soil textures; this assumption is generally feasible and practical for SSM estimations over natural surfaces. Figure 6 shows the result of the estimated SSM versus the simulated values for the eight selected cloud-free days at the Bondville site in 2001. According to the results, a reliable accuracy is found for the eight cloud-free days, with a RMSE from 0.030 to 0.037 m³ m⁻³ and an R^2 from 0.702 to 0.866. Moreover, the estimated SSM and simulated values are evenly distributed around the 1:1 line with a satisfactory accuracy (total RMSE=0.033 m³ m⁻³, $R^2=0.758$), which indicates that the previous bare SSM retrieval model is capable of directly estimating SSM under the condition that the underlying surface is associated with spatially variable vegetation and soil textures.

In addition to the simulated data, a preliminary validation using ground measurements from the Bondville site is also presented. For the validation, the observed diurnal cycles of the LST and NSSR are primarily used to fit the elliptical relationship and to obtain the ellipse parameters (x_0 , y_0 , a and θ) for the SSM estimation. Furthermore, the meteorological data collected at the Bondville site are included to create

simulated data via the CoLM simulation and to acquire the five model parameters n_i ($i = 0, 1, 2, 3, 4$). Finally, the estimated SSM values are calculated by the SSM retrieval model in Equation (1) using both the ellipse parameters (x_0, y_0, a and θ) and the five model parameters n_i ($i = 0, 1, 2, 3, 4$) for each cloud-free day. In total, the measured SSM on 14 cloud-free days throughout the growing season in 2007 are used to validate the retrieval SSM. Figure 7 depicts the comparison of the estimated SSM versus the measured SSM on 14 cloud-free days; an $R^2=0.328$ with a $RMSE=0.058 \text{ m}^3\text{m}^{-3}$ is obtained. Moreover, a $bias=0.020 \text{ m}^3\text{m}^{-3}$ is found for the estimated SSM compared with the measured values. Considering the possible uncertainties in the measurements and the inherent error in the SSM retrieval model, the estimated SSM and the measured values generally exhibit a consistent trend according to the preliminary validation.

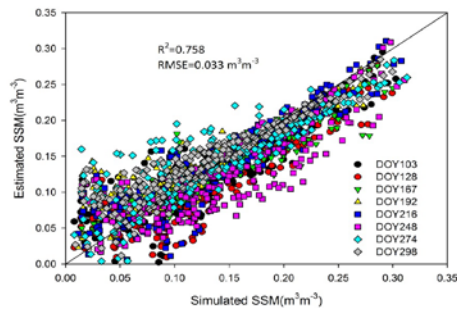


Figure 6. Comparison of the estimated SSM versus the simulated values on the eight cloud-free days in 2001 at Bondville site.

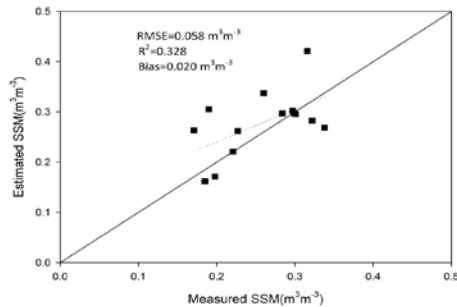


Figure 7. Comparison of the estimated SSM versus the measured SSM on the 14 cloud-free days in 2007 at Bondville site.

4 CONCLUSIONS

In this study, we analyzed the effects of vegetation and soil texture on a previously developed bare soil SSM retrieval model. The analysis is primarily based on simulated data from the CoLM. The results of the analysis determine the vegetation and soil texture

conditions with respect to the quantitative SSM retrieval using ellipse parameters derived from an elliptical relationship between the diurnal cycles of the LST and NSSR. The conditions were described as that the fractional vegetation in the presence of spatially variable vegetation cover ranging from 0 to 0.7, with a clay content of the soil lower than 30%. In general, the FVC range covers the vegetation conditions from bare soils to moderate and high vegetation coverage. Because most of the continent has a clay content of 30% or less, according to the present global soil datasets (an exception is tropical rain forests and other forest ecosystems), these conditions are practical for SSM estimations over natural surfaces. The results from the simulated data show that the previous bare SSM retrieval model produces generally acceptable accuracy when the FVC has a range of 0-0.7 and a clay content lower than 30%. For the eight cloud-free days, the total RMSE and R^2 reach $0.033 \text{ m}^3\text{m}^{-3}$ and 0.758, respectively, which indicates that the previous bare SSM retrieval model is feasible for obtaining SSM in such conditions. In addition to the simulated data, a preliminary validation using ground measurements is also presented, and an $R^2=0.328$ with a $RMSE=0.058 \text{ m}^3\text{m}^{-3}$ are obtained for the 14 cloud-free days at the Bondville site.

This study methodologically achieves quantitative SSM retrievals using a uniform expression with an underlying surface associated with spatially variable vegetation cover and soil textures using simulated data, and a preliminary validation was conducted to support the results. However, more intensive validations and further applications with satellite data are vital to ongoing research that aims to improve the SSM retrieval model.

ACKNOWLEDGMENT

The work described in this article was supported in part by the National Nature Science Foundation of China [grant number 41271379]; partly supported by the CAS (Chinese Academy of Sciences) Key Research Program “Hydrological Impacts from Degrading Permafrost in the Sources Area of the Yellow River” [grant number KZZD-EW-13]; and also partly supported by the CAS Action-Plan for West Development [grant number KZCX2-XB3-15].

REFERENCES

- Anderson, W., Zaitchik, B., Hain, C., Anderson, M., Yilmaz, M., Mecikalski, J., and Schultz, L., 2012, Towards an integrated soil moisture drought monitor for East Africa. *Hydrology and Earth System Sciences*, 16, 2893-2913.
- Bailey, R., and Spackman, E., 1996, A model for estimating soil moisture changes as an aid to

- irrigation scheduling and crop water-use studies: I. Operational details and description." *Soil Use and Management*, 12, 122-128.
- Carlson, T., Gillies, R., and Schmugge, T., 1995, An interpretation of methodologies for indirect measurement of soil water content. *Agricultural and Forest Meteorology*, 77, 191-205.
- Huang, J., van den Dool, H., and Georgakakos, K., 1996, Analysis of model-calculated soil moisture over the United States (1931-1993) and applications to long-range temperature forecasts. *Journal of Climate*, 9, 1350-1362.
- Jackson, T., Schmugge, T., and Wang, J., 1982, Passive microwave sensing of soil moisture under vegetation canopies. *Water Resources Research*, 18, 1137-1142.
- Leng, P., Song, X., Li, Z.-L., Ma, J., Zhou, F., and Li, S., 2014, Bare surface soil moisture retrieval from the synergistic use of optical and thermal infrared data. *International Journal of Remote Sensing*, 35, 988-1003.
- Leng, P., Song, X., Li, Z.-L., and Wang, Y., 2013, Evaluation of the effects of soil layer classification in the Common Land Model on modeled surface variables and the associated land surface soil moisture retrieval model. *Remote Sensing*, 5, 5514-5529.
- Li, Z.-L., Tang, B., Wu, H., Ren, H., Yan, G., and Wan, Z., 2013, Satellite-derived land surface temperature: Current status and perspectives. *Remote Sensing of Environment*, 131, 14-37.
- Li, Z.-L., Tang, R., Wan, Z., Bi, Y., Zhou, C., Tang, B., Yan, G., and Zhang, X., 2009, A review of current methodologies for regional evapotranspiration estimation from remotely sensed data. *Sensors*, 9, 3801-3853.
- Li, Z.-L., Wu, H., Wang, N., Qiu, S., Sobrino, J., Wan, Z., Tang, B., and Yan, G., 2013, Land surface emissivity retrieval from satellite data. *International Journal of Remote Sensing*, 34, 3084-3127.
- Meyles, E., Williams, A., Ternan, L., and Dowd, J., 2003, Runoff generation in relation to soil moisture patterns in a small Dartmoor catchment, southwest England. *Hydrological Processes*, 17, 251-264.
- Mozny, M., Trnka, M., Zalud, Z., Hlavinka, P., Nekovar, J., Porop, V., and Virag, M., 2011, Use of a soil moisture network for drought monitoring in the Czech Republic. *Theoretical and Applied Climatology*, 107, 99-111.
- Penna, D., Tromp-van Meerveld, H., Gobbi, A., Borga, M., and Dalla Fontana, G., 2011, The influence of soil moisture on threshold runoff generation processes in an alpine headwater catchment. *Hydrology and Earth System Sciences*, 15, 689-702.
- Porporato, A., D'Odorico, P., Laio, F., and Rodriguez-Iturbe, I., 2003, Hydrologic controls on soil carbon and nitrogen cycles. I. Modeling scheme." *Advances in Water Resources*, 26, 45-58.
- Price, J., 1980, The potential of remotely sensed thermal infrared data to infer surface soil moisture and evaporation. *Water Resources Research*, 16, 787-79.
- Sandholt, I., Rasmussen, K., and Andersen, J., 2002, A simple interpretation of the surface temperature/vegetation index space for assessment of surface moisture status. *Remote Sensing of Environment*, 79, 213-224.
- Scipal, K., Drusch, M., and Wagner, W., 2008, Assimilation of a ERS scatterometer derived soil moisture index in the ECMWF numerical weather prediction system. *Advances in Water Resources*, 31, 1101-1112.
- Song, X., Leng, P., Li, X., Li, X., and Ma, J., 2013, Retrieval of daily evolution of soil moisture from satellite-derived land surface temperature and net surface shortwave radiation. *International Journal of Remote Sensing*, 34, 3289-3298.
- Su, C.-H., Ryu, D., Young, R., Western, A., and Wagner, W., 2013, Inter-comparison of microwave satellite soil moisture retrievals over the Murrumbidgee basin, Southeast Australia. *Remote Sensing of Environment*, 134, 1-11.
- Wanders, N., Karssenbergh, D., Bierkens, M., Parinussa, R., de Jeu, R., van Dam, J., and de Jong, S., 2012, Observation uncertainty of satellite soil moisture products determined with physically-based modeling. *Remote Sensing of Environment*, 127, 341-356.
- Wei, S., Dai, Y., Duan, Q., Liu, B., and Yuan, H., 2014, A global soil data set for earth system modelling. *Journal of Advances in Modeling Earth Systems*, 6, 249-263.
- Yurova, A., and Lankreijer, H., 2007, Carbon storage in the organic layers of boreal forest soils under various moisture conditions: A model study for Northern Sweden sites." *Ecological Modelling*, 204, 475-484.
- Zhao, W., and Li, Z.-L., 2013, Sensitivity study of soil moisture on the temporal evolution of surface temperature over bare surfaces. *International Journal of Remote Sensing*, 34, 3314-3331.
- Zhao, W., Li, Z.-L., Wu, H., Tang, B., Zhang, X., Song, X., and Zhou, G., 2013, Determination of bare surface soil moisture from combined temporal evolution of land surface temperature and net surface shortwave radiation. *Hydrological Process*, 27, 2825-2833.

Land Surface Temperature Product Validation by Using an Autonomous TIR Data Acquisition System Setup in Meteorological Stations

Raquel Niclòs¹, José A. Valiente², Maria J. Barberà¹, César Coll¹, José A. Benavent¹

¹ *Earth Physics and Thermodynamics Department, University of Valencia, 50 Dr. Moliner, E-46100 Burjassot (Spain).*

² *Instituto Universitario Centro de Estudios Ambientales del Mediterráneo – CEAM-UMH, 14 Charles Darwin, E-46980 Paterna (Spain).*

Raquel.niclos@uv.es

ABSTRACT - *An autonomous system for field thermal-infrared data acquisition was developed with the aim of being deployed at any meteorological tower station. The system scans angularly sky and land hemispheres by means of a single infrared radiometer. We describe the development of the autonomous and angular system for ground land surface temperature (LST) measurements and show the first validation results for LST products retrieved from MSG-SEVIRI and EOS-MODIS images using the measurements of the system deployed in field conditions as ground-truth data.*

1 INTRODUCTION

Dedicated ground-truth experimental campaigns for thermal-infrared (TIR) radiometric measurements are used to validate remotely sensed Land Surface Temperature (LST) products. The generation of more accurate LST retrieval algorithms, e.g. with angular-dependent coefficients and angular-dependent emissivity input data, requires also more detailed ground measurements at convenient equipped monitoring stations. Additionally, this kind of ground radiometric observations can be used to better understand many land-atmosphere interactions, such as the net radiation partitioning into latent and sensible heat fluxes or the monitoring of partly cloudy sky TIR emission for the appropriate correction of the downward atmospheric reflected radiance effect in the LST retrieval. All these requirements lead to the convenience of using a specific device to scan sky and surface temperatures at different azimuth and zenith angles.

Therefore, an autonomous system for field TIR radiance measurements at different observation angles by a single radiometer has been developed to be easily deployed at any meteorological tower station to obtain surface radiative properties and remotely sensed LSTs.

2 EXPERIMENTAL SYSTEM AND SETUP

The system developed makes possible routinely angular TIR measurements with a single TIR radiometer, rather than using radiometers fixed at fixed viewing angles (Fiebrich et al. 2003). The convenience of this configuration is the acquisition of complete scans of both land and sky hemispheres by means of sweeping measurements at predefined angles

and the use of only one TIR radiometer, with one single calibration, avoiding intercomparison problems.

The system has a 25-cm diameter plate that rotates around a tube, playing this tube the role of the system axis (Fig. 1). A ball bearing is inserted between the latter two elements allowing the rotation of the plate around the tube to attain any specific azimuth observation angle. A servomotor and a gear wheel below the plate are the mechanical parts in charge of driving the system to the specific azimuth positions. A second servomotor, whose axis is attached in parallel to the bottom face of the plate, controls the zenith positioning of the radiometer. The radiometer is inserted into a head to connect with the axis of this second and smaller servomotor. This head acts as a radiation shield to prevent the detector from solar heating, and contains also a digital inclinometer that allows a precise knowledge of the actual observation angle. Besides, a reed switch in combination with a magnet in the proximity of the rotation axis is used to obtain the precise positioning azimuth angle. The axis tube of the system allows the insertion of a 40-mm mast and the selection of a fixed height along the pole where measurements are to be taken. Many meteorological towers end in a mast, and the system can be integrated in such towers at a level not necessarily being the highest, allowing accommodation for other sensors.

The movement of the system is controlled by an extensively used CR1000 Campbell datalogger, which was firstly configured for 10 azimuth and 6 zenith equally-spaced positions (azimuth angles of 18, 54, 90, 126, 162, 198, 234, 270, 306, 342 degrees from North, and zenith angles of 18, 45, 72, 108, 135, 162

degrees from Zenith). However, the acquisition azimuth and zenith angles can be modified by the user. For this specific configuration, both sky and land hemispheres can be swept twice in a 10-min period, with clockwise and counter clockwise scans. The system takes the 6 consecutive zenith angle measurements in the same vertical plane, moves to the following azimuth angle through a horizontal sweep and takes the next 6 measurements at the zenith angles. The time period elapsed between one single measurement and the following was set as 4 seconds to change position, wait for accommodation of the radiometer response, and take the measurement.

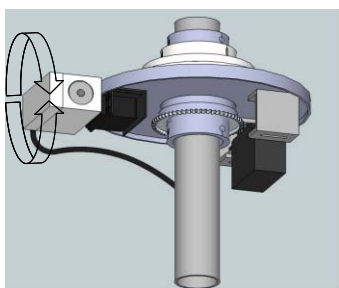


Fig. 1. The system for the angular positioning of the TIR radiometer.

The 8-14 μm *Apogee Instruments* radiometer model SI-121 was selected for the integration in the system (www.apogeeinstruments.com) not only by its reduced size and mass (190g) but also by its good quality-price ratio, as proved in calibrations with traceable blackbodies. Radiometric temperature accuracies for the SI-121 radiometer used for the study were obtained through calibrations against: (a) a Landcal Blackbody Source P80P with temperatures from 278 K to 303 K, and (b) a National Institute of Standards and Technology (NIST) blackbody with temperatures from 283 K to 303 K during a TIR radiometer comparison campaign organized by the Committee on Earth Observation Satellites (CEOS). Temperature accuracies of ± 0.2 K were obtained at temperatures from 278 K to 303 K with (a), and better than ± 0.2 K at 293-303 K with (b) (Theocharous et al. 2010, Niclós et al. 2011). The SI-121 half angle field-of-view (FOV) is 18 degree, which corresponds to the radius of a hemispherical circle from which 98% of the radiation viewed by the radiometer detector is being emitted. However, an observation angle relative to the center of the detector of 10 degree means a 90% of the incoming radiation that is emitted by the target. The response time of the radiometer is less than one second. However, small fluctuations are observed in a period greater than one second if the radiometer is exposed to target temperature changes of ~ 20 K.

Taking a wider time period for the radiometer accommodation avoids the problem and increases the measurement reliability.

A prototype of the described autonomous and angular system was deployed at an experimental site located in a ~ 100 km², flat and homogeneous area of rice crop fields (39.274°N, -0.317°E in WGS-84; 2.5 m above sea level) in August, 2012. This area has been extensively used in experimental calibration and validation campaigns of satellite TIR sensors and LST products (Coll et al. 2005, 2006, Niclós et al. 2011). The cultivated-rice area has a full vegetation cover from July to September, until harvesting is done, then it is flooded from December to January and also in June, and the land cover changes from wet to dry bare soils from February to May. Therefore, different surface conditions can be studied overtime. For this particular location, the system was affixed to the top of a 3-m mast erected on a farming plot ridge. With this configuration, there exist some system observation angles where the ridge is partly viewed by the radiometer and other angles have representative and homogeneous views of the crop.

3 DATA ANALYSIS AND PROCESSING

3.1. Data analysis

As the system acquires large amount of data, we developed a MATLAB program tool to read, select, filter and plot the data. The software tool is able to read several months of data, select the data to work with, calculate solar position for the measurements, store transformed data, filter data with thresholds, integrate hemispherically data, and interpolate and extrapolate values in the polar hemispherical space based on the measurements. Additionally, the tool represents the data with different output plots, e.g., daily time series of the whole set of directional data and for a selected land viewing zenith angle (Fig. 2), polar projections of the data for sky and land hemispheres rendering the interpolated field at the background level (Fig. 3), and cross sections at selected azimuth angles in a hemispherical map to extract the zenith angular behavior (Fig. 4).

3.2. Ground-truth LST retrieval

The TIR radiance measured by the band i of a radiometer observing a surface at ground level at an angular direction can be expressed as follows:

$$L_i(\theta, \phi) = \varepsilon_i(\theta, \phi) B_i(LST) + (1 - \varepsilon_i(\theta, \phi)) L_i^{\downarrow atm, hem} \quad (1)$$

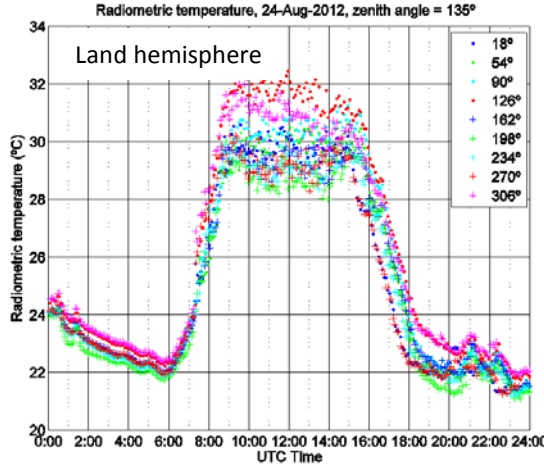


Fig. 2. Radiometric temperature time series for different azimuthal angles at a land observation zenith angle (135°). Cloudless day (24 August, 2012).

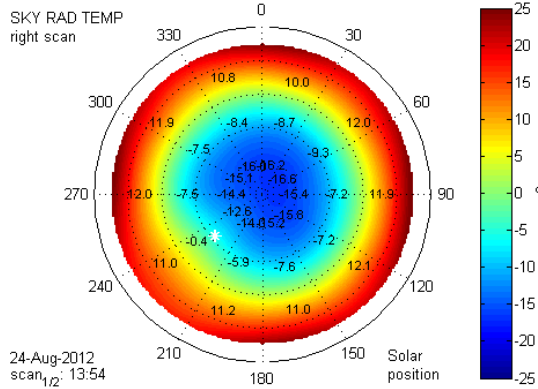


Fig. 3. Polar projections of the radiometric temperatures for the sky hemisphere in a cloudless day (24 August, 2012, 13:54 UTC).

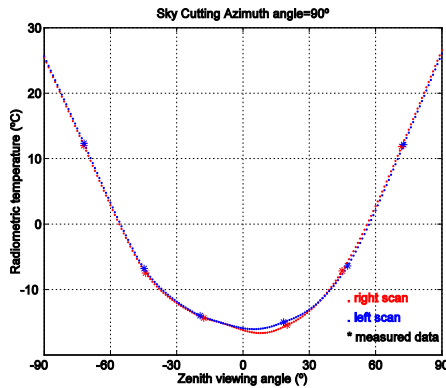


Fig. 4. Zenith angular behaviour of the sky radiometric temperature at a selected azimuth angle (90°) for the same cloudless day.

where $B_i(LST)$ is the averaged Planck's function for the band i and a temperature LST ; $\varepsilon_i(\theta, \phi)$ is the directional surface emissivity; and $L_i^{\downarrow atm, hem}$ is the hemispheric downwelling radiance (the downwelling irradiance divided by π), which can be obtained by integration of the radiance coming from different viewing directions. In case of totally cloudless or cloudy conditions, the sky radiances can be approximated as (Nicolòs et al. 2005a):

$$L_i^{\downarrow atm}(\theta, \phi) = L_i^{\downarrow atm}(\theta) \approx L_i^{\downarrow atm}(0^\circ) \cos^{-x_i}(\theta) \quad (2)$$

$$L_i^{\downarrow atm, hem} = \frac{2}{2 - x_i} L_i^{\downarrow atm}(0^\circ) \quad (3)$$

Cloudless conditions are required to retrieve LST from satellite TIR observations and thus to validate their data by comparison with ground LST measurements. Therefore, equations (2)-(3) can be used to obtain

$L_i^{\downarrow atm, hem}$ from the angular system $L_i^{\downarrow atm}(\theta)$ measurements (see Fig. 4). Emissivity measurements were performed in field conditions with TIR multiband CE-312 radiometers (www.cimel.fr) using different techniques depending on the land cover (Mira et al. 2009): the Temperature-Emissivity Separation (TES) method, the Box Method, and a portable infrared Designs & Prototypes 102 spectroradiometer (2–16 μm). Results showed a near-grey body spectrum with $\varepsilon \approx 0.983 \pm 0.005$ and negligible spectral variation between 8 and 13 μm for the fully-vegetated rice crops. Emissivity values of around 0.970 were obtained for bare soil conditions and water emissivities for flooded soils were obtained from Nicolòs et al. (2005b, 2014). Finally, equation (1) was used to obtain ground LSTs from the system radiance measurements taken at four azimuth angles and zenith angles of 162 or 135 degree (i.e., 18 or 45 degree from Nadir). These angles were selected because the radiometer footprints were entirely over the crop, avoiding ridges as mentioned before. Ground LST uncertainties were obtained as the quadratic sum of the ground LST dispersion for the different observations within a scan and the uncertainty calculated with the propagation through equation (1) of uncertainties in the input terms.

4. VALIDATION OF SATELLITE LST PRODUCTS

LST products generated from the METEOSAT Second Generation (MSG) Spinning Enhanced Visible and Infrared Imager (SEVIRI) and EOS Moderate Resolution Imaging Spectroradiometer (MODIS) data were validated against the ground LST data obtained by the system setup in the rice crop area.

4.1. MSG-SEVIRI LSA SAF LST product

We used the MSG-SEVIRI LSA SAF LST product (HDF5_LSASAF_MSG_LST), which is generated every 15 minutes by the EUMETSAT LSA SAF using an adaptation of the Generalized Split-Window algorithm proposed first by Wan and Dozier (1996) (Trigo et al. 2008, Niclòs et al. 2011). Concurrent MSG-SEVIRI LSA SAF LSTs and ground LST data retrieved from the system data as described in section 3.2 were compared every 15 minutes during two totally cloudless days (24 and 27 August, 2012). Ground data acquired by the system scan closest to the SEVIRI acquisition time over the experimental site were considered. Fig. 5 shows the diurnal cycle of the MSG-SEVIRI and ground LSTs for the 24 August, 2012. Ground LST error bars represent the measurement uncertainties and MSG-SEVIRI LST error bars were obtained from the LSA SAF LST product. Fig. 6 shows that MSG-SEVIRI LSA SAF LST product tends to overestimate the ground LSTs. Statistics of the differences between MSG-SEVIRI LSA SAF and ground LST values show a median of +0.6 K and a robust standard deviation ($RSD = 1.4826 \text{ median}(|\text{dif}_j - \text{median}(\text{dif}_j)|)$) of ± 1.0 K, which yields a quadratic sum of both values (R-RMSE) of ± 1.2 K. This comparison shows a LSA SAF LST product overestimation, but with an uncertainty, i.e., R-RMSE, within the expected values.

4.2. EOS-MODIS 11_L2 LST product

The MODIS LST/E 5-Minute L2 Swath 1 km product (MOD11_L2 and MYD11_L2 for MODIS onboard EOS Terra and EOS Aqua, respectively) was also validated with the ground data provided by the system (Fig. 7). This product, which is available at reverb.echo.nasa.gov, is also obtained with the Generalized Split-Window algorithm (Wan and Dozier 1996). Concurrent cloudless MODIS and ground LSTs were compared over a period of 18 days in summer of 2012, with full vegetation cover, and over a period of six months in 2012 and 2013 to include different surface covers (full vegetation cover, bare soil and flooded soil). In this case, not only the single pixel covering the system location was considered for the comparison, but also mean values for a 3×3 pixel array centered in the location. Statistical results show a negligible MODIS LST underestimation of $-0.10 \text{ K} \pm 1.3 \text{ K}$ (R-RMSE of $\pm 1.3 \text{ K}$) for 1 pixel and of $0.0 \text{ K} \pm 1.1 \text{ K}$ (R-RMSE of $\pm 1.1 \text{ K}$) for 3×3 pixels in the summer period, i.e., with full vegetation cover. Similar results were obtained for all land covers together, with slight underestimations and R-RMSE of $\pm 1.7 \text{ K}$ both for 1 pixel and the 3×3 pixel array.

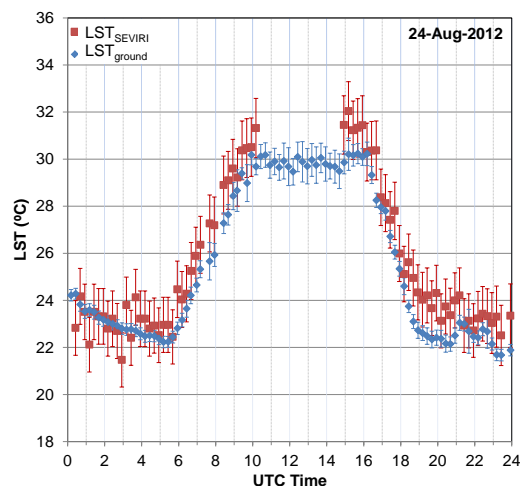


Fig. 5. Diurnal cycle of the MSG-SEVIRI LSA SAF and ground LST data for the 24 August, 2012.

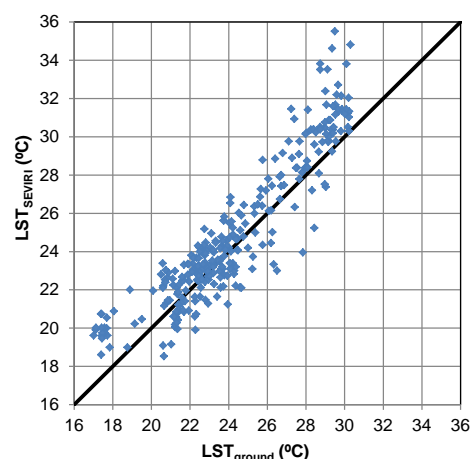


Fig. 6. LSA SAF LSTs against ground LST data.

5 CONCLUSIONS

The experimental data obtained by the angular system set up in an extensive and homogeneous area of rice-crop were used as ground-truth data to validate MSG-SEVIRI and EOS-MODIS LST products retrieved with the Generalized Split-Window algorithm (Wan and Dozier 1996). The first validation results showed that both products work with expected accuracies. However, an overestimation of $+0.6 \pm 1.0 \text{ K}$ (R-RMSE of $\pm 1.2 \text{ K}$) is observed for the MSG-SEVIRI LSA SAF LST product. A negligible underestimation is observed in the case of the EOS-MODIS 11_L2 LST product, with R-RMSEs from $\pm 1.3 \text{ K}$ to $\pm 1.7 \text{ K}$.

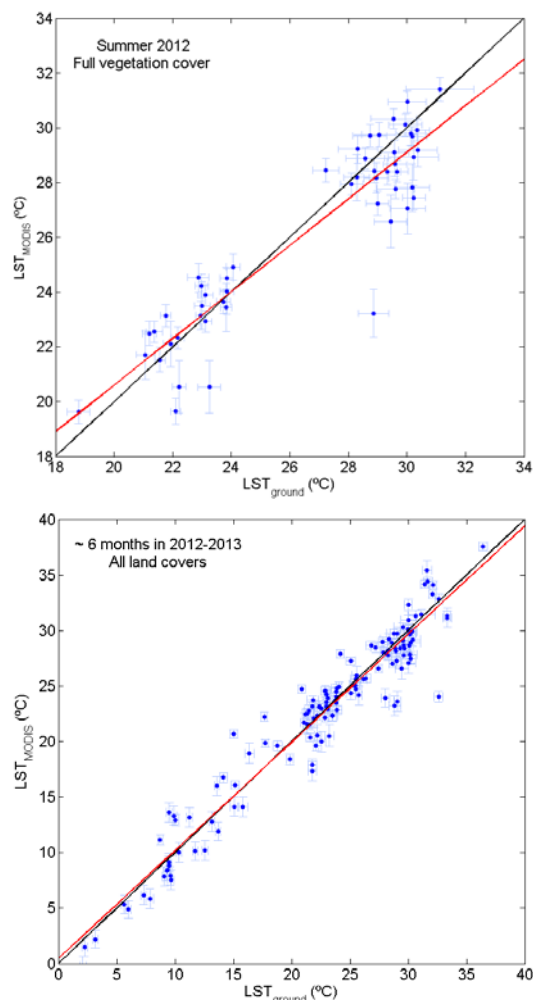


Fig. 7. MOD/MYD11_L2 LSTs against ground LSTs for a full vegetation cover in summer (top) and all land covers (bottom).

6 ACKNOWLEDGMENTS

This study was supported by the Spanish Ministerio de Economía y Competitividad (project CGL2011-30433-C02-02/01; and Dr. Niclòs “Ramón y Cajal” Research Contract). The Instituto Universitario CEAM-UMH is partly supported by the Generalitat Valenciana.

7 REFERENCES

Fiebrich, C.A., Martinez, J.E., Brotzge, J.A., and Basara, J.B., 2003, The Oklahoma Mesonet's skin temperature network. *Journal of Atmospheric and Oceanic Technology*, 20, 1496-1504.

Coll, C., Caselles, V., Galve, J.M., Valor, E., Niclòs, R., Sánchez, J.M., and Rivas, R., 2005, Ground measurements for the validation of land surface temperatures derived from AATSR and MODIS data, *Remote Sensing of Environment*, 97, 288-300.

Coll, C., Caselles, V., Galve, J.M., Valor, E., Niclòs, R., and Sánchez, J.M., 2006, Evaluation of split-window and dual-angle correction methods for land surface temperature retrieval from Envisat/AATSR data. *Journal of Geophysical Research*, 111, 12105 doi 10.1029/2005JD006830.

Mira, M., Schmugge, T.J., Valor, E., Caselles, V. and Coll, C., 2009, Comparison of thermal emissivities retrieved with the two-lid box and TES methods with laboratory spectra. *IEEE Transactions on Geoscience and Remote Sensing*, 47(4):1012-1021.

Niclòs, R., Caselles, V., Coll, C., Valor, E., and Sánchez, J.M., 2005a, In situ surface temperature retrieval in a boreal forest under variable cloudiness conditions. *International Journal of Remote Sensing*, 26(18), 3985-4000.

Niclòs, R., Valor, E., Caselles, V., Coll, C., and Sánchez, J.M., 2005b, In situ angular measurements of thermal infrared sea surface emissivity – Validation of models. *Remote Sensing of Environment*, 94(1), 83-93.

Niclòs, R., Galve, J.M., Valiente, J.A., Estrela, M.J. and Coll, C., 2011, Accuracy assessment of land surface temperature retrievals from MSG2-SEVIRI data, *Remote Sensing of Environment*, 115, 2126-2140.

Niclòs, R., Doña, C., Bisquert, M., and Valor, E., 2014, Thermal-infrared emissivity characterization of crude and seawater, *IEEE Transactions on Geoscience and Remote Sensing*, 52(9), 5387-5395.

Theocharous, E., Usadi, E., and Fox, N.P., 2010, NPL Report OP3: CEOS comparison of IR brightness temperature measurements in support of satellite validation. Part I: Laboratory and ocean surface temperature comparison of radiation thermometers; National Physical Laboratory (NPL); Teddington, UK.

Trigo, I.F., Monteiro, I.T., Olesen, F., and Kabsch, E., 2008, An assessment of remotely sensed land surface temperature. *Journal of Geophysical Research*, 113 (D17108), doi: 10.1029/2008JD010035.

Wan, Z., and Dozier, J., 1996, A generalized split-window algorithm for retrieving land surface temperature from space, *IEEE Transactions on Geoscience and Remote Sensing*, 34(4), 892-905.

Calibration of Landsat-8 TIRS Bands with Ground-Truth Data over Different Land Covers at the Valencia Test Site

Raquel Niclòs¹, Juan M. Sánchez², José A. Valiente³, Maria J. Barberà¹, César Coll¹, Vicente Caselles¹, and Diego Caselles¹

¹ Earth Physics and Thermodynamics Department, University of Valencia, 50 Dr. Moliner, E-46100 Burjassot (Spain).

² Applied Physics Department, University of Castilla-La Mancha, 1 Pl. Manuel Meca, E-13400 Almadén (Spain).

³ Instituto Universitario Centro de Estudios Ambientales del Mediterráneo – CEAM-UMH, 14 Charles Darwin, E-46980 Paterna (Spain).

Raquel.niclos@uv.es

ABSTRACT- The Landsat-8 (L8) was launched on February 2013, and operational acquisitions started in middle April 2013. The L8 Thermal Infrared Sensor (TIRS) has two thermal bands aimed to provide more accurate Land Surface Temperatures (LST). The first studies by the L8 calibration team showed TIRS temperature offsets using reference data measured in water bodies, and in November 2013 they proposed subtracting $0.29 \pm 0.12 \text{ Wm}^{-2}\text{sr}^{-1}\mu\text{m}^{-1}$ ($\sim 2.1 \pm 0.8 \text{ K}$) and $0.5 \pm 0.2 \text{ Wm}^{-2}\text{sr}^{-1}\mu\text{m}^{-1}$ ($\sim 4.4 \pm 1.8 \text{ K}$) from radiances measured by band 10 and 11, respectively, and in February 2014 the L8 TIRS archive was reprocessed to remove the offsets. The aim of this study is to contribute to the L8 TIRS calibration efforts. Ground LST data measured along transects performed in a 100 km², flat and thermally homogeneous area of rice-crop fields close to Valencia-Spain (Valencia Test Site) were used to evaluate the calibration of the L8 thermal bands. Different surface conditions were covered during the measurement period, from flooded soil (water surface) to dry bare soil, with LSTs ranging from 10 °C to 40 °C, and a variety of environmental condition. Although more measurements are required, the first results show that the reprocessed L8 TIRS brightness temperatures underestimate the simulated brightness temperatures in both thermal bands using the LST data acquired in the Valencia Test Site as reference.

1 INTRODUCTION

The Landsat Data Continuity Mission (LDCM), renamed Landsat-8 (L8), was launched on February 2013, and operational acquisitions started middle April 2013. The L8 Thermal Infrared Sensor (TIRS) has two thermal bands, 10 (11.60-11.19 μm) and 11 (11.50-12.51 μm), aimed to provide more accurate Land Surface Temperatures (LST) than the Landsat-7 ETM+, at 100-m spatial resolution. The on-board calibration of the L8 TIRS was monitored by the L8 calibration team over water bodies and the first results showed TIRS temperature offsets. In November 2013, the L8 calibration team proposed subtracting $0.29 \pm 0.12 \text{ Wm}^{-2}\text{sr}^{-1}\mu\text{m}^{-1}$ ($\sim 2.1 \pm 0.8 \text{ K}$) and $0.5 \pm 0.2 \text{ Wm}^{-2}\text{sr}^{-1}\mu\text{m}^{-1}$ ($\sim 4.4 \pm 1.8 \text{ K}$) from radiances measured by band 10 and 11, respectively, with a root mean square variability for the recalibration of $\pm 0.12 \text{ Wm}^{-2}\text{sr}^{-1}\mu\text{m}^{-1}$ ($\pm 0.8 \text{ K}$) and $\pm 0.2 \text{ Wm}^{-2}\text{sr}^{-1}\mu\text{m}^{-1}$ ($\pm 1.8 \text{ K}$) for bands 10 and 11, respectively (landsat.usgs.gov). The offsets represent an average error introduced by stray light coming from outside the TIRS field of view for temperatures between 10-30 °C. Due to the larger calibration uncertainty associated with band 11, it was

recommended that users refrain from relying on band 11 data in quantitative analysis of the TIRS data, such as the use of split window techniques for atmospheric correction to retrieve LSTs. In February 2014, the entire L8 archive was reprocessed to remove these calibration offsets (TIRS digital numbers being modified). The aim of this study is to contribute to the TIRS calibration efforts using ground LST measurements performed in the Valencia Test Site concurrently to L8 overpasses.

2 DATA AND METHODOLOGY

2.1 Experimental site and ground data

The Valencia Test Site is a $\sim 100 \text{ km}^2$, flat and thermally homogeneous area of rice-crop fields (39.267°N, -0.308°E in WGS-84, at sea level) close to Valencia-Spain (Niclòs et al. 2011, Coll et al. 2012). Flooded soil (water surface) to dry bare soil covers were considered for the study to enlarge the LSTs range from around 10 °C to 40 °C, and account for a variety of environmental conditions. Four TIR radiometers were used to perform the transects: two CIMEL CE 312-1 with four bands (8–13, 11.5–12.5,

10.5–11.5, and 8.2–9.2 μm) and two CIMEL CE 312-2 with six bands (8–13, 8.1–8.5, 8.5–8.9, 8.9–9.3, 10.3–11.0, and 11.0–11.7 μm) (www.cimel.fr). The CE 312 radiometers showed uncertainties within ± 0.2 K for all bands at 20–30 $^{\circ}\text{C}$ (Coll et al. 2012). The radiometers were carried back and forth along transects of 100m in length, and temperatures measured within 3 min centered at the satellite overpass time were averaged as a compromise between sufficient sampling and not introducing too much temporal variability. Downwelling sky radiance was also measured to account for the atmospheric correction of the ground measurements. Emissivity measurements were also performed in field conditions using different techniques depending on the land cover on the L8 acquisition date (Mira et al. 2009, Sánchez et al. 2011): the Temperature-Emissivity Separation (TES) method, the Box Method, and a portable infrared Designs & Prototypes 102 spectroradiometer (2–16 μm). Water surface emissivities considered for flooded surface conditions were obtained from Niclòs et al. (2005a, 2014). The standard deviation of the ground LSTs in each transect was calculated as a measure of the spatial and temporal LST variability and the quadratic sum of this deviation and the standard deviation of the data measured by the four radiometers was used to show the LST variability in the test site (from $\pm 0.3\text{K}$ to $\pm 1.7\text{K}$ depending on the surface cover)

2.2 L8 TIRS data

Six daytime L8 scenes were acquired over the Valencia Test Site between January and June 2014 (see Table 1), and were downloaded from the United States Geological Survey EROS Data Center (earthexplorer.usgs.gov). L8 thermal band data are given as 16-bit digital numbers (DN) that are calibrated to at-sensor radiances ($L_{\text{sen},i}$) as:

$$L_{\text{sen},i} = M_{Li} \text{DN}_i + A_{Li} \quad (1)$$

where M_{Li} are band-specific multiplicative rescaling factors, and A_{Li} are band-specific additive rescaling factors (see Table 2). The brightness temperature, T_{bi} , is obtained from the at-sensor radiance as:

$$T_{bi} = \frac{k_{2i}}{\ln\left(\frac{k_{1i}}{L_{\text{sen},i}} + 1\right)} \quad (2)$$

where k_{1i} and k_{2i} are band-specific thermal conversion constants (Table 2). The location of the Valencia Test Site falls within two different L8 paths (198 and 199) and a single row (33), although the cloudy events at the test site limited the available data. The processing level of the scenes was L1T, which provides systematic radiometric and geographic accuracy using

ground control points and digital elevation model as well. Data were collected at 100 m spatial resolution but resampled to match the OLI spectral bands using cubic convolution to 30 m.

2.3 Methodology

The MODTRAN-5 radiative transfer model (Berk et al., 2006), together with re-analysis atmospheric profiles from the National Center for Environmental Prediction (NCEP), interpolated to the site location, date and time, were used to calculate the atmospheric transmittance and emitted radiance in the spectral range of the L8 TIR bands. Atmospheric transmittance (τ_{λ}) and radiance emitted towards the sensor (L_{λ}^{\uparrow}) were obtained at nadir. We also calculated the downwelling atmospheric radiance, $L_{\lambda}^{\downarrow}(\theta)$, at twelve zenith angles from $\theta=0^{\circ}$ to 89° , which were used to obtain the hemisphere-integrated downwelling radiance. The radiance measured by the sensor, L_i , can be simulated using the atmospheric transmittance and emitted radiances (forward simulation). L_i can be approximated for a surface at temperature LST and with emissivity ε_i using:

$$L_i = [\varepsilon_i B_i(\text{LST}) + (1 - \varepsilon_i) L_i^{\downarrow}] \tau_i + L_i^{\uparrow} \quad (3)$$

The brightness temperature, T_{bi} , corresponding to the simulated at-sensor radiance L_i is usually lower than the LST in (3) due to atmospheric and emissivity effects. Equation (3), with $\tau_i=1$ and $L_i^{\uparrow}=0$, was used to correct the ground measurements from emissivity and downwelling radiance effects, with the emissivities measured in field conditions.

Table 1. L8 TIRS scenes used in the study.

Case	Date, UTC time, path/row	Surface condition
1	January 27, 10:45, 199/33	Flooded
2	February 12, 10:44, 199/33	Wet bare soil
3	March 16, 10:44, 199/33	Dry bare soil (non-tilled)
4	April 10, 10:37, 198/33	Dry bare soil (tilled)
5	May 3, 10:43, 199/33	Dry bare soil (tilled)
6	June 4, 10:43, 199/33	Flooded

Table 2. Band-specific rescaling factors, and thermal conversion constants.

TIRS band i	M_{Li}	A_{Li}	k_{1i}	k_{2i}
10	0.000334	0.1	774.89	1321.08
11	0.000334	0.1	480.89	1201.14

The hemisphere-integrated downwelling radiance defined was calculated as the radiance measured by the CE 312 radiometers at zenith multiplied by a factor (of around 1.5) dependent on the spectral band and the atmospheric water vapor content (Nicolòs et al. 2005b, García-Santos et al. 2012), which was estimated from the NCEP profiles. Equation (3) was also used to derive the LST from the satellite-measured at-sensor radiance L_i (inverse simulation).

3 RESULTS AND DISCUSSION

Ground measurements were compared with L8 TIRS data for the vicarious calibration of bands 10 and 11. This comparison was performed in terms of: a) L8 TIRS at-sensor brightness temperatures, T_{bi} , and radiances, L_i (forward simulation), and b) at-surface temperatures, LSTs (inverse simulation). In the first case, L8 TIRS L_i values were simulated using (3) with LST being the ground-measured temperature. The atmospheric parameters required in (3) were simulated for the TIRS bands using NCEP atmospheric profiles and the MODTRAN 5 model as explained in section 2.3. Emissivity values for the L8 TIRS bands were estimated for each surface condition from the CE 312-1 (CE 312-2) measurements, described in section 2.1, at the 10.5–11.5 μm (10.3–11.0 μm) and 11.5–12.5 μm (11.0–11.7 μm) bands, respectively (see in Table 2).

Table 3 shows the ground-measured LSTs, LST_g , with standard deviations from $\pm 0.3\text{K}$ to $\pm 1.7\text{K}$, together with the emissivities used for bands 10 and 11 in each case, depending on the land cover, for which uncertainties of ± 0.007 were obtained. Table 4 shows the L8 TIRS acquired L_i and T_{bi} . With the purpose of calibrating the original data acquired by the L8 TIRS (data without reprocessing), the abovementioned recalibration radiance offsets, removed with the reprocessing, were added to the TIRS data after February 3, 2014. L8 TIRS data shown in Table 3 were obtained from mean values of DN in a 17 x 17 pixel array around the geographic coordinates of the test site. Since TIRS data are resampled from 100m to 30m, a 17 x 17 pixel array was used to cover the extension of 5 x 5 original pixels. Very similar results were obtained for one pixel due to the thermal homogeneity of the experimental site, as the low spatial variation in 17 x 17 pixel shown in terms of T_{bi} proves ($< 0.4\text{ K}$ in all cases). Figure 1 shows L_i simulated from LST_g (forward simulation) against L8 TIRS L_i for both thermal bands (with and without the reprocessing), together with linear regression equations that can be used as recalibration equations to adjust L8 TIRS L_i . Table 5 shows the statistical results (mean (bias), standard deviation (SD) and quadratic sum of bias and SD (RMSE)) of the differences between L_i and T_{bi} values measured by the L8 TIRS

without reprocessing and simulated from LST_g data, both for 17 x 17 pixels and 1 pixel. Close results were obtained in both cases due to the thermal homogeneity of the site. Table 5 shows the statistics when using the reprocessed data for 17 x 17 pixels. As shown in Figure 1 and Table 5, L8 TIRS L_{10} and T_{b10} without reprocessing are just slightly higher than those simulated from LST_g in the Valencia Test Site, with differences of $0.06 \pm 0.09\text{ W m}^{-2}\text{ sr}^{-1}\mu\text{m}^{-1}$ in L_{10} and $0.5 \pm 0.6\text{ K}$ in T_{b10} , instead of $0.29 \pm 0.12\text{ W m}^{-2}\text{ sr}^{-1}\mu\text{m}^{-1}$ and $\sim 2.1 \pm 0.8\text{ K}$ estimated with ground data measured in water bodies by the L8 Calibration Team. A significant L8 TIRS overestimation is observed for band 11, with differences of $0.27 \pm 0.08\text{ W m}^{-2}\text{ sr}^{-1}\mu\text{m}^{-1}$ in L_{11} and $2.3 \pm 0.7\text{ K}$ in T_{b11} without reprocessing. The L8 Calibration Team also pointed out the existence of a significant offset in band 11 data, which was even larger than the values obtained in our site ($0.5 \pm 0.2\text{ W m}^{-2}\text{ sr}^{-1}\mu\text{m}^{-1}$ and $\sim 4.4 \pm 1.8\text{ K}$). However, a common underestimation of $\sim 0.24 \pm 0.09\text{ W m}^{-2}\text{ sr}^{-1}\mu\text{m}^{-1}$ in L_i and $\sim 2.0 \pm 0.7\text{ K}$ in T_{bi} is obtained for both bands when using the reprocessed L8 TIRS data (see in Table 6), as a consequence of the removal of higher offsets than required for our test site in the reprocessing.

The comparison between L8 TIRS data and ground measurements was also performed in terms of at surface temperature LST (inverse simulation). In this case, TIRS radiances were corrected for the emissivity and atmospheric effects to obtain a LST value from each band, LST_i , by solving (3) for LST. The obtained LSTs were compared with the ground-measured LSTs, LST_g . Table 7 shows the LSTs obtained from the L8 TIRS data shown in Table 3. L_i values of 17x 17 pixels are used in this case, with very similar values for one pixel. Figure 2 also shows LST_g against LST_i obtained from the L8 TIRS radiances (with and without reprocessing), together with linear regression equations. The LST_i values obtained from TIRS data without reprocessing overestimate the ground data in both bands, but mainly for band 11, with a mean difference of $2.9 \pm 0.9\text{ K}$ (with RMSE of $\pm 3.1\text{ K}$). However, LST_i values obtained from the TIRS data after the reprocessing underestimate the ground data in $2.0 \pm 0.8\text{ K}$ and $2.7 \pm 0.9\text{ K}$ for bands 10 and 11, respectively.

Table 3. Ground LST data, LST_g , and emissivities.

Case	LST_g (°C)	ϵ_{10}	ϵ_{11}
1	12.7 ± 0.3	0.991	0.985
2	15.3 ± 0.6	0.977	0.978
3	27.6 ± 1.3	0.959	0.959
4	36.8 ± 1.7	0.958	0.956
5	40.1 ± 1.1	0.969	0.963
6	30.6 ± 0.9	0.991	0.985

Table 4. L8 TIRS radiances L_i and brightness temperatures T_{bi} with and without the reprocessing (in italics).

Case	L_{10} ($W\ m^{-2}\ sr^{-1}\ \mu m^{-1}$)	T_{b10} ($^{\circ}C$)	L_{11} ($W\ m^{-2}\ sr^{-1}\ \mu m^{-1}$)	T_{b11} ($^{\circ}C$)
1	7.39 (7.68)	10.2 (12.5)	6.85 (7.36)	8.5 (13.2)
2	7.46 (7.75)	10.8 (13.1)	6.92 (7.43)	9.1 (13.8)
3	8.88 (9.17)	21.7 (23.8)	8.11 (8.62)	19.8 (24.2)
4	9.70 (9.99)	27.6 (29.6)	8.74 (9.25)	25.2 (29.4)
5	10.60 (10.88)	33.6 (35.5)	9.46 (9.97)	31.1 (35.1)
6	9.38 (9.67)	25.3 (27.4)	8.45 (8.96)	22.8 (27.0)

Table 5. Statistical results of the differences between L_i and T_{bi} values measured by the L8 TIRS (without reprocessing) and simulated from LST_g for 17 x 17 pixel array (and 1 pixel).

	L_{10} ($W\ m^{-2}\ sr^{-1}\ \mu m^{-1}$)	T_{b10} ($^{\circ}C$)	L_{11} ($W\ m^{-2}\ sr^{-1}\ \mu m^{-1}$)	T_{b11} ($^{\circ}C$)
bias	0.06 (0.06)	0.5 (0.4)	0.27 (0.27)	2.3 (2.3)
SD	0.09 (0.11)	0.6 (0.8)	0.08 (0.09)	0.7 (0.7)
RMSE	0.11 (0.13)	0.8 (0.9)	0.28 (0.29)	2.4 (2.4)

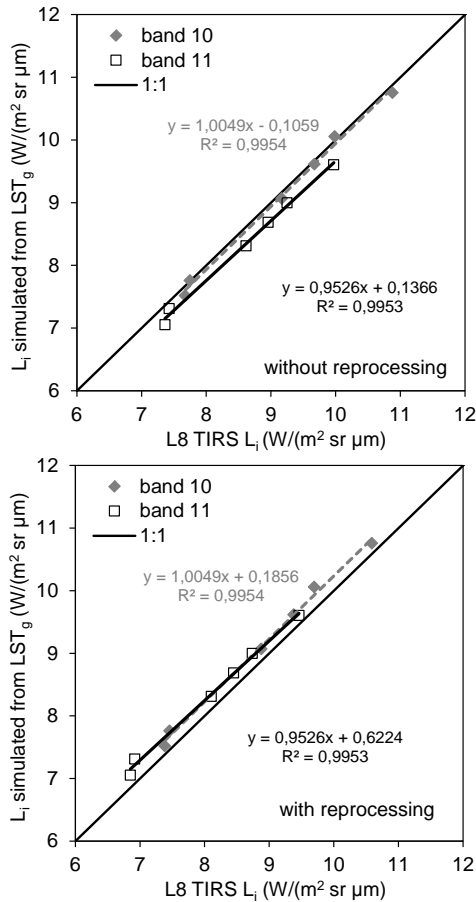


Fig. 1. Radiances simulated from LST_g against L8 TIRS radiances for band 10 and 11 without (top) and with reprocessing (bottom), together with linear regression equations.

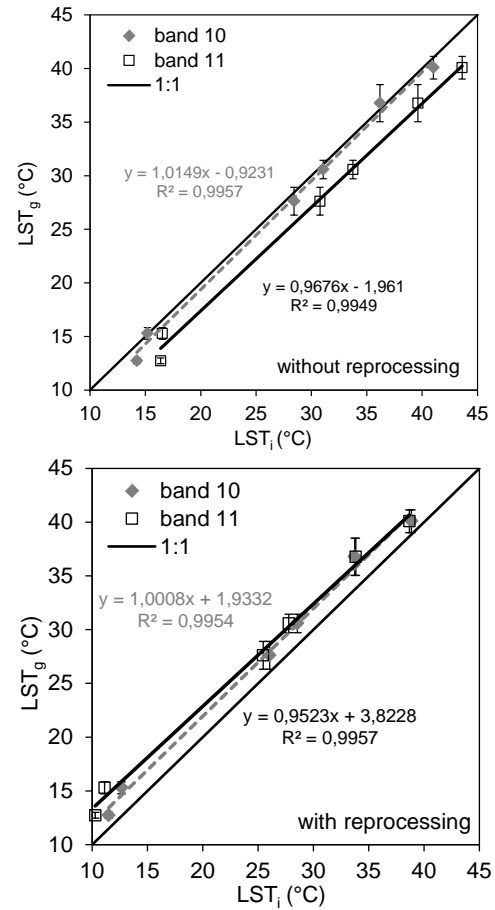


Fig. 2. Ground-measured LST_g against LST_i obtained from the L8 TIRS radiances without (top) and with reprocessing (bottom), together with linear regression equations.

Table 6. Statistical results of the differences between L_i and T_{bi} values measured by the L8 TIRS (with the reprocessing) and simulated from LST_g for 17x17 pixel array.

	L_{10} ($W\ m^{-2}\ sr^{-1}$ μm^{-1})	T_{b10} ($^{\circ}C$)	L_{11} ($W\ m^{-2}\ sr^{-1}$ μm^{-1})	T_{b11} ($^{\circ}C$)
bias	-0.23	-1.7	-0.24	-2.1
SD	0.09	0.6	0.08	0.8
RMSE	0.25	1.8	0.25	2.3

Table 7. Statistical results of the differences between LST_i obtained from the L8 TIRS radiances L_i with and without reprocessing (in *italics*) and LST_g for 17 x 17 pixel array.

	$LST_{10} - LST_g$ ($^{\circ}C$)	$LST_{11} - LST_g$ ($^{\circ}C$)
bias	-2.0 (0.5)	-2.7 (2.9)
SD	0.8 (0.8)	0.9 (0.9)
RMSE	2.1 (0.9)	2.8 (3.1)

4 CONCLUSIONS

At-sensor radiances and brightness temperatures were simulated for the L8 TIRS band 10 and 11 from ground LST measurements taken in the Valencia Test Site with different surface conditions given by the rice-crop phenology. They were compared with the L8 TIRS data acquired over the test site on the six cloudless dates from January to June 2014. Differences between L8 TIRS data without reprocessing and simulated values from ground LST were obtained, which showed L8 TIRS overestimations for both thermal bands for the site, with slight overestimation for band 10 (0.5 ± 0.6 K in terms of brightness temperature) and significant overestimation for band 11 (2.3 ± 0.7 K). The L8 Calibration Team observed different overestimations for the TIRS bands in water bodies, of $\sim 2.1 \pm 0.8$ K and $\sim 4.4 \pm 1.8$ K for bands 10 and 11, respectively, in terms of brightness temperatures, and reprocessed the TIRS data archive to remove the corresponding radiance offsets. Consequently, L8 TIRS data after reprocessing underestimate the brightness temperatures simulated from ground-measured LSTs in the Valencia Test Site in 1.7 ± 0.6 K and -2.1 ± 0.8 K for bands 10 and 11, respectively. Nevertheless, more ground measurements (e.g., including rice-crop vegetation covers) are required to confirm the calibration results.

5 ACKNOWLEDGMENTS

This study was supported by the Spanish Ministerio de Economía y Competitividad (projects CGL2011-30433-C02-02/01, CGL2013-46862-C2-01/02; and Dr. Niclòs "Ramón y Cajal" Research Contract) and Generalitat Valenciana (PROMETEU/2014/086).

The Instituto Universitario CEAM-UMH is partly supported by the Generalitat Valenciana. The authors thank the assistance of the students involved in the experimental campaign.

6 REFERENCES

- Berk, A., Anderson, G.P., Acharya, P.K., L.S. Bernstein, L. Muratov, J. Lee, M. Fox, S.M. Adler-Golden, J.H. Chetwynd, M.L. Hoke, R.B. Lockwood, J.A. Gardner, T.W. Cooley, C.C. Borel, P.E. Lewis & E.P. Shettle., 2006. "MODTRAN5: 2006 Update," Proc. SPIE, Vol. 6233, 62331F.
- Coll, C., Caselles, V., Valor, E. and Niclòs, R., 2012, Comparison between different sources of atmospheric profiles for land surface temperature retrieval from single channel thermal infrared data. *Remote Sensing of Environment*, 117, 199-210.
- García-Santos, V., Galve, J.M., Valor, E., Caselles, V., and Coll, C., 2013, Estimation of atmospheric water vapour content from direct measurements of radiance in the thermal infrared region. *Remote Sensing Letters*, 3(1), 31-38.
- Mira, M., Schmugge, T.J., Valor, E., Caselles, V. and Coll, C., 2009, Comparison of thermal emissivities retrieved with the two-lid box and TES methods with laboratory spectra. *IEEE Transactions on Geoscience and Remote Sensing*, 47(4):1012-1021.
- Niclòs, R., Valor, E., Caselles, V., Coll, C., and Sánchez, J.M., 2005a, In situ angular measurements of thermal infrared sea surface emissivity – Validation of models. *Remote Sensing of Environment*, 94(1), 83-93.
- Niclòs, R., Caselles, V., Coll, C., Valor, E., and Sánchez, J.M., 2005b, In situ surface temperature retrieval in a boreal forest under variable cloudiness conditions. *International Journal of Remote Sensing*, 26(18), 3985-4000.
- Niclòs, R., Galve, J.M., Valiente, J.A., Estrela, M.J. and Coll, C., 2011, Accuracy assessment of land surface temperature retrievals from MSG2-SEVIRI data, *Remote Sensing of Environment*, 115, 2126-2140.
- Niclòs, R., Doña, C., Bisquert, M., and Valor, E., 2014, Thermal-infrared emissivity characterization of crude and seawater. *IEEE Transactions on Geoscience and Remote Sensing*. 52(9), 5387-5395.
- Sánchez, J.M., French, A.N., Mira, M., Hunsaker, D.J., Thorp, K.R., Valor, E., and Caselles, V., 2011, Thermal infrared emissivity dependence on soil moisture in field conditions. *IEEE Transactions on Geoscience and Remote Sensing*, 49, 4652-4659.

Validation of a Forage Production Index derived from MODIS fCover time series - Methodology and main results

A. Roumiguie⁽¹⁾, A. Jacquin⁽¹⁾, G. Sigel⁽²⁾, H. Poilvé⁽²⁾, and O. Hagolle⁽³⁾

¹ Université de Toulouse, Institut National Polytechnique de Toulouse, Ecole d'Ingénieurs de Purpan, UMR 1201 DYNAFOR, France.

² AIRBUS Defence and Space, France.

³ CESBIO UMR 5126 CNES-UPS-CNRS-IRD; Toulouse, France.

Antoine.Roumiguie@purpan.fr

ABSTRACT - An index-based insurance solution is developed to estimate and monitor the near real-time forage production in France. It is based on an indicator called the Forage Production Index - FPI -, used as a surrogate of the grassland production, corresponding to the integral of the Fraction of green Vegetation Cover derived from medium spatial resolution - MR - remotely-sensed time series images and calculated at the scale of an elementary unit of 3600ha. The scope of this paper is to present the method implemented for the scientific validation of this indicator and the main results. An up-scaled approach is chosen based on a direct and an indirect validation, by comparing the FPI respectively with biomass ground data and high spatial resolution - HR - time series. The experimental site is localized in the Lot and Aveyron provinces, in the South-West of France. Two types of data are collected: biomass ground measurements of grassland plots over 28 farms for years 2012 and 2013; 26 and 17 HR images covering the Lot province respectively in 2013 and 2014. The coefficients of determination are medium to low which are explained by various factors affecting the quality of the validation data. In the perspective of the Sentinel-2 data availability, this study provides valuable information on the strengths and weaknesses to develop index-based insurance product from HR time series images.

1 INTRODUCTION

An index-based insurance solution is developed by Pacifica Crédit Agricole Assurances and AIRBUS Defence & Space to estimate and monitor the near real-time forage production in France. It is based on an indicator called Forage Production Index (FPI). FPI is derived from the Fraction of green Vegetation Cover (fCover) integral and used as a surrogate of the forage production (Equation 1).

$$FPI_n = \sum_{i=01/02}^{i=31/10} (fCover_{Grassland_i} - i \times NPf) \quad (1)$$

The FPI is calculated for year n and is the sum of daily fCover between February 1st and October 31st ($fCover_i$) from which a part characterising the proportion of non-productive vegetation (NPf) is subtracted.

fCover is a biophysical parameter obtained from medium spatial resolution (MR) MODIS / MERIS time series. It is calculated with Overland Software application developed by AIRBUS Defence & Space. This tool extracts biophysical parameters from vegetation by inverting a radiative transfer model while simultaneously considering scene and atmosphere models (Poilvé, et al. 2012). OverlandTM is built on recognized biophysical models (Jacquemoud, et al., 2009), LOWTRAN (Kneizys, et al., 1988) for the atmospheric component and PROSPECT (Jacquemoud and Baret, 1990) and SAIL

(Verhoef, 1984) for the vegetation component. The soil reflectance, which is needed as an input to the SAIL model, is obtained by capturing a spectral signature of the local soil from the satellite image, then by considering that this reflectance may locally vary, both in time and space, depending on wetness and roughness of the soil surface. This processing makes it possible to obtain biophysical parameter images of vegetation while taking into account characteristics of both sensors and directional conditions (Sun and viewing angles).

Because one MR pixel may contain different types of land cover, a spectral unmixing model based on a statistical approach is applied to determine fCover time series for grassland (Di Bella, et al., 2004). Consequently, FPI is calculated at an Elementary Unit (EU) scale of 3600 ha. In the insurance product, payouts are indexed on the ratio between the annual FPI and the Olympic average of FPI of the last five years.

For efficiently using the FPI in the insurance product, a validation of the remote sensing information produced is mandatory. An ad hoc two-step validation protocol has been defined. In the first step, a direct comparison between in-situ grassland biomass measurements and FPI derived from high spatial resolution (HR) fCover time series was conducted. Results indicate that fCover can be successfully used as a proxy of grassland biomass production

(Roumiguie et al. In revision). The second step consists of assessing whether the ratio of annual FPI can be used to estimate interannual biomass variation at a kilometric scale. Because the validation of MR satellite products still remains a challenge, a bottom-up validation approach is designed to deal with the change scale issue, based on the recommendations of Baret, et al. (2006), Morissette, et al. (2006), Weiss, et al. (2007) and Camacho, et al. (2013). At a defined EU, ratio of annual FPI obtained with MR fCover grassland time series (Δ FPI MR) are compared to those derived from production data (direct validation) and from HR fCover grassland time series (indirect validation). Hereafter, the objectives are first to describe the method used for the second validation step of the FPI and, then, to present the results. The study site is located in the Aveyron and Lot provinces, in the South-West of France. This agricultural region is focused in livestock farming. Grassland is a key element of the landscape and covers approximately 43 % of the provinces' surface.

2 DIRECT VALIDATION

Direct validation consists in evaluating the performance of the ratio of annual FPI derived from MR fCover grassland time series (Δ FPI MR) to estimate interannual biomass variation, with comparing it to actual production data.

2.1.1 Production data

Biomass production measurements are realized during 2012 and 2013 in 28 farms located in the study site. The dataset contains 275 (605 ha in 2012) and 541 (1278 ha in 2013) natural and temporary grassland plots. On each plot, and for each mowing period, the biomass production expressed in dry matter is estimated by multiplying the total number of bales of hay harvested with the average yield of one bale. To obtain this latter data, measurements of weight and moisture are realized with a pallet scale and a portable moisture meter on around 5% of the bales from each plot. Then, the annual biomass production estimation of the plot ($Production_{Plot}$) corresponds to the sum of the biomass production observed during each mowing period. Finally, a $Production_n$ index is computed using Equation 2 in which $Surface$ is the area of a plot. It provides the annual biomass production estimation at a defined EU level in tones of Dry Matter.

$$Production_n = \frac{\sum_1^j (Production_{Plot_i} \times Surface_i)}{\sum_1^j (Surface_i)} \quad (2)$$

2.1.2 Method of analysis

At the EU level, the Δ FPI MR index given by the Equation 3 is correlated with the Δ Production index characterizing the variation of biomass estimated by production data (Equation 4). For both indexes, the

period of monitoring is the same. It starts from February 1st and ends the day the plots are harvested for the last time in the EU. This information is defined thanks to the ground observations collected.

$$\Delta FPI MR = \frac{FPI_{MR 2013}}{FPI_{MR 2012}} \quad (3)$$

$$\Delta Production = \frac{Production_{2013}}{Production_{2012}} \quad (4)$$

The relationships between the indexes are quantified using the coefficient of determination (R^2) and the root mean square error (RMSE). The difficulty of acquiring data over a large scale and the necessity to create a representative sample of grassland requires a new shape of the EU. In each area where plots data are collected in 2012 and 2013, the surface of the EUs is decreased (from 3600 ha to 1152 ha) and their limit are drawn according to the spatial distribution of the plots sampled (Figure 1). As a consequence, the percentage of grassland sampled is higher (from 2% for EU of 3600 ha to 14% for resized EU of 1152ha). It may also improve the quality of the biomass production estimations from the plots data. A total of 13 EUs of 1152 ha are analyzed.

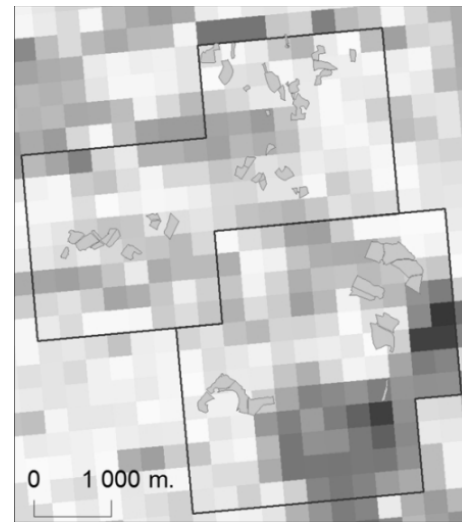


Figure 1. Examples of new EUs designed for FPI direct validation.

2.1.3 Results

Figure 2 presents the relationship between Δ FPI MR and Δ Production. The coefficient of determination is equal to 0.45 and the RMSE to 0.49. The level of sensitivity is similar. The variability observed is between 0.6 and 2.4 for Δ FPI MR and ranges from 0.9 to 2.1 for Δ Production.

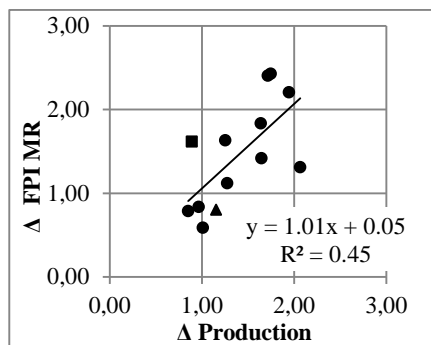


Figure 2. Scatterplot of the linear regression between ΔFPI_{MR} and $\Delta Production$ measured on 13 resized EUs of 1152ha for 2012 and 2013.

In 11 of the 13 EUs (illustrated by dots on Figure 2), ΔFPI_{MR} varies in the same way as the $\Delta Production$. The two others EUs (symbolized by a square and a triangle on Figure 2) correspond to situations with opposite responses of indexes: a triangle when the production measured is higher in 2013 than 2012 while the FPI_{MR} is lower in 2013 than 2012; a square for the contrary. These results should be interpreted with caution regarding the limited number of EUs monitored in this experiment.

In the direct validation of the FPI, the collection of production data is time-consuming and can lead to considerable expenditure. In consequence, it is not easy to replicate these accurate measurements over a large area. So, an indirect validation is carried out with HR remote sensing data.

3 INDIRECT VALIDATION

Indirect validation consists in assessing the performance of the ratio of annual FPI derived from HR and MR fCover grassland time series to estimate interannual biomass variation, without comparing them to production data. In this part, the study site is reduced to the Lot province because of the HR images time series spatial coverage.

3.1.1 HR fCover grassland time series

In 2013, 26 HR images from four different sensors acquired between February 16th and October 10th are analyzed (Spot-6: 2 images @ 6 m; DEIMOS: 1 image @ 22 m; Landsat-8: 12 images @ of 30 m; Spot-4: 11 images @ 20 m). In 2014, 17 HR images (14 Landsat-8 images and 3 DEIMOS images) acquired between February 2nd and September 1st are processed. Spot-4 images are supplied by Centre National d'Etudes Spatiales (CNES) in the framework of the Take-Five program. Spot-6 and DEIMOS images are delivered by AIRBUS Defence & Space and Landsat-8 by USGS. All images – supplied orthorectified – are re-projected in Extended Lambert-2 and re-sampled to a resolution of 10m.

For all images, the OverlandTM software developed by AIRBUS Defence & Space is applied to identify cloud free pixels and to calculate their fCover. For the specific case of the SPOT-4 images that are pre-processed in “top of atmosphere” reflectance (Level 1C) in the framework of the Take Five program, a modification to the OverlandTM processing algorithm is required to convert TOA reflectance to radiance before producing the biophysical variables.

In order to be consistent with the FPI_{MR} , only HR fCover pixels belonging to grassland plots within the EUs analyzed are selected. The register of declaration made by the farmers in the context of CAP Policies is used to identify the grassland plots. Last version available is updated in 2012. From this land cover database, we define as grassland all plots classified as natural or temporary grassland, moors and heathland. Then, HR fCover is scaled-up, first at the grassland plot level, for all grassland plots containing at least 60% of their surface covered by fCover information, and, second, at the EU level, by computing a weighted average of HR fCover grassland plot values contained in an EU. From this process, it results a HR fCover grassland time series composed of a variable number of images for each EU depending on the cloud cover. For the indirect validation, we only keep EUs that present a missing HR fCover period no longer than 40 days. On the Lot province, from 178 potential EUs, we analyze 69 due to an important cloud cover in 2013. For those EUs, an interpolation function – spline method - is applied between each HR fCover data to obtain daily HR fCover. Finally, the calculation of FPI_{HR} is carried out at the EU level using Equation 1.

3.1.2 Method of analysis

The relationship of ΔFPI_{MR} (given by Equation 5) with FPI computed from HR fCover images (ΔFPI_{HR} given by the Equation 6) is assessed. The indexes are summed from March 1st to August 1st according to the temporal coverage of the HR images time series in 2013 and 2014.

$$\Delta FPI_{MR} = \frac{FPI_{MR} 2014}{FPI_{MR} 2013} \quad (5)$$

$$\Delta FPI_{HR} = \frac{FPI_{HR} 2014}{FPI_{HR} 2013} \quad (6)$$

As for the direct validation, the relationships between the indexes are quantified using the coefficient of determination (R^2) and RMSE.

The indirect validation presents two major advantages compared to the direct. The surfaces of grassland monitored are larger and all the grassland plots within an EU are fully identified as illustrated on Figure 3. Therefore, the number of analyzed EUs is more important and, consequently, the quality of the statistical analysis is improved

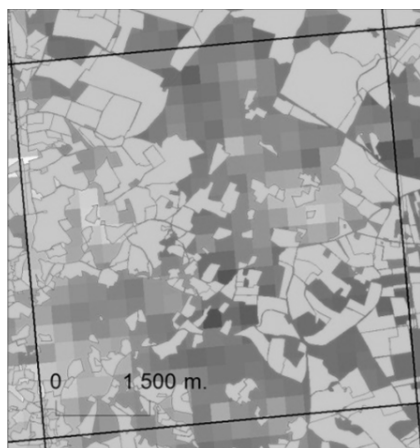


Figure 3. Example of grassland plots within an EU used for FPI indirect validation.

3.1.3 Results

Fig. 4 illustrates the scatterplot of the linear regression between FPI_{HR} and FPI_{MR} for 2013 and 2014.

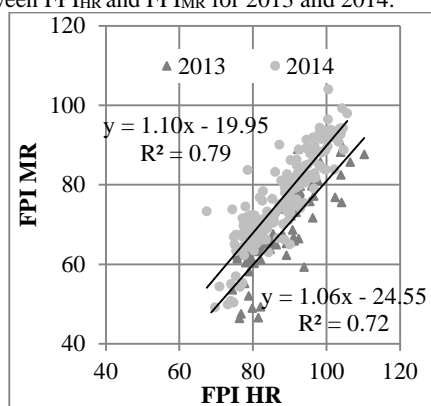


Figure 4. Scatterplot of the linear regression between FPI_{HR} and FPI_{MR} and measured on 69 and 173 EUs of 3600ha for 2013 and 2014.

The slopes of the equations are close to 1 with a coefficient of determination equal to 0.72 in 2013 and 0.79 in 2014. These results tend to demonstrate that FPI_{MR} is highly correlated with FPI_{HR} . But there is still existing variability. RMSE attached to the linear regression of 2013 and 2014 data are equal to 5.95 and 5.17. The percentage of grassland surface in the EU is one explanation. Figure 5 illustrates the relationship between 2014 FPI_{HR} and FPI_{MR} according to the percentage of grassland surface in the EU for the 69 EUs where data are available for both years. The variability decreases as the percentage of grassland surface increases (from 8% to 71%). For the study of the ΔFPI relation, only the 34 EUs with more than 40% of their surface in grassland are selected to limit the error coming from the annual FPI.

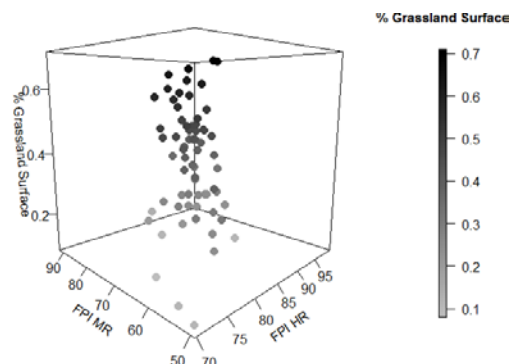


Figure 5. Linear regression for 2014 between FPI_{MR} and FPI_{HR} according to the percentage of grassland surface in the EU for 69 EUs of 3600 ha.

Then, RMSE of 2013 is slightly higher than the one of 2014. The different number of EUs used for the analysis may have an influence: $n=69$ in 2013 whereas $n=173$ in 2014. Indeed, the year 2013 was cloudy and, even though the number of acquired images is higher than in 2014 (26 images in 2013 vs 17 in 2014), the time series is less regular and locally, the period without HR fCover data can be longer than 40 days (threshold fixed to allow interpolation of daily fCover between two dates).

Hereafter, ΔFPI_{MR} and ΔFPI_{HR} are compared. Fig. 6 presents the scatterplot of the relation obtained. ΔFPI_{HR} ranges between 0.94 and 1.11 while the ΔFPI_{MR} is between 0.92 and 1.01. The variability seems to be slightly better for the index calculated from HR than from MR images (0.17 in HR vs 0.09 in MR). Then, the coefficient of determination is low ($R^2 = 0.27$) compared to the one obtained in the direct validation ($R^2 = 0.45$). It can be explained by the poor variability of biomass production observed between 2013 and 2014 (range of $\Delta FPI_{MR} = 0.09$) compared to the one recorded between 2012 and 2013 (range of $\Delta FPI_{MR} = 1.8$).

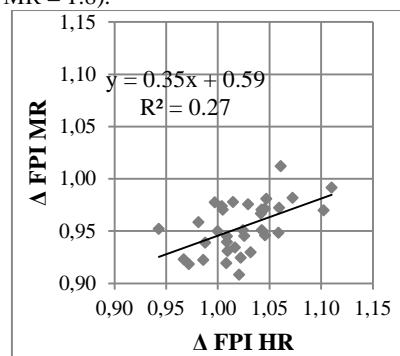


Figure 6. Scatterplot of the linear regression between ΔFPI_{MR} and ΔFPI_{HR} measured on 34 EUs of 3600ha characterized by at least 40% of their surface in grassland for 2013 and 2014.

4 CONCLUSION

Within the development of the index-based insurance product, this paper presents a bottom-up approach to validate the potential to use the ratio of annual FPI as a surrogate of the interannual biomass variation at a kilometric scale.

Results with the validation dataset collected in the Lot and Aveyron provinces during the period 2012-2014 lead to two major conclusions.

Validating MR satellite products directly with production data remains very difficult. Results obtained in the case of the FPI validation ($R^2=0.45$) could be qualified as good if we consider the various sources of uncertainty included in the dataset used. Collecting enough production data with a high quality of biomass measurement to meet the requirements for a statistical meaningful dataset at the scale of a 3600ha Elementary Unit is very difficult. A significant effort was engaged within this experiment (275 plots in 2012 and 541 in 2013). To be able to monitor this high number of plots, a compromise was made on the method to measure the biomass, resulting in a decrease of the quality of the data collected. Despite this effort, at the 3600ha EU scale, the sampling rate stayed low (an average of 2%). To reach a more satisfying grassland sample rate, the EUs were resized according to the spatial distribution of the grassland plots. Nevertheless, there is a remaining bias linked to the non-randomly selection of the plots within an EU. Plots belong to one or two farmers. As a consequence, the representativeness of the production data may not be guaranteed.

Validating MR satellite products indirectly with HR comparable products gives satisfaction. The number of EUs studied is increased (from 13 EUs of 1152ha in the direct validation to 69 EUs of 3600ha in the indirect validation), improving the robustness of the analysis. In addition, results of the relation between annual FPI computed from HR or MR fCover grassland time series are very good ($R^2=0.72$ in 2013 and $R^2=0.79$ in 2014). Concerning the results of the relation between ratios of annual FPI computed from HR or MR fCover grassland time series, it is not possible to make conclusions for one major reason: the biomass production in 2013 was very similar to the one of 2014 for this study site. An additional analysis is thus undergoing on the forage production area of the Crau region (South-East of France) where a HR fCover grassland time series is available for many years.

Above all, in the perspective of HR data time series accessibility (Landsat-8, SPOT-4 Take 5, SPOT-5 Take5, Sentinel-2), the methodology implemented and the results gave valuable information on the strengths and weaknesses to develop the index in the insurance product with the FPI_{HR} .

5 REFERENCES

- Baret, F., J.T. Morisette, R.A. Fernandes, J.L. Champeaux, R.B. Myneni, J. Chen, et al. 2006. Evaluation of the representativeness of networks of sites for the global validation and intercomparison of land biophysical products: proposition of the CEOS-BELMANIP. *Geoscience and Remote Sensing, IEEE Transactions on* 44: 1794-1803. doi: 10.1109/TGRS.2006.876030.
- Camacho, F., J. Cernicharo, R. Lacaze, F. Baret and M. Weiss. 2013. GEOV1: LAI, FAPAR essential climate variables and FCOVER global time series capitalizing over existing products. Part 2: Validation and intercomparison with reference products. *Remote Sens. Environ.* 137: 310-329. doi: <http://dx.doi.org/10.1016/j.rse.2013.02.030>.
- Di Bella, C., R. Faivre, F. Ruget, B. Seguin, M. Guerif, B. Combal, et al. 2004. Remote sensing capabilities to estimate pasture production in France. *International Journal of Remote Sensing* 25:5359-5372. doi:10.1080/01431160410001719849.
- Jacquemoud, S. and F. Baret. 1990. PROSPECT: A model of leaf optical properties spectra. *Remote Sens. Environ.* 34: 75-91. doi: [http://dx.doi.org/10.1016/0034-4257\(90\)90100-Z](http://dx.doi.org/10.1016/0034-4257(90)90100-Z).
- Jacquemoud, S., W. Verhoef, F. Baret, C. Bacour, P.J. Zarco-Tejada, G.P. Asner, et al. 2009. PROSPECT+SAIL models: A review of use for vegetation characterization. *Remote Sens. Environ.* 113, Supplement 1: S56-S66. doi: <http://dx.doi.org/10.1016/j.rse.2008.01.026>.
- Poivlé, H. 2012. BioPar Product User Manual - MERIS FR products. GEOLAND2. 50p.
- Kneizys, F.X., S. E.P., W.O. Gallery, A. L.W., S. J.E.A., C. J.H., et al. 1988. Users Guide to Lowtran 7 Air Force Geophysics Laboratory.
- Morisette, J.T., F. Baret, J.L. Privette, R.B. Myneni, J.E. Nickeson, S. Garrigues, et al. 2006. Validation of global moderate-resolution LAI products: a framework proposed within the CEOS land product validation subgroup. *Geoscience and Remote Sensing, IEEE Transactions on* 44: 1804-1817. doi:10.1109/TGRS.2006.872529.
- Roumiguié A., Jacquin A., Sigel G., Poivlé H., Lepoivre B. and Hagolle O., In revision. Development of an index-based insurance product: Validation of a Forage Production Index derived from medium spatial resolution fCover time series. *Giscience & Remote Sensing*.
- Verhoef, W. 1984. Light-Scattering by leaf layers with application to canopy reflectance modeling - The SAIL Model. *Remote Sens. Environ.* 16: 125-141. doi:10.1016/0034-4257(84)90057-9.
- Weiss, M., F. Baret, S. Garrigues and R. Lacaze. 2007. LAI and FAPAR CYCLOPES global products derived from VEGETATION. Part 2: validation and comparison with MODIS collection 4 products. *Remote Sens. Environ.* 110: 317-331. doi:<http://dx.doi.org/10.1016/j.rse.2007.03.001>.

BEAM 5 and Sentinel Toolbox functions for image analysis and validation purposes

Ana B. Ruescas, Norman Fomferra, Carsten Brockmann
Brockmann Consult GmbH
ana.ruescas@brockmann-consult.de

ABSTRACT With the requirement to create an open platform for scientists and operational users as well as software developers, ESA laid the foundation for a sustainable and successful open-source software development project, BEAM. The Sentinel toolboxes will build on this heritage and will be both a toolbox supporting a wide range of optical sensors for Earth Observation and a development platform that allows users to easily create their own visual and data processing tools.

1 INTRODUCTION

BEAM is an open-source toolbox and development platform for viewing, analysing and processing of remote sensing raster data. Originally developed to facilitate the utilisation of image data from Envisat's optical instruments, BEAM now supports a growing number of other raster data formats such as GeoTIFF and NetCDF as well as data formats of other EO sensors such as MODIS, AVHRR, LANDSAT, AVNIR, PRISM and CHRIS/Proba. Various data and algorithms are supported by dedicated extension plug-ins.

ESA is developing three new open source toolboxes for the scientific exploitation of the Sentinel-1, Sentinel-2 and Sentinel-3 missions. The toolboxes are based on the Sentinel Application Platform (SNAP) which is the evolution of the proven ESA BEAM/NEST architecture inheriting all current BEAM and NEST functionality, including multi-mission support for SAR and optical missions to support ESA and third party missions to come.

In this paper, the attention is focused on the presentation of the newest BEAM 5 functionalities for analysis and validation of data, together with the introduction of the SNAP Sentinel 2 and Sentinel 2 Toolboxes.

2. BEAM 5.0

The latest version of BEAM was released in May 2014. Some of the newest tool developments for analysis and validation of data – made in the framework of several ESA and EU projects – are briefly explained and illustrated in this section.

A general impression of the BEAM software components can be summarized in three points:

- VISAT - An intuitive desktop application to be used for visualization, analysis and processing of remote sensing raster data.

- A set of scientific tools running either from the command line or invoked by VISAT, entirely written in Java.
- A rich Java API for the development of new remote sensing applications and BEAM extension plug-ins.

2.1. Analysis Tools

Improved Spectrum View Tool

When an image is open, it is possible to inspect the spectra for one or several given pixel positions. This can be done by opening the Spectrum View tool and moving the cursor over the image view. The spectrum view will display the spectra for the current pixel position. Now it is possible to change the symbol and line style of a spectrum. This is especially useful when working with different pixel positions (for instance, related to different surfaces in the image) when plotting the spectra selected and saved with the pin manager (Figure 1). While the mouse cursor is moved around a region in the image, the diagram axes are automatically adjusted according to the min/max values of the displayed spectral band values

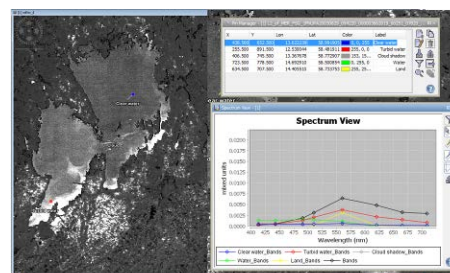


Figure 1. The spectrum view has been extended to display multiple spectra at the same time, and each with its own style

Magic Wand

A new tool called Magic Wand has been implemented. The purpose of this tool is allows to create region of interests (ROIs) within images comprising pixels that are similar to a set of manual picked pixels. The similarity takes into account any number of bands or the entire spectra. Different similarity metrics are provided which may operate either on the derivative, integral or the plain spectrum.

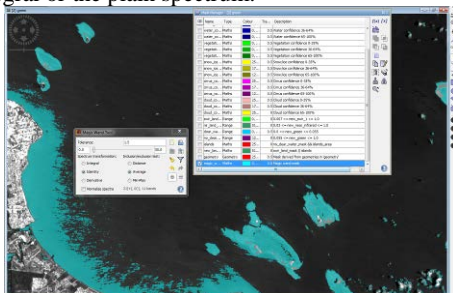


Figure 2 Shallow areas close to the coast and around small islands selected with the Magic Wand tool and saved as a mask

ROI Statistics Tool

Basic statistics can now be simultaneously estimated in several ROIs, combining the vector importing and the statistics tool. One image has to be read before importing the vector data (for instance ESRI shape files with water bodies as the ones shown in Figure 3). The set of statistical information displayed comprises:

- The total number of pixel.
- The minimum/maximum geophysical value
- The arithmetic mean of the geophysical value.
- The standard deviation of the geophysical value.
- Several percentile thresholds.

Additionally, two diagrams are displayed: the histogram and the thresholds for all percentiles.

In command line mode, there is a Statistics Operator which allows the calculation and exports individual spreadsheets as output for each ROI.

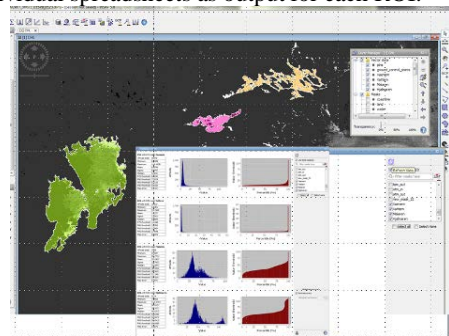


Figure 3. ROIs imported as ESRI shape files for three lakes in Sweden. Statistics and diagrams are calculated by ROI using the “Use ROI mask” option

2.2 Validation Tools

Correlative Plot

It allows plotting an imported variable against a raster variable. The parameter (i.e. a ship track) has to be imported into the opened raster image first. It is possible to select an existing or new defined ROI mask to filter the data to be displayed.



Figure 4. Correlative plot of in situ data vs. image pixel values. Several options are available for the display, including the box or macropixel size, tolerance range and regression line

Pixel Extraction Tool

The tool allows to extracts pixel values given by a user-specified list of geographic coordinates from a prearranged list of data products. A number of additional parameters must be passed to the tool: the size of the area around the geographic coordinate (macropixel size), the time difference allowed (if looking for match-ups) or the valid pixel expression to filter the appropriate data. The output generated is a comma separated value file, with averages per macropixel (if pre-selected) or raw data per pixel. It writes a file for each product type found in the list of data used. It is also possible to export sub-scenes containing at least all coordinates found in one product

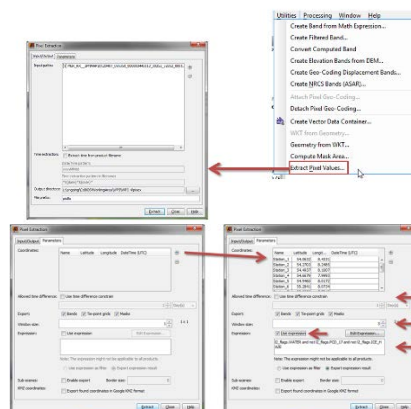


Figure 5. Input and output panes of the Pixel Extraction tool

Time Series Tool

Within the Time Series Tool, a time series is specified by several source products and variables. Every product comprising remote sensing bands is used as a source product. However, all products need to share at least one remote sensing band or variable, in order to create a meaningful time series. This tool consists of four modules: the time series manager, the time series graph, the matrix and the player. It is a complex and powerful tool for managing and visualisation of parameter on a spatio-temporal scale.

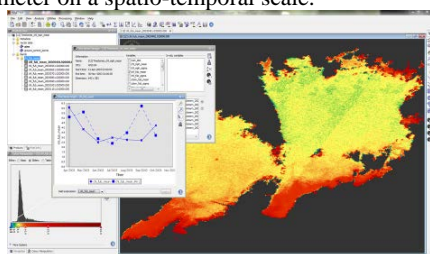


Figure 6. Time Series Manager and Graph of the chlorophyll_a parameter on Lake Vanern in Sweden

3 SENTINEL-2 TOOLBOX

The Sentinel-2 toolbox is an evolution of BEAM which supports the Sentinel-2 products (L1b, L1c) and which includes ESA processors to Level 2A. This comprises the cloud screening and the atmospheric correction. The BEAM data model will evolve to support the multi-resolution bands of Sentinel-2, already available in the last version of the Landsat reader in BEAM 5. The development of the tool is led by C-S France, who brings in the rich high resolution analysis functionality of the Orpheo ToolBox (Inglada et al., 2009).

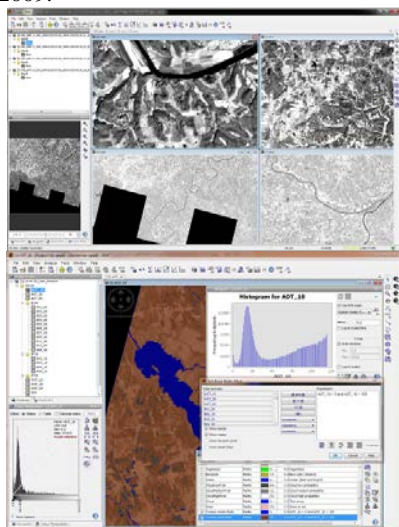


Figure 7 Sentinel-2 MSI Level-1C and L2A test datasets in the Sentinel-2 Toolbox

4. SENTINEL-3 TOOLBOX

The Sentinel-3 toolbox is an evolution of BEAM with specific support of the optical instruments on Sentinel 3, OLCI and SLSTR. The Sentinel-3 Toolbox supports all products including L1b, L2 and the synergy product L1c combining OLCI and SLSTR bands. It also exploits the uncertainty information provided along with the upcoming Sentinel 3 data products and which are standard ancillary datasets for most of the ESA CCI's essential climate variables.

Important processors from BEAM are adapted to the Sentinel-3 products (Case2Regional, CoastColour, fAPAR, etc.) and new processors will be made available, such as the SST processor from Reading University. Brockmann Consult is leading the Sentinel-3 Toolbox development

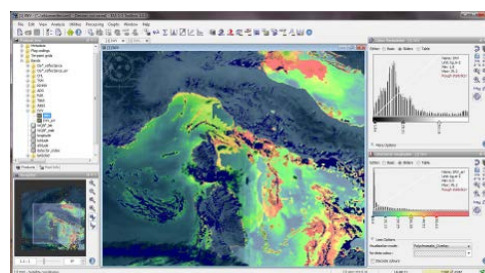


Figure 8. The uncertainty information plotted on a scene using the polychromatic overlay option

5. SENTINEL APPLICATION PLATFORM

The Sentinel-1, -2 and -3 toolboxes are based on a common development platform, SNAP. The 3 development teams meet regularly in a dedicated developer forum, under leadership of Brockmann Consult, to agree on a common development plan and technical details. External partners, like NASA (SeaDAS development) will join the developer forum.

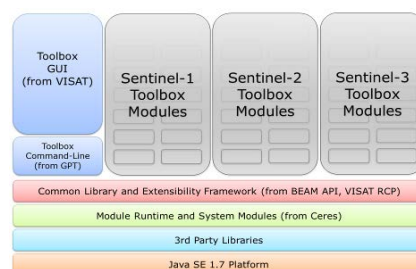


Figure 9: SNAP concept and structure

6. TOOLBOXES BATCH PROCESSING & THE CALVALUS SYSTEM

The Graph Processing Framework (GPF) allows constructing directed acyclic graphs (DAG) of

processing nodes. A node in the graph refers to a GPF operator, which implements the algorithm to be executed. The node also has the role to configure the operation by specifying the source nodes and providing values for the processing parameters. Many operators are included in the GPF: data binning, collocation, merging, mosaicking, PCA, Pixel Extraction, Statistics Operator, etc.

The CALVALUS processing system is based on Apache Hadoop and BEAM technology. In addition to various other bulk processing workflows, CALVALUS allows for mission wide matchup extractions and trend analyses including on-the-fly execution of BEAM GPF processors and Unix programs.

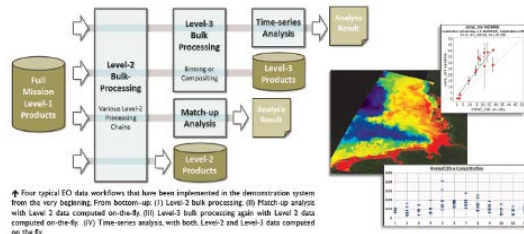


Figure 10. Complete mission processing is possible using the CALVALUS system

7. REFERENCES

BEAM:

<http://www.brockmann-consult.de/cms/web/beam>
 Inglada, J.; Christophe, E., "The Orfeo Toolbox remote sensing image processing software," Geoscience and Remote Sensing Symposium, 2009 IEEE International, IGARSS 2009, vol.4, no., pp.IV-733, IV-736, 12-17 July 2009
 doi: 10.1109/IGARSS.2009.5417481
 URL: <http://ieeexplore.ieee.org/stamp/stamp.jsp?tp=&arnumber=5417481&isnumber=5417310>

SEADAS: <http://seadas.gsfc.nasa.gov/>

SNAP project :

<https://sentinel.esa.int/web/sentinel/toolboxes/jsessionid=157B677586E79734AA95F1A3188DB7D8.eodisp-prod4040>

Consistency assessment of PROBA-V and SPOT-VEGETATION GEOV1 LAI, FAPAR and FCover products for the continuity of the Copernicus Global Land Service.

J. Sánchez ⁽¹⁾, F. Camacho ⁽¹⁾, R. Lacaze ⁽²⁾, B. Smets ⁽³⁾

⁽¹⁾ EOLAB, Parc Científic Universitat de València. Catedrático José Beltrán, 2. 46980 Paterna (Valencia), Spain, ⁽²⁾ HYGEOS, Toulouse, France, ⁽³⁾ VITO, Mol, Belgium.

jorge.sanchez@eolab.es

ABSTRACT - This study investigates the scientific quality of the GEOV1 Leaf Area Index (LAI), Fraction of Absorbed Photosynthetically Active Radiation (FAPAR) and Fraction of Vegetation Cover (FCover) products based on PROBA-V observations. The procedure follows, as much as possible, the guidelines, protocols and metrics defined by the Land Product Validation (LPV) group of the Committee on Earth Observation Satellite (CEOS) for the validation of satellite-derived land products. This study is focused on the consistency of SPOT/VGT and PROBA-V GEOV1 products developed in the framework of the Copernicus Global Land Services, providing an early validation of PROBA-V GEOV1 products using data from November 2013 to May 2014. Several criteria of performance were evaluated including product completeness, spatial consistency, temporal consistency, intra-annual precision and accuracy. Firstly, and inter-comparison with both spatial and temporal consistency were evaluated with reference satellite products (SPOT/VGT GEOV1 and MODIS C5) are presented over a network of sites (BELMANIP2.1). Secondly, the accuracy of PROBA-V GEOV1 products was assessed against a number of agricultural sites. The ground data was collected in the context of the FP7 ImagineS project in support of the evolution of Copernicus Land Service. Our results demonstrate that GEOV1 PROBA-V products were found spatially and temporally consistent with similar products (SPOT/VGT, MODIS C5), and good agreement with limited ground truth data with overall performance (RSME) of 0.75 for LAI, 0.07 for FAPAR and 0.1 for FCover.

1 INTRODUCTION

From 1st January 2013, the Copernicus Global Land Service is operational, providing in near real time a set of biophysical variables over the whole globe. Leaf Area Index (LAI), Fraction of Absorbed Photosynthetically Active Radiation (FAPAR) and Fraction of Vegetation Cover (FCover) are delivered at 1 km resolution and 10-days frequency. These vegetation biophysical variables play a key role in several surface processes, including photosynthesis, respiration and transpiration. The first version of LAI, FAPAR and FCover variables, called GEOV1, was based on SPOT/VGT observation until the end of the mission in May 2014 (Baret et al., 2013). A SPOT/VGT GEOV1 archive of 15 years is now available (1999-2014) at the Global Land service. The continuity of the GEOV1 products is based on PROBA-V observations at 1 km. To provide continuity of the variables at 1km, the processing chains are to be updated towards the new PROBA-V mission which started its lifetime in November, 2013. Although the sensor of the latter mission is very compatible with the former mission, a spectral correction is to be performed to continue the 15-year time series at 1km resolution in a consistent manner.

Therefore a pre-processing module is developed that performs next to the spectral correction a transformation of the new PROBA-V input data into SPOT-VGT compatible input data. Validation of PROBA-V GEOV1 is thus mandatory before delivering the products to the users.

This paper describes the main results of the early scientific quality assessment of PROBA-V GEOV1 LAI, FAPAR, FCover products. This preliminary validation is focused on the consistency with SPOT/VGT GEOV1 products during the overlap period (November 2013 - May 2014). MODIS C5 LAI/FPAR products are also considered for the intercomparison

The procedure follows the guidelines and metrics defined by the Land Product Validation (LPV) group of the Committee on Earth Observation Satellite (CEOS) for the validation of satellite-derived land products. Several criteria of performance were evaluated including product completeness, spatial consistency, temporal consistency, intra-annual precision and accuracy.

The accuracy of PROBA-V GEOV1 products was evaluated against a number of agricultural sites. The ground data was collected in the context of the FP7 ImagineS project (<http://fp7-imagines.eu>) in support of

the evolution of Copernicus Land Service (Camacho et al., this issue).

The quality assessment method is briefly described in Section 2. Section 3 shows the main results; conclusions are provided in Section 4.

2 QUALITY ASSESSMENT METHOD

Several criteria of performance were assessed in agreement with previous global LAI validation exercises (Camacho et al., 2013), the OLIVE (On Line Validation Exercise) tool hosted by CEOS cal/val portal (Weiss et al., 2014), and with the recent CEOS LPV Global LAI product validation good practices (Fernandes et al., 2014). First and intercomparison with the existing global products was conducted to examine the spatial and temporal consistency of GEOV1 PROBA-V products. Second, a direct validation approach was conducted using found reference maps to quantify the overall uncertainties of the products.

2.1 Intercomparison Approach

The reference global satellite products used are: GEOV1 based on SPOT/VGT observations (Baret et al., 2013) and Terra MODIS LAI/FAPAR (MOD15A2) collection 5 (Yang et al., 2006).

The products were intercompared over the BELMANIP2.1 (Weiss et al., 2014) network of sites that was designed to represent globally the variability of land surface types. Furthermore, the products are analysed for 6 generic classes, namely: Evergreen Broadleaf Forest, Evergreen Deciduous Forest, Needle-leaf Forest, Croplands, Herbaceous and Shrub/Sparse/Bare Areas. The different products must be compared over a similar spatial support area and temporal support period. The intercomparison was conducted using an average value over 3x3 pixels to reduce coregistration errors between products and differences in their sensor Point Spread Function (PSF) which determines the actual footprint of the data. The temporal support period for the quantitative assessment is 10-days with monthly composites. The original temporal sampling was used for compute missing values, histograms and the smoothness.

The following criteria of performance and metrics are assessed:

- **Product Completeness:** corresponds to the absence of spatial and temporal gaps in the data. Temporal variations of GEOV1 missing values for SPOT/VGT and PROBA-V LAI products have been computed over the whole images.
- **Spatial Consistency:** can be quantitatively assessed by comparing the spatial distribution of a reference validated product with the product under study. Global histograms of residuals at a monthly basis were analyzed. This analysis is complemented by

the analysis of Probability Density Function (PDFs) of retrievals per biomes.

- **Temporal Consistency:** The consistency of temporal variations of the vegetation variables are qualitatively analyzed as compared to reference validated products.
- **Intra-annual precision (smoothness):** corresponds to temporal noise assumed to have no serial correlation within a season. In this case, the anomaly of a product LAI value from the linear estimate based on its neighbors can be used as an indication of intra-annual precision or smoothness. It can be characterized as suggested by Weiss et al., (2014): for each triplet of consecutive observations, the absolute value of the difference between the center $P(d_{n+1})$ and the corresponding linear interpolation between the two extremes $P(d_n)$ and $P(d_{n+2})$ was computed:

$$\delta = \left| P(d_{n+1}) - P(d_n) - \frac{P(d_n) - P(d_{n+2})}{d_n - d_{n+2}} (d_n - d_{n+1}) \right| \quad (1)$$

Histograms of the smoothness are presented adjusted to a negative exponential function. The exponential decay constant is used as quantitative indicator of the typical smoothness value.

- **Relative Uncertainties:** The inter-comparison of products offers an indirect means of assessing uncertainties (systematic or random) between products. The global statistical analysis is performed over BELMANIP2.1 sites considering all the dates available.

2.2 Direct Validation

The accuracy assessment was performed against ground truth data processed according to CEOS LPV guidelines for validation of LAI products. The data set used to validate is the ground data collected in the framework of the ImagineS project over agricultural sites for the period under study. Up-scaling of ground data was achieved with high-resolution satellite image using an empirical transfer function (Camacho et al., 2014, this issue). Four additional sites were made available for the accuracy assessment for 2014 coming from FP7 ImagineS (Table 1).

Site Country	Lat (deg)	Lon (deg)	Land Cover	Dates	LAI	FAPAR	FCover
25Mayo_1 Argentina	-37.907	-67.75	Crop	02/14	1.30	0.39	0.32
25Mayo_2 Argentina	-37.939	-67.79	Shrub	02/14	0.42	0.19	0.16
LaReina Spain	37.82	-4.86	Crops	05/14	1.08	0.30	0.29
Albufera Spain	39.2743	-0.316	Crops	06/14	0.58	0.22	0.182
				08/14	5.78	0.85	

Table 1: Characteristics of the validation sites from ImagineS project for 2014 and associated ground biophysical values.

Due to the limited number of concomitant ground measurements, the number of ground reference maps was increased by using data from a different year (forest and grassland sites) from Camacho et al., 2013 and from CEOS OLIVE Cal/Val portal. These sites have been filtered by analyzing the stability of the temporal variations of MODIS C5 FAPAR products. Only the stable forest and grassland sites have been used.

3 RESULTS

3.1 Product Completeness

Figure 1 shows the temporal evolution of missing values for SPOT/VGT and PROBA-V GEOV1 LAI products. Over the six month overlap period (November 2013 - May 2014), SPOT/VGT and PROBA-V provides consistent results, with SPOT/VGT showing a slightly better fraction of valid observations (around 5%). It can be partly explained due to the different overpass time between PROBA-V and SPOT/VGT satellites.

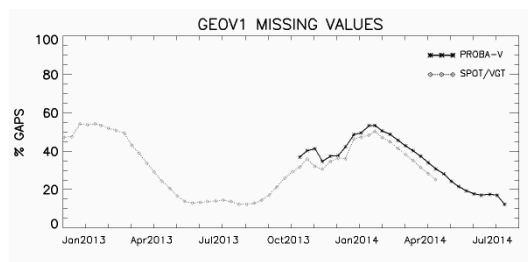


Figure 1: Temporal variations of GEOV1 missing values for SPOT/VGT and PROBA-V LAI products.

The length of the missing values, evaluated over BELMANIP2.1 sites (Figure 2), shows very similar distributions for PROBA-V and SPOT/VGT GEOV1 products, with around 50% of the gaps shorter than 30 days. On the other hand, the length of the gaps in MODIS C5 is shorter, with around 60% of gaps corresponding to one missing observation.

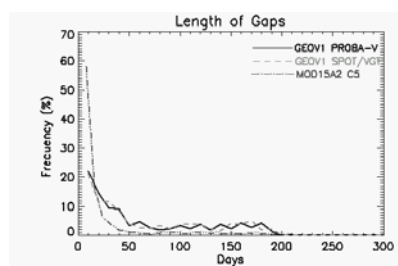


Figure 2: Distribution of the temporal length of the missing values over BELMANIP2.1 sites during the

Nov13-May14 period for PROBA-V GEOV1, SPOT/VGT GEOV1 and MODIS C5 products.

3.2 Histograms of residuals

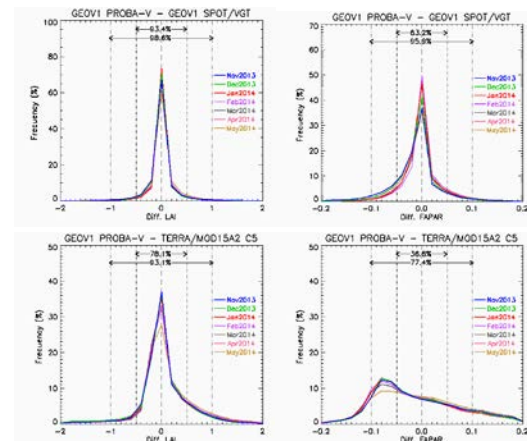


Figure 3: Distribution of differences between PROBA-V and SPOT/VGT GEOV1 (Top) and between PROBA-V GEOV1 and MODIS C5 (Bottom) for LAI (Left side) and FAPAR (right side) products.

Histograms of differences among the global products under study were analyzed monthly (Figure 3). For LAI differences, above 93% of values (in average) are within ± 0.5 LAI units for all the dates evaluated, which corresponds with a good spatial consistency, and 98% of difference values lies between ± 1 LAI units between both GEOV1 products (PROBA-V and SPOT/VGT). PROBA-V GEOV1 and MODIS C5 LAI differences are larger with a 78% of values between ± 0.5 and 93% between ± 1 LAI units. For FAPAR, a good agreement is found between PROBA-V and SPOT/VGT GEOV1 products with a percentage around 83% of differences within ± 0.05 and up to 96% for the ± 0.1 interval, which means also quite good consistency, but showing an asymmetric histogram with a slight negative bias (i.e. larger FAPAR values from SPOT/VGT observations). Large spatial discrepancies were found between PROBA-V GEOV1 and MODIS C5 global products. The histogram of residual shows the peak around -0.075 and large scattering (Figure 3), 77% of FAPAR differences belong to the ± 0.1 interval, and only 36% of difference values lies between ± 0.05 .

3.3 Distribution of retrievals

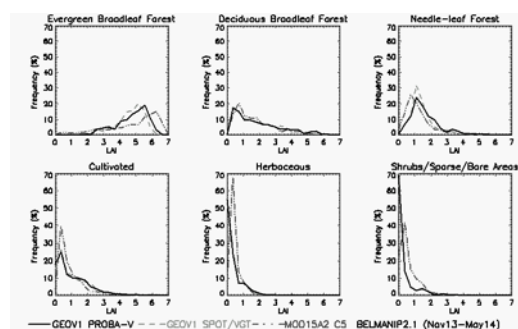


Figure 4: Distribution of LAI values of each product for the BELMANIP2.1 sites during Nov13-May14 period for each biome type.

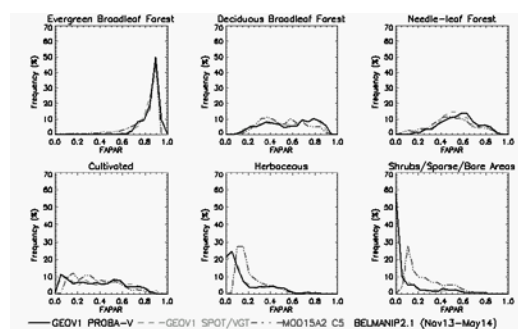


Figure 5: Distribution of FAPAR values of each product for the BELMANIP2.1 sites during Nov13-May14 period for each biome type.

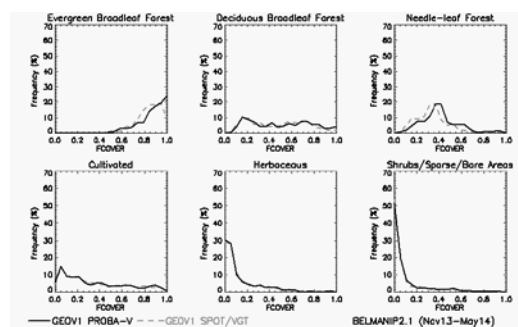


Figure 6: Distribution of FCover values of each product for the BELMANIP2.1 sites during Nov13-May14 period for each biome type.

Figure 4 shows the statistical distributions of LAI retrieved values per biomes for the several satellite products under study. Very similar distributions were found for both GEOV1 products (PROBA-V and SPOT/VGT) for all biome type. As compared with MODIS C5, the main discrepancies were found for evergreen broadleaf forest. Larger values for MODIS C5 over herbaceous and shrubs and bare areas are found, as well as a negative bias over needle-leaf

forest. Figure 5 shows the FAPAR histograms. A good agreement is found between MODIS and GEOV1 distributions for forest and cultivated areas. MODIS shows larger values for herbaceous, shrubs and bare areas, in agreement with previous validation exercises (Camacho et al., 2013). Figure 6 shows the FCover histograms, where PROBA-V and SPOT/VGT GEOV1 retrievals display consistent results for all biome type except for evergreen broadleaf forest and needle-leaf forest, with slight larger values of PROBA-V products.

3.4. Temporal Consistency

Over the South West cropland area (SouthWest_1, Figure 7) a very good temporal consistency for both GEOV1 is observed, showing similar trajectories. The agreement of SPOT/VGT GEOV1 with ground truth is pretty good, reproducing well the seasonality of this agricultural site. Figure 8 shows the temporal trajectories over the rice agricultural site located in Albufera (Spain). The seasonal variations of both GEOV1 products are consistent, and also with MODIS C5 products which are however more noisy. Note that PROBA-V and SPOT/VGT GEOV1 products saturate the FCover value during the peak of vegetation.

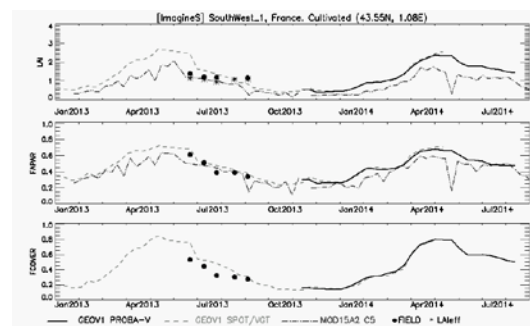


Figure 7: Temporal profiles of the products under study for over South West (France) validation site. For the LAI, asterisk symbol represent LAIeff observation.

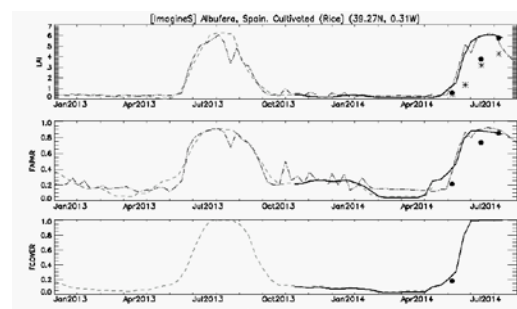


Figure 8: Temporal profiles of the products under study for over Albufera (Spain) validation site. For the LAI, asterisk symbol represent LAIeff observation.

3.5 Intra-Annual Precision

The distributions δ FAPAR were analyzed over the BELMANIP2.1 set of sites (Figure 9). The cumulative histograms of the delta values (smoothness) show better results for both GEOV1 products (PROBA-V and SPOT/VGT) than MODIS C5, with highest frequencies for the lowest δ FAPAR.

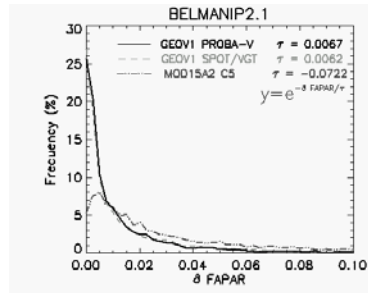


Figure 9: Histograms of the delta function (smoothness) for FAPAR products for BELMANIP2.1 sites during Nov13-May14 period. The curves are adjusted to an exponential function and the exponential decay constant is presented.

3.6 Relative Uncertainties

The consistency of PROBA-V GEOV1 with the reference global products was evaluated over BELMANIP2.1 sites at 10-days frequency during the November 2013 to May 2014 period. Uncertainty metrics (RMSE, Bias, correlation) are shown in Table 2

(X vs Y)	R ²	RMSE	Bias (X-Y)
LAI			
PROBA-V vs SPOT/VGT	0.96	0.29	0.011
PROBA-V vs MODIS	0.84	0.67	0.055
SPOT/VGT vs MODIS	0.84	0.68	0.024
FAPAR			
PROBA-V vs SPOT/VGT	0.98	0.03	-0.004
PROBA-V vs MODIS	0.9	0.09	0.004
SPOT/VGT vs MODIS	0.89	0.09	0.011
FCover			
PROBA-V vs SPOT/VGT	0.98	0.04	0.009

Table 1: Intercomparison exercise: Performance between the different global products over BELMANIP2.1 sites for Nov13-May14 period.

PROBA-V and SPOT/VGT GEOV1 are highly correlated, with R² better than 0.96 for LAI, FAPAR and FCover. Very low bias and low RMSE is observed between both GEOV1 products. On the other hand, the performance between both GEOV1 (PROBA-V and SPOT/VGT) and MODIS is relatively consistent with high correlations (better than 0.84) and mean bias

close to zero, however large bias is expected over some regions or periods (see Figure 3). Both GEOV1 products present very similar discrepancies as compared to MODIS in terms of RMSE. These results seem consistent with the previous validation exercise (Camacho et al., 2013) performed for a two year period (2004-2005).

3.7 Direct Validation

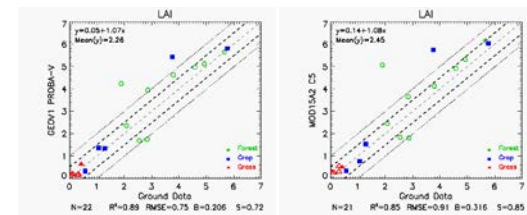


Figure 10: Direct validation results: comparison of each LAI product with the LAI ground-based maps. Filled symbols refers to coincident year, unfilled symbols refers to a different year.

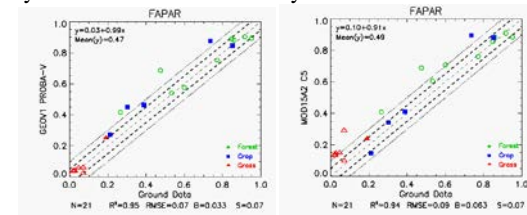


Figure 11: Direct validation results: comparison of each FAPAR product with the FAPAR ground-based maps. Filled symbols refers to coincident year, unfilled symbols refers to a different year.

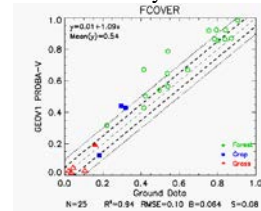


Figure 12: Direct validation results: comparison of PROBA-V GEOV1 FCover product with the FCover ground-based maps. Filled symbols refers to coincident year, unfilled symbols refers to a different year.

For the LAI (Figure 10), the overall accuracy of PROBA-V GEOV1 is 0.75 and the correlation is 0.89. Note that GEOV1 provides a good agreement for the whole range of LAI values, and only some overestimation for highest values was observed. Similar results were obtained with MODIS.

For the FAPAR (Figure 11), GEOV1 shows correlations with ground maps better than 0.95, with an overall accuracy of 0.07 and almost no bias. The offset of the linear fit is close to zero (0.03) and the

slope 0.99. The overall performance is better than MODIS, where a positive bias is observed, mainly for low values

For the FCover (Figure 12), the overall accuracy of GEOV1 is 0.1 and the correlation is 0.89. However, a positive bias over forest sites (non concomitant) is found.

4 CONCLUSIONS

In this study, an early scientific validation of GEOV1 (LAI, FAPAR and FCover) products based on PROBA-V observation was performed for the overlap period between SPOT/VGT and PROBA-V. The methodology used follows the guidelines proposed by the CEOS LPV group for validation of remote sensing vegetation products. First, an intercomparison with existing global products (SPOT/VGT GEOV1 and MODIS C5) was performed. The BELMANIP2.1 network of sites was used to perform the global statistical analysis at 3x3 km² and at a 10-days time step. Second, the uncertainties were quantified by direct comparison with ground-based reference maps.

GEOV1 LAI, FAPAR and FCover estimates from PROBA-V data were found consistent with that of GEOV1 based on SPOT/VGT observations. The completeness of PROBA-V GEOV1 products is similar to that of SPOT/VGT GEOV1 products (around 5% lower).

Both PROBA-V and SPOT/VGT shows consistent spatial distribution of retrievals, whereas discrepancies between PROBA-V and MODIS are larger, mainly for the FAPAR product (large discrepancies). The temporal variations of PROBA-V were found also consistent with that of SPOT/VGT GEOV1 products.

The overall consistency between SPOT/VGT and PROBA-V evaluated in term of RMSE over BELMANIP-2 is better than the CEOS requirements on accuracy (0.5 for LAI, 0.05 for FAPAR), which demonstrates the good consistency between both products.

The direct validation shows good match of PROBA-V GEOV1 products with ground truth, slightly better than MODIS C5, for a limited ground dataset. The overall performance of PROBA-V GEOV1 is 0.75 for LAI, 0.07 for FAPAR and 0.1 for FCover, with correlations better than 0.89, and a slight positive for FCover.

In conclusion, the preliminary assessment of PROBA-V GEOV1 products shows a similar level of quality than SPOT/VGT GEOV1 products. However, a longer dataset is necessary to better assess the quality of the PROBA-V products. These products are available since end of May, 2014 as a demonstration version on the Copernicus Land Service website (<http://land.copernicus.eu/global/>).

5 REFERENCES

- Baret, F., M. Weiss, R. Lacaze, F. Camacho, H. Makhmara, P. Pacholczyk, B. Smets (2013). GEOV1: LAI and FAPAR essential climate variables and FCOVER global time series capitalizing over existing products. Part1: Principles of development and production. *Remote Sensing of Environment* 137: 299–309.
- Camacho, F., Cernicharo, J., Lacaze, R., Baret, F., and Weiss, M. (2013). GEOV1: LAI, FAPAR Essential Climate Variables and FCover global time series capitalizing over existing products. Part 2: Validation and intercomparison with reference products. *Remote Sensing of Environment* 137: 310–329.
- Camacho, F., Lacaze, R., Latorre, C., Baret, et al. (2014). A network of Sites for Ground Biophysical Measurements in support of Copernicus Global Land Product Validation. This issue.
- Fernandes, R., Plummer, S., Nightingale, J., et al. (2014). Global Leaf Area Index Product Validation Good Practices. CEOS Working Group on Calibration and Validation - Land Product Validation Sub-Group. Version 2.0: Public version made available on LPV website.
- Weiss, M., Baret, F., Block, T., Koetz, B., Burini, A., Scholze, B., Lecharpentier, P., Brockmann, C., Fernandes, R., Plummer, S., Myneni, R., Gobron, N., Nightingale, J., Schaepman-Strub, G., Camacho, F., Sanchez-Azofeifa, A (2014). On Line Validation Exercise (OLIVE): A Web Based Service for the Validation of Medium Resolution Land Products. Application to FAPAR Products. *Remote Sensing*. 2014. 6(5):4190-4216.
- Yang, W., Huang, D., Tan, B., Stroeve, J. C., Shabanov, N. V., Knyazikhin, Y., et al. (2006). Analysis of leaf area index and fraction of PAR absorbed by vegetation products from the Terra MODIS sensor: 2000–2005. *IEEE Transactions on Geoscience and Remote Sensing*, 44(7):1829–1842

GEOV2: Near real time estimation of LAI, FAPAR and cover fraction variables from VEGETATION data within Copernicus Global Land service

A. Verger^{1,2,*}, F. Baret², M. Weiss², B. Smets³, F. Camacho⁴, R. Lacaze⁵

¹ CREAF, Cerdanyola del Vallès 08193, Catalonia, Spain

² INRA UMR114 EMMAH, UMT CAPTE, 84914 Avignon, France

³ VITO, 2400 Mol, Belgium

⁴ EOLAB, 46980 València, Spain

⁵ HYGEOS, 31400 Toulouse, France

* verger@creaf.uab.cat

ABSTRACT - The GEOV2 algorithm for continuous, consistent and near real time estimation of Leaf Area Index (LAI), fraction of absorbed photosynthetic active radiation (FAPAR) and vegetation cover fraction (FCOVER) from daily VEGETATION satellite data is here described. Similarly to the first version, GEOV1, of Copernicus Global Land product, GEOV2 capitalizes on the development and validation of already existing products and the use of neural networks which ensure consistency and similar accuracy levels in the derived products. GEOV2 significantly improves GEOV1 in terms of continuity (only 1% of missing data in GEOV2 as compared to 20% in GEOV1) and smoothness, especially at high latitudes, and Equatorial areas, due to the use of daily observations and temporal techniques which also allows to process products in near real time. Global GEOV2 products at 1/112° spatial resolution for the period 1999-2014 will be freely available at Copernicus portal (<http://land.copernicus.eu>). The adaptation of the algorithm and processing chain to PROBA-V ensures service continuity and near real time estimates at global scale.

1 INTRODUCTION

Near real time (NRT) estimation of global biophysical variables from moderate spatial resolution satellite sensors are of high interest in a range of application areas including numerical weather forecasting, monitoring of rapid land surface changes (e.g. droughts, hurricanes, forest fires, floods) and support policies on environment and water management, agriculture and food security. Although many studies point out the crucial need of NRT vegetation products, only very few deal with near real time series, and up to now, there is no delivery of NRT global vegetation products.

A first version of Leaf Area Index (LAI), fraction of absorbed photosynthetic active radiation (FAPAR) and vegetation cover fraction (FCOVER) from SPOT/VEGETATION data (hereafter called VGT) within Copernicus Global Land service, called GEOV1, was already developed (Baret et al. 2013) and freely distributed at the Copernicus website (<http://land.copernicus.eu/global>). Time series of GEOV1 estimates from 1999 to 2014, are delivered globally at 1/112° spatial sampling. These GEOV1 products are updated every 10 days, with a temporal basis for compositing of 30 days and delivered with a 12-day lag in NRT. GEOV1 has been demonstrated to

outperform current existing products both in terms of accuracy and precision (Camacho et al. 2013). GEOV1, although one of the smoothest available product still includes some problems, particularly over cloudy areas. A significant fraction of missing data was observed for GEOV1, specially at high latitudes and Equatorial areas.

The second version of Copernicus Global Land vegetation products derived from VGT, called GEOV2, aims to be consistent with GEOV1 in terms of accuracy. At the same time, GEOV2 products are expected to improve GEOV1 in terms of continuity and smoothness. To comply with user requirements, GEOV2 production and delivery of LAI, FAPAR and FCOVER variables are to take place in NRT and are complemented by the constitution of time series from 1999 to present (offline processing of historical (HIST) past time series).

This paper describes the principles of the GEOV2 algorithm with due attention to the differences with the GEOV1 approach. Then, the GEOV2 estimates are evaluated based on the comparison with GEOV1.

	GEOV1	GEOV2
Inputs of neural networks	Temporal composites of Top of the Canopy directionally normalized surface reflectances	Daily Top Of Atmosphere reflectances, 3 angles of sun and view directions, ozone and water content
Temporal composition	Composition of input reflectances based on a 30-day temporal window with Gaussian weighting	Composition at the level of biophysical estimates using a Savitzky-Golay filter with an adaptive composition window within 30- and 60-day semi-periods defined by the availability of 6 valid observations at each side of the date being processed
Temporal smoothing and gap filling	Not applied	Application of TSGF (Temporal Smoothing and Gap Filling) and CACAO (Consistent adjustment of Climatology to Actual Observations) filters
Near Real Time	12-day lag delivery	Near Real Time projection

Table 1: Algorithm differences between GEOV2 and GEOV1 products.

2 PRINCIPLES OF ALGORITHM DEVELOPMENT

The GEOV2 algorithm (Verger et al. 2014) for the estimation of global LAI, FAPAR, and FCOVER from VGT data consists of three main steps:

(1) Neural networks to provide instantaneous estimates from daily VGT-P reflectances. Similarly to GEOV1, GEOV2 capitalizes on the development and validation of already existing products: CYCLOPES version 3.1 and MODIS collection 5, and the use of neural networks (Baret et al. 2013; Verger et al. 2008). GEOV2 uses daily top of atmosphere (TOA) reflectances in the red, NIR and SWIR bands, 3 angles of sun and view directions, ozone and water content as input data. An explicit atmospheric correction is not applied to the input VGT data contrarily to GEOV1 (Table 1).

(2) A multi-step filtering approach based on an iterative upper envelope process and expert knowledge on the expected seasonality was applied to eliminate noisy data mainly affected by atmospheric effects and snow cover.

(3) A temporal composition ensures consistency and continuity of the LAI, FAPAR and FCOVER time course every 10 days. TSGF (Temporal Smoothing and Gap Filling) (Verger et al. 2011) and CACAO (Consistent adjustment of Climatology to Actual Observations) (Verger et al. 2013) temporal techniques were applied. TSGF combines a Savitzky-Golay filter with an adaptive asymmetric composition window within 30- and 60-day semi-periods defined by the availability of 6 valid observations at each side of the date being processed, and linear interpolation for filling gaps. CACAO consists in fitting the climatology (defined as the interannual average of GEOV1 time series) to actual observations for each growth season by scaling the magnitude and shifting the phenology. CACAO allows to better cope with missing and noise contaminated data as compared to

standard methods (Verger et al. 2013) and allows time projection.

The combination of the TSGF local fitting and the projection capacity of CACAO allows to process in NRT when only past observations are available. To avoid the instability in NRT estimates and improve the consistency with offline processing (past time series), the products are updated each time when a new dekad is available and processed (real-time estimates). This results in the delivery of successive updates of the recent past values of the products in a convergence period of 60-day (Verger et al. 2014). Therefore, products will be updated during six dekads and then remain stable.

Further details on the algorithm are provided in Verger et al. (2014). The differences between the GEOV2 and GEOV1 algorithms are summarized in Table 1.

3 QUALITY ASSESSMENT

A preliminary evaluation of GEOV2 estimates has been achieved, mostly based on the quality indicators associated to the products and the comparison with GEOV1.

3.1 Associated uncertainty and quality assessment

The following quality indicators are associated to each GEOV2 product:

- The number of valid VGT observations, n , used within the temporal composition of final products. The more observations, the more reliable are the products.
- The length in days of each semi-period (before and after the dekadal date) of the compositing window. The shorter the periods, the more reliable are the products.
- The RMSE of the final product as compared to the daily P observations in the compositing period.

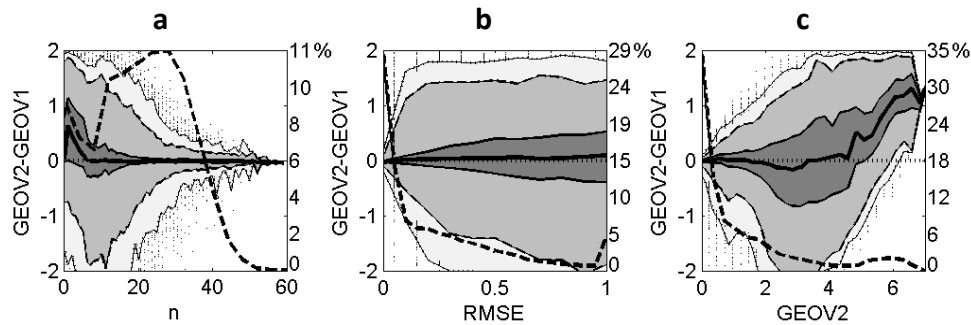


Figure 1. Evaluation of the differences between GEOV2 and GEOV1 products over the BELMANIP2 sites for the years 2008-2010 as a function of the number n of valid VGT-P observations in the composition period (a), the $RMSE$ associated to GEOV2 product (b), and the GEOV2 product value (c). The several gray values correspond to 75% (dark gray), 90% (medium gray) and 95% (light gray) of the population, and the dots to 5% percentile of residual outliers. The bold back solid line corresponds to the median value of the differences. The dotted line is the 0:0 line. The dashed line shows the distribution of values of the variable in the abscissa which frequencies are indicated in the vertical axis on the right. Case of LAI products.

The comparison of GEOV2 with GEOV1 shows an overall good agreement. However, the agreement degrades when the number of available observations in the composition period, n , is lower than approximately $n=10$ (Figure 1a). The distribution of n (Figure 1a, dashed bold line) shows that in most situations it is in between 10 to 30. For the lower values of n , a small positive bias is observed, due to the effect of cloud contamination not detected in GEOV1. Note that the maximum number of observations is 60 which corresponds to the minimum composition window.

The $RMSE$ computed between actual valid daily LAI estimates and GEOV2 (Figure 1b) is closely linked with the difference between GEOV2 and GEOV1. This results from the increasing number of available observations, n , as well as from the ‘scaling’ effect: the $RMSE$ GEOV2-GEOV1 (Figure 1c, right) tends to increase with the GEOV2 value. Note that the distribution of $RMSE$ values (Figure 1b, dashed bold line) shows that most values are lower than 0.1.

3.2 Temporal consistency

Few BELMANIP2 and DIRECT sites (Weiss et al. 2014) showing typical features have been selected to illustrate the performance of GEOV2 algorithm for HIST and NRT processing as compared to GEOV1 product and ground based measurements.

For sites having enough high quality data (Figure 2a), NRT and HIST solutions are very close and show a good agreement with GEOV1 product. Reasonable performances and no significant differences were found in this case between the solutions of NRT algorithm in the converge period (NRT-0, NRT-3) and the consolidated one (NRT-6).

For sites near the equator having a significant percentage of missing data and noise due to persistent

clouds (Figure 2b), GEOV2 still provides reliable solutions both for HIST and NRT cases. Note that in this case GEOV2 product clearly outperforms GEOV1 in terms of continuity. The background information provided by the climatology and the CACAO fitting approach allows adequate gap filling in these difficult situations. Further, the outlier rejection allows eliminating contaminated data while keeping the expected level of LAI as the good agreement with ground data indicates.

For sites situated at very high latitudes (Figure 2c), GEOV1 shows some artifacts and anomalous seasonality in winter time (e.g. unexpected increment of LAI in October-November). These problems are probably due to the instabilities in BRDF correction in extreme illumination conditions as well as possible residual snow pixel contamination. These artifacts were corrected in GEOV2 because (1) the sun angle was explicitly considered in the NNT, (2) outliers were rejected and (3) CACAO and climatology background information increase robustness. Further GEOV2 shows continuity in the temporal profiles with a base level of LAI in winter time given by CACAO. Some problems were also found in GEOV1 for these high latitude sites in the summer period due in part to the significant amount of noise in the data which negatively bias the solution. These problems were mostly corrected in the HIST and consolidated NRT-6 GEOV2 products but some remaining difficulties were found in NRT-0 to converge to the expected upper solution during the growing season. GEOV2 estimates show some temporal inconsistencies at the end of the growing season (longer seasons than expected) over forest areas at northern high latitudes $>50^\circ$ where GEOV2 is very sensitive to the high level of noise in input TOA VGT reflectances.

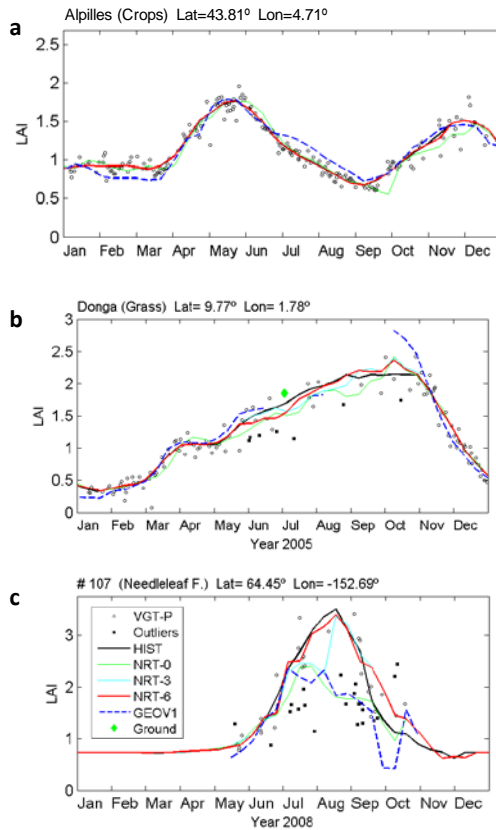


Figure 2. Temporal profiles of near real time LAI estimates for n=0,3,6 dekads after the date being processed (NRT-n) as compared to the historical (HIST) GEOV2 estimates and GEOV1 LAI products over (a) non-problematic, (b) Equatorial and (c) high latitude sites. The valid and filtered VGT-P LAI estimates as well as the available ground measurements are shown. The title of each plot indicates the DIRECT site name or BELMANIP2 site number, the GLOBCOVER biome class, the latitude and longitude in degrees.

3.3 Temporal smoothness

LAI variable results from incremental bio-physical processes. It is therefore expected to show relatively smooth temporal variations except in extreme situations such as flooding, fire or changes in the land-use. High variability in the temporal profiles would indicate a lack of reliability of the derived products. The smoothness of the LAI temporal series was evaluated based on the absolute value of the difference, δLAI , between $\text{LAI}(t)$ product value at date t and the mean value between the two closest bracketing dates in a maximum δt period of 60 days

(Verger et al. 2011). The smoother the temporal evolution, the smaller the δLAI difference should be. The histogram of δLAI over the whole dataset of BELMANIP2 sites in the 2003-2010 period (Figure 3) shows that both GEOV1 and GEOV2 products are very smooth with differences lower than 0.25 for most of cases. However, GEOV2 shows generally smoother temporal profiles as attested in Figure 3.

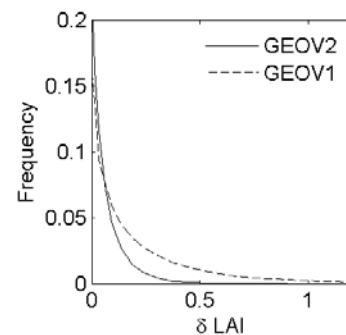


Figure 3. Histogram of the δLAI absolute difference representing temporal smoothness for GEOV2 and GEOV1 LAI products. Evaluation over the BELMANIP2 sites for the 2003-2010 period.

3.4 Temporal continuity

The continuity of GEOV2 time series is evaluated by the fraction of missing data based on the 445 BELMANIP2 sites during the 2003-2010 period. Only 1% of the potential dekads are missing globally, i.e. much less than for GEOV1 showing about 20% of missing data (Figure 4). GEOV1 products are missing if less than 2 observations exist in the 30-day compositing window. GEOV2 benefits from the use of the TSGF and the CACAO climatology based techniques for filling gaps. GEOV2 data are missing only if the GEOV1 climatology is not available due to too large discontinuities in the data.

The climatological values are used to fill large gaps in 10% to 55% of the cases depending on the biome type as displayed in Figure 4. The fraction of dekads that were not filled but with available observations are slightly higher than those observed for GEOV1 due to the use of daily estimates and a larger compositing window. Identical patterns per biome are observed with lower fraction of high quality observations for evergreen broadleaf forests which are mostly located in areas with continuous cloud cover around the Equator. In this particular case, the fraction of non filled data is higher for GEOV1 because in GEOV2 a high fraction of noisy data is filtered out in the outlier rejection process.

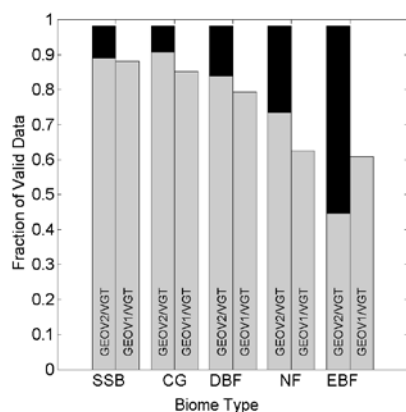


Figure 4. Average fraction of valid GEOV2 and GEOV1 products per biome. The biome classes are derived from the GLOBCOVER global landcover: Shrubs/Savana/Bare soil (SSB), Crops and Grassland (CG), Deciduous Broadleaf Forests (DBF), Needleleaf Forest (NF), and Evergreen Broadleaf Forest (EBF). For GEOV2, high quality products (grey) and products with less than 2 valid observations in the compositing period (black) are distinguished. Evaluation over the BELMANIP2 sites for the 2003-2010 period.

4 CONCLUSIONS

GEOV2 LAI, FAPAR and FCOVER products capitalize on the efforts undertaken in the first version of products GEOV1 through a three-step procedure including: 1) NNT to provide instantaneous estimates from VGT-P reflectances; 2) a multistep filtering approach to eliminate data mainly affected by atmospheric effects and snow cover; and 3) temporal techniques to ensure consistency and continuity as well as short-term projection of the product dynamics. First validation results show that GEOV2 products have high consistency with previous GEOV1 products and show similar accuracy levels as compared to ground measurements. At the same time, GEOV2 provides global estimates at near real time and significantly improves GEOV1 in terms of consistency (smoother products less affected by noise in the data) and continuity (less than 1% of missing data as compared to the 20% of gaps in GEOV1). Some remaining problems at northern very high latitudes $>50^\circ$ were identified in GEOV2 due to the high levels of noise in the data. An explicit atmospheric correction may improve the reliability of GEOV2 estimates in these difficult observational conditions. Global GEOV2 past time series (1999-2014) and near real time GEOV2 estimates every 10 days at $1/112^\circ$ spatial resolution will be freely available at Copernicus portal (<http://land.copernicus.eu>). The adaptation of the algorithm and processing chain to PROBA-V ensures continuity after 2014.

5 ACKNOWLEDGEMENTS

This research was partially supported by the European Earth observation programme Copernicus, and the GIOBIO (32-566) and LONGLOVE (32-594) projects. A. Verger is the recipient of a *Juan de la Cierva* postdoctoral fellowship from the Spanish Ministry of Science and Innovation.

6 REFERENCES

- Baret, F., Weiss, M., Lacaze, R., Camacho, F., Makhmara, H., Pacholczyk, P., & Smets, B. (2013). GEOV1: LAI, FAPAR Essential Climate Variables and FCOVER global time series capitalizing over existing products. Part1: Principles of development and production. *Remote Sensing of Environment*, 137, 299-309
- Camacho, F., Cernicharo, J., Lacaze, R., Baret, F., & Weiss, M. (2013). GEOV1: LAI, FAPAR Essential Climate Variables and FCOVER global time series capitalizing over existing products. Part 2: Validation and intercomparison with reference products. *Remote Sensing of Environment*, 137, 310-329
- Verger, A., Baret, F., & Weiss, M. (2008). Performances of neural networks for deriving LAI estimates from existing CYCLOPES and MODIS products. *Remote Sensing of Environment*, 112, 2789-2803
- Verger, A., Baret, F., & Weiss, M. (2011). A multisensor fusion approach to improve LAI time series. *Remote Sensing of Environment*, 115, 2460-2470
- Verger, A., Baret, F., & Weiss, M. (2014). Near real time vegetation monitoring at global scale. *IEEE Journal of Selected Topics in Applied Earth Observations and Remote Sensing*, DOI: 10.1109/JSTARS.2014.2328632
- Verger, A., Baret, F., Weiss, M., Kandasamy, S., & Vermote, E. (2013). The CACAO method for smoothing, gap filling and characterizing seasonal anomalies in satellite time series. *IEEE transactions on Geoscience and Remote Sensing*, 51, 1963-1972
- Weiss, M., Baret, F., Block, T., Koetz, B., Burini, A., Scholze, B., Lecharpentier, P., Brockmann, C., Fernandes, R., Plummer, S., Myneni, R., Gobron, N., Nightingale, J., Schaepman-Strub, G., Camacho, F., & Sanchez-Azofeifa, A. (2014). On Line Validation Exercise (OLIVE): A Web Based Service for the Validation of Medium Resolution Land Products. Application to FAPAR Products. *Remote Sensing*, 6, 4190-4216

Estimation of atmospheric water vertical content from MSG2-SEVIRI

Xiaoyu Zhang, Jing Pang and Bing Wang

School of Environment and Resources, Shanxi University, Taiyuan, Shanxi Province, PR China

Corresponding author. E-mail address: zhang_xyhz@sxu.edu.cn

ABSTRACT - Measurements in the 10.8 and 12.0 μ m channels have been widely used to retrieve total water vapor content (WVC). The study compared of three WVC retrieval methods using MSG-SEVIRI data and European Centre for Medium-Range Weather Forecasts(ECMWF) reanalysis data, which one is proposed by Li et al.(2003) using split-window covariance-variance ratio based on spatial moving window(denotes as $WVC_{spatial}$), and the other is proposed by Schroedter-Homscheidt et al. (2008) from MSG-SEVIRI split-window channel data over varying surface temperature(denotes as $WVC_{temporal2}$), at the same time, WVC is also estimated using Li's method but based on temporal moving window(denotes as $WVC_{temporal}$). The results shows that Li's method based on spatial moving window performed better than the others, root mean square error (RMSE) of WVC is 0.8, 0.94 and 1.26(g/cm²) for $WVC_{spatial}$, $WVC_{temporal}$ and $WVC_{temporal2}$ respectively, RMSE of fraction errors is 0.77, 0.94 and 0.89 for $WVC_{spatial}$, $WVC_{temporal}$ and $WVC_{temporal2}$ respectively. The pixel numbers that can be calculated are 2098, 2411 and 709 for $WVC_{spatial}$, $WVC_{temporal}$ and $WVC_{temporal2}$ respectively

1 INTRODUCTION

Total column water vapor content (WVC) is very important in climate research and weather prediction etc, defined as the vertical integration of atmospheric water vapor mass. It is also crucial in atmospheric correction especially for near-IR and middle-IR and thermal-IR image (Chen, X. H., and Huang, X. L., 2014).

Due to these reasons, more and more approaches about the retrieval of WVC from satellite data are developed. According to the wavelength used, the approaches can be divided into three categories: visible and near-IR method; thermal-infra method and microwave method.

The visible and near-IR method is based on detecting the absorption by water vapor of the reflected solar radiation after it has transferred down to the surface and backup through the atmosphere. The total vertical amount of water vapor can be derived from a comparison between the reflected solar radiation in the absorption channel, and the reflected solar radiation in nearby non-absorption channels. The method needs to have at least one channel in the water absorption band (0.94 μ m), at the same time, the similar spectral characters for the two channels are needed in the method. No channel in the near-IR water absorption band is available for SEVIRI on board MSG; the near-infrared technique, therefore, cannot be applied to SEVIRI data and one applicable technique is the thermal infrared technique. For the thermal-IR, WVC can be derived from retrieval of water vapor vertical profiles based on hyperspectral sounding such

as Atmospheric Infrared Sounder (AIRS) (pougachev, et al., 2009). A split-window technique has been used by many researchers to retrieve WVC in the thermal-IR without explicit retrieval of water vapor vertical profile. The technique utilizes a linear assumption that atmospheric attenuation of the surface infrared emission is linearly proportional to the radiance difference between two split-window channels (Sobrino, et al., 1994). Li et al. (2003) estimated precipitable water from ATSR split-window channel data over land area using split-window covariance-variance ratio(SWVCR) from BT9 and BT10 data of surrounding clear skies assuming that the atmospheric state is approximately the same and the emissivity ratio of two channels are also the same and equals to 1 for the spatial neighboring pixels. Schroedter-Homscheidt et al. (2008) retrieved total WVC from MSG2-SEVIRI split-window channel data over varying surface temperature under the assumption of constant WVC over several hours. The paper aims to compare the use of the method proposed by Li with that proposed by Schroedter-Homscheidt for MSG-SEVIRI measurements over European and African land surfaces. At the same time, Estimation of WVC using temporal-based moving window is also done similar to spatial-based moving window in Li's method.

Section2 introduces the Schroedter-Homscheidt's and Li's method and describes the datasets used in the study. The comparison of the three methods is delineated in Section 3. Further conclusions and discussions are presented in Section 4.

2 THEORY AND DATASET

2.1 Theory of Li's method

On the basis of radiative transfer theory and the first Taylor series of the Planck function $B_i(T)$ around some mean temperature T , Under the condition that the atmosphere and directional surface emissivity in channel i are constant or the effects of their spatial variations are not larger than the combined effects of both instrument noise over the N neighboring pixels and the linear approximation of Plank function, the variation of radiance measured from space in channel i at the zenith angle θ due to the change of surface temperature can be expressed as:

$$B_i(T_{i,k}(\theta)) - B_i(\bar{T}_i(\theta)) = \varepsilon_i(\theta) \tau_i(\theta) [B_i(T_{s,k}) - B_i(\bar{T}_s)] \quad (1)$$

Eq. (1) can be expressed in terms of temperature difference as:

$$(T_{i,k} - \bar{T}_i) = \varepsilon_i \tau_i (T_{s,k} - \bar{T}_s) \quad (2)$$

Similarly, for measurements in channel j , one has

$$(T_{j,k} - \bar{T}_j) = \varepsilon_j \tau_j (T_{s,k} - \bar{T}_s) \quad (3)$$

Dividing equation (2) by equation (3) gives

$$(T_{i,k} - \bar{T}_i) \frac{\tau_j \varepsilon_j}{\tau_i \varepsilon_i} = (T_{j,k} - \bar{T}_j) \quad (4)$$

If the assumption made above holds for N neighboring pixels, then, by least squares analysis of equation(4), the transmittance ratios in two channels, τ_j/τ_i can be derived from

$$\frac{\tau_j}{\tau_i} = \frac{\varepsilon_j}{\varepsilon_i} R_{ji} \quad (5)$$

$$R_{ji} = \frac{\sum_{k=1}^N (T_{i,k} - \bar{T}_i)(T_{j,k} - \bar{T}_j)}{\sum_{k=1}^N (T_{i,k} - \bar{T}_i)^2}$$

In practice, the emissivity ratio is assumed to be unity, leading to

$$\frac{\tau_j}{\tau_i} = R_{ji} \quad (6)$$

The ratio of atmospheric transmittances in the two channels is related to WVC. Jiang et al.(2007) give the specific expression of WVC and τ_j/τ_i for MSG-SEVIRI data as follows:

$$WVC = (4.15 + 10.495 \cos \theta) - (3.78 + 10.468 \cos \theta) * \tau_j/\tau_i \quad (7)$$

where θ is view zenith angle.

In the method, the linear correlation coefficient ($R^2 \approx 1$) of two measurements T_i and T_j is used to check whether the assumption is met.

$$R^2 = \frac{(\sum_{k=1}^N (T_{i,k} - \bar{T}_i)(T_{j,k} - \bar{T}_j))^2}{\sum_{k=1}^N (T_{i,k} - \bar{T}_i)^2 \sum_{k=1}^N (T_{j,k} - \bar{T}_j)^2} = R_{ji} R_{ij} \quad (8)$$

2.2 Theory of Schroedter-Homscheidt method

Kleespies and McMillin(1984,1990) pointed out that WVC can be related to brightness temperature measurements $T_{B,11}$ and $T_{B,12}$ at 10.8 and 12.0 μm as follows:

$$WVC = fct[\frac{1}{\sec(\theta)} \ln(\frac{T_{B,11} - T_A}{T_{B,12} - T_A})] \quad (9)$$

If the atmospheric state is approximately the same in varying surface temperatures situations, WVC can be described as a function of brightness temperatures and satellite zenith angle θ as follows:

$$WVC = fct[\frac{1}{\sec(\theta)} \ln(\frac{T_{B,11}^a - T_{B,11}^b}{T_{B,12}^a - T_{B,12}^b})] \quad (10)$$

Schroedter-Homscheidt (2008) gave the specific function of equation (10) for MSG-SEVIRI data, that is:

$$WVC = a + b(ratio) + c(ratio)^2 + d(ratio)^3 \quad (11)$$

$$ratio = \frac{1}{\sec(\theta)} \ln(\frac{T_{B,11}^a - T_{B,11}^b}{T_{B,12}^a - T_{B,12}^b})$$

$$a = 0.0001\theta - 0.0045\theta + 8.7092$$

$$b = 0.0094\theta - 0.0685\theta + 188$$

$$c = -0.03\theta + 0.1858\theta - 226.6$$

$$d = 0.0294\theta - 0.1854\theta + 151.0$$

Fig1a and 1b gives the specific flowcharts of three methods.

2.3 Dataset

MSG2-SEVIRI provides images every 15min in 12 spectral channels covering both optical and thermal spectrum at a spatial sampling of 3km at nadir. Visible, thermal, and the cloud mask images for August 5, 2005 were acquired to estimate WVC using three different methods.

ECMWF reanalysis is used to compare the three methods. The dataset has a spatial resolution of 1.0 latitude by 1.0 longitude and 21 vertical levels with geospatial coverage of latitude from 10°S to 60°N and longitude from 20°W to 160°E. 6-hourly humidity profiles on August 5, 2005 are used to derive actual total WVC.

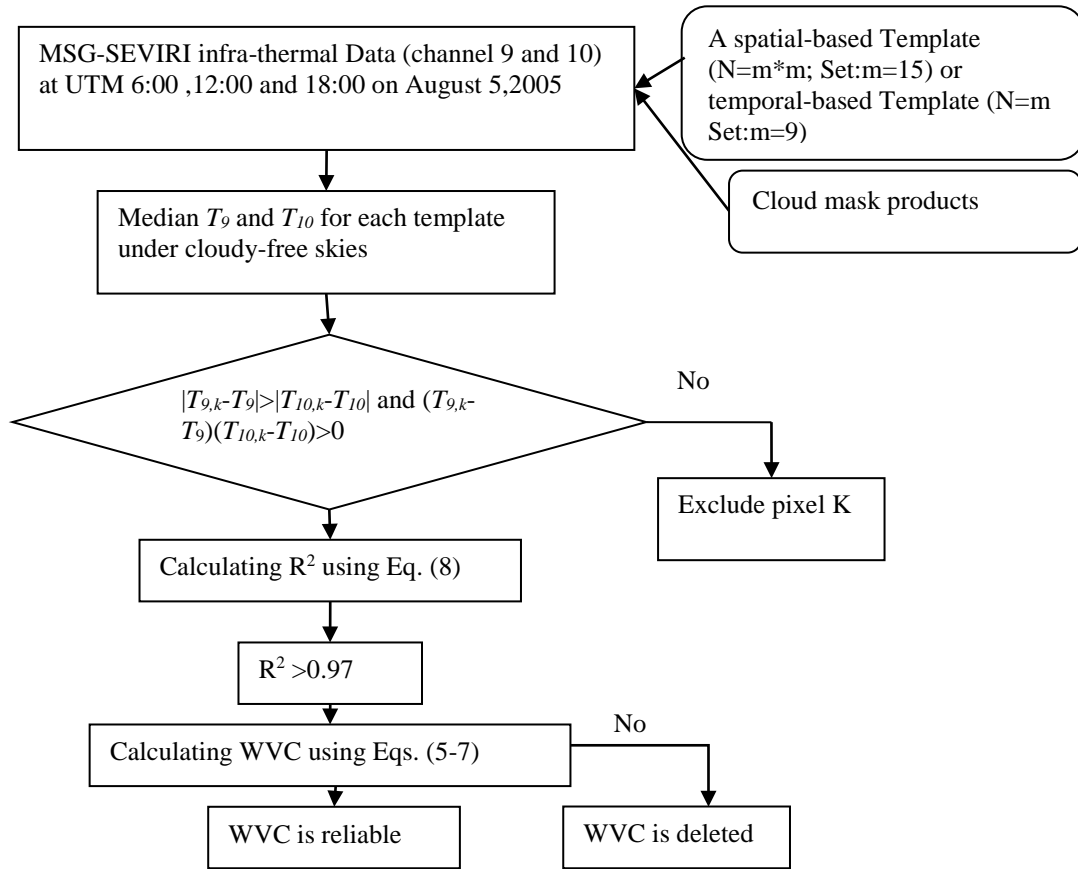


Figure 1a: The flowchart of Li's method

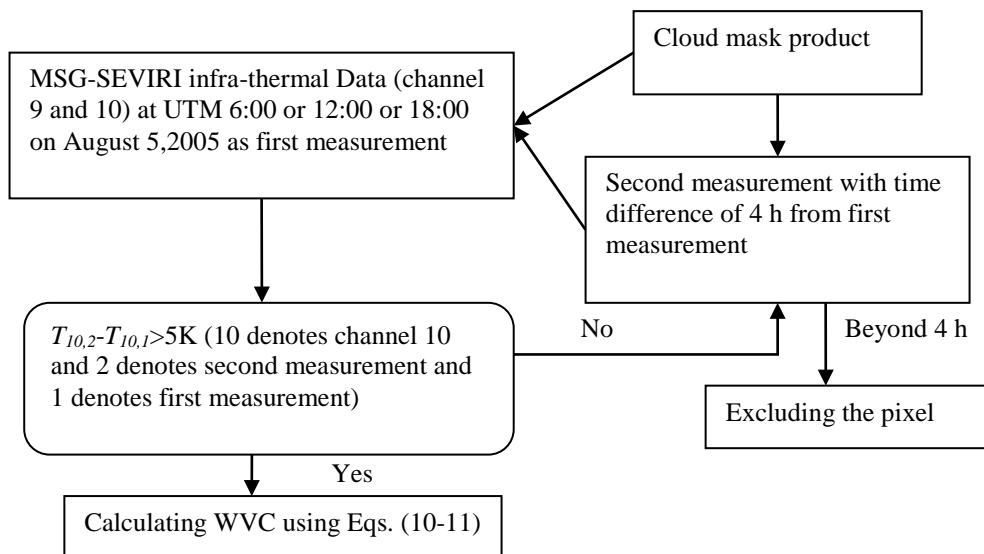


Figure 1b: The flowchart of Schroedter-Homscheidt's method

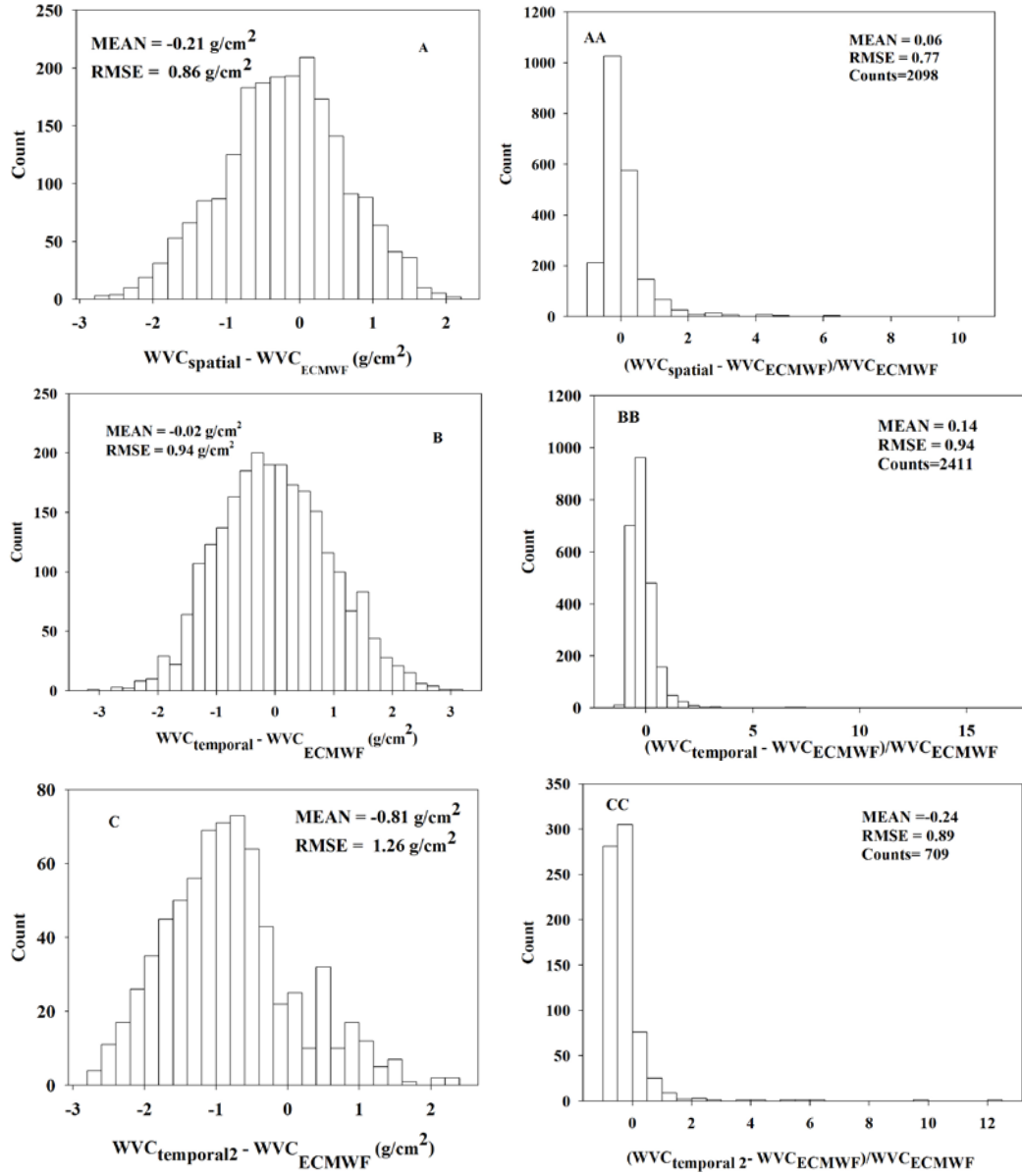


Fig2: Histogram of errors of the WVC from ECMWF and that estimated by three methods (A,B,C for difference between the WVC from ECMWF and that estimated by three methods; AA,BB,CC for fraction difference between the WVC from ECMWF and that estimated by three methods)

3 COMPARISON OF WVC ESTIMATED BY THREE METHODS

$WVC_{spatial}$ denotes the WVC estimated by Li's method using spatial-based moving window, $WVC_{temporal}$ denotes the WVC estimated by Li's method using temporal-based moving window, and

$WVC_{temporal2}$ denotes the WVC estimated by Schroedter-Homscheidt's method. Accounting for the spatial scale difference of MSG-SEVIRI ($0.03^{\circ} \times 0.03^{\circ}$) and ECMWF ($1^{\circ} \times 1^{\circ}$), WVC estimated from MSG-SEVIRI data are aggregated into the same resolution as WVC extracted from ECMWF using mean weight method.

Fig.2 gives the histogram of differences between WVC estimated with three methods and that from ECMWF. We define the fraction difference as $(WVC_{\text{spatial}} - WVC_{\text{ECMWF}}) / WVC_{\text{ECMWF}}$. The RMSEs of such fractional difference are 77%, 94% and 89% for WVC_{spatial} , WVC_{temporal} and $WVC_{\text{temporal2}}$ respectively. RMSE is 0.86g/cm^2 with a mean difference of -0.21g/cm^2 for WVC_{spatial} , RMSE is 0.94g/cm^2 with a mean difference of -0.02g/cm^2 for WVC_{temporal} , and RMSE is 1.26g/cm^2 with a mean difference of -0.81g/cm^2 for $WVC_{\text{temporal2}}$, respectively. And the pixel numbers that can be estimated are 2098, 2411 and 709 for WVC_{spatial} , WVC_{temporal} , and $WVC_{\text{temporal2}}$, respectively. So, among the three methods, WVC_{spatial} is better than the others, but the mean difference is the minimum for WVC_{temporal} , and the pixel numbers that can be estimated are the most. Li's methods can be performed under the condition that the atmosphere and directional surface emissivity in channel i are constant or the effects of their spatial/temporal variations are not larger than the combined effects of both instrument noise over the N spatial neighboring pixels and the linear approximation of Plank function. WVC_{spatial} is better than WVC_{temporal} shows that the influence to the retrieval of WVC coming from temporal variance of atmosphere are larger than that from spatial variance of atmosphere and directional surface emissivity although the directional surface emissivity are the same for the different time. $WVC_{\text{temporal2}}$ displayed poorest result shows that it is unfitted assuming that atmosphere is the same in four hours. More conditions can be met to estimate WVC by Li's method using temporal-based moving window.

4 CONCLUSIONS

WVC is a very important factor in atmospheric correction especially for near-IR and middle-IR and thermal-IR image. The study compares three methods for the retrieval of WVC using MSG-SEVIRI thermal-IR channel data ($10.8\mu\text{m}$ and $12.0\mu\text{m}$). The Li's method displayed the best result regarding RMSE between estimated WVC and that from ECMWF, while Li's method using temporal-based moving window displayed the minimum mean bias, at the same time, the pixel numbers that can be calculated by the method are the most, and Schroedter-Homscheidt's method shows poorest result.

Considering the assumption of three methods, we can conclude that the influence from temporal variance of atmosphere to the retrieval of WVC is larger than that from spatial variance of atmosphere and directional surface emissivity although the directional surface emissivities are the same for the different time. Schroedter-Homscheidt's method displayed poorest result shows that it is unfitted

assuming that atmospheric state is the same in four hours.

5 ACKNOWLEDGMENTS

This work was supported by the National Natural Science Foundation of China (41271381). We also thank EUMETSAT for providing the MSG2-SEVIRI data.

6 REFERENCES

- Chen, X. H., and Huang, X. L., Usage of differential absorption method in the thermal IR: A case study of quick estimate of clear-sky column water vapor. *Journal of Quantitative Spectroscopy & Radiative Transfer*. 2014, 140:99-106.
- Jiang, G. Retrieval of Land Surface Emissivity and Land Surface Temperature from MSG1-SEVIRI Data. Ph.D. Dissertation, University of Strasbourg, Strasbourg, France, 2007.
- Kleespies, J.T., & McMillin, L.M. Physical retrieval of precipitable water using the split window technique. *Conference on Satellite Meteorology, Remote Sensing and Applications (AMS)*. 1984, 55-57.
- Kleespies, J.T., & McMillin, L.M. Retrieval of precipitable water from observations in the Split window over varying surface temperatures. *Journal of Applied Meteorology*, 1990, 29, 851-862.
- Li, Z.-L., Jia, L., Su, Z.B., Wan, Z.M., and Zhang, R.H., A new approach for retrieving precipitable water from ATSR2 split-window channel data over land. *International Journal of remote sensing*. 2013, 24: 5095-5117.
- Pougatchev, N., August, T., Calbet, X., Hultberg, T., Oduleye, O., and Schlusell, P., IASI temperature and water and water vapor retrievals-error assessment and validation. *Atmos Chem Phys*, 2009: 6453-6458.
- Schroedter-Homscheidt, M., Drews, A., and Heise, S., Total water vapor column retrieval from MSG-SEVIRI split window measurements exploiting the daily cycle of land surface temperatures. *Remote sensing of environment*, 2008, 12: 249-258.
- Sobrino, J.A., Li, Z.-L., Stoll, M.P., Becker, F., Improvement in the split window technique for land surface temperature determination. *IEEE Trans Geosci Remote sens*. 1994, 32: 243-253.

Comparison of Split-Window and Single-Channel Methods for Land Surface Temperature Retrieval from Landsat-8

Yu-Ze Zhang¹, Hua Wu², Zhao-Liang Li^{3,4}, Xiao-Guang Jiang^{1,5,6*}, Yu-Zhang Du¹, En-Yu Zhao¹

1 University of Chinese Academy of Sciences, Beijing, 100049, China;

2 State Key Laboratory of Resources and Environmental Information System, Institute of Geographic Sciences and Natural Resources Research, CAS, Beijing, 100101, China

3 Key Laboratory of Agri-informatics, Ministry of Agriculture / Institute of Agricultural Resources and Regional Planning, Chinese Academy of Agricultural Sciences, Beijing, 100081, China;

4 ICube, Uds, CNRS, 300 Bld Sebastien Brant, CS10413, 67412 Illkirch, France

5 Key Laboratory of Quantitative Remote Sensing Information Technology, Academy of Opto-Electronics, CAS, Beijing, 100094, China

6 Guilin University of Technology, Guilin, Guangxi, 541004, China

E-mail address: zhangyuze999@126.com *Corresponding author: xgjiang@ucas.ac.cn

ABSTRACT—Landsat-8 carries two instruments: the Operational Land Imager (OLI) and the thermal infrared sensor (TIRS). Unlike the former satellites in Landsat program, for instance, the TM sensors on Landsat 4 and 5, and ETM+ on Landsat 7, there are two thermal bands on TIRS sensor which make the split-window algorithm to be feasible to retrieve Land Surface Temperature (LST) from Landsat-8 data. In this study, we aimed to make a full comparison for the performance in retrieving LST from Landsat-8 data with the split-window (SW) method and the single-channel (SC) method. However, as the discrepancies have been noted between calibrated TIRS Bands 10 and 11 data, we use the simulated data instead. Furthermore, two types of errors on surface emissivity and brightness temperature are also involved. The results show that the root mean square errors (RMSEs) of the retrieved LST of SC method are usually larger than that of SW method if the sensor-dependent coefficients and parameters are provided accurately, especially for wet atmospheric profiles. But, when considering the errors in retrieved LST, only for the dry atmospheric profiles, SC method could then have a better accuracy than the SW method.

1 INTRODUCTION

Landsat-8 is an American Earth observation satellite launched on February 11, 2013, which is also known as the Landsat Data Continuity Mission (LDCM). It is the 8th satellite in the Landsat program and provides repetitive acquisition of high resolution multispectral data of the Earth's surface on a global basis. Landsat-8 carries two instruments, i.e., the Operational Land Imager (OLI) and the thermal infrared sensor (TIRS). The OLI measures data for visible, near infrared, and short wave infrared spectral bands at 30 m (15 m panchromatic band) spatial resolution. The TIRS measures the TIR radiance at 100 m spatial resolution using two bands between 10 and 12 μm (Irons et al., 2012; Jiménez-Muñoz et al., 2014).

In TIR applications, land surface temperature (LST) is no doubt an important variable derived from TIR data. LST is a key parameter in the processes controlling energy, water, and biogeochemical fluxes

over the interface between land surface and atmosphere (Holmes et al., 2009). Generally, the common algorithms for LST retrieval can be roughly grouped into three categories: single-channel methods, multi-channel methods, and multi-angle methods. The single-channel methods are based on the inverse formula of the radiance measured by the satellite sensor and the split-windows methods use the different water vapor absorption in two adjacent TIR channels to retrieve LST. Unlike the multi-channels method, the theory of multi-angle algorithm is based on the differential atmospheric absorption (Z.-L. Li et al., 2013).

The main goal of this paper is to compare the performance of different methods in LST retrieval from Landsat-8 data. And when considering the applicability of the algorithms to Landsat-8 data, only two methods are finally involved. They are the single-channel method and the split-window method. Two types of errors were also introduced to make full

comparisons. However, due to the larger calibration uncertainty associated with TIRS band 11, we used simulated data in this paper.

2 ALGORITHM AND DATA

2.1 Single-channel algorithm

The SC^{JM&S} algorithm involved in this paper can be expressed as follow (Jiménez-Muñoz and Sobrino, 2003):

$$T_s = \gamma \left[\frac{1}{\varepsilon} (\Psi_1 L_{sen} + \Psi_2) + \Psi_3 \right] + \delta \quad (1)$$

where ε is the surface emissivity, and (γ, δ) are two parameters given by:

$$\gamma \approx \frac{T_{sen}^2 c_2}{\lambda L_{sen}} \quad (2)$$

$$\delta \approx T_{sen} - \frac{T_{sen}^2 c_2}{\lambda} \quad (3)$$

where T_{sen} is the at-sensor brightness temperature, with $c_2 = 1.43877e4 \mu\text{m} \cdot \text{K}$, and Ψ_1, Ψ_2, Ψ_3 are obtained from the atmospheric parameters, also called the atmospheric functions (AFs). The details are as follow:

$$\Psi_1 = \frac{1}{\tau}; \Psi_2 = -L^\downarrow - \frac{L^\uparrow}{\tau}; \Psi_3 = L^\downarrow \quad (4)$$

where τ is the atmospheric transmissivity, L^\downarrow is the downwelling atmospheric radiance, and L^\uparrow is the upwelling atmospheric radiance. AFs can also be empirically obtained through the water vapor content, given by:

$$\begin{bmatrix} \Psi_1 \\ \Psi_2 \\ \Psi_3 \end{bmatrix} = \begin{bmatrix} c_{11} & c_{12} & c_{13} \\ c_{21} & c_{22} & c_{23} \\ c_{31} & c_{32} & c_{33} \end{bmatrix} \begin{bmatrix} w^2 \\ w \\ 1 \end{bmatrix} \quad (5)$$

where coefficients $c_{i,j}$ are obtained from simulated data, and w is water vapor content.

Note that all λ in this paper means the effective wavelength for the channel (TIRS band 10 for SC), given by:

$$\lambda_{\text{effective}} = \frac{\int \lambda f(\lambda) d\lambda}{\int \lambda d\lambda} \quad (6)$$

where $f(\lambda)$ is the response function of TIRS band 10 (Jiménez-Muñoz and Sobrino, 2010; Jiménez-Muñoz et al., 2009).

2.2 Split-window algorithm

The split window method (Wan and Dozier, 1996) is used to retrieve the LST based on the different water vapor absorption in two different infrared bands and the algorithm can be expressed as:

$$T_s = a_0 + \left(a_1 + a_2 \frac{1-\varepsilon}{\varepsilon} + a_3 \frac{\Delta\varepsilon}{\varepsilon^2} \right) \frac{T_i + T_j}{2} + \left(a_4 + a_5 \frac{1-\varepsilon}{\varepsilon} + a_6 \frac{\Delta\varepsilon}{\varepsilon^2} \right) \frac{T_i - T_j}{2} \quad (7)$$

where T_i and T_j are the TOA brightness temperatures measured in TIRS band 10 ($10.89 \mu\text{m}$) and 11 ($12.0 \mu\text{m}$); ε is the average emissivity given by:

$$\varepsilon = \frac{\varepsilon_{b10} + \varepsilon_{b11}}{2} \quad (8)$$

and $\Delta\varepsilon$ is the emissivities difference between the two adjacent bands, the expression goes as follow:

$$\Delta\varepsilon = \varepsilon_{b10} - \varepsilon_{b11} \quad (9)$$

where ε_{b10} and ε_{b11} are, respectively, the surface emissivities, and coefficients $a_0 \sim a_7$ are derived from simulated data.

2.3 Simulated Data

In order to generate the simulated Landsat-8 data and get the sensor-dependent coefficients, the ASTER Spectral Library, the Thermodynamic Initial Guess Retrieval (TIGR) database and the atmospheric radiative transfer model MODTRAN 4.0 were used in this study.

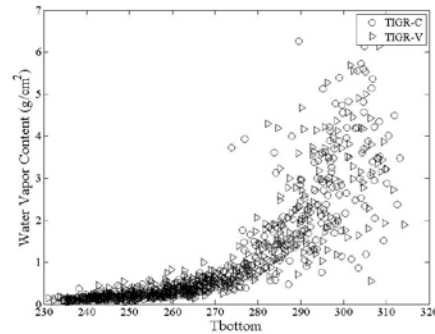


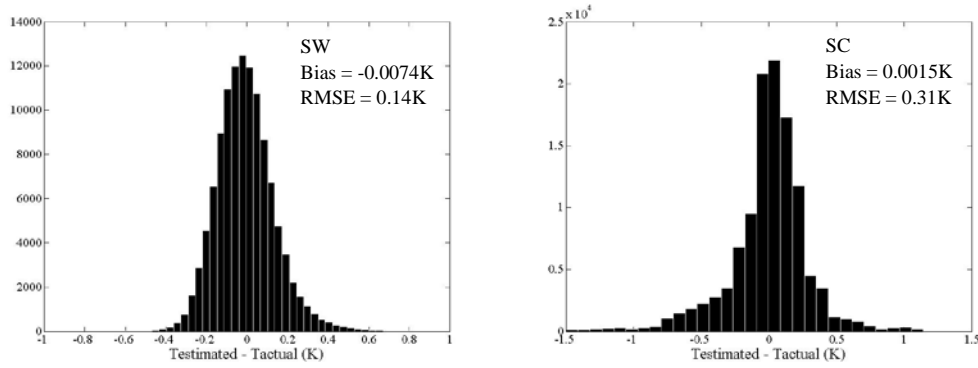
Fig.1. The water vapor content as function of the atmospheric temperature in TIGR-C and TIGR-V

Table 1. Coefficients of SW algorithm obtained from TIGR-C for the sub-range $w \in [0, 1.5] \text{ g/cm}^2$

SW	a_0	a_1	a_2	a_3	a_4	a_5	a_6
	-2.0261	1.0090	0.1574	-0.2993	3.1858	13.6912	0.5922

Table 2. Coefficients of SC algorithm obtained from TIGR-C for the sub-range $w \in [0, 1.5] \text{ g/cm}^2$

SC($c_{i,j}$)	j=1	j=2	j=3
i=1	0.0287	0.0528	1.0279
i=2	-0.5423	-0.9669	-0.1127
i=3	0.2779	0.6208	0.0591

**Fig.2.** Difference between estimated T_s and actual T_s obtained from TIGR-V for the sub-range $w \in [0, 1.5] \text{ g/cm}^2$

To test the accuracies of the coefficients, the TIGR2000 database was divided into two groups: TIGR-C and TIGR-V. The distribution of each group's water vapor content is shown in Fig.1.

3 RESULTS AND DISCUSSION

All coefficients and parameters in algorithms were obtained through the TIGR-C and then evaluated by TIGR-V. We also divided the water vapor content (WVC) into six sub-ranges for improving the accuracies of the algorithm coefficients (B.H. Tang et al., 2008). ([0, 1.5], [1.0, 2.5], [2.0, 3.5], [3.0, 4.5], [4.0, 5.5], [5.0, 6.5]) However, as the RMSEs of the LST retrieved with SC method would be terrible under the condition of higher WVCs, which have been listed in Table 3, only the first two sub-ranges were considered. Coefficients of these two methods, for the sub-range $w \in [0, 1.5] \text{ g/cm}^2$, are shown in Table 1 and 2, and the corresponding ΔT_s (estimated T_s - actual T_s) are shown in Fig.2. Similar results are obtained for the sub-range $w \in [1.0, 2.5] \text{ g/cm}^2$.

Then the retrieval results with different errors of

surface emissivity and of brightness temperature were compared. In addition, two types of errors were considered: bias error and standard deviation (std) error. The bias errors on surface emissivity ranged from 0 to ± 0.01 with a step of 0.002 and from 0 to $\pm 0.5\text{K}$ for brightness temperature with a step of 0.1K. The std errors ranged from 0 to 0.02 for surface emissivity with a step of 0.002 and from 0 to 0.5 with a step of 0.1K for brightness temperature. The results with errors on surface emissivity are provided in Fig.3.

Table 3. RMSEs of SW and SC methods for different sub-ranges

WVC(g/cm ²)	SW(K)	SC(K)
[0,1.5]	0.14	0.32
[1.0,2.5]	0.24	1.10
[2.0,3.5]	0.40	1.98
[3.0,4.5]	0.48	3.12
[4.0,5.5]	0.63	2.95
[5.0,6.5]	0.93	4.05

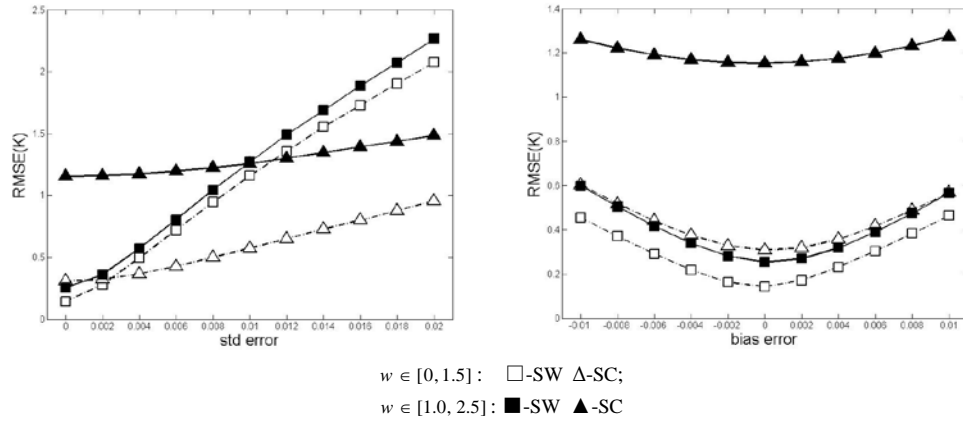


Fig.3. The RMSEs between actual and estimated T_s with errors on emissivity for the sub-ranges $w \in [0, 1.5]$ and $w \in [1.0, 2.5]$ g/cm^2

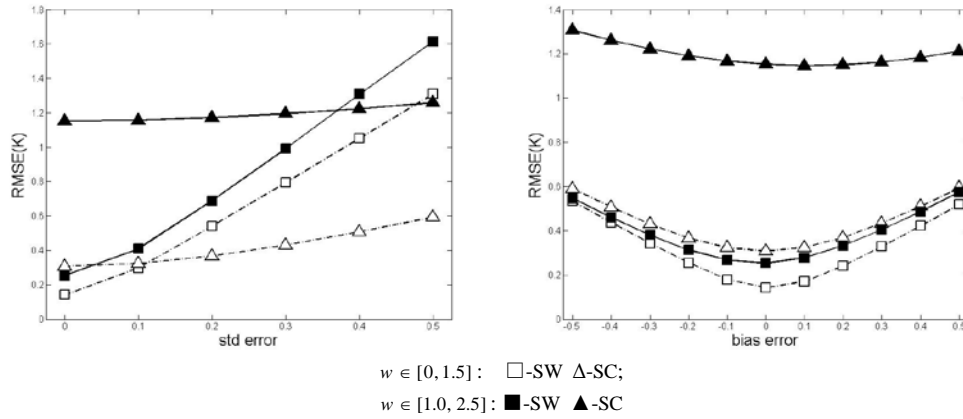


Fig.4. The RMSEs between actual and estimated T_s with error on brightness temperature for the Sub-ranges $w \in [0, 1.5]$ and $w \in [1.0, 2.5]$ g/cm^2

From Fig 3, one can see that SW method was always better than SC method if coefficients and parameters were provided accuracy. However, it was evident that the SW method was much sensitive to std error than SC method. The difference between maximum and minimum RMSE of SW method was about 1.9K, which was just about 0.6K for SC method, with std errors for the sub-range $w \in [0, 1.5]$ g/cm^2 . Furthermore, the difference of SC method would even be smaller under the condition of a higher WVC. For example, it was only about 0.3K larger with a std error of 0.02 for the sub-range $w \in [1.0, 2.5]$ g/cm^2 . In addition, it is also obvious that the trends of RMSEs of these two methods would go into sharp reverse when the std error was larger than a certain value, which we called error threshold. As was shown in Fig.3, when the std error on emissivity was less than about 0.002 for the sub-range $w \in [0, 1.5]$ g/cm^2 and with no bias error, the RMSEs of SW method were always smaller

than SC method, but it would come to a completely opposite conclusion if the std error was larger than 0.002. And the difference in RMSE of these two methods would then become larger and larger with increase of std error. Just as shown in Fig.3, when the std error reached 0.02, the RMSE of SW method was almost 1K larger than that of SC method. On the other hand, from Fig.3 one can also see that the SC method was highly sensitive to WVC. The RMSE of SC method was about 0.3K with no errors for the first sub-range, but it would be about 1.1K for the second sub-range. On the contrary, the RMSEs of SW method were relatively stable for both sub-ranges. The difference was only about 0.2K. The results with bias errors showed that the trend of these two methods were similar, however, unlike the results with std errors, the error threshold was not found here, which means the accuracy of SW method was usually better than SC method.

Fig.4 shows the results with errors on brightness temperature and similar conclusions were obtained. The important thing to note, however, is that a bias error of 0.002 on emissivity might have a similar impact on RMSEs to that with a bias error of 0.1K on brightness temperature.

4 CONCLUSIONS

In this paper, two general methods for retrieving LST from Landsat-8 data are compared with simulated data. For more comprehensive analysis, two types of errors are also considered in retrieved LST. The results demonstrate that the SW method is little better than SC method with a low WVC, which means a dry atmospheric profile. However, the accuracy of SC method will then become unacceptable with the increase of WVC, which means that these two methods are only comparable for very dry atmospheric profiles. Furthermore, taking into account the errors on emissivity and brightness temperature in LST retrieval, we find only when the std error is small than a certain value, which depends on the specific condition of WVC, does the accuracy of SW method is better than SC method—that is, SC method might be a high-accuracy method under a specific condition. Therefore, according to the fewer parameters in SC method, it might be a preferred one to retrieve LST from Landsat-8 if the WVC is low enough, while the SW method will be an appropriate choice for wet atmospheric profiles. However, when errors are known a priori, it will depend on the specific condition to choose the right method to retrieve LST.

ACKNOWLEDGEMENTS

This work was supported by the National Natural Science Foundation of China (41231170 and 41471297), by the National Key Basic Research Program (973 Program, 2013CB733402), and by the National High Technology Research and Development Programme of China (2012AA121103)..

REFERENCES

- Bohui Tang, Yuyun Bi, Zhao-Liang Li and Jun Xia, "Generalized Split-Window Algorithm for Estimate of Land Surface Temperature from Chinese Geostationary FengYun Meteorological Satellite (FY-2C) Data", *Sensors* 2008, 8(2), 933-951.
- Juan C. Jiménez-Muñoz, José A. Sobrino, Dražen Skoković, Cristian Mattar and Jordi Cristóbal, "Land Surface Temperature Retrieval Methods From Landsat-8 Thermal Infrared Sensor Data", *IEEE Geoscience and Remote Sensing Letters*, vol. 11, No.10, pp. 1840-1843, Oct. 2014.
- Juan C. Jimenez-Munoz and Jose A. Sobrino, "A generalized single-channel method for retrieving land surface temperature from remote sensing data", *Journal of Geophysical Research*, vol. 108, D22, pp. 4688, Nov. 2003.
- Juan C. Jiménez-Muñoz and José A. Sobrino, "A Single-Channel Algorithm for Land-Surface Temperature Retrieval From ASTER Data", *IEEE Geoscience and Remote Sensing Letters*, vol. 47, No. 1, pp.339-349, Jan. 2009
- Juan C. Jiménez-Muñoz, Jordi Cristóbal, José A. Sobrino, Guillem Soria, Miquel Ninyerola, and Xavier Pons, "Revision of the Single-Channel Algorithm for Land Surface Temperature Retrieval From Landsat Thermal-Infrared Data", *IEEE Transactions on Geoscience and Remote Sensing*, vol. 47, No. 1, pp.339-349, Jan. 2009
- T.R.H. Holmes, R. A. M De Jeu, M. Oew, and A. J. Dolman, "Land surface temperature from Ka band (37GHz) passive microwave observations," *J. Geophys. Res.*, vol.114, no. D4, pp.1-15, Feb. 2009.
- Wan, Z.; Dozier, J. "A generalized split-window algorithm for retrieving land-surface temperature from space", *IEEE Transactions on Geoscience and Remote Sensing*, Vol.34, No.4, pp.892-905, 1996.
- Z.-L. Li, H. Wu, N. Wang, S. Qiu, J. A. Sobrino, Z. Wan, B.-H. Tang, and G. Yan, "Land surface emissivity retrieval from satellite data," *Int. J. Remote Sens.*, vol. 34, no. 9/10, pp. 3084–3127, 2013.

Study on the methods of quantitative retrieval of farmland soil salinity based on remote sensing characteristic index——A Case Research in Xinjiang Shihezi Farming Area

Shi Chen^{a,b}, Chao Gao^b, Bin Xu^a, Yunxiang Jin^a, Jinya Li^{a,d}, Hailong Ma^a, Fen Zhao^a, Jian Guo^a, Xiuchun Yang^{a,c,*}

^a Key Laboratory of Agri-informatics, Ministry of Agriculture / Institute of Agricultural Resources and Regional Planning, Chinese Academy of Agricultural Sciences, Beijing 100081, China; ^b College of Territorial Resources and Tourism, Anhui Normal University, Wuhu 241000, China; ^c College of Environment and Planning, Shangqiu Normal University, Henan 476000, China; ^d State Key Laboratory of Urban and Regional Ecology, Research Center for Eco-Environmental Sciences, Chinese Academy of Sciences, Beijing 100085, P.R. China

Shi Chen(shic11@126.com); Xiuchun Yang(yangxiuchun@caas.cn)

ABSTRACT- Salinized soil has posed severe threat to the sustaining cultivation of land and grain production safety. It is of great significance for the sustainable development of Xinjiang Agriculture to monitor, prevent and treat soil salinization. On the basis of remote sensing image from Landsat-8 OLI and 72 sampling points' soil salinity data from field sampling measurement, this paper contrasted the correlativity among sensitive bands, characteristic remote sensing index and ground soil salinity. Based on PLSR and BP neural network, this paper quantitatively inverted the soil salinity of Farming Area of Shihezi in Xinjiang, establishing high accuracy soil salinity inversion model. The research showed that (1) a good correlation existed between the characteristic remote sensing index and ground soil salinity; (2) compared with inversion model of remote sensing sensitive band for inversion soil salinity, it can be more accurate and dependent to utilize characteristic remote sensing index; (3) characteristic remote sensing index had better inversion effect of soil salinity on the BP neural network platform, with the model verification root-mean-square error and average relative error respectively 3.07 and 0.34, and the inversion accuracy reached up to 66%; comparing to the former inversion methods of soil salinity, it improved the accuracy to some extent, and had significant scientific reference value to the improvement, prevention and treatment of soil salinization.

1 INTRODUCTION

Global climatic change has made the soil salinization increasingly obvious at the middle and low latitude (Pankova et al. 2013; Li et al. 2012), particularly causing great losses to the crop yield and regional production of Xinjiang of the arid and semi-arid (Danierhan et al. 2013). Timely inverting soil salinity of the farming area by using remote sensing technology has great significance to the prevention and treatment to soil salinization of the farming area (Wang et al. 2006; Li et al. 2014).

There have been a large number of studies on quantitative inversion of soil salinity by utilizing remote sensing images at home and abroad (Jiang et al. 2014; Liu et al. 2013; Farifteh et al. 2007; Summers et al. 2011), and these studies mainly include the following two aspects. ① After variant mathematical manipulation of reflectivity on remote sensing images, screen the most sensitive band in response to soil

salinity. Adopt the analytical methods of geographical information system for quantitative inversion of soil salinity (Xu et al. 2014). Some studies show that positive correlation exists between the band reflectivity on the remote sensing images and corresponding soil salinity. The construction of relation model between the sensitive band and actually-measured soil salinity can better reflect the soil salinity of the researched district (Pu et al. 2012). ② Jianli Ding made mathematical manipulation on remote sensing images to highlight the information beneficial to research, and utilized Modified Soil-adjusted Vegetation Index (MSAVI), Humidity Index (HI) and Salt Index (SI) to build the remote sensing inversion model of soil salinity, providing a new orientation for soil salinity inversion (Ding et al. 2013; Zhang et al. 2013). In the inversion methods, scholars mostly utilized PLSR and BP artificial neural network to build inversion models, in which BP artificial neural network method has higher accuracy (Fu et al. 2007).

Generally, at present utilizing remote sensing image for quantitative inversion of the soil salinity of ground surface is mainly to build the inversion model between remote sensing sensitive band and soil salinity, fewer use the characteristic remote sensing index of variant representation soil salinity on the remote sensing image to inverse the soil salinity.

During the remote sensing inversion process, the factors such as ground surface soil brightness, soil humidity, soil salt cover degree and soil radiation level would indirectly reflect the salinity in remote sensing pixels. This paper adopts the indicators like Soil Brightness Index (SBI), Soil Moisture Index (SMI), Soil Salt Cover Index (SSCI) and Soil Radiation Level Index (GRLI) to build characteristic remote sensing index, then inverts the soil salinity of Shihezi Farming Area based on BP neural network. It establishes soil salinity inversion model of high-accuracy BP neural network, providing a new way for the quantitative inversion of ground surface salinity, as well as offering scientific reference for the prevention and treatment of soil salinity.

2 MATERIALS AND METHODS

2.1 Study site

The study area is located in Manas County and Shawan County of Shihezi City, the Northern Farming Field, Xinjiang Uygur Autonomous Region, with the geographical coordinate scope of 84°07'~86°33'E and 43°28'~45°08'N (Figure 1). This area is located at the south edge of Junggar Basin, the northern foot of Tianshan Mountain, the south edge of Gurbantunggut Desert. It is characterized by typical temperate continental drought climate, severe cold in winter and extremely hot in summer, with annual precipitation of 125.0-207.7mm and average sunshine duration of 2721-2818 hours, quick temperature rise in Spring and fall in Autumn, large temperature differences between the daytime and night, and 450.8m mean altitude. The river flows into Junggar Basin from south to north, with shallow groundwater. Groundwater flows slowly, easily causing salt accumulation greater than the discharge rate.

2.2 Data resources

Field sampling points were taken from April 23 to 28, 2013. Investigations were made to areas with different contents in soil moisture and salt, 0-30cm salinized soil of soil surface was collected as specimens(Zhao et al. 2008), 72 ground soil salinity specimens were obtained, and 8 ion assay measurement method was adopted to get the soil salinity of sampling points.

Landsat 8 OLI series remote sensing data resources of medium spatial resolution were selected with the strip belt No. Path:144 and Row:29, 30m of spatial resolution. The imaging date was April 13, 2013. The sparse ground vegetation growth of the

period and good climatic conditions were beneficial to the ground soil salinity inversion. Geometrical correction method for retaking examples was utilized by using quadratic polynomial and bilinear interpolation methods, outputting UTM projection and spheroid of WGS84. All control points' errors and overall error shall be guaranteed within 0.5pixel. By utilizing ENVI5.0 atmospheric correction modules, the calibration parameter was selected for atmospheric correction.

2.3 Research methods

2.3.1 Selection of the sensitive bands

It has become an important means to invert soil salinity by using the sensitive band of remote sensing images. We calculated the correlation coefficient and diagnosing index between the reflectivity of band 1 to band 7 from the remote sensing data of Landsat 8 OLI and the corresponding ground soil salinity of 72 sampling points. From the analysis of Figure 1, the correlation coefficient and diagnosing index of band 3 to band 6 in Landsat 8 OLI were higher than those of other bands, so these bands were suitably used as sensitive bands for inversion of the ground soil salinity.

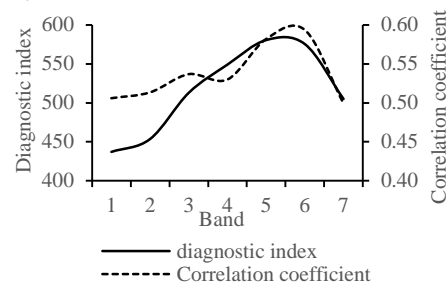


Figure 1. Correlative coefficient and diagnosing index of reflectivity and salinity from band 1 to band 7 of Landsat8 OLI

2.3.2 Determination of characteristic remote sensing index

The inversion of soil salinity from remote sensing image data is liable to be affected by soil humidity, brightness, soil salt cover degree and radiation level. In order to improve the inversion accuracy, the characteristic remote sensing index were sorted out which represented higher soil salinity correlation coefficient from Landsat 8 OLI remote sensing images, including the factors of Soil Brightness Index (SBI), Soil Moisture Index (SMI), Soil Salt Cover Index (SSCI) and Soil Radiation Level Index (GRLI). Soil Brightness Index (SBI) and Soil Moisture Index (SMI) can be obtained from tasseled cap transformation. Soil Salt Cover Index (SSCI) can be obtained through decomposing mixed pixels by taking oil, saline soil and vegetation as end members. Soil

Radiation Level Index (GRLI) was obtained from LBV change. Through the analysis of SPSS, the correlation coefficients between SBI, SMI, SSCI, GRLI and the ground soil salinity of 72 sampling points can be obtained as 0.708, -0.621, 0.699 and 0.698, which were higher than those between sensitive bands and soil salinity.

To study the fit goodness between the sensitive band in Landsat 8 OLI, the characteristic remote sensing index of SBI, SMI, SSCI and GRLI and ground points soil salinity, the linear and nonlinear methods were utilized in SPSS to fit the relation of band reflectivity, characteristic remote sensing index value and the ground points soil salinity. The study showed that the optimum fitting R^2 between the reflectivity of sensitive band in Landsat 8 OLI and soil salinity was smaller than the degree of fitting of the characteristic remote sensing index and ground soil salinity (Figure 2).

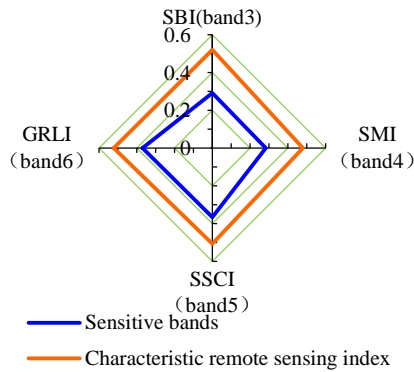


Figure 2. Correlativity among the sensitive band, characteristic remote sensing index and ground soil salinity

To further explore the fit goodness between characteristic remote sensing index of SBI, SMI, SSCI and GRLI and soil salinity of ground surface points, we utilized linear and nonlinear methods to fit the relation between all kinds of characteristic remote sensing index value and soil salinity of ground surface points. The study showed that the best fitting result of SBI was nonlinearity index method, and the fit goodness R^2 reached 0.521. SMI optimum fitting method was quadratic polynomial, and R^2 was 0.480. The best fitting method of SSCI and GRLI was power function. The values of fit goodness R^2 were 0.506 and 0.522 respectively. Thus it can be seen that the correlation between characteristic remote sensing index value and soil salinity was high.

2.3.3 Characteristic remote sensing index and sensitive band PLSR for inversion soil salinity

PLSR is widely used in the inversion modeling (Farifteh et al. 2007). The method is used to contrast and analyze the accuracy of characteristic remote

sensing index and sensitive band for inversion of the of ground surface salinity. In SPSS, characteristic remote sensing index of SBI, SMI, SSCI and GRLI and band 3, band 4, band 5 and band 6 are taken as the independent variables, and the ground soil salinity of 52 sampling points are taken as the dependent variables so as to construct PLSR inversion model. At last, randomly reserved 20 soil sample data were adopted for accuracy verification of models. Specifically, two verification indicators REE and RMSE were adopted. The smaller the REE and RMSE were, the higher the accuracy of inversion model was, with the calculating formula as follows.

$$REE = \sqrt{\frac{\sum [(T_i - P_i) / P_i]^2}{N}} \quad (1)$$

$$RMSE = \sqrt{\frac{\sum (T_i - P_i)^2}{N}} \quad (2)$$

In this formula, T_i was the ground point measured value of the sampling point's soil salinity; P_i was the inversion predicted value of the sampling point's soil salinity; N was the number of samplings to verify the inversion accuracy of soil salinity.

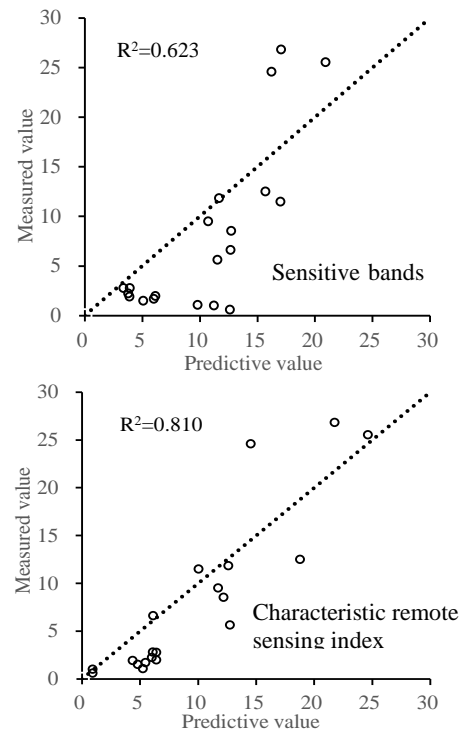


Figure 3. PLSR inversion accuracy verification between sensitive band and characteristic remote sensing index

Seen from the verification result of inversion model set up from PLSR, the inversion effect of characteristic remote sensing index was better than that of sensitive band. Their degrees of fitting R^2 were

0.810 and 0.623 respectively (Figure 3). The accuracy verification indicators RMSE were 4.111 and 5.914 respectively with REE respectively as 0.480 and 0.545, and the model accuracy were 52% and 45.5% respectively.

3 INVERSION OF SOIL SALINITY BASED ON BP NEURAL NETWORK

3.1 Structure of the inversion model of BP neural network for soil salinity

Through the above correlation analysis and accuracy comparison, it is derived that the inversion of ground soil salinity by using characteristic remote sensing index is more accurate. BP neural network has strong linear and nonlinear simulation ability comparing to other inversion models, with some certain summarizing and generalizing capacity, particularly adaptable to simulate the internal mechanism complex relationship between remote sensing image features and soil salinity, which can invert the actual ground soil salinity through remote sensing images. Therefore, we can take MATLAB as the research platform, and design structure of BP neural network, as well as take the SBI, SMI, SSCI and GRLI data of 52 pixels of remote sensing images to as input factor, then set up inversion model with the corresponding ground soil salinity of 52 sampling points. Finally we utilized the randomly reserved 20 groups of SBI, SMI, SSCI and GRLI data and soil salinity for verification.

3.2 Comment and verification of BP soil salinity inversion accuracy

The test demonstrated that the training speed was quick to construct good BP model, and the simulation accuracy was high (Figure 4). The simulation effect of simulation salt salinity and true salinity was satisfactory, and the corresponding degree of the two aspects was basic identical. The simulation degree was high, and the relation degree R^2 of predicted value and measured value of inversion model reached 0.999, with simulation value and predicted value basically on the linear trend line. It can be seen that nerve network model has strong nonlinear goodness of fit, which demonstrated that the effect of inverting soil salinity by utilizing remote sensing index was satisfactory. Thus, this high-accuracy training model can be utilized for the inversion of the soil salinity of other pixels on the remote sensing images.

From the scatter diagram of verifying measured value and predicted value we can know that the goodness of fitting R^2 between measured value and predicted value was 0.917 (Figure 5). The accuracy verification indicators RMSE and REE of inversion model shall be 3.07 and 0.34, and the accuracy model was 66%. Comparing to the effect of the inversion of soil salinity utilizing the sensitive band of CBERS

made by Zhang et.al (Zhang et al 2013), the training sample and verification sample were basically same. The obtained training nerve cell verification R^2 was 0.751, smaller than the simulation result of this paper. Thus, through the above BP neural network accuracy verification analysis, it was found that the inversion of soil salinity through BP neural network by utilizing remote sensing index had great advantages.

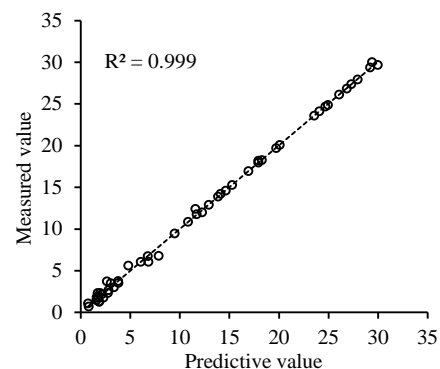


Figure 4. The precision results of inversion model training of neural network

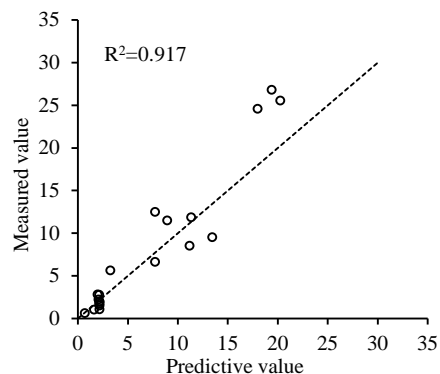


Figure 5. The validation scatter plot of using BP Neural network to invert soil salinity

3.3 The analysis of the spatial pattern of remote sensing inversion of soil salinity

Based on well-trained high-accuracy nerve cell for inversion the soil salinity of each pixel of cotton field of research area, the spatial pattern figure of soil salinity of cotton field can be obtained (Figure 6). The figure illustrated that the grade of salinization was obvious and clear in hierarchy. In terms of administrative layer, the influence was dominant in cotton field of Shawan County, further exceeding Manas County and Shihezi City. The areas with higher salinization were mainly distributed in the village areas like 135 Round Field of Shawan County, Xiabahu Village, 132 Round Field, Red Flag Farm,

and Wutongshu Village. Manas County was less influenced by salinization. The salinization degree of 149 Round Field was high. The cotton field soil salinization within Shihezi City was below Level 2, with less harm. Seen from the distribution pattern of soil salinization degree of research area, it demonstrated the pattern of “One Belt and One Area”. “One Belt” was the strip with higher salinization degree formed by Manas Drainage Basin, represented by 135 Round Field, Zhabankou Village and Erping Village from northwest the southeast. “One Area” covered the typical salinization area composing 132 Round Field, 134 Round Field, Red Flag Farm and Wutongshu Village. Thus, while considering taking the preventing and treating measures of salinization, it was feasible to implement treatment by combining the “One Belt and One District” focus area proposed in this paper.

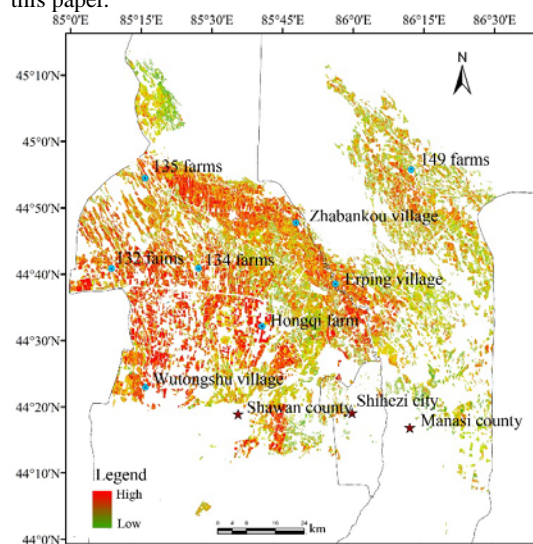


Figure 6. The spatial pattern of inversion of soil salinity in the cotton field

4 DISCUSSION

In the inversion research of ground salinity, most scholars utilize remote sensing data for direct or indirect inversion of ground soil salinity. Direct inversion means to excavate the indicators of higher correlation with the ground soil salinity from remote sensing images (Metternich et al. 1997; Ben-Dor et al. 2002), and obtain the inversion of the ground salinity from these indicators. Indirect inversion means to monitor the vegetation sensitive to salinity through remote sensing data, so as to obtain the salinity of soil indirectly from sensitive vegetation (Dehaan et al. 2002; Metternich et al. 2003). In remote sensing data sources, multispectral or hyperspectral data are adopted for the inversion of soil salinity so as to utilize the mathematical manipulation and correlation

analysis, to study the correlation of remote sensing data TM(An et al. 2008), HJ-1A(Ma. 2014), Aster(Wang et al. 2009) and Hyperion(Liu et al. 2009; Tang et al. 2010) and soil salinity, so as to determine the respective sensitive band and obtain the inversion of ground soil salinity.

Dealing with the features of soil salinity represented at the images, this paper held that the differences of remote sensing index SBI, SMI, SSCI and GRLI of salinized soil would influence the inversion accuracy of soil salinity of the ground surface. The study showed that the accuracy of inversion soil salinity would be improved based on comprehensive considering the characteristic remote sensing index of the above several features. However, the information like the soil distribution, degree, nature and scope of salinization would change with time. Thus multi-temporal remote sensing data may be combined to synthesize inversion. It was required to study further on whether other remote sensing data sources had better effect. This research was only suitable for the remote sensing images with the soil salinity of ground point. The inversion and generalization of inversion model of soil salinity in other years was beneficial to learn the dynamic process of soil salinization change.

5 CONCLUSIONS

There have been a great number of inversion studies on ground soil salinity with remote sensing technology. With the advancement of science and technology, the inversion methods are developed rapidly. This paper takes Landsat-8 OLI as the remote sensing resource, and utilizes sensitive band and characteristic remote sensing index, then respectively adopts the methods of PLSR and BP nerve network to build inversion model of ground soil salinity, finally proposes a set of high-accuracy remote sensing soil salinity inversion model.

ACKNOWLEDGEMENTS

This study was supported by the Doctorial Fund Project of Xinjiang Production and Construction Corps (2012BB001), the Project of Scientific and Technological Support to Xinjiang of Xinjiang Production and Construction Corps (2013AB017), International Science & Technology Cooperation Program of China (2013DFR30760).

REFERENCES

- An, Y. Q., Y. H. Qu, H. Y. Gao, X. L. Duan, J. W. Wu, and A. P. Chen., 2008, Supervising the Salted Land Distribution of Hetao Irrigation Area in Inner Mongolia by Using Remote Sensing. *Remote Sensing Technology and Application*, 23: 316-322.

- Ben-Dor, E., K. Patkin, A. Banin., 2002, Mapping of several soil proper-ties using DAIS-7915 hyperspectral scanner data:A case study over clayey soils in Israel. *International Journal of Remote Sensing*, 23: 1043-1062.
- Danierhan, S., A. Shalamu, H. Tumaerbai, D. H. Guan., 2013, Effects of emitter discharge rates on soil salinity distribution and cotton (*Gossypium hirsutum* L.) yield under drip irrigation with plastic mulch in an arid region of Northwest China. *Journal of Arid Land*, 5: 51-59.
- Dehaan, R. L., G R Taylor., 2002, Field-derived spectra of salinized soils and vegetation as indicators of irrigation-induced soil salinization. *Remote Sensing of Environment*, 80:406-417.
- Ding, J. L., J. Qu, Y. M. Sun., 2013, The retrieval model of soil salinization information in arid region based on MSAVI-WI feature space: A case study of the delta oasis in Weigan-Kuqa watershed. *Geographical Research*, 32: 223-232.
- Farifteh,J., F. V. D. Meer, C. Atzberger., 2007, Quantitative analysis of salt-affected soil reflectance spectra:A comparison of two adaptive methods (PLSR and ANN). *Remote Sensing of Environment*, 110: 59-78.
- Fu, Q. H., S. X. N, S. X. Wang., 2007, Retrieval of salt content base on remote sensing. *Transactions of the CSAE*, 23: 48-54.
- Jiang, H. T., T. Tashpolat, S. Mamat., 2014, Study on spatial and temporal dynamics change of soil salinization in Keriya Oasis. *Chinese Journal of Soil Science*, 45: 123-129.
- Li, J. G., L. J. Pu, M. Zhu., 2012, The present situation and hot issues in the salt-affected soil research. *Acta Geographica Sinica*, 9: 1233-1245.
- Li, J., G. X. Zhao, C. Y. Chang., 2014, Land salinization information extraction method based on HSI hyperspectral and TM imager. *Spectroscopy and Spectral Analysis*, 34: 520-525.
- Liu, D. d., Q. Wang., 2009, Inversion Model of BP Neural Network for Soil Salinity. *Journal of Northeast Agricultural University*, 37: 88-90.
- Liu, L. J., Y. G. Wang, X. Y. Li., 2013, Spatial distribution pattern of soil dissolved inorganic carbon in an arid oasis. *Chinese Journal of Ecology*, 32: 2539-2544.
- Ma, C., 2014, Research on soil salinization using remote sensing of HJ-1A hyper spectral images. *Journal of Arid Land Resources and Environment*, 28: 180-184.
- Metternichit, G., J. A. Zinck., 1997, Spatial discrimination of salt and sodium affected soil surfaces. *International Journal of Remote Sensing*, 18: 2571-2586.
- Metternicht, G. I., J.A.Zinck., 2003, Remote sensing of soil salinity: potentials and constraints. *Remote Sensing of Environment*, 85: 1-20.
- Pankova, Y. I., A. F. Novikova,A. Kontoboytseva., 2013, The New Map of Soil Salinity and Regularities in Distribution of Salt-Affected Soils in Russia. In *Developments in Soil Salinity Assessment and Reclamation*, Berlin: Springer-Verlag, pp. 99-111.
- Pu, Z., R. D. Yu, C. Y. Yin., 2012, Optimal hyperspectral indices for soil salt content estimation on typical saline soil in arid areas. *Bulletin of soil and Water Conservation*, 32: 129-133.
- Summers, D., M. Lewis, B. Ostendorf., 2011, Visible near-infrared reflectance spectroscopy as a predictive indicator of soil properties. *Ecological Indicators*, 11: 123-131.
- Tang, Y., 2010, Study on inversion of soil salinity. *Engineering of Surveying and Mapping*, 19: 65-67.
- Wang, G. M., D. Li, Z. Z. Wang, and Y. Xing., 2009, Research on Remote Sensing Inversion of Salt Content in Saline-alkali Soil in Song Liao Plain. *Research of Soil and Water Conservation*, 16: 235-237.
- Wang, H., P. Gong, G. H. Liu., 2006, Multi-scale spatial variations in soil salt in the Yellow River Delta. *Geographical Research*, 25: 649-658.
- Xu, C., J. S. Huang., 2014, A study of quantitative hyperspectral inversion of soil salt content. *China Rural Water and Hydropower*, 4: 1-3.
- Zhao, R. F., Y. N. Chen, C. X. Hong., 2008, Study on spatial variability and pattern of soil salinity of the oasis in the headstreams of the Tarim River Basin: A case study on Yuepuhu oasis. *Geographical Research*, 27: 145-154.

Roughness parameterization for soil moisture optimum retrieval over the Valencia Anchor Station

Fernandez-Moran, R. ^(1, 2), Wigneron, J.-P. ⁽²⁾, Lopez-Baeza, E. ⁽¹⁾, Salgado-Hernanz, P.M. ⁽¹⁾, Kerr, Y. ⁽³⁾, Mialon, A. ⁽³⁾, Parrens, M. ^(2, 3), Miernecki, M. ⁽²⁾, Coll-Pajaron, A. ⁽¹⁾, Alyaari, A. ⁽²⁾, Wang, S. ^(2, 5), Schwank, M. ⁽⁴⁾

(1) University of Valencia. Faculty of Physics. Dept. of Earth Physics & Thermodynamics. Climatology from Satellites Group. Calle Dr Moliner, 50, Burjassot. 46100 Valencia. Tel: 963544048, Fax: 963543385.

(2) INRA, UR1391 ISPA, F-33140 Villenave d'Ornon, Centre INRA Bordeaux Aquitaine, France

(3) CESBIO, CNES/CNRS/IRD/UPS, UMR 5126, 18 Avenue Edouard Belin, Toulouse, France

(4) Swiss Federal Research Institute WSL, Birmensdorf, Switzerland

(5) Institute of Remote Sensing and Digital Earth, Chinese Academy of Sciences, Beijing 100094, China

E-mail: roberto.fernandez@uv.es / ernesto.lopez@uv.es

ABSTRACT - Satellites as SMOS (Soil Moisture and Ocean Salinity) and SMAP (Soil Moisture Active Passive) operate at L-band in the aim of providing global maps of SM. The protected L-band is optimum for SM estimation, for what is necessary to account for soil roughness and vegetation.

Different combinations of the values of the model parameters which accounts for soil roughness effects (H_R , Q_R , N_{RH} and N_{RV}) in the L-MEB model (L-band Microwave Emission of the Biosphere) were evaluated. The evaluation was made by comparing the in situ measurements of SM to the SM retrievals based on the L-MEB inversion. We used here two retrieval methods: the classical 2-Parameter (2-P) retrieval method (SM and τ_{NAD} (vegetation optical depth at nadir) are retrieved) and a 3-Parameter (3-P) method, accounting also for the structural effects of vineyards.

Using the 2-P method and setting N_{RP} ($p=H$ or V) equal to -1 the best soil moisture estimations in terms of correlation and unbiased Root Mean Square Error (ubRMSE) was found, especially when Q_R was set equal to 0.1). The assumption that $N_{RV} = N_{RH} = -1$ simplifies the τ - ω model and τ_{NAD} and H_R can be grouped and retrieved as a single parameter (the Simplified Retrieval Method (SRP)). A main advantage of the SRP method is that is not necessary to calibrate the value of H_R to perform SM retrievals. Using the 3-P method, improved results were obtained in the SM retrievals in terms of correlation and ubRMSE.

Keywords: ELBARA-II, L-MEB, SMOS, soil moisture, soil roughness, Valencia Anchor Station.

1 INTRODUCTION

Soil moisture is a parameter which has an important influence in hydrological and meteorological processes. Passive microwave radiometry at L-band (1.4 GHz) has a key role in the estimation of soil moisture (SM). Satellites as SMOS (Soil Moisture and Ocean Salinity) and SMAP (Soil Moisture Active Passive) operate at L-band in the aim of providing global maps of soil moisture (Kerr et al., 2010, Entekhabi et al., 2010(b)). The protected L-band is optimum for SM estimation due to the fact that microwave brightness temperatures (TB) are highly related to the soil dielectric constant which is mainly determined by SM. In spite of this, TB is also affected by other factors such as soil texture and roughness,

vegetation cover and litter (Grant et al., 2007) and soil and vegetation temperatures (Wigneron et al., 2007).

The Valencia Anchor Station (VAS) is currently a long term site for the validation of SMOS. Inside this area, there is a vineyard field called MELBEX-III (Mediterranean Ecosystem L-band Characterization Experiment). Since this area is dedicated to the production of wine, different agricultural practices are performed along the year in the aim of improving the field conditions for a good grape development. These agricultural practices include plowing, vine shoot pruning, tying up long branches to trellis wires, sulfurizing and grape harvest. All of these practices and strong rainfall events bring changes in soil roughness.

The European Space Agency (ESA) selected the VAS for the installation of one of the ELBARA-II radiometers in September 2009, under the responsibility of the Climatology from Satellites Group of the University of Valencia. This is an L-band microwave radiometer which measures brightness temperatures (TB) in dual polarization over the MELBEX-III site.

The L-MEB (L-band Microwave Emission of the Biosphere) model is the basis for the SMOS level 2 soil moisture processor for the retrieval of both vegetation optical depth (TAU) and SM (Wigneron et al., 2007).

This study aims to better understand the effect of soil roughness in soil moisture retrievals at L-band in agricultural areas as the Valencia Anchor Station. For that purpose, it is searched the optimum parameterization of the roughness effects to achieve an improved retrieval of SM. Several combinations of values of the roughness parameters H_R , Q_R and N_{RP} were evaluated, by comparing the SM retrievals with the in situ SM measurements, considered here as the reference. The evaluation was made using all available ELBARA-II observations at 6 am and 6 pm over 2013.

2 MATERIALS AND METHODOLOGY

2.1 Materials

Results shown in this paper are based on measurements made by ELBARA-II over the MELBEX-III site in 2013. This site is located in "Finca El Renagado" (39° 31' 18.18" N, 1° 17' 29.64" W), a field of vineyards with a grapes variety of "tempranillo". Several instruments are deployed there including the L-band ELBARA-II radiometer and several automatic instruments used to characterize the soil and vegetation conditions. ELBARA-II is a dual polarization L-band microwave radiometer with two measuring channels (1400-1418 MHz and 1409-1427 MHz) mounted on a 23.5 dB gain horn antenna. The observed TBp (p=H, V) used in this study is an average of the TB values measured in the two measuring channels. The radiometer is placed on a 15 m height platform to measure continuously the brightness temperature in both polarizations (TBV, TBH) over the vineyard. It is possible to change the antenna inclination, therefore increasing the field of view, in a large incidence angle (θ) range (30 – 150°). The radiometer automatically performs measurements following a protocol which consists in: (i) sky calibration measurements (every day at 23:55) at $\theta = 150^\circ$ (relative to nadir) (ii) angular scans ($\theta = 30^\circ, 35^\circ, 40^\circ, 45^\circ, 50^\circ, 55^\circ, 60^\circ, 65^\circ$ and 70°) every 30 min and (iii) observations at a fixed angle of $\theta = 45^\circ$ every hour at 10, 20, 40 and 50 min (Schwank et al., 2012). Brightness temperatures measured by ELBARA-II were filtered out when the presence of radiofrequency interferences (RFI) is suspected.

Two Delta-T ML2x soil moisture probes are placed in the MELBEX site to estimate SM. They provide the volumetric soil moisture (m³/m³) of the top 0-6 cm soil layer. One ThetaProbe is placed close to a vine stump and the other one is placed in the middle of two vine rows. The average of the two probes, which is considered to be representative of the moisture conditions over the whole field, was taken into account to compute the in situ SM values used in this study. Precipitations for the year 2013 were obtained from "Confederación Hidrográfica del Júcar" (Jucar River Basin Authority).

2.2 General methodology

The SM retrievals were based on the inversion of the L-MEB (L-band Microwave Emission of the Biosphere) model. L-MEB is based on the zero-order radiative transfer τ - ω model (Mo et al., 1982) to model the vegetation effects. According to the τ - ω model, soil emissivity (e_{GP}) can be calculated as follows:

$$e_{GP}(\theta) = 1 - r_{GP}(\theta) \quad (1)$$

where θ is the incidence angle, r_{GP} the soil reflectivity, which is function of the soil reflectivity of a plane surface r_{GP}^* (p = H, V). r_{GP}^* can be computed from the Fresnel equations as a function of the incidence angle and of the soil dielectric constant (ϵ). This constant was computed here as a function of SM, soil effective temperature (T_G), and soil texture in terms of clay fraction (C) (Mironov et al., 2013).

A semi-empirical approach developed originally by Wang and Choudhury (1981) was used to model the roughness effects as function of four roughness parameters Q_R , H_R and N_{RP} (p=V and p=H) (Wigneron et al., 2007):

$$r_{GH}(\theta) = [(1 - Q_R(\theta))r_{GH}^*(\theta) + Q_R(\theta)r_{GV}^*(\theta)]\exp[-H_R\cos^{N_{RH}}(\theta)] \quad (2)$$

$$r_{GV}(\theta) = [(1 - Q_R(\theta))r_{GV}^*(\theta) + Q_R(\theta)r_{GH}^*(\theta)]\exp[-H_R\cos^{N_{RV}}(\theta)] \quad (3)$$

where r_{GP}^* (p=H, V) is the Fresnel reflectivity and H_R accounts for the decrease in reflectivity due to soil roughness effects (r_{GP} (p=H, V) decreases generally as H_R increases), Q_R accounts for polarization mixing effects, and N_{RP} governs the changes in the angular dependence of reflectivity.

Using the τ - ω model, the emission from the soil-vegetation medium can be calculated for each polarization as a sum of (i) the direct vegetation emission (ii) the soil emission attenuated by the canopy and (iii) the vegetation emission reflected by the soil and attenuated again by the canopy layer (4)

$$TB_p(\theta) = (1 - \omega_p)[1 - \gamma_p(\theta)][1 + \gamma_p(\theta)r_{GP}(\theta)]T_c + [1 - r_{GP}(\theta)]\gamma_p(\theta)T_g \quad (4)$$

where T_G and T_c are respectively the soil and vegetation effective temperature, γ_p is the vegetation

attenuation factor and ω_p ($p = H, V$) is the effective scattering albedo (Kurum et al., 2013). This latter is generally considered to be close to zero over low vegetation covers (Wigneron et al., 2010, Kurum et al., 2013). In this study, ω was set equal to zero.

The vegetation attenuation factor γ_p is related to τ_p as follows:

$$\gamma_p = \exp[-\tau_p / \cos(\theta)] \quad (5)$$

where the optical thickness at polarization p (τ_p) can be also expressed as function of the optical thickness at nadir τ_{NAD} (referred to as τ_{NAD} in the following):

$$\tau_p(\theta) = \tau_{NAD} [\sin^2(\theta) tt_p + \cos^2(\theta)] \quad (6)$$

where tt_v and tt_h are parameters used to quantify the dependence of τ_p on incidence angle.

Following Wigneron et al. (2012) and Miernecki et al. (2014), some assumptions were made in this study. The soil effective temperature T_G was set equal to the vegetation canopy T_c , and we considered here a single parameter called the composite soil-vegetation surface temperature T_{GC} (Jackson, T. J., et al., 1980, Wigneron et al., 2007). Retrievals were performed at 6 am / 6 pm, in correspondence with the SMOS observations, at a time close to the soil hydraulic near-equilibrium state. Values of T_{GC} were obtained from the ERA-INTERIM 0-7 cm soil temperature product, with a temporal resolution of three hours and a spatial resolution of 1.5 degree. Following these assumptions, equation (4) can be simplified as follows:

$$TB_p(\theta) = T_{GC} [1 - \gamma_p^2(\theta) r_{GP}(\theta)] \quad (7)$$

Using equations (2), (3), (5), (6) and (7), TB_p can be expressed as:

$$TB_p(\theta) = T_{GC} [1 - r_p'(\theta) \exp \left(-2\tau_{nad} \frac{\cos^2(\theta) + tt_p \sin^2(\theta)}{\cos(\theta)} - H_R \cos^{N_{RP}}(\theta) \right)] \quad (8)$$

In this study, SM estimations were obtained from the inversion of L-MEB using the ELBARA-II multi-angular observations according to 2 main approaches:

- 2-Parameter (2-P) retrievals: SM and τ_{NAD} were retrieved simultaneously and the tt_v and tt_h parameters were set equal to 1 (the angular dependence of τ_p was neglected). This case corresponds to the most classical L-MEB inversion approach (Wigneron et al., 1995, 2000, 2003, 2007) and is currently used in the SMOS algorithm (Kerr et al., 2012).
- 3-Parameter (3-P) retrievals: SM, τ_{NAD} and the tt_v vegetation parameter are retrieved simultaneously (while tt_h is set equal to 1), as in Wigneron et al. (2012) and Miernecki et al. (2014). In that case the angular dependence of τ_p is accounted for in the V polarization, considering the vertical structure of the vine vegetation (mostly stems and vine stocks).

The inversion was based on ELBARA-II measurements made in the 30-55 degrees. We did not considered SM retrievals when the angular range of the available multi-angular data was lower than 10 degrees. The L-MEB inversion was based on the minimization of a cost function (χ) using a least-squares iterative algorithm (Wigneron et al., 2007):

$$\chi = \frac{\sum (T_{Bmes} - T_B^*)^2}{\sigma(T_B)^2} - \sum \frac{\sum (P_i^{ini} - P_i^*)^2}{\sigma(P_i)^2} \quad (9)$$

where T_{Bmes} is the TB value measured by ELBARA-II and $\sigma(T_B)$ is the standard deviation associated with the TB measurements (it was set here to 1 K, Schwank et al., 2012), P_i^{ini} ($i = 1, \dots, N$) is the initial value of each parameter in the retrieval process that corresponds to an a priori estimate of the parameter P_i , $\sigma(P_i)$ is the standard deviation associated with this estimate and P_i^* ($i = 1, \dots, N$) is the value of the retrieved parameter.

After each SM retrieval, the RMSE between the measured (ELBARA-II) and simulated TB values was calculated (referred to as $RMSE_{TB}$). High errors in the retrieval process were filtered out by deleting SM values when $RMSE_{TB} > 12$ K, avoiding bad quality retrievals. Also SM values were filtered so as to delete SM values outside the 0 - 0.5 m³/m³ range (Juglea et al., 2010).

To evaluate the different parameterizations of the roughness effects taken into account in this study, the SM retrievals were compared with the in situ SM measurements, considered here as the reference. The statistic scores used in this study are the correlation coefficient (R), the bias and the unbiased root mean square error. The latter was computed as a function of the bias and the root mean square error (RMSE) (Entekhabi et al., 2010(a)):

$$ubRMSE = \sqrt{RMSE^2 - bias^2} \quad (11)$$

3 RESULTS

In this section, different combinations of the values soil roughness effects (H_R , Q_R , N_{RH} and N_{RV}) are analyzed. Each statistic score (R , bias and $ubRMSE$) was used separately to find which roughness parameterization leads to the "best" SM retrievals, considering highest R values, and lowest bias and $ubRMSE$ values.

First, we present results for correlations between measured and retrieved SM values for different values of H_R , Q_R and N_{RP} ($P=H, V$), for 2-P and 3-P retrievals. For 2-P retrievals, the SRP configuration leads to the highest correlation values in the case $Q = 0$ ($R = 0.68$) or $Q = 0.1$ ($R = 0.71$). In both cases, for all other roughness parameterizations than SRP, R decreases as H_R increases. As noted in section General methodology, the retrieved value of SM does not depend on H_R for the SRP method. Also, setting H_R equal to 0 produces the same SM retrievals as the SRP method, whatever the used value of N_{RV} and N_{RH} . The

two parameterizations where the values of N_{RH} and N_{RV} are different lead to lower R values when $H_R \geq 0.4$. For 3-P retrievals (when t_{tv} is retrieved simultaneously to SM and τ_{NAD}), correlation values (R) depend on H_R for the SRP parameterization (contrary to what was obtained for 2-P retrievals). However, whatever the value of H_R , considering 3-P Parameters, leads to improved correlations (R ranging from 0.71 to 0.82) in comparison to 2-P retrievals. Furthermore, for a given roughness configuration, 3-P retrieval performs better in terms of correlation values than 2-P in all cases. The increase of H_R , leads generally to a decrease of the R values (except for the SRP method).

Second, we present the results of the bias between measured and retrieved SM values. For 2-P retrievals, the range of bias values was similar when $Q=0$ (the bias ranged from $-0.046 \text{ m}^3/\text{m}^3$ (SRP method) to $0.113 \text{ m}^3/\text{m}^3$) and when $Q=0.1$ (bias varied from $-0.078 \text{ m}^3/\text{m}^3$ (SRP method) to $0.077 \text{ m}^3/\text{m}^3$). For both $Q=0$ and $Q=0.1$, it appeared that the bias increases, from negative values to positive values, almost linearly with increasing values of H_R . Setting $Q=0.1$ generally leads to lower retrieved SM values. When $Q=0$, a bias equal to zero can be reached for values of H_R in the range 0.3 - 0.7, depending on the values of N_{RH} and N_{RV} . When $Q=0.1$, a bias equal to zero can be reached for higher values of H_R (≥ 0.5). Bias for the SRP method was found to be high when $Q=0.1$ ($-0.078 \text{ m}^3/\text{m}^3$) but better if $Q=0$ ($-0.046 \text{ m}^3/\text{m}^3$).

Using 3-P retrievals, similar results to 2-P retrievals were obtained, except that lower SM values were retrieved generally (bias ranging from $-0.077 \text{ m}^3/\text{m}^3$ to $0.051 \text{ m}^3/\text{m}^3$ for $Q=0$, and $-0.091 \text{ m}^3/\text{m}^3$ to $0.040 \text{ m}^3/\text{m}^3$ for $Q=0.1$). For 3-P retrievals the range of bias values is slightly lower compared to 2-P retrievals. A bias equal to zero was achieved in the range of H_R from 0.5 to 0.8 when $Q=0$ and for values of H_R larger than 0.6 when $Q=0.1$. For the specific parameterization $N_{RV} = N_{RH} - 1$ (as for the SRP method), the bias is almost constant (bias ranging from $-0.062 \text{ m}^3/\text{m}^3$ to $-0.080 \text{ m}^3/\text{m}^3$ for $Q=0$, and $-0.082 \text{ m}^3/\text{m}^3$ to $-0.091 \text{ m}^3/\text{m}^3$ for $Q=0.1$).

Finally we considered the results for the unbiased RMSE. Varying the value of H_R does not affect the ubRMSE values for the SRP parameterization. For the other parameterizations, the ubRMSE values generally increases with increasing values of H_R .

For 2-P retrievals, the lowest value of ubRMSE was reached with SRP (ubRMSE = $0.056 \text{ m}^3/\text{m}^3$ for $Q=0$ and ubRMSE = $0.044 \text{ m}^3/\text{m}^3$ for $Q=0.1$) while the highest values was $0.106 \text{ m}^3/\text{m}^3$ for $Q=0$ and $0.097 \text{ m}^3/\text{m}^3$ for $Q=0.1$. Whatever the value of H_R , the parameterizations in which N_{RH} is not equal to N_{RV} produced higher ubRMSE.

For the 3-P retrievals, results are relatively similar to 2-P retrievals except that lower values of ubRMSE can be obtained (ubRMSE varying from $0.035 \text{ m}^3/\text{m}^3$

to $0.086 \text{ m}^3/\text{m}^3$ for $Q=0$, and from $0.035 \text{ m}^3/\text{m}^3$ to $0.089 \text{ m}^3/\text{m}^3$ for $Q=0.1$). As for 2-P retrievals, the configurations leading to lowest ubRMSE values are the ones in which $N_{RP} = -1$ ($P = H, V$). In summary, in terms of ubRMSE, 3-P retrievals provided improved results in comparison to 2-P retrievals, while setting $Q=0.1$, instead of $Q=0$, provided improved results only in the case of the 2-P retrievals.

4 CONCLUSIONS

The aim of this study was to analyze the roughness modelling in soil moisture retrievals over the VAS site, taking advantage of the observations of the L-band ELBARA-II radiometer and in situ measurements of soil moisture and roughness in a vineyard field. Several values of the roughness parameters (H_R , Q_R , N_{RV} , N_{RH}) were tested as input for the L-MEB model when retrieving soil moisture simultaneously to vegetation optical depth τ_{NAD} (2-P retrieval) and simultaneously to both τ_{NAD} and the vegetation parameter t_{tv} (3-P retrieval).

It was found that when setting $N_{RP} = -1$ ($P=H, V$) in the 2-P retrievals, the original formulation to compute TB as defined in the τ - ω model can be simplified (SRP method). In this case, it is mathematically possible to account for the combined impact of soil roughness (H_R) and vegetation (τ_{NAD}) through a single parameter (TR). In that case H_R does not need to be calibrated, as it is included within the TR parameter which is retrieved simultaneously to SM . Based on the data set acquired over the VAS area in 2013, it was found that the SRP method gave the best retrieved SM values in terms of correlation and ubRMSE when compared with SM measured in situ over all the year 2013. Conversely, the lowest bias was found with other combinations of the roughness parameters. Using SRP, the retrieved SM values underestimated the measured ones for all tested configurations (2-P or 3-P retrievals for $Q=0$ or $Q=0.1$) and the bias was in the $[-0.08 \text{ m}^3/\text{m}^3, 0.04 \text{ m}^3/\text{m}^3]$ range.

However as noted before, the sampling depths of the retrieved SM data (~ 0 -3 cm) and of the in situ measurements (~ 0 -6cm) are not the same.

Considering the parameter t_{tv} as a free parameter in the retrievals (3-P retrievals), generally led to improved results in terms of correlation and ubRMSE, but the bias between measured and retrieved SM data was generally larger. For instance, when $N_{RV} = N_{RH} = -1$, the correlation increased from $R = 0.68$ -0.71 (considering $Q=0$ or $Q=0.1$) for 2-P retrievals (corresponding to the SRP method) to $R = 0.77$ -0.82 for 3-P retrievals.

This improvement could be due to the fact that the specific structural characteristics of the vineyards, with a preferential vertical orientation of the vine stems and stocks could be accounted for in the 3-P retrievals, where the free parameter t_{tv} parameterizes the dependence of the optical depth at V-polarization

(τ_v) on the incidence angle. Conversely, in 2-P retrievals, both tt_v and tt_h were set equal to a constant value ($tt_v = tt_h = 1$), corresponding to isotropic conditions, which could not account for the changes in the vegetation structure in relation with the vegetation cycle (growth and senescence) and the agricultural practices.

Although, at the VAS, the 3-P retrieval was found to be the most performant approach in terms of correlation and ubRMSE, this method presents the traditional disadvantages of requiring of the calibration of the H_R parameter. However, in the case when $N_{rv} = N_{RH} = -1$, the statistics criteria (R and ubRMSE) were found to only slightly dependent on the value of H_R .

So in summary, for both 2-P and 3-P retrievals, it was found that the most performant approaches in terms of correlation (R) and ubRMSE were those corresponding to the case $N_{rv} = N_{RH} = -1$ (i.e. the SRP method in the case of 2-P retrievals). In both cases, the SM retrievals were either independent for 2-P retrievals (for SRP) or only slightly dependent for 3-P retrievals on the value of H_R .

In conclusion, the results of this study suggest the use of the SPR method is an interesting alternative approach to calibrate the roughness parameters. More studies evaluating the improvement of soil moisture retrievals using the SRP method from spaceborne observations will be crucial to consolidate this method as a feasible option in the determination of SM at global scale.

5 REFERENCES

- Entekhabi, D., Njoku, E. G., O'Neill, P. E., Kellogg, K. H., Crow, W. T., Edelstein, W. N., Entin, J. K., Goodman, S. D., Jackson, T. J., Johnson, J., et al., 2010a. The soil moisture active passive (smap) mission. *Proceedings of the IEEE*, 98 (5), 704–716.
- Entekhabi, D., Reichle, R. H., Koster, R. D. & Crow, W. T., 2010b, Performance metrics for soil moisture retrievals and application requirements. *Journal of Hydrometeorology*, 11, 832–840.
- Grant, J. P., Wigneron, J. -P., Van de Griend, A. A., Kruszewski, A., Søjberg, S. S., & Skou, N., 2007, A field experiment on microwave forest radiometry: L-band signal behaviour for varying conditions of surface wetness. *Remote Sensing of Environment*, 109(1), 10-19.
- Juglea, S., Kerr, Y. H., Mialon, A., Wigneron, J. -P., Lopez-Baeza, E., Cano, A., Albitar, A., Millan-Scheidig, C., Carmen Antolin, M. & Delwart, S., 2010, Modelling soil moisture at SMOS scale by use of a SVAT model over the Valencia Anchor Station. *Hydrology and Earth System Sciences*, 14, 831–846.
- Kerr, Y. H., Waldteufel, P., Richaume, P., Wigneron, J. -P., Ferrazzoli, P., Mahmoodi, A., Al Bitar, A., Cabot, F., Gruhier, C., Juglea, S. E., Leroux, D., Mialon, A. & Delwart, S., 2012, The SMOS Soil Moisture Retrieval Algorithm. *IEEE Transactions on Geoscience and Remote Sensing*, 50(5), 1384-1403.
- Kerr, Y. H., Waldteufel, P., Wigneron, J. -P., Cabot, F., Boutin, J., Escorihuela, M. J. et al., 2010, The SMOS mission: new tool for monitoring key elements of the global water cycle. *Proceedings of the IEEE*, 98(5), 666-687.
- Kurum, M., 2013, Quantifying scattering albedo in microwave emission of vegetated terrain. *Remote Sensing of Environment*, 129, 66–74.
- Mierniecki, M., Wigneron, J. -P., Lopez-Baeza, E., Kerr, Y., De Jeu, R., De Lannoy, G. J. M., Jackson, T. J., O'Neill, P. E., Schwank, M., Fernandez-Moran, R. et al., 2014, Comparison of SMOS and SMAP soil moisture retrieval approaches using tower-based radiometer data over a vineyard field. *Remote Sensing of Environment*, 154, 89-101.
- Mironov, V., Kerr, Y., Wigneron, J.-P., Kosolapova, L. & Demontoux, F., 2013, Temperature- and Texture-Dependent Dielectric Model for Moist Soils at 1.4 GHz. *IEEE Geoscience and Remote Sensing Letters*, 10(3), 419-423.
- Mo, T., Choudhury, B., Schmugge, T., Wang, J., Jackson, T., 1982, A model for microwave emission from vegetation-covered fields. *Journal of Geophysical Research*, 87(C13), 11229–11237.
- Schwank, M., J. -P. Wigneron, et al., 2012, L-Band Radiative Properties of Vine Vegetation at the SMOS Cal/Val Site MELBEX III. *IEEE Transactions on Geoscience and Remote Sensing*, 50(5), 1587-1601.
- Wang, J. R. & Choudhury, B. J., 1981, Remote sensing of soil moisture content over bare field at 1.4 GHz frequency. *Journal of Geophysical Research*, 86, 5277–5282.
- Wigneron, J. -P., Calvet, J. -C., Chanzy, A., Grosjean, O. & Laguerre, L., 1995, A composite discrete-continuous approach to model the microwave emission of vegetation. *IEEE Transactions on Geoscience and Remote Sensing*, 33(1), 201-211.
- Wigneron, J. -P., Calvet, J. -C., Pellarin, T., Van de Griend, A. A., Berger, M., Ferrazzoli, P., 2003, Retrieving near-surface soil moisture from microwave radiometric observations: current status and future plans. *Remote Sensing of Environment*, 85(4), 489-506.
- Wigneron, J. -P., Kerr, Y. H., Waldteufel, P., Saleh, K., Escorihuela, M. -J., Richaume, P., Ferrazzoli, P., de Rosnay, P., Gurney, R., Calvet, J. -C., Guglielmetti, M., Hornbuckle, B., Matzler, C., Pellarin, T., and Schwank, M., 2007, L-band Microwave Emission of the Biosphere (L-MEB) Model: description and calibration against experimental data sets over crop fields. *Remote Sensing of Environment*, 107(4), 639–655.
- Wigneron J. -P, Kerr, Y. H., Mialon, A., Novello, N., Cabot, F., Delwart, S. et al., 2010, First evaluation of SMOS observations and Level-2 products over agricultural sites in temperate regions. *Proceedings of the 3rd International Symposium on Recent Advances in Quantitative Remote Sensing: RAQRS'III*, 678-681.
- Wigneron, J. -P., Schwank, M., López-Baeza, E., Kerr, Y. H., Novello, N., Millan, C. et al., 2012, First Evaluation of the simultaneous SMOS and ELBARA-II observations in the Mediterranean region. *Remote Sensing of Environment*, 124, 26-37.
- Wigneron, J. -P., Waldteufel, P., Chanzy, A., Calvet, J. -C., Kerr, Y., 2000, Two-Dimensional Microwave Interferometer Retrieval Capabilities over Land Surfaces (SMOS Mission). *Remote Sensing of Environment*, 73(3), 270-282.

Potential of X-band SAR data from TerraSAR-X and COSMO-SkyMed sensors to retrieve physical soil properties

A. Gorraab^{1,2}, M. Zribi¹, N. Baghdadi³, Z. Lili Chabaane² and B. Mougenot¹

1-CESBIO (CNRS/UPS/IRD/CNES), 18 av. Edouard Belin, bpi 2801, 31401 Toulouse cedex 9, France.

2-INAT/Université de Carthage, 43 av. Charles Nicolle 1082, Tunis, Mahrajène Tunisie.

3-IRSTEA, UMR TETIS, 500 rue François Breton, 34093 Montpellier cedex 5, France.

Emails: azzagorrab@gmail.com; zribim@cesbio.cnes.fr; nicolas.baghdadi@teledetection.fr; bernard.mougenot@ird.fr; Zohra.lili.chabaane@gmail.com

ABSTRACT - We propose in this study to analyze the potential of TerraSAR-X and COSMO-SkyMed SAR measurements to retrieve surface parameters over bare soils. We consider a statistical analysis of the relationships between X-band SAR backscattering signals function of soil moisture and different roughness parameters (the root mean square height H_{rms} , the Z_s parameter and the Z_g parameter) at HH polarization and for an incidence angle equal to 36° . Results have shown a high sensitivity of real radar data to the two soil parameters: roughness and moisture. A linear relationship is obtained between volumetric soil moisture and radar signal with the strongest correlation observed with gravimetric moisture measurements at 2 cm depth. A logarithmic correlation is observed between backscattering coefficient and all roughness parameters. The highest dynamic sensitivity is obtained with Z_g parameter. We compared, then the performance of different physical and semi-empirical backscattering models (IEM, Baghdadi-calibrated IEM and Dubois models) with SAR measurements at HH and VV polarization. The results show that the IEM model simulates correctly the radar response only for $H_{rms} < 1.5\text{cm}$ using exponential correlation function in HH polarization and for $H_{rms} < 1.5\text{cm}$ using exponential correlation function and $H_{rms} > 1.5\text{cm}$ with Gaussian function in VV polarization, at 36° . Important discrepancies (over or under estimation) are generally observed between the measured X-band SAR signals and the Dubois simulated backscatters. Considerable improvement of the the performance of IEM model was observed using the IEM Baghdadi-calibrated version.

1 INTRODUCTION

Geometric and dielectric soil properties, as roughness, moisture content and soil texture, assessment are needed for many scientific applications, particularly hydrological and erosion modeling, agriculture and sustainable natural resources management. Soil parameters are characterized by a very high spatial and temporal variability. Conventional soil moisture and roughness measurement methods, as gravimetric, time-domain reflectometry (TDR), and pine profiler, are not sufficient to describe their variability. Besides, these methods consume generally much time and may disturb the soil structure.

Active microwave sensors have demonstrated their potential to measure and monitor effectively soil surface characteristics with meter-scale resolution. Over bare agricultural areas, backscattered radar signal is very sensitive to physical soil parameters particularly roughness, water content and soil composition (Baghdadi et al., 2008; Aubert et al., 2011). Consequently, different radar backscattering models (theoretical, semi-empirical and empirical)

were developed to better understanding the relationship between backscattering coefficient and the parameters used to characterize the soil. Various studies have shown a linear relationship between radar signal and soil moisture (Anguela et al., 2010) while a logarithmic function is observed between roughness and backscattering coefficient Ulaby et al., 1986).

An accurate analysis and interpretation of the backscattering behaviour of bare soils is important to retrieve soil parameters by inverting backscattering models. In this context, the objective of the present research is to analyze the sensitivity of X-band SAR measurements (TerraSAR-X and COSMO-SkyMed) as a function of different physical soil parameters, and to evaluate the accuracy of the most commonly used backscattering models with real data. Firstly, we presented our ground and satellite data. Secondly, we considered statistical analysis of the relationships between backscattered radar coefficients and soil parameters. Thirdly, we compare the performance of the different backscattering models. Finally, we presented our conclusions.

2 MATERIAL AND METHODS

2.1 Study site description

Our study area is located in central Tunisia (9°23'–10°17'E, 35°1'–35°55'N). The climate in this region is semi-arid, with an average annual rainfall of approximately 300 mm/year, characterized by a rainy season lasting from October to May, with the two rainiest months being October and March (Zribi et al., 2011). As is generally the case in semi-arid areas, the rainfall patterns in this area are highly variable in time and space. The landscape is mainly flat, and the vegetation is dominated by agricultural production (cereals, olive groves, fruit trees, and market gardens).

2.2 Ground and spatial data availability

a) Satellite database

Twelve radar images (X-Band ~9.65 GHz) were acquired with two sensors TerraSAR-X and COSMO-SkyMed at different configurations. Table 1 summarizes the main characteristics of these SAR images collected on Kairouan site. Seven TerraSAR-X data were acquired in Spotlight dual-polarization (HH and VV) at high incidence angle (36°) and with ground pixel spacing about 2 m. For COSMO-SkyMed, we have five images acquired at HH and HV polarization, in two incidence angles (26° and 36°) with pixel spacing about 8 m. The images were firstly multi-looked using the NEST software to reduce speckle then, they were radiometrically calibrated to enable the derivation of backscattering coefficients σ° . After that, they were geo-referenced. Finally, we calculated the mean radar signals for each training plot.

b) In situ database

Ground campaigns were realized in central Tunisia between November 2013 and January 2014. During twelve dates, ground campaigns were carried over agricultural bare soil fields with radar measurements acquired in different configurations (multi-polarizations, multi-incidences, multi-resolution). Fifteen test bare soil fields were considered, with different types of roughness ranged between smooth and ploughed surfaces. For each date, we measured physical soil parameters (soil moisture content, soil roughness, soil bulk density and soil texture).

Soil moisture:

Different in situ methods are used for measuring soil moisture content over our test fields: i) Thetaprobe instrument ii) Gravimetric sampling. For each training plot, about 6 to 10 different gravimetric samples were monitored (at 2 cm depth) and about 20 thetaprobe

readings were taken at 5 cm depth. The gravimetric soil moisture content was calculated by dividing the mass of water by the mass of dry soil then it was converted to volumetric soil moisture using soil bulk density (six samples per field). Important variations of the volumetric soil moisture content were observed using the thetaprobe instrument and gravimetric sampling measurements. They are ranging from 4.7% to 31.6% using the thetaprobe and from 1.2 % to about 40 % with gravimetric method.

Table1. Main characteristics of X-band SAR images:
Pol: Polarization, Inc: Incidence Angle.

Date of acquisition (dd/mm/yy)	Sensor	Pol Mode	Inci. Ang	Geometric resolution (m)
06/11/13	CSK1	HV/HH	26°	7.9
09/11/13	TSX	HH/VV	36°	1.8
11/11/13	CSK1	HV/HH	36°	7.9
20/11/13	TSX	HH/VV	36°	1.8
22/11/13	CSK1	HV/HH	26°	7.9
01/12/13	TSX	HH/VV	36°	1.8
04/12/13	CSK4	HV/HH	26°	7.9
05/12/13	CSK2	HV/HH	36°	7.9
12/12/13	TSX	HH/VV	36°	1.8
23/12/13	TSX	HH/VV	36°	1.8
14/01/14	TSX	HH/VV	36°	1.8
25/01/14	TSX	HH/VV	36°	1.8

Soil roughness:

To characterize soil roughness, we considered 1 m long pin profiler with a resolution equal to 2 cm. Ten roughness profiles, 5 parallel and 5 perpendicular to the tillage row direction, were established in all test fields at three different ground campaigns. Two main surface roughness parameters, the root mean square surface height (Hrms) and the correlation length (l) are calculated from the mean correlation function which is determined from the digitalized soil profiles (Ulaby et al., 1986; Baghdadi et al., 2008). Significant variations of the Hrms values were observed between the ground campaigns ranging from 0.24cm (very smooth soils) to 3.4 cm (ploughed soils). This is mainly due to the rain effect and cultural practices (tillage, sowing...).

Soil texture:

For each test field, we collected various soil samples to characterize soil texture. After several measurement steps in the laboratory, we calculated the percentage of sand, silt and clay particles to determine soil texture.

3 RESULTS AND INTERPRETATION

In this section, we present firstly the results of our statistical analysis of the backscattering coefficient behaviour as a function of volumetric soil moisture and various roughness parameters at 36° and for HH polarization. Secondly, we evaluated the performance of different backscattering models currently used.

3.1 Relationship between radar and surface roughness parameters (H_{rms} , Z_s and Z_g)

In order to analyze the influence of the soil roughness on X-band SAR radar signal, we considered the sensitivity of TerraSAR-X and COSMO-SkyMED backscattering coefficients to three different roughness parameters: i) the root mean surface height H_{rms} , ii) the parameter $Z_s = \frac{H_{rms}^2}{l}$ developed by (Zribi and Dechambre, 2003) and iii) the parameter $Z_g = H_{rms} \left(\frac{H_{rms}}{l} \right)^\alpha$ introduced by (Zribi et al., 2014) at 36° and for HH (Figure 1). To take into account only the effect of roughness, we separated soil moisture into two groups: Low volumetric moisture $mv < 10\%$ and high volumetric moisture $mv > 25\%$. Results show a high sensitivity of the X-band SAR signal to all roughness parameters (H_{rms} , Z_s and Z_g). These relationships can be represented by a logarithmic function in which backscattering coefficient σ^0 increases clearly with increasing values of roughness parameters. This behaviour was also observed in several studies, as Baghdadi et al., 2008 and Anguela et al., 2010. For high soil moisture, graphics show the highest dynamic and correlation of the X-SAR signal versus roughness parameters compared to low moisture.

Comparing separately the roughness parameters in the case of high volumetric soil moisture, results show that the sensitivity becomes more strongly correlated when we represent σ^0 with Z_s ($R^2=0.7$) and Z_g ($R^2=0.8$) than with the H_{rms} ($R^2=0.6$). This behaviour can be explained that for the case of Z_s parameter, the latter combines the influence of both the soil's H_{rms} and its correlation length. In addition, it introduces the slope's effect (H_{rms}/l) which is an important soil feature in the estimation of σ^0 . The strongest correlation behaviour is obtained with Z_g parameter with a high dynamic range observed at small values of Z_g , and near saturation about 0.4 cm. This result is in agreement with Zribi et al., 2014 and it can be explained by the fact that Z_g takes the influence on radar backscattering behaviour of H_{rms} , l and the correlation function shape into account.

3.2 Relationship between radar and soil moisture content

Figure 2 shows the behaviour of σ^0 according to volumetric soil moisture derived from: i) thetaprobe measurements and ii) gravimetric measurements.

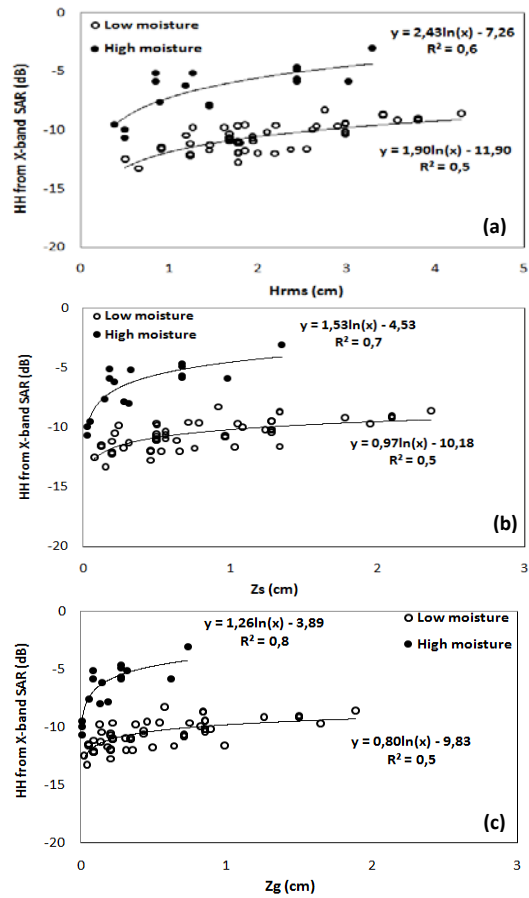


Figure 1: Relationship between X-band SAR signal and roughness parameters: a) H_{rms} , b) Z_s and c) Z_g , at HH polarization, for incidence angle about 36° .

A linear relationship is observed between σ^0 and volumetric soil moisture. Several studies obtained this linear correlation (Paloscia et al., 2008; Le Morvan et al., 2010). Moreover, the graphics show that the strongest correlation are obtained with gravimetric measurements with a coefficient of determination R^2 about 0.77. These results are explained by the fact that the 0–2 cm soil layer is relatively thin and it is the most influenced by the two extremely moisture conditions (rapid increase or decrease under wettest and driest conditions consecutively). In fact, during a significant precipitation event, the storage capacity of the thin surface layer is quickly satisfied, particularly

along the lower porosity. In addition, this depth is the upper surface layer so it is the most affected by the evaporation fluxes under very dry conditions. These results are in agreement with Famiglietti et al., 1998 observations. The highest correlation observed with gravimetric measurements confirms that gravimetric water content measurements are the most accurate methods and perform better the ground truth moisture variability.

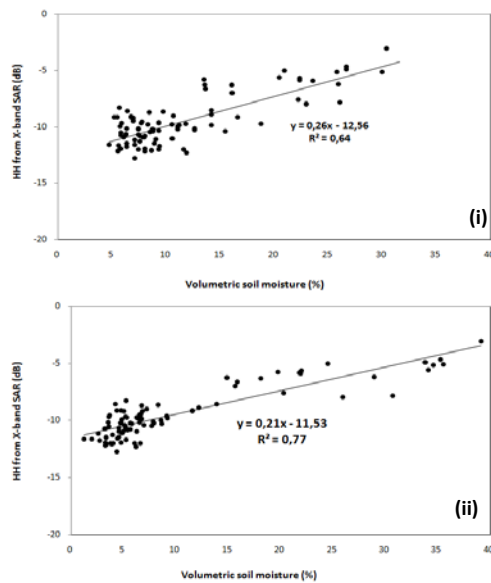


Figure 2: Relationship between backscattering coefficient and volumetric soil moisture measured by i) thetaprbe instrument “5 cm depth” ii) gravimetric sampling “2 cm depth”, for HH polarization.

3.3. Evaluation of backscattering models

To evaluate the accuracy of various backscattering models: IEM model; Dubois model; and the Baghdadi-calibrated IEM model, we compared the predicted signal strengths with the remotely sensed radar data at 36° for HH and VV polarization.

a) IEM model

The Integral Equation Model (IEM) is a physical radar backscattering model, developed by Fung and Chen, 1992. For bare agricultural soils, it simulates the σ_{HH}^0 , σ_{HV}^0 and σ_{VV}^0 radar backscattering coefficients as a function of various radar configurations and soil parameters. Two types of surface correlation function, exponential or Gaussian, are used in the IEM backscatter model simulations.

The results show that the IEM simulations are in good agreement with the remotely sensed signals under certain conditions only (Figure3):

- In the HH polarization, for $H_{rms} < 1.5$ cm, with an exponential correlation function: bias=-0.7 dB and RMSE=1.96 dB. On the other hand, the IEM model tends to over-estimate the backscattering coefficient σ_{HH}^0 in the following case: $H_{rms} > 1.5$ cm with a Gaussian correlation function: bias approximately - 3.08 and RMSE equal to 3.5 dB.

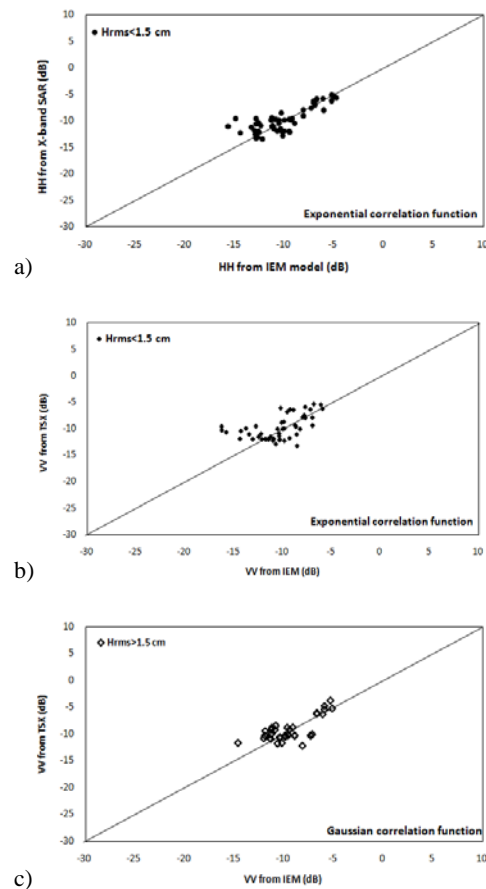


Figure 3: Comparison between measured X-band data and IEM simulations only for: a) HH polarization using exponential correlation function; b) VV polarisation using exponential correlation function; c) VV polarization using Gaussian correlation function.

- In the VV polarization, for $H_{rms} < 1.5$ cm, with an exponential correlation function: bias=0.63 dB and RMSE=2.4 dB. For $H_{rms} > 1.5$ cm, with a Gaussian correlation function: at 36°, bias=0.24 dB and RMSE=1.66 dB.

Using X-band data and various incidence angles in the range between 25° and 52°, Baghdadi et al., 2011 observed that the IEM correctly simulates the values of σ_{HH}^0 and σ_{VV}^0 for the following two cases: H_{rms}

<1.5 cm with an exponential correlation function; and $H_{rms} > 1.5$ cm with a Gaussian function.

b) Dubois model

The Dubois model is a semi empirical backscattering model, developed by Dubois et al. 1995. It simulates the σ_{HH} and σ_{VV} radar backscatter coefficients using as input the incidence angle (θ°), the dielectric constant, the H_{rms} surface height, and the radar wavelength. Figure 4 shows that this model is in good agreement with the measured σ_{VV} data for the case where $H_{rms} > 1.5$ cm with a corresponding bias of -0.18 dB and RMSE of 1.75 dB. The Dubois model often tends to over-estimate the SAR backscattering coefficients when $H_{rms} > 1.5$ cm, with a bias of approximately -2.6 dB and an RMSE of 3.4 dB. On the other hand, this model underestimates the radar signal in the case of low surface roughness ($H_{rms} < 1.5$ cm), with a bias of approximately 2.32 dB and an RMSE of 3.25 dB in the HH polarization, and a bias of approximately 3.5 dB and an RMSE of 3.9 dB in the VV polarization.

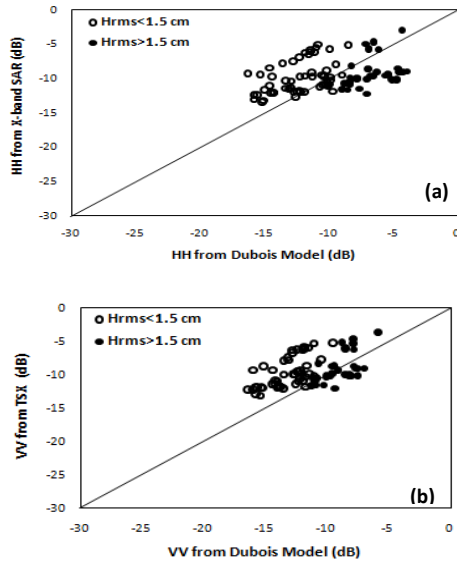


Figure 4: Comparison between X-band data and Dubois simulations: (a) HH polarization, (b) VV polarization, at 36° incidence.

c) Baghdadi calibrated IEM version

In this paragraph, the semi-empirical calibration of the IEM model developed by Baghdadi et al., 2011 is applied, in order to minimize the mismatch between the IEM simulations and the observed backscattered signal. In this new version of the IEM, the measured

correlation length is replaced by a fitting parameter "L-opt", whatever the range of H_{rms} . The results show that the implementation of L-opt leads to an improved agreement between the IEM simulations and the SAR data and it also allows the IEM's domain of validity to be extended, to include even high values of surface roughness. These modifications are proposed for the Gaussian correlation function shape, which leads to the best agreement between simulations and data, when the new fitting parameter L-opt is used.

Figure 5 compares the measured radar data with simulated signals obtained with the initial version (using the measured correlation length), and with the empirical calibrated version (using the fitting parameter L-opt) of the IEM model.

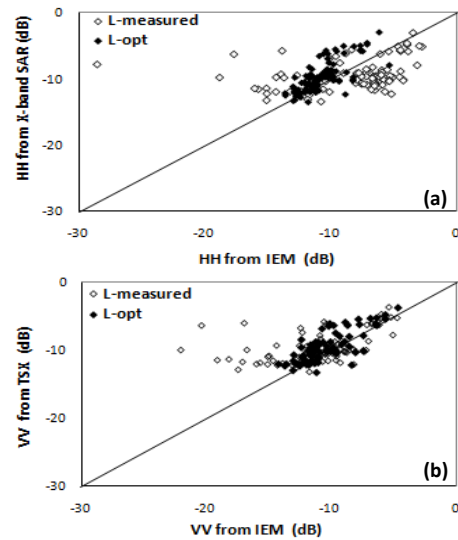


Figure 5: Comparison between X-band radar signals and Baghdadi-calibrated IEM (Baghdadi et al., 2011) simulations: (a) HH polarization; (b) VV polarization, at 36° .

In the HH polarization, the results predicted by the semi-empirical IEM calibration are found to be in good agreement with the measured backscatter coefficients, with a bias of approximately 0.9 dB, and an RMSE of approximately 1.8 dB. In the VV polarization, the bias is 0.84 dB and the RMSE is equal to 1.67 dB. Application of the initial version of the IEM (using the measured correlation length) leads to considerable discrepancies, with an RMSE of 6.5 and 6.9 dB in the HH and the VV polarization respectively. The results determined using the semi-empirical calibration are in good agreement with those obtained by Baghdadi et al., 2011 and lead to a significant improvement in the IEM backscattering

predictions. The calibrated IEM approach thus provides a robust model for the simulation of radar backscattering from agricultural soils.

4 CONCLUSIONS

We analyzed in this paper the sensitivity of TerraSAR-X and COSMO-SkyMed signal backscattering to physical soil parameters to retrieve these latter by inverting backscattering models. Logarithmic functions are observed between backscattering coefficient and roughness parameters: the rms height (Hrms), the Zs and the Zg parameters for HH polarization and at 36°. The highest correlation is obtained with Zg because its expression takes into account all the other roughness parameters. A linear correlation is observed between the X-band SAR signal and volumetric soil moisture. The strongest sensitivities are obtained from the thetaprobe moisture measurements made at 0-5 cm. This result reveals that thetaprobe measurements made at 5 cm can lead to more accurate estimations of soil moisture than those made at a depth of only 2 cm. The performance of the IEM, Dubois, and Baghdadi-calibrated IEM models are also discussed. The results provide an indication of the limits of validity of the IEM and Dubois models (over- or underestimations), for various radar configurations and roughness conditions. Considerable improvements in the IEM model performance are observed using the Baghdadi-calibrated version of this model.

5 ACKNOWLEDGEMENTS

This study was funded by the French IRD ('Institut de Recherche pour le Développement'), the ANR AMETHYST (ANR-12 TMED-0006-01) and TOSCA/CNES projects. The CSK images used in this analysis was supported by public funds received in the framework of GEOSUD, a project (ANR-10-EQPX-20) of the program "Investissements d'Avenir" managed by the French National Research Agency. We would also wish to thank all of the technical teams of the IRD and INAT (Institut National Agronomique de Tunisie) for their strong collaboration and support in implementing the ground-truth measurements.

6 REFERENCES

- Anguela, T.P., Zribi, M., Baghdadi, N., Loumagne, C., 2010. Analysis of Local Variation of Soil Surface Parameters With TerraSAR-X Radar Data Over Bare Agricultural Fields. *IEEE Trans. Geosci. Remote Sensing*, 48, 874-881.
- Aubert, M., Baghdadi, N., Zribi, M., Douaoui, A., Loumagne, C., Baup, F., El Hajj, M., Garrigues, S., 2011. Analysis of TerraSAR-X data sensitivity to bare soil moisture, roughness, composition and soil crust. *Remote Sens. Environ.*, 115, 1801-1810.
- Baghdadi, N., Zribi, M., Loumagne, C., Ansart, P., Anguela, T.P., 2008. Analysis of TerraSAR-X data and their sensitivity to soil surface parameters over bare agricultural fields. *Remote Sens. Environ.*, 112, 4370-4379.
- Baghdadi, N., Saba, E., Aubert, M., Zribi, M., Baup, F., 2011. Evaluation of radar backscattering models IEM, Oh, and Dubois for SAR data in X-band over bare soils. *IEEE Geosci. Remote Sens. Lett.* 8, 1160-1164.
- Dubois, P., Van Zyl, J., Engman, T., 1995. Measuring soil moisture with imaging radars. *IEEE Transactions on Geoscience and Remote Sensing*, 33, 915-926.
- Famiglietti, J.S., Rudnicki, J.W., Rodell, M., 1998. Variability in surface moisture content along a hillslope transect: Rattlesnake Hill, Texas. *Journal of Hydrology*, 210, 259-281.
- Fung, A. K., Li, Z., Chen, K. S., 1992. Backscattering from a randomly rough dielectric surface. *IEEE Transactions on Geoscience and Remote Sensing*, 30, 356-369.
- Le Morvan, A., Zribi, M., Baghdadi, N., Chanzy, A., 2008. Soil moisture profile effect on radar signal measurement. *Journal of Sensors, Sensors*, 256-270.
- Paloscia, S., Pampaloni, P., Pettinato, S., Santi, E., 2008. A comparison of algorithms for retrieving soil moisture from ENVISAT/ASAR images. *IEEE Trans. Geosci. Remote Sens.*, 46, 3274-3284.
- Ulaby, F.T., Moore, R. K., and Fung, A. K., 1986. "Microwave Remote Sensing Active and Passive", Norwood: Artech House, Inc, 3, pp 1098.
- Zribi, M., and Dechambre, M., 2003. A new empirical model to retrieve soil moisture and roughness from Radar Data. *Remote Sens. Environ.*, 84, 42-52.
- Zribi, M., Gorraeb, A., Baghdadi, N., 2014. A new soil roughness parameter for the modelling of radar backscattering over bare soil. *Remote Sensing of Environment*, 152, 62-73.
- Zribi, M., Chahbi, A., Lili Chabaane, Z., Duchemin, B., Baghdadi, N., Amri, R., Chehbouni, A., 2011. Soil surface moisture estimation over a semi-arid region using ENVISAT ASAR radar data for soil evaporation evaluation. *Hydrol. Earth Syst. Sci.*, 15, 345-358.

Predictability of short-term quantitative precipitation nowcasting from radar scans using optical flow method

Yu Liu^{a,b}, Du-Gang Xi^c, Zhao-Liang Li^{d,e,*}

a. Institute of Geographic Sciences and Natural Resources Research, Chinese Academy of Sciences, Beijing, 100101, China.

b. Institute of Remote Sensing and Digital Earth, Chinese Academy of Sciences, Beijing 100101, China

c. The PLA Information Engineering University, Zhengzhou, 450001, P.R. China

d. Key Laboratory of Agri-informatics, Ministry of Agriculture/Institute of Agricultural Resources and Regional Planning, Chinese Academy of Agricultural Sciences, Beijing 100081, China

e. ICube, UdS, CNRS, 300 Bld Sebastien Brant, CS10413, 67412, Illkirch, France

* Authors to whom correspondence should be addressed: lizhaoliang@caas.cn

ABSTRACT - Short-term Quantitative Precipitation Nowcasting (QPN) from consecutive radar scans plays a quite important role in navigation, flood forecasting, and other numerous hydro-meteorological applications. This study analyzed the predictability of QPN from Radar images from five aspects which includes the spatial resolution of Radar, the character of precipitation system, the number of input data, the QPN method, and the length of leading time. And this is carried out based on a new algorithm called Pixel-based Pyramid Lucas-Kanade optical flow method (PPLK) which is composed of three steps: employing a Pyramid Lucas-Kanade Optical Flow method (PLKOF) to estimate cloud advection, projecting rainy cloud considering the advection and evolution pixel by pixel, interpolating QPN imagery based on space-time continuum of cloud patches. The results show that the predictability of QPN is mainly determined by precipitation weather system and the length of leading time. The proposed PPLK improved the predictability of QPN compared to the other three widely used QPN methods with higher accuracy and less time consumption. The spatial resolution of radar has complicate influence on QPN, and the number of the input data has slight influence.

1 INTRODUCTION

Short-term high-resolution extrapolation-based Quantitative Precipitation Nowcasting (QPN) is referred as forecasting future precipitation within a very short time (e.g., 0~ 2 hour) from current observations (e.g., radar and satellite imageries). The predictability of QPN has important implications for the hydro-meteorological concerns, such as flash-flood warning, navigation safety.

Predictability of precipitation is a fundamental and intrinsic property of nonlinear systems stemming from complex dynamic and microphysical processes. It is depend as well on the particular forecasting model considering it is a concept better taken in a relative sense-relative to a method of forecasting.

The predictability of precipitation study began in 1976 when the McGill Weather Radar Observatory started sending 1-6-h rainfall forecasts to the local weather office (Bellon and Austin 1978). Since then some related techniques have been presented (Bellon et al., 2005; Lee and Zawadzki, 2005; Mecklenburg et al. 2000; Seed 2003), a recent effort of the analysis of the predictability of precipitation is the based on

Continental Radar Images by Lagrangian extrapolation (MAPLE) algorithm by Germann and Zawadzki team (Part I: Description of the Methodology; Part II: Probability Forecasts; Part III: Operational Nowcasting Implementation (MAPLE); Part IV: Limits to Prediction) from the aspects of the lifetime patterns of rainfall rates, the scale dependence of predictability and so on (Germann and Zawadzki, 2002, 2004; Turner et al., 2004; Germann et al., 2006). Much less effort has been devoted to evaluate the predictability of QPN from comprehensive perspective. In addition, attempts at analysing precipitation forecast skill are mainly based on Lagrangian persistence methods which always have difficulty in hydro-meteorological applications for significant computational cost and limitation in accurate tracking thunderstorms such as the Traditional widely pixel-based QPN methods, such as the Maximum Correlation Method (MCM) (e.g., Smythe and Zrnic, 1983; Tuttle and Foote, 1990), Variational Echo Tracking (VET) (Germann and Zawadzki, 2002), the performance of different methods has not been analysed.

Thus, this work aims to analyse factors affecting the predictability of QPN systematically using a newly developed extrapolation model which is Pixel-based QPN using Pyramid Lucas-Kanade Optical Flow method (PPLK) which was introduced in the next section.

In this paper, section 2 describes applied data sets. The method of analysing predictability was introduced in section 3. Section 4 explored the relationship between influence factors and the skilful forecast time of precipitation. Section 5 concludes the results.

2 DATA

Three typical rainfall events (1500-2100 UTC on 4 September 2013, 0900-1400 on 3 July 2010 and 1400-1720 on 7 June 2010) (Table 1) of a ground-based radar precipitation data were used in this study. They were provided by the Tsinghua University with spatial resolution 90 m and a frequency of 5min. The Radar covered a radius of 36km in the Tsinghua University, Beijing, China (116.32°E, and 40.01°N). The precipitation estimation work was carried out by the department of hydraulic engineering of Tsinghua University and Sichuan University.

Considering the co-existence of several storms in a single imagery, those 166 imageries consist of main kinds of rain events that occurred in Beijing.

Table 1 information for 3 rainfall event, including time, length, and rainfall system character

No.	*Duration length (hour)	No. of imageries	Rainfall system character
1	5.5	66	(a) 1500-1730.Convection is week; (b) 1745-18:30. A wide spread stratus moved in the Radar covering area from non-radar area; (c) 1830-2100. Strong convection.
2	5	60	(a) 0900-1230.Convection is relative week; (b) 1230-1300. Strong convection; (c) 1300-1400 convection getting week.
3	3.33	40	(a) 1400-1720.Convection is relative week; (b) 1620-1720.strong convection.

*No.1: the rainfall event of 1500-2100 UTC on 4 September 2013; No.2: the rainfall event of 0900-1400 on 3 July 2010; No.2: the rainfall event of 1400-1720 on 7 June 2010.

3 METHODOLOGY

3.1 Implement of the QPN

Considering that the traditional widely pixel-based QPN methods, such as The Maximum Correlation Method (MCM) (eg., Tuttle and Foote, 1990; Laroche and Zawadzki, 1995), Variational Echo Tracking (VET) (Germann and Zawadzki, 2002), the coupled hierarchical-tracking approaches and mesh-based

models of image deformation (Zahraei et al., 2012), always have difficulty in hydro-meteorological applications for significant computational cost and limitation in accurate tracking thunderstorms. Thus, this study used a new algorithm PPLK which is composed of three processes: utilizing the pyramid Lucas- Kanade optical flow method (LKOF) to improve the cloud advection estimation; projecting rain pixel based on liner extrapolation method considering the cloud advection and evolution; and adding a precipitation interpolation process based on the space-time continuum of cloud patches to reduce the projection discontinuities. The steps are described as follows.

(a) Pixel-based cloud tracking. Firstly, establish pyramid multi-resolution imageries. Then, estimate the derivative of rainy pixel from the top to the bottom of pyramid using Lucas- Kanade optical flow with a Gaussian kernel before processing. This study averaged the forward and backward cloud advection to avoid some unreasonable points.

(b) Rainfall extrapolation. Project rain images considering the cloud advection and evolution.

(c) Spatial interpolation. Interpolate QPN imageries obtained in step (b) using the inverse distance method on the assumption that the topological relationships of cloud pixels do not change in consecutive imageries.

The parameters of PPLK are composed of two types: (1) Parameters of PLKOF for the cloud advection estimation. Level of pyramid: 4; The size of searching window: 5×5; Matrices of filter function in the extension process of pyramid: (0.25- $\alpha/2$, 0.25, α , 0.25, 0.25- $\alpha/2$), where $\alpha = 0.4$; (2) Parameters of precipitation extrapolation. Searching radius of spatial interpolation for the forecasted image was set as “leading time×3/forecasting step+6”.

3.2 Analysing the predictability of QPN

This study analysed the predictability of QPN of Radar images from three aspects that were inputs, model type and outputs.

The influence of model inputs on the predictability of QPN can be indicated by the character of precipitation system, the spatial resolution of Radar, and the number of input data. To analyse the effect of spatial resolutions, the accuracy of four spatial resolutions (90m, 180m, 270m, and 360m) were compared. The character of precipitation system was indicated by the performance of three rainfall storms which involves the rapid development of cloud patch, movement of outside cloud, and so on. The effect of number of input data was shown by different number of prior radar imageries (t1, t2... t5).

To demonstrate the influence of the method of forecasting, this study compared four QPN models

using different advection extracting methods: precipitation now casting using liner extrapolation method (PLE), maximum correlation method (PMC), Horn-Schunck optical flow method (PHS), and PLKOF. The first one is the most widely method used in QPN (e.g., Tuttle and Foote, 1990). The second one has been newly applied recently years (Cheung and Yeung, 2012; Han et al., 2008). The third one is the proposed method in this study.

The effect of model outputs on the predictability of QPN was shown by the length of leading time. This study compared the accuracy of 0-1 hour predictions with the step of 5 min.

The predictability of precipitation from gestational satellite images was demonstrated by the time consumption and forecasting accuracy. In order to demonstrate the accuracy, five performance measures are used including: the relative bias (Bias), the coefficient of correlation (Corr), the normalized mean square error (NMSE), the probability of detection (POD), the false-alarm rate (FAR), and the critical success index (CSI). The former three parameters (the Bias, NMSE and Corr) measure the agreement between forecast and observation. The latter three (the POD, FAR, and CSI) can describe the skill of predicting the occurrence of precipitation. Those measures can be found in Liu et al. (2014).

All this study was carried out on a personal computer of ASUS UX32VD.

4. RESULTS

4.1 Spatial resolutions

Fig. 2 presents the averaged accuracy of a rainfall event for 0-60 min predictions vs. different spatial resolutions (90m, 180m, 270m, and 360m). The results show that coarser spatial resolutions reduced the NMSE and Corr, while has complex influence on Bias which decrease first and then increase. For example, the Bias, Corr and NMSE of QPN with 180m is 0.82, 0.67, 1.10, 1.08times of the original spatial resolutions (90m), while they are 1.43-1.75, 0.56-0.70, 0.98-1.01 times for the spatial resolutions between 270-360m. The coarser spatial resolutions has less influence on NSE compared to on Bias and Corr.

As for performance on the existence of rainfall events, it shows that POD increased 4.26%, -3.98%, -7.33% when it increased 1, 2 and 3 times from the original, while FAR reduced 2.67%, 6.93%, and 7.24%, CSI increased 3.38%, -0.15%, and -2.81%. Therefore, it shows better prediction skill on rainfall events with spatial resolutions increase from 90-180m, while the prediction accuracy reduced with spatial resolutions greater than 180m.

The reason for this lies in that the coarser resolution helps to improve the QPN performance by

reducing the image noise, and while it might fail to predict smaller-scale thunderstorms for decreasing accuracy of cloud advection extraction.

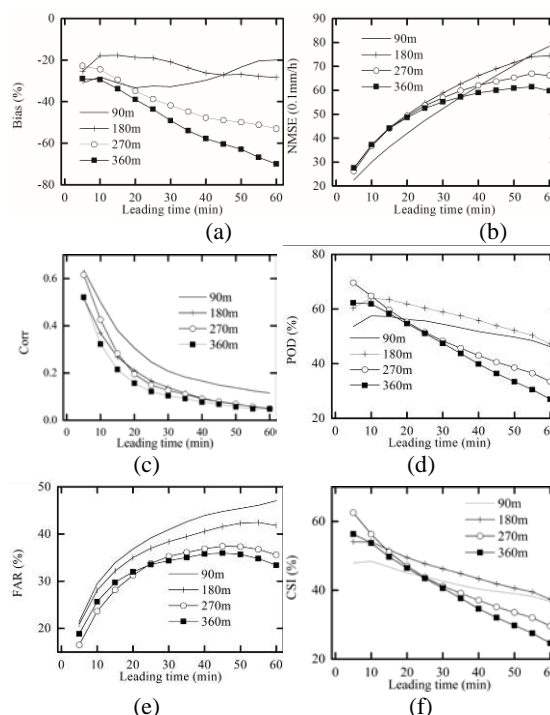


Fig. 2 6 average measures (Bias, Corr, NMSE, POD, FAR and CSI) vs. leading time for QPN with different spatial resolutions

4.2 The character of precipitation system

Fig.3 presents measures of QPN for different precipitation systems of 2.5hours in the first rainfall event (1630-1900 UTC on 4 September 2013). The rainfall event can be divided into three periods: (a) 1630-1730. Convection was relative weak and cloud patches were dispersed and small; (b) 1745-1830. A stratus moved in the Radar covering area from southwest direction, the cloud patches spread wide and were well organized; (c) 1830-1900. Rainfall system developed rapidly and the stratus cloud in the middle-east was replaced by convection cloud and the new birth, disperse, and merging process appeared continually.

It shows that rainfall system has significant influence on the predictability of QPN. The curve of various measures fluctuate greatly, the highest value is several times, even thousands times of lowers ones. Taking the Corr as example, the accuracy of QPN with the leading time of 10min, 20min, 40min, and 60min can arrive 0.7, 0.58, 0.4, and 0.38, while lowest Corr is only 0.002-0.1. The rainfall systems influence QPN in the following aspects: (1) the scale of cloud patches.

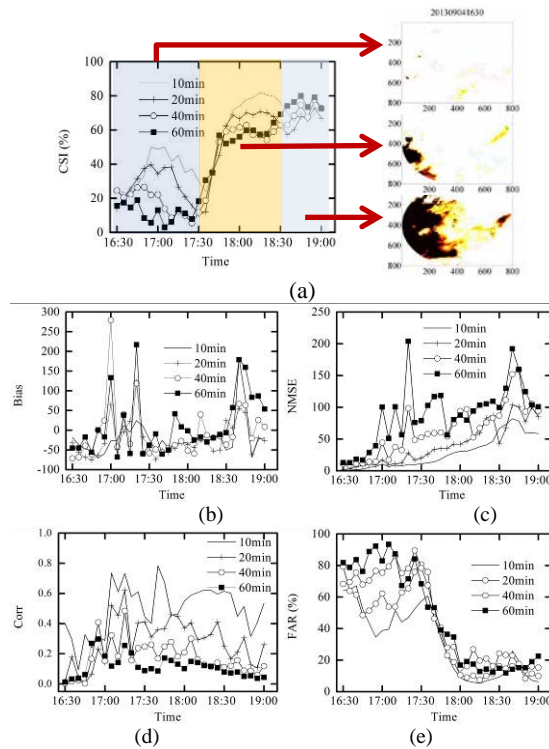


Fig.3 average measures vs. leading time of 10, 20, 40, and 60min for the precipitation systems of 1630-1900 UTC on 4 September 2013

The QPN performed bad in 1630-1730 when the disperse cloud patches take the predominate with the CSI of 20-50%, 18-40%, 5-25%, 3-20% for the QPN of 10min, 20min, 40min, and 60min, respectively. It get better when the small cloud patches were replaced by bigger ones during 1630-1730 with the CSI of 55-80% for the leading time of 60min; (2) the movement of cloud patches. The performance of QPN during 1745-1830 was not so good due to limit coverage of Radar which makes it hard to predict the southwest cloud moving in the Radar area from outside. However, the accuracy of QPN improved greatly after the main body of cloud patches moved in; and (3) the complex development of cloud patches. During the third period (1830-1900), the Corr, Bias, and NMSE are low despite of the high CSI, which indicate that the QPN can predict the existence of rainfall events well but fail to forecast the quantity of rain. The reason lie in that cloud tracking methods always treat cloud patch as robust and assume the relative position of cloud pixels do not change. However, it is observed that the new birth, dispersion and merge of cloud patches take places widely. Thus, the present cloud tracking methods have difficulties in accurate QPN due to failing to capture the complex development of cloud patches.

4.3 the number of the prior Radar data

Fig.4 is the average measures of QPN for 1-5 previous Radar data (t_1, t_2, \dots, t_5) used. It shows that number of prior Radar data used in QPF has no obvious influence on the Corr, NMSE, CSI and FAR. The Bias increased and POD reduced with the increasing number of prior Radar data. The increasing number of input prior imageries does not help to improve the accuracy of QPN. Thus, it is feasible to use only one prior Radar data as input.

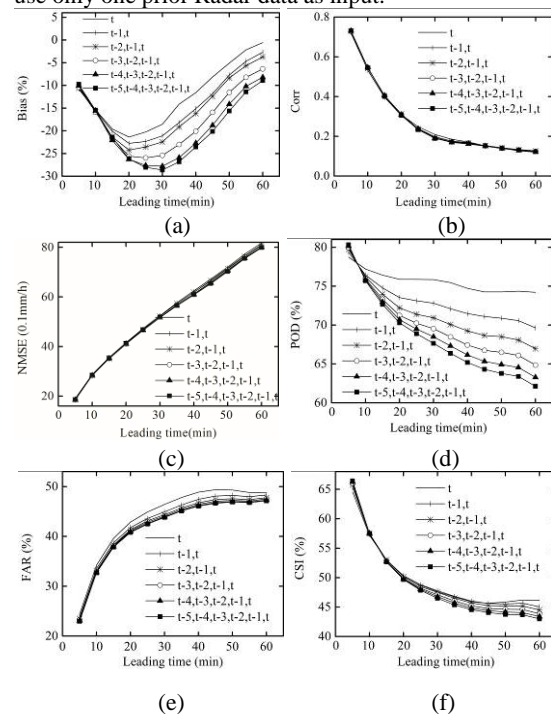


Fig.4 average measures vs. leading time for QPN with 1-5 prior Radar data used

4.4 QPN method

This study compared the average time consumption of QPN for different methods with leading time 0-1 hour. The result shows that the time consumption of MCM and PHS were 18.2min and 16.56min while that is only 0.006min for PPLK in the cloud tracking. PPLK has obvious advantage of time efficiency comparing with PMC and PHS. Thus, the PPLK method improves the predictability of 8-16min.

Fig.5 is the comparisons of PPLK vs. PMC and PHS and observations for the Bias, Corr, NMSE, POD, FAR and CSI averaged over imageries of the first rainfall case. It shows that the optical flow based-QPN, both PPLK and PHS outperformed the PMC method with great improvement in the predictability of rainfall in terms of 6 measures. For example, the

average NMSE of 0-1-hour leading time are 4.11mm/h, 1.13mm/h, 0.99mm/h, and 5.36mm/h for liner extrapolation, MCM, PHS and PPLK, respectively. PPLK improved the CSI by 17.38%, 13.63% and 1.96%, and increased POD by 39.94%, 29.25% and 14.67%, compared the liner extrapolation, MCM, and PHS. In addition, compared to the PHS, PPLK has better performance in identifying rainfall events despite of more FAR of 8.69%.

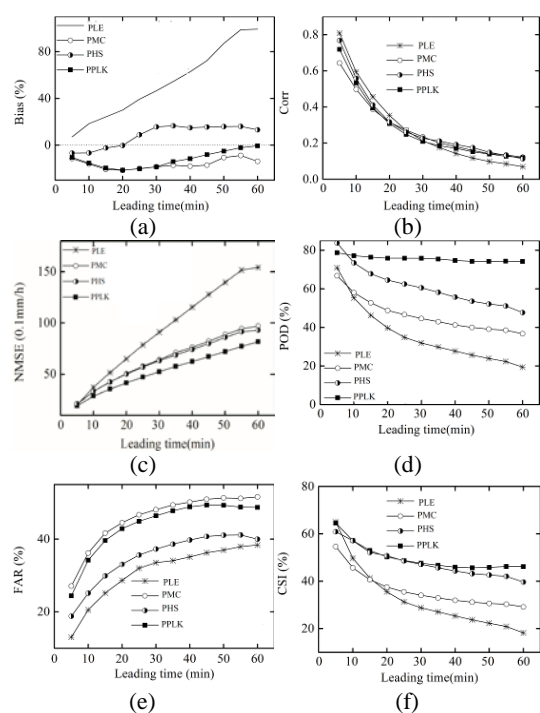


Fig.5 average measures vs. leading time for four QPN methods

4.5 the length of leading time

Fig.6 is the average measures of QPN with 0-60min leading time. It shows that the accuracy of QPN reduced rapidly with the increasing lead time. The Bias, Corr, NMSE, POD, FAR and CSI of QPN with 60min leading time are -13.75%, 0.12, 8.92mm/h, 56.29%, 47.73% and 40.72%, respectively. It is suggested that the forecast leading time should not greater than half hour with Bias, Corr, NSE, NMSE, POD, FAR, and CSI are -16.37%, 0.20, 31.89mm/h, 5.37mm/h, 61.74%, 41.58%, and 44.99%, respectively. QPN with long leading time have limited accuracy lies in shortage of extrapolation-based QPN method, complex development of rainfall system, and limit coverage of Radar.

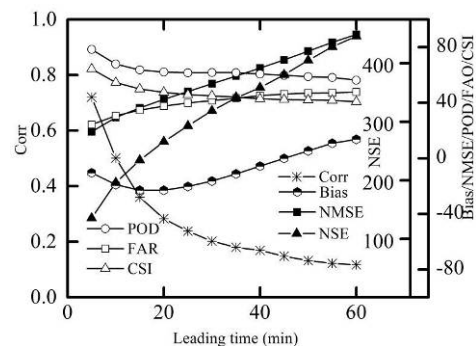


Fig. 6. average measures vs. leading time

This study compared the QPN by PPLK and other methods carried in other studies despite different cases used. Considering that the cases used in this study were more difficult for less Radar coverage and more complex rainfall systems which involved the movement of cloud from non-radar coverage area in addition to the cloud development in Radar area, the comparison is reasonable. The result shows that the method used in this study has obvious advantage over other methods. The accuracy of 60 min QPN for PPLK is even comparable to that of 30min for other methods. PPLK improved the POD of 30min by 16-34% and reduced FAR by 27-44%, comparing to the PBN which was the best method of four popular methods according to the study of Zahraei et al. (2012). It increased POD by 28-44% and reduced FAR by 27-44% for QPN with 60min leading time.

5. SUMMARY AND CONCLUSIONS

In this study, five factors affecting the predictability of QPN of Radar were analysed based on a new QPN algorithm PPLK: the spatial resolution of Radar, the character of precipitation system, the number of input data, the QPN method, and the length of leading time based on a QPN algorithm PPLK. The result shows that:

(1) The predictability of QPN is mainly determined by precipitation weather system in which the accuracy indexes vary greatly for strong convection clouds and stratiform clouds. In addition, the movement of cloud from non-radar coverage area complicated the precipitation forecasting substantially. And the development character of clouds also make the precipitation forecasting quite difficult, such as cloud new birth, merge, and dispersion, etc.

(2) The spatial resolution of radar has complicate influence on QPN. Low spatial resolution can not only helps to improve the accuracy of cloud tracking by lessening image noise, but also reduces accuracy of QPN for missing some minor convection clouds which may develop rapidly and produce strong rainfall.

According to the experiments, it shows that the accuracy with spatial resolution of 90-180m is better than that of 270m and 360m.

(3) The number of the prior Radar data used in QPN has no obvious influence on the accuracy of QPN. It is feasible to use only one prior Radar data as input in QPN.

(4) The proposed PPLK method improved the predictability of precipitation by outperforming the other three comparison methods (Linear extrapolation method, MCM and PHS) with significantly improved accuracy and slightly reduced time consumption.

(5) The accuracy of QPN reduced rapidly with the increasing leading time. It is suggested that the leading time should not greater than half hour. The proposed PPLK with 60min lead time is even comparable the comparison studies of 30min QPN despite different cases and scans used.

ACKNOWLEDGMENT

This work was supported by the National Natural Science Foundation of China under Grant 41301379. The authors would like to thank TshingHua University for providing Radar data.

REFERENCES

- Bellon, A., Austin, G. L., 1978, The evaluation of two years of real-time operation of a short term precipitation forecasting procedure (SHARP). *Journal of Applied Meteorology*, 17, 1778–1787
- Bellon, A., Lee, G., Zawadzki, I., 2005, Error statistics of VPR corrections in stratiform precipitation. *Journal of Applied Meteorology*, 44, 998–1015
- Germann, U., Zawadzki, I., 2002, Scale-dependence of the predictability of precipitation from continental radar images. Part I: description of the methodology. *Monthly Weather Review*, 130, 2859–2873
- Germann, U., Zawadzki, I., 2004, Scale-dependence of the predictability of precipitation from continental radar images. Part II: probability forecasts. *Journal of Applied Meteorology*, 43, 74–89.
- Germann, U., Zawadzki, I., Turner, B., 2006, Predictability of precipitation from continental radar images. Part IV: limits to prediction. *Journal of the Atmospheric Sciences*, 63, 2092–2108.
- Lee, G., Zawadzki, I., 2005, Variability of drop size distributions: Time-scale dependence of the variability and its effects on rain estimation. *Journal of Applied Meteorology*, 44, 241–254
- Liu, Y., Xi, D. G., Li, Z.-L., Shi, C. X., 2014, Analysis and Application of the Relationship between Cumulonimbus (Cb) Cloud Features and Precipitation Based on FY-2C Image. *Atmosphere*, 5, 211–229
- Tuttle, J.D., Foote, G.B., 1990, Determination of the boundary layer airflow from a single Doppler radar. *Journal of Atmospheric and Oceanic Technology*, 7, 218–232.
- Turner, B. J., Zawadzki, I., Germann, U., 2004, Predictability of precipitation from continental radar images. III: Operational nowcasting implementation (MAPLE). *Journal of Applied Meteorology*, 43, 231–248
- Zahraei, A., Hsu, K., Sorooshian, S., Gourley, J. J., Hong, Y., Behrangi, A., 2013. Short-term quantitative precipitation forecasting using an object-based approach. *Journal of Hydrology*, 483, 1–15
- Zahraei, A., Hsu, K., Sorooshian, S., Gourley, J. J., Hong, Y., Lakshmanan, V., Bellerby, T., 2012. Short-term quantitative precipitation forecasting: a Lagrangian pixel based approach. *Atmospheric Research*, 118, 418–434.
- Cheung, P., Yeung, H.Y., 2012. Application of optical-flow technique to significant convection nowcast for terminal areas in Hong Kong. The 3rd WMO International Symposium on Nowcasting and Very Short-Range Forecasting (WSN12), 6–10 August 2012, Rio de Janeiro, Brazil
- Han, L., Wang, H. Q., Lin, Y. J., 2008. Application of Optical Flow Method to Nowcasting Convective Weather. *Acta Scientiarum Naturalium Universitatis Pekinensis*. 44, 751–755 (in Chinese)
- Zinner, T., Mannstein, H., and Tafferner, A., 2008, Cb-TRAM: Tracking and monitoring severe convection from onset over rapid development to mature phase using multi-channel Meteosat-8 SEVIRI data. *Meteorology and Atmospheric Physics*, 101, 191–210.

A statistical calibration for a combined Optical-Passive microwave method using remote sensing and reanalysis data

C. Mattar¹, A. Santamaría-Artigas¹, J.P. Wigneron² and P. de Rosnay³.

1. Laboratory for Analysis of the Biosphere (LAB), University of Chile

cmattar@uchile.cl

2-EPHYSE, INRA-Aquitaine, France.

3-European Centre for Medium-Range Weather Forecasts, Reading, United Kingdom.

ABSTRACT - This work presents a statistical calibration of a semi-empirical combined optical-passive microwave remote sensing method to estimate surface soil moisture at regional scale. The proposed method uses satellite data provided by different sensors such as: bi-polarized brightness temperature (HV polarizations) at L-band given by the Soil Moisture and Ocean Salinity Mission (SMOS) brightness temperature level 3 product (TBL3), the Normalized Difference Vegetation Index (NDVI) and Land surface Temperature (LST) derived from MODIS (MOD13Q1 and MOD11A1 respectively), the LST obtained by GOES GEOLAND2 products, the Surface Soil Moisture (Volumetric soil water layer 0 – 7 cm) and Skin Temperature provided by the ECWMF (ERA-interim). Results show that the use of vegetation indices such as the NDVI improves the calibration of the semi-empirical approach. The improvements of the coefficient of determination (r^2) increase between 2 and 20% when using NDVI in comparison to setting NDVI equal to zero. The use of LST in the calibration of the semi-empirical approach can be considered as a possible indicator of the effective temperature. A partial evaluation of the soil moisture estimates was performed without statistical significant results. Finally, this work contributes to the use of synergic optical-passive microwave approaches, which can improve the soil moisture estimation based on remote sensing data at regional scale.

Keywords: Soil Moisture, Microwave Radiometry, L-band, SMOS

1 INTRODUCTION

Soil moisture plays a key role in meteorological and hydrological forecast as it controls the evaporation process between land surface and atmosphere. During the few last decades new technologies have been developed to perform soil moisture estimates at different spatial and temporal scales. Moreover, the relevance of soil moisture maps at global or continental scales area a crucial parameter for climate change studies (Douville and Chauvin, 2000), surface-atmosphere interactions (Koster et al., 2004), weather forecast (Drusch, 2007) and agriculture applications (Shin et al., 2006), among others. Therefore, the importance of soil moisture information has conditioned many scientists to generate reliable soil moisture estimates from land surface modelling, remote sensing techniques, or a combination of both through land data assimilation systems. (Albergel et al., 2013a and references there-in).

One of the most relevant techniques to provide soil moisture maps at global scale is by using active/passive microwave remote sensing. At present, new satellite missions working on L-band passive microwave range were being developed in order to improve the surface soil moisture estimations and ocean salinity at global scale (Kerr et al. 2001; Kerr et al., 2012; Lagerloef et al 2008; Entekhabi et al., 2010). One of these is the Soil Moisture and Ocean Salinity

Mission (SMOS). This satellite mission was specially designed for monitoring soil moisture, acquiring data at the suitable frequency for soil moisture retrieval (1.4 GHz) and providing global maps of soil moisture every three day at nominal spatial resolution of 43 km with an accuracy goal of 0.04 m³/m³ (Kerr, 2010). The surface soil moisture delivered from SMOS data is performed by the SMOS Level 2 algorithms. These routines are an iterative approach which aims at minimizing a cost function whose main component is the sum of the squared weighted differences between measured and modelled TB data for a collection of incidence angles (Kerr et al., 2012). The TB measured is obtained by SMOS and the upwelling set of TB values is modelled using the L-band Microwave Emission of the Biosphere (L-MEB) model (Wigneron et al., 2007). The L-MEB model uses a tau-omega (τ - ω) emission model calculated over a wide range of land covers given by the ECOCLIMAP database (Masson et al., 2003)

This τ - ω approach was tested in several land uses at in-situ and global scale considering the vegetation parameter as an indicator of the vegetation optical depth (Saleh et al., 2006; Wigneron et al., 2007; Parrens et al., 2012; Mattar et al., 2012), the τ - ω model proposed by Mattar et al (2012) was calibrated and validated using the Normalized Difference Vegetation Index (NDVI) as an indicator of τ .

Nevertheless, this model was only tested with in-situ data from the SMOSREX site (de Rosnay et al., 2006), and no applications at regional or continental scale have been demonstrated yet. Thus, the aim of this work is to analyse the semi-empirical approach developed by Mattar et al. (2012) by using vegetation indices such as the NDVI at regional scale. For this end, satellite data from SMOS, the Geostationary Operational Environmental Satellite (GOES), the Moderate Resolution Imaging Spectroradiometer (MODIS) and reanalysis data from ERA-interim were applied over the agricultural central-southern zone of Chile

2 STUDY AREA & DATA

The study area is located in the Central-Southern region of Chile in between the Coast and the Andes Mountains (Figure 1). This area is the most agricultural productive zone of Chile and fruit orchards cover it and several crops mainly rice, maize and wheat. The climate condition ranges between Mediterranean to Austral type with seasons clearly marked by dry summers and wet winters. Although there is rainfall throughout the year, the months where rainfall is concentrated are June, July and August. The average rainfall amount is close to 538 mm in the north of the study area and almost 3000mm in the southern zone. It presents a high thermal oscillation in all seasons between maximum and minimum daily temperatures.

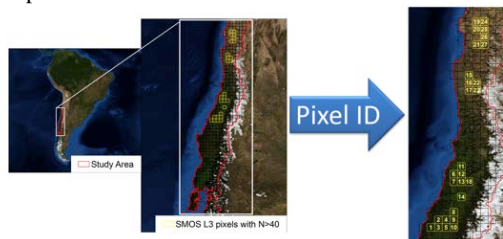


Figure 1. Study area and the SMOS pixels used in this work. In black is the whole data set and in yellow the pixel with a data count (for SMOS, GOES, MODIS and ERA) higher than 40 per year.

2.1 MODIS

Two data sets from MODIS were used in this work concerning land surface temperature and vegetation indices. These products are the MOD11A1 V5 Land Surface Temperature product (Wan, 1999) which was used to obtain daily surface temperature values at 1x1 km spatial resolution and the MOD13Q1 V5 Vegetation Index product (Huete et al., 1999) which includes 16-day composite Normalized Difference Vegetation Index (NDVI) data at a 0.25 x 0.25 km spatial resolution.

2.2 GOES

The GOES land surface products derived from Geoland2 (Lacaze et al., 2011) were also used in this work. The Geoland2 land surface temperature (LST) product was generated globally using METEOSAT, GOES and MTSAT imagery. The LST data is calculated by using a generalized split-window method based on several atmospheric profiles databases and a radiative transfer code. The 3 hourly LST derived from GOES satellite at 8 x 8 km were used.

2.3 SMOS L3 product

The bi-polarized brightness temperature (vertical (TBV) and horizontal (TBH)) at 42.5° from SMOS-level 3 products (TBL3) was used in this study. The TBL3 data set corresponds to daily values of brightness temperature at L-band available at different view angles in the EASE spatial grid (25 x 25 km). More details of the TBL3 products appear in Kerr et al (2012).

2.4 ERA-interim

Finally, the ERA-Interim reanalysis produced by the European Centre for Medium-Range Weather Forecasts (ECMWF) is a reliable source of meteorological data for scientific research and development (Dee et al., 2011). ERA-Interim data is available from 1979 to present day and includes global meteorological data at different temporal and spatial resolutions. Several works have compared the soil moisture with microwave remote sensing and in-situ observations demonstrating the reliability of the soil moisture products (Albergel et al., 2012; 2013a; 2013b). For this work, two different ERA-Interim products were used, the skin temperature (i.e. the temperature of a surface at radiative equilibrium that forms the interface between soil and the atmosphere) and the volumetric soil water layer (i.e. the water content between the surface and the first 7 cm of soil), both data sets have a spatial resolution of 0.125° x 0.125° latitude – longitude

3 METHOD

3.1 Theoretical Approach

The theoretical basis of the semi-empirical regression used in this work consists in the tau-omega model applied to vegetation covers (Ulaby et al., 1986). The p -polarized brightness temperature $T_b(\theta, p)$ was written as a function of the single scattering albedo $\omega(\theta, p)$, the optical depth $\tau(\theta, p)$, the soil reflectivity $\Gamma_s(\theta, p)$, the downward atmospheric and galactic brightness temperature $T_{b\theta}^{SKY}$ and the soil and vegetation effective temperatures (T_s^E and T_v^E , respectively):

$$Tb_{(\theta,p)} = (1 - \omega)(1 - \gamma) \left(1 + \gamma \Gamma_{S(\theta,p)} \right) T_V^E + \gamma \left(1 - \Gamma_{S(\theta,p)} \right) T_S^E + Tb_{\theta}^{SKY4} \Gamma_{S(\theta,p)} \gamma^2 \quad (1)$$

where $\gamma = \gamma(\theta, p)$ is the p -polarized transmissivity of the vegetation layer, which can be expressed as a function of the optical thickness $\tau(\theta, p)$, and the incidence angle θ .

$$\gamma_{(\theta,p)} = \exp \left(-\frac{\tau_{(\theta,p)}}{\cos(\theta)} \right) \quad (2)$$

Some simplification can be made without introducing significant errors such as considering the effective soil and vegetation temperatures as equal ($T_S^E = T_V^E = T_C = \text{effective soil temperature}$) (Jackson et al., 1995) and the upward and downward atmospheric emission can be neglected (Wigneron et al., 2004). A semi-empirical approach was initially developed by Wigneron et al. (2004) considering that scattering effects can be neglected, which generally is a good approximation at L-band [35], so equation (1) can be written as:

$$Tb_{(\theta,p)} = T_C (1 - \Gamma_{S(\theta,p)} \gamma_{(\theta,p)}^2) \quad (3)$$

The measured surface emissivity $e(\theta, p)$ defined as $e(\theta, p) = Tb_{(\theta,p)} / T_C$ can be written as

$$e_{(\theta,p)} = 1 - \Gamma_{S(\theta,p)} \gamma_{(\theta,p)}^2 \quad (4)$$

Soil reflectivity can be assumed proportional to surface soil moisture according to

$$\Gamma_{S(\theta,p)} \cong Ap_{(\theta)} w_s^\alpha \quad (5)$$

where $Ap(\theta)$ and α are site dependent coefficients that implicitly accounts for the sensor configuration and all the soil characteristics that determine soil emission: mainly soil texture and structure and surface roughness, among others. Thus, replacing equation (5) in (3) the soil moisture can be written as a function of the vegetation optical thickness $\tau(\theta, p)$, surface effective temperatures and bi-polarized brightness temperature $Tb_{(\theta,p)}$. Wigneron et al (2004) tested the equation (5) over barren areas. However, Mattar et al (2012) adapted this approach for a vegetated area including a vegetation indicator described as follows:

$$\log(w_s) = a + b * (\log(1 - \Gamma\theta, H)) + c * (1 - \Gamma\theta, H) + d * Veg \quad (6)$$

Where a , b , c and d are the regression coefficients, w_s is the soil moisture, Γ is the bi-polarized and angular dependent passive microwave reflectivity defined as $\Gamma = 1(Tb/T_C)$ where Tb and T_C are the L-band Brightness and effective temperature respectively and Veg is a surface vegetation indicator. So, eq(6) can be rewritten as:

$$\log(w_s) = a \left(\log \left(1 - \frac{Tb_{(\theta,H)}}{T_C} \right) \right) + b \left(\log \left(1 - \frac{Tb_{(\theta,V)}}{T_C} \right) \right) + c * VEG + d \quad (7)$$

Eq. (7) was tested over the SMOSREX site using the NDVI as a vegetation indicator and obtained significant results related to soil moisture estimation improvements.

3.2 Calibration and Validation

The whole set of data was resampled to the same spatial grid (EASE V1 grid at 25 x 25 km). Once the whole data sources were given the same spatial grid for the whole data period, an extract procedure was applied in order to characterize each EASE pixel by date/hour, SMOS Tb (ascending, descending), SMOS science flags, ERA (soil moisture and skin temperature), MODIS (LST and NDVI) and GOES (LST) for the whole period. Then, a quality filter was applied for the whole time series in order to select data reliable for the calibration and the remaining observations were matched to the SMOS observations overpass time. After filtering, the EASE pixels which presented a pair of data equal or higher than 40 (equivalent to the 40% of the whole period) were selected for the calibration process.

To calibrate eq(7) a step forward statistical regression was applied to each EASE pixel which presented more than 40 pairs of data over all the data sets (those with observations for all the data sources at a given time). Based on the filtered data, a statistical calibration process was carried out to obtain the best statistical correlations between soil moisture, orbit dependent brightness temperature, land surface temperature and NDVI. These results were compared to the same statistical results obtained when NDVI was set equal to zero. In this way, the potential improvements obtained when NDVI was included in the retrieval process could be evaluated. Additionally, the data sources could also be evaluated in order to see influences of geostationary, polar or reanalysis data. The best statistical correlations were evaluated by the statistical significance of the regression coefficients in addition to the coefficient of determination (r^2). The calibration was carried out for each year of data (2010, 2011 and 2012) separately.

To evaluate the soil moisture estimates and the influences of the vegetation indicator, the soil moisture estimates using NDVI and NDVI set equal to zero were evaluated with the soil moisture provided by ERA for the years not used in the calibration (e.g. calibration in 2010 and evaluation in 2011 and 2012). The magnitude of improvements were evaluated using the Root Mean Square Error (RMSE) which was expressed as $\sqrt{bias^2 + \sigma^2}$ where bias and σ are the average and the standard deviation of the difference between the estimated and the observed values respectively.

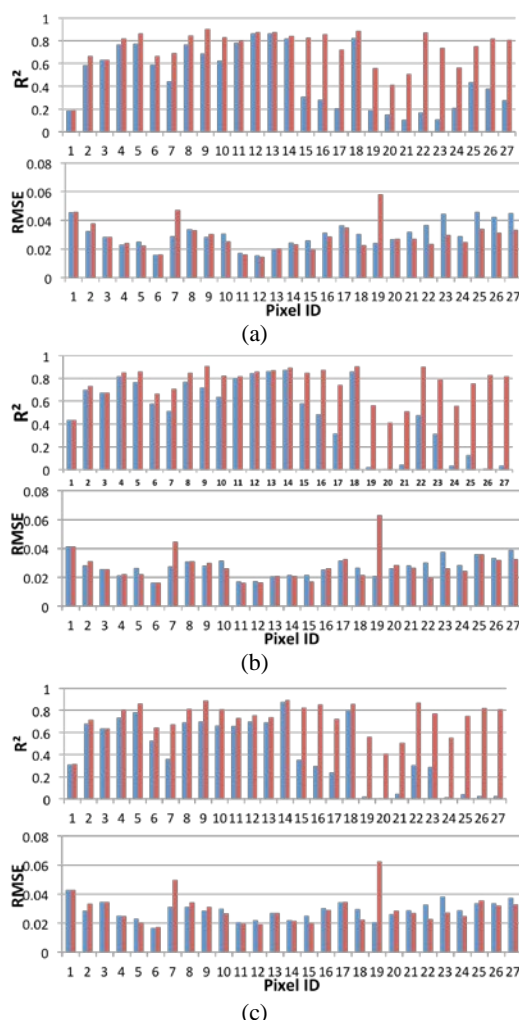


Figure 2. Coefficient of determination for the regressions of year 2010 and RMSE for the evaluations on years 2011 and 2012 using NDVI=0 (blue bars) and NDVI=MOD13Q1 (red bars) for ERA (a), GOES (b) and MODIS (c).

4 RESULTS

The use of NDVI improved the calibration of eq (7) in comparison to when NDVI was not considered. The best improvement was obtained for year 2010 and for Ascending SMOS orbits and MODIS-LST (Table 1). Figure 2 shows the Coefficient of Determination (r^2) for the year 2010 (calibration) and 2010-2011 (Evaluation). For this period, the RMSE and estimations of soil moisture using NDVI from MOD13Q1 and NDVI =0 are shown for ERA, GOES and MODIS respectively.

5 CONCLUSIONS

The optical passive-microwave approach calibration is improved (between 2 and 20% of the r^2) when using a vegetation indicator such as the NDVI to account for the vegetation influence in the soil moisture estimation. The use of LST on the semi-empirical method can be also used a possible indicator of the thermal influences on the proposed approach.

However, further work needs to be conducted in order to analyse the effects of replacing the effective temperature by the LST. The results presented here show the potential of applying the combined optical-passive microwave at regional scales in order to improve soil moisture estimates.

6 ACKNOWLEDGMENTS

This Work is partially funded by the project Fondecyt-Initial 11130359 and U-Inicia VID 4/0612. The authors also acknowledge to ECMWF for the free distribution of ERA-interim data, CATDS for SMOS data, NASA for the free distribution of LST-MODIS products and Geoland2 for GOES products.

7 REFERENCES

- Albergel, C., et al. 2012. Evaluation of remotely sensed and modelled soil moisture products using global ground-based in-situ observations. 2012. *Remote Sensing of Environment*, 118, 215 – 226.
- Albergel, C., et al. 2013a. Monitoring multi-decadal satellite earth observation of soil moisture products through land surface reanalyses. *Remote Sensing of Environment*, 38, 77 – 89.
- Albergel, C., Dorigo, W., Reichle, R., Balsamo, G., De Rosnay, P., Muñoz-Sabater, J., Isaksen, L., De Jeu, R., Wagner, W. 2013b. Skill and Global Trend Analysis of Soil Moisture from Reanalyses and Microwave Remote Sensing. *Journal of Hydrometeorology*, 14, 1259 – 1277.
- Dee, D.P., et al. 2011. The ERA-interim Reanalysis: configuration and performance of the data assimilation system. *Quarterly Journal of the Royal Meteorological Society*, 137, 553 – 597.

- De Rosnay, et al. 2006. SMOSREX: A long term field campaign experiment for soil moisture and land surface processes remote sensing. *Remote Sensing of Environment*, 102, 377 – 389.
- Douville, H., and Chauvin, F. 2000. Relevance of soil moisture for seasonal climate predictions: A preliminary study. *Climate Dynamics*, 16, 719 – 736.
- Drusch, M. 2007. Initializing numerical weather predictions models with satellite derived surface soil moisture. Data assimilation experiments with ECMWF's integrated forecast system and the TMI soil moisture data set. *Journal of Geophysical Research*, 113.
- Entekhabi, D., et al. 2010. The Soil Moisture Active Passive (SMAP) mission. *Proceedings IEEE* 98(5), 704 – 716.
- Huete, A. and Justice, C. 1999. MODIS Vegetation Index (MOD13) Algorithm Theoretical Basis Document.
- Jackson, T. J., Le Vine, D. M., Swift, C. T., Schmugge, T. and Schiebe, F.R. 1995. Large area mapping of soil moisture using the ESTAR passive microwave radiometer in Washita 92. *Remote Sensing of the Environment*. 54:27-37.
- Kerr, Y., Waldteufel, P., Wigneron, J. -P., Martinuzzi, J.M., Font, J., and Berger, M. 2001. Soil moisture retrieval from space: The soil moisture and Ocean Salinity (SMOS) mission. *IEEE Transactions on Geoscience and Remote Sensing*, 39(8), 1729 – 1735.
- Kerr, Y., et al 2010. The SMOS mission: New tool for monitoring key elements of the global water cycle. *Proceedings IEEE*, 98(5), 704 – 716.
- Kerr, Y., et al. 2012. The SMOS soil moisture retrieval algorithm. *IEEE Transactions on Geoscience and Remote Sensing*, 50(5), 1384 – 1403.
- Koster, R., Dimeyer, P., Guo, Z., Bonan, G., Chan, E., Cox, P., et al. (2004). Regions of strong coupling between soil moisture and precipitation. *Science*, 305, 1138 – 1140.
- Lacaze, R., et al. 2011. Geoland 2 - Towards an operational GMES Land Monitoring Core Service: the Biogeophysical Parameter Core Mapping Service. *Proceedings of the 34th International Symposium of Remote Sensing of Environment*.
- Lagerloef, G., et al. 2008. The Aquarius/SAC-D mission: Designed to meet the salinity remote-sensing challenge. *Oceanography*, 21(1):68–81.
- Masson, V., Champeau, J. -L., Chauvin, F., Meriguet, C., & Lacaze, R. 2003. A global database of land surface parameters at 1 km resolution in meteorological and climate models. *Journal of Climate*, 16, 1261–1282.
- Mattar, C., et al. 2012. A Combined Optical–Microwave Method to Retrieve Soil Moisture Over Vegetated Areas. *IEEE Transactions on Geoscience and Remote Sensing*, 50(5), 1404–1413
- Parrens, M. et al. 2012. Comparing soil moisture retrievals from SMOS and ASCAT over France. *Hydrology and Earth System Sciences*, 16:423–440.
- Saleh, K., Wigneron, J. P. and Rosnay, P. de. 2006. Semi-empirical regressions at L-band applied to surface soil moisture retrievals over grass. *Remote Sensing of Environment*, 101:415–426
- Wan, Z. 1999. Modis Land-Surface Temperature Algorithm Theoretical Basis Document.
- Wigneron, J. -P., et al. 2004. Soil moisture retrievals from biangular L-band passive microwave observations. *IEEE Geoscience and Remote Sensing Letters*, 1, 277–281
- Wigneron, J.-P., et al. 2007. L-Band Microwave Emission of the Biosphere (L-MEB) Model: Description and Calibration against Experimental Data Sets over Crop Fields. *Remote Sensing of Environment*, 107 (4): 639–55.

LAB-net the First Chilean soil moisture network for Remote Sensing Applications

C. Mattar¹, A. Santamaría- Artigas¹, C. Durán-Alarcón¹, L. Olivera-Guerra¹, & R. Fuster².

1. Laboratory for Analysis of the Biosphere (LAB), University of Chile

cmattar@uchile.cl

2. Laboratory for Territorial Analysis (LAT), University of Chile.

ABSTRACT - Soil moisture has been defined as one of the essential climate variables by several worldwide climate and earth observation expert panels. During the last decades several explorer mission have been launched in order to obtain reliable soil moisture estimations at global scale. The most recent and successfully launched project is the Soil Moisture and Ocean Salinity Mission (SMOS) working at L-band and providing soil moisture maps at global scale with a revisit time of less than 3 days. In Chile, remote sensing applications related to soil moisture and evapotranspiration estimates have increased during the last decades because of the drought and the water use conflicts which generated a strong interest on water demand quantification. To address the problem of water balance estimation at large scales by using remote sensing imagery, LAB-net was created as the first soil moisture measurement network in Chile for remote sensing applications. The network's land cover types are vineyards and olive orchards, located in the semi-arid region of Copiapo valley; a well irrigated raspberry crop located in the central zone of Tinguiririca Valley; and a green grassland located in Chile's austral region. In each site, a well implemented meteorological station is continuously recording the 5 minute averages of the following parameters: Soil moisture and temperature at two ground levels (10 and 20 cm), air temperature and relative humidity, net radiation, global radiation, brightness temperature (8 – 14 μ m), rainfall and ground fluxes. This is the first approach of an integrated soil moisture network in Chile. The data generated by this network is freely available for any research or scientific purpose related to current and future soil moisture satellite missions.

Keywords: Soil moisture network, meteorological station, remote sensing, LAB-net

1 INTRODUCTION

Soil moisture (SM) is one of the most essential climate variables which control the hydrological and meteorological response of land's surface. It also plays a main role in land-atmosphere interactions due to its control on evapotranspiration (Cheruy et al., 2013). In situ SM measurements can now be routinely achieved with an accuracy as high as 0.025 m³/m³ (Walker et al, 2004). However, considering the high spatial variability of SM and the poor density of in situ measurement sites, it is not possible to produce accurate large-scale estimate of SM from in-situ measurement networks (Dorigo et al., 2011; Vivoni et al, 2008). A major alternative to estimate SM at the large scale is to rely on remote sensing satellites which offer global coverage and high revisit time, although they are only sensitive to a shallow layer of the soil. During the last decades, several remote sensing missions have been launched in order to retrieve reliable soil moisture maps at global scale such as AMSR-E (Njoku, 2004), ASCAT (Wagner et al., 2013) or SMOS (Kerr et al., 2012)

However, it is a current necessity to calibrate and validate the soil moisture products provided by the

models which uses satellite information. In fact, accurate SM initialization is crucial to the quality of most water-related environmental forecasts up to at least seasonal forecasts, including numerical weather predictions (NWP) (Al-Yaari, et al., 2014).

Despite the significant effort for provide a robust soil moisture network at global scale to calibrate satellite products and to provide data on numerical models, the south hemisphere does not present a high density grid of soil moisture stations (Dorigo et al., 2011). In this context, in-situ soil moisture measurements are required to improve remote sensing products also in order to provide reliable information for the users.

The objective of this work is to present the first Chilean soil moisture network "LAB-net" which can be used for several remote sensing applications including calibration/validation of remote sensing products and model retrieval evaluations.

2 EXPERIMENTAL SET UP

LAB-net is based on the contribution of two national research projects focused in soil moisture (Fondecyt-Initial) and Irrigation Efficiency in semi-arid regions (Fondef-IDEA). LAB-net was

implemented in four different crops: Olive orchards (27°19'13.46"S; 70°32'22.56"W) and vineyards (27°17'41.69"S; 70°27'7.49"W), both located in a semi-arid region close to the Atacama desert a raspberry crop in the central zone of Chile (34°43'39.67"S; 70°58'46.16"W); and a green grassland located in South part of Chile (40°53'6.07"S; 73° 6'31.41"W). The stations located in these sites are detailed as follows. Some examples of the stations at the different locations are showed in figure 1.

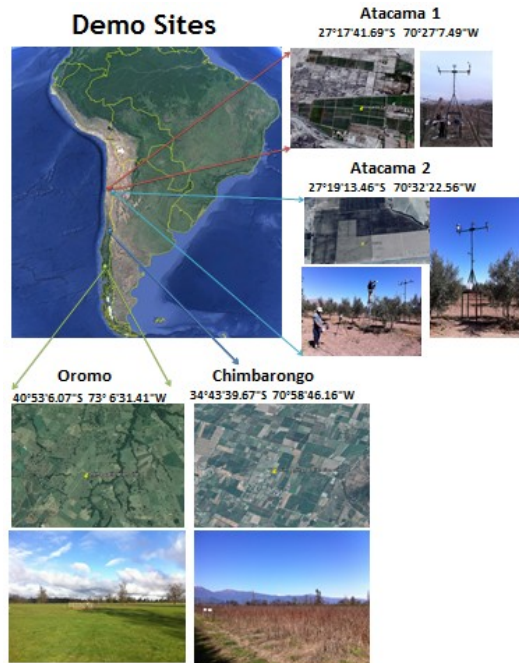


Fig 1. LAB-net sites along different land covers of Chile.

2.1 Stations

The four LAB-net sites were installed and mounted in order to provide the basic meteorological parameters and fluxes and energy balance data. These sites were implemented between October 2013 and July 2014. The instrumentation is detailed in table 1.

Data is measured every minute and then averaged and recorded every 5 minutes. Recording data are stored and transmitted weekly by using a GPRS system. The back-up is performed two times per month in order to avoid any data loss.

TABLE 1. Parameters and land cover characteristics for each LAB-net site.

Parameters	Oromo	Chimbarongo	Atacama 1	Atacama 2
Land cover	Green grass	Raspberry	Vineyards	Olives
Area (ha)	150	14	35	100
Air Temp at 2m (°C)	✓	✓	✓	✓
Relative Humidity (%)	✓	✓	✓	✓
Wind Speed (m/s)	✓	✓	✓	✓
Wind Direction (°)	✓	✓	✓	✓
Rainfall (mm)	✓	✓	✓	✓
Radiometric Temperature (K)	✓	✓	✓	✓
Net Radiation (W/m ²)	✓	✓	✓	✓
Soil Moisture 0-10 cm (m ³ /m ³)	✓	✓	✓	✓
Soil Moisture 10-20 cm (m ³ /m ³)	✓	✓	✗	✗
Soil Temperature 10 cm (K)	✓	✓	✓	✓
Soil Temperature 20 cm (K)	✓	✓	✗	✗
Ground Flux (W/m ²)	✓	✗	✓	✓
GPRS communication (7 days)	✓	✓	✓	✓
Start Validated data	07/14/2014	10/16/2013 Over Maize crop 07/17/2014 Moved to Raspberry	07/26/2014	07/28/2014
Linked to International Projects	ISMN	MIXMOD-E Imagined		

2.2 Assimilation data

LAB-net data can be used for several applications such as calibration and validation, for comparison between in-situ observation and land surface energy fluxes and water balance models, soil irrigation models, among others. LAB-net data is also complemented by in-situ measurements acquired during seasonal field campaigns where transects are performed. These transects consists in several measurements of surface reflectance acquired by an ASD Fieldspec Handheld spectroradiometer, infrared (8 – 14 μm) brightness temperature provided by an Apogee SI-111 infrared radiometer and soil moisture provided by a Campbell HS2 probe. Finally, LAB-net data is related to a remote sensing data base for different sensors such as SMOS, MODIS and Landsat-8. These remote sensing images are continuously downloaded and matched for each coordinates where LAB-net stations are located. These data base is assimilated and compiled in order to apply several applications such as soil moisture evaluation

3 APPLICATION

In this manuscript, a time series of SMOS SM and LAB-net data is presented. Figure 2 shows the time series of in-situ volumetric water content (m³/m³) at 10 cm, rainfall (mm) and the SMOS soil moisture (m³/m³) derived from the Level-3 daily SM product (CLF31) for Oromo and Chimbarongo sites respectively. The SMOS data was obtained from nearest EASE pixel to the LAB-net stations.

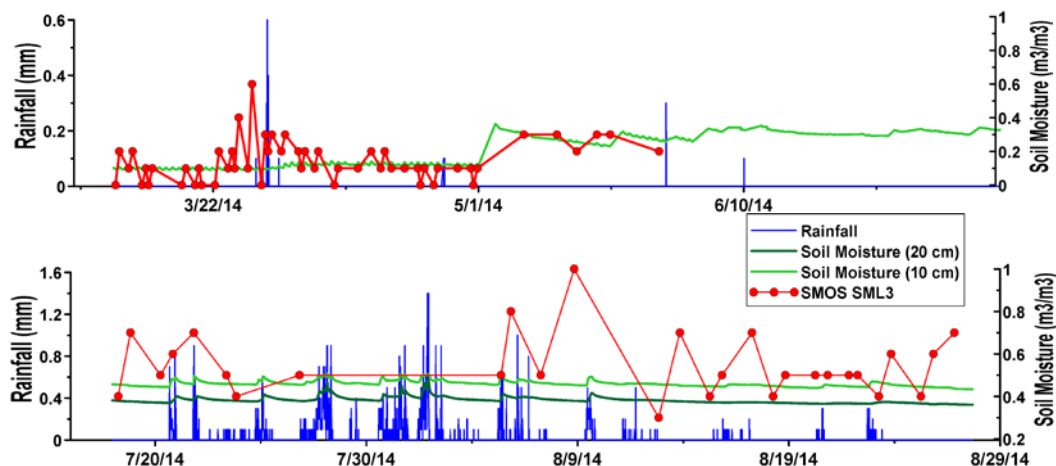


Fig 2. Rainfall, in-situ soil moisture at 10 and 20 cm and soil moisture from SMOS CLF31 product for Chimbarongo (top) and Oromo (bottom) sites.

It seems that soil moisture retrieved by SMOS is following the rainfall events evidenced in both LAB-net sites. The maximum soil moisture value retrieved by SMOS is evidenced in the south part of Chile

Regarding the maximum SM value in the Oromo site, it could be attributed to ponding zones widely present in the southern part of Chile where the agricultural soil present a low irrigation. Some details of the Oromo soil characterization which reflects the ponding effect is described in Casanova et al (2013).

In the case of Chimbarongo, the soil moisture values measured at 10 cm are similar to the soil moisture values provided by SMOS L3 after January (Dry and irrigation season). The major part this agricultural central zone of Chile is covered by annual crops.

These crops were planted and harvested between September and March. After this period, the wet edge can be evidenced in the in-situ soil moisture values.

4 CONCLUSIONS

LAB-net is the first Chilean soil moisture network for remote sensing applications. The network Data is freely available and it can be downloaded from the following web site: <http://www.biosfera.uchile.cl/lab-net.html>. Flux and water balance instruments will be implemented in each LAB-site in order to improve the land surface parameters provided by this network.

5 ACKNOWLEDGMENTS

This Work is partially supported by Fondecyt-Initial 11130359 and the project FONDEF-IDeA CA13I10102.

6 REFERENCES

- Al-Yaari, A., and Co-authors 2014. Global-scale evaluation of two satellite-based passive microwave soil moisture datasets (SMOS and AMSR-E) with respect to Land Data Assimilation System estimates. *Remote Sensing of Environment*, 149, 181 – 195.
- Casanova, M. et al. 2013. The soils of Chile. Ed Springer link. ISBN: 978-94-007-5948-0, 185 pp.
- Cheruy, F., and Co-authors 2013. Combined influence of atmospheric physics and soil hydrology on the simulated meteorology at the SIRTa atmospheric observatory. *Climate Dynamics*, 40, 2251–2269.
- Dorigo, W. and Co-authors 2011. The International Soil Moisture Network: A data hosting facility for global in situ soil moisture measurements. *Hydrology and Earth System Sciences Discussions*, 8.
- Kerr, Y. and Co-authors. 2012. The SMOS soil moisture retrieval algorithm. *IEEE Trans. Geosci. Remote Sensing*, 50(5), 1384 – 1403.
- Njoku, E. G. 2004. AMSR-E/Aqua L2B Surface Soil Moisture, Ancillary Params, & QC EASE-Grids. Version 2. Boulder, Colorado USA: NASA DAAC at the National Snow and Ice Data Center.
- Vivoni, E. R. and Co-authors 2008. Comparison of ground-based and remotely-sensed surface soil moisture estimates over complex terrain during SMEX04. *Remote Sensing of Environment*, 112, 314–325.
- Wagner, W. and Co-authors. 2013. The ASCAT Soil Moisture Product: A Review of its Specifications, Validation Results, and Emerging Applications. *Meteorologische Zeitschrift*, 22(1), 5 – 33.
- Walker, J. P., Willgoose, G. R., & Kalma, J.D. 2004. In situ measurement of soil moisture: A comparison of techniques. *Journal of Hydrology*, 293, 85–99.

Synergistic usage of ERS, ASAR and PALSAR data for PSI based mining induced subsidence monitoring

Nesrin Salepci, Christian Thiel, Arvid Kuehl & Christiane Schmullius

Friedrich-Schiller-University Jena, Dept. of Earth Observation, Loebdergraben 32, 07743 Jena, Germany

nesrin.salepci@uni-jena.de, christian.thiel@uni-jena.de, arvid.kuehl@uni-jena.de, c.schmullius@uni-jena.de

ABSTRACT- *The present work investigates the ground surface dynamics over a field of deep mining in Sondershausen, Germany based on multi-temporal Synthetic Aperture Radar (SAR) images. The C- and L-band acquisitions of the sensors ERS-1/2 (1995–2005), Envisat-ASAR (2004–2010) and ALOS-PALSAR (2007–2010) are used to derive 15 years of subsidence information by means of Persistent Scatterer Interferometry (PSI) technique. The deformation maps derived by PSI analysis of each SAR dataset indicate a subsidence trough located in the urban area of Sondershausen. The combination of information from deformation maps of different sensors indicates a non-linearly decreasing trend of subsidence values. The validation of the PSI results in reference to the available leveling measurement suggests a good correlation between these sets of estimations. However, the absence of persistent scatterers at a critical area in the ERS deformation map degrades the detected spatial pattern of the subsidence. The problem of undersampling in critical areas, which is a common limitation of the PSI approach, is addressed by the synergistic usage of PSI estimations from different satellite sensors. The integration of points from ASAR or PALSAR deformation maps result in an improvement in the modeled geometry of the subsidence trough in the period of ERS acquisitions. With this improvement the correlation coefficient calculated for the ERS model is increased from 0.92 to 0.97. The application demonstrates the synergistic potential of multi-sensor PSI analysis to improve the interpretation of ground subsidence characteristics and, thus, to increase the confidence of risk assessment.*

1 INTRODUCTION

Ground subsidence, originating from human activity or occurring naturally, is a geological hazard which has the potential to pose risk to life and surface structures, as well as damage the environment. Consequently, the assessment of the risk is an important objective in land-use planning and providing appropriate engineering design for the surface structures (Bell, 2002). In order to assess the risk and reduce the impact of subsidence, the behavior of the phenomenon needs to be understood (Bell, 2002). Spaceborne radar remote sensing is capable of providing precise measurements of deformation over a large area with moderate to low cost. Furthermore, this technique provides the option for retrieving deformation information by the SAR images acquired in the past.

With the development of the interferometric SAR technique, the displacement occurring in the line-of-sight of the radar can be estimated by interfering two or more SAR images acquired from different viewing angles and at different dates. However, changes in imaging geometry and surface scattering properties from one image to another limit the applicability of this method. Furthermore, even if the measurement is possible, the deformation signal is affected by variations in the atmosphere and errors in satellite orbit information. These limitations challenge in particular the detection of slow deformation processes by standard SAR interferometry (Hooper et al. 2012). To overcome

these shortcomings, techniques for processing multiple acquisitions are developed by the end of 1990s. One approach of time series analysis involves identifying “persistent scatterers” pixels, whose scattering properties remain stable throughout the monitoring period. Temporal stability of scattering properties enables the computation of reliable deformation estimations in millimeter scale, since the atmospheric contributions as well as the orbit and DEM errors can be estimated and removed (Ferretti et al., 2001).

Numerous studies in the literature utilize PSI for mapping ground surface displacements. Rich SAR data archives providing deformation information since 1991 contribute to the increasing applications of PSI in deformation monitoring. In addition to the SAR data from already existing sensors, the forthcoming SAR missions, ensuring data continuity, contribute to an increase in PSI applications for the detection of displacements. With the developing technology, noise and other error sources will be addressed by the new generation missions (Hooper et al., 2012). Furthermore, by the combination of data from different sensors with various spatial resolutions and sensitivities to the displacement, a more accurate and detailed determination of the displacement characteristics can be achieved (Froger et al., 2007). Accordingly, several studies utilize multi-sensor SAR data to explore the different sensibilities of sensors in order to improve the spatio-temporal description of the deformation by

synergy of different sensors (e.g. Froger et al., 2007, Lan et al., 2007, Walter et al., 2009).

Based on these insights in this study, multi-sensor SAR data is utilized for long-term monitoring of the mining induced subsidence in Sondershausen. Since the impact of subsidence on the surface structures depends on the component of the displacement on the ground surface, the initial identification of the areas with highest risk requires determination of subsidence profile. Therefore, this study additionally comprises geometric modeling of the subsidence by the displacement rates measured at persistent scatterers. Promoted by the upcoming SAR data acquisitions from various missions, the need for development of new methodologies to explore the synergy between multi-sensor data grows. Motivated by this growth, the present work proposes a novel methodology for the synergistic usage of the PSI observations from multiple sensors to tackle the common problems of spatial gaps at critical areas in the single sensor PSI results. The proposed approach allows the combination of subsidence information derived from PSI analysis of different SAR datasets with different temporal coverage and/or spatial resolution in order to refine the initial geometric model. As a consequence of such improvements, the confidence of hazard assessment also increases (Lan et al., 2013).

2 STUDY SITE & DATASET

2.1 Study site

Ground subsidence affecting the town of Sondershausen, Germany in the form of a subsidence trough is induced by the intensive mining activities for a century until the termination of salt production in 1991. During the period of mining, the rate of subsidence has increased gradually reaching to a critical deformation rate of around 25 cm/year accompanied by seismic events (Fliss et al., 2011). In order to stabilize the subsidence, the corresponding part of the mine is backfilled after 1991, as a consequence, the subsidence rates are gradually decreasing.

2.2 SAR data

Considering the long history of mining induced subsidence in Sondershausen, multiple sets of SAR data from different sensors are utilized. The available SAR scenes cover the period of backfilling between 1995 and 2010. The displacement rates for the first ten years (1995-2005) are derived by 74 ERS-1/2 scenes. The following years (2004-2010) are monitored by an Envisat-ASAR stack including 21 images. In addition, for the span of 3 years from 2007 to 2010, 15 ALOS-PALSAR scenes are used.

3 METHODOLOGIES

3.1 PSI analysis and geometric models

Deformation patterns are extracted by means of persistent scatterer interferometry, a technique that exploits the spatio-temporal characteristics of interferometric signatures from persistent scatterers (Werner et al., 2003). The Interferometric Point Target Analysis (IPTA) package of GAMMA Remote Sensing software is employed for the PSI processing. The linear component of displacement and the topographic phase associated with DEM errors show a linear dependence to the phase change of the pixel through the time series and can be estimated by utilizing a linear model (Werner et al., 2003). Therefore, in IPTA analysis, a linear subsidence model is used. However, the linear model assumption used in PSI analysis can have a negative influence for areas characterized by non-linear deformation. Especially in the main deformational areas showing significantly non-linear motion, the final PSI maps may lack PSs, due to the fact that the observed PS phases do not fit to the linear phase model (Crosetto et al., 2010). In such cases, the linear model assumption can be a critical limitation, because PSI may be unable to provide estimations over the most interesting area with large deformation rate (Crosetto et al., 2010).

Since the impact of movements due to subsidence on surface structures varies spatially, initial identification of the high-risk areas requires the knowledge of subsidence profile (Bell, 2002). Therefore, the point estimations at persistent scatterer locations are extended by kriging interpolation to a surface of estimations to model the geometry of the subsidence trough. By this way, geometric models of the subsidence trough for the periods of ERS, ASAR and PALSAR stacks are generated.

3.2 Model refinement: synergy of multi-sensor PSI estimations

The persistent scatterer interferometry is an effective tool for deformation monitoring; however, PSI deformation maps may often be restricted by the spatial gaps in the high-risk areas (Lan et al., 2013).

In this study, the insufficient sampling of critical areas in the single sensor PSI result (e.g. ERS deformation map in Figure 2) is addressed by the methodology developed for the synergistic usage of PSI based estimations from different sensors (ASAR and PALSAR). With the objective of filling the spatial gap in the main deformational area, the methodology estimates missing information by transferring the PSI point observations found in a deformation map of a different sensor.

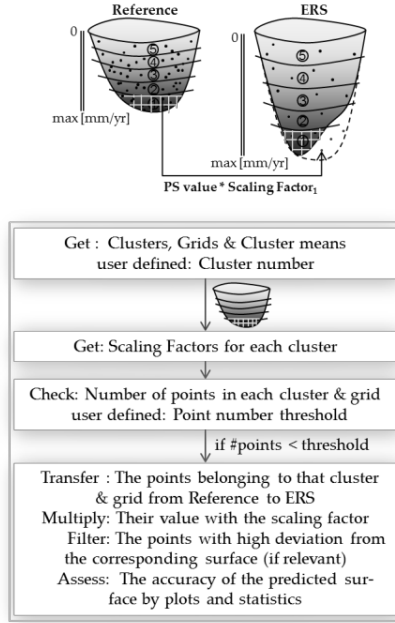


Figure 1: Principle and flow chart of model refinement algorithm. The parallel lines on the surfaces represent the cluster boundaries; in this sketch 5 clusters are defined. The points stand for the PS points from which the surfaces are generated. The thin light gray lines at the bottom represent the grids for the first cluster. The dash line is the expected shape of ERS surface and also represents the area defined as gap, in other words, the surface aimed to be predicted after the integration.

Since the deformation maps of different sensors represent different temporal regime of subsidence in this application, the point values should be scaled before the integration. In case of Sondershausen, the PSI deformation maps indicate a constant pattern of the subsidence trough with varying depths due to changes in the subsidence rates in time. Therefore, the strategy to integrate PSI results is based on the assumption that the spatial pattern of the subsidence trough is not changing for the entire period of PSI monitoring. Under this assumption, the scale factors are derived by the

local ratio of the geometric models to account for the variations in surface tangent slopes. As summarized and depicted in Figure 1, first of all the reference (ASAR or PALSAR) and the ERS models are divided into equal number of clusters for the computation of the local scale factors. With the calculation of cluster means for each cluster, the scale factors assigned to every cluster are computed by,

$$S_k = \frac{\bar{C}_{k-ERS}}{\bar{C}_{k-Ref}} \quad k = (1, \dots, n) \quad (1)$$

where S_k is the scale factor of the cluster k , n indicates the total number of clusters, \bar{C}_{k-ERS} represents the cluster mean of the ERS surface and \bar{C}_{k-Ref} is the cluster mean of the reference surface. After obtaining the scale factors, the value of i^{th} point in the reference surface (Pt_{i-Ref}) is scaled with the factor of corresponding cluster (k) to derive the point value for ERS (Pt_{i-ERS}) with,

$$Pt_{i-ERS} = Pt_{i-Ref} \times S_k \quad (2)$$

Aiming at keeping the originality of the ERS surface as much as possible by filling only the gap, gridwise search of points is used to control the inclusion of unnecessary points. Following this objective, the number of ERS points is calculated for each grid and cluster. If the number is smaller than the user defined threshold, the points found in the reference stack are transferred to the ERS point list with the values being multiplied by the scale factor belonging to that cluster.

One important point to consider at this stage is that the multiplication of a value means also the multiplication of the uncertainty. In this application, the accuracy of PALSAR estimates is particularly low, mainly due to the small number of SAR scenes in the stack and low sensibility of the measurements due to long wavelength. If every point from PALSAR is included in the transfer list for the new map of ERS, the filled area looks noisy. In order to cope with that, a filtering is applied where the upper and lower thresholds for filtering are set to the numbers calculated by multiplication of scale factor with the cluster minimum and maximum of the reference model. In this case the points which have larger distance to the interpolated surface are filtered out.

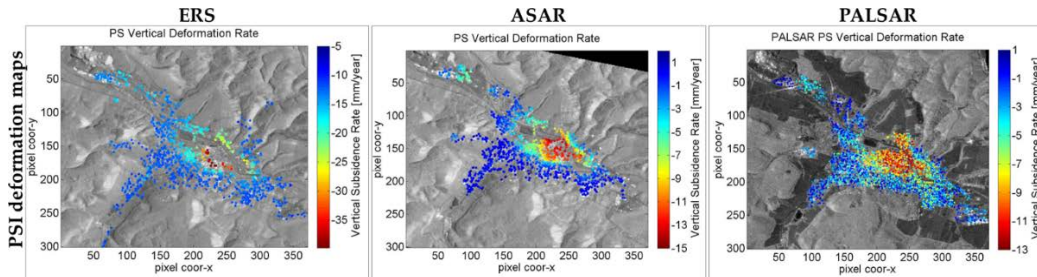


Figure 2: PSI deformation maps of ERS (1995-2005), ASAR (2004-2010) and PALSAR (2007-2010) stacks.

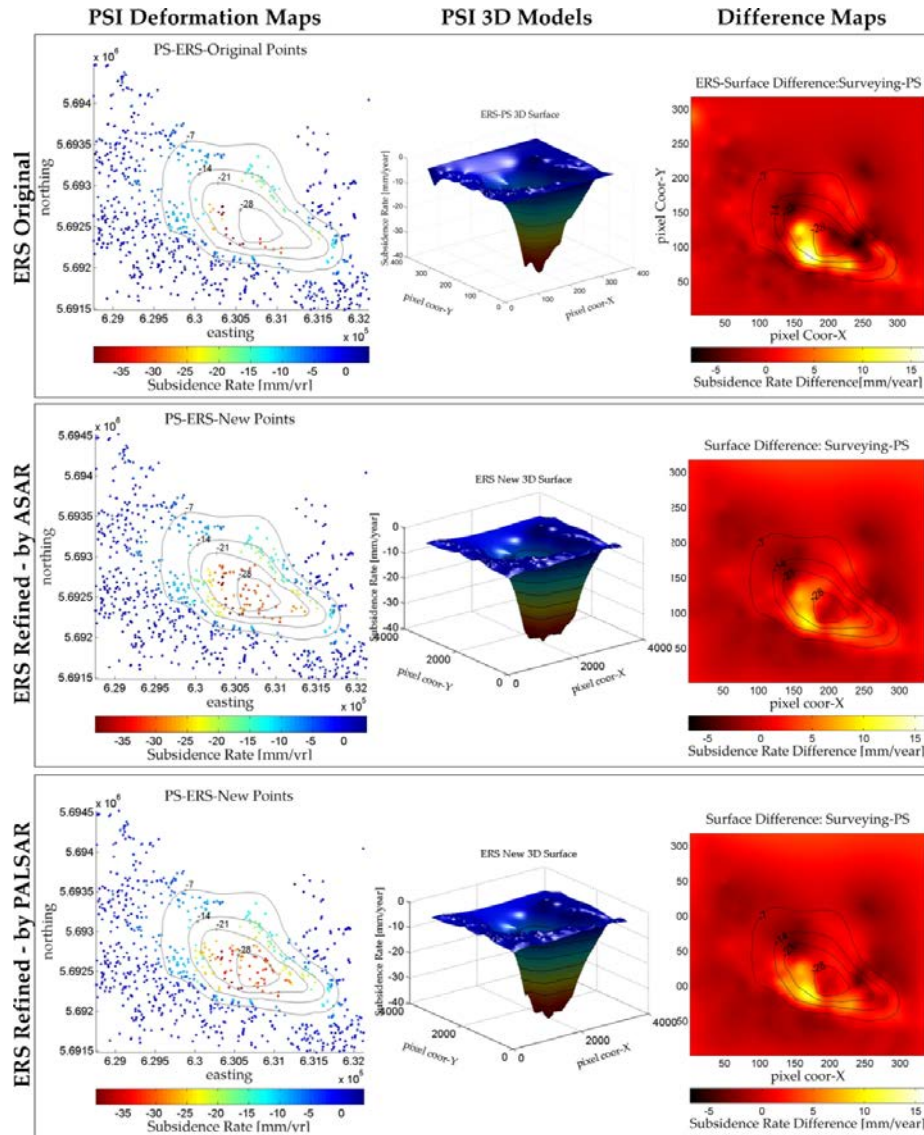


Figure 3: Results of integration. In the first column of figures the PSI deformation maps (with the contours stemming from the surfaces derived from the surveying measurements) are presented. The figures in the second column are the geometric models derived from the corresponding PSI maps. The third column represents the difference maps generated by the subtraction of the PSI based surface from the surveying based surface.

The results are validated with the surfacewise difference maps produced by subtraction of the surfaces derived by PSI and surveying estimations. The degree of correlation is tested with the correlation coefficient.

4 RESULTS

The usage of multi-sensor data providing opportunities for synergistic analysis has an impact in both, temporal and spatial dimensions. In temporal framework,

deriving subsidence rates for multiple time spans enables the extension of the monitoring period as well as the derivation of a more detailed model of temporal evolution. In case of the Sondershausen subsidence, 15 years of continuous monitoring with millimeter accuracy is achieved by PSI analysis of ERS, ASAR and PALSAR data. The estimated rates for the first 10 years by ERS indicate around 38 mm/year of maximum subsidence.

In the following years this value drops to approximately 14 mm/year in ASAR, and 13 mm/year in PALSAR estimations (see the PSI deformation maps in Figure 2). These values have two implications, (i) the rate of subsidence is decreasing over time, which confirms the effectiveness of backfilling of the mine, (ii) the trend of subsidence is non-linear. Although the PSI analysis is restricted to the estimation of linear deformation rates, the combination of information from different sensors reveals the non-linear nature of the subsidence. In spatial framework, the distribution of displacement estimations in all sets of PSI results corresponds to an ellipsoidal shape extending from northwest to southeast over the urban areas of Sondershausen with a major axis around 3 km (see Figure 2).

The validation of PSI measurements with the available levelling data indicate good agreement between these estimations (correlation coefficients are above 0.91 for the geometric models derived from the deformation maps shown in Figure 2). However, the accuracy is also degraded by various factors. For instance, due to the small number of images in the PALSAR stack, the individual PSI estimations in the deformation map are unreliable. Furthermore, the ERS result suffers from a lack of PS measurements at the critical location mainly due to the linear subsidence model used in the PSI analysis since the non-linear component of the subsidence is significant in this period. Inherently, the models generated for those results are also affected. Owing to its high precision and favorable distribution of the PS measurements, the largest correlation between surveying and PSI models is obtained by the ASAR model (0.977). Although, the general outline of the subsidence trough is estimated efficiently with the PALSAR model, a much lower coefficient is calculated (0.912) due to the fluctuations between the individual estimations. On the other hand, a slightly higher correlation is obtained with the ERS surface (0.928), however, more critical deviations in the high gradient area are found. Therefore, model refinement by multi-sensor synergy is applied to the ERS result.

With the integration process, 83 ASAR and 92 PALSAR points are added separately to the original ERS point list, yielding two new maps for the period of 1995 to 2005. Although several PALSAR points are filtered out, a sufficient number of points with good distribution are transferred to the new map. The scale factors are calculated around 2.8 for ASAR and 3.1 for PALSAR. Considering the fact that subsidence rates decrease by time due to backfilling, a slightly higher scale factor for PALSAR can be expected. The number of clusters has an impact on the scale factors as well as the filtering, since the factors and the thresholds for filtering are derived from cluster mean, minimum and

maximum. In this example 10 clusters are used for the integration.

Referring to the objective of integration, the region inside the -21 contour line is successfully filled (see the integrated ERS maps in Figure 3); furthermore, both solutions (from ASAR and PALSAR) are in good agreement considering the spatial pattern and the estimated rates by the integration. The refined models of ERS generated by interpolation of the new point lists are also presented in Figure 3.

The validation of the refined model suggests an improvement in the correlation of two datasets. The deviation of 5 mm/year in the underestimated area is diminished (the black region in the difference maps presented in Figure 3). The maximum deviation in the overestimated area is also decreased from 15 mm/year to 10 mm/year, implying a correction for the overestimation of the interpolation algorithm due to the absence of PS estimations in the vicinity. With these improvements, the correlation coefficient calculated for the ERS surface is increased from 0.928 to 0.975 with ASAR and 0.962 with PALSAR points (Table 1). Therefore, ASAR integration can be used as the final version. However, 10 mm/year of difference is still observed (see the difference maps in Figure 3). The high deviation persisting after the refinement is caused by the overestimation of the original persistent scatterers found in this region. Due to the presence of the original ERS points, this area is not addressed by the synergy.

Table 1: Surfacewise validation results of the original and refined PSI models. The differences are calculated by the subtraction of the model by PSI measurements from the one derived by the surveying estimations.

Surfacewise validation	ERS original	ERS-ASAR integration	ERS-PALSAR integration
correlation coeff.	0.928	0.975	0.962
max. diff. (mm/yr)	-5/+15	-1/+10	-2/10

5 CONCLUSIONS AND DISCUSSIONS

Integration of information from different data sources can provide improvements in the understanding of surface dynamics both, in temporal and spatial dimension. In the temporal dimension, the synergistic approach combines the multi-source information to derive the temporal evolution of the deformation. A non-linearly decreasing trend was determined in Sondershausen by combining the information from three different measurements in time. Although, the subsidence curve of a point was modeled to a certain extent by a piecewise linear function with three lines

(the linear estimations from 3 sensors), the essential temporal characteristics of the deformation was successfully derived. In the spatial dimension, the synergistic approach improves the initially modeled geometry from single sensor estimations. The improvement gained by the refinement in the area of spatial gaps (the underestimated area by the ERS model) provides a precision of maximum 1 mm/year deviation from the values modeled by the surveying dataset. Furthermore, the deviation in the overestimated area is reduced to a certain extent by the synergistic approach; although, this area is not inside the gap, i.e. there are original PSI points. With the objective of filling only the gap and preserving the already existing information, this area is not directly addressed by the refinement algorithm. Therefore, the improvement in this area is restricted to the refinement in another region. However, a further refinement can be easily employed for this area by using a point number threshold larger than 1 in the integration algorithm. Thereby, new points can be transferred to the grid cells where the original PSI points overestimate the surface to reduce the impact of overestimation of PSI points.

Based on these insights, the study indicates that PSI is a powerful technique to study the surface dynamics in Sondershausen, although the analysis is restricted by certain factors. Furthermore, the application demonstrates the potential of synergy to overcome the common problem of gaps in the PSI results, thereby, to improve the PSI based description of the spatio-temporal behavior of the deformation. Since the effect of subsidence on the surface structures varies spatially along the subsidence profile, the improvements gained by synergy in the estimated subsidence profile will also increase the confidence of risk assessment. Especially the new generation satellites with better resolutions and more frequent acquisitions, furthermore, the new advances in the PSI methodologies and SAR technologies promise developments in the field of deformation monitoring and modeling. Relying on the growing SAR archives and upcoming missions, synergy offers further advancements in the ground subsidence studies.

6 ACKNOWLEDGMENTS

This research was carried out in the framework of multidisciplinary project INFLUINS. The authors also thank to ESA for providing the SAR data, as well as GSES mbH and GVV mbH for their collaboration and for providing the essential surveying data.

7 REFERENCES

- Bell, F. G., 2002, Geological hazards: their assessments, avoidance and mitigation (Taylor & Francis e-Library).
- Crosetto, M., Monserrat, O., Iglesias, R., and Crippa, B., 2010, Persistent Scatterer Interferometry: Potential, Limits and Initial C- and X-band Comparison. *Photogrammetric Engineering and Remote Sensing* 76, no. 9, pp. 1061–1069.
- Ferretti, A., Prati, C., Rocca, F., 2001, Permanent Scatterers in SAR Interferometry. *IEEE Transactions on Geoscience and Remote Sensing*, 39, no. 1, pp. 8–20.
- Fliss, T., Marx, H., Thoma, H., Staubert, A., Lindenau, A., and Lack, D., 2011, Proceedings of MINEFILL 2011. Backfilling and Pillar Re-Mining in Potash Industry. International Conference on Mining with Backfill, Cape Town South Africa, 21-25 March.
- Froger, J. L., Fukushima, Y., Tinard, P., Cayol, V., Souriot, T., Mora, O., Staudacher, T., Durand, P., Fruneau, B. and Villeneuve, N., 2007, Proceedings of FRINGE 2007 Workshop. Multi sensor InSAR monitoring of volcanic activity: the February & April 2007 eruptions at Piton de la Fournaise, Reunion Island, imaged with Envisat-ASAR and ALOS-PALSAR data. Frascati, Italy, 26 – 30 November.
- Ge, L., Chang, H. C., and Rizos, C., 2007, Mine Subsidence Monitoring Using Multisource Satellite SAR Images. *Photogrammetric Engineering and Remote Sensing*, 73, no. 3, pp. 259–266.
- Hooper, A., Bekaert, D., Spaans, K., and Arikian, M., 2012, Recent advances in SAR interferometry time series analysis for measuring crustal deformation. *Tectonophysics*, 514-517, pp. 1–13.
- Lan, H., Gao, X., Liu, H., Yang, Z., and Li, L., 2013, Integration of TerraSAR-X and PALSAR PSI for detecting ground deformation. *International Journal of Remote Sensing*, 34, no. 15, pp. 5393–5408.
- Walter, D., Wegmuller, U., Spreckels, V., Hannemann, W., and Busch, W., 2009, Proceedings of ISPRS Hannover Workshop 2009, WG I/2, I/4, IV/2, IV/3, VII/2, High-Resolution Earth Imaging for Geospatial Information. Interferometric monitoring of an active underground mining field with high-resolution SAR sensors. Hannover, Germany, 2 - 5 June.

Performance comparison of downscaling methods on improving microwave soil moisture data spatial resolution with optical/infrared data

Wei Zhao, Ainong Li*, Huaan Jin, Jinhu Bian, Zhengjian Zhang, Xi Nan

Institute of Mountain Hazards and Environment, Chinese Academy of Sciences, Chengdu 610041, China

Email: ainongli@imde.ac.cn

ABSTRACT - Soil moisture plays a vital role in various land surface processes, and it is a crucial parameter for a large number of applications. Microwave remote sensing is widely used because of the physically based relationship between the land surface emission observed and soil moisture. However, the application of the retrieved soil moisture data is restricted by its coarse spatial resolution. To overcome this weakness, method should be proposed to downscale the microwave soil moisture data to fine resolution. The traditional method is the microwave-optical/IR synergistic approach, in which land surface temperature (LST), vegetation index and surface albedo are key parameters. Based on the primary method, a number of methods are developed in these years. Several typical methods are selected in this study. To compare the performance of the developed methods on downscaling microwave soil moisture, the methods are applied to the Zoige Plateau in China with Advanced Microwave Scanning Radiometer on the Earth Observing System (AMSR-E) Land Parameter Retrieval Model (LPRM) soil moisture product and optical/thermal data of MODIS. The coarse resolution LPRM soil moisture is disaggregated into the resolution of MODIS product finally. The surface soil moisture measurements of the Maqu soil moisture observation network located in the plateau was used to validate the downscaling results. Comparative results are finally provided in the study to address the problems of the application of current methods in plateau area. The further direction for the improvement is also pointed out.

1. INTRODUCTION

Soil moisture plays an important role in land surface energy and material exchange process (Western et al., 2004), and it is a crucial parameter for a large number of applications such as weather prediction, flood forecasting, agricultural drought assessment, water resources management and so on. Although field measurement is able to obtain accurate soil moisture at different soil depth, the high spatial variation of soil moisture induces the big uncertainty in interpolating point-scale measurements to spatial distribution of soil moisture.

Recent years, numerous works have been done to retrieve regional or global distribution of surface soil moisture by using remote sensing methods, and microwave remote sensing is widely used because of the physically based relationship between the observed land surface emission and surface soil moisture content. Until now, many passive microwave sensors have been launched. Among these sensors, the Scanning Multichannel Microwave Radiometer (SMMR; 1978–1987), the Tropical Rainfall Measuring Mission (TRMM) Microwave Imager (TMI; since 1997), the Advanced Microwave Scanning Radiometer E for the Earth Observing System (AMSR-E; 2002–2011), and the L-band SMOS (Soil Moisture and

Ocean Salinity), have been in operation to provide regional scale mean surface soil moisture measurements on a global scale. However, all of these instruments are characterized by coarse spatial resolution (approximately 25 to 50 km), even for the forthcoming SMAP (Soil Moisture Active and Passive) mission which will provide soil moisture data at 10 km resolution. Although the coarse spatial resolution is adequate for many global applications, but it is certainly not suitable for regional studies with not resolution demanded from 1 to 10 km (Crow et al., 2000; Entekhabi et al., 1999). An important task ahead is how to get high spatial resolution soil moisture data.

Compared with microwave remote sensing, optical remote sensing offers a wide range of land surface remote sensing data with the spatial resolutions from several tens of meters to kilometers. Although optical remote sensing has potential to monitor soil moisture, the indirect relationship between optical signature and soil moisture makes the soil moisture retrieval impractical. Therefore, the integration of low-resolution microwave and high-resolution optical data seems to be a good way to get high resolution soil moisture.

Under the assumption of the soil moisture impact on the triangle distribution between land surface temperature (LST) and vegetation index, a popular direction for microwave soil moisture downscaling is

developed with different methods by combining optical remote sensed LST and vegetation index with microwave soil moisture data (Chauhan et al., 2003). In order to investigate the performance of these methods, comparison study was conducted in this study to analyze the downscaling results for different methods to find the most suitable method when it is applied to Tibetan Plateau area.

2. METHODOLOGY

The development of a synergistic approach using microwave-optical/IR products is usually based on the schematic relationship of the triangle space among soil moisture, vegetation index, and LST. It is purely empirical by using polynomial-fitting method and has been developed into different formats. From the first version of the downscaling method proposed by Chauhan et al. (2003), different types of the methods are developed by revising the model expression or adding some additional variables to the model. The methods are listed in table 1 and noted as M1 to M5. M2 and M3 are modified based on M1. In these two models, enhanced vegetation index (EVI) is introduced in M2 to replace NDVI in M1 and diurnal LST difference (DT) is included in M3 to replace LST in M1. A is surface albedo. T_b is the observed brightness temperature by microwave sensor. All the variables in the model expression are normalized by their maximum and minimum values.

Table 1. Triangle-Based empirical downscaling models

Ref.	No.	Model
Chauhan et al. 2003	M1	$SSM = \sum_{i=0}^2 \sum_{j=0}^2 \sum_{k=0}^2 a_{i,j,k} T^{*(i)} NDVI^{*(j)} A^{*(k)}$
	M2	$SSM = \sum_{i=0}^2 \sum_{j=0}^2 \sum_{k=0}^2 a_{i,j,k} T^{*(i)} EVI^{*(j)} A^{*(k)}$
	M3	$SSM = \sum_{i=0}^2 \sum_{j=0}^2 \sum_{k=0}^2 a_{i,j,k} DT^{*(i)} NDVI^{*(j)} A^{*(k)}$
Choi et al. 2012	M4	$SSM = a_1 + a_2 A^* + a_3 NDVI^* + a_4 T^* + a_5 A^* NDVI^* + a_6 T^* NDVI^* + a_7 A^* T^*$
Piles et al. 2011	M5	$SSM = \sum_{i=0}^2 \sum_{j=0}^2 \sum_{k=0}^2 a_{i,j,k} T^{*(i)} NDVI^{*(j)} T_b^{*(k)}$

According to the models listed in table 1, two steps are separated to finish the downscaling process. The first step is: aggregate the fine resolution optical remote sensing data into microwave remote sensing spatial resolution, normalize the variables in the five models according to their maximum and minimum values, and apply regression analysis between microwave soil moisture data and the aggregated data to get the coefficients in each model. In the second step, the downscaling models are applied to the optical remote sensing data to get fine resolution soil moisture data with the estimated coefficients.

3. STUDY AREA AND DATA

The Zoige plateau located at the northeast part of Tibetan Plateau is selected as the study area (Fig. 1). Its average elevation is above 3000m. Therefore, there will be a significant freezing and thawing process during the end and the start of each year. Due to the high elevation, the major land cover type is grassland accompanied with some wetland and bare soil. The different vegetation cover and soil moisture conditions in this area enables the triangle space of the scatter plot between vegetation index and LST for the whole region.

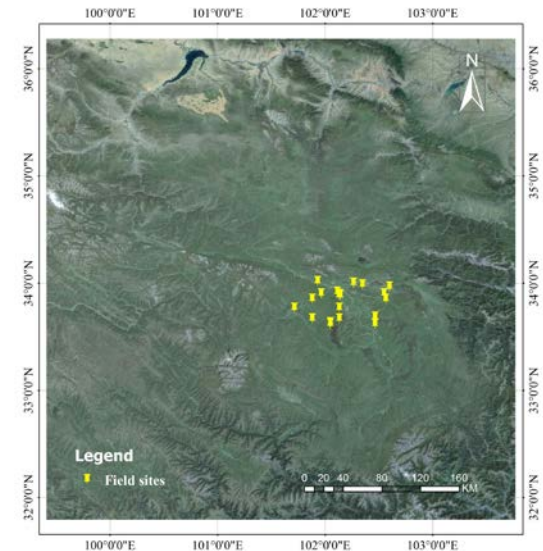


Fig. 1 Location of the study area and the Maqu soil moisture observation network

To evaluate different downscaling methods, MODIS Aqua land products (Vegetation index, LST and albedo) and LPRM AMSR-E ascending soil moisture product V002 from July, 2008 to August, 2009 were downloaded to downscale AMSR-E soil moisture data to MODIS 1km spatial resolution for the study area. The Maqu soil moisture observation network located in the plateau can provide hourly surface soil moisture measurements to evaluate the downscaling results. The network includes 20 separated sites.

4. RESULTS

4.1 AMSR-E soil moisture data evaluation

Before conducting the downscaling process with the above five methods, the LPRM AMSR-E soil moisture data was firstly compared with field measurements. The average values of observation network at Aqua satellite overpass are compared with the AMSR-E soil

moisture data over the same region. Fig. 2 presents the scatter plot of both datasets. Two periods are shown in the figure: one for the winter season and one for the non-winter season. It is clear that the freezing of soil water in the winter season induces big uncertainty in AMSR-E soil moisture estimation result. In the non-winter season, the correlation generally obeys the 1:1 line. The determination coefficients (R^2) is of 0.2 and the RMSE is of $0.06\text{m}^3/\text{m}^3$. It partly confirm the reliability of AMSR-E soil moisture product under accuracy the goal of less than $0.06\text{m}^3/\text{m}^3$ specified by the microwave observation project. Therefore, to remove the impact of snow and ice on microwave soil moisture estimation, the downscaling methods comparison work was conducted for the data in the non-winter months.

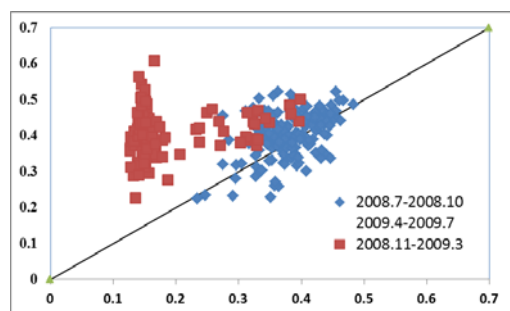


Fig. 2 scatter plot between AMSR-E soil moisture data and field measurements

4.2 Downscaling methods fitting results comparison

In the downscaling process, an important part to evaluate the downscaling accuracy is to access the fitting results of each downscaling method.

For each day in the non-winter months, the clear sky MODIS pixels are aggregated into the AMSR-E pixel scale by using a simple aggregation method that the average values of MODIS pixels in one AMSR-E pixel is set to the right value of the coarse resolution pixel. In the aggregation, a rule should be abided that the percent of clear MODIS pixels in one AMSR-E pixel should be no less than 90%, and the number of the available coarse resolution pixels for the fitting should be no less than 50.

With the aggregated parameters and AMSR-E soil moisture data, polynomial fitting was performed for each method for each day, and the regression statistics of each method are calculated to investigate their fitting performances. Table 1 presents the average values of R^2 and RMSE for each method in the non-winter months. The values indicate that all the methods have similar R^2 and RMSE with the value around 0.65 and $0.1\text{m}^3/\text{m}^3$ respectively. Only M3 has poorer fitting results when compared with other methods.

Table 2. Average R^2 and RMSE of fitting results for each method

Method	M1	M2	M3	M4	M5
R^2	0.676	0.683	0.593	0.651	0.656
RMSE	0.098	0.097	0.110	0.102	0.103

The fitting statistics indicate that all the methods cannot fully explain the relationship between soil moisture, land surface temperature, surface albedo, and vegetation index for the study area under specific climatic condition. Consequently, the uncertainty in the downscaling model fitting results (close to $0.1\text{m}^3/\text{m}^3$) will transfer to the final downscaling results. The fitting uncertainty should be considered during the downscaling process.

4.3 Downscaling results comparison at network scale

In addition to downscaling model fitting result assessment, the downscaled soil moisture at MODIS pixel scale of each method within the whole period are compared with field measurements at observation network.

A comparison over the whole network is undertaken firstly to evaluate the downscaling methods. Fig. 3 illustrates the scatter plot between the field measured soil moisture and the downscaled soil moisture over the region. One point represents one day. Due to the heavy cloud cover in Zoige plateau, it can be found from fig. 3 that number of pixels is smaller than the number of days in the non-winter months. Especially for M3, day and night LST are both used in the method. However, this condition is hardly satisfied in the operation. Therefore, the points in the figure are obviously fewer than those of other methods.

The statistics shown in fig. 3 indicate that M1, M2 and M3 have better correlation with field observation with the R^2 of 0.19, 0.17 and 0.19 respectively. The R^2 s are close to the comparison result of AMSR-E soil moisture data in fig. 2. M2 has poorer performance than the other two methods because of its bigger RMSE. For M4 and M5, the R^2 s keep to low value. In general, the comparison work shows that the downscaling methods cannot effectively improve the accuracy of the downscaled soil moisture when validated at network scale. The uncertainty in the downscaling process influences the downscaling results.

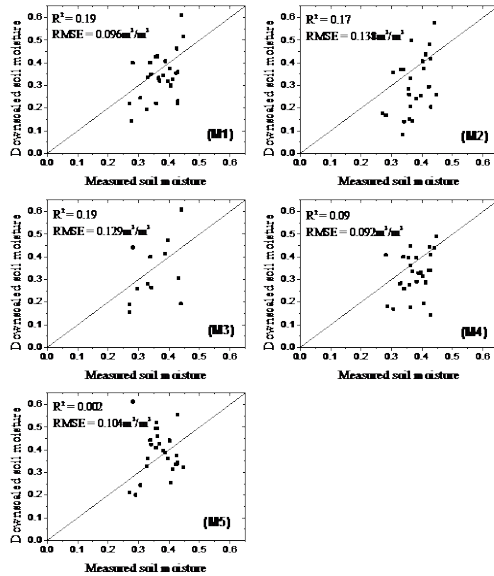


Fig. 3 Comparison between downscaled soil moisture from five method and field observations at network scale.

4.4 Downscaling results comparison at site scale

The network scale comparison has proved the relatively poorer performance of five methods to downscale soil moisture over a big region. However, it is still needed to evaluate their ability to give more reliable spatial variability. Therefore, site scale comparison was conducted by comparing the downscaled soil moisture with the field measurement at each site for the whole non-winter months.

Fig. 4 shows the scatter plot for the downscaled soil moisture of each method with field measurements for all the sites. Generally, the downscaled soil moisture is reasonably within the range of 0 to 1 m^3/m^3 . However, from the points' distribution, it is clear that downscaled soil moisture of all the methods is poorer correlated with site observation. All the methods have similar performance in this comparison. Except the error in soil moisture estimation from AMSR-E microwave data, the reason can be partly attribute to the comparison method. Because all the sites and all the available days are involved in the comparison, and both spatial and temporal change information are mixed in the figure, it is hard to distinguish the spatial and temporal correlation ability for downscaled soil moisture. The correlation for different sites may have different characteristic. The other reason can be referred to the spatial representativeness of one point soil moisture measurement in one MODIS pixel. The sparse field measurements cannot effectively validate the accuracy

of the downscaled soil moisture. The final reason should be related to the uncertainty in the downscaling method, as indicated in section 4.2 and 4.3, there are still enough space to improve the downscaling method.

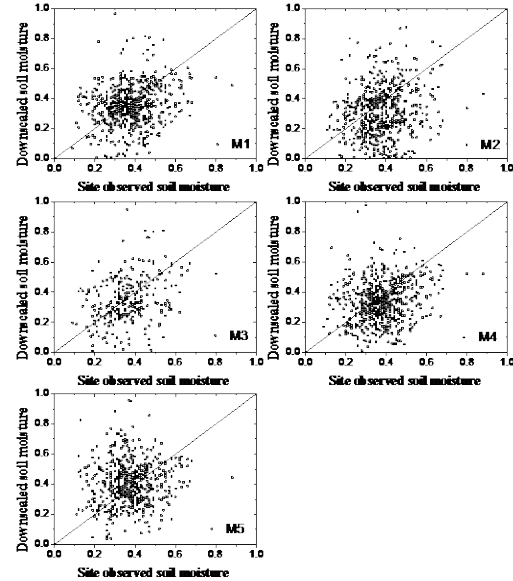


Fig. 4 Comparison between downscaled soil moisture from five method and field observations at site scale.

5. SUMMARY AND CONCLUSIONS

Five microwave soil moisture downscaling methods are tested in this study to evaluate their ability to downscale soil moisture in Zoige Plateau. Comparison work is separated into three directions to evaluate the performance of the five methods. The results suggest that the selected five empirical downscaling methods cannot derive reliable fine resolution soil moisture data in this area because of the uncertainty in downscaling model and spatial representativeness of point measurement. It is important to analyze the impacts from surface soil moisture on the parameters in the downscaling methods to improve the sensitivity of downscaling methods on soil moisture variation. Meanwhile, for a more sophistic validation on soil moisture with a relatively large scale, higher density field observations are necessary in future study.

ACKNOWLEDGMENT

The work described in this publication has been partly supported by the National Natural Science Foundation of China under Grant 41401425, the "Hundred Talents" Project, and International Cooperation Partner Program of Innovative Team (Grant No. KZZD-EW-TZ-06) of Chinese Academy of Sciences.

REFERENCES

- Chauhan, N.S., Miller, S. and Ardanuy, P., 2003, Spaceborne soil moisture estimation at high resolution: A microwave-optical/IR synergistic approach. *International Journal of Remote Sensing*, **24**, 4599–4622.
- Choi, M., and Hur, Y., 2012, A microwave-optical/infrared disaggregation for improving spatial representation of soil moisture using AMSR-E and MODIS products. *Remote Sensing of Environment*, **124**, 259–269.
- Crow W., Wood E., and Dubayah R., 2000, Potential for downscaling soil moisture maps derived from spaceborne imaging radar data, *Journal of Geophysical Research*, **105(D2)**, 2203–2212.
- Entekhabi D., Asrar G., Betts A., Beven K., Bras R., Duffy C., Dunne T., Koster R. S., Lettenmaier D., McLaughlin D., Shuttleworth W., van Genuchten M., Wei M., and Wood E., 1999, An agenda for land surface hydrology research and a call for the second international hydrological decade, *Bulletin of the American Meteorological Society*, **80(10)**, 2043–2058.
- Piles, M., Camps, A., Vall-Llossera, M., Corbella, I., Panciera, R., Ruediger, C., Kerr, Y.H., and Walker, J., 2011, Downscaling SMOS-derived soil moisture using MODIS visible/infrared data. *IEEE Transaction on Geoscience and Remote Sensing*, **49**, 3156–3166.
- Western, A.W., Zhou, S.L., Grayson, R.B., McMahon, T.A., Blöschl, G., Wilson, D.J., 2004, Spatial correlation of soil moisture in small catchments and its relationship to dominant spatial hydrological processes. *Journal of Hydrology*, **286**, 113–134.

Operational soil moisture mapping using multitemporal ASAR/Wide Swath ENVISAT data

M. Zribi¹, F. Kotti², A. Gorraab^{1,2}, N. Baghdadi³, Z. Lili Chabaane², R. Amri²

1 CESBIO (CNRS/UPS/IRD/CNES), 18 av. Edouard Belin, bpi 2801, 31401 Toulouse cedex 9, France

2-INAT/Université de Carthage, 43, Avenue Charles Nicolle 1082 -Tunis- Mahrajène TUNISIE

3 IRSTEA, UMR TETIS, 500 rue François Breton, 34093 Montpellier cedex 5, France

E-mails: mehrez.ribi@cesbio.cnes.fr

ABSTRACT - *In this paper, an operational algorithm is proposed for the mapping of surface moisture over the northern and central parts of Tunisia, in North Africa. A change detection approach is applied, using 160 multi-incidence Envisat ASAR Wide Swath images acquired in the horizontal polarization over a 7-year period. Parameterization of this algorithm is considered for three classes of vegetation cover density ($NDVI < 0.25$, $0.25 < NDVI < 0.5$ and $NDVI > 0.5$), retrieved from SPOT-VGT decadal images. A relative soil moisture index, ranging between 0 (for the driest surfaces) and 1 (for saturated soils), is proposed for each date, with a resolution of 1 km. The retrieved soil moistures are validated by means of ground measurements based on continuous thetaprobe measurements, as well as low resolution (25 km) ERS and ASCAT soil moisture products from the Vienna University of Technology (TU Wien).*

1 INTRODUCTION

Soil moisture is a key state parameter of the land surface, influencing the manner in which rainwater is shared between the phenomena of evapotranspiration, infiltration and runoff (Beven et al., 1996; Koster et al., 2004). In the case of semi-arid regions, this parameter is particularly important for irrigation management (Bastiaanssen et al., 2000). If water resources, which are often very limited, are to be optimized and protected, an accurate estimation of the soil's water content is needed in order to determine the expected evapotranspiration flux. Considerable efforts have thus been devoted to improving the evaluation of soil moisture and evapotranspiration, and to understanding its relationship with the vegetation cover and the soil's water content (Allen et al., 2005).

Radar remote sensing has demonstrated its strong potential for monitoring of soil moisture over the last twenty years (Wagner et al., 1998, Zribi et al., 2010). Using Synthetic Aperture Radars (SARs), it is possible to estimate the soil moisture at a high spatial resolution. Among the proposed approaches, the "linear approach", which relates the surface soil moisture to calibrated and validated SAR (Synthetic Aperture Radar) measurements expressed in decibels (dB) (SIRC, ERS, RADARSAT, Envisat ASAR, TerraSAR-X...), is widely used.

In recent years, different operational algorithms have been proposed, based on a change detection approach. This is particularly relevant for low-resolution spaceborne scatterometers (active

microwave) and passive microwave instruments. In this context, (Wagner et al., 2008) proposed a modified approach for the operational estimation of soil moisture at medium spatial resolutions, using the Global and Wide Swath modes of the Advanced Synthetic Aperture Radar (ASAR). (Van Doninck et al., 2012) proposed an adapted algorithmic approach, providing a more accurate analysis of seasonal vegetation effects over Calabria in Italy. The study sites are often in Europe, and often corresponding to humid regions. The major difficulty encountered when applying a change detection algorithm on humid sites is that of under-estimating the radar signal's sensitivity to soil moisture, determined from the difference between the signals acquired for the driest and wettest signals. In practice, it is difficult to retrieve extremely dry surfaces present in humid regions, when using a limited SAR database for the development of a retrieval algorithm.

In the case of semi-arid regions, seasonal analysis of the influence of vegetation could lead to errors in the estimation of soil moisture. In fact, as a consequence of frequent periods of drought, the dynamics of the vegetation cycle can be highly variable, from one year to another, and even from one period to another within the same agricultural season (Amri et al., 2012). The aim of the present study is thus to apply an operational change detection approach, based on developed methodologies, which takes the particularities of the climate and vegetation cover of semi-arid regions into account. The algorithms proposed in the present study are expected

to be highly beneficial for the upcoming SENTINEL-1 mission, for which an operational algorithm will be needed for the mapping of soil moisture. This mission is based on the Sentinel constellation of two C-band radar satellites, of which the first is launched in 2014. Given the large data volume generated by Sentinel-1, the techniques developed for the ASAR detection of soil moisture changes are likely to be applicable to, and improved for, this new instrument.

In Section 2, the studied site and database are presented. In Section 3, the algorithm proposed for the estimation of the soil moisture index is presented and validated. Finally, our conclusions are presented in Section 4.

2 DATABASE

2.1 Study site

The study area (Amri et al., 2012) corresponds to the central and northern parts of Tunisia, situated in North Africa, covering an area approximately 200 km in width and 300 km in length (see Figure 1). The south of the selected site borders to the Sahara desert, which is of limited interest since it is characterized by extremely low variations in soil moisture. The climate in this region is semi-arid, with an average annual rainfall ranging between approximately 200 mm per year in the south and 1000 mm per year in the north.



Figure 1: Map of the studied site

2.2 Satellite data

a) Envisat ASAR data

The ENVISAT satellite was launched by ESA (European Space Agency) on March 1st, 2002, and was functional until April 8th, 2012. One of its nine Earth-

observation instruments, ASAR, was a multi-mode sensor working in the C-band (5.3 GHz), at several polarizations (HH, VV, HV and VH) and at various incidence angles and spatial/radiometric resolutions, depending on its operational mode. At the C-band frequency atmospheric perturbations can be considered to have a negligible influence on the instrumental performance. The ASAR data used in the present study was provided by ASAR's ScanSAR Wide Swath (WS) observation mode at HH polarization, with a spatial resolution of 150 m and incidence angles ranging between 16 and 43 degrees. Between May 2004 and December 2011, 160 images were acquired at various incidence angles over the central and northern regions of Tunisia.

b) SPOT/VGT data

The ten-day synthesis (S10) is a full resolution product (1 km resolution), providing 10-day NDVI (Normalized Difference Vegetation Index) data. The NDVI can be related to the green vegetation cover or to the vegetation abundance, and is expressed by: $NDVI = (R_{NIR} - R_{RED}) / (R_{NIR} + R_{RED})$, where R_{NIR} is the near-infrared (NIR) reflectance and R_{RED} is the red reflectance.

c) ERS and ASCAT/METOP moisture products

The ERS and ASCAT/METOP scatterometer radars (active microwave) operate in the C - band (5.3 GHz), in the vertical polarization. The ERS mission was based on two European Remote Sensing Satellites ERS - 1 (1991–1996) and ERS - 2 (1995 up to 2011). The ASCAT radar is one of the 12 instruments carried by the European Space Agency's METOP-A satellite (launched in 2006). Soil moisture data is retrieved from the backscattering coefficient, through the use of a change detection method developed by the microwave remote sensing team of the Vienna University of Technology (TU Wien), and described by Wagner et al. (1998).

2.3 ASAR data processing

Radar data processing was carried out in three steps: Firstly, all images were geo-referenced using a single radar reference image, resulting in an RMS control point error of approximately 0.5 pixel. Secondly, all of the images were re-sampled (averaged) to a 1 km resolution. This was needed, to allow the radar data to be compared with SPOT-VGT data, which has a 1 km resolution. A positive side effect of this spatial aggregation is the improved radiometric accuracy of the resulting images. A mask was developed, to allow cities and high terrain to be eliminated. The cities were retrieved from a classification of LANDSAT images covering the studied area.

3 METHODOLOGY

3.1 Incidence angle normalization

In order to implement a change detection approach, the data must be normalized with respect to the incidence angle under which it is recorded. For the extrapolation of backscatter measurements to a reference angle of 30° a linear model as previously employed by (Wagner et al., 2008, Van Doninck et al., 2012) is used:

$$\sigma_0(30^\circ) = \sigma_0(\theta) - \beta(\theta - 30^\circ) \quad (1)$$

where θ is the local incidence angle, σ_0 is the backscattering coefficient in dB, and β is a slope parameter used to normalize the data to a 30° incidence angle. This parameter is very sensitive to the vegetation's characteristics (Wagner et al., 1998, Van Doninck et al., 2012) and to the local topography. For each pixel (x,y) three possible normalizations were thus considered, depending on the vegetation density encountered in this pixel. The S10 SPOT-VGT NDVI database was used to classify the vegetation into one of the following classes:

- Class I, with NDVI<0.25, corresponding to bare soils and/or very sparse vegetation;
- Class II, with 0.25<NDVI<0.5, corresponding to the vegetation encountered during the growing season in annual agricultural areas, and pastures during the wet season;
- Class III, with NDVI>0.5, corresponding to dense vegetation (forests, agricultural areas at their maximum annual growth ...).

3.2 Development of a surface moisture index

A change detection approach, similar to that described in other scientific studies (Wagner et al., 2008, Van Doninck et al., 2012), is proposed here: a relative surface soil moisture index, ranging between 0 and 1 (0 for the driest conditions, 1 for the wettest conditions) is defined for each pixel (x,y) by:

$$I_m(x, y) = \frac{\sigma^0(x, y) - \sigma_i^{dry}(x, y)}{S_i(x, y)} \quad (2)$$

where $S_i(x, y) = \sigma_i^{wet}(x, y) - \sigma_i^{dry}(x, y)$

In the above expression, $\sigma_i^{dry}(x, y)$ is the dry reference backscattered signal in dB, at pixel (x,y), for the i^{th} vegetation class (where $i = I, II$ or III). This parameter is defined as the average value of the 5% lowest backscatter coefficients in the Class I time series, and corresponds to the driest conditions for this pixel.

$\sigma_i^{wet}(x, y)$ is the wet reference backscattered signal in dB, at pixel (x,y), for the i^{th} vegetation class (where $i = I, II$, or III). This parameter is defined as the average value of the 5% highest backscatter coefficients in the Class I time series, and corresponds to the wettest

conditions for this pixel. By using these average values for the dry and wet radar signals, any noise, which could have a strong influence on the accuracy of moisture estimations, is reduced.

For each pixel (x,y), $S_i(x, y)$ is the sensitivity of the backscatter coefficient to soil moisture variations, for each vegetation class (I, II or III). The sensitivity is defined as the difference between $\sigma_i^{dry}(x, y)$ and $\sigma_i^{wet}(x, y)$

As for the slope maps, the sensitivities were not computed for all pixels on the studied site. S1 was computed mainly in the south, which is characterized by sparse vegetation. S3 was estimated mainly in the north, which is characterized by the presence of forests and dense annual agriculture. As could be expected, the highest values of sensitivity are observed for bare soils and low dispersion vegetation, and the lowest values of sensitivity are observed for high vegetation densities, with values ranging between 2.8dB and 14dB

3.3 Validation of retrieved soil moistures

a) Validation through ground measurements

As described in section 2, ground soil moisture measurements are made only in the Kairouan plain in central Tunisia, such that this is the only part of the studied site for which ground measurement validations could be considered.

Figure 2 compares the ground measurements acquired using **two** thetaprobes during the period from 2009 to 2011 with the proposed inversions over two local areas in central Tunisia. Each point on this chart corresponds to a single date, on which ASAR data and ground measurements are compared. The data plotted in Figure 2 is reasonably well correlated ($R^2=0.49$), and has an RMS error equal to 0.13 (approximately 3.5% as volumetric moisture). Simultaneous satellite acquisitions and ground measurements were recorded on only a small number (27) of dates. The highest value of soil moisture, for which a strong discrepancy was observed between the value retrieved from ASAR (0.91) and that measured on the ground (0.62), was preceded by a small rainfall event some hours before the radar acquisition. This rainfall event would have been sufficient to strongly increase the soil moisture down to a depth of a few millimeters, or perhaps down to one to even two centimeters, but not to the greatest depth of the thetaprobe measurements, which are made between approximately 3 and 7 cm. This discrepancy could thus be explained by the fact that the C band has a limited penetration depth under wet conditions. This type of scenario arises frequently in semi-arid conditions, as a result of the frequent occurrence of brief rainfall events, combined with a high rate of evaporation, which limits the depth to which the rainwater can infiltrate.

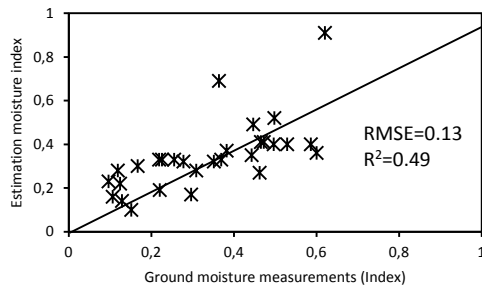


Figure 2: Inter-comparison between the estimated soil moisture indexes proposed for ASAR WS data and ground moisture measurements

b) Inter-comparison with ERS/ASCAT products

An inter-comparison between the retrieved indices and the scatterometer products (ASCAT and ERS/WSC) was carried out in the present study, for two scatterometer pixels situated in the Kairouan plain. For the ASAR products, a mean value was calculated for each scatterometer pixel. The comparisons were made for dates common to two different types of measurement, thereby limiting the number of illustrated points. Figure 3 shows that the data is in excellent agreement for the two pixels, with a correlation coefficient respectively equal to 0.8 and 0.81, an RMS error equal to 0.13 and 0.087 (approximately 3.5% and 2.3% in terms of volumetric moisture).

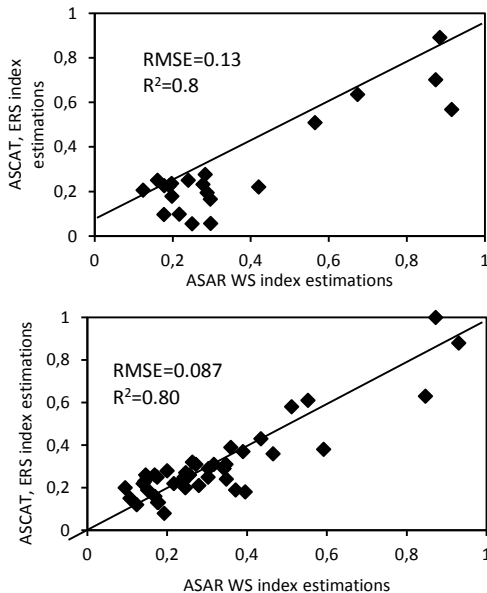


Figure 3: Inter-comparison between the ASAR WS index and the ASCAT/METOP (Vienna University) and ERS indexes, determined over the Kairouan plane, a) a pixel in the north of Kairouan plane, (b) a pixel in the south of Kairouan plane

Figure 4 illustrate two soil moisture maps showing high spatial and temporal variations. These variations are correlated to reprecipitations events.

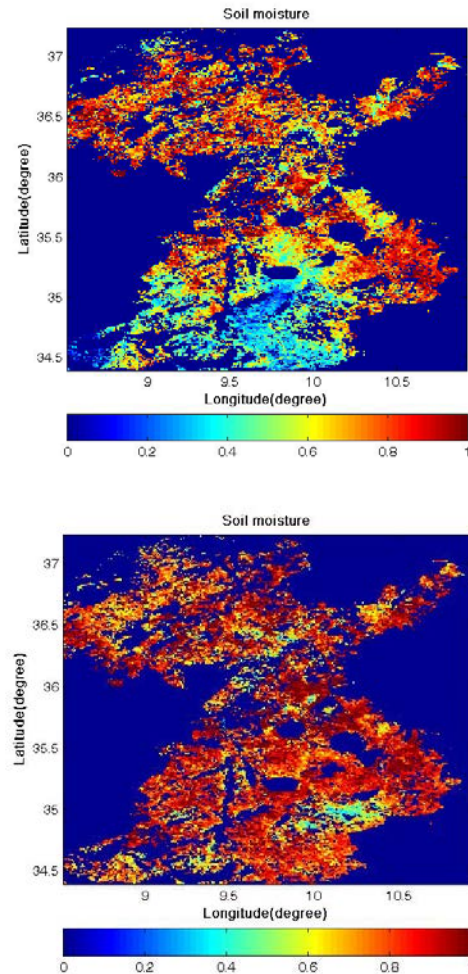


Figure 4: Soil moisture index maps determined for different two dates.

4 CONCLUSIONS

In this paper, a change detection approach, based on the interpretation of 160 Envisat ASAR WS radar images, is proposed for the operational retrieval of soil moisture over a semi-arid region in North Africa. The backscattered signal, normalized to a 30° incidence angle, was scaled between the lowest and highest values of the studied database. The influence of vegetation, which in these semi-arid regions is characterized by high temporal variations associated with seasonal influences and periods of drought, is

taken into account by ranking the radar pixels according to three vegetation classes, through the use of empirical thresholds defined by: $NDVI < 0.25$, $0.25 < NDVI < 0.5$ and $NDVI > 0.5$. The proposed moisture index was validated firstly through the use of ground measurements and ASCAT products recorded in central Tunisia. These analyses clearly demonstrate the potential of SENTINE-1 data, when combined with optical data (Sentinel-2 or other products), for the development of operational soil moisture products at a medium resolution and a high temporal frequency.

5 ACKNOWLEDGEMENTS

This study was funded by METASIM/SICMED, ASCAS/CNES and AMETHYST (ANR-12-TMED-0006-01) ANR projects. Envisat ASAR data were kindly provided by the European Space Agency (ESA) through ENVISAT-AO 356. We wish to thank VITO for kindly providing us with its SPOT-VEGETATION NDVI products, and the ISIS program for providing us with SPOT images.

6 REFERENCES

- Allen, R. G., Pereira, L. S. Smith, M. Raes D., and Wright J., 2005. FAO-56 dual crop coefficient method for estimating evaporation from soil and application extensions, *Journal of Irrigation and Drainage Engineering*, vol. 131, 1(2).
- Amri, R., Zribi, M., Lili-Chabaane, Z., Wagner, W., Hauesner, S., 2012. Analysis of ASCAT-C band scatterometer estimations derived over a semi-arid region, *IEEE Trans. Geosci. Remote Sens*, vol. 50, 7, Part I, 2630-2638.
- Bastiaanssen, W. G. M., D. J. Molden, and I. W. Makin, 2000. Remote sensing for irrigated agriculture: examples from research and possible applications. *Agr. Water Manage*, 46, pp. 137-155.
- Beven, K. G., and Fisher J., 1996. Remote Sensing and Scaling in Hydrology, in: *Scaling in Hydrology Using Remote Sensing*, edited by: Stewart, J. B., Engman, E. T., Feddes, A., and Kerr, Y., Wiley, New York, 93-111.
- Hornacek, M., Wagner, W., Sabel, D., Truong, H.L., Snoeij, P., Hahmann, T., Diedrich, E., & Doubkova, M. (2012). Potential for High Resolution Systematic Global Surface Soil Moisture Retrieval via Change Detection Using Sentinel-1. *IEEE Journal of Selected Topics in Applied Earth Observations and Remote Sensing*.
- Koster, R. D., P. A. Dirmeyer, Z. Guo, G. Bonan, E. Chan, P. Cox, C. T. Gordon, S. Kanae, E. Kowalczyk, D. Lawrence, P. Liu, C. H. Lu, S. Malyshev, B. McAvaney, K. Mitchell, D. Mocko, T. Oki, K. Oleson, A. Pitman, Y. C. Sud, C. M. Taylor, D. Verseghy, R. Vasic, Y. Xue, and T. Yamada (2004), Regions of Strong Coupling Between Soil Moisture and Precipitation, *Science*, vol. 305, pp. 1138-1140, doi:10.1126/science.1100217.
- SPOT Vegetation User's Guide, 2008: <http://www.spot-vegetation.com/vegetationprogramme/Pages/TheVegetationSystem/userguide/userguide.html>.
- Van Doninck, J., Peters, J. Lievens, H. De Baets, B., and Verhoest N. E. C., 2012. Accounting for seasonality in a soil moisture change detection algorithm for ASAR Wide Swath time series, *Hydrol. Earth Syst. Sci.*, vol. 16, pp. 773-786.
- Wagner, W. (1998), Soil Moisture Retrieval from ERS Scatterometer Data", PhD dissertation, Vienna University of Technology, Austria.
- Wagner, W., G. Lemoine, and H. Rott (1999), A method for Estimating Soil Moisture from ERS Scatterometer and Soil Data, *Remote Sens. Environ.*, vol. 70, pp. 191-207.
- Wagner, W., Pathe, C., Doubkova, M., Sabel, D., Bartsch, A., Hasenauer, S., Blöschl, G., Scipal K., Martínez-Fernández J., and Löw A., 2008. Temporal Stability of Soil Moisture and Radar Backscatter Observed by the Advanced Synthetic Aperture Radar (ASAR)," *Sensors*, vol. 8, pp. 1174-1197.
- Zribi, M., Paris Anguela, T., Duchemin, B., Lili, Z., Wagner, W., Hauesner, S., Chehbouni, A., 2010. Analysis of relationship between soil moisture and vegetation in the Kairouan plain region of Tunisia using low spatial resolution satellite data, *Water Research Ressources*, VOL. 46, W06508, doi:10.1029/2009WR008196.

Cloud screening and pixel characterization: moving to Sentinel requirements

C. Brockmann, M. Paperin, A. Ruescas, O. Danne, G. Kirches, K. Stelzer,
Brockmann Consult GmbH
 carsten.brockmann@brockmann-consult.de

ABSTRACT -Higher level processing of Sentinel data requires characterisation of each individual pixel into land, water or clouds. Further characterisation information is required in order to apply specific correction methods or algorithms. Such characterisation includes: presence of cirrus clouds, cloud shadow, spatially mixed cloud-land or water-land, coastline, submerged vegetation in water pixels, just to name some important cases. A method called Pixel Identification or IdePix was developed for ENVISAT sensor images, and it is now being adapted to the requirements of the Sentinel 2 and 3 sensors.

1 INTRODUCTION

The term pixel Identification or “Idepix” refers to a classification of a measurement with the purpose of identifying properties of the pixel that are influencing further algorithmic processing steps, specifically cloud and clear sky screening. The IdePix method can be adapted to several sensors, even if it was primarily design for MERIS & AATSR. It calculates a certain set of features (physical or other type) and a probabilistic combination of these features in order to calculate a set of pixel classification attributes. Only the implementation of how the features are calculated is instrument specific. The IdePix classifier for MERIS is actually available in BEAM 5 from the CoastColour module.

2 METHODOLOGIES

While the information about a pixel located over water or land can be taken from a static map as a good first guess -provided the geo-location is better than the size of the pixel-, the cloud coverage is spatially and temporally highly variable and needs to be derived from the measurement itself. After knowing whether a pixel is cloudy or clear, in the clear sky case the land-water information can be refined. This is particularly necessary in the coastal zone where the actual land-water boundary is constantly changing due to tides, whether the pixel size is small enough to resolve this difference.

The feature based probabilistic arithmetic approach enables decoupling the sensor specific measurements from the physically based features and the logical combination. After the feature values have been derived from a sensor measurement, all subsequent calculations do not depend on the sensor anymore. Thus the pixel identification developed here is mainly sensor independent and can be considered as unique for any optical sensor.

The uniqueness consists of a certain set of features, which are calculated for each instrument and probabilistic combination of these features in order to calculate a set of pixel classification attributes. The implementation how the features are calculated is instrument specific (Figure 1).

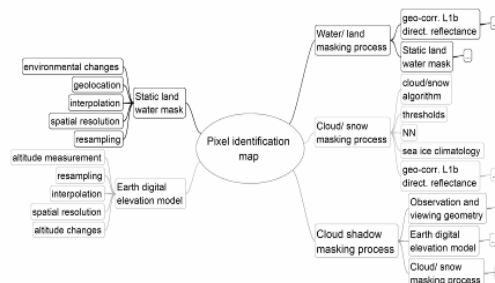


Figure 1. Pixel Identification sources on the right part of the graph; common source of error on the left part

Features are combined by simple arithmetic averaging. For example two features, f1 and f2, which do have no dependency from each other, and both being an indication that a third feature, f3, is true. Then, f3 is the average of f1 and f2:

$$f3 = (f1 + f2) / 2 \quad (1)$$

The introduction of the probability scale [0 ... 1] has further the advantage that it enables decoupling of feature values from the instruments.

Not every feature can be calculated for every instrument. In such cases the feature value is constant equal to 0.5. This convention allows formulating the logical combination of features even if a feature is not available for a certain instrument, and hence the logical combination can be formulated instrument independently.

2.1 Pixel Identification features

The following features are currently used for cloud detection:

- Brightness - integral reflectance in visible bands
- Whiteness - average slope in visible bands
- Height - derived e.g. from absorption by atmospheric gases (e.g. O₂ or water vapour), or from thermal measurements
- Temperature - derived from measurements in the thermal domain
- Spatial pattern - derived from spatial context
- Temporal consistency - derived from time series (currently implemented as separate step)
- Cloud probability - a special feature derived from training a neural network with the manually classified pixels of the PiBox dataset
- Improvements are expected from time series based cloud filtering and by exploiting the synergy and new bands in Sentinel 3 OLCI and SLSTR.

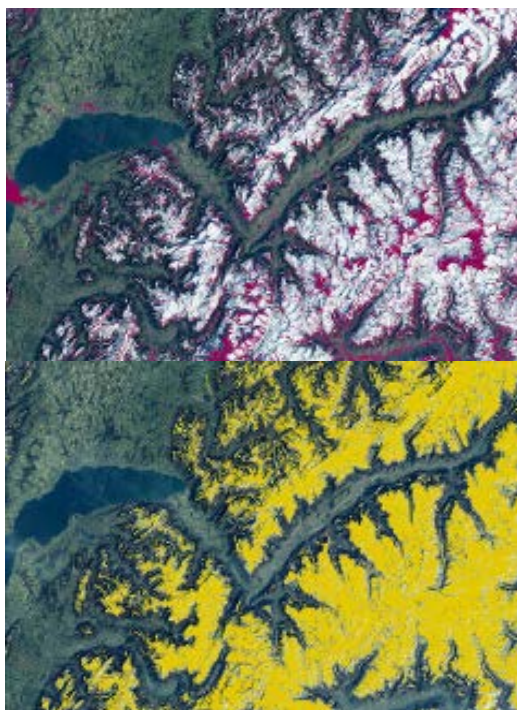


Figure 2. Landsat 8 -20 March 2014 lake Geneva-distinction snow-cirrus clouds still a challenge

2.2 Pixel Identification results

Some examples on the resulting flags are shown in this section. For instance the mixed pixel flag identifies a pixel with mixed spectrum, which is the sum of the pure spectra of each component within the IFOV, weighted by the spatial proportion of each material.

When scattered photons interact with multiple components, the mixture has the potential of becoming nonlinear. This happens more often over land with low resolution sensors. These mixed pixels are classified as land, water or cloud -within one unique category- when they can really contain a portion of each. There is a need of a better screening of pixels in sub-pixel level and identification and flagging as mixed pixel. For doing this, it is assumed a linear relationship within the different components of the spectrum's pixel, and an analysis based on their mixture is done by means of a spectral mixture analysis (SMA). One example of the application of this flag can be found in Figure 3. The mixed pixel flag identifies floating cyanobacteria bloom as well as sub-pixel size islands. Related marine reflectance spectra are shown in inset.

Improvements on cirrus and contrail detection on Landsat 8 (base sensor for S2 MSI) is also possible using in IdePix a similar approach to the one followed by Zu and Woodcock (2012) in the Fmask method.

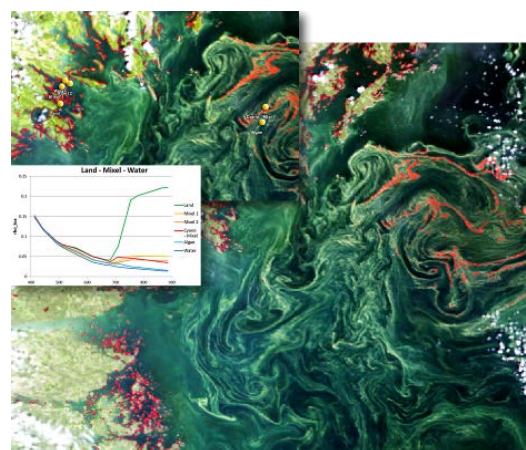


Figure 3. Baltic Sea MERIS scene with a cyanobacteria bloom and the mixed pixel identification flag in red

Figure 4 shows a case of the use of the Fmask on one Landsat 8 image on Lake Geneva. The big difference in the detection of almost transparent clouds and airplane contrails is easily visible when comparing the default mask with the new approaches (Figure 4).

Further improvements could include also the cloud shadow detection (Figure 5). The proposed algorithm contains three main parts:

- Step 1: Cloud top height (CTH) and cloud base (CBH) estimation;
- Step 2: potential cloud shadow area identification;
- Step 3: cloud shadow identification

An advantage of the proposed algorithm is its independence from cloud height retrievals. It should work with fixed cloud top height and base height.

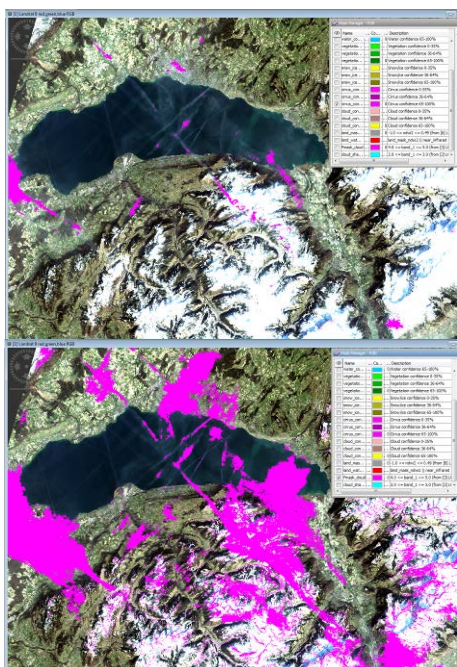


Figure 4. Original L8 mask versus Idepix approach

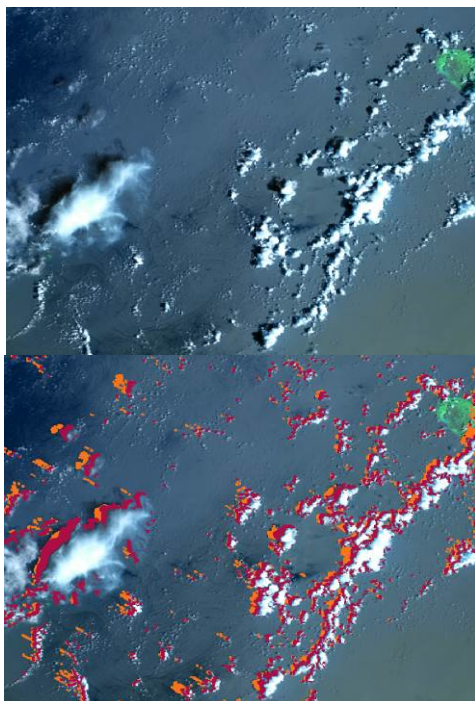


Figure 5. RGB and Cloud shadow mask (red IdePix cloud shadow versus new algorithm)- MERIS-FSG 24. September 2011 16:31:44

3 VALIDATION

The validation of the pixel identification information is not easy because it is not a physical quantity but context related qualitative information. It is also not self-consistent information but has to be considered in connection with further processing: clouds can be semitransparent, or the pixel is a mixture of land and water. Processing, e.g. with an atmospheric correction, depends on the ability of this further processing to correct for such ambiguities.

A large database of manually classified pixels, called PixBox, has been compiled for MERIS Reduced Resolution (110 000 pixels) and Full Resolution (40 000 pixels), SPOT VGT (40 000 pixels) as well as AVHRR (16 000 pixels). MODIS (60 000) has been recently added in the framework of the METIMAGE project (Figure 6). IdePix has been already used in LandCover CCI, Ocean Colour CCI, CoastColour and GlobAlbedo processing.

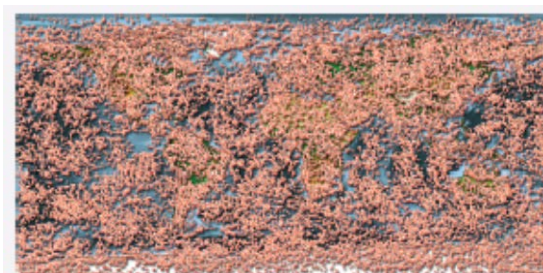


Figure 6. Spatial distribution of PixBox sampling for MODIS (60 000 points). The sampling was done on images from 2007, using 4 days per season, in the spectral channels of the visible and thermal (including a temperature image calculated with a split window algorithm)

This PixBox dataset can be updated in the future with Sentinel 2 and 3 data, if future projects that involve these sensors permit it. The pixel information assigned comprises clear sky, totally cloudy and mixed cases, further classified as by attributes such as land surface type, climate zone, water body type and atmospheric turbidity.

The database is used for validation, by means of confusion matrices as the one shown in Figure 7 and 8. It has also been used to develop the neural network cloud probability. Improvements are expected from time series based cloud filtering and by exploiting the synergy and new bands in Sentinel 3 OLCI and SLSTR.

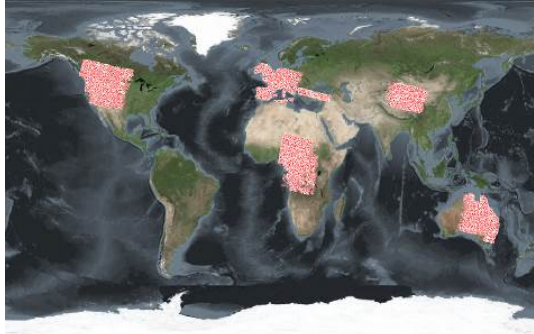


Figure 7. Spatial distribution of the validation sampling points (MERIS FSG 2005-2009)

		Database				Users Accuracy
		CLOUD	LAND	WATER	SNOW/ICE	
IdePix	CLOUD	9762 / N _{tot}	271 / N _{tot}	18 / N _{tot}	611 / N _{tot}	0.92
	LAND	3008 / N _{tot}	3624 / N _{tot}	8 / N _{tot}	8 / N _{tot}	0.55
	WATER	22 / N _{tot}	46 / N _{tot}	57 / N _{tot}	0 / N _{tot}	0.46
	SNOW/ICE	47 / N _{tot}	1 / N _{tot}	24 / N _{tot}	182 / N _{tot}	0.72
Producers Accuracy		0.76	0.92	0.53	0.23	Overall Accuracy 0.77 N _{tot} =17689

Figure 8. Validation results: confusion matrix with statistics

3.1 Application to Sentinel 2 and Sentinel 3

Application of IdePix to Sentinel 2 and Sentinel 3 offers new features to be added due to additional bands or the synergistic exploitation of OLCI and SLSTR, in the case of Sentinel 3. In particular the

latter will be a great advantage compared to the current performance. Weighting coefficients need to be defined according to the quality of the derived feature.

Figure 9 shows some cases of feature definition using the two new instruments, together with the bands that are used for the derivation of those features. One of the synergistic cases will be the use of the temperature bands from SLSTR where there is coincidence with the OLCI pass; taking advantage as well of the higher OLCI resolution.

Feature	Instrument - S2	Bands (nm)
Brightness, whiteness	MSI	B2(490), B3(560), B4(665)
Height	MSI	B9(940), B10(1375)
Temperature	Not applicable	
Spatial consistency	MSI	B2(490), B3(560), B4(665)
Snow/ice	MSI	B11(1610), B12(2190)
	Instrument - S3	Bands
Brightness, whiteness	OLCI	All visible bands (new: 400)
Height	OLCI	O2 absorption bands
Temperature	SLSTR	S8 and S9
Spatial consistency	OLCI, SLSTR	Visible (OLCI) and thermal (SLSTR)
Snow/ice	SLSTR	S3(865) and S5(1610)

Figure 9. Indicative features that can be derived from Sentinel 2 and Sentinel 3 sensors and the bands use in each case

4 REFERENCES

BEAM:

<http://www.brockmann-consult.de/cms/web/beam/CoastColour/>

<http://www.coastcolour.org/>

Zhu, Zhe and Woodcock, Curtis E., 2012, Object based cloud and cloud shadow detection in Landsat imagery, Remote Sensing of the Environment 118, 83-94

Integration of earth observation technologies in field-crop advisory services provided by sigAGROasesor platform.

F.L.M. Padilla¹, M.P. González-Dugo¹, F. De la Cruz², A. Armesto³, N. Abdat¹, J. Sillero¹, H. Lopez-Corcoles², A. Castilla¹, F. Perea¹, G. Besga⁴, J. Serra⁵, M. Jabargo⁵, A. Mestre⁶, M.R. Botey⁶, A. Lafarga³

¹ IFAPA. Consejería de Agricultura, Pesca y Desarrollo Rural. Apdo. 3092 Córdoba, Spain
Ph: +34671532700, Fax: +34957016043,

e-mail: franciscol.munoz @juntadeandalucia.es

² ITAP, Instituto Técnico Agronómico Provincial S.A. Avd. Gregorio Arcos, 19. 02005 Albacete, Spain.

³ INTIA, Instituto Navarro de Tecnologías e Infraestructuras Agroalimentarias. Avd. Serapio Huici, 22. 31610 Villava (Navarra) Spain.

⁴ NEIKER tecnalia, Berreaga 1, 48160. Derio (Bizkaia) Spain.

⁵ Fundació MAS BADIA, Mas Badia, s/n. 17134 La Tallada d' Empordà (Girona), Spain.

⁶ AEMET, Agencia Estatal de Meteorología, Spain.

ABSTRACT - The sigAGROasesor project aims to develop an on-line platform that will support farmer's decisions with a customized GIS advisory tool. This platform is designed to provide economic and environmental sustainability indicators for field crops management and the traceability of agricultural products and activities. The current version of SigAGROasesor platform offers Decision Support Tools (DST) for the sustainable management of extensive crops, including tools for fertilization and irrigation scheduling, crop cultivar selection, control of diseases and sustainability indicators. This work presents the first results of the integration of remotely sensed data into these DST. Despite the long history of agricultural applications of remote sensing, little operational services are directly offering this technology to farmers. This work represents a joint effort to integrate remote sensing data in daily farmer's decisions for crop management.

1 INTRODUCTION

In the framework of the environmental EU LIFE program, sigAGROasesor project (2012-2015) aims to develop an on-line platform that will support farmer's decisions with a customized GIS advisory tool. This platform is designed to provide economic and environmental sustainability indicators for field crops management and the traceability of agricultural products and activities. In line with current smart agriculture policies, sigAGROasesor offers a state-of-the-art technology platform with Decision Support Tools (DST) for the sustainable management of extensive crops, including tools for fertilization and irrigation scheduling, crop cultivar selection, control of diseases and sustainability indicators. A second version of the platform is currently under development, and farmers will validate it during the next growing season (2014-2015) over different regions of Spain.

The objective of this work is to evaluate the integration of remotely sensed data into these DST and it analyzes the perspectives for a fully operative service. For this task, three main applications have been explored using remotely sensed data: irrigation

scheduling, nitrogen fertilization and potential yield prediction.

2 STUDY AREA AND REMOTE SENSORS

In the framework of this project, several crops (wheat, corn, barley, oats) and fields have been monitored in 5 Spanish regions during the 2013 and 2014 crop growing seasons using different remote sensors. Figure 1 shows the study area.

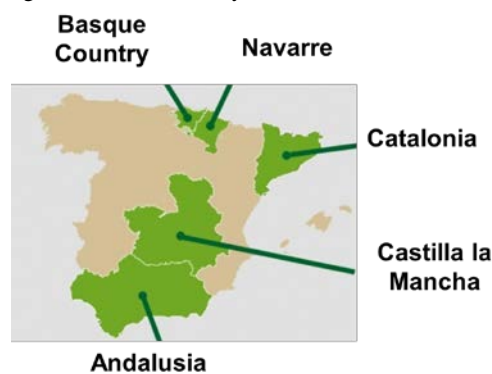


Figure 1: Study areas

Remote sensors used in the sigAGROasesor project are:

- DEIMOS-1
- Landsat-8 (OLI)
- UAV (Multispectral sensor 250-850nm)
- Airborne FLIR SC655 thermal imaging camera and hyperspectral sensor Micro-Hyperspec VNIR
- ASD-FieldSpec spectroradiometer
- Rapidscan CS-45

3 HAD IRRIGATION (irrigation scheduling)

DST-irrigation uses weather forecasts provided by AEMET over the Iberian Peninsula to recommend irrigation at field scale using FAO-56 crop water requirements computation guidelines. Previous studies (Gonzalez-Dugo et al., 2009 and 2013, Mateos et al., 2013) supported the use of multispectral vegetation indices to assist the estimation of plant transpiration through the computation of basal crop coefficients, both sensitive to plant ground cover fraction. The evaluation of this approach in different Spanish regions within sigAGROasesor pilot areas is presented here.

3.1 Materials and Methods

Several experimental sites grown with corn (*Zea mays*) were monitored during the 2013 growing season in the framework of the project. For each field, crop water requirements were estimated, using FAO-56 approach. The basal crop coefficient of these fields was computed from satellite-derived vegetation indices (SAVI). Figure 2 briefly describes the methodology employed.

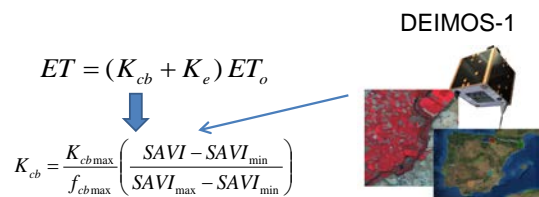


Figure 2: Methodology used to compute basal crop coefficient using DEIMOS imagery.

The methodology has been evaluated by comparing their results with that obtained by the methods traditionally used in irrigation engineering, which either take crop coefficient values directly from published tables or modify these values to adapt it to local conditions.

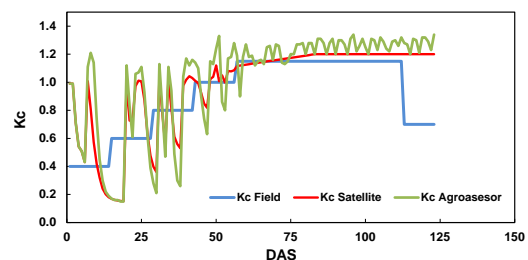
- 1.- Kc-satellite = satellite-estimated basal crop coefficient + Ke
- 2.- Kc-agroasesor = basal crop coefficient tabulated in FAO + Ke

3.- Kc-field = single crop coefficient adjusted for local conditions, without an independent calculation of soil evaporation (Ke)

The evaporation coefficient (Ke) for the first two simulations was computed following FAO-56 procedures.

3.2 Results

Figure 3 shows the evolution of the single crop coefficient in a corn field of 22 ha, located in Córdoba (Spain), during 2013, using the three different approaches (only the basal crop coefficient differs between them).



DAS = Days after sowing

Figure 3: Evolution of the single crop coefficient of a corn field in 2013.

Evolution of the single crop coefficient following the Kc-satellite approach was similar to the single crop coefficient adjusted for local conditions. Only one field is showed in this publication. However multiple simulations were made with good results in all cases.

4 HAD FERTILIZATION (nitrogen fertilization)

In sigAGROasesor platform, DST-fertilization recommends application rates (nitrogen, phosphorus and potassium) at field scale by keeping track of the main incoming and outgoing nutrient's fluxes throughout the growing season. In the framework of the project, several remote sensing methodologies and vegetation indices are being evaluated with the intention of integrating the results into this DST-fertilization.

The ability of the canopy chlorophyll concentration index (CCCI) to infer differences in nitrogen status (related to chlorophyll "a" concentration) is addressed in this study.

4.1 Materials and Methods

A wheat experiment (randomized block design) was conducted in Cordoba (Spain) during 2014 with four replicates and five treatments (five levels of nitrogen application (0, 90, 135, 180, 225 kgN/ha)).

Field canopy reflectance and SPAD measurements were performed over all the experimental plots using an ASD FieldSpec radiometer and a SPAD meter on March 6th, April 7th and May 13rd, 2014. Three thermal and hyperspectral images were also acquired over the experimental area on the same days. The CCCI nitrogen index (Barnes et al., 2000; Clarke et al., 2001) was calculated for each experimental plot and date.

The CCCI is a two-dimensional index, calculated as follows:

$$CCCI = \frac{NDFR - NDFR_{min}}{NDFR_{max} - NDFR_{min}} \quad (2)$$

The NDFR index is a combination of spectral reflectance measured at 790 and 720 nm, and is sensitive to plant chlorophyll content and nitrogen status (El-Shikha et al., 2007).

$$NDFR = \frac{\rho_{790} - \rho_{720}}{\rho_{790} + \rho_{720}} \quad (3)$$

The boundaries ($NDFR_{max}$ and $NDFR_{min}$) were empirically determined for maximum (N-sufficient = 225 kgN/ha treatment) and minimum (N-deficient = 0 kg/ha treatment) conditions, as a function of Normalized Difference Vegetation Index (NDVI). A linear relationship between NDFR and NDVI was then assumed for both high and low nitrogen conditions.

4.2 Results

Figure 4 shows one hyperspectral image acquired over the experimental area on April 7th.

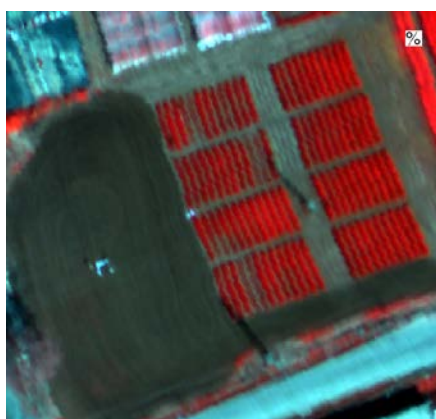


Figure 4: False colour composite image of the experimental plots (April 7th).

Limits used to define high (Max) and low (Min) chlorophyll “a” content (linear relationship between NDFR and NDVI for the wheat experiment) is presented in figure 5.

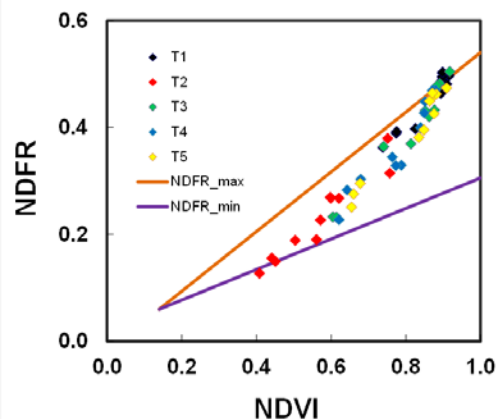


Figure 5: Relationship between NDVI and NDFR for the wheat experiment conducted in Córdoba. T1= 225; T2=0; T3=180; T4=90; T5=135 [kgN/ha]

In this experiment, the NDFR versus NDVI plots showed a typical distinctive curvilinear shape. The data ranges ($NDFR_{max} = f(NDVI)$ and $NDFR_{min} = f(NDVI)$) were delineated visually using plots with extreme treatment, T1 = 225 kg/N and T2 = 0 kg/N.

$$NDFR_{max} = 0.5581 \times NDVI - 0.0181 \quad (4)$$

$$NDFR_{min} = 0.2857 \times NDVI + 0.02 \quad (5)$$

The CCCI was calculated using eq.2 for each experimental plot and date. Figure 6 shows the relationship between CCCI and leaf chlorophyll “a” for the wheat experiment (all treatments are shown).

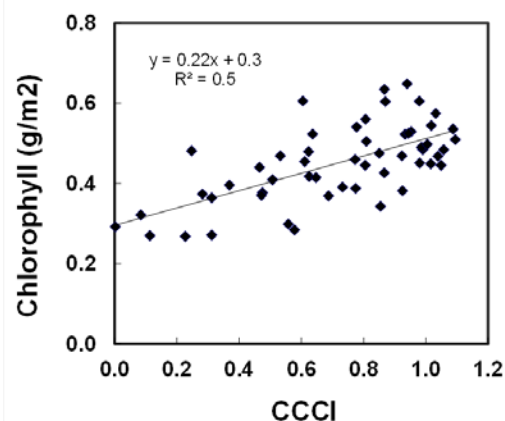


Figure 6: Relationship between CCCI and Chlorophyll “a” concentration for DOY 65, 97 and 133.

The r^2 was 0.5 for the relationship between CCCI and leaf chlorophyll “a” concentration in this experiment. Although there is substantial scatter, CCCI appears to

offer information about the leaf chlorophyll “a” concentration measured in all experimental plots in this study.

5 POTENTIAL YIELD PREDICTION

An estimation of the potential crop production is required to compute future nutrients outgoing for the balance of DST-fertilization. A methodology for estimating potential yield prediction using remote sensing is proposed and tested in this study.

5.1 Materials and Methods

Yield data provided by farmers at field scale during 2013 and distributed yields measured by a precision harvesting device, combined with historical series of climatic data were used to calibrate and validate the biomass model of Monteith (Monteith, 1972).

5.1.1 The biomass model of Monteith

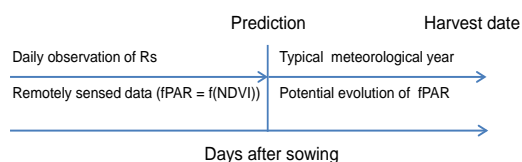
The biomass model of Monteith allows the estimation of the increase in crop biomass over time by accumulating the product of APAR (absorbed photosynthetically active radiation) and a parameter representing light-use efficiency (ϵ) (i.e., the amount of biomass produced per unit of APAR). In this approach the parameter fPAR (the fraction of PAR absorbed by the plant canopy) is needed for computing APAR. This model can include a harvest index (HI) that can be used for estimating crop yield. The model is expressed as follow:

$$Yield = \int_0^t fPAR \cdot PAR \cdot \epsilon \cdot HI \cdot dt \quad (6)$$

5.1.2 Methodology for early prediction

The biomass model in combination with an average harvest index was calibrated using yield maps from 21 commercial wheat fields located in Navarre (Spain). Once the model was calibrated, yield estimations were made on January 7th, April 21st, May 4th and June 12nd, for a different set of 20 commercial wheat fields using DEIMOS imagery to obtain fPAR.

A methodology for early prediction is proposed and tested in this study. Figure 7 shows a diagram of the proposed methodology.



From planting date to the day where predictions are made, daily observation of solar radiation and remotely sensed data are used. To complete the set of data beyond that date (ie. future weather conditions and canopy development), a typical meteorological year and a potential evolution of PAR is used.

5.2 Results

Fig.8 and 9 shows wheat yield predictions for commercial wheat fields in Navarre plotted versus the corresponding observed (farmer-reported) yields.

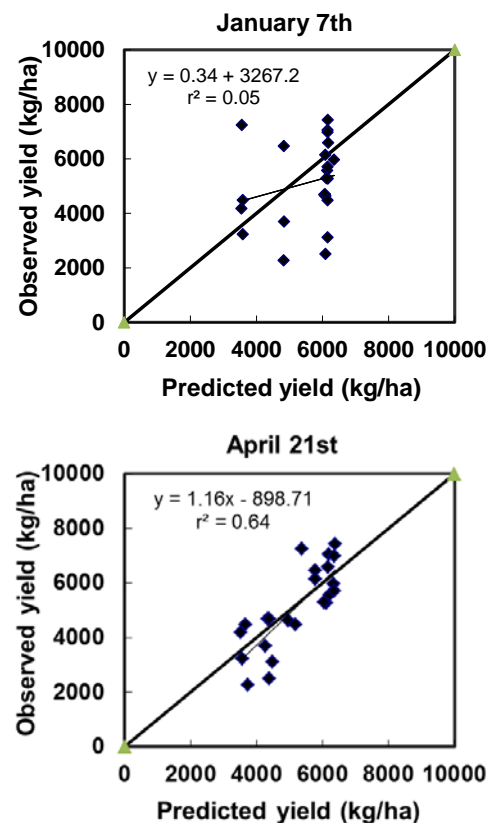


Figure 8: Wheat yield estimations on January 7th and April 21st for commercial fields using the Monteith model and DEIMOS satellite imagery.

The points in Fig. 8 (only on April 21st) and Fig. 9 (both dates) tended to cluster along the 1:1 line. Scatter among the points about the 1:1 line is substantial, with average absolute errors (AAE, the average amount that the yield for an individual field is over- or under-estimated) of 1302, 779, 853 and 884 kg ha⁻¹ for the estimations made on January 7th, April 21st, May 4th and June 12nd, respectively. These error values represented 26%, 15%, 17 % and 17%, respectively of the average observed yields for the 20 fields in this study.

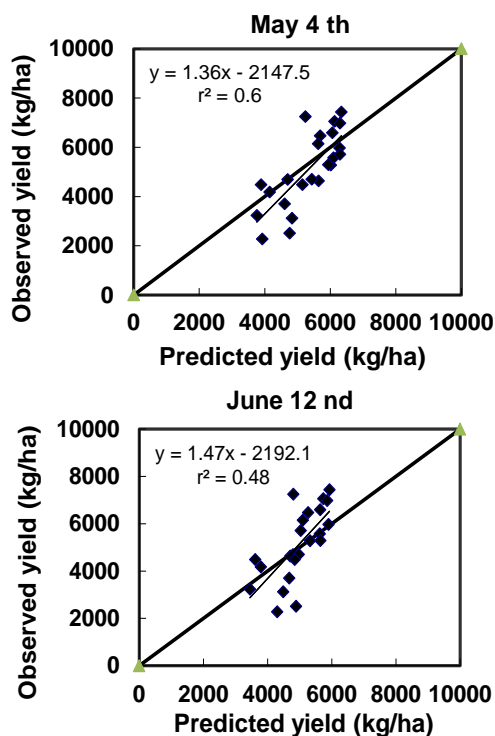


Figure 9: Wheat yield estimations on May 4th and June 12nd, for commercial fields using the Monteith model and DEIMOS satellite imagery.

6 CONCLUSIONS

Satellite-estimated basal crop coefficients for the commercial corn fields were generally consistent with basal crop coefficients adjusted for local conditions during the growing season. The combination of remote sensing-derived basal crop coefficients with FAO-56 methodology is an operative tool for estimating crop water requirements. It is planned to implement this approach into the next operative version (May-2015) of the HAD irrigation within the sigAGROasesor platform.

Since chlorophyll “a” leaf concentration is related to crop nitrogen status, the CCCI computed for wheat experimental plots appears to provide valuable nitrogen status information. However, further research is required to evaluate whether this technology may be useful for the HAD Fertilization.

The Monteith model, along with a harvest index and satellite imagery, was a practical and appropriate option for monitoring wheat yields with a reasonable degree of accuracy. This methodology will be validated in other agricultural areas in Spain before a definitive implementation into the sigAGROasesor platform.

Although further research is required, it seems that remote sensing technologies can provide valuable information for the decision support tools, incorporated into the sigAGROasesor platform. Next version of the platform will integrate one of the applications evaluated in this work (remote sensing for irrigation scheduling) and further applications are currently under study.

7 REFERENCES

- Barnes, E.M., Clarke, T.R., Colaizzi, P., Haberland, J., Kostrzewski, M., Riley, E., Moran, S., Waller, P., Choi, C., Thompson, T., Richards, S., Lascano, R., Li, H., 2000, Coincident detection of crop water stress, nitrogen status and canopy density using ground-based multispectral data. In: Proceedings of the Fifth International Conference on Precision Agriculture, 16-19 July, at Blooming, MN, USA.
- Clarke, T.R., Moran, M.S., Barnes, E.M., Pinter Jr., P., Qi, J., 2001, Planar domain indices: a method for measuring a quality of a single component in two-component pixels. In: IEEE International Geoscience and remote Sensing Symposium Proceedings (IGARSS 2001) Scanning the Present and Resolving the Future, 9-12 July 2001, Sydney, Australia. CD-ROM, pp 1279-1281.
- El-Shikha, D.M., Waller, P., Hunsaker, D., Clarke, T., Barnes, E., 2007, Ground-based remote sensing for assessing water and nitrogen status of broccoli. *Agricultural Water Management*, 92, 183-193.
- González-Dugo, M.P., Escuin, S., Cano, F., Cifuentes, V., Padilla, F.L.M., Tirado, J.L., Oyonarte, N., Fernández, P., Mateos, L., 2013, Monitoring evapotranspiration of irrigated crops using crop coefficients derived from time series of satellite images. II. Application on basin scale. *Agricultural Water Management*, 125, 92-104.
- González-Dugo, M.P., Neale, C.M.U., Mateos, L., Kustas, W.P., Prueger, J., Anderson, M.C., Li, F., 2009, A comparison of operational remote-sensing-based models for estimating crop evapotranspiration. *Agricultural Forest Meteorology*, 149, 1843-1853.
- Mateos, L., González-Dugo, M.P., Testi, L., Villalobos, F.J., 2013, Monitoring evapotranspiration of irrigated crops using crop coefficients derived from time series of satellite images. I Method Validation. *Agricultural Water Management*, 125, 81-91.

Spatial analysis of the homogeneity of the Land Surface Temperature in three Spanish test sites

D. Skoković, J. A. Sobrino, J. Carlos Jiménez-Muñoz, G. Sòria and Y. Julien
Global Change Unit (UCG), Image Processing Laboratory (IPL), University of Valencia
(UVEG).
drazen.skokovic@uv.es

ABSTRACT- Calibration and validation (cal/val) are key activities to test the data quality acquired from satellite-based instruments, as well as to report the accuracy of derived products such as the Land Surface Temperature (LST). Calibration of Thermal Infra-Red (TIR) data and Validation of LST products at low spatial resolution requires the identification of large and homogeneous areas, which is a difficult task. In this work, we analyze the spatial and temporal homogeneity of the Land Surface Temperature (LST) over three Spanish regions: the agricultural area of Barrax, the marshland of Doñana, and the natural park of Cabo de Gata. For this purpose, very high spatial resolution (~ 3 m) imagery acquired with the Airborne Hyperspectral Scanner (AHS) in the framework of different field campaigns and high-medium spatial resolution (~ 100 m) imagery acquired with the TIR Landsat-8 sensor have been used to retrieve homogeneity of high-medium and low spatial resolution sensors respectively. Different LST retrieval algorithms were applied to AHS and TIRS sensors to compare the LST for a given pixel against the LST of neighbor pixels through the computation of the Root Mean Square Error (RMSE). Results obtained from the analysis of LST derived from AHS data over Barrax and Doñana test sites show that part of these regions have a RMSE lower than 1K, which is consistent with the accuracy of the LST validation (between 0.5 K and 1.5 K). The temporal analysis of LST derived from the TIR sensor shows that some parts of Doñana and Cabo de Gata sites have a mean RMSE of 1 K along the year, which is lower than the accuracy of the LST validation (~ 2 K). The results show the usefulness of these three test sites to perform cal/val activities for both low and high spatial resolution sensors. The methodology presented in this study also allows the identification of suitable areas for future cal/val activities.

Keywords: calibration, validation, LST, homogeneity, AHS, TIR Landsat-8.

1 INTRODUCTION

Radiometric calibration of Earth Observation Sensors (EOS) is a critical component to provide accurate global measurements of environmental variables at useful spatial and temporal resolutions. The calibration techniques used for most thermal infrared sensors includes a pre-launch calibration, performed in similar fashion as it would be performed for any instrument, on board calibration, using a blackbody source and, finally, a ground-reference calibration or vicarious calibration that uses in situ measurements from ground test sites (Slater et al., 1996; Thome et al., 1997; Tonooka et al., 2005). This last part is the most problematic, since the measurements performed in situ has higher resolution than the measurements obtained from the EOS. For this reason, it is necessary to study what test sites are the most suitable for the installation of the infrared radiometers, as these should be representative of the pixel size to be studied.

An ideal test site to develop calibration and validation (cal/val) activities must to accomplish several critical characteristics that are essential to simplify cal/val tasks (Thome, 2001).

These characteristics can be resumed in:

- High-spatial uniformity (homogeneity) over a large area minimizes the errors of in situ measurements.
- Knowledge of temporal variations of test sites implies the knowledge of the changes of the emissivity, which is important to know the Land Surface Temperature (LST).
- An elevation of at least 1 km reduces the atmospheric associated errors.
- High probability of cloud-free days.
- Easy accessibility of the test site is also an important factor.

One of the most important characteristics is the homogeneity. If the area is not homogeneous for the size of sensor pixel, it not will be valid for the development of cal/val activities. Also it is important to know that the in situ measurements do not cover the same size as an EOS pixel, so it is necessary to install multiple sensors in situ and have a lot of personnel to cover the pixel to be measured. Usually it is not possible to have the equipment and personnel needed to cover all the area to be measured due to its high cost. Furthermore, it is not always clear how to combine the different measurements to represent the

pixel because the satellite image does not have to match with the measurements (especially for sensors with low spatial resolution).

To solve these difficulties a detailed knowledge of the area is necessary in terms of homogeneous for a different periods of time. In other words, it is necessary to perform in the test site a spatial and temporal study, covering all the changes that may occur. Some studies about the characterization of different areas have been made before to perform cal/val activities. All of these studies (Coll et al. 2005; Hale et al. 2011) are based on the determination of LST homogeneity using the most common statistics, such as minimum, maximum and standard deviation values (the last author use semivariograms to obtain these statistics). All of them use high resolution EOS such as Landsat-7 Enhanced Thematic Mapper Plus (ETM+) or ASTER Thermal Infrared (TIR) to analyze the variation of the LST in an area similar to the size of low resolution sensor pixel such as Moderate Resolution Imaging Spectroradiometer (MODIS) or Spinning Enhanced Visible and Infrared Imager (SEVIRI).

In this study, the data obtained from the Airborne Hyperspectral Scanner (AHS) instrument was used to characterize, with high resolution images, the homogeneity in three candidate test sites in the framework of the Spanish CEOS-Spain project, aimed to setting-up experimental sites in Spain for the purpose of calibration and validation of EOS. The use of AHS sensor guarantees that an airborne sensor pixel had a similar size and representatively of a measurement performed in situ in the same pixel. Moreover, a Landsat-8 TIR images were used to obtain the changes in the homogeneity during the year.

2 METHODS AND SENSOR DATA

2.1 Sensor data

Two sensors were used in this work: The AHS sensor, used to obtain the LST homogeneity for areas covered by the high-medium resolution sensors (100m or less) and the Landsat-8 TIR, used for a areas covered by the low resolution sensors (2000m or less).

Landsat-8 carries two sensors, the Operational Land Imager (OLI), and the TIR Sensor. OLI collects data at 30m spatial resolution with 8 bands located in the Visible and Near-Infrared (VNIR) and in the Short-Wave Infrared (SWIR) regions of the electromagnetic spectrum, plus an additional panchromatic band at 15 m spatial resolution. TIR sensor measures the TIR radiance at 100m spatial resolution using two bands (Band 10 and 11) located in the atmospheric window between 10-12 μm (Irons et al., 2012). Only the Band 10 was used in this work as has been shown more stable than the Band 11.

The AHS sensor is operated by the Spanish Institute of Aeronautics (INTA) and it was placed onboard the aircraft CASA 212-200 Paternina. The most important specifications of the sensor for this work are: 3m of spatial resolution, FOV of 90° ($\pm 45^\circ$), 80 bands in four ports (VNIR, SWIR, MWIR, and LWIR) 10 of them in TIR bands (from 8 μm to 13 μm) and 750 samples per line (Sobrino et al. 2006). Only the parts of the image when the view zenith angle is lower than 30° were be considered to minimize the angular effects.

2.2 Requirements

To obtain the homogeneity of our test sites in terms of LST, bias, standard deviation (σ) and Root Mean Square Error (RMSE) were be computed in an area of n pixels for a AHS and TIR images as shows Figure 1:

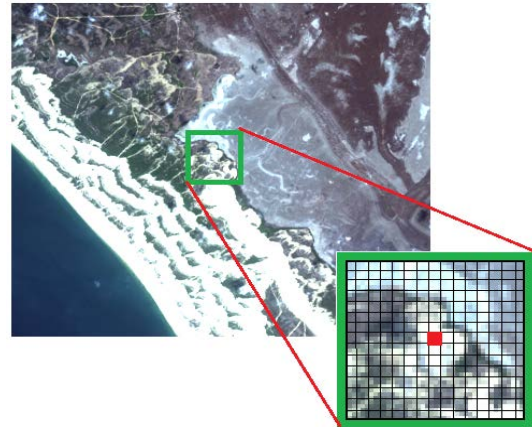


Figure 1. Example of selected area to compute the RMSE in a Landsat-8 image over Doñana test site.

Bias, standard deviation and Root Mean Square Error of the area of figure 1 can be expressed as follows:

$$BIAS = \frac{1}{n} \sum_{i=0}^n |T_C - T_i| \quad (1)$$

$$\sigma = \sqrt{\frac{1}{n-1} \sum_{i=0}^n |T_i - \bar{T}|^2} \quad (2)$$

$$RMSE = \sqrt{BIAS^2 + \sigma^2} \quad (3)$$

where T_C is the LST of the central pixel of selected area, T_i is the LST of the pixels over the study area, \bar{T} is the mean LST of the study area and n is the pixel number of the area, that depends of the sensor image used. Equation 1 is the mean differences between the

chosen pixel and the neighbour pixels, equation 2 is the variability of the selected area and, finally, equation 3 gives the total error of the central pixel for the selected area. In other words, is the total error due to homogeneity, in a given spatial resolution, when we made measurements in a chosen pixel. This process was repeated for all pixels of the AHS and TIR images

2.3 LST estimation from sensors

Due to the change of the atmospheric conditions between areas in the same test site and differences in the emissivities of the surfaces, an estimation of the LST is needed to minimize the RMSE. For this propose, the Temperature and Emissivity Separation (TES) algorithm (Guillespie et al., 1998) and the Single-Channel algorithm (Jiménez-Muñoz et al., 2014) was used to estimate LST for the AHS sensor and the TIR sensor respectively. The atmospheric parameters (τ , L_d , L_u) and total column atmospheric water vapor were obtained from MODIS atmospheric profiles (MOD07 product) and MODTRAN (version 5) radiative transfer code (Beck et al., 1999).

3 TEST SITES

Three test sites in Spain (Barrax, Doñana and Cabo de Gata) with different natural land cover and climate were considered for the cal/val activities (see figure 2). Barrax is an agricultural area located in Albacete (39°N, 2°W) with flat terrain and the presence of large, uniform land-use units (approx. ~100 ha). Doñana National Park is located in Huelva (37°N, 6.4° W) and is noted for its marshland that covers half of its extension (approx. ~27,000 ha). Cabo de Gata Natural Park is located in Almeria (36.9°N, 2° W) and has a volcanic origin with an extension of 38,000 ha.

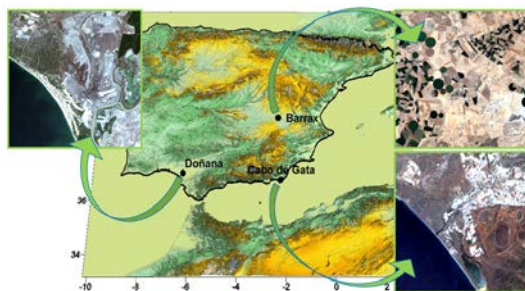


Figure 2. Test sites location in Spain, and the Landsat-8 images of them.

4 RESULTS

4.1. Validity of the results

To consider a valid pixel for carrying out cal/val activities, the RMSE value must be lower than a certain value that depends of the EOS accuracy and

the error of algorithm used to obtain the LST. For example, for high resolution sensors (~ 100 m), the LST estimation errors are ranging between 0.5-1.5 K as described in Hook et al (2007) or Coll et al (2010) and for low resolution sensors (> 1000 m), the estimation errors are about 2 K as obtained in the validations performed by Wan (2014) and Coll et al. (2009) for MODIS sensor. According this values, the RMSE obtained in AHS image and TIR sensor image must be lower than 1.5 K and 2 K respectively to consider the pixel suitable for cal/val activities.

The AHS pixel resolution covers approximately the same size as the in situ measurements, but the pixel resolution of the TIR sensor is lower than the AHS sensor and seems not representative for the in situ measurements. For this reason, to demonstrate the representativity of TIR images, a resize of the AHS images to TIR resolution and the subsequent analysis of the RMSE in a square of 2 km, following the methodology proposed for the three test sites, was performed. The results shows that the zones where TIR image are representative (where RMSE of both images are the same) match with the zones where the homogeneity for high-medium resolution sensors is high.

4.2. Homogeneity for high-medium resolution EOS

Figure 3 shows the RMSE obtained with AHS sensor for an area of 100x100 m or 33x33 pixels. Three zones can be considered for the cal/val activities due to high homogeneity: Marshland in Doñana, with a RMSE values lower than 1.5 K; Some parts of Cabo de Gata, where the RMSE ranges between 1 K and 2 K and some fields of Barrax where the RMSE is lower than 1 K. If a measurements of a 3 m (as AHS pixel size) of spatial resolution were be performed in one pixel of this zones, we can be sure that the error due to homogeneity is less than the RMSE retrieved only if a comparison is made with a high-medium resolution EOS.

4.2. Homogeneity for low resolution EOS

Figure 4 shows the RMSE for an area of 2000x2000 m or 20x20 pixels obtained with the TIR sensor. The RMSE retrieved (big image in every one of the three test sites) is an average of twelve images downloaded from April 2013 to April 2014. The small images are the RMSE average of winter season (top left) and the RMSE average of summer season (bottom right).

Only analyzing the zones previously selected, when the TIR sensor is representative of AHS measurements, the marshland of Doñana and Cabo de Gata presents values of RMSE from 0.5 K to 1.5 K, while Barrax is not recommended by their low homogeneity. These values of RMSE are representative only for a low resolution EOS.

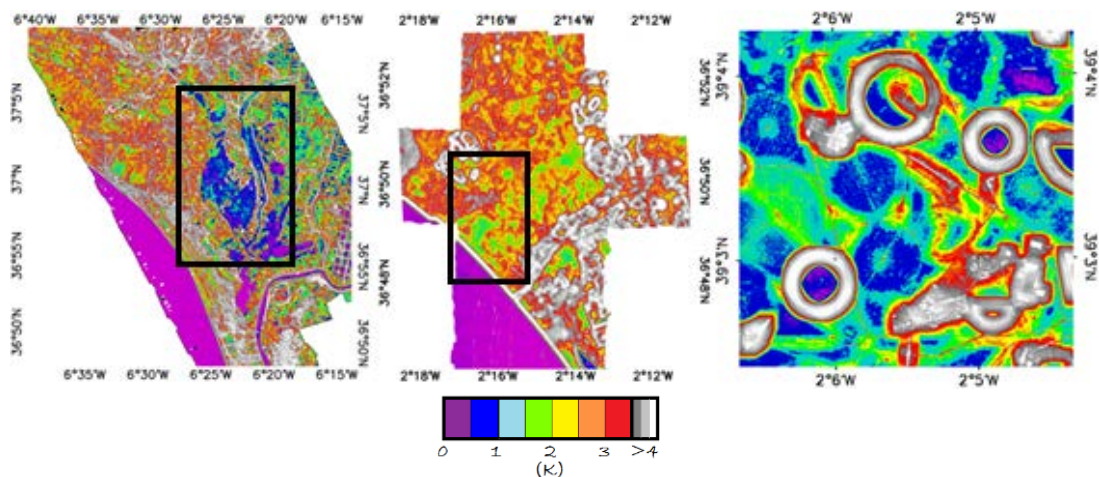


Figure 3. From left to right: Doñana, Cabo de Gata and Barrax RMSE retrieved for a high-medium resolution EOS with AHS sensor.

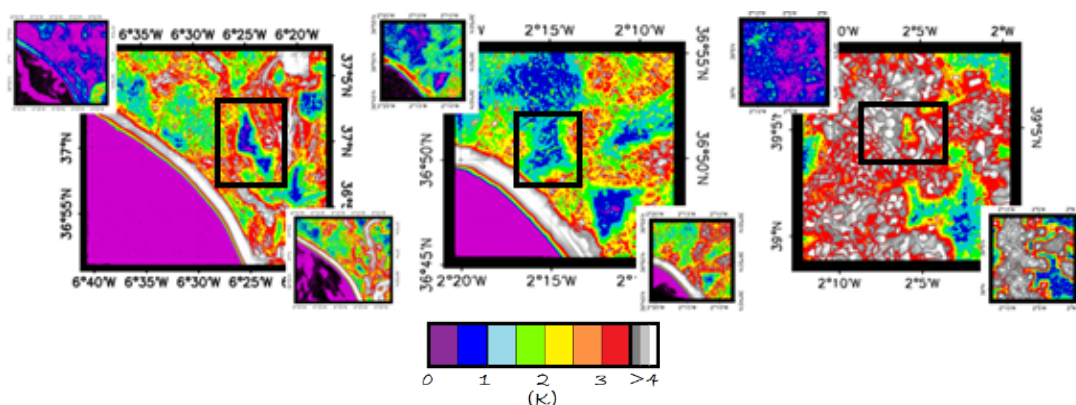


Figure 4. From left to right: Doñana, Cabo de Gata and Barrax RMSE retrieved for a low resolution EOS with TIR sensor. Central figure for each test site represents the mean RMSE along the year; Top left figure represents the mean winter RMSE and Right bottom figure represents the mean summer RMSE.

Temporal analysis of the TIR images shows that in winter the homogeneity is higher than in summer with values of RMSE lower than 1 K in all zones. In summer, the RMSE is higher, and only in some parts of marshland and Cabo de Gata the RMSE is lower than 2 K.

4 CONCLUSION AND DISCUSSION

The cal/val areas must meet certain requirements in order to make the most accurate measurements as possible. One of this requirements is the homogeneity that is important because the ground-based measurements used for comparison are usually of much finer spatial resolution than the instantaneous field of view of the satellite-based instrument. For

these reason the homogeneity of three Spain test sites were analyzed to obtain the error due to homogeneity. Assuming that the AHS spatial resolution is the same than the in situ measurements and demonstrating that the TIR Landsat-8 sensor is representative of the AHS pixels, only when the homogeneity is high, we can obtain the RMSE for a high-medium and low resolutions EOS in our test sites.

For high-medium resolution EOS, the lowest RMSE were retrieved in Barrax and in the marshland of Doñana with values around 1 K. In Cabo de Gata, the values are little higher (~ 1.5 K) but acceptable as the accuracy of LST validation is similar. These values of RMSE were obtained in the summer period, so the RMSE in other seasons will be lower, especially in

winter. Consequently, the RMSE of figure 3 is overestimated for the other seasons. For low resolution EOS, the marshland of Doñana and Cabo de Gata have demonstrated the lowest values of RMSE (~ 1 K) during the year, with a maximal homogeneity in winter (< 1 K) and minimal in summer (< 2 K).

In conclusion, these three test sites offers high homogeneity for a high resolution sensors (TIR Landsat-8, EMT+ Landsat-7 or TIR ASTER) and a low resolution sensors (MODIS TERRA/AQUA, VIIRS Suomi NPP or SLSTR Sentinel-3) to perform cal/val activities.

5 ACKNOWLEDGEMENTS

This work was supported by the European Union (CEOP-AEGIS, project FP7-ENV-2007-1 Proposal No. 212921), the Ministerio de Economía y Competitividad (CEOS-Spain, project AYA2011-29334-C02-01).

6 REFERENCES

- Coll, C., Caselles, V., Galve, J. M., Valor, E., Niclos, R., Sanchez, J.M., 2005, Ground measurements for the validation of land surface temperatures derived from ATSR and MODIS data. *Remote Sensing of Environment*, 97, 288–300.
- Coll, C., Wan Z., Galve J.M., 2009, Temperature-based and radiance-based validation of the V5 MODIS land surface temperature product *Journal of Geophysical Research*, 114, p. D20102
- Coll, C., Galve J.M., Sanchez J.M., Caselles V., 2010, Validation of Landsat-7/ETM + thermal-band calibration and atmospheric correction with ground-based measurements. *IEEE Transactions on Geoscience and Remote Sensing*, 48 pp. 547–555
- Gillespie, A., Rokugawa, S., Matsunaga, T., Cothorn, J. S., Hook, S., & Kahle, A. B., 1998, A temperature and emissivity separation algorithm for advanced spaceborne thermal emission and reflection radiometer (ASTER) images. *IEEE Transactions on Geoscience and Remote Sensing*, 36, 1113–1126.
- Hale, R. C., Gallo, K. P., Tarpley, D., and Yu, Y., 2011, Characterization of variability at in situ locations for calibration/validation of satellite-derived land surface temperature data, *Remote Sensing Letters*, vol. 2, no. 1, 41-50.
- Hook, S. J., Vaughan, R. G., Tonooka, H. and Schladow S. G., 2007, Absolute radiometric in-flight validation of Mid and Thermal Infrared data from ASTER and MODIS using the Lake Tahoe CA/NV, USA automated validation site; *IEEE Trans. Geosci. & Rem. Sens.* 45 1798–1807.
- Irons, J. R., Dwyer, J. L., & Barsi, J. A., 2012, The next Landsat satellite: The Landsat Data Continuity Mission. *Remote Sensing of Environment*, 122, 11-21.
- Jiménez-Muñoz J. C., Sobrino J. A., Skoković D., Mattar C. and Cristóbal J., 2014, Land Surface Temperature Retrieval Methods From Landsat-8 Thermal Infrared Sensor Data, *IEEE Geoscience and Remote Sensing Letters*, vol. 11, no. 10.
- Slater P.N., Biggar S.F., Thome K.J., Gellman D.I. and Spyak P.R., 1996, Vicarious radiometric calibrations of EOS sensors, *Journal of Atmospheric and Oceanic Technology*, vol. 13, pp. 349-359.
- Sobrino, J.A., Jiménez-Muñoz, J.C., Zarco-Tejada, P.J., Sepulcre-Cantó, G. and De Miguel, E., 2006, Land surface temperature derived from airborne hyperspectral scanner thermal infrared data. *Remote Sensing of Environment*, 102, pp. 99–115.
- Thome K., Markham B., Barker J., Slater P., and Biggar S., 1997, Radiometric calibration of landsat,” *Photogramm. Eng. Remote Sens.*, vol. 63, pp. 853–858.
- Thome, K.J., 2001, Absolute Radiometric Calibration of Landsat 7 ETM+ Using the Reflectance-Based Method. *Remote Sensing of Environment*, 78(1-2): 27–38.
- Tonooka H., Palluconi F. D., Hook S. J. and Matsunaga T., 2005, Vicarious Calibration of ASTER Thermal Infrared Bands, *IEEE Transactions on Geoscience and Remote Sensing*, vol. 43, no. 12.
- Wan, Z., 2014, New refinements and validation of the collection-6 MODIS land-surface temperature/emissivity product *Remote Sensing of Environment*, 140, pp. 36–45

AUTHOR INDEX

A

Abaoui, J., 297
Abdat, N., 533
Afán, I., 195
Alavipanah, S.K., 48, 54
Alyaari, A., 488
Amri, R., 524
Anderson, M.C., 310
Andreu, A., 310
Aouade, G., 297
Aragonés, D., 195
Ardö, J., 327
Armesto, A., 533

B

Baghdadi, N., 401, 493, 524
Bahir, M., 292, 304
Bakhtiari, M., 48
Ballabrera, J., 396
Bao, Y.H., 172
Barberà, M.J., 442, 447
Barbu, A., 406
Baret, F., 410, 431, 467
Barsi, J.A., 415
Bartholomeus, H.M., 230
Baruth, B., 243
Becedas, J., 420
Belaqziz, S., 297
Benarchid, O., 262, 267
Benavent, J.A., 442
Benkaddour, A., 297
Berjamy, B., 297
Besga, G., 533
Bi, Y., 322, 390
Bian, J., 519
Bigéard, G., 297
Borel, C., 139
Boschetti, M., 410

Bossio, D., 410
Botey, M.R., 533
Boudhar, A., 297
Boulet, G., 292, 297, 304
Brockmann, C., 457, 529
Brom, J., 349
Buck, P., 22
Bustamante, J., 195

C

Calvet, J.-C., 406
Camacho, F., 7, 327, 410, 426, 431, 461, 467
Campbell, P.E., 144
Campos-Taberner, M., 7, 283, 426
Camps-Valls, G., 7
Caño, A.B., 380
Carbonero, M.D., 380
Carpintero, E., 310
Carrara, A., 338
Carrer, D., 406
Carretero, L., 11
Caselles, D., 447
Caselles, V., 447
Castilla, A., 533
Castrignano, A., 410
Chávez, R.O., 190
Chehbouni, G., 297
Chen, B.R., 172
Chen, S., 184, 355, 482
Chen, Z., 255
Cheng, Y.-B., 144
Chernetskiy, M., 277
Chirouze, J., 297, 304
Claverie, M., 108
Clevers, J.G.P.W., 190, 230
Colin, J., 127
Coll, C., 442, 447
Coll-Pajaron, A., 488
Corbera, J., 103

Corp, L.A., 144
Coudert, B., 292, 297
Courault, D., 37

D

Danne, O., 529
Daughtry, C.S.T., 144
De la Cruz, F., 410, 431, 533
de Miguel, E., 11, 86
de Rosnay, P., 505
Demarez, V., 410
Di, S., 316
Di Bella, C., 410
Diarra, A., 297
Díaz-Delgado, R., 195
Dörnhöfer, K., 121
Drapeau, L., 297
Driouech, F., 297
Du, Y., 75
Du, Y.-Z., 477
Duan, S.-B., 390
Dupont, S., 133
Durán-Alarcón, C., 112, 288, 376, 510
Duveiller, G., 243

E

El Adnani, M., 297
El Fazziki, A., 297
El Mandour, A., 297
Er-Raki, S., 297
Ezzahar, J., 297

F

Fairbairn, D., 406
Fakir, Y., 297
Fan, X., 16
Fang, H., 410
Fanise, P., 292, 297
Fernández-Morán, R., 488
Fernández-Rebollo, P., 380

Fernández-Renau, A., 86
Filali, N., 297
Fomferra, N., 457
Font, J., 396
Franch, B., 108
Freile-Aranda, M.D., 28
Fuster, R., 288, 510

G

Gallego-Elvira, B., 304
Gao, C., 75, 482
Gao, F., 310
Gao, T., 98
García Contado, S., 243
García-Haro, F.J., 7, 283, 327, 410, 426
García-Moreno, A., 380
Gascoin, S., 297
Gelati, E., 406
Gerace, A., 415
Gevaert, C., 283
Gilabert, M.A., 7, 327, 338
Gillespie, A. R., 271, 361
Gobron, N., 277
Gómez-Amo, J.L., 28, 32
Gomez-Dans, J., 277
Gómez-Giráldez, P.J., 380
Gonzalez, M.P., 410
González, C., 420
González, G., 420
González-Dugo, M.P., 310, 380, 533
Gorrab, A., 401, 493, 524
Göttsche, F-M., 203
Guillevic, P., 37
Guo, J., 355, 482
Gutiérrez de la Cámara, Ó., 86

H

Hagolle, O., 297, 452
Hai, Q.S., 172
Hajhouji, Y., 297
Hanich, L., 297

Hesslerová, P., 116
Hook, S.J., 415
Huemmrich, K.F., 144
Hulley, G.C., 203
Huo, H., 75, 386

I

Ibouh, H., 297
Irvine, M., 133

J

Jabargo, M., 533
Jacquin, A., 452
Jarlan, L., 292, 297, 304
Jenerowicz, A., 94, 161
Jia, L., 127, 237, 249
Jiang, X., 75
Jiang, X.-G., 477
Jiménez, M., 11, 86
Jiménez-Muñoz, J.C., 112, 209, 221,
376, 538
Jin, H., 519
Jin, Y., 42, 184, 355, 482
Jin, Y.X., 98, 172, 214, 370
Julien, Y., 221, 538

K

Kaminski, P., 94
Kane, J., 361
Kane, V., 361
Kayitakire, F., 366
Kerr, Y., 297, 488
Khabba, S., 297
Kharrou, M.H., 297
Khusfi, M.E., 48
Kirches, G., 529
Knapp, K., 150
Kotti, F., 524
Kuehl, A., 513
Kullmann, L., 199

Kussul, N., 410
Kustas, W.P., 144, 310
Kutsch, W., 327

L

Lacaze, R., 410, 431, 461, 467
Lafarga, A., 533
Laftouhi, N., 297
Lagouarde, J.-P., 133, 292, 304
Landis, D.R., 144
Latorre, C., 410, 431
Latorre, M.J., 420
Lattanzio, A., 150
Le Page, M., 297
Leblanc, M., 297
Leng, P., 60, 436
Lewis, P., 277
Li, A., 519
Li, J., 42, 184, 355, 482
Li, J.Y., 98, 214, 370
Li, W., 42
Li, X., 386
Li, X.Y., 172
Li, Z.-L., 16, 60, 64, 69, 80, 90, 178, 226, 316,
322, 344, 386, 390, 436, 477, 499
Li, Z.W., 172
Liang, S., 271
Lili-Chabaane, Z., 292, 493, 524
Linés, C., 86
Liu, J., 255
Liu, S., 98
Liu, Y., 499
Liu, Z., 386
López-Baeza, E., 488, 410
López-Corcoles, H., 533
López-Lozano, R., 243
Lu, J., 316, 322

M

Ma, H., 184, 355, 482
Ma, H.L., 98, 214, 370

Malhi, Y., 209
 Mangiarotti, S., 297
 Marah, H., 297
 Marchane, A., 297
 Marcos, C., 32
 Markham, B.L., 415
 Marloie, O., 37
 Martín, M.P., 333
 Martínez, B., 7, 327, 338, 426
 Martínez, E., 396
 Martínez, J., 396
 Martínez-Lozano, J.A., 28, 32
 Maselli, F., 338
 Mattar, C., 112, 209, 288, 376, 410, 505, 510
 Matthews, J., 150
 Meliá, J., 7, 327, 426
 Menenti, M., 127, 237, 249
 Merlin, O., 297, 304
 Mestre, A., 533
 Meurey, C., 406
 Mialon, A., 488
 Middleton, E.M., 144
 Miernecki, M., 488
 Mira, M., 37, 304
 Mokssit, A., 297
 Montanaro, M., 415
 Moreno, A., 7, 327, 338
 Morera, M., 103
 Mougénot, B., 292, 297, 493
 Mushkin, A., 271, 361

N

Nan, X., 519
 Nerry, F., 64, 127, 237, 386
 Nestola, E., 410
 Ni, Z., 386
 Niclòs, R., 442, 447

O

Olesen, F.S., 203

Oliosio, A., 37, 292, 304
 Olivera-Guerra, L.E., 288, 510
 Olmedo, E., 396
 Oppelt, N., 121
 Orych, A., 94, 161

P

Pacheco-Labrador, J., 333
 Padilla, F.L.M., 533
 Pang, J., 472
 Paperin, M., 529
 Parrens, M., 488
 Pattey, E., 410
 Pedrera, F., 420
 Pedrós, R., 32
 Peng, S., 226
 Perea, F., 533
 Pérez, F., 103
 Pérez, R., 420
 Pérez-Hoyos, A., 366
 Piccard, I., 410
 Piles, M., 338, 396
 Pipia, L., 103
 Poilvé, H., 452
 Pokorný, J., 116
 Pons, X., 37
 Prado, E., 86
 Procházka, J., 349

Q

Qian, Y., 75
 Qin, Z., 42, 355
 Qin, Z.H., 214, 370
 Qiu, J.J., 214

R

Raibi, F., 297
 Raissouni, N., 262, 267
 Raqueno, N.G., 415
 Rezaei, A.A., 48

Rezvani, M.M., 54
 Rivalland, V., 37, 292, 304
 Roebeling, R., 150
 Romano, J., 139
 Roosjen, P.P.J., 230
 Rosario, D., 139
 Roumiguié, A., 452
 Roupioz, L., 127, 237
 Rudiger, C., 410
 Ruescas, A.B., 457, 529
 Ruiz Casas, A., 103
 Russ, A.L., 144

S

Saaïdi, A., 297
 Sabol Jr., D.E., 22
 Salepci, N., 513
 Salgado-Hernanz, P.M., 488
 Sánchez, J., 461,
 Sánchez, J.M., 447
 Sánchez, S., 327
 Sanchez-Azofeifa, A., 410
 Sánchez-Ruiz, S., 7, 338
 Santamaría-Artigas, A., 288, 505, 510
 Savin, I., 410
 Schmullius, C., 277, 513
 Schott, J.R., 415
 Schulz, J., 150
 Schwank, M., 488
 Seguini, L., 243
 Semmens, K., 310
 Serra, J., 533
 Shao, K., 64, 69
 Sigel, G., 452
 Sillero, J., 533
 Simonneaux, V., 297
 Skokovic, D., 221, 538
 Smets, B., 461, 467
 Sobrino, J.A., 112, 209, 221, 262, 376,
 538
 Song, C., 42
 Song, X., 60, 80, 436

Sòria, G., 221, 538
 Stelzer, K., 529
 Stöckli, R., 150
 Szintai, B., 199

T

Takahashi, M., 150
 Tang, B., 60
 Tang, B.-H., 16, 64, 69, 90, 178, 226, 316, 390
 Tang, R., 69, 90, 178, 226, 316, 322, 344, 390
 Tardà, A., 103
 Tavernier, A., 297
 Thiel, C., 513
 Tóth, H., 199
 Toumi, J., 297

U

Uhl, F., 121
 Utrillas, M.P., 28, 32

V

Valiente, J.A., 442, 447
 Vall-llossera, M., 396
 van der Tol, C., 1
 Verger, A., 467
 Verhoef, W., 1
 Vermote, E.F., 108
 Vinciková, H., 349

W

Walczkowski, P., 155, 161, 166
 Wang, B., 472
 Wang, D., 255, 436
 Wang, F., 42
 Wang, G., 271
 Wang, R., 80
 Wang, S., 488
 Wang, Y., 60, 436

Wang, Z.L., 370
Weiss, M., 410, 431, 467
Wierzbicki, D., 166
Wigner, J.-P., 488, 505
Wilinska, M., 166
Wu, H., 16, 64, 69, 90, 178, 226, 316,
390, 477
Wu, M.Q., 370
Wu, Q., 172, 214, 271

X

Xi, D.-G., 499
Xin, X.P., 172
Xu, B., 42, 98, 184, 214, 355, 370, 482

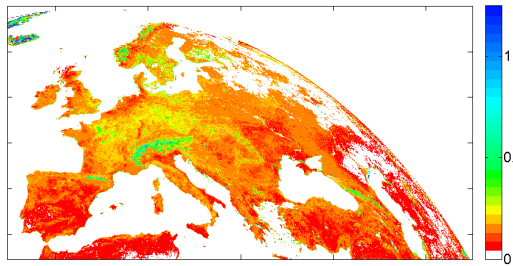
Y

Yan, G., 16
Yan, R.R., 172
Yang, X., 184, 355, 482
Yang, X.C., 98, 214, 370
Yang, Z., 98
Yu, H., 184
Yu, H.D., 98

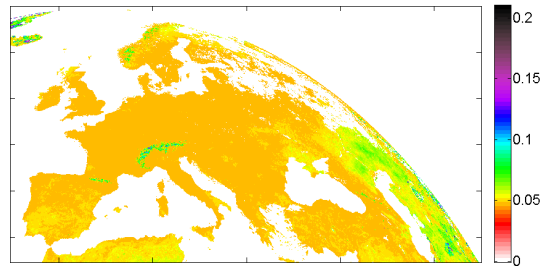
Z

Zhang, B.H., 172
Zhang, D., 69
Zhang, H.B., 172
Zhang, J., 370
Zhang, Q., 144
Zhang, X., 472
Zhang, Y., 75
Zhang, Y.-Z., 477
Zhang, Z., 519
Zhao, E.-Y., 75, 477
Zhao, F., 184, 214, 355, 482
Zhao, L., 355
Zhao, S., 42
Zhao, W., 519
Zhong, X., 178
Zhou, F.-C., 80
Zhou, G., 64
Zhou, J., 249
Zhou, Q., 255
Zhu, X., 184
Zribi, M., 401, 410, 493, 524

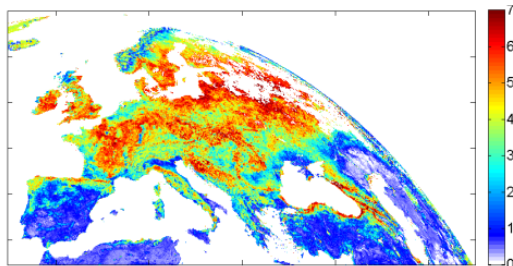
FIGURES IN COLOUR



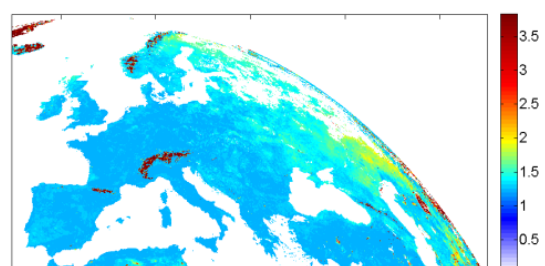
(Page 8) Figure 3. Canopy water content (Kg^2/m^2) estimated map retrieved with GPR (2013 June the 11th).



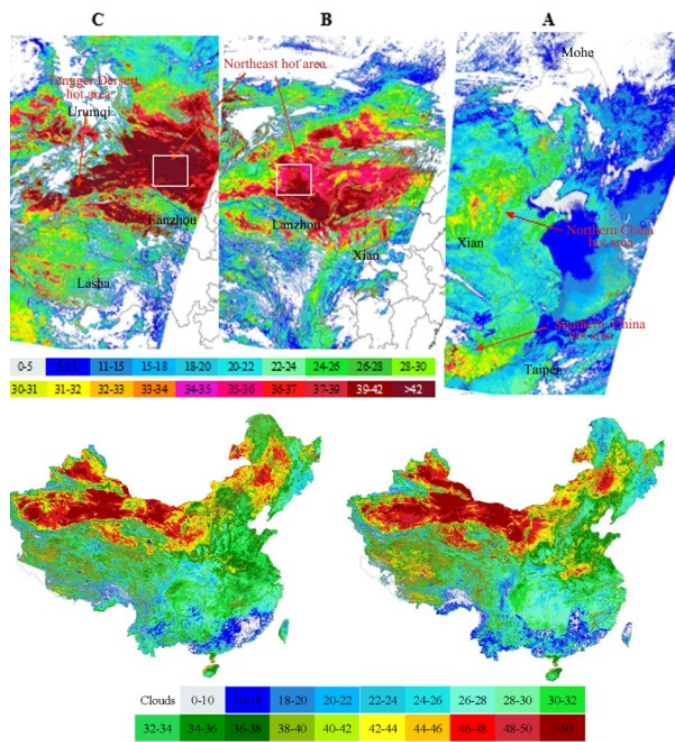
(Page 8) Figure 4. Confidence map (σ) retrieved with GPR for canopy water content (Kg^2/m^2) (2013 June the 11th).



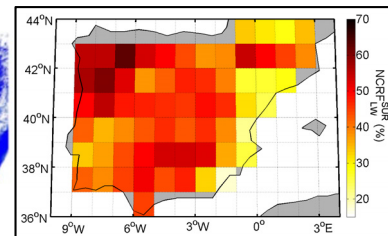
(Page 8) Figure 5. Leaf area index (m^2/m^2) estimated map retrieved with GPR (2013 June the 11th).



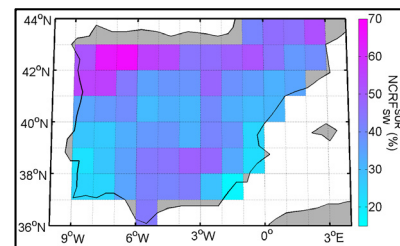
(Page 8) Figure 6. Confidence map (σ) retrieved with GPR for leaf area index (m^2/m^2) (2013 June the 11th).



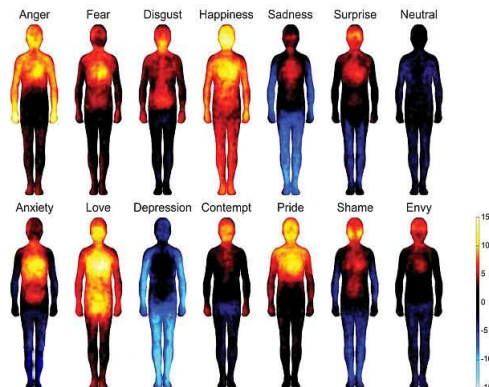
(Page 45) Figure 2 Spatial distribution of MODIS LST in China



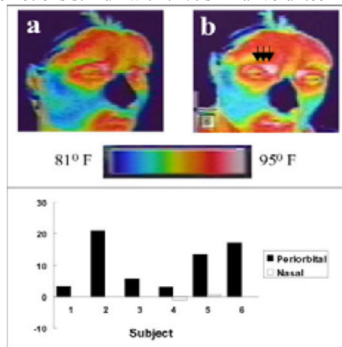
(Page 31) Figure 9: Daily mean of NCRF_{LW} at surface in the Iberian Peninsula (04/05/2012).



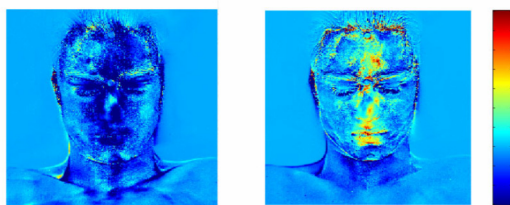
(Page 31) Figure 10: Daily mean of NCRF_{SW} at surface in the Iberian Peninsula (04/05/2012).



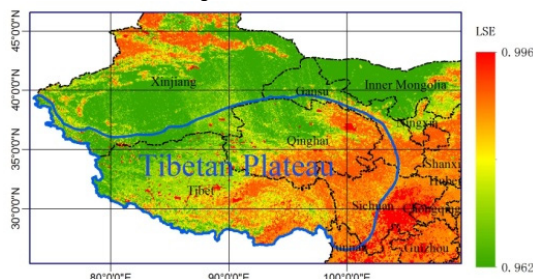
(Page 55) Fig. 2: result of study on 701 volunteers to extract affected regions of body by emotions stimuli with 71% similar volunteer response.



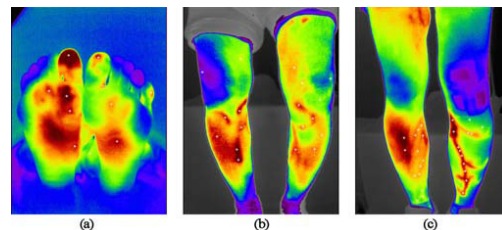
(Page 55) Fig. 3: Thermal images of the face for a subject (a) before and (b) 300 msec after an instantaneous startle. Arrows indicate local warming in the periorbital area. The color bar depicts the false coloring scheme from the lowest (81.0 F) to the highest (95.0 F) temperature. (c) Changes of the average pixel value in the periorbital and nasal areas with auditory startle. The changes are depicted for each subject ($n=6$ subjects). Positive deviation represents local warming and negative deviation, cooling.



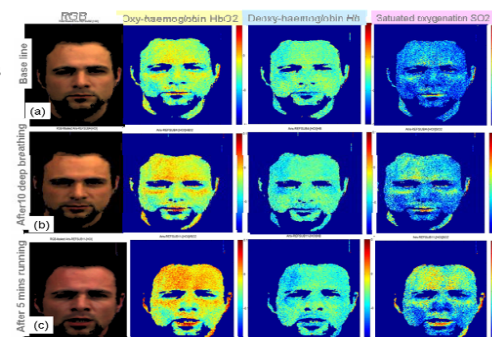
(Page 56) Fig. 6: Overall average of the cutaneous blood perfusion rate for one of the volunteers (in arbitrary units). On the left, the average distribution while watching sport movies; on the right, the average distribution while watching erotic content movies.



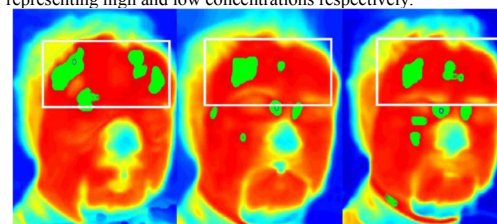
(Page 62) Figure 1. LSE in S-VISSR channel IR1 (10.3-11.3μm) on 5 August 2008



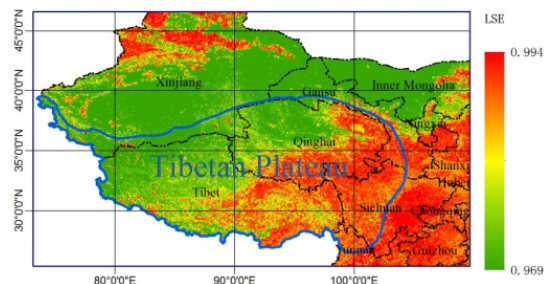
(Page 56) Fig. 8: Detection results of the suspicious pain regions. White asterisk marks represent those regions. (a) Foot of the glycosuria patient. (b) The degenerative arthritis. (c) The varicose vein.



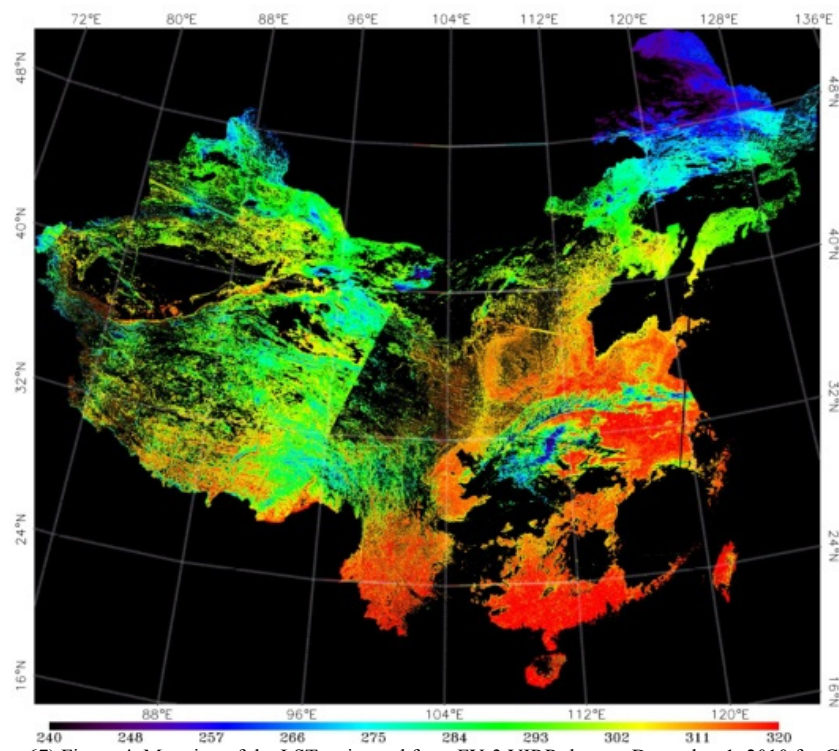
(Page 57) Fig. 10: shows the result for the detection of physical stress by sensing the increases of blood oxygenation using HSI technique. The experiment is arranged by requesting a subject to (a) sit on chair for rest as the base line condition, heart beat ~80BPM, (b) slow but deep breathing for 10 times while remain seated, heart beat increases to 90BPM, (c) after running for 5 minutes, heart beat increases to 140BPM. As in fig 4 all maps are presented in false colours with All maps are shown in false colours with hot (red) and cold (blue) colours representing high and low concentrations respectively.



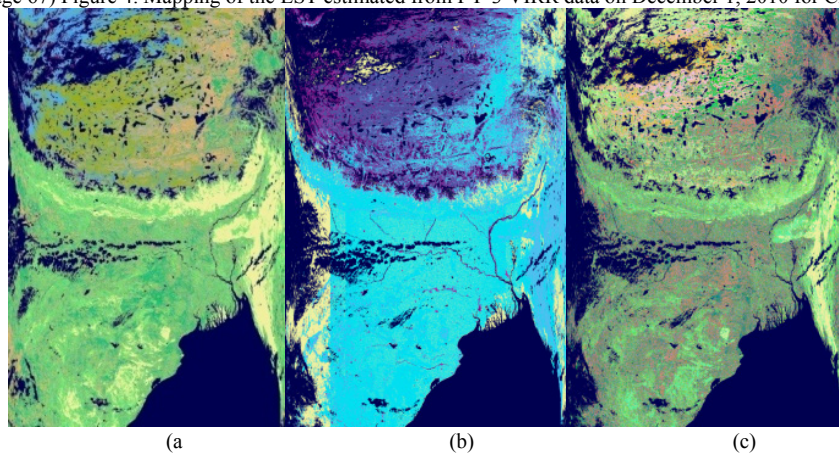
(Page 57) Fig. 11: shows the averaged thermal images of the subject after the emotional (left) and physical (middle and right) stressors are applied. All images are projected onto an arbitrary pose by using an image registration technique, and they are then averaged to give a more faithful representation of the thermal signatures due to various stressors.



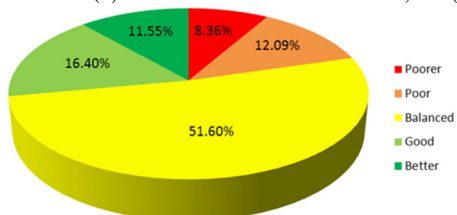
(Page 62) Figure 2. LSE in S-VISSR channel IR2 (11.5-12.5μm) on 5 August 2008



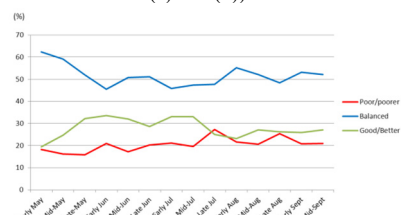
(Page 67) Figure 4. Mapping of the LST estimated from FY-3 VIRR data on December 1, 2010 for China.



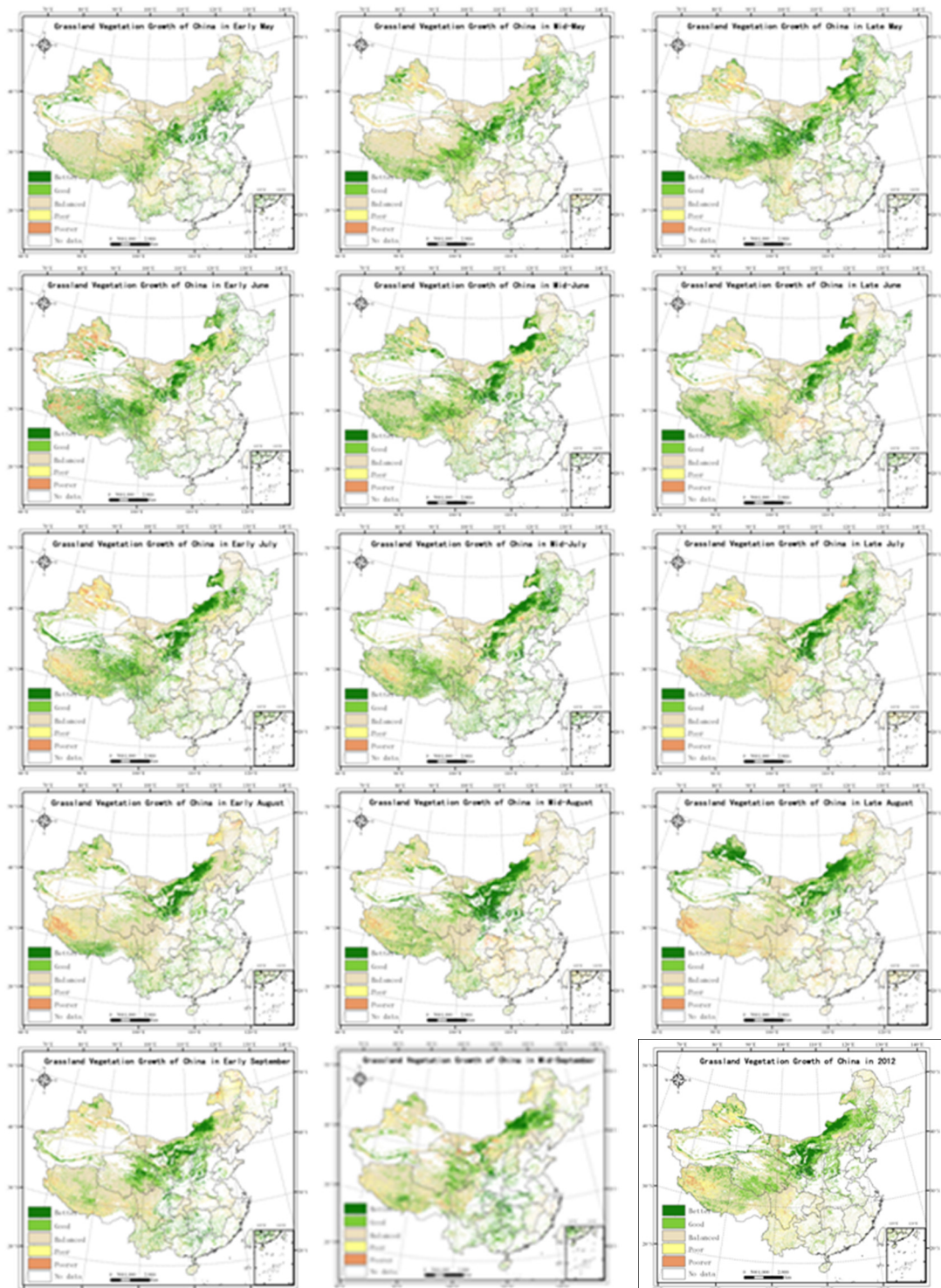
(Page 92) Figure 4. Mapping of LSEs obtained with different methods ((a) with NDVI method; (b) with classification-based method; and (c) the difference LSEs between (a) and (b)).



(Page 100) Figure 1. The production for Grassland vegetation growth of China in 2012

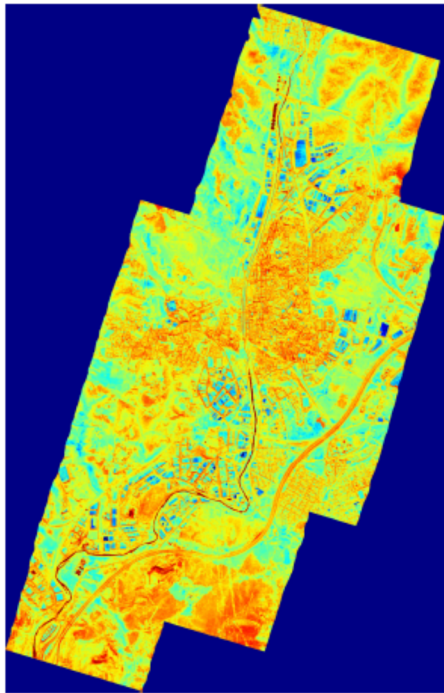


(Page 100) Figure 2. Ten-day dynamic change of grassland vegetation growth in China over May-September 2012 compared with the same period of 2011

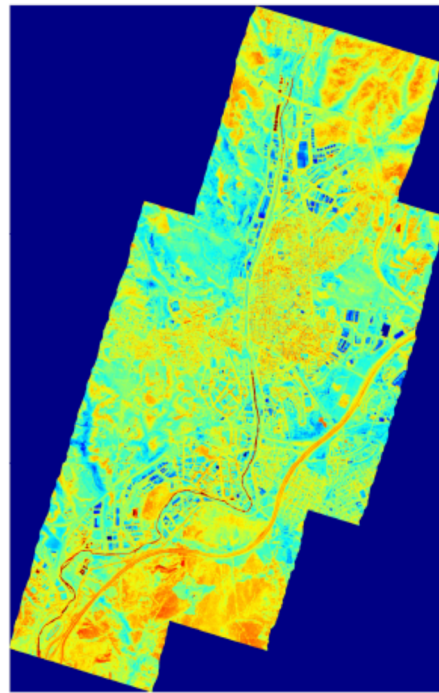


(Page 101) Figure 3. Spatial distribution map of vegetation growth during early May to mid-September 2011 compared with every ten-day period growth in 2011

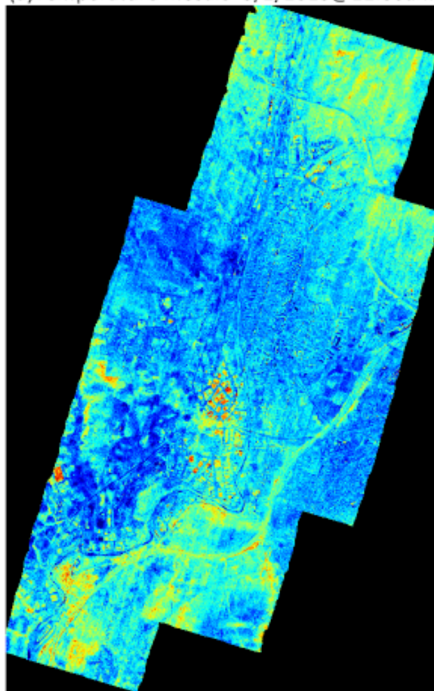
(Page 101) Figure 4 Spatial distribution map of grassland vegetation growth in 2012



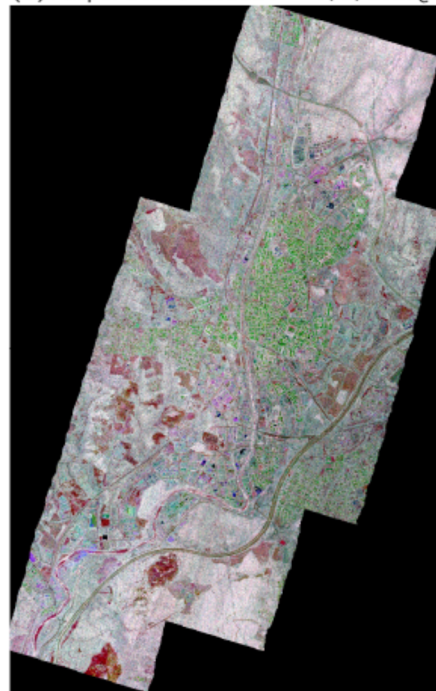
(a)Temperature mosaic -5/2/2013@12:00am



(b)Temperature mosaic - 5/2/2013@06:00

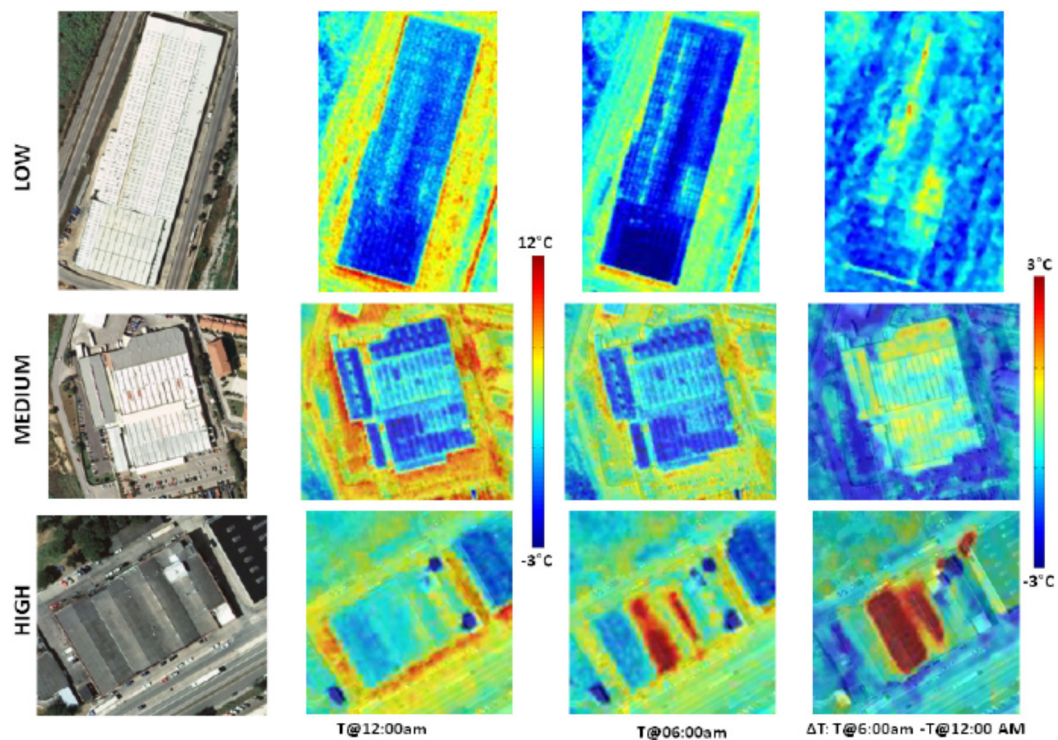


(c) ΔT mosaic: $T@6:00am - T@12:00am$

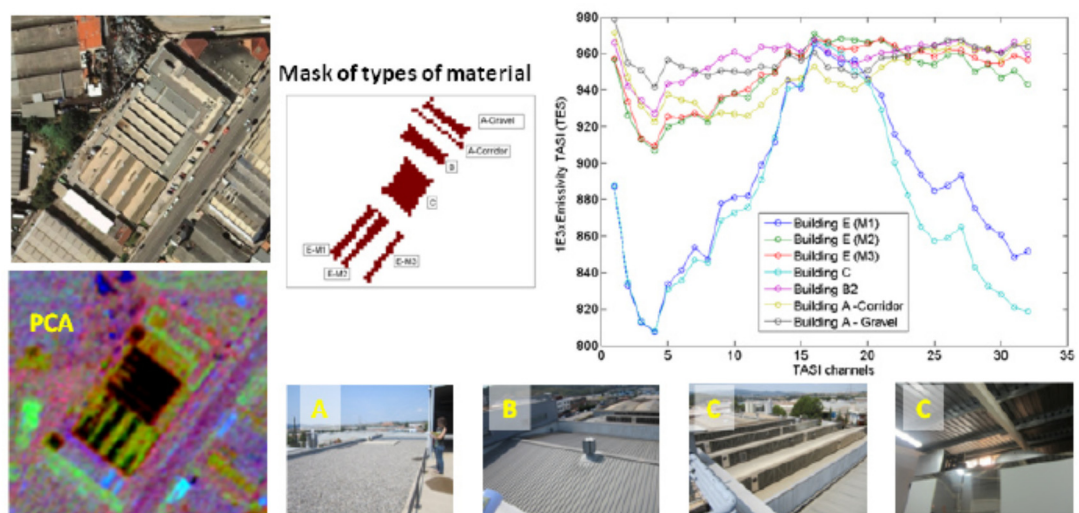


(d) $\langle \epsilon \rangle$ mosaic: $[\epsilon@6:00am + \epsilon@12:00am]/2$

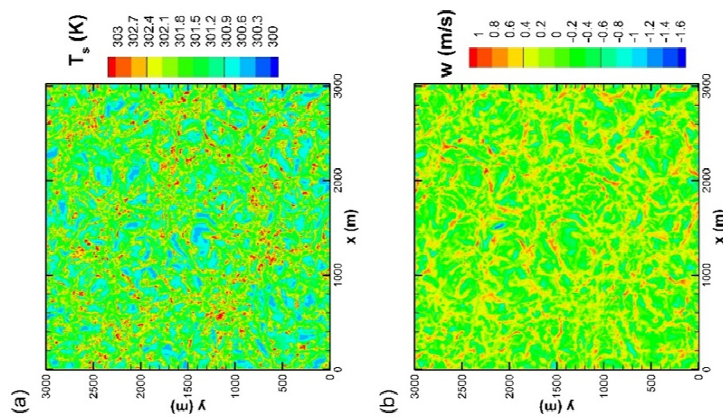
(Page 105) Figure 2 – Mosaicks of temperature Mosaics in Rubi at 12am (a) and 6am (b), temperature gradient (c) and of emissivity at 9.6 μm (red), 8.6 μm (green) and 8.2 (blue) (d).



(Page 106) Figure 3 – Examples of industrial estates belonging to low (up), medium (centre), and high (bottom) temperature gradient classes.

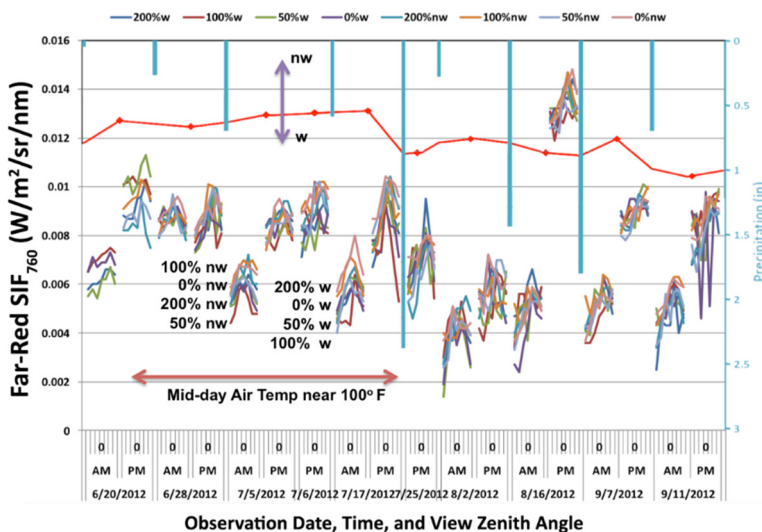


(Page 107) Figure 4 – Example of industrial facility cover in Rubi. RGB image from PCA is used to detect homogeneous areas and create a mask to estimate spatially-averaged 32-band emissivity profiles accounting for different materials.



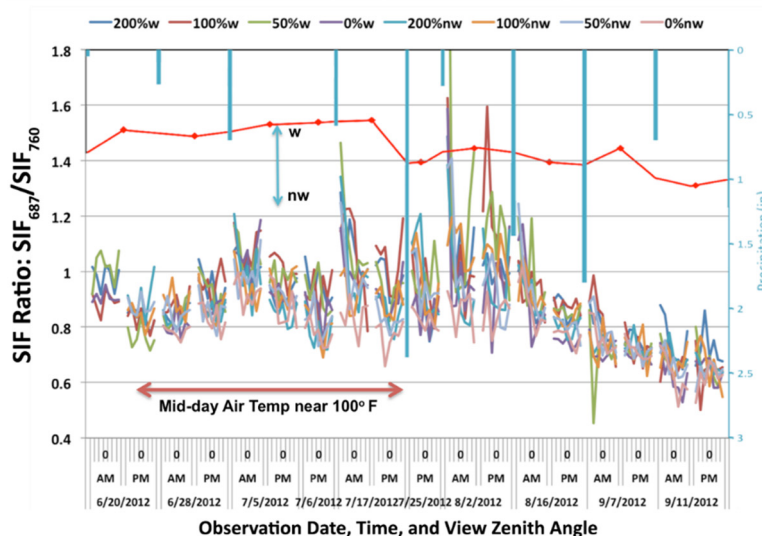
(Page 136)

Figure 3. Snapshot of the tree top surface temperature T_s (a) and vertical wind velocity w at canopy top (b) as simulated by the LES model over a Maritime pine stand under convective condition.



(Page 147)

Figure 2. The bidirectional emission distribution functions for the far-red SIF retrieved for SIF_{760} are shown for the data matching the PRI (Fig. 1). As with the PRI, significant anisotropy is apparent in the bidirectional emission for SIF_{760} . Note that the bidirectional emissions have inverted bowl shapes for almost all of the measurement sets, but that the highest SIF is emitted by the non-watered treatment groups whereas the least stressed groups had lower SIF. However, there was considerable overlap of the bidirectional emission and no consistent gradient from most to least SIF values. SIF_{760} is lower in mornings than in afternoons, but afternoon SIF_{760} is similar throughout the growing season.



(Page 148)

Figure 3. The bidirectional emission distribution functions for the Red/Far-Red SIF Ratio (SIF_{687}/SIF_{760}) are shown as in Figs. 1 and 2. These curves exhibit overlapping and variable shapes across the SPP, so that the anisotropy is suppressed relative to that expressed by SIF_{760} . However, this ratio exhibits perturbations after rain events before stability is achieved. Within each measurement set, the highest values are typically associated with healthiest watered treatment groups. A general decline in the SIF_{687}/SIF_{760} ratio indicates a similar reduction in canopy photosynthetic efficiency.

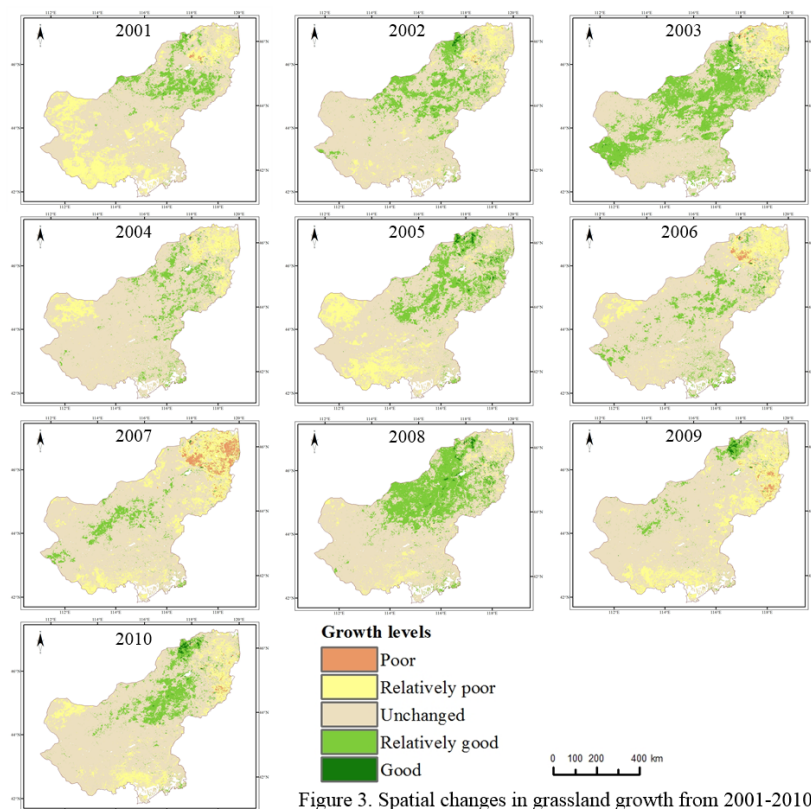
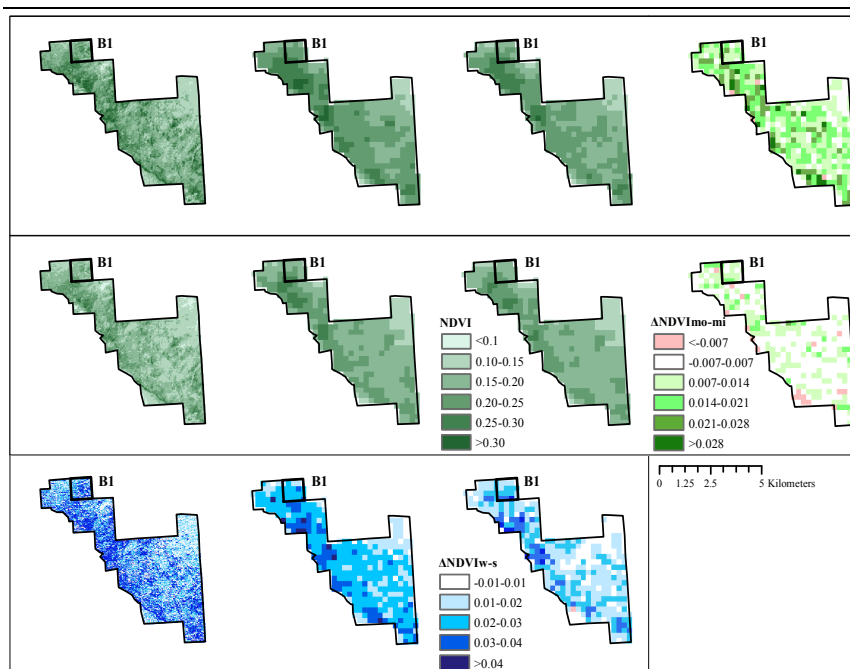
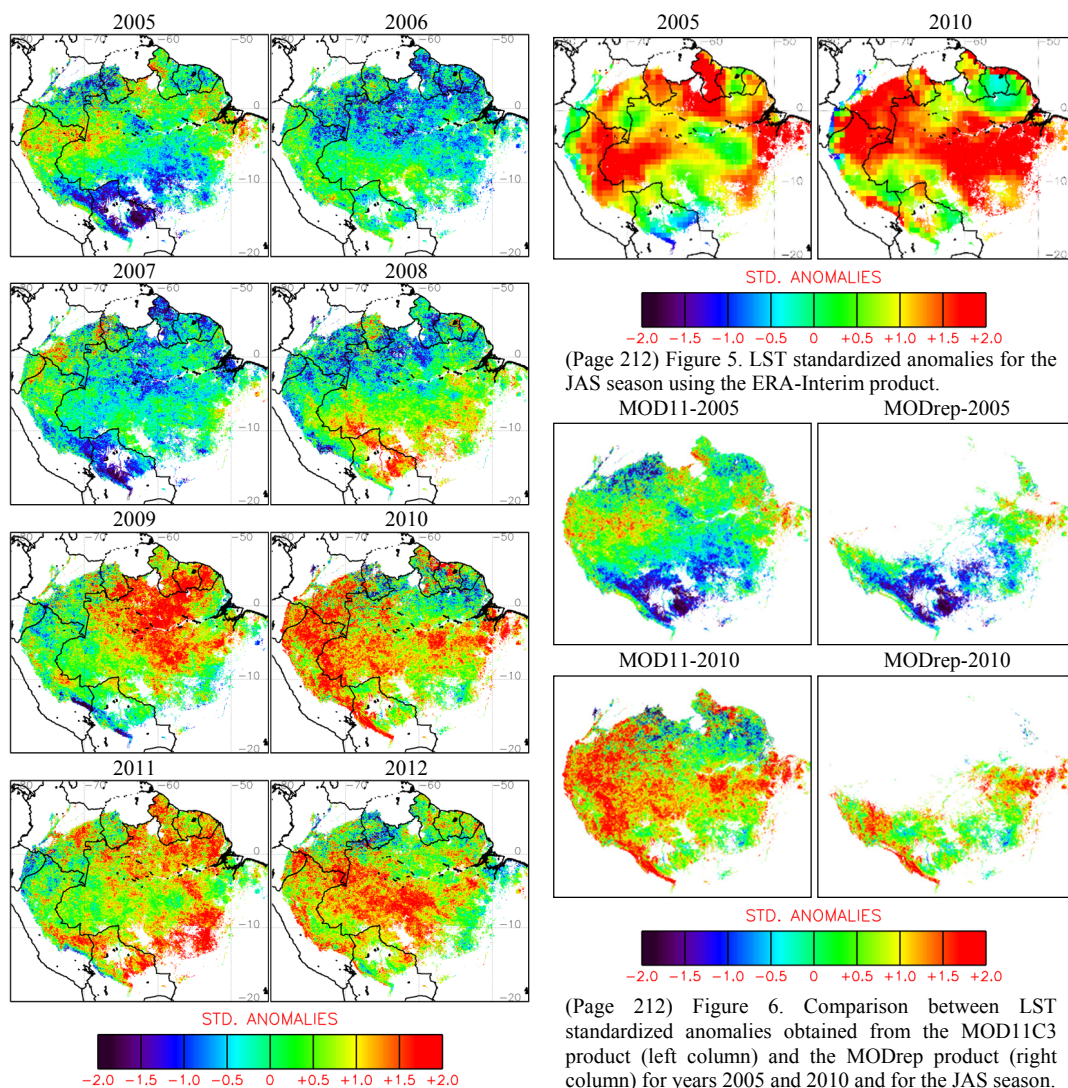


Figure 3. Spatial changes in grassland growth from 2001-2010

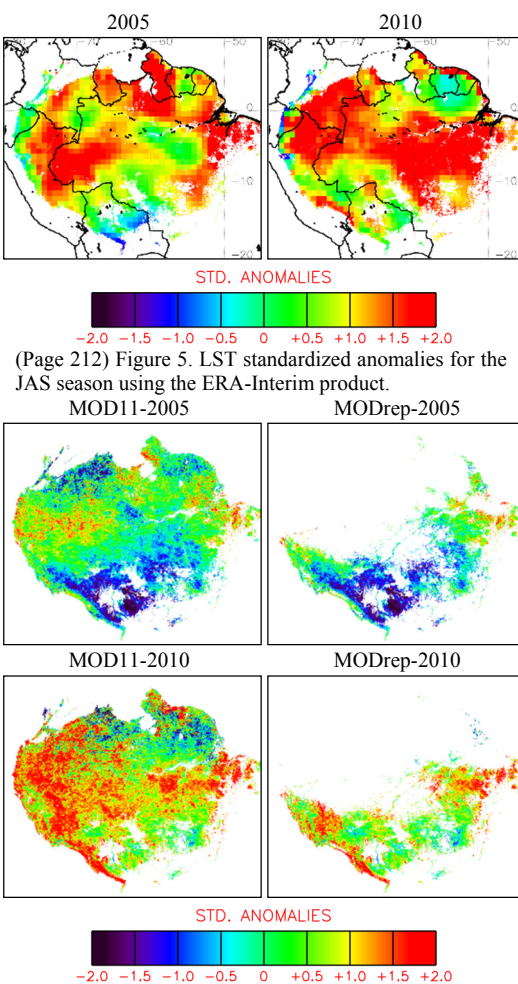
(Page 189)
Figure 3.
Spatial changes in
grassland growth from
2001-2010



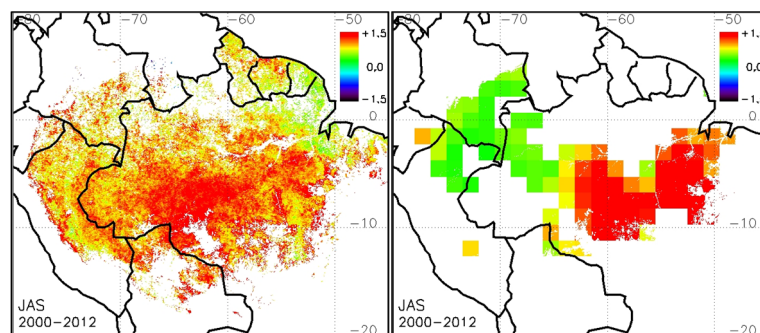
(Page 194)
Figure 11: NDVI values
at pixel level of all
Bellavista plantation
stands in the winter of
2007 (first row), the
summer of 2006-2007
(second row), and the
 ΔNDVI_{w-s} of 2007 (third
row) obtained from
Landsat images (first
column), MODIS-Terra
images (second column),
and MODIS-Aqua
images (third column).
The fourth column
corresponds to the
 $\Delta\text{NDVI}_{mo-mi}$ in winter
(first row) and summer
(second row) based on
Terra (morning) and
Aqua (midday).



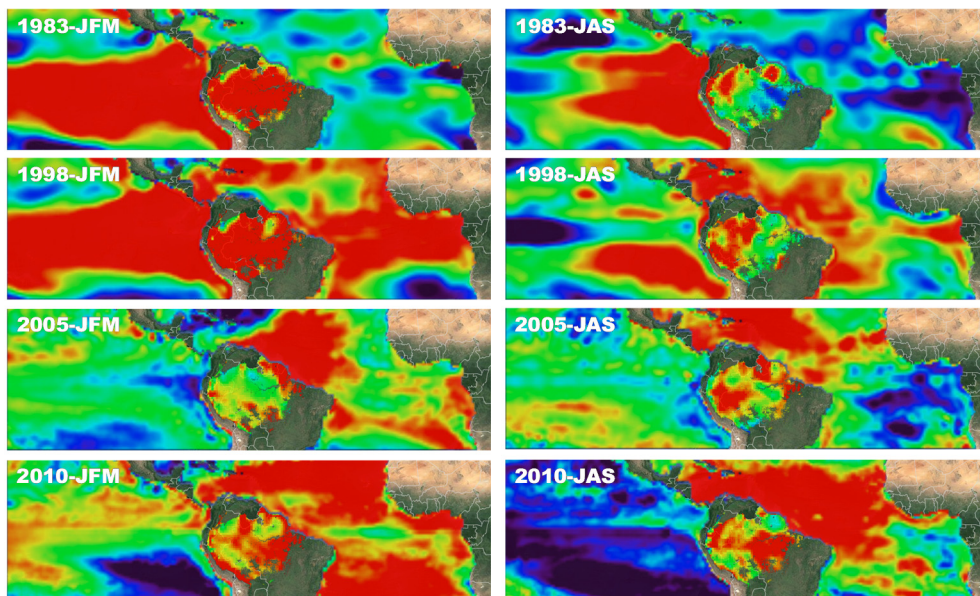
(Page 211) Figure 4. LST standardized anomalies for the JAS season using the MODIS product MOD11C3.



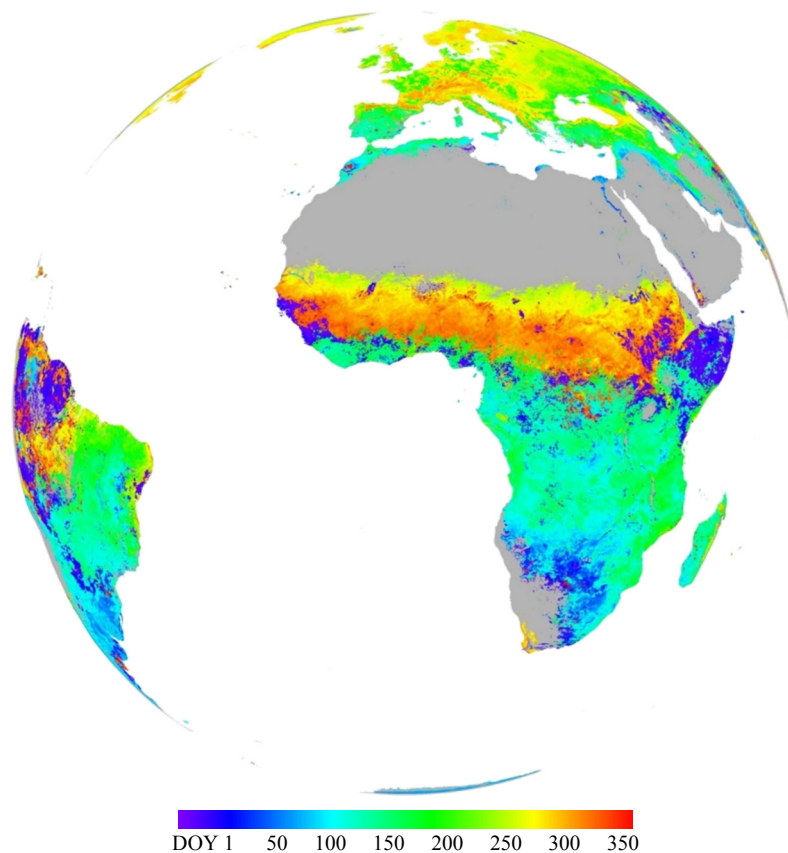
(Page 212) Figure 6. Comparison between LST standardized anomalies obtained from the MOD11C3 product (left column) and the MODrep product (right column) for years 2005 and 2010 and for the JAS season.



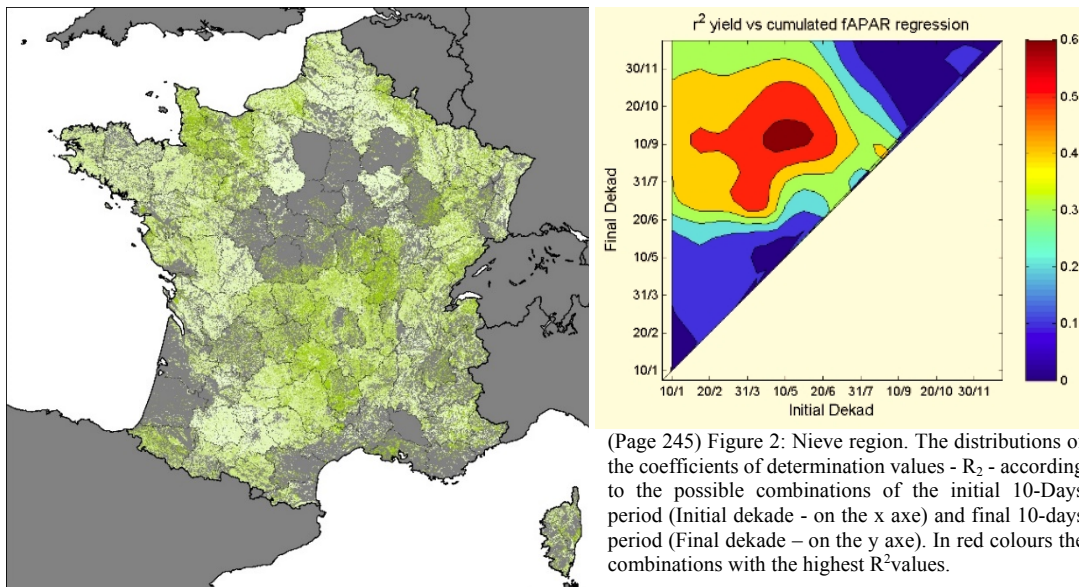
(Page 212) Figure 7. Trends (°C/decade) in LST anomalies for the JAS season and the period 2000-2012 using MODIS product (top) and ERA-Interim reanalysis (bottom). Only pixels with $p < 0.05$ are displayed.



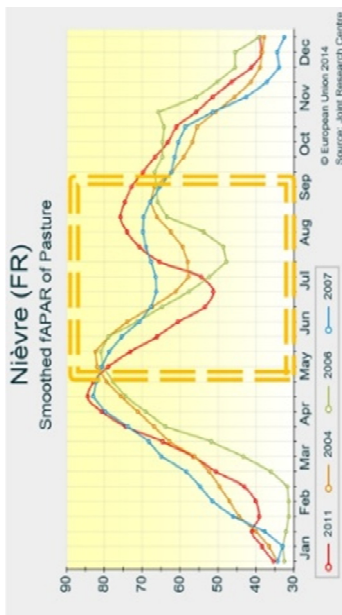
(Page 213) Figure 9. Sea and Land Surface Temperature anomalies for different seasons (JFM and JAS) and different years (1983, 1998: El Niño events; 2005, 2010: severe droughts over Amazonia). Pictures extracted from Thermal Amazonia Viewer.



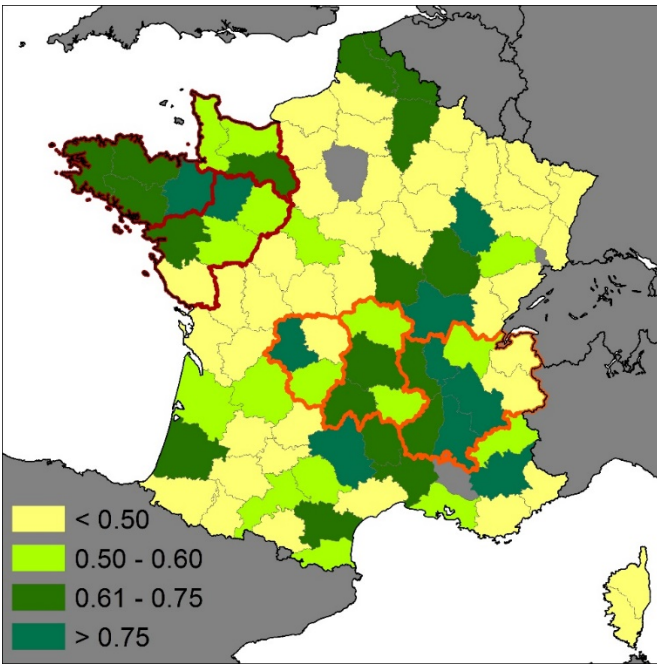
(Page 224) Figure 4. End Of Season (EOS) dates for year 2013 as retrieved from MSG-SEVIRI NDVI time series.



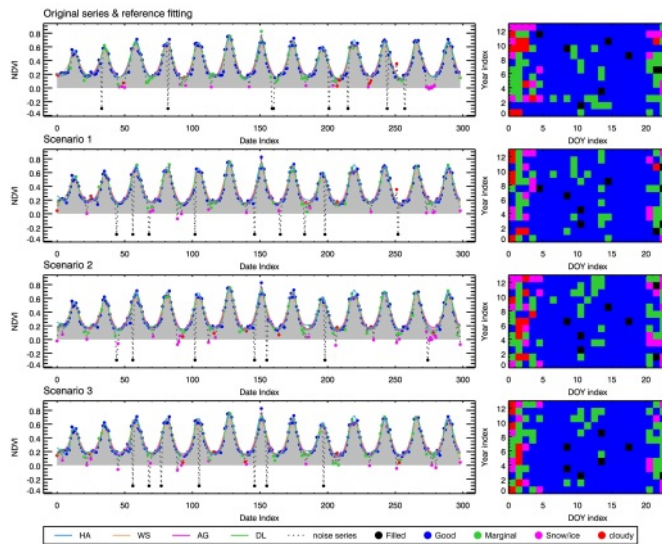
(Page 244) Figure 1: the distribution of pasture areas according to the CAPRI definitions of GRAE and GRAI.



(Page 245) Figure 3: Nièvre region. Example of optimal windows and its overlap to several time fAPAR seasons profiles. The window corresponds to the highest R^2 values as visible in Figure 2

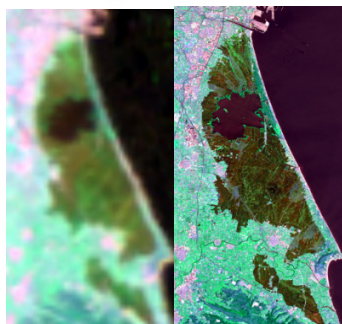
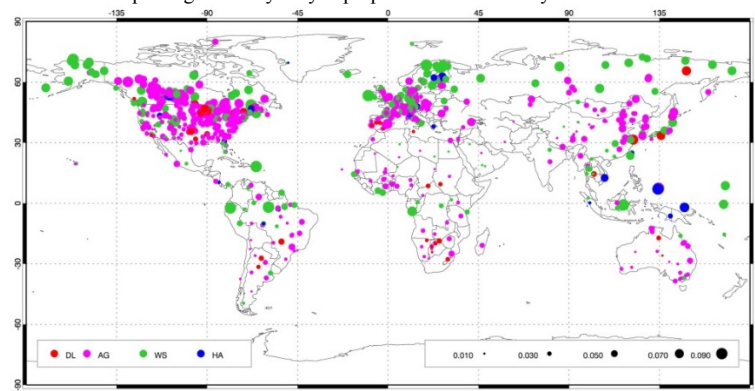


(Page 247) Figure 5: Geographical distribution of the R^2 across the France territory. The R^2 are divided into four ranges with decreasing values as displayed in the legend. In red and orange are marked the group of regions that were analyzed in §3.3.

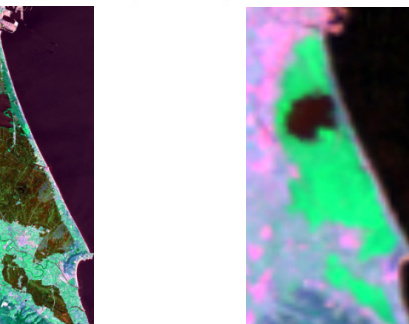


fn_cnduocrp | Duolun_cropland | 42.0456N, 116.6714E

(Page 252) Fig. 3 The reference series and three scenarios for simulated noisy series and their reconstruction results by different candidate reconstruction methods. Left panel gives the yearly superposition of reliability information

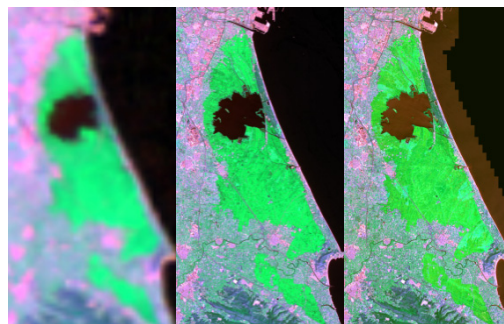


(a)



(b)

(Page 285) Figure 4. The base pair ($M(t_0)$, $L(t_0)$) used to predict surface reflectance for each $M(t_k)$. (a) MODIS composite from May, 25 – June, 10th; (b) Landsat 8/OLI image on June 4.

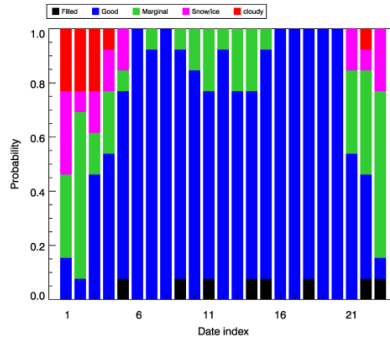


(a)

(b)

(c)

(Page 286) Figure 5. Results of data fusion in a case with significant temporal change: using June 3th as a base date to predict reflectance on September 1st. (a) The MODIS composite of August 21-September 6, 2014; (b) the predictions using STRUM. (b) a reference (unused) Landsat image on September 1st. All images are displayed with the band combination R:Red, G:NIR, B: SWIR.

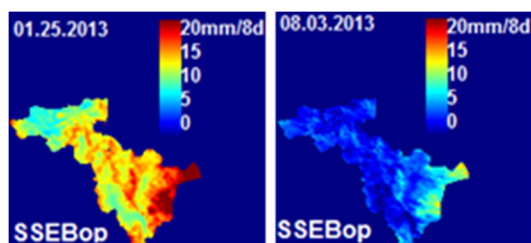


(Page 252)

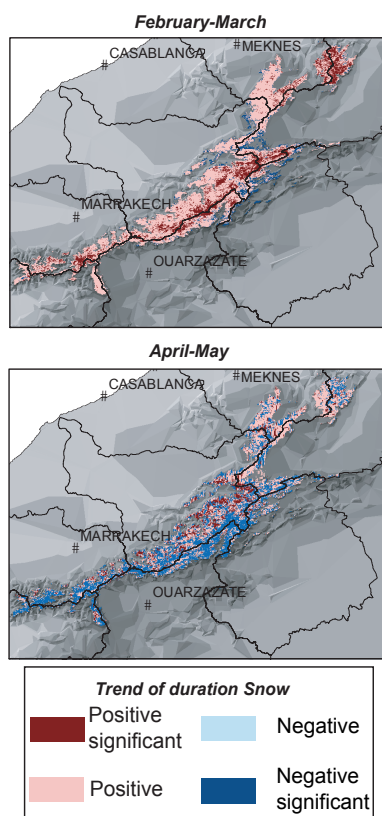
Fig.4. The probability distribution of the quality of NDVI observations from Duolun_cropland site. For each composition day, we assume the quality for different level follow multinomial distribution, with which random noisy series scenarios are simulated.

(Page 253) Fig.5.

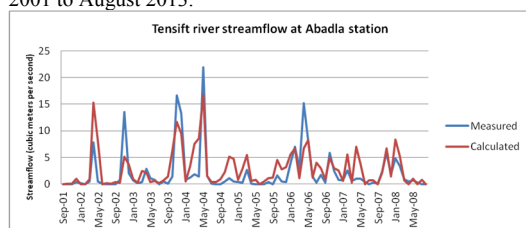
The Evaluation results for 1211 MODIS subset field sites. Coloured circles indicate the optimal reconstruction method for different sites. The smallest reconstruction error among all candidate methods is presented by different size of circles.



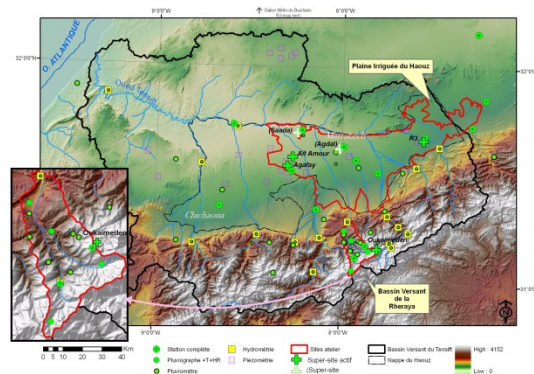
(Page) Figure 3. Evapotranspiration at dry (25-Jan-2013) and wet (03-Aug-2013) edges over the study area.



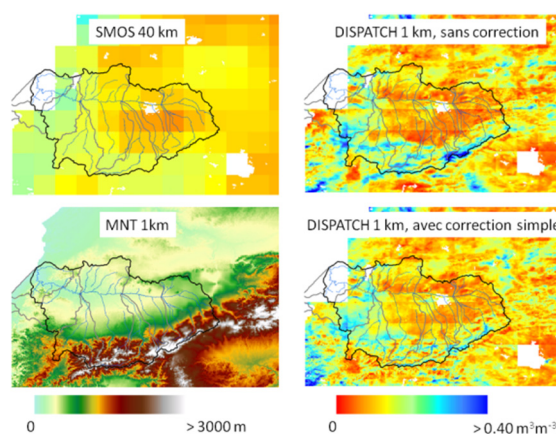
(Page) Figure 4 : Trend of snow cover duration (SCD) for February-March (up) and April-May (down) from September 2001 to August 2013.



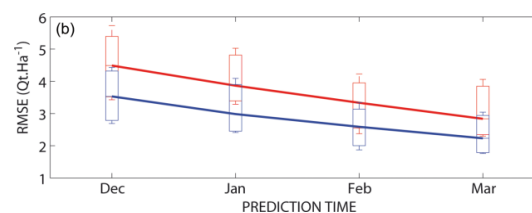
(Page) Figure 6 : Measured and predicted streamflow of the SAMIR-WEAP-MODFLOW tool at the plain outlet (Abadla station) without calibration.



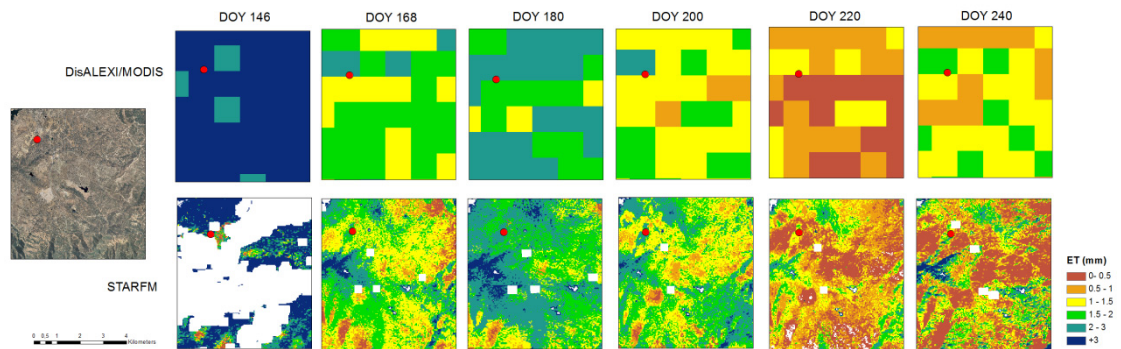
(Page) Figure 2 : Experimental design of the TENSIFT observatory.



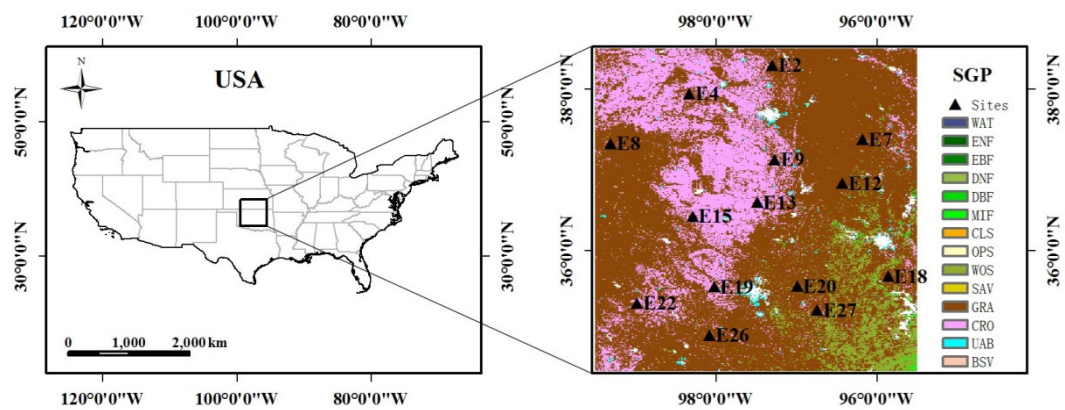
(Page) Figure 3 : disaggregated soil moisture : SMOS at full resolution, disaggregated product at 1 kms with and without temperature correction, MNT.



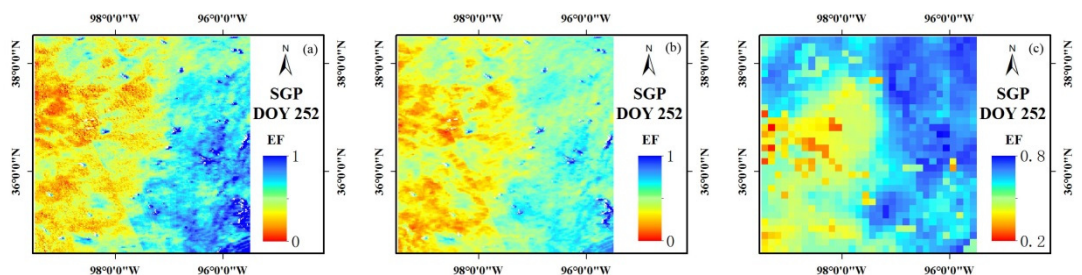
(Page) Figure 5: Evolution of rmse between predicted cereal grain yields and province statistics for the 11 most productive province in Morocco as a function of prediction time from December to March (about 2 months before harvest) ; (red) Multi-linear regression ; (blue) Support Vector Machine



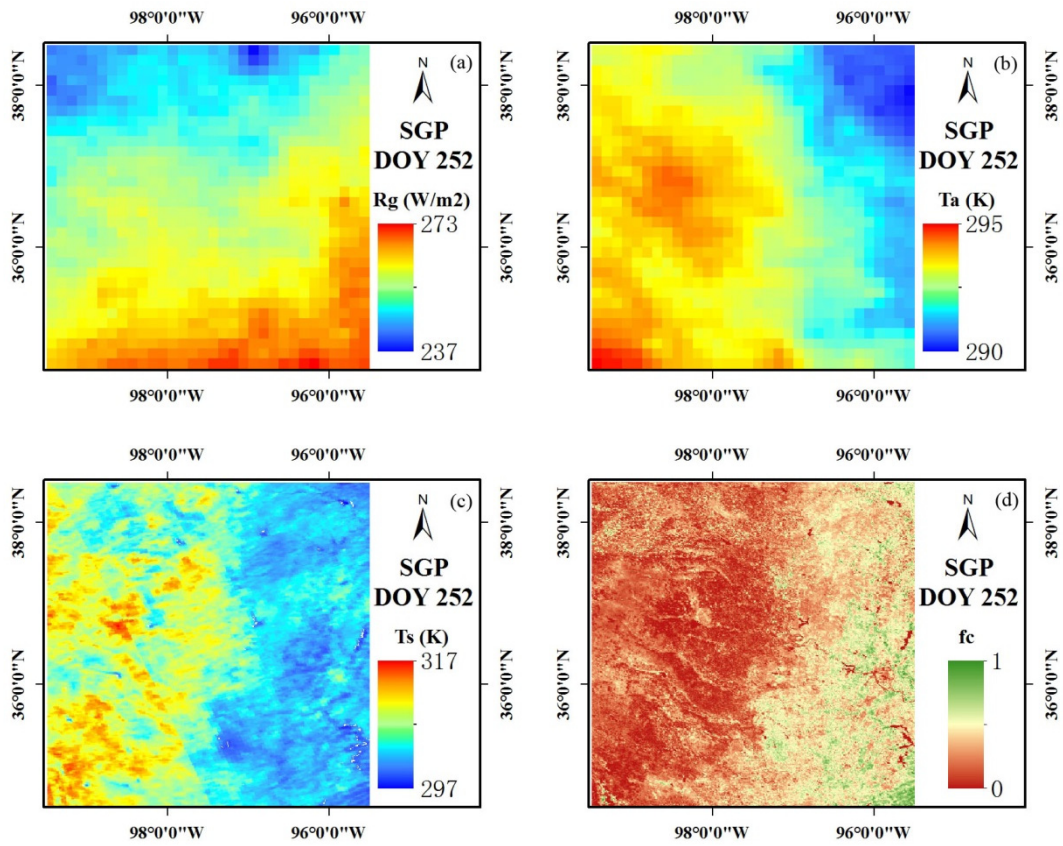
(Page 314) Figure 4. Maps of spatial distribution of daytime-integrated ET (mm) on different days between DOY 141-240



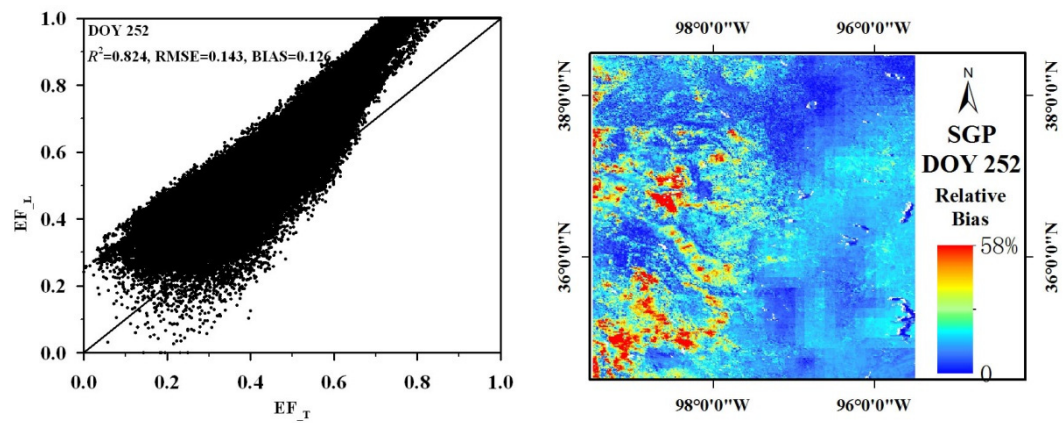
(Page 323) Fig. 1. The location of the Southern Great Plains and the distribution of Energy Balance Bowen Ratio sites



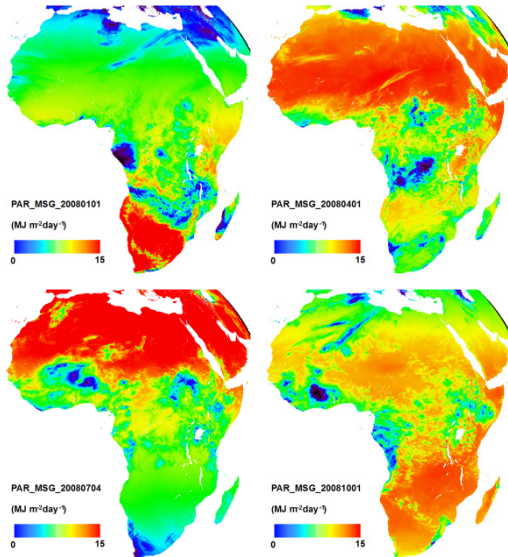
(Page 324) Fig. 2. The EF distribution over the Southern Great Plains from (a) the EF_L method, (b) the EF_T method, and (c) NLDAS-2



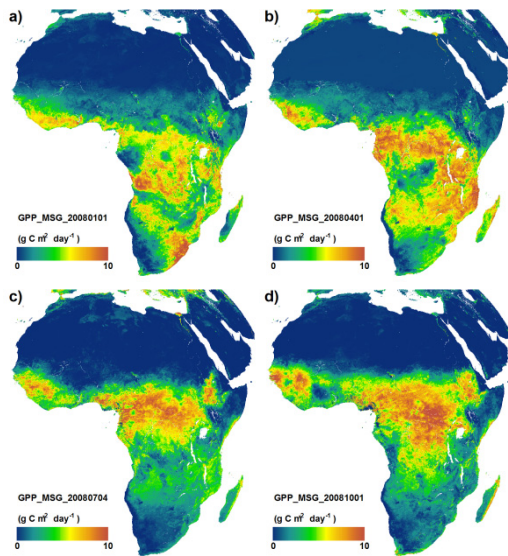
(Page 324) Fig. 3. Spatial distribution of (a) R_g , (b) T_a , (c) T_s , and (d) f_c over the SGP region



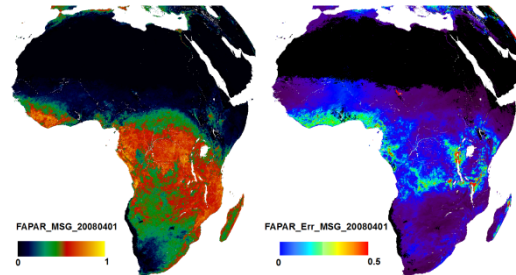
(Page 325) Fig. 4 (a) Comparisons of EF estimates between the EF_L and EF_T methods and (b) the spatial distribution of their absolute relative bias



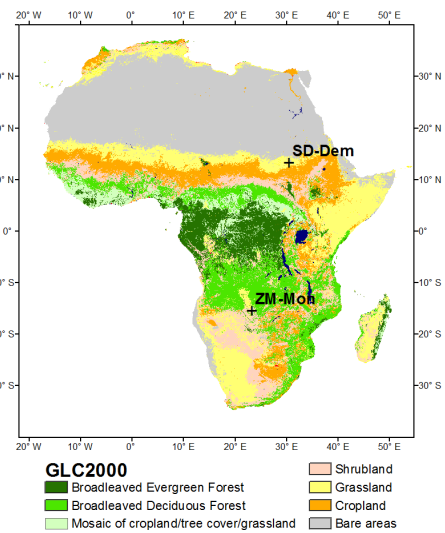
(Page 328) Figure 1. PAR derived from the daily downwelling surface shortwave radiation flux (DIDSSF) product for four dates.



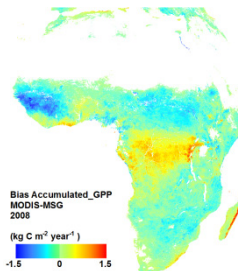
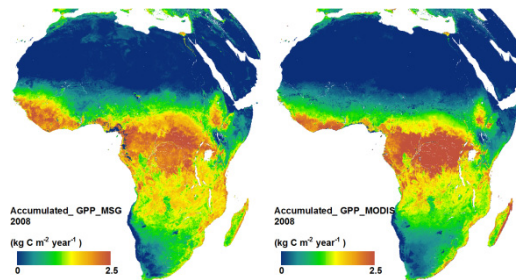
(Page 330) Figure 5. Daily GPP derived from MSG data for four dates along the 2008.



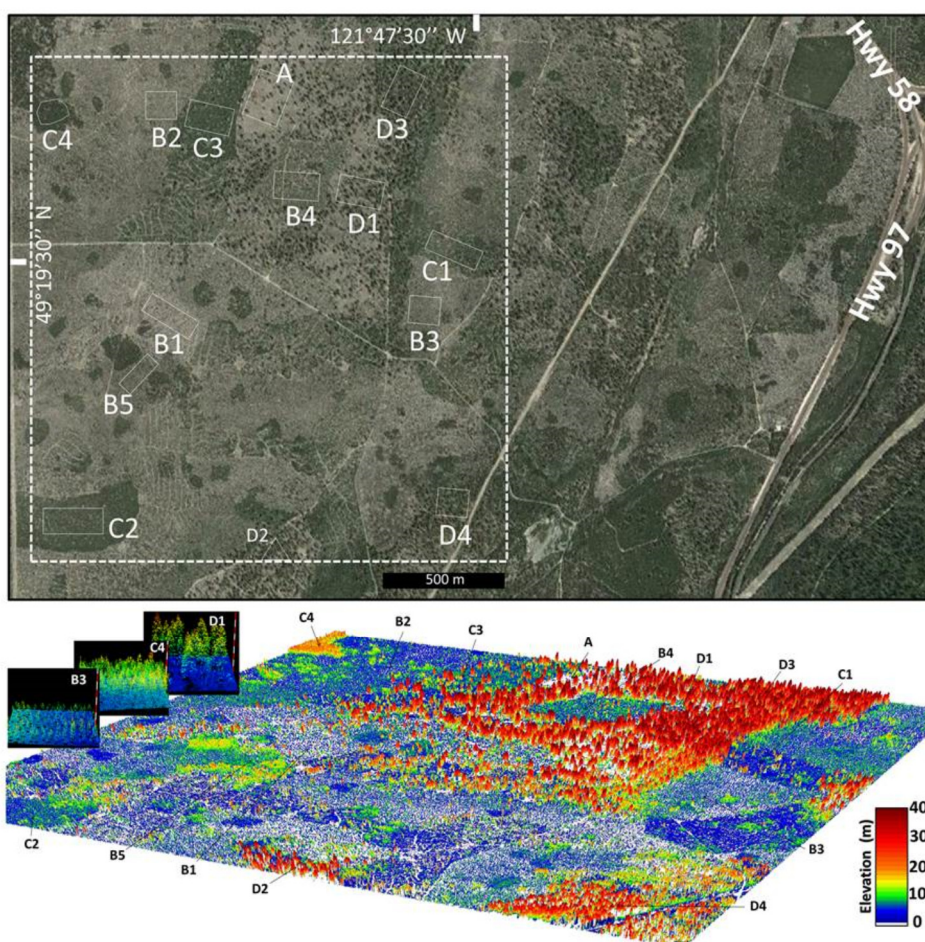
(Page 328) Figure 3. f_{APAR} filtered (left) product with its error (right) for April 1st, 2008.



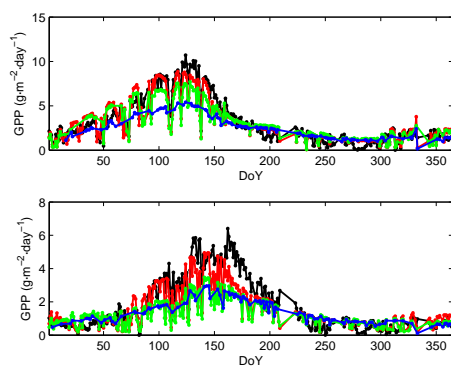
(Page 329) Figure 4. Distribution of 6 major biomes in Africa derived from the 23-class Global land cover 2000 (GLC2000). Locations of the two EC flux towers considered.



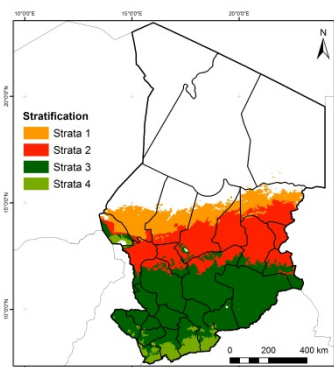
(Page 331) Figure 8. Annual MSG and MODIS GPP for 2008 (top) and bias between accumulated MODIS and MSG (bottom).



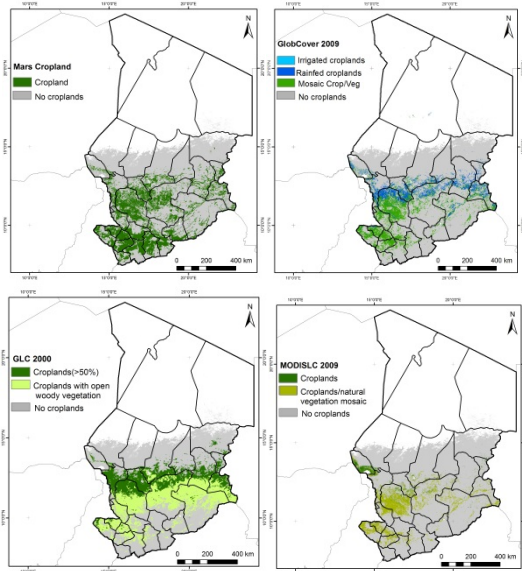
(Page 363) Figure 3. Google Earth image of the study site (top) and a 1 m/pixel canopy surface model (bottom) for the 4×4 km area boxed in white. Insets are point-cloud rendering of the LiDAR data used for the surface model. The different classes of forest stands are marked in both images.



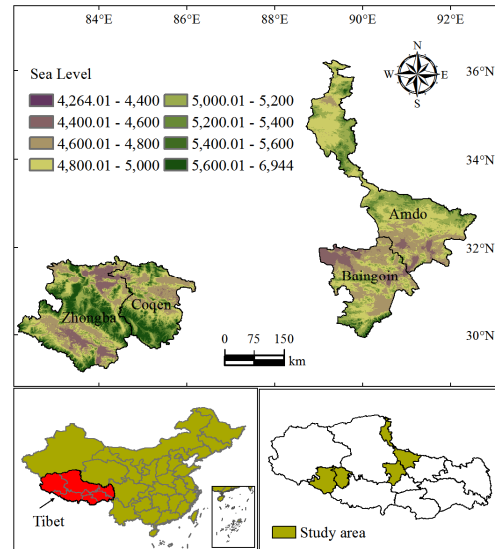
(Page 342) Figure 7. Temporal variation for the year 2011 of GPP estimated EC data (black), and calculated by equation (1) with $\epsilon(W) = C_{ws}^1$ (red), $\epsilon(W) = C_{ws}^2$ (green), and $\epsilon(W) = C_{ws}^3$ (blue). Top: Las Majadas del Tiétar. Bottom: Cortes de Pallás.



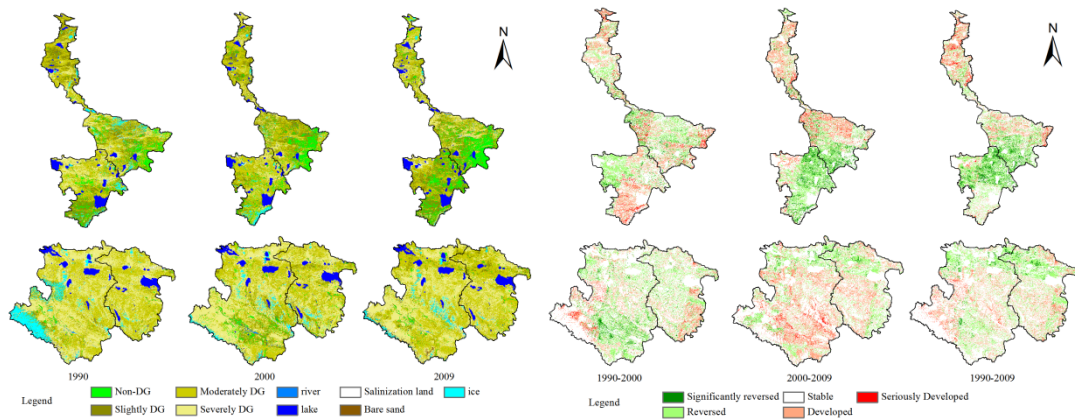
(Page 368) Figure 3. Stratification of Chad based on MODIS dataset.



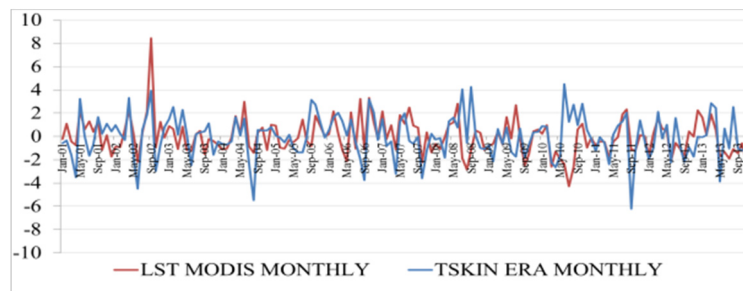
(Page 368) Figure 4. Top-left) Crop mask compared to top-right) GlobCover, bottom-left) GLC2000 and bottom-right) MODIS Land Cover.



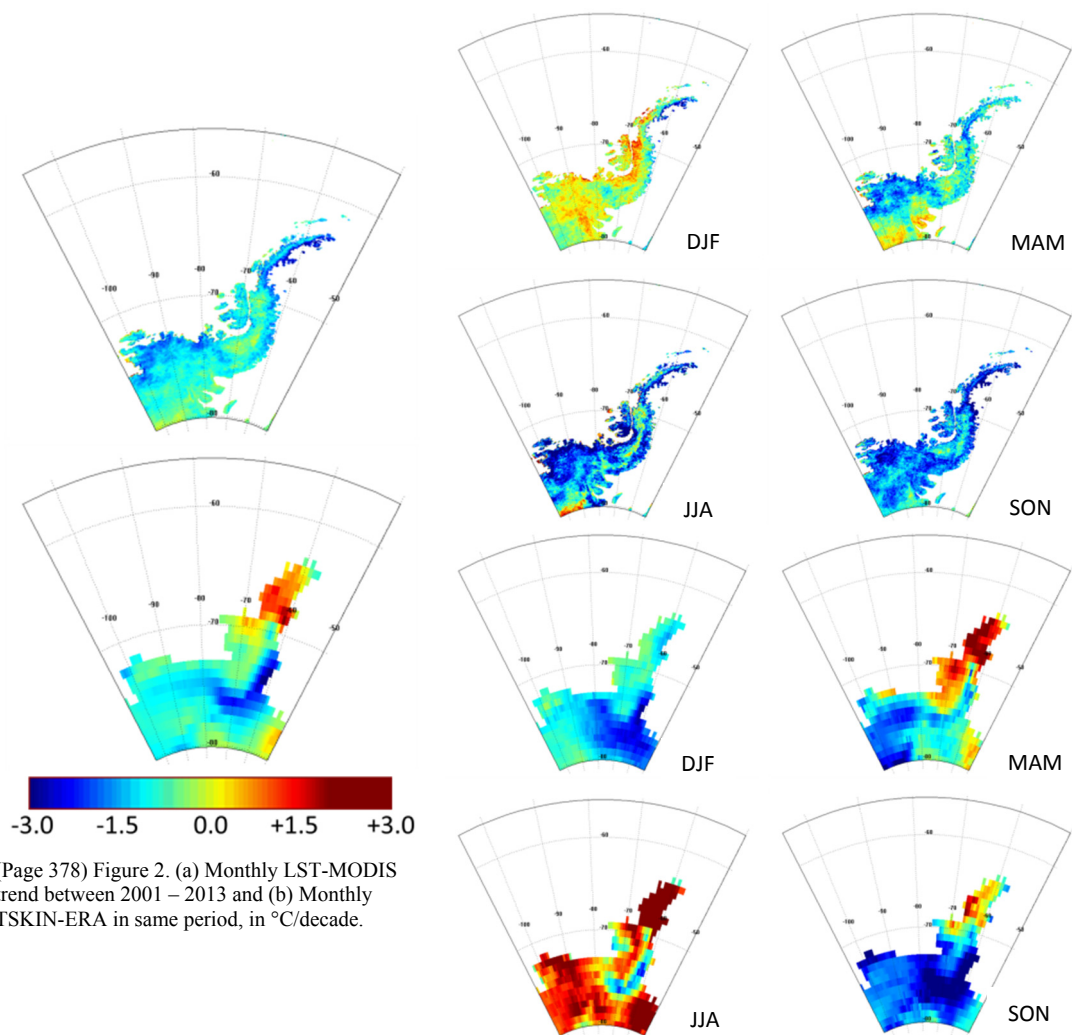
(Page 371) Fig.1 Location of Study Area



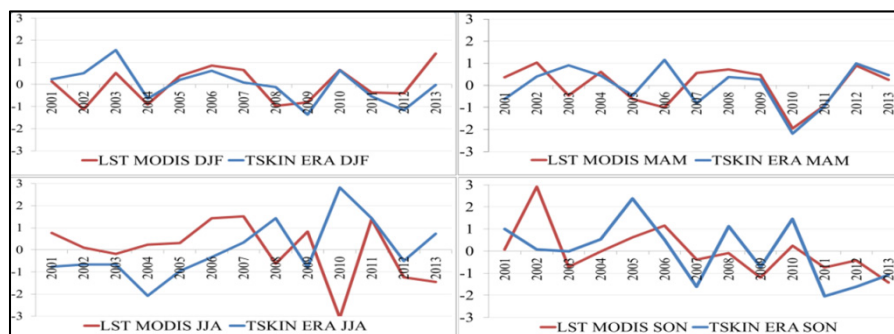
(Page 373) Fig. 2 Chart of Soil Coverage Type Change, such as (Page 374) Fig. 3 Dynamic Change Chart of the Grassland Tibetan Grassland Desertification

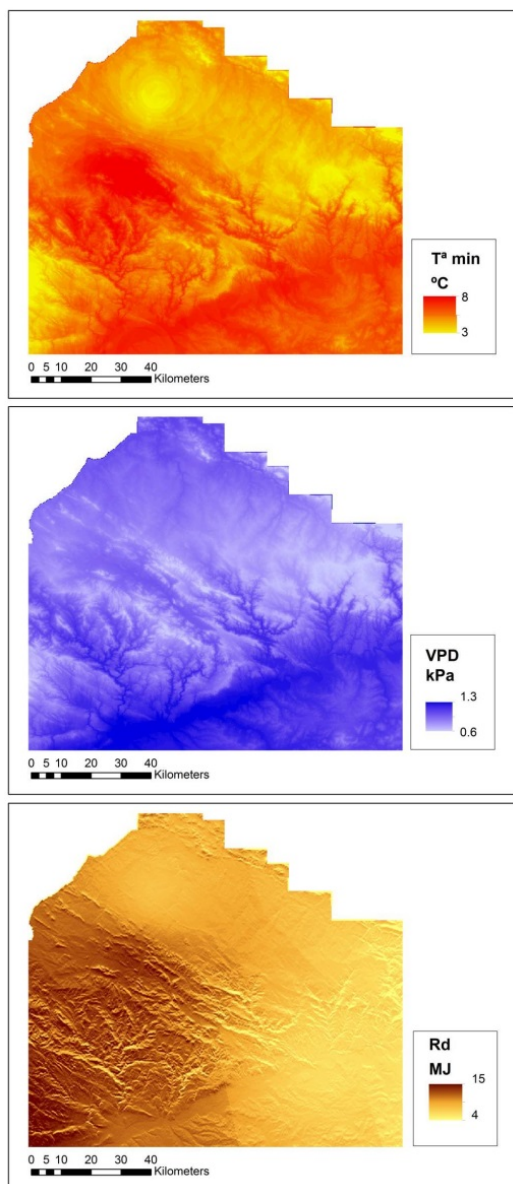


(Page 378) Figure 3. Monthly anomalies (°C) of LST-MODIS (red line) and TSKIN-ERA anomalies (blue line) between 2001 and 2013.

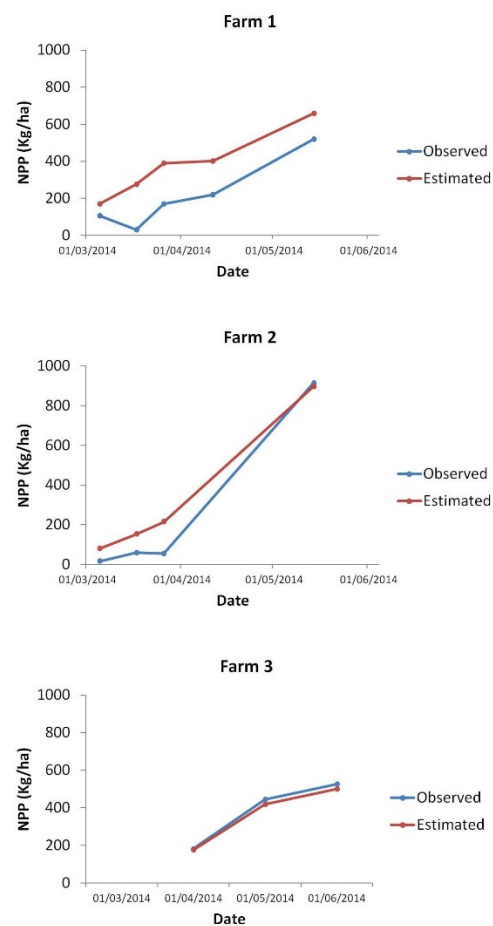


(Page 378) Figure 4. Seasonal LST-MODIS trend (in a) and Seasonal TSKIN-ERA (in b) between 2001 – 2013.

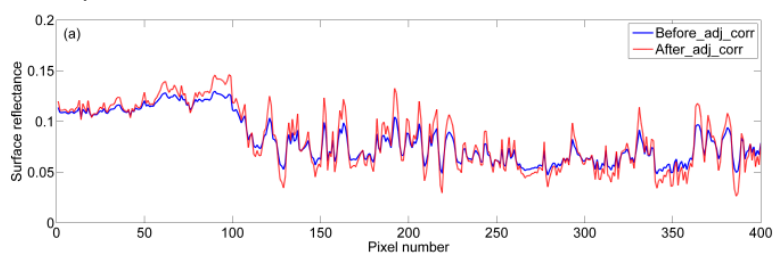




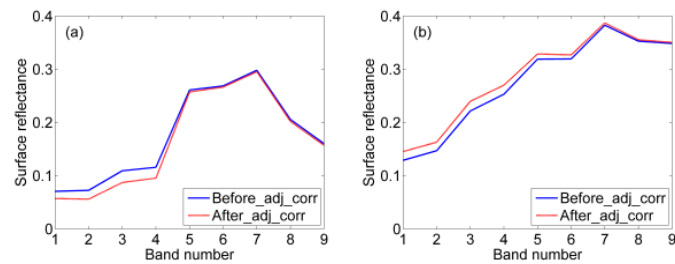
(Page 382) Figure 2. Spatial interpolation of Rd, Tmin and VPD for the 28th of February, 2014.



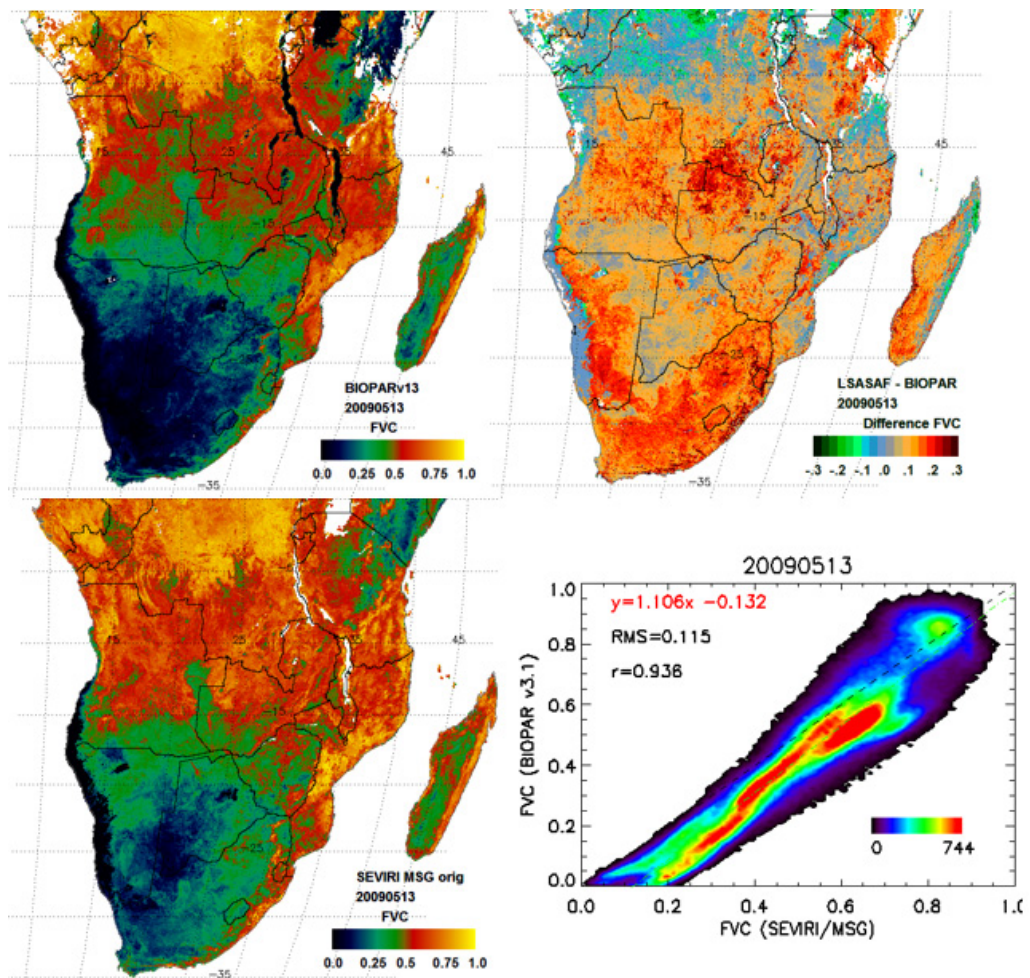
(Page 383) Figure 5. Temporal evolution of observed and estimated NPP in the three validation farms.



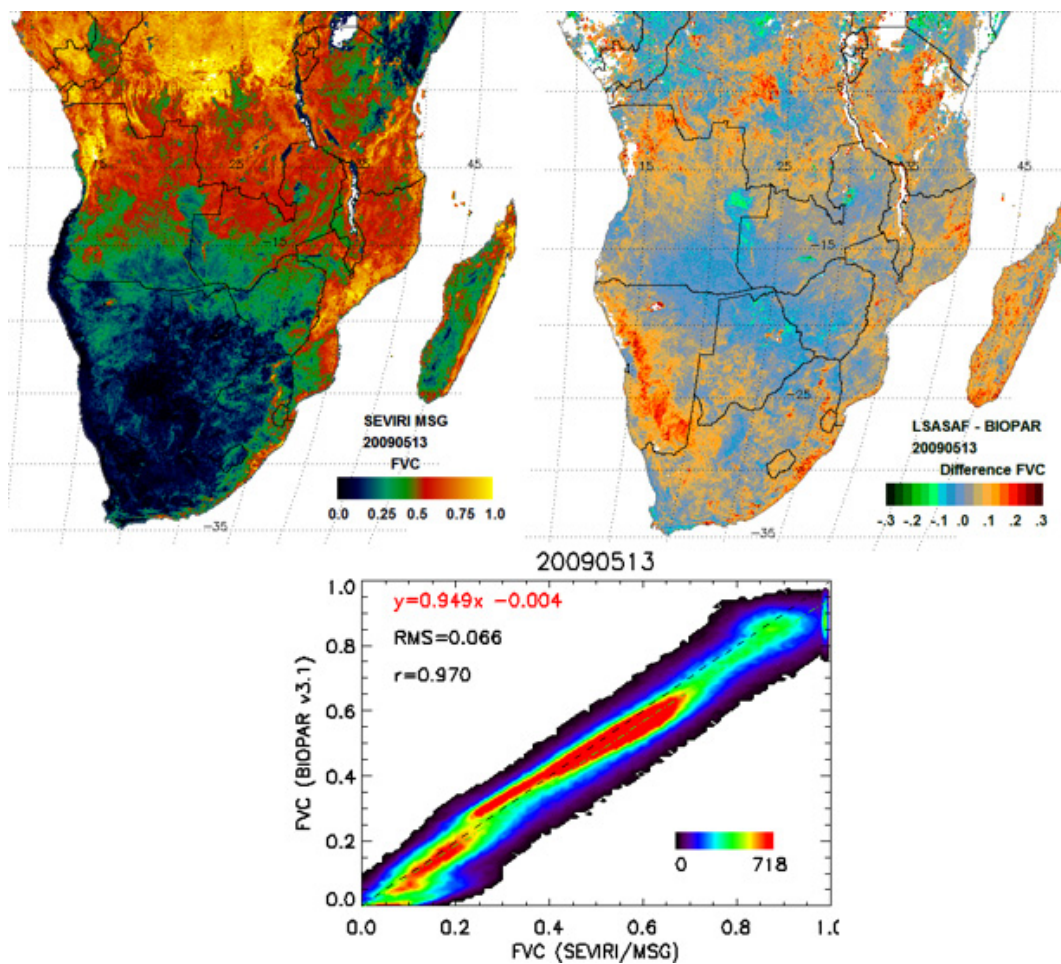
(Page 393) Figure 5. Surface reflectance profiles before and after the adjacency effects were corrected for ALI band 1p (443 nm).



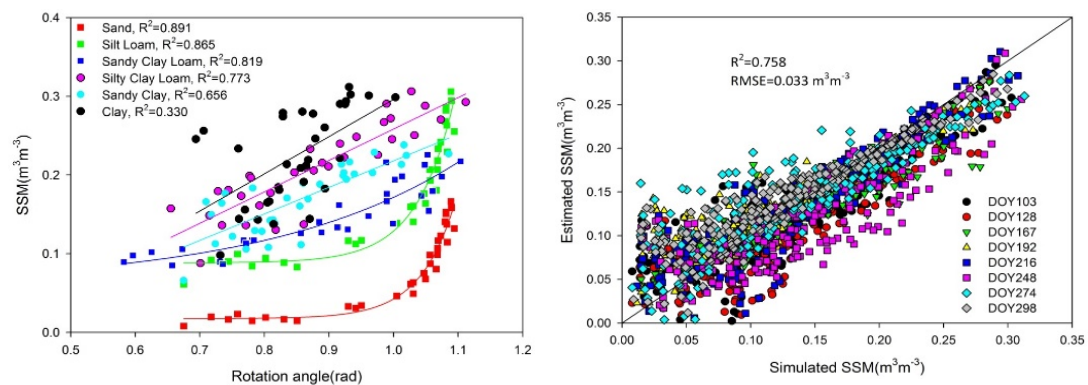
(Page 394) Figure 6. A comparison of the surface reflectance before and after the adjacency effects were corrected over (a) vegetated and (b) bare soil pixels.



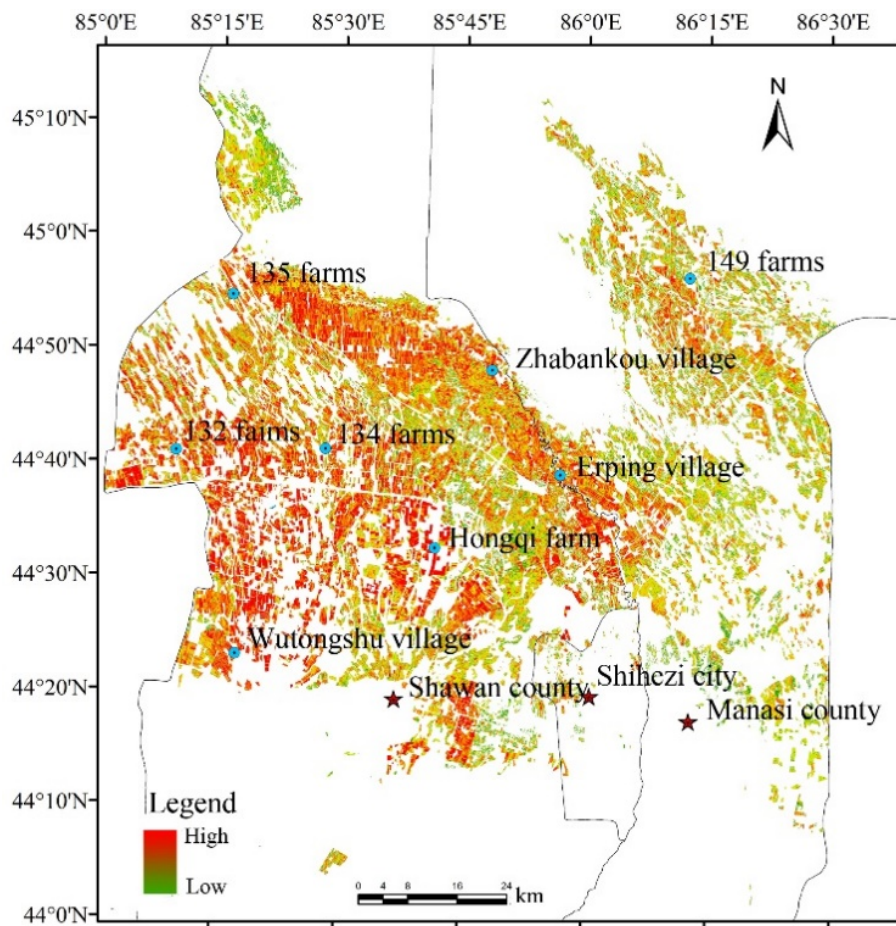
(Page 428) Figure 2. Comparison (image maps, difference and scatterplot) between SEVIRI FVC (currently available in LSA SAF) and Copernicus Global Land (VGT, GEOV1), products on mid May, 2013.



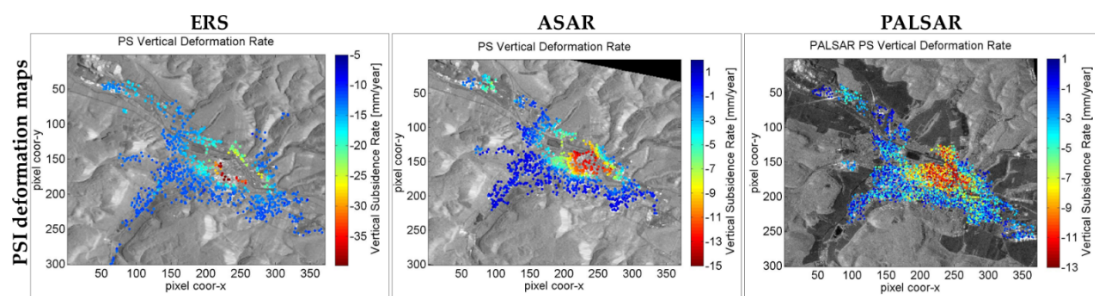
(Page 429) Figure 3. Comparison (image maps, difference and scatterplot) between SEVIRI FVC (resulted from the new LSA SAF algorithm) and Copernicus Global Land (VGT, GEOV1), products on mid May, 2013.



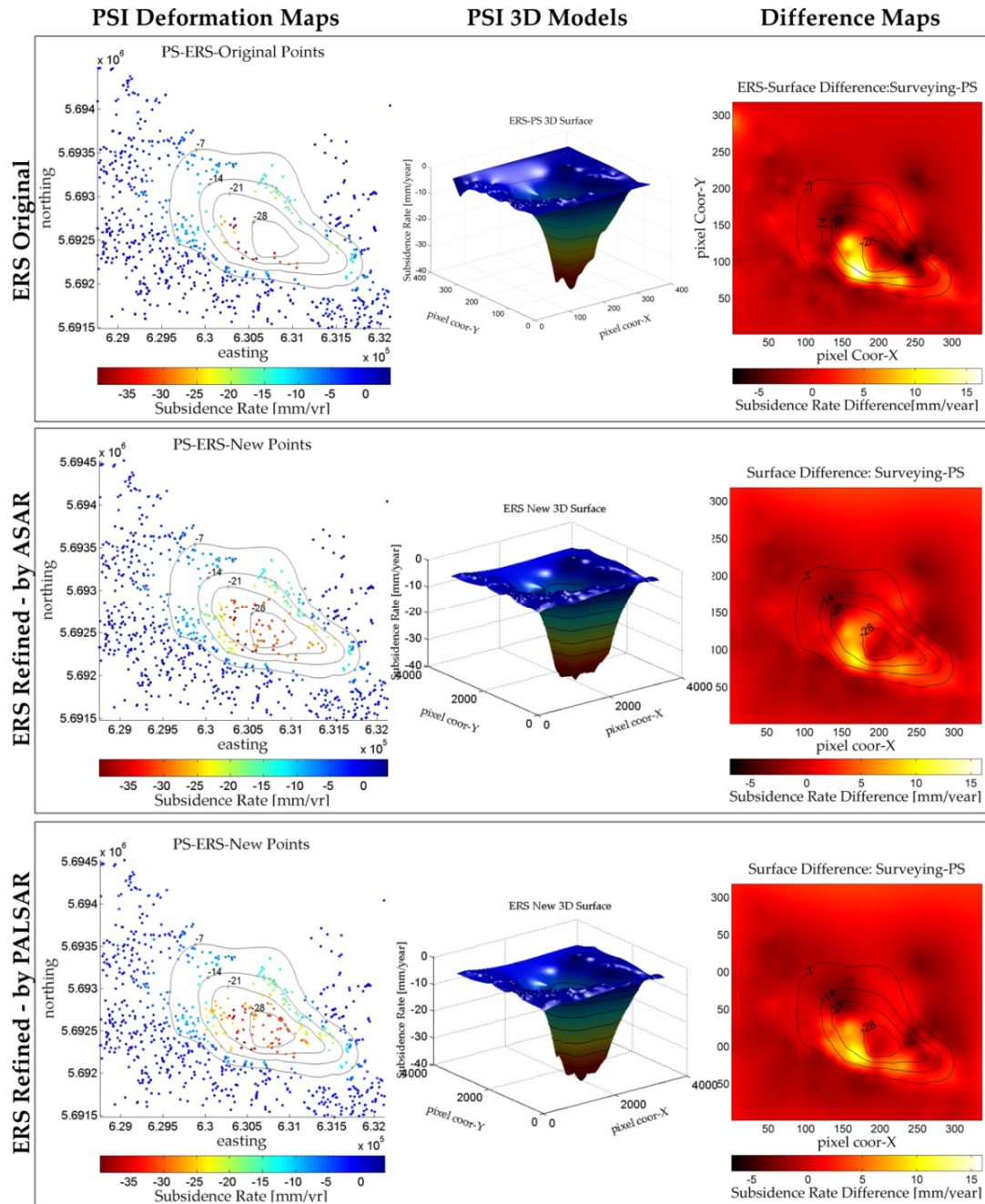
(Page 439) Figure 4. Relationships between SSMs and rotation (Page 440) Figure 6. Comparison of the estimated SSM versus the simulated values on the eight cloud-free days in 2001 at Bondville site.



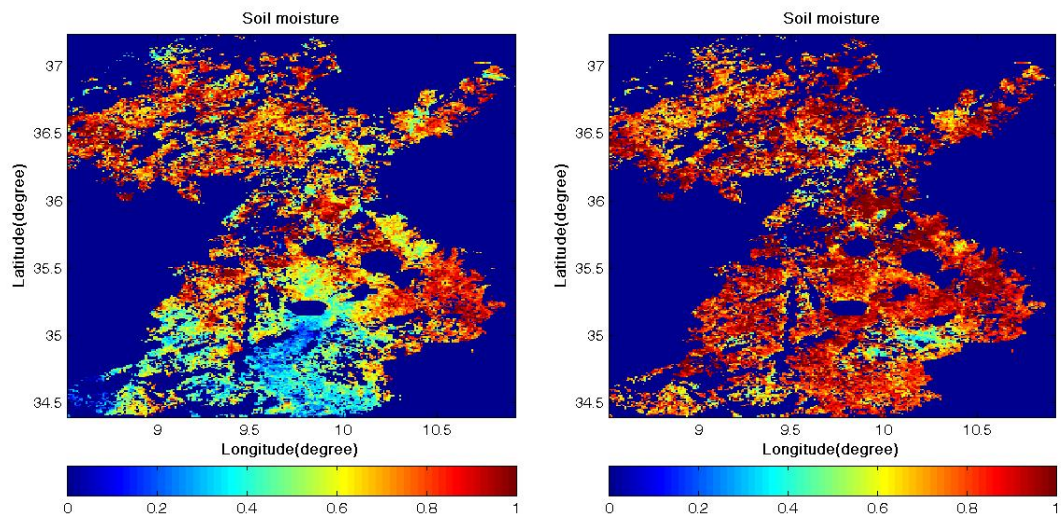
(Page 486) Figure 6. The spatial pattern of inversion of soil salinity in the cotton field



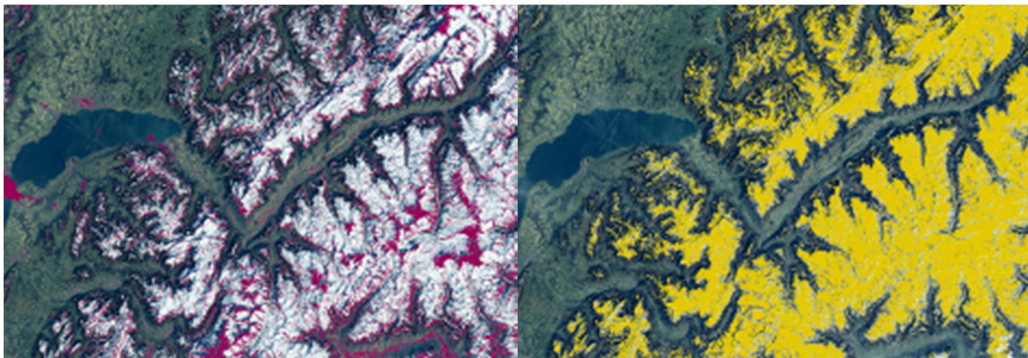
(Page 515) Figure 2: PSI deformation maps of ERS (1995-2005), ASAR (2004-2010) and PALSAR (2007-2010) stacks.



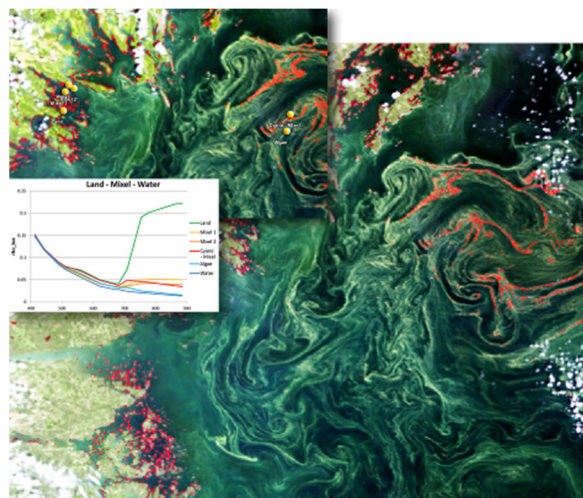
(Page 516) Figure 3: Results of integration. In the first column of figures the PSI deformation maps (with the contours stemming from the surfaces derived from the surveying measurements) are presented. The figures in the second column are the geometric models derived from the corresponding PSI maps. The third column represents the difference maps generated by the subtraction of the PSI based surface from the surveying based surface.



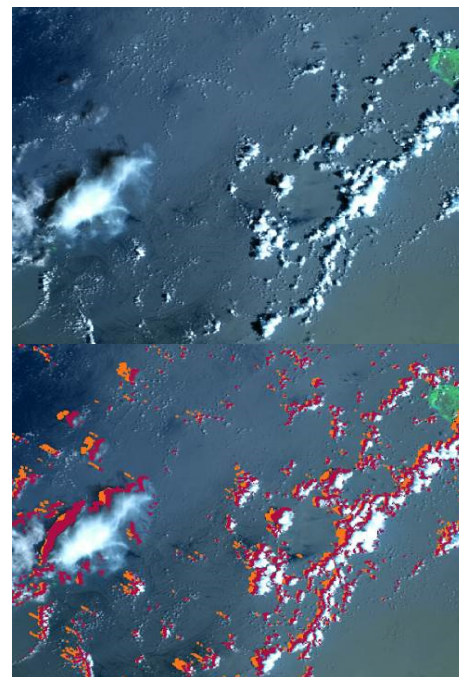
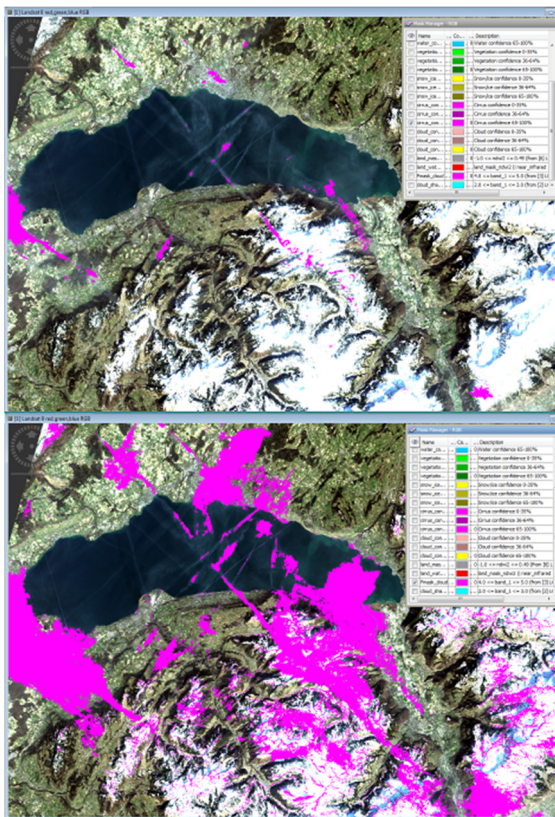
(Page 527) Figure 4: Soil moisture index maps determined for different two dates.



(Page 530) Figure 8. Landsat 8 -20 March 2014 lake Geneva- distinction snow-cirrus clouds still a challenge



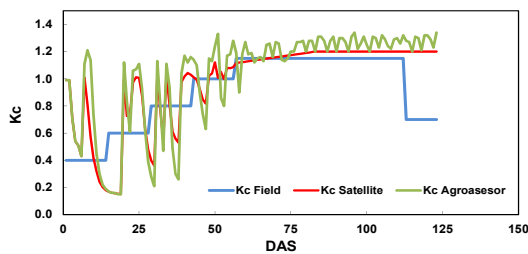
(Page 530) Figure 9. Baltic Sea MERIS scene with a cyanobacteria bloom and the mixed pixel identification flag in red



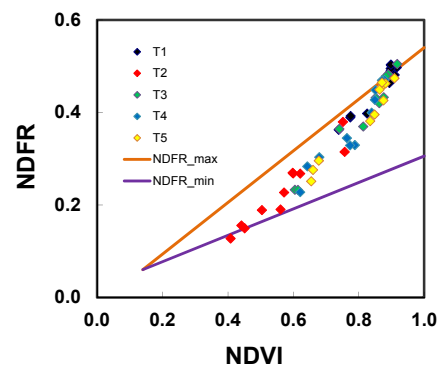
(Page 531) Figure 11. Original L8 mask versus Idepix approach

(Page 531) Figure 10.RGB and Cloud shadow mask (red IdePix cloud shadow versus new algorithm)-MERIS-FSG 24. September 2011 16:31:44

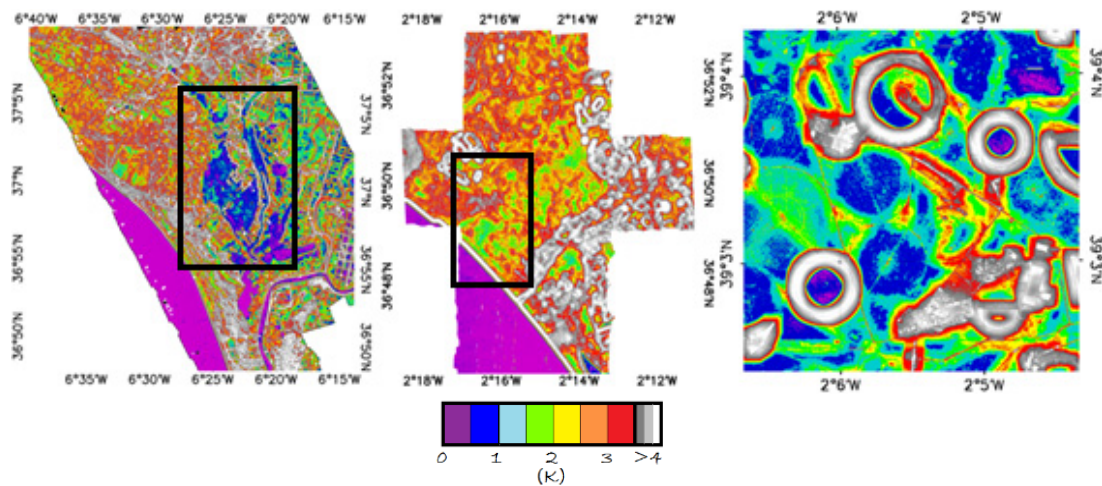
(Page 531) Figure 12. Spatial distribution of PixBox sampling for MODIS (60 000 points).



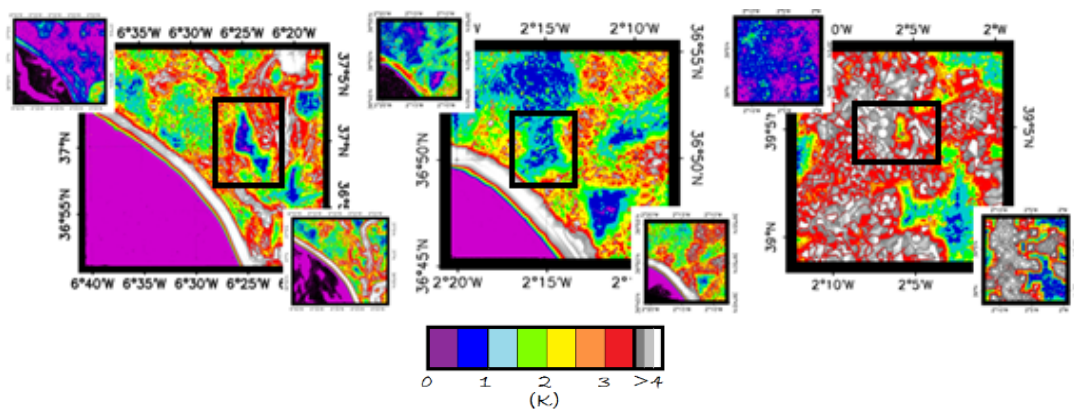
DAS=Days after sowing
(Page 534) Figure 3: Evolution of the single crop coefficient of a corn field in 2013.



(Page 535) Figure 5: Relationship between NDVI and NDFR for the wheat experiment conducted in Córdoba. T1= 225; T2=0; T3=180; T4=90; T5=135 [kgN/ha]



(Page 541) Figure 3. From left to right: Doñana, Cabo de Gata and Barrax RMSE retrieved for a high-medium resolution EOS with AHS sensor.



(Page 541) Figure 4. From left to right: Doñana, Cabo de Gata and Barrax RMSE retrieved for a low resolution EOS with TIR sensor. Central figure for each test site represents the mean RMSE along the year; Top left figure represents the mean winter RMSE and Right bottom figure represents the mean summer RMSE.

